BOOK OF ABSTRACTS


16MCM
04–09 September 2022
Brno, Czech Republic
TESCAN
WARMLY WELCOMES YOU
AT BOOTH #2
Image taken by Stefan Diller with TESCAN MIRA 3 electron microscope

16th Multinational
Congress on Microscopy

16MCM

04–09 September 2022

Brno, Czech Republic

#16MCM

BOOK OF ABSTRACTS

Editors:
Vladislav Krzyžánek, Kamila Hrubanová, Pavel Hozák, Ilona Müllerová,
and Miroslav Šlouf

Publishers:
Czechoslovak Microscopy Society

ISBN 978-80-11-02253-2

ThermoFisher SCIENTIFIC

The world leader in serving science

We supply innovative solutions for electron microscopy and microanalysis to take customers from questions to usable data by combining high-resolution imaging with physical, elemental, chemical, and electrical analysis across scales and modes—through the broadest sample types.

Please visit our booth to learn about our exciting new innovations!

Learn more at **thermofisher.com/em**

thermo scientific

Content

Plenary Lectures 1

Instrumentation and Methods (IM) 11

IM1: Multi-dimensional image processing: Facing the data interpretation challenge 11

IM2: Multi-modal and correlative microscopy 28

IM3: Diffraction-based techniques and spectroscopy in electron microscopy 73

IM4: Advances in electron optics and beam shaping for electron microscopy 106

IM5: Cryogenic, in situ and environmental electron microscopy 120

IM6: Low energy electrons related science and technology 154

IM7: Advances in sample preparation techniques for material and life sciences 169

Life Sciences (LS) 194

LS1: Electron microscopy in health, diagnostics, nanomaterials and regenerative medicine 194

LS2: Microscopy for healthier environment: Microorganisms, plants, and Host-Pathogen Interactions 212

LS3: Structural studies from macromolecules to tissues 233

LS4: Advances in fluorescence and super-resolution microscopy 261

LS5: Advances in probes and sample preparation in microscopy 281

LS6: Multi-parametric and functional imaging in life sciences 290

LS7: Advances in volume electron microscopy and image processing 306

Material Science (MS) 322

MS1: Metals, alloys and intermetallics 322

MS2: Ceramics, rocks and minerals 369

MS3: Polymers, biomaterials and soft materials 382

MS4: 2D-materials, thin films, coatings, surfaces and interfaces 407

MS5: 1D-materials (nanowires, nanotubes, nanorods etc.), nanoparticles and nanostructures 452

MS6: Materials for energy related applications 485

MS7: Micro- and nanomechanical characterization of materials 507

Index of Authors 540

From nano to macro in femtoseconds.

ZEISS Crossbeam laser

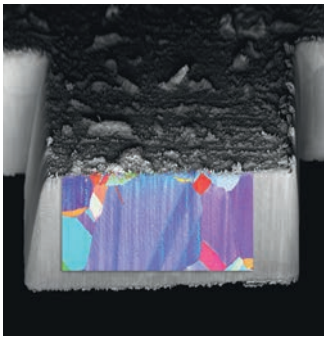

The LaserFIB enhances your *in situ* studies. Gain rapid access to deeply buried structures, if needed guided by X-ray microscopy data in a multi-modal setup. Prepare cross-sections up to mm in width and depth for EBSD within minutes. Machine meso-scale large structures for mechanical tests. Minimize sample damage and avoid contamination of your FIB-SEM chamber as you perform work with the femtosecond laser in a dedicated chamber.

zeiss.com/crossbeam

ZEISS

Seeing beyond

Plenary

Type of presentation: Plenary

Plenary-3051 The electron cryomicroscopy revolution in structural biology

Henderson R.[1]

[1]MRC Laboratory of Molecular Biology, Francis Crick Avenue, Cambridge CB2 0QH

Email of the presenting author: rh15@mrc-lmb.cam.ac.uk

In the last decade, single particle electron cryomicroscopy (cryoEM) has experienced an enormous leap in its capability, due to improved electron microscopes, better detectors and better software, and this has revolutionised structural biology [1,2]. I will show some topical examples, including our recent work [3] on interaction of human erythrocyte catalase with the air-water interface [figure], and discuss how further technical improvements [4] might help to complete the structural biology revolution. There is also a desperate need to expand access to the methodology by developing low-cost cryoEM equipment, so I will also describe some of our efforts in this direction [5,6,7,8].

References:

1. Subramaniam, S., Kühlbrandt, W. & Henderson, R. IUCrJ 3, 3-7 (2016). CryoEM at IUCrJ: a new era.
2. Vinothkumar, K.R. & Henderson, R. Quart. Rev. Biophysics 49, e13, 1-25 (2016). Single particle electron cryomicroscopy: trends, issues and future perspective.
3. Chen, S., Li, J., Vinothkumar, K.R. & Henderson, R. Microscopy 71(S1), i51-i59 (2022). doi.org/10.1093/jmicro/dfab037. Interaction of human erythrocyte catalase with air-water interface in cryoEM.
4. Naydenova, K., Kamegawa, A., Peet, M.J., Henderson, R., Fujiyoshi, Y. & Russo, C.J. Ultramicroscopy 237, 113512 (2022). On the reduction in the effects of radiation damage to two-dimensional crystals of organic and biological molecules at liquid-helium temperature.
5. Peet, M., Henderson, R. & Russo, C.J. Ultramicroscopy 203, 125-131 (2019). The energy dependence of contrast and damage in electron cryomicroscopy of biological molecules.
6. Naydenova, K., McMullan, G., Peet, M.J., Lee, Y., Edwards, P.C., Chen, S., Leahy, E., Scotcher, S., Henderson, R. & Russo, C.J. IUCrJ 6, 1-13 (2019). CryoEM at 100 keV: a demonstration and prospects.
7. Russo, C. & Henderson, R. Microsc.Microanal. DOI: 10.1017/S1431927620022175 (2020) Elements of a Purpose-Built Electron Cryomicroscope for Single-particle cryoEM.
8. El-Gomati, M.M., Wells, T., Zha, X., Sykes, R., Russo, C.J., Henderson, R. & McMullan, G. Journal of Vacuum Science and Technology B39, pp. 062804-1 to 062804-6 (2021). doi: 10.1116/6.0001275. 100 keV vacuum sealed field emission gun for high resolution electron microscopy.

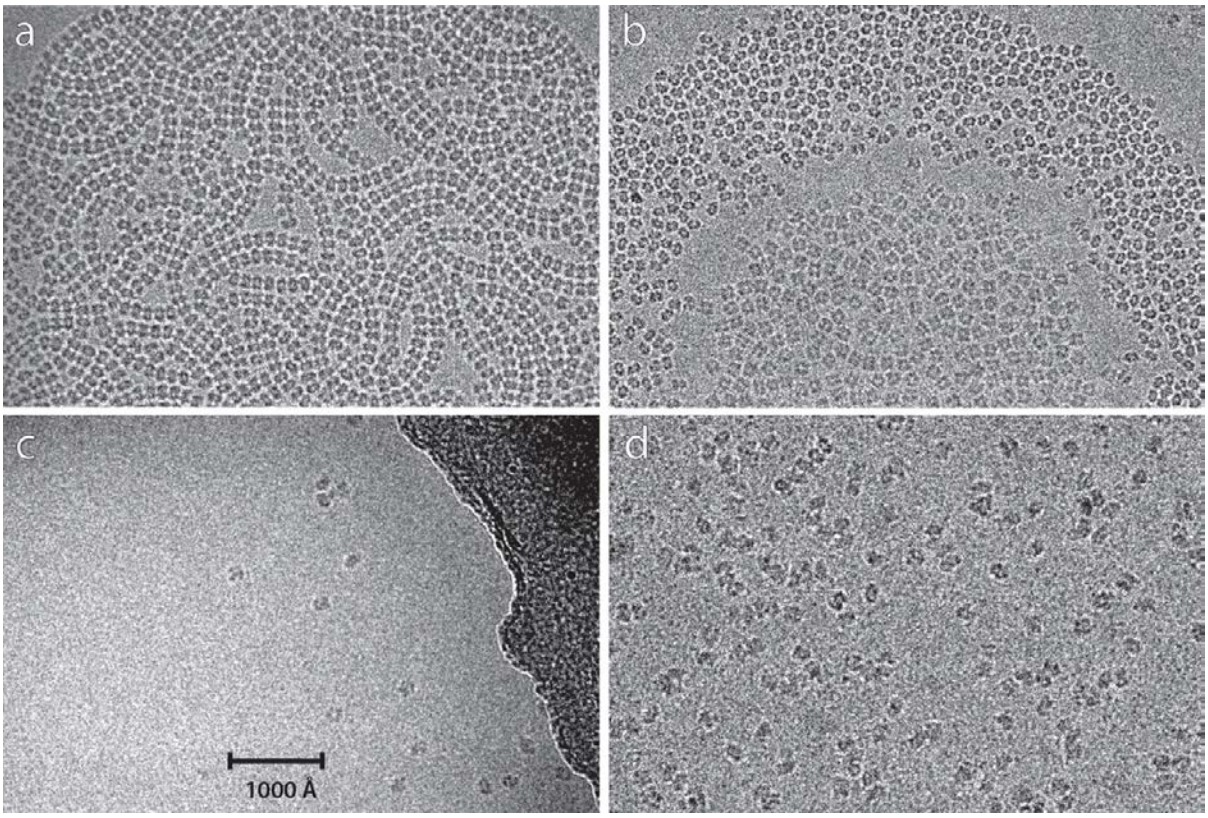

Fig. 1: Behaviour of human erythrocyte catalase at the air-water interface. (a) ribbons of catalase molecules are produced from 0.05 mg/ml catalase in detergent-free buffer when blotted to form a very thin film. The catalase molecules adopt a single “edge” orientation with respect to the air:water interface and interact with one another to form the ribbons. (b) 0.1 mg/ml catalase in 0.2 mM DDM after blotting to form a thin film. In this case, the catalase molecules are still concentrated at the air-detergent-water interface but have a weaker interaction with each other. The molecules in the central region form a raft with their short axis oriented perpendicular to the film; a gap with very few molecules separates this central raft from another crowded region with molecules in an edge orientation. In the gap, a few molecules showing a dumbbell view are also seen. Outside these crowded central regions, very few molecules are found, which is consistent with their low bulk protein concentration. (c) 1 mg/ml catalase in 4 mM Fos-choline-8 detergent shows few molecules in many different orientations but no rafts or ribbons (d) 40 mg/ml catalase in 8 mM CHAPSO, with good distribution. The last two panels show a distribution of catalase molecules with the expected particle count due to the absence of any surface interaction.

Type of presentation: Plenary

Plenary-2901 Recent Progress in High-Resolution Electron Energy Loss Spectroscopy in the Scanning Transmission Electron Microscope

Ramasse Q. M.[1,2], Kepaptsoglou D. M.[1,3], Hage F. S.[1,4]

[1]SuperSTEM Laboratory, Daresbury, United Kingom, [2]Schools of Chemical and Process Engineering & Physics and Astronomy, University of Leeds, Leeds, United Kingdom, [3]Department of Physics, University of York, York, United Kingdom, [4]Department of Physics, University of Oslo, Oslo, Norway

Email of the presenting author: qmramasse@superstem.org

Instrumentation advances have pushed the energy resolution of electron energy loss spectroscopy (EELS) in monochromated scanning transmission electron microscopes (STEMs) into the meV range, all the while retaining atomic-sized probes [1]. This now allows for probing the chemical and electronic structure of a wide range of materials systems with unprecedented detail, from the core-loss to the vibrational spectroscopy regimes. This contribution will review a number of recent developments achieved using a monochromated Nion UltraSTEM100 MC across the energy loss scale.

The energy loss near-edge structure (ELNES) arising from core-level excitation provides a wealth of information on chemical bonding between atoms, and can be interpreted by first-principles calculations in favourable cases. Here, the increased sensitivity and resolution were used to obtain real-space maps of π* and σ* states in epitaxial graphene multilayers observed in side view. Interpretation relies crucially on understanding how the beam propagation through the sample affects the observed ELNES, using combined multi-slice and density functional theory calculations, and pave the way towards using ELNES to map electronic orbitals in real space. [2]

In the low loss regime, a dark field (DF) EELS detection geometry can be used to map atomic scale variations in acoustic and optical phonon excitations in materials, down to atomically thin singlelayer graphene. Individual point defects such as a single-atom dopants substituted in the graphene host lattice (figure 1) can also be shown to have a characteristic vibrational response [3]. Optimising signal levels thanks to highly-sensitive direct electron detectors and custom-developed annular apertures reveals the emergence of locally resolved fine structure in the phonon spectra:figure 2. In addition to a further direct interrogation of the chemical bonds in a system consisting of Bi_2Se_3 films grown by chemical vapor deposition on epitaxial graphene, it is thought these observations could also be linked to the interplay between the various phonon modes and the Dirac plasmons in the topological insulator Bi_2Se_3.

Finally, the prospects for observing the excitation of spin waves, or magnons, arising from the collective excitation of the electrons' spin in a lattice and which qualitatively occupy the same energy range as phonons, are explored through preliminary experiments and the development of a theoretical framework based on the diffuse scattering of electrons due to magnons. [4]

[1] QM Ramasse, 180 (2017), 41-51
[2] FS Hage et al., Phys. Rev. Lett. 122 (2019), 16103
[3] FS Hage et al., Science 367 (2020), aba1136
[4] K Lyon et al., Phys. Rev. B 104 (2021), 214418

Acknowledgement: SuperSTEM is the UK National Research Facility for Advanced Electron Microscopy, supported by the Engineering and Physical Sciences Research Council (EPSRC).

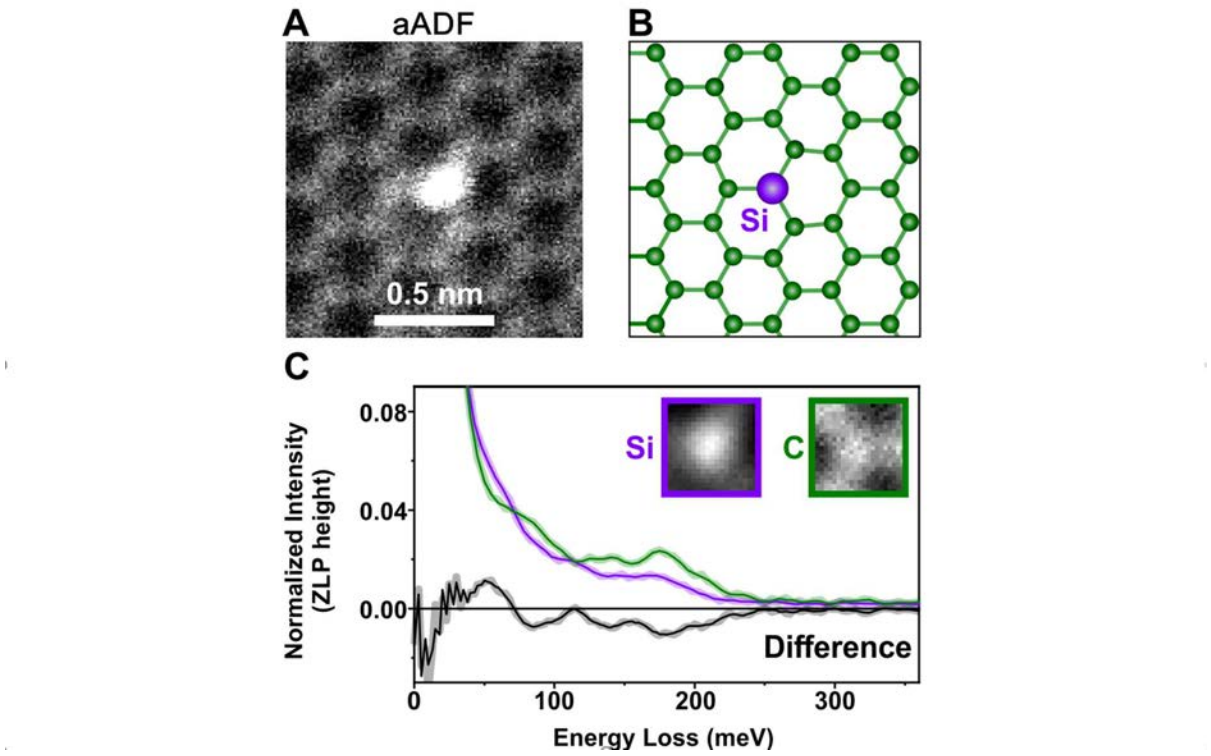

Fig. 1: (A) aADF image (thus named due to the off-axis geometry) and (B) model of a single substitutional Si dopant in graphene. (C) Vibrational spectrum of the Si atom ("Si") and of a defect-free part of the graphene a few atoms away from the Si atom ("C"). The difference spectrum is calculated by subtracting the C spectrum from the Si spectrum. [3]

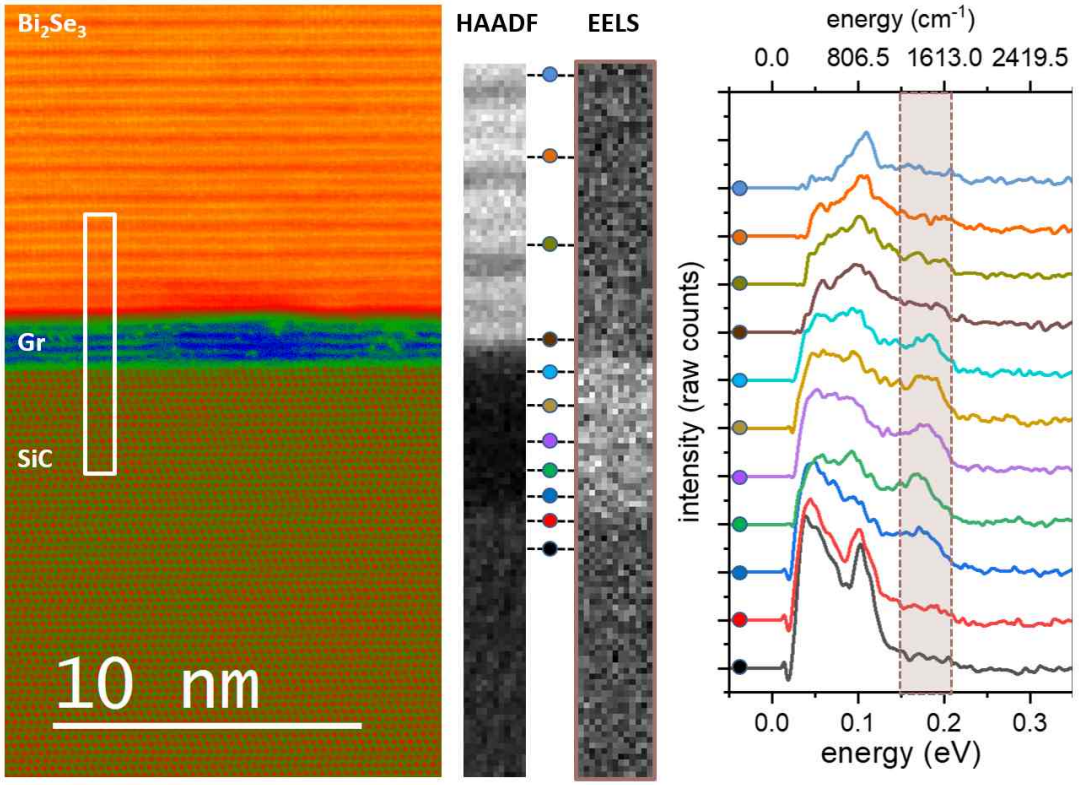

Fig. 2: Left: STEM image of a SiC /Graphene/Bi2Se3 heterostructure. A rectangle indicates the region over which an EELS spectrum image was recorded. Centre: simultaneous ADF and integrated EELS signal (over the energy window indicated in the extracted spectra, right), showing atomically-resolved phonon signal over the 5 graphene layers.

Type of presentation: Plenary

Plenary-3038 Determining and modifying properties of two-dimensional inorganic and organic materials using low-voltage TEM - challenges and solutions

Kaiser U. A.[1]

[1]Ulm University, Central Facility of Electron Microscopy

Email of the presenting author: ute.kaiser@uni-ulm.de

Two-dimensional materials are one of the current brightest stars on the horizon of materials and promise the realization of completely new technologies with further miniaturized component. In these materials, the properties often depend on the position of the individual atoms in the crystal structure. Using aberration-corrected low-voltage TEM, atomic positions can be determined with picometer accuracy, however the imaging atoms at the same time can modify the structure. A detailed understanding of beam electron-sample interactions is therefore required gained from atomically-resolved, time-dependent in-situ TEM imaging of two-dimensional (2D) transition metal dichalcogenides (TMDs) using the chromatic- and spherical-aberration-corrected low-voltage SALVE instrument operating between 80kV and 20kV [1,2]. We elucidate the accelerating-voltage-dependent formation of single atomic defects and find that elastic and inelastic interactions are strongly connected, resulting in a two-step interaction process [3]. When the material under electron irradiation is transformed from an ordered to an unordered structure, the evaluation of this structure is performed by U-net-based neural network (NN).
We further discuss the formation of defects in 2D inorganic crystals. We analyse in-situ structural and chemical transformations of different freestanding TMDs and of rarely reported TMPTs (TM phosphorus tri-chalcogenides). Complementary ab-initio calculations prove the stability of the newly formed phases and predict their properties [4]. As the TMPTs are often very oxygen-sensitive, they were prepared with the help of a newly-developed polymer-assisted sample preparation method. Furthermore, we present in-situ studies of a miniaturized electrochemical cell, where reversibly single-crystalline bilayer graphene is lithiated and delithiated in controlled manner using an electrochemical gate confined to a device protrusion [5] with special emphasis on the Li crystal nucleation mechanism.
Knowledge gained from the study of 2D inorganic materials we apply to the study of 2D polymers and 2D metal-organic frameworks (MOFs). We present key strategies to achieve highest resolution in high-resolution TEM images of imine-based 2D polymer films [6,7]. Finally, we show that differentiating between the bond nature of two metal atoms is now possible [8].
[1] U. Kaiser et al., Ultramicroscopy, 111, 8, (2011) 1239
[2] M. Linck, et al. PRL 117, (2016) 076101
[3] S. Kretschmer and T. Lehnert, et al, Nano Lett. 20, (2020) 2865
[4] J. Köster et al., Nanotechnology 32 (2021) 075704
[5] M. Kühne, F. Börrnert et al., Nature 564 (2018) 234
[6] H. Qi et al., Science Advances 6, (2020) eabb5976
[7] B. Liang et al. Nature Communication accepted.
[8] K. Cao et al., Science Advances 6 (2020) eaay5849

Acknowledgement: We gratefully acknowledge the funding from DFG (German Research Foundation) SFB-1415 as well as the financial support GrapheneCore3, Grant Agreement No. 881603.

Type of presentation: Plenary

Plenary-2891 When microscopy meets crystallography: Crystal structure analysis by 3D electron diffraction

Palatinus L.[1]

[1]Institute of Physics of the CAS, Na Slovance 2, Prague 8, Czechia

Email of the presenting author: palat@fzu.cz

Electron microscopy has always been a prominent technique for investigating crystalline materials, especially thanks to its unrivalled spatial resolution. Ab initio determination of complicated crystal structures, however, was for a long time considered out of reach of electron microscopy and electron diffraction, and it remained mostly the realm of x-ray diffraction methods. Single crystal x-ray diffraction is still the method of choice for structure elucidation, but it requires relatively large crystals, much larger than 1μm. However, modern material science, chemistry and biochemistry work with more and more complex materials and synthetic routes that often do not yield sufficiently large single crystals. The structures of these materials were then extremely difficult or even impossible to determine.

The situation has changed with the advent of three-dimensional electron diffraction (3D ED). The basic principle of the method is the collection of a sequence of diffraction patterns from a slowly rotating crystal. This approach allows collecting a large amount of electron diffraction data on a single nanocrystal, and then applying standard crystallographic techniques to determine the crystal structure from these data.

Single crystal structure analysis by 3D ED faces a number of fundamental as well as technical problems, for example the radiation damage of some classes of materials, instrumental stability and tracking of the crystal during the data acquisition, and correct modelling of diffracted intensities that needs to include the multiple scattering effects. However, all these problems have been at least partly solved in the past few years, and the fast development of the method has received a lot of attention and positive reception in the crystallographic community.

At present, 3D ED methods are being used in many laboratories almost routinely to analyse the structures of a wide variety of materials, ranging from metals, oxides and other inorganic materials through minerals, framework and porous materials to organic molecular crystals and macromolecular crystals [1]. Some of the recent breakthroughs in accurate structure analysis include detailed structure analysis of beam sensitive materials including the localisation of hydrogen atoms [2] or the determination of absolute structure of organic crystals [3]. With improving data quality and accuracy of data processing, advanced applications like charge density analysis from 3D ED data are also becoming feasible.

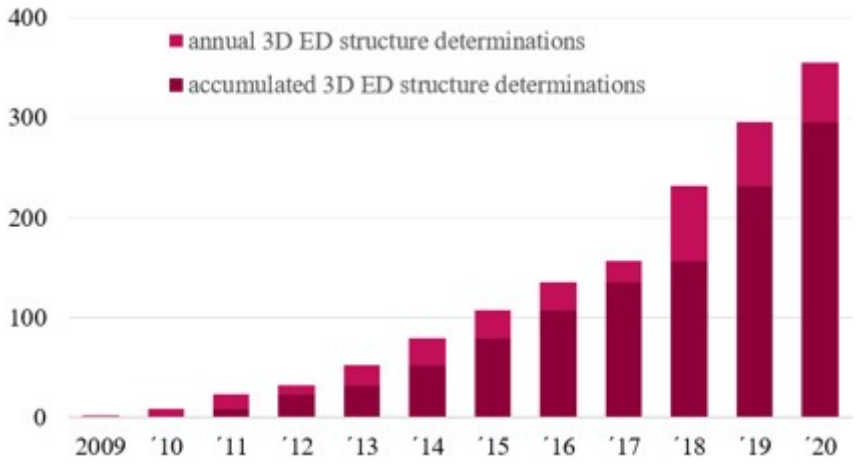

Fig. 1: Annual and accumulated number of published crystal structures solved by 3D ED methods since 2009. Image and underlying data analysis by Paul Klar.

Type of presentation: Plenary

Plenary-2872 Watching and shaping memories in the brain with optical methods

Losonczy A.[1]

[1]Department of Neuroscience, Columbia University, New York, United States

Email of the presenting author: al2856@columbia.edu

Learning is a fundamental capacity of the brain, but a mechanistic understanding of neural processes supporting learning in complex circuits of the mammalian brain remains a longstanding challenge in the field of neuroscience. In the hippocampus, a key brain region for spatial and episodic learning, a striking form of feature selectivity can be found in the spatial receptive fields of 'place' cells. Indeed, much of our current understanding of memory operations comes from investigations of hippocampal place cells ensembles. However, to date, it remains unknown whether and how neuronal architecture at single-cell and circuit levels regulates the emergence of place cells. Likewise, we know puzzlingly little about how the same neuronal architecture can support long-term storage of memories. High-resolution functional imaging of neural activity with genetically encoded sensors has recently emerged as a promising tool for fast optical recordings of neural circuit dynamics in vivo. To interrogate dynamic interactions of individual hippocampal neurons with their surrounding microcircuitry, we used multi-photon imaging of calcium and voltage sensors in combination with single-cell labeling and optogenetics. In my talk, I will summarize recent results related to local circuit and cellular mechanisms of place cell formation and memory consolidation. Together, our findings support the emerging notion that cellular and microcircuit processes jointly and flexibly regulate learning and memory in mammalian brain circuits.

Type of presentation: Plenary

Plenary-3049 Mature Holographic Microscopy

Chmelík R.[1,2], Bouchal P.[1,2], Ďuriš M.[1], Dostál Z.[1,2], Veselý P.[1], Zicha D.[1]

[1]CEITEC – Central European Institute of Technology, Brno University of Technology, Brno, Czech Republic, [2]Institute of Physical Engineering, Faculty of Mechanical Engineering, Brno University of Technology, Brno, Czech Republic

Email of the presenting author: radim.chmelik@vut.cz

Holographic microscopy (HM) is a prominent Quantitative Phase Imaging (QPI) [1] technique. QPI has been gaining popularity in biomedical imaging, providing high-contrast images of unstained living cells and measuring their area dry-mass density distribution and its dynamics [1]. Other applications make QPI increasingly important also in materials science and modern optics [2,3].
A coherent illumination required by the classical HM impairs the reconstructed image with coherence artifacts. Transition to low-coherent light eliminates these effects and returns HM's resolving power to the wide-field microscopy standard. However, the most significant benefit of low coherence is the coherence-gate effect blocking the light scattered by the unwanted parts of a specimen. This effect is typically used for imaging through disordered media by least-scattered (ballistic) light.
Our concept of the holographic incoherent-source QPI (hiQPI) makes off-axis holography fully compatible with incoherent illumination. The setup with spatially separated reference and object arms fits better live-cell imaging [4]. The single-path setup separating both beams by polarization encoding using geometric-phase optics is suitable for measuring phase effects of metasurface optical elements [2] and generally for the characterization of the object beam polarization state [3].
Nevertheless, we have taken one more step to exploit the potential of hiQPI fully. While the standard holographic record characterizes the low-coherent interfering beams only partially, the hiQPI method allowed us to characterize them more completely, thus unlocking unique extra imaging capabilities. This way, we accomplished hiQPI through scattering medium with the non-ballistic light. Further, by combining ballistic and non-ballistic images, we synthesized images of quality superior to the ballistic-light-only approach [5]. Also, applying this procedure to the system of a specimen and a diffraction grating, we increased the hiQPI resolution substantially beyond Abbe's diffraction limit while keeping a large field of view of low-NA objectives [6].
Compared to classical holographic recording, the proposed approach provides more information about the observed object, thus providing hiQPI with the capability of improved resolution for both 2D and 3D objects.

References

[1] Park, Y., Depeursinge, C. and Popescu, G. Nature Photonics 12, 578-589 (2018).
[2] Bouchal, P. et al. Nano Letters 19, 1242-1250 (2019).
[3] Bouchal, P. et al. Scientific Reports 9, 3608 (2019).
[4] Sheridan, J. T. et al. Journal of Optics 22, 123002 (2020).
[5] Ďuriš, M. and Chmelík, R. Optics Letters 46, 4486 (2021).
[6] Ďuriš, M., Bouchal, P., Rovenská, K. and Chmelík, R. APL Photonics 7, 046105 (2022).

Acknowledgement: The work is supported by the Czech Science Foundation (21-01953S), ERDF (CZ.02.1.01/0.0/0.0/18_046/0016045), MEYS CR (LM2018129), and BUT (FSI-S-20-6353).

IM1 Multi-dimensional image processing: Facing the data interpretation challenge

Type of presentation: Invited

IM1-IN-2973 Writing and sustaining analysis tools for large and complex microscopy data

Nord M.[1]

[1]Department of Physics, Norwegian University of Science and Technology, Trondheim, Norway

Email of the presenting author: magnus.nord@ntnu.no

Within the field of transmission electron microscopy (TEM), the amount of data being generated during a typical experimental session has historically been modest. Due to this small amount of datasets, it has been possible to analyse each of them manually. Even for complex data types such as diffraction, atomic resolution images or spectra. However, in recent years this has changed, due to the advent of direct electron detectors for use in TEM.

One example of this is the fast pixelated electron detector, which can acquire over 1000 images per second. Utilizing this detector in Scanning TEM (STEM), one can acquire a diffraction pattern for each position in a scan. In this scanning electron diffraction technique (or 4D-STEM) a dataset can easily consist of 250.000+ diffraction patterns. With such large amount of patterns, it is clearly not feasible to analyse each of them manually. Some type of automation is needed. For simple data processing, such as making a virtual bright field image by summing each diffraction pattern, this is fairly easy to implement. However, for more complex data processing, this requires a different approach: as it needs to be i) efficient enough so the processing doesn't take forever, ii) robust enough so it doesn't produce false results.

This presentation will outline the challenges and solutions in writing software for doing complex analysis of very large dataset. Specifically how the microscopy community can utilize the experience from the wider open source community, both in the use of software development tools, organizational structure and how to make software useable to the wider community.

[1] "Four-Dimensional Scanning Transmission Electron Microscopy (4D-STEM): From Scanning Nanodiffraction to Ptychography and Beyond", Colin Ophus, Microscopy and Microanalysis, Volume 25, Issue 3, 2019

Acknowledgement: Research Council of Norway for funding NORTEM (197405), and "In-situ Correlated Nanoscale Imaging of Magnetic Fields in Functional Materials", InCoMa (315475).

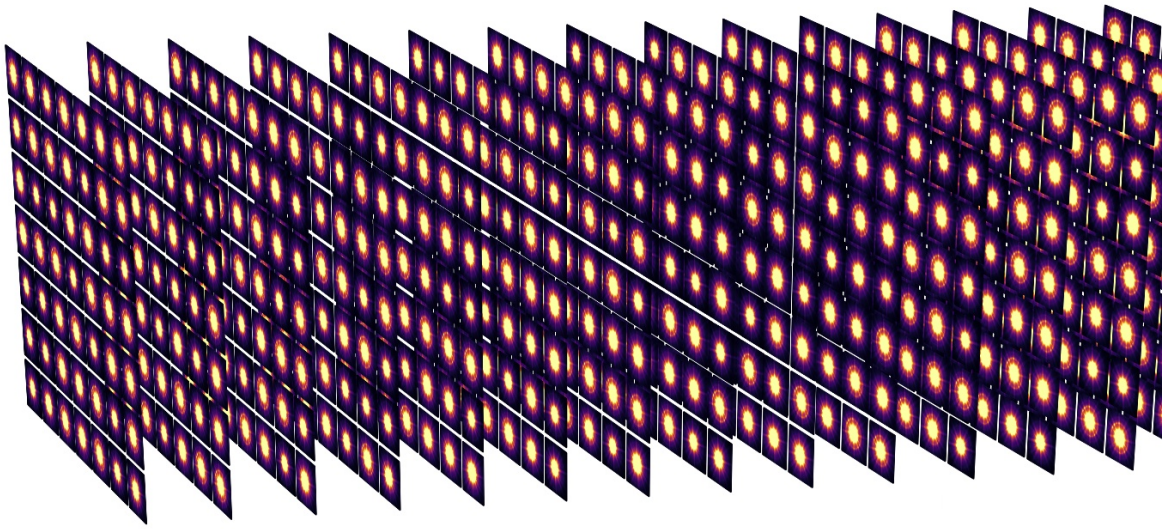

Fig. 1: Showing a large number of diffraction patterns acquired using scanning electron diffraction.

Type of presentation: Oral

IM1-O-2569 Making Every Electron Count: Improving STEM Quantification, Speed, and Data Throughput with Solid State Detectors and Pulse Counting Hardware

Peters J.[1], Mullarkey T.[1,2], Moldovan G.[3], Garel J.[4], Jones L.[1,5]

[1]School of Physics, Trinity College Dublin, Dublin, Ireland, [2]Centre for Doctoral Training in the Advanced Characterisation of Materials, AMBER Centre, Dublin, Ireland, [3]point electronic GmbH, Erich-Neuss-Weg 15, D-06120, Halle (Saale), Germany, [4]El-Mul Technologies Ltd, Rehovot, Israel, [5]Advanced Microscopy Laboratory, Centre for Research on Adaptive Nanostructures & Nanodevices (CRANN), Dublin

Email of the presenting author: jonathan.peters@tcd.ie

STEM is a core technique yielding simultaneous imaging and spectroscopy with easy interpretability. However, despite the interpretability of ADF STEM, true quantitative measurements are not trivial, needing simulation and thorough calibration of the microscope [1]. Fundamentally, individual electrons contribute differently to image intensity due to their stochastic interaction with the detector. Moreover, tiny imperfections such as leakage currents, thermal instabilities and digitisation noise result in non-zero dark values and arbitrary or irreproducible pixel values. Further, conventional acquisition systems must employ a wider data bandwidth, creating unnecessary bottlenecks. Here we show an optimised approach to STEM through electron counting using a combination of Si-based detector and gradient thresholding.

For the case of electron counting, when a single electron hits the detector, a minute current pulse is induced, amplified, compared with a threshold, and then added to a digital count in the corresponding image pixel. The resultant image intensity has values in units of electron counts, therefore counted images provide an easy path for image quantification, with a true zero dark level, uniform detector efficiency, as well as deliver a narrower data bandwidth without any loss of information (Fig. 1). In contrast with conventional STEM, the upper limit to usable dose is determined by electron pile-up, where multiple detection events occur rapidly and cannot be distinguished. By comparison with simple thresholding, we show that gradient thresholding not only increases the upper limit, but also achieves higher detection efficiency (Fig. 2a) [2].

A strength of counting is that it can be retrofitted to existing scintillator-based detectors, not only integrated to new systems. However, the upper limit is strongly limited by the slow response of standard scintillator-based detectors. We compare this with a Si-based Opal 6 segment detector (El-Mul Technologies) [3], showing not only narrower electron pulses, but also superior detector uniformity (Fig. 2b). Further, the independence of counting events over the detector segments can be used to mitigate the pile-up limit. Conventional STEM scanning systems are not compatible with such high speed, multiple parallel counting signals, therefore we use a scanning systems from point electronic (Fig. 3). Altogether, our work sets a standard for optimum image quantification using conventional and state-of-the-art hardware, extending the capabilities and lifetime of new and existing microscopes.

[1] L. Jones et al., Nano lett, 14, (2014) 6336–6341
[2] T. Mullarkey et al., Microsc. Microanal, 27 (2020) 99-108
[3] A. Seifer et al., Microsc. Microanal, 27, (2021) 1476-1487

Acknowledgement: We acknowledge SFI awards URF/RI/191637 and 19/FFP/6813, as well as SFI-EPSRC CDT-ACM awards 18/EPSRC-CDT-3581 and EP/S023259/1.

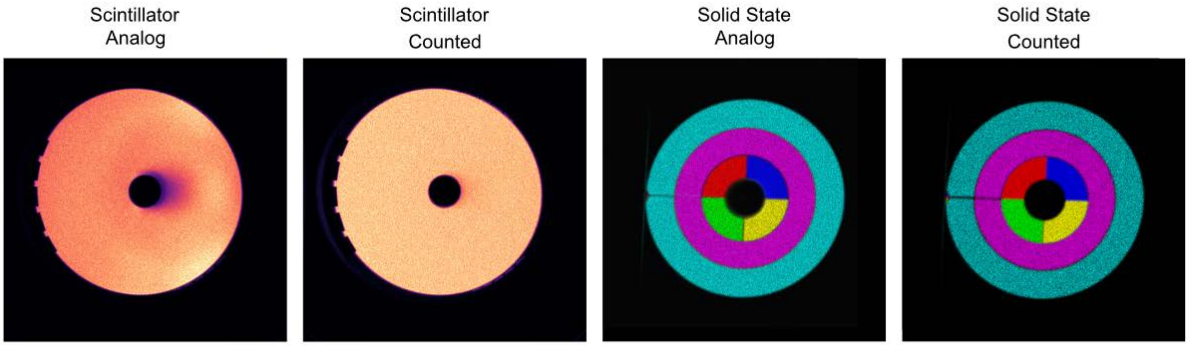

Fig. 1: Recorded maps of scintillator and Si-based solid state detectors, with and without counting.

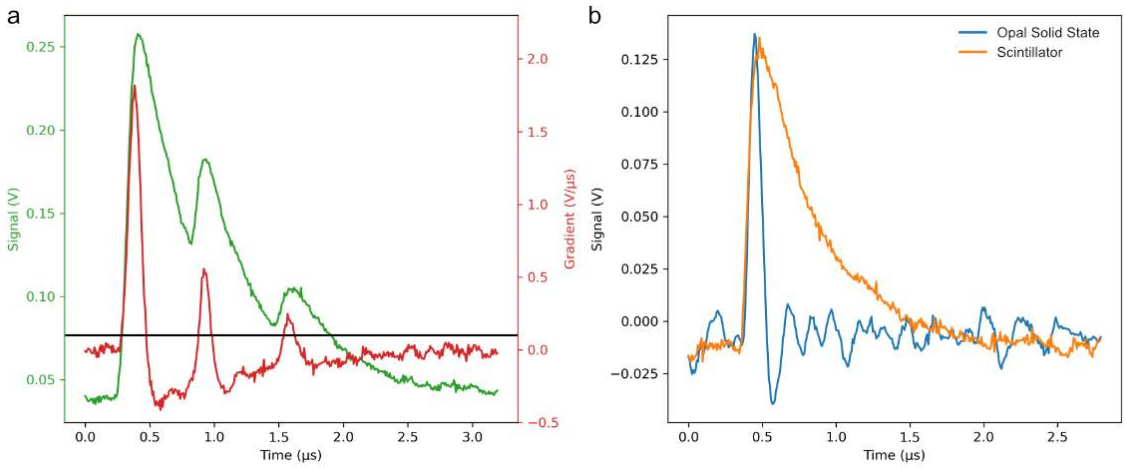

Fig. 2: **a** Example of detection pile-up showing how the signal gradient can detect all events using an appropriate threshold (horizontal line). **b** Pulse profile from scintillator and Opal solid state STEM detector, El-Mul Technologies.

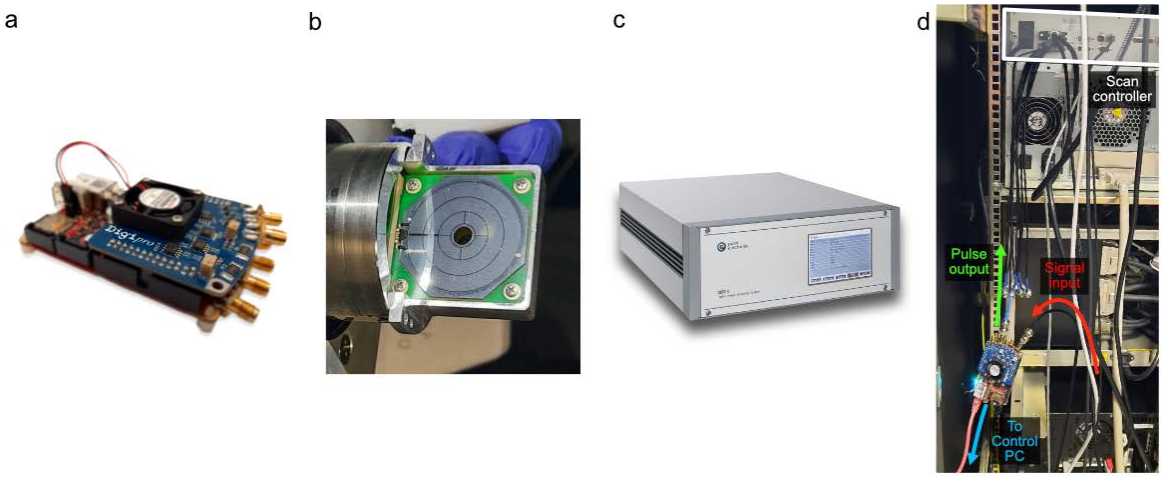

Fig. 3: **a** Digi-pro pulse counting hardware. **b** Opal solid state STEM detector. **c** DISS6 scan generator and image acquisition. **d** experimental configuration showing the DISS6 scan generator and Digi-pro.

Type of presentation: Oral

IM1-O-2853 4D-STEM Imaging for 3D Stereo Reconstruction by Deep Learning Neural Networks

Ganeeva G.[1], Altingövde O.[2], Ong Khac Q.[3], Stellacci F.[3], Fua P.[2], Oveisi E.[4], Hébert C.[1]

[1]Electron Spectrometry and Microscopy Laboratory (LSME), EPFL, Lausanne, Switzerland, [2]Computer Vision Laboratory (CVLab), EPFL, Lausanne, Switzerland, [3]Supramolecular Nanomaterials and Interfaces Laboratory (SuNMIL), EPFL, Lausanne, Switzerland, [4]Interdisciplinary Centre for Electron Microscopy (CIME), EPFL, Lausanne, Switzerland

Email of the presenting author: gulnaz.ganeeva@epfl.ch

Three-dimensional (3D) stereo reconstruction of dislocation structures from the transmission electron micrographs is an effective reconstruction technique compared to conventional electron tomography. Many advantages to this approach were brought by the development of the tilt-less imaging technique where a stereo-pair of images is acquired in scanning TEM (STEM) mode [1]. However, following post-processing and 3D reconstruction remained slow and required manual treatment.

Hence, we developed an approach based on deep learning convolutional neural networks (CNN) to automatically reconstruct the dislocations network in the 3D volume of a sample. Our technique allows to automatically detect the dislocations and match them on both views to finally obtain their 3D distribution in its crystallographic coordinates [2]. Our neural networks have been trained with a large dataset of dislocation images in three materials under various imaging conditions which makes it a versatile tool and a worthy alternative to tomography.

By applying tilt-less 3D imaging [1] on a fast pixelated STEM detector [3] and using our algorithm, we demonstrate the 3D reconstruction of dislocations from virtual stereo-images extracted from the 4D STEM dataset. Pairs of virtual stereo BF-STEM images with approximately 6 degrees stereo-tilt can be formed by selecting the intensity from the two counterpart regions of the direct disc. Fig. 1 depicts the 3D reconstruction procedure from the 4D STEM dataset. Images are treated by CNNs to provide a 3D reconstruction. Our approach delivers the possibility to obtain a larger stereo-angle between the views as well as increases the number of the views on the sample for the following 3D reconstruction and improves its precision.

We also extended the tilt-less 3D imaging technique to study the 3D distribution of nanoparticles in cryo condition. We performed the 3D cryo-STEM imaging using an annual detector with four segments on the nanoparticles in vitrified ice followed by 3D reconstruction. Fig. 2 depicts our 3D reconstruction pipeline for measuring the 3D depth of nanoparticles in the sample. We first perform circle detection on denoised images to detect nanoparticles. When our search algorithm finds consistent detections in all four images for a value of shift on the lines, it is assigned to the particle as its depth. Collecting four images via single-shot STEM imaging noticeably economizes the time of the experiment and reduces the electron damage of the sample.

[1] E Oveisi, A Letouzey, D T L Alexander, et al., Scientific Reports, 7.1 (2017).
[2] O Altingövde et al., Ultramicroscopy, 234 (2022).
[3] C Ophus, Microsc Microanal. (2019), 563-582.

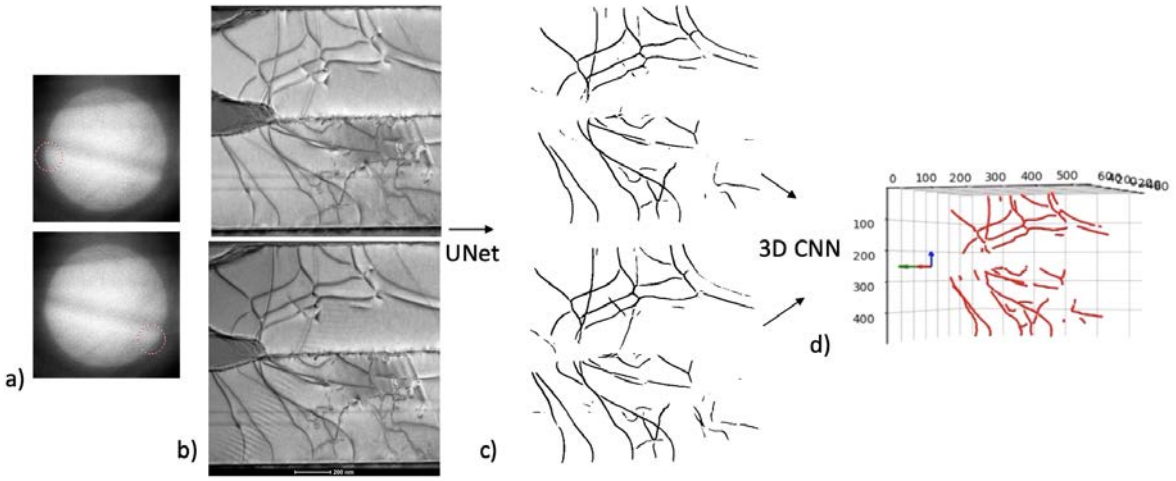

Fig. 1: 3D reconstruction procedure from 4D STEM dataset: a) diffraction pattern in 2-beam condition g=(200) acquired on a pixelated detector, b) stereo-pair of virtual BF-STEM images acquired by collecting the intensity in the regions highlighted by circles in a), c) corresponding detected dislocations by UNet, d) 3D reconstruction by 3D CNN.

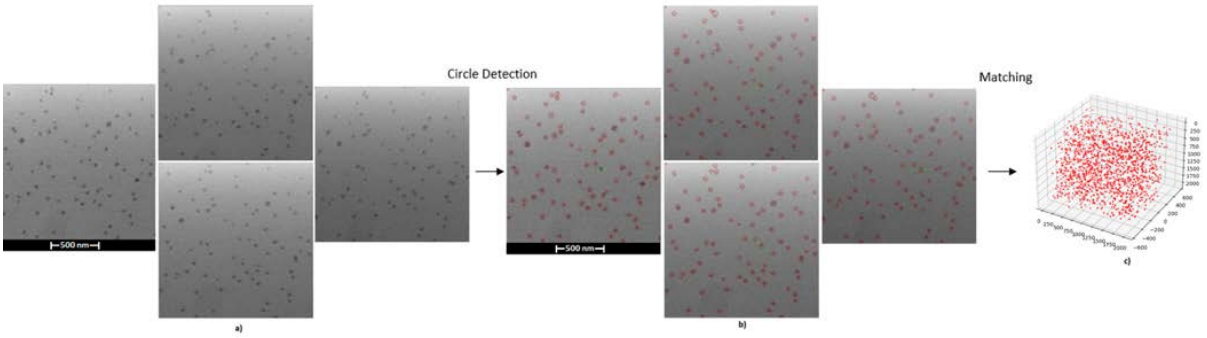

Fig. 2: 3D reconstruction of nanoparticles in vitrified ice: a) images from A, B, C, and D regions of the detector (shown clock-wise), b) detected particles are shown in red circles, c) if consistent detections are found in all 4 images, a suitable depth value is assigned to the particle.

Type of presentation: Oral

IM1-O-2679 Integrated topographic SEM imaging for software assisted fractography

Hemmleb M.[1], Bettge D.[2], Schmies L.[2], Sonntag U.[3], Botsch B.[3]

[1]point electronic GmbH, Halle, Germany, [2]Bundesanstalt für Materialforschung und prüfung (BAM), Berlin, Germany, [3]Gesellschaft zur Förderung angewandter Informatik e.V. (GFaI), Berlin, Germany

Email of the presenting author: mh@pointelectronic.de

The aim of a fractographic investigation is the evaluation of macroscopic and microscopic fracture surface characteristics and, as a result, the determination of the fracture mechanism of a component from a failure case. The basis for such evaluations of fracture characteristics comes from actual comparative mechanical testing and from the literature. A fractographic analysis can be very complex and, in any case, requires considerable experience.

Machine learning methods enables the quantitative determination of fracture characteristics and fracture mechanisms utilizing digitized expert knowledge [1]. Although the application of SE images provides promising results, additional information is required to obtain reliable solutions. As expected, BSE and 3D information helps to improve the classification (Fig. 1). But only a fast, widely integrated, and automated topography measurement can provide the required amount of referenced surface data for the application of machine learning methods.

To fulfil these requirements, topographical data are obtained from a BSE detector with four symmetric segments (4Q-BSE) using shape-from-shading technology [2]. Surface height calculation is performed live during image acquisition and provides immediate feedback in three dimensions. All available signals (SE, BSE and more if applicable) are recorded simultaneously together with the surface topography and stored in a multichannel data file. This guaranties the same geometrical reference for all data, which is required for further analysis (Fig. 2).

When applying machine learning methods to topographic data together with SEM images, topographic information must be provided as depth image. Consequently, a unique height scale is required for all applied data with different magnifications. This requires a calibrated height measurement, which is ensured with the integrated 3D calibration of the topographic acquisition and a dedicated calibration sample. Thus, a large number of data sets from different fracture samples was generated and used as training data for machine learning.

In the joint research project “iFrakto”, a software is developed, which quantitatively determines fracture characteristics and fracture mechanisms from SEM images and topographic data (Fig. 3). In the medium term, a software tool should provide knowledge-based suggestions for the evaluation of fracture surfaces in real time during SEM work or at subsequent evaluation. As a basis for this, round robins were carried out among experts to create a knowledge base, to query the practice-relevant requirements for such tools and to carry out first practical tests.

[1] M. X. Bastidas-Rodriguez et al, DOI: 10.1016/j.engfailanal.2020.104532

[2] M. Hemmleb et al, DOI: 10.1002/EMC2016.0709

Acknowledgement: Thanks to Quynh-Hoa Le, Michaela Buchheim and Anna Yarysh for support and data acquisition. The joint project (“iFrakto”) is founded by AIF (IGF, 21477N).

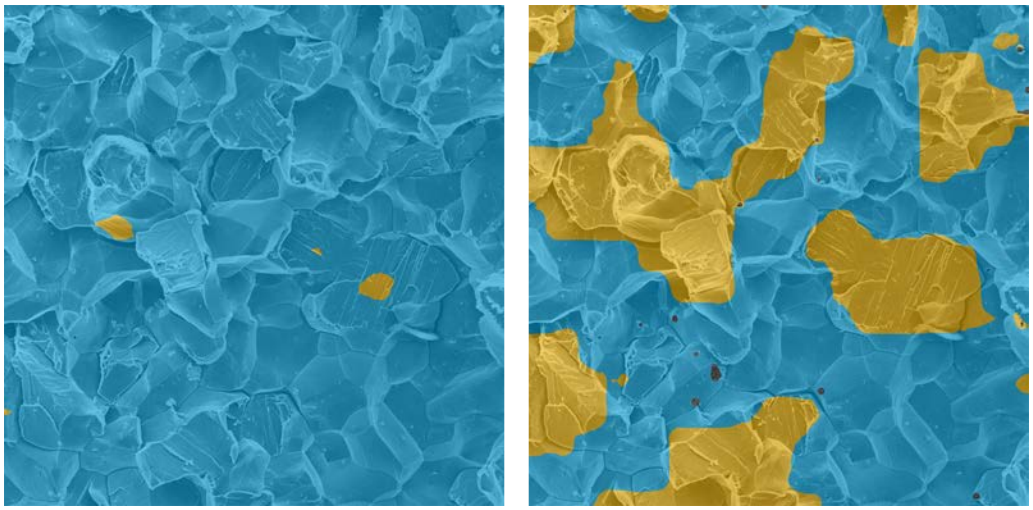

Fig. 1: Classification results without applying topographic information (left) and improved results with additional application of BSE and topographic information on same dataset. Blue areas are predictions for exposed grain boundaries and orange for cleavage planes.

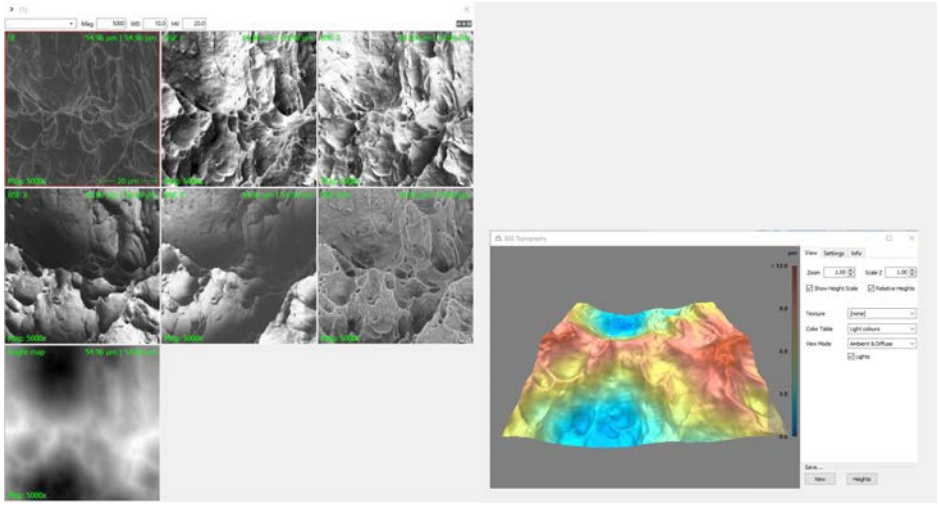

Fig. 2: Multichannel SEM data acquisition. SE image, quantitative BSE signals and height data are acquired from the fracture sample at the same time. Height data are shown in additional scan window as 16-bit image and in separate 3D viewer. Height scale is provided from integrated calibration with dedicated 3D reference sample.

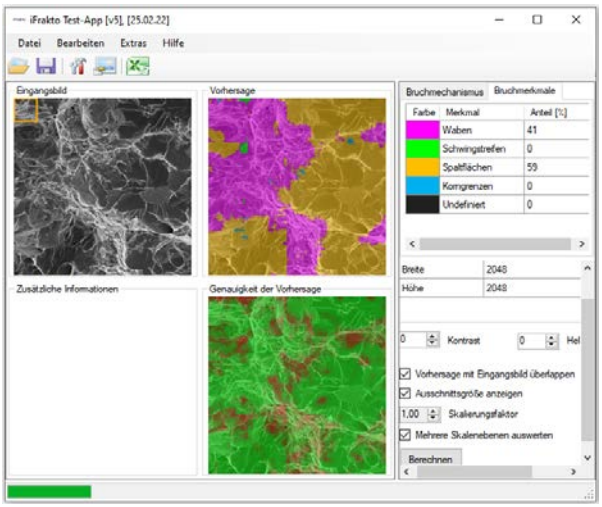

Fig. 3: Software tool for classification of surface characteristics and fracture mechanism. In addition to SE and BSE images, also height maps can be used as input data.

Type of presentation: Invited

IM1-IN-2752 Image Analysis Workflow for Phase-Contrast Optical Microscopy Images

Erdem Y. S.[1], Ayanzadeh A.[2], Mayalı B.[1], Balıkçi M.[3], Belli Ö. N.[3], Uçar M.[1], Yalçın Özyusal Ö.[3], Pesen Okvur D.[3], Önal S.[4], Iheme L. O.[5], Töreyin B. U.[2], Ünay D.[1]

[1]Electrical and Electronics Engineering, Izmir Democracy University, İzmir, Turkey, [2]Informatics Institute, Istanbul Technical University, İstanbul, Turkey, [3]Molecular Biology and Genetics, Izmir Institute of Technology, İzmir, Turkey, [4]Biotechnology and Bioengineering Graduate Program, Izmir Institute of Technology, İzmir, Turkey, [5]Virasoft Software Inc., İstanbul, Turkey

Email of the presenting author: unaydevrim@gmail.com

Phase-contrast optical microscopy (PCM) is a recent label-free imaging technique, which is preferred by cell biology researchers for understanding morphology and dynamics of cells - invasive and metastatic capacities of cancer cells in particular - and therefore is used for the analysis (quantification, segmentation, and tracking) of living-cells in different biomedical applications [1]. Accordingly, in this work automated analysis of PCM time-lapse images collected from wound healing and cell motility assays of breast cancer cell lines are studied.

Three different cell lines with varying morphology and motility characteristics are imaged: MDA-MB-231 invasive breast cancer cell line in mesenchymal morphology, MCF7 non-invasive breast cancer cell line in epithelial morphology, and MCF10A normal breast cell line in epithelial morphology. High-resolution images are obtained every 15-minutes using a confocal laser scanning Leica TCS SP8 microscope. Wound fronts and cell boundaries in the acquired images are manually annotated by experts using ImageJ and an online manual annotation tool.

Deep learning methods have pivotal effects on the improvement of segmentation accuracy and facilitate the process of analysis in many clinical applications [2]. Accordingly, here various deep learning-based solutions - such as the popular U-Net and its modified version, SegNet, ResNet, and VGG - are developed for automated segmentation of wound fronts and isolated cells. An extended version of this abstract is under review for publication as a book chapter [3]. Experimental evaluations showed that our deep learning based solutions outperformed their classical rivals in both segmentation tasks.

As for the quantification, various biologically-important features are automatically computed from the segmentation results, such as length and width of wound area, curvature of wound front, size and shape of isolated cells, total distance traveled by each cell, and average cell speed. These quantified features - together with segmentation results - provide important ques for cell biology researchers in understanding morphology and dynamics of cells, like invasive and metastatic behavior, as well as tumor aggressiveness.

[1] Jaccard N. et al. "Automated method for the rapid and precise estimation of adherent cell culture characteristics from phase contrast microscopy images." Biotechnol. Bioeng. 111.3 (2014): 504-517.
[2] Shen D. et al. "Deep learning in medical image analysis." Annu. Rev. Biomed. Eng. 19 (2017): 221-248.
[3] Erdem Y.S. et al. “Automated Analysis of Phase-Contrast Optical Microscopy Time-Lapse Images: Application to Wound Healing and Cell Motility Assays of Breast Cancer” in Diagnos. Biom. Sig. Im. Proc. Appl., eds Polat K. & Ozturk S., Elsevier (in preparation).

Acknowledgement: This work is supported by the Scientific and Technological Research Council of Turkey (TUBITAK) under grant no 119E578.

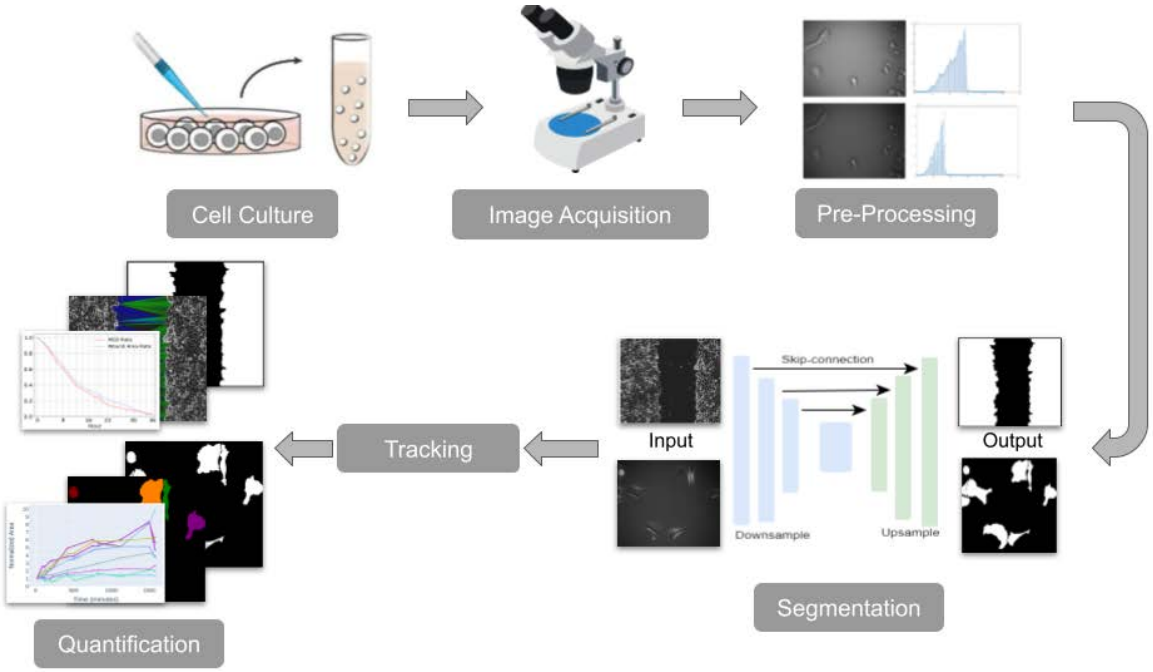

Fig. 1: Flowchart of the proposed workflow for the automated analysis of phase-contrast optical microscopy images. The proposed workflow consists of pre-processing, segmentation, tracking, and quantification steps for the acquired phase-contrast optical microscopy time-series images of wound healing and cell motility assays of breast cancer cell lines.

Type of presentation: Oral

IM1-O-2681 Precipitate size estimation using image feature detection

Ederer M.[1], Löffler S.[1]

[1]University Service Centre for Transmission Electron Microscopy, TU Wien, Wiedner Hauptstraße 8-10/E057-02, 1040 Wien, Austria

Email of the presenting author: manuel.ederer@tuwien.ac.at

With the amount of data TEM imaging produces, manual evaluation and comparison of images is becoming excruciatingly difficult. It is a time consuming, generally non-reproducible and subjective process. We present an algorithm based on feature detection that automatically calculates the difference between the image and a reference image and demonstrate its manifold uses on the example of detecting precipitates.

This feature detection algorithm is based on the scale invariant feature transform (SIFT) [1]. In a reference image, regions in scale space that fully define the image are found, characterized and compared to the same locations in an image of interest. The result is a single number fully representing the difference between the images and, provided that the reference image is the theoretical optimal case, the image quality. In principle, this metric is applicable to any case involving TEM images. Due to the characteristics of feature detection, however, the algorithm exceeds in HRTEM and low dose imaging. Compared to a difference metric more conventionally used, the mean squared error (MSE), image regions of high contrast are inherently weighted more strongly, thus reducing the influence of background noise.

We demonstrate this on the example of determining the size of ZrO_2 precipitates in a Nb_3Sn substrate. HRTEM images of a 21.1 nm thick sample of Nb_3Sn are simulated using the multi-slice algorithm. The image for an infinite electron dose is used as the reference image. For simplicity, we simulate a spherical precipitate of ZrO_2 in the center of the sample, although arbitrary positions and shapes are equally feasible for the method. The upper row of Figure 1. shows the resulting HRTEM images for a ZrO_2 precipitate with a diameter of 5.2 nm and varying degrees of shot noise. The image difference algorithm compares each unit cell individually to a unit cell of the reference image. In order to get a measure for the precipitate diameter, unit cells with an image difference exceeding an electron dose dependent threshold are counted.

Application of the image difference metric is not limited to this illustrative case and can easily be extended to experimental HRTEM images. In the future, we plan on using the algorithm for optimizing experimental parameters in energy filtered STEM images in order to improve the signal-to-noise ratio.

[1] D. G. Lowe, International Journal of Computer Vision, 60, 91-110 (2004)

Acknowledgement: The authors gratefully acknowledge funding from FWF under grant nr. I4309-N36.

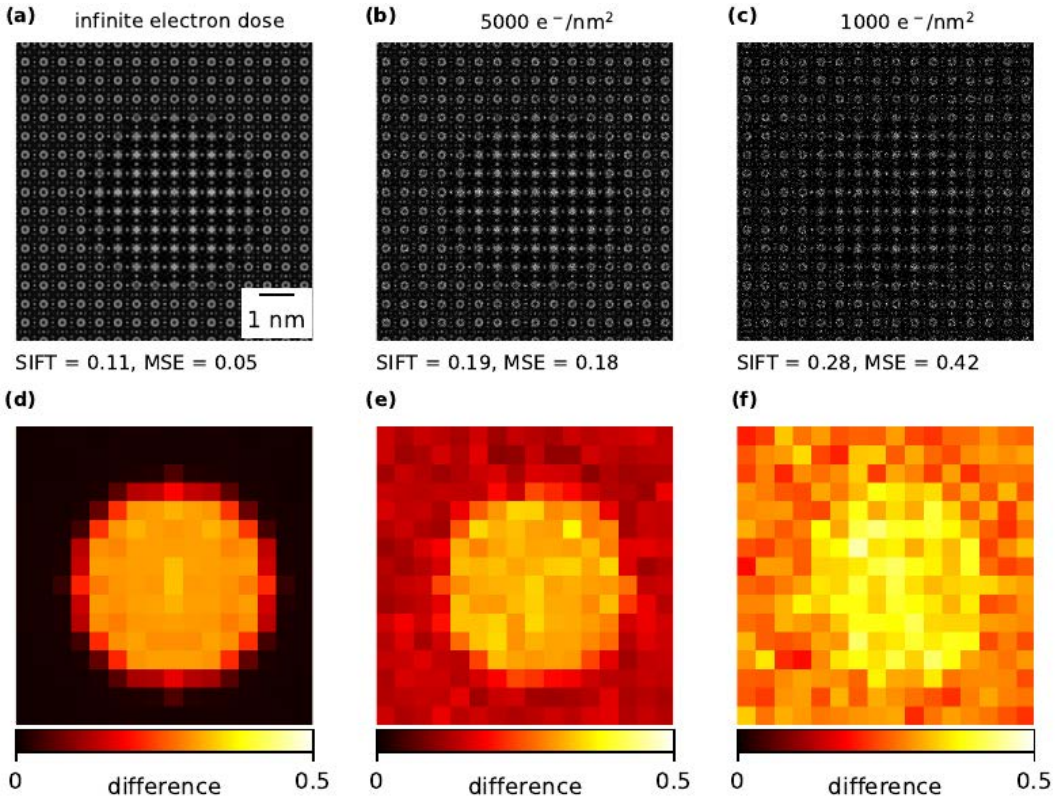

Fig. 1: **(a)**, **(b)**, **(c)** Nb_3Sn with a spherical precipitate of ZrO_2 with a diameter of 10 unit cells (5.2 nm) in the center, for a total sample thickness of 21.1 nm. **(d)**, **(e)**, **(f)** SIFT image difference of each unit cell of the images in **(a)**, **(b)** and **(c)**, respectively, to the reference image of pure Nb_3Sn.

Type of presentation: Poster

IM1-P-2686 Deep-learning model for automatic detection of cells in microscopy images

Mateašík A.[1], Marček Chorvátová A.[1,2], Čunderlíková B.[1,3], Chorvát D.[1]

[1]Dept. of Biophotonics, International Laser Centre, CVTI SR, Bratislava, Slovakia, [2]Dept. of Biophysics, FNS, Univ. Ss Cyril and Methodius in Trnava, Slovakia, [3]Faculty of Medicine, Comenius University in Bratislava, Slovakia

Email of the presenting author: dusan.chorvat@cvtisr.sk

A large number of image processing and computer vision methods have been used to address automatic cell detection in microscopy images, among which machine-learning methods, especially deep learning, have gained great popularity recently [1, 2]. However, this task still remains challenging due to various image acquisition techniques, low image contrast, large variance in cell shapes and/or cell counts, and presence of arbitrary cell occlusions in two dimensional microscopy images. In this work, we present a novel method utilizing trained model of a fully convolutional neural network for cell detection in microscopy images. The architecture of used convolutional network is based on the well-known U-Net architecture and it is used to produce an intensity probability map of cells existing in a given image with the local maxima attributed to cell centroids. The cell images taken in different experimental scenarios can have significantly different statistical intensity distributions for various types of cells or acquisition techniques, which could hamper convergence of the model. Therefore, U-Net was modified with introduction of the batch normalization operation at the input of every neuron to regularize the statistical distributions of its input data. Next modification counted the reduction of convolution kernels in each convolution layer, to improve convergence even for smaller datasets. To train the model, three image datasets were used: 40 fluorescence images of *Chlorella sp* algae cells, 40 bright-field images of KYSE-450 cells and 50 bright-field images of Jurkat cells. The traditional scheme 80 - 20 was employed during training with F-score of 97.60%. Experimental results demonstrated that the proposed model was capable of successful processing of variable-size images containing dense cell clusters with various level of cell densities, counts and occlusions.

Acknowledgement: The research leading to these results has received funding from LASERLAB-EUROPE (EU Horizon 2020 grant agreement no. 871124).

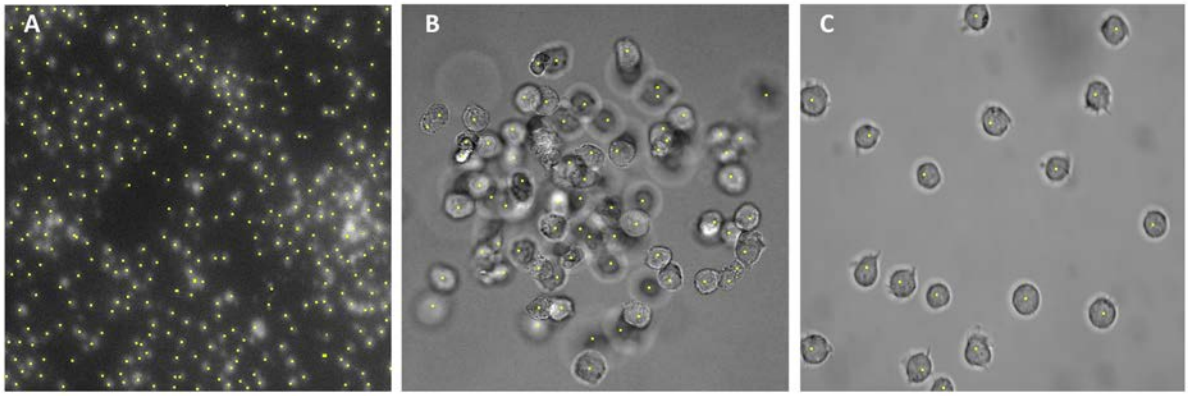

Fig. 1: Results of automated detection of cells in three different microscopy scenarios. From left: A) fluorescence image of *Chlorella sp* algae, B) bright-field image of KYSE-450 cells, and C) bright-field image of Jurkat cells. The yellow dots represent the detection output and indicate the centroid of detected objects.

Type of presentation: Poster

IM1-P-2611 Estimation of Pancreatic Islets Volume from Single Projection.

Janáček J.[1], Radochová B.[1], Habart D.[2]

[1]Laboratory of Biomathematics, Institute of Physiology ASCR, Prague, Czech Republic, [2]Diabetes Centre, Institute for Clinical and Experimental Medicine, Prague, Czech Republic

Email of the presenting author: jiri.janacek@fgu.cas.cz

Pancreatic islets (PI) grafts volume is routinely estimated using 2D images from light microscopy. Our goal is a precise PI volume estimator using contours of the 2D projections calibrated by measurement of 3D images from lightsheet microscope.

We processed 3D images of PI by minimization of the total variation functional with L1 data term (TV-L1) and segmented them by thresholding. The objects were then projected in the direction of the eigenvector corresponding to the least eigenvalue of the second moment tensor to obtain 2D contours of PI.

We constructed 3D model of PI by extruding 2D contour by union of balls which equatorial circles are inside the contour. The height of the extruded object was efficiently calculated using digital Euclidean distance transform [1]. Then we modified the height by a factor depending on the size of the contour to reflect increasing flatness in bigger islets. The single parameter of the factor function was estimated from 3D data by nonlinear regression.

In total, 850 islets were measured. Coefficient of determination was 0.98 in the nonlinear regression. The flatness factor decreased from 1.0 to 0.8 for the biggest islets.

[1] Breu H., Gil J., Kirkpatrick D., Werman M.: Linear time euclidean distance transform algorithms, IEEE Trans. PAMI 17 (1995), 529-533.

Acknowledgement: Supported by AZV CR (NU22-01-00141) and by MEYS (Czech-Bioimaging LM2018129).

Type of presentation: Poster

IM1-P-2696 Project „Pattern“ – an online tool for spatial analysis of immunolabeling in electron microscopy

Pinkas D.[1], Vlcak E.[1], Raabova H.[1], Janacek J.[2], Filimonenko V.[1,3], Hozak P.[3]

[1]Institute of Molecular Genetics ASCR v.v.i., Microscopy Center, Electron Microscopy Core Facility, Prague, Czech Republic, [2]Institute of Physiology ASCR v.v.i., Prague, Czech Republic, [3]Institute of Molecular Genetics ASCR v.v.i., Department of Biology of the Cell Nucleus, Prague, Czech Republic

Email of the presenting author: dominik.pinkas@img.cas.cz

Evaluation of immunolabelling in EM often lacks unbiased quantitative approach. We have developed an easy-to-use online tool for semi-automatic multi-stage analysis of immunolabeling on EM images spanning particle detection and classification, mathematical and statistical evaluation and visualization of results. This builds on previous work of Philimonenko et al. [1] and Schofer et al. [2]. The tool detects basic particles (“big” and “small” spheres) automatically and results of detection and identification can be manually reviewed and edited. Spatial relations can be analyzed in 2D and 3D microscopic data and along linear structures such as membranes and filaments. The tool uses pair correlation and pair cross-correlation functions for clustering and colocalization evaluation with results presented both numerically and graphically. Labelled structures are visualized via mapping and their spatial relations to other structures or particles are further evaluated as shown by Philimonenko et al. [3]. Statistical significance of detected patterns is calculated and presented in a comprehensive way without requiring a deep insight into statistical analysis. All results and respective settings can be exported. Particle coordinates can be kept on the server for prolonged periods of time to be reused with new settings or compared to new datasets. Projects can be shared with colleagues. For routine analysis, useful results should be available in just a few clicks. The tool is provided to the broad scientific community in open access mode by the IMG within the Czech-BioImaging research infrastructure. The tool emphasizes convenience and understandability of the interface and provides detailed explanations of all results, steps, values and options. The platform is modular and can be expanded with more capabilities in the future.
[1] doi:10.1006/jsbi.2000.4326
[2] doi: 10.1016/j.jsb.2004.01.014
[3] doi: 10.1007/s00418-013-1178-6

Acknowledgement: MEYS CR (LM2018129, LTC19048), ERDF (No. CZ.02.1.01/0.0/0.0/16_013/0001775 No. CZ.02.1.01/0.0/0.0/18_046/0016045)., TACR (TE01020118), IMG grant (RVO: 68378050)

IM2 Multi-modal and correlative microscopy

Type of presentation: Invited

IM2-IN-2637 Combining AFM with FIB/SEM in Nanofabrication

Winkler R.[1]

[1]Christian Doppler Laboratory for Direct-Write Fabrication of 3D Nano-Probes (DEFINE), Institute of Electron Microscopy and Nanoanalysis, Graz University of Technology, 8010 Graz, Austria

Email of the presenting author: robert.winkler@felmi-zfe.at

The ongoing trend towards miniaturization of components in electronics and other technologies is driving the development of suitable fabrication- and analysis tools for nanoscale structures. Versatile tools in this context are dual beam microscopes that combine a Scanning Electron Microscope (SEM) with a Focused Ion Beam (FIB). These beams enable nanofabrication via subtractive structuring (FIB milling, etching) and additive manufacturing (Focused Particle Beam Induced Deposition), as well as obtaining a variety of information about the sample (e.g. different imaging modes, X-ray spectroscopy). In contrast, for complementary information such as the quantitative sample morphology in 3D, mechanical, electrical and magnetic surface properties, Atomic Force Microscopy (AFM) is often the method of choice. While usually both techniques are done one after the other, for many questions it is advisable or even partly unavoidable to apply FIB/SEM and AFM in situ, in parallel or simultaneously. Therefore, integrating an AFM into a FIB/SEM chamber can provide new insights that are not accessible with stand-alone microscopes.
In this contribution we first discuss the benefits of AFM measurements in vacuum compared to ambient conditions. In a first use cases we present 3-dimensional reconstructions of sample volumes where the physical properties (e.g. mechanical, magnetic, electrical) can be mapped for each layer using advanced AFM modes and then correlated with information obtained by FIB/SEM. The individual layers can be produced either by FIB-slicing (subtractive tomography) or by layer-by-layer growth (additive tomography). Figure 1 shows subtractive tomography of polymer beads in an aluminum matrix, where the stiffness in each FIB slice was measured by the AFM. An example of additive tomography is given in Figure 2, where the electron beam was used to deposit single layers of material (FEBID), while the AFM monitored the layer-by-layer growth in situ [1]. In other applications, the SEM can be used to select the region of interest and precisely position the AFM for mechanical testing of nanostructures. In addition, we present correlative characterization of FIB cuts in a multilayer system combining FIB-SEM-EDX and AFM techniques. Again, we go beyond simple AFM based height and phase imaging and use more advanced AFM modes (magnetic/electric force, conductive AFM) to obtain comprehensive information of the sample. However, such AFM modes require specialized nanoprobes, therefore, we briefly outline the fabrication route of such advanced AFM tips via 3D-nanoprinting. The selected examples all demonstrate the advantages of correlative microscopy of a FIB-SEM dual beam microscope with an in situ AFM.

[1] C. Yang et al. ACS Appl. Mater. Interfaces 9, 24456 (2017)

Acknowledgement: Many thanks go to Harald Plank, Gerald Kothleitner, Jakob Ihrenberger, Lukas Seewald, Michele Brugger-Hatzl, Melanie Hannebelle, Chen Yang, and QD Microscopy

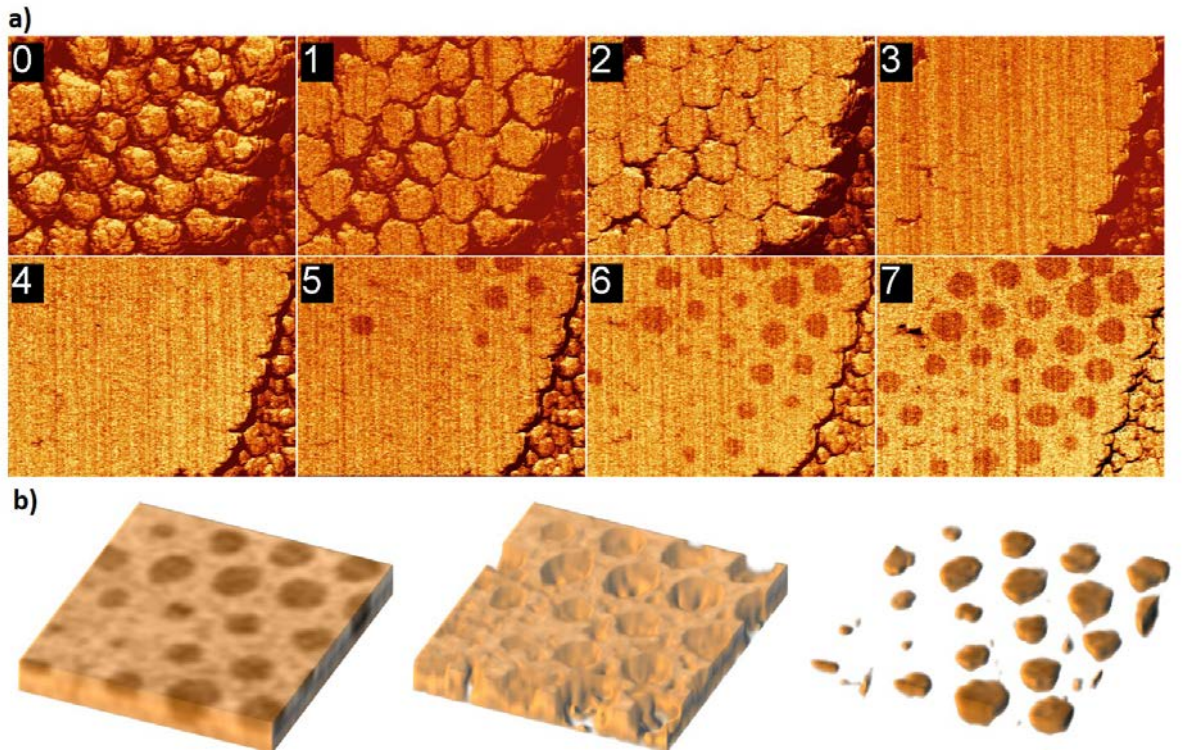

Fig. 1: Subtractive tomography of polymer beads embedded in sputtered aluminum. The AFM maps in a) display the stiffness of selected FIB slices. b) 3D-reconstruction of the volume with segmentation of matrix and PS beads

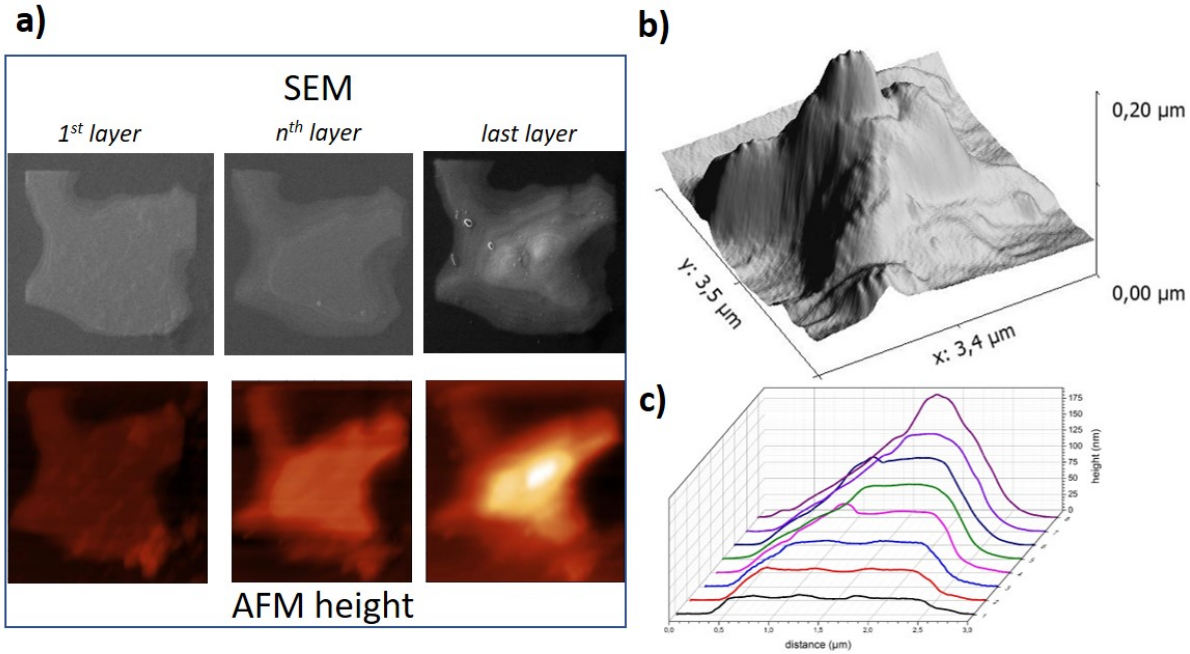

Fig. 2: Additive nanofabrication of a Platinum Matterhorn miniature grown by Focused Electron Beam Induced Deposition. a) After each layer SEM and AFM images were acquired, to monitor the growth process. b) AFM based 3D-reconstruction of the Matterhorn model. c) AFM height profiles for different layers

Type of presentation: Oral

IM2-O-2571 Combining Light, Raman, and Electron Microscopy in Imaging Viral Factories of Avian Reovirus

Ďurinová E.[1,2], Kaščáková B.[1], Mojzeš P.[3], Tůma R.[1]

[1]Faculty of Science, University of South Bohemia in České Budějovice, Czech Republic, [2]Biology Centre, Czech Academy of Sciences in České Budějovice, Czech Republic, [3]Faculty of Mathematics and Physics, Charles University, Prague, Czech Republic

Email of the presenting author: evadurinova12@gmail.com

Avian reovirus (ARV), a dsRNA virus of Reoviridae family, significantly affects the world poultry industry. The available vaccine is not economical and often inefficient due to new emerging ARV strains. The ARV replication is a promising target for viral inhibition and therefore for the design of lacking antiviral drugs. However, ARV replication and assembly mechanisms are poorly understood because it takes place in dense cytoplasmic inclusion bodies, the so-called viral factories (VF). Here we characterize the nature of VFs and follow their formation in cells.
First, we have established stable mammalian cell lines expressing non-structural (NS) proteins (μNS and σNS) which were fused to various fluorescent proteins (eGFP and mCherry). The cells were subsequently infected by an ARV S1133 vaccine strain. In addition, we studied the formation of VF-like bodies in solution using purified NS proteins. The resulting VFs were studied by various imaging techniques (refractive index tomography, epi-fluorescence live cell imaging, Raman microscopy, fluorescence recovery after photobleaching and transmission electron microscopy).
We observed the formation of VFs in real time at different stages of the viral infection. During the first stage the globules spontaneously arise by liquid-liquid phase separation and remain fluid, exhibiting high protein concentration (Figure 1). Expression of μNS in mammalian cells leads to fluid VF-like globules even in the absence of other viral components. However, viral infection is necessary for separation of □NS into VFs.

Acknowledgement: This project is supported by Czech-BioImaging LM2018129 and by ERDF CZ.02.1.01/0.0/0.0/15_003/0000441.

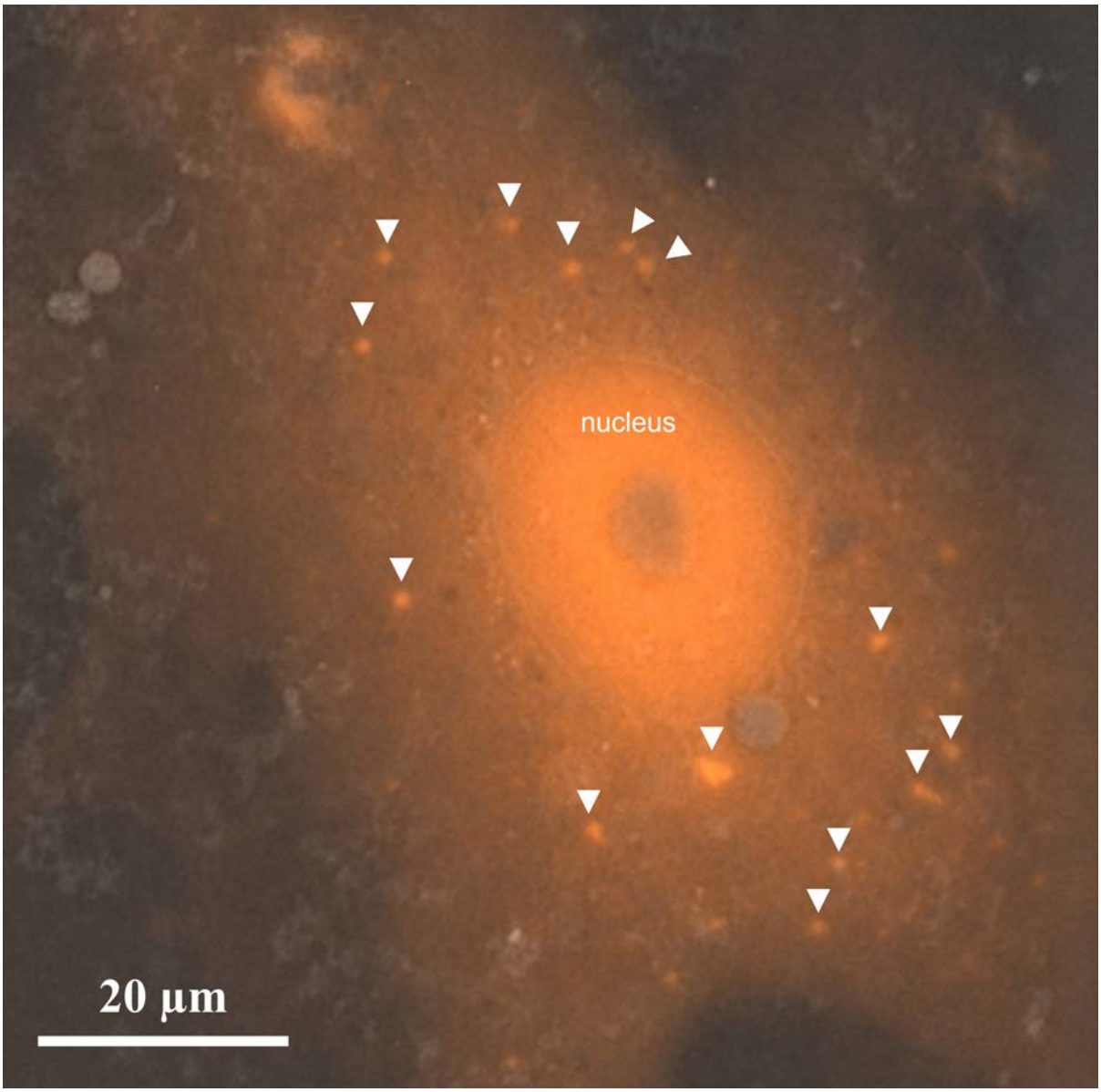

Fig. 1: An image of a mammalian cell (overlay of refractive index contrast and epifluorescence, taken by 3D Cell Explorer, Nanolive) producing fluorescently labelled viral protein σNS. With the advancing ARV infection, the protein is recruited into the viral factories (indicated by arrows).

Type of presentation: Oral

IM2-O-2520 In-situ electrical analysis with EBIC STEM: developments and applications

Hammer R.[1], Conlan A. P.[2], Moldovan G.[1], Cooper D.[2]

[1]point electronic GmbH, Halle (Saale), Germany, [2]Univ. Grenoble Alpes, CEA, LETI, Grenoble, France

Email of the presenting author: grigore.moldovan@pointelectronic.de

An emergent area in TEM is the ability to directly relate structure and composition with electrical properties, at different biasing conditions and with high spatial resolution. Several techniques can be applied, such as electron holography, pixelated STEM, differential phase contrast (DPC) STEM and electron beam induced current (EBIC) STEM. From these, EBIC STEM brings the ability to reveal internal electric fields, measure diffusion lengths and determine recombination strengths. Here, we present recent instrument developments and applications of EBIC STEM, with a particular focus on automatic quantification for measurement of fundamental material properties, and in-situ characterisation of nano structures and devices.

The technique is very straightforward, the focused electron beam is used as a virtual electrical probe to induce a minute current into the in-situ device, which is measured using a biasing holder connected to a low-noise high-speed imaging unit. Image interpretation for the case of simple structures is also very straightforward, as induced current is only present in areas with an internal electric field, which may be locally broadened by diffusion of charge carriers, and locally reduced by increased recombination activity at defect sites. Interpretation becomes more difficult for the case of complex structures, not only because the amount of induced current depends on the local energy loss, but also because Secondary Electrons (SE) give rise to an additional current overlaying onto the induced current [1]. Examples of application to test structures and new devices will be used to illustrate these important points, where EBIC has been performed in a probe corrected FEI Titan Ultimate [2,3].

We will show that the key advantage of EBIC STEM over other techniques is the ability to bridge between experimental images and device modelling as it measures the signal in the µA to fA range at each point on the sample. Therefore, image interpretation can always be assisted by an understanding of quantified values, from simple 2D devices to complex heterostructures with varying composition. Measurable effects of TEM sample preparation on charge carriers will be presented. It will also be illustrated how Monte Carlo simulations is used to support interpretation of data with overlapping SE and EBIC currents. Key to in-situ characterisation, examples of EBIC at different biasing conditions will be presented, including links to device modelling.

[1] WA Hubbard, M Mecklenburg, HL Chan, and BC Regan, Phys. Rev. Applied 10, 044066 (2018)

[2] AP Conlan, G Moldovan, L Bruas, E Monroy and D Cooper, J. Appl. Phys. 129, 135701 (2021)

[3] AP Conlan, MA Luong, P Gentile, G Moldovan, MI Den Hertog, E Monroy and D Cooper, Nanotechnology 33, 035712 (2022)

Acknowledgement: Cross-Disciplinary Program on Instrumentation and Detection of CEA, and “Recherches Technologiques de Base” Program of the French Ministry of Research.

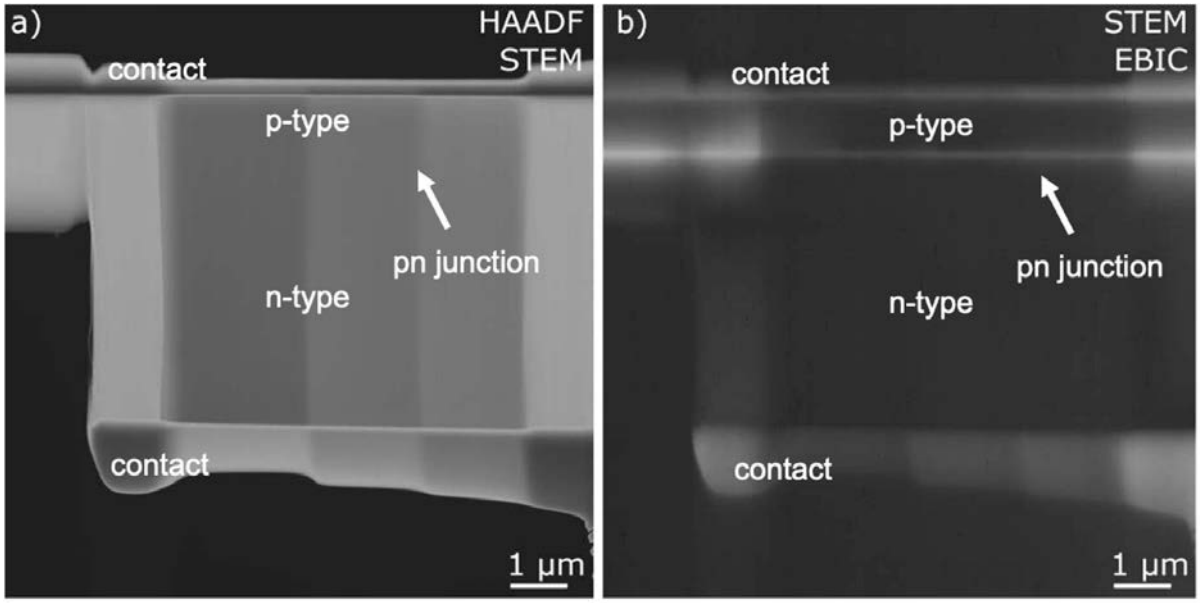

Fig. 1: (a) Simultaneous HAADF STEM and (b) EBIC STEM images of a Si diode test structure, prepared at increasing lamella thickness

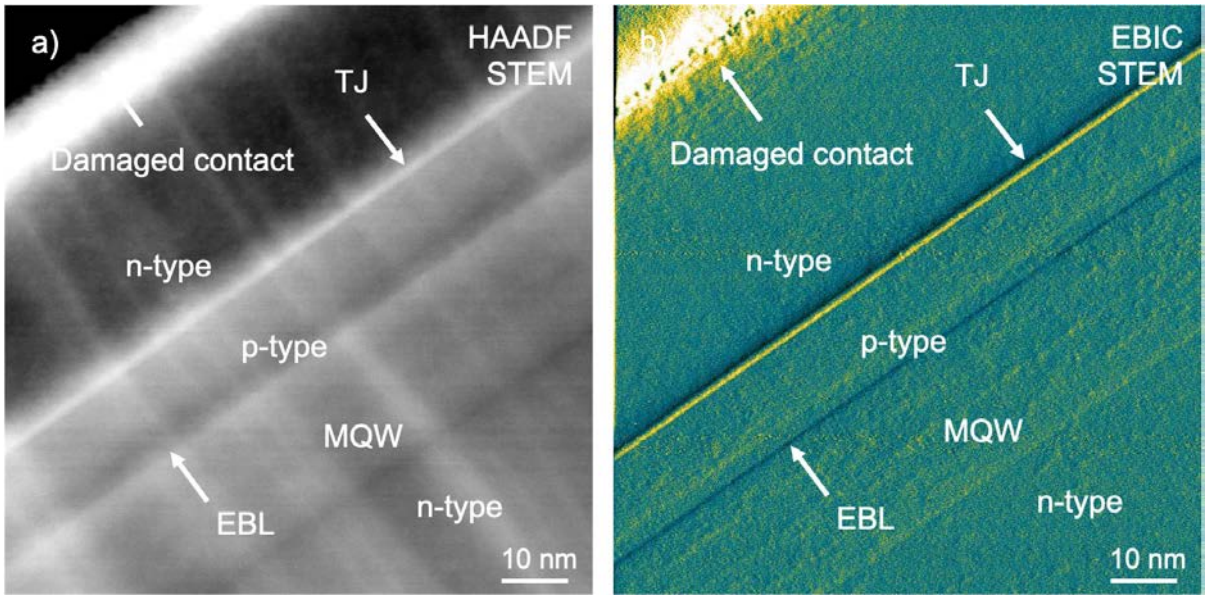

Fig. 2: (a) Simultaneous HAADF STEM and (b) pseudo-color EBIC STEM images of an AlGaN/GaN LED device showing Multiple Quantum Wells (MQW), a Tunnel Junction (TJ) and an Electron Blocking Layer (EBL).

Type of presentation: Oral

IM2-O-2612 Proof-of-Concept study for high-resolution correlative multimodal imaging and big data of a mouse brain

Fernandez-Rodriguez J.[1], Axer M.[2], Micaroni M.[1], Camacho R.[1], Amunts K.[2], Handschuh S.[3], Gloesmann M.[3], De Felipe J.[4], Merchan A.[4], Eberle A. L.[5], Ruland S.[2], Jaeger C.[6], Casares A.[6]

[1]Centre for Cellular Imaging, Shalgrenska Academy, University of Gothenburg, Sweden, [2]Institute of Neuroscience and Medicine, Forschungszentrum Jülich, Germany, [3]VetCore/Imaging, University of Veterinary Medicine, Vienna, Austria, [4]Instituto Cajal, Universidad Politécnica de Madrid, Spain, [5]Carl Zeiss MultiSEM GmbH, Oberkochen, Germany, [6]Carl Zeiss Microscopy GmbH, Oberkochen, Germany

Email of the presenting author: juliafer@cci.sahlgrenska.gu.se

The future of bioimaging is in the synergy between modalities, in the hard-to-navigate waters of the interdisciplinary divide. While 'omics' communities attempt to reduce complexity through advances in single-cell technologies, imaging communities are attempting to broaden their existing single-cell technologies to tackle the complex spatial systems biology of three-dimension (3D) models or entire organs (e.g., the brain), and pathological tissues such as tumors. Given the age-old trade-off between sample size and resolution, and between imaging structure and function, these challenges will only be met by designing new and more automated Correlative Multimodal Imaging (CMI) workflows that daisy-chain microscopes together to capture images of nanoscale biological processes across scales within a single organism.
The CMI approach aims at gathering information from a specimen with multiple imaging modalities that – when combined – create a highly informative, composite view of the specimen. It is a holistic approach that spans a large spatial resolution range from from mm to nm, and provides complementary information about the structure, function, dynamics, and the molecular composition of the sample. CMI is of strategic importance to a large and wide group of national and international life scientists, supporting many research activities, such as, to characterise synaptic changes and pathological protein aggregation underlying neurological diseases. In this context we have created in 2019 a European consortium, Big mUltimodal hIgh-resolution atLas Data Management, BUILD, to design a proof-of-concept approach to study and understand the brain's nerve fiber architecture and the resulting structural connectivity (e.g., to address diseases that affect myelination, such as MS). During the study the same sample was shipped to the different expert facilities all over Europe. We first prepared and visualized a mouse brain section with a low-resolution polarized microscopy, (Figure 1A). The same brain section was sent to a second facility where is prepared for scanning electron microscopy and X-ray tomography (1B). We then defined the volume of interest with X-ray tomography (1C), creating a reference 3D image dataset. After a successful evaluation of the X-ray the images were correlated with different scanning electron microscope systems to image the volume at high resolution for advanced analysis (SEM single and multi-beam systems and FIB-SEM, see Figure 1 D-F). Finally, datasets will be transferred to the Fenix infrastructure for segmentation analysis test and final storage. Thus, the combined usage of these interdisciplinary approach will finally enable the generation of unique brain atlases of different species, such non-human and human primates.

Acknowledgement: This work was supported by the Swedish Foundation for Strategic Research (SSF), for founding the Research Infrastructure Fellow program no. RIF14-0079.

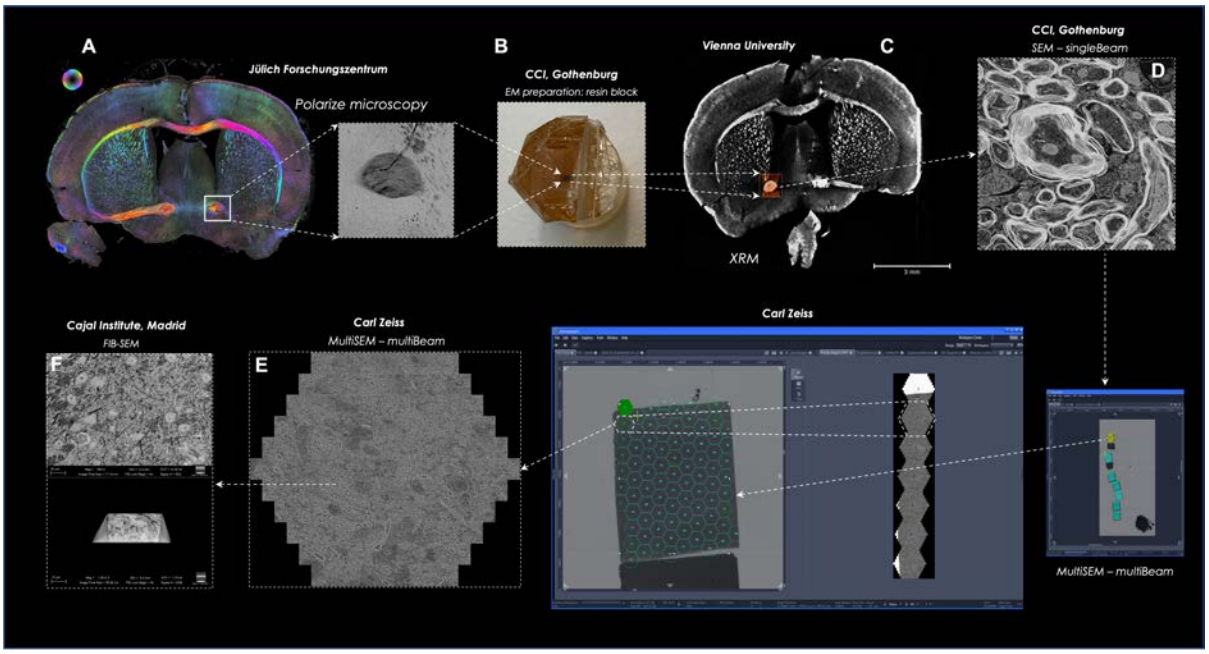

Fig. 1: Correlated multimodal imaging workflow of a mouse Brain section: (A) Polarize microscopy image; (B) Resin block prepared for electron microscopy; (C) X-ray image; (D) Image of the brain section taken with the SEM singlebeam; (E) Overview image taking with the MultiSEM multibeam microscope; (F) Image acquired with the focused ion beam.

Type of presentation: Oral

IM2-O-2635 3D-Nanoprinting of Magnetic Force Microscopy Tips

Brugger-Hatzl M.[1,2], Winkler R.[1], Seewald L.[1], Kothleitner G.[2,3], Plank H.[1,2,3]

[1]Christian Doppler Laboratory for Direct-Write Fabrication of 3D Nano-Probes, Graz University of Technology, Austria, [2]Graz Centre for Electron Microscopy, Steyrergasse 17, 8010 Graz, Austria, [3]Institute of Electron Microscopy and Nanoanalysis, Graz University of Technology, Austria

Email of the presenting author: michele.brugger-hatzl@felmi-zfe.at

Magnetic devices play an important role in modern electronics and data storage. To analyze magnetic nanoscale features, Magnetic Force Microscopy (MFM), an advanced mode of Atomic Force Microscopy (AFM), is an often used as characterization technology. To induce the magnetic sensitivity, commercial MFM cantilevers mostly use non-magnetic standard tips, which are covered with thin magnetic coatings. Such additional layers, however, increase the apex radii, which consequently reduce the lateral resolution capabilities in both, AFM and MFM scans. Furthermore, mechanical stress during scanning can lead to local delamination of the magnetic coating, which changes or even removes the magnetic sensitivity. To overcome those issues, a solid, magnetic nanoscale tip would be required, which can be a tough challenge when aiming on full cantilever chips. Following that motivation, we here demonstrate the application of Focused Electron Beam Induced Deposition (FEBID) for additive, direct-write 3D-nanoprinting of magnetic tips on prefinished AFM cantilevers.
After a brief introduction to 3D-FEBID, we turn into fabrication details of magnetic nano-tips from $HCo_3Fe(CO)_{12}$ precursor. We discuss the impact of process parameters such as electron energies, beam currents and patterning sequences revealed by SEM, EDX and TEM for consistent morphological, chemical and structural insights. Next, the basic performance of such MFM tips is demonstrated with special focus on lateral resolution, magnetic phase shift and signal-to-noise ratio. For further optimization, tip geometries were adjusted (see Figure 1) and subjected to different post-processing procedures such as post-irradiation with electrons/ions, thermal treatments and purification protocols to exploit their full potential. Finally, optimized FEBID-MFM tips were then tested on various magnetic samples (magnetic multilayer system (Figure 2), hard disc drives, magnetic recording tapes) and benchmarked to commercially available MFM tips (Figure 3). Finally, we briefly show two application examples in the field of correlative-microscopy, where SEM, EBSD, TEM, AFM and MFM are used on duplex steel and CuNiFe material systems. In summary, this contribution presents 3D-nanoprinting of novel MFM tips, the elaboration of a suitable fabrication parameter set and the application of those special tips in (correlative) microscopy experiments on various samples.

Acknowledgement: Many thanks go to Thomas Radlinger, and Stefan Mietsche for experimental support.

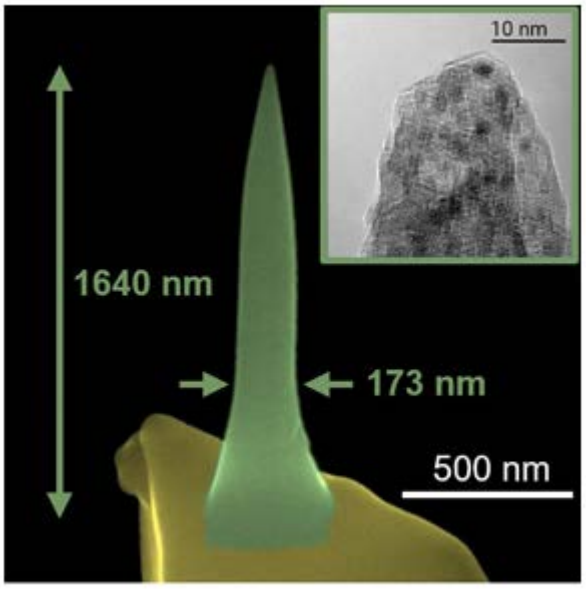

Fig. 1: SEM image of a Co_3Fe MFM tip fabricated by 3D-FEBID on a cantilever. The cone shaped tip is indicated in green, whereas the cantilever is indicated in yellow. The inset top right shows a TEM image of the tip apex.

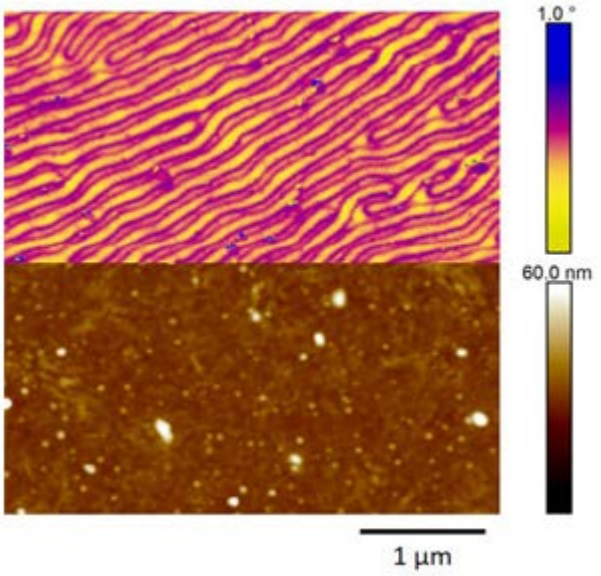

Fig. 2: MFM image (top) and topography image (bottom) of a magnetic multilayer system measured with a Co_3Fe tip.

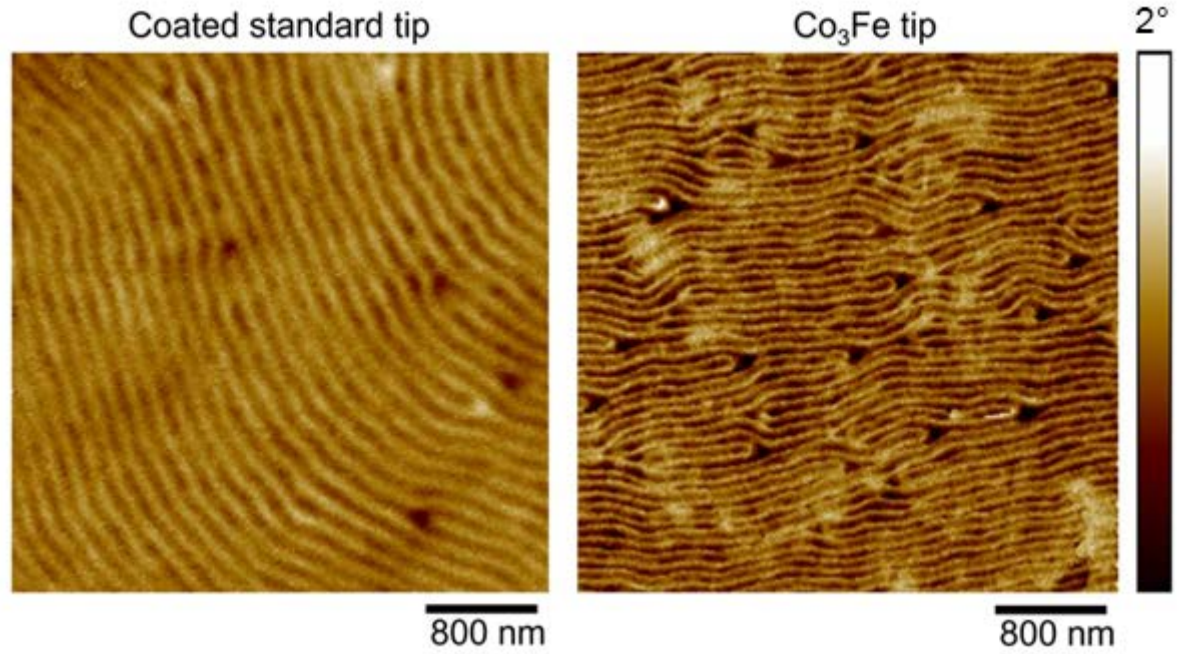

Fig. 3: Comparison of MFM images of a standard coated tip (commercial) and a Co_3Fe tip.

Type of presentation: Oral

IM2-O-2791 Correlative super-resolution and electron microscopy in plant samples

Franek M.[1], Koptašíková L.[2], Olšinová M.[2], Dvořáčková M.[1], Benda A.[2], Fajkus J.[1]

[1]Mendel Centre for Plant Genomics and Proteomics, Central European Institute of Technology (CEITEC), Masaryk University, Kamenice 5, CZ-62500 Brno, Czech Republic , [2]Charles University, Faculty of Science, Biology Section, Imaging methods core facility at BIOCEV, Průmyslová 595, 252 50 Vestec, Czech Republic

Email of the presenting author: 357550@mail.muni.cz

Super-resolution microscopy was experimentally established over 15 years ago [1,2,3] and soon found its way into the basic research of cellular structures in mammalian systems. Plant sciences are lagging behind in the application of these techniques for several reasons. First of all, sample preparation is more complicated and applying super-resolution microscopy in complex tissues such as roots or leaves is problematic due to high sample background fluorescence. Our work highlights common problems encountered during sample preparation (either isolated nuclei or whole-mount detection) for super-resolution microscopy. Moreover, we establish new approaches to facilitate the application of super-resolution microscopy in plant samples and test the uses of correlative light-electron microscopy in studying nuclear structures and genome replication. Taking advantage of replication tagging using the ethynyl deoxy-uridine (EdU)/Click-IT detection system, we optimized a protocol for the simultaneous detection of cell-cycle progression and ultrastructural analysis of plant nucleoli. Importantly, we demonstrate that Lowicryl embedding of EdU-tagged plant roots permits in-situ labeling of replication on semi-thick (500 nm) sections, which allows us to correlate spinning-disk images of replication profiles with thin sections for electron microscopy in the same root. Crucially, we show that dSTORM super-resolution imaging can be performed in Lowicryl-embedded sections with a high number of localizations and low background. Overall, we show that physical sectioning of plant tissues dramatically improves dSTORM performance and Lowicryl embedding is compatible with subsequent dSTORM imaging. It remains to be seen whether alternative labeling protocols, such as Halo-Tag or SNAP-tag protein labeling, can be used in the same setup. Using the protocols mentioned above, we were able to observe replication foci in S-phase colocalizing in low-contrast nucleolar regions, termed fibrillar centers and detect changes in nuclear/nucleolar volume related to cell-cycle progression.

References:

[1] Gustafsson MGL, 2000. Surpassing the lateral resolution limit by a factor of two using structured illumination microscopy. J. Microsc. 198:82-87. doi.org/10.1046/j.1365-2818.2000.00710.x

[2] Hell SW, Wichmann I, 1994. Breaking the diffraction resolution limit by stimulated emission: stimulated-emission-depletion fluorescence microscopy. Optics Lett. 19: 780-782. doi: 10.1364/OL.19.000780.

[3] Betzig et al., 2006. Imaging intracellular fluorescent proteins at nanometer resolution. Science 313:1642-1645.

Acknowledgement: We acknowledge support from CSF project 19-11880Y, project INTER-COST LTC18048 and LTC20003, ERDF - Project “SINGING PLANT“ and the Czech Bioimaging initiative.

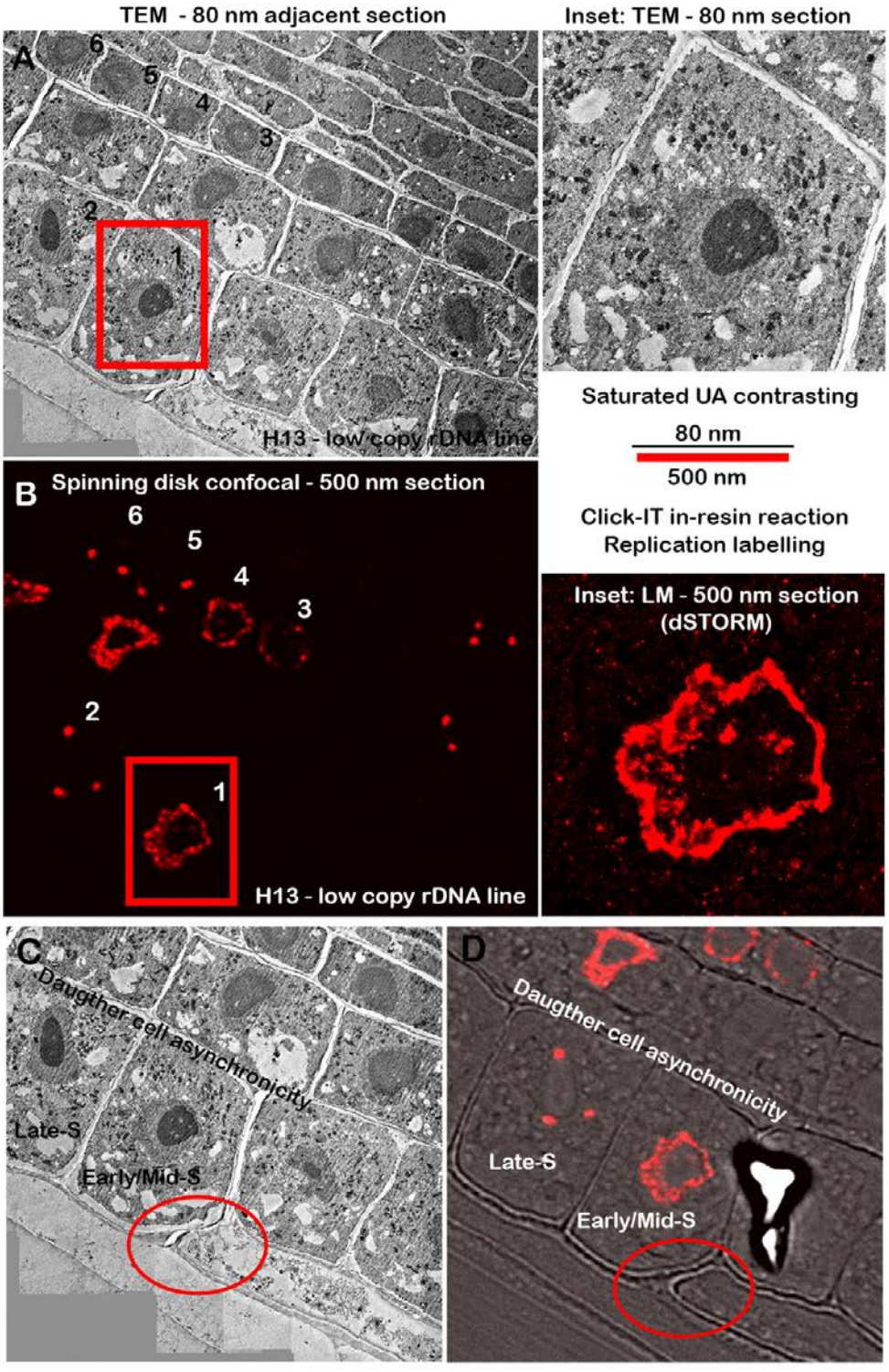

Fig. 1: Imaging of 80 nm and 500 nm root sections with transmission electron microscopy and light microscopy (A and B, respectively). Asynchronicity of adjacent (daughter) cells is apparent in figures C and D, where the distribution of EdU is different in early/mid-S-phase (diffuse pattern) and late S-phase (focal spots in chromocenters).

Type of presentation: Oral

IM2-O-2695 Atomically Sharp Domain Walls in an Antiferromagnet

Michalička J.[1], Křížek F.[2], Reimers S.[3,4], Kašpar Z.[2], Man O.[1], Rusz J.[5], Idrobo J. C.[6], Wadley P.[3], Jungwirth T.[2]

[1]CEITEC, Brno University of Technology, Czech Republic, [2]Institute of Physics of Czech Academy of Science, Prague, Czech Republic, [3]School of Physics and Astronomy, University of Nottingham, UK, [4]Diamond Light Source, Harwell Science and Innovation Campus, Didcot, UK, [5]Department of Physics and Astronomy, Uppsala University, Sweden, [6]Center for Nanophase Materials Sciences, ORNL, Oak Ridge, USA

Email of the presenting author: jan.michalicka@ceitec.vutbr.cz

Efficient manipulation of antiferromagnetic (AF) domains and domain walls has opened up new avenues of research towards ultrafast, high-density spintronic devices **[1,2]**. AF domain structures are known to be sensitive to magnetoelastic effects, but the microscopic interplay of crystalline defects, strain and magnetic ordering remained largely unknown. Recently, we have explored antiferromagnetic CuMnAs thin films in which imaging by x-ray photoemission electron microscopy (XPEEM) revealed that its AF domain structure is dominated by nanoscale crystalline defects **[3]**. The results emphasized the crucial role of these defects in determining the AF domains and domain walls, and provided a route to optimizing device performance in term of scaling limits for the data density in the bulk of the antiferromagnet. However, even smaller magnetic objects were indirectly observed in the material, but they remained below the detection limit of the used established XPEEM methods.

Here, we achieve atomic resolution imaging of abrupt AF magnetic domain walls in CuMnAs epilayers by utilizing scanning transmission electron microscopy (STEM), differential phase-contrast (DPC) and 4D-STEM techniques **[4]**. Identification of the magnetic domain DPC signal is based on the specific symmetry of the CuMnAs crystal, where the opposite magnetic Mn sublattices occupy crystallographically distinct noncentrosymmetric sites, **Fig. 1A**. With focus on small field-of-view high-resolution imaging, we could associate the DPC-STEM signals with two types of abrupt Néel vector reversals, schematically illustrated in **Fig. 1C and D**: The first type occurs at a crystallographic antiphase boundary defect (**Fig. 1C**), while the second type forms in a part of the epilayer with no crystallographic perturbation detectable by STEM (**Fig. 1D**). **Fig. 2** and **Fig. 3** then show the DPC-STEM imaging and signal analysis of each type of the domain wall. Experimental and analytical DPC-STEM measurement setup and discussion of structural artifacts potentially influencing the DPC signal will be presented together with a perspective on applications of devices based on CuMnAs.

References:

[1] Jungwirth, T. et al. Antiferromagnetic spintronics. Nature Nanotechnology, 11(3), pp. 231–241 (2016)

[2] Wadley, P. et al. Electrical switching of an antiferromagnet. Science, 351(6273), pp. 587–590 (2016)

[3] Reimers, S. et al. Defect-driven antiferromagnetic domain walls in CuMnAs films. Nature Communications, 13(1), pp. 724 (2022)

[4] Křížek, F. et al. Atomically sharp domain walls in an antiferromagnet. Science Advances, 8(13), pp. eabn3535 (2022)

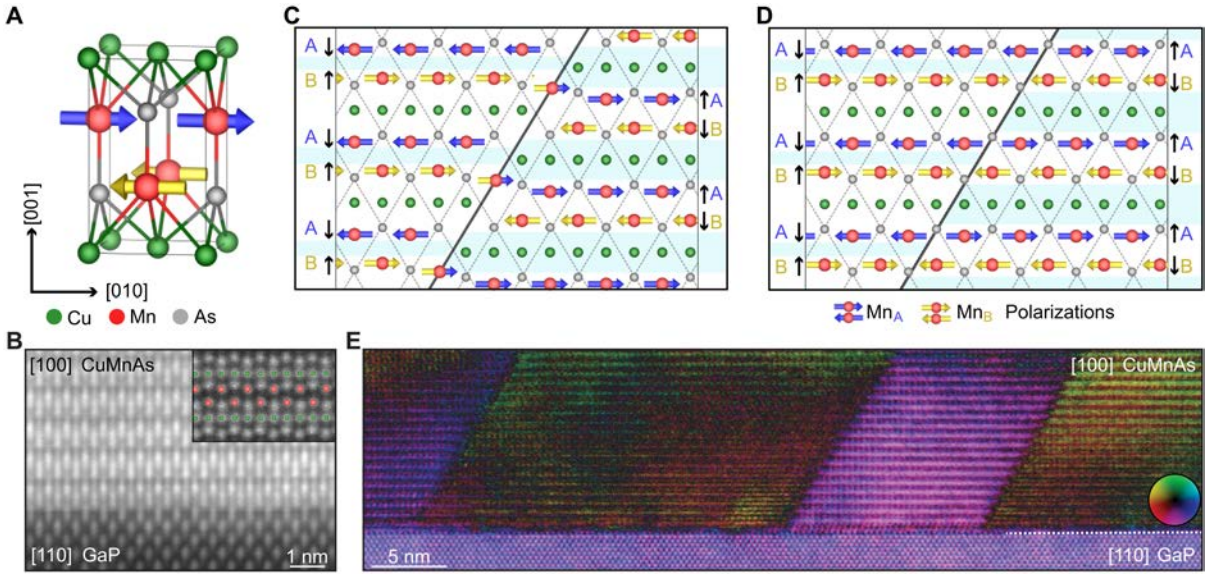

Fig. 1: (A) CuMnAs unit cell. (B) HAADF–STEM of [100] CuMnAs epilayer on GaP. (C,D) Atomically sharp domain walls at antiphase boundary defect and in unperturbed area of the CuMnAs single crystal, respectively. Black arrows represent Lorentz force direction at individual sublattices. (E) DPC-STEM overview of atomically sharp domain walls in CuMnAs.

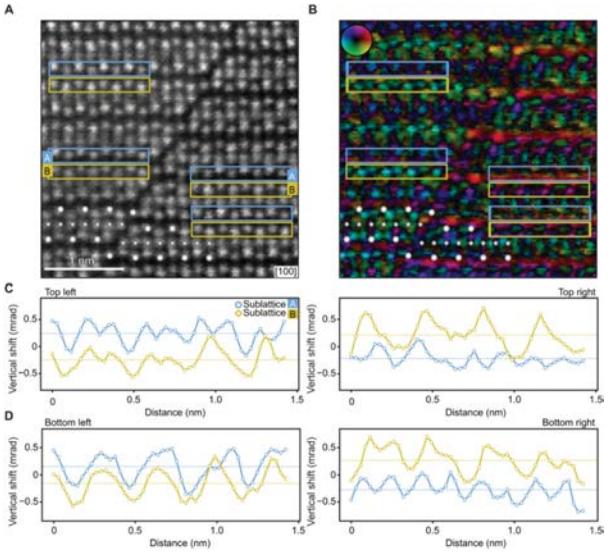

Fig. 2: (A) HAADF-STEM of CuMnAs with antiphase boundary defect. Rectangles A (blue) and B (yellow) label upper and lower Mn sublattices. (B) DPC-STEM of the area. (C) DPC horizontal line profiles from selected top areas on each side from the boundary corresponding to Mn_A and Mn_B sublattice. (D) Same as (C) for the bottom areas.

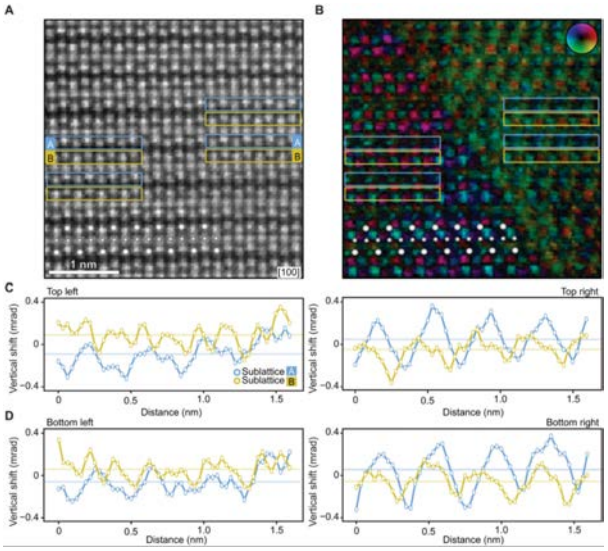

Fig. 3: Same as (A) to (D) in Fig. 2 for the domain wall in a part of the CuMnAs without a detectable crystal defect. The used experimental method, including the applied digital mask, is identical to Fig. 2.

Type of presentation: Oral

IM2-O-2563 Correlative Raman microscopy, SEM and EDS – The combined evaluation of a whole sample mapping of a Chelyabinsk meteorite fragment

Fitzek H.[1], Schmidt R.[1,2], Nachtnebel M.[1], Rattenberger J.[1], Zankel A.[1,2], Hofer F.[1,2], Schroettner H.[1,2]

[1]Graz Centre for Electron Microscopy, Steyrergasse 17, Austria, [2]Institute of Electron Microscopy and Nanoanalysis, NAWI Graz, Graz University of Technology, Steyrergasse 17, Austria

Email of the presenting author: harald.fitzek@felmi-zfe.at

The correlation of different microscopic techniques has seen increased interest in recent years due to the possibility of combining the strengths of multiple techniques. In addition to the practical challenges with regard to sample preparation, instruments design and the need for operators experienced in multiple techniques, unique data treatment challenges arise when combining data sets with different resolutions and contrast mechanism. Two key questions arise. How can a SEM image with a pixel resolution of 30 nm, an EDS mapping with a pixel resolution of 100 nm and a Raman mapping with a pixel resolution of 1 µm that are distorted against each other (different contrast mechanism) be combined into a single map? How can we evaluate the resulting map that consist of Raman bands, EDS-elemental concentrations and SEM contrast values? We want to address these questions (on the example of a whole sample Raman-SEM-EDS-mapping of the Chelyabinsk meteorite), but please note that these approaches generalize to other combinations.
The basic approach of our workflow is shown in figure 1. Starting from the separated mapping data, we start with an evaluation of the separated data as far as possible. This serves the purpose of both reducing the amount of data as well as preserving the advantages of established evaluation routines as far as possible. The second step is to correlate the mappings based on common features visible in all mappings and interpolating everything to the resolution of the most high-resolution technique (BSE in this case). This way a combined “super-spectral-map” is generated that contains all the relevant analytical information of the separated mappings. In the final step a variety of option are available to evaluate the combined data. In this case we opted for a random forest algorithm for the classification of the phases of the meteorite fragment (figure 2a). Note that none of the initial techniques (SEM, EDS, Raman) is capable of differentiating all of the phases on its own, which is one of the main benefits of correlative microscopy. In a second evaluation step we used the combination of the random forest classification and the at-%-quantification from the EDS for a further analysis of the phase. The example of the pyroxene phase, which divides into two compositional clusters is shown in figure 2 (b,c).
To sum up we aim to provide a workflow for correlating and combining large datasets of various microscopic techniques, whilst also pointing out some of the best options for evaluating those combined mappings, using the fascinating example of a meteorite fragment.

Acknowledgement: Financial support: “HRSM-Projekt ELMINet Graz” (BMBWF), “TIMELY” (SP-2020-02, ACR, BMDW), “Inno. Mat.” (SP2016-002-006; ACR)

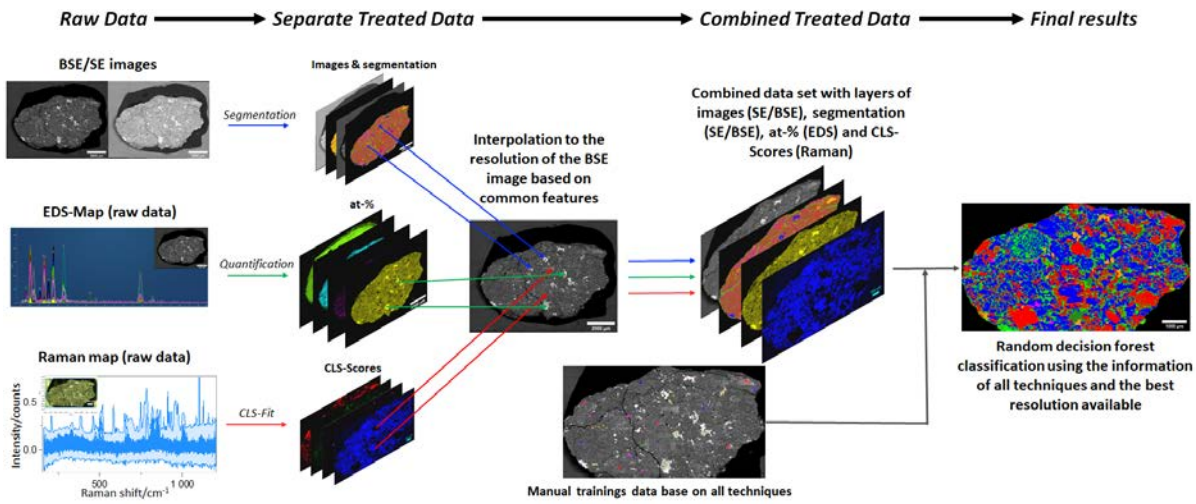

Fig. 1: Summary of the workflow used to correlate, combine and evaluate the Raman, SEM and EDS mappings of the Chelyabinsk meteorite. The detailed results are shown in figure 2 below.

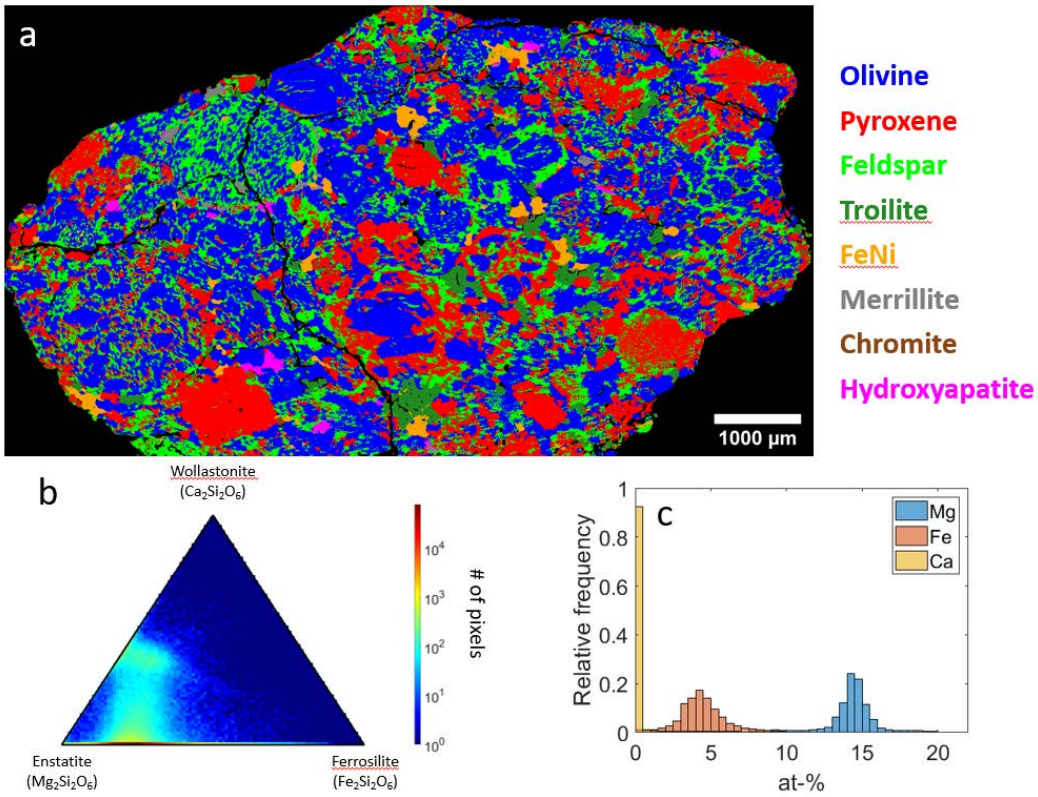

Fig. 2: (a) Random forest evaluation of the phase distribution of the Chelyabinsk meteorite fragment using a combined SEM, Raman, EDS mappings. (b) & (c) Evaluation of the composition of the pyroxene phase in the Wollastonite-Enstatite-Ferrosilite triangle (b) and in terms of the at-% in (c) based on the data in (a).

Type of presentation: Oral

IM2-O-2719 Integrated light-4D-STEM: from fluorescence microscopy and sample thickness mapping to powder diffraction analysis

Skoupy R.[1,2,3], Boltje D. B.[2,4], Hoogenboom J. P.[2], Jakobi A. J.[1,3]

[1]Bionanoscience, Delft University of Technology, Delft, NL, [2]Imaging Physics, Delft University of Technology, Delft, NL, [3]Kavli Institute of Nanoscience, Delft University of Technology, Delft, NL, [4]Delmic B.V., Delft, NL

Email of the presenting author: r.skoupy@tudelft.nl

Multimodal and correlative imaging is one of the hot topics in the microscopy field. There is a wide variety of techniques including correlative light and electron microscopy (CLEM). By combining different techniques in a single setup, more information from the ROI can be collected with higher positioning accuracy. We demonstrate how a fluorescence microscope (FM) integrated into a SEM chamber can be transformed into a high-resolution 2D-STEM detector of transmitted electrons. Such a detector can be operated in both fluorescence/light and electron detecting mode: ROI selection can be done by fluorescence imaging, while secondary or backscatter electron imaging allows analysis of sample ultrastructure and deep analysis of scattering/diffraction patterns provide the geometrical and crystalline composition of the sample. The system is geometrically calibrated for sample thickness mapping [1] and enables such analysis together with other 4D-STEM methods.

We demonstrate the utility of the setup on Powder Nanobeam Diffraction (PNBD) [2] analysis of mouse lung tissue including inhaled TiO2 nanoparticles (Fig. 1a; thin section; thickness approx. 100 nm). Regular analytical techniques available in an SEM would enable identification of the presence of TiO2 particles without access to information on the crystal form, whereas the resulting PNBD radial profile indicates the presence of tetragonal anatase (Fig. 1g). The initial blurring of individual diffraction patterns can be suppressed by deconvolution with a point spread function estimated from the same dataset (Fig. 1c-e).

The light-based 4D-STEM detector may be combined with a focused ion beam for precise determination of sample thickness during sample preparation, or used at low temperatures when a suitable detector is available [3]. As the result, a combined FM-cryo-FIB-4D-STEM microscope is created and can be used for deep analyses of diverse samples.

References:
[1] Skoupy, R. and Krzyzanek, V., Microsc. Microanal. 2021, 27 (Suppl 1), pp. 1602.
[2] Slouf, M. et al., Materials 2021, 14, 7550.
[3] D. Boltje et al., Microsc. Microanal. 2021, 27 (Suppl 1) , pp. 3228 – 3229.

Acknowledgement: The authors acknowledge funding by the Dutch Research Council (NWO-TTW no.17152) and the European Research Council (ERC-StG-852880).

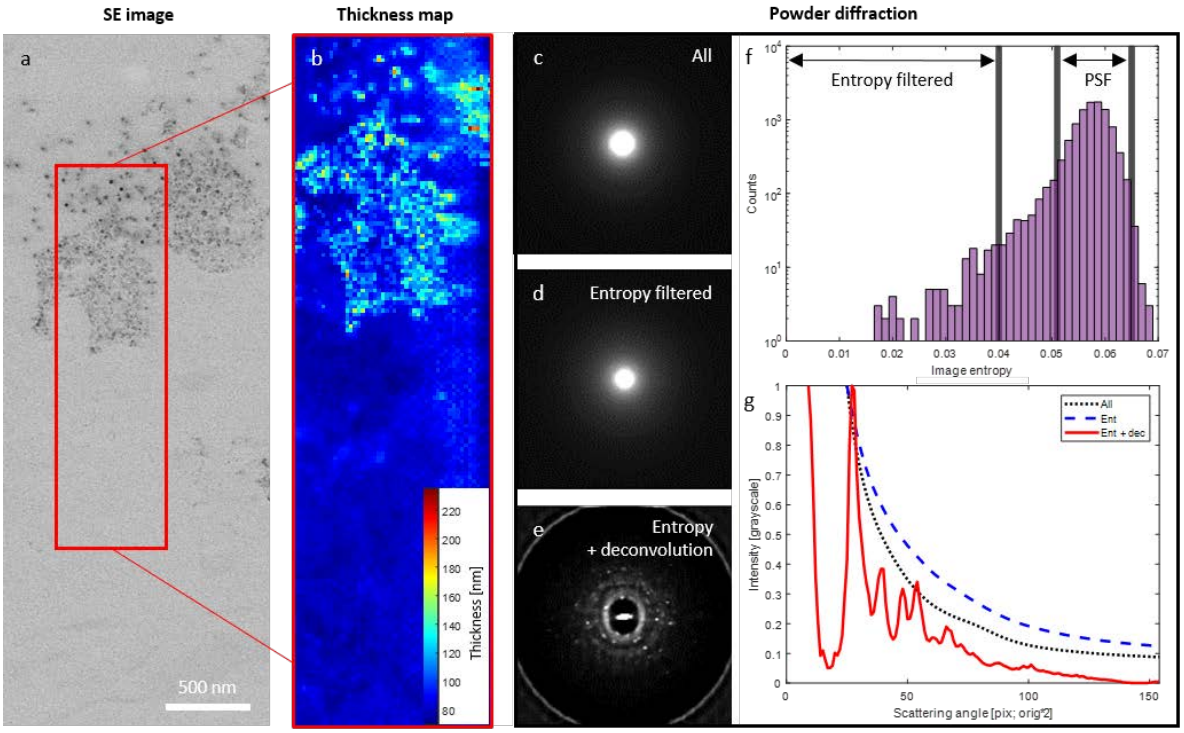

Fig. 1: (a) Mouse lung thin section with high-density particle clusters. (b) Local thickness map (dataset 50×200 points; for Embed812 resin). (c-e) Powder diffraction patterns with different processing. (f) Entropy histogram. (g) Powder diffraction radial profiles indicate TiO2 in the tetragonal crystal form of anatase.

Type of presentation: Oral

IM2-O-2528 Analysis of sampled airborne particles by correlative microscopy

Schumann J.[1], Dziurowitz N.[1], Thim C.[1], Peters T.[1], Meyer-Plath A.[1]

[1]BAuA - Federal Institute for Occupational Safety and Health, Unit 4.5, Berlin, Germany

Email of the presenting author: Schumann.John@baua.bund.de

While breathing, humans inhale a large variety and number of airborne objects that are part of the so-called exposome [1]. Nonetheless, origin, composition, shape and concentration of inhaled solid objects are mainly unknown as they depend on many details of the natural surroundings and the living or working environment and vary in the course of a day. They generally comprise natural and manufactured particles and fibres as well as bioaerosols, e.g., microorganisms, viruses or pollen. Depending on their aerodynamic properties, they may reach different compartments of the respiratory tract. Particular attention must be paid to objects that are toxic either due to chemical composition or biologic activity, or due to biodurability and respirability. It is therefore necessary to improve knowledge about the presence and nature of the respirable solid fraction of the exposome. Here, we describe our approach to an automated detection, classification and quantification methodology for solid airborne objects. It quantifies particles and fibres collected on track-etched membrane filters by first imaging filter areas representing a specific sampled air volume with scanning electron microscopy (SEM). High-resolution images allow localising and morphologically classifying objects based on secondary electron (SE) contrast. Elemental information is acquired by energy dispersive X-ray spectroscopy (EDS). Whenever elemental data is insufficient for identification, e.g., for carbon-based materials, complementing optical and Raman microscopic analyses are performed. All involved microscopes are operated with respect to stage control as well as images and spectra recording by our fully automatic in-house software [2]. Using constellation matching algorithms for the filter pores, objects of interest that are visible only in SEM can be located in the confocal Raman microscope with a spatial precision better than the optical diffraction limit [3]. This way, all optical and SE images as well as spectral mapping data are spatially correlated. Artificial neural network-based object segmentation allows to attribute compositional information to individual particles and fibres aiming at classifying them by means of shape, elemental composition and chemical characteristics.

[1] Wild, C.P. The exposome: from concept to utility. Int. J. Epidemiol. 2012, 41, 24–32, doi:10.1093/ije/dyr236

[2] Schumann, J.; Bäger, D.; Dziurowitz, N.; Thim, C.; Meyer-Plath, A. Retrieving SEM sample positions under limited relocation accuracy using digital image processing. Proceedings of the MC2019 Conference 2019, Berlin; pp 391–392

[3] Meyer-Plath, A. Correlating SEM and Raman Imaging of Nucleopore Filter Sampled Nanofibers: doi: 10.13140/RG.2.2.11130.72641. Virtual Raman Imaging Poster Summit 2020

Acknowledgement: I would like to acknowledge Matthias Hemmleb (point electronic GmbH) for the collaboration.

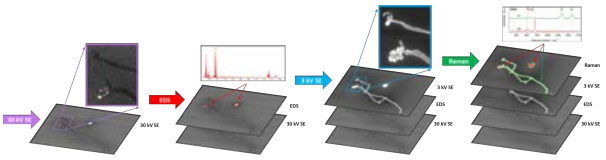

Fig. 1: Correlative microscopy with SEM-SE, EDS and Raman signals

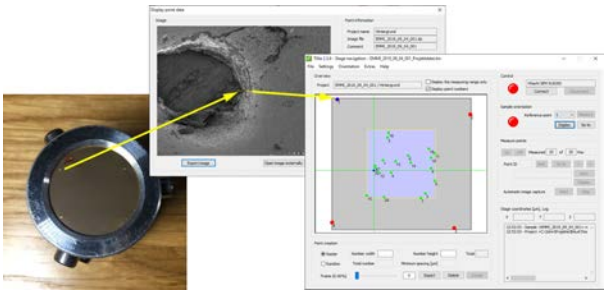

Fig. 2: Stage navigation software TiNa with sample orientation

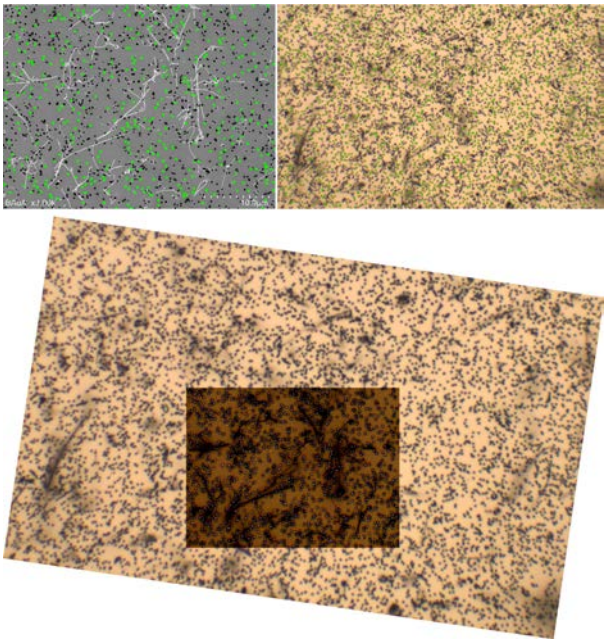

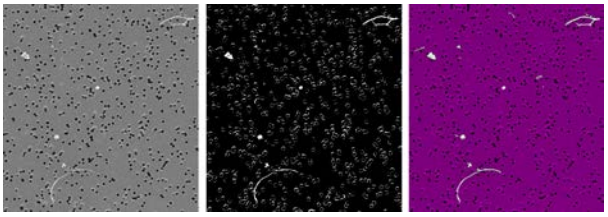

Fig. 4: Comparison of object segmantation, left: original SEM-SE image, middle: segmentation with classical image processing algorithms, right: segmentation with artificial neural network

Fig. 3: Image matching between SEM-SE image and Raman optical image using a constellation matching algorithm

Type of presentation: Oral

IM2-O-2693 Micro X-ray computed tomography as an extension to light microscopy and FIB/SEM

Löffler M.[1,2], Rellinghaus B.[1,2]

[1]Dresden Center for Nanoanalysis (DCN), Technische Universität Dresden, Dresden, Germany, [2]Center for Advancing Electronics Dresden (cfaed), Technische Universität Dresden, Dresden, Germany

Email of the presenting author: markus.loeffler@tu-dresden.de

Laboratory X-ray imaging and X-ray computed tomography (XCT) provide non-destructive characterization capabilities across a range of length scales, allowing for the observation of features with sizes from millimeters to micrometers down to several 10 nanometers. Especially µXCT can be seen as an established extension to conventional light microscopy to full three-dimensional imaging even for light-opaque objects. With a resolutions down to 700 nm, µXCT can not only provide insights into materials in a non-destructive manner, but is also capable of in-operando or in-situ imaging of whole devices. Due to absorption and/or phase contrast imaging, the method is suitable for samples of low or high atomic numbers alike. As such, µ-XCT is also an ideal extension of conventional FIB/SEM imaging to larger volumes for e.g. hierarchical or multi-scalar characterization concepts. Furthermore, the technology enables scientists to answer questions where the relevant structures are inaccessible to other methods of imaging and where the 3D imaging data can serve as a starting point for elaborate finite-element models.

The talk will briefly introduce the basic concepts of X-ray tomography and discuss some advantages and limitations of the technology with respect to the Zeiss Versa 520 X-ray microscope. The presented application examples of hard and soft materials include through-silicon-via structures, which were screened for defects, micro-opto-electro-mechanical systems (MOEMS) tested in-situ and low-Z materials imaged using propagation phase contrast.

Acknowledgement: The authors acknowledge our partners from Fraunhofer IZM-ASSID and Technische Universität Dresden for providing the respective samples.

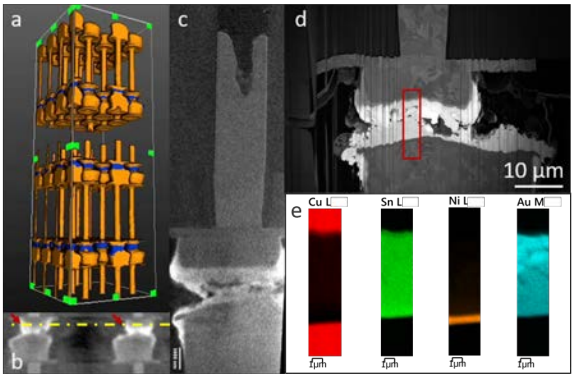

Fig. 1: Multiscalar analysis of a multi-layer through-silicon-vias (TSV) and solder bumps test chip using a,b) µXCT, c) nXCT, d) FIB/SEM and e) EDX. Sample courtesy of Fraunhofer IZM-ASSID. Several pecularities can be identified: a,c) incomplete TSV-filling, b,c) anomalous solder flow and void formation, d,e) void and intermetallic phase formation.

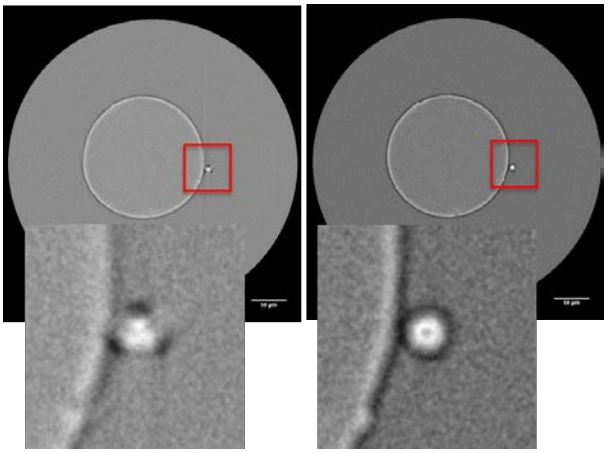

Fig. 2: Reconstructed center slice thorugh a silica sphere and a carbon fibre obtained using propagation phase contrast imaging. Left: Raw data, Right, aligned data. The use of phase objects allows for a precise alignment of the angle-dependent stage shifts and improves the 3D resolution of the tomographic reconstructions

Type of presentation: Oral

IM2-O-2938 From mammalian neuronal circuits to synapses: correlative multimodal imaging using hard X-rays

Bosch C.[1]

[1]Sensory Circuits and Neurotechnology lab, The Francis Crick Institute, London, UK

Email of the presenting author: carles.bosch@crick.ac.uk

Integrating physiology and structure at the neuronal circuit scale can provide a mechanistic understanding on how that circuit works. A correlative multimodal imaging pipeline that combines in vivo 2-photon microscopy (2P), synchrotron X-ray computed tomography with propagation-based phase contrast (SXRT) and serial block-face electron microscopy generates these multimodal maps reliably. In it, SXRT brings subcellular context over multi-mm3 landscapes non-destructively. SXRT also enables a bridging use: 2P and SXRT datasets can be warped at single-cell accuracy, informing on optimal specimen trimming strategies. Finally, this pipeline is compatible with other complementary hard X-ray imaging modalities: X-ray nano-holotomography resolves lateral dendrites of mitral and tufted neurons of known physiological profiles, and X-ray ptychographic tomography can resolve synapses in tissue. Altogether, this experimental approach enables harnessing the resolving power of multiphoton, hard X-ray and volume electron microscopy technologies to create detailed multimodal maps of brain circuits.

Type of presentation: Oral

IM2-O-2629 Automated and correlative SEM-EDX-Raman particle analysis on fine dust filters of extreme events: New Year's Eve and Sahara dust

Nachtnebel M.[1], Schroettner H.[1,2], Rattenberger J.[1,2]

[1]Graz Centre for Electron Microscopy (ZFE), Steyrergasse 17, 8010 Graz, Austria, [2]Institute of Electron Microscopy and Nanoanalysis (FELMI), NAWI Graz, Graz University of Technology, Steyrergasse 17, 8010 Graz, Austria

Email of the presenting author: manfred.nachtnebel@felmi-zfe.at

Various natural or manmade events can have major impacts on the local and nationwide air quality. This includes Sahara dust events and fireworks during New Year´s Eve nights, where high fine dust concentrations are registered. To obtain information about the presence of the different elements and materials in particulate matter (PM) in the air, various qualitative and quantitative methods are available. In this study scanning electron microscopy (SEM) combined with energy dispersive spectroscopy (EDX) and Raman spectroscopy were used to analyse PM at fine dust filters. Although quantifying the element concentration via EDX is not permissible in this particle size fraction, the composition of each individual particle can still be revealed.
To enable this, absolute filters tapes (AFT) were investigated in a correlative microscope. These filters are standardly used in air quality monitoring to measure the fine dust concentration at various sites on an hourly basis. To obtain initially a good spatial resolution in the used SEM (Zeiss, Sigma 300 VP), the electrically non-conductive filter was coated by carbon evaporation. Three of the recorded samples are shown in this abstract, while several thousand of particles are automated recorded each: New Year's Eve 2017/18, New Year's Eve 2020/21 and a measurement at the night 23th of December 2020. The weather propagation conditions of the three nights are comparable as always an atmospheric inversion and a comparable windspeed prevailed [1]. Figure 1 shows the comparison of the fine dust concentration at both New Year's Eve nights. It can clearly be seen that the fine dust pollution of New Year's Eve 2017/18 is about ten times higher than 2020/21. The comparison of a few selected elements shows, that some concentrations are significantly higher at the Silvester nights, e.g. Pb, Sr or Bi, while others like Fe can be counted to the background elements.
Subsequent correlative Raman spectroscopy investigations of particular particles are planned. Therefore, the samples have to be investigated in the available low vacuum mode of the used RISE (Raman imaging and scanning electron microscopy) System [2]. This should give a comprehensive insight into the toxicity of particles in the air during such events.

[1] https://www.umwelt.steiermark.at/cms/ziel/2060750/DE/ ; Onlinedaten Kontinuierliches und mobiles Messnetz; Land Steiermark (last call: 08.04.2022)
[2] R. Schmidt, H. Fitzek, M. Nachtnebel, C. Mayrhofer, H. Schroettner, and A. Zankel, "The Combination of Electron Microscopy, Raman Microscopy and Energy Dispersive X-Ray Spectroscopy for the Investigation of Polymeric Materials," Macromol. Symp., vol. 384, no. 1, pp. 1–10, 2019

Acknowledgement: The authors thank Th. Pongratz from the air quality monitoring Styria, the ACR (P.Nr.: SP2018-003-001) and the agency's FFG (P.Nr. 856321).

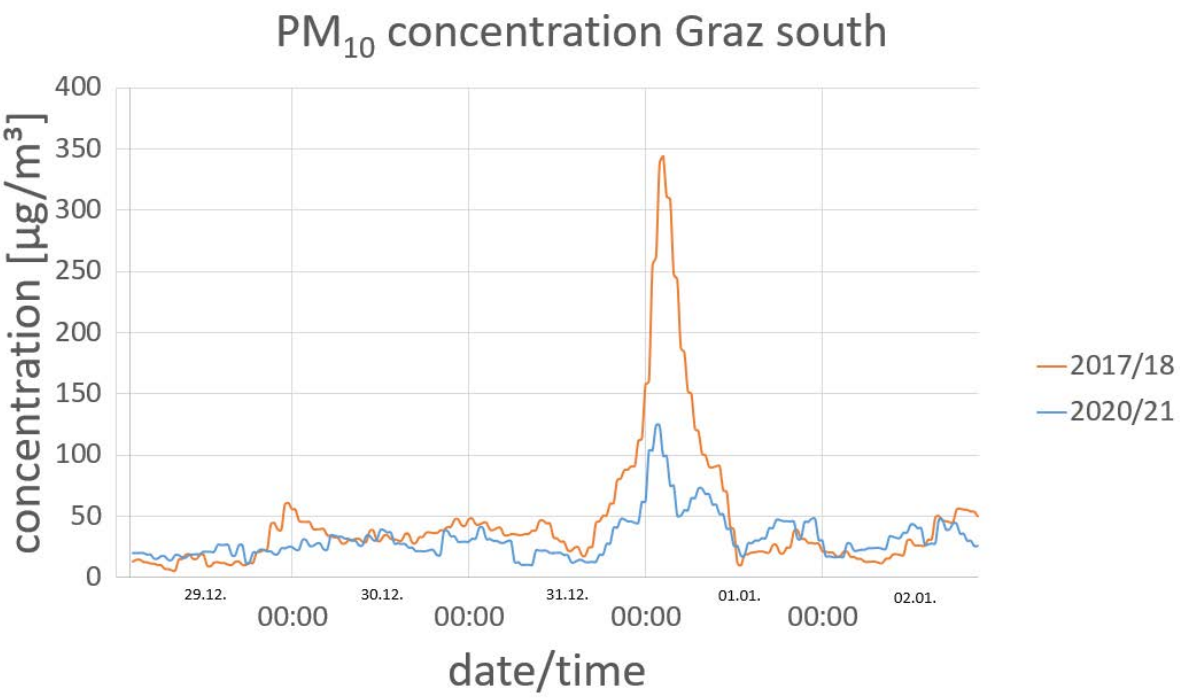

Fig. 1: Comparison of the PM10 concentration at both analyzed Silvester nights at the investigated air quality monitoring site Graz south.

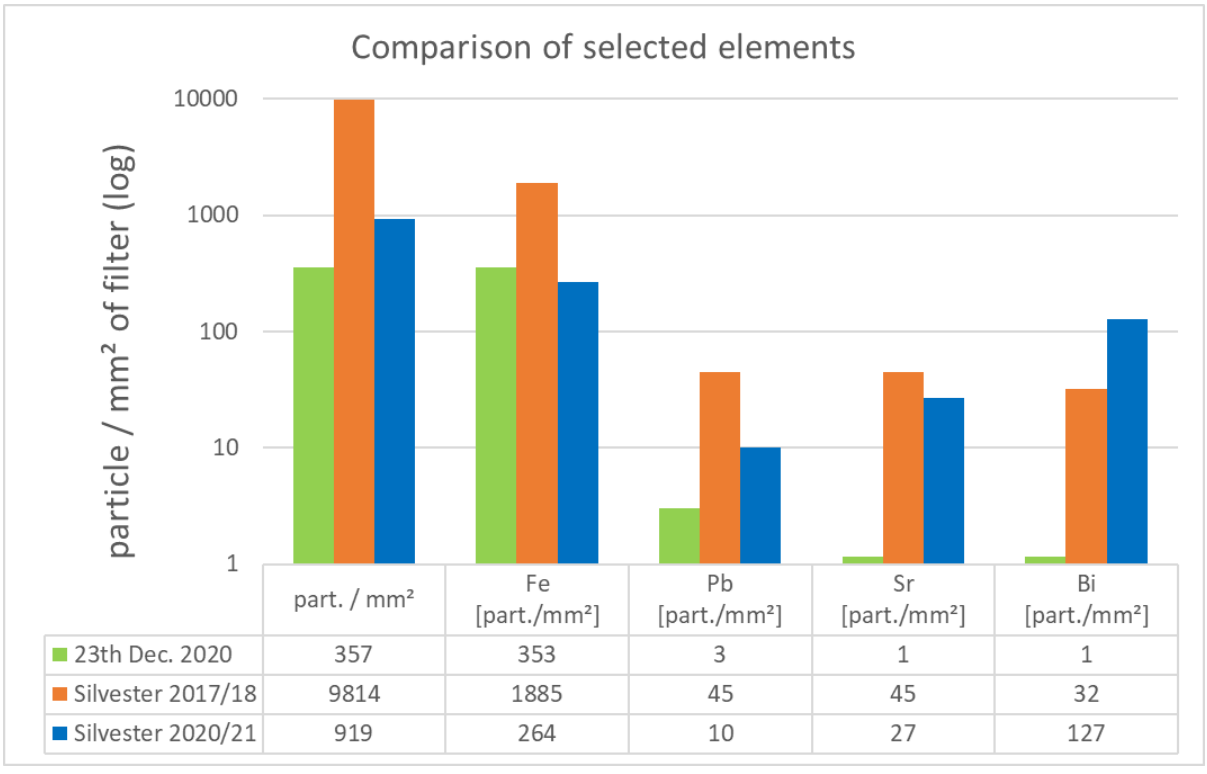

	part. / mm²	Fe [part./mm²]	Pb [part./mm²]	Sr [part./mm²]	Bi [part./mm²]
23th Dec. 2020	357	353	3	1	1
Silvester 2017/18	9814	1885	45	45	32
Silvester 2020/21	919	264	10	27	127

Fig. 2: Comparison of few selected elements (Fe, Pb, Sr, Bi) at three nights, while first row column shows the total detected particle per mm² of investigated filter (note logarithmic scale).

Type of presentation: Poster

IM2-P-2633 Multimodal Microscopy for very large 2D & 3D Imaging

Casares A.[1]

[1]Carl Zeiss Microscopy GmbH

Email of the presenting author: antonio.casares@zeiss.com

Modern microscopy labs are typically outfitted with a suite of instruments, capable of capturing data across a range of length scales in 2D- and 3D, from the centimeters to the sub-nanometers.

These imaging instruments are often complimented by analytical techniques, such as spectroscopic chemical characterization platforms or mass spectrometry and are designed to produce a comprehensive depiction of the material under investigation.

Recently, a novel multi-beam SEM (mSEM®) technology for imaging of large sample areas has been developed by ZEISS. The MultiSEM family features 61 or even 91 electron beams scanning in parallel, resulting in an imaging throughput of up to 2 TeraPixels per hour is now achievable, therefore enabling extremely large-scale imaging experiments in 2D and 3D.

The mSEM® technology with its high degree of automation for instrument tuning, will be an enabler for many research areas where statistically significant are studied [1,2,3].

The presentation will give an overview of unique advancement enabling correlative microscopy to pull together data from light-, electron-, Ion-, and X-Ray Microscopy (XRM), its potential application space for very large 2D & 3D Imaging and the challenges in data handling imposed by the enormously increased data rate.

[1] Crosby K, Eberle AL, Zeidler D (2016) Multi-beam SEM Technology for High Throughput Imaging. MRS Advances, 1 (26):1915–1920
[2] Double cones and the diverse connectivity of photoreceptors and bipolar cells in an avian retina J. Neurosci 2021; 10.1523/JNEUROSCI.2495-20.2021
[3] Jeff W. Lichtman lab, USA. A Browsable Petascale Reconstruction of the Human Cortex, June 2021
https://ai.googleblog.com/2021/06/a-browsable-petascale-reconstruction-of.html

Type of presentation: Poster

IM2-P-2850 Imidazole-osmium reduces elution of lipids from cryofixed rat hepatic tissue for correlative TEM/NanoSIMS analysis

Dürr S.[1], Krššák M.[1], Fürnsinn C.[1], Scherer T.[1], Ehret V.[1], Philippe C.[2], Schintlmeister A.[3], Cyran N.[4], Gruber D.[4], Reipert S.[4]

[1]Department of Medicine III, Medical University of Vienna, Austria, [2]Department of Biomedical Imaging and Image-Guided Therapy, Medical University of Vienna, Austria, [3]Large-Instrument Facility for Environmental and Isotope Mass Spectrometry, University Vienna, Austria, [4]Core Facility Cell Imaging and Ultrastructural Research, University of Vienna, Austria

Email of the presenting author: sabine.duerr@meduniwien.ac.at

Introduction

For semi-correlative TEM/NanoSIMS (transmission electron microscopy/ nanoscale secondary ion mass spectrometry) analysis, structures of interest, such as lipid droplets, have to stay intact and elution of intracellular substances has to be avoided. Imidazole, a highly polar heterocyclic compound, has been shown to enhance the binding ability of osmium tetroxide to lipids and thereby improving their visualization in TEM [1]. This study aimed to investigate the effect of imidazole-osmium application before and during cryopreparation to prevent elution from lipid droplets.

Methods

Perfusion-fixed (4.5 % phosphate buffered formaldehyde, pH 7) hepatic tissue from male Sprague-Dawley rats (n=6; 8 weeks old) on high fat diet (60% of calories as fat; fed for 4 weeks) was processed for cryopreparation. We added 1% OsO4 and 0.1M imidazole to the substitution medium, acetone, and developed an appropriate freeze-substitution protocol. Specimens were embedded in Agar 100 resin, and the ultrastructure was analyzed in ultrathin sections (70 nm, Leica EM UC7; ZEISS Libra 120 TEM).

Results

By including imidazole, a significant improvement in preservation of lipids was achieved. In contrast to the control (Figure A), tissue treated in this way displayed homogeneously osmificated lipid droplets (Figure B).

Conclusion

We suggest that osmium-imidazole prevented the elution of lipid content during freeze substitution. Further investigations including NanoSIMS will be conducted to confirm this hypothesis.

Reference

[1] S. Angermüller, H. D. Fahimi, The Histochemical journal, 14 (5), 823–835 (1982)

Acknowledgement: The authors acknowledge funding by the WWTF.

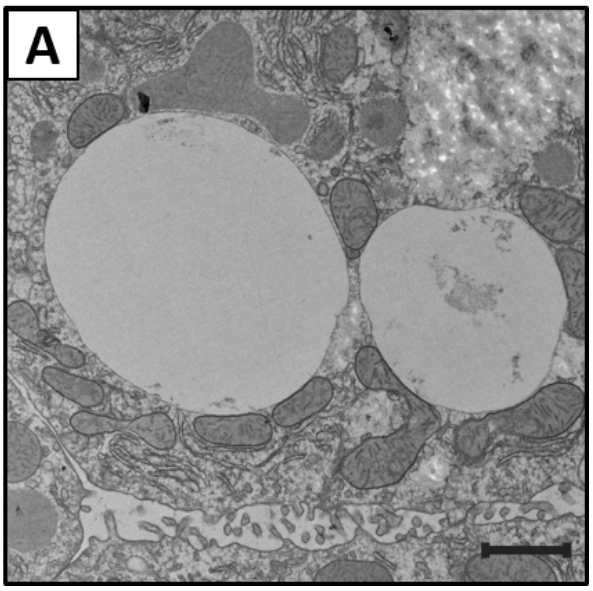

Fig. 1: Lipid droplets (LD) in tissue without imidazole treatment. Lipid content is apparently missing. Scale bar, 1 µm.

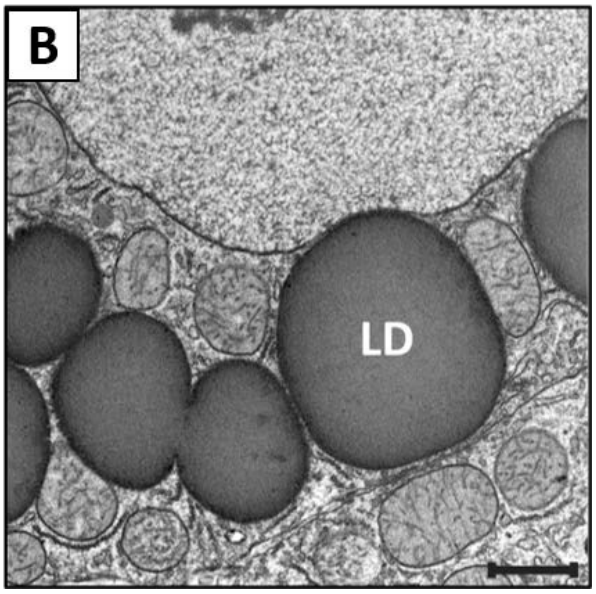

Fig. 2: Entirely homogeneous lipid droplets after osmium-imidazole mediated freeze substitution. Scale bar, 1 µm.

Type of presentation: Poster

IM2-P-2604 Towards correlating light and electron microscopy with immersion objectives at cryogenic temperatures

Faul N. A.[1], Chen S. Y.[1], Lamberz C.[1], Dienemann C.[2], Burg T. P.[1]

[1]Integrated Micro-Nano-Systems Lab, Technical University of Darmstadt, Darmstadt, Germany, [2]Department of Molecular Biology, Max Planck Institute for Multidisciplinary Sciences, Göttingen, Germany

Email of the presenting author: n.faul@micronano.tu-darmstadt.de

Light microscopy (LM) attains the highest level of resolution when immersion objectives can be employed. At cryogenic temperature, this is a challenge due to the direct contact between the sample and the objective lens through the immersion medium. Importantly, to perform correlation between cryoimmersion-light and cryo-electron microscopy (cryoimmersion-CLEM), the immersion medium must be removed prior to the electron microscopy.
Here we investigate the possibility of cryoimmersion-CLEM, using a cryo-compatible immersion objective with a refractive index matched immersion medium (numerical aperture (NA) of 1.15), that has been described previously by our group [1].
Cryo-LM is an intermediate step in the workflow of cryo-CLEM (Figure 1) and therefore the sample quality must not degrade during LM and subsequent sample transfer. Three factors are particularly detrimental for the usability of the sample in cryo-electron microscopy (cryo-EM) or tomography: ice-contamination, mechanical damage, and devitrification.
We demonstrate the cryoimmersion-CLEM approach using U2OS cells, plunge frozen on EM grids (Figure 2). The vitrified samples were embedded in a cryoimmersion medium and imaged with widefield to localise regions of interest. Confocal laser scanning microscopy (LSM) was then used to reveal subcellular structures. After cryo-LM the samples were rinsed by dissolving the cryoimmersion medium to avoid mechanical damage. During the entire process, the sample temperature was kept below the devitrification limit (-135°C) [2]. Subsequently, the samples were transferred to a transmission cryo-electron microscope and the collected data was correlated with the confocal LSM images.

The main feature of cryoimmersion-LM is the gain in image quality due to high-NA objectives, reducing the exposure time when acquiring weak signals. In addition, embedding samples in cryoimmersion medium protects the sample from contamination by atmospheric humidity and enables extremely long imaging sessions of more than 7 hours to investigate samples in detail. We demonstrate that the samples survive cryoimmersion-LM without any detectable degradation with our method, opening new possibilities for cryo-CLEM. Particularly super-resolution microscopy can benefit greatly from high-NA objectives.

References

[1] Faoro, R., Bassu, M., Mejia, Y. X., Stephan, T., Dudani, N., Boeker, C., Jakobs, S., & Burg, T. P. (2018). Aberration-corrected cryoimmersion light microscopy. Proceedings of the National Academy of Sciences, 115(6), 1204–1209
[2] Schultz, P. (1988). Cryo-electron microscopy of vitrified specimens. Quarterly Reviews of Biophysics, 21(2), 129–228

Acknowledgement: This project has received funding from the European Research Council under the European Union's Horizon 2020 research and innovation programme (No. 772441).

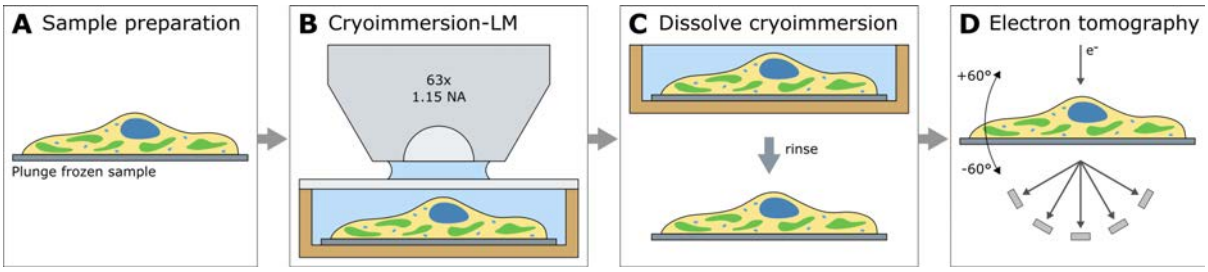

Fig. 1: Schematic workflow for cryoimmersion-CLEM.
A Fluorescently labelled cells are plunge frozen on EM grids. **B** The cryoimmersion-objective is used to image the sample embedded in cryoimmersion medium **C** which is dissolved to rinse the sample. **D** TEM imaging and correlation with LM images to reveal subcellular structures on reconstructed tomograms.

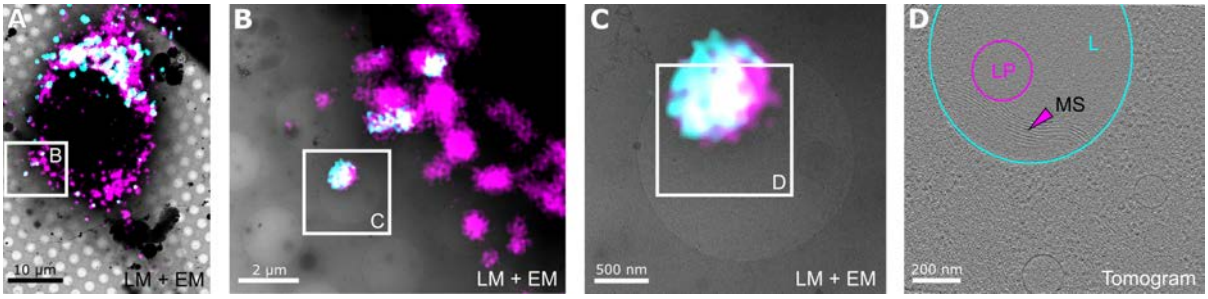

Fig. 2: Correlation of cryoimmersion-LM and EM data.
U2OS cells were labelled with MitoTracker Green (magenta) and LysoTracker Red (cyan) and plunge frozen on EM grids. **A-C** Correlation of confocal LSM and cryo-EM data reveals **D** subcellular details of Lysosomes (L), Lipid particle (LP) and membrane stack (MS). No residue of cryoimmersion fluid was detected.

Type of presentation: Poster

IM2-P-2691 IPHYS Bioimaging Facility

Hadraba D.[1]

[1]IPHYS Bioimaging Facility

Email of the presenting author: daniel.hadraba@fgu.cas.cz

Institute of Physiology of the Czech Academy of Sciences (IPHYS) Bioimaging Facility provides open-access to several confocal and multiphoton microscopic systems and other imaging tools and skills that are highly supported by the Czech-BioImaging project. Our primary focus is on advanced fluorescence microscopic and image analysis techniques. In microscopy, our unique specialization is multiphoton and fluorescence lifetime microscopy including related non-linear techniques, for instance SHG/PSHG/CARS. The techniques were enriched by implementing phosphorescence lifetime imaging (PLIM) in 2016, installing the upright two-photon microscope Bruker Ultima (2018) dedicated to live animal imaging, CARS system (2021) or a brand new Leica Stellaris 8 (2021). In addition to that, The Bruker Ultima microscope, optic fibre confocal microscope Cellvisio and Bruker µCT/PET create a complementary family of instruments that provide a significantly framework for imaging living animals. For the large samples, our facility provides optical projection tomography (OPT) technique and brand you lightsheet system (Leica Stellaris 8 DSL). A major part of our work is dedicated to the image acquisition, processing and analysis of the biological data including technical support, experiment planning, image reconstruction or stereology.

Acknowledgement: The work was supported by the MEYS CR (Large RI Project LM2018129 Czech-BioImaging).

Type of presentation: Poster

IM2-P-2502 Magnetic field imaging with electron energy loss spectroscopy based on Babinet's principle

Horák M.[1], Křápek V.[1], Konečná A.[1], Hrtoň M.[1], Šikola T.[1]

[1]Brno University of Technology, Brno, Czech Republic

Email of the presenting author: michal.horak2@ceitec.vutbr.cz

Localized surface plasmon resonances are self-sustained collective oscillations of free electrons in metallic nanostructures. Mapping of localized surface plasmon modes with high spatial and energy resolution is necessary to understand their nature and spatio-spectral characteristics. This can be done by scanning transmission electron microscopy (STEM) combined with electron energy loss spectroscopy (EELS) which measures the energy transferred from electrons to the LSP. Importantly, EELS is sensitive to the electric near field component of localized surface plasmon modes parallel with the electron beam and cannot be directly associated with the magnetic near field.

In our contribution, we use the Babinet's principle to facilitate characterization of both the electric and the magnetic near field of plasmonic antennas. Babinet's principle relates the properties of a planar plasmonic antenna (particle) and a complementary plasmonic antenna (aperture) in a thin metal film of the same size and shape. In particular, the energies of LSPR in both types of antennas shall be identical and the magnetic near-field distribution of the particle antenna shall correspond to the electric near field distribution of the complementary aperture antenna. The spatially resolved EELS mapping of the aperture antennas can thus help to deduce the magnetic near fields associated with the localized surface plasmon resonances in particle antennas and vice versa [1,2], see also Figure 1. We demonstrate such use of Babinet's principle in a combined experimental and theoretical study for disc-shaped antennas/apertures [1] and plasmonic bow-tie and diabolo antennas/apertures with electric/magnetic hot spots [2]. Moreover, we will also discuss optimal experimental conditions in STEM-EELS for achieving the best signal-to-background ratio [3].

[1] M. Horák et al., Sci. Rep. **9**, 4004 (2019).

[2] V. Křápek et al., Nanophotonics **9**, 623-632 (2020).

[3] M. Horák, T. Šikola, Ultramicroscopy **216,** 113044 (2020).

Acknowledgement: Supported by EU Horizon 2020 (SINNCE, 810626), Czech Science Foundation (17-25799), MEYS CR (CzechNanoLab, LM2018110), and TFS-CSMS scholarship 2019.

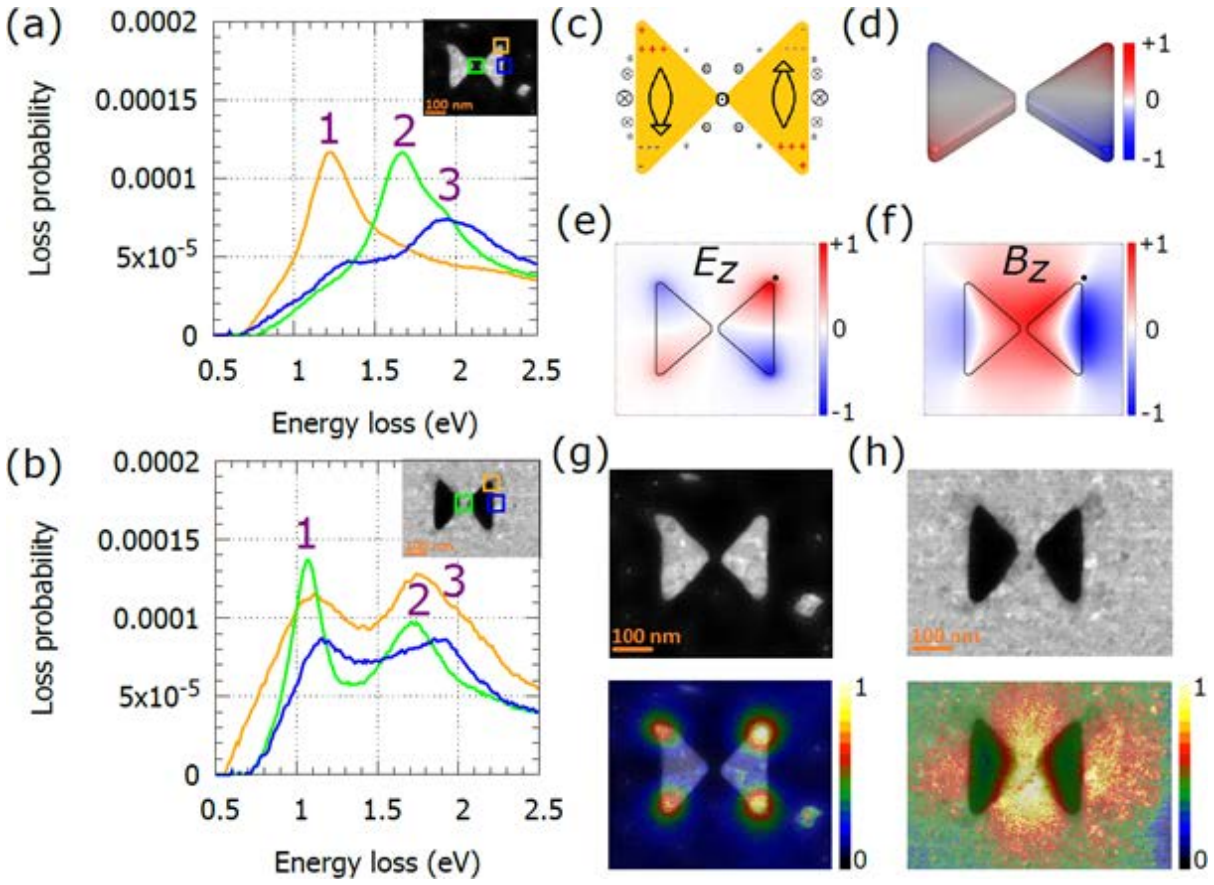

Fig. 1: Transverse dipolar mode [peak 1 in (a,b)] in a bow-tie antenna. EEL spectra of bow-tie (a) and inverted bow-tie (b) antenna. Schematic representation the TD mode (c), calculated surface charge (d), electric (e) and magnetic (f) out-of-plane near-field distributions. STEM micrographs and EELS maps of the bow-tie (g) and inverted bow-tie (h) antenna.

Type of presentation: Poster

IM2-P-2816 KPFM in SEM - Simultaneous Kelvin Probe Force Microscopy and Scanning Electron Microscopy

Kovařík M.[1], Konečný M.[2], Šikola T.[1,2], Kolíbal M.[1,2]

[1]CEITEC Brno University of Technology, Brno, Czech Republic, [2]Institute of Physical Engineering, Brno University of Technology, Brno, Czech Republic

Email of the presenting author: martin.kovarik@ceitec.vutbr.cz

With the introduction of Atomic Force Microscope (AFM) to the Scanning Electron Microscope (SEM), some yet unexplored ways of sample characterization have opened up. Kelvin Probe Force Microscopy (KPFM) is an AFM-based technique for measuring surface electrical properties at nanoscale [1] and allows to measure local surface potential or visualize trapped charge, for example. The simultaneous combination of KPFM and SEM imaging provides a new direct view on the complex interaction between electron beam and the sample.

To our knowledge, there is no published study about simultaneous KPFM and SEM imaging. We use small and compact NenoVision LiteScope AFM that can be inserted into various SEM chambers [2]. In this contribution, we present our first advances in this topic, focusing on basic principles of operation and data interpretation. We will demonstrate and discuss measurements performed on simple systems (lateral metallic heterostructures) as well as advanced materials (graphene) .

[1] Melitz, W. et al., Surface Science Reports, Volume 66, Issue 1, January 2011, p. 1-27
[2] Novotna, V. et al., Microscopy Today, Volume 28, Issue 3, May 2020, p. 38-46

Type of presentation: Poster

IM2-P-2699 Assembly for Cryo-SEM/Raman Microspectroscopy sample analysis

Laznicka T.[1], Hrubanova K.[1], Jezek J.[1], Kizovsky M.[1], Bernatova S.[1], Mrazova K.[1], Obruca S.[2], Zemanek P.[1], Krzyzanek V.[1]

[1]Institute of Scientific instruments, The Czech Academy of Sciences, v.v.i., Kralovopolska 147, 612 00 Brno, Czech Republic, [2]Faculty of Chemistry, Brno University of Technology, Purkynova 112, 612 00 Brno, Czech Republic

Email of the presenting author: lazna@isibrno.cz

Correlative imaging using different methods of observation is now becoming more and more popular. It allows the interconnection of various information of the sample accessible only by individual techniques. It is crucial to find and observe the same place on the sample. The same objects and their locations (cell shape and arrangement) can be correlated with each other, especially with software when 2 different imaging devices were used. Combination of the Cryo-Scanning Electron Microscopy (Cryo-SEM) and Cryo-Raman Micro-spectroscopy (Cryo-Raman) gives many benefits. Surface, structure or morphology of the sample can by studied using Cryo-SEM, and detection and identification of elements or compounds in the examined sample using Cryo-Raman. For observation of various, especially biological samples, their freezing to the temperature of liquid nitrogen is used. The motivation was to design an assembly for motion and observation using Cryo-Raman and its connection with commercial holders used for the observation of vitrified samples by Cryo-SEM. Assembly allows movement of the sample to a known position and measuring the cryogen level using LabVIEW software.
Our assembly consists of a Dewar vessel, which contains liquid nitrogen. The stage is inside the Dewar vessel below the liquid level and is made by 3D printing and enables 3 positions for individual types of sample holders (Leica microsystems, Gatan and Quorum technologies). The Dewar vessel lies on piezoelectric stage allowing movement in both X and Y direction. The stage is connected to the Raman spectrometer table providing displacement in the Z direction. The Dewar vessel is covered with Plexiglas to minimize contamination. Assembly was tested on dried samples and polystyrene in cryo temperatures with known spectrum to verify functionality. Then biological samples including C. necator H16 were tested.
System allows more efficient correlation between individual analyses of microorganisms containing biopolymer particles. For example, several representatives of soil microorganisms, such as bacteria C. necator H16 which are able to produce polyhydroxyalkanoates (PHA) [1]. PHAs are polyesters of hydroxyalkanoic acids, which serve as energy storage. PHAs attract attention as an alternative to petrochemical plastics, which can be biotechnologically produced from waste streams of some industrial processes.
It was proved that the combination of Raman spectroscopy with the cryo-SEM technique can provide a deeper insight into the chemical and mechanical properties of polymeric granules inside the bacterial cells and it will serve for future research [2].

References:
[1] Obruca, S. at al, PLoS ONE, 2016, 11(6), e0157778
[2] Kucera, D. at al, Applied Microbiology and Biotechnology, 2016, 100(3), pp. 1365–1376

Acknowledgement: The research was supported by the Technology Agency of the Czech Republic (TN01000008) and the Czech Academy of Sciences (MSM100652102).

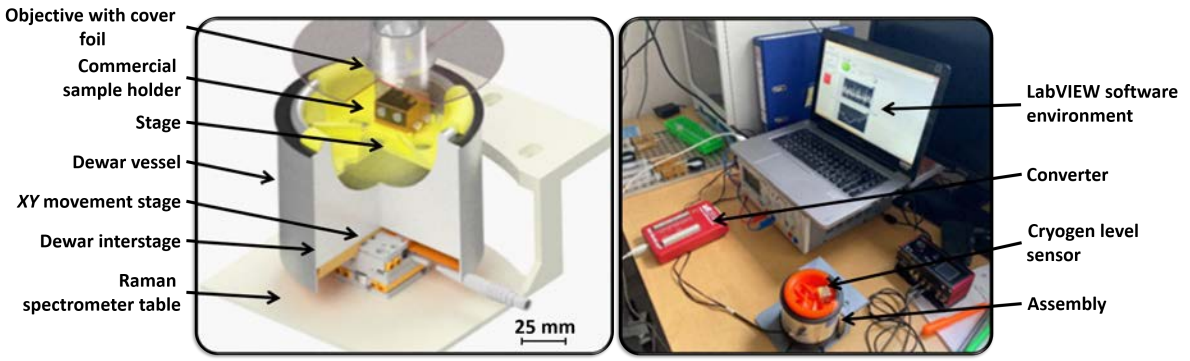

Fig. 1: Description of the Cryo-Raman assembly with systematic arrangement during the test.

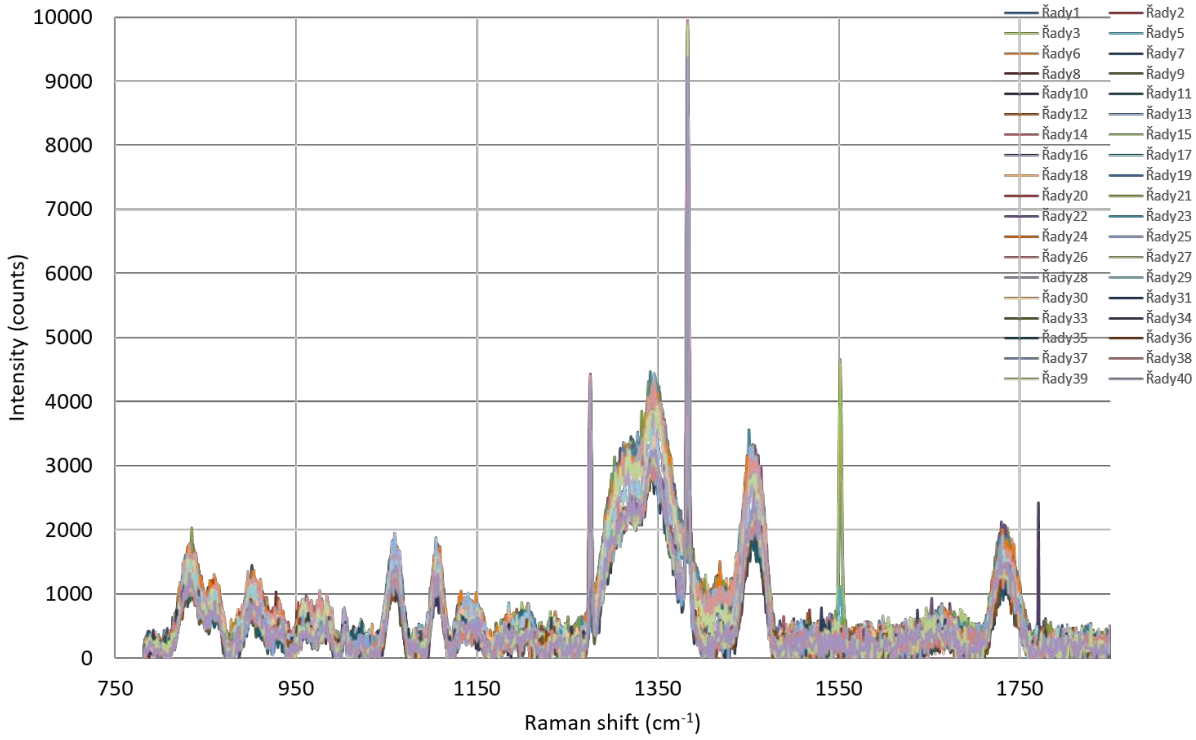

Fig. 2: Spectral analysis of the C. necator H16 containing PHAs granules (830, 1450 and 1730 cm^{-1}) measured by cryo-Raman micro-spectrometer. Over time, a small layer of icing began to form on the sample, causing increasingly visible peaks in 1274, 1381 cm^{-1} (probably dry ice - CO_2) and 1550 cm^{-1} (O_2).

Type of presentation: Poster

IM2-P-2527 AFM-in-SEM solution for correlative microscopy in material sciences

Neuman J.[1], Hegrova V.[1], Dao R.[1]

[1]NenoVision s.r.o., Brno, Czech republic

Email of the presenting author: conference@nenovision.com

Correlative in-situ microscopy is one of the hot topics in material sciences nowadays. As it combines the benefits of different imaging systems, it has become an essential tool helping us understand the complexity of the sample properties. When we imagine combining two complementary techniques, atomic force microscopy (AFM) and scanning electron microscopy (SEM), this setup has several advantages, such as multimodal measurement, under in-situ conditions, and precise localization to the area of interest.

To combine these techniques, a unique Atomic Force Microscope (AFM), LiteScope™, was developed for easy „plug & play“ integration into the SEMs. The connection of AFM and SEM enables to merge the strengths of both techniques, resulting in effective workflow and possibilities of complex sample analysis that was difficult or readily impossible by conventional, separate AFM and SEM instrumentation. Additionally, Correlative Probe and Electron Microscopy, shortly CPEM, is a unique method allowing for precise AFM and SEM data correlation (Fig. 1). The images are acquired simultaneously from both devices in the same coordinate system and undter the same conditions. Thus, the resulting 3D CPEM view can combine multiple channels from AFM and SEM, enabling thorough sample analysis and clear data interpretation.

In material sciences, a lot of effort is spent on a fundamental understanding of the surface properties of metals and alloys, thin materials, or batteries. In the case of Mg-Ca-Zn alloy (Fig. 2), a biocompatible and biodegradable material, it is studied for medicinal applications. The content of Zn and Ca has a significant influence on the mechanical properties of the alloy. Certain conditions can lead to the precipitation of a Ca-rich phase, which hardens the material by blocking dislocation movement. However, such precipitates are often hard to find and distinguish from other features on the surface using each imaging technique separately. They can be easily recognized using AFM-in-SEM and imaged by the Kelvin Probe Force Microscopy (KPFM) technique, which maps the contact potential difference between the tip and sample. Thanks to the differences in the potential between both phases, we were able to distinguish the hardening precipiate from other islands (not relevant) presented on the sample surface.

Thus, the AFM-in-SEM solution allows us multimodal analyses of AFM modes – such as 3D topography, electrical, magnetic, or mechanical properties – and SEM capabilities like fast imaging, chemical analysis, or surface modification. This way, the Correlative in-situ Microscopy is essential not only in Material sciences but also in Nanotechnology, Semiconductor, Life sciences, and other areas in both research and industry.

Acknowledgement: I wish to acknowledge the group of Jörg F. Löffler, Metal Physics and Technology, ETH Zürich for providing the sample.

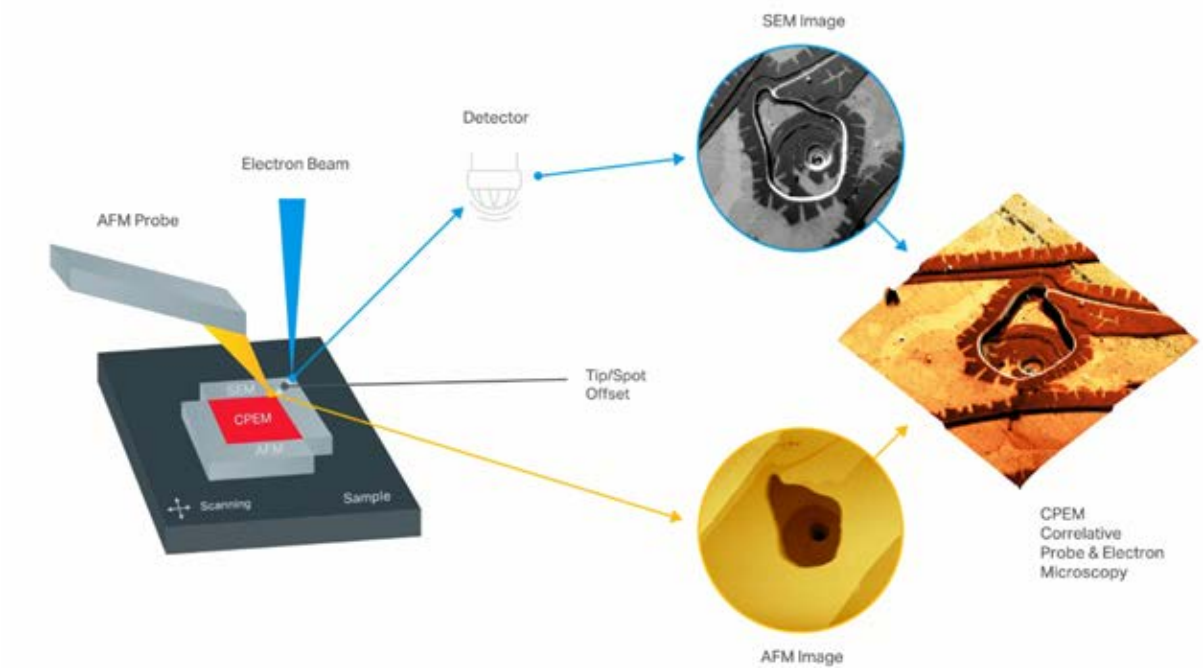

Fig. 1: Scheme of CPEM Technology.

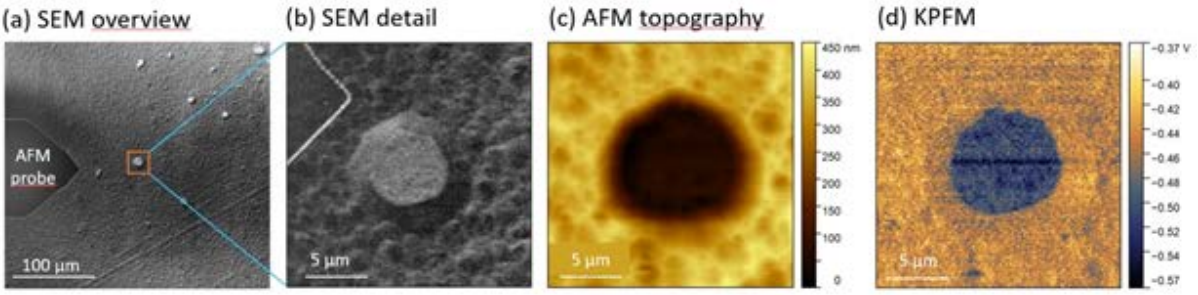

Fig. 2: Mg-Ca-Zn alloy with Ca-rich precipitation: (a) SEM overview with detail, (b) AFM topography with surface potential image of the precipitate.

Type of presentation: Poster

IM2-P-2677 Miro proteins and their role in horizontal transfer of mitochondria via tunneling nanotubes in cancer cells

Novák J.[1, 2], Nahácka Z.[1], Lánský Z.[1], Henrichs V.[1], Gryčová L.[1], Neužil J.[1, 3]

[1]Czech Academy of Sciences, Institute of Biotechnology, Vestec, Czech Republic, [2]Charles University in Prague, Faculty of Science, Prague, Czech Republic, [3]Griffith University, School of Pharmacy and Medical Science, Sydney

Email of the presenting author: novakj70@natur.cuni.cz

Intercellular communication between the same and different cell types is essential for tissue homeostasis in multicellular organisms. Similarly, cancer cells communicate with the surrounding stroma to enhance their proliferative and metastatic potential. A striking example of intimate communication between cancer and stromal cell involves exchange of whole organelles including mitochondria. Tumour cells with damaged mitochondria can renew their proliferative potential by replacement of malfunctioning organelles via the import of healthy mitochondria from stromal cells, presumably via tunneling nanotubes (TNTs). TNTs are transient physical membranous connections of the cytoplasm of donor and recipient cells containing cytoskeletal structures with tubulin fibers acting as tracks for organelle movement, which is governed by adaptor and motor proteins.

Miro proteins are small GTPases related to the family of Rho GTPases, anchored in the outer mitochondrial membrane facing toward the cytoplasm. Miro proteins play a multifaceted role in mitochondrial physiology, their major function being to regulate organelle movement along tubulin fibers. Miro proteins interact with various adaptor and motor proteins associated with both tubulin and actin filaments, coordinating mitochondrial localization within the cell, and they are involved in the intercellular transfer of mitochondria. However, the exact role of Miro proteins in the movement of mitochondria from one cell to another remains unknown. This work aims to elucidate the mechanisms by which Miro proteins contribute to the ability of cancer cells to import mitochondria from stromal cell via TNTs.

We have been utilizing total internal reflection or interference reflection microscopy (TIRF/IRM) of the reconstituted system of microtubules, adaptor and motor proteins, plus mitochondria with or without Miro to quantitatively describe the role of Miro proteins in mitochondrial movement along microtubules. To capture these relatively rare events of TNTs connection transferring mitochondria between donor and acceptor cells, we have been utilizing a co-culture microfluidic device. This allows us to spatially separate the populations of donor and acceptor cells to subsequently localize events of transfer for further characterization of TNTs containing mitochondria with multiple microscopy approaches. We aim to investigate the dynamics of mitochondrial movement over several micrometre long TNTs with the use of low phototoxicity live-cell imaging (e.g. holographic microscopy) followed by ultrastructural analysis of TNTs and the mobilized mitochondria with superresolution microscopy and, ultimately, correlative light and electron microscopy.

Acknowledgement: Imaging Methods Core Facility at BIOCEV, Luděk Štěpánek. This work was supported by GAUK, GACR, MEYS CR, IBT CAS and BIOCEV ERDF.

Type of presentation: Poster

IM2-P-2800 Microscopy and in vivo imaging in aid for visualization of dynamic processes - example of brain damage evolution after ischemic brain stroke

Petrinec D.[1], Hamer D.[1], Srakočić S.[1], Josić P.[1], Ister R.[1], Radmilović M.[1], Škokić S.[1], Glasnović A.[1], Skukan L.[1], Berecki M.[1], Gajović S.[1]

[1]Laboratory of regenerative neuroscience, Croatian Institute for Brain Research, University of Zagreb School of Medicine, Šalata 12, Zagreb, Croatia

Email of the presenting author: daniela.petrinec@mef.hr

In modern animal experiments, it is necessary to apply the 3R principle but another challenge is a visualization of the dynamic processes which change through time especially if combined with methods with different magnification ranges. Besides light, other visualization modalities can be applied, for example, magnetic resonance or microCT. Subsequently, a platform was organized for in vivo imaging of the laboratory mice, which allowed multiple imaging sessions during a single experiment. This was applied to study the mice model of human ischemic stroke, where brain lesion was caused by transient middle cerebral occlusion (tMCAO). Two imaging modalities were used, magnetic resonance imaging (MRI) and optical imaging of bioluminescence (BLI). Obtained in vivo imaging results were combined with histological analysis and immunohistochemistry of the mouse brain. Moreover, the imaging results were related to the functional outcomes obtained by neurological deficit scoring. This approach was used to compare the mice deficient for the receptor on the microglia, Tlr2, to which particles of necrotic cells bind and subsequently elicit neuroinflammation. The experimental paradigm included the follow-up of mice for 28 days after ischemic lesion. The imaging sessions allowed to compare the brain consequences between Tlr2-deficient to control wild-type mice. Tlr2-deficient mice survived better after ischemic lesion, however, had bigger lesions and neurological scores. After 28 days Tlr2-deficient mice were comparable to their controls. The same was shown by modeling the relation between ischemic lesion and functional outcome indicating that Tlr2-deficient mice recovered better than the wild-type controls. It is known that the phenotype changes after ischemic stroke occur, which is visible by the change in the morphology of microglia and astrocytes. Microglia morphology is ramified in the healthy brain and varies among brain regions which facilitate the maintenance of homeostasis through cellular surveillance. After ischemic stroke transformation from a highly ramified into a less ramified or amoeboid cell shape is visible . Microglia and astrocytes were visualized under a confocal microscope (Olympus FV3000) using immunohistochemistry on thin cryoslices. Specific antibodies for glial fibrillary acidic protein in astrocytes and ionized calcium-binding adaptor molecule 1 in microglia were used. It was shown that astrocytes were missing which suggests necrosis in the area affected by ischemic stroke. On the other hand, microglial cells were present in the ischemic lesion. Overall, the in vivo imaging modalities combined with other microscopy methods provided a multimodal approach giving insight into the time-dependent changes of the mouse brain after ischemic lesion.

Acknowledgement: Supported by EU project “Sinergy of molecular markers and multimodal *in vivo* imaging during preclinical assessment of the consequences of the ischemic stroke.”

Type of presentation: Poster

IM2-P-2544 High-resolution electron beam induced current study of AlN epitaxial layer

Pongrácz J.[1,2], Vacek P.[3], Gröger R.[1,2]

[1]Institute of Physics of Materials, Czech Academy of Sciences, Brno, Czech Republic, [2]Central European Institute of Technology (CEITEC), Brno, Czech Republic, [3]Department of Materials science & Metallurgy, University of Cambridge, Cambridge, United Kingdom

Email of the presenting author: pongracz@ipm.cz

Heteroepitaxial growth of hexagonal (wurtzite) AlN on (111)-oriented Si substrates results in 19% lattice misfit and produces a large density of threading dislocations (TDs). In particular, the density of TDs in MOCVD-grown film of 200 nm AlN/Si(111) is about 10^{10} cm^{-2}. Because TDs act as nonradiative recombination centres and scattering sites for free electrons, their presence in semiconductor structures reduces the efficiency of optoelectronic devices such as photovoltaic cells, light emitting diodes (LEDs) and laser diodes (LDs). The recombination activity of individual TDs can be characterized by scanning the sample surface by electron beam, and measuring the current flowing into the external circuit, the so-called Electron Beam Induced Current (EBIC).

The objective of this work is to compare the measurements made using two methods: (i) the standard EBIC method as implemented in the Mighty EBIC 2.0 system coupled with FEMTO preamplifier [1], and (ii) the near-field (high-resolution EBIC) measurements made using the SPM LiteScope [2]. Both devices are coupled with SEM TESCAN Lyra 3, which serves as the source of electron beam. The planar Schottky contact for the method (i) is made by depositing 5nm of 80%Pt+20%Pd on the AlN surface and creating an ohmic contact on Si surface, as shown in Fig. 1(a). For the method (ii), no special surface treatment is needed, because the Schottky contact is created when the AFM tip approaches the AlN surface, as shown in Fig. 1(b). Here, we use the Pt-coated Bruker AFM probe OSCM-Pt R3 connected via probe holder to the SPM LiteScope that processes the measurements. Both types of measurements are compared in Fig. 2, where the panel (c) is the EBIC measured using the standard method, and (d) the map acquired using the high-resolution EBIC. However, this signal contains a significant contribution from back-scattered electrons that needs to be eliminated. Our solution to this problem is to use a two-pass measurement. In the first pass, the tip is in contact with the AlN surface and the external ammeter registers the sum of EBIC and the current due to backscattered electrons. In the second pass, the tip is lifted a few microns above the surface, and the measurement provides only the signal from backscattered electrons. Subtracting the map obtained in the second pass from that in the first pass gives the required EBIC map.

References:

[1] P. Vacek, P. Kostelník, R. Gröger, Correlation of structure and EBIC contrast from threading dislocations in AlN/Si films. Phys. Stat. Sol. B 256 (2019) 1900279.

[2] K. Smaali, M. Troyon, Application of nano-EBIC to the characterization of GaAs and InP homojunctions, Nanotechnology 19 (2008) 155706.

Acknowledgement: This research was supported by the “GEFSEM” No. W01010183 funded by the TACR, and by the Innovation Voucher CZ.01.1.02/0.0/0.0/20_358/0027762.

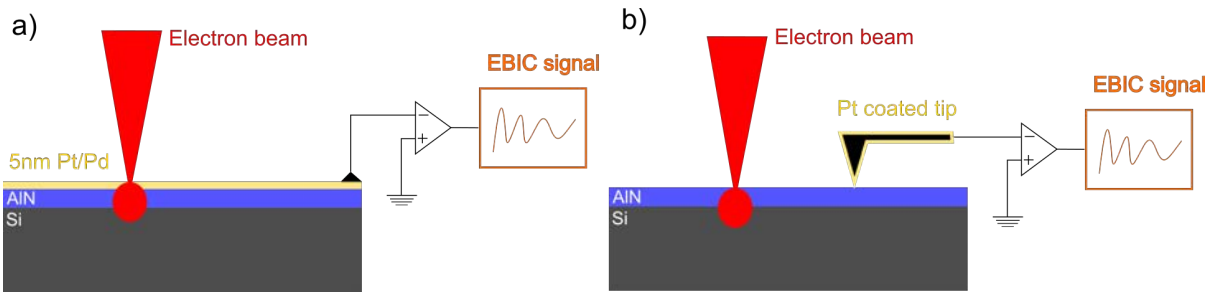

Fig. 1: Schematic representation of (a) regular EBIC with Pt planar Schottky junction, and (b) high-resolution EBIC measured through Pt-coated AFM tip.

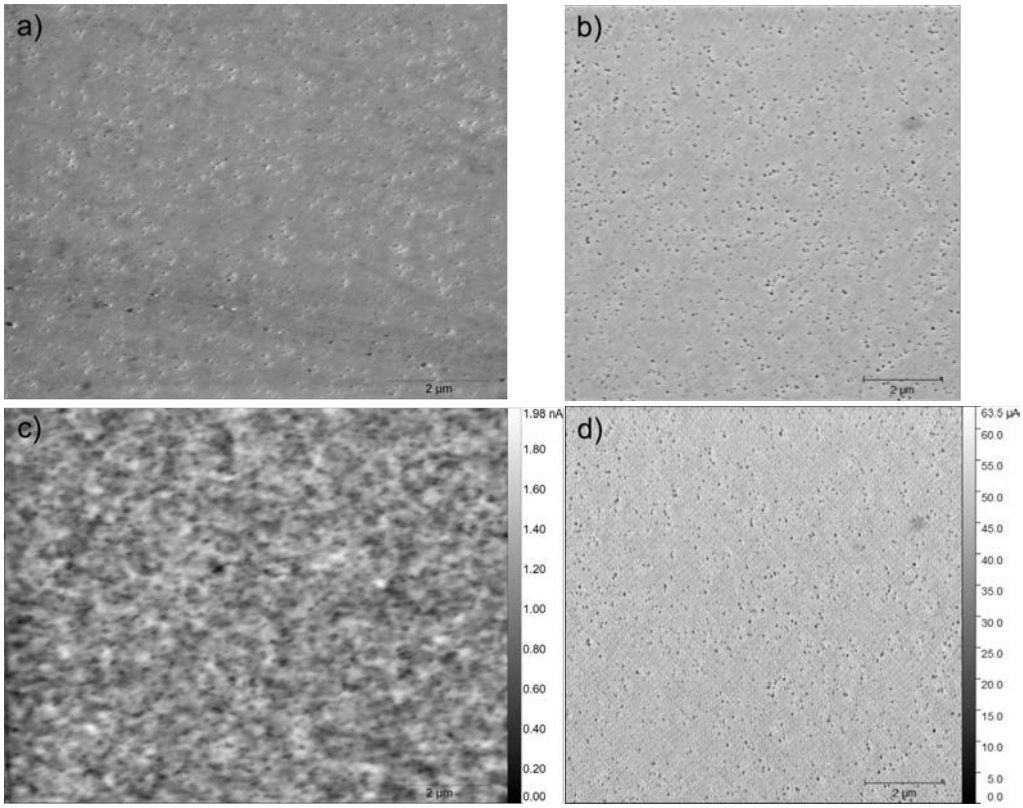

Fig. 2: Comparison of EBIC measurements made using the standard method and high-resolution EBIC: (a) SEM and (c) the corresponding EBIC current measured using the standard method; (b) SEM, and (d) the high-resolution EBIC measured through Pt-coated AFM tip.

Type of presentation: Poster

IM2-P-2545 Extensive material characterization for series production of 3D printer components

Schroettner H.[1, 2], Mayrhofer C.[1], Haider H.[3]

[1]Graz Centre for Electron Microscopy (ZFE), Steyrergasse 17/3, 8010 Graz, Austria, [2]Institute for Electron Microscopy and Nanoanalysis (FELMI), NAWI Graz, Graz University of Technology, Steyrergasse 17/3, 8010 Graz, Austria, [3]OFI, Franz-Grill-Straße 5, Objekt 213, 1010 Vienna, Austria

Email of the presenting author: hartmuth.schroettner@felmi-zfe.at

In the last decade, 3d printing technology has undergone rapid development. From the original technology for the production of prototypes or special applications in medicine, racing or aerospace, to individual production and economically competitive series production. Additive manufacturing opens up a variety of possibilities to manufacture even geometrically complex components from metallic, ceramic or polymeric materials [1].
The joint research project “Material and process optimization for series production of 3D printer components” aims to develop fundamentals for optimizing 3d printed polymeric components. Since components from 3d printing behave significantly differently than, for example, injection moulded parts, they also have to be designed and dimensioned differently. The differences can be found also in the material properties and in the processing-related material structure and surface morphology.
Hence there is the necessity to characterize the resulting mechanical, morphological and chemical properties and the ageing behaviour of the versatile polymers (e.g. ABS, PA, PC, PLA, PP, TPU, … or fibre reinforced plastics) used for the different 3d printing processes (FDM, FFF, SLA, SLS,…) under different printing parameters. Therefor a special test specimen was designed (Figure 1). For the dimensioning of printed components, a detailed description of the material properties under application conditions must be provided. This requires knowledge of the material strength and the reduction of strength under mechanical stress. For a general description of this behavior, reduction factors have been determined to define the nominal design stress according to the given load cases, e.g. static or dynamic mechanical loads, notching effects, elevated operation temperature or aging / exposure.
Surface morphology is monitored with large area and detailed Environmental Scanning Electron Microscopy (ESEM). Atomic Force Microscopy (AFM) can connect the surface structure with local mechanical properties. Computed tomography (CT) enables an insight into the component (defects and cavities). For a local detailed structure analysis the samples are cross-sectioned with microtomy techniques and then characterized with a multiscale approach of different microscopic methods. From stitched Light Microscopy (LM) images in the mm range (Figure 2), via Scanning Electron in the µm range, up to interfaces investigated with Transmissions Electron Microscopy (TEM) in the nm range. Raman Integrated Scanning Microscopy (RISE) provides correlative elemental and chemical information by combining EDXS and Raman spectroscopy (e.g. fibre reinforcement, distribution of additives, fillers and pigments) [2].

Acknowledgement: The author wants to thank BMDW for the financial support of the project (SP-2020-08).

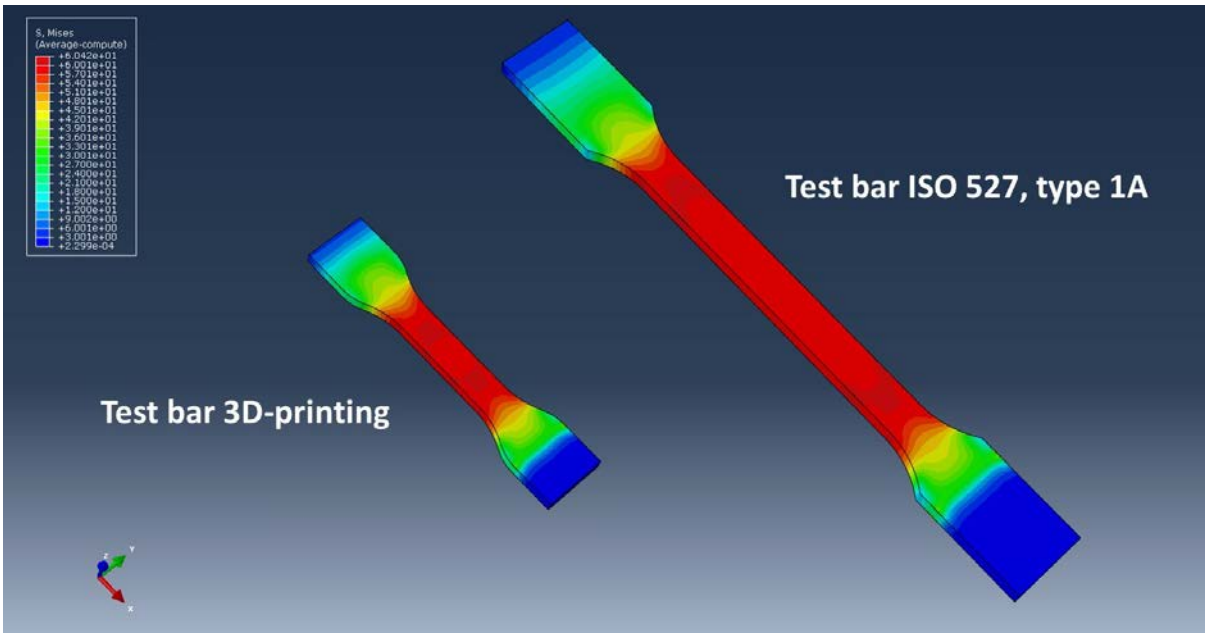

Fig. 1: To improve the results of all mechanic analysis (static, dynamic, creep and fatigue), a separate test specimen was dimensioned especially for 3D printing parts. Small parts with the largest possible sample cross-section must provide comparable results to standard specimens, like test bar ISO 527, type 1A.

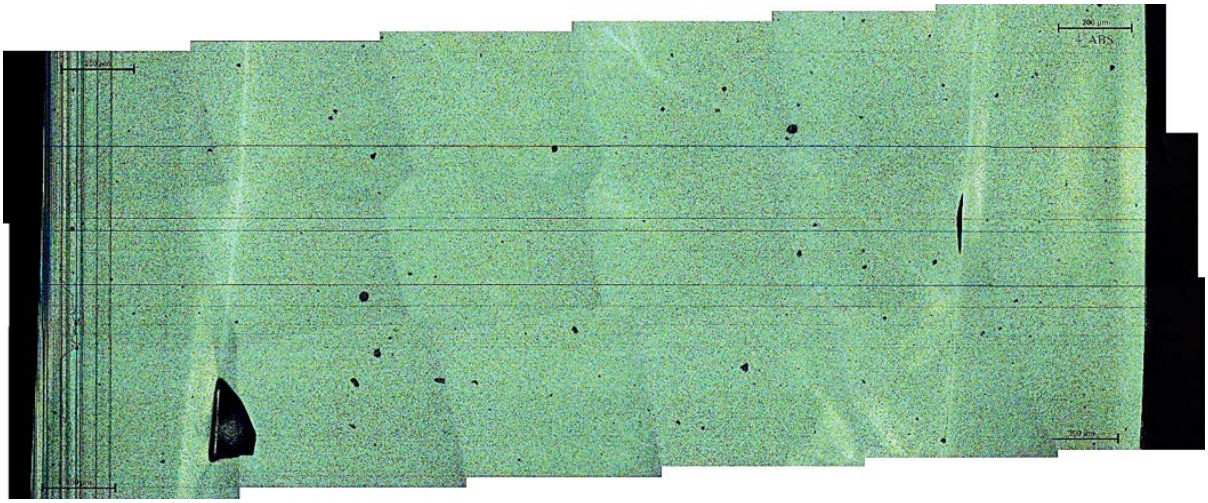

Fig. 2: Stitched Light Microscopy image of a cross section of a FDM printed sample made of ABS in standing structure direction, as it is clamped for the tensile tests.

IM3 Diffraction-based techniques and spectroscopy in electron microscopy

Type of presentation: Invited

IM3-IN-3015 Pushing at the limits of low-dose in 4D-STEM and electron ptychography

Nellist P. D.[1], Ding Z.[1], Kirkland A. I.[1,2,3]

[1]Department of Materials, University of Oxford, United Kingdom, [2]Electron Physical Sciences Imaging Centre, Diamond Light Source Ltd., Didcot, United Kingdom, [3]The Rosalind Franklin Institute, Harwell Science and Innovation Campus, Didcot, United Kingdom

Email of the presenting author: peter.nellist@materials.ox.ac.uk

Many candidate materials for important applications in energy conversion and energy storage are highly susceptible to damage under the irradiating electron beam and so an important current challenge is to develop methods that can allow the high-spatial resolution structural determination of these materials. Hitherto, the scanning transmission electron microscope (STEM) has not been widely regarded as an instrument appropriate for low dose studies, in part because the most common STEM imaging modes, such as annular dark-field imaging (ADF), only collect a small fraction of the incident electrons. The development of fast pixelated detectors now allows the full diffraction pattern from each illuminating STEM probe position to be recorded for each illumination STEM probe position, thus forming a 4D-STEM data set that records almost all the transmitted electrons. It will be shown how ptychography can be used for structural analysis of beam sensitive materials including Li ion battery cathode materials and polymers.
The instrumental requirements for low-dose work will be discussed, in particular the balance between detector dynamic range and speed. Even diffraction patterns containing fewer than 100 electrons per probe position can reveal the structure of a zeolite sample [1]. It will be discussed how different 4D-STEM and ptychography data processing methods cope with noise arising from low-doses. For imaging soft-materials, an energy-filter is often used to reduce the large image background arising from inelastic scattering. By reconstructing structures from energy-filtered 4D-STEM data (Figure 1), we show that filtering the inelastic scattering leads to worsened contrast and signal to noise.

[1] CM O'Leary, et al., Applied Physics Letters 116 (2020) 124101

Acknowledgement: Support from JEOL UK, PNDetector, EPSRC (EP/K040375/1, EP/M010708/1, EP/P033229/1), The Henry Royce Institute, EU 823717 ESTEEM3

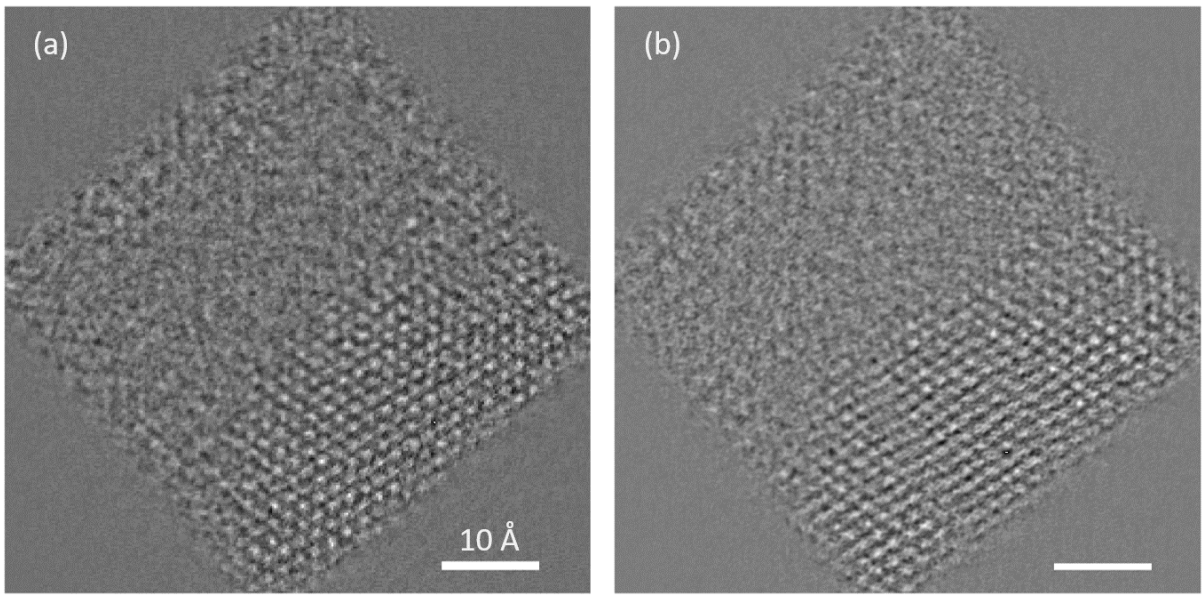

Fig. 1: Figure 1 | Ptychographic phase reconstructions of the edge of a Au nanoparticle (a) without energy filtering, i.e. elastic and inelastic scattered electrons are both recorded, and (b) with energy filtering, i.e. only elastic scattered electrons are recorded. Defocus value is -14 nm.

Type of presentation: Oral

IM3-O-2671 High-resolution Powder Nano-Beam Diffraction in Scanning Electron Microscopy

Slouf M.[1], Skoupy R.[2], Pavlova E.[1], Krzyzanek V.[2]

[1]Institute of Macromolecular Chemistry of the Czech Academy of Sciences, Prague, Czech Republic , [2]Institute of Scientific Instruments of the Czech Academy of Sciences, Brno, Czech Republic

Email of the presenting author: slouf@imc.cas.cz

We have recently introduced a novel SEM method which yields powder electron diffraction patterns [1] that are fully comparable to standard TEM/SAED powder diffractograms [2]. This opens quite new possibilities in the field of SEM microscopy. The only hardware requirement is that the SEM microscope must be equipped with a pixelated detector of transmitted electrons.

The pixelated detectors (2D-array detectors) for STEM-in-SEM have been commercialized recently. They can be used routinely to collect a high number of electron diffraction patterns from individual nanocrystals and/or locations [3]. This is called 4D-STEM, as we obtain 2D diffractogram for each pixel of the 2D scanning array. The 4D-STEM datasets are easy to collect, but the individual 4D-STEM diffractograms are difficult to analyze due to the random orientation of nanocrystalline material. In our method, all individual spotty diffractograms are combined into one composite powder diffraction pattern (Fig. 1). Consequently, the method was called 4D-STEM/PNBD (Powder NanoBeam Diffraction) The final 4D-STEM/PNBD diffractogram can be analyzed easily by means of standard programs for TEM/SAED, such as ProcessDiffraction [4].

To make the 4D-STEM/PNBD analysis as simple as possible, we developed a freeware Python program package STEMDIFF [5]. The package converts 4D-STEM datasets to powder diffractograms with a minimal user input. The recent STEMDIFF version includes a fast entropy-based filtering module (selecting of strongly diffracting locations and ignoring the amorphous regions) and deconvolution module (reducing the effect of primary beam spread), which improve the 4D-STEM/PNBD resolution to a TEM/SAED level (Fig. 2).

References:

[1] *Nanomaterials* 11 (2021) 962; doi: 10.3390/nano11040962
[2] *Materials* 14 (2021) 7550; doi: 10.3390/ma14247550
[3] *Microsc Microanal* 23 (2017) 554; doi: 10.1017/s1431927617003452
[4] *Microsc Microanal* 18 (2012) 406; doi:10.1017/S1431927611012803
[5] https://pypi.org/project/stemdiff

Acknowledgement: We thank Thermo Fisher Scientific for a high-resolution SEM with pixelated detector within the projects TN01000008 (TACR) and GA21-13541S (CSF).

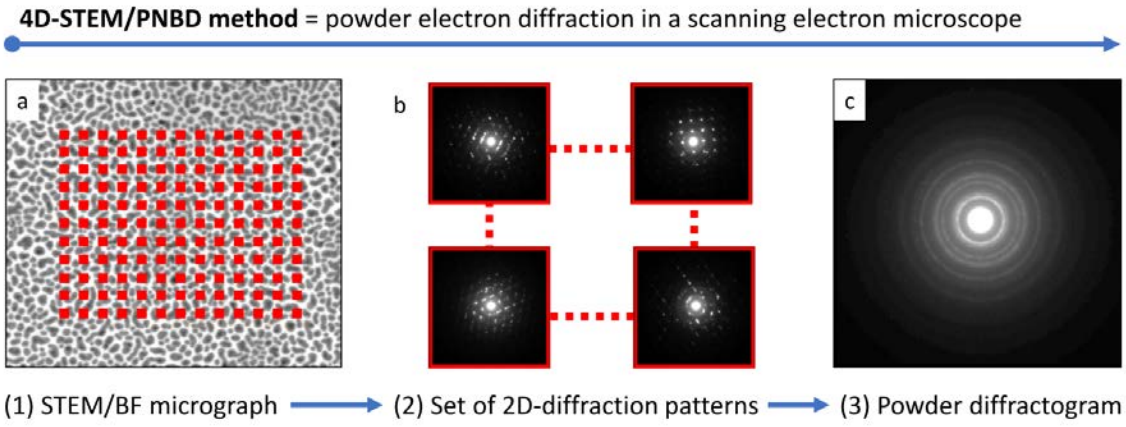

Fig. 1: Principle of 4D-STEM/PNBD method: (a) Standard STEM/BF image of a sample with a scanning matrix (represented by red points), (b) diffraction patterns captured from the individual locations (all red points in fig. (a)) and (c) powder diffraction pattern obtained by summation of all individual diffraction patterns (shown schematically in fig. (b)).

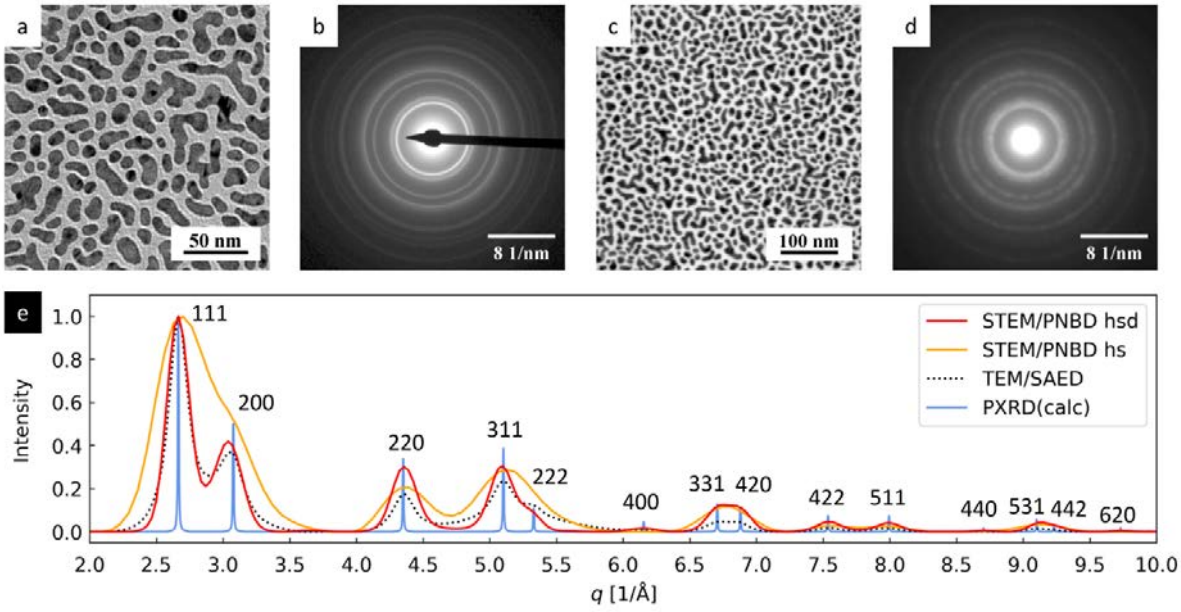

Fig. 2: Comparison of 4D-STEM/PNBD, TEM and PXRD results for Au nanoislands: (a) TEM/BF, (b) TEM/SAED, (c) STEM/BF, (d) 4D-STEM/PNBD, and (e) the comparison of radially averaged results from 4D-STEM/PNBD method with deconvolution (red line), 4D-STEM/PNBD without deconvolution (orange), TEM/SAED (black), and theoretically calculated PXRD (blue).

Type of presentation: Oral

IM3-O-2896 A New Approach for 3D Quantitative STEM Using Defocus Corrected Electron Ptychography

Mostaed A.[1], Liberti E.[1,2], Huang C.[2], Nellist P.[1], Kirkland A. I.[1,2,3]

[1]Department of Materials, University of Oxford, Oxford OX1 3PH, UK, [2]The Rosalind Franklin Institute, Harwell Campus, Didcot OX11 0FA, UK, [3]electron Physical Science Imaging Centre (ePSIC), Diamond Light Source, Didcot OX11 0DE, UK

Email of the presenting author: ali.mostaed@materials.ox.ac.uk

Electron ptychography is a powerful technique exploited to study the atomic structure of materials including those containing both light and heavy elements. In electron ptychography, first, a series of electron diffraction patterns (i.e. a 4D STEM dataset) are collected by scanning an electron beam (probe) across a specimen. Then, some mathematical algorithms (e.g. SSB, WDD and ePIE) are used to deconvolve the probe and object transfer functions from the 4D STEM dataset. The key assumption in these algorithms is that the probe function is constant for all the probe positions since the aberrations of the microscope's electromagnetic lenses are almost constant during the very short time of data acquisition. Although the lens aberrations can be assumed to be constant for each probe position in a dataset, the probe function is not unique since the geometry of the specimen at each probe position across the imaging area alter the defocus value of the probe (Figs. 1(a-c)). Thus, we have to use a defocus-corrected probe function for each probe position to calculate the object transfer functions. Here we show that it is possible to calculate the probe's defocus value using electron ptychography. Moreover, we demonstrate that 3D models of nanoparticles can be obtained from 4D-STEM datasets acquired simultaneously with HAADF images. Here, we calculated the number of Pd atoms for each atom column observed in a HAADF image from a Pd nanocube (Fig. 2(d)), and then we measured the height of those columns from their apparent defocus extracted from the WDD ptychographic phase reconstructed from a 4D-STEM dataset acquired simultaneously with the HAADF image. Finally, the 3D model of the Pd nanocube were simply reconstructed as we had the number of atoms in each column as well as the height of those columns (Fig. 2(e-g)). We expect this approach to be applicable to reconstruct not only an accurate ptychographic phase but also a 3D model of any other nanostructure.

Acknowledgement: The authors thank funding from the ESTEEM3 program under Grant No 823717 and access the Diamond Light Source's instrument E02, Proposal Nos MG20431 and MG22317

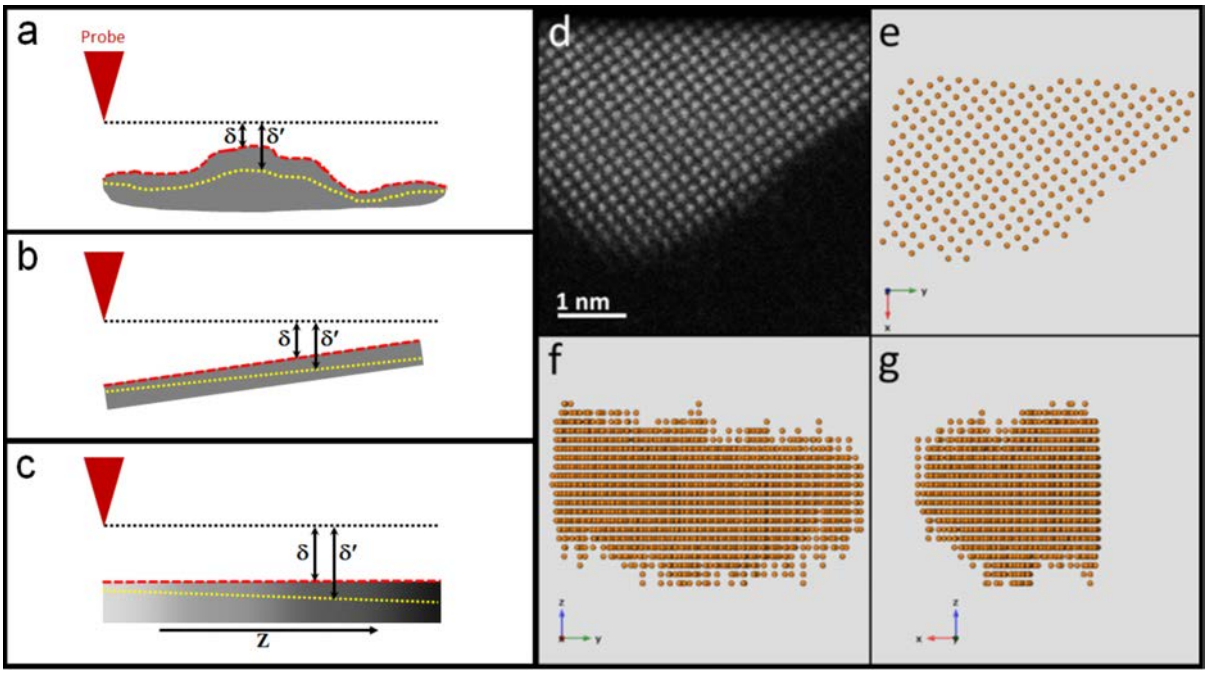

Fig. 1: Absolute defocus (δ) and apparent defocus (δ') levels for (a) a sample with an uneven surface, (b) tilted sample and (c) sample with compositional variation. (d) ADF image obtained from a Pd nanocube. (e-g) 3D reconstructed model in three different viewing direction for the nanocube shown in (d).

Type of presentation: Invited

IM3-IN-2626 Challenges in the characterization of complex nanomaterials with analytical STEM

Knez D.[1], Lammer J.[2], Oberaigner M.[1], Šimić N.[2], Haberfehnler G.[1], Fisslthaler E.[2], Krisper R.[2], Radlinger T.[1], Grogger W.[1,2], Hofer F.[1,2], Kothleitner G.[1,2]

[1]Institute of Electron Microscopy and Nanoanalysis, Graz University of Technology, Graz, Austria, [2]Graz Centre for Electron Microscopy, Graz, Austria

Email of the presenting author: daniel.knez@felmi-zfe.at

Aberration corrected electron optics, novel detection techniques in combination with advanced computational capabilities have turned scanning transmission electron microscopy (STEM) into one of the most powerful characterization techniques for a wide range of nanomaterials. Its versatility stems from the availability of different imaging and diffraction modes as well as analytical techniques such as electron energy-loss (EELS) and energy dispersive X-ray spectroscopy (EDX), which enables one to deduce information about structure, elemental composition and chemical bonding with atomic resolution [1]. This has paved the way for many breakthroughs in understanding fundamental phenomena in physics, chemistry and material science in recent years.

In practice, however, structural and chemical characterization on an atomic level, such as the detection of impurities, dopants or point defects within a crystal, is often impeded by experimental challenges in sample preparation, limitations in signal-to-noise ratios (SNR), instrumental instabilities and the high current densities introduced by a highly focused electron beam. This leads to steady, yet often unrecognized specimen transformations [2], especially when applying spectroscopic techniques, which in general require higher acquisition doses. This is particularly true for experiments that aim to determine concentrations or defects quantitatively [1, 3]. As a consequence, many highly relevant material systems such as battery materials, materials with a high amount of low-coordinated surface atoms (nanoporous materials and nanoclusters) and organic/biological materials, require the development of novel methodologies in preparation, characterisation and data analysis.

The talk will give an overview over acquisition and analysis strategies for STEM spectroscopy tackling the above-mentioned challenges by exemplary showcasing some selected research questions, with different material systems like complex oxides, metallic clusters and energy materials.

Exemplary, the column-by-column quantification of barium lanthanum ferrate and the compositional characterization of Au@Ag and Ag@Au core-shell nanoclusters will be discussed. Emphasis will be placed on the use of direct detection detectors for EELS and complementary high-sensitivity EDX.

[1] G. Kothleitner et al., Phys. Rev. Lett. 112 (2014), doi:10.1103/PhysRevLett.112.085501.
[2] D. Knez et al., Ultramicroscopy. 192, 69–79 (2018), doi:10.1016/j.ultramic.2018.05.007.
[3] J. Lammer et al., Ultramicroscopy 234, 113477 (2022), doi:10.1016/j.ultramic.2022.113477.

Acknowledgement: Financial support by the EU Horizon 2020 program under Grant 823717-ESTEEM3 and by the Austrian Science Fund (FWF) under grant nr. I4309-N36.

Type of presentation: Oral

IM3-O-2824 The choice of the right beam energy for analytical (scanning) transmission electron microscopy

Stöger-Pollach M.[1]

[1]USTEM, TU Wien, Vienna, Austria

Email of the presenting author: stoeger@ustem.tuwien.ac.at

Analytical electron microscopy aims for the detailed analysis of pristine specimens. Although this sentence sounds so trivial and self-evident, it contains a task that is indeed difficult to master. It is the preservation of the original state of the sample without generating radiation damage through electron bombardment. The best-known forms of radiation damage are knock-on damage and radiolysis. While radiolysis is mainly a problem for organic samples and increases with lower radiation energy, knock-on damage is a significant problem for inorganic samples at elevated electron energies. Knock-on damage does not necessarily mean that atoms have to be knocked out of the sample. It also describes the creation of point defects. The latter often cannot even be detected by means of high-resolution microscopy. Nevertheless, they can massively influence the analytical signal in terms of quenching and the generation of additional signals [1].
Another aspect for the correct choice of acceleration voltage is the generation of unwanted signals, which can overlap with the signals of interest. These include the Vavilov-Cerenkov radiation in the cathodoluminescence (CL) signal [2] and the corresponding energy losses in electron energy loss spectrometry (EELS) [3] but also the corresponding surface excitations, also known as light guide modes. The latter are excited on the top and bottom surface of the sample and can generate significant interference patterns in thin samples.
As a consequence, modern electron microscopes require a Consequently, modern electron microscopes require great flexibility in terms of the accelerating voltages available not only for imaging but also for spectroscopy. While CL analyses can be performed independently of the beam energy, since the optical components do not have to be adapted to the electron energy, this is different in EELS. Here, too, great energy flexibility is required.
In the present work, we show the influence of the beam energy on the CL and EELS signal for different semiconductor materials. For this purpose, we use our EEL spectrometer with high angular resolution and various high voltages. In comparison, CL spectra are recorded to quantify the Vavilov-Cerenkov radiation. Additionally, we study beam damage by observing quenching in CL, which is the most sensitive measure in this context.
[1] M. Stöger-Pollach et al., Ultramicroscopy 200 (2019) 111-124
[2] M. Stöger-Pollach et al., Ultramicroscopy 214 (2020) 113011
[3] M. Horak and M. Stöger-Pollach, Ultramicroscopy 157 (2015) 73-78

Type of presentation: Oral

IM3-O-2555 Tomography of surface phonon polarition fields by electron energy loss spectroscopy

Haberfehlner G.[1], Li X.[2], Hauer R.[1], Hohenester U.[3], Stéphan O.[2], Kociak M.[2], Kothleitner G.[1,4]

[1]Institute of Electron Microscopy and Nanoanalysis, Graz University of Technology, Graz, Austria, [2]Université Paris-Saclay, CNRS, Laboratoire de Physique des Solides, Orsay, France, [3]Institute of Physics, University of Graz, Graz, Austria, [4]Graz Centre for Electron Microscopy, Graz, Austria

Email of the presenting author: georg.haberfehlner@felmi-zfe.at

Surface phonon polaritons (SPPs) are coupled photon-phonon excitations that emerge at the surfaces of dielectric ionic nanostructured materials. Using a highly monochromated electron beam in a scanning transmission electron microscope (STEM), SPPs can be excited by the electron beam and mapped by electron energy loss spectroscopy (EELS). A tilt series of EELS spectrum images recorded at a number of tilt angles can be used as the basis for tomographically reconstructing the complete three-dimensional (3D) vectorial picture of the local photonic density of states (LDOS) [1] (Fig. 1). Knowing the full 3D LDOS promises insights into nanoscale physical phenomena and is invaluable to the design and optimization of nanostructures for fascinating new uses.

In this work, we perform a thorough examination of the tomography scheme introduced in [1]. Tomographic reconstruction of the LDOS is done by means of minimizing the difference between reprojected EELS maps of a reference structure and the simulated (or measured) EELS maps of the real structure (Fig. 2). The reprojected maps are calculated based on an eigenmode decomposition, dependent on the used reference structure. This reference structure is not necessarily equivalent to the real structure of the system, but may be a simplified representation of its geometry and ignore changes in the surroundings, such as the substrate.

Based on a previous approach used for surface plasmon reconstruction [2, 3], a generalized scheme, usable for the quasistatic case was performed to deal with mode mixing and symmetry breaking, which allows for using idealized reference structures in the reconstruction. To validate this approach, in simulation studies, we consider the impact of the choice of reference structure and the type of eigenmodes used. Finally, we apply these findings to the 3D reconstruction of experimental EELS data on more complex structures (Fig. 3).

[1] X Li et al., Science 371 (2021) p. 1364.
[2] A Hörl et al., Nat. Commun. 8 (2017) p. 37.
[3] G Haberfehlner et al., Nano Lett. 17 (2017) p. 6773.

Acknowledgement: This project has received funding from the European Union's Horizon 2020 research and innovation programme under grant agreement No. 823717 (ESTEEM3).

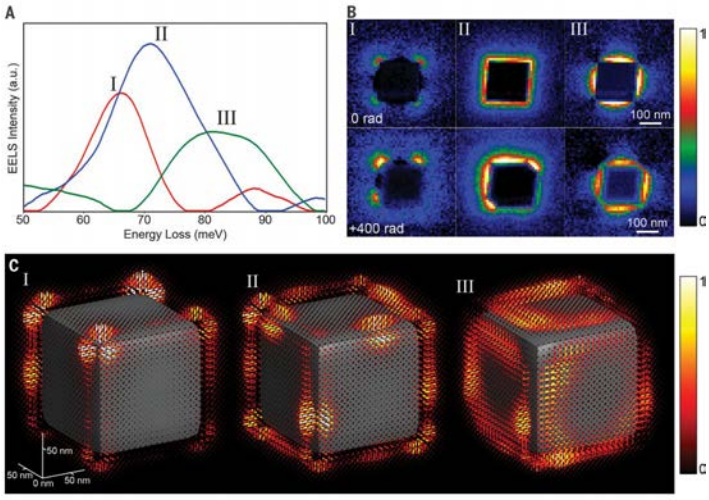

Fig. 1: 3D vectoral reconstruction of the phononic LDOS on a MgO-cube. (a) NMF components and (b) NMF maps at two different tilt angles for three main modes. (c) 3D reconstruction of the phononic LDOS of the three modes [1].

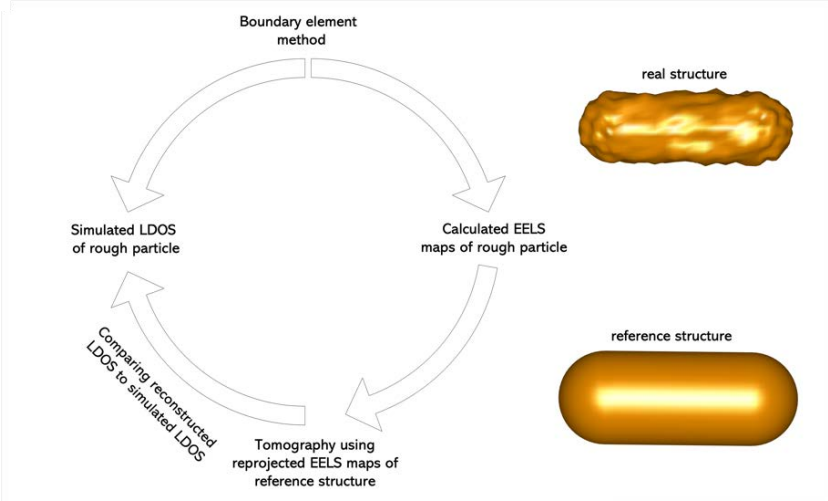

Fig. 2: Route for validation of tomography scheme based on simulated data.

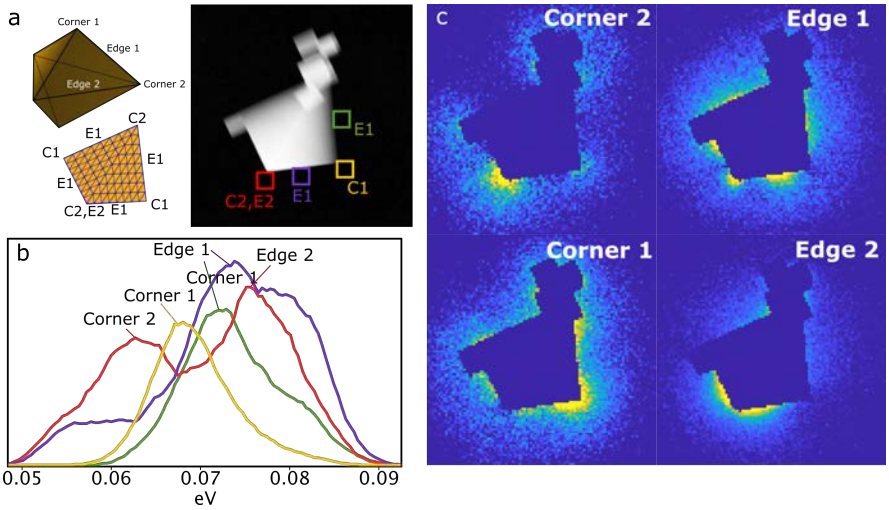

Fig. 3: 2D EELS results on a MgO bipyramid: (a) Morphology, (b) EELS spectra, (c) EELS maps

Type of presentation: Poster

IM3-P-2650 Investigation the origin of TiO2 nanoparticles in human pancreas using different TEM techniques

Brontvein O.[1]

[1]Electron Microscopy unit, Chemical Research Support Department, Weizmann Institute of Science, Rehovot, Israel

Email of the presenting author: olga.brontvein@weizmann.ac.il

Ti-O system has several stable phases, where TiO2 compound has 3 different stable structures: Anatase, Brokite and Rutile. Different structures of same compound have different mechanical, electrical, optical and more properties. As part of matter analysis obtained from the human pancreas, were found several types of nanoparticles while crystalline TiO2 and crystalline Fe(O)OH, were most commonly found. In this case different TiO2 structure has a different particle origin. The white colored food or medication pigment is TiO2 Anatase, and the wall pigment of paints is TiO2 Rutile. This work is focused on an analysis of TiO2 nanoparticles using different TEM techniques. High resolution TEM and SAED revealed that those particles are crystalline. However, d-spacings of known TiO2 structures are close one to the other, so it was not conclusive in this case. Using EELS measurements, it can be easily detected TiO2 phase according to Ti-O pick shape, but the quantitative analysis was not correct. On the other hand EDS quantitative analysis was informative and correct. As can be seen every TEM technique separately can't give us the full information, however their combination gave us all needed information to investigate TiO2 nanoparticles and as a result to understand their origin in human pancreas.

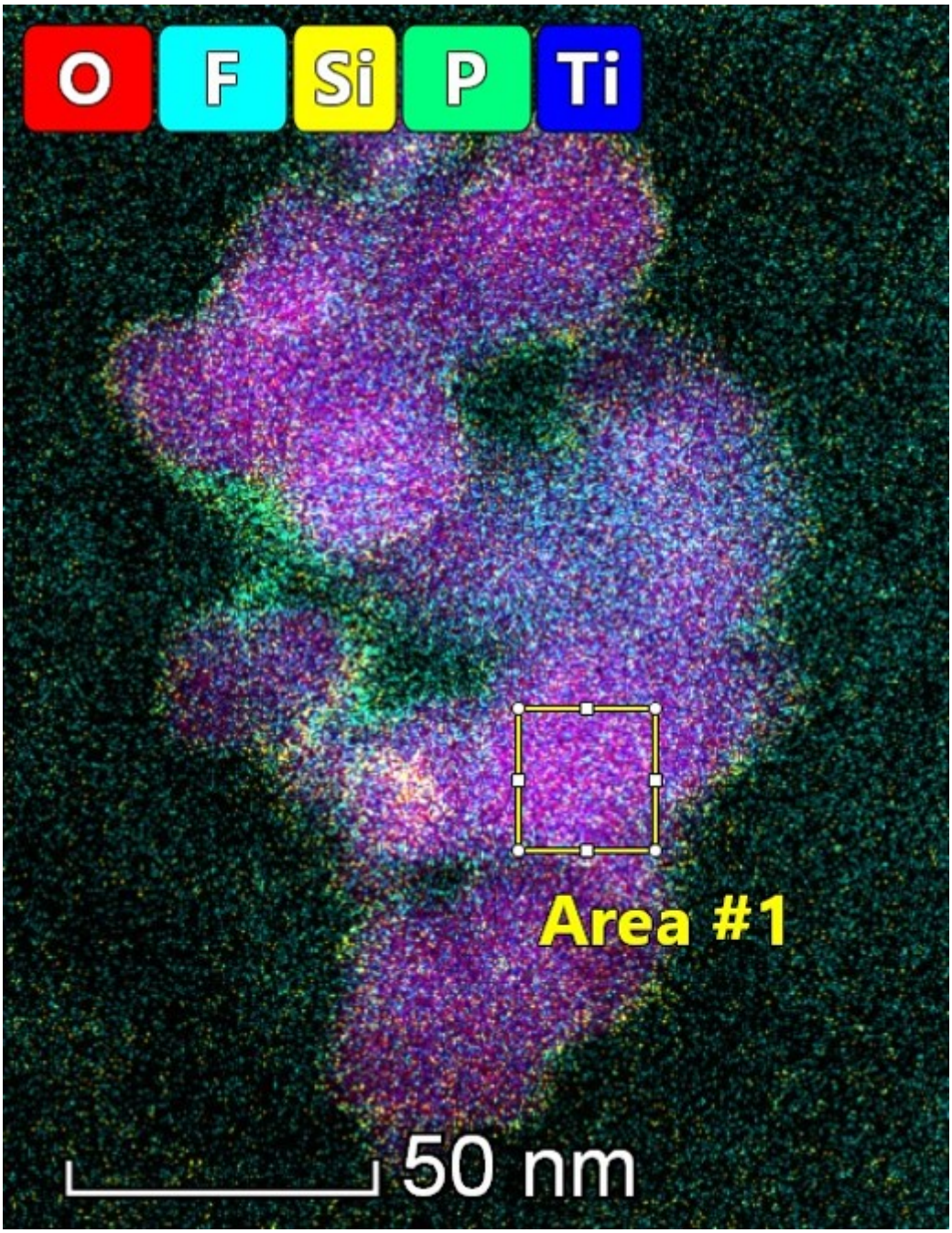

Fig. 1: HAADF STEM EDS

Type of presentation: Poster

IM3-P-2631 Precession Electron Diffraction and its Applications in Semiconductor Heterostructures

Brozyniak A.[1], Truglas T.[1], Navarro-Quezada A.[2], Groiss H.[1]

[1]Christian Doppler Laboratory for Nanoscale Phase Transformations, Center for Surface and Nanoanalytics, Johannes Kepler University Linz, Altenberger Str. 69, 4040 Linz, Austria, [2]Institute of Semiconductor and Solid State Physics, Johannes Kepler University Linz, Altenberger Str. 69, 4040 Linz, Austria

Email of the presenting author: aleksander.brozyniak@jku.at

Since its introduction in 1994, precession electron diffraction (PED) has become a powerful and indispensable mode in transmission electron microscopy (TEM) [1]. In contrast to standard diffraction patterns (DP), where dynamical effects are inevitable, PED yields quasi-kinematical diffraction patterns through precessing the electron beam (Fig. 1). The integration over the patterns from the varying diffraction angles during precession produces a significantly broader range of present diffraction reflections and compensates for small variations of sample thickness or misorientation. With the high spatial resolution resulting from the small probe size, PED offers vast possibilities in nanostructure analysis.

In this work, we demonstrate the potential of (scanning) nanobeam PED in a JEOL 2200FS TEM, equipped with a TVIPS-manufactured universal scan generator using a fast 4k x 4k CMOS camera. The influence of various beam precession (tilting) angles between 0° and 3° is shown for DPs parallel to the strong dynamical <110> zone axis of Si, to demonstrate the possible parameter space and reached accuracy of our setup. Subsequent intensity analysis of individual (forbidden) spots helps to find the optimum precession angle [2]. By scanning the precessed beam over a sample area full 2D DPs arrays are obtained. The resulting large data sets can be used for phase identification and orientation mapping, as well as for detailed lattice and strain analysis.

The strain and phase mapping capabilities of PED with a nanobeam diffraction setup are shown for Fe_yN nanocrystals (NCs) embedded in phase-separated GaδFeN layers, a hybrid material system combining semiconductors and magnetic nanostructures (Fig. 2) [3]. The Al concentration in the $Al_xGa_{1-x}N$ buffer layers determines the number of dislocations threading from the interface with the sapphire substrate to the surface of the system. The threading dislocations (TDs) act as NCs nucleation sites, and the strain-related TD density influences the ratio of the cubic γ-Fe_4N and the hexagonal Ɛ-Fe_3N NCs with differently oriented magnetic easy axes. Along with the strain and phase maps obtained with PED (Fig. 3), we demonstrate the reduction of TDs through an additional AlN interlayer with weak-beam dark-field microscopy.

[1] R. Vincent, P.A. Midgley, Ultramicroscopy **53**, 271 (1994).
[2] A.S. Eggeman, T.A. White, P.A. Midgley, Ultramicroscopy **110**, 771 (2016)
[3] A. Navarro-Quezada, K. Gas, T. Truglas, V. Bauernfeind, M. Matzer, D. Kreil, A. Ney, H, Groiss, M. Sawicki, A. Bonanni. Materials, **13**, 3294 (2020)

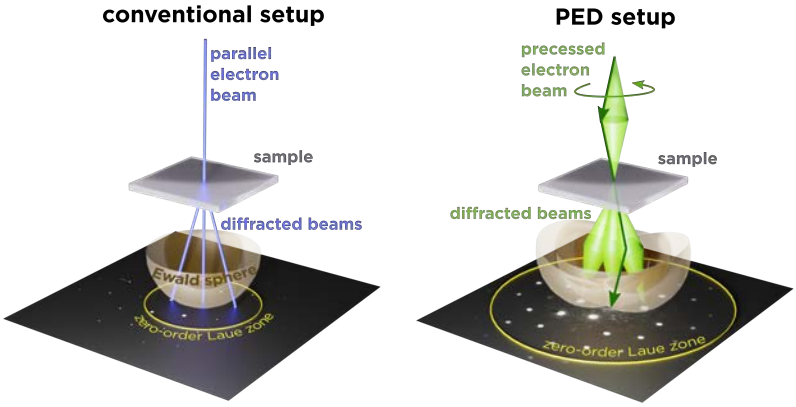

Fig. 1: Comparison between the principles of the conventional and the PED TEM diffraction on a Si [110] specimen. The DP in PED mode is an integration over all patterns acquired during precession.

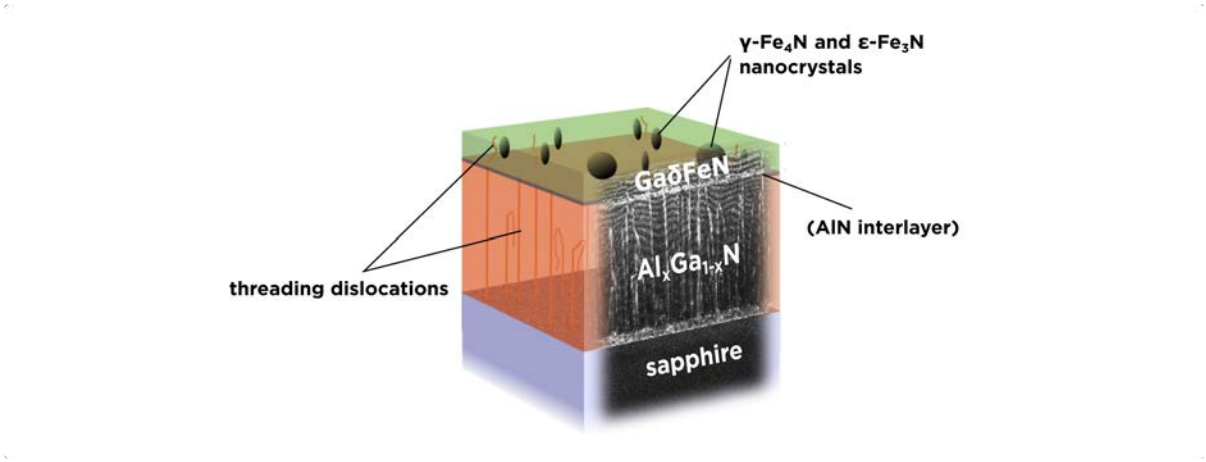

Fig. 2: Structure of the investigated system: $Al_xGa_{1-x}N$ buffer layers grown on sapphire. An optional AlN interlayer can further influence the dislocation density, affecting the nanocrystals in the topmost GaδFeN layer. A **g**-3**g** weak-beam dark-field image features the dislocations stopped by the AlN interlayer.

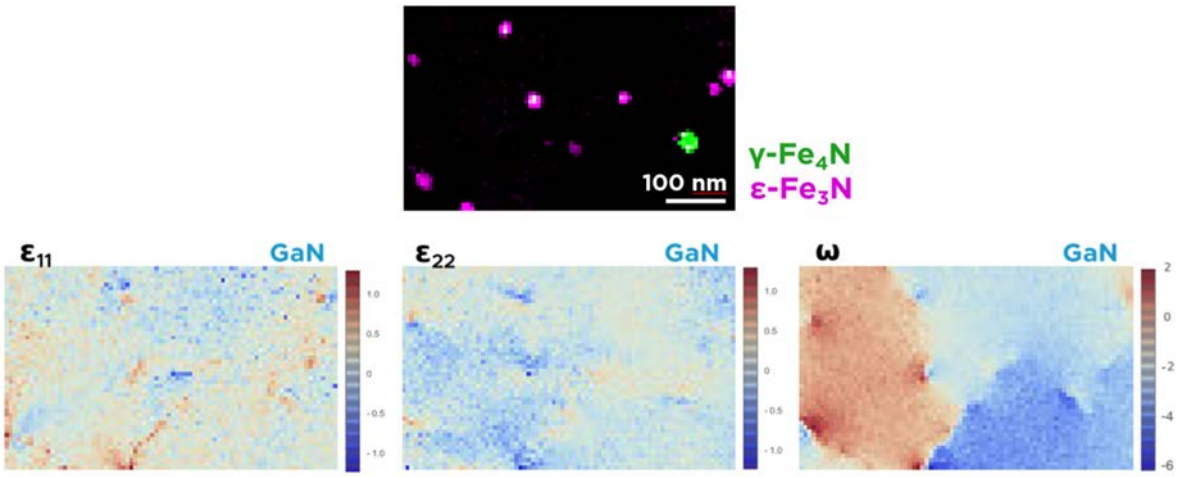

Fig. 3: Exemplary PED phase map identifying the location of γ-Fe_4N and Ɛ-Fe_3N nanocrystals embedded in a GaN buffer (upper image). Exemplary PED strain maps of the corresponding GaN buffer (lower images).

Type of presentation: Poster

IM3-P-2579 3D Electron Diffraction on Ferroelectric Perovskites.

Griesi A.[1], Vit V.[2], Lanza A.[5], Orlandi F.[3], Righi L.[4], Gemmi M.[5]

[1]Center for Convergent Technologies CCT@Morego, (IIT), Genova, Italy, [2]CNR-IMEM, Parma, Italy, [3]ISIS Neutron and Muon Facility, Rutherford Appleton Laboratory–STFC, UK, [4]Department of Chemistry, Life Sciences and Environmental Sustainability, University of Parma, Parma, Italy, [5]Istituto Italiano di Tecnologia, Center for Materials Interfaces, Electron Crystallography, Pontedera, Italy

Email of the presenting author: andrea.griesi@iit.it

The doubly ordered perovskites AA'BB'O_6 have been known since 1984, but detailed structural studies have only been carried out in recent years. Perovskites have structural and compositional flexibility, which allows us to alter the conduction bandwidth and strength of the magnetic super-exchange interactions. As such, they provide a mechanism for fine-tuning the electrical, magnetic, and optical properties[1].
The crystal structures of several doubly ordered AA'BB'O_6 perovskites have proven to be more complex than originally thought. Previous studies report complexity of the structure, such as compositional and/or positional modulations and twinnig of the octahedral tilt system[1].
NaLaCoWO6, a promising ferroelectric material, is one example of this structural complexity, showing a monoclinic average structure and a still unexplained temperature-dependent modulation[2].
Moreover, NaLaCoWO6 can only be obtained in nanocrystalline form, thus making single-crystal XRD methods not applicable and powder methods extremely difficult. In such cases, 3D precession electron diffraction is the method of choice as it makes it possible to collect 3D diffraction data from single nanocrystals. This allows us to observe and resolve the modulation and reveal investigate local features of the structure[3].
Tiny changes of the crystal structures determine alterations of electric properties and could represent the key to understand the chemical mechanism governing the electric field-induced transitions. From our studies on $NaLaCoWO_6$ with 3D PED at variable temperature, we could determine the modulation vector and superspace symmetry. Combining PED data with NPD and XRPD, we solved the (3+1)D modulated structure. An additional challenge is to use electron diffraction to reveal the structural changes induced by the application the of an electric field on $NaLaCoWO_6$.
[1] G. King, J. Mater - Chem 2010, 20, 5785-5796;
[2] P. Zou, C. Darie et al. - Inorg. Chem. 2019, 58, 81−92;
[3] A. Lanza, M. Gemmi et al. - Acta Cryst. (2019). B75, 711-716.

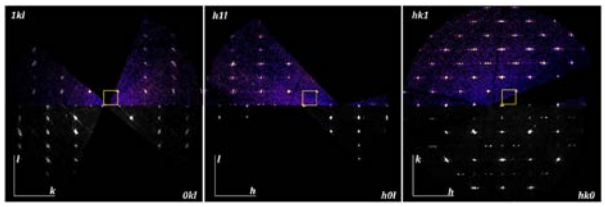

Fig. 1: Reconstruction of the $NaLaCoWO_6$ reciprocal space obtained from the 3D ED data showing the modulation along the a* direction. The black zones, devoid of reflections, are areas of the reciprocal space that are not measured due to the geometrical constrain of the experiment.

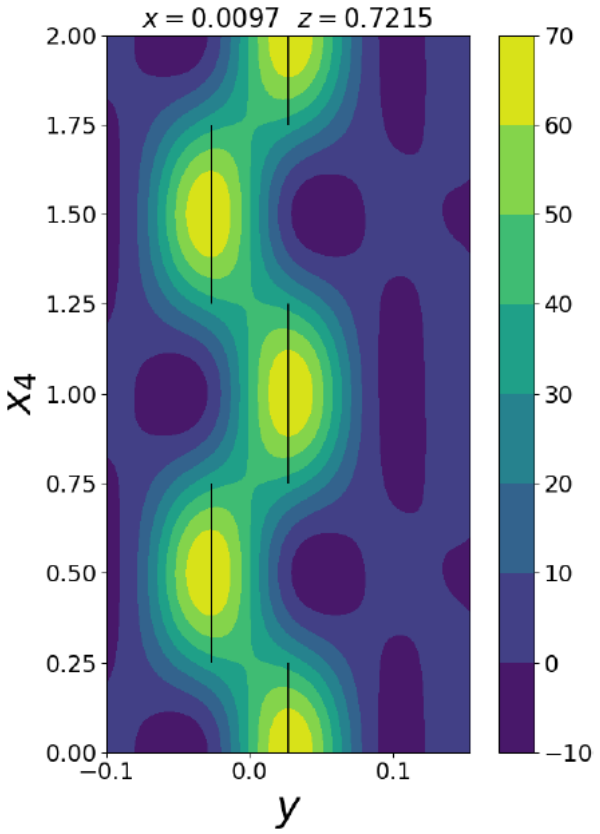

Fig. 2: Fourier map calculated around the O1 position showing the discontinuous occupancy of the split positions along the x4 direction.

Type of presentation: Poster

IM3-P-2642 Analytical electron tomography of CuNiFe magnetic spinodal alloys

Kormilina T. K.[1], Haberfehlner G.[2], Radlinger T.[2], Kothleitner G.[1,2]

[1]Graz Centre for Electron Microscopy, Graz, Austria, [2]Institute of Electron Microscopy and Nanoanalysis, Graz University of Technology, Graz, Austria

Email of the presenting author: tatiana.kormilina@felmi-zfe.at

Many properties and effects connected to the microstructure of materials are being redefined and expanded with the development of 3D characterization techniques. In this manner, magnetic spinodal alloys of copper-nickel-iron have already proven themselves a valuable material for applications ranging from electric motors to data storage and spintronics. Despite their long investigation history and the consistent reports of variations in microstructure having influence on mechanical and magnetic properties [1,2], the whole picture is still not understood. The exact relationship between the microstructural anisotropy and material performance remains an active field of research.

Analytical techniques play important role in visualization and quantification of the chemical composition and morphology of the alloy constituents. Electron energy loss spectroscopy (EELS) and energy-dispersive X-ray spectroscopy (EDXS) were used to define the precipitates in $Cu_{75}Ni_{20}Fe_5$ alloys [3]. 3D study using high-angle annular dark field (HAADF) STEM tomography and 3D data analysis tools were shown effective and insightful for high entropy alloys [4] and, combined with analytical tools, were used to describe the complex phases of alnico alloys [5].

In this study we incorporate EDXS and EELS measurements in the process of HAADF tilt series acquisition (Figure 1) to create three complementary 3D representations of $Cu_{52}Ni_{34}Fe_{14}$ alloy sample. Samples are prepared with focused ion beam as 200-300 nm thick pillars to allow full 180° tomography acquisition angle. Elemental mapping in 3D is used to analyse chemical composition of Cu and Ni+Fe rich platelet-like phases and quantify the spinodal wavelengths in three dimensions. Explored are also the ligament interconnectivity and relationship between structure anisotropy and magnetic properties.

[1] Findik, F. "Improvements in spinodal alloys from past to present." Materials & Design 42 (2012): 131-146.

[2] Kobayashi, S. et al. "Magnetization Characteristics of Oriented Single-Crystalline NiFe-Cu Nanocubes Precipitated in a Cu-Rich Matrix." Molecules 25.14 (2020): 3282.

[3] Kang, S. et al. "Microstructural evolutions of a Cu75-Fe5-Ni20 alloy depending on the isothermal annealing temperatures." Metals and Materials International 18.3 (2012): 521-525.

[4] Sosa, J. M., et al. "Three-dimensional characterisation of the microstructure of an high entropy alloy using STEM/HAADF tomography." Materials Science and Technology 31.10 (2015): 1250-1258.

[5] Guo, W. et al. "Correlative energy-dispersive X-ray spectroscopic tomography and atom probe tomography of the phase separation in an alnico 8 alloy." Microscopy and Microanalysis 22.6 (2016): 1251-1260.

Acknowledgement: This project has received funding from the European Union's Horizon 2020 Research and Innovation Program under grant agreement No. 823717-ESTEEM3.

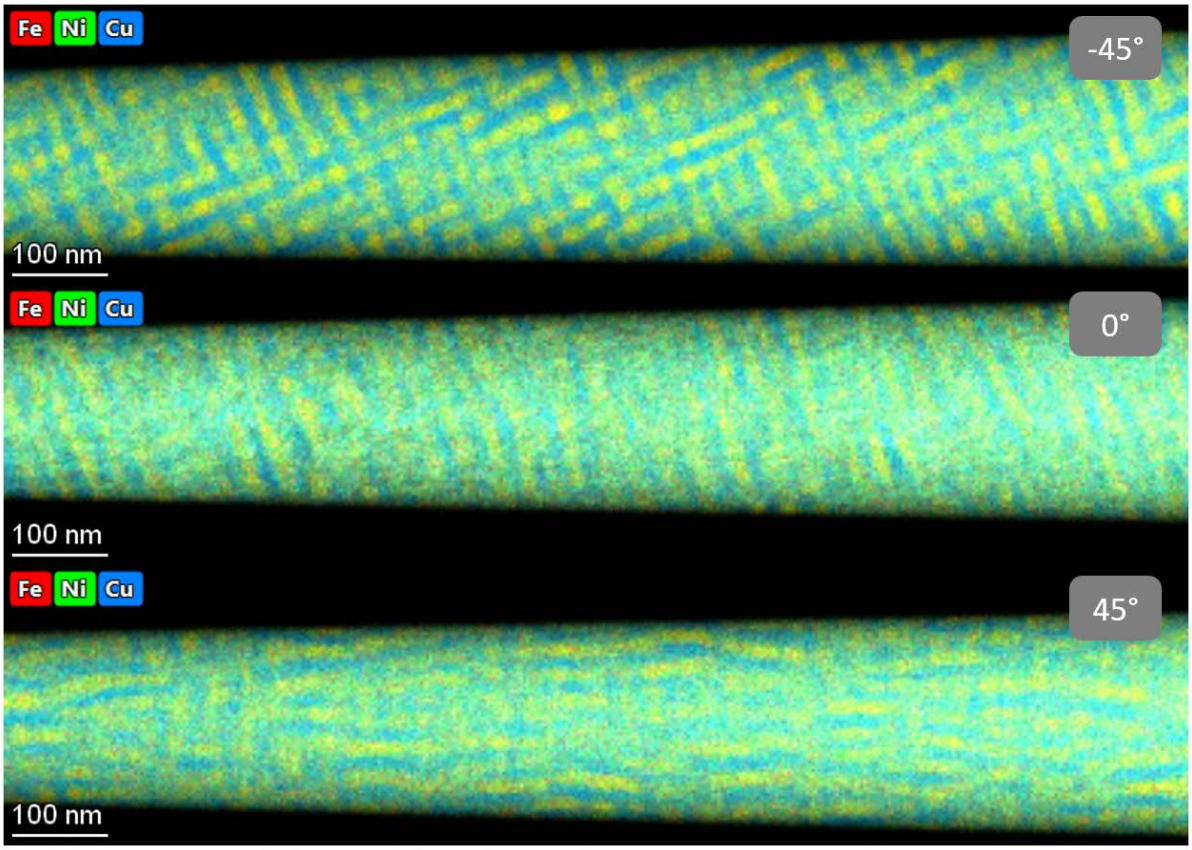

Fig. 1: Color mix view of EDXS projections taken at -45, 0, and 45 degree tilt, revealing Cu rich and Ni+Fe rich phases with the direction of longest dimension appearing respectively diagonal, perpendicular and parallel to the pillar axis.

Type of presentation: Poster

IM3-P-2781 Application of the DiffMap program to PtSi thin films

Lábár J. L.[1], Pécz B.[1], Nemouchi F.[2], Lefloch F.[2], Vethaak T. D.[2]

[1]EK MFA, Konkoly Thege M. u. 29-33, H-1121 Budapest, Hungary, [2]Univ. Grenoble Alpes, CEA, LETI, F-38000 Grenoble, France

Email of the presenting author: labar.janos@ek-cer.hu

A computer program, named DiffMap, was recently published for evaluation of four dimensional electron diffraction (4D-ED) datasets to calculate orientation maps and phase maps from them [1]. The dataset is measured with a nearly parallel nanoprobe in a scanning transmission electron microscope (STEM) by scanning the electron probe over a rectangular area and recording a two-dimensional (2D) diffraction pattern at each position of the probe (i.e. at each pixel of the relevant 2D STEM image). The 4D-ED dataset manifests in the recorded several thousand electron diffraction patterns, which serve as the input of the DiffMap program.
PtSi thin film samples were selected to demonstrate the operation of this program. PtSi has been an important contact material in the electronic industry, specifically in CMOS silicon technology. A new application of this material is planned in the development of new quantum technology within a Quant-ERA project “Superconducting Silicon Qubit in CMOS Technology (SIQUOS)”, which started on 1 April 2022. An important property of PtSi is that it becomes superconducting at very low temperatures (1 K). The SIQUOS project will use it to realise and study a Si gatemon qubit, a gate tuneable transmon qubit composed of a Si Josephson field-effect transistor (JoFET) coupled to a microwave resonator. The Si JoFET is a Si transistor with superconducting source and drain (S&D) contacts, whose non-dissipative supercurrent can be modulated by an electrostatic gate. CMOS-compatible metal silicides will be used as the superconducting S&D contacts. One of them is PtSi.
The 4D-ED dataset was recorded in a Titan Themis G2 200 (Thermo Fisher Scientific,Waltham, MA, USA) STEM, operated at 200 kV and controlled by the TIA program of Thermo Fischer. A high-angle annular dark-field (HAADF) detector (E.A. Fischione Instruments, Inc., Pennsylvania, PA, USA) recorded the STEM image. A 4k*4k CETA 16 CMOS (optical fiber coupled, indirect detection) camera recorded the diffraction patterns, converted into TIF format. The microprobe STEM operation mode of the Themis ensured probe convergence angle of 0.24 mrad. With this nearly parallel probe the spatial resolution of the STEM HAADF image is not as good as in the usual STEM mode, but the recorded diffraction patterns are composed of small spots, similarly to the selected area electron diffraction (SAED) patterns, without the application of a selected area aperture (SAA). Spatial localization of the diffraction information is done by the restricted illumination provided by the small diameter electron probe.

Acknowledgement: Financial support of the Quant-ERA SIQUOS and
VEKOP-2.3.3-15-2016-00002 of ESIF is acknowledged.

A·thin·TEM·lamella·was·prepared·by·Ar-ion·beam·from·the·backside·of·a·layer-on-top-of-a-substrate·sample.·A·10·nm·thick·Pt·layer·was·deposited·on·top·of·a·Si·substrate·and·heat·treated·to·350·°C·that·resulted·in·a·reaction·between·the·Pt·and·Si.·Heat·treatment·was·done·under·a·protecting·thin·layer,·which·was·removed·prior·to·the·examination.·Backside·thinning·resulted·in·a·thin·plane-view·sample·with·the·nanograins·(containing·both·Pt·and·Si)·seen·laterally·side-by-side.·The·phase·in·these·nanograins·was·automatically·identified·from·the·4D-ED·dataset·by·the·Diffmap·program.·2500·diffraction·patterns·were·processed·(from·a·50*50·pixel·STEM·image).·The·pixel·size·is·4·nm,·so·the·entire·field·of·view·is·200·nm.·It·turned·out·that·the·only·crystalline·phase·found·in·the·layer·is·PtSi·(an·orthorhombic·phase,·space·group·62).·Neither·part·of·the·original·Pt,·nor·Pt_2Si,·nor·Si·remained·in·crystalline·form·in·that·part·of·the·examined·thin·layer.·The·orientation·map·of·PtSi·is·presented·in·Fig.·1.·It·is·seen·that·the·grains·are·not·larger·than·20·nm·in·diameter·and·many·very·different·orientations·appear·in·the·layer,·with·[010]·orientation·for·the·majority·of·the·grains·pointing·to·the·Z-direction·of·the·Lab-system·(which·is·the·direction·of·the·electron·beam·of·the·STEM).·It·shows·a·degree·of·local·texture·in·this·small·area.·Relation·to·any·possible·texture·in·a·larger·area·is·to·be·examined·later.¶

[1]·János·L.·Lábár:·"DiffMap:·A·new·free·computer·program·to·process·scanned·electron·diffraction·patterns",·Resolution·and·Discovery·DOI:·10.1556/2051.2022.00090¶

Fig. 1: .

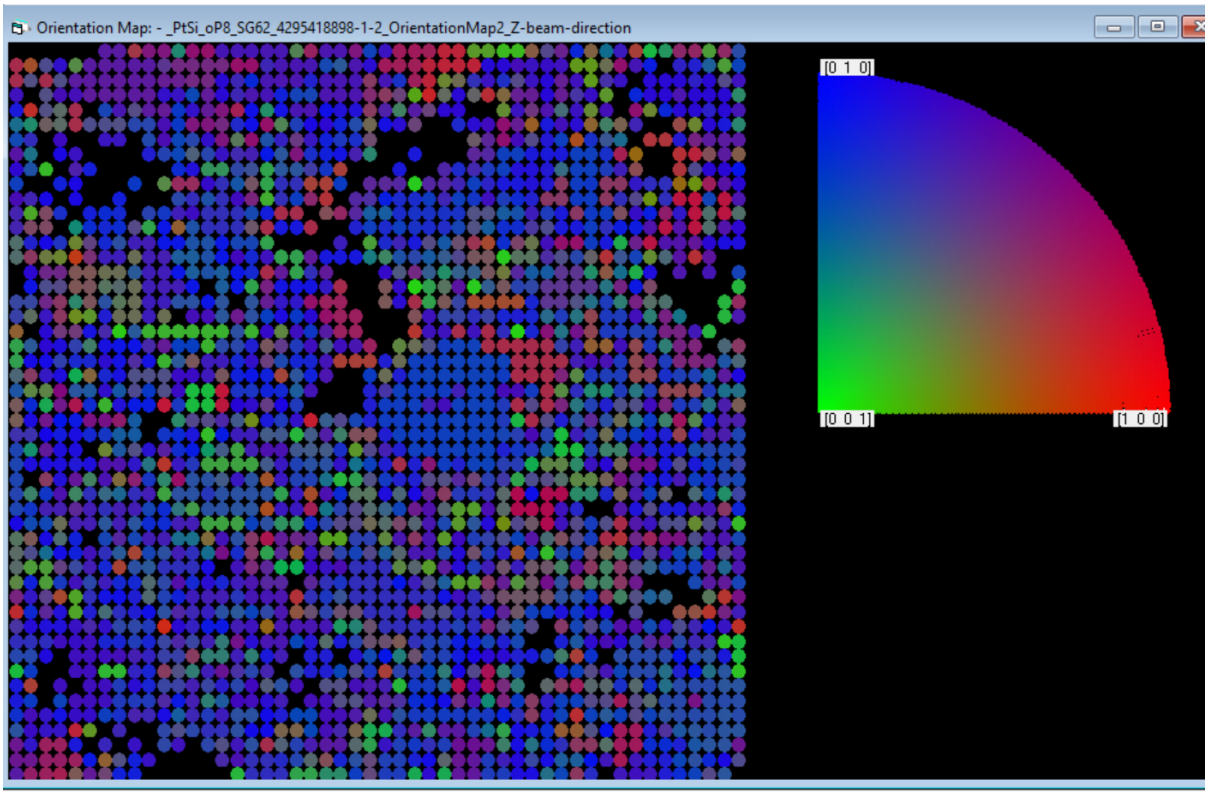

Fig. 2: Orientation distribution of PtSi grains seen from the electron beam direction (Z-direction of the Lab-system). The colour code shows the real space direction coordinates of the individual grains pointing to this Z-direction. Pixel size is 4 nm in this 50*50 pixel STEM image. Black colour indicates uncertain identification.

Type of presentation: Poster

IM3-P-2678 Temporal correlations in coherent cathodoluminescence

Scheucher M.[1,2], Schachinger T.[3,4], Preimesberger A.[1], Spielauer T.[1], Stöger-Pollach M.[3,4], Haslinger P.[1]

[1]Vienna Center for Quantum Science and Technology, Atominstitut, TU Wien, Vienna, Austria, [2]IQOQI Vienna, Austrian Academy of Sciences, Vienna, Austria, [3]University Service Centre for Transmission Electron Microscopy (USTEM), TU Wien, Vienna, Austria, [4]Institute of Solid State Physics, TU Wien, Vienna, Austria

Email of the presenting author: alexander.preimesberger@tuwien.ac.at

We recently [1], developed a novel method to separate coherent and incoherent contributions of cathodoluminescence (CL) by using temporal correlations. This technique allows us to unveil different photon generation mechanisms by investigating the arrival time of consecutive photons. While incoherent CL (e.g., resulting from excitation of quantum systems within the sample) exhibits a certain lifetime, coherent CL is produced within the electron – sample interaction time (on the order of femtoseconds). By using a fiber-based Hanbury Brown and Twiss interferometer we recorded the temporal correlations of the photons. Since coherent CL generation is a probabilistic process, each electron has a certain probability to generate one, two or more photons as it interacts with the sample. The strong temporal constraint for coherent CL, posed by the electron – sample interaction time, leads to a pronounced peak in the second order correlation function $g(2)(\tau)$ at $\tau=0$. This can be attributed to these coherent interaction mechanisms, as we have confirmed for Cherenkov radiation via an additional measurement (high-tension scanning).
In the here presented data, we studied Cherenkov radiation, which is generated by electrons going faster than the speed of light in the sample. This type of coherent CL exhibits many interesting features. Its emission characteristics can be modified, if we produce these photons in mode-selected geometries [2] such as tinniest Fabry-Pérot cavities or optimized 3D-printed structures. Furthermore, electron-photon pairs which are produced by the Cherenkov effect are strongly correlated by energy/momentum conservation, which we will exploit in future experiments.

Acknowledgement: [1] Scheucher, Michael, et al., arXiv preprint arXiv:2110.05126 (2021)

[2] Auad, Yves, et al., Nano letters (2021)

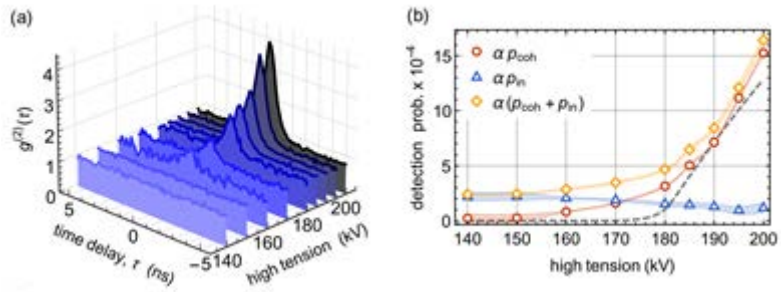

Fig. 1: a) Second order correlation function g(2)(τ) for different settings of the high tension.
b) Coherent, incoherent and total photon detection probability, αp_{coh}, αp_{in} and $\alpha(p_{coh} + p_{in})$, respectively, as a function of the applied high tension.

Type of presentation: Poster

IM3-P-2815 Hybrid-pixel detectors for TEM

Stroppa D. G.[1], Meffert M.[1], Piazza L.[1]

[1]DECTRIS Ltd., Taefernweg 1, 5405 Baden-Daettwil, Switzerland

Email of the presenting author: daniel.stroppa@dectris.com

25 years of advances in aberration correction have clearly shifted the TEM characterization limits from the electron optics to other factors, among them the electron detectors. Recent improvements on electron detection technology clearly impact the TEM characterization on both Materials Sciences and Life Sciences, particularly when beam-sensitive samples are involved [1]. Hybrid-pixel detector (HPD) [2] is one of the approaches to directly detect and count electrons, with the distinctive advantage of flexible design with respect to the sensor material and electronics for optimization to different applications.
Building from its successful HPD technology for X-rays detectors, recently DECTRIS optimized its design to enable the precise detection of electrons. Among the required adaptations were the determination of optimal threshold values for counting electrons with zero read-out noise within a wide energy range and the retrigger technology fine-tuning to allow counting from 1 to 107 counts/pixel/second [3].
These characteristics already indicate that HPDs are fit to variety of TEM applications, including low-dose imaging with single-electron sensitivity, and 4D-STEM and EELS experiments with simultaneous high dynamic range and frame rate up to 18 kHz. An application example is the flexible EELS collection from zero-loss peak (ZLP) to zero-noise core-loss (CL) region in the same acquisition range (Figures 1 adapted from reference [3]). Ongoing developments hint that improved frame rates and dynamic range can be expected with the next HPD generation.
References:

[1] A. R. Faruqi et al., Nucl. Inst. Methods Phys. Res., A 878, 180-190 (2018).
[2] N. Bochenek et al., IEEE Trans Nucl Sci 65 (6), 1285-1291 (2018).
[3] B. Plotkin-Swing et al., Ultramicroscopy 217, 23-30 (2020).

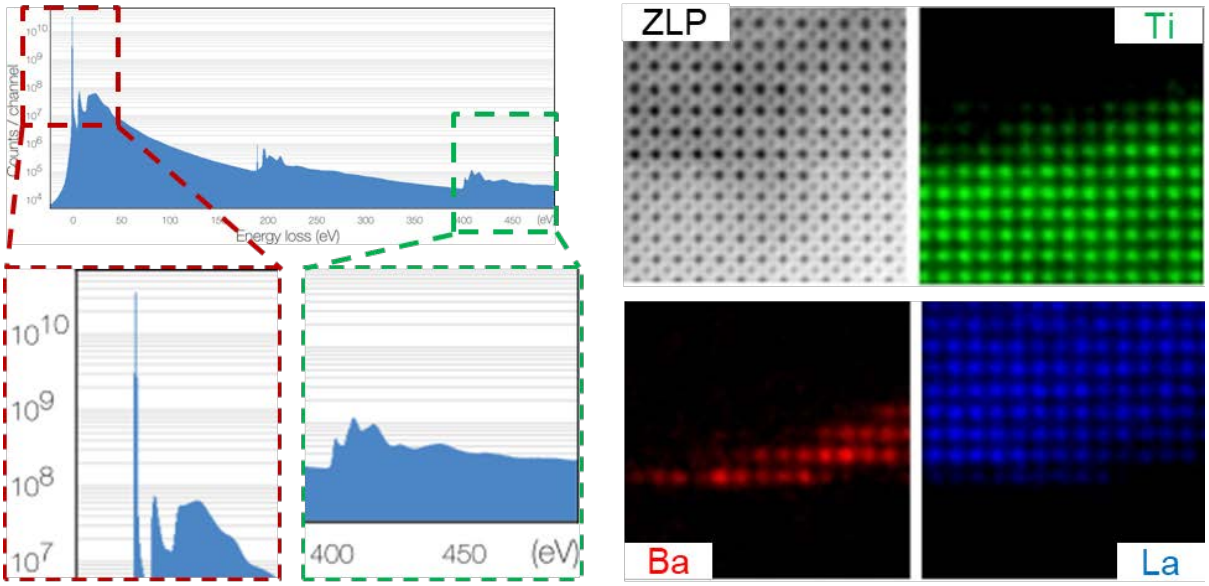

Fig. 1: (left) EELS spectrum of h-BN at 60kV. Simultaneous ZLP and CL collection without saturation across 6 orders of magnitude. (right) Spectrum imaging of STO/BTO/LSMO. Flexible elemental mapping with multipass EELS allowed by zero-readout noise.

Type of presentation: Poster

IM3-P-2510 Phase Analysis of (Li)FePO4 by Selected Area Electron Diffraction in Transmission Electron Microscopy

Šimić N.[1], Knez D.[2], Hanzu I.[3], Grogger W.[2]

[1]Graz Centre for Electron Microscopy (ZFE), Graz, Austria, [2]Institute of Electron Microscopy and Nanoanalysis, Graz University of Technology, Graz, Austria, [3]Institute for Chemistry and Technology of Materials, Graz University of Technology, Graz, Austria

Email of the presenting author: nikola.simic@felmi-zfe.at

Lithium iron phosphate ($LiFePO_4$) is a well-studied compound with a lot of promise as cathode material in rechargeable batteries. Due to its low cost, low toxicity, safety and the abundance of iron LFP is considered a very attractive energy storage option for the automotive industry.

$LiFePO_4$ has an orthorhombic crystal structure with Pnma space group [1]. During the discharge process lithium intercalates from a graphite anode into the $FePO_4$ cathode, where it is stored in between FeO_6 octahedra and PO_4 tetrahedra, thus slightly changing the lattice vector length of the unit cell while maintaining the same crystal structure as seen in figure 1.

To better understand the lithium deintercalation process various studies were performed with methods such as x-ray diffraction [2] and precession diffraction [3] to identify charged and discharged (L)FP particles by measuring lattice spacings.

This work shows the identification process of (Li)$FePO_4$ particles via selected area electron diffraction (SAED) with comparison of theoretical calculations of respective crystal models. SAED patterns have been recorded for numerous particles with size of approximately 200 nm in either lithiated ($LiFePO_4$) or delithiated ($FePO_4$) samples with results matching expectations. Through rigorous experiments the presented methodology has been deemed reliable and applied to samples that are either fully lithiated ($LiFePO_4$), partially delithiated ($LixFePO_4$), or fully delithiated ($FePO_4$). A comparison of chemically and electrochemically delithiated samples is made with both SAED as well as Raman spectroscopy.

[1] T.V.S.L. Satyavani, A. Srinivas Kumar, P.S.V. Subba Rao, et. al., Engineering Science and Technology, an International Journal, 19 (1), 178-188 (2016)
[2] C. Delmas, M. Maccario, L. Croguennec, et. al., Nature Materials, 7 (1), 665–671 (2008)
[3] G. Brunetti, D. Robert, P. Bayle-Guillemaud, et. al., Chem. Mater., 23 (20), 4515-4524 (2011)

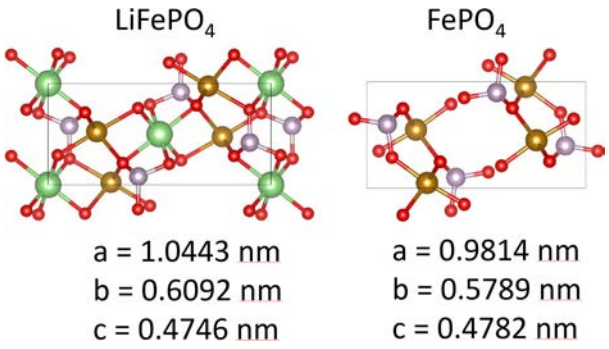

Fig. 1: $LiFePO_4$ and $FePO_4$ models, differing only in Li content and lattice spacing.

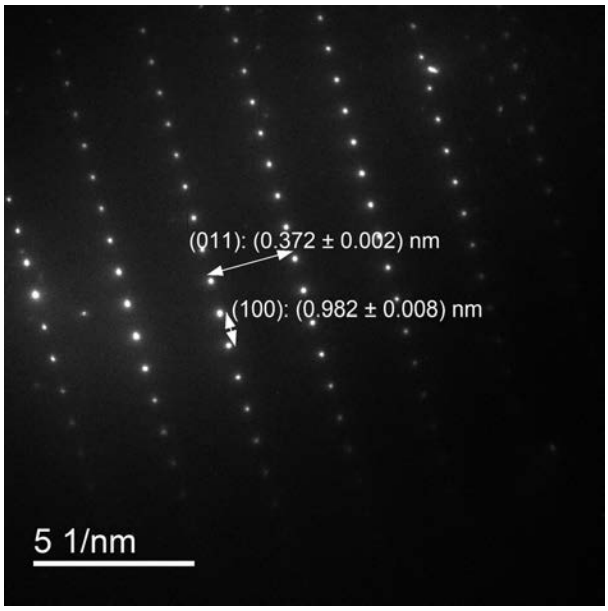

Fig. 2: SAED Pattern of chemically delithiated FePO4 in 0-11 direction. The lattice plane distance shows that the particle is indeed delithiated.

Type of presentation: Poster

IM3-P-2683 Scanning electron diffraction study of TiFeAl alloy microstructure

Vacek P.[1], Mellor R. F.[1], Jones N. G.[1], Fairclough S. M.[1], Stone H. J.[1], Midgley P. A.[1]

[1]Department of Materials Science and Metallurgy, University of Cambridge, 27 Charles Babbage Road, Cambridge, CB3 0FS, UK

Email of the presenting author: pv305@cam.ac.uk

Novel Ti-based alloys have attracted much interest as materials for efficient transportation and energy generation applications. However, the microstructure of these alloys needs to be carefully assessed in order to understand its influence on the material's structural properties. Scanning electron diffraction (SED, also known as 4D-STEM) has risen in popularity with the availability of new electron detectors and fast computational analysis [1]. Using SED, an electron probe with low convergence angle is scanned across the area of interest and a diffraction pattern is recorded at every pixel in the scan. This approach offers much higher spatial resolution when compared to traditional methods like selected area diffraction (SAD), and can be used to determine crystal structure, orientation, strain, or construct virtual dark/bright field images.

In this work, the microstructure of a novel TiFeAl alloy is investigated using SED. The microstructure composes of body-centered cubic (BCC) matrix and lenticular precipitates in three mutually perpendicular orientations. The long axis of the lens is aligned parallel to the <100>□ direction in the BCC matrix. Therefore, if viewed along a particular <100> direction they can appear in plan view or cross section as shown in Figure 1(a). However, there is much finer structure inside the precipitate lens itself. The SAD pattern (Figure 1(b)) is composed of overlapping diffraction from the matrix, and lenses at all orientations. Therefore, SED was used to differentiate between the phases inside the lens. The lens is composed of two phases. One is a partially ordered B2 phase (CsCl structure) and the other an orthorhombic phase (Cmcm). In the lens, the orthorhombic phase exists in two mutually perpendicular orientations. The orientation relationship for the B2 and orthorhombic phase is $(110)_{B2}/(001)_{orth}$ $[100]_{B2}/[100]_{orth}$ and $(110)_{B2}/(010)_{orth}$ $[100]_{B2}/[100]_{orth}$, respectively. Representative SED patterns and virtual dark field images from reflections corresponding to B2 and orthorhombic phase are shown in Figure 2. The information gained using SED was compared with high-resolution scanning electron microscopy (STEM). The STEM high-angle annular dark field (HAADF) image of the lens in plan view (Figure 3) confirms the microstructure described using SED. There are near-square B2 precipitates (highlighted in pink) and two orientations of orthorhombic precipitates in the "corners" of the B2 precipitates (highlighted in red and teal). Additionally, there is a thin layer of atoms (<1 nm) separating the B2 precipitates which was not directly visible in the SED data.

[1] D. Johnstone, P. Midgley, Scanning Electron Diffraction of 'Soft' Materials–Application to Organic and Hybrid Systems, Microsc Microanal. 26 (2020) 1732–1733.

Acknowledgement: The authors thank the EPSRC for funding under grant number EP/V007750/1 and the European Union Horizon 2020 research and innovation programme (ESTEEM3): 823717.

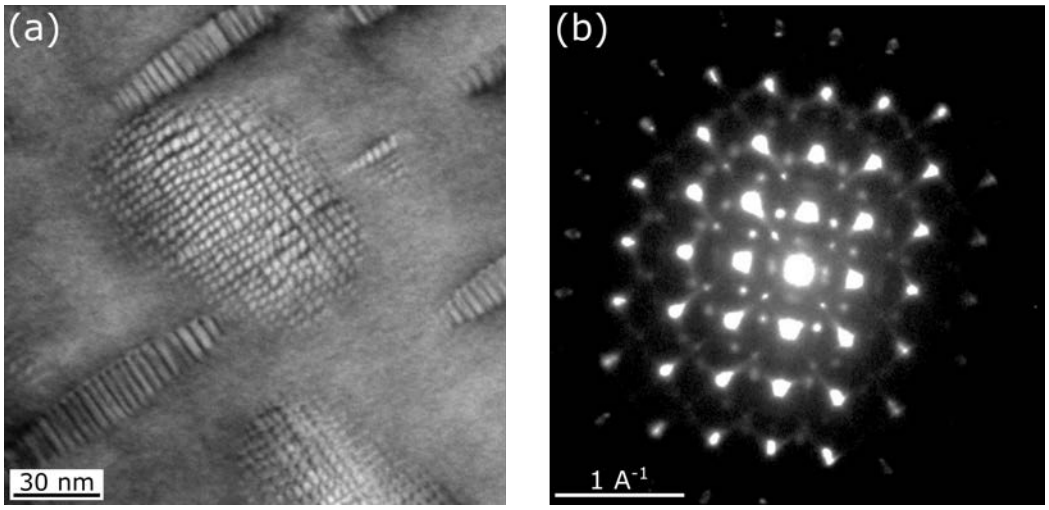

Fig. 1: (a) STEM HAADF image recorded parallel to a $[100]_{bcc}$ direction of precipitate lenses in plan view and cross section showing several lenses and finer structure inside the lenses and (b) corresponding SAD pattern.

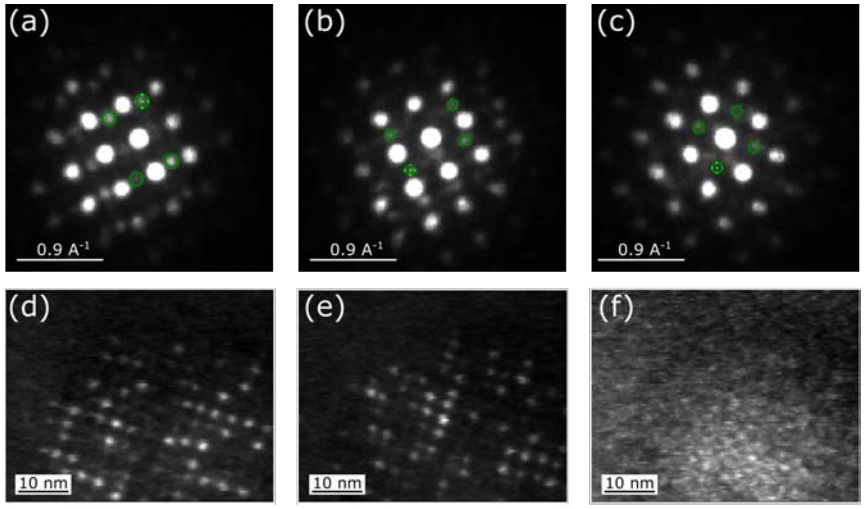

Fig. 2: $<100>_{bcc}$ diffraction patterns (a-c) and virtual dark field images (d-f) from the orthorhombic phase in each orientation (a,b,d,e) and from the superlattice reflection of the B2 phase (c,f). Virtual apertures used for dark field images are shown as green circles in the diffraction patterns.

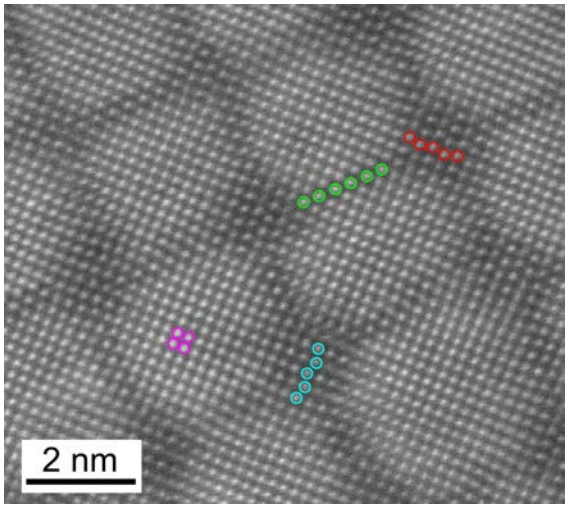

Fig. 3: High-resolution STEM HAADF image of precipitate lens recorded parallel to a $[100]_{bcc}$ direction. The high-resolution pattern of individual phases is highlighted in pink, green, red, and teal for cubic B2 phase, single atomic layer separating the B2 phase, and the two orientations of orthorhombic phase, respectively.

Type of presentation: Poster

IM3-P-2825 Improved mapping algorithms: combating data sparsity in SEM EDS

Vaňatka M.[1], Wandrol P.[1], Klusáček J.[1], Vaverka O.[2], Šembera O.[1], Tůma T.[1], Stephens S.[3]

[1]Thermo Fisher Scientific, Brno, Czech Republic, [2]Edhouse, Uherské Hradiště, Czech Republic, [3]Thermo Fisher Scientific, East Grinstead, United Kingdom

Email of the presenting author: marek.vanatka@thermofisher.com

Energy-dispersive X-ray spectroscopy (EDS) is a wide-spread analytical technique used in a broad range of scientific and industrial applications. Advances in detector and pulse processor design have enabled EDS analysis at high throughputs and with excellent spectral resolution. Throughputs in the order of 100,000 counts/s are now routine, allowing for a point-mode analysis to be completed in seconds. However, the throughput remains a significant bottleneck to high-speed spectral imaging. E.g., 768x512px resolution spectral image with 1 million X-rays collected (10s job with the above throughput) averages only 2.5 counts/px. We argue that advanced computational methods can be combined with deeply integrated, always on EDS system to significantly shorten the time needed to achieve high-quality outputs even using such sparse data sets.

Firstly, we can demonstrate how our quant mapping, compared to the traditional count mapping, can serve as a fast gateway into the composition mapping. We increase the counting statistics using smart feature-based (rather than traditional square-shaped) pixel grouping (binning) based on the BSE contrast [1] which sacrifices only minimum of spatial details. Then each bin is processed using identical quantification like in point-mode analysis (standardless peak fitting with peak deconvolution, and Phi-rho-Z (PROZA) [2] matrix corrections). The algorithm is highly optimized, providing live access to full quality, deconvolved and quantitative chemical imaging with no need to post process.

Secondly, we break the implicit assumption of the independence of individual pixels or sample regions by performing component-based phase mapping using multivariate statistical analysis. Here, the dominant components within the dataset are computed and used to define the elementally unique phases [3]. The components are calculated by determining the variance-covariance of the data and then creating a matrix of the variances, from which matrix transformation calculations eigenvectors and eigenvalues are obtained. Such an approach performs particularly well on sparse data sets, as it is less susceptible to noise despite no prior knowledge of the elemental constituents or their relationships within the data set. The obtained phases are then quantified or matched to a library.

In conclusion we demonstrate that computational methods including feature-based quantitative mapping and multivariate phase analysis can greatly improve the accuracy and information content of spectral maps, thereby reducing the time to data and accelerating EDS workflows in science and industry.

[1] Tuma, T., et al., US. Patent No. 16533291 (2021).
[2] Bastin G. F., et al., Scanning, 8, p. 45 (1986).
[3] Kotula, P., et al., Microscopy and Microanalysis, 9, pp. 1-17 (2003).

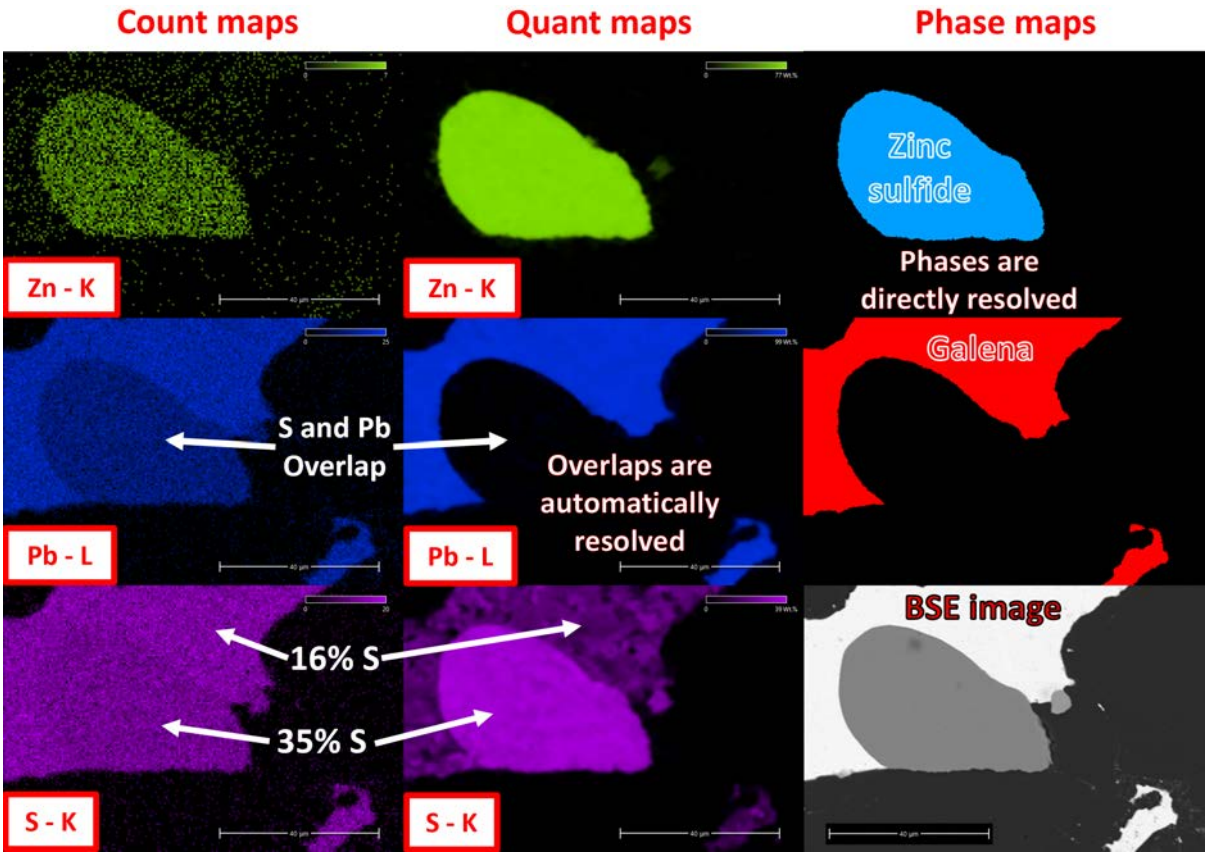

Fig. 1: EDS mapping of ZnS and PbS. Left: count maps of the individual elements. Center: quant maps (feature-based segmentation) with correctly deconvolved S and Pb. Right: correctly recognized phase maps that can be consecutively quantified or matched to a database. The dataset contains 1 Mcounts (2.5 counts per pixel) at HV=15 kV.

Type of presentation: Poster

IM3-P-2831 New possibilities enabled by correlative low-kV STEM-in-SEM imaging and Transmission Electron Diffraction

Zakopal P.[1], Vystavěl T.[1], Unčovský M.[1]

[1]Thermo Fisher Scientific, Vlastimila Pecha 12, 627 00 Brno, Czech Republic

Email of the presenting author: petr.zakopal@thermofisher.com

Scanning transmission electron microscopy conducted in low kV on FIB/SEM systems is gaining traction in the fields of material science, semiconductor development and life science. By combining lamella preparation and high-resolution imaging and diffraction examination on one platform, an entire experimental workflow can be performed without sample transfer to TEM. In semiconductor industry, ever thinner lamellae are examined, while in material and life sciences, beam-sensitive and low-Z samples are often under scrutiny. These requirements favor lower electron energies, due to lower radiation damage and better scattering contrast. Here we report on transmission diffraction analysis enabled by Timepix pixelated detector supported in recent Helios 5 FIB/SEM.

Recently, significant increase in resolution of FIB/SEM platforms down to 3 Å in STEM mode was enabled by introduction of Helios platform with retractable pole-piece for high-resolution STEM imaging [1]. Later Helios 5 version supports the retractable Timepix hybrid pixelated detector from the Medipix detector family [2], thus enabling correlative STEM and diffraction analysis of thin samples.

In our experiments, STEM in SEM images of several samples were obtained using in-lens mode and segmented STEM detector. Subsequently by inserting the Timepix based detector under the sample, 4D STEM dataset was obtained in the region of interest. Post-processing the diffraction patterns by custom Python algorithms enables creating Virtual Dark Field maps revealing strain and defects or visualizing of grains and material phases in polycrystals (Results in Fig. 1).

By continually tilting the sample and acquiring diffraction patterns (Micro Electron Diffraction/MicroED), the electron density of the molecules in sample can be revealed. Diffraction patterns from several samples (Fig. 2) show high quality of obtained raw data for MicroED studies using the low kV approach and Timepix based detection.

Other uses of the described setup may include combined SE/STEM/diffraction analysis of nanoparticles (Fig. 3), or of thin 2D materials like graphene. Furthermore, due to high sensitivity of diffraction pattern to crystalline sample tilt, precise zone axis alignment of lamella for high resolution STEM imaging is possible. Eventually, TKD (Transmission Kikuchi Diffraction) orientation maps may be also constructed. As in the former examples, high dynamic range and noise-less operation of the Timepix detector due to its direct electron detection enables precise analysis of the diffraction patterns.

[1] Vystavěl, T., Tůma, L., Stejskal, P., Unčovský, M., Skalický, J., & Young, R. (2017). Microscopy and Microanalysis, 23(S1), 554-555.
[2] http://medipix.web.cern.ch/medipix/

Acknowledgement: This research was supported by the Technology Agency of the Czech Republic, grant number TN01000008.

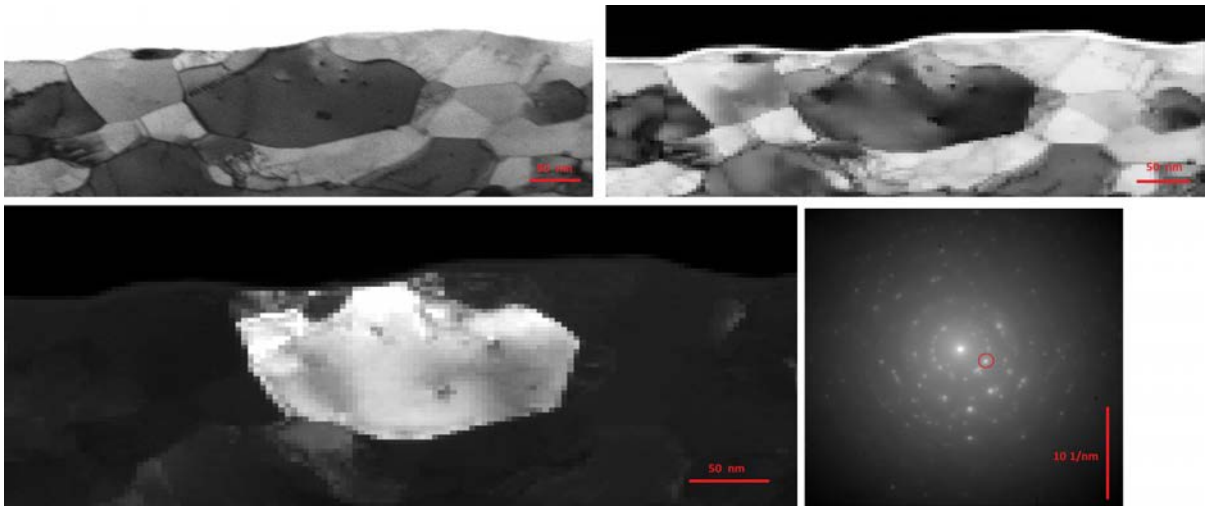

Fig. 1: (Clockwise from top left): Bright field STEM image of Al alloy (conventional solid-state detector);Reconstructed bright-field image from Timepix (using virtual central aperture); Averaged diffraction pattern from the 4D STEM map with a selected band aperture (red circle); Integral signal from the selected band highlights specific grain.

Fig. 2: Transmission diffraction patterns from (left to right): paracetamol, asbestos and flufenamic acide, acquired on Timepix detector at 30 kV electron energy.

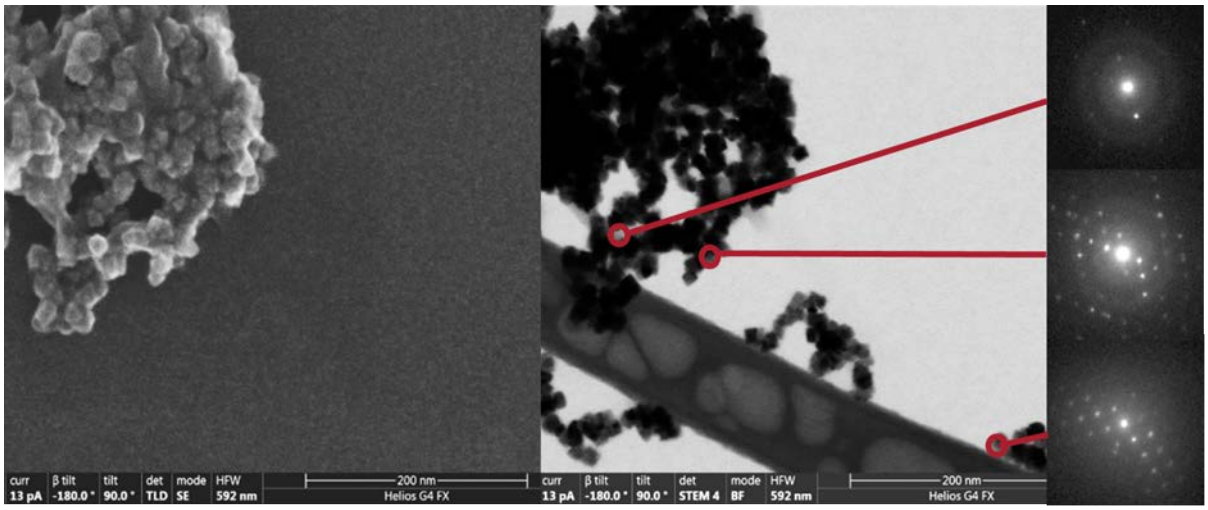

Fig. 3: (Left to right) SE image; Bright field solid-state STEM image; individual diffraction patterns from nanoparticles of CeO2 on both sides of thin carbon film, acquired on Timepix detector at 30 kV electron energy.

IM4 Advances in electron optics and beam shaping for electron microscopy

Type of presentation: Invited

IM4-IN-2573 Electrons and Light: Ponderomotive Beam Shaping and Optical Near-field Electron Microscopy

Juffmann T.[1]

[1]University of Vienna, Faculty of Physics / Max Perutz Labs

Email of the presenting author: thomas.juffmann@univie.ac.at

Electron induced damage is one of the major challenges in imaging biological matter with electron beams. We will discuss two techniques that open possibilities for dose-effective measurements:

First, we will discuss ponderomotive electron beam shaping [1]. An electron beam interacts with a shaped high intensity laser pulse, which induces a phase-shift proportional to the local light intensity. Since the light intensity distribution can be shaped arbitrarily, we can use this to arbitrarily shape the wavefront of an electron beam. We demonstrate concave and convex electron lensing and the ability to program complex electron deflection patterns. This beam shaping technique is lossless, and doesn't induce inelastic scattering. It can be used for the realization of a phase plate, an aberration correction plate, or for adaptive measurement schemes.

Second, we will discuss optical near-field electron microscopy (ONEM) which has been proposed as a way to circumvent electron-induced damage [2]: In ONEM, a sample is probed non-invasively using light, and the resulting near-field interference patterns are converted into an electron current using a photocathode.
The emitted electrons are then imaged with nanometric resolution using an aberration corrected Low Energy Electron Microscope (LEEM). For sample-photocathode distances much smaller than the optical wavelength (z□λ) this allows for label-free superresolution microscopy of interfaces. After introducing the basics of this new imaging concept, we will discuss first steps towards the implementation of ONEM in an existing LEEM system [3].

[1] Marius Constantin Chirita Mihaila, Philipp Weber, Matthias Schneller, Lucas Grandits, Stefan Nimmrichter, Thomas Juffmann, Transverse Electron Beam Shaping with Light. ArXiv:2203.07925 (2022)

[2] Marchand, R., Šachl, R., Kalbac, M., Hof, M., Tromp, R., Amaro, M., van der Molen, S. J. & Juffmann, T., Optical Near-Field Electron Microscopy. Physical Review Applied 16, 014008 (2021)

[3] Geelen, D., Jobst, J., Krasovskii, E. E., van der Molen, S. J. & Tromp, R. M., Nonuniversal Transverse Electron Mean Free Path through Few-layer Graphene. Physical Review Letters 123, 086802 (2019)

Acknowledgement: These projects have received funding from the European Union's Horizon 2020 program under Grant Agreement No. 101017902 and No. 758752.

Type of presentation: Invited

IM4-IN-2672 Advanced measuring schemes using new electron optics ideas

Grillo V.[1]

[1]Centro S3, Istituto di Nanoscienze-CNR, 41125 Modena, Italy

Email of the presenting author: vincenzo.grillo@cnr.it

While electron microscopy has reached incredible spatial and energy resolution thanks to more sophisticated and bulky electron-optics, a new field is emerging with the idea of giving arbitrary wave shapes to the electron beam. The new probes and analysis methods can improve the measurement sensibility, give access to new quantities (e.g. for EMCD experiments [1]) or reduce the required dose in experiments.
We will show that this can be based on 2 approaches: miniaturised electrostatic optical elements [2] or electron light interaction [3].
The miniaturised optics is based on Micro-electromechanical systems (MEMS) and has allowed the realisation of the electrostatic OAM-sorter [2], and a controlled, aberration free realisation of vortex beams [4].
The electron-light interaction in based on using a Spatial Light Modulator to control the light field and transfer this phase/amplitude modulation to the electrons. This is potentially even more flexible than MEMS methods but it is a less mature technology and it is now starting to show its possibilities (vortex beams, imaging phase plates).
I will review results in both directions and how to use both methods for new concepts like or conformal mapping or computational ghost imaging [5][6]. With the latter imaging method, inspired by optics, we can introduce a novel imaging mode that is hybrid between scanning and extended wave imaging and has important advantages in terms of dose.
Finally I will highlight the revolution that subtends all these experiments: the use of artificial intelligence to guide and automatize all complex alignments [7].

References

[1] E Rotunno et al. Physical Review B 100 , 224409 (2019)
[2] AH Tavabi, et al. Physical Review Letters 126, 094802 (2021)
[3] GM Vanacore et al. Nature materials 18, 573-579 (2019)
[4] AH Tavabi et al. arXiv preprint arXiv:2203.00477 (2022)
[5] A Konečná et al. arXiv:2203.07332 (2022)
[6] A Kallepalli et al. https://doi.org/10.21203/rs.3.rs-1111193/v1 (2021)
[7] E Rotunno, et al. Ultramicroscopy 228, 113338 (2021)

Acknowledgement: This work is part of the SMART-electron project that has received funding from the EU's Horizon 2020 Programme under grant agreement No 964591.

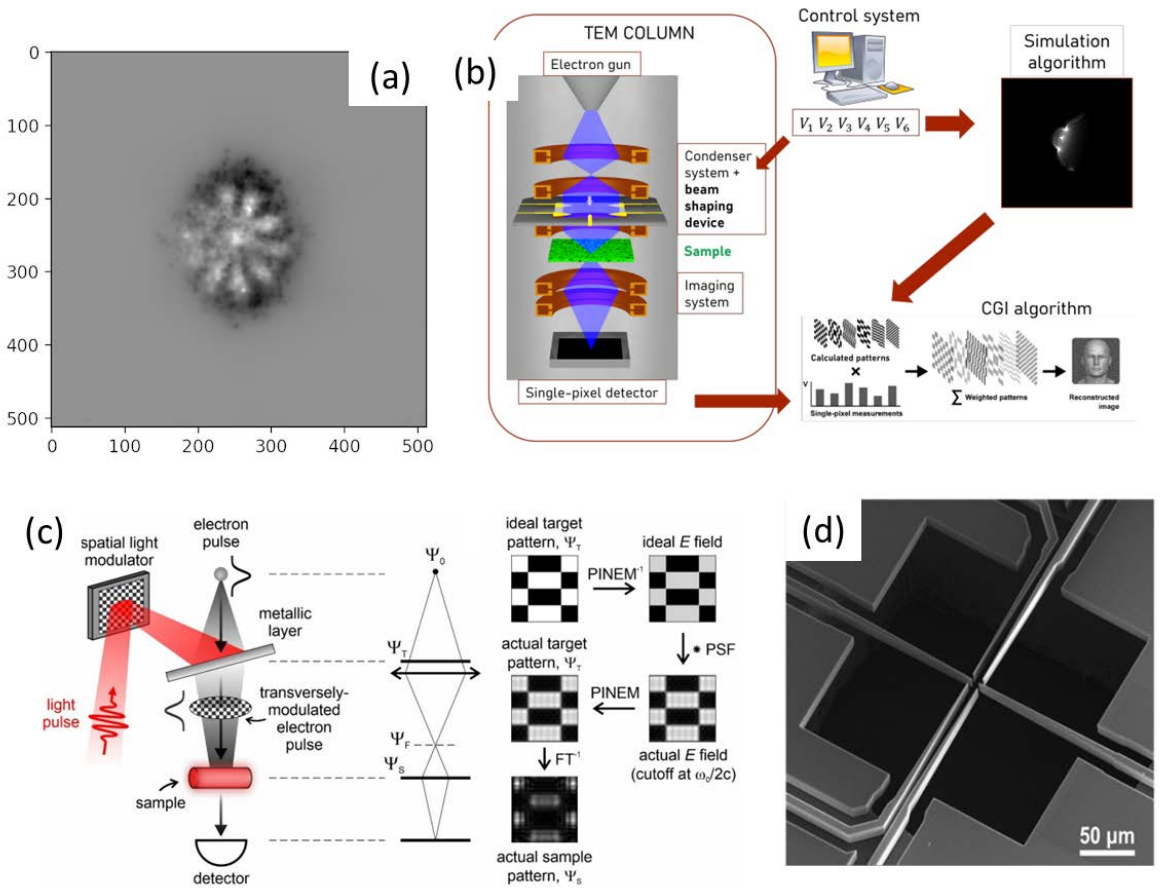

Fig. 1: a) example of experimental computational ghost imaging (CGI) reconstruction, b,c) schemes of CGI with MEMS b) and light electron interaction c) . Fig d) example of MEMS.

Type of presentation: Oral

IM4-O-2570 A User Adjustable Pole-piece Gap as a Route to Improve the Sustainability of TEM Infrastructure

McBean P.[1,2], Murphy P.[1], Sagawa R.[3], Jones L.[1,2]

[1]School of Physics, Trinity College Dublin, Dublin, Ireland, [2]Advanced Microscopy Laboratory, CRANN, Dublin, Ireland, [3]JEOL Ltd., Akishima, Toyko, Japan

Email of the presenting author: mcbeanp@tcd.ie

The transmission electron microscope (TEM) is a powerful characterisation instrument used widely in both physical and life sciences. It is a significant investment for any research institution due to both the high initial cost, followed by the running and cooling energy costs (leading to non-trivial carbon emissions), support staff costs, and maintenance contracts for perhaps another 15 years.

The specification of the objective lens pole-piece gap is crucial in determining the capabilities and performance of the instrument [1]. While a smaller gap results in reduced spherical and chromatic aberrations, and thus improved resolution, a larger gap offers wider flexibility for sample-tilting, tomography, in-situ experiments, or energy-dispersive x-ray spectroscopy (EDX) collection efficiency. As the former is typically preferred by the physical science community, but the latter by the analytical/life-science communities, an inherent trade-off is required. If multiple columns must be purchased to avoid performance compromises, then this duplication of both up-front and running costs raises significant sustainability considerations.

As an alternative approach, we propose a User Adjustable Pole-piece (UAP) with a pole gap that can be adjusted by the microscopist to suit a variety of experiments, reducing wasteful duplication [2]. To be of practical use, the proposed UAP must be; adjustable while under high vacuum, mechanically stable with ultra-precise alignment about the optic axis, and be realignable to a good tuning without a specialist engineer present.

Our proposed adjustable pole-piece design, based around the current JEOL 200/300kV geometry, is shown in Figure 1. In the smallest gap, we naturally expect the lowest aberrations, while in the largest gap we expect full 180-degree rotation for tomography.

Candidate designs for the UAP were evaluated and compared using multiphysics modelling software to guide its construction; evaluating geometric predictions for EDX collection solid-angles, attainable tilt-ranges of several customised holders, contrast transfer functions, and aberration coefficient estimations for different pole-gaps. An example of one of these customised holders, along with preliminary magnetic field simulations, are visible in Figures 2 and 3.

In this presentation we will elaborate on our progress in the design and manufacture of the UAP. We will present our preliminary results which confirm that the larger pole gaps yield better tilt/access for experiments, while the smaller gaps yield reduced aberrations.

[1] K. Tsuno and D. A. Jefferson, Ultramicroscopy, vol. 72, no. 1–2, pp. 31–39, 1998.
[2] P. McBean, D. O'Mahony, and L. Jones, in European Microscopy Congress Proceedings, Mar. 2020, p. 322.

Acknowledgement: The authors would like to acknowledge financial support from SFI, AMBER, and Enterprise Ireland. We also thank JEOL Tokyo for fruitful discussion and support.

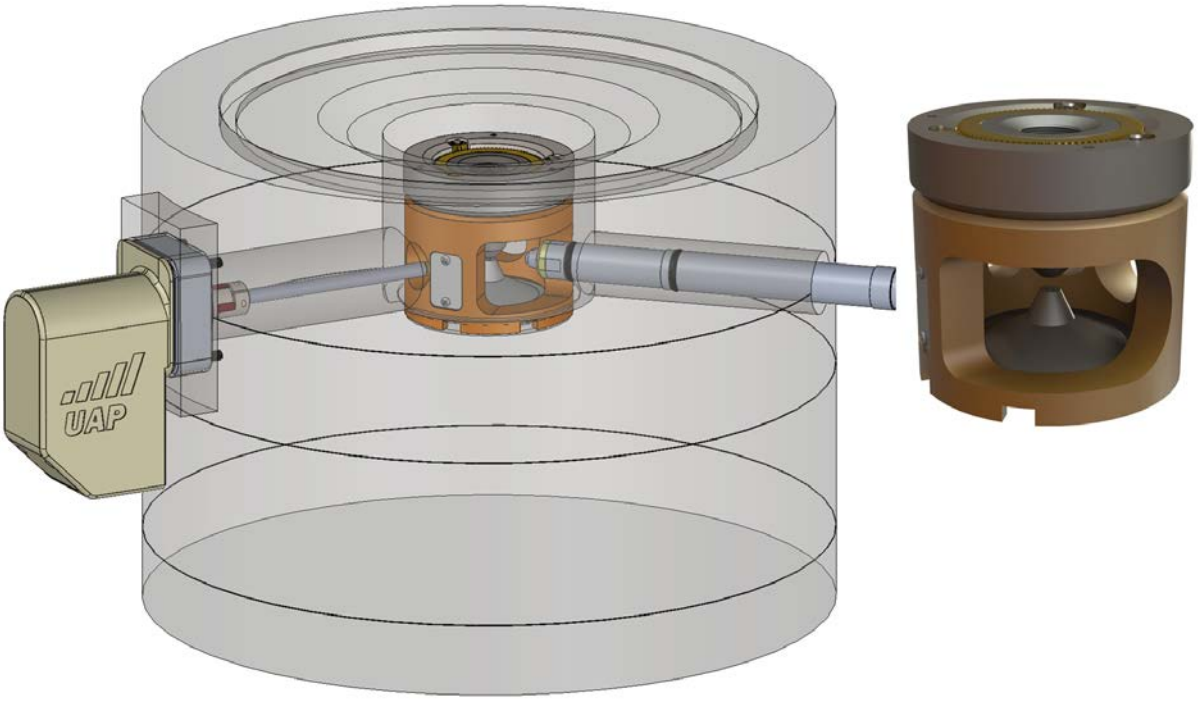

Fig. 1: (Left) Integration of the User Adjustable Pole-piece in the existing objective lens module of a JEOL GRAND ARM. Also visible are a custom feedthrough system for adjusting the UAP, and a bespoke sample rod containing an endoscope. (Right) Close up of the UAP, currently positioned at an intermediate pole gap of 4.0 mm.

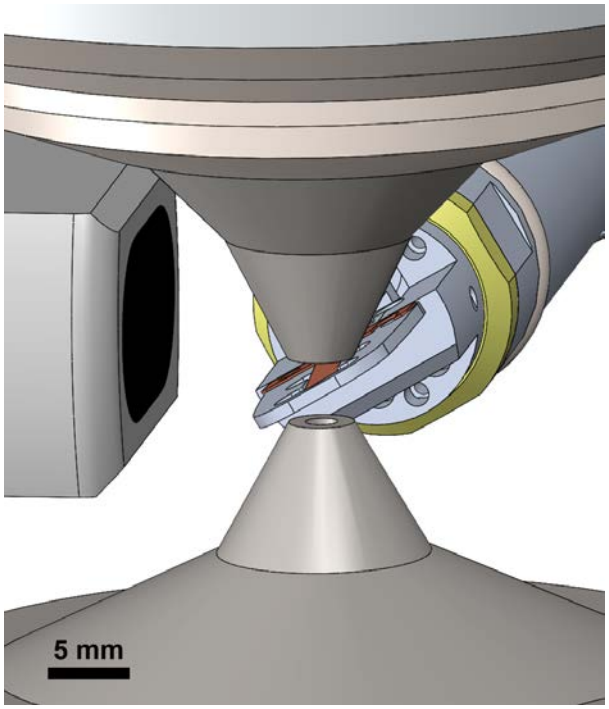

Fig. 2: Insertion of a customised holder tip to measure tilt-range and EDX collection solid-angles for each specified gap of the UAP.

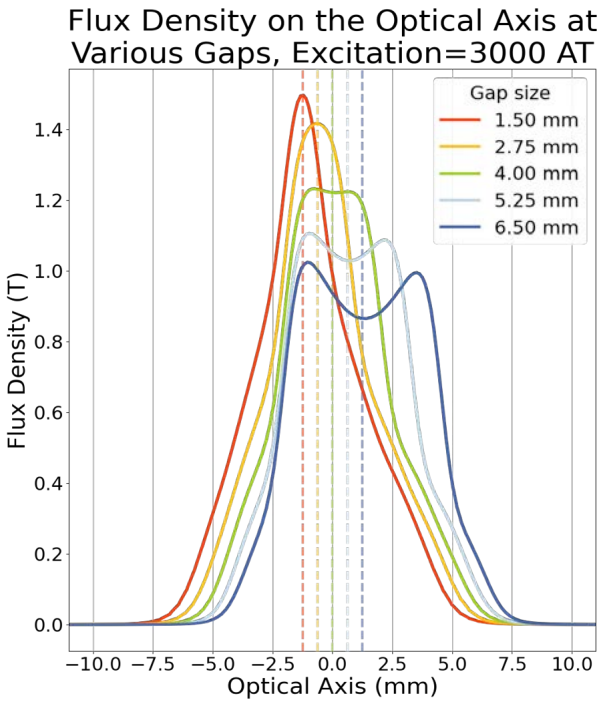

Fig. 3: Preliminary computer simulations using COMSOL of the magnetic field along the beam direction for the five UAP pole-piece gap settings.

Type of presentation: Oral

IM4-O-2506 Measurement and Correction of Phase Aberrations in Scanning Transmission Microscopy by Artificial Neural Networks

Bertoni G.[1], Rotunno E.[1], Marsmans D.[2], Tiemeijer P.[2], Grillo V.[1]

[1]Istituto Nanoscienze, Consiglio Nazionale delle Ricerche, Modena, Italy, [2]Thermo Fisher Scientific, Eindhoven, Netherlands

Email of the presenting author: giovanni.bertoni@cnr.it

The ultra-high-resolution in scanning transmission microscopy (STEM) resides in the ability to correct aberrations of the probe forming lenses, to obtain atomically resolved images with Z-sensitive contrast. The idea of this contribution is to test artificial neural networks (ANN) to measure the aberrations from a single image of the stationary probe on an amorphous region (Ronchigram). The aim is to assist the user in his tuning or to improve the existing routines available with probe correctors with faster ones. Recent deep learning approaches were demonstrated to be promising in optimizing the STEM aperture [1,2].

In our study, we have built a dataset of 24k images with different aberrations values. These were suitably patterned and passed to the ANN for training (Figure 1). The ANN is a custom VGG16 consisting of 2D convolution layers followed by 2D pooling and dropout layers before the final flatten layers. For demonstration purposes, we limited our study to the principal aberrations in the aberration phase $\chi(q)$: defocus (C_1), two-fold astigmatism (A_1), coma (B_2), three-fold astigmatism (A_2), and spherical aberration (C_3). The ANN has reached convergence, with predicted errors on the aberration values of ~5% with respect to the range limits. In the case of A_1, the mean absolute error is 4 nm. Despite this apparently poor precision, the ANN succeeds in the correction of synthetic data in a few iterations. Figure 2 shows an example, by comparing the image before and after ANN correction. The improved resolution is evident, and can be calculated by using the quarter-wave criterion to determine the STEM optimal aperture of semi-angle $\alpha = \min(|\chi(q)| \leq \pi/4)$. The spatial resolution can be estimated from the Rayleigh criterion as $0.61(\lambda/\alpha)$, giving an improvement in this example from ~4 Å to 0.8 Å.

However, the effectiveness of the ANN prediction in real experiments is related to the accuracy of the model in describing the experimental images, such as i) patterning the Ronchigram images [3] to build an optimized ANN input; ii) defining a simple but realistic model of the sample potential, usually treated as a noise grating [2]; iii) including the detector point spread function and counting noise. On experimental data the ANN resulted to give aberrations values in agreement with the ones measured with the commercial built-in software (CEOS), making this approach promising for quick tuning.

[1] C. Zhang et al. Microscopy & Microanalysis 27 (2021) p. 810-812.

[2] N. Schnitzer et al. Microscopy & Microanalysis 26 (2020) p. 921-928.

[3] A.R. Lupini et al. Ultramicroscopy 110 (2010) p. 891-898.

Acknowledgement: The authors acknowledge funding from the European Union's Horizon 2020 Research and Innovation Programme under Grant Agreement No 964591 'SMART-electron'.

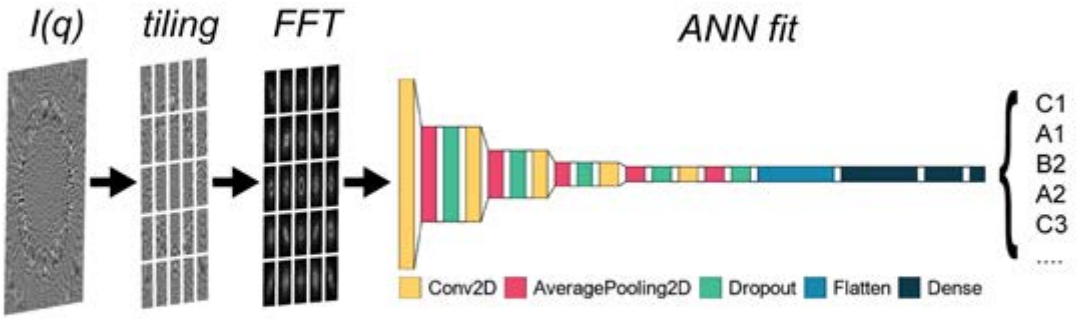

Fig. 1: Schematic view of ANN fitting of Ronchigram images. We limited our study to main aberration values (C_1, A_1, B_2, A_2, C_3). Higher-order aberrations up to 5th order were randomly generated as residual aberrations.

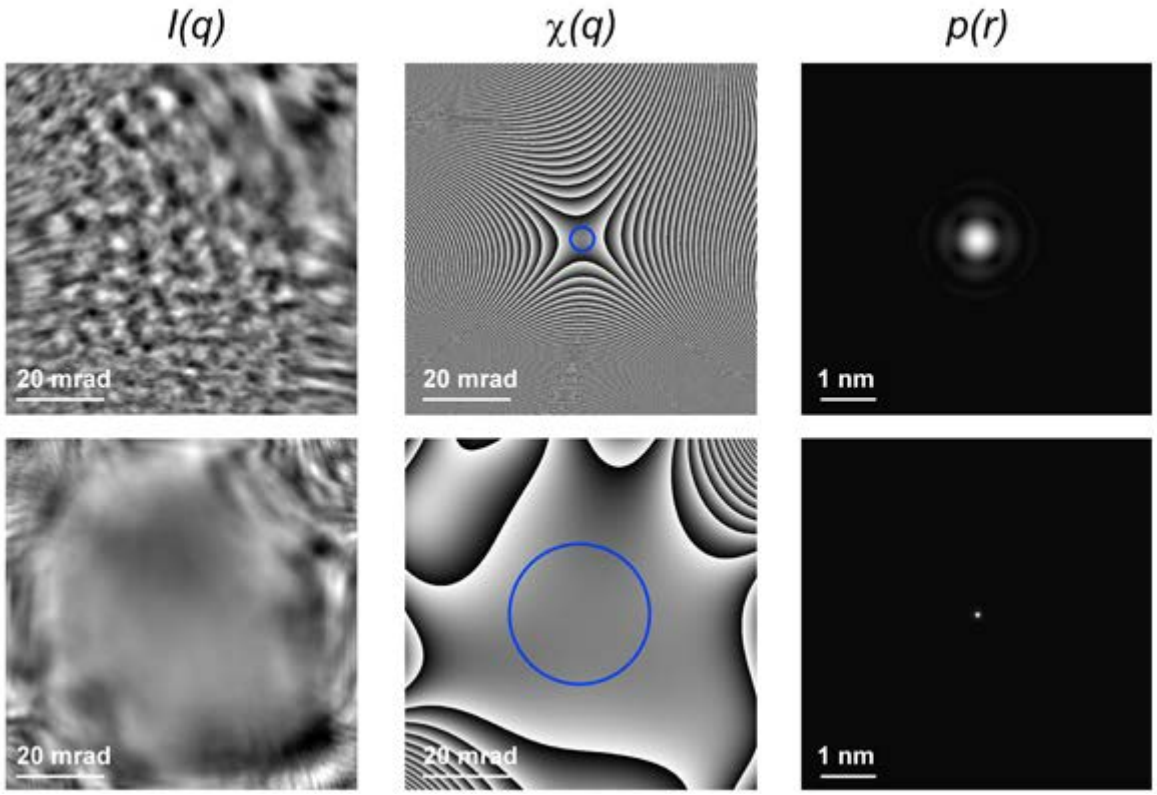

Fig. 2: Simulated images to illustrate the ANN correction capability. Ronchigram *I(q)*, aberration phase *χ(q)*, and probe *p(r)* images before ANN correction (top) and after 3 iterations of the ANN (bottom). The blue circle is the optimal probe aperture to estimate the resolution with the Rayleigh criterion.

Type of presentation: Oral

IM4-O-2867 Concept of Aberration Corrected Low-Voltage Transmission Electron Microscope

Bačovský J.[1], Kolařík V.[1], Jánský P.[1], Mynář M.[1]

[1]Research laboratory, Delong Instruments a.s., Brno, Czech Republic

Email of the presenting author: jaromir.bacovsky@delong.cz

Aberration correctors have become a standard component of high-end conventional transmission electron microscopes. However, the integration of the corrector to the commercially produced low voltage transmission system (5-25kV) has not been proposed yet. Low voltage systems are very specific because of the high importance of chromatic aberration compared to conventional systems. Instrument operating at 25kV benefits from low voltage, meaning extraordinary high contrast, but the deteriorative effect of spherical and chromatic aberration is already comparable. Thus the individual correction of spherical aberration is already beneficial. According to these facts, a miniaturized hexapole corrector based on permanent magnet technology seems to be a promising solution for the correction of the primary spherical aberration.
In this work, we come up with a full concept of transmission electron microscope corrected for the primary spherical aberration. The complete design of electron optics from gun to screen is presented.
The incorporated corrector follows the electron-optical concept of LVEM25. Due to the unique design consisting of permanent magnets, it allows to preserve compact dimensions and low complexity of the instrument and at the same time significantly improves the spatial resolution.
Our developed solution is beneficial, especially for STEM mode, which is not sensitive to the additional energy broadening of the electron beam given by the sample itself. However, the microscope is intended to operate also in uncorrected TEM mode. Although STEM regime minimises chromatic deterioration caused by electron passage through the sample, the best performances are expected in a combination of the above-mentioned corrected system with a monochromator and/or CFE gun.
[1] ROSE, H., WAN, W., Aberration Correction in Electron Microscopy. Proceedings of the 2005 Particle Accelerator Conference. IEEE. 44-48, 2005. DOI: 10.1109/PAC.2005.1590354. ISBN 0-7803-8859-3. Available from: http://ieeexplore.ieee.org/document/1590354/.
[2] HAIDER, M., MÜLLER, H., UHLEMANN S., Advances in Imaging and Electron Physics. Volume 153, Hawkes ed., Springer, Heidelberg, 2008. ISBN 978-0123742209.
[3] Štěpán, P., Delong, A., Low voltage electron microscope III- Present and future possibilities. Proceedings of 12th European Congress on Electron Microscopy (EUREM), Brno, 2000. ISBN 80-238-5501-8.

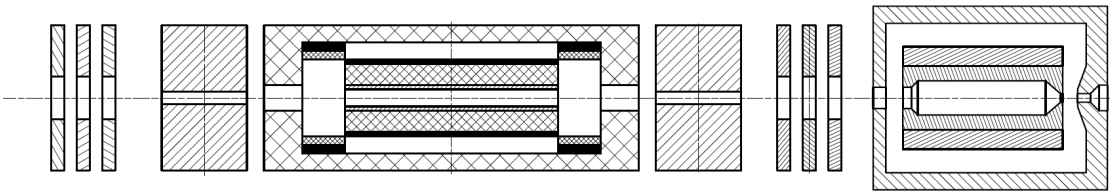

Fig. 1: Scheme of novel design of corrected LVEM. From left to right. electrostatic preparative lens, hexapole corrector with permanent magnet dublet, electrostatic elimination lens, and doublet condensor-objective based on permanent magnet technology.

Type of presentation: Oral

IM4-O-2591 Enhancing Electron Computational Ghost Imaging Using Artificial Neural Networks

Viani L.[1], Rosi P.[2], Rotunno E.[2], Frabboni S.[1], Balboni R.[3], Migliori A.[3], Grillo V.[2]

[1]Department of Physics, IT and Mathematics, University of Modena and Reggio Emilia, Modena, Italy, [2]Consiglio Nazionale delle Ricerche (CNR)-NANO, Modena, Italy, [3]Consiglio Nazionale delle Ricerche (CNR)-IMM, Bologna, Italy

Email of the presenting author: lorenzo.viani@unimore.it

Computational Ghost Imaging (CGI) [1, 2], or single-pixel imaging, consists in recovering the transmission function of the sample by using structured illumination in the form of an illumination pattern. It was first developed in the field of light optics. We propose an experimental setup to adapt the technique to electron optics. The process is schematized in Figure 1: a pattern generator is introduced at the condenser system level. The electron beam passes through it and turns into a structured probe dependent on six biases, then propagated to the sample. The transmitted beam is imaged on a single-pixel detector and integrated as an intensity. The illumination pattern is predicted by an Artificial Neural Network (ANN) depending on the six biases. Combining the calculated patterns and the measured intensities allows recovering the image.

Two main factors determine the quality of the reconstruction: the level of control over the complexity of the generated patterns and the correspondence between the calculated patterns and the actual ones used while measuring.

About the former, we propose a new electro-optical device based on the Micro ElectroMechanical System (MEMS) technology to use as an optical modulator for electrons. It consists of a planar arrangement of six microscopic needles that can be biased independently to produce an electrostatic potential distribution that imparts a position dependent phase to the beam. The generator allows for controlled beam shaping in Fraunhofer condition, with six degrees of freedom and fast pattern generation.

For the latter, we know that for traditional algorithms it is difficult to incorporate machine-dependent effects, that are hard to implement in the code. We decided to train a Convolutional Neural Network (CNN) [3] because it could predict the patterns starting from the six biases applied to the generator while accounting for machine-dependent effects, improving the resulting image. Also, it is faster than traditional algorithms. An example of final image is shown in Figure 2.

Compared to TEM imaging, electron CGI combines the use of low electron dose for each pattern with the efficiency of compressed sensing methods, providing accurate retrieval of the transmission function with good contrast. In this initial implementation CGI allows observing amplitude objects, making it complementary to electron Ptychography, and can be seen as a sort of generalized STEM.

[1] M J Padgett, R Aspden, G Gibson, M Edgar, and G Spalding, Optics & Photonics News 27 (October 2016), p. 38-45

[2] J H Shapiro, PHYSICAL REVIEW A78, p. 061802(R)

[3] E. Rotunno, A.H. Tavabi, P. Rosi, S. Frabboni, P. Tiemeijer, R.E. Dunin-Borkowski and V. Grillo, Ultramicroscopy 228 (2021), p. 113338

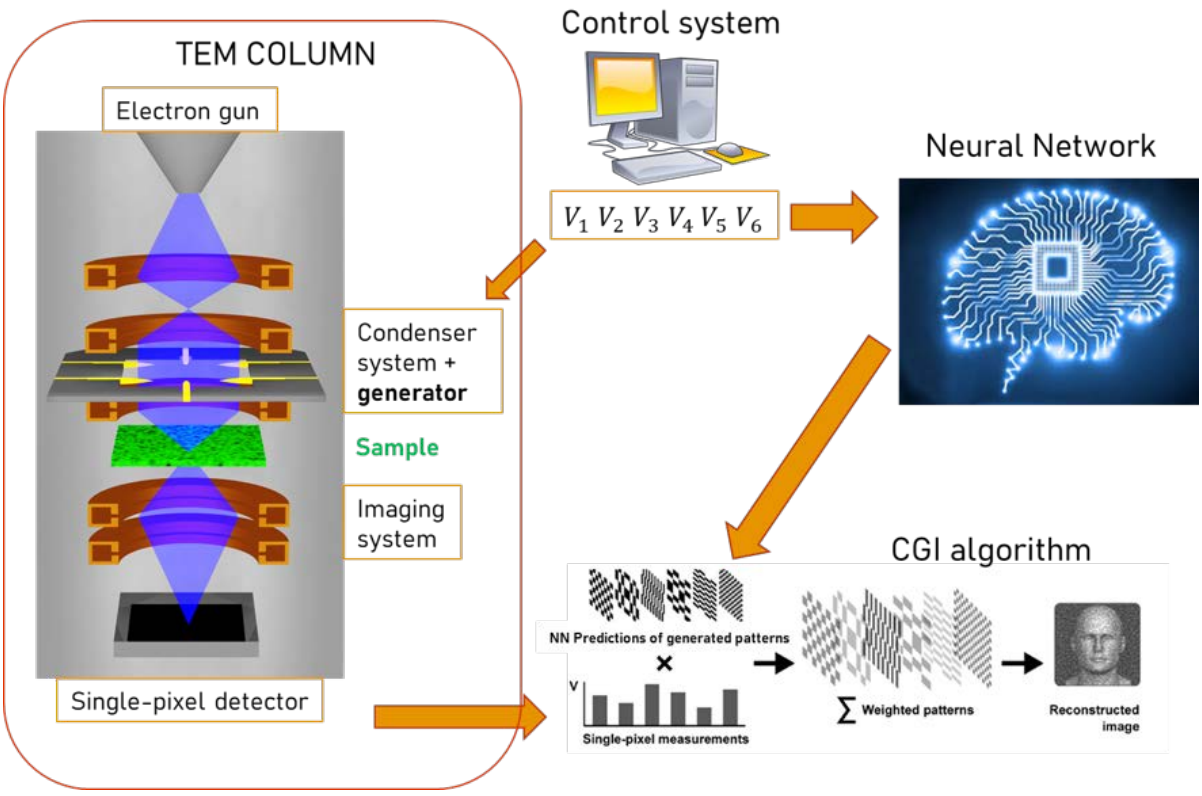

Fig. 1: Proposed experimental setup.

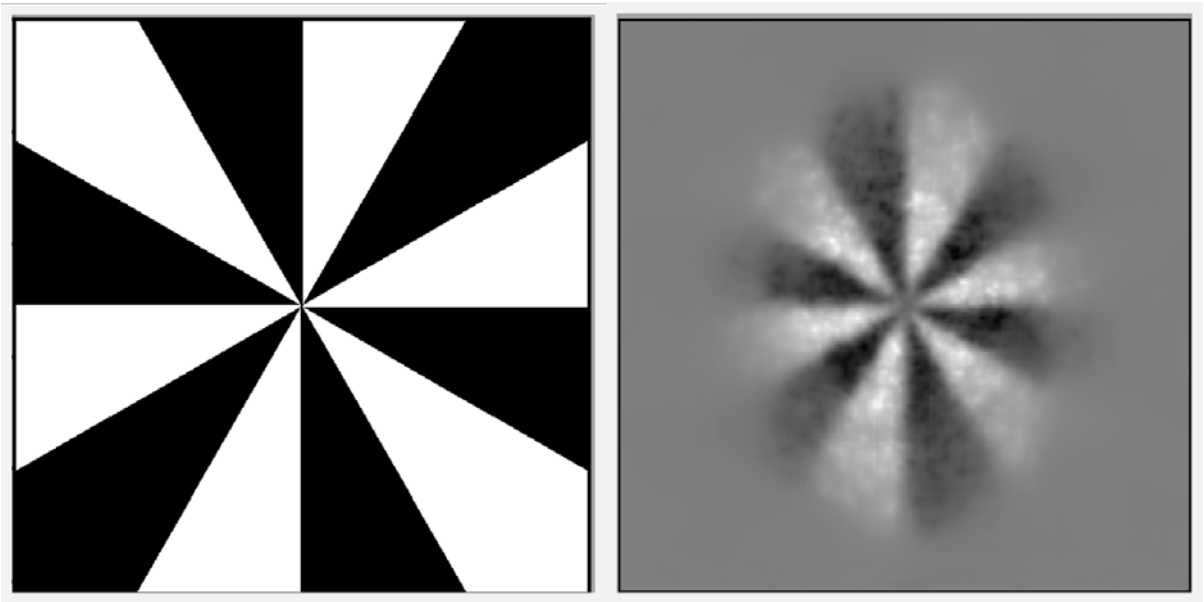

Fig. 2: Comparison of the Siemens star target of choice (left) and simulated reconstruction with 5000 summed patterns (right).

Type of presentation: Poster

IM4-P-2584 Simplified electron vortex generator with aberration correction

Schachinger T.[1,2], Lau A. J.[3], Li X.[3], Dellby N.[4], Kociak M.[3], Schattschneider P.[1,2]

[1]USTEM, TU Wien, Wiedner Hauptstraße 8-10/E057-02, Vienna, Austria, [2]Institute of Solid State Physics, TU Wien, Wiedner Hauptstraße 8-10/E138-03, Vienna, Austria, [3]Laboratoire des Physique des Solides, Universit´e Paris Saclay, CNRS, Orsay, France, [4]Nion Company, 11511 NE 118th Street, Washington, USA

Email of the presenting author: thomas.schachinger@tuwien.ac.at

The principle of astigmatic mode conversion (MC), known from light optics [1a], has been successfully applied in electron optics to form a singular and high-purity electron vortex beam [1b]. Such a vortex generator is based on a quadrupole (QP) doublet. The drawback of this setup is the fact that the QP doublet must be "borrowed" from the aberration corrector, which is then out of function. Ideally, separate QPs in front of the aberration correcting elements should be used. In the case of the NION C3/C5 aberration corrector [2], employed e.g., in the NION UltraSTEM instrument, there is a set of quadrupoles to couple the beam coming from the condenser into the first octupole, which can be repurposed for MC.

Furthermore, it is shown that the standard mode converter geometry as described in [1a] can be simplified inasmuch as the Hilbert phase plate (HPP) can be positioned inside the QP doublet. For a proof of principle experiment, an optical setup is proposed where the HPP is placed in the sample holder in between two astigmatic line foci produced by the QP component of the first QP/octupole element, see Figure 1. Wave optical simulations of the propagation of the electron through the optical elements of the proposed configuration show that the characteristic azimuthal vortex phase and ring like intensity distribution can be produced, see Figure 2. It turns out that the currents for the appropriate focal widths of the QPs in order to function as a vortex generator lie all within the accessible range for the NION UltraSTEM.

Even though the proposed setup leaves the probe corrector in operation, there are two major drawbacks. Firstly, the extremely low convergence angle (~70 µrad) produces a rather large STEM probe of ~43 nm (which facilitates beam testing in a proof-of-principle experiment). Secondly, the sample stage is occupied by the HPP. Future directions include the placement of the HPP in an upgraded condenser aperture holder. This enables STEM imaging with the MC vortex probe and enhance the achievable convergence angle to roughly one mrad. However, for atomic resolution imaging as well as e.g., testing new quantum computation schemes [3] a dedicated QP doublet with demagnification- and magnification-stage is proposed.

[1] a) Beijersbergen et al., Astigmatic laser mode converters and transfer of orbital angular momentum, Optics Communications, 96, 123-132 (1993), b) T. Schachinger et al., Experimental realization of a π/2 vortex mode converter for electrons using a spherical aberration corrector, Ultramicroscopy, 229, 113340 (2021)
[2] O.L. Krivanek et al., An electron microscope for the aberration-corrected era, Ultramicroscopy, 108, 179–195 (2008)
[3] S. Löffler et al., A quantum logic gate for free electrons, (2022), submitted

Acknowledgement: PS and TS acknowledge funding by the FWF (P29687-N36). This project received funding from the EU's Horizon 2020 research and innovation programme (NO 823717).

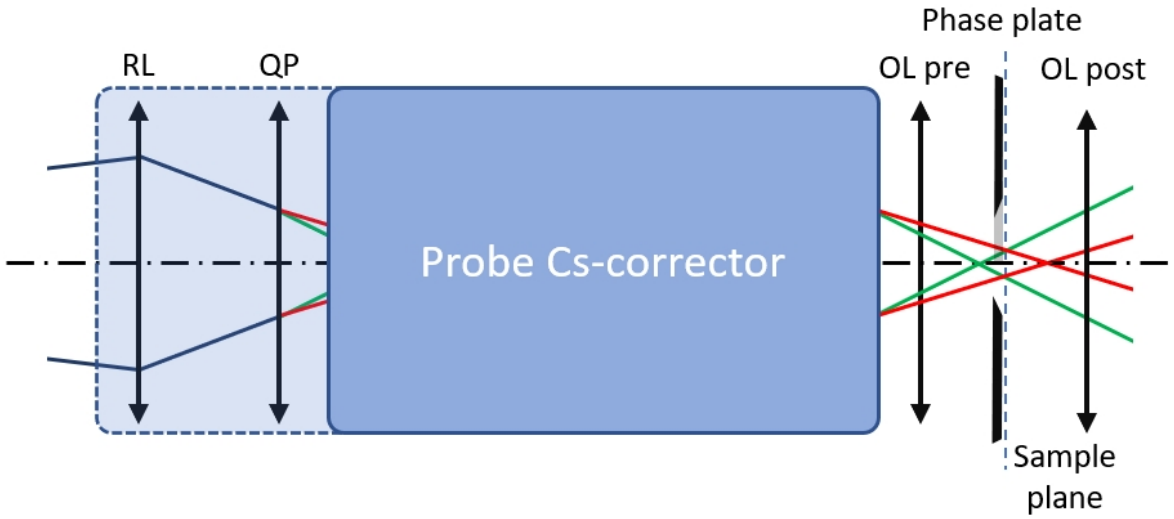

Fig. 1: Schematics of a vortex generator realized in a dedicated STEM instrument with operational probe corrector. The round lens (RL), formed by QPs in the corrector, prepares an astigmatic low convergence angle beam in the objective lens (OL) with the OL being switched off. A HPP is placed in between the two astigmatic line foci to facilitate MC.

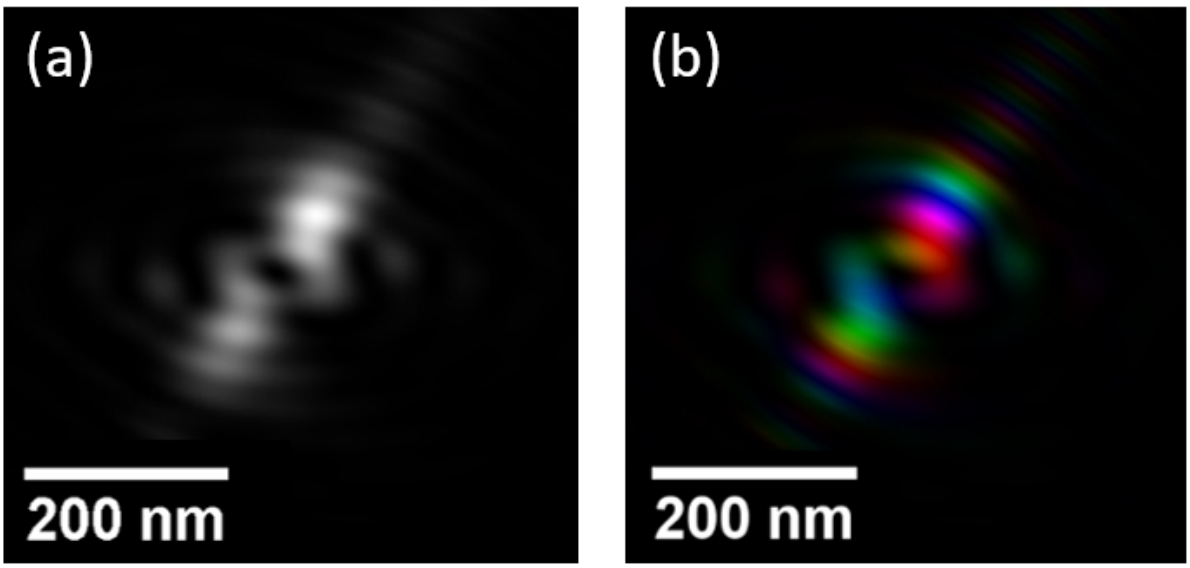

Fig. 2: Wave optical electron beam simulation results showing the intensity distribution (a) and (b) hue color coded phase of the vortex probe for the MC setup proposed in Figure 1.

IM5 Cryogenic, in situ and environmental electron microscopy

Type of presentation: Invited

IM5-IN-2617 Do you know the relevant conditions for in situ heating experiments in the TEM?

Grogger W.[1,2], Krisper R.[2], Fabbro R.[3], Fisslthaler E.[2]

[1]Institute of Electron Microscopy and Nanoanalysis (FELMI), Graz University of Technology, Steyrergasse 17, Graz, Austria, [2]Graz Centre for Electron Microscopy (ZFE), Steyrergasse 17, Graz, Austria, [3]ams-OSRAM AG, Tobelbader Strasse 30, Premstätten, Austria

Email of the presenting author: werner.grogger@felmi-zfe.at

In many fields of materials science in situ experiments in the TEM have proven to be paramount complements to conventional static investigations. These types of experiments allow for a real-time observation of the sample's response to a specific external stimulus. In terms of the impact of thermal energy (i.e. heating) the advent of MEMS (microelectromechanical systems) based heating holders for the TEM has greatly enhanced the choice of experimental possibilities. Due to the small size of MEMS-based heating elements, rapid temperature changes and a high stability can be achieved. In addition, the amount of emitted infrared radiation is sufficiently small so in situ nanoanalysis using X-ray spectrometry (EDXS) can be used up to 1000 °C [1].
What remains a challenge, however, is the knowledge of the relevant experimental conditions. For instance, the sample temperature is often only estimated from the heating holder readout. This temperature might significantly deviate from the local temperature of the area of interest. Therefore, different methods are available for determining the sample's temperature more accurately like electron diffraction or plasmon energies [e.g. 2, 3]. On the other hand, the performance of the X-ray detector will change when exposed to a large amount of infrared radiation, which might render quantitative analysis results questionable [4].
In this contribution we will focus on the performance of the EDXS detector and the quality of the obtained spectra when exposed to a heated sample. As shown in figure 1 the energy resolution of an SDD EDXS detector degrades significantly for temperatures above 500 °C. This can be attributed to the increasing emission of infrared radiation from the hot parts of the sample and the heating holder. When plotting the measured infrared intensities in an Arrhenius plot, a good correspondence to calculations can be found.
As an application example, the in situ investigation of a vertical cavity surface emitting laser (VCSEL) device is also shown. In terms of reliability one critical part in oxide defined VCSELs is the aperture, which might undergo secondary oxidation and furthermore cause stress in the structure and degrade the device performance. Such an aperture was prepared in plan-view and is shown in fig. 2 [5]. During in situ heating experiments the generation of so-called dark line defects could be observed. Preparations for in situ biasing experiments are currently ongoing and we hope to be able to show first experimental results.

[1] https://denssolutions.com/products/wildfire/ (as of 06.04.2022)
[2] F. Niekiel et al. Ultramicroscopy 176 (2017) 161
[3] M. Mecklenburg et al. Science 347 (2015) 629
[4] R. Krisper et al. Ultramicroscopy 234 (2022) 113461
[5] R. Fabbro et al. Micron (2022) in print

Acknowledgement: We acknowledge financial support from the iRel 4.0 (H2020 876659) and the ESTEEM3 (H2020 823717) projects and the Austrian Cooperative Research Facility.

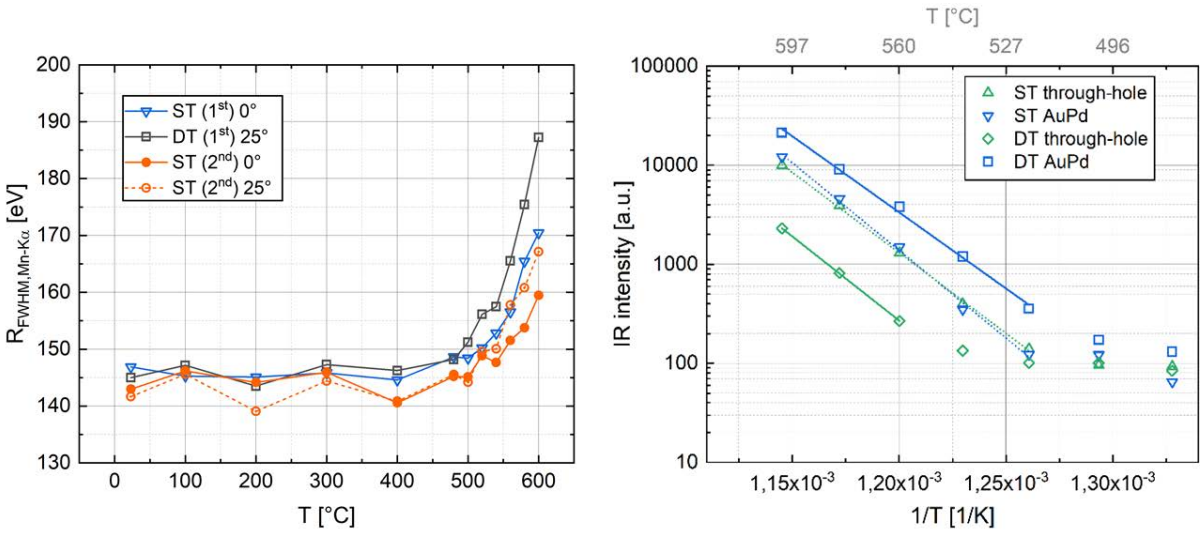

Fig. 1: (left) Energy resolution (Mn-Kα) for a single tilt (ST) and double tilt (DT) heating holder at 0° and 25° tilt with a multi-detector system at specimen temperatures up to 600 °C. (right) Detected infrared emission for the same specimen holders at 25° for two regions (hole, AuPd thin film).

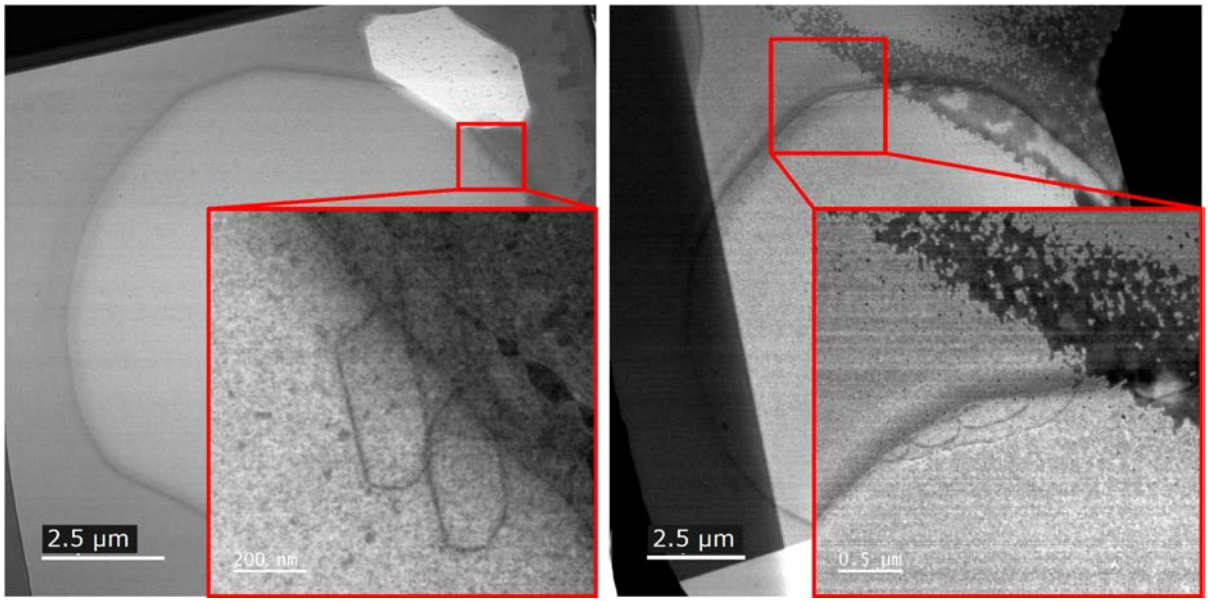

Fig. 2: STEM HAADF images of the aperture in a VCSEL (plan view) showing the creation of defects at the aperture edges (two different temperature cycles).

Type of presentation: Oral

IM5-O-2894 Graphene liquid cell for electron microscopy analysis of nanoparticle interaction with solutions: the case of titanium oxide nanoparticles and phosphates

Batra N.[1], Gautron E.[1], Poizot P.[1], Le Caer S.[2], Moreau P.[1], Abellan P.[1]

[1]Institute Des Materiaux De Nantes, CNRS-Nantes University, Nantes, France, [2]Université Paris-Saclay, CEA, CNRS, NIMBE, UMR 3685, 91191, Gif-sur-Yvette, France

Email of the presenting author: nitinkumar.batra@cnrs-imn.fr

Liquid cell electron microscopy (LCEM) is a very powerful technique to visualize dynamic reactions in liquid samples.[1] Both biological and nanomaterials have been studied using LCEM. Conventionally, silicon based chips, along with dedicated transmission electron microscopy (TEM) holders, are used for enclosing liquid samples between two silicon nitride membranes. Even though, there are many advancements with these silicon nitride based chips, it is difficult to obtain nanometer resolved imaging at nanoparticles interfaces. The major factor for the limited spatial resolution in LCEM is the radiation damage that nanomaterials and solvents endure during electron irradiation, the choice of membranes materials is also key.
In the last decade, graphene has been explored as a LCEM membrane to collect high-resolution structural information from various materials. Yuk et al. developed graphene liquid cells by enclosing the nanoparticle solution between two graphene layers and established a process to perform high-resolution imaging of Pt nanoparticles.[2] Graphene is composed of a single layer of carbon atoms. The thermal, electrical, mechanical and chemicals properties of graphene makes it an ideal candidate for replacement of silicon nitride membranes, as it is impermeable to most of liquids. Moreover, Graphene has shown to reduce the electron beam damage in the beam-sensitive nanomaterials as well as biomolecules.[3]
There has been a lot of work done with the graphene liquid cells, however, it is difficult to assemble these liquid cells and the success rates are low. In this work, we will present steps to transfer graphene to TEM grids (as shown in Figure 1) and challenges associated with it. Further, the methods to assemble graphene liquid cells will be presented (Figure 2). The graphene liquid cells are utilized to analyse TiO2 nanoparticles interactions with phosphate molecules. It has been observed that ultrafine (<20 nm) TiO2 nanoparticles can cause DNA or cell damage in human organs. There is little understanding of the effect of crystal orientation and facets of TiO2 nanoparticles interaction with biological organs and the first results in order showing this interaction will be presented.

References:
[1] Williamson, M. J., Tromp, R. M., Vereecken, P. M., Hull, R. & Ross, F. M. Dynamic microscopy of nanoscale cluster growth at the solid–liquid interface. Nature Mater 2, 532–536 (2003).
[2] Yuk, J. M. et al. High-Resolution EM of Colloidal Nanocrystal Growth Using Graphene Liquid Cells. Science 336, 61–64 (2012).
[3] Zan, R. et al. Control of Radiation Damage in MoS 2 by Graphene Encapsulation. ACS Nano 7, 10167–10174 (2013).

Acknowledgement: The authors would like to thank the financial support by the French National Research Agency (ANR) through the project PRC ACETONE (reference ANR-20-CE09-0010).

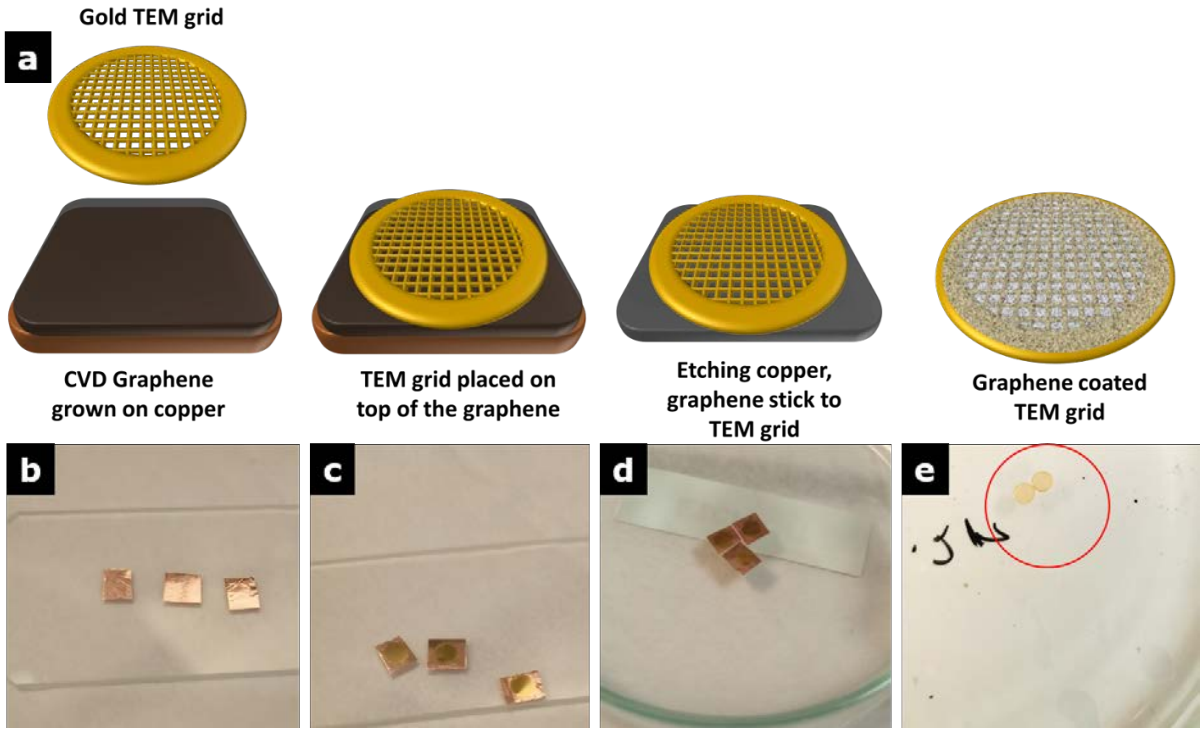

Fig. 1: a) Schematic steps for direct graphene transfer to the TEM grids, b) square pieces of the CVD graphene-Cu foil, c) gold TEM grids placed onto the graphene-Cu foil and holey carbon making contact to the graphene, d) gold TEM grid + Graphene-Cu foil system floating on copper etchant, e) graphene coated TEM grids floating in water bath.

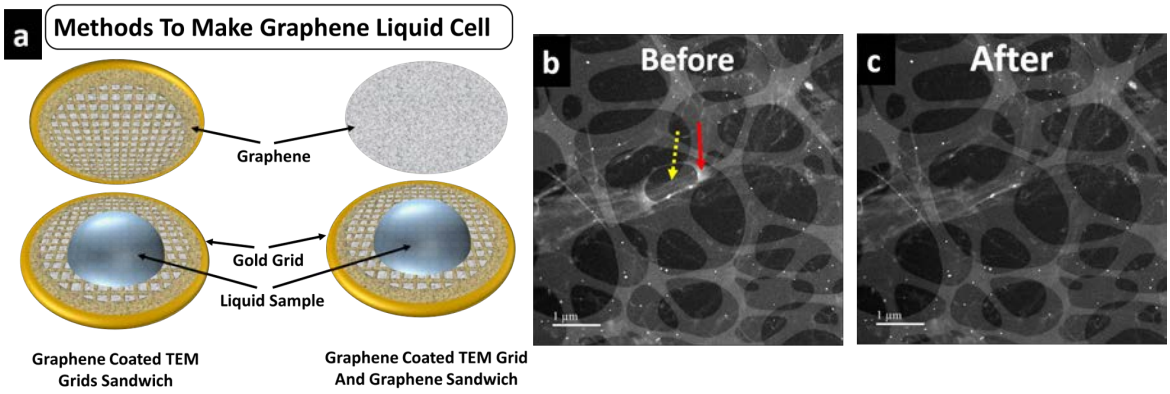

Fig. 2: a) Schematic of methods to prepare a graphene liquid cel usedl, b) and c) STEM images of graphene liquid cells with water pockets, before and after beam exposure respectively. Red arrow shows the presence of water, while yellow arrow shows the bubble formation.

Type of presentation: Oral

IM5-O-2649 Integration of EBSD acquisition into fully automated in-situ thermo-mechanical testing for high temporal and spatial resolution

Donoghue J. M.[1], Smith A. D.[2], Martinez F.[3], Taylor M.[1], Yang Z.[1], Lunt D.[1,4], Gholinia A.[1]

[1]Henry Royce Institute, Department of Materials, The University of Manchester, UK, [2]TESCAN-UK, Cambridge, UK, [3]NewTec Scientific, Caveirac, France, [4]United Kingdom Atomic Energy Authority (UKAEA), Culham Science Centre, UK

Email of the presenting author: jack.donoghue@manchester.ac.uk

In situ experiments within a SEM are increasingly exploited for quantifying the thermomechanical performance of materials at the sub-micron scale. A typical workflow for such an experiment is summarised in Fig. 1a. Traditionally, these tests are performed manually and are labour intensive as different systems are usually required for each stage of the test. Furthermore, experimental time is limited by operator working hours and each data collection step requires time to carry out due to the detail required from the capture. These time constraints can restrict the type of experiment to be carried out, limiting either the size of the region(s) investigated or reducing the number of strain/temperature steps considered. This is particularly true when Electron Backscatter Diffraction (EBSD) is sought for phase and crystallographic information as this is often the most time-consuming step (even allowing for CMOS based fast detectors).

Presented here is an integrated solution developed at the University of Manchester, in collaboration with TESCAN and NewTec Scientific, that allows for the automated acquisition of EBSD maps during in situ experiments. The solution allows the acquisition of images and EBSD maps at user defined intervals throughout complex straining/temperature experiments. Particular attention is paid to the ability to automatically track regions of interest and maintain focus. The stability of the system allows these experiments to run continuously without user intervention over several days. Automation minimises user error and potentially allows triple the data that could be achieved in standard working hours (Fig. 1b).

Several case studies are presented. These include a static heating experiment where a high strength low alloy steel is taken to 1000°C to completely transform to the high temperature austenite phase and then slowly cooled in order to study the transformation to bainite (Fig. 2). The automated solution presented here allows for increased temporal resolution enabling phenomena such as the effect of twins and carbide pinning on grain boundaries to be fully investigated in terms of their influence on the transformation behaviour. A further study presented demonstrates the system's ability to automatically track a region and maintain focus during a loading experiment. A nickel-based superalloy (Inconel 718) is deformed in tension to 15%, where EBSD is acquired at incremental steps to understand the evolution of plastic strain within the microstructure and provide crucial information for crystal plasticity simulations (Fig. 3). In this case, the advantages of automation are exploited to collect larger datasets at each individual strain step for increased statistical relevance rather than increase the temporal resolution.

Acknowledgement: Authors are grateful to the Henry Royce Institute for Advanced Materials, funded through EPSRC grants EP/R00661X/1, EP/S019367/1, EP/P025021/1 & EP/P025498/1

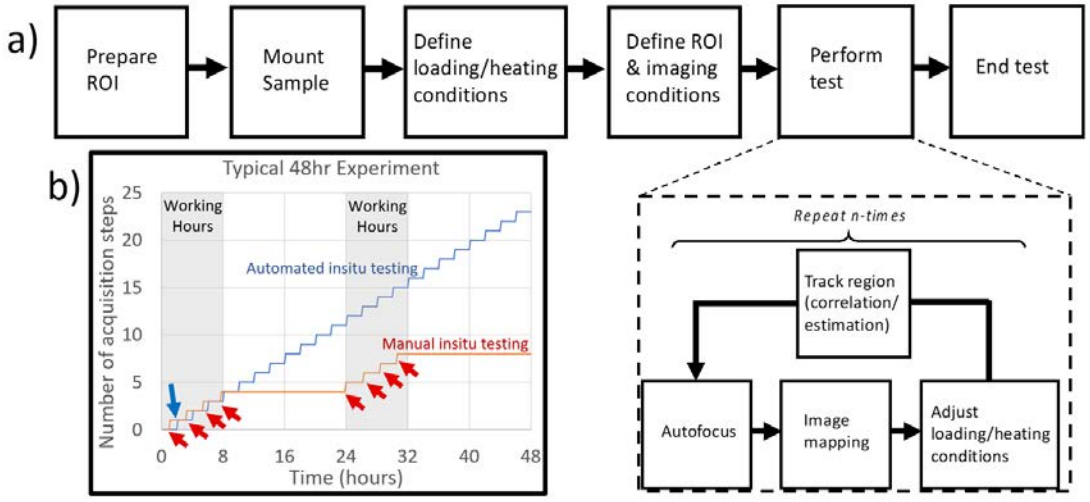

Fig. 1: The typical workflow of an in situ experiment. With automation the steps in the dashed box can be repeated without user intervention. The temporal resolution difference between automated in situ and manual testing is shown in (b). Also shown are the requirement for user interaction (arrows).

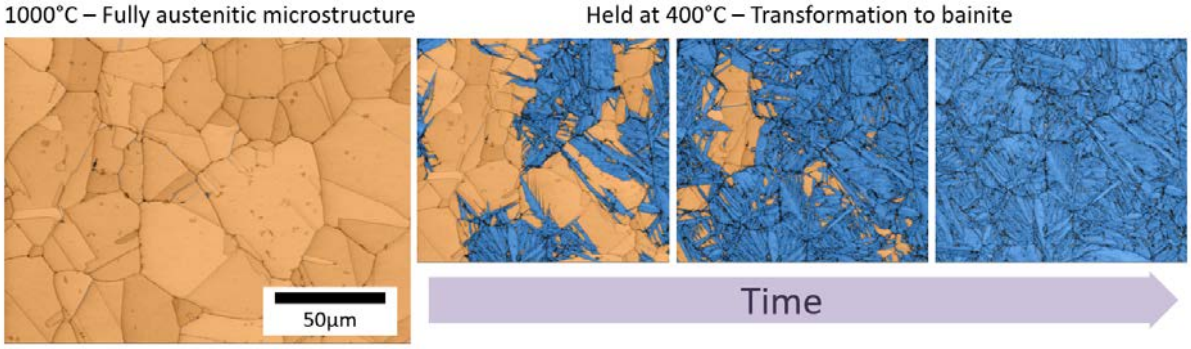

Fig. 2: EBSD phase maps following the transformation from austenite (orange) at 1000°C to bainite (blue) in a high strength low alloy steel at 400°C. Only selected frames of the acquired transformation data are shown due to the size of the dataset.

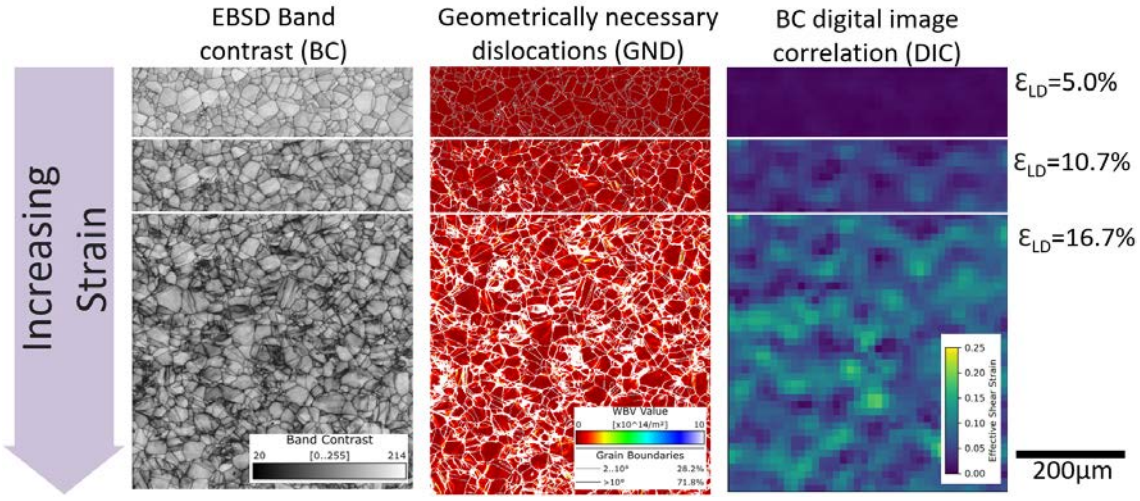

Fig. 3: Selected EBSD maps of Inconel 718 acquired in situ at strain. Band contrast pattern quality maps are displayed alongside GND density measured from the weighted Burgers' vector approach, and DIC maps calculated from the band contrast maps allowing the strains within the region to be determined.

Type of presentation: Invited

IM5-IN-2999 Microsystems for in situ cryofixation and correlative cryomicroscopy

Burg T. P.[1], Chen S. Y.[1], Faul N. A.[1], Lamberz C.[1], Szabo G. V.[1], Thiem D.[1]

[1]Department of Electrical Engineering and Information Technology, Technische Universität Darmstadt, Darmstadt, Germany

Email of the presenting author: thomas.burg@tu-darmstadt.de

In this talk I will present recent work of our group towards correlating cryogenic electron microscopy, cryogenic fluorescence microscopy, and live cell imaging with *in situ* cryofixation.

Before entering the high vacuum of an electron microscope, biological samples need to be fixed chemically or frozen. Due to the time required for this preparation, it is difficult to correlate high-resolution EM images of cell structure with millisecond dynamics observable in the light microscope. We have been able to overcome this limitation by cryofixing cells and small model organisms directly in the light microscope through ultra-rapid *in situ* cooling. The approach differs fundamentally from methods based on plunge freezing, jet freezing, or high-pressure freezing, which rely on a rapid shift between a warm and a cold equilibrium state. Instead, a microfluidic chamber is maintained in a state far from thermodynamic equilibrium during live cell imaging. The microfluidic device is in contact with an LN2-cooled solid heat sink, and power lost to the heat sink is balanced precisely by an electrical heater that is optimized to exhibit high uniformity and low thermal resistance. By lowering or cutting the power to the heater, the sample can be cooled without mechanical interference at controlled rates of several ten thousand degrees per second. We are currently working towards elucidating the ultimate limits of this approach regarding the size of the object, temporal resolution, and minimizing or eliminating the need for cryoprotectants. Another part of our research focues on the ability to image in situ cryofixed samples by high numerical aperture cryofluorescence microscopy. To this end we designed a new type of light microscope for immersion imaging below the glass transition temperature of water (-135 °C). The technology is compatible with conventional correlative light and electron microscopy workflows. We therefore expect that our platform will be of interest for studying a wide range of questions involving temporal relationships between cell stimulation, dynamic cell function, and structural alterations at the nanometer scale.

Acknowledgement: This project has received funding from the European Research Council (ERC) under the European Union's Horizon 2020 programme (MICROCRYO, No. 772441)

Type of presentation: Oral

IM5-O-2703 In-situ Microscopy of Catalytic Oxidation of CO to CO2 over Platinum Surfaces.

Vařeka K.[1], Janák M.[2], Jaroš A.[2], Hrůza D.[2], Bábor P.[1,2], Kolíbal M.[1,2], Šikola T.[1,2]

[1]CEITEC - Central European Institute of Technology, Brno University of Technology, Brno, 61200, Czech Republic, [2]Institute of Physical Engineering, Faculty of Mechanical Engineering, Brno University of Technology, Technická 2896/2, Brno, 616 69, Czech Republic

Email of the presenting author: karel.vareka@ceitec.vutbr.cz

Exhaust gases released into the atmosphere by global industrialisation constitute a significant contributor to deterioration of the environment. Carbon monoxide (CO) arises from the incomplete combustion of fossil fuels and is a domain feature in the development of alternative fuels. As an unwanted by-product during the production of methanol in CO2 hydrogenation, excessive CO feeds to hydrogen fuel cells may cause decay in their electro-generation performance [1]. Therefore, the development of efficient catalytic processes with high CO conversion rates is essential for the modernisation of our industry sectors and the minimisation of waste production as a result of a circular economy.

Catalysis is a process that increases the rate of a reaction by lowering the activation barrier. Although, throughout the reaction, the catalyst remains undepleted, in the long term, the surface can exhibit sintering, faceting, or poisoning that lead to the catalytic activity lowering [2]. Conventionally, heterogeneous catalysis experiments are carried out by ex-situ high-vacuum microscopy techniques to determine the effect of ambient atmospheres on a catalyst. Nevertheless, to avoid atmospheric contamination and to directly correlate surface processes with external influences (pressure, temperature), the real-time in-situ characterisation of surface and on-surface dynamics is of particular interest for catalysis research.

The kinetics of the adsorption and diffusion mechanisms of gas-phase and temperature-induced processes during CO oxidation give rise to spatial- and temporal-dependent behaviour on polycrystalline platinum surfaces (see Figure 1). Many conventional surface science techniques may be adapted, yet not all offer sufficient chemical, spatial, and temporal resolution. In our group, we employed state-of-the-art UHV in-situ scanning electron microscope (SEM) and in-situ static secondary ion mass spectrometry (SSIMS) for real-time observations. Correlative approach is carried out to compare the chemical composition of the surface layers (SSIMS) with the changes in the work function (SEM) with the mass spectrometer gas flow data. In addition, we employed atomic force microscopy (AFM) capable of in-situ measurements within the microscope chamber (see Figure 2). The correlative probe electron imaging is set to reveal a connection between self-promoting wave behaviour and the surface active sites as any facets boundaries are visible in the topography. We aspire to investigate the tip-sample interaction between adsorbed gases during several AFM modes.

[1] Holton, O. T., Stevenson, J. W., 2013, Platinum Metals Rev., vol. 48, pp. 259-271.
[2] Imbihl, R., Ertl, G., 1995, Chem. Rev., vol. 95, pp. 697-733

Acknowledgement: We acknowledge CzechNanoLab Research Infrastructure supported by MEYS CR (LM2018110).

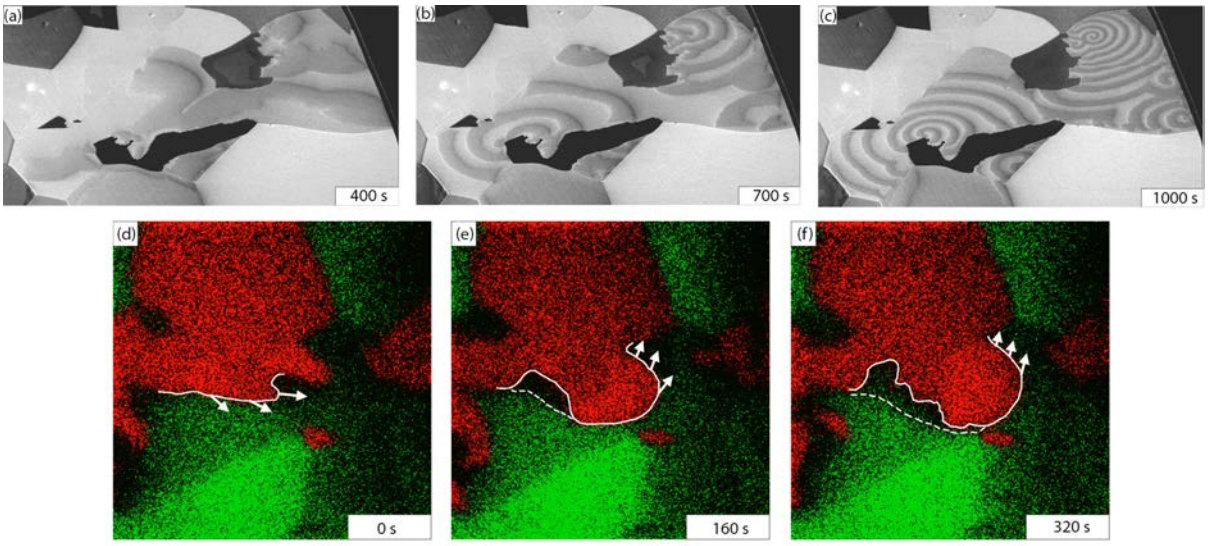

Fig. 1: Time evolution of elliptical patterns observed on an active Pt(4,1,10) grain measured by (a)-(c) in-situ UHV-SEM TESCAN and (d)-(f) by TOF-SIMS5 IONTOF at T = 443 K, p_O2 = 1.5 × 10−3 Pa, p_CO = 3 × 10−4 Pa. Red areas denote oxygen coverage, green CO coverage. White arrows highlight the moving wavefront of adsorbed species.

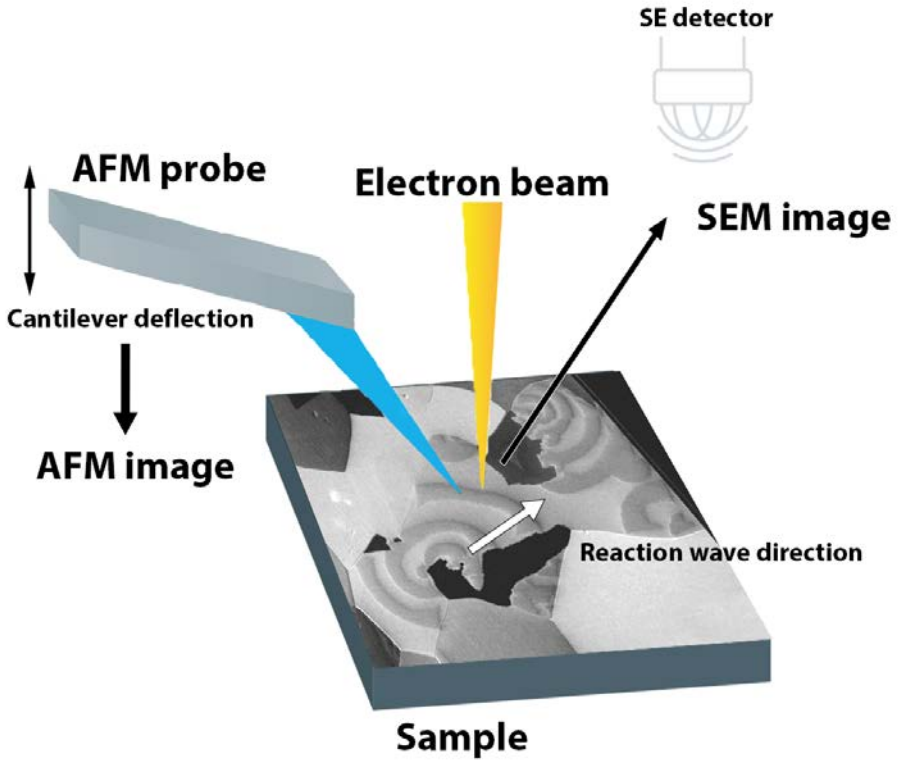

Fig. 2: Scheme of correlative probe and electron microscopy of real-time reaction wave observations. Adapted from: AFM in SEM LiteScope Correlative microscopy-NenoVision, URL (https : //www.nenovision.com/litescopetm/correlative − microscopy/).

Type of presentation: Oral

IM5-O-2542 Transmission electron microscope modification for light-induced in situ imaging of specimens in liquid on example of photodynamic therapy

Żak A. M.[1], Kaczmarczyk O.[2], Grzęda J.[1], Piksa M.[3], Matczyszyn K.[2]

[1]Faculty of Mechanical Engineering, Wroclaw University of Science and Technology, Wrocław, Poland, [2]Faculty of Chemistry, Wroclaw University of Science and Technology, Wroclaw, Poland, [3]Institute of Immunology and Experimental Therapy, Polish Academy of Science, Wroclaw, Poland

Email of the presenting author: andrzej.zak@pwr.edu.pl

Antimicrobial Photodynamic Therapy (aPDT) is an effective alternative to fight drug-resistant infections. It consists of a non-toxic substance called photosensitizer (PS) which via illumination with a suitable light wavelength produces reactive oxygen species leading to the pathogen death. However, the molecular mechanism of aPDT is still not fully understood. There is a debate the location of the PS action, the ability to penetrate into the structure of pathogens and the final impact of PS penetration. For this reason, we decided to make a setup that will allow for this phenomenon imaging in electron microscope.

Despite the significant development of in situ techniques, light-induced research is a relatively rarely used approach. The most popular solutions include the use of dedicated specimen holders or introduction of an optical fiber or a laser beam within the objective lens side ports. The first solution limits the possibility of multifaceted impact on the sample, and the second one offers nonuniform lighting or forces the sample to be tilted. For this reason, we decided to introduce a top-mounted system in place of the removed STEM deflection system. The first generation of the system used LED light source [1], and the final used glass optical fiber and a tunable 1W laser light source. The design of an illuminator, adapted to the Hitachi H-800 microscope (Fig. 1), has been published for wide use [2].

To ensure observation in the hydrated state, a carbon-carbon liquid cell was used with the concentration of bacteria selected so that they are separated and surrounded by PS. Initial tests were carried out on *Staphylococcus aureus* and methylene blue excited by 660 nm.

The biggest issue with observing hydrated samples in TEM is the electron beam itself. Because in the absence of the factory dose measure, a new method of measuring and controlling dose has been proposed, which has been shown to be particularly useful at the lowest available doses [3]. Preliminary experiments [1,2] were carried out at doses exceeding lethal doses; however, strict control of the total dose in illuminated and control trials allowed the light-induced effects to be separated. The exemplary results (Fig. 2) showed that in the combination of the microorganism and PS used, the outer envelope of the bacteria is damaged first. Further work is directed towards reconstructing the system on a modern TEM to minimize dose and maximize resolution, also on different groups of microorganisms and photosensitizers.

Literature

[1] Zak A. et al., Photodiagnosis Photodyn Ther, DOI: 10.1016/j.pdpdt.2021.102463
[2] Zak A. et al., Ultramicroscopy, DOI: 10.1016/j.ultramic.2021.11338
[3] Zak A., Micron, DOI: 10.1016/j.micron.2021.103058

Acknowledgement: The research was financed by the Miniatura grant (2019/03/X/NZ3/02100, National Science Center, Poland).

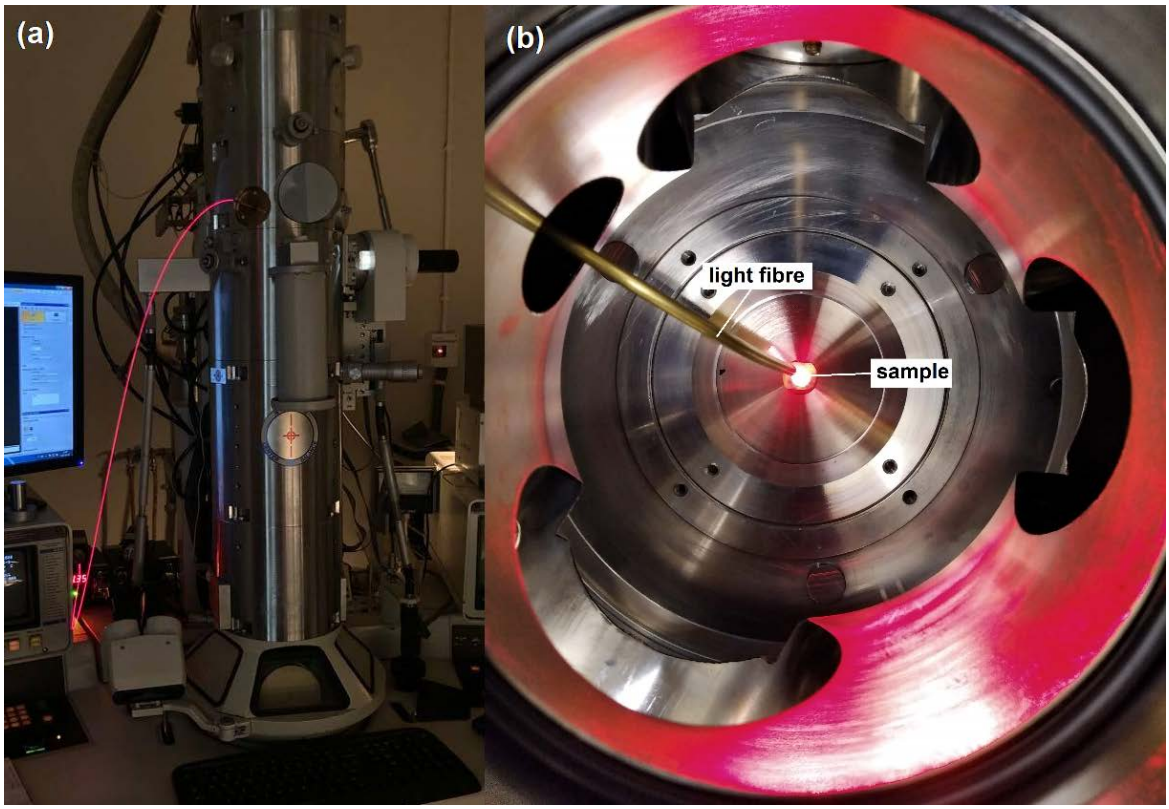

Fig. 1: TEM with working illuminator (a) and illumination system inside the microscope, after removing the condenser system [1].

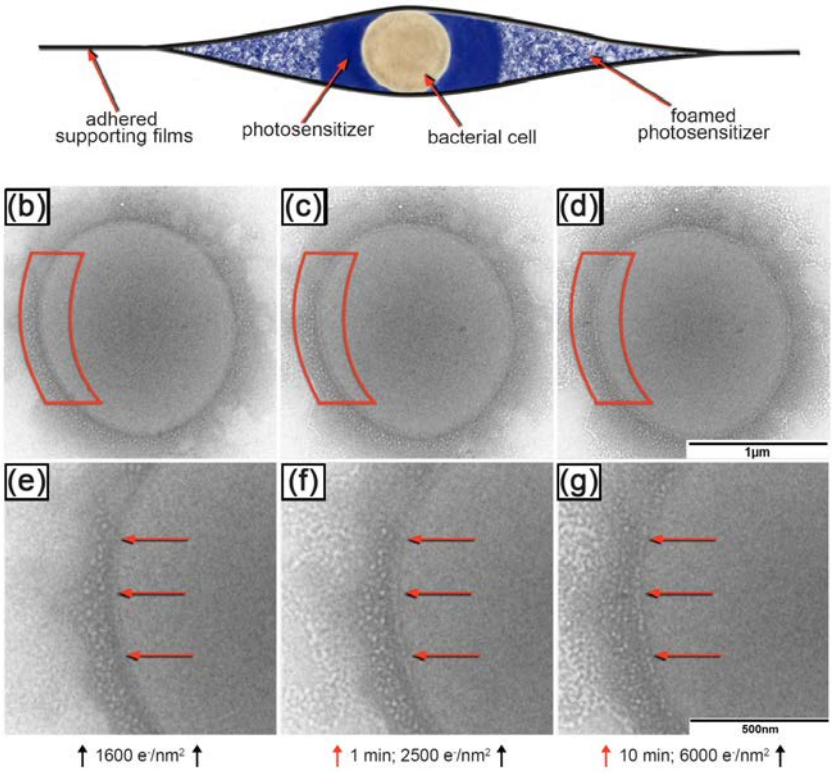

Fig. 2: Schematic representation of the cell encapsulated with the photosensitizer between two carbon films (a). The cell before light illumination (b,e) is characterized by the regular edge. The changes can be observed within the cell wall after light illumination for 1 min (c,f), which are more visible after 10 min (d,g) [2]

Type of presentation: Poster

IM5-P-2651 The power of speed: DED EELS for analytical in situ TEM

Fisslthaler E.[1], Krisper R.[1], Šimić N.[1], Knez D.[2], Grogger W.[2]

[1]Graz Centre for Electron Microscopy (ZFE), Steyrergasse 17, Graz, Austria, [2]Institute of Electron Microscopy and Nanoanalysis (FELMI), Graz University of Technology, Steyrergasse 17, Graz, Austria

Email of the presenting author: evelin.fisslthaler@felmi-zfe.at

With the advent of advanced *in situ* TEM, speed and precision gained considerably in importance for dynamic TEM experiments. Collecting information at just the right time became significantly more crucial. Powerful techniques and hardware that allows capturing images and analytical data with high speed got into focus to be able to monitor fast dynamic processes with both the lateral and the temporal resolution that is needed for adequate description.
Due to various challenges of geometrical and physical nature that might arise in EDXS analysis with MEMS (microelectromechanical systems) heaters [1,2], using EELS is often beneficial for analytical analysis during *in situ* TEM experiments. This is especially true for the investigation of precipitation in light alloys. They requires systems capable of tilting along two axes, and detectors that provide ample signal not only for the main metallic components, but also for light elements like Li or B (used as additives for grain refinement or strengthening). The properties of these materials can be modified by subjecting them to accurately defined temperature treatments that trigger an artificial ageing process [3]. Using certain threshold temperatures, some systems can even be “cycled” – i.e. restored to their original supersaturated state and “aged” again [4]. *In situ* (S)TEM can provide detailed insight into various stages of precipitation. However, a key condition for the use of a structure with dimensions in the micro- and nanometer range to illustrate processes in a bulk system is the exact knowledge of the local stoichiometry. Consequently, concomitant analytical analysis that is fast enough to observe changes in the chemical composition of the sample during the experiment is extremely valuable for the reliable interpretation of *in situ* TEM results.
In this study, we use direct electron detection EELS (DED EELS) from Gatan (Quantum ERS GIF with K2 camera) to perform 2D chemical analysis during a STEM heating experiment. The material that is described is AlCu4, an aluminum alloy with 4% of copper that can be strengthened by precipitation hardening. We capture and describe the changes of the system during different stages of precipitate formation (see Figure 1), using fast EELS techniques to track the chemical composition of the whole system.
Especially when compared to EDXS analysis, this approach is more powerful in terms of speed, providing the capability to perform detailed chemical analysis of a complex light element system at various stages of transformation.

[1] https://denssolutions.com/products/wildfire/ (as of 06.04.2022)
[2] Krisper et al., Ultramicroscopy 234 (2022) 113461
[3] Ashby, Engineering Materials 2 (2013) Elsevier
[4] Zandbergen et al., Nature Scientific Reports 7 (2017) 2184

Acknowledgement: We acknowledge financial support by Austrian Cooperative Research project “INSIGHT” (SP-2021-04).

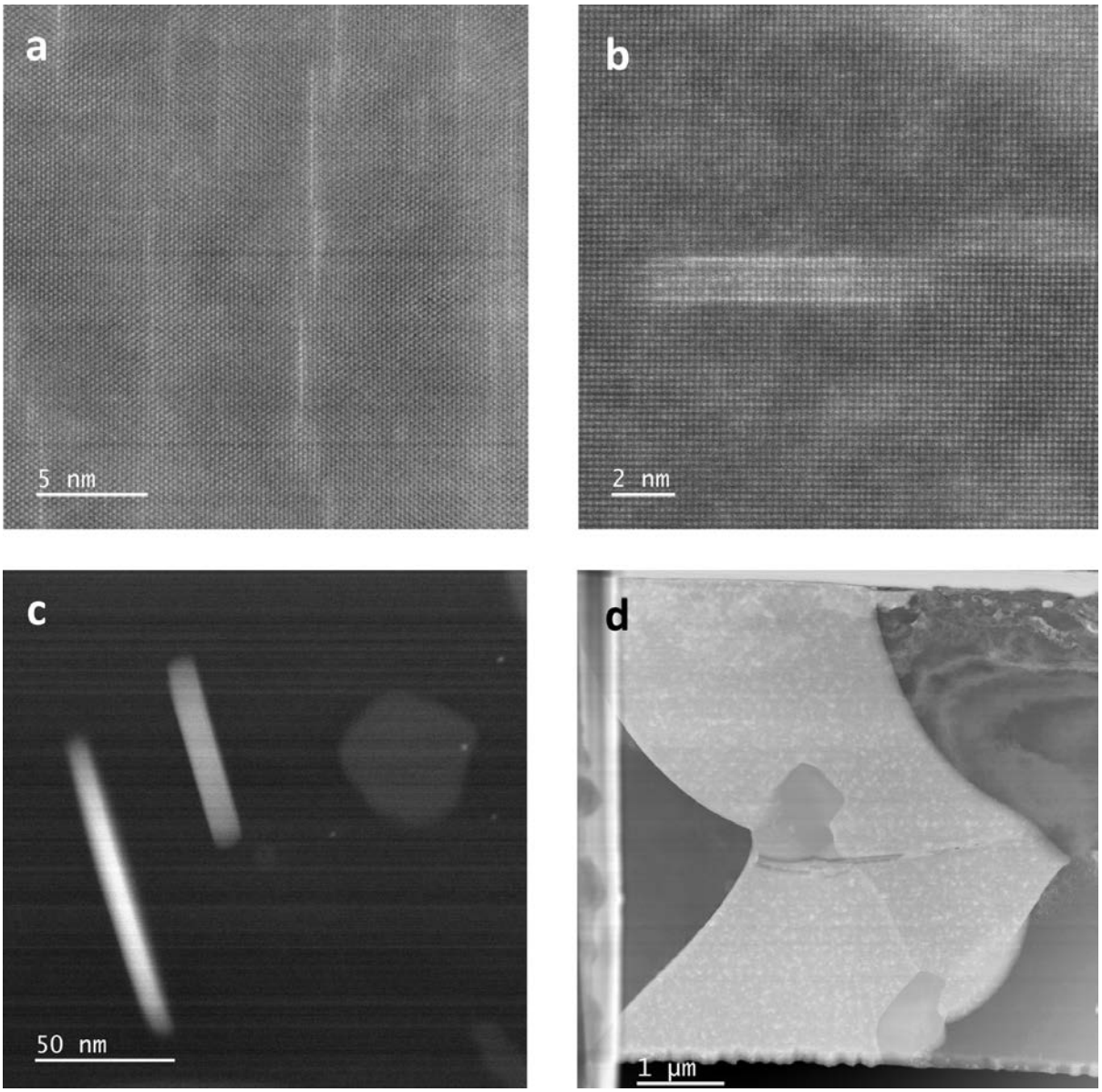

Fig. 1: HR STEM images of various stages of precipitate formation in AlCu4 ((a): monolayer Guinier-Preston I (GP I) zones, (b) and (c): growing multiple layer GP II zones/θ“, (d) θ precipitates ($CuAl_2$))

Type of presentation: Poster

IM5-P-2664 Efficient preparation of MEMS carriers with plan-view specimens: a case study of in situ TEM experiments with thin epitaxial layers

Groiss H.[1], Šantić N.[1], Minenkov A.[1]

[1]Christian Doppler Laboratory for Nanoscale Phase Transformations, Center for Surface and Nanoanalytics, Johannes Kepler University Linz, 4040 Linz, Austria

Email of the presenting author: heiko.groiss@jku.at

Comprehensive characterization is of principal importance for the controlled synthesis and application of nanomaterials. *In situ* TEM, which has recently evolved by the introduction of cutting-edge MEMS-based sample carriers [1], is an excellent tool for real-time observation of nanoscale structural changes induced by different stimuli such as heat or bias.
One of the major challenges for successful *in situ* TEM experiments is a suitable MEMS carrier preparation with an electron transparent specimen. This is particularly challenging when examining free surfaces from layered samples in plan-view geometry. In combination with cross-sectional samples, such specimens are crucial to provide detailed three-dimensional information on the morphological evolution of thin films [2].
To make a step in solving this challenge we elaborate a novel method for sample preparation, suitable for a vast variety of fragile materials. It is especially developed for *in situ* TEM heating in plan-view geometry of thin epitaxial layer systems [3]. It involves a broad primary mechanical thinning of the sample by the wedge-polishing technique followed by FIB-assisted installation on the MEMS-based carrier (Fig. 1). The synergy of the two techniques allows us to combine the advantages of both approaches minimizing invasive effects such as mechanical load and ion beam illumination. Moreover, the broad wedge-shaped specimens are well-suited for cutting multiple lamellae from the same sample giving ground to studying materials properties in a systematic fashion.
The principle of the proposed method is demonstrated by new insights into the thermal-induced strain relaxation and stability of Ge Stranski-Krastanov islands on Si during *in situ* TEM heating (Fig. 2). We thoroughly traced the morphological and structural changes on the fly in a single heating-cooling cycle via HRTEM and SAED. To highlight the inherent strain of the SK islands the two-beam condition has been utilized. Major strain relaxation in the islands occurs through the formation of stacking faults at 625°C induced by the different thermal expansion coefficients of the inherent materials. These findings can be barely achieved without applying the elaborated method that, in particular, proves its conceptual applicability for thin epitaxial layers.

[1] J.T. van Omme et al, Ultramicroscopy 192 (2018), p. 14.
[2] A. Minenkov, H. Groiss, Journal of Alloys and Compounds 859 (2021), 157763.
[3] A. Minenkov et al., MRS Bulletin 47 (2022), pp.1-4.

Acknowledgement: The authors thank J. Aberl, L. Vukušić and M. Brehm from the Institute of Semiconductor and Solid-State Physics (JKU Linz) for providing the MBE grown samples.

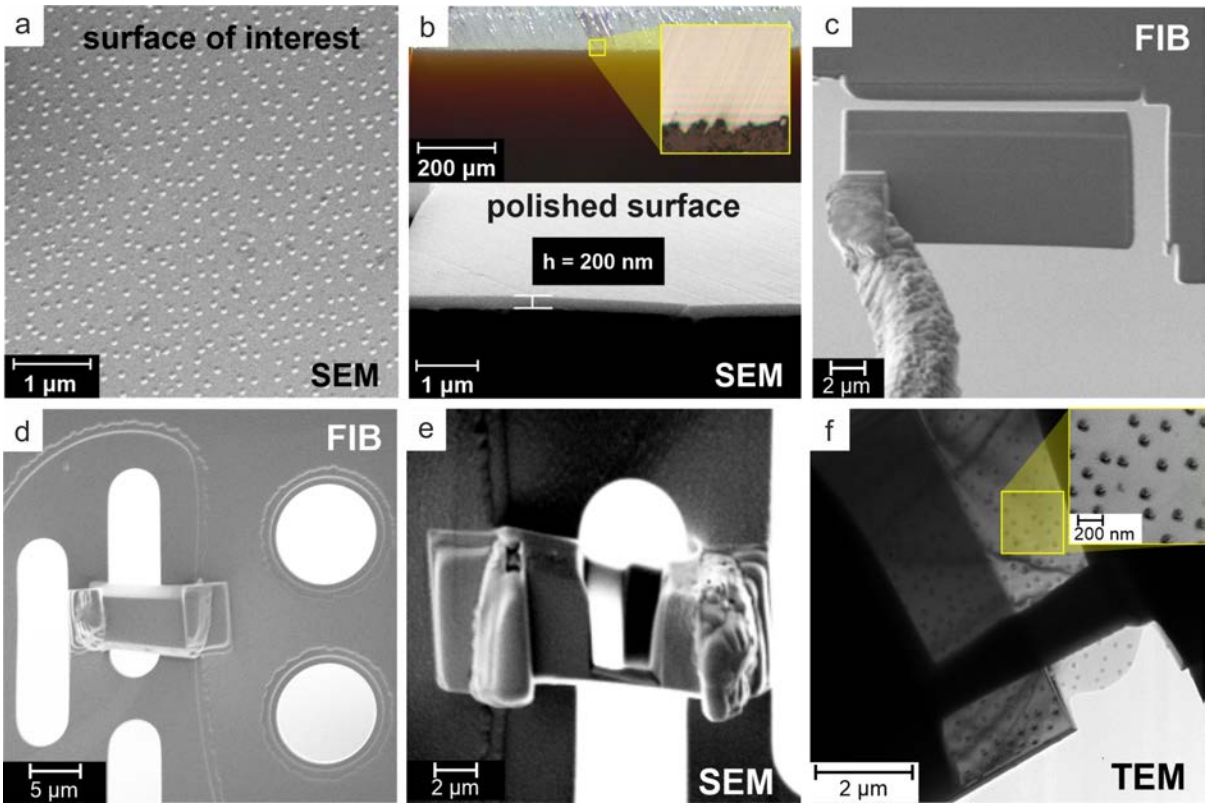

Fig. 1: Preparation of a MEMS heating chip: (a) SEM of the Ge islands before preparation, (b) light microscopy and SEM of a wedge polished sample with its thin edge, (c) FIB lift out, (d) installation of the lamella on the chip, (e) final thinning to electron transparency, (f) TEM images of the Ge islands on the chip.

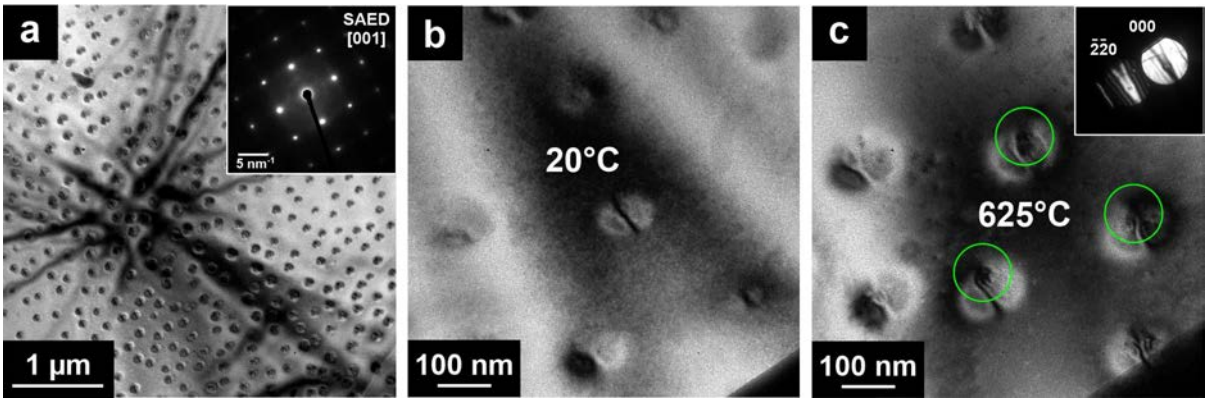

Fig. 2: (a) TEM of the Ge islands aligned along [001] and the corresponding SAED pattern, (b, c) selected snapshots of the sample at different temperatures taken at two-beam condition (inset) and recorded during a continuous *in situ* heating experiment. The formation of dislocations within the Ge islands at 625°C is highlighted with green circles.

Type of presentation: Poster

IM5-P-2797 Real-time atomic-resolution observation of coherent twin boundary migration in rocksalt transition metal nitride

Chen Z.[1], Löfler L.[2], Holec D.[2], Zhang Z.[1]

[1]Erich Schmid Institute of Materials Science of the Austrian Academy of Sciences, [2]Department of Materials Science, Montanuniversität Leoben, A-8700 Leoben, Austria

Email of the presenting author: zhuo.chen@stud.unileoben.ac.at

It is well known that most crystal structures do not possess simple geometric arrangements, which determines their more complex deformation mechanism. For complex material deformation, Kronberg proposed a synchronous slip and twinning deformation mechanism in 1957, whereby two shears operate in opposite directions on adjacent atomic planes [1]. This mechanism has been shown to operate in the Laves phase and α-Alumina [2, 3]. However, due to the difficulty of characterization of complex materials, there has been no in-situ experimental evidence to support this deformation mechanism for many years. In this work [4], using in-situ atomic-resolution electron microscopy, we report two different twin boundary defect (TD) nucleation and CTB migration modes at the CTB/ITB (incoherent twin boundary) and CTB/surface junctions. A new twin defect nucleation and CTB migration mode are observed from the CTB/surface junction. We show that such CTB migration is associated with a boundary structure alternating from an N-terminated to Cr-terminated, involving Cr and N atom respective motion, i.e., asynchronous CTB migration (as seen in Fig.1). We further reveal the dynamic and thermodynamic mechanism of such asynchronous migration through strain analysis and DFT simulations. Our findings uncover an atomic-scale dynamic process of defect nucleation and CTB migration in a binary system, which provides new insight into the atomic-scale deformation mechanism in complex materials.

Reference:

[1] M.L. Kronberg, Plastic deformation of single crystals of sapphire: Basal slip and twinning, Acta Metallurgica 5(9) (1957) 507-524.
[2] M.F. Chisholm, S. Kumar, P. Hazzledine, Dislocations in Complex Materials, Science 307(5710) (2005) 701-703.
[3] N. Shibata, M.F. Chisholm, A. Nakamura, S.J. Pennycook, T. Yamamoto, Y. Ikuhara, Nonstoichiometric Dislocation Cores in α-Alumina, Science 316(5821) (2007) 82-85.
[4] Z. Chen, Y. Zheng, L. Löfler, M. Bartosik, H. Sheng, C. Gammer, D. Holec, Z. Zhang, Real-time atomic-resolution observation of coherent twin boundary migration in CrN, Acta Materialia, Volume 208, 2021, 116732.

Acknowledgement: The authors thank Dr. M. Bartosik and Prof. P.H. Mayrhofer for the help of this work. This work is supported by FWF P 33696 (Z.Z. and Z.C.).

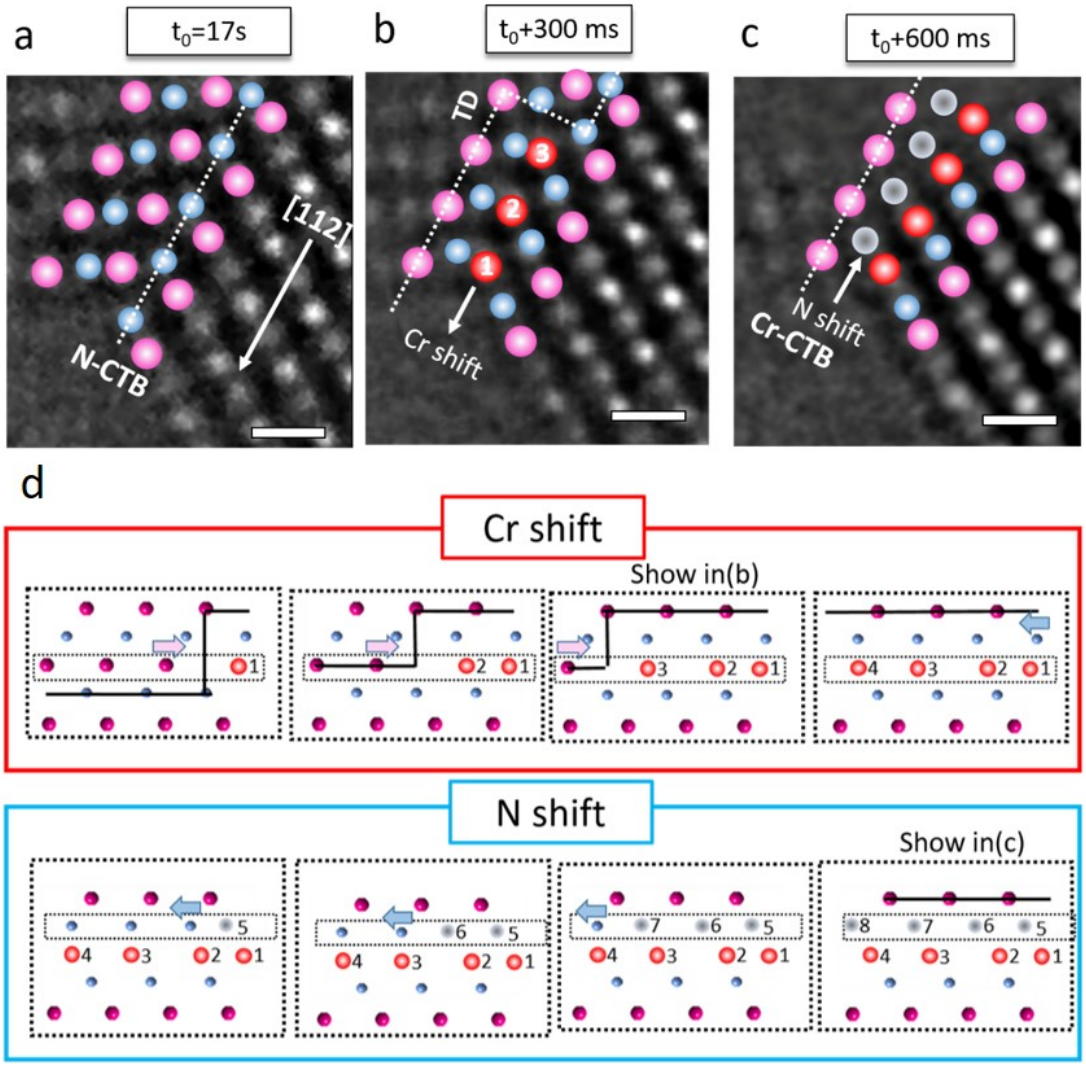

Fig. 1: (a)-(c) HRTEM images (snapshots of Movie) of the initial state, transitional state, and final stage of CTB migration from N-terminated to Cr-terminated, respectively. (d) Schematic sequence of asynchronous CTB migration and the TD movement.

Type of presentation: Poster

IM5-P-2628 Field induced oxygen vacancy migration in anatase thin films studied by in situ biasing TEM

Knez D.[1], Krisper R.[2], Chaluvadi S. K.[3], Orgiani P.[3], Dienstleder M.[2], Kothleitner G.[1,2], Ciancio R.[3]

[1]Institute of Electron Microscopy and Nanoanalysis, Graz University of Technology, Graz, Austria, [2]Graz Centre for Electron Microscopy, Graz, Austria, [3]Istituto Officina dei Materiali-CNR, Area Science Park, Trieste, Italy

Email of the presenting author: daniel.knez@felmi-zfe.at

Titanium dioxide TiO_2 is the most prominent representative within the class of transition metal oxides and is interesting for a large number of applications due to its optical properties, memristive behaviour, catalytic activity and electrochemical stability. Among the different polymorphs of TiO_2, anatase is the preferred configuration for many applications. Even though stoichiometric anatase is a wide band gap semiconductor with an indirect optical band gap of 3.2 eV, its electronic and optical properties are largely determined by the presence of excess electrons, which can be induced by dopants or intrinsic defects such as oxygen vacancies (VO). VO are inherently present in anatase and act as donors in the n-type semiconductor. Their presence induces localized electronic states within the band gap, correlated to the formation of Ti^{3+} ions [1]. Recently we were able to show that VO form periodic oxygen concentration variations along specific crystallographic directions without breaking the continuity of the anatase structure, contradicting the previously proposed formation of shear planes [2].
Related to the formation of such VO superstructures is the question about the origin of the memristive behaviour of anatase. There is theoretical evidence for the mobility of VO along the [100] and [010] crystallographic direction of the crystal in an electric field [3]. The structural implications of such field induced VO diffusion have however not yet been studied.
Here, we present an in situ biasing TEM study of the atomic structure of oxygen deficient anatase thin films, epitaxially grown on $LaAlO_3$ substrates by Pulsed Laser Deposition (PLD). The TEM micrographs in Figure 1 depict such a film in its initial state (a) and after increasing the voltage to 3.5 V over 30 min (b). The periodic contrast variations typical for the presence of vacancy superstructures in TiO_2 films are already visible in the initial oxygen deficient state (Fig. 1a). After applying an E-field along the [100] orientation they are, however, found to significantly increase. This finding points towards an increase of VO which preserve the overall structural arrangement and the relative distances between the defective planes of the modulated structure in the observed region.
Our experimental approach enables us to apply an E-field parallel to the in-plane direction of the film by using a standard MEMS-based in situ biasing platform (DENS Solution Lightning), which allows to shed light on the underlying mechanisms in electromigration and electroforming in TiO_2 thin films.

[1] B. Gobaut et al., ACS applied materials & interfaces, 9, 27,23099, 2017.
[2] D. Knez et al., Nano letters 20 (9), S. 6444, 2020.
[3] A. Paris, S. Taioli, J. Phys. Chem. C 120 (38), S. 22045–22053, 2016.

Acknowledgement: The authors acknowledge financial support by the European Union's Horizon 2020 research and innovation program under Grant 823717-ESTEEM3.

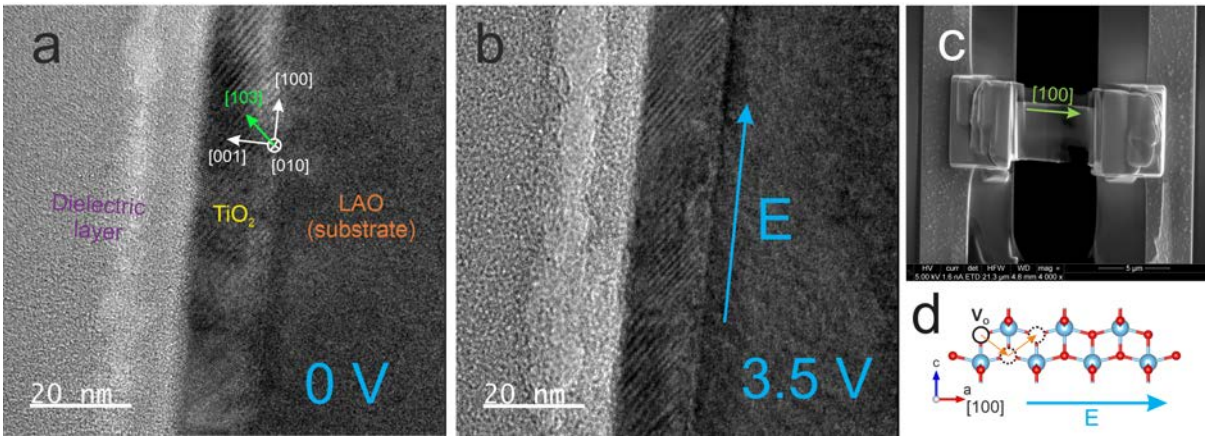

Fig. 1: TEM BF micrographs of the anatase thin film in its initial state (a) and after application of an electric field along [100] (b). (c) shows a SEM image of the mounted lamella on the DENS solutions MEMS chip. (d) illustration of the VO migration process along [100] in an applied E field [3].

Type of presentation: Poster

IM5-P-2530 In situ deformation observation via EBSD and EDS during high temperature tensile testing

Krauß S.[1], Bale H.[2], Boese M.[1], Tordoff B.[1]

[1]Carl Zeiss Microscopy GmbH, Carl-Zeiss-Straße 22, 73447 Oberkochen, [2]Carl Zeiss X-ray Microscopy Inc, 5300 Central Parkway, Dublin, CA 94568

Email of the presenting author: sebastian1.krauss@zeiss.com

Tensile testing is the backbone of mechanical characterization for materials science. The possibility to combine mechanical testing with advanced imaging and characterization methods and the option to operate at high temperatures up to 800°C opens a large variety of possibilities for materials research. In this work in situ annealing experiments are shown, where the grain growth is observed via EBSD over the course of the experiment. Different annealing states are achieved and tested after cooling to room temperature. Using the EBSD information, high Schmid factor grains can easily be identified and monitored during the in situ tensile experiment and therefore even the first yielding grains are captured. Further in situ high temperature tensile tests on steel samples up to a temperature of 800 °C are presented. An example of a tested steel specimen is shown in Figure 1. Here, slip band formation is easily observable in BSD contrast. By enabling feature tracking, the chosen region of interest remains in the field of view and is imaged correctly. By applying this method the deformation of the material can be imaged directly and a clearer interpretation of the deformation behavior is possible due to supporting structural or chemical information over the course of the experiment.
Such experimental capability pave the way for high throughput material data collection to build up a database of microstructural characteristics in combination with macroscale material performance. This work describes a number of use cases demonstrating the new automated capabilities.

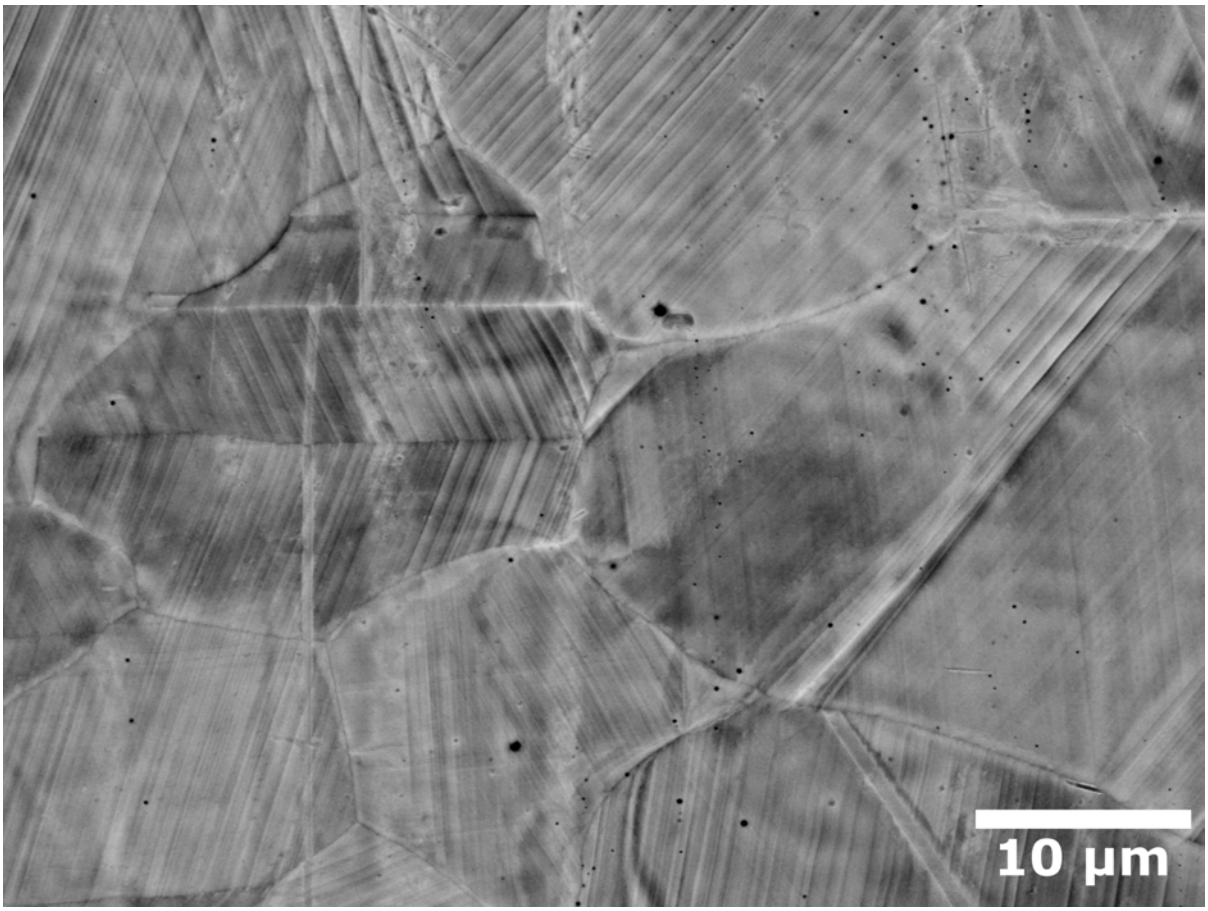

Fig. 1: Slip band formation in stainless steel during in situ experiment in BSD contrast.

Type of presentation: Poster

IM5-P-2833 Cryogenic Sample Holder with Electrical Contacts for UHV SEM/SPM

Krutil V.[1], Dupák L.[1], Fořt T.[1], Matějka M.[1], Srnka A.[1], Vlček I.[1], Urban P.[1]

[1]The Czech Academy of Sciences, Institute of Scientific Instruments, Královopolská 147, 612 64 Brno, Czech Republic

Email of the presenting author: krutil@isibrno.cz

We present a cryogenic sample holder with ten spring-loaded electrical contacts specially designed for an ultra-high vacuum scanning electron microscope combined with a scanning probe microscope (UHV SEM/SPM) working in the temperature range of 20 K – 300 K [1]. The contacts serve for the electrical connection of a removable transport pallet carrying a sample to the holder. Besides the sample, the transport pallet can be equipped with a low-temperature sensor, a heating element, and ten solid pins. Two quadruples of contacts allow precise four-wire measurement of electrical properties and temperature of the sample and the remaining pair allows two-wire connection of the heating element. The contact function was successfully verified by measuring the transient electrical resistance at the fixed and the spring contact sections within the whole range of the working temperatures. During the test, the transport pallet was repeatedly loaded into the holder. The limit temperature 22 K of the pallet was reached with a cryogenic helium flow cooling system embedded in a test vacuum chamber at the ambient temperature (~ 300 K). To minimize the effect of water ice condensation on the cold contact surfaces at low temperatures, a cooled thermal shield surrounding the sample holder was used as a water vapour trap. In this configuration, the limit temperature of the pallet was decreased down to 20.5 K. A thorough research study of commercially available sample holders indicates that the holders for the intended use are not available on the market.

References

[1] Vojtěch Krutil, Libor Dupák, Tomáš Fořt, Milan Matějka, Aleš Srnka, Ivan Vlček, Pavel Urban, Design of Cryogenic Sample Holder with Electrical Contacts for UHV SEM/SPM, The 15th Cryogenics 2019, IIR Conference, Prague, Czech Republic, April 8-11, 2019, DOI: 10.18462/iir.cryo.2019.0031.

Acknowledgement: We acknowledge the support of the TACR under Grant Project No. TE01020233 and the institutional support RVO:68081731.

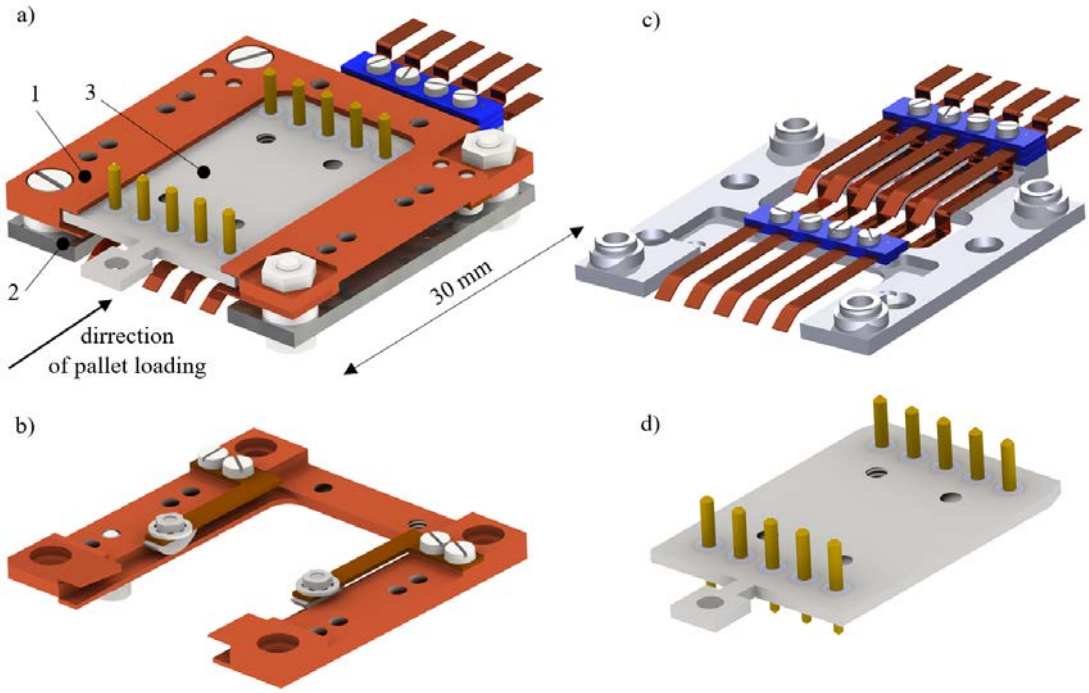

Fig. 1: a) Cryogenic sample holder with ten spring-loaded electrical contacts (square base 30 x 30 mm): 1 – pallet holder, 2 – electrical contacts holder, 3 – transport pallet; b) bottom view of the pallet holder assembly; c) top view of the electrical contacts holder assembly; d) top view of the transport pallet assembly.

Type of presentation: Poster

IM5-P-2864 Batteries in situ testing in SEM

Novák L.[1], Kundrát V.[1,2], Klvač O.[1,3], Kazda T.[3]

[1]Thermo Fisher Scientific, Vlastimila Pecha 12, Brno, 627 00, CZ, [2]Department of Chemistry, Faculty of Science, Masaryk University, Kotlarska 2, Brno, 611 37 CZ, [3]Department of Electrical and Electronic Technology, Faculty of Electrical Engineering and Communication, BUT, Technicka 10, Brno, 616 00, CZ

Email of the presenting author: libor.novak@thermofisher.com

We present in situ battery testing holders for SEM and FIB-SEM systems. Two types of in situ holders were newly developed, which assure transfer to SEM in a protective environment (in argon or high vacuum), electrical testing and heating of battery samples in SEM. When connected to SEM stage, the holders provide electrical contacting to the sample area and allow testing (galvanostatic cycling, cyclic voltammetry and other electrochemical testing) of a battery inside SEM. Micron sized batteries can be created on the in situ holders using FIB preparation of electrodes (Fig. 1). Consequent placement of electrolyte between the electrodes is possible in the vacuum of the SEM chamber as well. We will present example of electrical testing of a lithium titanium oxide (LTO) battery created by FIB on the in situ testing holder, which uses ionic liquid as the electrolyte. MEMS heating plate can be connected in the in situ holder, allowing heating of battery materials (up to 1200°C) during in situ SEM imaging. Optionally, reactive gases such as pure hydrogen, oxygen, or hydrogen sulfide, can be injected into a small reaction volume around the sample. This technique allows for real time SEM imaging of battery materials synthesis under realistic conditions that are used during battery materials development and manufacturing. We will present examples of in situ synthesis of tungsten oxide (Fig. 2) and tungsten sulfide nanowires, which are possible materials for sulfur based batteries. Moreover, the presented holders can be used for transfer of larger air sensitive samples to and from SEM, allowing SEM imaging of larger parts of batteries in SEM as well as FIB preparation of TEM lamellae from selected parts of the battery and consequent transfer of the lamellae to TEM without contact with air.

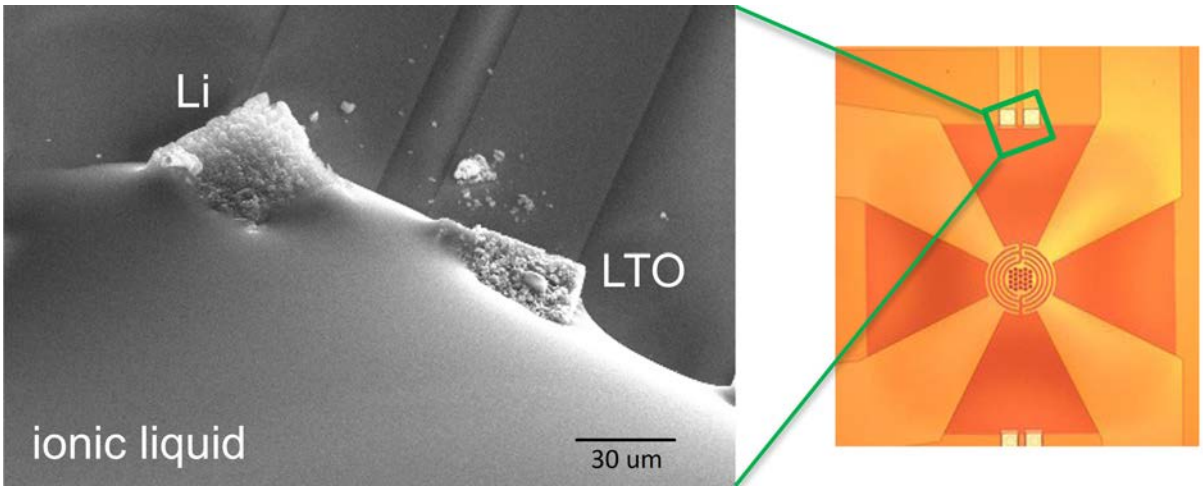

Fig. 1: LTO battery prepared by FIB on the in situ testing holder.

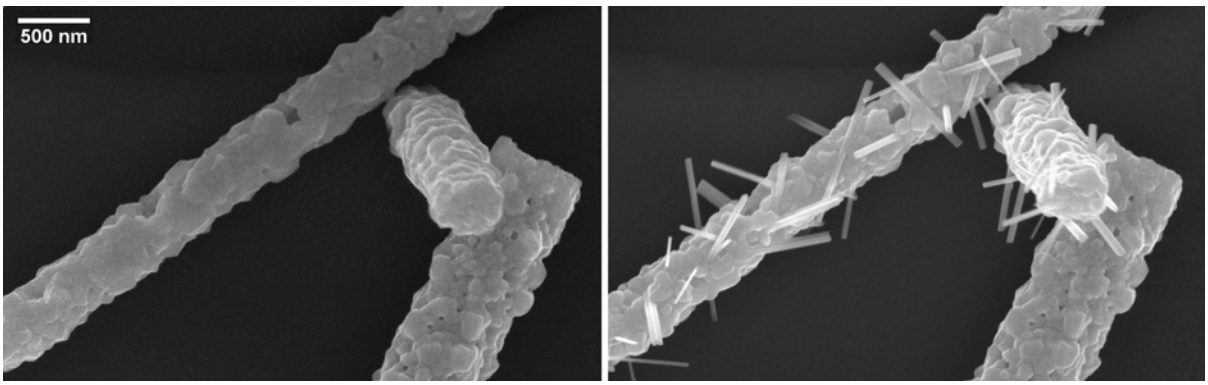

Fig. 2: $WO_3P_2O_5$ wires heated in hydrogen (100 Pa, 800°C) on the MEMS heating plate, forming $W_{18}O_{49}$ nanowires, which can further be changed to WS_2 in H_2S environment.

Type of presentation: Poster

IM5-P-2782 Cryo Volume Imaging: from cell nucleus to extracellular structure.

Rechav K.[1], Varsano N.[2], Addadi L.[2], Weiner S.[2], Gal A.[3]

[1]Department of Chemical Research Support, Weizmann Institute of Science, 76100, Rehovot, Israel, [2] Department of Structural Biology, Weizmann Institute of Science, 76100, Rehovot, Israel, [3]epartment of Plant and Environmental Sciences, Weizmann Institute of Science, 76100, Rehovot, Israel

Email of the presenting author: katya.rechav@weizmann.ac.il

Biological structures have been probed for more than 300 years, and a diverse array of instruments and methods are currently available including optical, electron and X-ray imaging techniques. However, deciphering these high-resolution structures at high resolution in their in vivo or as close as possible to the in vivo conditions, is still challenging to say the least.
Here we describe one of the newest methods for biological structural analysis that integrates the enormous benefits of cryo-imaging and analyzing large volumes, in 3 dimensions. Cryo-FIB-SEM (Focused Ion Beam-SEM) technique (Schertel et al., 2013) allows three-dimensional imaging of high pressure frozen or plunge-frozen biological samples under conditions that are very close to their native state, without any chemical treatment. The cryo-FIB-SEM can produce 3D image stacks of a volume of thousands of micrometers cubed at an image pixel size down to 5 nm, while keeping the sample in a hydrated state in vitreous ice. This method thus fills a valuable niche in biological cryo-imaging by closing the gap between light microscopy and TEM tomography.
Despite the Cryo FIB-SEM workflow is extremely fast, with compare to the traditional, room temperature, FIB-SEM technique, this method is still rarely used, and deemed exotic even.
We demonstrate here this methodology applying to objects, which we are actively investigating: mammalian cells, unicellular algae, tissues; we also discuss the advantages and challenges of this cutting-edge technique.

Acknowledgement: We thank the Moskowitz Center for Nano and Bionano Imaging for supporting the development of Cryo FIB methods.

Type of presentation: Poster

IM5-P-2634 Cryo-SEM to access the Microstructure of Colloidal Dispersions

Taylor M. S.[1]

[1]Quorum Technologies

Email of the presenting author: mark.taylor@quorumtech.com

The nature of colloidal dispersions can have a significant effect on the properties of foods such as texture and taste. Moreover, to meet the specified standards for consumer safety and acceptance, customarily they need to be stable against processes such as aggregation, coalescence and creaming for periods of months or even years.
Typically, food colloids are emulsions of oil-in-water (O/W) where the oil is dispersed in a continuous aqueous (water) phase, water-in-oil (W/O) where the aqueous (water) droplets are dispersed in a continuous oil phase or foams where a gas is dispersed in a continuous liquid phase. The stability of these food colloids is generally determined by the structure of the interface separating the two phases. The structure of this interface can be an extremely complex mixture of mono- and di-glycerides, lecithin, proteins, and casein micelles. Here I present the various methods to characterise the microstructure and stability of a range of colloidal dispersions using cryo-SEM.

Type of presentation: Poster

IM5-P-3010 New TDS software for computer-based optimisation of thermodynamic conditions in Advanced Environmental Scanning Electron Microscopy (A-ESEM)

Neděla V.[1], Tihlaříková E.[1], Macálka A.[2], Martinů P.[2]

[1]Environmental electron microscopy group, Institute of Scientific Instruments of the CAS, Brno, Czech Republic, [2]NUM Solution, Praha, Czech Republic

Email of the presenting author: vilem@isibrno.cz

Environmental scanning electron microscope (ESEM) allows direct observation of electrically non-conductive and fully hydrated samples from living and non-living nature with minimal preparation or in fully native state under elevated gas pressure (tens to thousands of Pa) and electron beam energy (1 - 20 keV). Dynamical in situ studies of sample hydration, drying or static observation under conditions of thermodynamic equilibrium are possible when water vapour pressure and sample temperature are precisely controlled. This is a key factor for successful observations, but also a major challenge, as these parameters are difficult to accurately measure in close vicinity to irradiated sample surface. Consequently, new observation methods based on mathematical and physical simulations (computational fluid dynamics, electron interactions etc.) are necessary. These methods, high efficiency detectors [1], custom designed hardware [2] and software for the Advanced ESEM (A-ESEM) [3] is developed by our scientific group.

New Thermo-Dynamic Software (TDS) for simulation of water vapour pressure, sample surface temperature and relative humidity (RH) was developed within a grant cooperation of Environmental electron microscopy group and private company NUM solution. The TDS allows very fast and precise determination of environmental conditions suitable for the different observation in ESEM Quanta 650 FEG. Parameters as working distance, type of the sample and sample holder geometry are considered and final working conditions (temperature/pressure/RH) are calculated according to operator's requirement. Thermo-dynamical conditions, calculated for the individual experiment guarantee successful results of observation in the A-ESEM. From these outputs, the user is able to see conditions in close vicinity around the sample, the gun above it and the detector, see Fig. 1.

TDS is based on combination of computational fluid dynamics (CFD), numerical simulations in ANSYS CFX and the support vector regression method (ε-SVR) which was used to predict the output results. The regression algorithm is based on machine learning - support vector machine which works on statistical learning theory.
Accuracy of the TDS software was tested in experimental measurements using humidity sensors. The ability of the TDS to simulate parameters for dynamical in-situ observation under 100% RH was tested on water droplet formation. Results show that the TDS software allow easy, fast and highly precise determination of working parameters directly according to requirements of the experiment, see Fig. 2.

[1] Neděla, V. et al., J. Ultramicroscopy 184(2018) 1-11
[2] Závacká, K. et al. Microsc. Microanal. 2021, 1-14
[3] Stelate, A. et al. Biomolecules. 2021; 11(10), 1407

Acknowledgement: The project was supported by the Grant Agency of Czech Republic [GA 19-03909S] and by the Ministry of Industry and Trade (CZ.01.1.02/0.0/0.0/17_176/0015020).

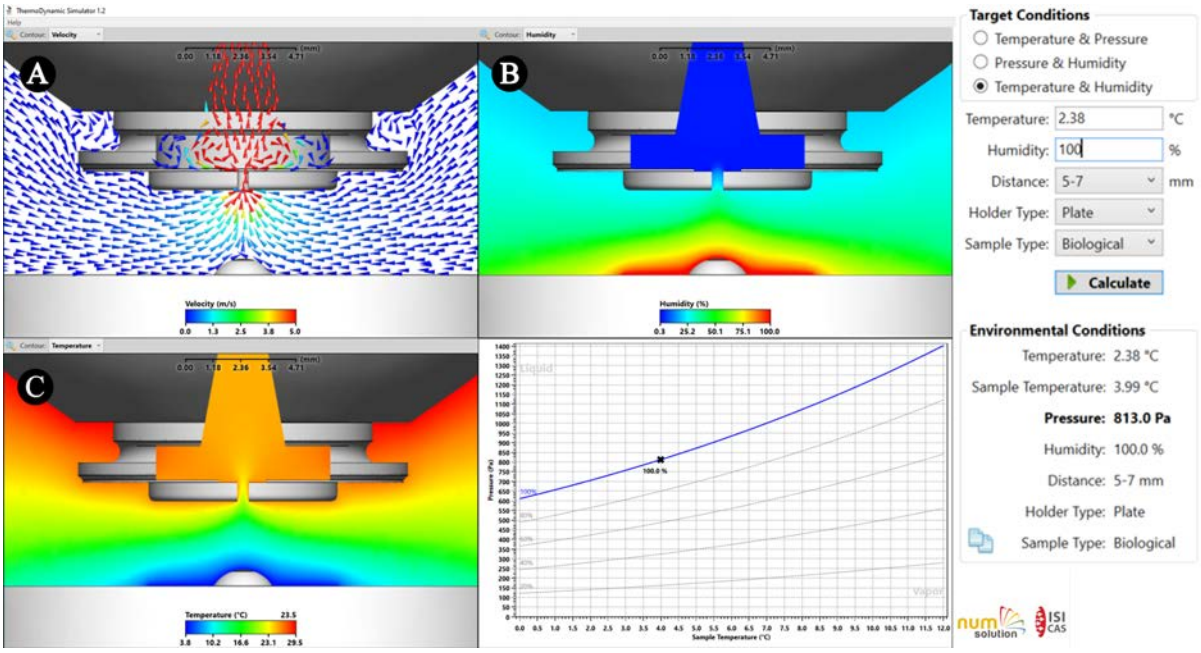

Fig. 1: TDS outputs - modules for contour visualization of the simulated results of velocity, humidity (B), temperature (C).

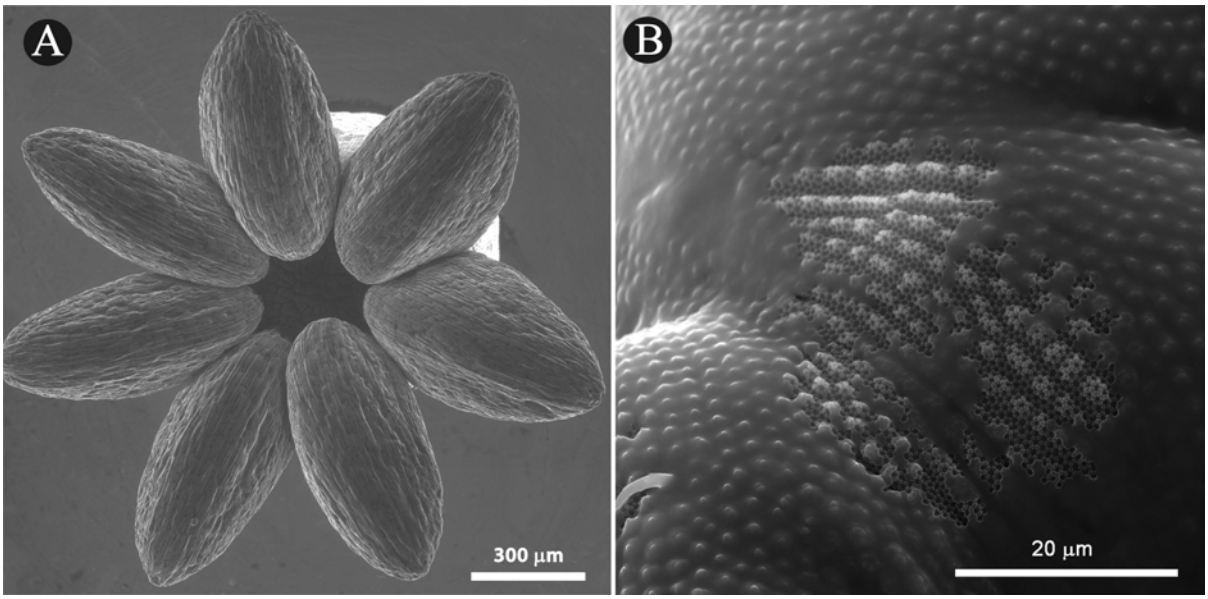

Fig. 2: Fresh cotyledon of meristem (RH 90%) (A); springtail skin covered with thin water layer (RH 100%) (B).

Type of presentation: Poster

IM5-P-2838 Effect of thermal radiation on the measurement of the sample holder temperature over the cryogenic range for various types of temperature sensor installations

Urban P.[1], Hanzelka P.[1], Králík T.[1], Srnka A.[1]

[1]The Czech Academy of Sciences, Institute of Scientific Instruments, Královopolská 147, 612 64 Brno, Czech Republic

Email of the presenting author: urban@isibrno.cz

We present how the thermal radiation (300 K) affects precision of temperature measurement of a sample holder (or sample) in an UHV SEM/SPM microscope working at the range down to 20 K for various ways of temperature sensor mounting. For reliable and precise temperature measurement at cryogenic temperatures, a correct installation of the temperature sensor including good thermal contact both of the sensor and its leads with measured object is essential. We tested a special copper casing designed by us [1] - Prismatic Sensor Bed (PSB) - for installation of Lake Shore temperature sensors (Cernox and Si diodes) encapsulated in SD packages [2]. The sensor is soldered in the bed of the casing using indium solder ensuring good thermal contact. The sensor leads are also thermally anchored to the casing but electrically insulated from it. We tested three ways of mounting of the sensors in PBS on a cooled plate imitating insufficient thermal anchoring of electrical wires to the plate and thermal shielding of the casing. In our test, we used CERNOX temperature sensors with declared uncertainty of 5 mK at 5 K. Comparative measurement was also performed with sensors in SD package mounted by the simplest possible way without using of PBS. We proved that our sensors casing PBS is suitable for intended application of temperature measurement of the sample holder (or directly of sample) in the UHV SEM/SPM microscope. In contrary, measurement precision by “unprotected” sensors proved to be absolutely unsuitable due to the high deviation of measured temperature from the correct value exceeding a required precision of about 1 K.

References

[1] Pavel Urban, Pavel Hanzelka, Tomáš Králík, Ivan Vlček, Aleš Srnka, Effect of thermal radiation on low temperature measurement for various types of temperature sensor installations, The 14th CRYOGENICS 2017 IIR International Conference, Dresden, Germany, DOI:10.18462/iir.cryo.2017.105.

[2] http://www.lakeshore.com/products/cryogenic-temperature-sensors/silicon-diodes/dt-670/pages/Downloads.asp 21.2.2017.

Acknowledgement: We acknowledge the support of the TACR under Grant Project No. TE01020233 and the institutional support RVO:68081731.

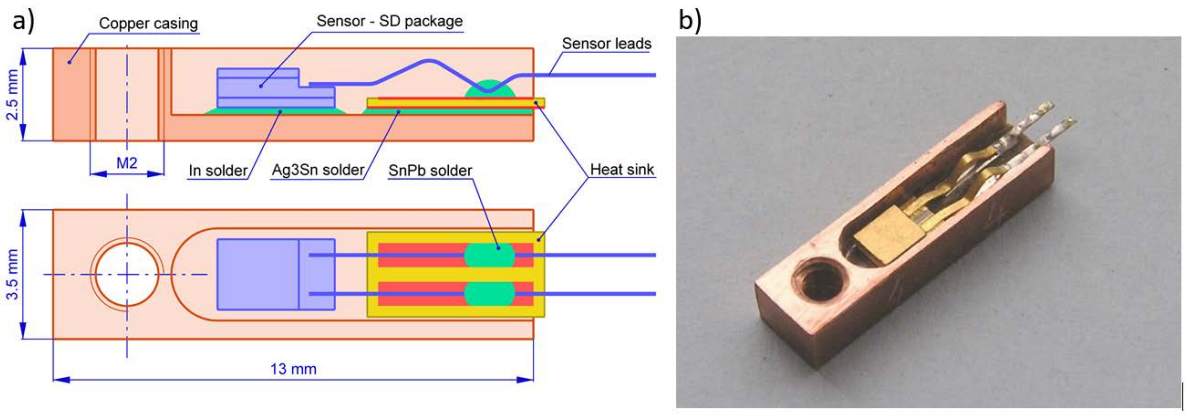

Fig. 1: Installation of Lake Shore temperature sensor in SD package into the Prismatic Sensor Bed (PSB): a) schematic cross-section and bottom view of PSB with installed temperature sensor; b) bottom view of the PSB with installed temperature sensor.

Type of presentation: Poster

IM5-P-2845 Low conductive thermal insulation pad with high mechanical stiffness

Hanzelka P.[1], Dupák L.[1], Krutil V.[1], Krzyžánek V.[1], Skoupý R.[1], Srnka A.[1], Vlček I.[1], Urban P.[1]

[1]The Czech Academy of Sciences, Institute of Scientific Instruments, Královopolská 147, 612 64 Brno, Czech Republic

Email of the presenting author: urban@isibrno.cz

Thermal conductivity and mechanical stiffness of sample holder mounting are two key properties that together affect the imaging quality of the scanning probe microscopes (SPM). Here we present the design of a thermal insulation pad (InBallPad) [1], characterized by low thermal conductivity and high mechanical stiffness, for mounting of the sample holder of an ultra-high vacuum SPM. The SPM operate at variable temperatures of the sample holder in the range of 20 K - 700 K. IBP is mounted between the upper plate of a piezoelectric scanner and the bottom of the sample holder. InBallPad consists of a top and bottom plate made of titanium alloy that are mutually separated by three specially designed ball supports. The design of ball supports is based on traditional kinematic couplings, called Kelvin Coupling, with three different types of bearings: tetrahedron, V-groove, flat plane [2]. The sample holder with variable temperature [3] is mounted on the top plate whereas the bottom plate serves for mechanical connection to the piezoelectric scanner of SPM with approximately room temperature. The main characteristics of IBP can be summarized as follow:

- Low thermal conductivity: heat flow 120 mW between top (bottom) plate at 20 K (300 K)
- High mechanical stiffness: 1×10^6 N/m
- Small dimensions and mass: diameter of 30 mm, height of 12 mm, mass of 34 g

References

[1] Pavel Hanzelka, Libor Dupák, Vojtěch Krutil, Vladislav Krzyžánek, Radim Skoupý, Aleš Srnka, Ivan Vlček, Pavel Urban, Low conductive thermal insulation pad with high mechanical stiffness, International Journal of Refrigeration 132 (2021) 92–99, DOI: https://doi.org/10.1016/j.ijrefrig.2021.09.019.

[2] Slocum, A., 2010. Kinematic couplings: A review of design principles and applications. Int. J. Mach. Tool Manuf. 50, 310-327. DOI: 10.1016/j.ijmachtools.2009.10.006.

[3] Vojtěch Krutil, Libor Dupák, Tomáš Fořt, Milan Matějka, Aleš Srnka, Ivan Vlček, Pavel Urban, Design of Cryogenic Sample Holder with Electrical Contacts for UHV SEM/SPM, The 15th Cryogenics 2019, IIR Conference, Prague, Czech Republic, April 8-11, 2019, DOI: 10.18462/iir.cryo.2019.0031.

Acknowledgement: We acknowledge the support of the TACR under Grant Project No. TE01020233 and the institutional support RVO:68081731.

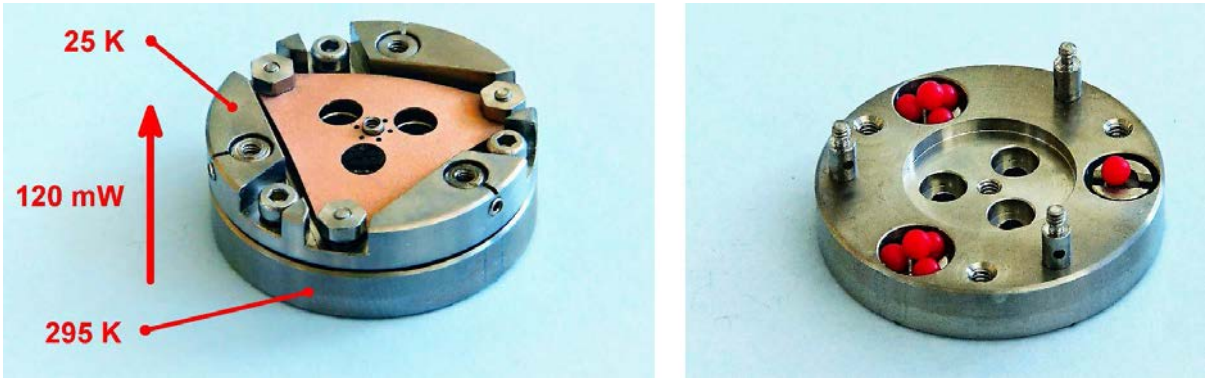

Fig. 1: The thermal insulation pad (InBallPad) for UHV SEM: a) top view of the InBallPad assembly. b) top view of the bottom plate of InBallPad with insulating balls made of fused silica (here red colored for ease of recognition).

IM6 Low energy electrons related science and technology

Type of presentation: Invited

IM6-IN-2513 Contrast mechanism and its application at landing energy near 0 eV in super low energy SEM

Aoyama T.[1], Mikmeková Š.[2], Kumagai K.[3]

[1]JFE Steel Corporation, [2]ISI CAS, [3]AIST

Email of the presenting author: to-aoyama@jfe-steel.co.jp

In recent years, the technique of scanning electron microscopy (SEM) observation with low landing energy of several keV or less has become common. When the landing energy is several eV or less, the signal electrons become sensitive to the electronic structure of the sample surface, and it is expected to be possible to obtain a new image contrast. We focused on the drastic contrast change seen at landing energy near 0 eV, and investigated the mechanism of contrast and its potential applications.
In order to elucidate the mechanism of contrast change near 0 eV, a sample in which Ni and Pt were pattern-deposited on a Si substrate was prepared. The sample was observed by SEM by changing the sample bias voltage with a constant acceleration voltage of 6018 V by UHV SLEEM [1], which can observe SEM images in an ultra-high vacuum. When the landing energy was increased in steps of 0.3 eV from -1.9 eV to 20.0 eV, the contrast of Si decreased significantly at 0.28 eV, after which the contrast of Ni decreased at 0.30 eV and the contrast of Pt decreased at 0.82 eV from the total mirror image. The order of the threshold energies corresponds to the order of the surface potentials separately measured by Kelvin probe force microscopy. From these results, it is considered that the incident electrons cannot reach the sample surface and are reflected in the region where the surface potential is higher than the incident electron energy, resulting in bright contrast. On the other hand, in the region where their surface potential is lower than the energy, incident electrons reach the sample surface and penetrate into the sample, is observed with dark contrast. The threshold energy differs depending on the material. It is expected that this phenomenon can be applied to the visualization of the materials or phases that are difficult to visualize with conventional SEM techniques. In this presentation, we will also discuss the results obtained with multi-phase steel [2], mild steel [3] and Cu [4] as application examples.
References

[1] I. Müllerová and L. Frank, Advances in Imaging and Electron Physics 128, 309-443 (2003).
[2] T.Aoyama et al., Ultramicroscopy, 204 (2019) 1-5.
[3] Š.Mikmeková et al., Surf Interface Anal., (2022) 1-10. doi:10.1002/sia.7079
[4] Š.Mikmeková and T.Aoyama, Ultramicroscopy, 220 (2020) 113144.

Type of presentation: Invited

IM6-IN-2598 Ab initio study of angle-resolved electron spectroscopy of graphene

Paták A.[1], Zouhar M.[1], Konvalina I.[1], Materna-Mikmeková E.[1], Průcha L.[1], Müllerová I.[1], Charvátová Campbell A.[2]

[1]Department of Electron Microscopy, Institute of Scientific Instruments of the CAS, v. v. i., Brno, Czech Republic, [2]Department of Nanometrology, Czech Metrology Institute (CMI), Brno, Czech Republic

Email of the presenting author: patak@isibrno.cz

Since the discovery of graphene in the first decade of the 21st century, this material and 2D-materials in general have attracted great attention due to their particularly distinctive properties. The corresponding scientific effort led to new and unexpected results, e.g. magic angle twisted graphene exhibiting superconductivity in the case of twisted bilayer graphene (TBG) [1]. The potential industrial and commercial applications are immense.

These materials are studied using many techniques, including e.g. optical microscopy, Raman spectroscopy, atomic force microscopy (AFM) and scanning tunneling microscopy (STM). Transmission electron microscopy (TEM) and electron energy loss spectroscopy (EELS) have been used to distinguish the number of graphene layers, their stacking order and twist. STM, TEM and EELS can provide a very good resolution and characterize these materials locally. Measurements at high TEM energies have destructive effects, due to knock-on damage, on the samples and hence it is desirable to decrease the energy of incident electrons. In order to quickly assess larger areas, scanning electron microscopy (SEM) represents a reasonable compromise - scanning larger areas with sufficient resolution. This includes both imaging and collecting spectra.

The above overview makes clear that electron microscopy is one of the important tools utilized in the studies of these materials. Theoretical investigations, e.g. ab initio simulations, may provide worthy insight into experimental results. We present the theoretical results obtained using the density-functional theory (DFT) and the many-body perturbation theory (MBPT). They include low energy momentum-resolved both reflectivity and EELS spectra, the first with phenomenological inclusion of inelastic effects. The EELS spectrum of graphene is shown in Fig. 1. A part of this spectrum was used to examine the momentum transfer present in our time-of-flight experiment already, see [2]. Furthermore, the theoretical simulations considered here predict that the Moiré patterns in TBG (typically accessible via STM) should be observable even in SEM equipped with a cathode lens (stage bias).

We predict that SEM is able to provide valuable spectroscopic information about unoccupied band-structure of 2D materials. Moreover, our findings imply that SEM at low landing energies should be able to display Moiré super-lattices. This significantly expands the class of electron microscopes that can be used to study and assess quality of these extremely interesting materials.

[1] Y. Cao et al.: Nature 2018, **556**, 43

[2] I. Konvalina et al.: Nanomaterials 2021, **11**(9), 2435

[3] P. Giannozzi et al.: J. Phys. Condens. Matter 2009, **21**, 395502; A. Marini et al.: Comput. Phys. Commun. 2009, **180**, 1392

Acknowledgement: This research was funded by the Technology Agency of the Czech Republic, grant number TN01000008. The authors acknowledge IT support provided by M. Valtr (CMI).

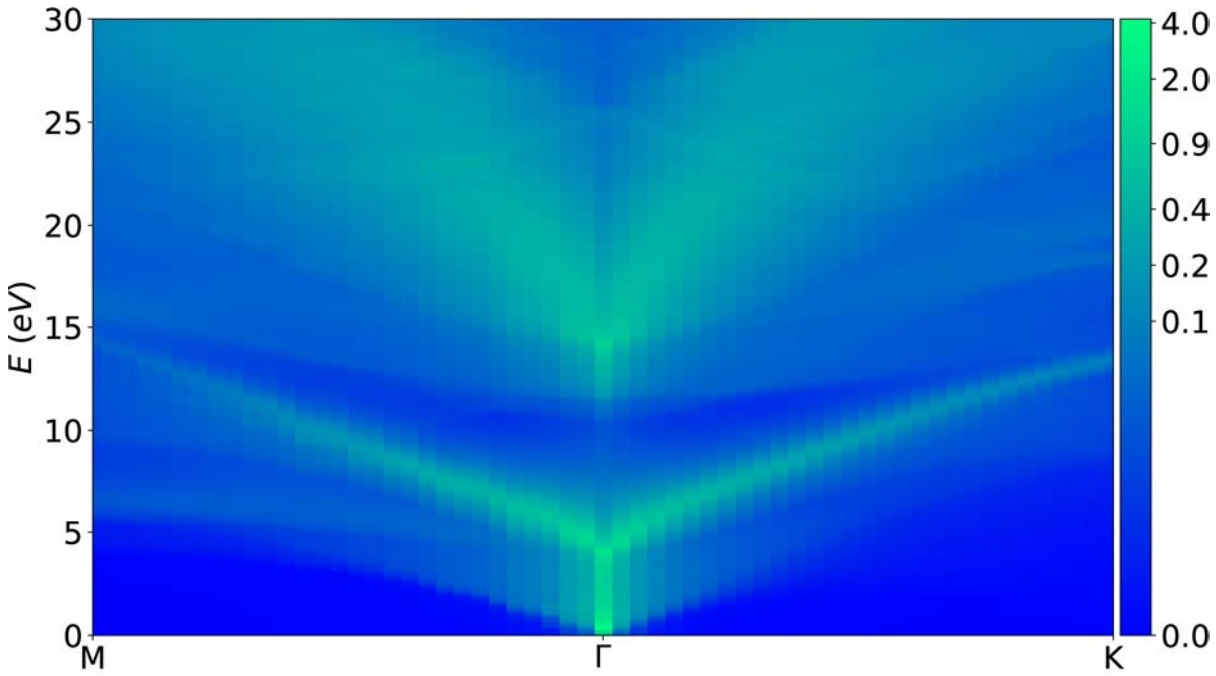

Fig. 1: Momentum-resolved EELS simulation for the free-standing graphene along M − Γ − K path in Brillouin zone. The heatmap of the EELS values is in arbitrary units. DFT calculations were performed using Quantum ESPRESSO, MBPT simulations were done using Yambo and yambopy [3] on top of that.

Type of presentation: Oral

IM6-O-2572 The Retrofittable Photoelectron Source: A Potential Improvement to Low Voltage SEM Imaging

Quigley F.[1,2], Downing C.[2], McGuinness C.[1], Jones L.[1,2]

[1]School of Physics, Trinity College Dublin, Dublin, Ireland , [2]Advanced Microscopy Laboratory, Centre for Research on Adaptive Nanostructures and Nanodevices (CRANN), Dublin, Ireland

Email of the presenting author: fquigley@tcd.ie

Improvements in low voltage scanning electron microscopy (<5 keV) are highly valuable to many different research areas. Such advances are of great interest to the semiconductor industry which benefits from the reduction in beam damage that low voltage imaging provides [1]. There are however a number of limitations holding back low voltage imaging in the scanning electron microscope (SEM), one of which includes the increased effect of chromatic aberration on resolution [2]. The chromatic defocus blur is proportional to the energy spread of the electron beam so decreasing this energy spread is one solution to increasing the resolution during low voltage imaging. Achieving this has commonly involved upgrading to a SEM which has a lower energy spread electron source such as a Schottky field emission gun ($\Delta E \approx 0.7eV$).

We propose an alternative design for a low energy spread electron emitter based on the photoelectric effect, where photons of a sufficient energy stimulate the direct release of electrons from a material. By choosing a laser diode as the light source and a low workfunction material such as Lanthanum Hexaboride (LaB_6) the emitted electrons would be nearly monochromatic. As LaB_6 crystals are already commonly found in thermionic electron guns a light source could be retrofitted to these instruments to create a low electron energy spread ($\Delta E=0.11eV$) [3] photoelectron emitter which would be ideal for low voltage imaging.

Using fiber optics, UV laser diodes, and 3D printed mountings we have created a prototype of our photoelectron emitter. This is retrofitted onto an existing thermionic LaB_6 electron gun in a ZEISS EVO SEM (**Figure 1 a)** and **b)**), where the protective laser covers have been removed to highlight the experiment. To separate the effects of photo stimulation and thermal heating, lasers of the same power but of different wavelength were used to verify that photoelectrons are forming the SEM images. Our photoelectron emitter using a laser of wavelength 405nm delivers a continuous electron beam and has successfully yielded SEM images (**Figure 2 a)**). **Figure 2 b)** was taken when the experiment was repeated with a laser of wavelength 650nm. The intensity of the SEM image is unchanged as the photons do not have the energy to produce photoelectrons. We present the design and development of this photoelectron emitter including discussing its performance as an electron source in the SEM. It is hoped that this retrofittable emitter will extend the performance and lifetime of existing thermionic SEMs, increasing their functionality and benefiting many areas in low voltage SEM research.

[1] J. B. Pawley, Scan. Electron Microsc. 3, (1984).
[2] D. C. Joy and C. S. Joy, Micron 27, 247 (1996).
[3] H. Sawa et al., J. Vac. Soc. Japan 60, 467 (2017).

Acknowledgement: FQ is supported by a Trinity College Provost's Award scholarship. LJ is supported by Science Foundation Ireland grant number URF/RI/191637.

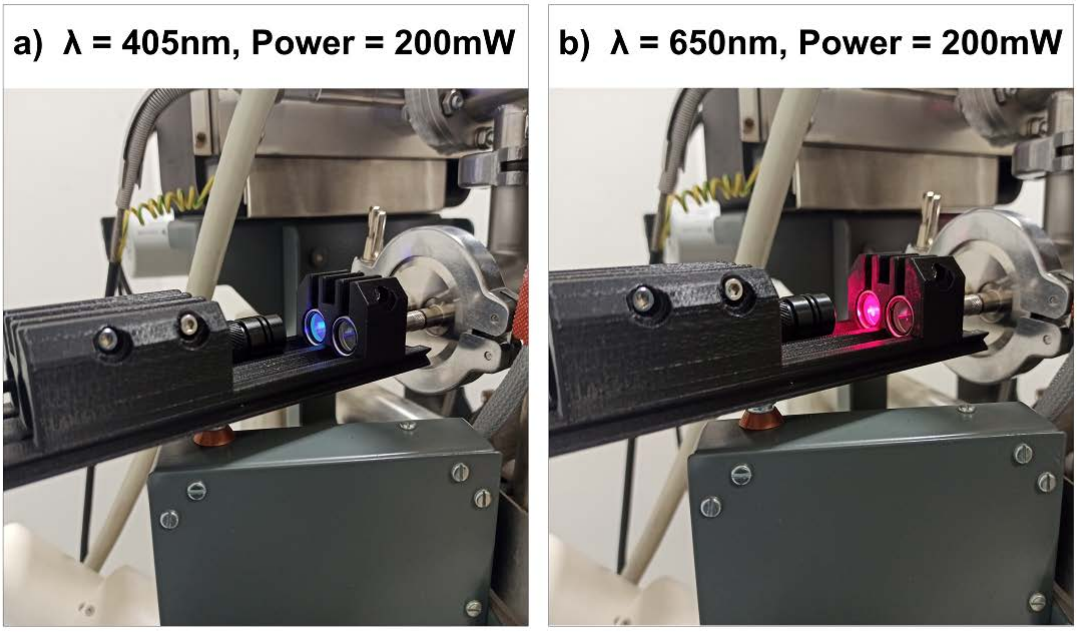

Fig. 1: **a)** and **b)** show the photoelectron system retrofitted on a SEM where a 3D printed holder supports the lasers so that they are directed at the collimators and the vacuum fiber optic feedthroughs that are fed up to the LaB_6 source. Both lasers have a power of 200mW and a wavelength of 405nm and 650nm for **a)** and **b)** respectively.

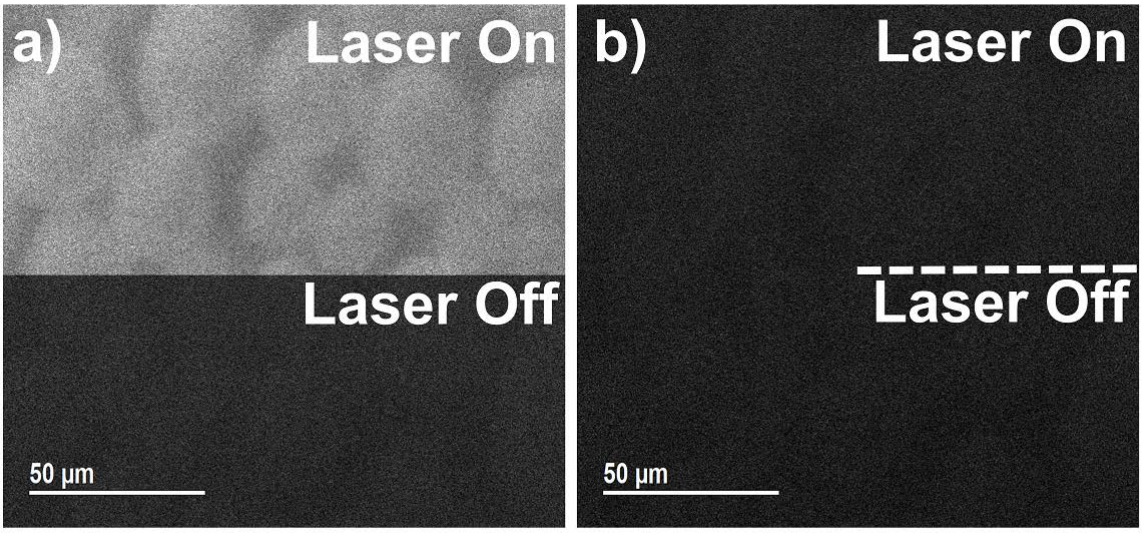

Fig. 2: **a)** is a SEM image produced from the retrofitted system where a laser of wavelength 405nm was turned on for the top half of the image and the LaB_6 source emitted photoelectrons. The laser was then turned off for the bottom half of **a)**. The same experiment in **a)** was repeated with a laser of wavelength 650nm and **b)** is the SEM image produced.

Type of presentation: Oral

IM6-O-2820 Time-of-Flight Spectrometer for Low Landing Energies

Konvalina I.[1], Daniel B.[1], Zouhar M.[1], Paták A.[1], Průcha L.[1], Piňos J.[1], Müllerová I.[1], Mikmeková E. M.[1]

[1]Department of Electron Microscopy, Institute of Scientific Instruments of the Czech Academy of Sciences, Brno, Czech Republic

Email of the presenting author: konvalina@isibrno.cz

New technological development and innovations of advanced 2D materials entail high demands on their analysis techniques. A detailed study of electron scattering in solids is essential for the design and diagnostics of the next generation materials, as well as in solid-state physics. The inelastic mean free path (IMFP) [1] is a key parameter of electron scattering in both bulk materials and thin foils.

At the Institute of Scientific Instruments of the Czech Academy of Sciences, we designed and assembled an ultra-high vacuum scanning low energy electron microscope (UHV SLEEM). The device is equipped with a time-of-flight (ToF) spectrometer [2], which operates in transmission mode. This allows us to use both electron microscopy and spectroscopy - powerful tools for obtaining information about the structure and properties of the analyzed materials.

We performed extensive experiments on a commercial monolayer graphene to obtain electron energy-loss spectra (EELS) for low landing energies. Graphene has unique properties, including remarkably high transparency and electrical conductivity. This makes it suitable for studying at very low energies in the transmission mode of UHV SLEEM.

We focus on the low landing energy interval (200, 800) eV and energy losses up to approximately 40 eV (which covers both π and π+σ graphene plasmon peaks). The experimental data are shown in Figure 1.

Applying the log-ratio method (see [3] for details) on the straight-line segment baseline-corrected EELS, we arrived at the effective IMFP values shown in Figure 2. Theoretical approaches to obtain IMFP include predictive formulas such as TPP-2M [4] or Bethe formula [5] (valid for amorphous materials).

One of the main advantages of our UHV SLEEM/ToF system is the possibility of using free-standing ultrathin samples. This eliminates the effect of the substrate and significantly reduces multiple inelastic scattering events. As a result, the analysis of EELS data is greatly simplified. Furthermore, the energy resolution of the ToF spectrometer, 0.5 eV at the landing energy of 50 eV, is more than acceptable for studying a graphene sample and thin foils.

References:

[1] M.P. Seah and W.A. Dench, Surf. Interface Anal. 1 (1979), p. 0142–2421. doi:10.1002/sia.740010103
[2] I. Konvalina et al., Microscopy and Microanalysis, 25(S2) (2019), p. 482-483. doi:10.1017/S1431927619003143
[3] I. Konvalina et al., Nanomaterials 11 (2021), 2435. https://doi.org/10.3390/nano11092435
[4] S. Tanuma, C.J. Powell and D.R. Penn, Surf. Interface Anal. 21 (1994), p. 165–176. doi:10.1002/sia.740210302
[5] H. Bethe, Ann. Phys. 397 (1930), p. 325–400. doi:10.1002/andp.19303970303

Acknowledgement: This research was funded by the Technology Agency of the Czech Republic, grant number TN01000008 together with institutional support RVO:68081731.

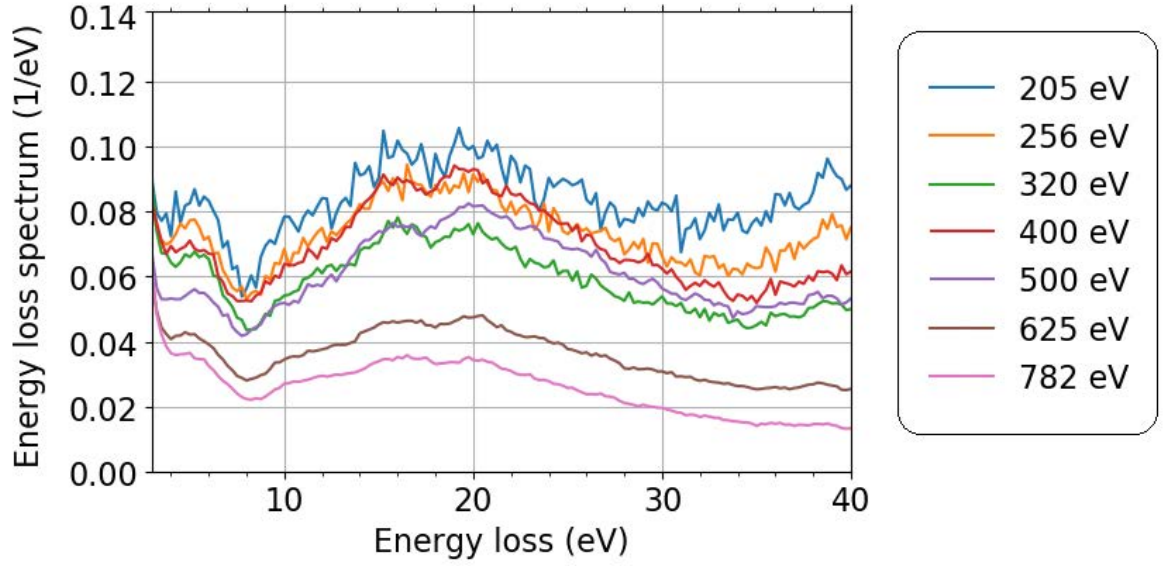

Fig. 1: ToF energy-domain spectra with similar values of momentum transfer for selected landing energies.

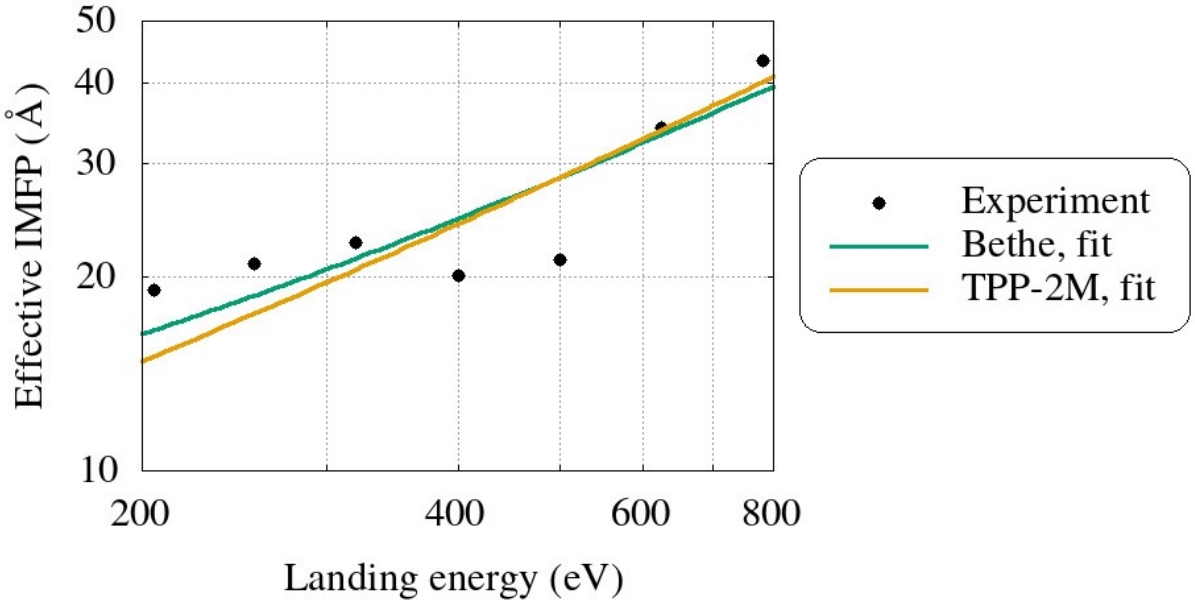

Fig. 2: Effective IMFP calculated from the ToF energy-domain spectra (displayed in Figure 1) compared to effective IMFP derived according to TPP-2M and Bethe formulae.

Type of presentation: Oral

IM6-O-2496 Imaging optical near-fields using a low energy electron microscope

Juffmann T.[1]

[1]Faculty of Physics, University of Vienna

Email of the presenting author: thomas.juffmann@univie.ac.at

Recently, optical near-field electron microscopy (ONEM) has been proposed as a way to circumvent electron-induced damage [1]: In ONEM, a sample is probed non-invasively using light, and the resulting near-field interference patterns are converted into an electron current using a photocathode.

The emitted electrons are then imaged with nanometric resolution using an aberration corrects Low Energy Electron Microscope (LEEM). For sample-photocathode distances much smaller than the optical wavelength (z□λ) this allows for label-free superresolution microscopy of interfaces.

After introducing the basics of this new imaging concept, we will discuss first steps towards the implementation of ONEM in an existing LEEM system [2], including illumination design, and the design of ONEM liquid cells for electrochemistry studies.

[1] MARCHAND, R., ŠACHL, R., KALBÁČ, M., HOF, M., TROMP, R., AMARO, M., VAN DER MOLEN, S. J. & JUFFMANN, T. (2021). Optical Near-Field Electron Microscopy. Physical Review Applied 16. http://arxiv.org/abs/2102.13010 (Accessed April 30, 2021).

[2] GEELEN, D., JOBST, J., KRASOVSKII, E. E., VAN DER MOLEN, S. J. & TROMP, R. M. (2019). Nonuniversal Transverse Electron Mean Free Path through Few-layer Graphene. Physical Review Letters 123. http://arxiv.org/abs/1904.13152

Acknowledgement: This project has received funding from the European Union's Horizon 2020 research and innovation program under Grant Agreement No. 101017902.

Type of presentation: Oral

IM6-O-2862 Delta – Detector for Scanning Electron Mirror Microscopy

Kolařík V.[1], Jánský P.[1], Bačovský J.[1], Mynář M.[1]

[1]Research laboratory, Delong Instruments a.s., Brno, Czech Republic

Email of the presenting author: vladimir.kolarik@delong.cz

Imaging using the impact of very slow electrons (down to zero energy - mirror microscopy) has important role in the investigation of the thin layers and surfaces of the various materials. One of the well-established method is LEEM - sample surface integral imaging down to 0eV primary beam impact energy. Contrary to LEEM, signal electrons detection in the scanning electron mirror microscopy is not consistently solved.

The most common arrangement places sample on the negative bias. This enables to detect backscattered signal electrons down to units of eV of the primary beam. In the region under 1eV all signal electrons are confined close to the optical axis which disable use of common axially symmetric detectors.

The challenging task is to separate primary and signal electrons once they have very similar energies and then naturally also trajectories. One of the logical solutions is use of the axially non-symmetric beam separator [1,2]. This arrangement enables to collect all signal electrons from 0eV to units of keV. Main requirement on the separator is not to disturb primary beam and simultaneously sufficiently deflect signal electrons towards to the off-axis detector [3].

One of the approaches is to use magnetic separator (Fig. 1). Main beam passes separator through “chicane” with 1:1 magnification in X and Y directions as well as with zero astigmatism and energy dispersion. The signal electrons are deflected by 90o and creates energy spectrum which allows to distinguish between secondary and backscattered electrons.

[1] P. Kruit, in Advances in Optical and Electron Microscopy, vol. 12, ed. by T. Mulvey (Academic, London, 1991), pp. 93-137
[2] J. Witzani and E.M. Hörl, Scanning electron mirror microscopy. Scanning, 4 (1981) 53-61
[3] V. Kolarik, M. Mankos, L. H. Veneklasen, Optik 87, No. 1 (1991) 1 – 12

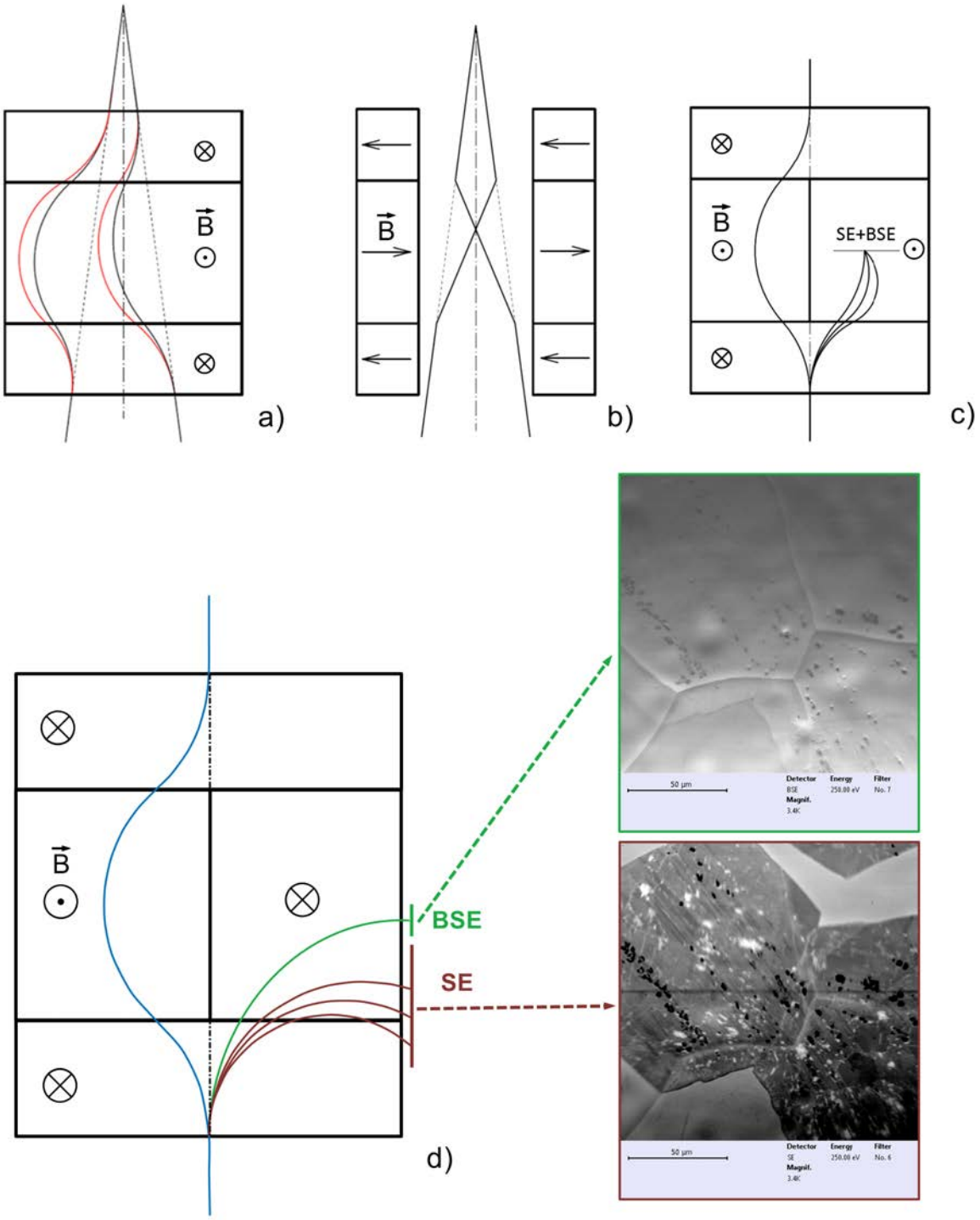

Fig. 1: a, b) Primary beam trajectory through chicane in X and Y planes,
c) Non-spectroscopic mode when all signal electrons are detected by one integral detector,
d) Spectroscopic mode when SE and BSE signal electrons are simultaneously detected by pair of solid state detectors.

Type of presentation: Poster

IM6-P-2879 Determination of the inelastic mean free path of electrons in selected Polymers, indenpent from optical data, considering surface excitations

Werner W. S.[1], Helmberger F. J.[1], Schürrer M. W.[1]

[1]Technical University Vienna, Faculty of Physics, Institute of Applied Physics, Vienna/Austria

Email of the presenting author: e11810754@student.tuwien.ac.at

The Inelastic Mean free Path (IMFP) of electrons in the Energy range from 500eV to 1600eV in selected polymers was measured by elastic peak electron spectroscopy. The IMFP is a crucial parameter in the description of solid-electron interactions. Since absolute measurements are difficult, reference samples of silicon and nickel were measured under the same conditions.
The electron-solid interaction and the resulting electron transport was determined using Monte Carlo simulations. The purpose of this work was to provide a method that calculates mean path lengths without the use of optical data. IMFP data from the authors Shinotsuka, Tanuma and Powell were available as reference values and are compared with our measured values. Surface excitations in the polymers were quantified by analyzing the inelastic back-scattering spectrum. Taking this into account, the evaluation of the elastic peak intensities gave IMFP values agreeing within 15% of the values reported by Shinotsuka and coauthors.

Acknowledgement: The authors acknowledge TU Wien Bibliothek for financial support through its Open Access Funding Programme and the VSC for providing computational resources.

Type of presentation: Poster

IM6-P-2620 Combining Low Energy Electron Microscopy and Thermal Raman Spectroscopy for Graphene Analysis

Průcha L.[1], Lejeune M.[2], Kizovský M.[1], Mikmeková E. M.[1]

[1]Department of Microscopy and Spectroscopy of Surfaces, Institute of Scientific Instruments of the CAS, v. v. i., Brno, Czech Republic, [2]Laboratories of Condensed Matter Physics, Université de Picardie-Jules Verne, Amiens, France

Email of the presenting author: prucha@isibrno.cz

Graphene as a very promising material for the semiconductor and battery industry has its indisputable advantages. Though it has been discovered almost two decades ago, we still have some gaps in knowledge regarding its behavior during temperature changes on different surfaces, even though it is critical for its use in practice.
Electron microscopy, and specifically Scanning Low Energy Electron Microscopy (SLEEM), is a very useful analyzing tool for graphene but it is not used very often. Its advantages are not only counting the number of graphene layers and low interaction volume but also because low energy electrons can clean the surface from the hydrocarbons adsorbed from the atmosphere which is necessary specifically for studying 2D materials [1]. On the other hand, Raman spectroscopy is one of the most common tools how to analyze this 2D material very quickly and precisely since the main peaks (2D, G, and D) in the spectra can very precisely tell much useful information about graphene, from the number of layers to lattice disorders [2]. These two analyzing methods together create a powerful duo for analyzing graphene that can be hardly replaceable. Our created graphene is thus analyzed not only by Raman microscope but also by confocal microscope and electron microscope.
In this study, we focused on graphene behavior under a very wide range of temperatures ranging from -190 to 600 °C measured during one sitting with the Raman microscope. Our CVD-grown graphene was placed onto different sample surfaces to study how the different thermal expansions affect graphene. In the past, some studies focused mainly on the graphene on the SiO2 surfaces with a lesser range of temperatures [3] but here we added to SiO2 also platinum, gold, and copper. From the Raman spectra, we calculated the Raman spectra thermal shift for all the different substrates. We also studied the thermal disintegration of carbon bonds in graphene not only through the rising D peak but also from the change in the changes in the whole spectrum. From the obtained data, we also proposed the possible temperature for each substrate at which the graphene irreversibly changes its form and thus is destroyed.

References:
[1] Frank, L., Mikmekova, E. & Lejeune, M. Treatment of surfaces with low-energy electrons. Appl. Surf. Sci. 407, 105–108 (2017).
[2] Childres, I., Jauregui, L., Park, W., Cao, H. & Chen, Y. Raman Spectroscopy of Graphene and Related Materials. New Dev. Phot. Mater. Res. (2013). DOI: 10.1016/B978-0-444-53175-9.00016-7.
[3] I. Calizo, F. Miao, W. Bao, C. N. Lau, and A. A. Balandin: Variable temperature Raman microscopy as a nanometrology tool for graphene layers and graphene-based devices. Appl. Phys. Lett. 91, 071913 (2007).

Acknowledgement: This research was funded by the Technology Agency of the Czech Republic, grant number TN01000008.

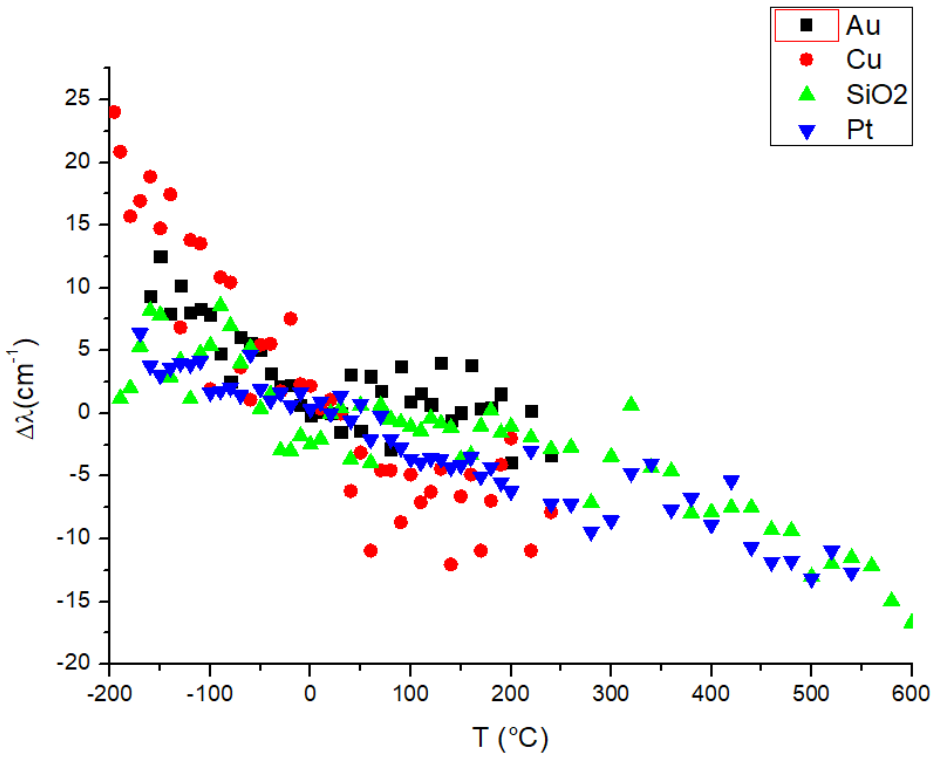

Fig. 1: The G peak shift in the Raman spectrum during the temperature change. With the rising temperature, there is a redshift in the G peak. The difference in the Cu shift is also noticeable, which corresponds with the different means of graphene attachment to the substrate surface.

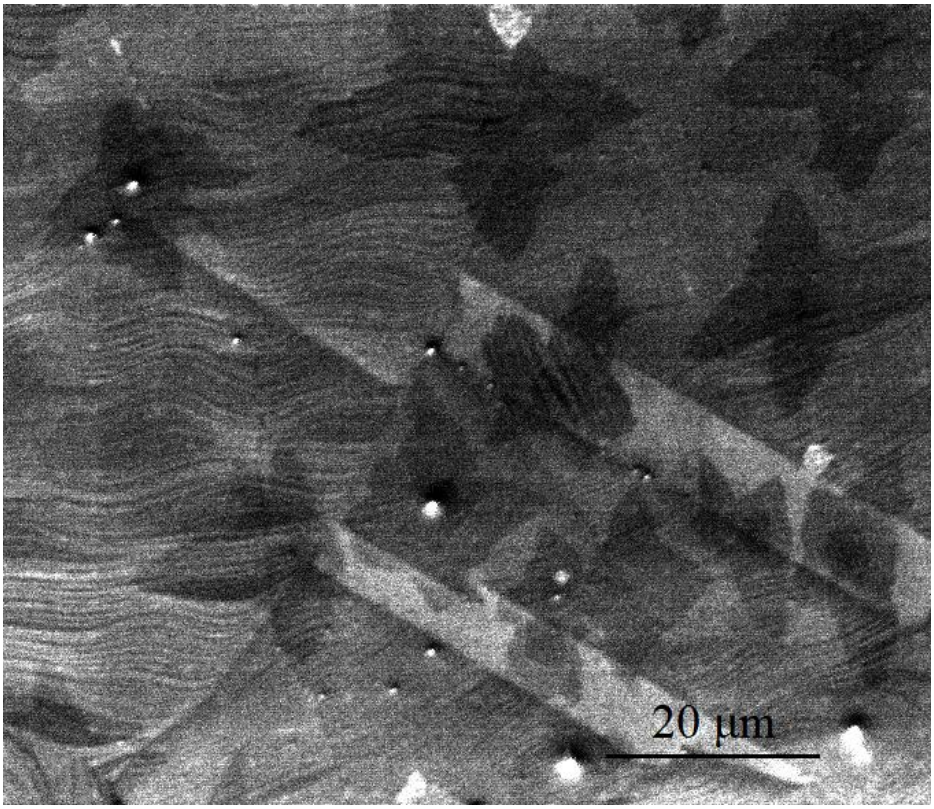

Fig. 2: Scanning Low Energy Electron Microscopy (SLEEM) can clearly distinguish the number of graphene layers and impurities on the surface. Here is the graphene on the Cu surface and the electron beam energy is 13 eV.

Type of presentation: Poster

IM6-P-2599 Effective IMFP of thin samples via the time-of-flight method

Zouhar M.[1], Daniel B.[1], Konvalina I.[1], Paták A.[1], Piňos J.[1], Materna-Mikmeková E.[1]

[1]Department of Electron Microscopy, Institute of Scientific Instruments of the CAS, v. v. i., Brno, Czech Republic

Email of the presenting author: zouharm@isibrno.cz

We built a custom ultra-high vacuum scanning low energy electron microscope. It allows us to measure transmitted electron spectra using the time-of-flight (TOF) method [1]. The cathode-lens principle, applying voltage bias to the sample (stage), allows us to measure at different landing energies ranging from 5 keV down to few eV. The setting of the voltages on active components can be optimised with respect to different quantities, e.g. length of the TOF spectra in the time-domain, keeping detected momentum transfer comparable across different landing energies etc.

We reconstruct the hyper-spectral data, TOF spectrum for each pixel in each scan of selected frames, from the collected primary data - a set of timestamps. Single TOF spectrum is obtained by selecting the region of interest, pixels corresponding to the best quality of the sample, and simply adding up the spectra from all the selected pixels. We present the methodology of the data processing and results obtained for a commercial single-layer graphene sample from the Ted Pella company. The experimental data were complemented by the density-functional theory and the many-body perturbation theory simulations [2, 3] and they corroborate our measurements and data processing methods.

We use the experimental data to estimate inelastic mean free path (IMFP) using the log-ratio method to sample the energy-profile of the IMFP within the regime of low landing energies. The resulting effective IMFP values for a single-layer graphene [2] are in good agreement with existing literature. We plan to study other 2D and thin materials of scientific and commercial interest as well.

[1] I. Konvalina et al.: "Time-of-Flight Spectrometer for Low Landing Energies" (companion contribution at this conference)
[2] I. Konvalina et al.: Nanomaterials 2021, 11(9), 2435; https://doi.org/10.3390/nano11092435
[3] A. Paták et al.: "Ab initio study of angle-resolved electron spectroscopy of graphene" (companion contribution at this conference)

Acknowledgement: Authors thank to colleagues I. Müllerová, L. Frank, T. Radlička, J. Sýkora and F. Hrubý. Funded by Czech Science Foundation (GACR), grant no. GA22-34286S.

IM7 Advances in sample preparation techniques for material and life sciences

Type of presentation: Invited

IM7-IN-2701 Rise to the occasion – high quality sample preparation for high resolution TEM

Dienstleder M.[1], Krisper R.[1], Lammer J.[1], Knez D.[2], Fisslthaler E.[1], Kothleitner G.[2]

[1]Graz Centre for Electron Microscopy (ZFE), [2]Institute of Electron Microscopy and Nanoanalysis (FELMI) Graz University of Technology

Email of the presenting author: martina.dienstleder@felmi-zfe.at

TEM sample preparation methods are as versatile as there are materials and examination methods.
During the last decades, they have advanced in parallel with the revolutionary development of the microscopes themselves. Nowadays, corrected ultra-high-resolution transmission electron microscopes and the option of *in-situ* real-time analyses, have provided access to the atomic scale and are critical for innovations in materials design based on accurate understanding of the properties of the latest materials under working conditions.

The characterization of materials is accompanied by the need to produce high quality samples through sophisticated and innovative sample preparation techniques, thus posing entirely new challenges for sample preparation.
Mechanical or ion-based (broad and focused ion beam) [1-3] sample preparations are now standard preparation techniques and yet, depending on the material, new preparation procedures must always be developed to minimize preparation-related artifacts [4-7] and to allow samples to be examined in as pristine a state as possible.
Preparations for *in-situ* heating and/or biasing experiments present many more challenges due to the MEMS chip geometry and the TEM investigation method, which have to be solved with ingenuity and creativity [8,9].

This talk will focus on recent developments in TEM sample preparation, with special attention on FIB lamella preparation for HR analytical STEM studies and *in-situ* TEM. First-hand experience and a variety of practical examples will provide a deep insight into a modern approach to a wide range of preparation techniques used at different stages of sample preparation.

[1] J. Ayache, et.al. “Sample preparation handbook for transmission electron microscopy” (2010)
[2] L. Reimer „Elektronenmikroskopische Untersuchungs- und Präparationsmethoden“ (1967)
[3] L.A. Giannuzzi et al., (2004) Springer Press ISBN 978-0-387-23116-7
[4] McCaffrey et al., (2001) Ultramicroscopy 87, pp. 97–104.
[5]. A. Barna et al., (1998) Ultramicroscopy, 70, p. 161
[6] Thompson, K., et al., (2006) microscopy and microanalysis, 12 (SUPPL. 2), pp. 1736-1737
[7] C.-M. Park et al., (2004) Applied Physics Letters 84, 3331; DOI: 10.1063/1.1715142
[8] L.A. Giannuzzi et al., (2015) Microsc. Microanal. 21, 1034–1048, doi:10.1017/S1431927615013720
[9] Kwon et al., (2020) Applied Microscopy, doi:10.1186/s42649-020-00043-6

Acknowledgement: We acknowledge financial support by ACR project “INSIGHT” and from the European Union's Horizon 2020 research programme "ESTEEM3".

„ God made the bulk; surfaces were invented by the devil “
Wolfgang Pauli

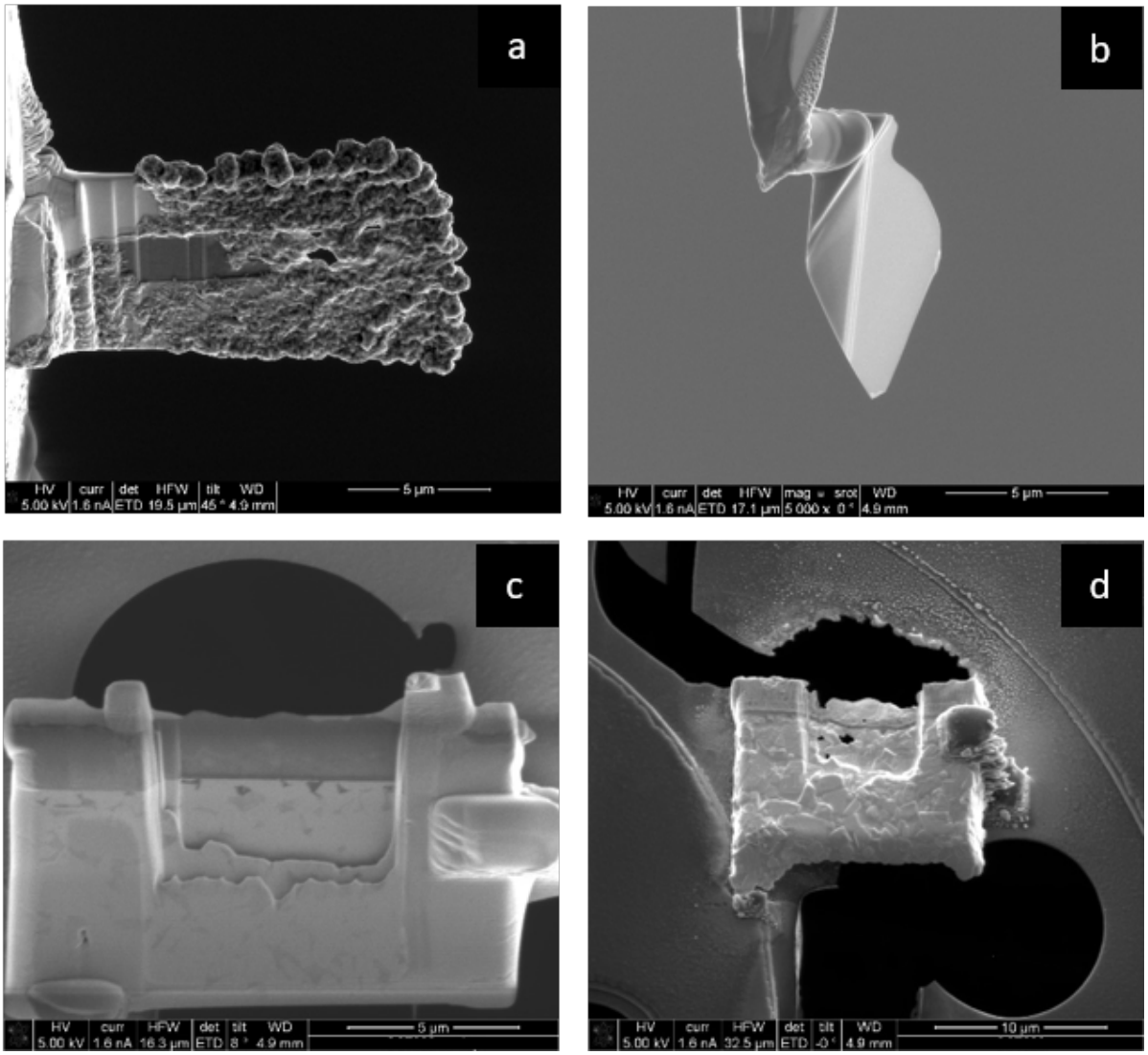

Fig. 1: a) Sulfur growths on a FIB lamella (Al-substrate) after overnight exposure to room air (t~16 hours).
b) FIB prepared sample inclusive low kV cleaning on a rotation in-situ micromanipulator needle before transfer on a MEMS chip.
c) FIB prepared lamella on a DENS heating MEMS chip before the heating test.
d) same FIB lamella (b) after the heating test.

Type of presentation: Invited

IM7-IN-2978 CLEM for FIB/SEM: A workflow for characterization of low-abundant samples on example of a parasitic flagellate Giardia intestinalis.

Tůmová P.[1], Nohýnková E.[1], Wanner G.[2]

[1]Institute of Immunology and Microbiology, First Faculty of Medicine, Charles University, Prague, Czech Republic, [2]Biocenter of Ludwig Maximilian University, Munich, Germany

Email of the presenting author: ptumo@lf1.cuni.cz

The limited number of some phylogenetically distant microorganisms hinders their ultrastructural analysis, necessary to understand their structural and functional cell architecture. Here, on the example of a single-celled eukaryote *Giardia intestinalis* (Metamonada), we present a correlative light and electron microscopy (CLEM) workflow, which allows the selection of individual cells – economical in terms of time and cost. The sample preparation in combination with adhesive coating of slides for fixation and ultrathin flat embedding resulted in excellent preservation of cell morphology of both non-adherent cysts and adherent trophozoites. Besides focused ion beam scanning electron microscopy (FIB/SEM), advanced SEM methods, such as high-resolution field emission scanning electron microscopy (FESEM) and energy-dispersive X-ray spectroscopy (EDX) analysis were applied on *Giardia* samples. FIB/SEM tomography enabled visualization of the fine cellular details in 3D, e.g. mitotic spindle organisation, kinetochores and rudimentary mitochondria in this non-model, phylogenetically divergent microorganism. This can help to understand cytological features shared by all, even distant, eukaryotes, which facilitate the genome and mitochondrial segregation.

Acknowledgement: We kindly acknowledge our funding sources: GAČR 20-06498S to E.N. and PRIMUS/20/MED/008 to P.T.

Type of presentation: Oral

IM7-O-2668 Faster Cryo TEM lamella preparation using optimised conditions and advanced workflows

Pinkas D.[1], Zachej S.[2], Havrankova J.[3], Javurek J.[3], Filimonenko V.[1,4], Hozak P.[4]

[1]Institute of Molecular Genetics ASCR v.v.i., Electron Microscopy Core Facility, Prague, Czech Republic, [2]TESCAN Brno, s.r.o., Libušina tř. 1, 623 00 Brno, Czech Republic, [3]TESCAN ORSAY HOLDING, a.s., Libušina třída 21, 623 00 Brno, Czech Republic, [4]Institute of Molecular Genetics ASCR v.v.i., Department of Biology of the Cell Nucleus, Prague, Czech Republic

Email of the presenting author: dominik.pinkas@img.cas.cz

Cryo-electron tomography of frozen-hydrated samples provides unparalleled level of details from native biological structures. Together with cryo-FIB lamella preparation, it allows us to peek deep inside a cell or even multicellular organism, that would otherwise be too thick to be directly accessible, without introducing any artefacts and deformations caused by more traditional sample preparation techniques such as chemical fixation or (cryo)ultramicrotomy. While the results provided by the method are exceptional, the workflow is technically challenging and requires expensive equipment and consumables and trained operators. Even though the method undergoes rapid development in terms of hardware improvements and software automation, currently the bottleneck is mainly the time that it takes to prepare a proper sample to be used in cryo-Transmission Electron Microscope (cryo-TEM).
Extensive optimizations of all steps are needed, both from the side of equipment manufacturers and users, to prevent heat, beam and mechanical damage as well as ice contamination during the whole process of sample preparation, lamella fabrication and transfer. Simplification of the whole process would not only shorten the time needed but also increase the success rate. We currently have all the necessary tools available at the electron microscopy core facility at IMG. Together with specialists from TESCAN and Leica Microsystems, we are working on simplification of the processes and we so far demonstrated the workflow on frozen hydrated bacteria, yeast, algae, mammalian cells, nematodes and crystalline materials using TESCAN AMBER Cryo FIB-SEM. Considering the amount of time invested in processing of a single sample, it is reasonable to be as precise as possible with selection and targeting of what to actually process. For that purpose, we utilize cryo-fluorescence microscope (Leica CryoCLEM) that allows us to quickly inspect the grids without going into the vacuum of SEM chamber. If the samples are fluorescent, we can pinpoint a specific object of interest and further save time and effort that would otherwise be wasted on suboptimal samples.
We have optimized the workflows for side entry TEM holders to make the method accessible to wider microscopic community compared to autoloader-cartridge focused work.
We are ready to provide cryo lamella-based microscopy techniques to users of our facility.

Acknowledgement: MEYS CR (LM2018129, LTC19048), ERDF (No. CZ.02.1.01/0.0/0.0/16_013/0001775 No. CZ.02.1.01/0.0/0.0/18_046/0016045)., TACR (TE01020118), IMG grant (RVO: 68378050)

Type of presentation: Oral

IM7-O-2593 High-Throughput TEM Sample Preparation with iNotch Technique

Krause M.[1], Moldovan G.[2], Schusser G.[1], Busch R.[1], Hoeche T.[1]

[1]Microstructure-Based Materials Processing, Fraunhofer Institute for Microstructure of Materials and Systems IMWS, Halle / Saale, Germany, [2]point electronic GmbH, Halle / Saale, Germany

Email of the presenting author: michael.krause@imws.fraunhofer.de

Sample preparation is a critical step for high resolution diagnostics in transmission electron microscopy (TEM). Whilst focused ion beam (FIB) tools have become one of the best routes for sample preparation, it is limited in practical operation to either accurate or fast milling, but not both at the same time [1]. Therefore, FIB techniques generally employ a sequence of milling steps, starting with fast but coarse excavation of material using high ion beam currents, and ending with precise, but very slow final thinning/polishing at low ion beam currents.

We introduce a novel FIB-based technique for high-throughput lamella preparation using an initial notch (iNotch), which overcomes this apparent contradiction of being either accurate or fast milling (Fig. 1a). iNotch is based on low-angle milling and self-masked geometry to exploit the effect of preferential milling of local surface elevations, and therefore to form receded terraces [2]. Because of the self-masked geometry, the ion beam does not necessarily have to have an optimal profile, thus allowing the use of the poorer beam shapes typical for high-current or low-energy conditions. iNotch therefore allows for fast removal of targeted material and, at the same time, for precise control of milling depth (Fig 1b). The patented technique does require though that an initial notch of calculated, well-defined geometry is cut before the area of interest.

Under the iNotch approach, terrace depth must match difference between the initial and the target thickness. It is simply determined by milling angle and notch width, therefore the only remaining dimension required is initial thickness. Whilst this initial thickness may be known for some cases, an approach is necessary to measure it in-situ, preferably before and after milling. Electron beam absorbed current (EBAC) is shown here as a suitable approach to determine thickness, as it provides fast and convenient measurements of thickness across the entire target area. The complete sample preparation geometrical calculation can therefore be encapsulated and automated into a simple workflow for the FIB operator.

This contribution will present the underlying physics and the geometrical aspects of notch milling, terrace formation and thickness measurements. First results of electron transparent samples prepared at nA-range ion beams using a Zeiss Auriga 40 will be presented. The broader potential of the novel approach will also be discussed for a range of applications, from depth-resolved electron backscatter diffraction (EBSD), to combined laser/broad-ion beam preparation.

[1] Bassim N, Scott K. and Giannuzzi LA MRS Bulletin 39, 317-325 (2014)
[2] Busch R, Krause M, Coyle S, and Höche T Micron 107, 35-42 (2018)

Acknowledgement: Financial support by the EU and the Investitionsbank Sachsen-Anhalt through the project "FIBNotch" under the grant number 2004/00071 is gratefully acknowledged.

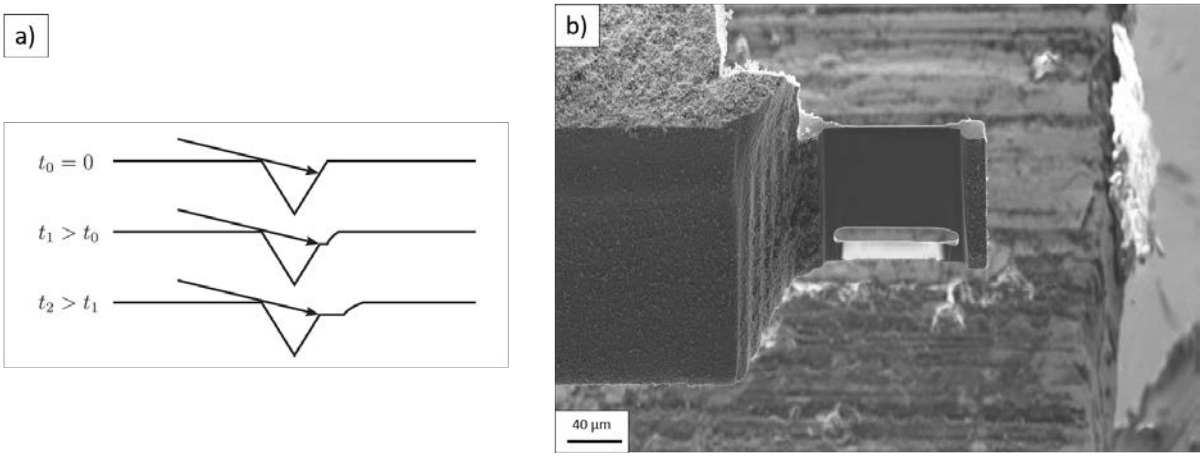

Fig. 1: a) Schematic diagram of the underlying principle for initial notches and b) SEM micrograph of a TEM lamella produced with the iNotch technique, using a Xe-PFIB at 180 nA.

Type of presentation: Oral

IM7-O-2590 FIB-based lamella preparation for in-situ TEM gas experiment

Park J.[1], Camara O.[1], Tempel H.[1], Kungl H.[1], Basak S.[1, 2], Eichel R. A.[1, 3]

[1]Institute of Energy and Climate Research - Fundamental Electrochemistry (IEK-9), Forschungszentrum Jülich GmbH, 52425 Jülich, Germany, [2]Ernst Ruska-Centre for Microscopy and Spectroscopy with Electrons, Forschungszentrum Jülich GmbH, 52425 Jülich, Germany, [3]Institute of Physical Chemistry, RWTH Aachen University, 52074 Aachen, Germany

Email of the presenting author: j.park@fz-juelich.de

The in-situ transmission electron microscope (in-situ TEM) method enables observing the morphological, structural, and chemical transition of the sample with stimuli such as heating or biasing via up to atomic resolution. For a successful in-situ TEM experiment, the sample should be prepared to fit the experimental requirements to stimulate correctly.
In the sintering process, heating and gas environments are required as stimuli. Compared to heating, the gas environment is a challenging stimulus because the inside of TEM is ultra-high vacuum (10-4 ~ 10-9 Pa) condition. Environmental TEM (ETEM) can form the gas environment up to 10 Pa, but many sintering processes are conducted at atmospheric pressure (106 Pa). Therefore, a nano-sized closed chamber is mandatory to replicate the real sintering process in TEM. Electron transmittable thin SiN film-coated micro-electromechanical system (MEMS) chips enable the formation of atmospheric conditions in the TEM.
If the sample is a nanoparticle, drop-casting on a MEMS chip is the simplest way to prepare. However, nanoparticle shape is not available to investigate the phenomena such as interaction on composite materials. The focused ion-beam (FIB) method is a useful preparation method for the TEM sample (lamella) from the bulk to analyze the sample beyond nanoparticles. The FIB-based preparation for the in-situ TEM method contains two processes; lamella preparation and lamella attachment on MEMS chip. Lamella preparation for MEMS chip is almost similar to regular TEM analysis, except if the stimulus is biasing. In the case of biasing experiment, the lamella should be prepared without the Pt layer, which is typically used as a protective layer during the FIB process. To obtain the lamella properly without Pt protection layer, the ion beam should be adjusted to lower electron voltage and lower current conditions.
Lamella attachment on the MEMS chip is the most challenging point. Electron beam imaging and ion beam imaging are generally used to recognize 3-dimensional movement during the attachment. In MEMS chips case, especially for gas experiments, ion beam imaging can break the thin SiN film. To avoid breaking the SiN film, lamella should be controlled mostly on electron beam and carefully checked with minimum ion beam dose as much as possible. We will introduce the FIB-based sample preparation and in-situ TEM gas experiment result to investigate the solid-state electrolyte sintering process.

Acknowledgement: J.P., O.C., H.T. and H.K., acknowledge the iNEW FKZ 03F0589A from BMBF. S.B. acknowledges “Electroscopy” (no. 892916) from the Marie Sklodowska-Curie action.

Type of presentation: Oral

IM7-O-2888 Imaging the Hard-Soft Bone Interface in near native conditions using Cryo FIB/SEM

Upadhyay A.[1], Galvani A.[2], Bideau J. L.[1], Geoffroy V.[2], Abellan P.[1]

[1]Nantes University, CNRS, Jean Rouxel Institute of Materials of Nantes (IMN), F-44000 Nantes, France, [2]Nantes University, INSERM U1229, Regenerative Medicine and skeleton Research Lab (RMES), 44042 Nantes, France

Email of the presenting author: aekta.upadhyay@cnrs-imn.fr

Recent technological advances in electron microscopy make it possible to image biological samples in near native conditions [1]. A very important aspect of this development and, in many cases, a main limiting factor, is the preparation of the samples preserving their structural integrity. In this context, particularly challenging is the preparation of samples for characterization of hard-soft interfaces. These interfaces, such as tooth-enamel interface exist in different regions of the body, and their characterization is crucial to the understanding of relevant biological mechanisms [2]. The two sides of a hard-soft interface exhibit mismatched behaviour in terms of bio (chemical), mechanical and physical properties [3].
Cryogenic fixation is one of the most effective methods to preserve the sample in as life-like state as possible. However, a limitation of this method is the depth of freezing sample. High pressure freezing (HPF) allows vitrification of water molecules to a depth of about 200 microns [4], with minimal ice crystal formation and artefacts. HPF followed by cryo-SEM combined with FIB allow gaining access to specific sites inside the 3D volume of a material in near native conditions. In order to image these interfaces (hard-soft tissue) and to produce 3D reconstructed volumes by cryo-SEM/FIB, three major challenges can be identified. These are: (a) preparation of samples preserving the structural integrity of biological species at both sides of the interface, (b) developing methodologies to acquire images with good resolution despite electron-beam sensitivity, charging effects and low contrast and (c) accessing the specific sites of interest buried within the volume of the sample. For our studies, we have chosen bone as a model system to develop a suitable protocol for simultaneous imaging of hard-soft tissue interfaces. In all our studies, front legs of three months old wild mice were dissected and chemically fixed immediately; to preserve the near native hydrated state of tissues. In this presentation, we will cover the challenges encountered on the development of a suitable method to prepare samples containing the hard-soft interface of bone using HPF and the optimization of milling parameters, deposition and 3D acquisition. These methodologies will open avenues for 3D visualisation of other relevant biological interfaces.

[1] Weston, A.N., Armer, H.E.J., Collinson, L.M. (2010) doi: 10.1007/s12154-009-0033-7
[2] Furqan, A.S., Krisztina, R. and Anders, P. 7 (2019) doi: 10.1038/s41413-019-0053-z
[3] Fang, Y., Yang, X., Lin, Y., Shi, J., Prominski, A., Clayton, C., Ostroff, E. and Tian, B. (2021) doi: 10.1021/acs.chemrev.1c00365
[4] Kach, A. https://www.zmb.uzh.ch/static/bio407/assets/Bio407_HPF_2013.pdf

Acknowledgement: The authors would like to thank financial support by the French National Research Agency (ANR) through the project JCJC VINCI (with reference ANR-20-CE11-0009).

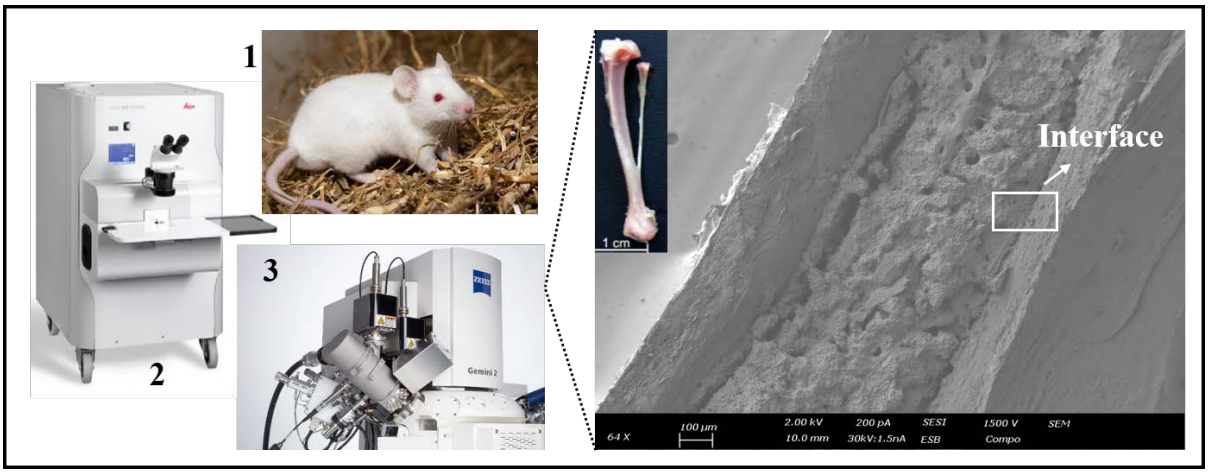

Fig. 1: represents the three main aspect of present study: 1: dissection of rat bone samples, 2: HPF and 3: FIB-SEM. Low magnification SEM image of bone showing the interface of hard-soft material (Right).

Type of presentation: Poster

IM7-P-2607 Imaging of uncoated samples with secondary electrons using in lens detection under optimum conditions – 'sweet spot' imaging

Boese M.[1], Krauss S.[1], Zhou F.[1]

[1]ZEISS Microscopy, Oberkochen, Germany

Email of the presenting author: markus.boese@zeiss.com

For materials characterization usually various signals can be used in the SEM. In this study we will focus on imaging uncoated samples formed by secondary electron (SE) images and the contrast between different materials. The Gemini column was originally developed to gain a good resolution at low voltages. This is achieved by using in-column beam deceleration, without immersing the sample in strong electric or magnetic fields. While decelerating the primary beam, the detectable electrons are accelerated towards the lens. This design also gave unique imaging contrast to the inlens detectors. One can tune the detection system towards optimized contrast conditions depending on the sample type. For different combinations of materials there are sweet spots, which can be used to image with a good contrast and a high signal to noise ratio. There are many examples shown in Literature, which use the detection pattern of the Gemini detection lens. Some recent examples, dealing with different material classes, are described in the following sections. A systematic mapping of imaging conditions (beam energy and working distance) is used for a differentiation of four types of carbide and nitride precipitates in a steel sample [1]. The material contrast was then confirmed by subsequent EDS measurements. By using a matrix mapping of imaging conditions, it becomes clear that the observed contrast of different carbides changes with the beam energy. Good material contrast is shown at 1 kV and 5 mm working distance. This condition is referred to as a sweet spot for imaging this material class. For the measurement of the dimensions of cellulose nanofibrils (CNF) [2], low voltage is used as well. Optimized imaging conditions are key to a precise measurement of CNF widths. A negative-contrast method is developed by using an Al thin foil as a substrate for sample preparation. The large difference of the dielectric properties of the CNF and the metal is utilized here to image under sweet spot conditions (1.5 KV and WD 5,5).
Using a cryo stage, frozen samples can be imaged. The effect of the acceleration voltage on the contrast formation in several types of specimens, focusing on materials formed mainly of carbon and oxygen, with low inherent contrast are examined [3]. Slight specimen charging is exploited to enhance contrast between different materials and phases. As an addition to the well-known yield dependent charge neutrality imaging condition, a sweet spot for high contrast imaging is exploited here, too.

[1] T. Nakamura et al., Materials Transactions, 60, 1591-1597 (2019)

[2] B.D. Mattos et al., Biomacromolecules, 20, 2657-2665. (2019)

[3] L. Liberman et al., Ultramicroscopy, 218, 113085 (2020)

Type of presentation: Poster

IM7-P-2822 Conventional TEM preparation of thin films by the method of "cross-section"

Drev S.[1], Čeh M.[2]

[1]Center for Electron Microscopy and Microanalysis, Jožef Stean Institute, Ljubljana, Slovenia,
[2]Center for Electron Microscopy and Microanalysis and Department for Nanostructured Materials, Jožef Stean Institute, Ljubljana, Slovenia

Email of the presenting author: sandra.drev@ijs.si

Conventional sample preparation has an important role in transmission electron microscopy (TEM). The basic concept of the conventional TEM sample preparation technique remains the same, but it has to modify due to new materials that are present. New materials that are coming have specific properties and have to be precisely treated. This poses ever new challenges, constant adjustments and improvements of advanced conventional and other TEM preparation techniques.
To describe the conventional TEM sample preparation technique by the method of “cross-section”, we present thin film samples on different substrates. We want to expose how important these techniques are and how high the quality of the sample we prepared with this type of preparation. In this chapter, we demonstrate the TEM sample preparation technique of multilayer film of Sr-Ti-Fe-O, La-Sr-Co-O, and Ce-Gd-O on ZrO2-Y2O3 substrate, thin film of Mn-Ni-Co-O on SiO2 covered with Al-Ni-Au electrode and thin film of TiSi on Si substrate. Samples were cut in a block dimension of 1.8x1.8mm and glued in a sandwich with high vacuum epoxy glue. The blocks were fitted into 3 mm brass cylinders using epoxy glue to improve strength. The TEM specimen was ground to a thickness of 100 μm and dimpled down to 15 μm at the disc center (Dimple grinder, Gatan Inc., Warrendale PA, USA). TEM specimen was finally ion-milled (PIPS, Precision Ion Polishing System, Gatan Inc., USA) using different energy for the specific material. Proper energy affects the final quality of the sample. Changing the parameters for the specific materials has an important impact to achieve the result.
Structural and analytical analysis of thin films was performed on a Jeol JEM-2010F transmission electron microscope at the Center for Electron Microscopy and Microanalysis of the Jožef Stefan Institute in Ljubljana and a Jeol ARM 200 CF scanning transmission electron microscope at the Institute of Chemistry in Ljubljana.

Type of presentation: Poster

IM7-P-2801 Washing brains or how to see things more clearly - Fluorescence microscopy can be used for visualization of blood vessels and neurons in the cleared mouse brain

Hamer D.[1], Petrinec D.[1], Berecki M.[1], Skukan L.[1], Gajović S.[1]

[1]Laboratory for Regenerative Neuroscience, Croatian Institute for Brain Research, University of Zagreb School of Medicine, Šalata 12, 10000 Zagreb, Croatia

Email of the presenting author: dominik.hamer@mef.hr

Structures of large samples or whole organs of the laboratory animals can be visualized using novel light sheet fluorescence microscopy (LSFM). The variety of tissue clearing procedures, which are necessary for imaging thick samples, are used for achieving sample transparency and the visualisation is based on labelling the structures of interest by fluorescence. The main goal of this research was to image the structures in the cleared mouse brain with a special task to verify if the clearing procedure can be beneficial even if “classical” easily available fluorescent microscopes were used for sample visualisation. The inverted fluorescence microscope (The EVOS® FL Auto Imaging System, ThermoFisher Scientific) was used for this purpose. For whole brain tissue clearing, four methods were used: ECi (optical clearing using ethyl-cinnamate), iDISCO (immunolabeling-enabled threedimensional imaging of solvent-cleared organs), PEGASOS (polyethylene glycol-associated solvent system) and FluoClearBABB (fluorescent-protein preserving using benzyl alcohol and benzyl benzoate). Previously naturally transparent parts of mouse embryos were also imaged using fluorescence microscopy by our group. The fluorescent staining 10 % fluorescein solution (Fluorescite, Alcon) and Isolectin GS-IB4 from Griffonia simplicifolia, Alexa Fluor 568 Conjugate (Invitrogen) was injected by help of stereotaxic apparatus (David KOPF Stereotaxic Instrument Small Animal Frame 5001 H7000). Moreover, mouse brains were isolated from two months old animals (Thy1-YFP-16 strain), which naturally expressed yellow fluorescent protein in neurons. As a third approach blood vessel visualization Lycopersicon Esculentum Lectin Texas Red (Invitrogen) was injected in the left heart ventricle of living mouse (Figure 1). In all three cases the mice were perfused by 1× PBS and 4 % formalin solution and subsequently cleared. Cleared mouse brain samples were cut on approximately 1 mm thick slices using mold (Alto Acrylic 1mm Mouse Brain Coronal 40-75gm, CellPoint Scientific), mounted subsequently on the glass slides in the drop of the final clearing solution, covered by coverslips, and imaged using inverted fluorescence microscope. The ECi method was preferred as the protocol for clearing lasted only one day and used chemicals were nontoxic. iDISCO clearing technique made brain slices brittle and difficult to handle. Even without using LSFM, it was possible to visualize fluorescently labelled structures in thick samples. It was still to be clarified if this type of imaging is suitable beside qualitative description of the samples, to quantitative measurements as well. In conclusion, the clearing of mouse brain produces thick slices suitable as well for imaging and analysis by fluorescence microscopy.

Acknowledgement: Supported by EU project “Sinergy of molecular markers and multimodal in vivo imaging during preclinical assessment of the consequences of the ischemic stroke.”

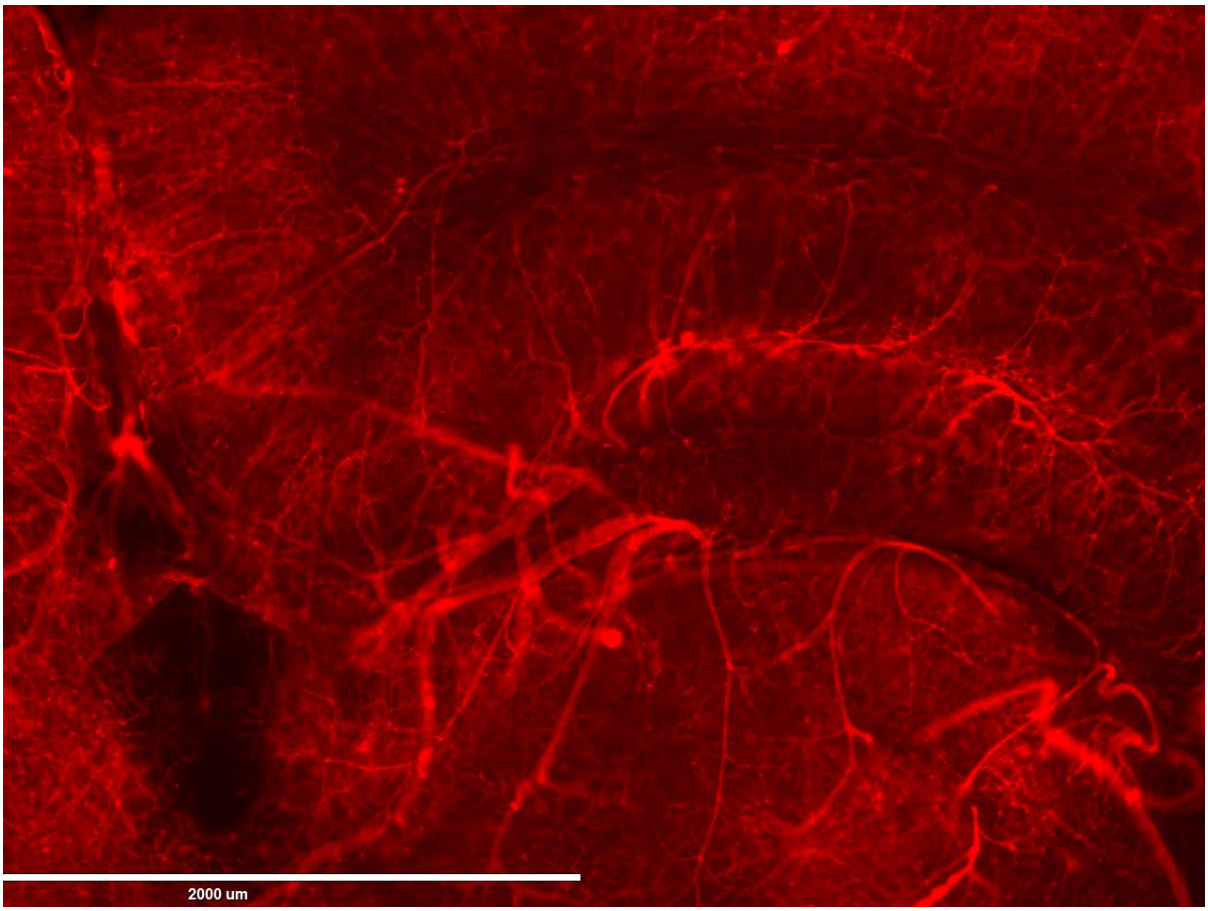

Fig. 1: Blood vessels in mouse brain labeled with LEL Texas Red using inverted fluorescence microscope (approximately 1 mm sample slice (sample sliced with Alto Acrylic 1mm Mouse Brain Coronal 40-75gm, CellPoint Scientific) cleared using ECi method; blood vessels labelled with Lycopersicon Esculentum Lectin Texas Red (Invitrogen)).

Type of presentation: Poster

IM7-P-2755 CANVAS: A System for Controlled Alteration of Nanomaterials in Vacuum Down to the Atomic Scale

Mangler C.[1], Meyer J. C.[1,2], Mittelberger A.[1,3], Mustonen K.[1], Susi T.[1], Kotakoski J.[1]

[1]Physics of Nanostuctured Materials, Faculty of Physics, University of Vienna, Vienna, Austria, [2]Currently: Institute for Applied Physics, University of Tuebingen, Tuebingen, Germany, [3]Currently: Nion Co, Kirkland, Washington, USA

Email of the presenting author: clemens.mangler@univie.ac.at

To get a true understanding of materials' properties, one has to assess their structure down to the atomic level. The next step is to enhance these properties by controlled and atomically precise alterations. While investigations of materials are usually carried out in high-resolution electron microscopes, their alteration typically has to be done in separate devices in controlled atmospheres, often ultra-high vacuum (UHV). This leads to the problem of sample transfer, where a major issue is their contamination. This is especially critical for low-dimensional materials due to their high surface-to-volume ratio.

To overcome this drawback, we have built one vast UHV system for the controlled alteration of nanomaterials in vacuum down to the atomic scale (CANVAS). The CANVAS system spans over two floors and consists of an aberration-corrected UHV scanning transmission electron microscope Nion UltraSTEM 100 [1] with a specially modified stage [2], an atomic force microscope (AFM) [3], and a manipulation chamber equipped with a plasma source, a 6W diode laser and various thermal and electron-beam evaporators. Insertion of samples is done via a fully computer-controlled loadlock which is attached to a glovebox under argon atmosphere. The individual parts of the system are all connected via a novel arbitrary-length UHV transfer system consisting of magnetically coupled transfer cars and a new sample-holder design, which can be accommodated by all devices in the system (cf. Figure 1 and Figure 2 for an overview).
The CANVAS system allows the controlled alteration of materials and even the growth of new ones by utilizing various parts of the apparatus and quickly moving samples between them. Typical workflows include experimental steps like the alteration of a materials by thermal evaporation or plasma irradiation augmented by quick checks at atomic resolution at the STEM.

[1] O.L. Krivanek, G.J. Corbin, N. Dellby, et al., Ultramicroscopy, 108 (3), 179 (2008)
[2] M.T. Hotz, G. J.. Corbin, N. Dellby, et al., Microscopy and Microanalysis, 22 (S3), 34 (2016)
[3] https://www.qd-microscopy.com/afsem/ (accessed April 29, 2022)

Acknowledgement: The authors thank V. Skákalová for suggesting the name of the system, G. Zagler, S. Hummel, W. Joudi and F. Herterich for help with construction.

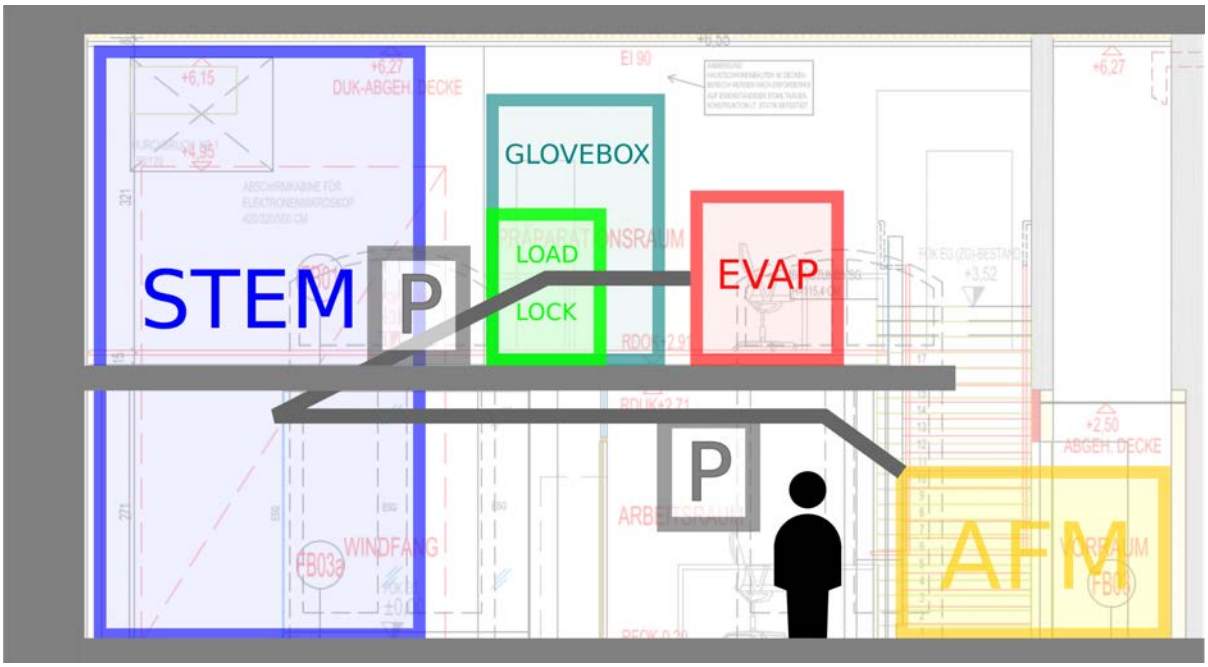

Fig. 1: Cross-section of the Vienna lab showing the CANVAS-system: scanning transmission electron microscope (STEM, blue), loadlock and glovebox (green/teal), evaporation chamber (EVAP, red), atomic force microscope (AFM, yellow) and sample storage (P, grey).

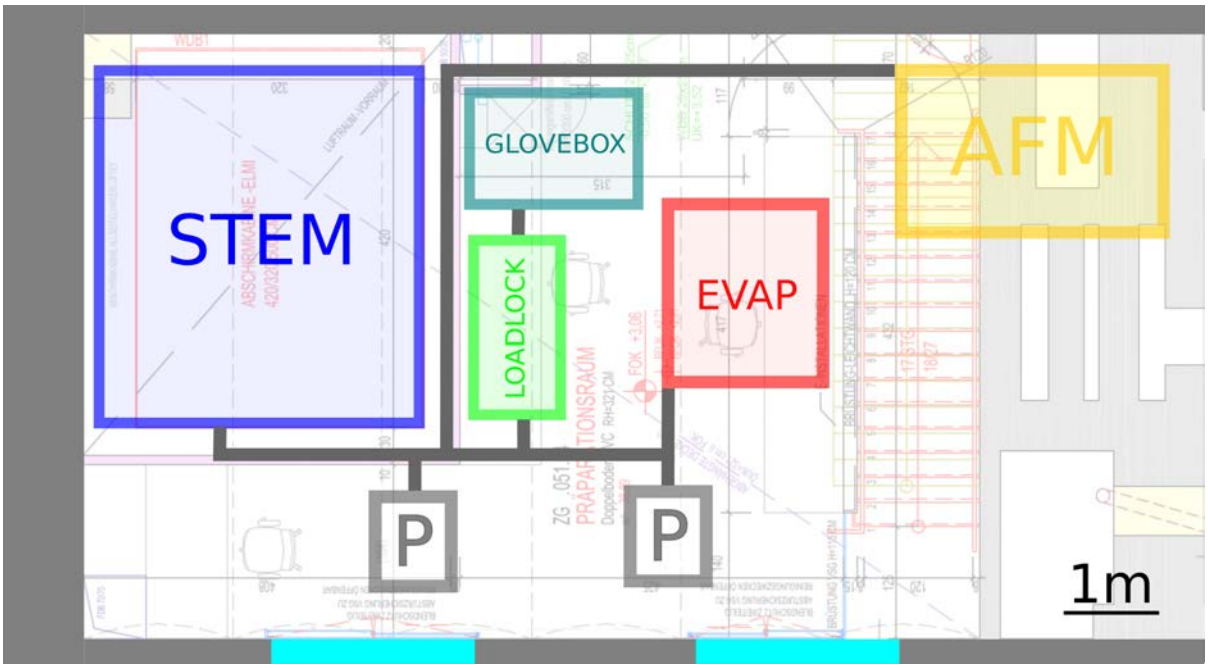

Fig. 2: Top-view of the Vienna lab showing the CANVAS-system: scanning transmission electron microscope (STEM, blue), loadlock and glovebox (green/teal), evaporation chamber (EVAP, red), atomic force microscope (AFM, yellow) and sample storage (P, grey).

Type of presentation: Poster

IM7-P-2537 The Hidden Power of Coffee – An Exceptional Replacement for Uranyl Acetate for Staining Biological Specimens in Transmission Electron Microscopy

Mayrhofer C.[1], Zandonella R.[2], Letofsky-Papst I.[2]

[1]Graz Centre for Electron Microscopy, Steyrergasse 17, Graz, Austria, [2]Institute of Electron Microscopy and Nanoanalysis, NAWI Graz, Graz University of Technology, Steyrergasse 17, Graz, Austria

Email of the presenting author: claudia.mayrhofer@felmi-zfe.at

The use of uranyl acetate, one of the most conventional contrast agents used for decades in electron microscopic examinations of biological specimens, is strictly regulated by law and in some cases banned from laboratories. In recent years, non-toxic or non-radioactive alternatives with similar staining results have been developed. These alternatives are not equally effective for all biological structures. Examples are Uranyl Acetate Replacement (UAR), Uranyless (UL) and Oolong tea extract (OTE) [1, 2]. In this work, two new alternatives, being coffee solution as well as one of its components, chlorogenic acid (CGA), have been studied [3].
Coffee contains a wide range of ingredients that are said to have health-promoting traits. A new outstanding but unknown property is that coffee can also be used to increase contrast of biological samples in electron microscopy. Figure 1 shows mitochondria in zebrafish, A) stained with UA, B) stained with coffee. Subjectively, both images show quite good contrast. This work illustrates how a subjective impression of either good or poor contrast can be converted into an objective and thus comparable numerical value using the Michelson contrast and a MATLAB algorithm (see Fig. 2), which makes a direct comparison of the different contrast agents possible. On comparing these contrast values for epithelial cells, cell membranes, muscle fibers tubules and mitochondria in zebrafish it turned out that coffee is even more suitable as a contrast agent than UA. Also chlorogenic acid, for its part, produces good image quality with high contrast values and is superior to UA concerning mitochondria, cell membranes, muscle fibers and epithelial cells. This method now allows the direct numerical comparison between differently stained specimens. For this research, primarily the excellently mapped zebrafish (Danio rerio) was used, but subsequently mouse kidney was also studied in detail.
[1] A.A. Miller, A.V. Simakova: Application of Method of OTE Staining of Ultrathin Sections Based on Example of Microsporidia; Cell and Tissue Biology 2010, Vol 4-1, pp. 109-115
[2] R.L. Santhana et al.: Modification of the Uranyl Acetate Replacement Staining Protocol for Transmission Electron Microscopy; Int. J. Med Nano Res 2016, Vol 3, Issue 1
[3] R. Zandonella: Can Coffee replace Uranium: Alternative Staining Agents for Biological Samples in Transmission Electron Microscopy, Master´s Thesis 2022, in press

Acknowledgement: Special thanks to W. Salvenmoser (University of Innsbruck) and I. Kufferath (Medical University of Graz) for providing the zebrafish and mouse kidney samples.

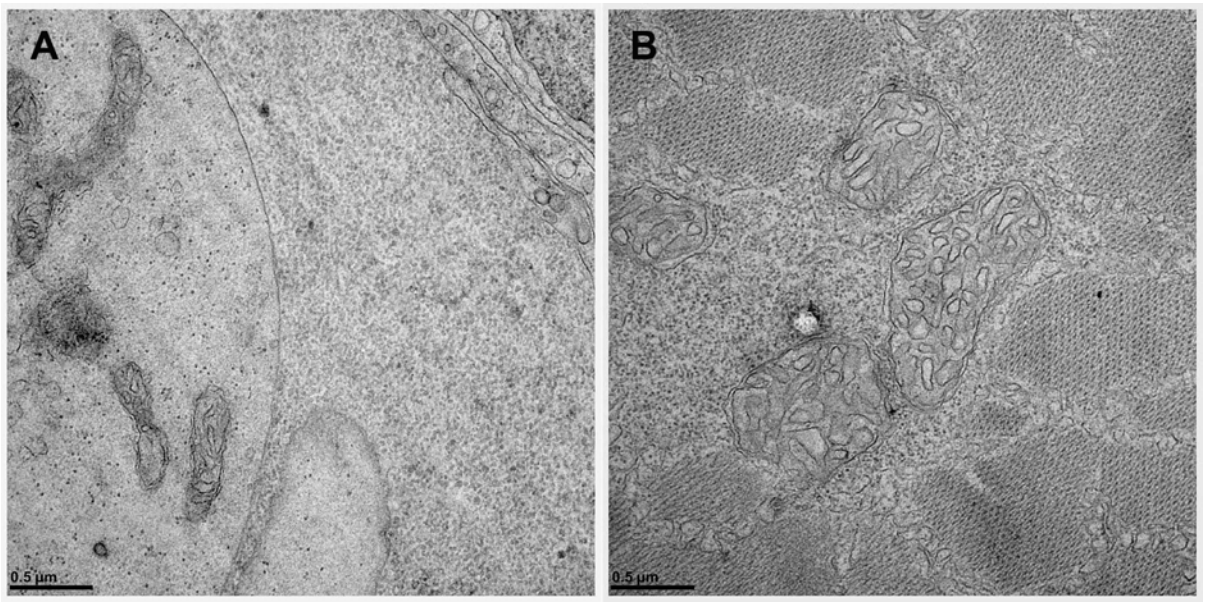

Fig. 1: Zebrafish specimen stained with uranyl acetate (A) and coffee (B)

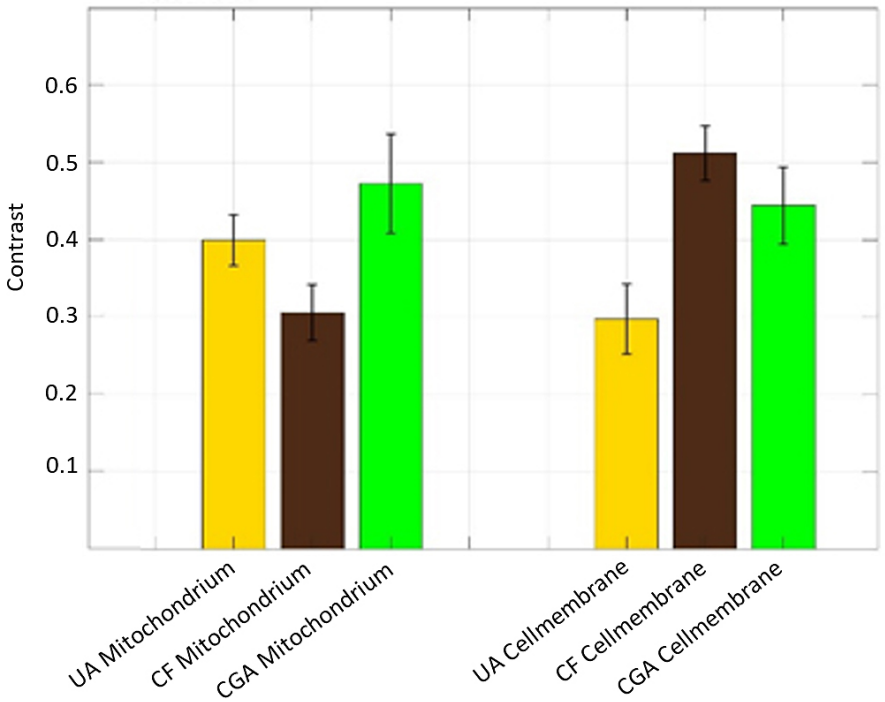

Fig. 2: Comparison of some MATLAB algorithm results for chlorogenic acid (CGA), coffee (CF) and uranyl acetate. (UA)

Type of presentation: Poster

IM7-P-2848 High-Throughput Cryo-Electron Tomography with a next generation platform

Mitchels J. M.[1], Rigort A.[3], Reyntjens S.[2], Kotecha A.[2]

[1]Thermo Fisher Scientific s.r.o., Brno, Czech Republic, [2]Thermo Fisher Scientific, Eindhoven, The Netherlands, [3]Thermo Fisher Scientific, Munich, Germany

Email of the presenting author: john.mitchels@thermofisher.com

Since the inception of cryo-lamella preparation methodology 10 years ago, cryo-electron tomography has become an indispensable tool for structural biology research. Thermo Fisher Scientific in conjunction with leading academic groups brought the technique to a wider community with the incremental introduction of new technology during this time. The Thermo Scientific Aquilos cryo-focused ion beam is in its second generation with new automation routines for lamella production. Cryo-lift-out and fluorescence microscopy options have been integrated to the system, and these have expanded the application range of the cryo-FIB to new samples and use cases. These improvements in cryo-FIB technology and the corresponding improvements in cryo-TEM (data collection, faster direct electron detectors and energy filters), have opened the door to the statistical domain [1]. This can be seen clearly by the steady increase in the number of publications in the field of structural biology and physiology [2].

In this contribution, the next big step in cryo-electron microscope technology development will be presented: a next generation cryo-FIB instrument. Similarly, to the introduction of the automated Krios cryo-TEM. This is as significant as the introduction of the automated Krios cryo-TEM. This system has been designed to be fully dedicated to production of cryo-lamellae for the cryo-electron tomography workflow. It features a state-of-the-art plasma ion source, an automated sample loading system, integrated fluorescence microscope, and the lowest contamination rates for pristine lamella and maximum productivity.

References:

[1] D Kwon, Nature 598, 558-560 (2021). doi.org/10.1038/d41586-021-02904-w
[2] Z Wang et al, Cell 184, 2135–2150.e1–e5, April 15, (2021). doi.org/10.1016/j.cell.2021.02.047

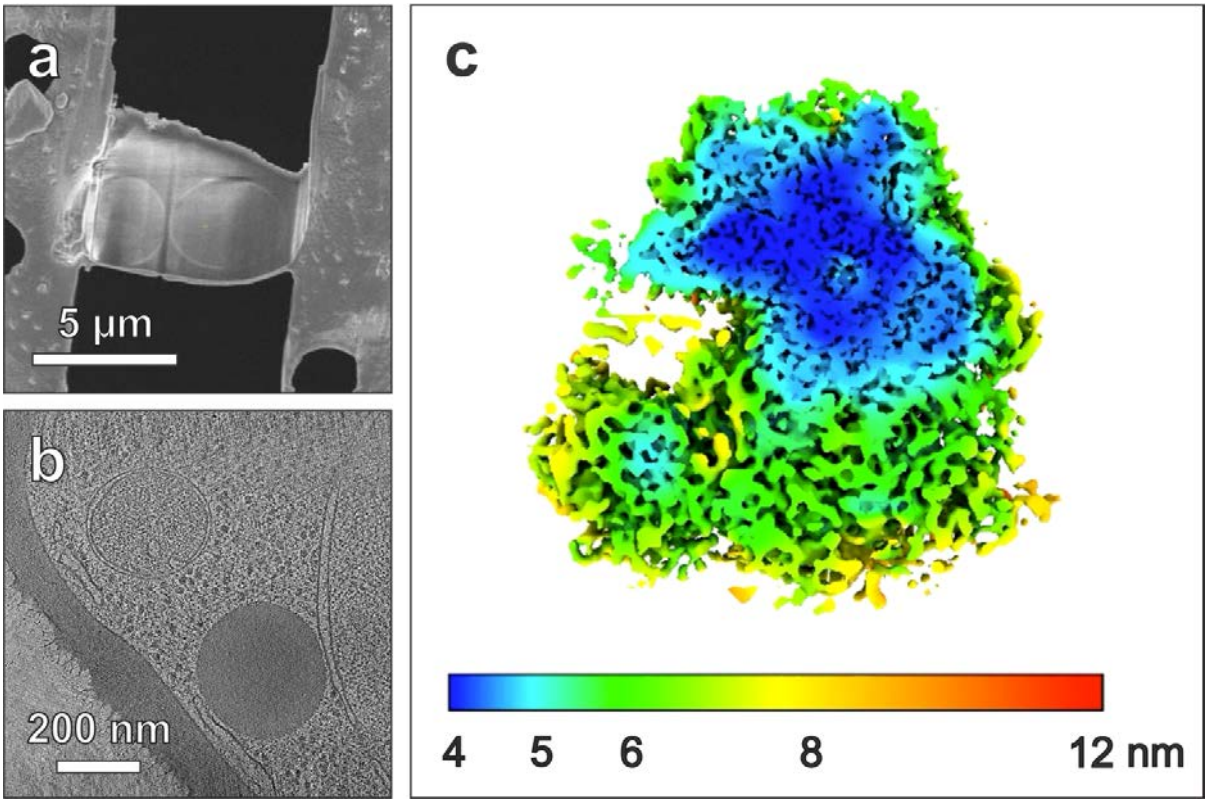

Fig. 1: (a) S. cerevisiae cryo-lamella produced by Xenon ion milling in the next generation cryo-Plasma-FIB system. (b) Slice from a tomographic reconstruction. (c) Corresponding sub-tomogram averaging yielding the 80S ribosome at a global resolution of 6.5Å from 7000 particles. The 60S large subunit reaches 4.5 Å local resolution.

Type of presentation: Poster

IM7-P-2818 Distribution of staining agents in samples of mice soft tissues prepared for Serial Block Face SEM.

Nebesarova J.[1,2,3], Durinova E.[1,3], Kitzberger F.[1,3], Skoupy R.[4], Tyc J.[1]

[1]Biology Centre, Czech Academy of Sciences, České Budějovice, Czech Republic, [2]Faculty of Science, Charles University, Praha, Czech Republic, [3]Faculty of Science, University of South Bohemia, České Budějovice, Czech Republic, [4]Institute of Scientific Instruments, Czech Academy of Sciences, Brno, Czech Republic

Email of the presenting author: nebe@paru.cas.cz

Serial block-face scanning electron microscopy (SBF SEM) uses an ultramicrotome installed inside the microscope to cut away ultrathin slices together with backscatter imaging to visualise each newly exposed layer. Such arrangement brings the possibility to acquire a series of images allowing reliable and precise volume reconstruction. The biggest challenges we face in SBEM are sample preparation, finding the region of interest (ROI) within the sample, sample charging during the imaging, and finally, data processing and storage. Insufficient contrast in specimens often seriously limits the visualisation and makes the sample preparation one of the crucial steps in the SBEM analysis.
The sample preparation is based on procedures standardly used for transmission electron microscopy. It starts with chemical fixation followed by dehydration, including en bloc staining. The process is finished by sample embedding in a hard epoxy resin. Several protocols have been developed by modifying the chemicals used, incubation times or temperatures [1-4]. This study compared these protocols and evaluated the resulting contrast for SBF SEM analysis of soft animal tissues like mouse brain, liver and kidney. The samples prepared according to these protocols were analysed using light microscopy, SBF-SEM examination, and EDX analysis.
We found out that the frequently used protocol suggested by Deerinck et al. [1] resulted in an unevenly contrasted sample, where only thin outer regions approx. up to 100 µm below the surface were osmificated sufficiently. The protocol suggested by Hua et al. [2] provided the homogenous stained layer with an almost double thickness (Fig. 1). The protocol using tannic acid as a mordant [3] gave an excellent result with minimal difference in contrast between the samples' central and edge areas. In contrast, a protocol called fBROPA [4], which omits uranyl acetate, led to weak and inhomogeneous contrast mainly in the central parts of the specimen.

[1] Deerinck, T. J. et al.: Microscopy, 6–8 (2010).
[2] Hua, Y. et al.: Nature Communications, 6(1), 7923 (2015)
[3] Katsumoto T. et al.: J. Electron Microscopy, 30(3), 177-182 (1981)
[4] Genoud, C. et al.: Frontiers in Neuroanatomy, 12, 1–8 (2018)

Acknowledgement: This work was supported by TACR (TN0100008), and MEYS CR (Czech BioImaging LM2018129).

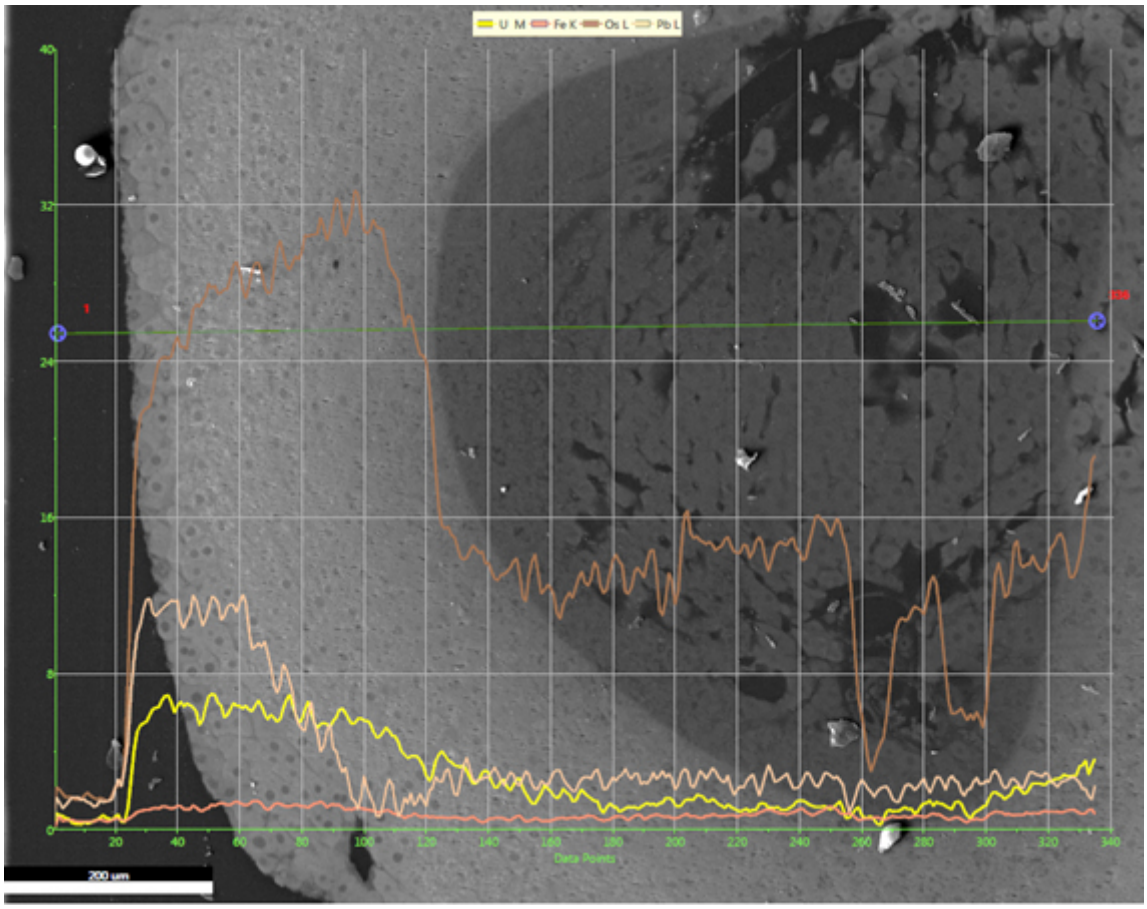

Fig. 1: The distribution of heavy atoms in the mouse liver tissue prepared for SBF-SEM according to Hua protocol. Fe (orange), Os (brown), Pb (beige), U (yellow)

Type of presentation: Poster

IM7-P-2790 Nanopatterned Surface for Super-resolution Microscopy localization of Cell Interactions

Pospíšil J.[1,2], Hrabovský M.[3], Bohačiaková D.[1,4], Hovádková Z.[3], Jurásek M.[3], Mlčoušková J.[5], Paruch K.[4,6], Nevolová Š.[4,7], Damborský J.[4,7], Hampl A.[1,4], Jaroš J.[1,4]

[1]Department of Histology and Embryology, MU, Brno, Czech Republic, [2]Core Facility Cellular Imaging, CEITEC, Brno,Czech Republic, [3]TESCAN Brno s.r.o., Brno, Czech Republic, [4]International Clinical Research Center, Brno, Czech Republic, [5]Department of Biology, MU, Brno, Czech Republic, [6]Department of Chemistry, MU, Brno, Czech Republic, [7]Department of Experimental Biology, MU, Brno, Czech Republic

Email of the presenting author: 357959@mail.muni.cz

Cellular behavior and cell fate are controlled not only by intrinsic processes but can be modulated also by the extracellular environment. Interactions with the environment usually occur at the nanoscale level and therefore it is complicated to evaluate their impact. To elucidate in more detail, the influence of the surrounding environment in vitro, we have to be able to prepare suitable biomaterials with controlled nano-distribution of selected molecules in a precise and reproducible manner. The main challenges are obtaining the nanoscopic features, high demand for biocompatibility, and finally, the necessity for transparent properties of prepared biomaterial, allowing subsequent super-resolution microscopy analysis. Recent progress in nanotechnology allows for mimicking of the microenvironment by the patterned distribution of biomolecules at the nanoscale level, particularly by using highly promising electron-beam lithography (EBL). Although this nanopatterning technique can generate nanostructures of good quality and resolution, it has been used, thus far, for the preparation of nanomaterials without a biological agent, and is mostly non-transparent, leaving its potential in biological applications unfulfilled. Here, we performed the EBL on conventional cell culture material coated with a transparent electron-conductive indium tin oxide layer, resulting in complex nanopatterns, further biofunctionalized via novel HaloTag recombinant protein. This biocompatible system allowed us to nanoprobe the cell interactions toward a specific region. We prove successful cellular localization by scanning electron microscopy and by super-resolution (SIM) microscopy. Furthermore, we suggest, that such a universal system can be effectively used for probing biological samples for the corelative-microscopy technique and may provide an understanding of cellular signaling mechanisms at a single-molecule level.

Acknowledgement: Acknowledge the core facility CELLIM supported by MEYS CR (LM2018129 Czech-BioImaging). Supported by ERDF project INBIO (No. CZ.02.1.01/0.0/0.0/16_026/0008451).

Type of presentation: Poster

IM7-P-2676 IMG Electron Microscopy Core Facility

Raabová H.[1], Pinkas D.[1], Vlčák E.[1], Filimoněnko V.[1,2]

[1]Core Facility for Electron Microscopy, Institute of Molecular Genetics CAS, Prague, Czech Republic, [2]Laboratory of Biology of the Cell Nucleus, Institute of Molecular Genetics CAS, Prague, Czech Republic

Email of the presenting author: helena.raabova@img.cas.cz

The Electron Microscopy Core Facility provides expertise and cutting-edge equipment for a broad range of biological sample preparation and ultrastructural imaging techniques. The core facility deals with various biological samples: human and animal cell cultures, plant and animal tissues, worms, microorganisms, lipid micelles, isolated DNA, or purified proteins. The sample preparation techniques include both standard and advanced techniques, such as routine chemical fixation and resin embedding, negative staining, cryofixation using plunge-freezing or high-pressure freezing, freeze-substitution, cryosectioning, freeze fracture replica labeling, pre- and post-embedding immunolabeling, the list being lately extended by cryoCLEM using specialized microscope.
Transmission electron microscopes (TEM) installed at the core facility include a standard 120 kV instrument for routine observation and an advanced 200 kV S/TEM providing the possibility of high-resolution TEM, 3D analysis by TEM- or STEM tomography, cryo-electron microscopy and STEM-EDS elemental analysis. High-pressure freezer with light stimulation module, two automatic freeze-substitution machines, cryo-ultramicrotomes, automated plunge-freezer, freeze-fracture replica making device, cryoCLEM microscope, as well as additional wet lab equipment are available.
The team has a long expertise in the development and optimization of sample preparation techniques, including fruitful collaborations with companies providing equipment for electron microscopy. The Electron Microscopy Core Facility is part of the IMG Czech-BioImaging node and Prague Euro-BioImaging node. We provide open access to our technologies and expertise and are ready to welcome users from all fields.

Acknowledgement: MEYS CR (LM2018129,LTC19048), ERDF (No.CZ.02.1.01/0.0/0.0/16_013/0001775 and No.CZ.02.1.01/0.0/0.0/18_046/0016045)., TACR (TE01020118), IMG grant (RVO:68378050)

Type of presentation: Poster

IM7-P-2662 Solutions for preparation and visualization of vitrified biological samples at IMG Electron Microscopy Core Facility

Vlcak E.[1], Pinkas D.[1], Zachej S.[3], Havrankova J.[4], Raabova H.[1], Philimonenko V.[1,2], Hozak P.[1,2]

[1]Institute of Molecular Genetics ASCR v.v.i., Electron Microscopy Core Facility, Prague, Czech Republic, [2]Institute of Molecular Genetics ASCR v.v.i., Department of Biology of the Cell Nucleus, Prague, Czech Republic, [3]TESCAN Brno, s.r.o., Libušina tř. 1, 623 00 Brno, Czech Republic, [4]TESCAN ORSAY HOLDING, a.s., Libušina třída 21, 623 00 Brno, Czech Republic

Email of the presenting author: erik.vlcak@img.cas.cz

Continual advancement in a broad range of interconnected cryo-electron microscopy pipelines has made the preservation and subsequent visualization of sensitive biological samples in close-to-native state more reliable and convenient than ever before. Cryo-electron microscopy has therefore become the new standard for dependable analysis of biological objects. Our facility has been continually updating the cryo-workflows to stay up-to-date with these advancements and to provide professional solutions for current scientific demands.
A 200 kV Jeol JEM-F200 transmission electron microscope with cryo polepiece, cold field emission electron gun, sensitive 4k CMOS camera TVIPS TemCam XF-416, and phase plate provides optimal configuration for a broad range of cryoTEM applications. The latter include observation of morphology of small objects sensitive to dehydration, such as e.g. small organisms or DNA origami, quality check of purified protein samples prior to SPA analysis, collection of diffraction patterns of frozen protein crystals, and cryo-electron tomography of subcellular structures.
The whole workflow of cryo-TEM tomography of frozen hydrated lamellae is currently available at the core facility due to the running collaborative project with TESCAN Company. The optimized on-grid workflow includes plunge freezing with Leica EM GP2, quality check in Leica THUNDER cryo-CLEM, mounting and transfer of sample to TESCAN Amber Cryo FIB-SEM for lamella fabrication, and final transfer of lamella into cryoTEM for tilt series acquisition. Successful observations and volume reconstructions of subcellular structures of C. elegans, S. cerevisiae, Chlamydomonas, Chlorella, and HeLa cells were performed using the workflow.
Several other skill-demanding workflows utilizing sample vitrification, such as freeze-fracture replica immunolabeling using multi-purpose sputter coater Leica EM ACE900, cryo-CLEM imaging with reliable correlation of images from both modalities, or cryo-sectioning followed by immunolabeling after Tokuyasu are established at the core facility. Samples vitrified by high-pressure freezing in Leica EM ICE HPF machine with light-stimulation module can be alternatively processed to resin blocks upon freeze-substitution in Leica EM AFS2 machines.
The EM CF, being a part of large imaging infrastructures Czech-BioImaging and Euro-BioImaging, provides open access to all described technologies with professional support on all steps of the user project.

Acknowledgement: MEYS CR (LM2018129, LTC19048), ERDF (No. CZ.02.1.01/0.0/0.0/16_013/0001775, No. CZ.02.1.01/0.0/0.0/18_046/0016045), TACR (TE01020118), IMG grant (RVO: 68378050)

LS1 Electron microscopy in health, diagnostics, nanomaterials and regenerative medicine

Type of presentation: Invited

LS1-IN-2535 Hyaluronic acid based nanoparticles are suitable carriers to muscle cells: the ultrastructural evidence

Carton F.[1], Repellin M.[2,3], Lollo G.[3], Malatesta M.[2]

[1]Department of Health Sciences, University of Piemonte Orientale 'A. Avogadro', 28100 Novara, Italy., [2]Department of Neurosciences, Biomedicine and Movement Sciences, University of Verona, 37134 Verona, Italy., [3]University of Lyon, Université Claude Bernard Lyon 1, CNRS, LAGEPP UMR 5007, 69100 Villeurbanne, France.

Email of the presenting author: flavia.carton@uniupo.it

Myotonic dystrophies (DMs) are neuromuscular diseases of genetic origin that involve multiple organs and tissues, with particular emphasis on skeletal muscles. Although only palliative treatments are administered, some molecules (e.g. pentamidine) have been proven to be efficient in mitigating the pathological halmarks of DMs. Actually, the therapeutic application of these compounds is impaired by their low bioavailability and high toxicity. To overcome these limitations, polymeric hyaluronic-acid-based nanoparticles (HA-NPs) were developed as a therapeutic strategy to efficiently deliver pentamidine (PTM) to skeletal muscle cells [1]. Howerver, to obtain HA-NPs suitable for clinical applications, it is mandatory to elucidate their behaviors and interactions with the biological milieu. Electron microscopy represents a suitable tecnique able to characterize, localize and track the fate of NPs inside cells thanks to its high resolution [2].
Firstly, morphological analysis of HA-NPs and PTM-loaded NPs was carried out using trasmission electron microscopy (TEM) and Cryogenic transmission electron microscopy (CryoTEM). As shown in Fig. 1 (A,B), both HA-NPs and PTM-loaded NPs formed monodispersed populations of rounded shaped particles.
Moreover, to precisely investigate NPs behaviour at the ultrastructural level, NPs must be unequivocally visualized. This is easily obtained for NPs containing electron dense components but it may be difficult for organic NPs having an intrinsic moderate electron density such as HA-NPs. A valid detection method to overcome this limitation is represented by the Alcian Blue (AB) staining, a long-estabilished histochemical technique [3]. In muscle cells treated with HA-NPs, the AB staining appeared as an irregular granular electron dense product found on weakly electron dense NPs (Fig.2) similar to those observed in cells processed for conventional ultrastructural morphology (Fig 3).
Once HA-NPs were unequivocally identified, their internalization and trafficking were investigated by TEM. As shown in Fig. 3 (A,B), HA-NPs were internalized individually via endocytosis and localized throughout the cytoplasms, being never observed inside the cell nuclei. HA-NPs rapidly escaped endosomes occurring free in cytosol and, after 24 h, they formed large cluster. However, no organelle damage or alteration was ever observed.
The results obtained underline the importance of transmission electron microscopy tecnique to investigate the behaviour of NPs inside cells and tissue, providing essential information on their actual spatial relationships with biological components.

References

[1] Carton F. et al., Int. J. Pharm., 569 (2019) 118526.
[2] Repellin M. et al., Microscopie, (2019) 30.
[3] Carton F. et al., Eur. J. Histochem., 63 (2019) 3086.

Acknowledgement: This project has received funding from EU Horizon 2020 GA No 754345 through the INVITE project.

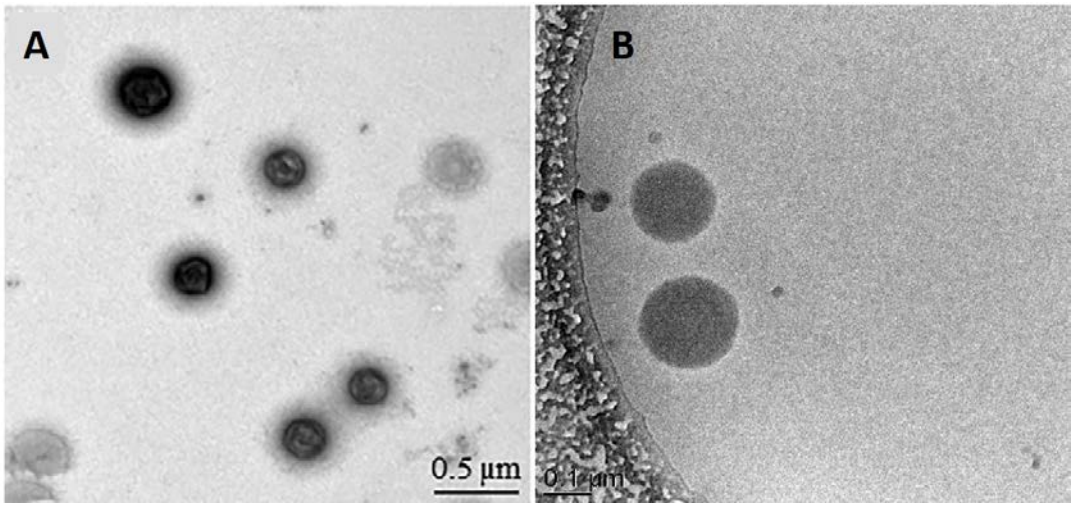

Fig. 1: TEM image of HA-NPs (A). Cryo-TEM image of PTM-loaded NPs (B). Bars: 0.5 µm (A), 0.1 µm (B). (Carton et al., Int. J. Pharm., 2019).

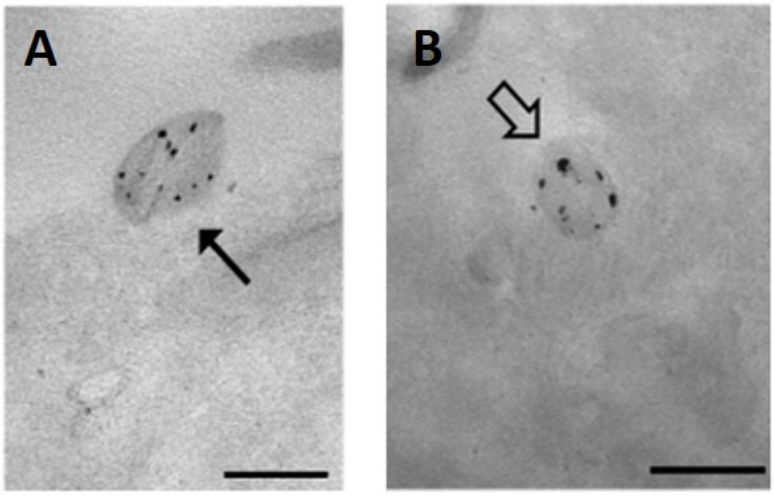

Fig. 2: TEM images of C2C12 myoblasts treated with HA-NPs. AB-labelled NPs occur at the cells surface (arrow in A) and free in the cytosol (open arrow in B). Bars: 200 nm. (Carton et al., Eur. J. Histochem., 2019).

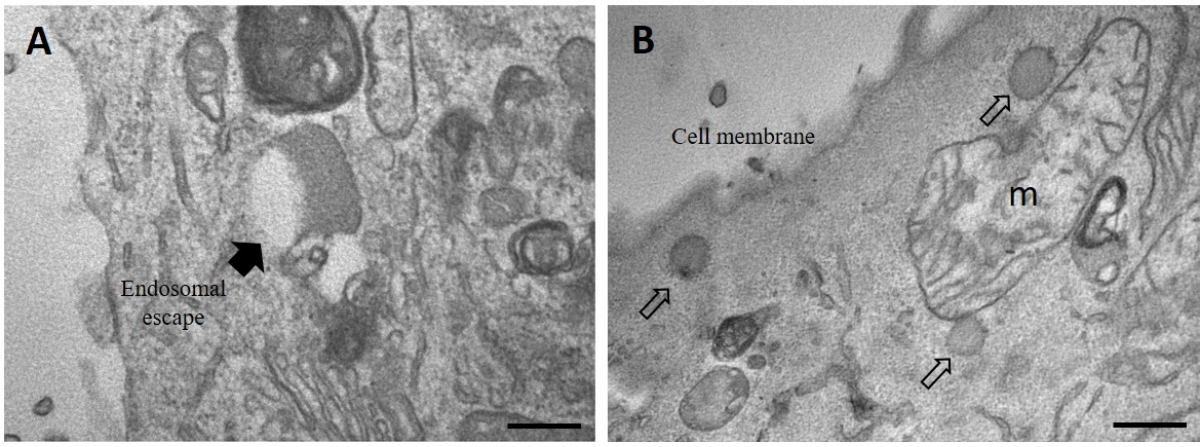

Fig. 3: TEM images of C2C12 myoblasts treated with HA-NPs. NPs were found to escape endosomes (arrowhead in A), thus accumulating free in the cytosol (open arrows in B). m, mitochondrion. Bars: 200 nm.

Type of presentation: Oral

LS1-O-2543 Antimicrobial photodynamic therapy effects on Gram-negative and Gram-positive bacteria observed using light-induced in-situ TEM

Kaczmarczyk O.[1], Maliszewska I.[1], Matczyszyn K.[1], Żak A. M.[2]

[1]Faculty of Chemistry, Wroclaw University of Science and Technology, Wroclaw, Poland, [2]Faculty of Mechanical Engineering, Wroclaw University of Science and Technology, Wroclaw, Poland

Email of the presenting author: olga.kaczmarczyk@pwr.edu.pl

Antimicrobial photodynamic therapy (aPDT) is a modern, non-invasive type of treatment, in which the cytotoxic effect is based on the generation of damaging reactive oxygen species upon the light irradiation of photosensitizer. As microbes are continuously becoming more resistant to known medicines, aPDT may one day become the only harmless cure for infections caused by highly pathogenic species. A profound understanding of the mechanism will help to improve the efficiency of the therapy, which depends on both type of photosensitizer and microbe[1]. In order to study the effects of aPDT in high resolution, it is necessary to go beyond the limits of light microscopy and take advantage of transmission electron microscopy (TEM). With a specially designed light illumination system consisting of a diode laser connected to the microscope column of Hitachi H-800 TEM via optical fibre, we performed in-situ observations of the aPDT processes in liquid. The antimicrobial effects were studied for a few bacteria-photosensitizer combinations. Liquid samples were prepared by sandwiching bacteria with solutions between two standard carbon films. The cells were illuminated for up to 30 minutes with an intensity of 250 mW/cm^2 and a light wavelength of 660 nm, which is strongly absorbed by photosensitizers used in the research. To decrease the unfavourable effects of the electron beam, the electron source was switched on only during taking the image. With low observation time and reduced electron dose, the damage was low enough to obtain reliable results as reported before[2,3]. The effect of light irradiation was studied on Gram-positive *Staphylococcus aureus* and Gram-negative *Acinetobacter baumannii* encapsulated with Methylene Blue. For both bacteria, the damage and oxidation products were visible at the cell-liquid interface (Fig. 1). To compare the effects of distinct photosensitizers, the research was also focused on the comparison of changes in *Staphylococcus aureus* cells illuminated in the same conditions, but with disulfonated hydroxyaluminum phthalocyanine instead. The results showed no significant changes in the cell's envelope, indicating that probably different antimicrobial mechanisms occurred for this photosensitizer (Fig.2). The presented results show a possibility to perform light-induced in-situ TEM imaging on cells with lowered electron damage as well as the method for observing the antimicrobial action of photosensitizers.

[1] F. Cieplik, D. Deng, W. Crielaard, W. Buchalla, E. Hellwig, A. Al-Ahmad, T. Maisch, Crit. Rev. Microbiol. 2018, 44, 571.
[2] A. M. Żak, O. Kaczmarczyk, M. Piksa, J. Grzęda, K. Matczyszyn, Ultramicroscopy 2021, 230, 113388.
[3] A. M. Żak, O. Kaczmarczyk, M. Piksa, K. Matczyszyn, Photodiagnosis Photodyn. Ther. 2021, 35, 102463.

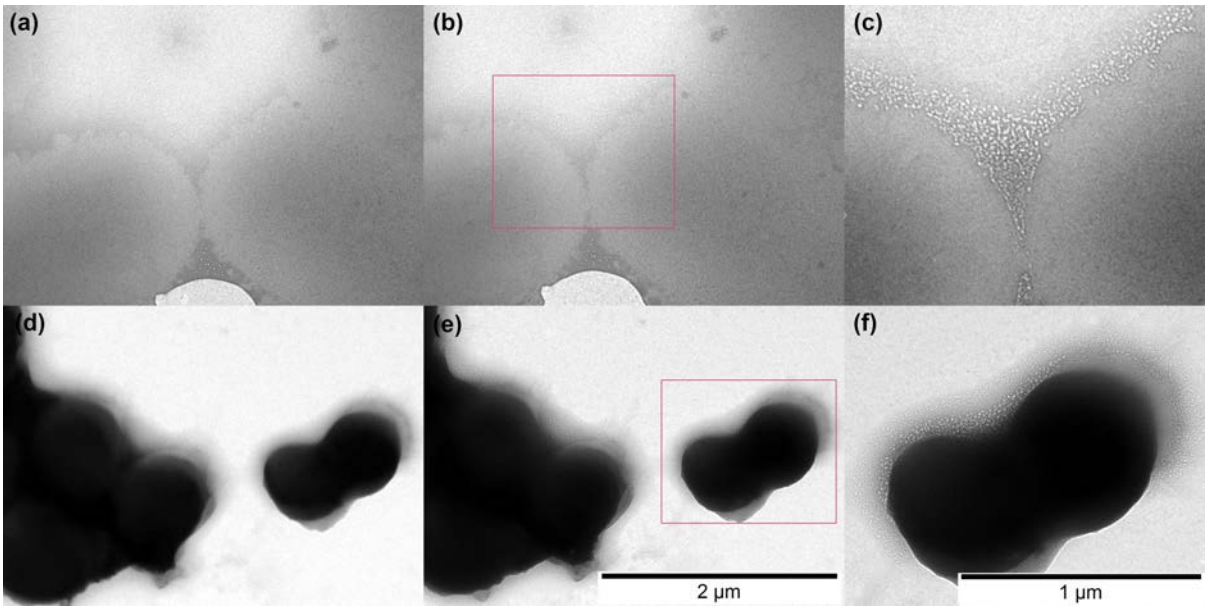

Fig. 1: TEM images of bacterial cells surrounded by Methylene Blue. The upper row presents *Acinetobacter baumannii* (a) before and (b) after 5 minutes of light illumination. The lower row shows *Staphylococcus aureus* (d) before and (e) after 8 minutes of light illumination. Images (c) and (d) present magnified areas indicated in (b) and (d).

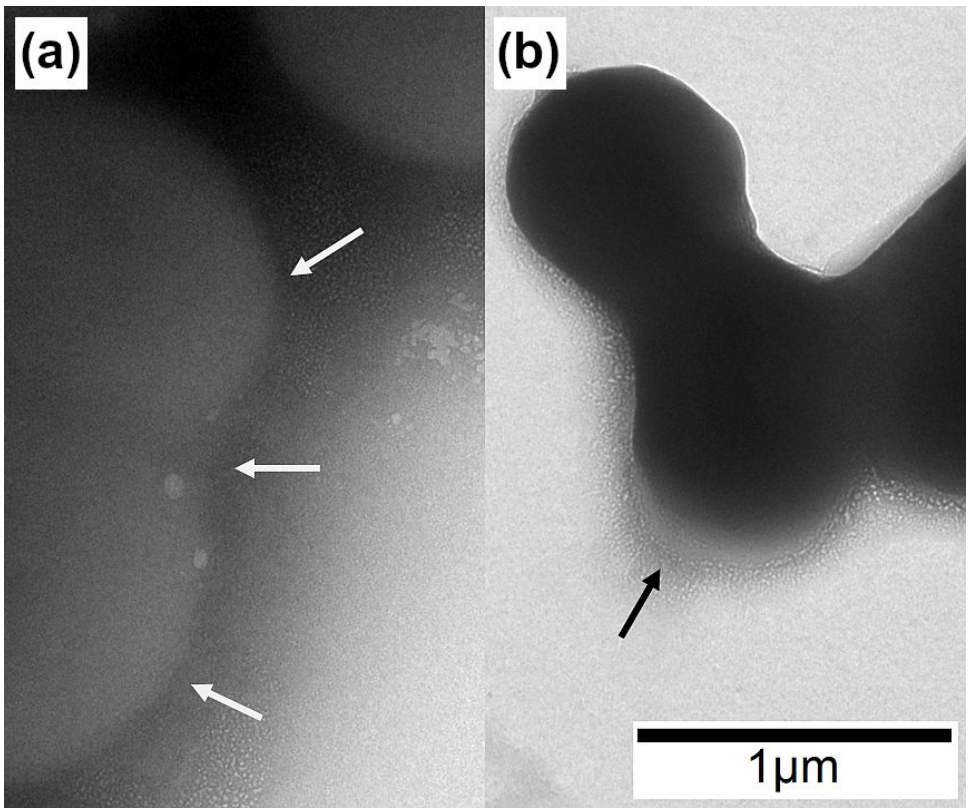

Fig. 2: TEM images of *Staphylococcus aureus* in disulfonated hydroxyaluminum phthalocyanine (a) and Methylene Blue solutions (b) after 20 minutes of light irradiation. The cells' outer layer near the interface with photosensitizer is damaged only in the case of Methylene Blue (b).

Type of presentation: Oral

LS1-O-2655 Why do Schwann cells like spider silk?

Ploszczanski L.[1], Peter K.[1], Sinn G.[1], Naghilou A.[2], Radtke C.[2], Lichtenegger H.[1]

[1]University of Natural Resources and Life Sciences, Institute of Physics and Materials Science, Vienna, [2]Med Uni Vienna/Vienna General Hospital, Plastic and Reconstructive Surgery, Vienna, Austria

Email of the presenting author: Leon.ploszczanski@boku.ac.at

Spider silk (SPSI) has been established as one of nature's most fascinating materials due to its unique properties. A remarkable application of the SPSI is its use in reconstructive medicine as nerve guidance structure/filament for nerve regeneration [1]. The Schwann cells (SCs), which are a crucial part of the nerve regeneration process adhere to SPSI and migrate along it to support axonal elongation [2]. SPSI degrades without inflammatory response or physiological pH changes. However, the interaction between the SCs and the silk and by that the SPSI properties, that promote SC adhesion are still unclear. The aim of this project is to elucidate material properties of SPSI, that are crucial for its unique performance in nerve regeneration. Not all spider silks show the same medical success, and we believe that properties such as composition, ultrastructure, and mechanical behaviour have a pronounced influence on the acceptance of SPSI by SCs. Therefore, by combining experiments consisting of in vitro studies and the material characterization of various SPSIs, the properties, which are responsible for the advanced success of SPSI in nerve regeneration, will be clarified.

[1] Radtke, C., et al., Spider Silk Constructs Enhance Axonal Regeneration and Remyelination in Long Nerve Defects in Sheep. PLOS ONE, 2011. 6(2): p. e16990.

[2] Kornfeld T, et al. Spider silk nerve graft promotes axonal regeneration on long distance nerve defect in a sheep model, Biomaterials, 2021 Feb 2;271:120692. doi: 10.1016/j.biomaterials.2021.120692.

[3] Riekel, C., et al., Nanoscale X-Ray Diffraction of Silk Fibers, Frontiers in Materials, 2019. 6(315).

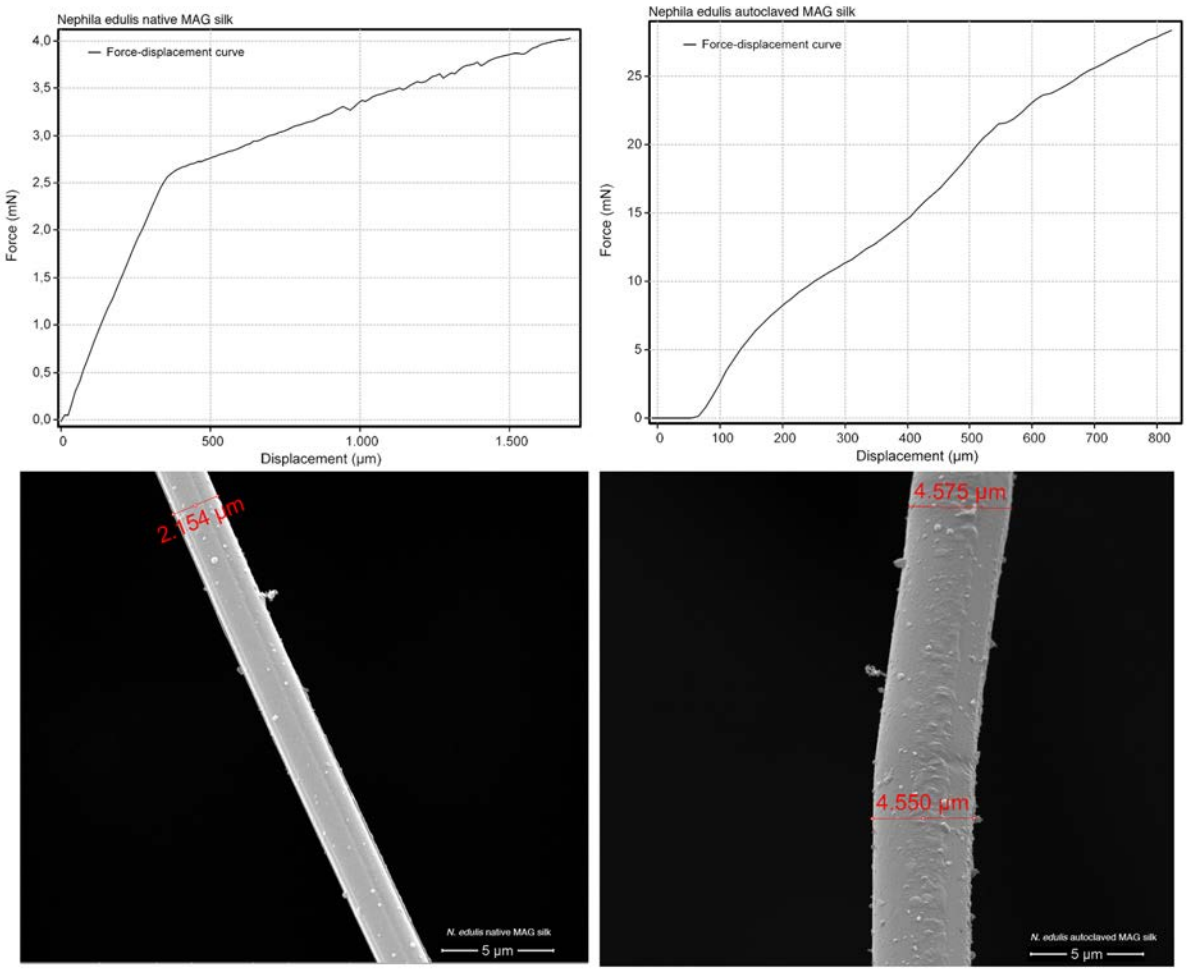

Fig. 1: Force-displacement curves and SEM micrographs of the native and autoclaved *N. edulis* MAG SPSI

Type of presentation: Invited

LS1-IN-3008 Transmission electron microscopy in research and diagnostics - new challenges in the omics era

Labudović Borović M. M.[1], Janković R. M.[2], Bogdanović L.[2], Seke M.[3], Rašić D. M.[4], Bajletić M. I.[1], Đorđević A.[3]

[1]Institute of Histology and Embryology „Prof. dr Aleksandar Đ. Kostić “, Faculty of Medicine, University of Belgrade, [2]Institute of Pathology, Faculty of Medicine, University of Belgrade, [3]University of Novi Sad, Faculty of Sciences, [4]Ophthalmology Clinic, Clinical Centre of Serbia

Email of the presenting author: sborovic2001@yahoo.com

The burden of innovative technologies in genomics, proteomics and transcriptomics puts a pressure in everyday diagnostics and makes us continually wondering whether techniques of light and transmission electron microscopy are sufficient, applicable, and precise enough to lead us to credible diagnosis that could be further confirmed with molecular methods.
The review is focused on the diagnostic issues recognized and proved by means of the transmission electron microscopy (TEM) as the first line in diagnostics followed by molecular methods. In these cases, the diagnostic protocols, employing TEM, are activated by specific set of patients' symptoms without previous knowledge of potential genetic causes. Protocols include tissue biopsy samples analysed by light microscopy and subsequently TEM analysis.
Special set of diagnostic items is the one where diagnosis was proved by means of TEM and then new scope of mutations was found accordingly. These include Cerebral Autosomal Dominant Arteriopathy with Subcortical Infarcts and Leukoencephalopathy – CADASIL where the TEM is still the primary diagnostic tool for the recognition of pathognomonic GOMs (granular osmiophilic material). Protocol where the diagnostics starts with the TEM lead us to the discovery of new, previously unknown, mutation in the scope of mutations causing CADASIL - Notch3 Gly89Cys on exon 3.
TEM proved useful in the diagnosis of a rare gastrointestinal disease with chronic pseudoopstruction - Hollov Visceral Myopathy. The indication was obtained at light microscopy and paraffin sections, and confirmed by TEM, while the final confirmation by means of genetics was obtained later.
Exclusive group of challenging issues for TEM experts are diagnostic dilemmas where initial diagnosis obtained with the light microscopy and immunohistochemistry needed additional confirmation with the TEM. These are myxofibrosarcoma conjunctivae, Merkel cell carcinoma of the eyelid and psammomatoid variant of juvenile ossifying fibroma.
TEM is, still, especially important in nephropathology as the primary diagnostic tool for the diagnosis of progressive hereditary nephritis - Alport Syndrome and nonprogressive hereditary nephritis - thin basement membrane disease.
Recently, a special diagnostic importance of TEM was found in the diagnosis of posttransplantational liver disease in children, where symptoms were followed by no morphological changes obvious on light microscopy, but recognizable at the TEM level.
Finally, the review will address to research problems in nanotechnology and nano systems for specific delivery of chemotherapeutics.

Acknowledgement: The research is supported by the Research grant No III45005 of the Ministry of Education and Science, Republic of Serbia.

Type of presentation: Oral

LS1-O-2804 Neurons and glial cells appear to store and release human brain ferritin at different rates

Leitinger G.[1], Sunkara S.[1], Radulovic S.[1], Lipovsek S.[2], Haybäck J.[3], Ropele S.[4]

[1]Division of Cell Biology, Histology and Embryology, Medical University of Graz, Graz, Austria, [2]Department of Biology, Faculty of Natural Sciences and Mathematics, University of Maribor, Maribor, Slovenia, [3]Institute for Pathology, Neuropathology and Molecular Pathology, Medical University of Innsbruck, Innsbruck, Austria, [4]Department of Neurology, Medical University of Graz, Austria

Email of the presenting author: gerd.leitinger@medunigraz.at

The main storage protein for iron in the human brain is ferritin [1]. Since iron overload can go along with a number of neurological disorders, it is important to study the mechanisms of iron storage. Ferritins store several thousand iron atoms in their core (e.g. [2]). This high concentration of iron within a few square nanometers allows using analytical electron microscopy for quantifying loaded ferritins. For this, human post mortem brain tissue is embedded in plastic and thin sectioned. The sections are visualized with a TEM and a Gatan GIF energy filter used to produce iron L-elemental maps. The maps allow quantifying those ferritin cores that are filled with iron, and an accompanying bright field overview of the respective brain area allows identifying the majority of the cell types involved. An example for bright field electron micrographs and an iron map is shown in Fig. 1.

We analyzed samples taken from four different brain areas of six deceased human subjects. We also determined the total iron concentration in neighboring samples using inductively coupled plasma mass spectrometry (ICPMS), and mapping the iron concentration R2*using quantitative magnetic resonance imaging (qMRI) of the same brain areas of the other brain half. We found two major changes in the ferritin content and in its cellular distribution.

First, the longer the post mortem interval, the less iron is found in ferritin cores [3]. In contrast, the total iron concentration as measured using qMRI an ICPMS fail to show post mortem a decline in iron concentration [3]. This indicates that ferritins may be degraded post mortem, but the iron remains in the brain in spite of ferritin degradation.

The second important finding was that the cellular iron distribution depends on the amount of iron stored in the brain [3]. Most loaded ferritins are always found in oligodendrocytes. But the percentage of loaded ferritins found in neurons increases with increasing iron load [3].

This may signify that glial cells and neurons store and release ferritin iron at different rates.

References:

[1] Finazzi, Dario and Arosio, Paolo (2014): Biology of ferritin in mammals: an update on iron storage, oxidative damage and neurodegeneration. In Archives of toxicology 88 (10), pp. 1787–1802. DOI: 10.1007/s00204-014-1329-0.

[2] Jian, Nan et al. (2016): Morphology of the ferritin iron core by aberration corrected scanning transmission electron microscopy. In Nanotechnology 27 (46), 46LT02. DOI: 10.1088/0957-4484/27/46/46LT02.

[3] Sunkara, Sowmya et al. (2022) Changes in cellular ferritin distribution of human brain tissue during autolysis revealed using analytical electron microscopy BioRXives. doi: https://doi.org/10.1101/2022.01.26.477869

Acknowledgement: Grant sponsor: Austrian Science Fund, P 29370, Medical University Graz
Ethics Approval 28-549 ex 15/16. Prof. Walter Gössler measured the iron concentrations.

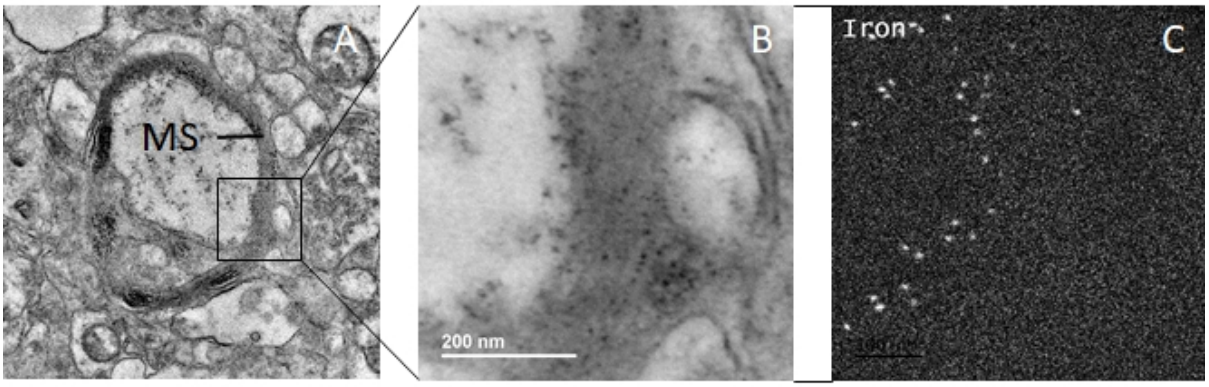

Fig. 1: A Bright Field electron micrograph of a sample of a human putamen. 2500 x. The myelin sheath (MS) is a marker for the axon and its surrounding oligodendrocyte. B Bright Field at 80 kx. C Corresponding iron L-elemental map showing ferritin cores as bright spots. Most ferritins appear associated with the myelin sheath.

Type of presentation: Oral

LS1-O-2870 Evaluation of elements impurities in drugs according to pharmacopoeia by use FESEM-EDS technique.

Doulab R. A.[1]

[1]Electron microscope unit, Pharmacy college, Basra university, Iraq

Email of the presenting author: rafid.doulab@uobasrah.edu.iq

Elemental Impurities in Pharmaceuticals industry is indispensable to ensure of pharmaceuticals safety, for 24 elements Although atomic absorption and inductively coupled plasma are used in the U.S Pharmacopeia and the European Pharmacopoeia, FESEM with energy dispersive spectrometers can be applied as an alternative analysis method for quantitative and qualitative results for a variety of elements without chemical pretreatment, unlike other techniques.
This technique characterizes by shortest time, with more less contamination, no reagent consumption and generation of minimal residue or waste as well as sample preparations time limiting, with minimal analysis error. Simple dilution for powder or direct analysis for liquid, we analyzed the usefulness of EDS method in testing with field emission scanning electron microscopy (FESEM, SUPRA 55 Carl Zeiss Germany) with an X-ray energy dispersion (XFlash6l10 Bruker Germany). The samples analyzed directly without coating by applied 5µ of known concentrated diluted sample on carbon stub with accelerated voltage according to sample thickness, the result for this spot was in atomic percentage and by Avogadro converted factor the final result will be in microgram.

Acknowledgement: FESEM technique in pharmacopeia as standard methods like inductively coupled plasma both ICP-AES, ICP-OES and ICP-MS.

Element	Series	Unn [wt%]	C norm. [wt%]	C atom. [at%]	C error [wt%]
Carbon	K-series	66.58	66.58	73.02	22.08
Oxygen	K-series	32.22	32.22	26.52	11.56
Sulfur	K-series	0.18	0.18	0.33	0.18
Chlorine	K-series	0.31	0.31	0.12	0.13
Lead	M-series	0.09	0.09	0.10	0.10
Total		100.00	100.00	100.00	

Fig. 1: Results of EDS analysis of lead chloride experiment sample

Element	Series	Unn [wt%]	C norm. [wt%]	C atom. [at%]	C error [wt%]
Carbon	K-series	67.31	67.31	77.81	22.35
Oxygen	K-series	18.80	18.80	16.31	7.07
Selenium	L-series	9.68	9.68	1.70	1.46
Nitrogen	K-series	4.21	4.21	4.17	2.30
Total		100.00	100.00	100.00	

Fig. 2: Results of EDS analysis of selenium experiment sample

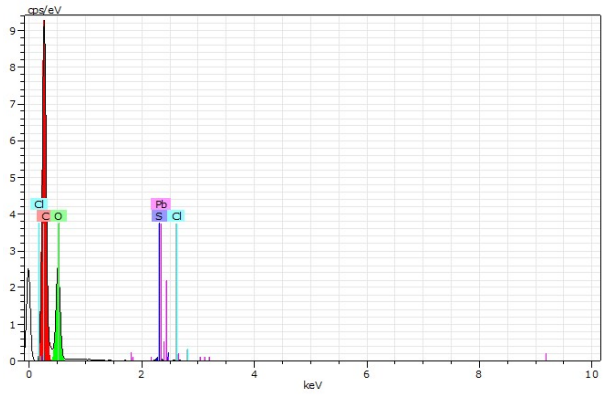

Fig. 3: Energy dispersive spectrum of lead chloride experimental sample.

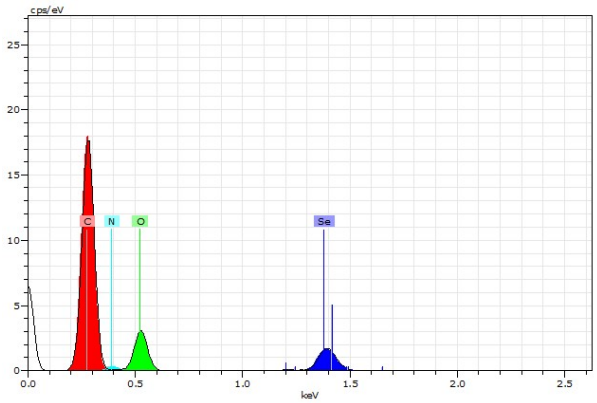

Fig. 4: Energy dispersive spectrum of selenium experimental sample.

Type of presentation: Poster

LS1-P-2519 Electron microscopy in the study of nanomaterial-cell interaction: involvement of autophagy

Condello M.[1], Meschini S.[1]

[1]National Center for Drug Research and Evaluation, National Institute of Health, Rome, Italy

Email of the presenting author: stefania.meschini@iss.it

The numerous and increasingly frequent applications of metallic nanomaterials in the biomedical field for the diagnosis and treatment of diseases have encouraged studies to rule out any toxicity. However, even in the absence of overt toxicity, electron microscopy can detect changes on the surface and inside the cell that can be correlated with cell physiology and biochemistry.
One of the phenomena observed following the interaction between cells and nanomaterials is the activation and/or deregulation of the autophagy process. Autophagy is an evolutionarily conserved cellular process in which organelles and macromolecules are delivered to lysosomes to be degraded. Many nanoparticles (NPs) can alter the autophagy pathway, leading to blockage of autophagic flux and accumulation of autophagosomes. The accumulation of the nanomaterial can be explained by an inhibition of the autophagy degradation capacity, inducing oxidative stress and inflammation.
Our electron microscopy observations have made a significant contribution to understanding the mechanism of NPs internalization, transport through the endo-lysosomal system and modification of autophagic flux. As shown by scanning electron microscopy (SEM) in Figure 1, colon cancer cells after interaction with ZnO-NPs have significant changes in surface area, swelling, rupture and loss of microvilli compared to the control. Transmission electron microscopy (TEM) observations showed aggregates of ZnO-NPs located in endocytic vacuoles (Figure 2A), which then combined with other vacuoles to form with undigested metal material. Some ZnO-NPs are located within the mitochondria, demonstrating the possible relationship between this organelle NPs and the induction of oxidative stress (Figure 2B).
TEM analysis of the immortalized mouse fibroblast cell line (Balb/3T3) showed that AuNPs are internalized and confined mainly to autophagosomes, endoplasmic reticulum and mitochondria (Figure 3). When AuNPs induce oxidative stress, cells activate the autophagy pathway as a survival mechanism to avoid cell death, if the intensity or duration of stress persists, activation of cell death is observed.
Finally, our study on the toxicity of Ag-NPs on the murine alveolar macrophage cell line MH-S showed that the nucleus and endoplasmic reticulum were morphologically well preserved, but mitochondrial destruction indicated oxidative damage. Figure 4 shows the deposition of NPs within large vesicles.
Our work has shown that morphological-ultrastructural analysis of different nanomaterials used for biomedical applications demonstrated the importance that maintaining a stable cellular oxidative system has in the delicate balance between normality and pathogenesis.

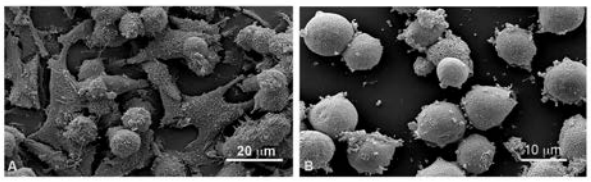

Fig. 1: SEM observations of untreated LoVo cells (A) and treated with ZnO-NPs (B).

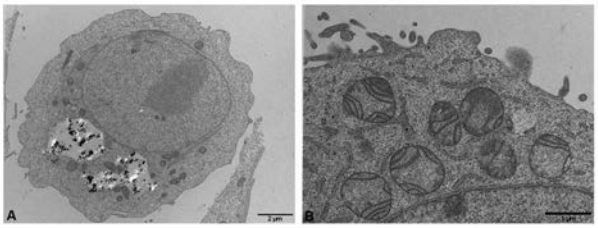

Fig. 2: TEM observations of LoVo cells treated with ZnO-NPs. (A) vacuoles containing ZnO-NPs. (B) oxidative stress induced by mitochondria damaged by ZnO-NPs.

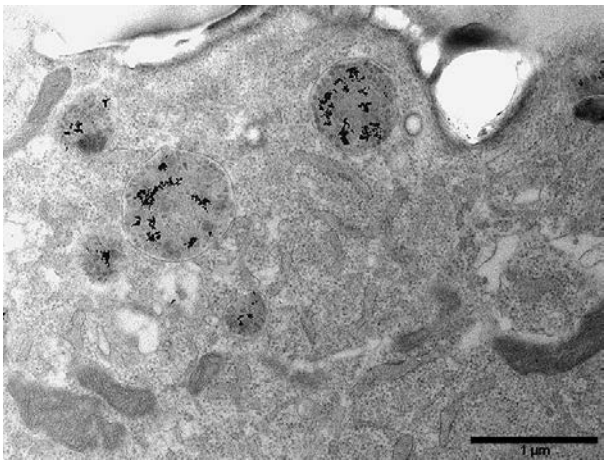

Fig. 3: Balb/3T3 cells showing huge vacuoles containing Au-NPs and material in the process of digestion.

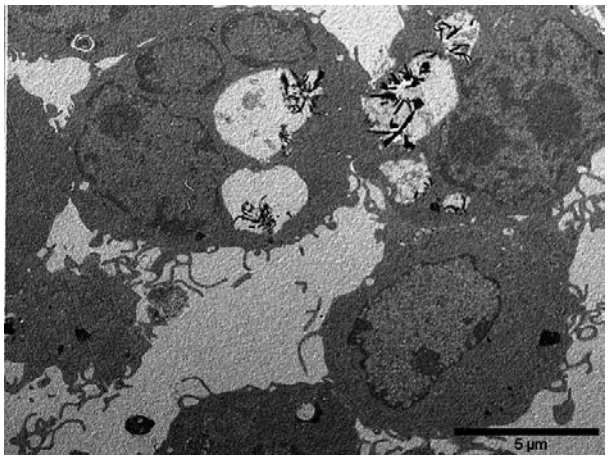

Fig. 4: TEM observations of MH-S cells, where Ag-NPs are deposited within large vesicles.

Type of presentation: Poster

LS1-P-2518 Ultrastructure analysis in the male reproductive system of different mammals exposed to ionizing radiation after the Fukushima accident: a comparative study

Gatti M.[1], Palmerini M. G.[2], De Rubeis M.[1], Mascitti I. A.[2], Yamashiro H.[3], Nottola S. A.[1], Macchiarelli G.[2]

[1]Department of Anatomy, Histology, Forensic Medicine and Orthopaedics, Sapienza University, Rome, Italy, [2]Department of Life, Health and Environmental Sciences, University of L'Aquila, L'Aquila, Italy, [3]Graduate School of Science and Technology, Niigata University, Niigata, Japan

Email of the presenting author: marta.gatti@uniroma1.it

Since the Fukushima Daiichi Nuclear Power Plant (FDNPP) accident, there was great attention on the exposure damages to low-dose-rate (LDR) radiation on the biological system [1]. Particularly, the male reproductive function is sensitive to ionizing radiation, with implications connected to infertility [1,2]. This preliminary study aimed to evaluate the effects of LDR on the male reproductive system of three different wild mammals captured from the FDNPP accident ex-evacuation area: 1) the Large Japanese field mouse (Apodemus speciosus), 2) the raccoon (Procyon lotor) and 3) the Japanese macaque (Macaca fuscata) [3]. We analysed the testis ultrastructure in Apodemus speciosus and Procyon lotor and the spermatozoa ultrastructure in Macaca fuscata. After collection, samples were fixed in glutaraldehyde 2.5%/PBS and subjected to the standard preparative for Light Microscopy (LM) and Transmission Electron Microscopy (TEM) [2]. Results showed general good preservation of seminiferous tubules both in mice and in raccoons. TEM analysis revealed the occasional presence of lipid droplets in the sperm cytoplasm and interstitial cells of Apodemus speciosus and Procyon lotor. Macaque spermatozoa were also well-preserved, with ovoid and flatheads, adherent plasma membranes, and large electron-dense nuclei covered by apical acrosomes. However, rare alterations to the mitochondrial and plasma membrane ultrastructure were noted in a few Macaca fuscata spermatozoa. In conclusion, although testes and spermatozoa are hypersensitive to radiation, long-term LDR exposure associated with the FDNPP accident had no significant effects on the male reproductive organs in wild animals. These ultrastructural data may be used for further studies on the male reproductive potential of Japanese mammals, inhabiting the Fukushima area and chronically exposed to LDR radiation.

References

[1] Takino S, Yamashiro H, Sugano Y, et al. Analysis of the effect of chronic and low-dose radiation exposure on spermatogenic cells of male large Japanese field mice (Apodemus speciosus) after the Fukushima Daiichi nuclear power plant accident. Radiat Res. 2017; 187:161-168.

[2] Komatsu K, Iwasaki T, Murata K, et al. Morphological reproductive characteristics of testes and fertilization capacity of cryopreserved sperm after the Fukushima accident in raccoon (Procyon lotor). Reprod Domest Anim. 2021;56(3):484-497.

[3] Hayama S, Nakiri S, Nakanishi S, et al. Concentration of radiocesium in the wild Japanese monkey (Macaca fuscata) over the first 15 months after the Fukushima Daiichi nuclear disaster. PLoS One. 2013;8(7):e68530.

Type of presentation: Poster

LS1-P-2817 Tundra TEM: tool 'easy of use' for new commers to Cryo EM

Hlavenkova Z.[1], Karia D.[2], Malinsky M.[1], Dolezal V.[1], Siwy R.[1], Cechmanek M.[1], Knippenberg B.[2], Cervinkova M.[1], Lingbo Y.[2]

[1]Thermo Fisher Scientific Brno s.r.o., Materials & Structural Analysis, Brno, Czech Republic , [2]Materials and Structural Analysis Division, Thermo Fisher Scientific, Achtseweg Noord, Eindhoven, Netherlands

Email of the presenting author: zuzana.hlavenkova@thermofisher.com

Cryo-electron microscopy (cryo-EM) , especially the Single Particle Analysis (SPA), is nowadays a widely used technique for getting answers of biological questions, finding novel structural and mechanistic perspectives of multitude of biological macromolecules. As the popularity of this technique increases, greater efficiency and accessibility is expected from both microscopic and biologic audience with no EM experience. Operating the electron microscope requires an experienced person with extensive training or a dedicated facility manager to support the microscope operation, optics alignment and data collection.
The Thermo Scientific Tundra Cryo-Transmission Electron Microscope (Cryo-TEM) was developed to accommodate the need of 'easy to use' cryo-TEM. Tundra operates on 100keV accelerating voltage, dedicated to the one SPA technique. New users will be able to operate the microscope and collect data after ~1-day of training, due to two major technical innovations: new cryo sample transfer – Semi Automated Loader and simplified user interface based on EPU SW with built-in fully automated microscope daily alignments.
The users can load the cryo sample to TEM column with minimal manual interaction, without the fear to break the microscope. The users can also set up optics according his experiment by one mouse click and then directly start to investigate the quality of the sample without need of any manual microscope alignment such as "center the beam" or "center the C2 aperture". The automated data collection can be set up in few minutes. The optics for high resolution i.e. astigmatism free and coma free, is fully automated and can be executed by a single click. to With benchmark protein apoferritin, we were able to achieve a resolution of 2.8Å (Fig. 1).
Tundra Cryo-TEM allows scientists to focus on science, to study the protein structure and to understand protein function, without a deep understanding the physics of electron microscope and extensive training.

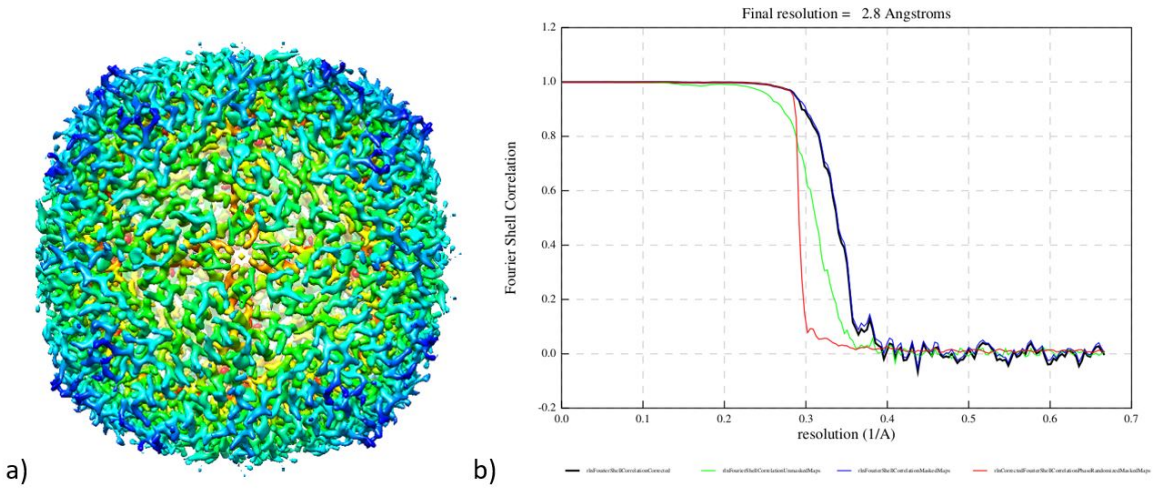

Fig. 1: Structure of Apoferritin protein determined at 100 keV. a) Visualization sharpened masked 3D reconstruction on 3Å resolution, b) Gold-standard FSC plot corresponding to the calculated map, showing the correlation between the phase-randomized (yellow), unmasked (blue) and masked (red) half-maps.

Type of presentation: Poster

LS1-P-2811 Histopathological and ultrastructural effects of chronic administrated high dose dehydroepiandrosterone on liver and kidney of male rats

Senturk G. E.[1], Sag F. B.[1], Sahin H.[1], Sezer Z.[1]

[1]Department of Histology and Embryology, Cerrahpasa Faculty of Medicine, Istanbul University-Cerrahpasa, Istanbul, Turkey

Email of the presenting author: hakan.ahin@gmail.com

Dehydroepiandrosterone (DHEA) is a steroidal hormone that acts as a precursor to androgens and estrogen. DHEA can be used exogenously as a dietary supplement. However, it has both beneficial and harmful effects on the cells according to literature. Our aim in this study is to investigate chronic and high dose administration of DHEA effects on the liver and kidney of young male rats on both light microscopic and electron microscopic levels. For this purpose, male 21-days old Sprague-Dawley rats were divided into control (n=4) and DHEA (n=8) groups. DHEA was injected at 60 mg/kg/day subcutaneously for a total of 28 days in the DHEA group while only sesame oil was injected to the control group. Next, the livers and kidneys of the animals were collected and prepared for both light microscopy and transmission electron microscopy (TEM) analyses. As a result, both the liver and kidney histomorphology showed severe damage under light microscopy. TEM also confirmed the ultrastructural changes in both tissues.

LS2 Microscopy for healthier environment: Microorganisms, plants, and Host-Pathogen Interactions

Type of presentation: Invited

LS2-IN-2966 Shedding new light on plant biology – automated long-term vertical-stage microscopy at high resolution

Malínská K.[1], Kashkan I.[1], Hauschild R.[2], Jelínková A.[3], Petrášek J.[1,3]

[1]Imaging Facility, Institute of Experimental Botany ASCR, Prague, Czech Republic, [2]Imaging & Optics Facility, Institute of Science and Technology Austria, Klosterneuburg, Austria, [3]Laboratory of Hormonal Regulations in Plants, Institute of Experimental Botany ASCR, Prague, Czech Republic

Email of the presenting author: malinska@ueb.cas.cz

Non-invasive *in vivo* imaging of living organisms in high resolution is the trend in microscopy today. One of the most significant challenges in plant *in vivo* microscopy is the orientation of the sample. Most microscopes mount the specimen horizontally, while plants grow vertically. For this reason, Imaging Facility of the Institute of Experimental Botany Czech Academy of Sciences (IFIEB) has installed a customized solution of a confocal microscope optimized for plant research.
Previously, when inspecting the root with a typical microscope, root attempted to bend downwards but it was constrained by a slide. The plant was therefore permanently gravistimulated. This influenced the obtained data by possible unwanted artefacts and made some experiments on growing roots completely impossible. In 2019, inspired by IST Vienna [1], local representatives of the Zeiss company have turned their Zeiss LSM 880 with Airyscan detector on its side at a 90 degree angle to optimize it for plant research in the IFIEB. In this setup, vertical sample mounting preserves the natural direction of plant growth and enables long-term imaging on plants acquired with confocal or Airyscan resolution. High magnification objectives (40x and 63x) with optimized immersion liquids are installed. In addition, our system is equipped with the stage rotary insert that enables further non-invasive application of gravistimuli on the seedlings, growing for a prolonged time under the microscope.
A long-term vertical-stage imaging opened up new challenges that needed to be addressed, including how to compensate for root growth outside of field of view. After initial tile scanning, root growth is now compensated by microscope stage movement, allowing time-lapse imaging in a single frame. In addition, plant leaves can be illuminated to preserve their photosynthetic activity. Our system is currently used to study processes of signal transduction and hormonal regulations during seed germination, root protophloem development or the impact of artificial plant root illumination. The possibilities of the system will be summarized in the talk.
[1] D. von Wangenheim, R. Hauschild, M. Fendrych, V. Barone, E. Benková, J. Friml “Live tracking of moving samples in confocal microscopy for vertically grown roots.” Elife, 6, e26792 (2017).

Acknowledgement: Supported by the MEYS CR (Large RI Project LM2018129 Czech-BioImaging).

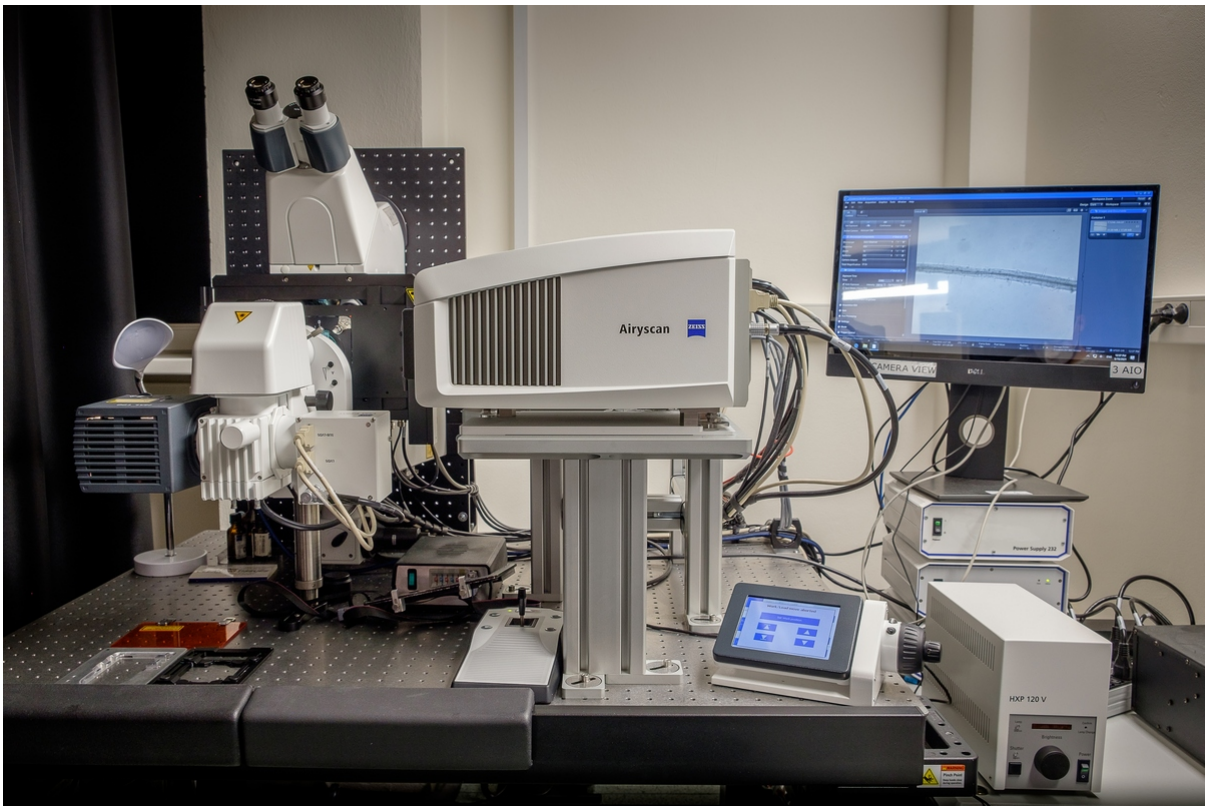

Fig. 1: Plant-optimized Zeiss LSM880 with Airyscan detector allowing vertical sample mounting.

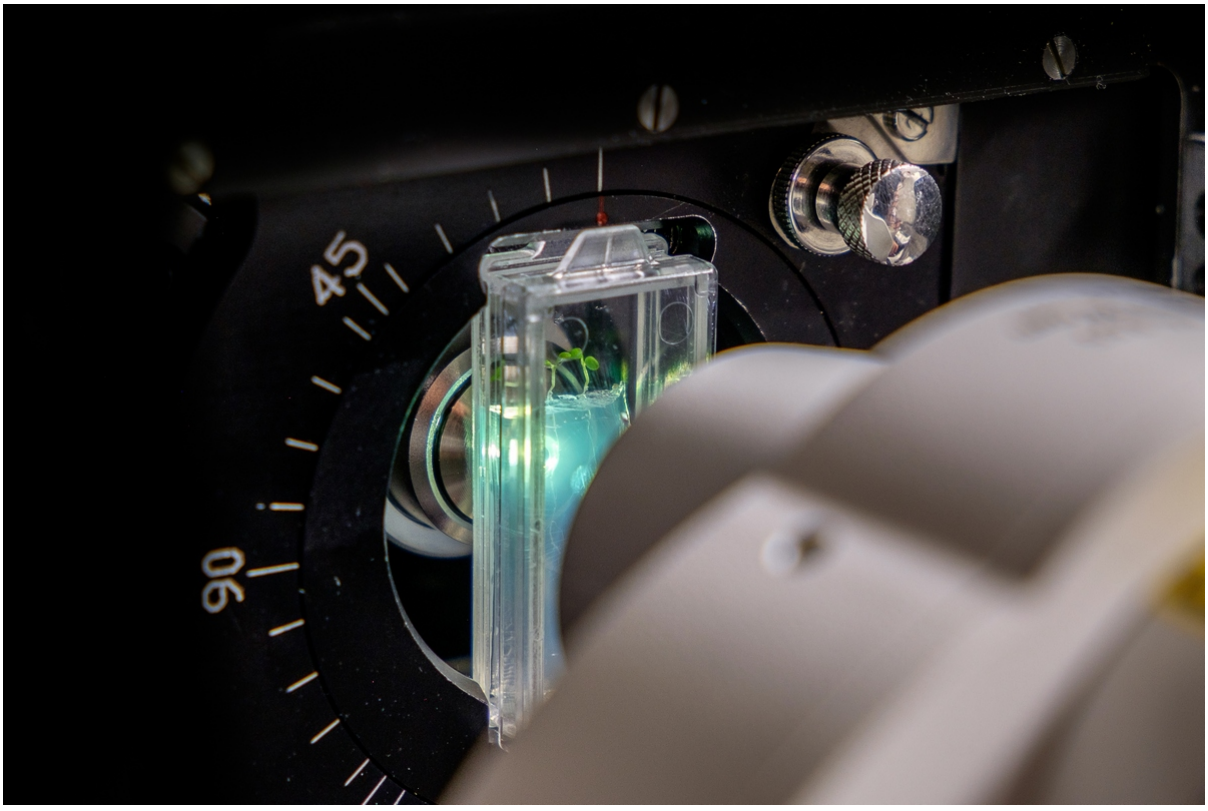

Fig. 2: Plant growing in a coverglass chamber during a long-term imaging.

Type of presentation: Invited

LS2-IN-2688 Recent advances in plant development and plant-microbe interactions employing light-sheet and super-resolution microscopy

Ovečka M.[1], Sojka J.[1], Tichá M.[1], Komis G.[1], Šamajová O.[1], Šamaj J.[1]

[1]Department of Biotechnology, Faculty of Science, Palacký University Olomouc, Šlechtitelů 27, 783 71 Olomouc, Czech Republic

Email of the presenting author: miroslav.ovecka@upol.cz

Plant growth and development can be visualized by different microscopy methods. However, live-cell imaging of plants is prone to several limitations depending on optical properties of plant cell surfaces, presence of vacuoles, and special environmental requirements for undisturbed growth and development during imaging. In addition, crop plant species are rather bulky, compromising the possibility to mount them onto a glass slide covered by coverslip used in classical microscopy imaging. Better understanding early plant development, cell patterning and organogenesis, as well as plant-microbe interactions, is indispensable for crop biotechnological research. However, it requires improvements and adaptations of traditional microscopy imaging approaches. Subcellular architecture, organization and dynamics of most organelles in cells of living plants can be monitored at the nanoscale using super-resolution microscopy methods, such as structured illumination microscopy (SIM) and Airyscan confocal laser scanning microscopy (ACLSM). On the other hand, light-sheet fluorescence microscopy (LSFM) is an ideal method for long-term bioimaging of living plants depicting their development at physiological conditions (Ovečka et al. 2018). We developed reliable and broadly applicable protocols for short-term bioimaging of plant cells using SIM (Komis et al. 2015) and long-term developmental imaging of plants using LSFM (Ovečka et al. 2015). We have used these advanced microscopy methods to address diverse scientific questions, such as visualization of microtubule and actin dynamics during plant morphogenesis, signalling by mitogen-activated protein kinase during cell division, nuclear changes in diverse root developmental zones and tissues, and contribution of vesicular trafficking to the growth of root hairs. Although most of these studies were performed in the model plant Arabidopsis thaliana, we successfully established LSFM imaging also in crops such as alfalfa (Medicago sativa) and barley (Hordeum vulgare). We have used advantage of LSFM and ACLSM to visualize M. sativa interactions with symbiotic nitrogen-fixing bacteria Sinorhizobium meliloti by employing transgenic plants carrying molecular marker for in vivo visualization of actin cytoskeleton. These new microscopy methods significantly broadened our understanding of molecular and cellular mechanisms involved in the plant development and interaction with microbes.

References

[1] Komis et al. (2015) Nature Protocols 10, 1248-1263.
[2] Ovečka et al. (2015) Nature Protocols 10, 1234-1247.
[3] Ovečka et al. (2018) Nature Plants 4, 639-650.

Acknowledgement: Supported by GAČR, project No. 19-18675S, and by ERDF project "Plants as a tool for sustainable global development", No. CZ.02.1.01/0.0/0.0/16_019/0000827.

Type of presentation: Oral

LS2-O-2638 Borrelia – host interactions: zoom in on the big picture

Strnad M.[1,2], Rego R.[1,2], Oh Y.[3], Hinterdorfer P.[3], Nebesářová J.[1,2], Vancová M.[1,2]

[1]Biology Centre CAS, Institute of Parasitology, Czech Republic, [2]Faculty of Science, University of South Bohemia, Ceske Budejovice, Czech Republic, [3]Institute of Biophysics, Johannes Kepler University Linz, Austria

Email of the presenting author: martin.strnad.cze@gmail.com

As opposed to pathogens passively circulating in the body fluids of their host, pathogenic species within the Spirochetes phylum are able to actively coordinate their movement in the host to cause systemic infections. The studies were conducted with the intention to bring together cutting-edge imaging methods and applications in order to illustrate how imaging can answer pathogenesis-related questions in Lyme disease at various resolution scale (Fig. 1). Correlative light and electron microscopy, atomic force microscopy-based single-molecule force spectroscopy and solution nuclear magnetic resonance have been used to shed light on the underlying mechanisms associated with Lyme disease Borrelia infection. Specifically, the key molecular players (decorin binding proteins) and interactions responsible for the variance in the pathogenicity and disease outcome of Borrelia species have been studied. The results show that spirochetes are able to leverage a wide variety of adhesion strategies through force-tuning transient molecular binding to extracellular matrix components, which concertedly enhance spirochetal dissemination through the host.

Acknowledgement: This work was supported mainly by the Grant Agency of the Czech Republic (17-21244S) and Czechoslovak Microscopy Society.

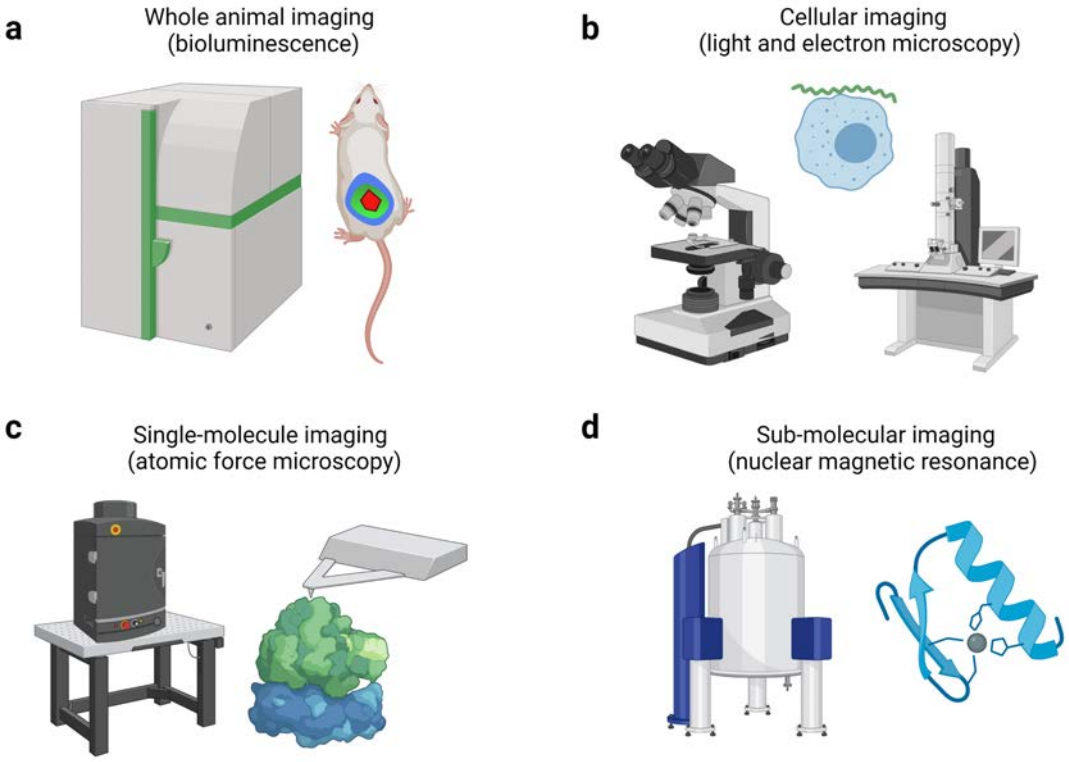

Fig. 1: Bioluminescence enables to follow the infection in a living animal (a). Light and electron microscopy provide cellular-level understanding of infection (b). Atomic force microscopy enables to study the interactions at the single-molecule level (c) and nuclear magnetic resonance can determine the binding site with amino acid precision (d).

Type of presentation: Oral

LS2-O-2661 Surface Coating-Modulated Phytotoxic Responses of Silver Nanoparticles in Chlorella vulgaris

Komazec B.[1], Lyons D. M.[2], Peharec Štefanić P.[1]

[1]Department of Biology, Faculty of Science, University of Zagreb, Zagreb, Croatia, [2]Center for Marine Research, Ruđer Bošković Institute, Rovinj, Croatia

Email of the presenting author: bruno.komazec@biol.pmf.hr

Silver nanoparticles (AgNPs) attract a great deal of attention due to their antimicrobial effects, for which they are implemented in a wide range of commercial products. However, due to their reactivity and toxicity, they pose a significant risk to aquatic ecosystems. To evaluate the impact of AgNPs on aquatic habitats, Chlorella vulgaris was used as a model organism. To assess the effect of AgNPs on C. vulgaris, algal cultures were grown in liquid BBM nutrient medium for 4 days after which they were exposed to AgNPs coated with citrate or CTAB, and to AgNO3 which was used as ionic Ag control. Concentration endpoints were obtained by growth inhibition test (72 h) and the estimated 25% growth rate inhibition (EC25) values for AgNP-citrate, AgNP-CTAB and AgNO3 were 0.188 mg L-1, 0.895 mg L-1 and 0.130 mg L-1, respectively. After 72h-treatment, the amount of synthesized oxygen, and photosystem II efficiency were analysed to address the impact of AgNPs on the photosynthetic apparatus. Furthermore, reactive oxygen species (ROS) levels and membrane lipid damage were analysed to investigate how well algae cells cope in the presence of AgNPs. To analyse ROS formation, algal suspensions were incubated with fluorogenic dyes (H2DCFDA and DHE) and visualized by a fluorescence microscope. To visualize ultrastructural changes, ultrathin sections of algal cells were analysed by transmission electron microscope (TEM). To further investigate the interaction between AgNPs and algal extracellular polymeric substances (EPS), cells were observed directly by TEM, and by fluorescence microscopy using FITC-labelled lectins. Obtained results indicate a differential effect of differently coated AgNPs on C. vulgaris since a significant reduction in newly synthesized oxygen and PSII efficacy after all treatments compared to the control were observed. Furthermore, differentially increased ROS content after all treatments (Fig. 1), in regard to used coatings, compared to control is suggestive of membrane lipids damage through ROS molecules. TEM analyses showed damaged ultrastructure (Fig. 2) with multiple NPs in EPS of algal cells (Fig. 3), while fluorescence microscopy showed increased EPS synthesis after all treatments, especially after AgNPs-CTAB, which could alleviate AgNPs toxic effect (Fig. 4). In conclusion, all forms of silver (AgNP-citrate, AgNP-CTAB and AgNO3) showed an adverse and detrimental effect primarily on the photosynthetic apparatus and membrane lipids mostly through increased synthesis of ROS molecules, where AgNP-citrate had most damaging effect. Due to the treatment with NPs, the synthesis of EPS increases, especially after AgNP-CTAB treatment, which can maintain and consequently reduce the harmful effect of AgNPs on the cells themselves.

Acknowledgement: Project funded by Croatian Science Foundation (grant number HRZZ-IP-2018-01-5351), PI: prof. Daniel Mark Lyons and is supported by University of Zagreb

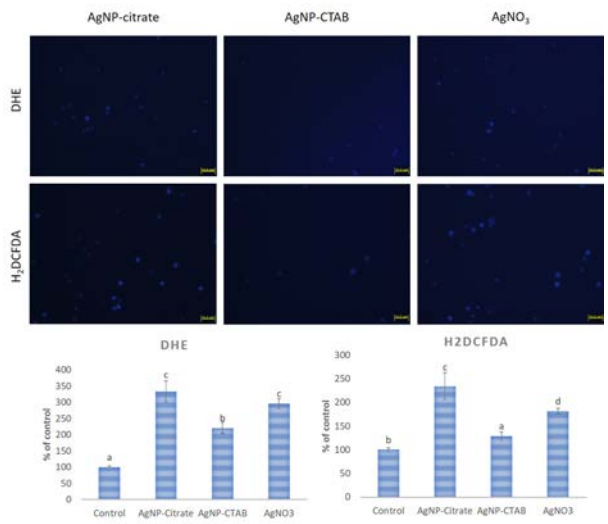

Fig. 1: Chlorella vulgaris cells after AgNP-citrate, AgNP-CTAB or AgNO3 treatment obtained by fluorescent microscopy showing increase in ROS content via fluorescent probes DHE or H2DCFDA (scale bar = 10.8 µm).

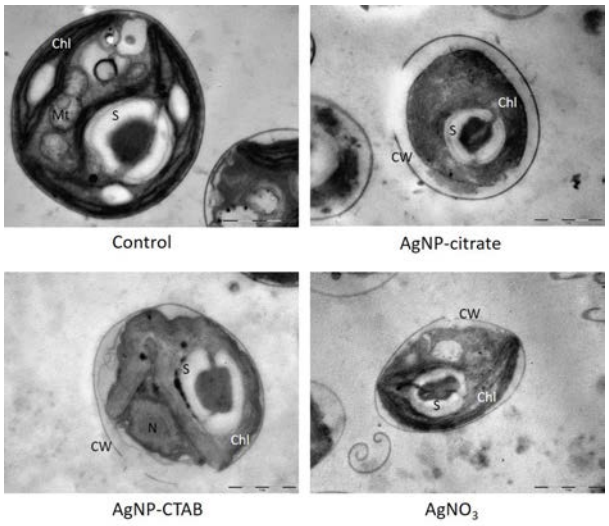

Fig. 2: Microphotographs of Chlorella vulgaris control cell and cells treated with AgNP-citrate, AgNP-CTAB or AgNO3 obtained by TEM (scale bar = 1 µm). CW-cell wall, Chl-chloroplast, S-starch, Mt-mitochondria, N-nucleus.

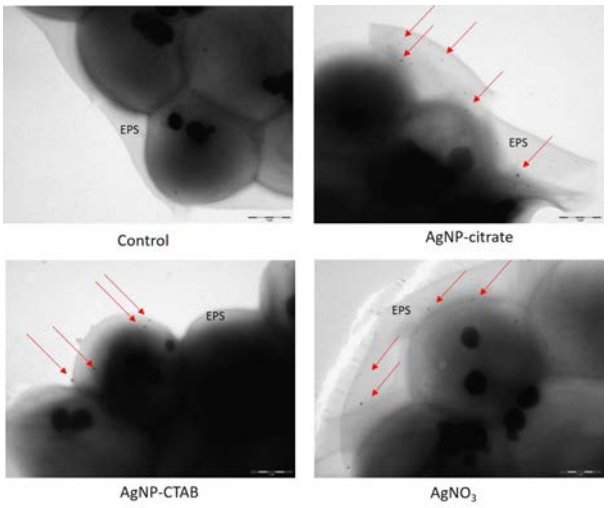

Fig. 3: Micrographs of EPS with NPs (arrows) around control cells and cells treated with AgNP-citrate, AgNP-CTAB or AgNO3 visualised by TEM (scale bar = 1 µm).

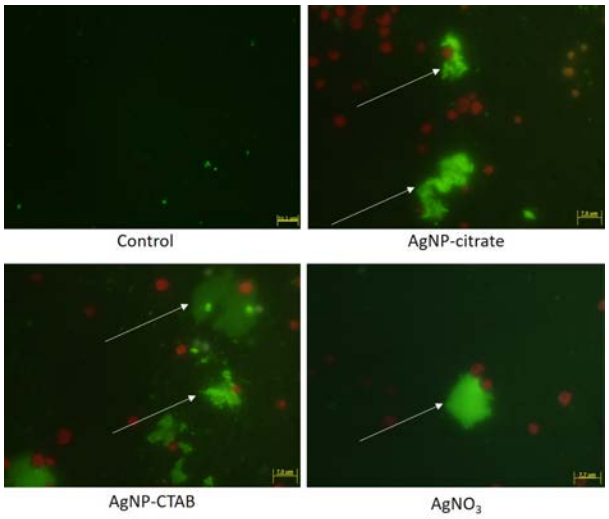

Fig. 4: Visualising EPS (arrows) around Chlorella vulgaris control cells and cells treated with AgNP-citrate, AgNP-CTAB or AgNO3 via FITC-labelled ConA lectins by fluorescent microscopy.

Type of presentation: Oral

LS2-O-2690 The use of SEM imaging and elemental mapping in the research of artificial bacterial aggregates

Hreščak J.[1], Rijavec T.[2], Deev D.[2,3], Lapanje A.[2], Čeh M.[1]

[1]Center for Electron Microscopy and Microanalysis, Jožef Stefan Institute, Ljubljana, Slovenia, [2]Department of Environmental Sciences, Jožef Stefan Institute, Ljubljana, Slovenia, [3]Jožef Stefan International Postgraduate School, Ljubljana, Slovenia

Email of the presenting author: jitka.hrescak@ijs.si

Hand in hand with the progress in technology and widespread use of electron microscopes, there has been an increasing trend of using these instruments also in microbiology and biotechnology fields. In this work, the SEM imaging together with EDS mapping helped in understanding the metabolic processes in constructed bacterial aggregates.

The anaerobic niches in artificial bacterial aggregates prepared by electrostatic modification of the cell surface by polyelectrolytes (PE) have the potential to be used as a model of interaction in multispecies microbial communities, such as biofilms or aggregates [1]. The alternative metabolic pathways could enable the anaerobic metabolism even under well-aerated conditions. One example of such pathway is the metabolization of heavy metals in polluted water. For instance, the bacterial strain *Shewanella oneidensis*, has been described to reduce metals in anaerobic conditions, including vanadium in the form of vanadate ion (V^{V}) to produce insoluble vanadyl ion (V^{IV}) [2].

The later bacterial strain was used in this study to construct the artificial aggregates. The bacterial cells were attached to each other according to the procedure described previously [1, 3]. The aggregates were then cultivated in a medium containing vanadium oxide. In order to preserve the physical structure of these aggregates, they were nitrified with liquid nitrogen and lyophilized prior to observation with SEM. The samples were then deposited onto the aluminium stub with adhesive C-tape, air-dried and coated with 10 nm of carbon. The Verios 4G HP (Thermo Fisher Scientific) Scanning Electron Microscope (SEM) with the Ultim Max 65 detector Energy Dispersive X-ray Spectroscopy (EDS) and AZtec software (Oxford Instruments) served for the imaging and EDS mapping.

SEM and EDS analysis revealed the presence of vanadium precipitates in the aggregates as shown in Figure 1. Based on the previous reports [2], this indicates the anaerobic activity of bacteria within the aggregates. These results confirm that construction of synthetic aggregates has a high potential in the control of metabolic activity of bacterial cells.

[1] D. Deev, I. Rybkin, T. Rijavec, A. Lapanje, Front. Mater. 2021, 8, 624631.

[2] W. Carpentier, K. Sandra, I. De Smet, A. Brigé, L. De Smet, J. Van Beeumen, Appl. Environ. Microbiol. 2003, 69, 6, 3636–39.

[3] I. Rybkin, D. Gorin, G. Sukhorukov, A. Lapanje, Front. Bioeng. Biotechnol. 2019. 7, 378.

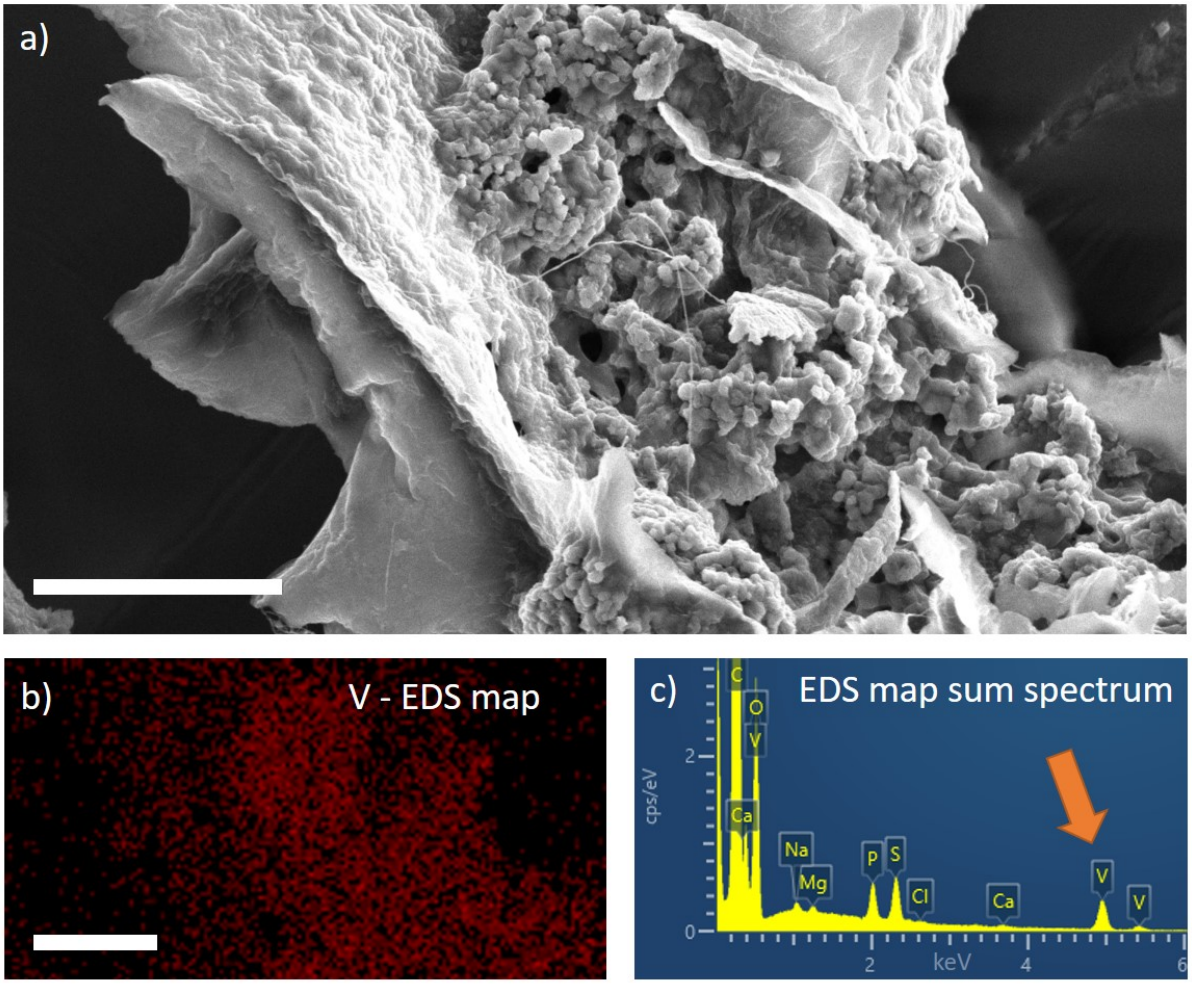

Fig. 1: a) SEM image of the prepared bacterial aggregate b) EDS map of vanadium (corresponding to the area shown on the SEM image) c) EDS spectrum from the imaged area, arrow enhancing the intense V peak. The markers show 5 µm.

Type of presentation: Oral

LS2-O-2684 Pyroplastics: A new Approach

Rattenberger J.[1], Fitzek H.[1], Korenjak Jausnik S.[2], Schroettner H.[1,2]

[1]Graz Centre for Electron Microscopy (ZFE), Steyrergasse 17, 8010 Graz, Austria, [2]Institute of Electron Microscopy and Nanoanalysis (FELMI), NAWI Graz, Graz University of Technology, Steyrergasse 17, 8010 Graz, Austria

Email of the presenting author: johannes.rattenberger@felmi-zfe.at

Pollution of aquatic ecological systems with different kind of plastics, from Nano- to Micro- and Macroplastics is a global problem and is shifting into the area of public interest mainly because these plastic particles can be found everywhere in the food chain.
Recent scientific publications reported about a new kind of plastic pollution of not well-known origin, pyroplastics [1]. Rock shaped and coloured formations of different polymers were found on beaches in south west England. The current theory of their formation is that plastic litter was burned incomplete near by the ocean or on the high seas. In comparison to previously published plastiglomerates the encapsulated material is usually plastic without a significant amount of extraneous material [2].
In the presented work a Raman microscope equipped with a heating stage was used to determine the maximum temperature pyroplastic was exposed. It can be seen that the structure of the samples starts to change above 225°C and above 275°C. The polyethylene bands between 800 cm-1 and 1800 cm-1 vanish and the amorphous carbon signal appears (figure 1). Additional experiments with the heating stage clearly showed that this effect is not heating time dependent and in combination with a light microscope, it could be shown that at about 80°C different pyroplastic stone fragments are melting together forming one solid piece.
Large area energy dispersive X-ray spectrometry (EDX) elemental mappings (in the cm² range) on a cross section were performed to get additional information about the present chemical elements (see figure 2). In contrast to previously published works no lead, chrome, bromide or antimony could be found, which would be a hint for special heat and UV stabilisers or flame-retardants.
Based on these findings and the fact that stones and sand on a beach can be heated up to 80°C, it can be possible that, additionally to combustion processes, pyroplastic stones are formed by the heat of the sun and the power of tides.
[1] Turner A., et. al. Marine pollution from pyroplastics. Sci. Total Environ., July 2019
[2] Corcoran, P.L., et. al. An anthropogenic marker horizon in the future
rock record. Geol. Soc. Am. Today 24 (6), 2014

Acknowledgement: The authors want to thank Prof. A. Turner (University of Plymouth) for the supply of pyroplastics and “TIMELY” (SP-2020-02, ACR, BMDW) for financial support.

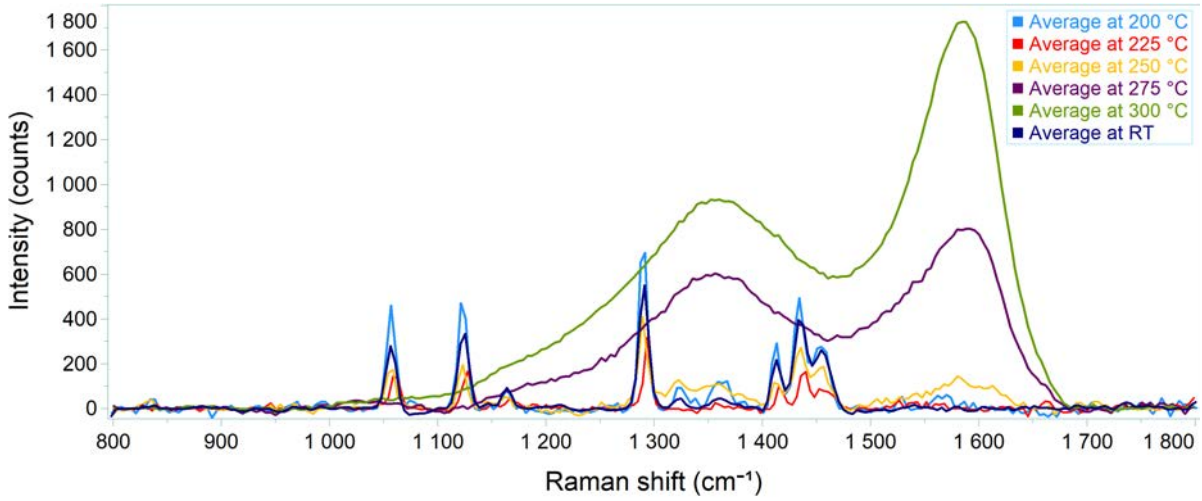

Fig. 1: Raman spectra of pyroplastic (average of 5 measurements at randomly selected positions) after different heat treatment in comparison to the Raman spectrum without heat treatment

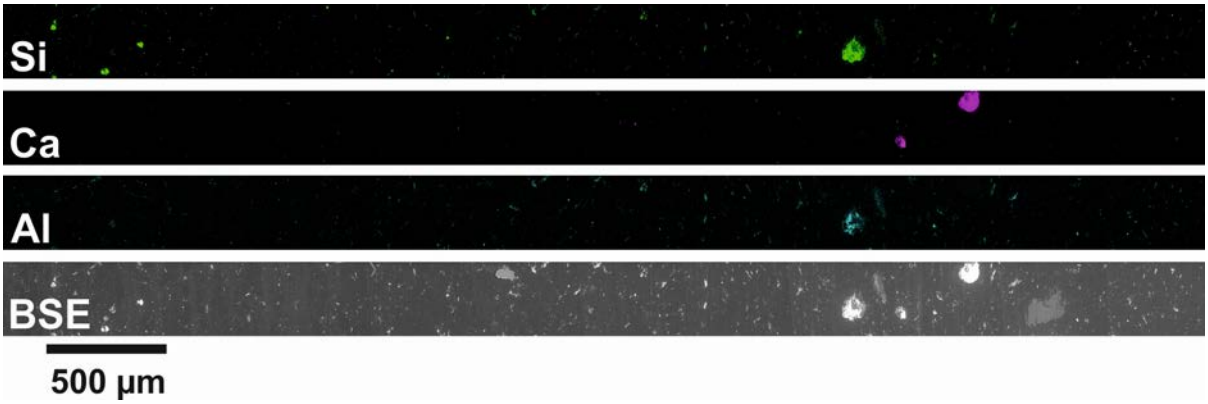

Fig. 2: Backscattered electron image and large area EDX elemental mappings of selected chemical elements

Type of presentation: Poster

LS2-P-2665 3D organization of photosynthetic membranes in cells of photosynthetic bacterium Sediminicoccus rosea

Bílý T.[1,3], Týč J.[3], Kopejtka K.[2], Gardiner A. T.[2], Singhal N.[2], Tomasch J.[2], Koblížek M.[2], Kaftan D.[1,2]

[1]University of South Bohemia, České Budějovice, CZ-370 05, [2]Institute of Microbiology CAS, Třeboň, CZ-379 81, [3]Biology Centre CAS, České Budějovice, CZ-370 05

Email of the presenting author: thomass@paru.cas.cz

The biogenesis of bacterial photosynthetic machinery involves coordinated gene expression and membrane remodelling, often negatively controlled by light. Photosynthetic microbial communities in polar regions experience half a year of constant daylight that would render the typical phototrophs devoid of any bacteriochlorophyll or photosynthetic reaction centres in just a few tens of hours.

Here we demonstrate the ultrastructure of a strain of bacterium formerly identified by Qu et al. as Sediminicoccus Rosea (Qu et al., 2013, J Gen Appl Microbiol. 59(6):463-8.), that we isolated from a creek in north-western Iceland near Raufarhöfn (66°16'22.4"N 15°48'24.5"W).

Electron tomography in TEM with sub-nanometre resolution showed an oval-shaped cell with a length of 1.7 μm and a width of 700 nm with their polar regions filled with numerous spherical vesicles presumably formed by chromatophores and a dense central region rich in ribosomes and chromosomal DNA.

Array tomography in SEM at resolutions 4 nm lateral and 70 nm in the Z-direction has been utilised for statistics for volume analysis of cells. This method allowed us to analyse the complete volume of several hundreds of cells and analyse volumes of single cells, cells before dividing and dividing cells.

Cell culture was prepared using a chemical way and embedded in a resin block.

For electron tomography: We cut 120 nm thick sections that we placed on a TEM grid, poststained by uranyl acetate and carbon coated. We collected tilt series images in the range +-65 with tilt step 1 on JEOL 2100 F equipped with K2 DED and controlled by SerialEM. We reconstructed tomograms and generated a 3D model in the etomo software package.

For array tomography: We cut 70 nm thick sections that we placed on a negatively charged wafer, poststained by uranyl acetate and lead citrate, finally carbon coated. We collected an array of images using MAPS software in Apreo SEM by Thermofisher Scientific. We roughly aligned images using the TrackEM package in ImageJ. We cut out individual cells and preciously aligned them in the etomo, which we used further for model generation and volume statistics.

Acknowledgement: Supported by MEYS CR (LM2018129 Czech-BioImaging), ERDF 003/0000441 and CSF PhotoGemm+ project GX19-28778X.

Type of presentation: Poster

LS2-P-2658 Preliminary morphological characterization of Schmallenberg Virus using cryo-TEM techniques

Guerra G. S.[1], Boshra H.[1,2], Aebischer A.[3], Beer M.[3], Abrescia N. G.[1,4]

[1]Structure and Cell Biology of Viruses Lab, CIC bioGUNE, Basque Research and Technology Alliance (BRTA), Derio, Spain. , [2]Department of Pathology, Fundamental and Applied Research for Animals & Health (FARAH), Faculty of Veterinary Medicine, University of Liège, Belgium. , [3]Friedrich-Loeffler-Institut, Greifswald, Insel Riems, Germany, [4]Ikerbasque, Basque Foundation for Science, Bilbao, Spain

Email of the presenting author: gsoares@cicbiogune.es

Schmallenberg Virus (SBV), from the Peribunyaviridae family and Orthobunyavirus genus, was first detected in late 2011 in Germany spreading all over Europe ever since. The virus causes a disease associated with dairy cattle that includes fever, drop on milk production, diarrhea and abortions, being its closely counterparts Bunyamwera virus (BUNV) and Akabane Virus. Its RNA (-) genome is divided into three segments, L, S and M, encoding the later for the two transmembrane spike glycoproteins, the smaller in size Gn and the bigger Gc [1]. The SBV particle is enveloped and pleomorphic, enclosing its ribonucleoproteins inside a lipid bilayer. While structural information on BUNV and its glycoproteins have already been described by cryo-EM [2], data on SBV and its spike structures are scarce. Only the crystal structure of Gc head domain (aa 465-874) fitted into a BUNV spike EM map is available [3].
The present work aims at describing the SBV morphology. We used purified SBV particles for both SPA and cryo-ET analyses (Fig. 1-2). An initial side-view 2D classification shows that density is present on the top of the corresponding bilayer (Fig. 3). Further, tilt series were collected on a Krios microscope at eBIC (Diamond LS, UK) and tomograms were reconstructed using the IMOD software [4] serving to assess the feasibility of the study and the setting up of a sub-tomogram averaging pipeline (Fig. 4).
Although still ongoing, this initial study on the SBV production and purification, along with cryo-TEM analyses will allow a more robust description on the viral spikes and contribute to expand the current knowledge on the SBV life cycle, a prerequisite to implement strategies for virus control since the Gc/Gn is the gateway for viral infection.
[1]Collins ÁB, Doherty ML, Barrett DJ, Mee JF. Schmallenberg virus: a systematic international literature review (2011-2019) from an Irish perspective. Ir Vet J. 2019 Oct 9;72:9.
[2]Bowden TA, Bitto D, McLees A, Yeromonahos C, Elliott RM, Huiskonen JT. Orthobunyavirus ultrastructure and the curious tripodal glycoprotein spike. PLoS Pathog. 2013;9(5):e1003374.
[3]Hellert J, Aebischer A, Wernike K, Haouz A, Brocchi E, Reiche S, Guardado-Calvo P, Beer M, Rey FA. Orthobunyavirus spike architecture and recognition by neutralizing antibodies. Nat Commun. 2019 Feb 20;10(1):879.
[4] Kremer JR, Mastronarde DN, McIntosh JR. Computer visualization of three-dimensional image data using IMOD. J Struct Biol. 1996 Jan-Feb;116(1):71-6. doi: 10.1006/jsbi.1996.0013. PMID: 8742726.

Acknowledgement: La Caixa Foundation ID100010434 LCF/BQ/DI19/11730041 Agencia Estatal de Investigacion RTI2018-095700-B-I00 Diamond/eBIC BI23872 Welcome Trust, MRC, BBRSC

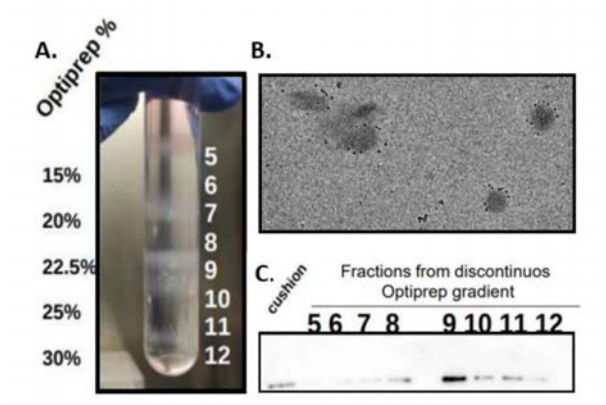

Fig. 1: **SBV purification. A.** Optiprep gradient used to purify SBV particles produced on BHK cells **B**. Negative stain immunolabeling of SBV particles using an anti-Gc as primary antibody bound to a secondary gold labelled antibody **C.** Immunoblot from the different Optiprep gradient fractions also using an anti-Gc antibody for primary staining.

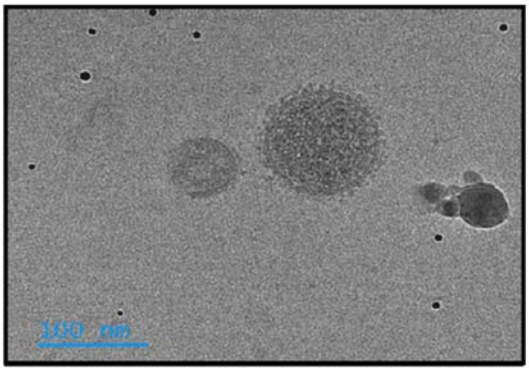

Fig. 2: **SBV particles visualized by cryoEM.** SBV particles derived from in-house purification were plunge-frozen and visualized with the presence of gold fiducials. The putative particles diameters ranged between 80 and 120 nm.

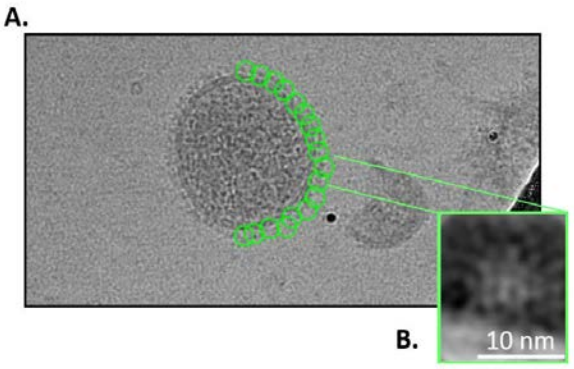

Fig. 3: **Initial 2D classification on SBV spike. A.** Particle picking from densities covering the viral membrane shown in green circles **B.** Preliminar 2D classification from the viral spike using Relion 3.0.

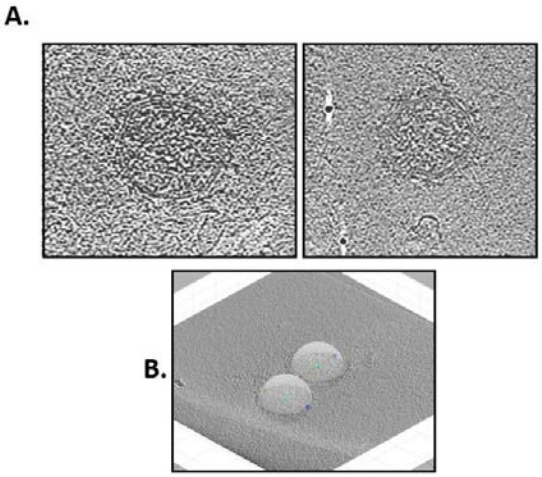

Fig. 4: **Tomography. A**. Examples from a central slice of two SBV reconstructed tomograms using IMOD **B.** Semi-automated particle picking from the surface of SBV tomograms (Dipole mode) in Dynamo.

Type of presentation: Poster

LS2-P-2532 Utilization of haematite nanoparticles by a flavin mediated iron uptake of roots

Keresztes Á.[1], Kovács Kis V.[2], Pankaczi F.[3], Fodor F.[3], Tolnai G.[4], Klencsár Z.[2], Solti Á.[3]

[1]Department of Plant Anatomy, Eötvös Loránd University, Budapest, Hungary, [2]Centre for Energy Research, Eötvös Loránd Research Network, Budapest, Hungary, [3]Department of Plant Physiology and Plant Molecular Biology, Eötvös Loránd University, Budapest, Hungary, [4]Kondorosi út 8/A, Budapest, Hungary

Email of the presenting author: keresztes.aron@ttk.elte.hu

The importance of iron is shown by chlorosis of the leaves, decrease of photosynthesis and so the crop production in iron deficient plants. As cca 30% of arable lands is depleted in iron, supplement is needed by inorganic salts, iron complexes or iron-containing nano-particles. The advantage of the latter is that it is less likely to be washed away from the soil, and its uptake is retarded.
We added nanohaematite (Fe_2O_3) particles to the liquid nutrient medium of iron deficient cucumber (*Cucumis sativus* L.) plants and observed that the chlorophyll content of the leaves was normalized within three days. Cucumber belongs to the group of plants which are able to obtain iron from soil particles, as they secrete flavins by their roots [1] and operate a reduction based iron uptake [2] in case of iron deficiency. Liberation of iron ions may happen either out of the root, or in the cell walls, or within the cells.
We examined ultrathin sections from meristematic (stem) cells of root tips covered by root cap in a Hitachi 7100 TEM and found aggregation of electron dense particles in the apoplast, namely in the middle lamellae between the adjacent cells (Fig. 1). We wanted to ascertain that they were nanohaematite particles, so we performed X-ray microanalysis (EDS) in a FEI Themis G2 HRTEM. It was found that the distribution of Fe followed the localization pattern of the particles in the apoplast (Fig. 2A&B). This was superimposed by Pb from the contrasting material, so this contributed to the density of the particles. HRTEM mode was applied for the atomic resolution imaging of the particles (Fig. 2C), and this showed the crystalline structure characteristic for haematite (Fig. 2D).
While the particle size was 10-20 nm in the original suspension, this decreased to 2-3 nm in the root apoplast, revealing a partial utilization of their iron content. Considering the pore size of the cell walls [3], it seems probable that a flavin-shuttle mediates the reduction of Fe(III) to Fe(II) ions supporting the transmembrane Fe(II) iron uptake into the cell interior.

References

[1] Satoh, J. *et al*. 2016. *Cucumis sativus* secretes 4'-ketoriboflavin under iron-deficient conditions. *Bioscience, Biotechnology and Biochemistry* 80. 363-367
[2] Sisó-Terraza, P. *et al*. 2016. Flavins secreted by roots of iron-deficient *Beta vulgaris* enable mining of ferric oxide via reductive mechanisms. *New Phytologist* 209. 733-745
[3] Kurczyńska, E. *et al*. 2021. Nanoparticles-plant interaction: What we know, where we are? *Applied Sciences* 11. 5473

Acknowledgement: Authors thank the grant VEKOP-2.3.3-15-2016-00002. V.K.K. was supported by János Bolyai Fellowship and ÚNKP-19-4.

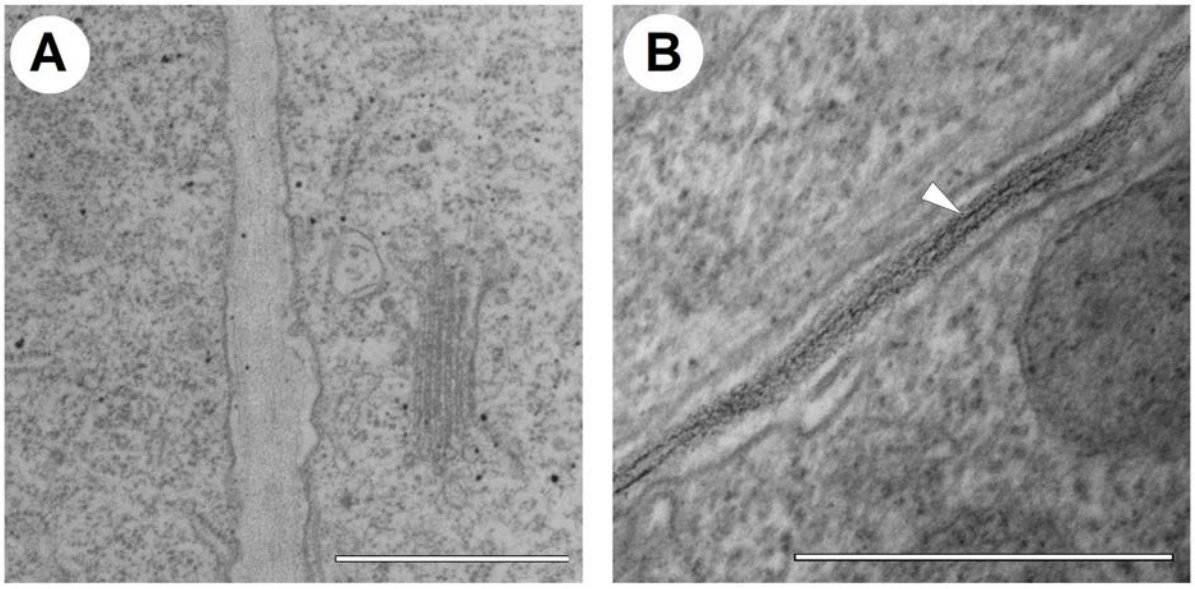

Fig. 1: Ultrastructure (examined in a Hitachi 7100 electron microscope) of the root tip meristem cells from the Fe(III)-EDTA grown (A) and nanohaematite treated (B) plants. Bars equal 1.0 μm (A) and 0.5 μm (B).

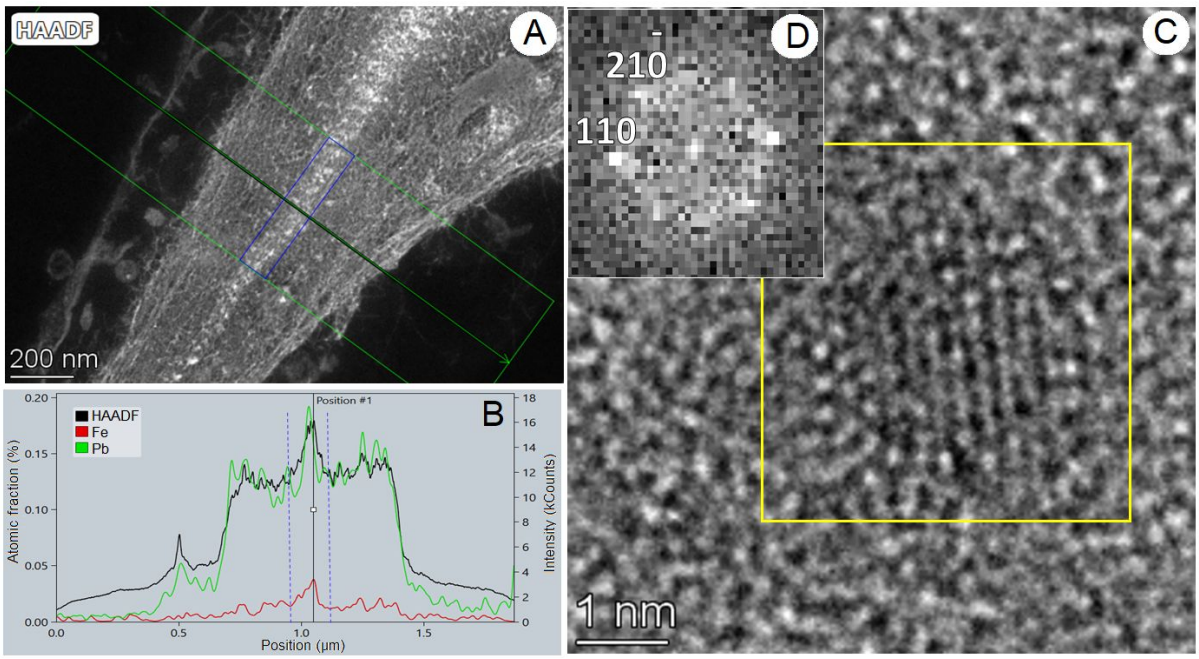

Fig. 2: STEM HAADF image (A) and EDS line profile analysis (B) across neighbouring cell walls of root tip meristem cells. HRTEM image (C) and corresponding Fourier transform (D) of an individual haematite nanoparticle viewed down the [001] zone axis.

Type of presentation: Poster

LS2-P-2585 Expression of the enzyme myrosinase type 1 in the root, the stem and the leaves of the plant nasturtium (Tropaeolum majus L.)

Kević N.[1], Restović I.[2], Kurić L.[1], Bočina I.[1], Bilušić T.[3], Vrca I.[3]

[1]Department of Biology, Faculty of Science, University of Split, Split, Croatia, [2]Faculty of Humanities and Social Sciences, University of Split, Split, Croatia, [3]Department of Food Technology and Biotechnology, Faculty of Chemistry and Technology, University of Split, Split, Croatia

Email of the presenting author: nkevic@pmfst.hr

Introduction: The enzyme myrosinase catalyses the hydrolysis of a group of low molecular weight compounds, the glucosinolates [1,2]. The myrosinase refers to a certain type of idioblasts called myrosin cells [2]. Myrosin cells are present in several tissues in the plant including the cotyledons and axis of the embryo as well as in the leaves, the stem, the root, the petals and the siliques of the adult plant [1]. Nasturtium (*Tropaeolum majus* L.) is a plant that belongs to the Tropaeolaceae family and is known for its ornamental and medicinal properties [3].
Objectives: The aim of the study was to investigate the expression of the enzyme myrosinase type 1 in the nasturtium leaf, stem and root regions in the different developmental stages after plant's sprout.
Materials and methods: The nasturtium tissues were cut into small pieces at different developmental stages after sprouting. The specimens were fixed in 4% paraformaldehyde in phosphate buffer pH 6.8, dehydrated in an ascending series of ethanol, cleared in xylene, and then embedded in paraffin wax. The paraffin sections cut on a rotary microtome were mounted on glass slides. After deparaffinization and rehydration, the sections were heated in a citrate buffer pH 6.0, cooled and a blocking buffer was applied to exclude unspecific staining. The sections were then incubated overnight at RT with TGG1 myrosinase 1 primary antibody, diluted 1/1000 in PBS. After washing in PBS, Alexa Fluor 488 secondary antibody, diluted 1/400 in PBS was applied for 1h and washed in PBS again. Then, the nuclei were stained with DAPI. All slides were studied using an Olympus BX51 epifluorescence microscope with digital camera a Nikon DS-Ri1 (Japan).
Results: Significant immunolocalization of the enzyme myrosinase type 1 was obtained in the phloem parenchyma cells, and through the ground tissue in the leaf region of the nasturtium in two different developmental phases (f0 and f4). An increasing signal of enzyme myrosinase type 1 was observed in the developmental stage 30 days (f4) after germination (Figure 1).
Conclusion: The myrosin cells are the subcellular compartments associated with the enzyme myrosinase. The glucosinolates are located in vacuoles and are separated from the myrosin cells. The presence of the glucosinolate−myrosinase system is characteristic of the Brassicales order, and it serves as a defense system against biotic and abiotic stressors.
References:
[1] A. S. Höglund, M. Lenman, L. Rask, Plant Sci. 1992, 85, 165.
[2] Y. Niu, A. Rogiewicz, C. Wan, M. Guo, F. Huang, A. Bogdan, B. A. Slominski, J. Agric. Food Chem. 2015, 63, 3078.
[3] G. A. Garzon, R. E. Wrolstad, Food Chem. 2009, 114, 44.

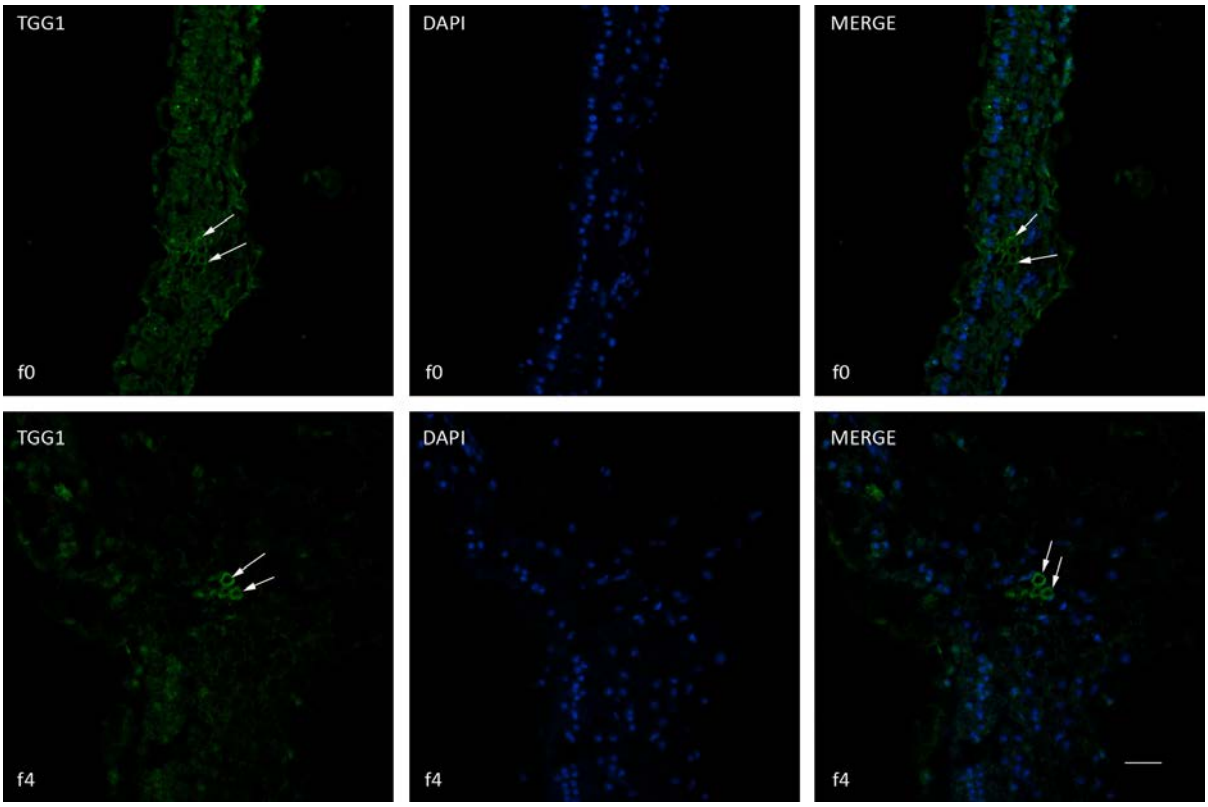

Fig. 1: Expression of the enzyme myrosinase type 1 in the ground tissue in the leaf region of the nasturtium (*Tropaeolum majus* L.) in two different developmental phases (f0 and f4). Magnification 40x; scale bar 100 µm. Merge = protein + DAPI.

Type of presentation: Poster

LS2-P-2663 Ultrastructural changes in prokaryotic microorganisms caused by long-term exposure to high salt and copper ion concentrations

Mrazova K.[1], Novackova I.[2], Hrubanova K.[1], Nebesarova J.[3,4], Obruca S.[2], Krzyzanek V.[1]

[1]The Institute of Scientific Instruments of the CAS, Brno, Czech Republic, [2]Faculty of Chemistry, Brno University of Technology, Brno, Czech Republic, [3]Biology Centre of the CAS, Ceske Budejovice, Czech Republic, [4]Faculty of Science, Charles University, Prague, Czech Republic

Email of the presenting author: mrazova@isibrno.cz

Cupriavidus necator is a soil bacterium known as a producer of polyhydroxyalkanoates (PHA), polyesters of hydroxyalkanoic acids. PHAs are polymers present in many prokaryotic organisms in the form of intracellular granules and serve as a source of carbon in the cell. Moreover, recent studies indicate, that the presence of PHA in the microbial cells enhances their robustness against various stress factors. Polyhydroxyalkanoates also attract attention as a potential substitute for petrochemical plastics. These biopolymers have similar properties as for example polypropylene, but since they are biodegradable, they will decompose in nature incomparably faster than conventional plastic materials. [1,2]
In our study, we focused on the PHA producer *Cupriavidus necator* in a long-term experiment, where the bacterial cells were exposed to high concentrations of salt (54 passages) and copper ions (64 passages). After cultivation, bacterial cells were harvested and analysed using the methods of electron microscopy, namely cryo-SEM and TEM.
Bacterial cells were centrifuged and fixed using the method of high-pressure freezing. For cryo-SEM analysis, bacterial cells were pipetted on the 0,2 µm side of the 6mm carrier type A and closed with the flat side of carrier type B without any treatment using lecithin or cryoprotectants. Frozen samples were then freeze-fractured and underwent freeze-etching procedure for 7min at -95°C. The cryo-SEM imaging was conducted at -120°C in a scanning electron microscope equipped with a cryo stage. For TEM analysis, 3mm carriers pre-treated with a 1% solution of lecithin were used and the frozen samples underwent freeze-substitution. The chosen freeze-substitution protocol was previously described in [3]. Samples cut to ultrathin sections and stained were then imaged in a transmission electron microscope using the electron beam of energy 80kV.
In the TEM images of Cu stress, it is possible to observe dense precipitates inside of the cells which can be correlated to cryo-SEM images where cells exposed to Cu^{+} show small hollows in the cytoplasm of similar shape and size as precipitates in TEM imaging. Also, cells exposed to high osmotic stress appeared to be smaller, than the control cultivation without any stress factors, and of a crescent shape. These findings indicate, that long-term exposure of microbial cells to stress conditions changes not only the production of intracellular polymers [4] but also their morphology and this phenomenon deserves to be studied further.
[1] Obruca S., et al.: Biotechnology Advances 36(2018), p. 856-870
[2] Obruca S., et al.: New Biotechnology 39(2017), p. 68-80
[3] Kourilova X., et al.: Microorganisms 9(2021), p. 909
[4] Novackova I., et al.: Biochemical Engineering Journal 151(2019), p. 107350

Acknowledgement: The authors gratefully acknowledge funding from the TACR (project TN01000008).

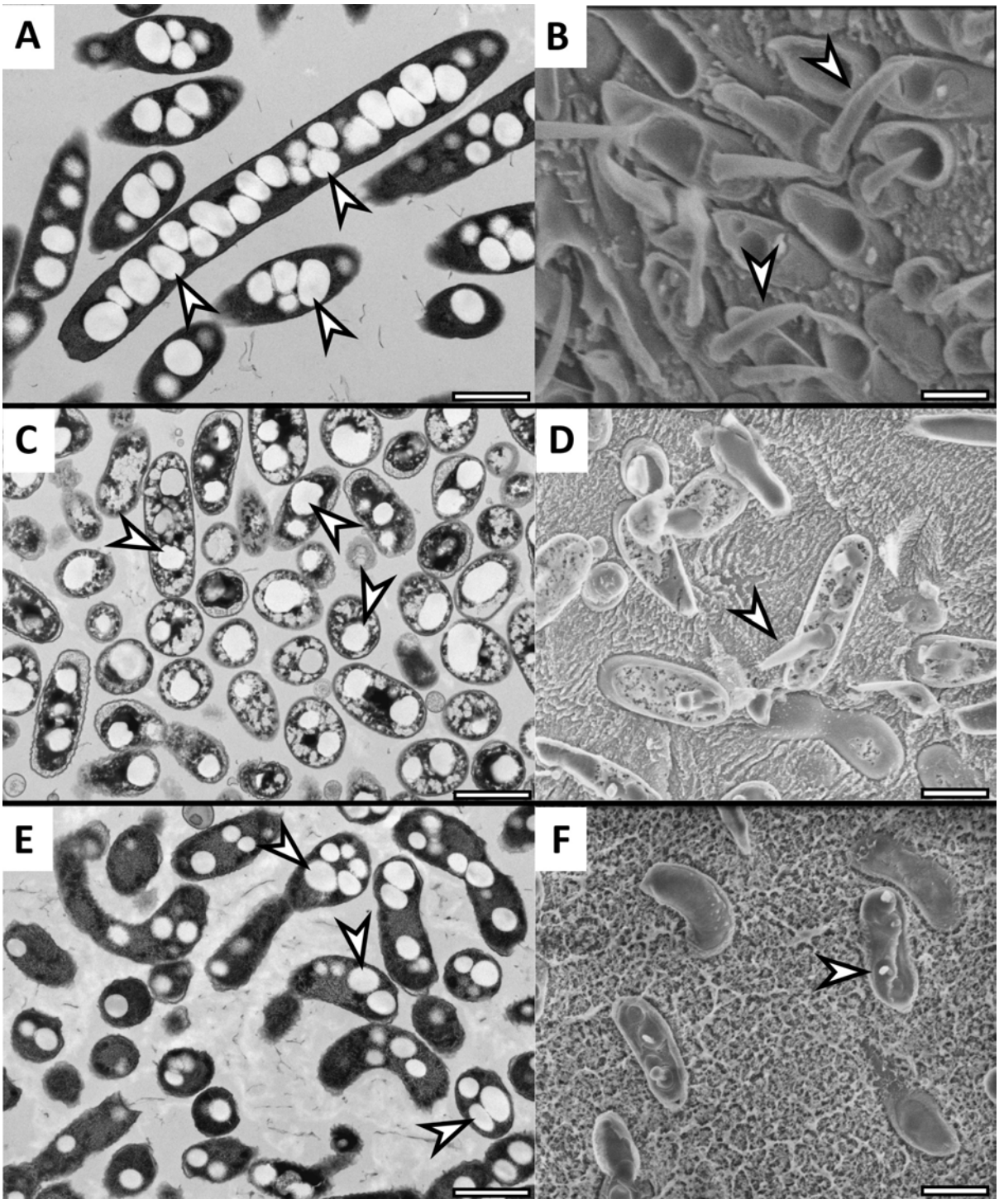

Fig. 1: EM images of *C. necator* A) cultivation without stress conditions, TEM; B) cultivation without stress conditions, cryo-SEM (sample coated with Ir); C) exposure to Cu^{+}, TEM; D) exposure to Cu^{+}, cryo-SEM; E) exposure to osmotic stress, TEM; F) exposure to osmotic stress, cryo-SEM; scale bar 1 µm; PHA granules marked with arrows

LS3 Structural studies from macromolecules to tissues

Type of presentation: Invited

Time-lapse microscopy reveals induction of entosis by TRAIL signalling

Bozkurt E.[1]

[1]Department of Genetics and Bioengineering, Faculty of Engineering, Izmir University of Economics, Izmir, Turkey

Email of the presenting author: emir.bozkurt@izmirekonomi.edu.tr

Entosis is a form of cell-in-cell (CIC) interaction where a living cell (“inner cell”) enters into another cell (“outer cell”) by activation of Rho-ROCK signalling. After invading into another cell, inner cells can stay alive, can undergo cell division, or can be released. However, most inner cells undergo degradation while being inside outer cells by entotic cell death. Entotic structures are evident in tumors of lung, head and neck, breast, colon, stomach, liver, and cervix; however, factors controlling entosis are not well understood. Here we show that besides activating apoptosis, TRAIL (Tumor necrosis factor-related apoptosis-inducing ligand) signaling induces entosis in colon cancer cells through TRAIL receptors, and structural presence but not catalytic activity of caspase-8. Although apoptosis and entosis are morphologically and biochemically distinct mechanisms, knockout of Bax and Bak, or inhibition of caspases inhibits entotic cell death and promotes survival and release of inner cells. Moreover, we provide evidence for an association of TRAIL signaling, CICs, and clinical outcome in colorectal cancer.

Type of presentation: Invited

Spheroids: in vitro 3D cell cultures of brown trout liver as a model for ecotoxicology research

Raskovic B.[1, 2, 3], Madureira T. V.[1, 2], Lopes C.[1, 2], Rocha E.[1, 2]

[1]Department of Microscopy, Institute of Biomedical Sciences Abel Salazar (ICBAS), University of Porto, Porto, Portugal, [2]Team of Histomorphology, Physiopathology and Applied Toxicology,Interdisciplinary Centre of Marine and Environmental Research (CIIMAR), University of Porto, Porto, Portugal, [3]Institute of Animal Sciences, Faculty of Agriculture, University of Belgrade, Belgrade, Serbia

Email of the presenting author: raskovic@agrif.bg.ac.rs

In 2018, approximately 10.5 million experimental animals were used in the EU for various testing purposes, and 26% of that number accounted for fish. The scientific community, regulatory agencies, and national and EU policymakers endorse the refinement, reduction, and replacement (3Rs) of assays to reduce the number of sacrificed experimental animals. Despite the guidelines in fish exposure assays being well established (such as OECD and US EPA) and the number of test animals kept as low as feasible, each exposure study still requires at least 105 fish. For this reason, many in vitro methods were developed or improved for use in fish assays, which provided a good platform for testing the effects of chemicals, complementing, or replacing in vivo studies. Methods from mammalian in vitro testing were used to develop primary piscine cultures and cell lines, typically cultured in monolayers, viz. two-dimensional (2D). The advantages of 2D cultures are rapid exposure tests, being easy for handling and requiring low-cost maintenance. However, the uses of 2D cultures also have downsides: cells cannot last for a long time and cannot mimic the organization of tissues since they are cultured in the bottom of flasks and plates. To solve these problems, researchers created three-dimensional (3D) cultures. The microarchitecture and physiology of cells in 3D cultures are closer to in vivo systems. 3D primary cultures in fish have been seldom used, but they may provide an excellent research tool for the toxicological assessment of chemicals. To further use fish spheroids in toxicology, we are expanding a protocol for routine isolation and culture/co-culture of cells from brown trout (Salmo trutta) liver. The protocol is compatible with exploring differential centrifugation of isolated cells to change the composition of spheroids in terms of the ratio of hepatocytes and biliary epithelial cells. After plating in non-adhesive plates, cells were cultured for 12 days until maturation, using orbital shakers, in which they slowly aggregated and formed spheroids in the incubator (at 18 °C). DMEM enabled the formation of spheroids with sufficient size, with an absence of significant necrotic centres, which usually occur in spheroids due to hypoxia. From day 12 to 18, liver spheroids were exposed to single or mixtures of endocrine disruptors (17α-ethinylestradiol and the progestins levonorgestrel and megestrol acetate) to assess their advert effects on cells. Spheroids were evaluated using light and electron microscopy (routine staining and immunohistochemistry), gene expression (a set of genes related to lipid metabolism, yolk proteins and vitellogenin), and biochemical assays (lactate dehydrogenase and resazurin assays). The spheroids were able to respond to the stimuli.

Acknowledgement: This study received funding from the EU's Horizon 2020 research and innovation programme under the Marie Sklodowska-Curie grant agreement No. 101038087.

Type of presentation: Oral

Endosome disruption enables enteroviruses to reach cell cytoplasm

Ishemgulova A.[1], Mukhamedova M.[1], Trebichalská Z.[1], Hrebík D.[1], Buchta D.[1], Škubník K.[1], Füzik T.[1], Šmerdová L.[1], Nováček J.[1], Plevka P.[1]

[1]Central European Institute of Technology, Masaryk University, Kamenice 5, Brno, 625 00, Czech Republic

Email of the presenting author: pavel.plevka@ceitec.muni.cz

Viruses infect cells by delivering their genomes across a biological membrane into the cell cytoplasm or nucleus. Enveloped viruses achieve this by membrane fusion; however, the cell entry of non-enveloped viruses is more diverse and less well understood. Enteroviruses, the causative agents of diseases ranging from the common cold to poliomyelitis, are one of the largest groups of non-enveloped viruses. To initiate infection, enteroviruses enter cells by receptor-mediated endocytosis. However, how enterovirus particles or RNA genomes cross the endosome membrane into the cytoplasm remains unknown. Here we used cryo-electron tomography of infected cells to show that endosomes containing rhinovirus 2, echovirus 30, echovirus 18 or enterovirus 71 deform, disintegrate, and release the virus particles into the cytoplasm. Blocking endosome acidification by bafilomycin A reduced the number of particles that released their genomes but did not prevent them from reaching the cytoplasm. In contrast, the inhibition of actin-dependent post-endocytic membrane trafficking by wiskostatin promoted enterovirus genome release. In addition, we show that endocytosis of very-low-density lipoprotein, the natural substrate of rhinovirus 2 receptor, results in deformation and disruption of endosomes. Our results show that endocytosis of enteroviruses activates a cellular membrane remodeling pathway that disrupts endosomes and thus releases the virus particles into the cytoplasm.

Type of presentation: Oral

Bacteriophage φ8 protein P4, an RNA binding molecular motor, studied by Cryo-EM

Gardian Z.[1,2], Kaščáková B.[1], Grinkevich P.[1], Tůma R.[1]

[1]Faculty of Science, University of South Bohemia, České Budějovice, Czech Republic, [2]Biology Centre of the Czech Acad. Sci, Institute of Parasitology, České Budějovice, Czech Republic

Email of the presenting author: gardian@prf.jcu.cz

Hexameric protein P4 (one subunit ~ 35 kDa) of bacteriophages (Cystoviridae) has multiple roles – it simultaneously acts as a channel and a translocating motor with RNA helicase activity. P4 with RNA interaction also has an ATPase activity and is important in packaging the genomic precursors and in the regulation of their replication. The structure of P4 was solved to 2.79 Å resolution by X-ray crystallography. However, structural and dynamical details of the RNA binding mechanism remain elusive due to the lack of P4-RNA complex structures. Cryo-EM is a method of choice for this project with its ability to reconstruct different conformers from one sample.
The purified and concentration-adjusted samples were prepared by plunge freezing on glow discharged holey carbon grids. Our initial studies were performed using a JEOL 2100F transmission electron microscope (TEM) operating at 200 kV and equipped with a Gatan K2 Summit direct electron detector (DED). To obtain a higher-resolution map of P4 protein, we used a ThermoFisher Krios TEM equipped with a K3 DED and a Bioquantum K3 imaging filter at CEITEC, Brno. Cryo-EM data were processed using cryoSPARC or RELION. We obtained electron density maps of at least two conformers. Based on them, the structural models of P4-RNA complex are being built using manual or automated modelling tools and also molecular dynamics flexible fitting.

Acknowledgement: This project was supported by European Regional Development Fund-Project No. CZ.02.1.01/0.0/0.0/15_003/0000441.

Type of presentation: Oral

Extending Capabilities of 120 kV LaB6 TEMs to Cryo-EM Reconstructions at Subnanometer Resolution

Masiulis S.[1], Staníček J.[2], Malínský M.[2], Raschdorf O.[1], Němeček D.[2]

[1]Materials and Structural Analysis Division, Thermo Fisher Scientific, Eindhoven, Netherlands,
[2]Materials and Structural Analysis Division, Thermo Fisher Scientific, Brno, Czech Republic

Email of the presenting author: daniel.nemecek@thermofisher.com

Life Science applications of 120-kV TEMs with the LaB6 electron source have been focused on imaging of plastic embedded cells and tissue, determination of molecular architecture of purified protein complexes and characterization of nanoparticles in general. Recent growth of high-resolution cryo-EM using the single particle analysis (SPA) has resulted in increased demand for optimization of cryo-EM samples to obtain optimal distribution of intact particles in random orientations within a very thin ice layer on a cryo-EM grid. Many cryo-EM facilities require such preliminary results as a proof of sample suitability for high resolution imaging to guarantee an efficient use of their instruments and resources. Cryo-EM capable TEM microscopes equipped with a LaB6 source and CMOS detectors have sufficient performance and sensitivity to detect individual nanoparticles in thin ice layers and are often used for initial characterization of purified biomolecules in thin ice before high-resolution cryo-EM SPA data collection. However, lower brightness and coherence of the LaB6 electron beam as well as lower sensitivity of used CCD and CMOS cameras than FEG equipped TEMs with direct electron detectors generally prevent to resolve internal protein structure and assess conformational homogeneity of imaged biomolecules. We analyzed performance of the Talos L120C microscope equipped with the LaB6 electron source and the Ceta F detector. The Ceta-F has been optimized for low dose applications and allows for collection of image fractions that can be used for beam induced motion correction in image processing of SPA datasets. Given the typical settings used in SPA cryo-EM imaging, parameters of the L120C optics and DQE of the Ceta-F camera, acquired images should contain information beyond 7-Å resolution for applied defocus below -1.5 µm (Figure 1). To validate these theoretical predictions, we imaged thin continuous carbon film of ~10 nm thickness to approximate scattering from a dense protein monolayer in ice. Experimental results indicate that CTF signal can be detected and fitted to 5–7 Å resolution in the defocus range from -0.5 to -1.5 µm (Figure 2). Cryo-EM images of densely packed apoferritin particles enabled CTF fitting to 5-7 Å resolution (Figure 3) and a 3D map of apoferritin was reconstructed to ~6 Å resolution, at which individual α-helices of ferritin subunits are well resolved. These results demonstrate that besides molecular architecture also protein secondary structure, fold and inter-subunit interfaces can be determined using the 120-kV LaB6 TEM with the Ceta-F camera.

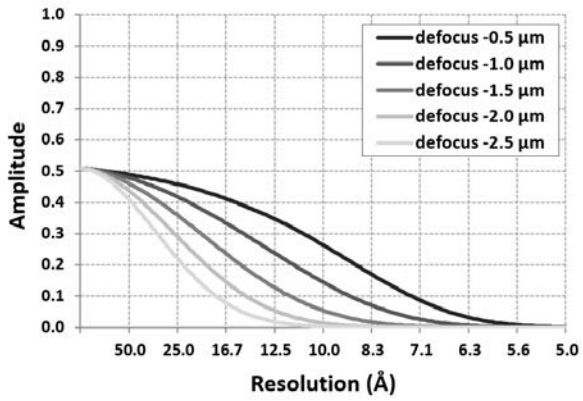

Fig. 1: Theoretical CTF envelope functions calculated at different defoci and weighted by Ceta-F detector DQE at 0.72 Å/pix pixel size.

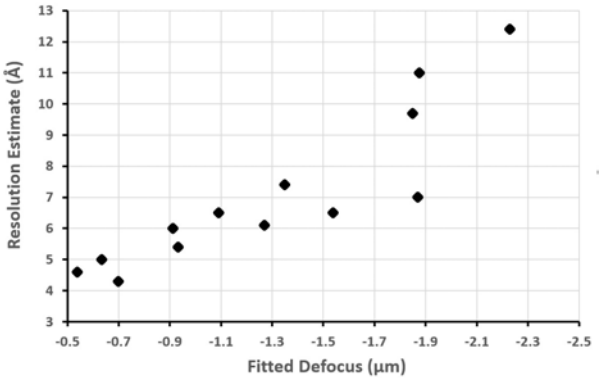

Fig. 2: Estimated resolution of CTF fits in images of thin carbon (~10 nm) collected at the typical cryo-EM settings (parallel illumination, 0.72 Å/pix, ~40 e–/Å2/s total electron dose).

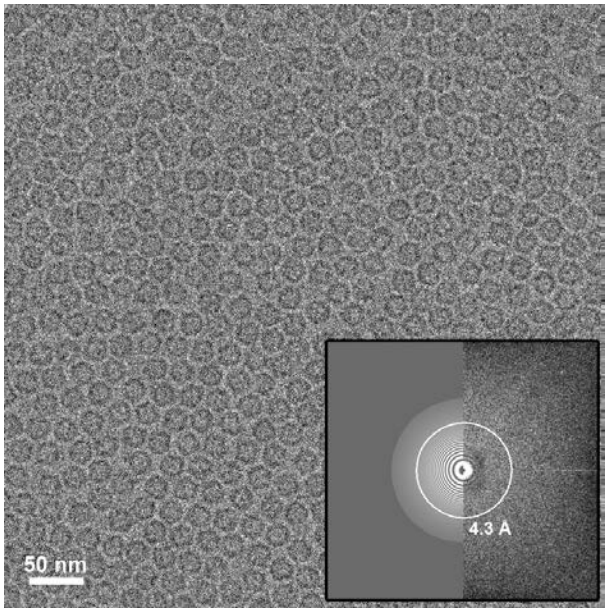

Fig. 3: Cryo-EM micrograph of apoferritin imaged using the Talos L120C equipped with Ceta-F detector: 10 fractions per movie, total electron dose 40 e–/Å2, applied defocus -1.0 µm. The inset shows the micrograph power spectrum and CTF fit up to 4.3-Å resolution.

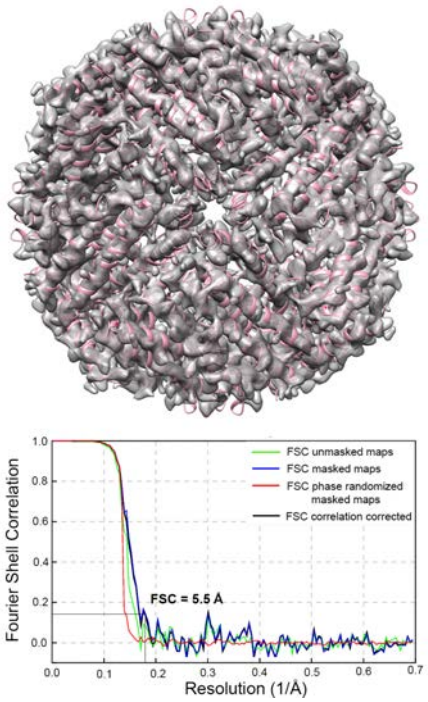

Fig. 4: Cryo-EM reconstruction of apoferritin (grey density) with rigid-body fitted atomic structure (PDB ID 6WX6). The gold standard FSC plot (below) indicates that achieved resolution of the map is better than 6 Å.

Type of presentation: Oral

LS3-O-2746 Exploring the unseen: quantitative phase imaging in cancer research

Nováková Z.[1], Křížová A.[1]

[1]Telight, Brno, Czech Republic

Email of the presenting author: zuzana.novakova@telight.eu

Cancer research is challenging due to intra-tumor heterogeneity and requires innovative methods for understanding the role of distinctive cell populations. Quantitative phase imaging (QPI) is an advanced, label-free method for live-cell analysis in diverse populations. Applying QPI in cancer research brings new opportunities for studying cells non-invasively but also quantitatively. QPI enables direct measurement of cell dry mass in pg/μm² and thus allows reliable analysis of cell viability, cell cycle and cell morphology profiling. The high detection sensitivity ranks QPI as the top-choice imaging method when aiming at correct cell segmentation while avoiding the toxicity of fluorescent labels. Due to uniform quality and precise background discrimination, QPI data are well suited for automatic cell segmentation and advanced image analysis using machine learning.

Apart from primary research of cancer cells, QPI represents a promising tool for testing novel chemotherapeutics. Because it is completely label-free and of minimal phototoxicity, it enables the evaluation of drug effect only. Effects of cytostatics on cell dynamics can be monitored in long-term non-invasive experiments. Also, the migrastatics can be studied non-invasively using QPI. In QPI data, the object trajectory and speed can be easily quantified and, in combination with morphological analysis, the drug's potential to lower the invasiveness can be evaluated. Thus, QPI is an innovative method to be applied in cancer research because without disturbing the population, it can capture rare cell events and detect unique cell phenotypes so these sub-populations, often responsible for the tumor resistance, can be targeted effectively.

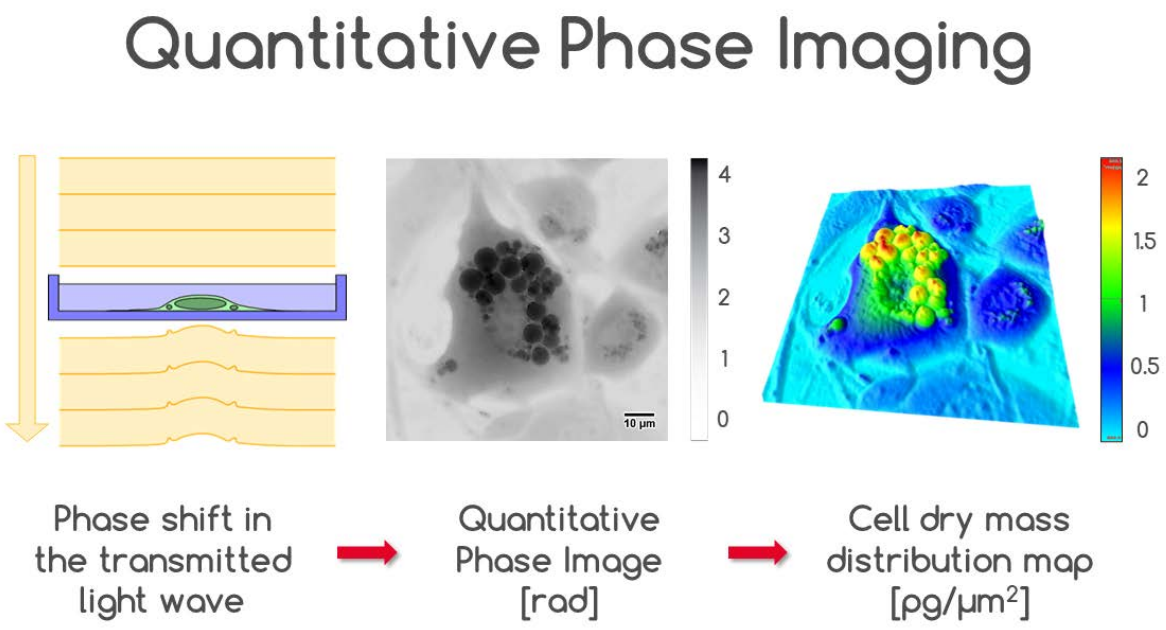

Fig. 1: Principle of Quantitative Phase Imaging.

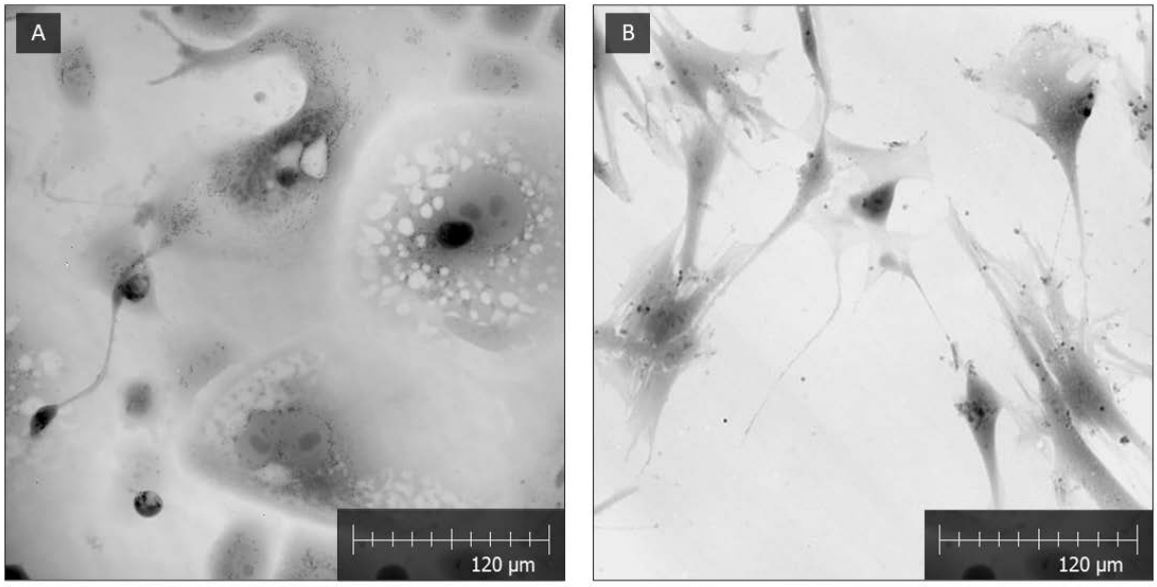

Fig. 2: QPI of cancer cells. Hypoxy-resistant metastatic prostate cancer cell line PC-3 (A) and human head and neck squamous cancer cell line (B). Magnification: 10x.

Type of presentation: Poster

LS3 -P-2504 Effect of arsenic(III) oxide on reproductive organs of female mices

Birinji A.[1], Lalošević D.[2], Marin M.[1]

[1]Faculty of Biology, University of Belgrade, Belgrade, Serbia, [2]Faculty of Medicine, University of Novi Sad,Novi Sad,Serbia

Email of the presenting author: ani.birinji@gmail.com

Arsenic is a toxic metalloid, widespread in nature, it occurs in several valence states, of which trivalent and pentavalent forms are important for the environment1. The higher toxicity of trivalent arsenic compounds compared to pentavalent forms is attributed to the higher affinity for generating reactive oxygen species2. Arsenic is deposited in the liver, kidneys, lungs, brain and skin, and data from scientific researches indicate that arsenic is a reproductive toxicant and a strong endocrine disruptor3. The aim of this study was to determine potentially harmful effect of arsenic(III) oxide in drinking water on morphological integrity of ovarian tissue and follicles of female mice. Mus musculus, strain NMRI female mices, were bred in the vivarium of the Institute for Antirabies Protection - Pasteur Institute, Novi Sad. The mices were housed in standard cages, with free access to water and food, the room temperature, humidity and light regime were controlled. Mices were divided into two groups, the control group received water from the water supply network, while the examined group drank water with dissolved concentration of 10.6 mg/l arsenic(III) oxide for 2 months. Determination of arsenic concentration used in this experiment was performed by converting the values of arsenic concentration from human to animal model (mice). Histological estimations were performed on haemotoxylin and eosin (H&E)-stained sections. No differences were observed between control and treated sections of ovarian tissue and corpus luteum, they had a normal appearance with no signs of hypertrophy (Figure 1. A,B). Beside the follicles contained an intact primary oocytes, organized granulosa layer and theca layer with a normal morphology (Figure 2.A), the results also showed an atretic follicles (Figure 2.B) which were characterized by the presence of a degenerating oocyte, disorganized theca cells and granulosa cell layer. It can be concluded that applied concentration of arsenic(III) oxide, did not cause pathological changes on ovary after 2 months of exposure.

[1] Aposhian HV, Aposhian MM. Arsenic toxicology: five questions. Chem. Res. Toxicol. 2006; 19: 1-15.

[2] Nesnow S, Roop BC, Lambert G, Kadiiska M, Mason RP, Cullen WR, Mass MJ. DNA damage induced by methylated trivalent arsenicals is mediated by reactive oxygen species. Chem. Res. Toxicol. 2002; 15: 1627-1634.

[3] Hughes MF. Arsenic toxicity and potential mechanisms of action. Toxicol. Lett. 2002; 133: 1-16.

Acknowledgement: Participation on the Conference is partly supported by: MPNTR 451-03-68/2022-14/ 200178

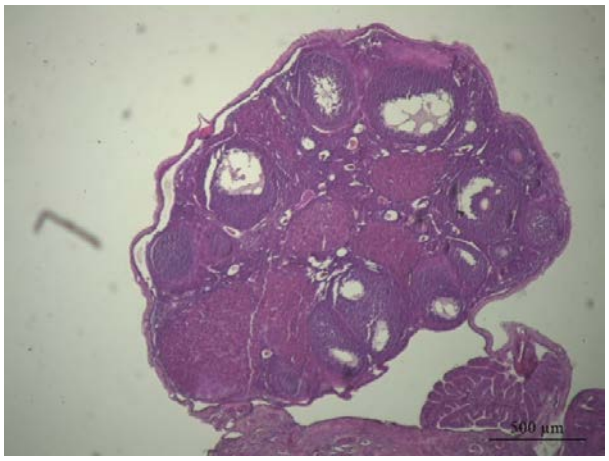

Fig. 1: Mouse ovarian sections, with Corpus luteum and follicular cells at different stages of development. H&E stained. Control ovary (A). Scale bars represent 500 µm.

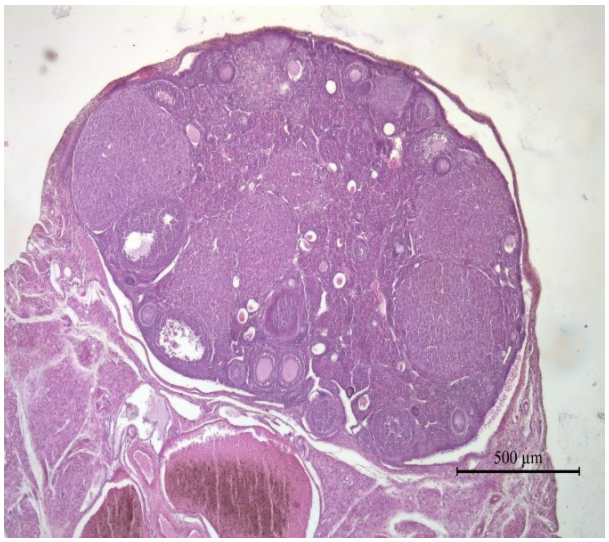

Fig. 2: Mouse ovarian sections, with Corpus luteum and follicular cells at different stages of development. H&E stained. Ovary after 2 months of exposure to arsenic (III) oxide (B). Scale bars represent 500 µm.

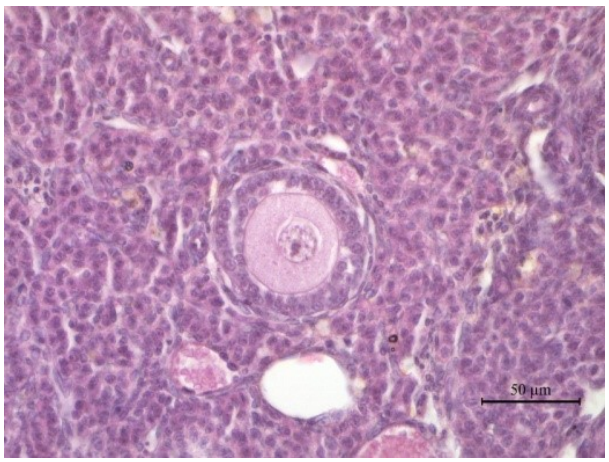

Fig. 3: Mouse ovarian sections after 2 months of exposure to arsenic (III) oxide. H&E stained. Primary oocytes (A). Scale bars represent 50 µm.

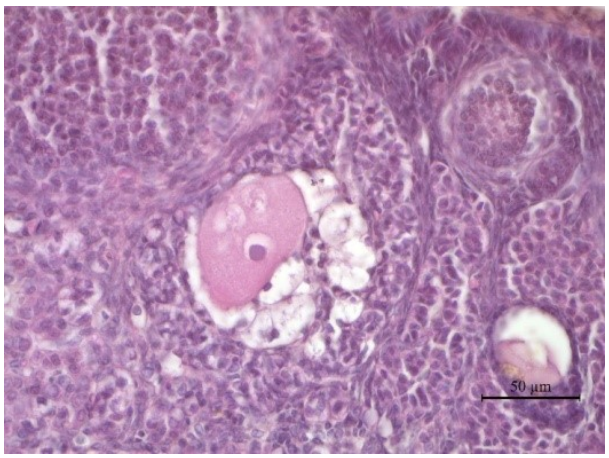

Fig. 4: Mouse ovarian sections after 2 months of exposure to arsenic (III) oxide. H&E stained. Atretic follicles (B). Scale bars represent 50 µm.

Type of presentation: Poster

LS3 -P-2805 Mitochondria activity evaluation under osmotic conditions

Ezati M.[1], Hashemi A.[1], Zumberg I.[1], Cmiel V.[1]

[1]Department of Biomedical Engineering, Faculty of Electrical Engineering and Communication, Brno University of Technology, Technicka 3082/12, 61600 Brno, Czech Republic

Email of the presenting author: 243468@vutbr.cz

Mitochondria generate large quantities of energy in the form of adenosine triphosphate (ATP), store calcium for cell signaling activities and play an important role in the maintenance of ionic balance. Mitochondria, however, are highly sensitive to any kind of stress in which they mainly respond by disturbance of respiration, and reactive oxygen species (ROS) production. Osmotic stress, in particular, generates ROS that degrades lipids, proteins, and DNA [1]. High accumulation of ROS also can disturb cellular redox homeostasis, and result in ion toxicity and oxidative damage. To respond to such conditions, the mitochondria may change shape and size. They also have been shown to join together in response to stress, which is known as mitochondria fusion. [2] This study aims to investigate the possible effects of KCl and NaCl on Bone marrow-derived (MSCs) mitochondria membrane potential (MMP), morphology and superoxide production. The cells were then stained with JC-10 dye (AAT Bioquest, Inc) for investigating the MMP and MitoLite Red FX600 (AAT Bioquest, Inc) for determining the cell's mitochondrial morphology. To determine the production of superoxide by mitochondria, MitoSOX (Red mitochondrial superoxide indicator, Invitrogen) was used. The morphology of the stained cells was studied using confocal fluorescent microscopy. The confocal microscope images indicated that both NaCl and KCl strongly decreased mitochondrial membrane potential after 3 and 24 hours (Fig 1). In addition, the mitochondria morphology analysis confirmed that in some cases, the mitochondria normal structure (tubular shape) changed to round shapes under the stress condition (Fig 2). The result of superoxide staining confirmed that the addition of NaCl and KCl in media induced mitochondrial superoxide production of MSCs after 24 h of culture (Fig 3). Overall these results suggested that putting mitochondria under environmental stress conditions may lead to a decrease in MMP, change in mitochondria structure, fusion into large networks to cope with the stressful situation, and higher production of superoxide which can result in oxidative damage.

[1] L. Michea, C. Combs, P. Andrews, N. Dmitrieva, and M. B. Burg, "Mitochondrial dysfunction is an early event in high-NaCl-induced apoptosis of mIMCD3 cells," American Journal of Physiology-Renal Physiology, vol. 282, no. 6, pp. F981–F990, Jun. 2002, doi: 10.1152/ajprenal.00301.2001.

[2] A. S. Rambold, B. Kostelecky, N. Elia, and J. Lippincott-Schwartz, "Tubular network formation protects mitochondria from autophagosomal degradation during nutrient starvation," Proceedings of the National Academy of Sciences, vol. 108, no. 25, pp. 10190–10195, Jun. 2011, doi: 10.1073/pnas.1107402108.

Acknowledgement: This study was supported by the Brno University of Technology and authors thankfully respected for financial support.

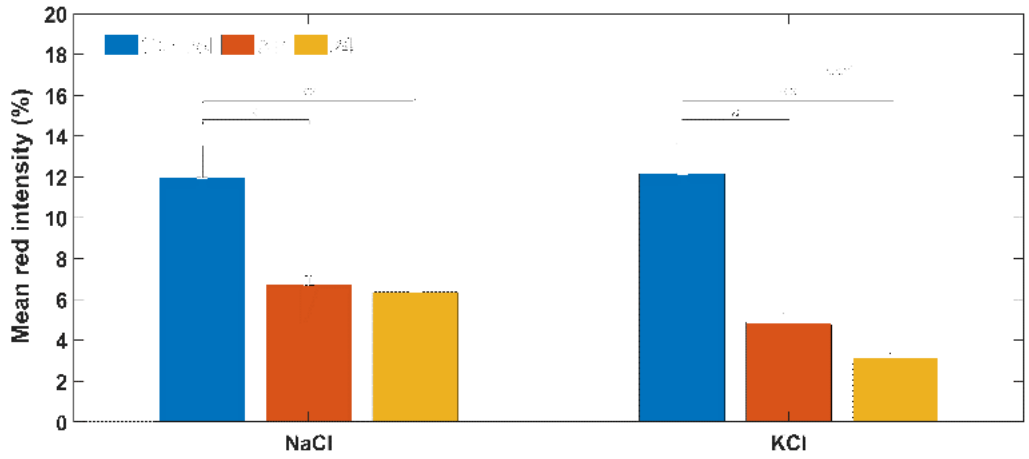

Fig. 1: Mitochondrial membrane potential assessment of MSCs exposed to 180 mM NaCl and 150 mM KCl for 3 and 24 h. Data are presented as mean ± SD; n = 3. *p<0.05 control compared to NaCl and KCl after 3 h, **p<0.05 control compared to NaCl and KCl after 24 h, ***p<0.05 KCl (3h) compared to KCl (24h).

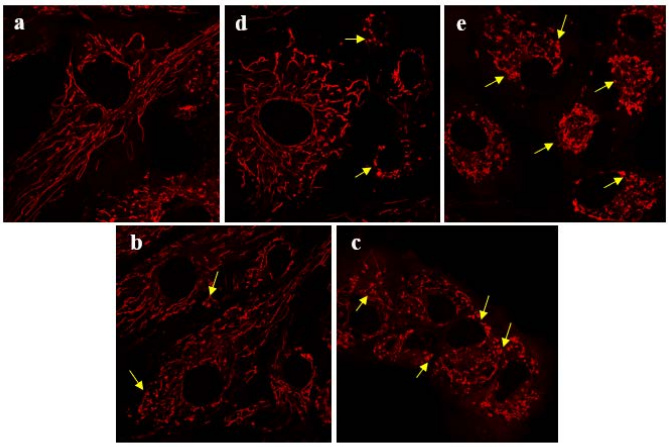

Fig. 2: Confocal fluorescence microscopic images of mitochondria morphology in MSCs in control (a), 3 h (b) and 24 h (c) after treatment with KCl and 3 h (d) and 24 (e) after treatment with NaCl. Yellow arrows show locations where mitochondria fusion can be seen. Scale bar 30 µm.

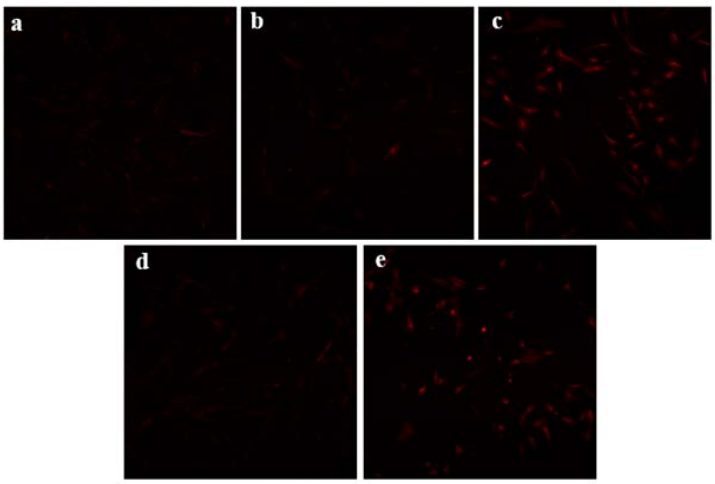

Fig. 3: Mitochondrial superoxide was detected by MitoSOX red mitochondrial superoxide indicator. Confocal fluorescence microscopic images of mitochondria in MSCs in control (a), 3 h (b) and 24 h (c) after treatment with KCl and 3 h (d) and 24 (e) after treatment with NaCl.

Type of presentation: Poster

LS3 -P-2916 Translation initiation stages of coupled transcription-translation

Hassan A. H.[1], Nagaraj P. H.[1], Chauvier A.[2], Walter N. G.[2], Demo G.[1]

[1]Central European Institute of Technology, Masaryk University, Brno, Czech Republic,
[2]Department of Chemistry and Centre for RNA Biomedicine, University of Michigan, Ann Arbor, MI, USA

Email of the presenting author: ahmed.hassan@ceitec.muni.cz

Transcription and translation are functionally coupled and highly coordinated in most bacterial species [1,2], with few exceptions such as Bacillus subtilis [3]. Translational riboswitches (cis-acting RNA structures) located in the 5' untranslated region of mRNAs can modulate transcription pausing or premature termination [4]. They can regulate both transcription and translation in a ligand-dependent manner and serve as an excellent model system to investigate the coordination of coupled transcription-translation.
Here we use a pre-queuosine1 (PreQ1) sensing riboswitch to understand the coordination of translation initiation and RNA polymerase (RNAP) pausing during transcription. Using cryo-electron microscopy as a primary approach we investigate the mRNA loading mechanism onto small ribosomal subunit (30S) and the coordination of translation initiation and transcription elongation. Our specific focus is to understand the dynamics of 30S binding to the mRNA riboswitch containing ribosomal binding site, formation and stabilization of pre-initiation complex and subsequent transient interactions during the initial steps of transcription-translation coupling.

1. M.W. Webster, M. Takacs, C. Zhu, et al. Science, 369, (2020), 1355–1359.
2. C. Wang, V. Molodtsov, E. Firlar, et al. Science, 369, (2020), 1359–1365.
3. G.E. Johnson, J.B. Lalanne, M.L. Peters et al. Nature, 585, (2020), 124–128.
4. S. Chatterjee, A. Chauvier, S.S. Dandpat, et al. Proc. Natl. Acad. Sci. U.S.A., 118, (2021), e2023426118.

Acknowledgement: This study was supported by LL2008 project with financial support from MEYS CR as a part of the ERC CZ program (to G.D.).

Type of presentation: Poster

LS3 -P-2654 NME6, a member of the NME/NDPK family resides in complexes at the interface of mitochondrial inner membrane and matrix

Proust B.[1], Radić M.[1], Škrobot Vidaček N.[1], Ačkar L.[1], Tokarska-Schlattner M.[2], Cottet C.[2], Ćetković H.[3], Schlattner U.[2], Herak Bosnar M.[1]

[1]Division for Molecular Medicine, Ruđer Bošković Institute, Zagreb, Croatia, [2]Laboratory of Fundamental and Applied Bioenergetics, Univ. Grenoble Alpes, Grenoble, France, [3]Division for Molecular Biology, Ruđer Bošković Institute, Zagreb, Croatia

Email of the presenting author: mherak@irb.hr

The nucleoside diphosphate kinases (NDPK/NME/Nm23) are a family of enzymes catalyzing the transfer of gamma phosphate from NTPs to NDPs. The family consists of 10 members in human. The family is divided in two groups. Group I (NME1-NME4) members are highly homologous among themselves and exhibit NDPK activity. Studies of cytosolic NME1/2 and mitochondrial NME3/4 revealed the enzymatic activity mechanism, which depends on the phosphorylation of a specific histidine in the catalytic site, and requires NMEs to assemble as hexamers. Group II (NME5-NME9) members display less homology and seem to be NDPK inactive. Extensive research has been conducted on Group I members after the discovery of NME1's role in metastasis suppression, while Group II remained largely unexplored. We focused our research on the barely explored Group II mitochondrial NME6 protein. We used immunofluorescence and live cell imaging together with time laps microscopy to confirm NME6 mitochondrial localization, and refined it using mitochondrial subfractionation. Fractionation of mitochondria by the swelling/shrinking procedure was analyzed by western blot and showed a NME6 distribution pattern highly similar to proteins of the matrix. It has also been revealed that overexpressing NME6 leads to downregulation of components oxidative phosphorylation chain. Although the proximity ligation assay indicated that NME6 forms complexes with mitochondrial proteins OPA1, NME4 and RCC1L the immunoprecipitation showed that the NME6 protein physically interacts only with RCC1L, a protein involved in coordination of the mitochondrial ribosome assembly. Together, these results provide precious clues for understanding the NME6 function and its possible impact on the respiratory chain and mitoribosomal translation and assembly.

1. Proust B, Radić M, Škrobot Vidaček N, Cottet C, Attia S, Lamarche F, Ačkar L, Godinić Mikulčić, Tokarska-Schlattner M, Schlattner U, Herak Bosnar M*. NME6 is a phosphotransfer-inactive, monomeric NME/NDPK family member and functions in complexes at the interface of mitochondrial inner membrane and matrix. Cell Bioscience 11, 1, 2021.

Type of presentation: Poster

LS3 -P-2924 Active transcription-translation coupling at the early translation elongation stages

Hiriyur Nagaraj P.[1], Slamova L.[1], Brabencova S.[1], Demo G.[1]

[1]Central European Institute of Technology, Masaryk University, Brno, Czech Republic

Email of the presenting author: Pradeep.Nagaraj@ceitec.muni.cz

In Bacteria and Archaea, mRNAs are translated by ribosomes simultaneously as they are transcribed. The physically coupled transcription and translation (CTT) mechanism was confirmed and visualized by cryo-electron microscopy (cryo-EM) [1,2]. The biochemical studies confirmed the synchronous rates of transcription and translation in *E. coli* suggesting a regulatory function of the leading ribosome on the RNAP propagation [3]. However, the *in-vitro* cryo-EM structures show stationary CTT complexes bridged by transcription factors NusG alone [1] or in combination with NusA [2]. These CTT complexes [1,2,3] lack the involvement of translation elongation factors such as EF-Tu or EF-G to activate translation phase in CTT.

Here we present biochemical and cryo-EM evidence of physically interacting bacterial 70S ribosome and RNA polymerase (RNAP). The sucrose gradient binding assays confirm the presence of RNAP in the elution peak of 70S ribosome with bound nucleic acid scaffold. The initial cryo-EM map reconstruction of the CTT complex shows poor RNAP occupancy due to its dynamic behaviour. Future studies are aimed to capture the early elongation steps of CTT using EF-Tu and GTP in a time-dependent manner. Time-resolved cryo-EM approach will enable the investigation of active transcription-translation coupling via EF-Tu initiated translation elongation process.

Reference

1. C. Wang, V. Molodtsov, E. Firlar, et al. Science, 369, (2020), 1359–1365.
2. M. W. Webster, M. Takacs, Ch. Zhu, et al. Science, 369, (2020), 1355–1359.
3. R. Kohler, R.A. Mooney, D.J. Mills, et al. Science, 356, (2017) 194–197.

Acknowledgement: This study was supported by the **LL2008** project with financial support from MEYS CR as a part of the ERC CZ program (to GD)

Type of presentation: Poster

LS3 -P-2652 Formation of cell junctions during integument morphogenesis in crustacean Porcellio scaber

Kunčič K.[1], Mrak P.[1], Žnidaršič N.[1]

[1]University of Ljubljana, Biotechnical Faculty, Department of Biology, Ljubljana, Slovenia

Email of the presenting author: katja.kuncic@bf.uni-lj.si

Epithelia function as selectively permeable barriers between the internal environment of the organism and the external environment in various organs. The architecture and function of epithelia crucially depend on cell-cell junctions. They have been shown to reorganise in relation to organ morphogenesis during development and epithelial renewal in adults. Invertebrate epithelial cells are mechanically connected mainly by adherens junctions (AJ), while septate junctions (SJ) restrict paracellular transport. The formation of cell junctions during invertebrate development has been rarely studied. Most research has been performed in the fruit fly (*Drosophila melanogaster*) epithelia [1]. Our study focuses on the ultrastructural aspects of the formation and remodelling of SJs in the epidermis of adult animals and selected embryonic and postembryonic (mancae) developmental stages of the crustacean *Porcellio scaber* (Latreille, 1804) [2]. The epidermis of arthropods is ectodermal in origin and secretes a chitinous matrix, a multi-layered cuticle that forms the exoskeleton. For the analysis, specimens were chemically fixed in aldehydes, post-fixed in 1% OsO_4, and embedded in epoxy resin Agar 100. Semithin (0.5 µm) and ultrathin (70 nm) sections were imaged by light and transmission electron microscopy, respectively. Our results show that individual septa of SJs, located basally to the AJs, are resolved at the earliest in the mid-embryonic stage. SJs' differentiation during further development involves a gradual increase in the number of septa and formation of long and continuous arrays of septa (Figs. 1A, B). A significant elongation of septa arrays in the epidermis is characteristic for the transition from embryonic to postembryonic development and for the release of the mancae from the female marsupium into the external environment. SJs in the epidermis of early postmarsupial stages architecturally resemble those of adults, although they are not so extensive (Figs. 1C, D). We noted a significant remodelling of SJs during cuticle renewal in molting marsupial mancae. Common features of SJs' biogenesis in functionally distinct ectodermal epithelia in arthropods are indicated [1, 3].

References:

[1] U. Tepass, V. Hartenstein, Dev. Biol. 1994, 161, 563–596.
[2] M. Milatovič, R. Kostanjšek, J. Štrus, J. Crustac. Biol., 2010, 30, 225–235.
[3] U. Bogataj, P. Mrak, J. Štrus, N. Žnidaršič, Arthropod Struct Dev, 2019, 50, 78–93.

Acknowledgement: The authors acknowledge financing from the Slovenian Research Agency (No. P1-0184) and the IC equipment MRIC I0-0022 (BF, UL) and I0-0004 IC NIB.

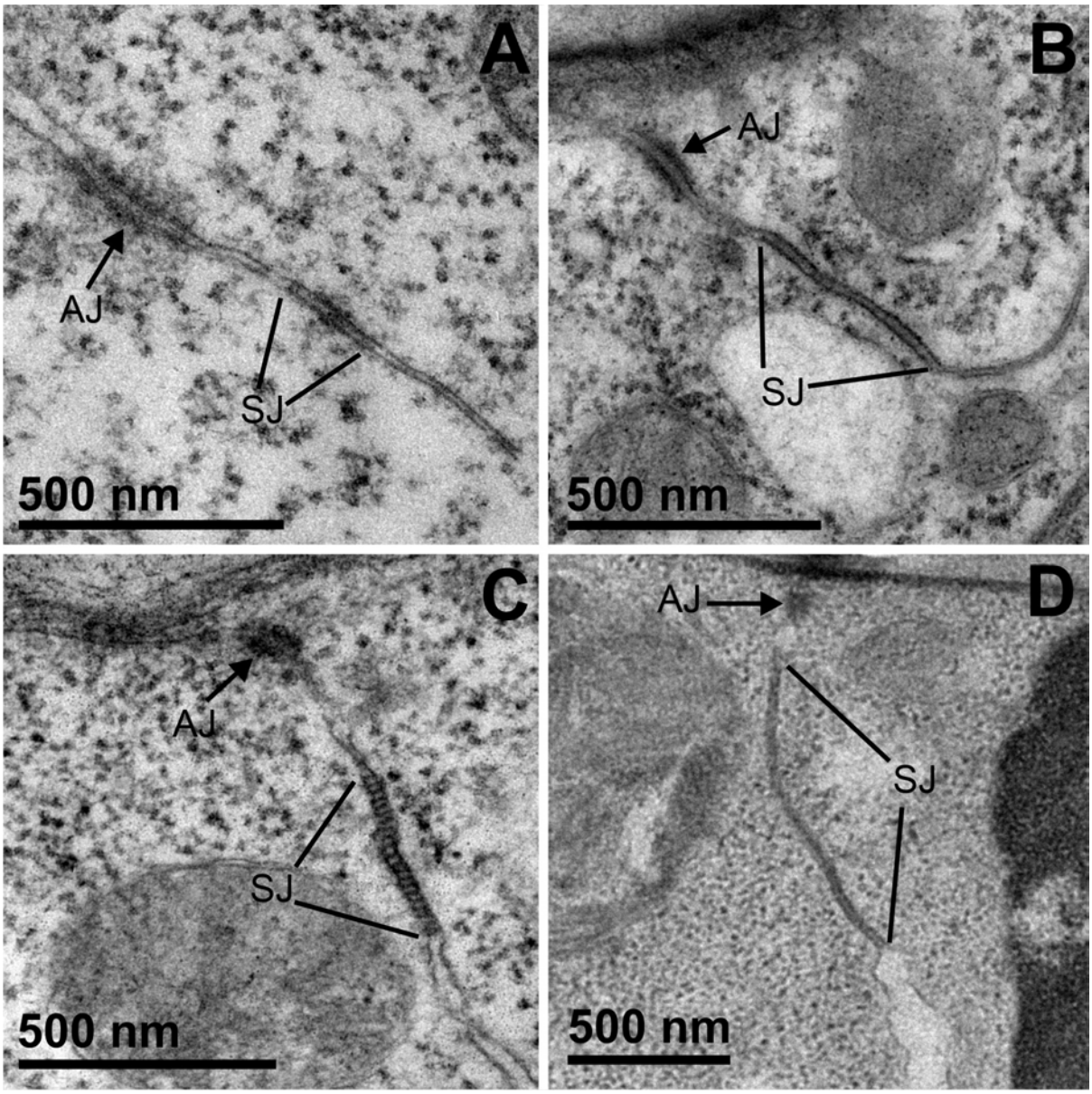

Fig. 1: Septate junctions' biogenesis in the epidermis of *Porcellio scaber*. A. Short arrays of septa are characteristic of the embryonic epidermis. B-C. Long and continuous arrays of septa span the intercellular space in postembryonic stages. D. Extensive SJs in the epidermis of adult animals. AJ: adherens junction, SJ: septate junction.

Type of presentation: Poster

LS3 -P-2799 Beneficial effects of ferroptosis inhibitor ferrostatin-1 on pancreatic islets in streptozotocin-induced diabetes

Markelić M. B.[1], Stančić A. T.[2], Katanić K. R.[3], Saksida T. A.[4], Veličković K. D.[1], Gajić D. M.[4], Grigorov I. I.[3], Otašević V. M.[3]

[1]Department of Cell and Tissue Biology, Faculty of Biology-University of Belgrade, Belgrade, Serbia, [2]Department of Molecular Biology, Institute for Biological Research "Siniša Stanković", University of Belgrade, Serbia, [3]Faculty of Biology-University of Belgrade, Belgrade, Serbia, [4]Department of Immunology, Institute for Biological Research "Siniša Stanković", University of Belgrade, Serbia

Email of the presenting author: milica.markelic@bio.bg.ac.rs

Ferroptosis is an iron-dependent regulated form of cell death characterized by the accumulation of lipid peroxides. In our recent study we have demonstrated involvement of ferroptosis in the β-cell loss under diabetogenic conditions *in vitro* [1]. This study proposed ferroptosis as a new potential target in the diabetes therapy approach, among the other β-cell death types which have been described previously. In addition, our preliminary *in vivo* results have demonstrated beneficial effects of ferroptosis inhibitor, ferrostatin-1 (Fer-1) in streptozotocin (STZ)-treated mice [1].
The aim of this study was to further elucidate the protective effects of Fer-1 treatment in β-cells' survival and protection under diabetogenic STZ-driven injury *in vivo*. For that purpose, male C57BL/6 mice were divided into three groups (n=8): diabetic (D, STZ-treated), diabetic Fer-1-treated (DF), and vehicle-treated (control, C) animals. STZ (40 mg/kg) and Fer-1 (1 mg/kg) were administered intraperitoneally, STZ from day 1-5; Fer-1 from day 1-21. All animals were sacrificed at day 22 of the experiment, pancreata were collected, paraffin-embedded and prepared for the light microscopic examinations.
Our results demonstrated that Fer-1-driven inhibition of ferroptosis in diabetic mice diminished diabetic insults of pancreatic islets and β-cells. Although islets' surface area remained decreased in both D and DF groups, without regard to Fer-1 treatment, statistically significant increase of islets' volume density has been noted in DF group (Fig. 1). In addition, average insulin immunopositivity of islets increased after Fer-1 treatment (Fig. 2), which is in line with lower glycaemia serum values in this group [1]. Immunofluorescence localization of xCT, a subunit of system Xc- (a cystine/glutamate antiporter system which provides the glutathione precursor L-cysteine), has demonstrated that Fer-1 prevents decrease and even increases its expression in islets' cells, including β-cells. In addition, immunoexpression of heme oxygenase-1 (HO-1), an enzyme involved in the protection against cell death, decreased significantly in islet cells of D group, while more cells with strong HO-1 immunoexpression were detectable in the islets of DF animals (Fig. 3).
Taken together, these results demonstrate that Fer-1 reduces damage of islets and β-cells in diabetes, clearly confirming ferroptosis involvement in the pathogenesis of this disease.

[1] Stancic A, Saksida T, Markelic M, Vucetic M, Grigorov I, Martinovic V, Gajic D, Ivanovic A, Velickovic K, Savic N, Otasevic V. Ferroptosis as a Novel Determinant of β-Cell Death in Diabetic Conditions. Oxid Med Cell Longev. 2022:3873420 (2022)

Acknowledgement: Serbian Ministry of Education, Science and Technological Development (No. 451-03-68/2022-14/200007); Science Fund of the Republic of Serbia (No. 6525651)

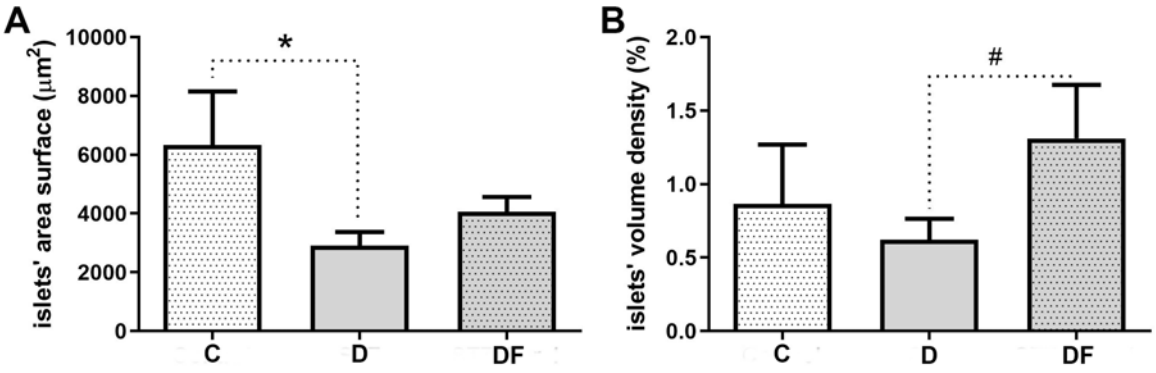

Fig. 1: Morphometric and stereological analyses of pancreatic islets of control, diabetic and diabetic ferrostatin-1 (Fer-1)-treated mice. A) Surface of islets area ($^{*}p<0.05$); B) volume density of islets ($^{\#}p<0.05$). Values presented as means ± SEM

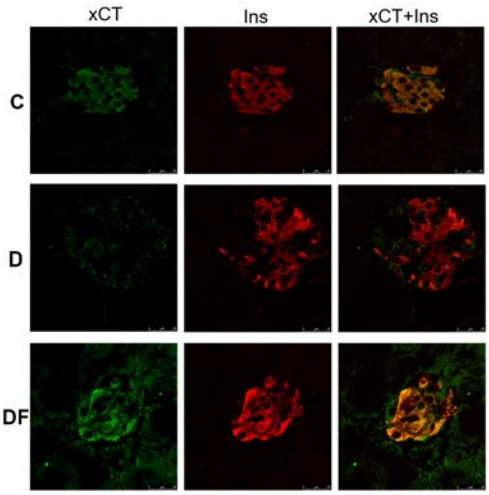

Fig. 2: Immunofluorescence detection of xCT and insulin (Ins) in pancreatic islets of control, diabetic and diabetic Fer-1-treated mice. Magnification x63, scale bar 25 μm

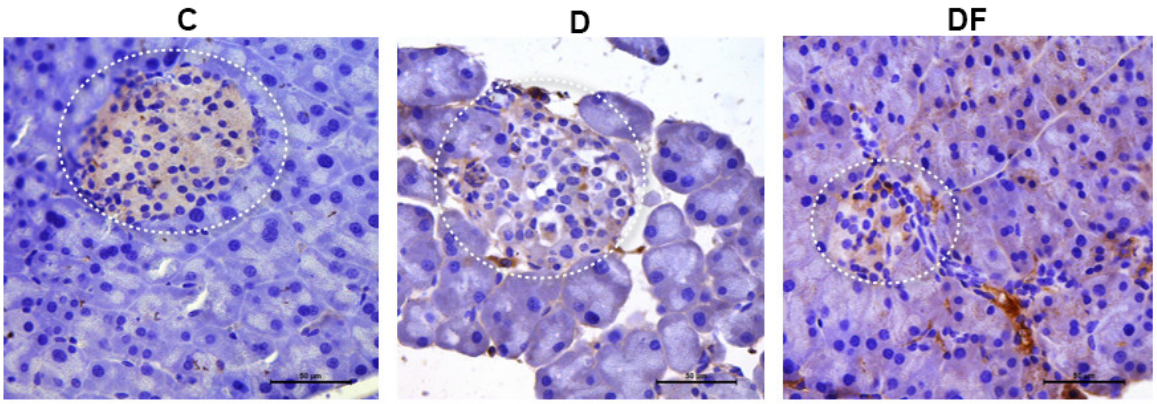

Fig. 3: Immunohistochemical detection of heme oxygenase-1 (HO-1) in pancreatic islets (encircled) of control, diabetic and diabetic Fer-1-treated mice. Magnification x40, scale bar 50 μm

Type of presentation: Poster

LS3 -P-2812 Beneficial effects of ferroptosis inhibitor ferrostatin-1 in diabetes-induced liver damage

Veličković K. D.[1], Markelić M. B.[1], Stančić A. T.[2], Saksida T. A.[3], Gajić D. M.[3], Grigorov I. I.[2], Martinović V. I.[2], Otašević V. M.[2]

[1]1Department of Cell and Tissue Biology, Faculty of Biology-University of Belgrade, Belgrade, Serbia, [2]Department of Molecular Biology, Institute for Biological Research , [3]Department of Immunology, Institute for Biological Research

Email of the presenting author: milica.markelic@bio.bg.ac.rs

Ferroptosis is a form of cell death and the main cause of tissue damage driven by iron overload and lipid peroxidation. Recently we have demonstrated the involvement of ferroptosis in the β-cell loss under diabetogenic conditions [1].

The aim of the present study was to explore the protective role of a ferroptosis inhibitor, ferrostatin 1 (Fer-1) in liver injury induced by diabetes mellitus (DM). Male C57BL/6 mice were divided in three groups (n=8): diabetic (D, streptozotocin (STZ)-treated), diabetic Fer-1-treated (DF), and control (C) group. STZ (40 mg/kg) and Fer-1 (1 mg/kg) were applied intraperitoneally, STZ from day 1-5; Fer-1 from day 1-21. Liver tissue was routinely prepared for histological, morphometric, stereological, and immunohistochemical analyses.

Microscopic signs of hepatocellular damage observed in D animals: extensive vacuolization, sinusoidal dilation, and inflammation were markedly reduced in DF group (Fig. 1A). Further, Fer-1 reduced liver fibrosis in D animals, as confirmed by stereological analysis (Fig. 1B). Regarding the hepatocyte size (measured as surface area; Fig.2A), statistical increase was noted in the D group, when compared to the C group. When hepatocytes of different liver lobules' zones were analysed, it became evident that this vacuolization effect of DM was more pronounced in periportal (Z1) than in pericentral zone (Z3), which was diminished in DF group. Hepatocytes were statistically larger in Z1 zone for both D and DF groups (Fig. 2B).

Taken together, our results indicate that Fer-1 decreases the accumulation of lipid peroxides in the diabetic liver and diminishes signs of damage. This suggests involvement of ferroptosis in DM-related liver damage and sheds new light on an antidiabetic strategy. Also, our results demonstrate different responses to DM insults among the lobule zones, confirming the necessity of a better understanding of the liver spatial organisation under physiological and pathological conditions.

[1] Stancic A, Saksida T, Markelic M, Vucetic M, Grigorov I, Martinovic V, Gajic D, Ivanovic A, Velickovic K, Savic N, Otasevic V. Ferroptosis as a Novel Determinant of β-Cell Death in Diabetic Conditions. Oxid Med Cell Longev. 2022:3873420

Acknowledgement: Serbian Ministry of Education, Science and Technological Development (No. 451-03-68/2022-14/200007); Science Fund of the Republic of Serbia (No. 6525651)

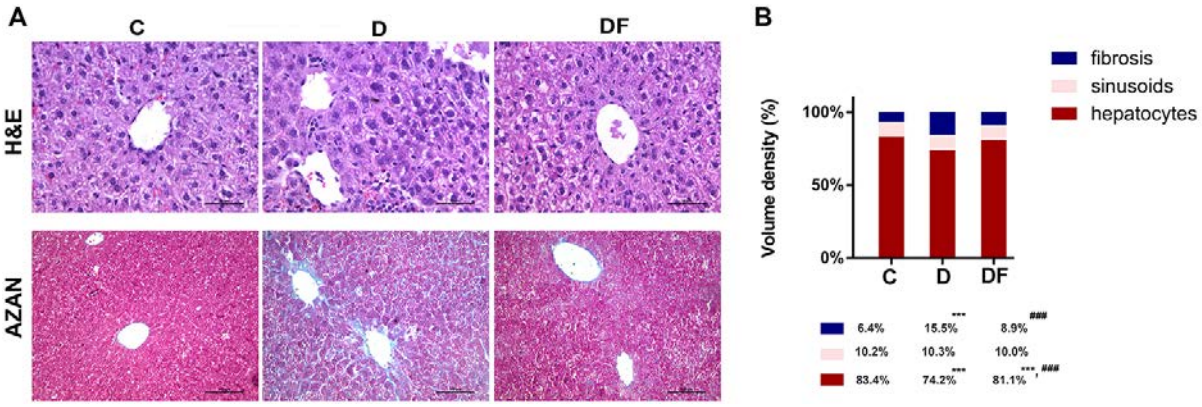

Fig. 1: Histological and stereological analysis of liver tissue. (A) Hematoxylin & eosin (H&E) and AZAN trichrome staining for detection of collagen (blue); scale bars: 50 μm (B) Volume density of hepatocytes, sinusoids, and fibrosis. Compared with the C group (***p<0.001); D vs. DF comparison (###p<0.001). Values presented as means ±SEM.

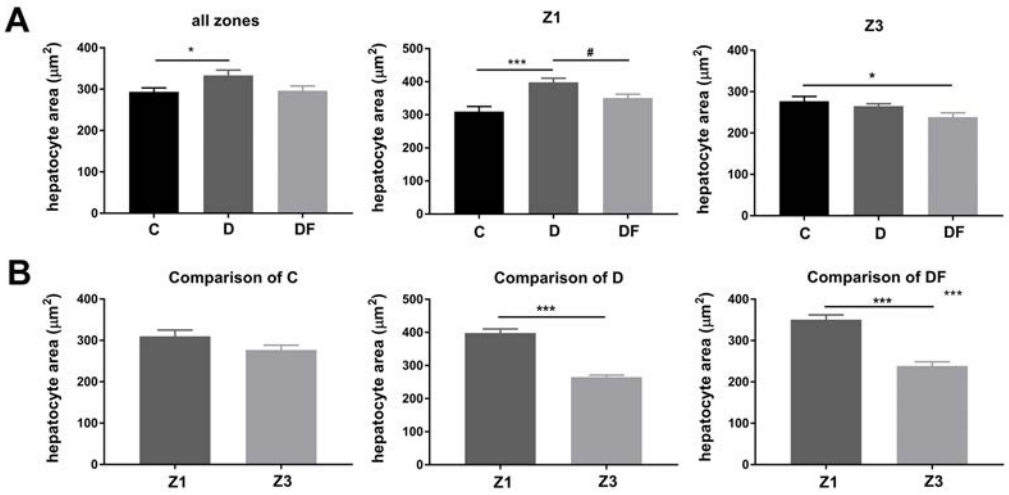

Fig. 2: Morphometric analyses of liver tissue: hepatocytes profile area of all zones, Z1 and Z3 zone, compared A) between groups and B) between the zones. Values presented as means ±SEM; statistical significance: *p<0.05, ***p<0.001, , #p<0.05

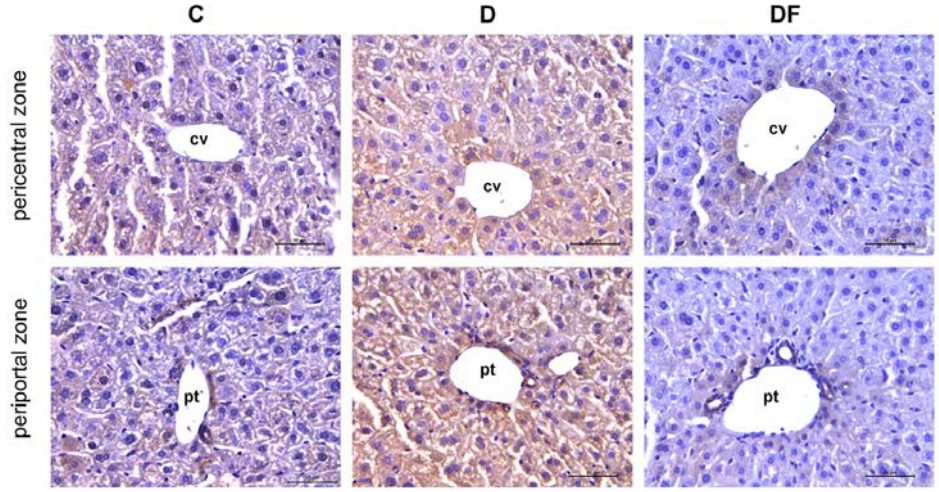

Fig. 3: Immunohistochemical analysis of 4-HNE in pericentral and periportal zones of the liver tissue of C, D and DF animals. cv - central vein, pt - portal triad; scale bars: 50 μm

Type of presentation: Poster

LS3-P-2704 Vitamin-D combined with resveratrol regulates islets hemostasis, β-cell regeneration, ER-stress and inflammation in fructose-fed diet/STZ-induced diabetic rats

Kaya-Dagistanli F.[1], Akdemir A. S.[1], Anapali M.[2], Aydemir D.[3], Tanriverdi G.[4], Ulusu N. N.[3], Ulutin T.[1], Ozturk M.[1]

[1]Istanbul University-Cerrahpasa, Cerrahpasa Faculty of Medicine, Department of Medical Biology, [2]Atatürk University, Faculty of Medicine, Department of Medical Biology, [3]Koc University, School of Medicine, Medical Biochemistry Department, Istanbul, Turkey, [4]Istanbul University-Cerrahpasa, Cerrahpasa Faculty of Medicine, Department of Histology and Embryology

Email of the presenting author: mozturk@iuc.edu.tr

High fructose diet with STZ is a model to mimic for type 2 diabetes (T2DM) (1). Inflammation and oxidative stress cause β-cell loss and insulin resistance (2,3).We investigated the effects of combined resveratrol(RSV) and vitamin-D(VitD) treatment on pancreatic islet cells activation and β-cell in fructose-fed diet/streptozotocin(STZ)-induced T2DM rats.
In diabetic groups, a single dose of STZ(40mg/kg) was injected after a 10% fructose diet(FD) for 2-weeks, then continued FD for 3-weeks. At the end of 5-weeks, rats were treated with combined RSV and VitD for 4-weeks. The tissue sections were immunostained with insulin, glucagon, somatostatin, active caspase3, PCNA, IL6, TNFα, IL1β, GRP78, CHOP antibodies. Glucagon, insulin, GIP, GLP1, PP, PYY, MCP1 serum levels were measured.TUNEL method was used to detect apoptotic cells. TEM was used for ultrastructural examination.
BG levels and serum insulin levels (IL) increased significantly in all diabetic groups compared with the control groups. In the combined treatment group, serum IL levels were similar to the control group, consistent with increased β-cell mass. Combined-treatment increased GLP1 levels whereas decreased glucagon levels in the controls (Fig1). In the combined group, markedly enhanced β-cell mass and clusters scattered in the exocrine tissue as well as around the ducts were observed compared to the diabetics (Fig2). Glucagon(+) cells significantly decreased in the islets of the combined group, consistent with the decreased serum GLP1 and increased glucagon levels compared to the diabetics.PCNA(+) cells were increased in the big size islets of the combined group compared to the diabetics. The expressions of IL1β, TNFα, IL6, GRP78, and CHOP were increased in islets of the diabetic group compared to the other groups. Active caspase-3(+)and TUNEL(+) apoptotic cells were increased in the islets of diabetic group compared to other groups. Ultrastructurally, apoptotic β-cells, also decreased insulin granules, dilated ER and autophagic vacuoles were seen in β-cells of the diabetic group, the islets and β-cells structures were close to the control group in the combined group.
We found that the combined therapy with RSV and VitD contributes to the improvement of islets morphology and hormonal secretion, tissue inflammation, β-cell regeneration, reduction of oxidative and ER stress, protection of β-cells from glucotoxicity and cytokine damage with their anti-inflammatory effect by providing the regulation of glucose and insulin homeostasis in the this diabetes model. We considered that the combined RSV+VitD usage might be beneficial in T2DM.
[1] Wilson RD, Islam MS. Pharmacol Rep. 2012; 64(1):129-39.
[2] Cerf ME Front Endocrinol (Lausanne). 2013;4:37
[3] Tsalamandris S, et al. Eur Cardiol. 2019;14(1):50-59.

Acknowledgement: The study was supported by the Research Fund of Istanbul University-Cerrahpasa, Istanbul, Turkey Project No. TSA-2019-32274

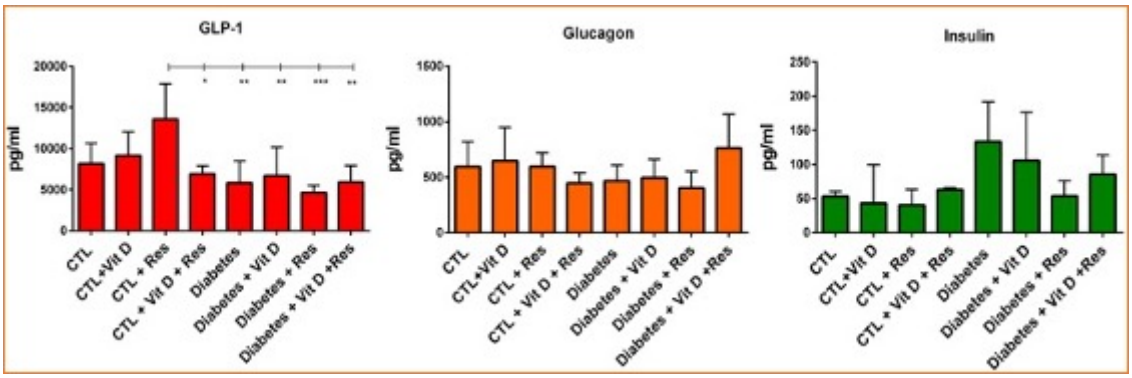

Fig. 1: Serum GLP-1, insulin and glucagon levels of rats in all experimental groups

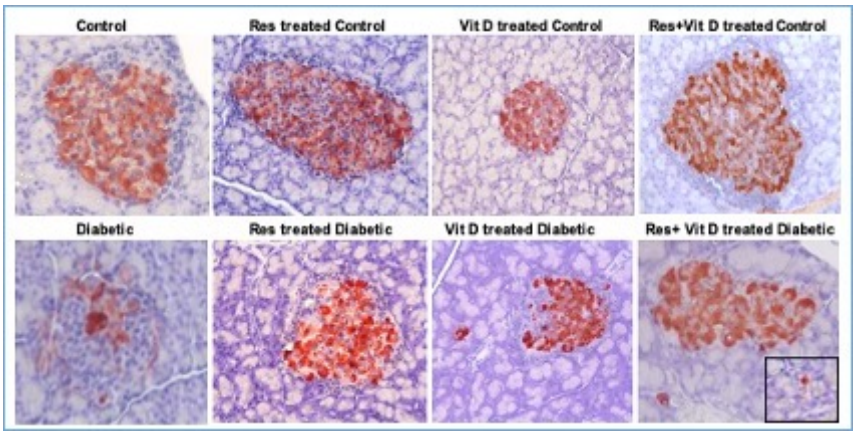

Fig. 2: Immunolocalization of insulin in the pancreatic islets of rats in all experimental groups. Res: Resveratrol. Immunostaining: Streptavidin-biotin peroxidase method. Magnifications: 200x

Type of presentation: Poster

LS3-P-2756 Differentiation of DDR1+ progenitor cells into β cells in neonatal rat diabetes

Ozturk M.[1], Kaya-Dagistanli F.[1], Argun Kurum G.[1]

[1]Istanbul University-Cerrahpasa, Cerrahpasa Faculty of Medicine, Department of Medical Biology, Istanbul, Turkey

Email of the presenting author: mozturk@iuc.edu.tr

Pancreatic islet cells originate from intra and extra islet progenitor cells. Pdx1 as a marker of β cell is detected predominantly in adult β cells[1]. DDR1 has been suggested as a bio-surface marker for endocrine progenitor cells, specifically in pancreatic islets[2]. DDR1 expression is observed during the embryonic stage in the pancreas as co-located with Pdx1 positive progenitor cells, suggesting a role for DDR1 in endocrine cell differentiation[2]. The distribution of DDR1 expression in islets under diabetic conditions is not clear. It has been shown that DPP4 inhibitor induces DDR1 expression in diabetic rats[3]. Neonatal diabetes models are recommended for detection of β cell regeneration. In this study, the relationship between β cells and DDR1 progenitor cells in short and long diabetes periods were investigated in order to determine the differantiation of progenitor cells into β cells in a STZ-induced neonatal diabetes model. The neonatal rats were divided into two main groups as control(C) and diabetic(D). Neonatal STZ diabetic group(n2-STZ) were created at the 2nd day of birth with a single dose of 100mg/kg STZ injection, then divided into subgroups; the short-term (3rd,5,7 and 10th days) and the long-term (30th day). Immunohistochemistry(IHC) were performed by using insülin(ins), Pdx1, PCNA and DDR1 antibodies, also stained double IHC for ins/DDR1. DDR1 plasma membrane(PM+) and/or cytoplasmic(C+) positive cells were evaluated. We found that after STZ the β cells reduced 5th day, then their numbers increased beginning of 7th day. The ins(+) cells in exocrine tissue, within duct epithelium and around of duct as a few cells or small β cell mass. In diabetics Pdx1(+) cells were decreased in islets whereas increased in extra islets areas in 3rd to 10th days compare to the controls. The β cell neogenesis and regeneration were increased from 7 to 10th days, whereas the rate of regeneration capacity were reduced at long term. DDR1 expression(C+) started in early stage (3rd and 5th days), whereas the membrane localization(PM+) were observed in the islet cells at the 7-10th day in n2-STZ dibetics. Double positive(ins/DDR1) cells were seen mainly in 7 and 10th days and rarely in the long term group(Fig 1). The results suggested that STZ induction stimulates DDR1 expression for β cell regeneration and differentiation in early stages of newborn rats. The β cell differantiation from DDR1+ progenitor cells increased from 7th day, whereas the rate of regeneration capacity is reduced at the long term diabetes. These results will provide direction for β cell regeneration studies.

[1] Kaya-Dagistanli F, Ozturk M. Acta Histochem 2020;122(7):151612
[2] Hald J, et al. Diabetologia 2012;55(1):154-65.
[3] Argun-Kurum G, et al. Pharmacol Rep. 2019;71(4):721-731.

Acknowledgement: This study was supported by the Research Fund of Istanbul University, Istanbul, Turkey. Projects; T-215/06032003 and 28090.

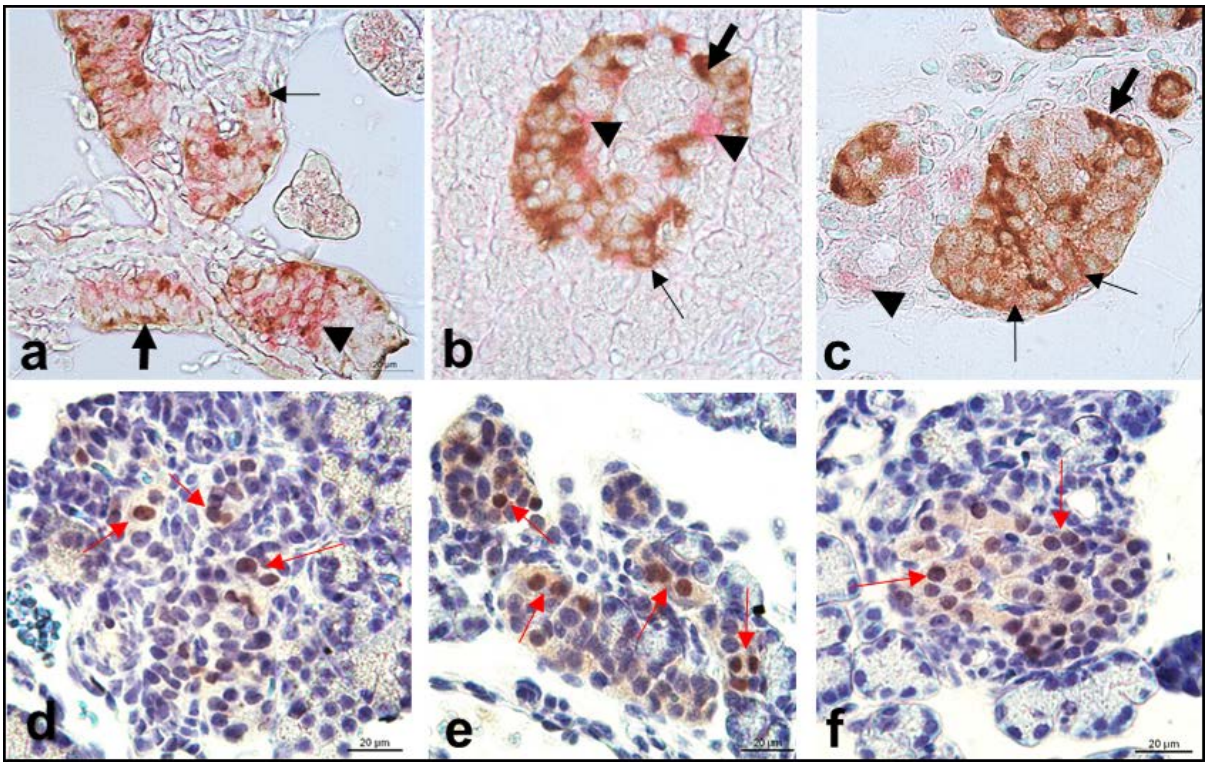

Fig. 1: Immunolocalizations in the pancreas sections of in neonatal STZ diabetic groups. ins/DDR1(+) (thin arrow), DDR (+) (arrow head), ins (+) (tick arrow), Pdx-1 nuclear (+) (red arrow) at the 5th (a,d), 7th (b,e) and 10th (c,f) days. Immunostaining; Streptavidin-biotin-peroxidase, Counterstaining for Pdx-1; Hematoxylin.

Type of presentation: Poster

LS3 -P-2643 Insect midgut epithelium architecture – focus on gut stem cells in larvae and adults

Žnidaršič N.[1], Bogataj U.[1], Mark P.[1], Žigon P.[2], Razinger J.[2], Sabotič J.[3]

[1]University of Ljubljana, Biotechnical Faculty, Department of Biology, Ljubljana, Slovenia, [2]Agricultural Institute of Slovenia, Plant Protection Department, Ljubljana, Slovenia, [3]Jožef Stefan Institute, Department of Biotechnology, Ljubljana, Slovenia

Email of the presenting author: nada.znidarsic@bf.uni-lj.si

Introduction

Stem cells are of increasing interest as they are crucial for development, tissue homeostasis and regeneration, but also play a role in aging and diseases. In general, stem cells can divide to self-renew and have the ability to give rise to the mature cell types that construct tissues and organs. Structure and function of stem cells is mainly studied in mammals. Data on stem cells in invertebrates is very incomplete and refers mainly to model organisms, e.g. the fruit fly (*Drosophila melanogaster*) [1]. The gut epithelium of insects is a highly regenerative tissue that serves as a physical and chemical barrier to the environment and responds to diverse physiological and pathophysiological stimuli [2]. To improve the understanding of the structure, function and regeneration of the insect gut and to gain new insights into invertebrate stem cells, it is necessary to study diverse insect gut epithelia in adults and in different developmental stages of the organism.

Material and methods

We have analysed the architecture of the midgut epithelia in larvae and adults of the spotted wing drosophila (*D. suzukii*) and in larvae of the Colorado potato beetle (*Leptinotarsa decemlineata*). To the best of our knowledge, no data on stem cells in these epithelia has been reported before. Dissected gut samples were fixed in aldehydes, embedded in resin and sections were imaged by light and transmission electron microscopy.

Results and discussion

The midgut epithelium of adult spotted wing drosophila comprises several cell types, with absorptive enterocytes being the most abundant cells (Fig. 1A). Individual stem cells can be distinguished at the base of epithelium. In the spotted wing drosophila larvae stem cells are more abundant and appear as clusters of cells in the basal region of the epithelium (Fig. 1B). In the midgut of Colorado potato beetle larvae columnar enterocytes with dense apical microvilli prevail and numerous stem cells reside in the basal part of the gut epithelium (Figs. 1C, D). Additional level of complexity relates to regional differences of the midgut along its anterior-posterior axis, reflected in variation of cell morphology, physiology and also stem cells' characteristics, which have been explained in detail for D. melanogaster [3], but have not been investigated in other species. Our current work focuses on further characterization of stem cells ultrastructure and comparative evaluation of differences in the midgut architecture along the anterior-posterior axis in *D. suzukii* and *L. decemlineata*.

References

[1] Curr Opin Cell Biol. 2021;73:58-68. doi:10.1016/j.ceb.2021.05.007
[2] EMBO Reports. (2020)21:e50047 https://doi.org/10.15252/embr.202050047
[3] eLife 2013;2:e00886. DOI: 10.7554/eLife.00886

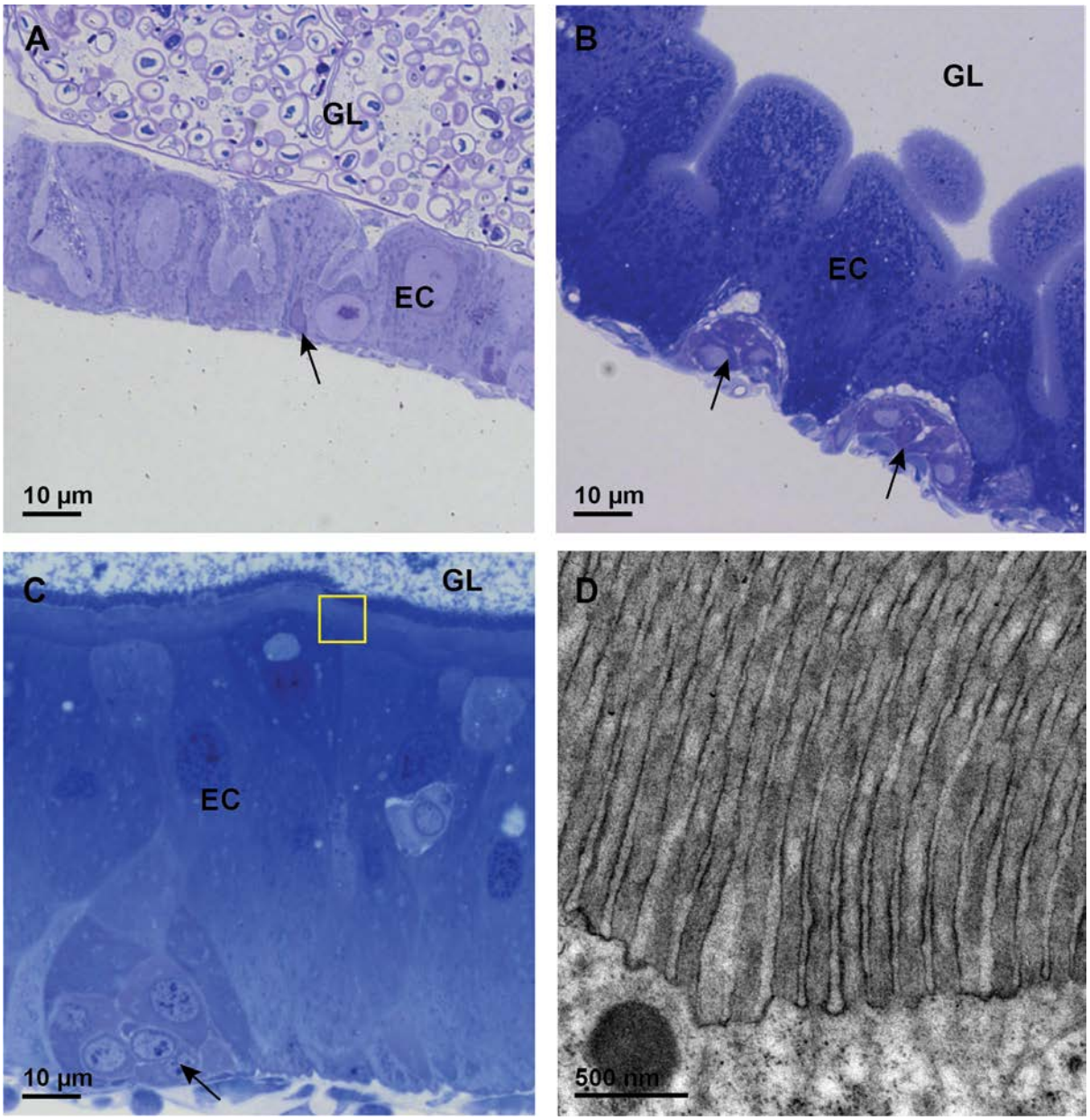

Fig. 1: Individual stem cells at the base of the midgut epithelium in adults (A) and clusters of stem cells in larvae of spotted wing drosophila (B). Clusters of stem cells in the midgut epithelium of Colorado potato beetle larvae (C) and microvilli on the apical surface of enterocyte (D). (EC) enterocytes, (GL) gut lumen, (arrow) stem cells.

LS4 Advances in fluorescence and super-resolution microscopy

Type of presentation: Invited

LS4-IN-2948 A DNA origami-based biointerface for probing the spatial requirements of cell surface receptor triggering

Hellmeier J.[1], Platzer R.[2], Eklund A. S.[3,4], Schlichthärle T.[3,4], Jungmann R.[3,4], Huppa J. B.[2], Sevcsik E.[1]

[1]Institute of Applied Physics, TU Wien, Vienna, Austria, [2]Institute for Hygiene and Applied Immunology, Medical University of Vienna, Vienna, Austria, [3]Max Planck Institute of Biochemistry, Martinsried, Germany, [4]Faculty of Physics and Center for Nanoscience, Ludwig Maximilian University, Munich, Germany

Email of the presenting author: eva.sevcsik@tuwien.ac.at

The nanoscale spatial organization of ligands and receptors is emerging as an important theme in regulating cell behavior yet inherently challenging to investigate. Antigen recognition by T-cells illustrates this conundrum: while central to adaptive immunity and with most molecular players already identified, knowledge on its operational principles is still limited. We have devised a DNA origami-based biointerface which allows the experimenter to adjust protein distances with nanometer precision as a means to enhance or disturb signaling while being responsive to large scale reorganization processes during cell activation. Combining this biointerface with advanced fluorescence microscopy methods to study the spatial requirements of T-cell activation we find that the smallest signaling-competent receptor unit consists of two stably ligated T-cell receptors (TCRs) within a distance of 20 nanometers. Spatial organization of the physiological ligand pMHC, however, is not a relevant parameter of antigen-mediated T-cell activation as single, well-isolated pMHC molecules efficiently stimulate T-cells.

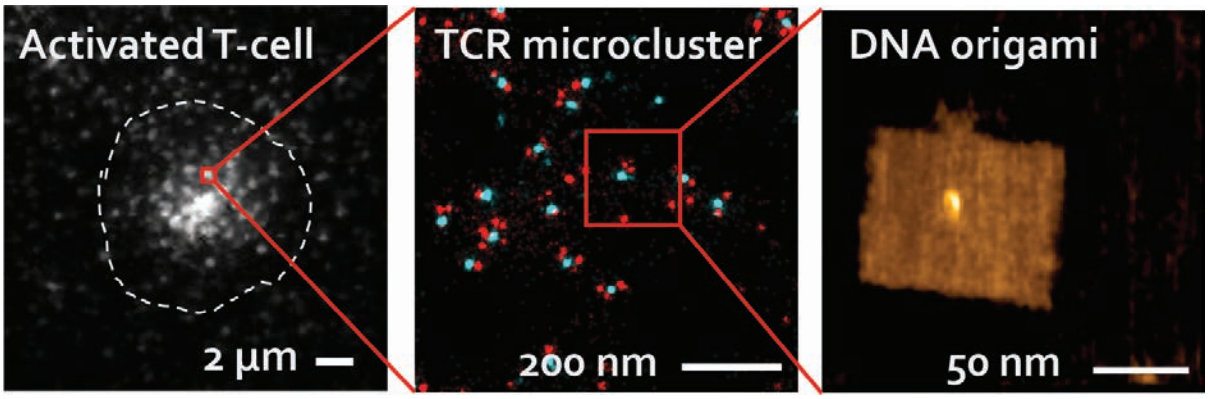

Fig. 1: Nanostructuring TCR microclusters using a DNA origami-based biointerface.

Type of presentation: Invited

LS4-IN-3001 Combining Super-resolution Optical Fluctuation Imaging (SOFI) With Structure Illumination and 3D Imaging

Grussmayer K. S.[1,2], Descloux A. C.[2], Navikas V.[2], Lukes T.[2], Mahecic D.[3], Manley S.[3], Yserentant K.[5], Wombacher R.[4], Herten D.[5], Radenovic A.[2]

[1]Grussmayer Lab, Department of Bionanoscience, TU Delft, Netherlands, [2]Laboratory of Nanoscale Biology, EPFL, Switzerland, [3]Laboratory of Experimental Biophysics, EPFL, Switzerland, [4]Department of Chemical Biology, MPImF, Germany, [5]Centre of Membrane Proteins and Receptors (COMPARE), College of Medical and Dental Sciences, Medical School & School of Chemistry, University of Birmingham, UK

Email of the presenting author: K.S.grussmayer@tudelft.nl

All fluorescence super-resolution microscopy techniques present trade-offs, for example between resolution, acquisition speed and live-cell compatibility. Diffraction-unlimited super-resolution imaging critically depends on the switching of fluorophores, often induced using intense laser light and specialized buffers or UV radiation. Recently, several spontaneously blinking dyes that switch between an open, fluorescent “on” state and a closed, colorless “off” state were introduced. Here, we exploit the synergy between super-resolution optical fluctuation imaging (SOFI) and self-blinking fluorophores for 2D imaging with up to 50-60nm resolution and for 3D imaging covering up to 10um depth [1,2]. We use two strategies for 3D imaging: an image-splitting prism for simultaneous multiplane acquisition [1] and remote focusing via adaptive optics [2]. SOFI is an alternative to localization microscopy that is less demanding in terms of fluorophore photoswitching and brightness, offering better time resolution and lower phototoxicity at the cost of a more moderate resolution gain. SOFI analyzes spatio-temporal fluctuations in fluorescence by calculating higher-order cumulants, a quantity related to correlations. Thus, even dyes that exhibit spontaneous blinking characteristics that are not suitable or suboptimal for single molecule localization microscopy can be used successfully for SOFI-based super-resolution imaging. We also demonstrate the combination of self-blinking SOFI with SIM, where we use SOFI as a source of non-linearity to further enhance the SIM resolution [3]. The two methods together reach a resolution beyond what is achievable with SIM alone without increased complexity of the experiment. We thus provide several robust routes for easy-to-use 2D and 3D high-resolution imaging.

[1] K. Grußmayer, Tomas Lukes, Theo Lasser, and Aleksandra Radenovic, ACS Nano 2020, 14, 7, 9156–9165; https://doi.org/10.1021/acsnano.0c04602, [2] V. Navikas, A. C. Descloux, K.S. Grussmayer, S. Marion, A. Radenovic, Nanophotonics 2021, 000010151520210108. https://doi.org/10.1021/acsphotonics.1c00668, [3] A. C. Descloux, K. S. Grußmayer, V. Navikas, D. Mahecic, S. Manley, and A. Radenovic, ACS Photonics 2021, 8, 8, 2440–2449, https://doi.org/10.1021/acsphotonics.1c00668

Type of presentation: Oral

LS4-O-2712 RNA export through the nuclear pore complex is directional

Shav-Tal Y.[1]

[1]The Faculty of Life Sciences and the Institute for Nanotechnology and Advanced Materials (BINA), Bar-Ilan University, Ramat Gan, Israel

Email of the presenting author: Yaron.Shav-Tal@biu.ac.il

The organization and compaction of mRNA into an mRNP during nucleo-cytoplasmic transport and export, are key steps in gene expression. Changes in mRNA organization after release from the gene, during nucleoplasmic diffusion and in preparation for export, are unknown. It is assumed that at the nuclear pore complex (NPC), the mRNP unfolds and enters 5'-first into the pore. We revisit this issue in mammalian cells to directly examine if this assumption holds as modus operandi, using single molecule RNA FISH to detect single RNAs (mRNAs and lncRNAs) by advanced microscopy including STED super-resolution microscopy. Thereby, we are able to uniquely and separately detect the fluorescent signatures and the spatial organization of the 5', middle and 3'-ends of the same single long transcripts in human cells. By performing imaging of single molecules in several colors we find that an mRNP is compact during nucleoplasmic travels compared to a more open structure after release from the gene. The mRNP is more open also in the nuclear periphery. Compaction levels of nuclear transcripts could be modulated by varying nuclear levels of RNA-bindng proteins and by changing global genome structure. The nuclear mRNPs were mostly rod-shaped with distant 5' and 3'-ends, although for some, the transcript ends were in proximity suggesting a circular formation. The latter was more abundant in the cytoplasm. Modifying the mRNA structure to distance the 5' and 3'-ends was only partly achieved by reducing the energetic status of the cell or inhibiting translation. Exit from the NPC was directly observed by labeling different parts of the same transcript in different colors together with endogenous labeling of single NPCs, exhibiting predominant 5'-first export for both mRNAs and non-translating lncRNAs. This analysis detected 'gene gating' in which several adjacent NPCs were engaged in the export of the same mRNA species. Altogether, using high-resolution microscopy we show that the mRNP is a flexible structure during travels, with 5'-directionality during export.

Type of presentation: Oral

LS4-O-2597 High-resolution structural and functional deep brain imaging using holographic endo-microsocpy

Uhlířová H.[1], Ondráčková P.[1], Stibůrek M.[1], Tučková T.[1], Turtaev S.[2], Šiler M.[1], Pikálek T.[1], Jákl P.[1], Gomes A.[2], Krejčí J.[3], Kolbábková P.[1], Krbková B.[1], Čižmár T.[1,2,4]

[1]Institute of Scientific Instruments of the CAS, Královopolská 147, 612 64 Brno, Czech Republic, [2]Institute of Photonic Technology, Albert-Einstein-Straße 9, 07745 Jena, Germany, [3]Institute of Biophysics of the CAS, Královopolská 135, 612 65 Brno, Czech Republic, [4]Institute of Applied Optics, Friedrich Schiller University Jena, Fröbelstieg 1, 07743 Jena, Germany

Email of the presenting author: huhlirova@isibrno.cz

Introduction:
Optical microscopy present nowadays a powerful tool not just to image biological tissue but also interogate its function via optogenetics. Often, it relies on delivering the light with desired spatial and temporal distribution towards the region of interest through highly scattering tissue. For investigation of structures lying deeper than ~1.6 mm, endoscopes are used as optical relays for illumination as well as signal readout. Among different types of endoscopes, the holographic endoscopes based on multi-mode optical fibres represent the far-most atraumatic way to image in unprecedented depth with diffraction-limited resolution dictated only by the numerical aperture of the fibre and the used wavelength. Up to now, holographic endoscopes have been used in pilot imaging experiments of neurons in cultures [1], acute brain slices [2, 3] and in vivo [1, 2]. The first indication that spatially-resolved functional imaging of intracellular calcium may be possible to implement through the means of holographic endoscopy has been shown in [1].
Results:
We advance the approach of holographic endo-microscopy pushing it to its current limits using: custom-designed computer interface, computing power of the GPU, computational refocusing, novel 'side-view' probes (Fig. 1a) and random access scanning. This enabled us to increase the resolution and field of view (Fig. 1b), image 3D volumes of the tissue without physical movement of the probe (Fig. 1c), stitch frames acquired along the path of the probe into extended fields of view (Fig. 1d) and measure changes of intracellular calcium (Fig. 1e) and blood flow velocity (Fig. 1f).
[1] Ohayon, S. et al., BIOMEDICAL OPTICS EXPRESS 9 (2018).
[2] Vasquez-Lopez, S. A. et al. LIGHT-SCIENCE & APPLICATIONS 7 (2018).
[3] Turtaev, S. et al., LIGHT-SCIENCE & APPLICATIONS 7 (2018).

Acknowledgement: MEYS (CZ.02.1.01/ 0.0/ 0.0/ 15_003/0000476, LO1212) ERC (724530), H2020-RIA (101016787), Freistaat Thuringen(2018-FGI-0022, 2020-FGI-0032), AS CR (RVO:68081731)

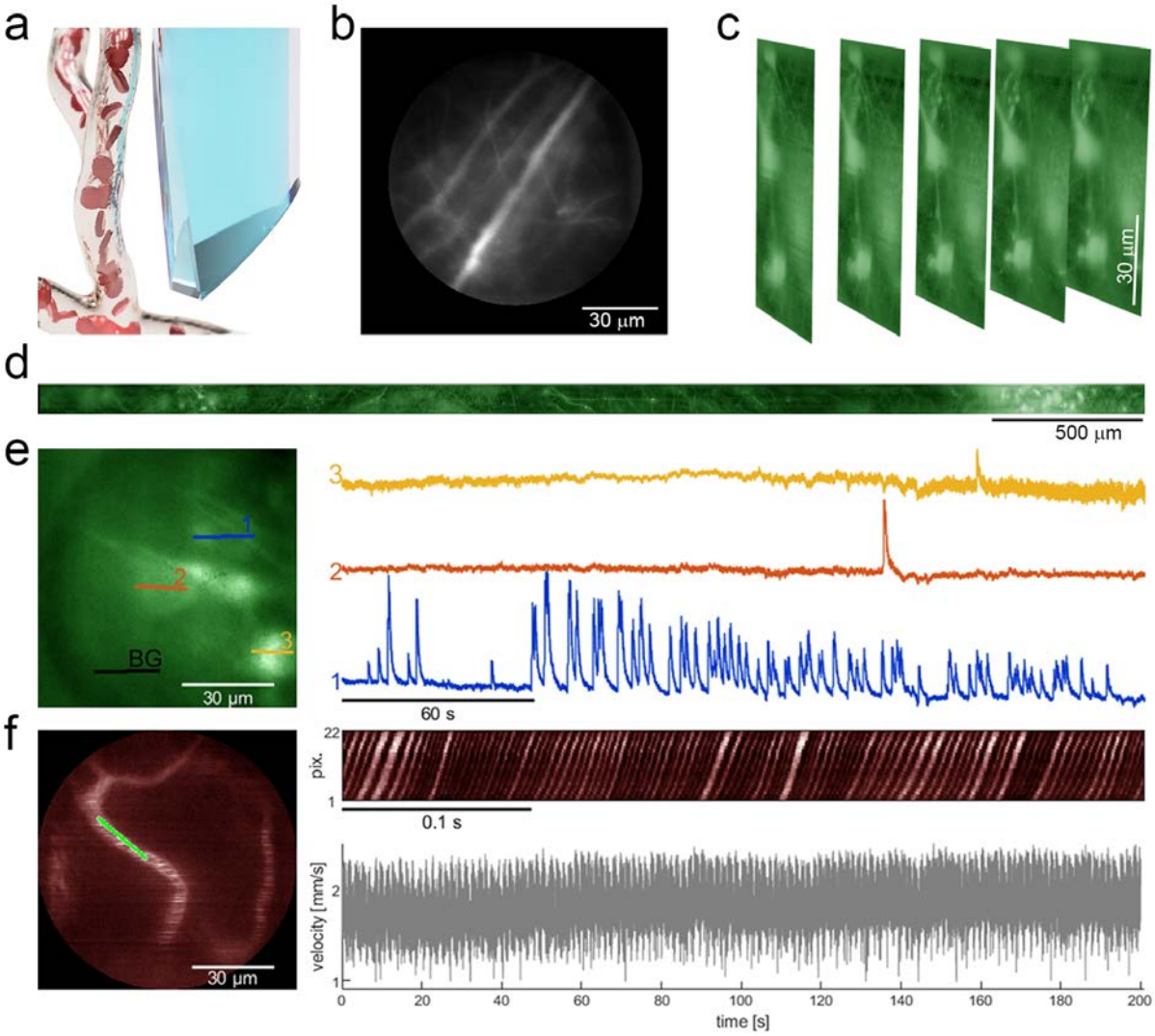

Fig. 1: **Imaging modalities of the holographic endoscope. a,** A ‘side-view probe’. **b,** Neuronal processes imaged in vivo. **c,** 3D imaging. **d,** An extended fiel of view along the fibre track. **e,** Intracellular calcium imaging. **f,** Measurement of blood flow.

Type of presentation: Oral

LS4-O-2587 Localization of Bacteria in Tumor Cells using Correlative Light and Electron Microscopy

Dadosh T.[1], Levin-Zaidman S.[1], Nejman D.[2], Straussman R.[2]

[1]Department of Chemical Research Support, Weizmann Institute of Science, Rehovot, Israel,
[2]Department of Molecular Cell Biology, Weizmann Institute of Science, Rehovot, Israel

Email of the presenting author: tali.dadosh@weizmann.ac.il

In recent years, bacteria have been shown as residents of human tumors, but whether their presence is advantageous to the tumors or to the bacteria themselves is still largely unclear. Characterization of the tumor microbiome is challenging because of its low biomass. In order to validate the presence of bacteria in human tumors, immunohistochemistry was conducted using antibodies against bacterial lipopolysaccharide and lipoteichoic acid to detect Gram-negative and Gram-positive bacteria, respectively. However verifying the presence of bacteria inside cancer cells is very challenging, due to the small size of the bacteria and its sparsity in the tumor tissue. We used Correlative Light-Electron Microscopy (CLEM) technique that allows localization of specific cellular components by fluorescence labeling and microscopy and visualization of high resolution details of the cell ultrastructure by electron microscopy. Fluorescent labeling has been used to identify desired targets over a large area of interest in a sample, and particularly beneficial in samples exhibiting a sparse number of targets or events. In this work we were able to validate the presence of bacteria inside cancer cells of human breast tumor. Combined fluorescence staining of bacteria and transmission electron microscopy imaging of the same cells clearly demonstrated the intracellular localization of bacteria in tumors.
[1] D. Nejman, I. Livyatan, G. Fuks, et al., The human tumor microbiome is composed of tumor type-specific intracellular bacteria, Science, 368 (6494) (2020), pp. 973-980.

Type of presentation: Oral

LS4-O-2854 Time resolved spectral detection for autofluorescence studies

Pala J.[2]

[1]Department of Pathophysiology, Third Faculty of Medicine Charles University in Prague, Czech Republic, [2]National Institute of Mental Health, Klecany, Czech Republic

Email of the presenting author: jan.pala@lf3.cuni.cz

Autofluorescence plays significant role almost everywhere and it is usually impossible to omit it completely during the microscopy work. There can be non-negligible contribution to detected fluorescence within labelled sample. The autofluorescence can occur in any kind of tissues and samples, and its level can increase or decrease with the sample preparation, mounting media, temperature, microenvironment of used fluorophores, pH, cell density and intercellular heterogeinity [1]. Several options can be used for the detection of the autofluorescence. The simplest way is to get full spectral response of control sample during the image acquisition with laser and detector setting to the recognized level of signal and apply the same setting for the image acquisition of labelled sample. The most precise approach is Fluorescence Lifetime Imaging Microscopy (FLIM) with different excitation pulsed laser lines and nanosecond resolving power. Other option for advanced autofluorescence detection is the combination of pulsed tunable laser source White Light Laser (WLL) and highly sensitive hybrid detectors (HyD) with LighGate (TimeGate) functionality. Autofluorescence excited by the picosecond tunable laser source can be spectrally detected in the different time windows of HyD detectors. These time windows are open in the range 0.0-12.0 ns with the minimum time gate 3.5 ns. Limited size of the time gate 3.5 ns and setting the time window with 0.1 ns step size restrict the time resolved measurements to different level than FLIM, but it can be used for complete removal of autofluorescence, for instance in chlorophyll [2] or localization of exocyst subunits at the plant–pathogen interface [3]. The goal of this contribution is to show options for the usage of combination of WLL with highly sensitive spectral HyD detectors with 1 nm spectral stepsize and TimeGate function for autofluorescence studies and removal.

Type of presentation: Poster

LS4-P-2839 Comparison of CLMS and super-resolution techniques to study meiotic proteins in plants

Bačovský V.[1], Novotná P.[1], Horáková L.[1]

[1]Department of Plant Developmental Genetics, Institute of Biophysics of the Czech Academy of Sciences, Kralovopolska 135, 612 65 Brno, Czech Republic

Email of the presenting author: Vbacovsky@seznam.cz

During the last decades, increased resolution, and significant advances in cytogenetic techniques (including sample preparation) allowed researchers to study nuclear and chromosome architecture beyond diffraction-limit of light. Nevertheless, in non-model species, the knowledge of chromatin organisation and cellular components at nanoscopic level is falling behind that of in Drosophila, mammals, or Arabidopsis. Here, we describe optimized methods of immune-localization, and the benefit of confocal (lightning, AiryScan) and super-resolution techniques (SIM, STED) to study meiotic protein architecture in plant Silene latifolia (2n=24, XY) and its relative species, S. vulgaris (2n=24). We show the major outcomes of lightning deconvolution for CLSM, comparing different modes of scanning of plant nucleus. Further, we tested individual techniques and their resolution on ASY1 protein complex (lateral element of the synaptonemal complex) during leptotene and zygotene of meiosis I. We show significant differences of ASY1 3D organization and different axis strength, evaluating its pattern, fibre width, and signal intensity. Moreover, using higher resolution we were able to determine specific features of the ASY1 element between the sex chromosomes, and its interspecies characteristics. We discuss the profit of CLSM and super-resolution methods for the analysis of meiotic protein components and show the main advances of tested techniques for the new model organisms.

Acknowledgement: This work was supported by the fellowship from the Czechoslovak Microscopy Society (CSMS) and by the Czech Science Foundation project No. 22-00301S.

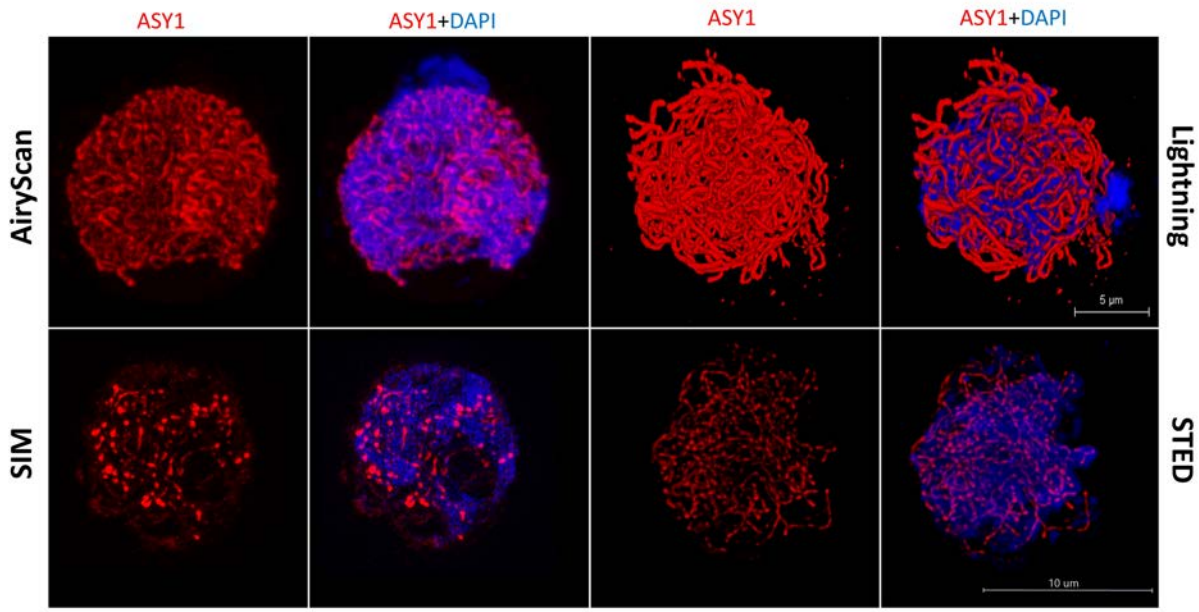

Fig. 1: The ASY1 element of meiosis I and the comparison of lightning deconvolution, AiryScan, SIM and STED technique to determine the ASY1 3D organization.

Type of presentation: Poster

LS4-P-2645 High-stability stage for cryo-light microscopy with immersion objectives

Paciu I.[1], Faul N. A.[1], Burg T. P.[1]

[1]Integrated Micro-Nano-Systems Lab, Technical University of Darmstadt, Darmstadt, Germany

Email of the presenting author: ion.paciu@stud.tu-darmstadt.de

Cryo-fluorescence microscopy is of great interest due to the excellent preservation of cellular ultrastructure by cryofixation. However, cryo-fluorescence imaging systems are still inferior to their room temperature counterparts because immersion objectives are not commonly used. One of the main obstacles is that contact between the objective lens and the sample through an immersion medium forms a thermal bridge and increases the risk of devitrification. To minimize the resulting heat flow, our group has recently developed a cryoimmersion objective in which a cold front lens is thermally shielded from the warm body of the objective [1]. This method limits the steady-state heat flow to approximately 10 W. However, to ensure distortion-free acquisition conditions, a vibration- and drift-free cryo-stage with sufficient cooling power is required. In addition, the stage must provide accurate temperature control that can keep the sample temperature below the devitrification limit of -135°C [2] while stabilizing the temperature at a point where the immersion medium is liquid and its refractive index matches the design of the objective [1].
Here we describe a gas-cooled microscopy cryostat for immersion objectives that fulfills the above requirements.
Cold gas is generated by evaporating liquid nitrogen in a dewar. A channel guides the stream of gas through a heat sink which cools the sample sitting on top of it. To prevent the transfer of vibrations from the gas generator to the cryo-stage, a gap is left as a mechanical separation (Figure 1).
Drift is mainly caused by the thermal expansion of stage components, which are not in thermal equilibrium. To minimize drifts, the heat sink is held by a glass-ceramic plate providing a very low thermal expansion coefficient. The plate sits on a temperature-controlled frame which eliminates the thermal expansion and thus prevents drift.
The temperature of the sample is controlled with a heater which allows us to keep the sample at a constant temperature adjustable down to -160°C.

The cryostat provides stable acquisition conditions for immersion objectives with a cooling power of 30 W, enabling distortion-free acquisitions. The precise temperature control enables to establish new immersion media with different refractive indices and expands the range of applicable immersion objectives. Additionally, the stage is designed in a simple and modular way to open up versatile fields of application. It can easily be deployed with different microscope systems.

References

[1] Faoro, R., Bassu, M., Mejia, Y. X., Stephan, T., Dudani, N., Boeker, C., Jakobs, S., & Burg, T. P., Proceedings of the National Academy of Sciences 115(6) (2018), 1204–1209
[2] Schultz, P., Quarterly Reviews of Biophysics 21(2) (1988), 129–228.

Acknowledgement: This project has received funding from the European Research Council under the European Union's Horizon 2020 research and innovation programme (No. 772441).

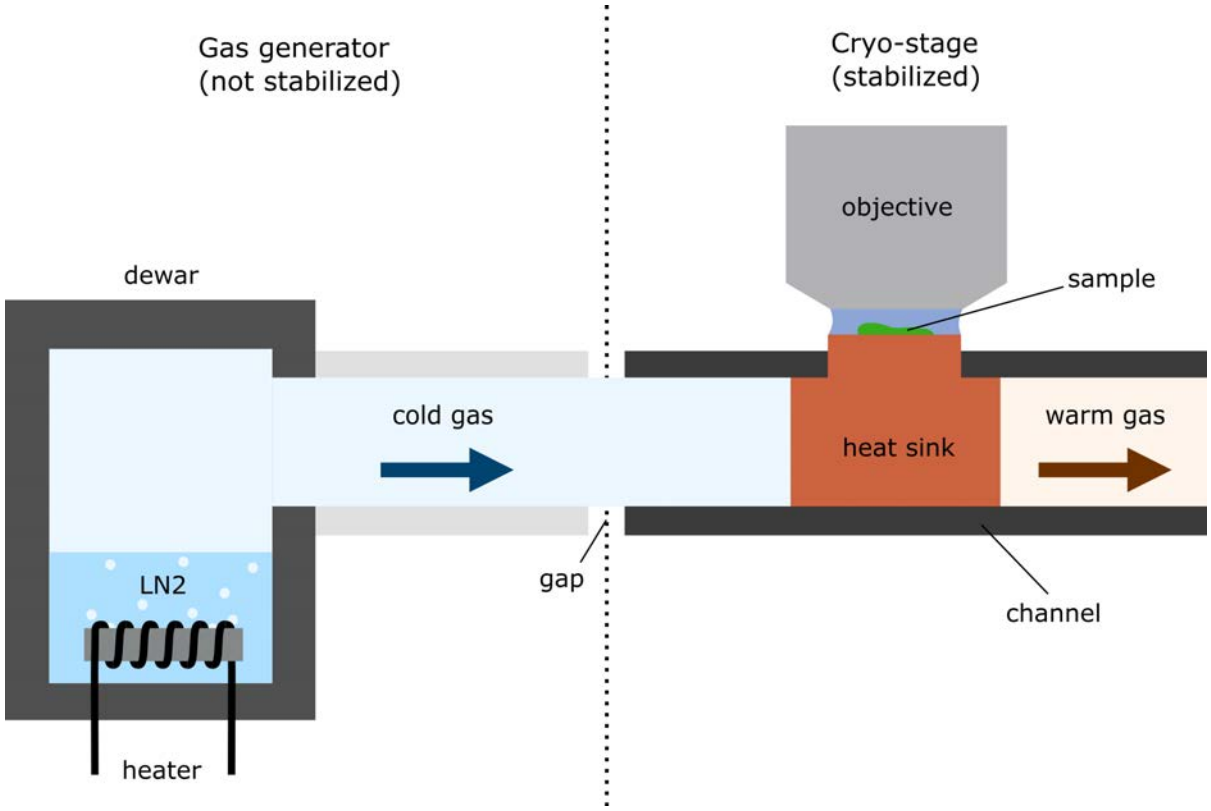

Fig. 1: Schematic cross-section of the gas generator and cryo-stage. The mechanical separation prevents vibrations from the gas generator from being transmitted to the cryo-stage.

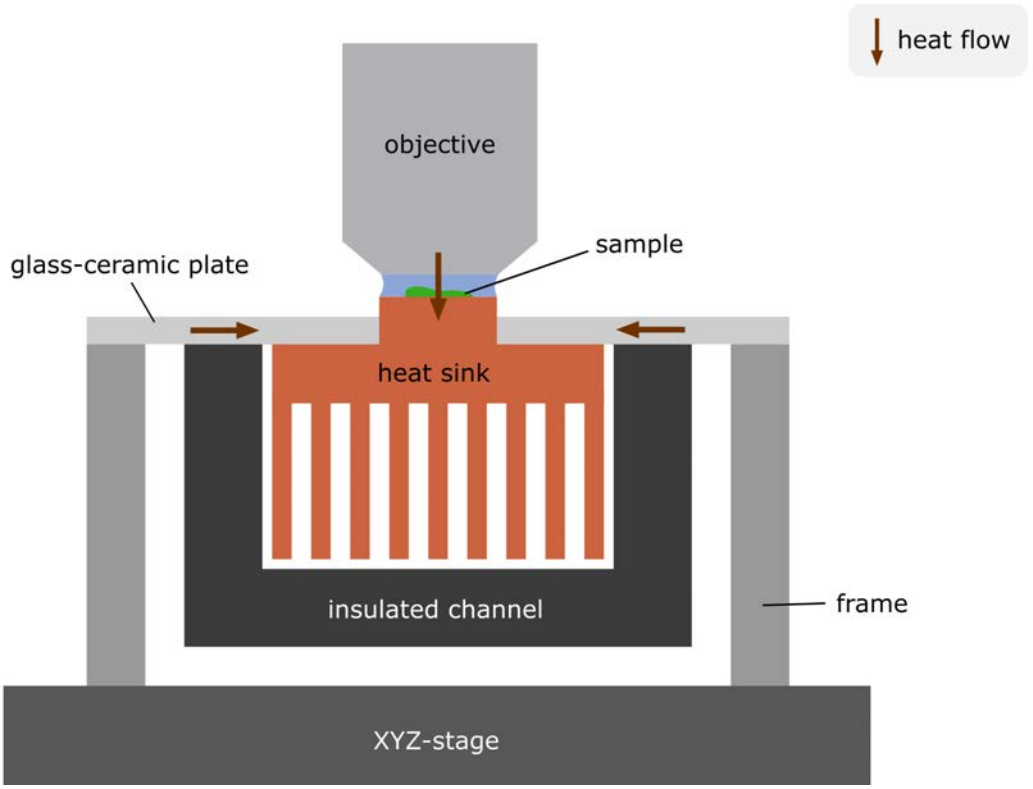

Fig. 2: Schematic cross-section of the cryo-stage showing the heat flow from the frame and objective to the heat sink. The temperature-stabilized frame prevents the sample from drifting. The insulated channel limits the parasitic cold loss.

Type of presentation: Poster

LS4-P-2498 Targeted photobiomodulation of cancer cells at 808 nm may improve efficacy of photodynamic therapy

Pevna V.[1], Tomkova S.[1], Wagnieres G.[2], Huntosova V.[3]

[1]Department of Biophysics, Faculty of Science, P.J. Safarik University in Kosice, Slovakia, [2]Laboratory for Functional and Metabolic Imaging, Institute of Physics, Swiss Federal Institute of Technology in Lausanne, Switzerland, [3]Center for Interdisciplinary Biosciences, Technology and innovation park, P.J. Safarik University in Kosice, Slovakia

Email of the presenting author: veronika.huntosova@upjs.sk

Photobiomodulation (PBM) is a relatively modern modality of adjuvant therapy that primarily uses near-infrared laser light to stimulate mitochondria in injured cells. Mitochondrial dysfunction is common in neurodegenerative diseases. Several studies reported beneficial effects of PBM on mitochondrial metabolic activity. In the present study, we administered rotenone at pathological concentrations to induce inhibition of complex I in the mitochondrial respiratory chain and to alter other subcellular compartments. We monitored the cisternae of the Golgi apparatus with confocal fluorescence microscopy. Fragmentation of the Golgi apparatus (Figure 1) and mitochondrial fission were detected in cells exposed to rotenone. Western blot analysis of autophagic proteins in these cells showed a change in autophagosome degradation in cells after PBM. Visualisation of LC3B-positive vesicles in the cells confirmed this observation. In addition, PBM increased the size of vesicles associated with the Golgi complex and induced the fusion of smaller cisternae into compact complexes. PBM is not an invasive method, and the photodamage induced by this process is more likely to be at the subcellular level. In addition to latent effects, PBM induced fusion of mitochondria and Golgi complex. We hypothesise that detoxification processes occur with the activation of antioxidant enzymes (superoxide dismutase and catalase) to reduce oxidative stress. However, the effect of PBM is not long-lasting. Thanks to its ease of use and low phototoxicity, PBM can be used repeatedly. Its application in cancer cells is questionable. We have recently shown that PBM can be combined with photodynamic therapy and improve the treatment outcome [1]. The targeted use of the photosensitizer is critical in such treatment. We used hypericin, which was mainly localised in the Golgi complex of cancer cells. Fluorescence microscopy studies showed that PBM induced autophagy in hypericin-treated cells. However, when these cells were PDT, autophagy transitioned to apoptosis. Our preliminary data suggest that appropriate design and targeted delivery may increase the efficacy of combination therapy.

[1] Pevna V., Wagnieres G., Huntosova V.: Autophagy and Apoptosis Induced in U87 MG Glioblastoma Cells by Hypericin-Mediated Photodynamic Therapy Can Be Photobiomodulated with 808 nm Light. Biomedicines 2021, 9(11), 1703; https://doi.org/10.3390/biomedicines9111703

Acknowledgement: Supported from projects of Slovak research agency APVV-20-0340 and EU H2020 research and innovation programme under grant agreement No. 952333, project CasProt.

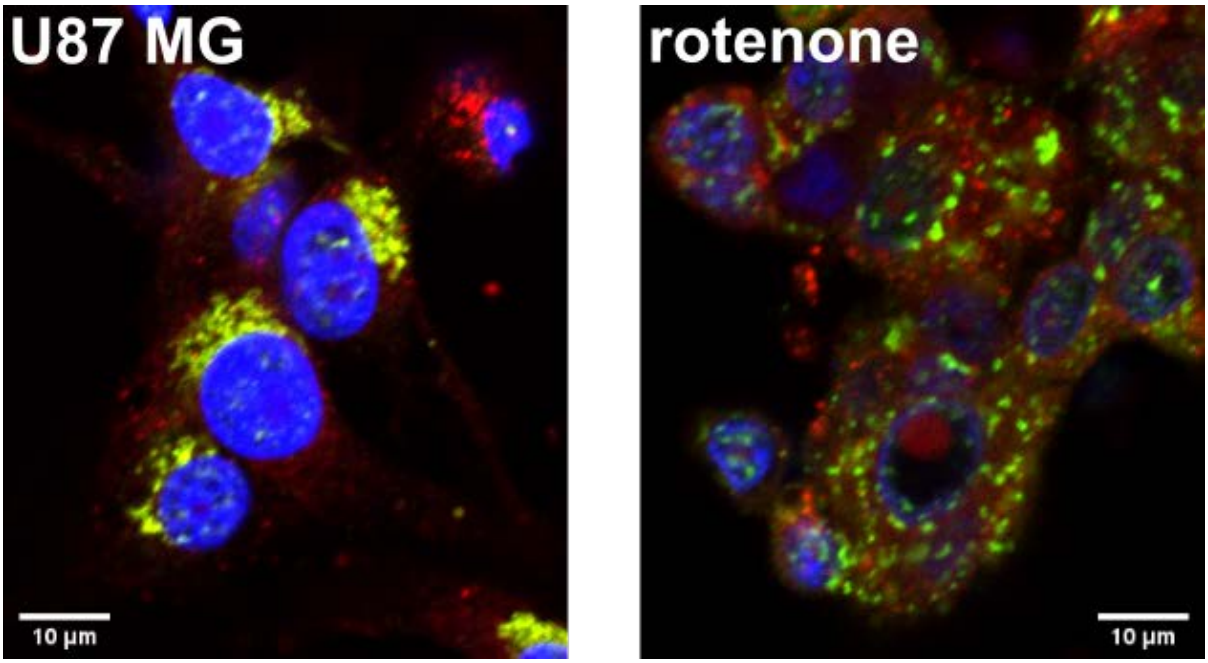

Fig. 1: Fragmentation of Golgi complex in A) U87 MG cells and in the presence of B) 10 µM rotenone for 24h (cathepsinB-red, Giantin-green and DAPI-blue).

Type of presentation: Poster

LS4-P-2499 Imaging of autophagic and mitochondrial proteins in 3D spheroids of U87 MG cancer cells during photodynamic therapy mediated with hypericin

Pevna V.[1], Huntosova V.[2]

[1]Department of Biophysics, Institute of Physics, Faculty of Science, P.J. Safarik University in Kosice, Slovakia, [2]Center for Interdisciplinary Biosciences, Technology and innovation park, P.J. Safarik University in Kosice, Slovakia

Email of the presenting author: viktoria.pevna@student.upjs.sk

Photodynamic therapy (PDT) is a treatment method that uses a light-sensitive molecule, a photosensitizer, and light of an appropriate wavelength. Hypericin, a hydrophobic molecule, is a model molecule that has interesting photodynamic properties for the diagnosis and treatment of cancer cells. Treatment results often differ in cell cultures in monolayers and in tissues under the same conditions. The intermediate stage between these two systems can be defined by 3D spheroids of cells. In this study, 3D spheroids were grown using the hanging drop method. Hypericin was administered 3 hours before PDT, and treatment efficacy was determined 24 hours after PDT induced with a homemade LED system at 590 nm and 4 J/cm^2. Spheroids were live-stained with fluorescent probes for mitochondrial potential, nuclei, and oxidative stress induced by the treatments. Confocal fluorescence microscopy was used to characterize live spheroids and spheroids immunostained after fixation. Autophagic and apoptotic proteins were detected in different layers of the spheroids. Caspase 3 levels were detected by NucView 488 and were preferentially localized in the peripheral layers after PDT. Increased LC3B levels were also detected in these cells (Figure 1). Heterogeneity was clearly demonstrated and supported by visualization of mitochondrial proteins in frozen sections of 3D spheroids. Western blot analysis is a complementary method to determine the amount of selected proteins because imaging is limited by the penetration of excitation light into the spheroids. A correlation was observed between fluorescence imaging and Western blot. Significant changes in LC3B, ATG16L1, SQTM1, ubiquitin, and M6PR protein levels were detected in cells after hypericin-induced PDT. Optimization of the therapeutic protocol is needed to better delineate the metabolic changes in tumor spheroids. Autophagy was found to be an important cellular response in PDT of 3D spheroids.

Acknowledgement: Supported from projects of Slovak research agency APVV-20-0340 and EU H2020 research and innovation programme under grant agreement No. 952333, project CasProt.

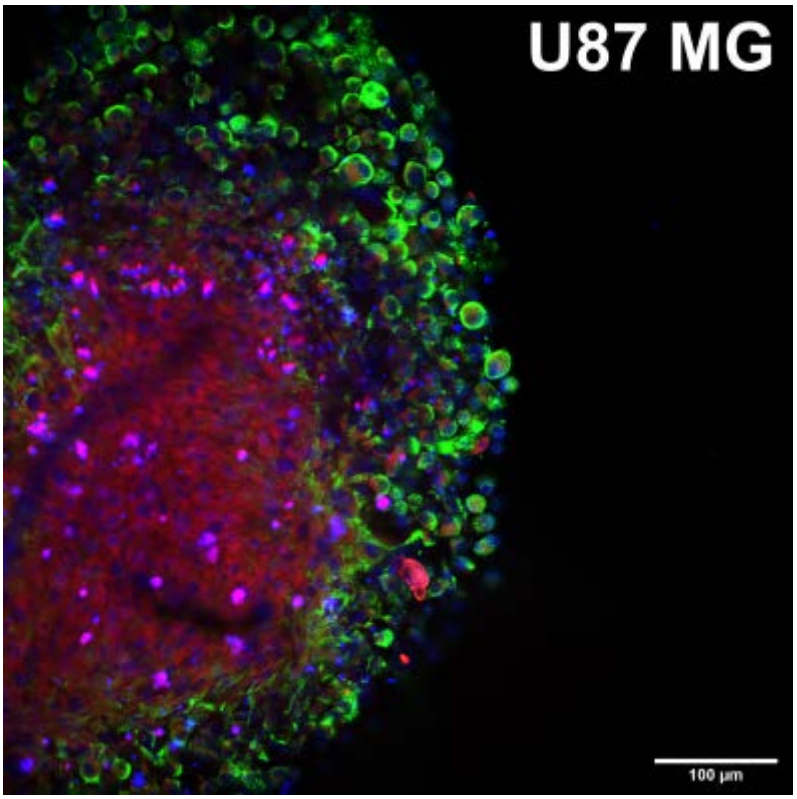

Fig. 1: Fluorescence image of U87 MG spheroid detected after PDT mediated with hypericin: LC3B-green, hypericin-red, Hoechst-blue.

Type of presentation: Poster

LS4-P-2606 Fluorescence confocal imaging via holographic endo-microscopy

Tučková T.[1], Pikálek T.[1], Jákl P.[1], Turtaev S.[2], Šiler M.[1], Ondráčková P.[1], Krejčí J.[4], Uhlířová H.[1], Čižmár T.[1,2,3]

[1]Institute of Scientific Instruments of the CAS, Brno, Czech Republic, [2]Lebniz Institute of Photonic Technology, Jena, Germany, [3]Institute of Applied Optics, Friedrich Schiller University Jena, Jena, Germany, [4]Institute of Biophysics of the CAS, Brno, Czech Republic

Email of the presenting author: tuckovat@isibrno.cz

In biological research, there is a desire to image and study cellular processes in deep areas of the tissue. The tissue has strong scattering properties that limit the imaging depth when using light microscopy. The ability to relay light into deeper regions of the tissue has motivated the development of different types of endoscopes based on GRIN lenses, fiber bundles, or multi-mode fiber (MMF). Among those, the MMFs provide the best ratio between resolution and probe diameter. Thus they enable far-most atraumatic way of imaging up to unprecedented depth in the living brain tissue while achieving diffraction-limited resolution [1]. However, the MMF acts as a turbid medium and the light after propagation comes out in a form of a random scrambled pattern. In order to counteract this scrambling, the light coupled into MMF can be modulated by spatial light modulators. In our case of MMF-based holographic endoscopy, the light is modulated using a digital micro-mirror device. At the distal end of the fiber, a single diffraction-limited spot is thus generated. This modulation enables imaging of the sample by scanning the spot across the field of view in the focal plane, similarly to a scanning microscope, and excites the fluorescence signal which is then collected by a bucket detector (PMT). However similarly to classical single photon excitation fluorescence microscopy, the images obtained through the MMF suffer from a decrease in contrast and resolution due to light scattered from out-of-focus planes. This effect is detrimental especially in highly-scattering dense tissue, such as the brain. In classical fluorescent microscopy, the out-of-focus light is suppressed using e.g. confocal approach. In the case of endoscopy, this confocal approach has also been demonstrated [2,3]. However, it is not optimal for fluorescence in vivo imaging. We introduce a new concept of MMF-based confocal imaging which allows the suppression of out-of-focus light and attenuation of the background signal. As we here present on the imaging of the fluorescent phantom sample and fixed brain slices, confocal filtration increases the contrast and resolution of the resulting images.

1. Turtaev, S., et al., High-fidelity multimode fibre-based endoscopy for deep brain in vivo imaging, Light: Science and Applications 7(2018); 2. Loterie, D., et al., Digital confocal microscopy through a multimode fiber, Optics Express (2015); 3. Loterie, D., et al., Confocal microscopy through a mulitmode fiber using optical correlation, Optics Letters (2015)

Acknowledgement: Holographic endoscopy for in vivo applications" (No. CZ.02.1.01/0.0/0.0/15_003/0000476) and its infrastructure by CAS (RVO:68081731).

Type of presentation: Poster

LS4-P-2673 Integrated Fluorescent Light Microscope (iFLM) - Applications Workflows

Vrbovská V.[1], Kuba J.[1], Krčmarský V.[1], Bublík A.[1], Dolník M.[1], Citterbardová K.[1], Hovorka M.[1], Mitchels J.[1]

[1]Thermo Fisher Scientific Brno, Brno, Czech Republic

Email of the presenting author: veronika.vrbovska@thermofisher.com

Cryo-electron tomography is a powerful tool for visualizing cellular structures in their native state and understanding the molecular interactions within the cells. To ensure lamellae for subsequent TEM analysis are being prepared from the desired target sites, it is important to identify the fluorescently labelled areas in the frozen sample.

The Correlative Light and Electron Microscopy (CLEM) approach enables to select specific cellular regions for ion beam milling, to further inspect the prepared lamellae, and validate they contain the specific protein or organelle of interest. This accelerates subsequent data acquisition in the cryo-TEM and delivers the assurance the correct structures are present in the tomography data.

Here we present the iFLM™ (Integrated Fluorescent Light Microscope) Correlative System and its application to the selected applications workflows. The solution streamlines the lamellae preparation process and addresses some of the challenges of the cryo-electron tomography workflow. The iFLM™ allows fluorescent samples to be imaged directly within the high vacuum chamber of the Aquilos 2 Cryo-FIB/SEM before, during and after cryo-lamella preparation. The combination of two imaging modalities within one system supports rapid identification of cell phenotypes and the selection of target sites for cryo-lamellae production. The correlation with the iFLM™ enables the lamella preparation process to be monitored step-by-step, and hence ensures that the target is contained in the final lamella. On-the-fly identification of the fluorescently labelled targets brings confidence that the 150-300 nm thin cryo-lamellae contain the region of interest. The automated lamella placement can further help find the right position of the region of interest. The integrated solution significantly reduces the sample contamination risk, and thus enhances the successful completion of the tomography workflow.

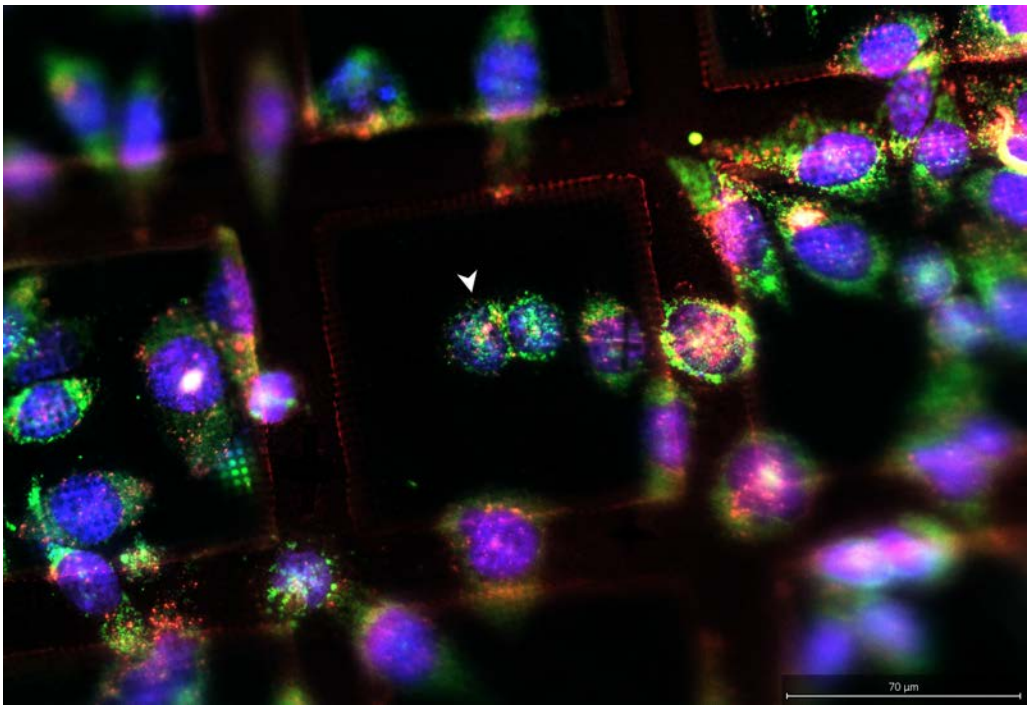

Fig. 1: Chinese hamster ovary (CHO) cells stained with Hoechst 33342 for nuclei, MitoTracker Green FM for mitochondria, and BODIPY TR Ceramide - Golgi red for Golgi body (Thermo Fisher Scientific). Cells are imagined by the iFLM system. The arrow marks the cell chosen for lamella milling, depicted in the next pictures.

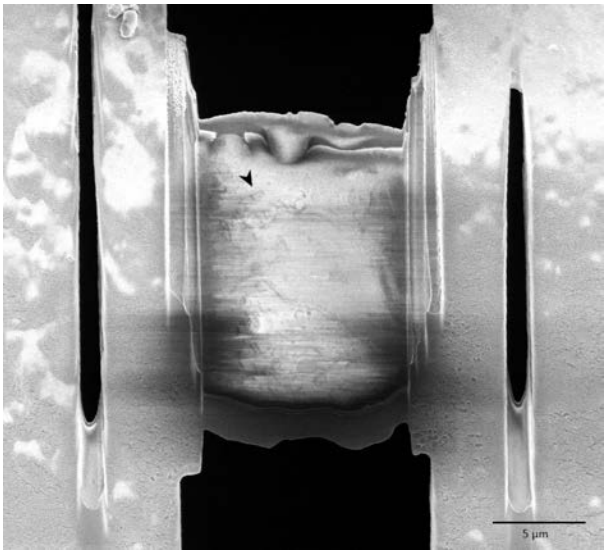

Fig. 2: SEM image of the final lamella polished to a thickness of approx. 200 nm acquired by Aquilos 2 Cryo FIB/SEM system. The arrow marks the mitochondrion identified also in the fluorescent data in figure 3.

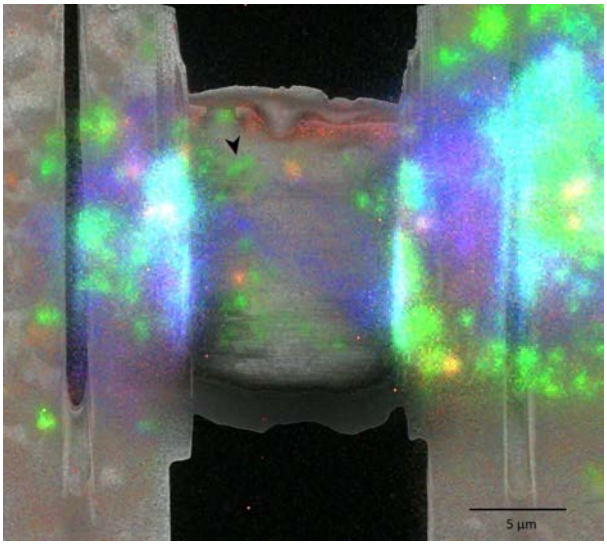

Fig. 3: Final-lamella SEM-image correlated with iFLM fluorescent data. In lamella, the nucleus (blue), mitochondria (green) and Golgi body (red-orange) are visible. The arrow marks mitochondrion visible also in figure 2.

LS5 Advances in probes and sample preparation in microscopy

Type of presentation: Invited

LS5-IN-3002 Multimodal microscopy in Type 1 diabetes research

Giepmans B. N.[1]

[1]UMC Groningen, The Netherlands

Email of the presenting author: b.n.g.giepmans@umcg.nl

Type 1 diabetes (T1D) results from the autoimmune destruction of insulin-producing beta cells in the Islets of Langerhans in the pancreas. While a cure is absent and the initial trigger(s) are not known, invasive insulin therapy is a lifesaver for (T1D) for over 100 years, albeit way less effective in controlling blood glucose compared to the beta cells. To study the disease using specialized techniques in labs all over the world the nPOD biobank (network for pancreas donors with T1D; jdrfnpod.org) has been initiated. We apply routine large-scale EM (nano-anatomy; nanotomy; nanotomy.org) on nPOD pancreas and built an EM database of the biobanked biomaterial. Nanotomy is now a routine technique in our facility: scanning entire EM sections at high resolution, comparable to scanners for histology. However, analysis is limited to the interpretation of the grey scale data. Correlated microscopy (fluorescence microscopy and EM) allows biological processes and/or cellular building blocks to be identified and dynamically studied followed by ultrastructural analysis, but the resolution of LM and EM do not match [1]. As an alternative, we optimized elemental dispersive X-ray analysis (EDX, 'ColorEM') to revisit areas of interest in the nanotomy maps, which we now also routinely use to identify endogenous structures, paint structures or label molecules based on elemental composition. All identification techniques above typically aid in identifying structures in large-scale EM maps and therefore their broad implementation will be highly useful in core facilities. In T1D research, these technique revealed anomalies in exocrine/ endocrine cells in (pre)diabetic patients [2]. Moreover, others found a diminished pancreas weight in (pre)diabetic patients, also hinting on a role of the exocrine pancreas in development of T1D [3]. However, a cause-consequence relationship could not be defined. Therefore, we now established a zebrafish larvae model to monitor in real time how stress in the Islets of Langerhans may be altered when modulating the exocrine tissue, which may be an initial trigger that ultimately destroys the insulin producing cells. Today, I will introduce the now routine techniques on Correlated microscopy, Nanotomy, ColorEM and include probes that help to identify molecules of interest. Moreover, I will highlight the benefit of an living model, the zebrafish larvae, for cell modulation and analysis using fluorescence microscopy in research [4] and discuss how these techniques may be further developed and implemented as valuable as generic tools for a broad microscopy and biomedical community.

References

[1] doi.org/10.1038/nmeth.3400
[2] doi.org/10.1038/s41467-020-16287-5
[3] doi.org/10.1001/jama.2012.15008
[4] doi.org/10.1002/1873-3468.14411

Type of presentation: Invited

LS5-IN-3045 Quantitative super-resolution microscopy of nuclear antigens in cells and tissues

Hoboth P.[1,2], Sztacho M.[1], Schatz M.[2], Sebesta O.[2], Akgul B.[3], Hozak P.[1,4]

[1]Dpt. of biology of the cell nucleus, Institute of Molecular Genetics CAS, Prague, Czechia, [2]Lab Confocal and Fluorescence Microscopy – IMCF Vinicna, Faculty of Science, Charles University, Prague, Czechia , [3]Institute of Virology, University of Cologne, Cologne, Germany, [4]Microscopy Centre, Institute of Molecular Genetics CAS, Prague, Czechia

Email of the presenting author: hoboth@img.cas.cz

Detection and precise localization of specific molecules in cellular context, their spatial patterns and mutual co-distributions is key for understanding of crucial biological processes, such as gene expression. Although classical models of gene expression were built using powerful tools of genetics and biochemistry, they had very limited consideration of the spatial and temporal organization of the process within the functional nuclear context. The genome is a complex and very dense viscoelastic polymer matrix and therefore it is difficult to visualize individual components of the transcription machinery with classical diffraction-limited light microscopy. Super-resolution imaging methods allows to control in time the emission of fluorophores by either deterministic or stochastic approach [1]. These frontier far-field optical modalities set new standards for the visualization, quantification and understanding of the nanoscale organization of cells and tissues. We will discuss the application of quantitative super-resolution microscopy approaches to study the nuclear landscape at nanoscale, with particular emphasis on nuclear phospholipids (Fig. 1). Although current models of gene expression that were built using super-resolution microscopy acknowledge the formation of protein and nucleic acid condensates as a driving force of gene expression, these models largely omit nuclear lipids and nuclear phosphatidylinositol phosphates (nPIPs) in particular. Nevertheless, accumulating evidence suggests the involvement of nPIPs in the regulation of gene expression [2,3]. However, the precise sub-nuclear distribution of nPIPs and their relationships with the gene expression machinery remains unclear. Therefore, we combined quantitative multi-color direct stochastic optical reconstruction microscopy, stimulated emission depletion microscopy and electron microscopy with biochemistry and evaluated the nPIP distribution within the gene expression compartments in human cultured cells and in human formalin-fixed paraffin-embedded biopsies (FFPE; Fig. 2 and 3). Taken together, using quantitative super-resolution microscopy we uncovered the nanoscale organization that supports the distinct roles of different nPIPs in the RNA polymerase II transcription. Moreover, we extended these analyses from cultured human cells to the human formalin-fixed paraffin-embedded biopsies to study their roles in physiological and pathological conditions.

[1] Hoboth et al., IJMS 2021
[2] hoboth et al., BBA - Mol Cell Biol Lipids 2021
[3] Sztacho et al., Cells 2021

Acknowledgement: CAS JSPS-20-06; IRC IMG RVO 68378050; MEYS CR COST Inter-excellence LTC19048 LTC20024. ERDF CZ.1.05/4.1.00/16.0347 and CZ.2.16/3.1.00/21515, CzBI LM2018129.

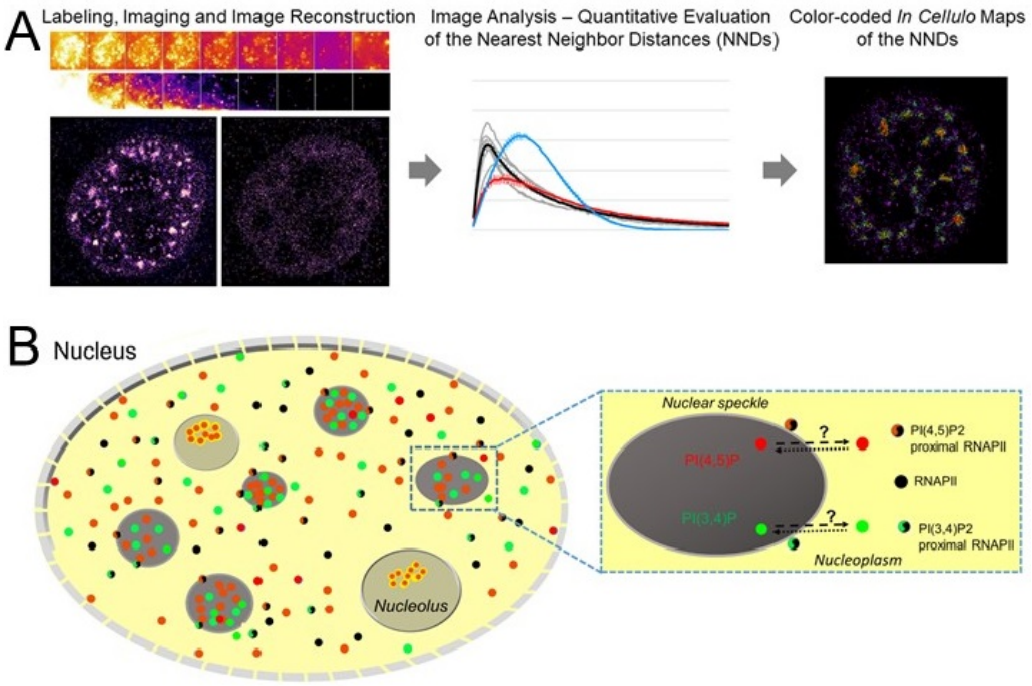

Fig. 1: Visualization of nuclear PIPs and nuclear speckle marker SON or RNAPII by dual-color dSTORM, nearest-neighbor distance (NND) analysis and in-cellulo visualization of NNDs (A). Nuclear PI(4,5)P2 and PI(3,4)P2 in nuclear speckles and nucleoplasm together with the subset of RNAPII foci (B).

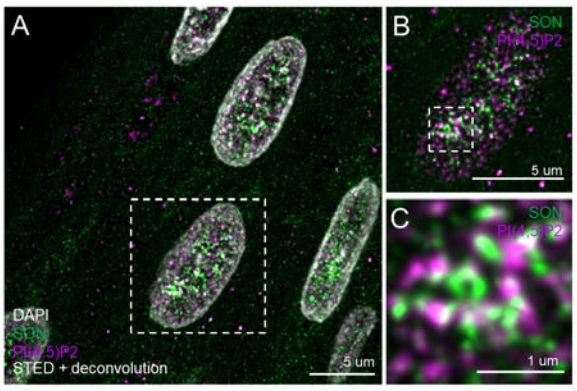

Fig. 2: (A) STED imaging with deconvolution of nuclear phosphatidylinositol 4,5-bisphosphate (green) and nuclear speckle marker SON (magenta) in human formaline-fixed paraffin-embeded biopsies counterstained with DAPI (white), (B) zoom into one nucleus, (C) zoom into the subnuclear region boxed in (B).

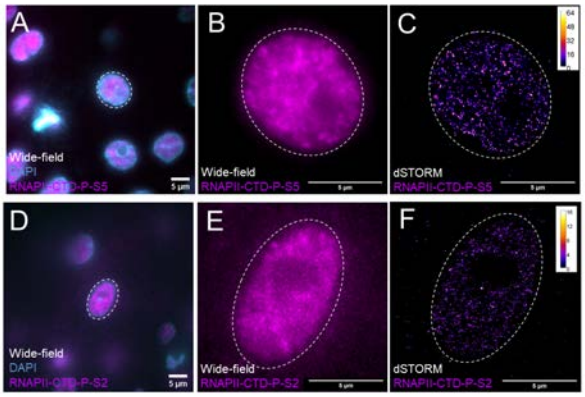

Fig. 3: The dSTORM imaging of immunolabeled RNA polymerase II phosphorylated at serine 5 (initiation marker P-S5; A-C) or 2 (elongation marker P-S2; D-F) of its C-terminal domain in humanFFPE biopsies. Wide-field (WF) overview (A, D) of a larger area counterstained with DAPI (cyan), WF P-S5/2 signal in a single nucleus (B, E), dSTORM image (C, F).

Type of presentation: Oral

LS5-O-2521 Novel method for simultaneous visualization and distinguishing Au nanoparticles on both sides of the ultrathin sections using low-energy STEM and BSE in HRSEM

Kitzberger F.[1,2], Yang S. M.[1,3], Týč J.[2], Bílý T.[1,2], Nebesářová J.[2,4]

[1]Faculty of Science, University of South Bohemia, České Budějovice, Czech Republic, [2]Biology Centre CAS, Institute of Parasitology, České Budějovice, [3]Biology Centre CAS, Laboratory of Evolutionary Protistology, Institute of Parasitology, České Budějovice, Czech Republic, [4]Faculty of Science, Charles University, Prague, Czech Republic

Email of the presenting author: frantisek.kitzberger@paru.cas.cz

A novel method for simultaneous detection of immunomarkers located on both sides of the ultrathin section is presented. This method uses High-Resolution Scanning Electron Microscope (HRSEM) operating in the Scanning Transmission Electron Microscopy (STEM) mode in combination with the detection of Backscattered Electrons (BSE). The combination of the information from the STEM and BSE signal at different accelerating voltages was shown successful in imaging and distinguishing the sides the AuNPs are located [1]. However, at precisely selected imaging parameters only one accelerating can be used for obtaining all necessary information. The STEM image provides us information about the ultrastructure of the specimen. The BSE image, acquired at the same time, gives us information about the localization of the immunomarkers (Au nanoparticles) – more precisely shows which are on the top of the ultrathin section and which are on the bottom. At these imaging conditions, the position of Au nanoparticles on top or bottom sides can be clearly differentiated, hence suggesting this method to be suitable for the straightforward multiple immunolabelling using Au nanoparticles as markers (Figure 1). Moreover, the visual difference can be amplified using a commonly available software. This amplified visual difference is so big, that automatic detection and resolution should be possible and rather straightforward. The Monte-Carlo simulation experiments support the theory of the effect of the used accelerating voltage on differentiation of top and bottom AuNPs and its´ relation to the section thickness.

[1] Nebesářová J., Wandrol P., Vancová M. (2016) Novel method of simultaneous multiple immunogold localization on resin sections in high resolution scanning electron microscopy Nanomedicine: Nanotechnology, Biology, and Medicine 12: 105-108.
DOI: 10.1016/j.nano.2015.09.008

Acknowledgement: This work was supported by TACR (TN0100008), MEYS CR (Czech BioImaging LM2018129) and Thermo Fisher Scientific – ČSMS scholarship 2021.

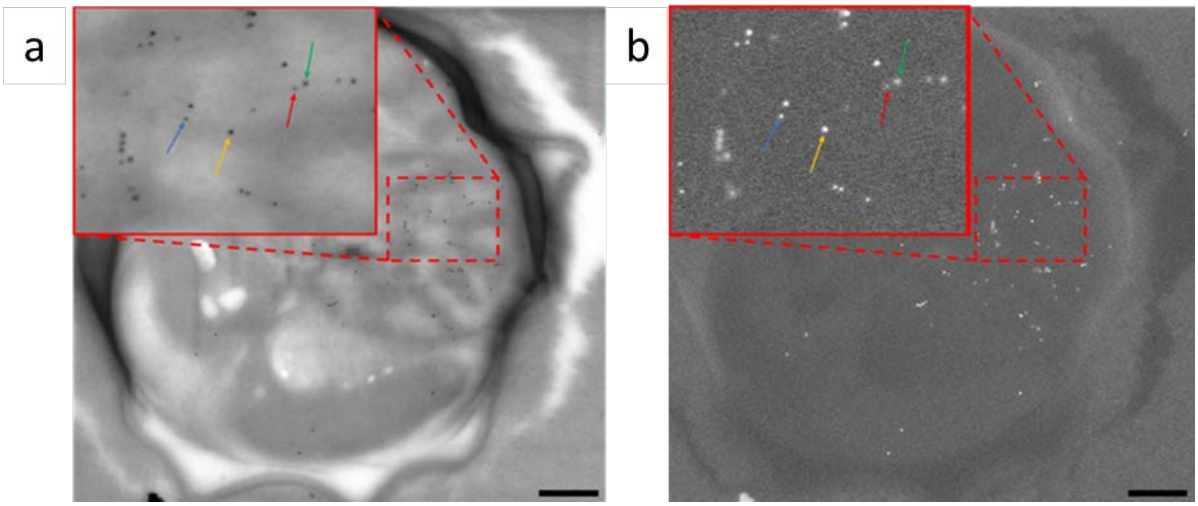

Fig. 1: Visual difference between Au nanoparticles of different sizes (10 and 15 nm) on both sides of 100 nm section on: a) STEM image; b) BSE image. Arrow color-coding: blue – 10 nm on top, yellow – 15 nm on top, red – 10 nm on bottom, green – 15 nm on bottom

Type of presentation: Oral

LS5-O-2697 Methods of leaf preparations for microscopic measurements of stomata and other epidermal cells

Veselá K.[1]

[1]Plant Biosystematic Group, Department of Botany and Zoology, Faculty of Science, Masaryk University, Brno, the Czech Republic

Email of the presenting author: 270432@muni.cz

Plant stomata regulate carbon dioxide uptake for photosynthesis and water transpiration. These critical physiological processes depend on the size and arrangement of stomata. Therefore, stomata and leaf epidermis are often the subject of physiologically-oriented studies and one of the most frequently microscopically observed plant structures. Most of these observations are done with cheap and fast imprint methods. While, these methods enable measurement of only a few stomatal parameters (e.g., their length and density) and are still of limited use for many plant species (e.g., those with hairy or fragile leaves, or when stomata are sunken in epidermis). This continues to limit current stomata research which could benefit from routine observation of stomata in directly on preparetes from leaf epidermis.However current methods of leaf and epidermis preparation are not yet routine, being demanding on laboratory equipment and experience and/or optimized only for model species. In the last years I have tested and combined different methods and approaches to prepare epidermal specimens for light (and confocal) microscopy, which could be used with minimal requirements on laboratory equipment and staff experience, as well as being universally applicable to vascular plants.

In this presentation, I intend to discuss the advantages and disadvantages of particular methods and present the optimized methods that I currently use to study stomata and leaf epidermis using light and confocal microscopy for a range of scientific questions. These methods enable a range of studies of stomatal parameters (such as stomatal pore length and stomatal conductance capacity) in hairy leaves or species with sunken stomata, including very old herbarium specimens, or in monocotyledons, where similar studies are still problematic for many species. With some of the proposed methods, epidermal samples can be easily prepared and stained for confocal microscopy, such as using DNA staining of nuclei to study endopolyploidy.

Acknowledgement: I acknowledge the core facility CELLIM supported by MEYS CR (LM2018129 Czech-BioImaging), J. Jaroš (Masaryk University) for assistance wih confocal microscope.

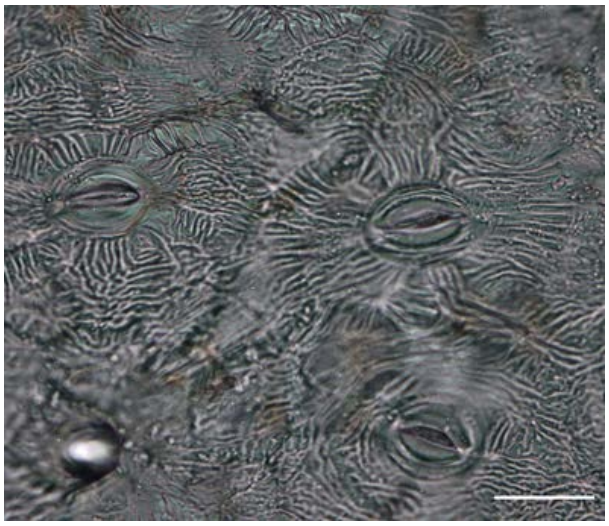

Fig. 1: Imprint method – Nail polish imprint of leaf epidermis of Aster linosyris, the edges of sunken stomata are not clearly visible. In addition, the start and the end of the aperture can not be clearly distinguished either. Scale bar is 50 µm (objective 40x).

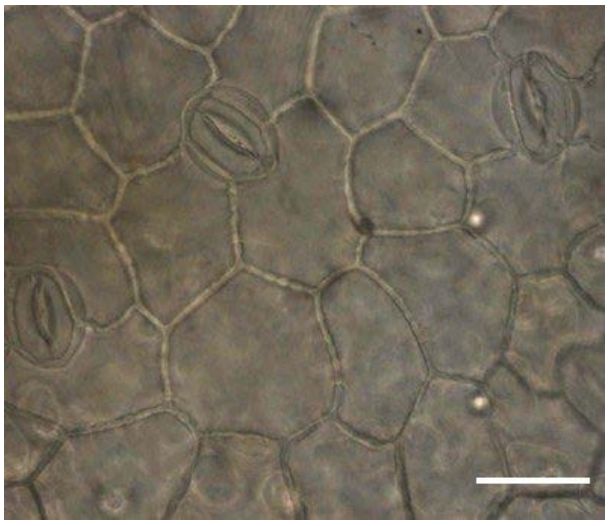

Fig. 2: Optimized cleaning method for light microscopy. Fixed (Carnoy fixative) and cleared (1M KOH) leaf epidermis of Aster linosyris with easily distinguished stomatal edges (guard cells) and stomatal aperture. Scale bar is 50 µm (objective 40x).

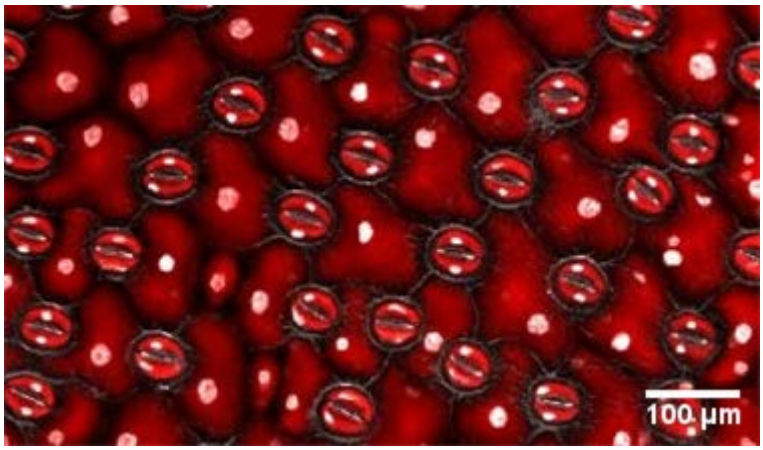

Fig. 3: Optimized staining method for confocal microscopy. Leaf epidermis of Satyrium coryiifolium with nuclei stained by Propidium iodide and cell walls stained with Calcofluor white. Colours were inverted to white for nuclei and to red for cell walls. Scale bar is 100 µm (objective 20x).

Type of presentation: Oral

LS5-O-2715 Correlative cathodoluminescence scanning electron microscopy for identification of cellular structures within vitrified samples at low electron beam energies

Vancová M.[1,2], Skoupý R.[3], Ďurinová E.[1,2], Bílý T.[1,2], Nebesářová J.[1,4], Krzyžánek V.[3], Kolouch A.[5], Horodyský P.[5]

[1]Institute of Parasitology, Biology Centre CAS, České Budějovice, Czech Republic, [2]Faculty of Science, University of South Bohemia, České Budějovice, Czech Republic , [3]Institute of Scientific Instruments CAS, Brno, Czech Republic, [4]Faculty of Science, Charles University in Prague, Prague, Czech Republic, [5]CRYTUR, spol. s r.o., Turnov, Czech Republic

Email of the presenting author: vancova@paru.cas.cz

Cathodoluminescence (CL) is the emission of photons from a material in response to excitation by accelerated electrons. CL-based imaging can be an alternative to integrated cryo-corelative light electron microscopy (e.g. photon ion electron microscopy [1]) for the identification of structures of interest in the cellular volume or on a surface of the structure of interest. Here, we show the potential of rare-earth element-doped nanocrystals [2], live-cell imaging agents from the group of luminescent transition metal complexes [3] as the CL probes, and the usage of polystyrene beads as the CL fiducials. In the cryo-SEM, the CL probes/fiducials enabled quick navigation to the freeze-fractured areas containing cells, identification of endocytic compartments with engulfed nanocrystals, and mapping of live-stained structures over larger areas of samples, and finally, to reveal the shapes of cells and nuclei positions. The consecutive secondary electron images add topographic data to determine further organelles' precise identification. The CL imaging can be easily integrated into simultaneous multimodal imaging offered by the modern SEM; therefore, we consider that CL can be used to select target regions before cryo-FIB milling or perform correlative CL-scanning electron microscopy (SEM) to identify structures within vitrified samples at low electron beam energies. This approach may unleash the potential of CL to localize structures using also the (cryo-) focused ion beam SEM, (cryo-) serial block-face SEM, and array tomography.

[1] Gorelick, S. et al. 2019. PIE-scope, integrated cryo-correlative light, and FIB/SEM microscopy. eLife 8, e45919.

[2] Keevend, K. et al. 2019. Ultra-Bright and Stable Luminescent Labels for Correlative Cathodoluminescence Electron Microscopy (CCLEM) Bioimaging. Nano Letters 19.

[3] Bader, C.A. et al. 2016. Imaging nuclear, endoplasmic reticulum and plasma membrane events in real-time. FEBS Let 590, 3051-3060.

Acknowledgement: We thank TACR (TN0100008), MEYS CR (Czech BioImaging LM2018129), CRYTUR comp., J. Vaněček (BC CAS), Prof. S. Plush and Prof. M. Massi.

LS6 Multi-parametric and functional imaging in life sciences

Type of presentation: Invited

LS6-IN-3013 Quantitative visualisation of membrane dynamics through photoactivation of fluorescent proteins

Rossy J.[1]

[1]Biotechnology Institute Thurgau at the University of Konstanz, Switzerland

Email of the presenting author: jeremie.rossy@bitg.ch

While they have been widely used for photoactivated localisation microscopy (PALM), photoactivatable or photoswitchable fluorescent proteins had initially been designed to assess protein dynamics. We have developed toolset based on photoactivation of fluorescent proteins that enabled us to generate quantitative information on endocytosis, incorporation into sorting and recycling endosomes, delivery from endosomes to the plasma membrane, and on the type of vesicles performing intracellular transport. We further adapted the same approach to measure the dynamics of proteins within clusters at the plasma membrane.
T cell activation involves the formation of a highly specialised cell-cell interface, the immunological synapse. Activation and formation of the synapse rely extensively on changes in the organisation of membrane proteins and the dynamics of these changes remain poorly understood. We applied our photoactivation-based microscopy approaches to obtain key information how the T cell receptor is transported through cell trafficking to a from the immunological synapse or how the co-receptor CD28 is maintained in stable clusters within the plasma membrane. Our data revealed a) a fast endocytic sorting pathway relying on the membrane proteins flotillins [1], [2] and b) how the BAR domain protein sorting nexin 9 regulate CD28 clusters stability and signalling [3].
[1] E. B. Compeer et al., “A mobile endocytic network connects clathrin-independent receptor endocytosis to recycling and promotes T cell activation,” Nature Communications, vol. 9, no. 1, p. 1597, 2018, doi: 10.1038/s41467-018-04088-w.
[2] G. M. I. Redpath et al., “Flotillins promote T cell receptor sorting through a fast Rab5–Rab11 endocytic recycling axis,” Nature Communications, vol. 10, no. 1, p. 4392, Dec. 2019, doi: 10.1038/s41467-019-12352-w.
[3] M. Ecker et al., “SNX9-induced membrane tubulation regulates CD28 cluster stability and signalling,” Elife, vol. 11, p. e67550, Jan. 2022, doi: 10.7554/eLife.67550.

Type of presentation: Oral

LS6-O-2622 Oscillatory intracellular patterns of the small GTPase Rac1

Šoštar M.[1], Marinović M.[1], Filić V.[1], Pavin N.[2], Weber I.[1]

[1]Ruđer Bošković Institute, Division of Molecular Biology, Zagreb, Croatia, [2]University of Zagreb, Faculty of Science, Department of Physics, Zagreb, Croatia

Email of the presenting author: iweber@irb.hr

Small GTP hydrolases from the Rho family regulate and coordinate a variety of processes driven by the actin cytoskeleton in eukaryotes, in particular the cell motility. Lifestyle of the highly motile *Dictyostelium discoideum* amoebae is remarkably reminiscent of the mammalian white blood cells, particularly neutrophils and phagocytes. Interestingly, the genomes of *Dictyostelium discoideum* and *Homo sapiens* both encode 20 Rho GTPases, although the two species diverged more than a billion years ago [1]. Here, we present a combined experimental and theoretical approach to investigate the intracellular dynamics of the small GTPase Rac1 and its effector DGAP1. Because *Dictyostelium* cytoskeleton remodels rapidly, in order to monitor its constitutive and regulatory proteins in living cells it is crucial to use fluorescent biosensors capable to follow these fast dynamics and to endure prolonged imaging at high recording rates. We developed a fluorescent probe highly specific for the active form of Rac1 with a low cytoplasmic background signal, which enables to resolve small variations of the Rac1 activity in the cell cortex [2]. Spatio-temporal distributions of fluorescently labelled active Rac1 and DGAP1 were recorded in living cells by point-scanning confocal microscopy, processed by QuimP software, and analyzed by principle component analysis. We observed the occurrence of three main types of patterns displayed by fluorescent probes: standing waves in the form of oscillations, travelling waves in the form of rotations, and stationary states in the form of stably polarized distributions (Fig.1). Beside these common patterns, we noticed that the dynamics of Rac1 activity and DGAP1 were mostly anti-correlated, with the exception of rare stationary patterns with overlapping distributions. To rationalize the observed patterns on the basis of underlying biochemical reactions, we applied mathematical modelling. The experimentally observed dynamic distributions were compared to the results of a reaction-diffusion model that includes Rac1 activation, Rac1 deactivation, and its interaction with DGAP1, described by simple mass action kinetics. Our theoretical model was able to reproduce almost all experimentally observed dynamical patterns (Fig. 1).

[1] Filić, V.; Mijanović, L.; Putar, D.; Talajić, A.; Četković, H.; Weber, I. Regulation of the Actin Cytoskeleton via Rho GTPase Signalling in Dictyostelium and Mammalian Cells: A Parallel Slalom. Cells 2021, 10, 1592. doi.org/10.3390/cells10071592.

[2] Marinović, M.; Šoštar, M.; Filić, V.; Antolović, V.; Weber, I. Quantitative Imaging of Rac1 Activity in Dictyostelium Cells with a Fluorescently Labelled GTPase-Binding Domain from DPAKa Kinase. Histochem Cell Biol 2016, 146, 267–279. doi:10.1007/s00418-016-1440-9.

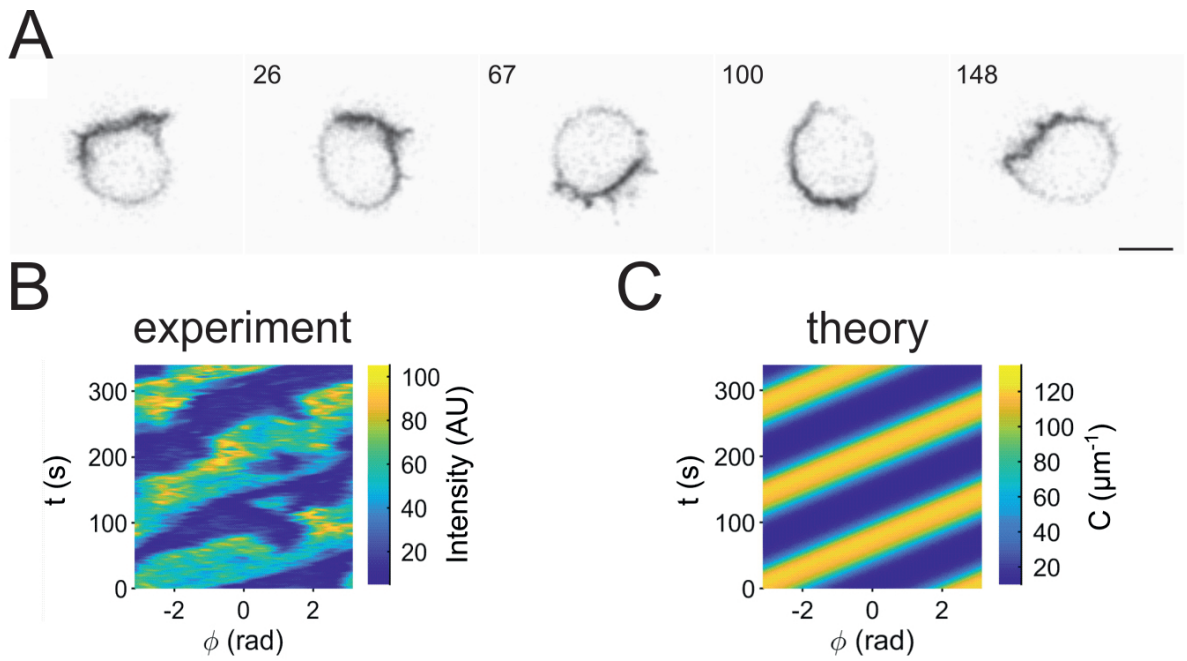

Fig. 1: A) Clockwise rotation of a single cortical domain labelled for active Rac1. Time is indicated in seconds. Scale bar: 5 μm. B) Kymograph of the measured fluorescence intensity of the active Rac1 probe along the cell circumference for a rotating pattern. C) A corresponding kymograph of the calculated linear concentration of active Rac1.

Type of presentation: Oral

LS6-O-2627 In-situ observations of metal nanoparticles interactions with living cells, in liquid environments directly in the Nanolive 3D CX-A microscope

Depciuch J.[1], Klebowski B.[1], Orzechowska B.[1], Parlinska-Wojtan M.[1]

[1]Department of Functional Nanomaterials, Institute of Nuclear Physics Polish Academy of Science

Email of the presenting author: joanna.depciuch@ifj.edu.pl

In recent years, focus has turned to therapeutic possibilities of nanoparticles (NPs). The hypothesis is made that the toxic effect of NPs on cells depends on the differences in the absorption dynamics, which, in turn, is directly related to the mechanical interaction between the cells and the NPs. These different interactions are caused by different shapes, sizes and chemical compositions of the NPs. To confirm this hypothesis, in situ, long-term, real-time experiments using high-resolution holotomographic microscope Nanolive 3D CX-A were performed. To investigate the correlation between the shape of NPs and absorption dynamics as well as accumulation place of NPs in cells, gold nanoparticles (Au NPs) with star-, sphere- and rod-like shapes as well as spherical Pd NPs, were used, Figure 1. Furthermore, to show the dependence between the dynamics of NPs absorption and cell type, four colon cell lines were used (three cancer lines with different grades, one control line), Figure 2.
The obtained results showed, that the dynamics of nanoparticle accumulation depends on the: (i) shape of nanoparticles, as well as on (ii) the type of cells. (i) Rod- and star-shaped Au NPs were accumulated on the membrane, outside the cells, while spherical Au NPs outside as well as inside the cells. Furthermore, the shortest time after which saturation of nanoparticles in cells occurred was observed for star-shaped Au NPs. (ii) Taking into account, the differences in the absorption of Pd NPs depended on the cell line, it was observed, that the highest volume of Pd NPs was observed for the most aggressive SW620 colon cancer cells.
The obtained results suggest, that absorption and accumulation place of different NPs with living cells, depend on the shape of NPs and type of cell line.

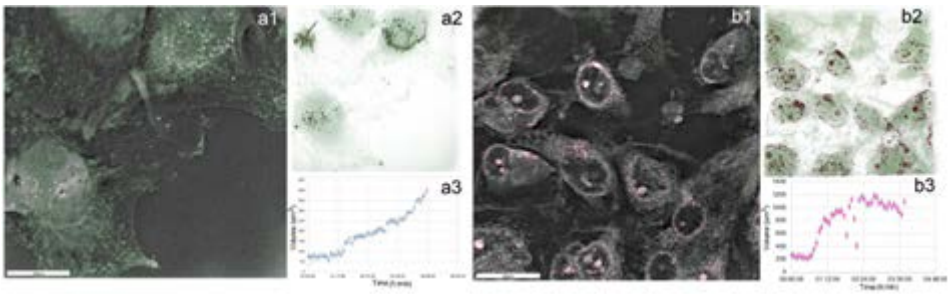

Fig. 1: Holotomographic images of U118 cells with marked Au NPs (red color) and cell membrane (green color); (a2, b2) Holotomographic images reconstructed based on the refractive index of Au NPs (red color) and cell membrane (green color); (a3, b3) Volumetric absorption of NPs by cells as a function time.

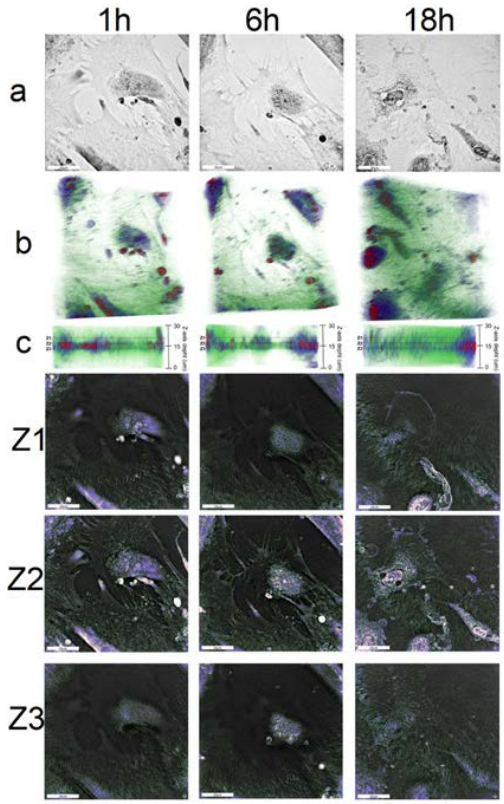

Fig. 2: a) Holotomographic images of SW480 cells cultured with Pd NPs. b) 3D reconstructed images based on the RI of: Pd NPs (red color), nuclei (blue color) and cytoplasm (green color). c) Z-axis reconstruction of holotomographic images with marked presented thickness of slices approximately 13μm (Z1), 17μm (Z2) and 21.6 μm (Z3).

Type of presentation: Invited

LS6-IN-2950 Large Area Brain Imaging

Pavone F.[1]

[1]University of Florence

Email of the presenting author: francesco.pavone@unifi.it

High-resolution microscopy methods based on nonlinear optical technique find numerous applications in brain imaging. Functional or structural information can be gain with different implementations. In this work large area reconstruction are obtained using a mesoscale light sheet system for structural analysis and a light sheet two-photon microscope for functional information. The mesoscale methodology developed allows analyzing the cytoarchitecture of the human brain in three dimensions at high resolution. The combination of experimental protocols, based on optical tissue clearing and autofluorescence enhancement, with an automated software analysis enable to expand the histological studies to the third dimension. Functional imaging has been used to investigate whole organ, like zebrafish larval brain activity, using standard scanning or light sheet two-photon illumination. Both modalities are capable to sample whole brain with single cell resolution, with light sheet imaging being capable to perform high rate volumetric imaging allowing to map in real time whole-brain calcium dynamics not affected by undesired visual stimulation artefacts, as occurring in one photon excitation fluorescence microscopy. Large area non linear imaging allows in general extended measurements of the neuronal activity in normal conditions (spontaneous activity), under pathological modeling of epilepsy (seizure activity) and during visual stimulation (sensorial stimulated activity).

Type of presentation: Oral

LS6-O-2615 The BUILD project: A multi-modal cross-scale approach to reveal characteristics of the human brain's nested connectome

Axer M.[1], Fernandez-Rodriguez J.[2], Amunts K.[1], Camacho R.[2], De Felipe J.[3], Eberle A. L.[4], Garbowski T.[4], Gloesmann M.[5], Handschuh S.[5], Jaeger C.[6], Merchan-Perez A.[3], Ruland S.[1], Micaroni M.[2], Casares A.[6]

[1]Institute of Neuroscience and Medicine, Forschungszentrum Jülich, Germany, [2]Centre for Cellular Imaging, Shalgrenska Academy, University of Gothenburg, Gothenburg, Sweden, [3]Instituto Cajal, Universidad Polit cnica de Madrid, Spain, [4]Carl Zeiss MultiSEM GmbH, Oberkochen, Germany, [5]VetCore/Imaging, University of Veterinary Medicine, Vienna, Austria, [6]Carl Zeiss Mic GmbH, Oberkochen, Germany

Email of the presenting author: m.axer@fz-juelich.de

Understanding the organizational principles of the human brain and the mechanisms of its function and dysfunction is crucial for basic and translational neuroscience. Human brain complexity is a major challenge in that respect. It comprises the highly folded cerebral cortex, the large number of specialized areas, a considerable inter-subject variability in brain structure, function and behavior, dynamic changes during the whole lifespan, and the sheer size of the brain with its nearly 86 billion neurons. The human brain is densely packed with unmyelinated and myelinated axons (fibers), which form via synaptic contacts highly complex networks – building the connectome. Recent developments in neuroimaging technologies have significantly enriched our knowledge about large fiber pathways connecting different brain regions. Diffusion MRI enables to study the entire human brain non-destructively from the mm-scale (in vivo) down to a few hundred µm (post mortem). However, information about individual fibers and their intricate circuits, particularly those within the cerebral cortex or interwoven white matter tracts, are not reliably obtainable with an MRI scanner to date. Sensitivity and resolution to target such neural microstructures at and beyond the µm-scale are rather accessible with light microscopy, X-ray scattering, or electron microscopy. Such high-resolution techniques are typically restricted to very small tissue samples as compared to an entire human brain, and often require their own tissue preparation protocols inhibiting true multi-modal imaging of the same samples.
In a proof-of-concept approach, we have started to develop brain preparation, scanning, and cross-correlation pipelines to utilize the virtues of complementary high-resolution neuroimaging techniques (MRI, 3D Polarized Light Imaging, X-ray tomography, 3D-SEM, mSEM, and FIB-SEM) serially applied to the same brain tissue. The main goal is to develop a scalable approach that facilitates the study of the human connectome from the millimeter to the nanometer domain in both the normal and the pathological brain (e.g., to address diseases that affect myelination, such as MS). To cope with the enormous amount of multi-modal data acquired at different research sites (high-performance computing, data sharing, storage, and dissemination), we are using the FENIX infrastructure (fenix-ri.de) coordinated by leading European centres for high-performance computing. The collected, cross-aligned connectome data will spatially be anchored and integrated into the publicly available Human Brain Atlas provided by the international, collaborative research infrastructure EBRAINS (ebrains.eu) developed in the context of the European Flagship Human Brain Project (HBP, humanbrainproject.eu).

Acknowledgement: BUILD is a partnering Project of the Human Brain Project (European Union's Horizon 2020 Framework Programme for Research and Innovation, SGA3, No. 945539).

Type of presentation: Oral

LS6-O-2639 Correlative 3D imaging workflow using X-ray micro-computed tomography and laser plasma focussed ion beam electron microscopy on biological soft tissues

Lawson M. J.[1], Donoghue J. M.[1], Gholina A.[1], Burnett T. L.[1], Sheratt M. J.[2], Withers P. J.[1]

[1]Henry Royce Institute, Department of Materials, The University of Manchester, Manchester M13 9PL, UK, [2]Division of Cell Matrix Biology and Regenerative Medicine, School of Biological Sciences, Faculty of Biology Medicine and Health, The University of Manchester, Manchester M13 9PT, UK

Email of the presenting author: matthew.lawson@manchester.ac.uk

Biological soft tissues, both human and animal, are formed of complex three-dimensional (3D), often hierarchical, structures that extend over many length scales (from sub-μm macro-molecular assemblies to mm scale tissue architectures). In order to better understand the risk factors for many common diseases it is necessary to visualise the 3D structure of tissues over this large size range. Current microscopy methods for imaging clinically relevant tissues commonly provide 2D images over a relatively narrow size range. Correlative microscopy approaches, which combine multiple techniques including 3D X-ray micro-computed tomography (μCT) and 3D volume electron microscopy (EM), can resolve the 3D structure of fixed soft tissues at multiple lengths scales [1]. The aim of this pilot study was to develop a correlative imaging workflow which builds on previous work to investigate clinically relevant tissue structures in 3D.

Mouse gut tissue, which had been infected with Trichuris muris [1], were used for development of the preliminary workflow. Each tissue sample was chemically fixed and stained in preparation for 3D imaging following standard EM protocols for soft tissue (step 1 figure 1). Each resin embedded soft tissue block (~1 cm3) was non-destructively μCT imaged using a Zeiss Versa 620 system (1-10 μm resolution, step 2 figure 1) to scout for regions of interest prior to EM imaging. Following inspection of the μCT data the tissue block was coated and placed in the Helios™ 5 Laser PFIB (Thermo Fisher). Using a combination of the laser and FIB milling a column (~500 μm diameter) of tissue centred around the region of interest was created with minimal surface damage (step 3 figure 1). Following extraction of the small column in the Laser P-FIB, further high-resolution 3D imaging (<1 μm resolution) was performed non-destructively with high resolution μCT. Destructive 3D imaging, using volume EM (<100 nm resolution, step 4 figure 1) was used if the features of interest were still not visible in the μCT scans.

This workflow (figure 1) effectively surveyed large volumes of tissue using μCT to identify previously difficult to find clinically relevant volumes of interest, which would be difficult to orient and slice with traditional methods. The laser milled column of tissue could then be imaged with both high-resolution μCT and volume EM. On a larger volume of tissue (up to 1 mm diameter), this workflow provided a more precise (than ultramicrotomy) and faster alternative to FIB milling for producing clinically relevant sub-volumes of soft tissue.

[1] O'Sullivan, J.D.B., et al. Characterisation of cuticular inflation development and ultrastructure in Trichuris muris using correlative X-ray computed tomography and electron microscopy. Sci Rep 10, 5846 (2020).

Acknowledgement: James O'Sulivan, Remco Guertes, Tristan Lowe, Billy Koe, Amin Garbout, Elizabeth Evans, NXCT, ERC, Henry Royce Institute

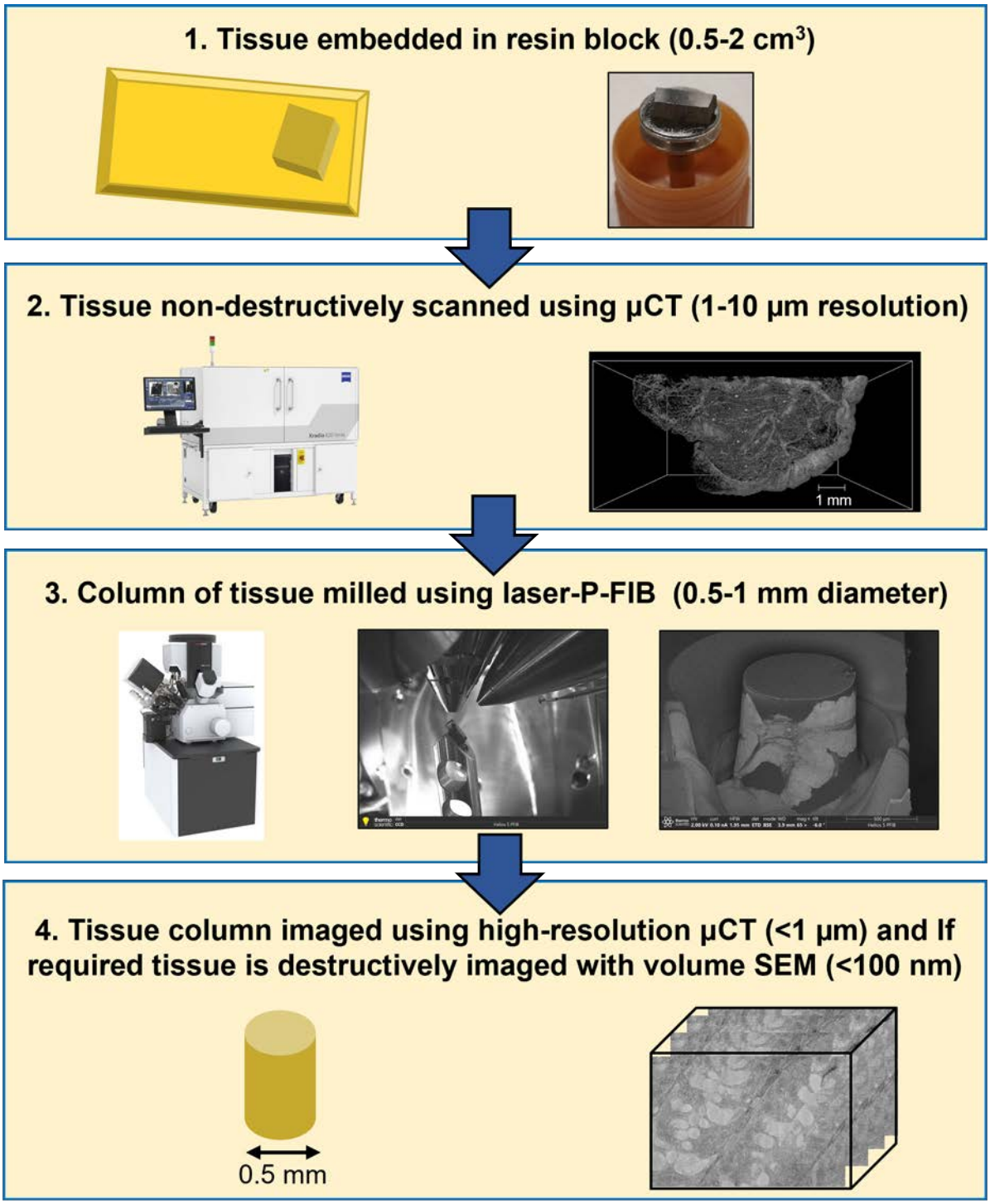

Fig. 1: Proposed workflow using a combination of using µCT and laser P-FIB electron microscopy on soft tissues. 1. Tissue prepared using standard EM protocols. 2. Tissue scanned using µCT to identify a region of interest. 3. Column of tissue is milled out using the laser and P-FIB. 4. Final high resolution 3D images captured with µCT and volume-EM.

Type of presentation: Poster

LS6-P-2881 A beetle that was a flea. Comparison of morphological adaptations in external parasites among Coleoptera and Siphonaptera, using light and scanning electron mic

Adamski Z.[1, 2], Konwerski S.[3], Sienkiewicz P.[4]

[1]Lab. Electron & Confocal Microscopy, F. of Biology, Adam Mickiewicz Univ. Poland, [2]Dept. Animal Physiology & Developmental Biology, F. of Biology, Adam Mickiewicz Univ., Poland, [3]Nat. History Collections, F. of Biology, Adam Mickiewicz University in Poznań, Faculty of Biology, Adam Mickiewicz Univ. Poland, [4]Dept. Entomology & Environmental Protection, Poznań Univ. of Life Sciences, Poznań, Poland

Email of the presenting author: zbigniew.adamski@amu.edu.pl

In ectoparasites living in the hair of mammals, adaptations to a specific environment are observed, consisting of modifications of various morphological structures. One of the most interesting examples of convergence in this ecological group can be seen between the beaver beetle Platypsyllus castoris belonging to the family Leiodidae (order Coleoptera) and fleas (order Siphonaptera). Interestingly, the beaver beetle was originally described as representative of a new flea family. Platypsyllus castoris lives almost exclusively in the hair of the European beaver (Castor fiber) and the North American beaver (Castor canadensis). In Europe, this beetle is relatively rare, and until recently it was considered an endangered species. The currently growing population of European beavers ensures also the survival of this interesting ectoparasite.
In the poster, the authors discuss similarities and differences between two parasitic species that inhabit similar environments. To show the convergence at the level of morphological features of certain body parts, the authors applied methods of light and scanning electron microscopy. The general body plan, and structure of the thorax, abdomen, and legs of the taxa in question will be analyzed and measured. Next, the ratio between the observed structures will be analyzed and compared.
The accurate measurements, using scanning electron microscopy, allow for precise comparison of the body-plan organization of two species that show morphological convergence and help in answering whether the ratio of the given structures is convergent, too. In the poster, the authors present the microscopic observations, correlate the morphology of organs of interest, and show the results of the measurements.

Type of presentation: Poster

LS6-P-2898 Correlation of Atomic Force Microscopy with other techniques: application on biosamples

Přibyl J.[1], Klimovič Š.[1], Kabanov D.[1]

[1]Core Facility NanoBioTechology, CEITEC MU, Masaryk University, Kamenice 5, CZ-62500 Brno

Email of the presenting author: jan.pribyl@ceitec.muni.cz

Atomic Force Microscopy (AFM) is a high-resolution microscopy technique [1] that is highly suitable for working with biospecimens, as it can operate under semi-physiological conditions. Moreover, the AFM may provide nano localized information about the sample's elastic [2] and other mechanical properties [3]. However, there are some characteristics that AFM can not provide, such as chemical composition, optical properties, and/or information about sample electrical properties.
A complex description of the sample is available by a combination of AFM with one or more correlative techniques. AFM with Raman microscopy enriches the topographic and mechanical mapping with information about the sample’s chemical composition. Polarizing microscopy can then help, for example, in the localization of collagen fibers. Fluorescence microscopy then adds the cell cytoskeleton structure to the information from elastic mapping. Another example of a correlative approach could be a combination of mechanical monitoring of cardiac contractions combined with electrical potential monitoring using a multielectrode array.
These and other examples of the correlative approach of combining scanning probe microscopy with other techniques will be shown in the presentation and discussed, including possibilities for further development and optimization.
[1] Horňáková, V., Přibyl, J. & Skládal, P: Monatsh Chem 147 (2016) 865–871.
[2] Raudenska M., Kratochvilova M., et al.: Scientific Reports 9 (2019) 1660, 1-11.
[3] Caluori G, Pribyl J, et al.: Biosens Bioelectron. 124-125 (2019) 129-135.

Acknowledgement: We acknowledge CF Nanobiotechnology of CIISB, Instruct-CZ Centre, supported by MEYS CR (LM2018127).

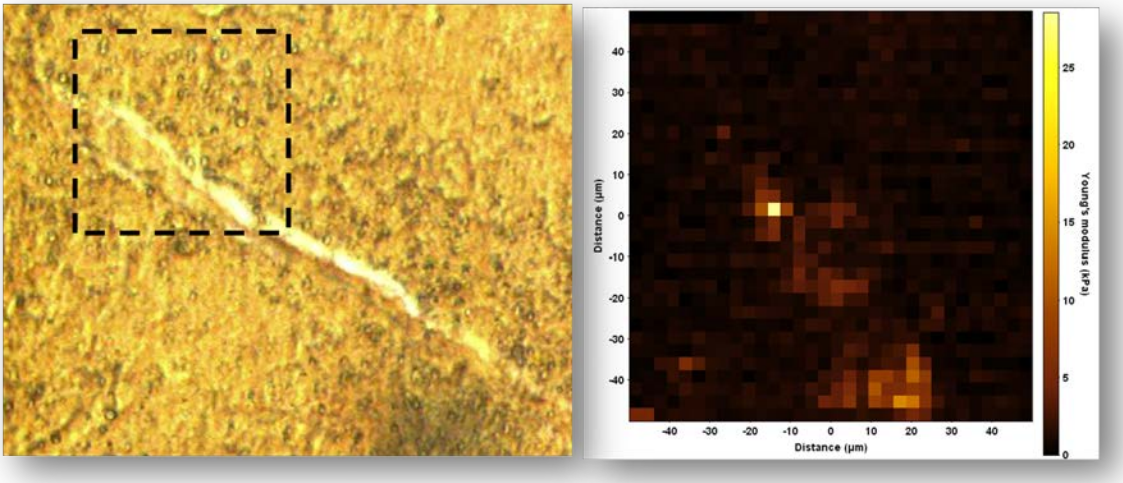

Fig. 1: Co-localization of collagen fibers in liver samples by polarization microscopy combined with AFM nanoindentation (sample property: M. Gregor, UMG CAS).

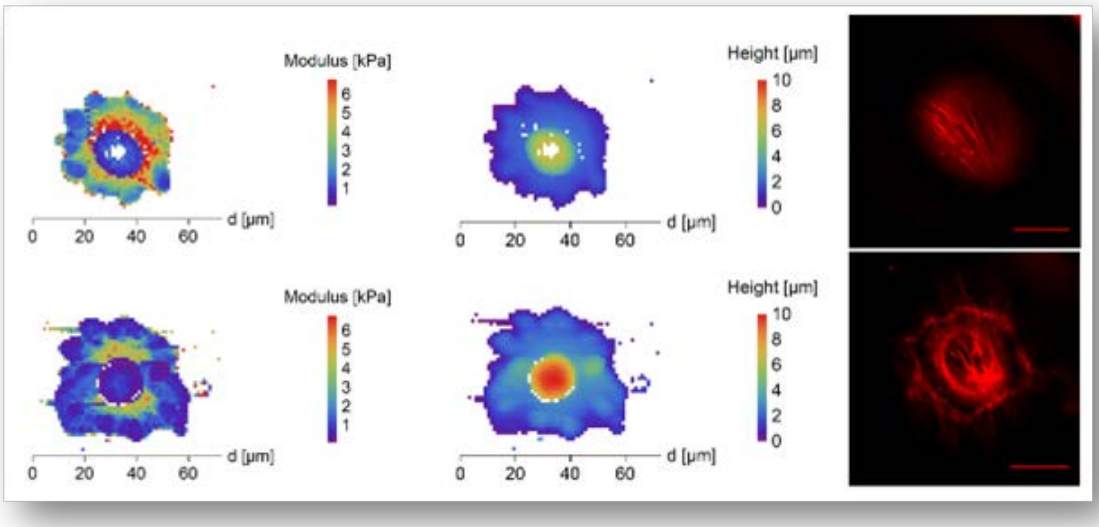

Fig. 2: Stiffness map and topography profile obtained by AFM nanoindentation correlated with actin filaments structure (fluorescence microscopy), fibroblast live cell study.

Type of presentation: Poster

LS6-P-2802 In situ cryo-electron tomography of enterovirus cell entry

Trebichalská Z.[1], Mukhamedova L.[1], Ishemgulova A.[1], Šmerdová L.[1], Füzik T.[1], Nováček J.[1], Plevka P.[1]

[1]Central European Institute of Technology, Masaryk University, Brno, Czech Republic

Email of the presenting author: 442024@mail.muni.cz

Enteroviruses from the family *Picornaviridae* are human pathogens that cause a range of diseases from the common cold to severe brain inflammation. Despite the societal and economic impact of enteroviruses, the available treatments are only symptomatic. The enterovirus cell entry and the release of the viruses from endosomes are potential targets for antiviral therapeutics. However, the details of these phenomena are not well understood.
Here, we used *in situ* cryo-electron tomography to visualize the cell entry and genome release of human rhinovirus 2. We observed endosome membrane remodelling and breakage followed by virus escape into the cytoplasm. We demonstrate that the endosome disruption is mediated by overactivation of a cellular mechanism by showing that endocytosis of very-low-density lipoprotein, the natural substrate of rhinovirus 2 receptor, also results in endosome disruption. The described mechanism of rhinovirus 2 cell entry is supported by data collected on other enteroviruses. Our results give evidence of the cellular mechanisms these viruses employ to enter cell hosts.

Acknowledgement: *We acknowledge the Cryo-electron microscopy and Tomography Core Facility of CEITEC MU for their support in data collection and analysis.*

Type of presentation: Poster

LS6-P-2849 Monitoring the endothelial cell behavior during flow stress induction using digital holographic microscopy.

Zumberg I.[1], Cmiel V.[1], Orlova L.[2], Hashemi A.[1], Jagos J.[2]

[1]Department of Biomedical Engineering, Faculty of Electrical Engineering and Communication, Brno University of Technology, Technická 3082/12, 616 00 Brno, Czech Republic, [2]Institute of Solid Mechanics, Mechatronics and Biomechanics, Faculty of Mechanical Engineering, Brno University of Technology, Technická 2896/2, 616 69 Brno, Czech Republic

Email of the presenting author: zumberg@vutbr.cz

The arterial endothelium is exposed to physical stress associated with blood flow and plays an essential role in maintaining vascular homeostasis in response to hemodynamic forces. Endothelial cells are in direct contact with flowing blood and their response to physiological and pathological flow dynamics affects the health of blood vessels [1]. The inclusion of computational modeling in cell mechanics research is a very promising tool for understanding the events taking place at the cellular level. A huge advantage of computational simulations is the possibility of connecting the cause and effect of behavior even for such values, which are either not possible or demanding to measure *in vivo*. The current hybrid computational model of a single endothelial cell considers all mechanically significant organelles [2], but suffers from a lack of information about the behavior of individual organelles. Such model can be optimized by comparing the model response with the real behavior of the cell under defined conditions. This study aims to monitor the elastic behavior of individual endothelial cells during fluid flow. A measuring set according to Fig. 1 is created for the implementation of experiments. The application of flow stimuli is provided by the microfluidic system Fluigent Flow EZ (FLUIGENT INC., Germany). First, a set of rectangular pressure pulses in Fluigent OxyGEN software is proposed. Then, pressure changes are converted to flow pulses by Fluigent Flow EZ controller. Finally, these flow pulses are applied to individual endothelial cells (Human umbilical vein endothelial cells) cultured in a channel slide (μ-Slide VI 0.1, ibidi). The video sequences of the cells are acquired with a T1000 digital holographic microscope (Lyncée Tec, Switzerland), which provides a label-free and minimally invasive technology for quantitative cell imaging. The microscopic images of selected cell before and during the experiment are shown in Fig. 2 and Fig. 3. They show that the cell mass is shifted in the direction of the fluid flow during application of a pressure pulse. The obtained real flow data together with analyzed cell responses on the flow stimuli are used to further analyze the shear stress applied to the endothelial cells and this can be used to later update of existing endothelial cell model.

[1] F. Tovar-Lopez, P. Thurgood, C. Gilliam, N. Nguyen, E. Pirogova, K. Khoshmanesh, and S. Baratchi, “A microfluidic system for studying the effects of disturbed flow on endothelial cells,” Frontiers in Bioengineering and Biotechnology, vol. 7, pp. 2296–4185, 2019.

[2] V. V. S. V. Jakka, and J. Bursa, “Impact of physiological loads of arterial wall on nucleus deformation in endothelial cells: A computational study,” Computers in Biology and Medicine, vol. 143, 2022.

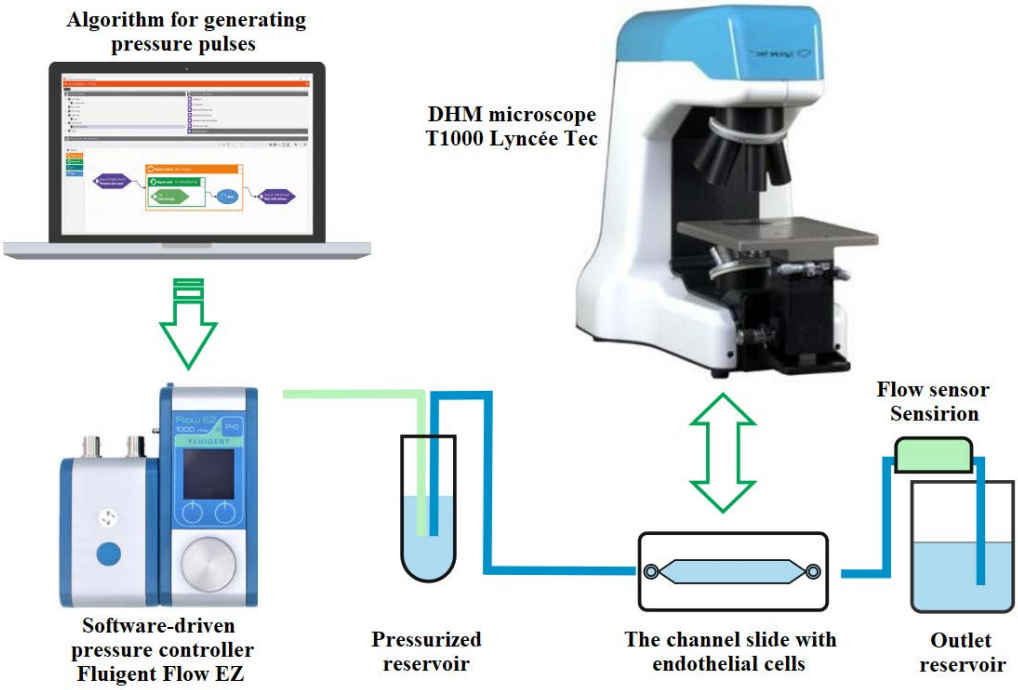

Fig. 1: Schematic of the implemented microfluidic-based measurement system with endothelial cell monitoring using digital holographic microscopy

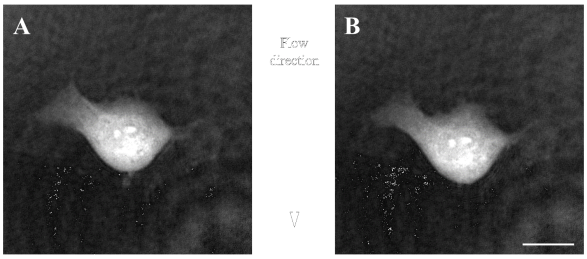

Fig. 2: The DHM microscopic images of endothelial cell before (A) and during (B) the application of fluid flow (flow rate 2.3 ml/min). Image resolution 790×790 px, 40x magnification, scale bar 20 µm

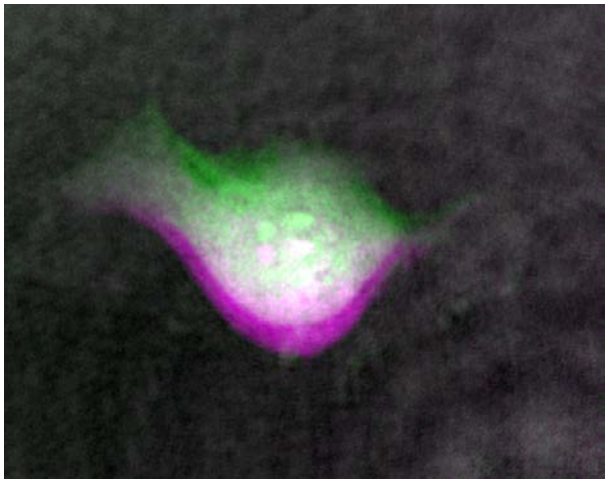

Fig. 3: Comparison of endothelial cell images before and during flow stress. Here, purple area shows the increase in brightness (or pixel values) and green area means the decrease in brightness, which represents the displacement of the cell in the flow direction

LS7 Advances in volume electron microscopy and image processing

Type of presentation: Invited

LS7-IN-3024 Chasing for efficacy: from manual and semi-automatic tools to convolutional neural networks in segmentation of microscopy datasets

Belevich I.[1], Vihinen H.[1], Jokitalo E.[1]

[1]Electron Microscopy Unit, Institute of Biotechnology, University of Helsinki, Finland

Email of the presenting author: ilya.belevich@helsinki.fi

Understanding the structure – function relationship of cells and organelles in their natural context requires multidimensional imaging techniques. As performance and access to such techniques are improving, the amounts of collected data are growing exponentially posing a question about processing, segmentation, and analysis of these datasets. To improve and facilitate the full utilization of acquired data, we developed Microscopy Image Browser (MIB) [1], which is an open-source solution with variety of tools for efficient processing, segmentation and analysis of multidimensional datasets. In my talk, I will concentrate on image segmentation and introduce semi-automatic tools of MIB, such as local thresholding, morphological operations and graphcuts - that significantly ease and speed-up the segmentation process.

Deep learning approaches are highly sought after solutions for coping with large amounts of collected datasets and becoming an essential part of imaging workflows. However, in most cases, deep learning is still considered as a complex task that only image analysis experts can master. In 2021, we released DeepMIB [2], which is a user-friendly package that is capable of training convolutional neural networks (CNN) on user's microscopy data. DeepMIB is bundled with MIB, forming a powerful suit to address all aspects of an imaging pipeline starting from basic processing of images (e.g., filtering, normalization, alignment) to manual, semi-automatic and fully automatic segmentation, proofreading of segmentations, their quantitation and visualization. It is easy to install, and its usage does not require any computer programming skills. I will demonstrate successful application of DeepMIB for semantic segmentation of 2D and 3D microscopy datasets as well as introduce the recently developed patch-wise workflow for processing 2D images. Both MIB and DeepMIB are written using Matlab language for scientific computing and distributed as an open-source code or as a compiled application for academic research.

References

[1] I. Belevich, M. Joensuu, D. Kumar, H. Vihinen E. Jokitalo, PLoS Biology 2016 Jan 4;14(1):e1002340.
[2] A I. Belevich, E. Jokitalo, PLoS Comput Biol. 2021 Mar 2;17(3):e1008374.

Acknowledgement: Biocenter Finland and Academy of Finland Research Infrastructure Funding, members of the Electron Microscopy Unit and MATLAB Central community

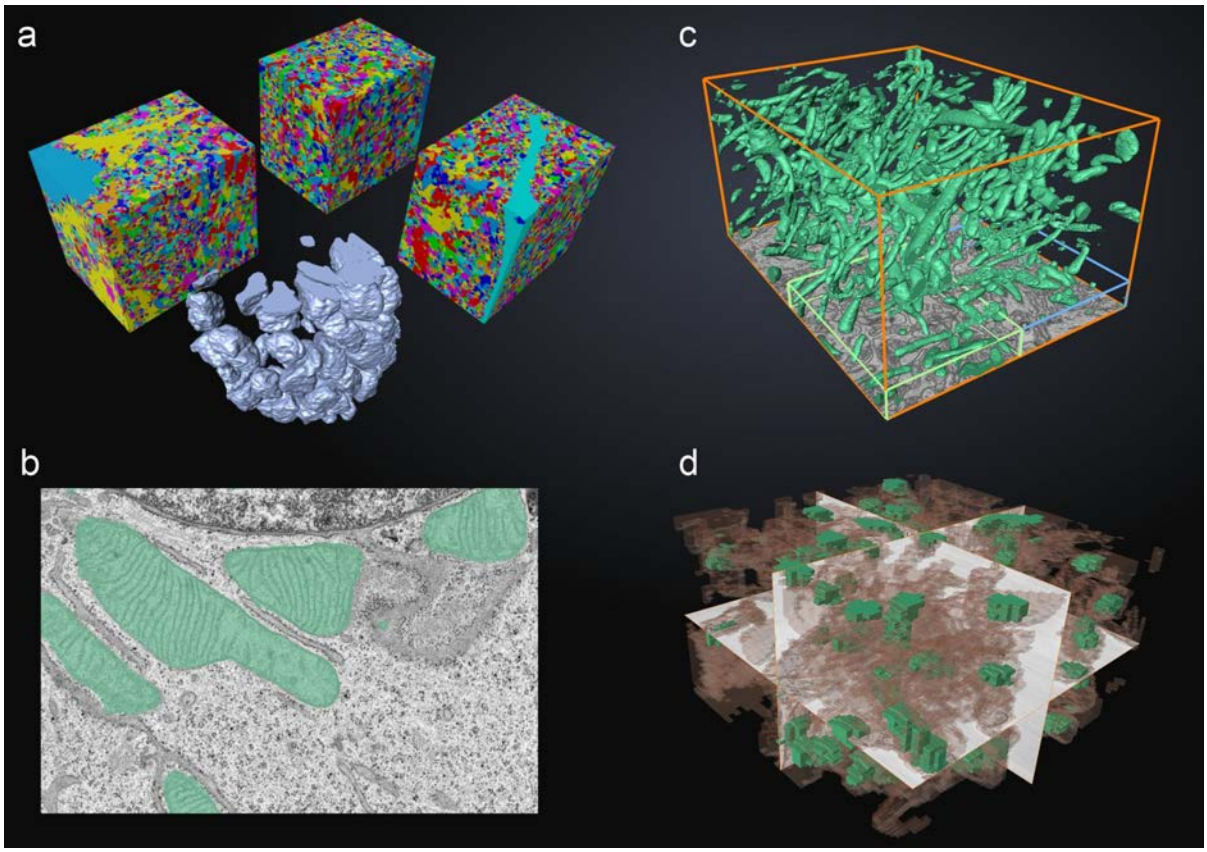

Fig. 1: Examples of image segmentation results. a) utilization of grid-graphcuts for segmentation of nuclei in large volume SBF-SEM; b) utilization of 2D CNN for detection of mitochondria in TEM; c) a model of mitochondria generated using 3D U-net from FIB-SEM; d) application of 2D patch-wise CNN for identification of nuclei in SBF-SEM

Type of presentation: Invited

LS7-IN-2525 Moving from two- to three- dimensional electron microscopy in the study of the synapse: a lesson from neurodevelopmental disorder models

Maiellano G.[1], Ghilardi A.[1], Francolini M.[1]

[1]Dept. of Medical Biotechnology and Translational Medicine, Università degli Studi di Milano – Via L. Vanvitelli, 32 – 20219 Milano, Italy

Email of the presenting author: maura.francolini@unimi.it

Electron microscopy is a widely used tool that has improved our knowledge of synapse ultrastructure and organization in the brain. Rearrangements of synapse structure following maturation and in synaptic plasticity have been broadly described and, in many cases, the defective architecture of the synapse has been associated to functional impairments. It is therefore important, when studying brain connectivity, to map these rearrangements with the highest accuracy possible to provide solid and reliable data about the structure of such a small complex. In the past two decades, traditional electron microscopy (EM) techniques has been implemented by the advent of three-dimensional (3D) EM techniques, among which Serial Block Face Scanning Electron Microscopy (SBFSEM); Focused Ion Beam-SEM (FIB-SEM) and serial sections Automated Tape collecting ultramicrotome-SEM (ssATUM-SEM). The volumetric data-sets obtained with such methodological approaches allow, in neurobiology research, the 3D reconstruction of neurons, neurites and their thinnest components within large volumes of tissues and to identify the shape and density of synapses, and finally to trace neuronal connections. Although the increasing interest and popularity raised by 3D EM, its diffusion is somehow limited by the amount of time required for the acquisition of the data-sets, the segmentation and reconstruction process and finally the analysis, particularly when considering brain specimens. In some cases, the necessity to move from 2D to 3D EM is questionable, since the results obtained by the first could lead to a reliable prediction of those obtained by 3D reconstruction. We recently demonstrated that several aspects of dendritic spines and of post synaptic densities (PSDs) of excitatory synapses (i.e. spine head and PSD size) can be carried out either by 2D and 3D EM, with comparable results [Colombo et al., 2021]. The strongest limitation of individual 2D projections is its inability to provide data regarding spines and PSDs shape and neuronal connections over long distances. Dendritic spines dysmorphism as well as alteration in the PSDs structure are hallmarks of impaired neuronal function mostly associated with the learning and memory defects that are typical of patients and models of neurodevelopmental disorders. In the past years we have extensively used both 2D and volume EM approaches to characterize these synaptic structural alterations and to link them to specific molecular defects and impaired function contributing to a certain extent to the comprehension of the relationship between neurodevelopmental disorders, learning and memory defects and neuronal connectivity and communication.

Acknowledgement: Acknowledgemnts: This research was funded by the Italian PRIN 2017, grant number 20172C9HLW to M.F

Type of presentation: Oral

LS7-O-2860 Volume electron microscopy and automatic segmentation of intracellular compartments in the urinary bladder umbrella cells

Hudoklin S.[1], Žerovnik Mekuž M.[2], Bohak C.[2, 3], Boneš E.[2], Marolt M.[2], Romih R.[1]

[1]Institute of Cell Biology, Faculty of Medicine, University of Ljubljana, Ljubljana, Slovenia, [2]Faculty of Computer and Information Science, University of Ljubljana, Ljubljana, Slovenia, [3]Visual Computing Center, King Abdullah University of Science and Technology, Thuwal, Saudi Arabia

Email of the presenting author: samo.hudoklin@mf.uni-lj.si

Introduction. Volumetric distribution of intracellular compartments and their temporo-spatial dynamics of interactions define the function and state of eukaryotic organisms. Urothelium is the epithelium of urinary bladder and represents a good model to study intracellular compartments involved in the formation and polarized transport of membranes. In superficial urothelial umbrella cells, ER-derived proteins (uroplakins) are processed in the Golgi apparatus (GA) to form 16-nm intramembrane particles that are organized into urothelial plaques in the post-Golgi compartments (fusiform vesicles, FVs) [1]. FVs transport urothelial plaques to the apical plasma membrane, where they provide the molecular basis for the blood-urine permeability barrier of the bladder [2]. Our aim was to define organization of these compartments crucially involved in urothelium functioning, using volume electron microscopy methods, and to develop new algorithms for their automatic segmentation.
Material, methods. Urinary bladders of C57B6 mice were cryo-fixed with a CPC device (Leica), freeze-substituted in AFS (Leica) with 2% OsO_4 in acetone, and embedded in Epon. Electron tomography (ET) was performed on 300 nm thick serial sections with a Tecnai 20 (FEI), running at 200 kV. Tomograms covered angles +65˚ to -65˚ in 1˚ steps. FIB-SEM analysis was done in Helios NanoLab 650 (FEI).The dimension of pixels was x=5.49 nm, y=5.49 nm, z=15.0 nm. For purpose of developing automatic segmentation pipelines and their evaluation, intracellular compartments were manually annotated with 3DSlicer in 5 FIB-SEM sub-volumes of size 256×256×256 voxels. Manual segmentation of tomograms was done with Imod.
Results and discussion. ET showed the differentiation-dependent organization of GA, mature and immature FVs, without membrane connections between them. FIB-SEM showed distribution of organelles in a larger volume of superficial urothelial cells. Manual segmentation proved to be time-consuming and represented a bottleneck. Therefore, we introduced a new publicly available annotated dataset (UroCell) and a novel segmentation pipeline based on deep convolutional neural networks (CNNs) to automatically segment GA, FVs, mitochondria and endo-lysosomal compartments [3].Our approach increased the robustness of segmentation through balanced sampling, improved contrast and transfer learning, and outperformed other compared segmentation methods in evaluation. In addition, to our knowledge, UroCell was the first public dataset not derived from brain tissue and unique in that it segments multiple intracellular compartments common to all eukaryotic cells.

[1] Wu, X.R., *et al*., Kidney Int, 2009. 75(11)
[2] Kreft, M.E., *et al*., Protoplasma, 2010. 246(1-4)
[3] Žerovnik Mekuč, M., *et al*., Comput Biol Med, 2020. 119

Acknowledgement: The authors would like to acknowledge and thank professor Margit Pavelka, who was for many decades an honoured advisor and a dear partner of our research team.

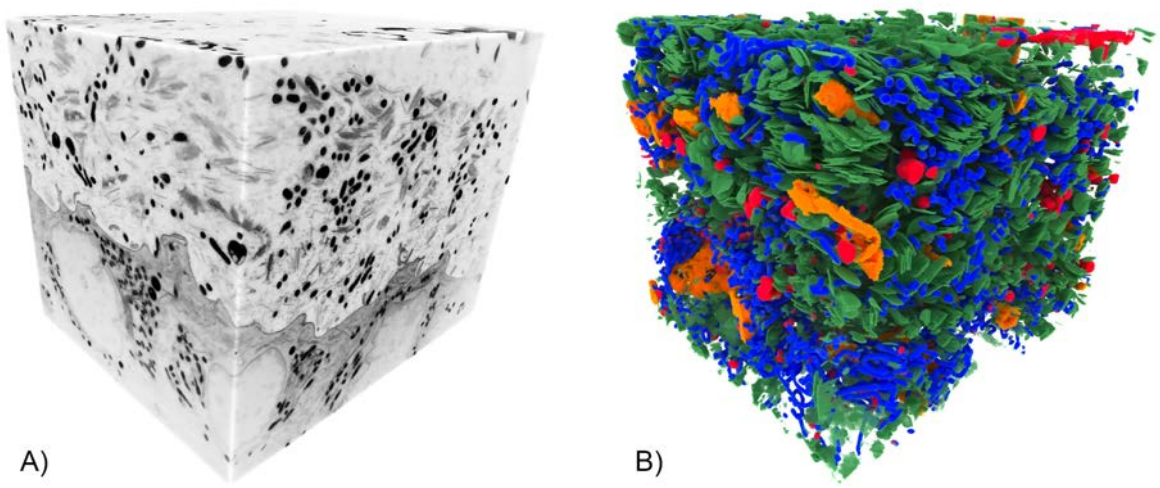

Fig. 1: Intracellular compartments in the urinary bladder umbrella cell obtained with FIB-SEM. A) Raw FIB-SEM volume. B) Visualization of Golgi apparatus (orange), fusiform vesicles (green), mitochondria (blue) and endo-lysosomal compartments (red) automatically segmented from the FIB-SEM volume with the proposed pipeline.

Type of presentation: Oral

LS7-O-2632 What does SARS-CoV-2 do to the lungs – what can 3D electron microscopy tell us

Týč J.[1], Palus M.[1,2], Hatmanstorfer A.[1,3,4], Coroianu A. M.[1,3,4], Hawlicek V.[1,3,4], Růžek D.[1,2], Vancová M.[1,3]

[1]Institute of Parasitology, Biology Centre, Czech Academy of Sciences, Budweis, Czech Republic, [2]Veterinary Research Institute, Brno, Czech Republic., [3]University of South Bohemia, Faculty of Science, Budweis, Czech Republic, [4]Johannes Keppler University, Faculty of Engineering & Natural Sciences, Linz, Austria

Email of the presenting author: jiri.tyc@paru.cas.cz

COVID19 pandemic lasts already over two years and has resulted in over 6 million deaths worldwide as of April 2022, according to WHO. Our knowledge about the disease is constantly increasing. Here we utilised a unique mouse model (Gasparo, 2021) that allows us to track the disease progression within the lungs over time in a controlled way. This cannot be done with human patients or in vitro cultures primarily used in other studies. We analysed three different mutations of the SARS-CoV-2 virus at 2 and 5 days post-infection. We use serial block-face scanning electron microscopy (SBEM) to visualise and decipher the COVID19 progress. Lungs are especially challenging tissue for 3D SEM because many empty spaces lead to charging and data processing (e.g. stitching) issues. Chemically fixed mouse lungs were processed with the "OTO" protocol and embedded in hard plus resin 812 (EMS). Images were acquired in 3D using Apreo SEM equipped with VolumeScope (Thermofisher Scientific) and variable pressure control. SBEM technology images regions of interest with dimensions up to several hundreds of µm, yielding large volumes for analysis. The final resolution at 7 nm (in X, Y axes) and 50-200nm (Z) facilitated the distinction of fine ultrastructural features within the cells, including viral particles and cells classification. We utilised the stereology approach using Microscopy Image Browser software to quantify such large volumes. This approach provided quantifiable estimations for statistical comparisons, saved time, and increased the throughput of the analysis (Ferguson 2017). Our study provides a deeper understanding of the cellular remodelling of the tissue after the SARS-CoV-2 infection. For example, we noted an increase in immune cells such as alveolar macrophages at the sites of infection, common congestions of blood vessels, necrosis of endothelial and pneumocyte cells and overall remodelling of the tissue due to fibroblasts activity.

Literature:

[1] De Gasparo R. et al. Bispecific IgG neutralises SARS-CoV-2 variants and prevents escape in mice. Nature. 2021

[2] Fergusson S. et al. Quantifying Golgi structure using EM: combining volume-SEM and stereology for higher throughput. Histochem Cell Biol. 2017

Acknowledgement: This work was supported by TACR (TE01000008) and Czech BioImaging (LM2018129).

Type of presentation: Oral

LS7-O-2827 Deep learning approaches for electron tomography under limited data acquisition conditions

Biagi G.[1], Ciuciu P.[2], Saghi Z.[1]

[1]Univ. Grenoble Alpes, CEA, LETI, Grenoble F-38000, France, [2]Univ. Paris Saclay, CEA-NeuroSpin, INRIA, Parietal, Gif-sur-Yvette, F-91191, France

Email of the presenting author: zineb.saghi@cea.fr

Electron tomography (ET) plays an important role in the three-dimensional (3D) characterization of a variety of nanostructures, including microelectronic devices, solid oxide fuel cells and organic/inorganic hybrid materials. To obtain faithful reconstructions, high-quality projection data must be acquired over the full 180° tilt range and at fine tilt increments of 1-2°. In practice, low-dose, limited-angle and sparse-view conditions are often employed due to the sample geometry and the electron beam damage. Compressed sensing (CS) approaches were recently introduced to overcome the limitations of classical reconstruction algorithms under limited data acquisition conditions [1]. While CS has demonstrated its superior performance for sparse-view acquisitions over the full tilt range, the reconstructions still suffer from artefacts related to low-dose noise and limited angle range [2-3].

In this work, we propose a data-driven deep learning (DL) approach to improve the quality of ET reconstructions under extreme acquisition conditions. We chose a deep neural network with U-Net architecture composed of four convolutional layers, which have 16, 32, 64, 128 filters respectively. A highly-sampled experimental dataset, consisting of 180 STEM-HAADF projections of a needle-shaped sample, was used to train the model (more information about the sample can be found in [1]).

Simultaneous iterative reconstruction technique (SIRT) was applied to generate the reference image (Figure 1 (left)), obtained with the complete dataset, and the degraded ones, obtained in artificially degraded conditions (Figure 1, middle column): (top) no added noise / -90°:10°:90°; (middle) added noise / -90°:3°:90°; (bottom) added noise / -60°:1°:60°. For each acquisition condition, 500 2D reconstructions through the needle were used for the training of the DL model, and 50 for the validation step. The obtained DL models were then employed to improve the reconstruction of a 2D slice, unseen during training. Figure 1 (right column) illustrate the images restored by the pre-trained DL models: in all three scenarios, the DL approach succeeds in retrieving fine details from highly corrupted SIRT images. We also report in Figure 2 the PSNR (peak signal-to-noise ratio) and SSIM (structural similarity index measure) values of the restored images, using the fully-sampled SIRT reconstruction (figure 1 (left)) as ground truth. A significant increase in both metrics is obtained with DL, suggesting that data-driven approaches are promising alternatives to model-based reconstruction methods, especially for low-dose and rapid experiments.

[1] M. Jacob et al., Ultramicroscopy 2021, 225:113289.
[2] Y. Jiang et al., Ultramicroscopy 2018,186:94.
[3] Z. Saghi et al., Ultramicroscopy 2016, 160:230.

Acknowledgement: This work, carried out on the Platform for Nanocharacterisation, was supported by the “Recherches Technologiques de Base” program of the French ANR.

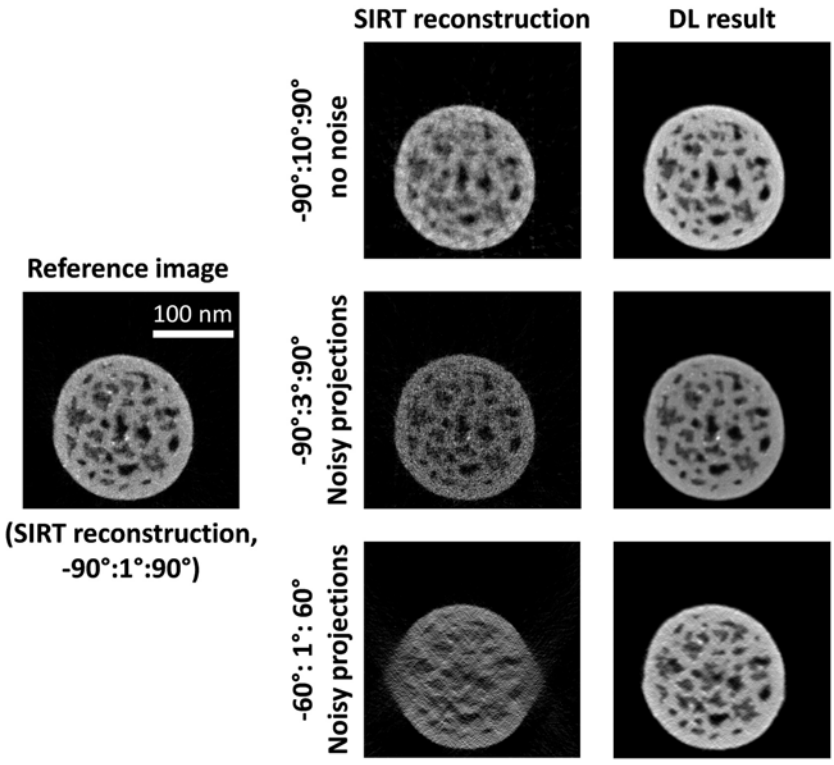

Fig. 1: DL-based image restoration under various conditions: 18 projections and full tilt range (top), 60 projections, full tilt range and added Poisson noise (middle), 120 projections, a limited tilt range (-60° to +60°) and added Poisson noise (bottom). The SIRT reconstruction obtained with the complete stack is shown in the left.

Tilt range	Number of projections	Poisson noise added	SIRT reconstruction PSNR / SSIM	DL output PSNR / SSIM
180°	18	no	22.5 / 0.782	25.8 / 0.807
180°	60	yes	19.8 / 0.675	26.1 / 0.806
120°	120	yes	19.6 / 0.633	25.8 / 0.823

Fig. 2: Summary of the different acquisition conditions, and the PSNR / SSIM values of the SIRT reconstructions and the restored images using the DL approach.

Type of presentation: Oral

LS7-O-2698 3D reconstruction of hydrated samples at the sub-micrometer scale using Liquid-Phase STEM at low voltage

Lebas L.[1], Bekel A.[1], Roiban L.[1], Masenelli-Varlot K.[1]

[1]Univ Lyon, INSA Lyon, UCBL, CNRS, MATEIS, UMR5510, 69621 Villeurbanne, France.

Email of the presenting author: louis-marie.lebas@insa-lyon.fr

Environmental electron microscopes have been developed for years to perform in situ studies in hydrated state, used in both material science and biology. They provide high resolution images, together with a fine control of the humidity state, thereby reducing the number of sample preparation steps. Moreover, dedicated sample holders allow the acquisition of complete tilt series and thus the reconstruction of the hydrated sample volume [1]. In this context, few challenges must still be overcome, among which the electron dose control especially for sensitive materials, the improvement of the spatial resolution down to a few nanometers [2] and the time resolution to monitor short duration events [3].
Our answer is called Liquid 3D STEM-in-ESEM. The technique is intended to operate scanning transmission electron microscopy tomography, in an environmental electron microscope. It relies on a home-made prototype of STEM tomography device specially built for liquid-phase studies, whose concept was proven on aqueous latex suspensions4. In this work, we automatise the acquisition of ± 75° tilt series in LPSTEM in less than 5 minutes. SE, BF and HAADF images are simultaneously recorded. Moreover, the electron dose can be precisely controlled.
In order to prove the capabilities of the technique, we will show tomograms acquired using a FEI QuattroS ESEM operated at 30 keV. Experiments are conducted on SBA latex and on silica aerogels. Both types of samples are deposited on a TEM grid coated with a holey carbon film. Images are recorded using our own software M-SIS using the Autoscript library based on Python. The tilt series are aligned with the TomoJ plugin of ImageJ, and data segmentation is performed with 3D Slicer.
We will show that Liquid 3D STEM-in-ESEM allows fast multi-modes acquisition of well-resolved tilt series with a precise dose control. Indeed, the 3D models produced exhibit a spatial resolution around 10 nm whereas the electron dose can be finely controlled and can be kept below the viability threshold of a biological cell. The limits will also be exposed in term of sample thickness, liquid film thickness control, spatial resolution, electron dose and total imaging time.
These advances pave the way for a more widespread use of Liquid 3D STEM-in-ESEM, for precise and easily reproducible multi-scale studies.

[1] Masenelli-Varlot, K. et al. (2014) ‘Wet-STEM Tomography: Principles, Potentialities and Limitations’, Microscopy and Microanalysis, 20(2).
[2] de Jonge, N. (2018) ‘Theory of the spatial resolution of (scanning) transmission electron microscopy in liquid water or ice layers’, Ultramicroscopy, 187.
[3] Jiao, X. et al. (2019) ‘Electron tomography on latex particles suspended in water using environmental scanning electron microscopy’, Micron, 117.

Acknowledgement: This work is part of the Liquid 3D STEM project (ANR). The authors thank the CLYM for providing access to the microscope.

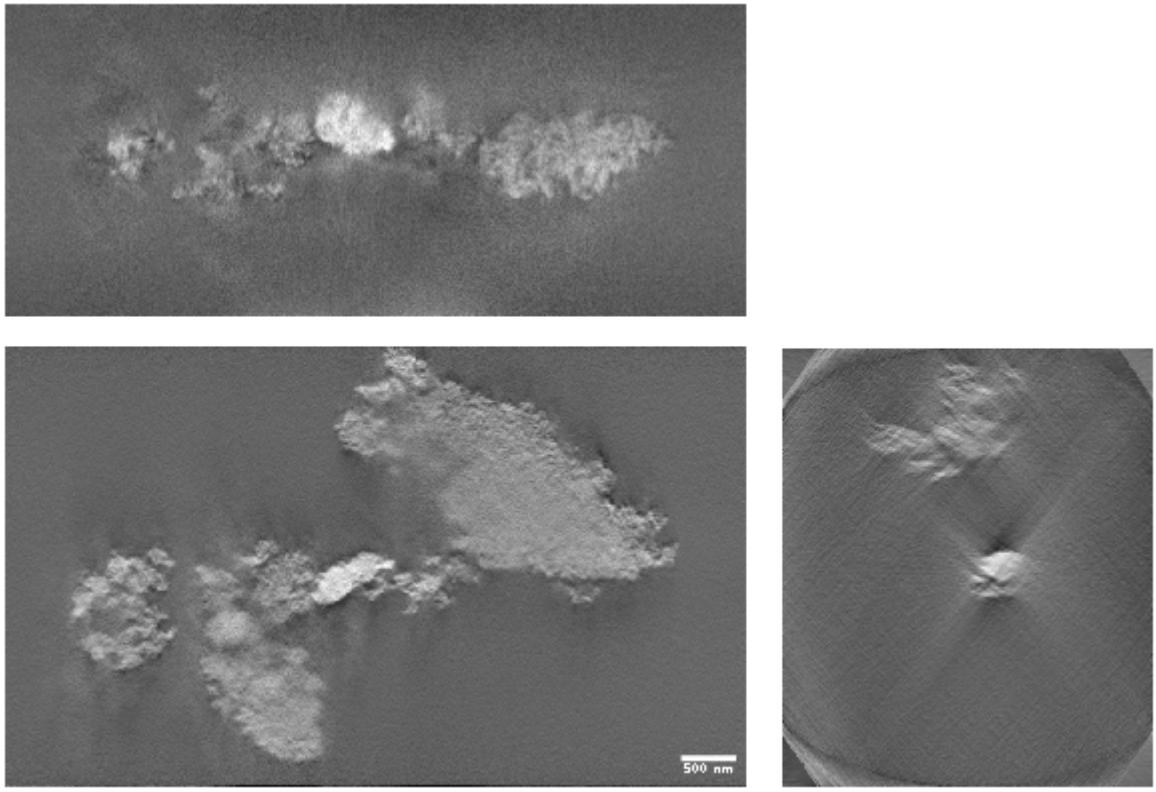

Fig. 1: From upper-left to bottom-right : YZ, XY and XZ ortho-slices of the reconstructed silica airgel volume from images recorded at different tilt angles in HAADF mode. Scale bar is 500 nm.

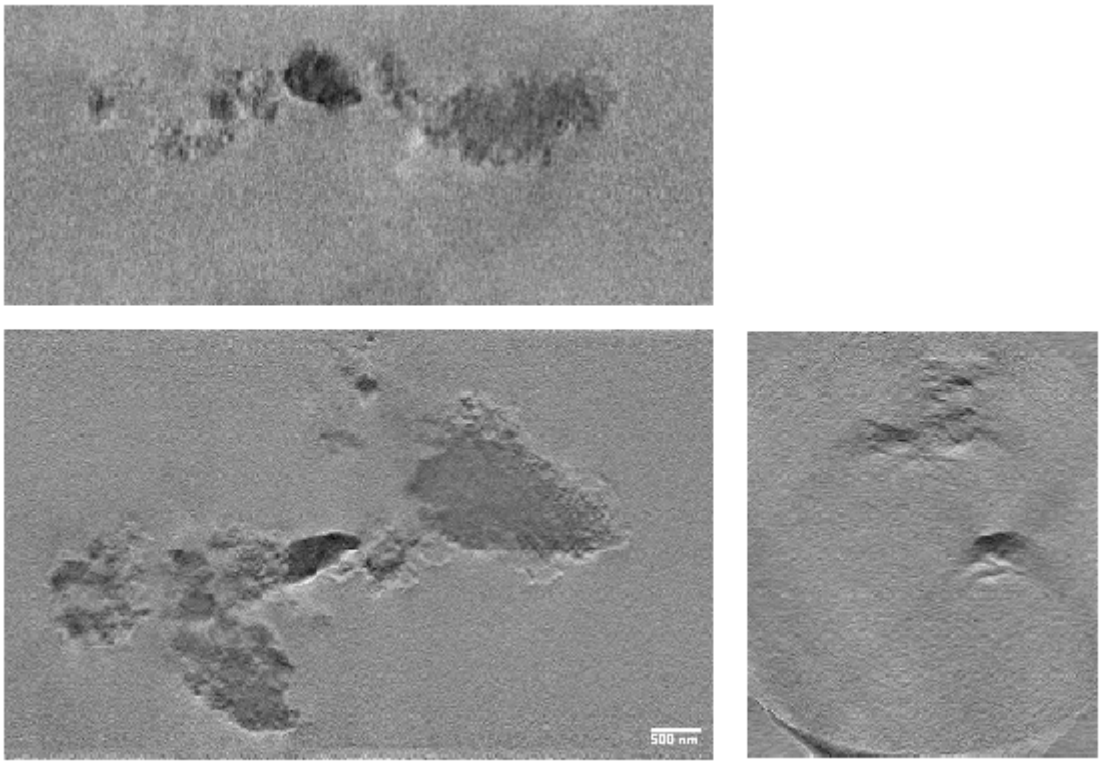

Fig. 2: From upper-left to bottom-right : YZ, XY and XZ ortho-slices of the reconstructed silica airgel volume from images recorded at different tilt angles in BF mode. Scale bar is 500 nm.

Type of presentation: Poster

LS7-P-2659 Modern SEM allows high-throughput 2D and 3D analyses on a single platform

Javurek J.[1], Koban M.[2], Machalkova M.[1], Searle S.[3], Hughes L.[4], Zachej S.[2]

[1]TESCAN ORSAY HOLDING, a.s., Brno, Czech Republic, [2]TESCAN Brno s.r.o., Brno, Czech Republic, [3]ConnectomX Ltd, Abingdon, United Kingdom, [4]Oxford Instruments NanoAnalysis, High Wycombe, United Kingdom

Email of the presenting author: jakub.javurek@tescan.com

Volume electron microscopy (volume EM) brings invaluable information about the three dimensional organisation of tissues and other biological materials, but traditional 2D imaging of samples remains an important function of any scanning electron microscope (SEM). Previously, volume EM techniques required dedicated SEM systems with limited usage for conventional imaging. For example, in-chamber microtomes for serial block face imaging (SBFI) have been associated with low reconfigurability when alternating between SBFI and other modes of operation.

Increasingly, life science electron microscopy research is concentrated into multi-user imaging centers, which provide a range of SEM applications, such as routine high-resolution imaging, chemical mapping with Energy Dispersive X-ray Spectroscopy (EDS), microscopy of cryogenically fixed specimens and various volume EM techniques. As demand for a wide range of methods rises, and with operational microscope and technician time at a premium, the ability to switch rapidly between different operating modes is an important factor for maintaining or increasing the productivity of microscopy facilities.

Our work demonstrates results from a range of applications including: (i) SBFI of resin embedded tissue to image ultrastructure over a large volume using the portable In-chamber Katana microtome, (ii) chemical volume mapping combining SBFI with EDS for multi-colour electron microscopy, (iii) analysis of a series of thin slices using the volume EM method of array tomography, and (iv) high resolution 2D surface imaging of biological samples. All of these techniques may be performed on a single system with little to no effort needed to switch between them. TESCAN CLARA SEM was proven as a flexible and universal SEM workstation providing a rapid turn-around between a diverse range of imaging techniques. Processing and visualisation of the resulting three-dimensional image and EDS datasets with TESCAN 3D Volume Analysis is also discussed.

Type of presentation: Poster

LS7-P-2582 Plasma FIB applications in Life Science: from large volumes to cryo-lamella preparation

Slamkova D.[1]

[1]Thermo Fisher Scientific, Vlastimila Pecha 1282/12, 627 00 Brno, Czech republic

Email of the presenting author: daniela.slamkova@thermofisher.com

The Thermo Scientific™ Helios Hydra™ Plasma FIB-SEM with the unique capability to deliver four ion species (Xe, Ar, O, or N) as the ion beam source is a novel technology in the life sciences space and can be a powerful method for multiscale analysis of biological samples.
The study of complex cellular processes often requires multiple levels of structural details and possibilitis for volume imaging or lamella preparation.
The ability to choose between different ions makes it possible to obtain curtain-free surfaces for a wide variety of resin-embedded biological samples as well as optimize and develop new strategies for cryo-lammela preparation and 3D volume-contextual imaging of bulk hydrated samples.
The Helios Hydra™ offers a new level of application flexibility for addressing scientific questions. It can bridge multiscale 3D to 3D correlation for precise targeting of the region of interest from uCT data to 3D Plasma FIB-SEM tomography (Figure 1). Its Spin Mill capability offers a unique alternative approach to 3D analysis, by planar milling of large-areas (up to 1 mm in diameter) (Figure 2), especially beneficial for accessing and investigating sparse regions of interest The multi-ion Plasma FIB is a powerful tool for analysis of cryo-immobilised, hydrated samples where different ions can be used for automated cryo-lamella preparation (Figure 3).

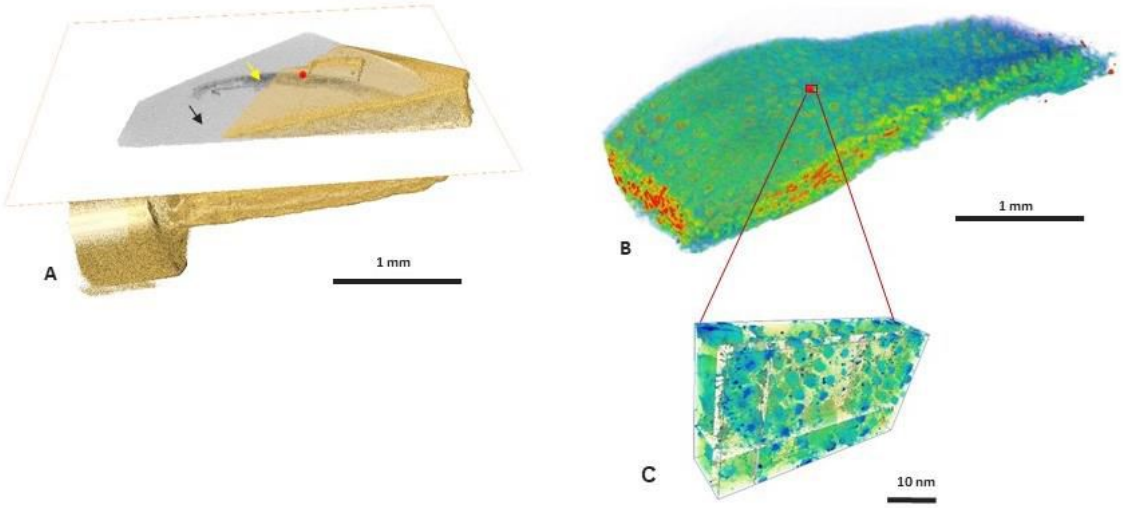

Fig. 1: A) 3D uCT data of a marine sponge sample, 1.2 mm x 1.2 mm x 3.3 mm. The sponge tissue (yellow arrow) is embedded in resin (black arrow). The red dot indicates targeted area of interest. B) uCT data used for 3D to 3D correlation. C) Auto Slice & View data of the targeted area acquired on Helios Hydra. Voxel size is 8 x 8 x 10 nm

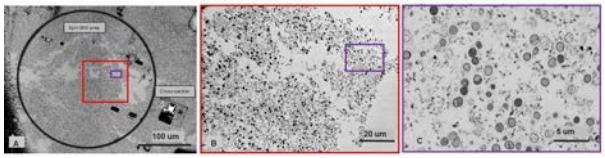

Fig. 2: Accessing large areas with Spin Mill. Staphylococcus infected by phage sample, embedded in Hard plus resin. A) Large area milling by Spin Mill is applied to the area defined by the circular marker (diameter 450 µm). B) First area of interest, field of view 100 µm, pixel size 16 nm. C) Second area of interest, field of view 20 µm, pixel size 4 nm.

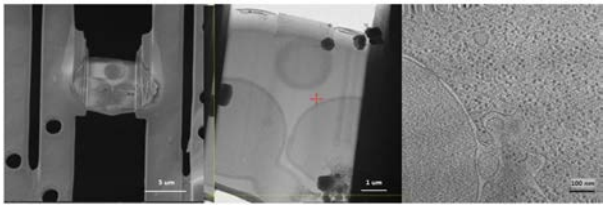

Fig. 3: Lamella of Yeast plunge frozen on a grid prepared with Hydra, using Xe as a primary ion species. AutoTEM Cryo 2.4 was used for automated lamellae preparation. Thickness of lamella 150 nm. Krios G4 was used for TEM evaluation, using 300 kV, Selectris energy filter and Falcon 4 direct electron detector.

Type of presentation: Poster

LS7-P-2625 Characterization of the Growth Plate-Bone Interphase Region Using Cryo-FIB SEM 3D Volume Imaging

Varsano N.[1], Kahil K.[1], Haimov H.[1], Rechav K.[2], Addadi L.[1], Weiner S.[1]

[1]Department of Chemical and Structural Biology, Weizmann Institute of Science, 76100 Rehovot, Israel, [2]Department of Chemical Research Support, Weizmann Institute of Science, 76100 Rehovot, Israel

Email of the presenting author: neta.varsano@weizmann.ac.il

Endochondral bone formation is a process in which first a cartilaginous matrix is formed, mineralized and then replaced by calcified bone tissue. This is the mechanism by which long bones are formed and then elongate. The process of elongation occurs near the edge of long bones at the interphase region between cartilaginous matrix called ‘growth plate’ and the mineralized and vascularized bone matrix (Figure 1A,B). The 3D structure of this interphase region is extremely complex, but its characterization is essential for better understanding the processes involved in bone elongation that include: mineralized cartilage formation, removal of the mineralized cartilage, bone formation and bone remodeling. Studying all these processes requires insights to extracellular matrices and contacts of cells with blood serum. Here we take advantage of the ability of cryo-FIB SEM to image all these very different components in 3D without the removal of the water, and in relatively large volumes of thousands of microns cubed (Figure 1C)[1]. We show that blood vessels are in intimate contact not only with cells, but in some locations also with mineralized tissues and confirm that there is an open pathway from the blood vessel extremities to the mineralizing cartilage. We document large multinucleated cells in contact with mineralized cartilage and possibly also with bone. In Several membrane bound mineralized particles were identified in these cells, as well as in blood serum, but not in the hypertrophic chondrocytes. Based on the sparsity of the mineralized particles, we conclude that mainly ions in solution are used for mineralizing cartilage and bone, but these are augmented by the supply of mineralized particles.

[1] Varsano, Neta, Keren Kahil, Heden Haimov, Katya Rechav, Lia Addadi, and Steve Weiner. "Characterization of the growth plate-bone interphase region using cryo-FIB SEM 3D volume imaging." Journal of structural biology 213, no. 4 (2021): 107781.

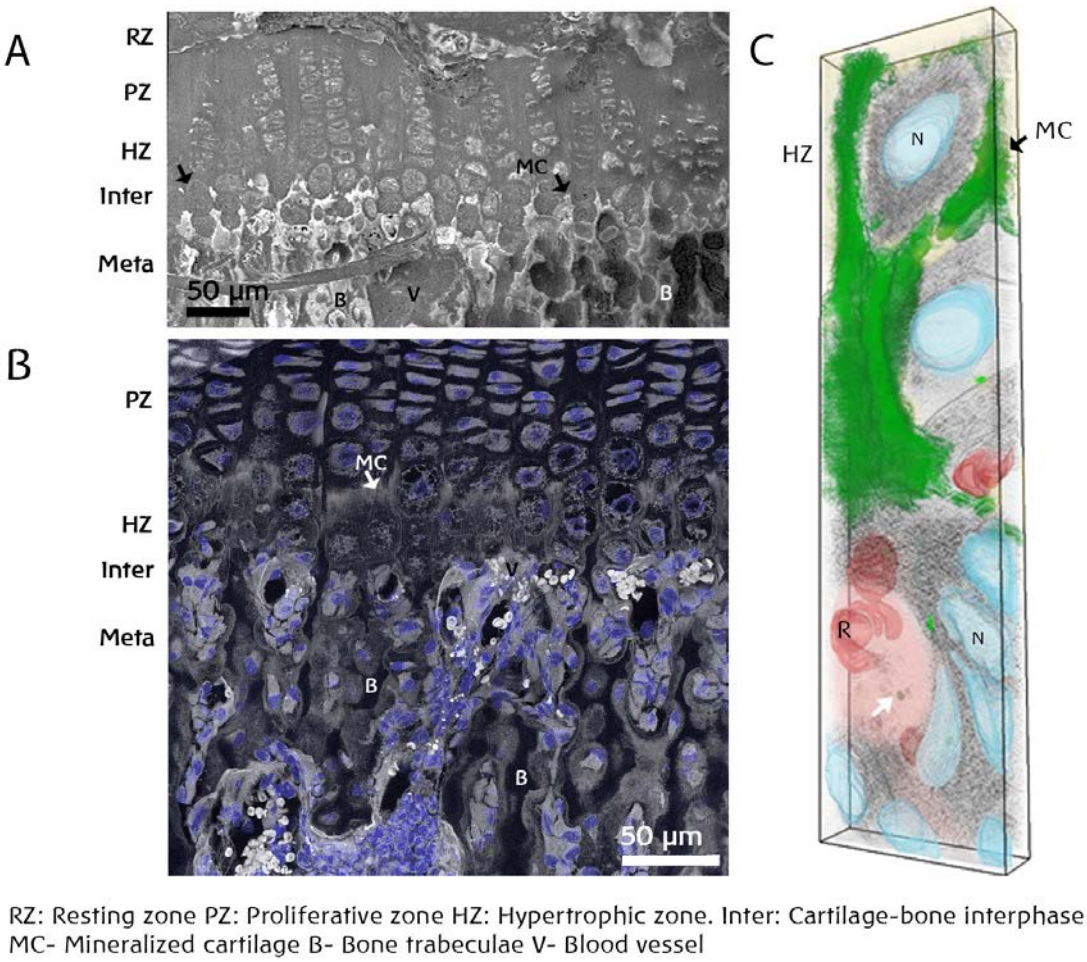

Fig. 1: (A, B) Cryo-SEM and Fluorescence image of a proximal growth plate (C) Volume of Cryo FIB-SEM taken from inter zone. Segmented components: mineralized areas (green), Un-mineralized cartilage (yellow), blood vessel (light red) and red blood cells (R, dark red), Nuclei (N, blue). White arrow points to mineralized particles.

MS1 Metals, alloys and intermetallics

Type of presentation: Invited

MS1-IN-2503 Quantitative STEM in the diffraction contrast regime

Dlouhý A.[1], Záležák T.[1], Bürger D.[2], Schneider M.[2], Agudo-Jácome L.[3]

[1]Institute of Physics of Materials, Academy of Sciences of the Czech Republic, Brno 616 62, Czech Republic, [2]Chair of Materials Science, Ruhr University, Bochum 44801, Germany, [3]Bundesanstalt für Materialforschung und Prüfung (BAM), Berlin 12205, Germany

Email of the presenting author: dlouhy@ipm.cz

We introduce a STEM BF&HAADF technique which provides an insight into 3D arrangements of objects in thin electron transparent foils. Contrary to high-tilt tomography methods, the technique enables a 3D perception and the reconstruction of foil surfaces using only TWO images acquired in a regime of diffraction contrast [1]. We show how the method can be extended by working in the scanning transmission electron microscope (STEM) mode of an analytical TEM equipped with a field emission gun (FEG TEM), bright field (BF) and high angular annular dark field (HAADF) detectors. Two STEM micrographs of a stereo pair combine into one anaglyph. When viewed with special colored glasses, the anaglyph provides a direct and realistic 3D impression of the microstructure, see Fig.1. A simple numerical treatment of the stereo-pair data yields a volumetric profile of the TEM foil including local foil thicknesses in any location within the investigated foil volume. Examples focused on microstructures formed during deformation in Medium Entropy Alloy and Advanced Ni-based Superalloy SX are presented [2,3].

[1] L. Agudo Jácome et al.: Ultramicroscopy 122 (2012) 48-59.
[2] F. Otto et al.: Acta Mater. 61 (2013) 5743-5755.
[3] D. Bürger et al.: Crystals 10 (2020) 134; doi:10.3390/cryst10020134.

Acknowledgement: Financial support from MŠMT (project CEITEC 2020 no. LQ1601) and DFG (projects A1 and A2 of the SFB/TR 103 center) is acknowledged.

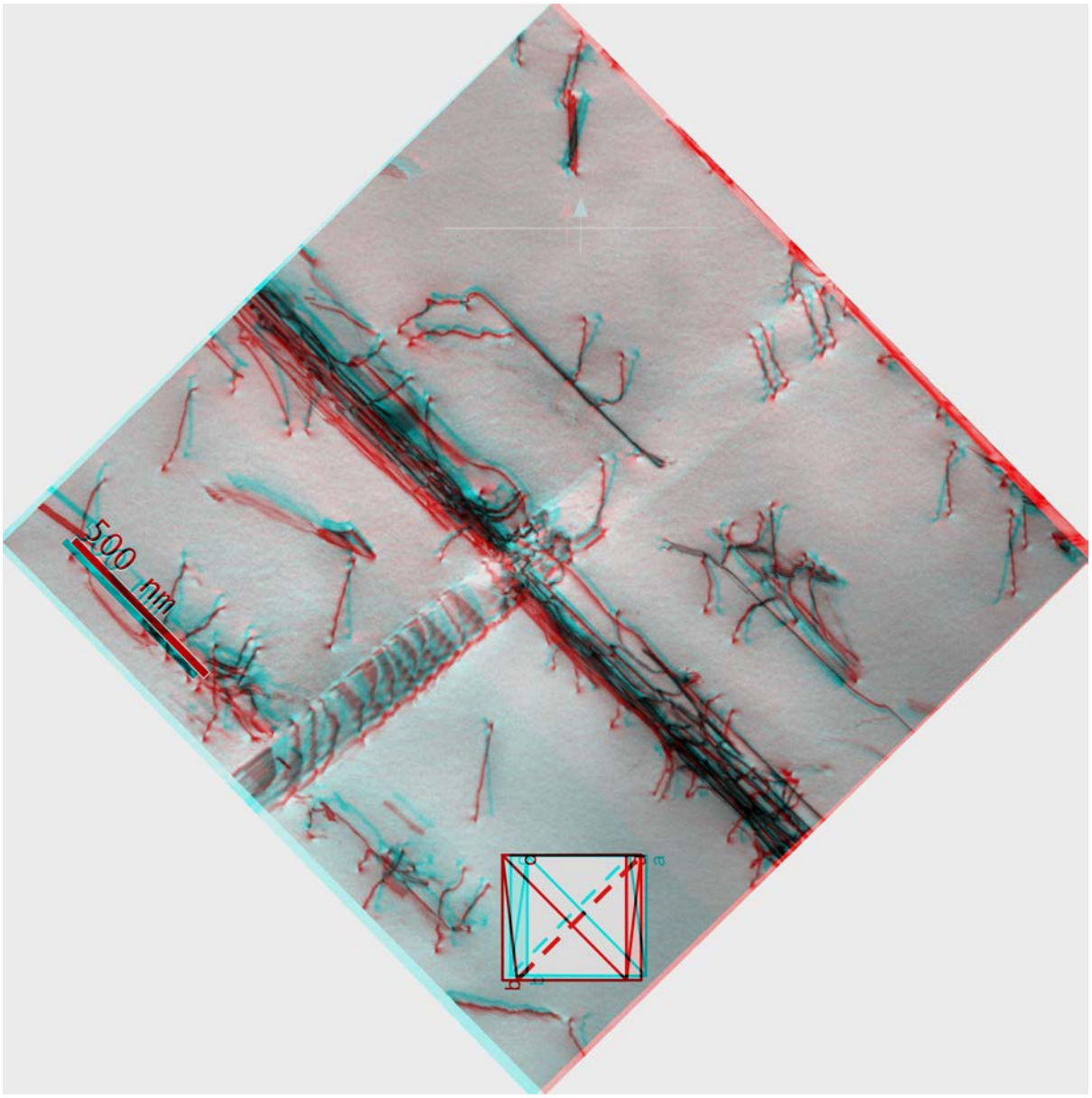

Fig. 1: An anaglyph providing a 3D perception of dislocation arrangement in CoCrNi alloy deformed at 77 K.

Type of presentation: Invited

MS1-IN-2915 Titanium-aluminide-silicide based alloys

Knaislová A.[1], Novák P.[2]

[1]Faculty of Mechanical Engineering, J. E. Purkyne University in Usti nad Labem, Pasteurova 3334/7, 400 01 Usti nad Labem, Czech Republic, [2]Department of Metals and Corrosion Engineering, University of Chemistry and Technology, Prague. Technická 5, 166 28 Prague. Czech Republic

Email of the presenting author: anna.knaislova@ujep.cz

Titanium alloys with other light elements (aluminum, silicon) are very promising materials for applications at higher temperatures. TiAl intermetallic alloys have already started to be used as turbochargers in passenger cars, aircraft engines, and their components. Titanium aluminides excel in low density and good resistance to oxidation at higher temperatures. However, TiAl alloys have low ductility at room temperature and fracture toughness.
The addition of silicon to TiAl alloys improves oxidation and corrosion resistance at elevated temperatures, as well as creep resistance. Silicon dissolves very little in TiAl alloys and, therefore, forms hard and brittle titanium silicides in the structure, mainly Ti5Si3 silicides, which have a strengthening effect. A major problem with Ti-Al-Si alloys is the brittleness of titanium silicides, so they must be as fine as possible.
The synthesis of TiAl intermetallic compounds is one of the important directions in the development of new materials with high thermal stability. The preparation of Ti-Al-Si alloy is very difficult using melting metallurgy. The melting and casting of Ti-Al-Si alloys produce hard and brittle titanium silicides Ti5Si3, and these coarse and randomly oriented sharp-edge silicide particles are undesirable in terms of the deterioration of some mechanical properties (especially fracture toughness). In this work, Ti-Al-Si alloys are prepared by powder metallurgy, the advantages of powder metallurgy include the acquisition of a finer and more homogeneous microstructure, which could cause an improvement in mechanical properties. Ti-Al-Si alloys prepared by a combination of reactive sintering and spark plasma sintering have in fact a significantly finer-grained and more homogeneous structure formed mainly by sharp-edged and unconnected particles of titanium silicides. Despite a slow cooling rate from the compaction temperature, cracks were found in the structure, especially in the titanium silicides.
For this reason, mechanical alloying followed by spark plasma sintering with a lower cooling rate is used. Mechanical alloying in combination with SPS led to a very fine microstructure of the Ti-Al-Si alloys. The distribution of Ti5Si3 is much more homogeneous because the brittle powder is crushed into very fine particles during the first step of mechanical alloying. The microstructure of Ti-Al-Si alloys prepared by mechanical alloying followed by spark plasma sintering is very homogeneous and fine-grained, which positively affects the mechanical properties, including fracture toughness [1].

[1] A. Knaislová, P. Novák, M. Cabibbo, L. Jaworska, D. Vojtěch, Development of TiAl–Si Alloys—A Review, 14 (2021) 1030.

Type of presentation: Oral

MS1-O-2601 Co-segregation of zinc, carbon and boron in a Σ5 iron grain boundary resolved by correlating atomic resolution STEM, APT and first-principles calculations

Ahmadian A.[1], Zhou X.[1], Scheiber D.[2], Gault B.[1,3], Romaner L.[2,4], Dehm G.[1], Liebscher C. H.[1]

[1]Structure and Nano-/ Micromechanics of Materials, Max-Planck-Institut für Eisenforschung GmbH, 40237 Düsseldorf, Germany , [2]Materials Center Leoben GmbH, Leoben, Austria, [3]Department of Materials, Royal School of Mines, Imperial College London, London, UK , [4]Montanuniversität Leoben, Leoben, Austria

Email of the presenting author: a.ahmadian@mpie.de

In polycrystalline materials, grain boundariy (GB) segregation has strong implications on mechanical properties by either embrittlement or increasing GB cohesion1 . Of great technological relevance is the liquid metal embrittlement (LME) of iron (Fe) by zinc (Zn) 2. The loss of ductility occurs at temperatures, where Zn is in its liquid form through an ingress along GBs. However, the role of Zn segregation ahead of the liquid front and its interaction with typical impurity elements such as carbon (C) and boron (B) are rarely explored.
Here, we investigated a bicrystal with a ∑5 [001] tilt GBs in ferritic Fe-2wt%Al. To introduce Zn into the system, we immersed the bicrystal into a Zn bath with a subsequent annealing step under high vacuum. The chemical composition was studied using aberration-corrected scanning transmission electron microscopy (STEM) in combination with energy dispersive X-ray spectroscopy (EDS) to probe the local variation of Zn concentration at the GB. Atom probe tomography (APT) experiments were conducted to reveal the interplay between Zn, B, C and Al.
Figure 1 shows STEM-EDS maps at viewed along the [001]- direction. A clear enrichment of Zn was observed (Figure 1), where the boundary is not homogeneously covered. Instead Zn-rich regions are forming. This was also substantiated by APT, where it was found that the Zn is arranged in regularly spaced linear segregation features along the [001] tilt axis (Figure 2). Furthermore, our APT investigations show the co-segregation of B and C, which are lower in concentration compared to the regions without Zn. Structural investigation of the boundary was performed by collecting the high-angle annular dark-field (HAADF) signal. It was found that the GB consists mainly of kite-type structural units (Figure 3) similar to predictions by first-principles calculations by Scheiber et al.3. However, the GB also contains a high number of defects leading to different local reconstructions, which locally change the boundary inclination angle. Our experimental findings were complemented by ab-initio density functional theory (DFT) calculations to determine the interplay of impurity segregation on the cohesive strength of the GB.

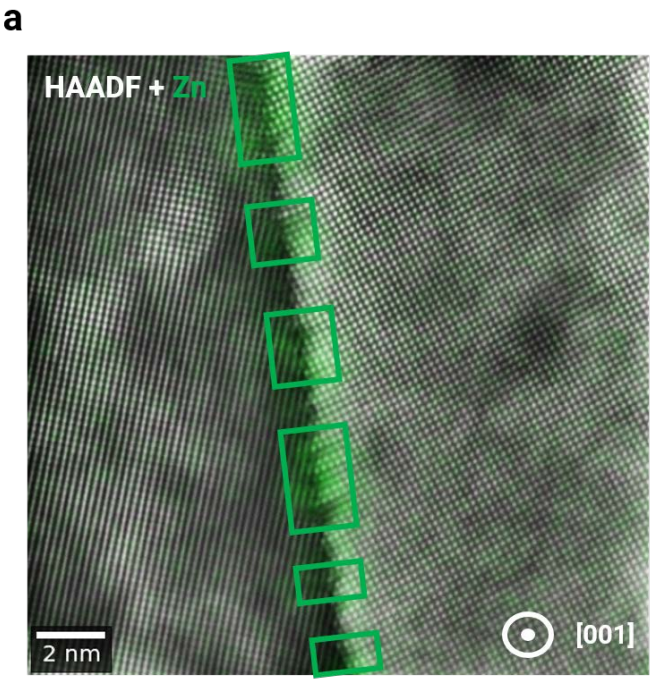

Fig. 1: STEM-EDS measurement showing the HAADF-STEM image overlaid with the elemental Zn map of the GB. Viewing direction is along the tilt axis. Zn segregated to GB forming clusters

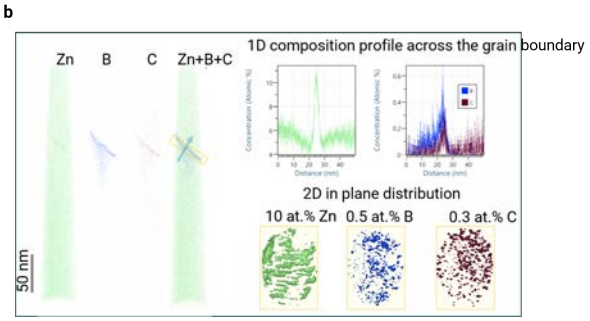

Fig. 2: Atom distribution of Zn, B and C to the boundary. The corresponding concentration profile extracted across the GB shows a peak concentration of Zn, B and C at the GB. The 2D in-plane distribution of this elements show a columnar arrangement of Zn, while B and C homogenously cover the boundary plane.

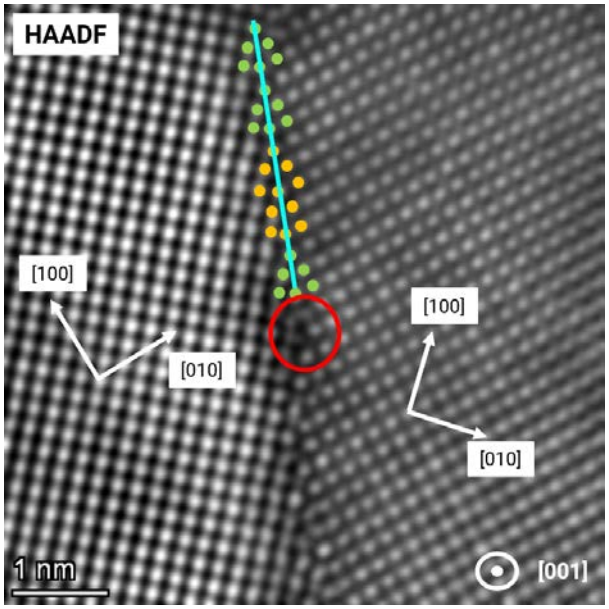

Fig. 3: HAADF-STEM image of a near-symmetric Σ5 [001] tilt GB with a misorientation of about 40° around the common [001] tilt axis. The GB structure has kite-type structural units, whereby the kites are not always connected to each other but contain on extra atom in between. Defects (marked in red) change the orientation of the boundary plane.

Type of presentation: Oral

MS1-O-2796 An in-depth investigation of liquid metal embrittlement sensitive grain boundaries in TBF steels

Akbari E.[1], Kürnsteiner P.[1], Hesser G.[1], Oberhumer P.[1], Groiss H.[1], Arndt M.[2], Gruber M.[2], Steineder K.[2], Sierlinger R.[2]

[1]Christian Doppler Laboratory for Nanoscale Phase Transformations, Center for Surface and Nanoanalytics, Johannes Kepler University Linz, Austria, [2]voestalpine Stahl GmbH, Linz, Austria

Email of the presenting author: elahe.akbari@jku.at

Automotive advanced high-strength steels, such as third-generation transformation induced plasticity assisted bainitic ferritic (TBF) steels with a Zn coating, are prone to a detrimental failure known as liquid metal embrittlement (LME) [1]. LME occurs for instance during resistance spot welding, while the steel is in contact with liquid Zn under external and thermal stress. Thus, the liquid Zn penetration toward the underlying steel can generate macroscopic cracks that cause premature brittle fracture [2]. In this respect, enormous research has been conducted so far to cast light on the effect of various alloying elements and the mechanism controlling LME in the Fe-Zn couple [3].

This study is aimed at systematically investigate the effect of B on LME behavior of electro-galvanized TBF steels. Hot tensile test results indicated that the presence of B even at extremely minute concentration reduces LME sensitivity. Therefore, electron backscatter diffraction (EBSD) was conducted on resistance spot welded specimens to reconstruct the prior austenitic matrix. Accordingly, the prior austenite grain (PAG) reconstruction enables us to study the high temperature microstructure at the time of LME crack generation. The results are shown in Fig. 1, verifying an intergranular penetration of Zn along high-angle prior austenite grain boundaries (PAGBs). In addition to this microstructural evaluation, transmission electron microscopy in conjunction with energy dispersive X-ray spectroscopy (EDS) was carried out to analyze grain boundary chemistry in B-free and B-added base steels, specifically to study the influence of B on the alloy element segregation at PAGBs. The identification of a PAGB with a misorientation angle of 52.5˚ for the TEM investigation and selected area diffraction patterns of the two neighboring grains alongside the selected PAGB is demonstrated in Fig.2. These findings suggest the effect of B on grain boundary energy in terms of grain boundary misorientation angle and plane orientation.

[1] N. Fonstein, Advanced High Strength Sheet Steels, Springer, (2015).

[2] J. H. Kang, D. Kim, D. H. Kim, and S. J. Kim, Fe-Zn reaction and its influence on microcracks during hot tensile deformation of galvanized 22MnB5 steel Surf. Coatings Technol, 357, 1069–1075 (2019).

[3] H. E. Emre and R. Kaçar, Resistance spot weldability of galvanize coated and uncoated TRIP steels, Metals, 6 (12), 299 (2016).

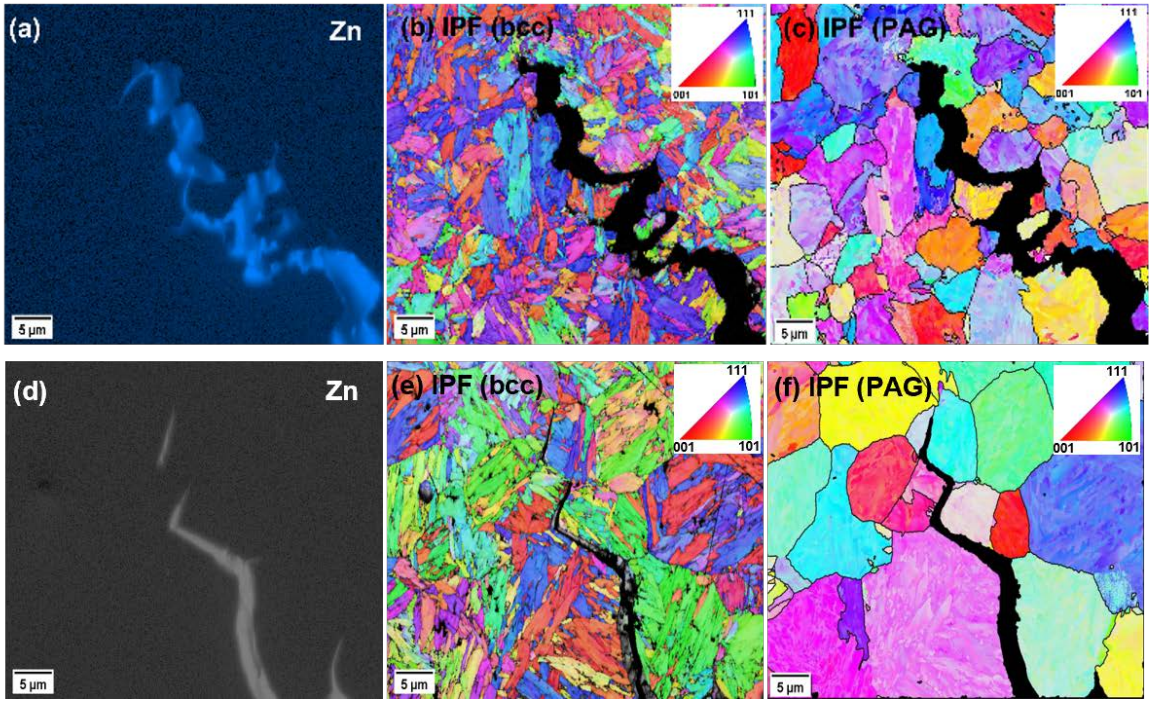

Fig. 1: EDS map of Zn at the cracking area in (a) B-free weld spot (d) B-added weld spot. EBSD IPF map around the cracking area in (b) B-free weld spot (e) B-added weld spot. EBSD IPF map of the reconstructed prior austenitic matrix of (c) B-free, (f) B-added

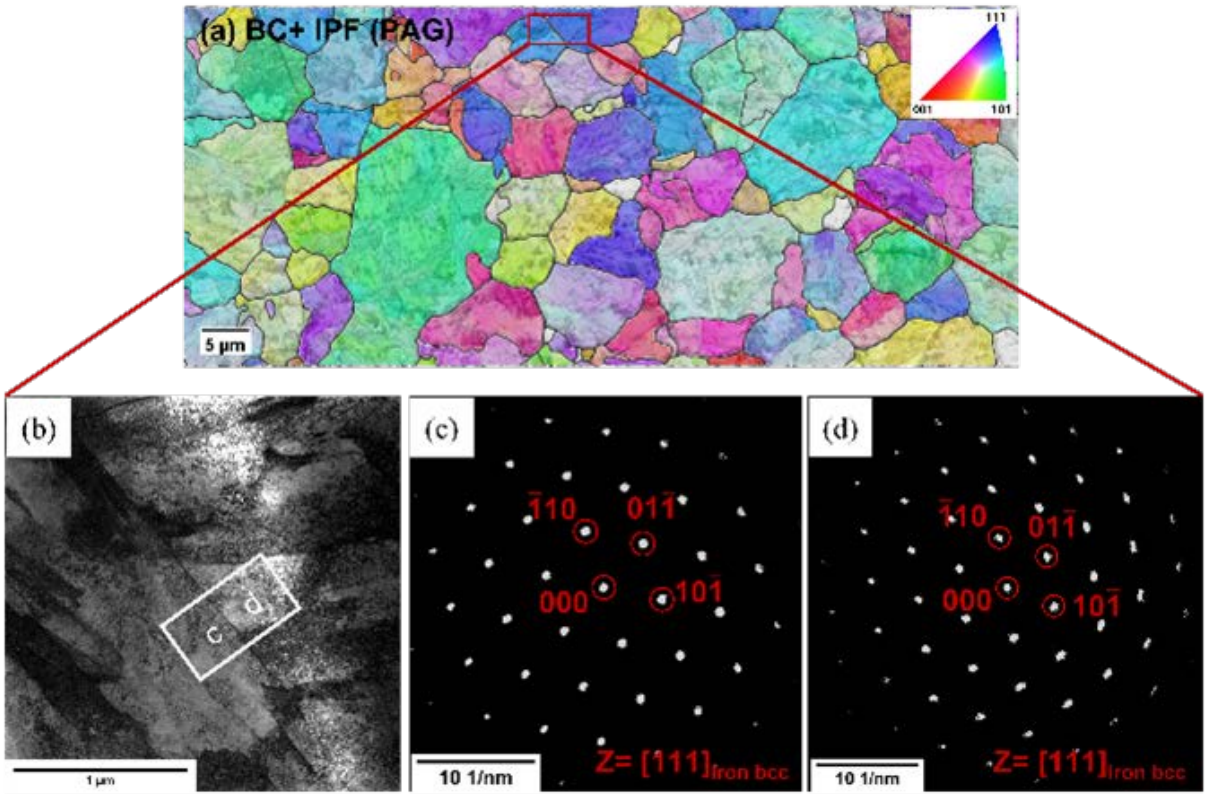

Fig. 2: Grain boundary investigation in B-added TBF steel (a) EBSD IPF map of reconstructed PAG overlaid with EBSD band contrast image of the bainitic-martensitic as-received sample, (b) TEM image of the PAGB marked in (a), (c) and (d) SAD patterns of the neighboring grains at the sides of the PAGB marked in (b)

Type of presentation: Oral

MS1-O-2857 Correlative electron microscopy and magnetism of CoCrFeNiZr high-entropy allos

Jelen A.[1], Vrtnik S.[1], Koželj P.[1], Guo S.[2], Kim H. J.[3], Guim H.[3], Meden A.[4], Dolinšek J.[1]

[1]Jožef Stefan Institute, Ljubljana, Slovenia, [2]Chalmers University of Technology, Göteborg, Sweden, [3]Korea Basic Science Institute, Daejeon, Republic of Korea, [4]University of Ljubljana, Faculty of Chemistry and Chemical Technology, Slovenia

Email of the presenting author: andreja.jelen@ijs.si

High-entropy alloys (HEAs) represent novel metals-based materials with complicated microstructure, where at least five different chemical elements, all in majority concentrations, are mixed on a simple crystal lattice at the atomic level (Fig. 1 d). Likewise, the materials are usually comprised of more than one phase on a different microscopic levels, raging from 10 nm – 1 mm. The complex atomic and phase structure, together with the choice of the elements and their concentrations, determine the physical properties (magnetic, electric and thermal) of the HEAs, which are usually not the compositional average of physical properties of the constituent phases [1-3].

For complete microstructural investigation of HEAs, the following electron microscopes with corresponding techniques were used: Scanning Electron Microscope (SE and BSE imaging, EDS, EBSD), Transmission Electron Microscope (HAADF, EDS) and Focused Ion Beam (channeling cont.).

In order to interpret the physical properties as accurately as possible, the microstructure has to be known at different orders of magnitude (multi-spatial-scale), using different types of electron microscopes (correlative microscopy) that enable such magnifications.

We have investigated the magnetism of CoCrFeNiZrx (x = 0.4–0.5) eutectic high-entropy alloys (HEAs) in relation to their microstructure by XRD, SEM, magnetization, specific heat and electrical resistivity measurements. Multylayered correlative electron microscopy of CoCrFeNiZr0.45 eutectic HEA is presented in Figure 1 with four panels, where each panel gives us a closer look of the same sample from 1 mm range to < nm range [1].

Two structural phases develop in the CoCrFeNiZrx HEAs, a Zr-free fcc solid solution and a Zr-containing C15 Laves-phase intermetallic compound, where in both phases magnetic transition elements Co, Cr, Fe and Ni substitute each other in a random-like manner.

Two magnetic structures coexist in the CoCrFeNiZrx HEAs. The first is a disordered ferromagnetic (FM) phase that develops in the interior of large dendrites of the fcc solid solution and in some larger lamellas of this phase. The second phase is superparamagnetic-like and originates from the remaining spins of the fcc solid solution fraction, located at the surfaces and in the interfaces, and from all spins of the C15 Laves-phase fraction. The relative magnitude of the disordered FM-state magnetization with respect to the superparamagnetic magnetization in the samples with different Zr concentration is predominantly determined by the volume fraction of the fcc bulky dendrites.

Acknowledgement: The author thanks Korea Basic Science Institute, Daejeon, Korea, for a Postdoc exchange.

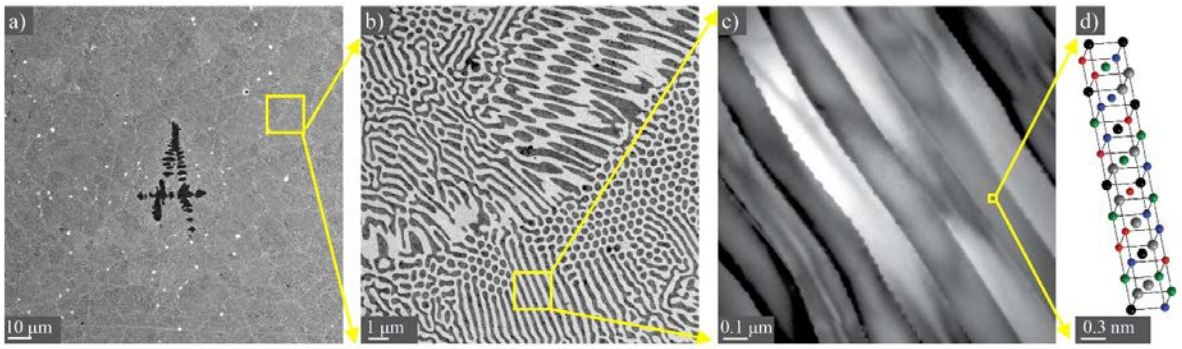

Fig. 1: (a) SEM BSE image of CoCrFeNiZr0.45 eutectic HEA at low magnification; (b) higher magnification SEM BSE image of the same sample shows finer details of the “grey” area in the panel (a); (c) TEM image shows lamellar structure; (d) schematic representation of HEA on an atomic scale.

Type of presentation: Oral

MS1-O-2765 Rejuvenation/relaxation in bulk metallic glasses: high-resolution transmission electron microscopy study

Ivanov Y. P.[1,2], Divitini G.[1], Greer A. L.[2]

[1]Electron Spectroscopy and Nanoscopy, Istituto Italiano di Tecnologia, Via Morego 30, 16163 Genova, Italy, [2]University of Cambridge, Department of Materials Science & Metallurgy, Cambridge CB3 0FS, UK

Email of the presenting author: iurii.ivanov@iit.it

Bulk metallic glasses (BMGs) lack long-range atomic order. It is increasingly appreciated that their disordered nature offers, even for a single composition, access to a wide range of structures and properties. This range can be characterized by energy – relaxation (ageing) taking the glass to lower-energy configurations, and rejuvenation to higher-energy configurations. A common method for BMGs relaxation (aging) is low temperature annealing. There is a growing interest in rejuvenation as a route to improving the plasticity of BMGs, as their lack of ductility is the main impediment to their wider exploitation in engineering applications. Rejuvenation of BMGs can be induced in several ways, for example by fast re-quenching, by elastostatic loading, by heavy plastic deformation, by cryothermal cycling between room temperature and liquid-nitrogen temperature (of particular interest as an easily applied, shape-preserving method), and - the most recent method - by constrained loading in compression.
Characterization of the structural changes in rejuvenation of a BMG remains challenging. Here we present a method by which BMG rejuvenation can be characterized by a combination of transmission electron microscopy (TEM) methods: electron diffraction (ED) and aberration-corrected high-resolution TEM (HRTEM). This study focuses on Zr-based BMGs and multilayer films relaxed/rejuvenated through low temperature annealing [1]/cryothermal cycling [2] or through plastic deformation [3]. ED provides information on the average volume per atom and on characteristic features of the short-range and medium-range order (SRO and MRO) at the microscale level. In complement to this, HRTEM allows extraction of such information locally (at nanoscale) with atomic resolution.
[1] Ketov, S. V.; Ivanov, Y. P. et al. Materials Today Advances 2019, 1, 100004.
[2] Ketov, S. V. et al. NPG Asia Materials 2018, 10, 137–145.
[3] Pan, J.; Ivanov, Y. P. et al. Nature 2020, 578 (7796), 559–562.

Acknowledgement: This work was supported by ERC Advanced Grant “ExtendGlass” (Grant ERC-2015-ADG-695487).

Type of presentation: Poster

MS1-P-2923 Reconstructing parent microstructures from EBSD based orientation measurements

de Kloe R.[1], Wright S. I.[2]

[1]EDAX, Tilburg, The Netherlands, 2EDAX LLC, Pleasanton, USA

Email of the presenting author: rene.de.kloe@ametek.com

When a material undergoes a transformation from one crystallographic phase to another, a grain in the original microstructure may transform into several different crystallographic variants. The transformed microstructure is generally quite different but often traces of the original microstructure are recognizable. It is difficult, if not impossible, to capture the microstructure of the high-temperature phase. It would be helpful to be able to characterize the microstructure (i.e., grain size, texture) of the high-temperature phase to optimize the full processing path of the material.
We have implemented the method by Ranger *et al.* [1] in conjunction with EBSD to allow reconstruction of the original high-temperature microstructures in a range of materials. The efficacy of the method was verified in the following metals:
• The observed high temperature grain structure in face-centred cubic β-cobalt obtained by an in-situ phase transformation experiment was compared against the reconstruction of the final low temperature hexagonal close-packed α-cobalt microstructure using the OR:
{1 1 1}β∥{0 0 0 1}α and <1 1-2>β∥<1-1 0 0>α.
• The austenite parent microstructure in steel from EBSD measurements on ferrite was reconstructed using the Nishiyama-Wasserman OR: {1 1 1}γ∥{1 1 0}α and <1 1 -2>γ∥<1 1 0>α. The fidelity of the reconstruction algorithm was confirmed by comparison to other algorithms.
• The original high temperature body-centred cubic b-Ti microstructure was obtained from EBSD measurements on a hexagonal close-packed α-Ti microstructure in additively manufactured Ti6Al4V containing a small fraction (2%) of retained β-Ti. The reconstruction was performed assuming an OR of {1 1 0}β∥{0 0 0 1}α and <1-1 1>β∥<1 1 -2 0>α. The retained original β-Ti phase in the microstructure provided a marker confirming the results of the reconstruction.
The results of the algorithm in reconstructing the pre-transformation parent microstructures in all three cases are shown in Figures 1, 2 and 3. Because local misorientations between adjacent pixels instead of entire grains are used to identify the phase relationships, also orientation gradients like those displayed within several of the grains in Figure 3(b) may be present in the reconstruction and can provide an indication of residual strain in the material prior to the phase transformation.
The parent grain reconstruction algorithm performs well and allows quantitative aspects of the pre-transformation microstructure such as grain size, crystallographic texture, and even residual strain to be reliably characterized.

References:

[1] C. Ranger, V. Tari, S. Farjami, M.J. Merwin, L. Germain, A. Rollett, Metall. Mater. Trans. A 49 (2018) 4521-4535

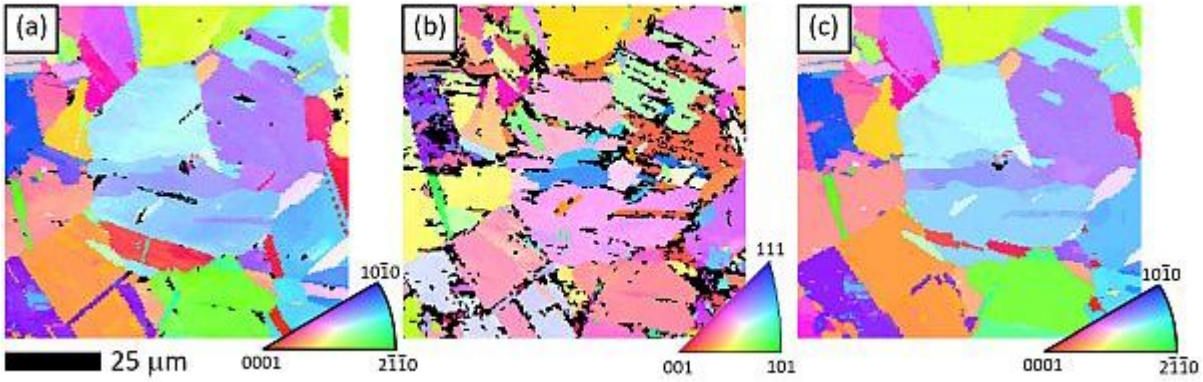

Fig. 1: Orientation maps from cobalt microstructures: (a) as-measured pre-transformation α-Co, (b) as-measured post transformation α-Co and (c) the as-reconstructed β-Co

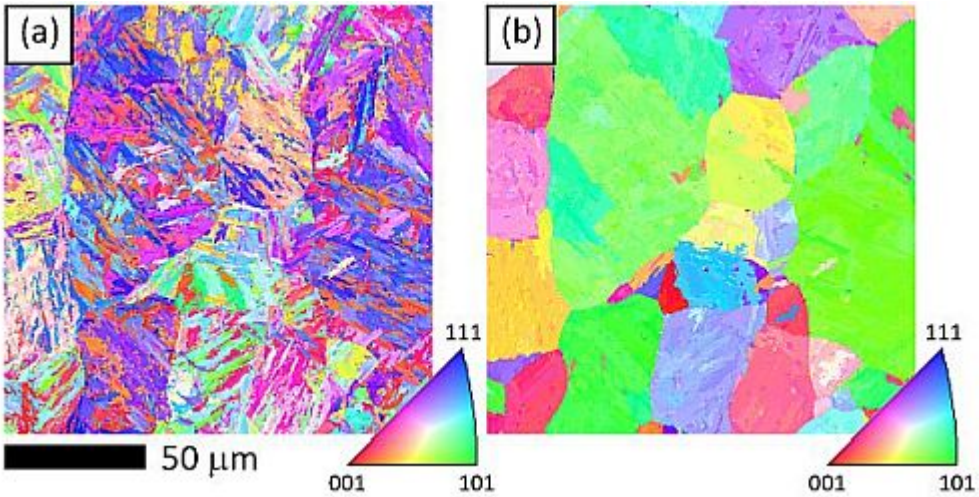

Fig. 2: Orientation maps from steel microstructures: (a) as-measured post transformation α-Fe and (b) the as-reconstructed γ-Fe

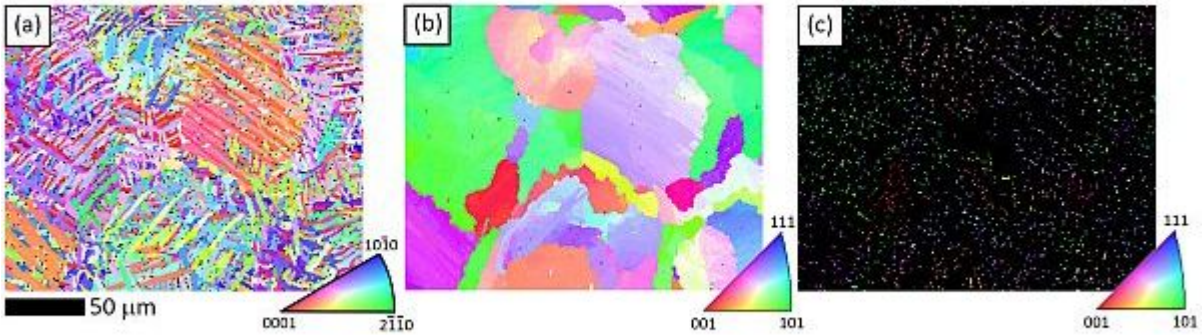

Fig. 3: Orientation maps from Ti6Al4V microstructures: (a) as-measured post-transformation α-Ti, (b) reconstructed pre-transformation β-Ti and (c) the as-measured retained β-Ti

Type of presentation: Poster

MS1-P-2794 Phase determination of dual phase steel using backscattered electron images and image analysis techniques

Jozefovič P.[1], Ambrož O.[1], Čermák J.[1], Mikmeková Š.[1]

[1]Institute of Scientific Instruments of the CAS, Brno, Czech Republic

Email of the presenting author: patjoz@isibrno.cz

For better understanding of behaviour of dual phase (DP) steels , their microstructure needs to be precisely determined. For characterization of the microstructure, a scanning electron microscope (SEM) is commonly used. The SEM allows better spatial resolution and higher possible magnification than optical or confocal microscopes. In order to separate the phases in DP steels in SEM micrograph, etching of the specimen is often used. Unfortunately, this process often results in over-etching one of the phases and prevent us from obtaining of precise structural information.
The other way of phase identification is by an electron backscatter diffraction (EBSD) method. The EBSD method has also several significant drawbacks, such as high requirements on the specimen surface quality and the specimen needs to be tilted which distorts the shape of the phases. To avoid the above-mentioned drawbacks, we have utilised a new technique for phase identification in the metastable austenitic stainless steel with induced α´-martensite transformation by a low cycle fatigue testing. As described in [1, 2, 3], the martensite phase shows an extraordinary bright contrast in comparison with all other phases in the SEM micrographs obtained at specific imaging conditions securing collection of the low take-off angle inelastic backscattered electrons.
Furthermore, a deep learning models for image analysis was used for automated phase determination in the SEM micrographs. Comparison between commercial software for phase segmentation and our pre-trained deep learning model were made to validate the performance of our model.

Acknowledgement: The research was financially supported by the Lumina Quaeruntur and strategy AV 21 by the Czech Academy of Sciences.

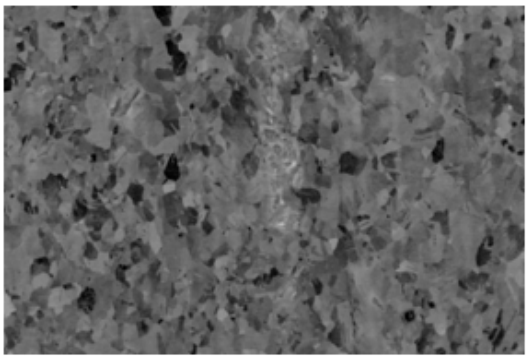

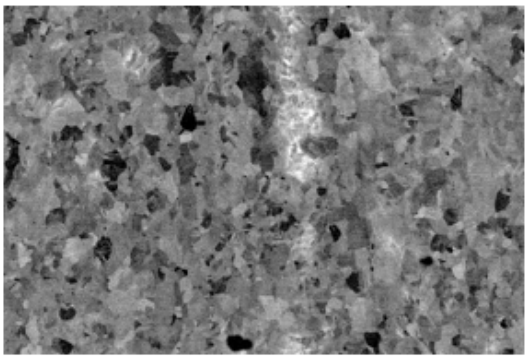

Fig. 1: Micrographs of the same location showing contrast evolution between α´-martensite and austenitic phase with respect to observing parameters of the SEM

Type of presentation: Poster

MS1-P-2657 Incommensurate structure of τ phase in the Al-Cu-Zn system

Klementová M.[1], Palatinus L.[1], Buršík J.[2], Zobač O.[2]

[1]FZU - Institute of Physics of the Czech Academy of Sciences, v.v.i., Na Slovance 2, Prague, Czechia, [2]Institute of Physics of Materials of the Czech Academy of Sciences, v.v.i., Zizkova 22, 616 00 Brno, Czechia

Email of the presenting author: klemari@fzu.cz

Dural alloys based on the Al-Cu-Zn system are of great technological importance for superior mechanical properties. They also exhibit shape-memory effect [1]. Recently, phase equilibria in this system were experimentally studied [2]. At 400°C, a single-phase field was found, containing three structural modifications of the ternary phase τ: cubic CsCl structure (τC), related rhombohedral structure type (τR), and an unknown structure with incommensurate modulation (τi), which is the topic of this study.

A sample was prepared from pure elements in the 40Al:45Cu:15Zn ratio (at%), i.e. in the region of the phase τi. It was then melted in evacuated quartz-glass ampoules, annealed at 400 °C for 648 hours and quenched in water. Overall composition was measured by SEM-EDX and the structure was analyzed by powder XRD, which confirmed the ternary phase τi.

More detailed structural evaluation of the incomensurate structure τi was done by electron diffraction (3D ED) [3]. A thin lamella cut out with FIB as well as a crushed sample prepared under liquid nitrogene were investigated. Data were collected on an FEI Tecnai G2 20 transmission electron microscope operated at 200 kV with LaB6 cathode, equipped with an ASI Cheetah direct detection camera (512x512 pixels) using the continuous rotation approach (tilt range +/-50deg, step 0.25deg). The data were processed in the PETS software [4]. Structure solution and refinement were performed in the computing system Jana2020 [5]. The structure was solved by the charge flipping algorithm using the program Superflip [6].

The basic structure has cubic symmetry and it is of the CsCl type with lattice parameter a = 2.91(1) Å. The modulation is quite complex (Fig. 1a) consisting of three independent modulation vectors and a non-standard centering, which only effects the satellite reflections. The centering vectors are (0,0,0,0.5,0.5,0), (0,0,0,0.5,0,0.5) and (0,0,0,0,0.5,0.5). The corresponding (3+3)D superspace group is Xm-3m (α,0,0) (0,α,0) (0,0,α) with α=0.386. The simple CsCl-type structure, in this case with the sites occupied by Al and Cu, is modified by the addition of Zn on the Al-site and vacancies on the Cu-site. The number of the vacancies increases from 4at% in τC to 17at% in τR and it is likely the cause of the modulation. The modulation (Fig. 1b) is mostly occupational even though slight deviations from the average atomic positions are also visible.

[1] L. Gomidzelovic et al., Trans. Nonferrous Met. Soc. China 25 (2015) 2630.
[2] O. Zobac et al., J. Material Science 55 (2020) 10796.
[3] M. Gemmi et al., ACS Cent. Sci. 5 (2019) 1315.
[4] L. Palatinus et al., Acta Cryst. B75 (2019) 512.
[5] V. Petricek, M. Dusek, L. Palatinus, Z. Krist 229-5 (2014) 345.
[6] L. Palatinus and G. Chapuis, J. Appl. Cryst. 40 (2007) 786.

Acknowledgement: CzechNanoLab project LM2018110 funded by MEYS CR is gratefully acknowledged as well as the EXPRO project 21-05926X supported by the Czech Grant Agency.

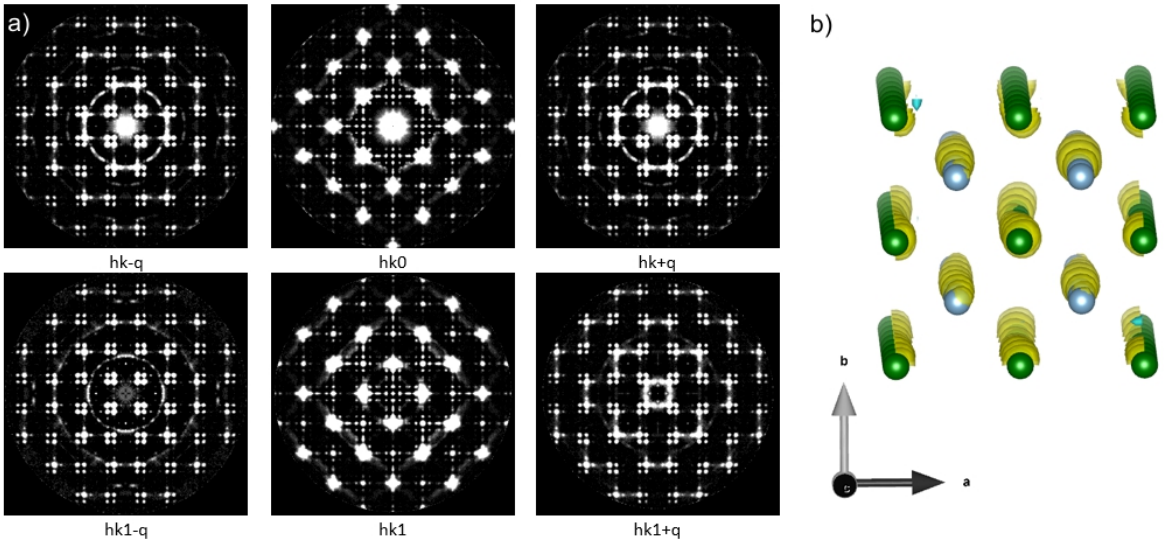

Fig. 1: 3D ED results. (a) Reciprocal space sections, (b) structure model of the ternary incomensurate phase τi (Al shown in grey and Cu in green). Modulation is highlighted by the changes in the electrostatic potential (in yellow), which clearly show the occupancy/position variations on both atomic positions.

Type of presentation: Poster

MS1-P-2656 The Use of Titanothermic Reduction for Processing of Deep-Sea Nodules

Klimša L.[1], Kopeček J.[1], Laufek F.[2], Michalcová A.[3], Tsepeleva A.[3], Kristianová E.[3], Chmelíková E.[3], Nováček D.[3], Dvořák P.[3], Novák P.[3]

[1]Department of Material Analysis, FZU – Institute of Physics of the Czech Academy of Sciences, Prague, Czech Republic, [2]Czech Geological Survey, Prague, Czech Republic, [3]Department of Metals and Corrosion Engineering, Faculty of Chemical Technology, University of Chemistry and Technology, Prague, Czech Republic

Email of the presenting author: klimsa@fzu.cz

The lack of color metals for advanced applications as well as the necessary improvement of nature protection open (again) the topic of the deep-sea nodule use. The aim of presented project is to prepare "natural alloy" and to construct as simple way as possible to reduce nodules into the usable alloy without wasting the energy, mainly to avoid the subsequent purification of individual metals. The aluminothermally reduced deep-sea nodules from Clarion-Clipperton Zone (Pacific Ocean) are investigated in this study. They contain manganese as the dominant element, whereas iron, nickel and copper are other major constituents besides aluminum and silicon.

The nodules were crushed and ground to a powder with titanium powder. Both the slag and produced metals were investigated by X-Ray Diffraction (XRD) and Scanning Electron Microscopy (SEM) to obtain phase composition. SEM investigations were performed using TESCAN FERA3 GM instrument. Phase content, thermal stability up to 1600 °C, hardness and tribological properties were investigated, but there is still a lot of unfinished work in comparison with the aluminothermic reduction [1, 2].

Using XRD three phases were found in the metal, whereas four phases were found in the slag. The phase composition of the metal is similar to aluminothermy with 0 % of aluminium excess. We determined β-Mn66Ni20Si14 major phase (P213 space group) and two other phases, (Mn,Cu)3(Al,Si) and Mn0.83Si0.17, detected in aluminothermally reduced nodules too.

The existence of other minor phases, such as manganese sulfide MnS, was proven using SEM with Electron BackScattered Diffraction/Energy Dispersive Spectroscopy coupled detectors (EBSD/EDS). SEM was equipped with EDAX analytical system – DigiView V EBSD camera and Octane Super EDS silicon drift detector – data were obtained by EDAX APEX acquisition software using ChI-Scan feature and processed by EDAX OIM Analysis 8 with NPAR (Neighbor Pattern Averaging & Reindexing) approach. Slag contained four phases, which were identified by XRD and determined by EBSD/EDS mapping as shown in Fig. 1.

[1] Novák, P.; Vu, N.H.; Šulcová, L.; Kopeček, J.; Laufek, F.; Tsepeleva, A.; Dvořák, P.; Michalcová, A. Structure and Properties of Alloys Obtained by Aluminothermic Reduction of Deep-Sea Nodules. *Materials* **2021**, *14*, 561. https://doi.org/10.3390/ma14030561

[2] Msallamová, Š.; Novák, P.; Miossec, P.; Kopeček, J.; Tsepeleva, A.; Rudomilova, D.; Fojt, J. Corrosion Properties of Mn-Based Alloys Obtained by Aluminothermic Reduction of Deep-Sea Nodules. *Materials* **2021**, *14*, 5211. https://doi.org/10.3390/ma14185211

Acknowledgement: We acknowledge Czech Science Foundation project 20-15217S and CzechNanoLab Research Infrastructure supported by MEYS CR (LM2018110).

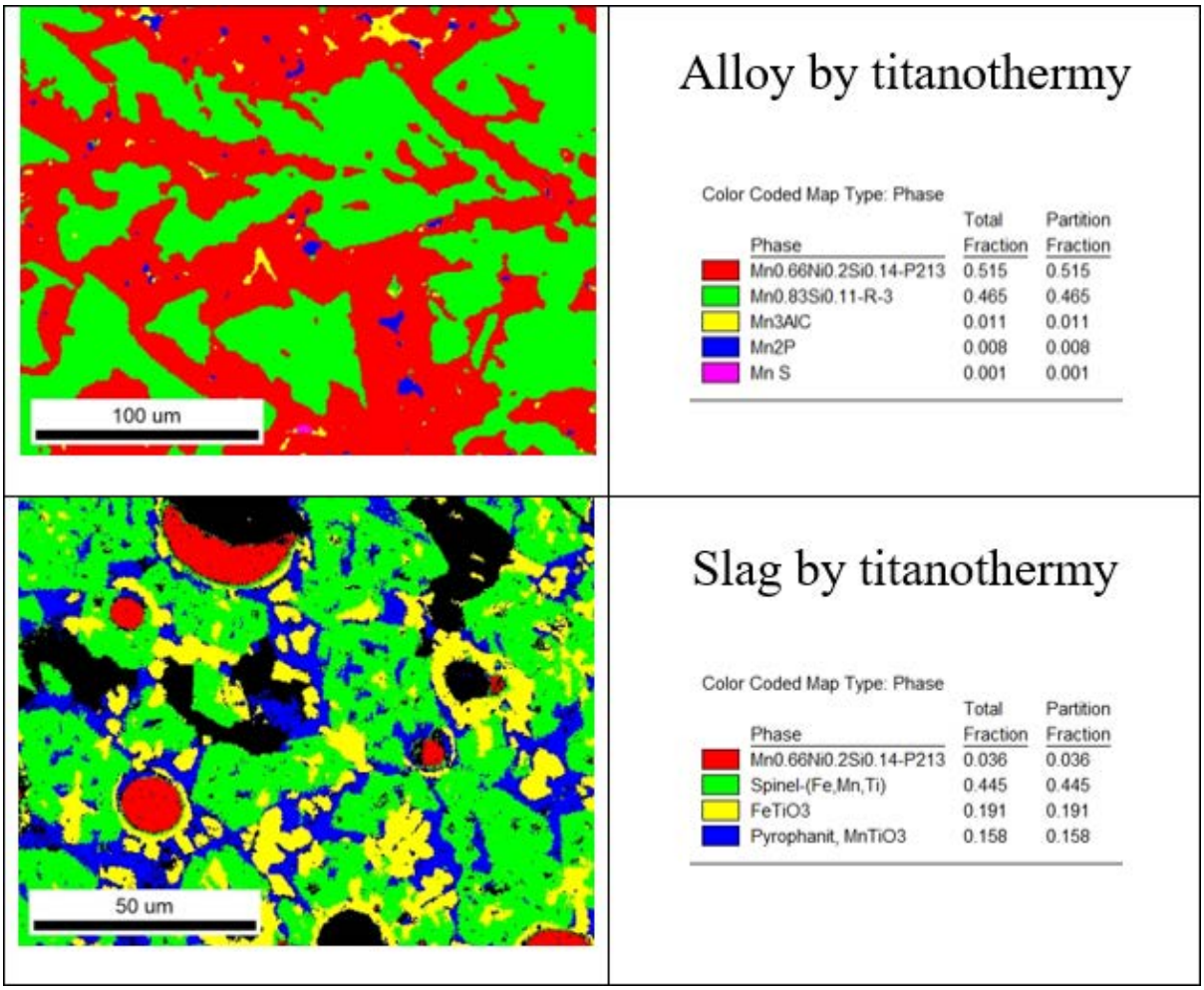

Fig. 1: The illustration sketches of the alloys prepared by titanothermy. The first row shows the phase composition of produced alloy and the second row the phase composition of the slag.

Type of presentation: Poster

MS1-P-2623 Aluminothermally reduced deep-sea concretion and its phase structure

Kopeček J.[1], Klimša L.[1], Laufek F.[2], Michalcová A.[3], Šulcová L.[3], Tsepeleva A.[3], Borkovcová K.[3], Nováček D.[3], Vu N. H.[3], Dvořák P.[3], Novák P.[3]

[1]FZU – Institute of Physics of the Czech Academy of Sciences, Department of Materials Analysis, Praha, Czech Republic , [2]Czech Geological survey, Praha, Czech Republic, [3]University of Chemistry and Technology in Prague, Department of Metals and Corrosion Engineering, Praha, Czech Republic

Email of the presenting author: kopecek@fzu.cz

The lack of color metals for advanced application as well the necessary improvement of nature protection opens the (again) the topic of deep-sea nodule use. The aim of presented project is to prepare “natural alloy”, to construct as simply as possible way to reduce nodules into the usable alloy without wasting the energy, mainly to avoid the purification of individual metals. The aluminothermally reduced deep-sea nodules from Clarion-Clipperton Zone (Pacific Ocean) are investigated in this study. They contain manganese as the dominant element, whereas iron, nickel and copper are other major constituents besides aluminum and silicon.
The nodules were crushed and ground to a powder with various excess of aluminum (0 %, 10 %, 20 % and 100 %). Both the slag and produced metals were investigated by XRD and SEM to obtain phase composition. Produced alloy shall be used as a filler to aluminum alloys and are extremally brittle. Beyond phase content investigation the thermal stability up to 1600 °C, hardness and tribological properties were investigated [1]. Later the study of corrosion resistance was performed [2].
Using XRD there were found from three to eight phases, some of them not listed in databases. Thus, phase investigation process was challenging. Some minor phases as sulfide MnS were proved using SEM with EBSD/EDS coupled detectors [1]. The alloys contain mayor manganese rich phase, which develops from β-Mn66Ni20Si14 phase (P213 space group) at 0 % of excess and β-Mn phase (P4132 space group) at 10 % of excess to α-Mn phase (I-43m space group) at 20 % of aluminum excess. The recently experimentally confirmed phases Mn2FeSi and Mn2FeAl were separated and both observed with Heusler alloy structure. The illustration sketches of the respective alloys can be seen in Fig. 1.
[1] Novák P, Nguyen H V, Šulcová L, Kopeček J, Laufek F, Tsepeleva A, Dvořák P, Michalcová A 2021 Materials 14 561.
[2] Msallamová Š, Novák P, Miossec P, Kopeček J, Tsepeleva A, Rudomilová D, Fojt J 2021 Materials 14 5211.

Acknowledgement: We acknowledge CzechNanoLab (LM2018110), project SOLID21 - CZ.02.1.01/0.0/0.0/16_019/0000760 by MEYS CR and CSF project 20-15217S for support.

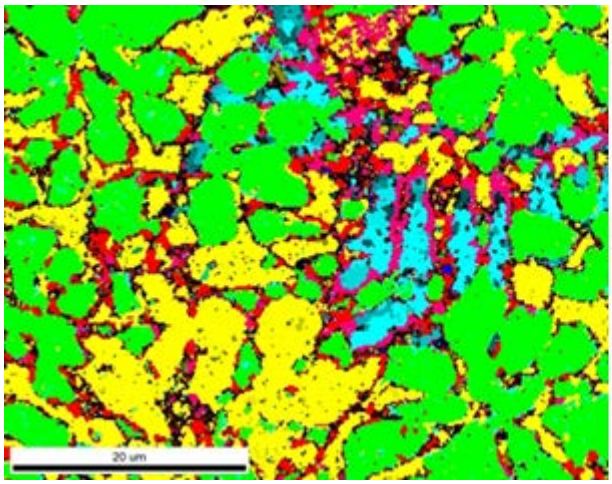

Phase	Total Fraction
Mn5Si3	0.112
Mn2FeAl	0.387
Mn-alfa	0.307
Mn2P	0.010
Mn3(Al,Si)	0.002
Mn(Fe)-Im3m	0.100
(Cu,Mn)3(Al,Si)	0.076
Mn S	0.005

Fig. 1: The illustration sketches of the alloys prepared by aluminothermy with 20 % of excess of aluminum. The phase compositions maps obtained by EBSD method are given.

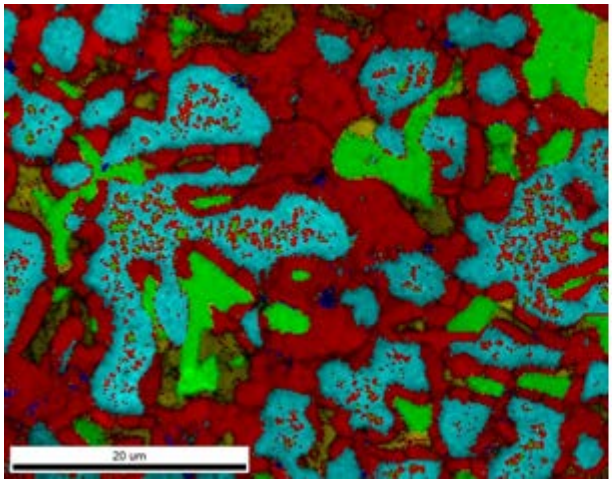

Color Coded Map Type: Phase

Phase	Total Fraction	Partition Fraction
Mn-beta	0.513	0.513
Mn0.83Si0.11-R-3	0.068	0.068
Mn2P	0.008	0.008
Mn2FeSi	0.110	0.110
Mn2FeAl	0.302	0.302

Fig. 2: The illustration sketches of the alloys prepared by aluminothermy with 10 % of excess of aluminum. The phase compositions maps obtained by EBSD method are given.

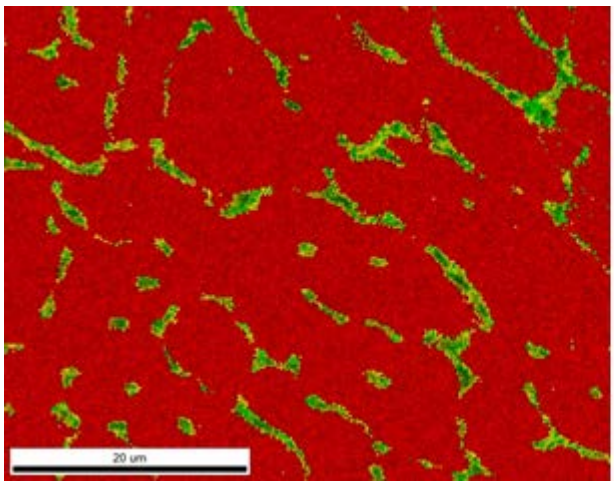

Phase	Total Fraction
Mn0.66Ni0.2Si0.14-P213	0.923
(Cu,Mn)3(Al,Si)	0.029
Mn2P	0.048

Fig. 3: The illustration sketches of the alloys prepared by aluminothermy with 0 % of excess of aluminum. The phase compositions maps obtained by EBSD method are given.

Type of presentation: Poster

MS1-P-2602 Phase Identification in Twin-Roll Cast Al-Steel Clad Composite

Křivská B.[1], Šlapáková M.[1], Veselý J.[1], Minárik P.[1], Králík R.[1], Grydin O.[2], Stolbchenko M.[2], Schaper M.[2]

[1]Faculty of Mathematics and Physics, Charles University, Prague, Czech Republic, [2]Faculty of Mechanical Engineering, Paderborn University, Paderborn, Germany

Email of the presenting author: krivska.barbora@seznam.cz

Aluminium-steel clad composites are applied in several industrial fields due to an advantageous combination of dissimilar properties of aluminium and steel. Steel brings high strength, while aluminium keeps the final material eligibly lightweight. This contribution focuses on identifying phases that form at the aluminium-steel interface when the material is exposed to high temperatures, which could come about through the manufacturing or the use of the composite. The type of phases and their thickness determines the final properties of the material [1-3]. In particular, Al-rich phases of the Al-Fe system [4] are reported to form at aluminium-iron or aluminium-steel joints: Orthorhombic Al5Fe2 (η-phase), monoclinic $Al_{13}Fe_4$ θ-phase [1, 5], or in case of the joint of aluminium with austenitic steel, similar structures are known with substitutions in some of the Fe sites by atoms of Cr or Ni [6].

The studied twin-roll cast aluminium-steel clad material consisted of a 2.5 mm thick layer of a technically pure aluminium EN AW-1070 and a 0.5 mm thick layer of austenitic steel type 1.4301. No intermetallic compounds were present at the interface after the casting process. The phase composition of the reaction layer was investigated on a lamella extracted by focused ion beam from the material annealed in an air furnace at 500 °C for 16 h. Phases were identified from selected area electron diffraction (SAED) patterns using transmission electron microscopes (TEM) JEOL 2000 FX and JEOL 2200 FS.

The reaction layer formed during the annealing was □5 μm thick and consisted of three separate layers. A fine-grained layer of a thickness □3 μm adjacent to steel (Fig. 1) matched the Al_5Fe_2 η-phase. The mid-layer of a similar thickness consisted of columnar grains, which were identified as the $Al_{13}Fe_4$ θ-phase (Fig. 2). The third layer bordering on Al was enriched by Si (see the overlayed BF image by elemental concentrations in Fig. 1) and it was identified as the bcc $Al_{19}Fe_4MnSi_2$ α-phase [7] (Fig. 3).

References

[1] Springer H, Kostka A, dos Santos J and Raabe D 2011 Mater. Sci. Eng. A 528 4630-4642
[2] Grydin O, Stolbchenko and M Schaper M 2017 Procedia Eng. 207 1695-1700
[3] Yang Y, Zhang F, He J, Qin Y, Liu B, Yang M and Yin F 2018 Vacuum 151 189-196
[4] Li X, Scherf A, Heilmaier M and Stein F 2016 J. Phase Equilib. Diffus. 37 162-173
[5] Li R, Yuan T, Liu X and Zhou K 2016 Scr. Mater. 110 105-108
[6] Liu B, Yang Q and Wang Y 2019 Results Phys. 12 514-524
[7] Barlock J G and Mondolfo L F 1975 Int. J. Mater. Res. 66 605-–611

Acknowledgement: This research was funded by the GAČR project 20-00355Y, SVV 260582 and the German Research Foundation in regard to the project SCHA 1484/21-1.

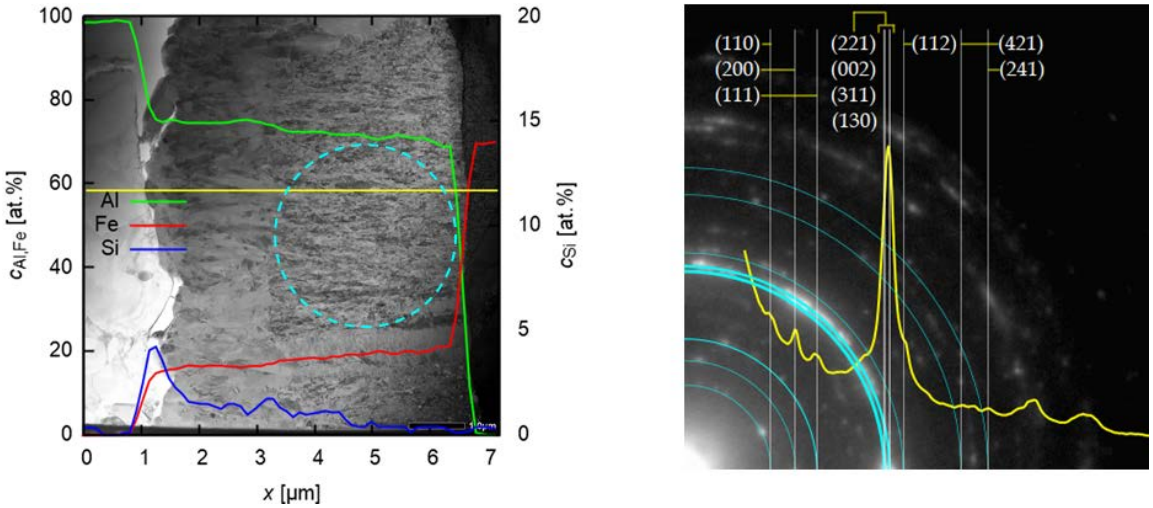

Fig. 1: TEM BF image of the reaction layers overlayed by concentration profiles measured along the yellow line by EDS in STEM; ring diffraction pattern of the fine-grained region (marked by a blue circle in the BF image) identified as Al_5Fe_2.

Fig. 2: TEM BF image showing columnar-grained layer; SAED pattern from the marked grain; simulated diffraction pattern corresponding to the $Al_{13}Fe_4$ θ-phase in the zone [120].

Fig. 3: TEM BF image showing Si-enriched region; SAED pattern from the marked grain; simulated diffraction pattern corresponding to the bcc α-phase in the zone [111].

Type of presentation: Poster

MS1-P-2722 Microstructural changes in DLMS IN939 due to low cycle fatigue investigated by advanced electron microscopy.

Kuběna I.[1], Šulák I.[1], Babinský T.[1], Fintová S.[1]

[1]Institute of Physics of Materials, Czech Academy of Science, Brno, Czech Republic

Email of the presenting author: kubena@ipm.cz

Heat-treated direct laser metal sintered IN939 nickel-based superalloy was subjected to deep microstructural analysis to reveal material response to the static and cyclic loading. Horizontal and vertical building directions were applied to prepare samples for tensile and fatigue testing. The prepared microstructure was characteristic of a columnar grain structure with a preferential orientation of <001>. Elongated dislocation substructures created during sintering remained after heat treatment. Present dislocation walls provided preferential sites for the formation of fine spherical γ' (Ni3(Ti,Al)) nanoprecipitates. As the precipitation of γ' dispersion during the heat treatment interacts with dislocations, they reduce dislocation mobility resulting in a considerable strength, which is, however, accompanied by lower ductility. Building direction was shown to have only a negligible effect on the static and cyclic properties.
Due to the grain size, which can be considered fine compared to the cast version of the material and present dislocation arrangement and formed nanoprecipitate dispersion, the material exhibit superior mechanical properties compared to the conventional cast alloy. Acting damage mechanisms are the combination of those observed for the cast alloy and materials containing fine dispersions.

Acknowledgement: This research was funded by European Union's Horizon 2020 research and innovation programme (H2020-WIDESPREAD-2018), under grant agreement No. 857124 (SIRAMM).

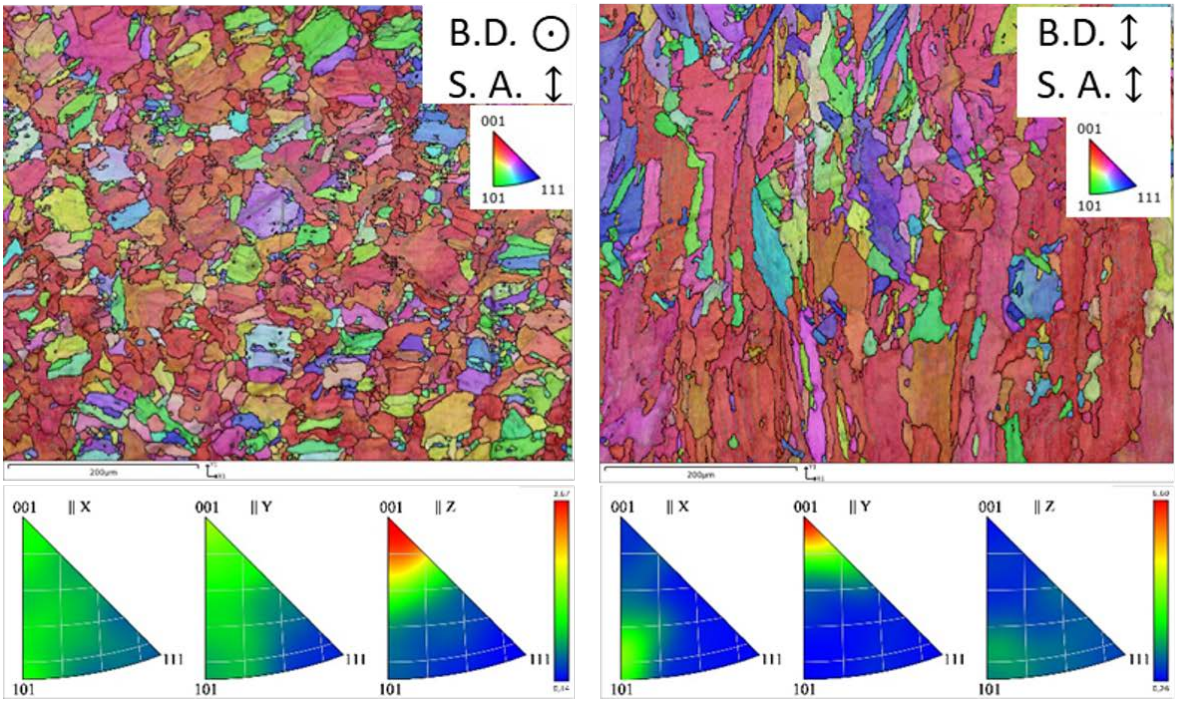

Fig. 1: EBSD maps with IPFs measured for horizontal (left) and vertical (right) building direction showing strong crystalographic <001> texture.

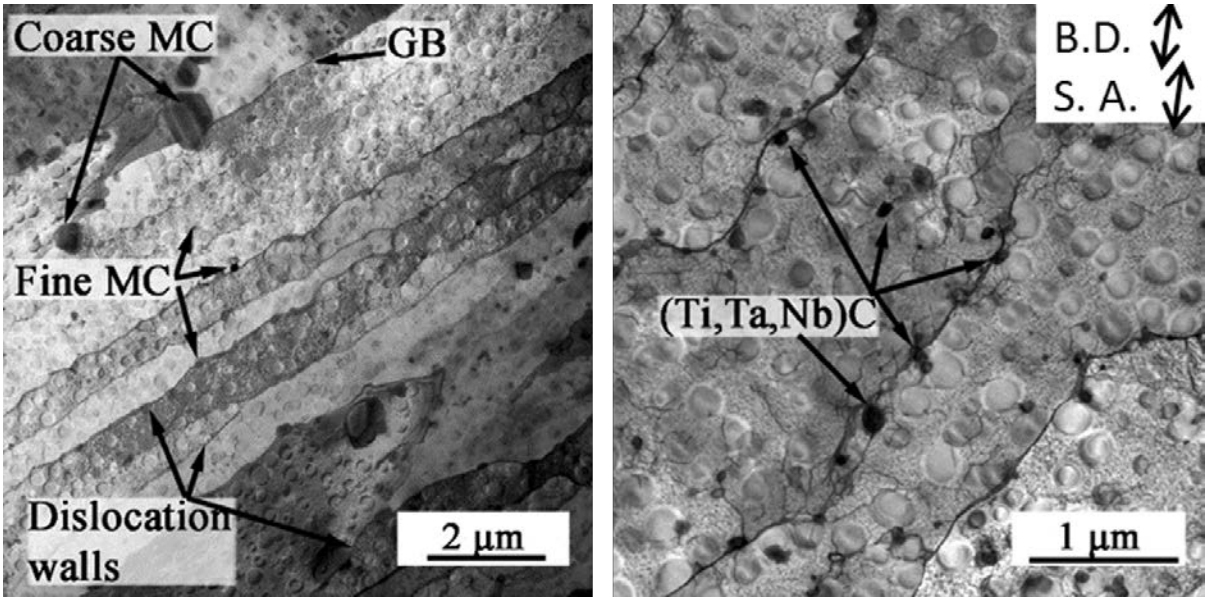

Fig. 2: TEM micrographs of heat-treated IN939 (left) elongated dislocation substructure with fine dispersion of carbides alongside dislocation walls; (right) detail of complex (Ti, Ta, Nb) nanocarbides with spherical morphology

Type of presentation: Poster

MS1-P-2826 Deep learning powered optical microscopy for steel research

Mikmeková Š.[1], Čermák J.[1], Ambrož O.[1], Jozefovič P.[1], Zouhar M.[1], Materna-Mikmeková E.[1], Konvalina I.[1], Materna J.[2]

[1]Institute of Scientific Instruments of the CAS, Brno, Czech Republic, [2]Machine Learning College, Brno, Czech Republic

Email of the presenting author: sarka@isibrno.cz

Steel is by far the world's most important, multi-functional, and most adaptable material. The excellent mechanical properties of steels are determined by their microstructure. The microstructure of advanced steels, such as advanced high strength steels (AHSS), is a combination of different phases or constituents with complex substructures [1] and its classification is extremely challenging. Traditionally used imaging techniques, such as light optical microscopy (LOM) or confocal microscopy (CM), turn out to be insufficient for precise structural characterization of the AHSS, and high-resolution imaging of their surface by state-of-the-art scanning electron microscopes (SEM) is required [1, 2]. However, common metallographic laboratories are equipped only with the LOM or the CM at best. As a result, they are not able to sufficiently characterize the structure of modern steels. In this work, we employ artificial intelligence techniques - namely deep learning - to enhance the OM micrographs of the AHSS in order to raise phase separation. Each training data-point consists of a trinity of corresponding micrographs obtained by the OM, the CM, and the ultra-high resolution SEM (Fig. 1). We will demonstrate that the deep learning methods have the potential to enhance the contrast among fine features in the OM micrographs and enable accurate secondary phase identification in the AHSS using LOM.

[1] Raabe, D., Sun, B., Kwiatkowski Da Silva, A. et al. Current Challenges and Opportunities in Microstructure-Related Properties of Advanced High-Strength Steels. Metall Mater Trans A 51, 5517–5586 (2020). https://doi.org/10.1007/s11661-020-05947-2

[2] www.worldautosteel.org

Acknowledgement: This research was funded by the Czech Academy of Sciences, LUMINA QUAERUNTUR.

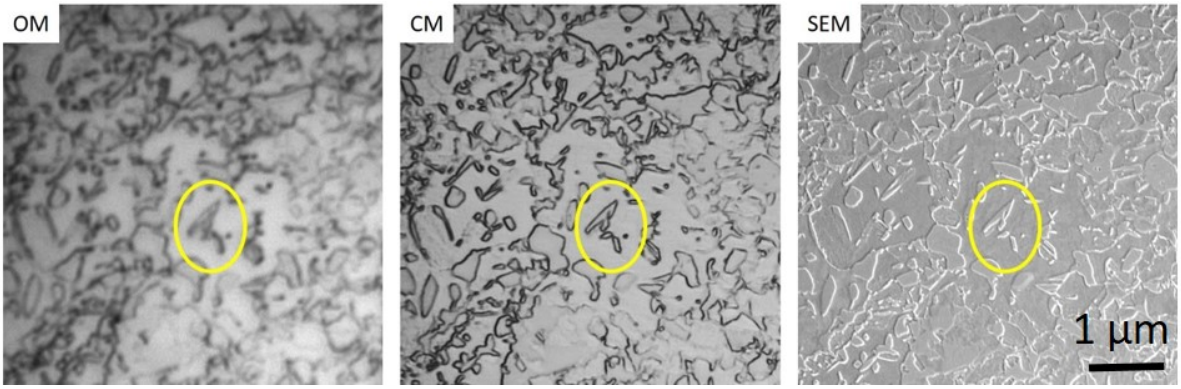

Fig. 1: Micrographs of the same region on the surface of the AHSS obtained by: light optical, confocal, and scanning electron microscopes (from the left). An example of secondary phases (martensite-austenite constituents) is marked by the yellow oval inside each image.

Type of presentation: Poster

MS1-P-2624 Modification of native oxide on magnesium powders for enhanced corrosion resistance

Nagy Trembošová V.[1,3], Nagy Š.[1], Nosko M.[1], Castro M.[2], Skiba J.[4], Beronská N.[1]

[1]Institute of Materials & Machine Mechanics, Slovak Academy of Sciences, Dúbravská cesta 9, 84513 Bratislava 4, Slovakia, [2]Centre of Excellence for advanced materials application, Slovak Academy of Sciences, Slovakia, [3]Faculty of Materials Science and Technology in Trnava, Slovak University of Technology, Slovakia, [4]Institute of High Pressure Physics, Polish Academy of Sciences, Poland

Email of the presenting author: ummstrem@savba.sk

Magnesium, the lightest among structural metals, with its suitable mechanical, thermal, and biodegradable properties makes it a proper candidate for advanced material from the aerospace industry to medicine. Still, among many advantages, a major drawback of fulfilling all possibilities is weak corrosion resistance. Despite the acknowledged insufficient protective shield on the magnesium surface, native magnesium oxide (MgO) can be transformed into a tenacious layer, which continuously covers the powder´s surface and ensures better corrosion stability. Moreover, this low-cost approach is environmentally safe and a modified surface ensures versatile application potential. In this work, we demonstrate the gradual hydration of the pure magnesium powders in a carbon dioxide atmosphere. Detailed microscopical study of surface changes on pure magnesium powders shows that hydration in the specific atmosphere can enhance the stability of magnesium powder and the native porous MgO can be chemically modified into a new layer of amorphous MgCO3 without the necessity of thermal treatment. The effect of hydration on corrosion and mechanical properties was further investigated on samples made from extruded powder. Microstructural modifications as well as powder interfaces of the compact after extrusion were extensively studied by means of SEM, EBSD, S/TEM, and EDS.

Acknowledgement: The authors gratefully acknowledge the financial support of the Slovak Grant Agency VEGA (Project 2/0085/22).

Type of presentation: Poster

MS1-P-2589 Microstructural characterization of sintered Iron and observation of oxides reduction after different conditions of sintering process

Orovčík L.[1], Beronská N.[1], Hájovská Z.[1], Gabalcová Z.[2], Nagy Š.[1], Nosko M.[1]

[1]Institute of Materials & Machine Mechanics, Slovak Academy of Sciences, Dúbravská cesta 9, 84513 Bratislava 4, Slovakia, [2]Faculty of Materials Science and Technology STU in Trnava, Paulínska 16, Slovakia

Email of the presenting author: ummsorov@savba.sk

Material for high-performance applications produced by the powder metallurgy (PM) process requires a pre-alloyed powder or powder mixture suitable for hardening/sintering. Pre-alloyed water atomized iron powders have become widely used in the PM industry. Alloying elements such as Cr, Ni, Cu, and Mn are most often used in PM. Chromium (Cr) is widely used as an alloying element in PM mainly due to its high hardening ability, corrosion resistance, low cost, and easy recyclability. Cr is generally sensitive to oxidation and water-atomized pre-alloyed iron powder during manufacturing. The barrier of Cr oxides on the surface affects the sintering of powder particles and the diffusion of elements such as Ni, which is added to the powder mixture to increase the dynamic properties. Other oxides to the powder particles reduce the mechanical properties. Therefore, our work is focused on the influence of sintering parameters on microstructural changes of Fe1.8% Cr + 2% Ni + 0.5% C alloy powder mixture. The powder mixtures were pressed under uniaxial pressure at 900 MPa and then sintered for 30 minutes at 1120, 1250, and 1350 °C. In the sintering process, the four atmospheres such as nitrogen (N2), hydrogen (H2), gas mixture (N2 + 5% H2), and (N2 + 10% H2), were used to reduce oxides in powder compacts, sinter powder particles, and distribute chemical elements into the microstructure of powder particles. The heating rate was set at 2 °C/min for better preheating the powder compacts and prolonging the oxide reduction time. The precipitation rate was set to 5 °C/min to obtain a soft microstructure formed by different amounts of austenite, ferrite, perlite, upper bainite, and martensite.
Samples were prepared by a standard metallographic process with a polishing step using OP-S. The observation of the samples was carried out by scanning electron microscope Jeol 7600F (SEM). Energy dispersive spectroscopy (EDS) was used for elemental mapping of elements distribution after various temperatures of the sintering process. Electron backscatter diffraction (EBSD) was used to determine changes in microstructure, main in high and low grain boundaries before sintering and after different parameters of the sintering process. For better characterization of austenite, ferrite, perlite, upper bainite, and martensite, samples were etched with Nital acid from 2 to 10 seconds, depending on microstructure. High-resolution transmission electron microscopy (HR-TEM) was used to observe oxides transformation in microstructure depending on various sintering process conditions.

Acknowledgement: This research was funded by the Slovak Research and Development Agency under the contract APVV-18-0508.

Type of presentation: Poster

MS1-P-2588 Real Time Observation of strain in the SEM copper sample

Piňos J.[1], Frank L.[1]

[1]Institute of Scientific Instruments of the CAS, v. v. i., Královopolská 147, 612 64, Brno, Czech Republic

Email of the presenting author: pinos@isibrno.cz

The scanning electron microscope (SEM) with various detector arrangements and analytical attachments is an irreplaceable tool in material research. One of the techniques available in most of contemporary microscopes is the scanning low energy electron microscopy. The beam deceleration allows controlling the information depth of the backscattered electrons (BSE) imaging within a wide range by altering the landing energy of electrons. [1]
The BSE micrographs show, among others the crystallographic contrast of the grains in polycrystals. Relaxed samples show a homogeneous signal intensity within a grain, while in heavily deformed samples gradual signal variations appear even inside single grain. [2]
Previous experiments on heavily deformed samples shows effect of deformation in microstructure of the samples.[3] We may ask how intense deformation is necessary to get visible effects in microstructure and whether this effect could be used to estimate the intensity of deformation. Using an in-situ tensile tester, the microstructure can be observed during the process.
Thermo Fisher Scientific Scios SEM with Trinity detection system allows to use low landing energy and simultaneously obtain SE and BSE images. The Scios column uses a biased A-tube to form a high energy primary beam and then decelerate to the required energy for observation. Signal electrons are detected by various detectors: ETD – standard SE detector; T1 – in-column, closest to the polepiece, detecting high-angle BSE T2 – in-column, higher in column detecting the low-angle BSE.
The observations were performed in the Optiplan mode at a working distance of 6.25 mm, using a landing energy of 2keV and an A-tube bias of 8 kV. The beam current was set as 1.6 nA.
Fig 1. shows images taken by the ETD, T1 and T2 detector and its changes from as inserted state to just before breakage. The effect of deformation on the crystalline structure is most visible in the images obtained by the T1 detector. This in-column detector collects mostly high-angle BSE electrons, which provide crystallographic information.
During the elastic deformation phase, the microstructure of the sample remains the same. The tensile test graph is shown in Fig. 2. The first observable changes in the microstructure starts to appear at a stress of about 120 MPa – the corresponding plastic deformation of about 4%. The development of the effect continued in Fig. 3. However, accurate quantification was not possible. We can conclude that deformations exceeding 5% can be identified in the microstructure.
References:
[1] I. Müllerová, L. Frank, Advances in Imaging and Electron Physics 128 (2003) 309-443.
[2] Š. Mikmeková et al., Key Engineering Materials 465 (2011) 338-341.
[3] Š. Mikmeková et al., Applied Surface Science 275 (2013) 403-408.

Acknowledgement: Funded by Strategy AV21, program Breakthrough Technologies for the Future – Sensing, Digitisation, AI and Quantum Technologies together and RVO:68081731.

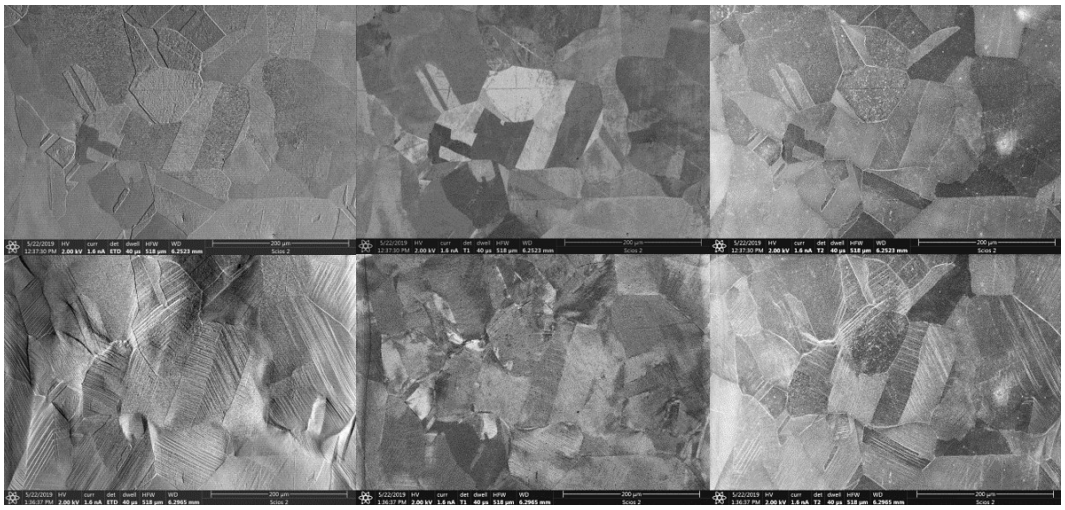

Fig. 1: Images from ETD, T1 and T2. Top row – undeformed sample, Bottom row – sample just before fracture.Tensile test diagram.

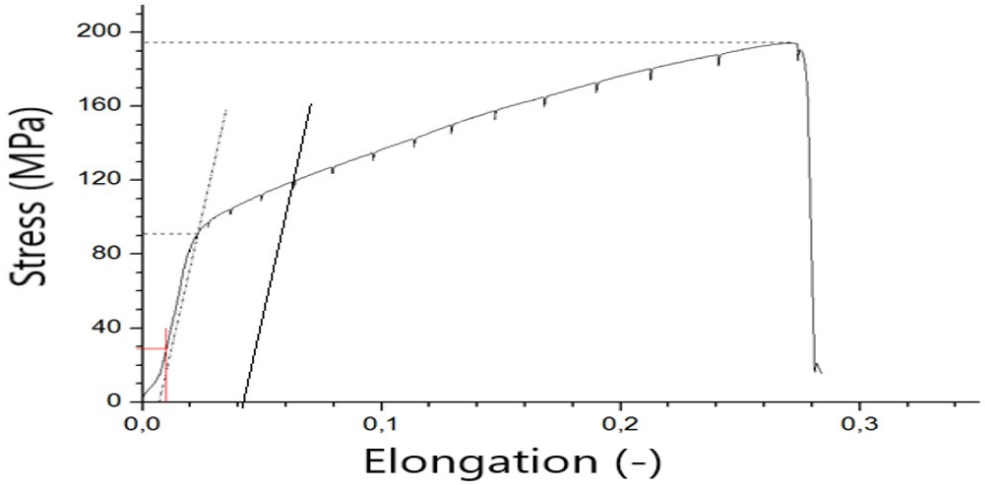

Fig. 2: Tensile test diagram.

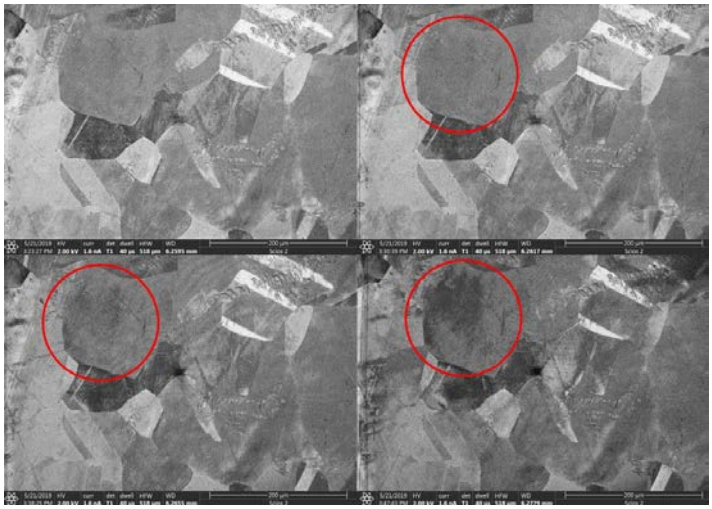

Fig. 3: Images taken by T1 at stress of 60, 90, 120, 150 MPa.

Type of presentation: Poster

MS1-P-2531 Exploring the magnetic microstructure of spinodal alloys with differential phase contrast scanning transmission electron microscopy (DPC-STEM)

Radlinger T.[1], Hofer F.[1,2], Kothleitner G.[1,2]

[1]Institute of Electron Microscopy and Nanoanalysis, Graz University of Technology, Steyrergasse 17, 8020 Graz, Austria, [2]Graz Centre for Electron Microscopy, Steyrergasse 17, 8020 Graz, Austria

Email of the presenting author: thomas.radlinger@felmi-zfe.at

Spinodal alloys are intriguing and promising materials for exploring the relationship between the chemical and the magnetic microstructure of magnetic alloys. The spinodal decomposition of such alloys due to heating treatments within the miscibility gap results in a segregation of a magnetic phase embedded in a non-magnetic matrix and is well known [1]. Although the compositional evolution of the microstructure and its manipulation has been subject of studies, little is known about the magnetic microstructure. Differential phase contrast (DPC) carried out in scanning transmission electron microscopy ((S)TEM) mode is an electron microscopy technique capable of doing so [2,3].
In this study, we investigated the chemical microstructure and the magnetic domain structure of spinodally decomposed $Cu_{52}Ni_{34}Fe_{14}$ and $Fe_{54}Cr_{31}Co_{15}$ alloys. We were able to shed light on the material microstructures by combining high-angle annular dark field imaging (HAADF), energy-dispersive X-ray spectroscopy (EDXS) elemental mapping and DPC-STEM imaging, revealing interesting relationships between compositional and magnetic properties of these alloys.
For $Cu_{52}Ni_{34}Fe_{14}$, overlaying EDXS elemental maps for Cu, Ni and Fe revealed a segregation of NiFe-rich platelets within a Cu-rich matrix. These platelets are ferromagnetic and form a pattern of small rectangular shaped 90° and 180° magnetic domains, which is displayed by the in-plane magnetic induction map acquired by DPC-STEM (Fig 1. (b)). There, the direction of the magnetic vector is plotted as a function of hue, which also helped to determine <111> as the magnetic easy axis for this alloy.
$Fe_{54}Cr_{31}Co_{15}$ segregates into ferromagnetic FeCo-rich particles embedded in a Cr-rich matrix. The induction map reveals a wavelike/lamellar and less regular magnetic domain structure compared to $Cu_{52}Ni_{34}Fe_{14}$, highlighting the deep insights into the magnetic domain structure gained by DPC-STEM.

References
[1] F. Fehim, Improvements in spinodal alloys from past to present, Materials and Design, 42, 131-146 (2012)
[2] J. Zweck, Imaging of magnetic and electric fields by electron microscopy, J. Phys.: Condens. Matter, 28, 403001 (2016)
[3] R. Nistico, F. Cesano, F. Garello, Magnetic Materials and Systems: Domain Structure Visualization and other Characterization Techniques for the Application in the Materials Science and Biomedicine, Inorganics, 8, 6 (2020)

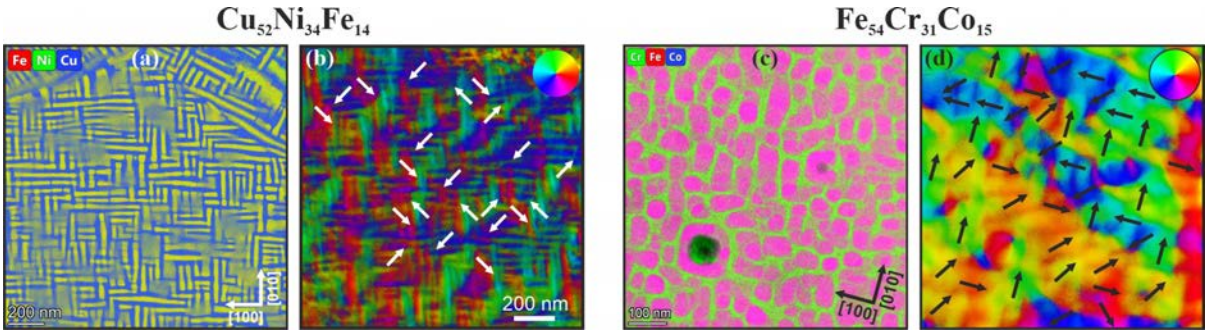

Fig. 1: Overlays of EDXS elemental maps and in-plane magnetic induction maps of spinodally decomposed $Cu_{52}Ni_{34}Fe_{14}$ and $Fe_{54}Cr_{31}Co_{15}$, respectively.

Type of presentation: Poster

MS1-P-2855 Morphological characterization of mill scales iron oxides products by SEM

Rajnovic D.[1], Balos S.[1]

[1]Faculty of Technical Sciences, University of Novi Sad, Novi Sad, Serbia

Email of the presenting author: draganr@uns.ac.rs

During manufacturing of the steel products by hot rolling a considerable amount of iron oxides is formed on the surface as mill scales [1-2]. The scales detach from the surface of steel products (bars, tubes, plates etc.) during further cooling and are accumulated as waste product. The amount of accumulated mill scales could become a pollution hazard as it contains large amount of iron oxides, heavy metals, lubrication oil and other potentially hazardous materials [2]. Thus, recycling and waste management off mill scales it's of great importance. Usually, mill scales are used as oxidizer in electric arc furnace steel making. However only the large size ones could be successfully used [1].
For that reason, in this paper a morphological characterization off mill scales produced during hot rolling of rebars is presented. Tree different size mill scales produced during different stages of rebar production ware studied (batch 1, 2, 3). Batches had a similar chemical mass. composition of: 78% Fe, 1.9%Al, 0.5%Mn, 0.12%Cu, 0.015%P, 0.015%S, 0.17%Ca, and rest - oxygen.
The morphological characterization was performed by scanning electron microscope JOEL JSM 6460LV.
It was founded that batch-1 is consisted of particles with different size and shape, that is small scales, irregular particles, and even spheres, with length 0.4-1 mm, Figure 1a. The thin scales had a thickness of about 50 μm, and had an elongated granular microstructure of cross section, while larger irregular particles had a more granular structure consisted of small equiaxial grains, Figure 1b. The batch-2 is more uniform, and is mostly consisted of larger thin scales, with size 0.7-1.4 mm, and thickness around 60 μm, Figure 2. The cross section of this scales exhibit appearance of brittle fracture with some amount of granules. The batch-3 represent the largest scales with few millimeters (3-5 mm) length, Figure 3. The thickness of this scales is similar to other batches, and is about 60 μm. The surface has a distinctive look of small grains of around 5 to 20 μm diameter, Figure 3b.
At the end, it can be concluded, that different mill scales are produced in different stages of rebar production. The mill scales are of characteristic size and shape, while thickness of scales is similar. Furthermore, additional processing, like grinding, pressing, bathing, vitrifying, annealing of batches, should be consider in order to reach desired particle size for further use.

[1] M.Z. Ruhiyuddin, D. Murizam, K. R. Ahmad, Synthesis and Characterization of Iron Produced from Iron Mill Scale. Key Engineering Materials, 594-595 (2013) 118–122
[2] M. Eissa, A. Ahmed, M. El-Fawkhry, Conversion of Mill Scale Waste into Valuable Products via Carbothermic Reduction, Journal of Metallurgy, (2015) 1-9

Acknowledgement: The research is supported by the project „Materials, joining and allied technologies“, at the DPE, Faculty of Technical Sciences, Novi Sad, Serbia.

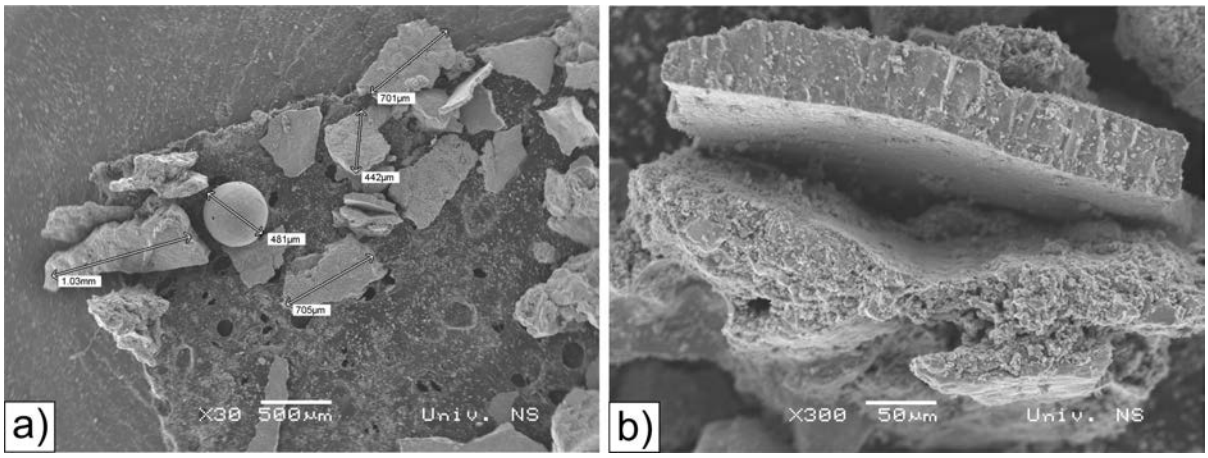

Fig. 1: Mill scales of the batch-1

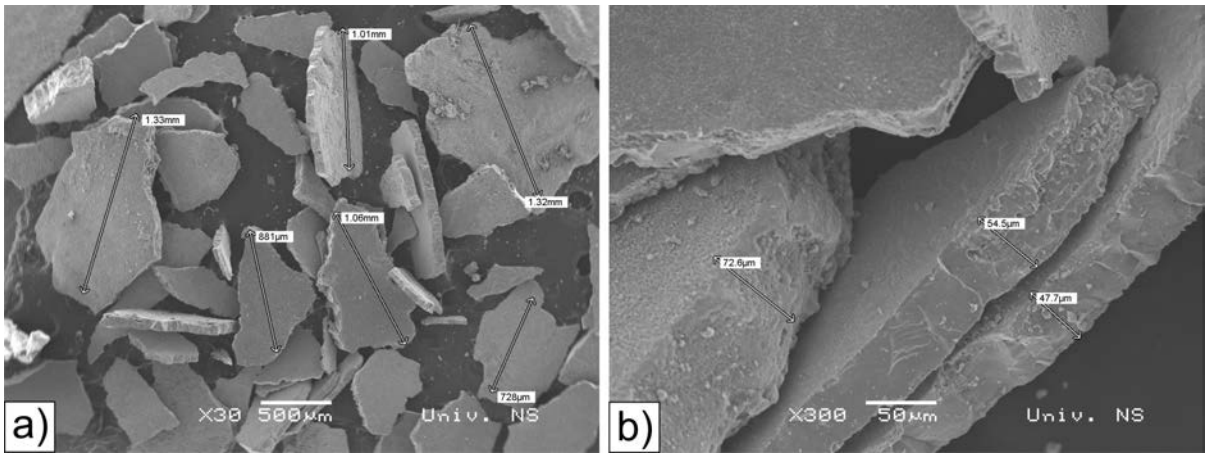

Fig. 2: Mill scales of the batch-2

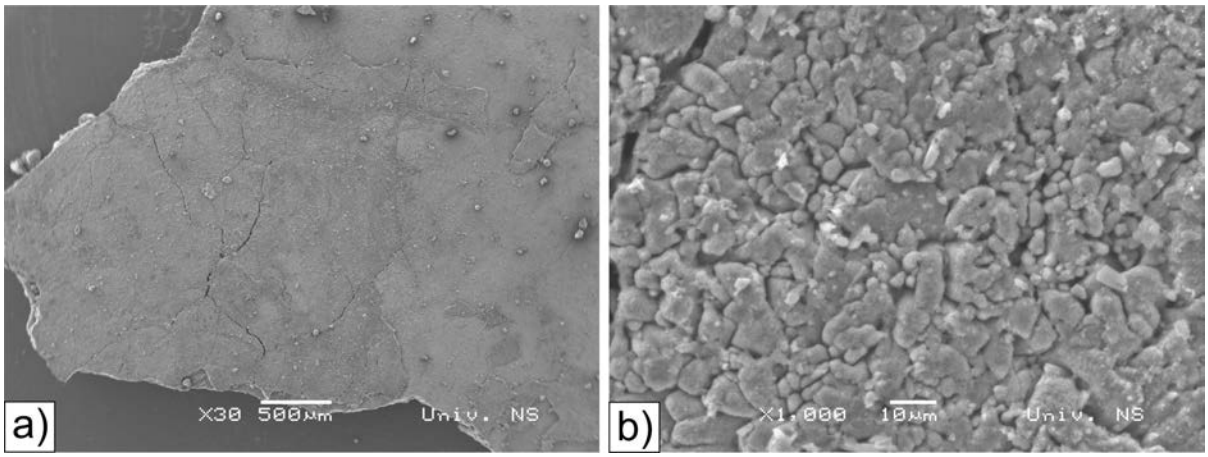

Fig. 3: Mill scales of the batch-3

Type of presentation: Poster

MS1-P-2856 Characterization of oil pipe weld localized corrosion and perforation

Rajnovic D.[1], Balos S.[1], Dramicanin M.[1], Janjatovic P.[1]

[1]Faculty of Technical Sciences, University of Novi Sad, Novi Sad, Serbia

Email of the presenting author: draganr@uns.ac.rs

Uniform or localized corrosion of oil pipes could occur due to chemical, electro-chemical or bio-chemical interactions with the working fluid or environment [1, 2]. Especially critical place of corrosion occurrence is welded zone due to introduction of different welding material, weld geometry, and generated internal stresses [1]. Localized corrosion introduces localized perforation trough which an oil or gas can leak causing serious damage and losses to the environment and the industries involved.

In this study a microscopical characterization off weld and corrosion products is presented. A localized perforation occurred in the weld connecting pipes made of standard steel API 5L, PSL1 grade B (ISO 3183, steel L245) used for transport of fluid consisted of 6% oil and 94% water. Characterization was performed by: light microscope Orthoplan, Leitz; scanning electron microscope JOEL JSM 6460LV; and energy dispersive spectroscopy (EDS) Inca, Oxford Instruments.

It was founded that perforation occurred due to localized corrosion of weld metal, Figure 1. Corrosion products (Figure 2 and Table 1) are consisted primary of Fe_2O_3, with traces of Mn and Si as residue of corroded steel. In the corrosion products minerals from water Al, Si, K, Ca, and particle of $BaSO_4$ (spec. 9) are present, also. A number of corrosion zones have a significant amount of S (spec 4, 8 i 9). The Sulphur content could originate from dissolved H_2S in oil, or it is generated by sulfate-reducing bacteria (SBR) [2]. Furthermore, amount of Ca is increased in EDS results due to formation of calcium carbonates ($CaCO_3$) scale from mineralized water.

Finally, it can be concluded that weld represent a critical place for localized corrosion and subsequent perforation, while corrosion is due to formation of scale on the weld, further development of SRB under scale, and final chemical corrosion of weld metal due to generated H_2S.

[1] M. Azam, M. Abdullah, T. Shimoda, Corrosion of weld area at internal surface of pipeline used in oil and gas industry, Journal of Advanced Manufacturing Technology, 14 (2020) 63–73

[2] X. Li, D. Shang, H. Yu, C. Chen, Research progress on oil & gas pipeline corrosion induced by SRB, Surface Technology, 50/2 (2021) 211–220

Acknowledgement: The research is supported by the project „Materials, joining and allied technologies“, at the DPE, Faculty of Technical Sciences, Novi Sad, Serbia.

Fig. 1: Perforation of the pipe

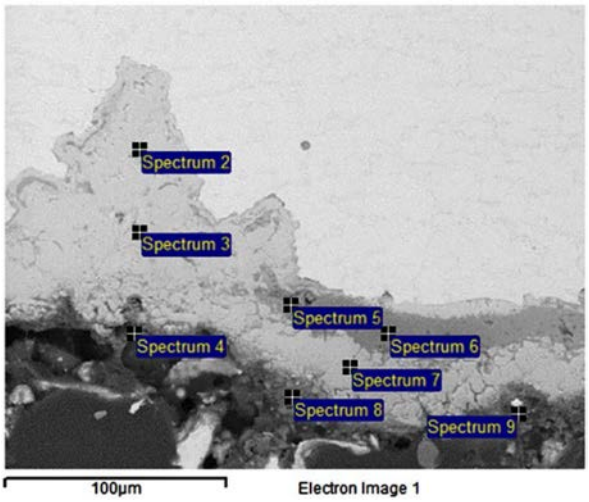

Fig. 2: EDS analysis of corrosion products

Table 1 - Chemical composition of corrosion products from Figure 2 [at. %]

	C	O	Al	Si	S	K	Ca	Mn	Fe	Ba
Sum Spec.	50.80	20.36	0.23	0.44			0.29	0.24	27.64	
Spec. 2		49.70						0.36	49.94	
Spec. 3		51.29		0.79				0.34	47.58	
Spec. 4	73.64	11.84	0.16	0.53	0.53		1.18		12.11	
Spec. 5	26.58	51.27					14.43		7.72	
Spec. 6	25.49	55.83					1.06	0.16	17.45	
Spec. 7		54.03							45.97	
Spec. 8	72.08	14.98	0.36	0.84	2.26	0.05	0.25	0.11	9.07	
Spec. 9	76.40	13.21	0.14	0.15	3.30		0.62		3.41	2.77

Fig. 3: Chemical composition of corrosion products from Figure 2 [at. %]

Type of presentation: Poster

MS1-P-2852 Influence of melting and AM-SLM processing on microtexture of Fe-Si soft magnetic materials – Is one-step manufacturing of electrical steels possible?

Sever T.[1], Steiner Petrovič D.[1], Donik Č.[1], Paulin I.[1], Godec M.[1], Petrun M.[2]

[1]Physics and Chemistry of Materials, Institute of Metals and Technology, Ljubljana, Slovenia,
[2]Institute of Electrical Power Engineering, Faculty of Electrical Engineering and Computer Science, University of Maribor, Maribor, Slovenia

Email of the presenting author: tina.sever@imt.si

Introduction

Silicon steels (SS) are fundamental for the economy of electrical appliances. The following properties are crucial: high permeability and induction reduce size and weight; low magnetic losses diminish generation of Joule heat and energy consumption; low magnetostriction reduces noise. They depend on material texture. The ideal texture of non-oriented SS is cubic texture with grains with the (001) or (110) plane parallel to the plane of the sheet, and uniform distribution of [100] direction.
Soft magnetic intermetallic alloys with high Si content (up to 6.5 wt% Si) possess excellent properties. However, as the Si content increases, the material becomes brittle and producing thin sheets is difficult.
Additive manufacturing (AM) has a huge potential in designing and industrial manufacturing of magnetic materials. Selective laser melting (SLM) is a promising method [1 – 3] as it could overcome the issue with magnetization reduction with insulation, significantly increase the eddy current loss via high electrical resistance, and the specific power of the electrical core could surpass traditional laminated cores [2, 3]. Moreover, reducing of the cut-edge effects on the power losses is imperative.

Materials & methods

In the study, crystallographic textures of soft magnetic materials are compared: conventional SS made of Fe-2Si-1Al alloy; remelted 45 µm Fe-6.5Si alloy powder, and AM-SLM material made of same powder. Microtextures are characterized using scanning electron microscopy with electron backscatter diffraction (ZEISS Crossbeam 550 FIB-SEM with EBSD system Hikari Super plus, Edax).

Goals & future work

The goal of the study is characterization of crystallographic textures developed with different manufacturing processes. Influence of powder remelting and AM-SLM processing parameters is compared to conventionally produced SS.
Future work will include extensive characterization of chemical, thermal, and mechanical properties of 3D printed soft magnetic materials, along with measurements of the materials' electromagnetic characteristics.

References

[1] V. Chaudhary, S.A. Mantri, R.V. Ramanujan, R. Banerjee, Prog. Mater. Sci., 114, 100688, 2020.
[2] T.N. Lamichhane, L. Sethuraman, A. Dalagan, H. Wang, J. Keller, M.P. Paranthaman, Mater. Today Phys., 15, 100255, 2020.
[3] F. Bernier, M. Ibrahim, M. Mihai, Y. Thomas, J.-M. Lamarre, Met. Powder Rep., 75, 6, 334-343, 2020.

Acknowledgement: The authors would like to acknowledge SIJ-ACRONI d.o.o. for the supply of the steel, and Slovenian Research Agency for the project funding.

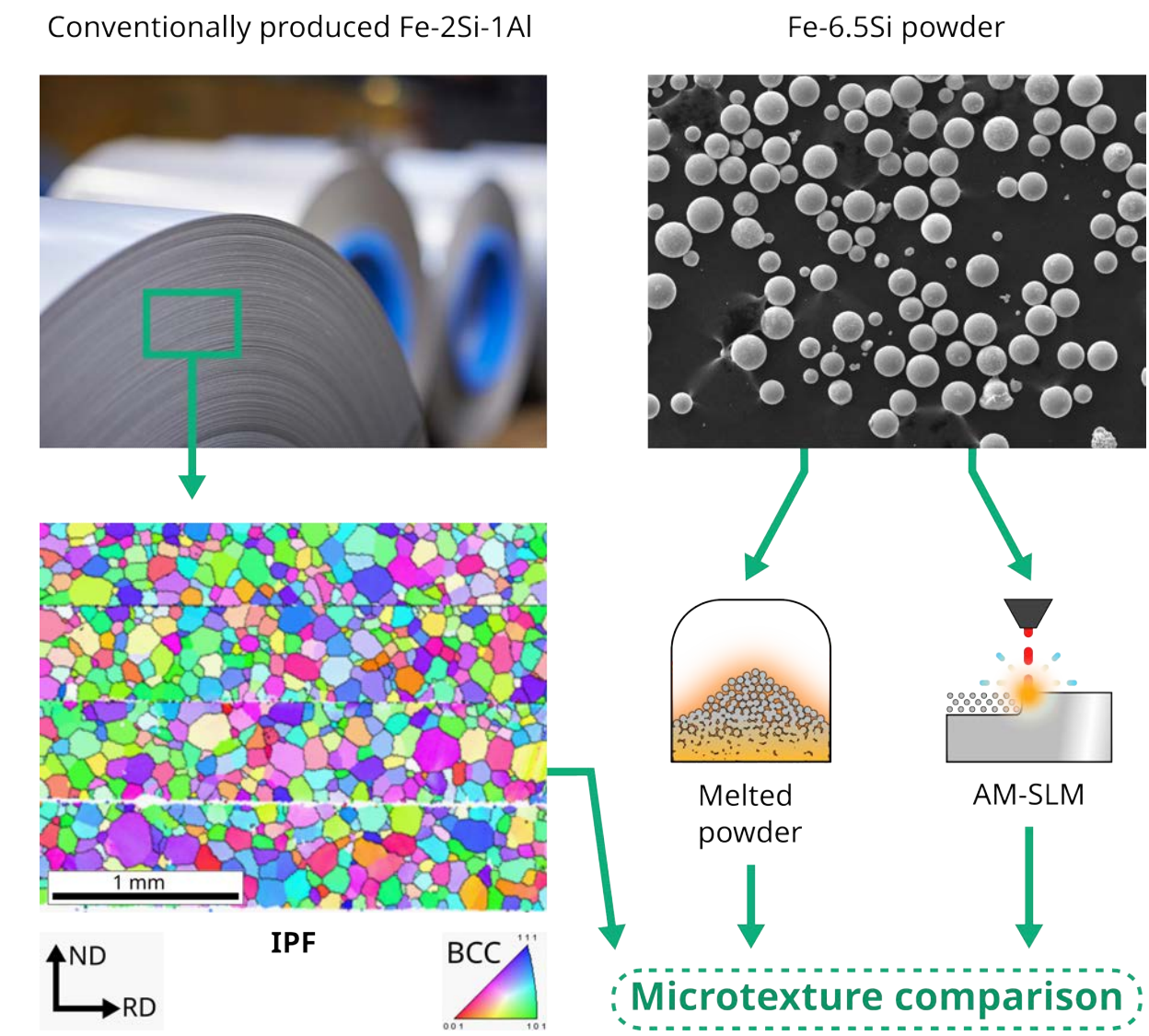

Fig. 1: Scheme of experiments.

Type of presentation: Poster

MS1-P-2490 In-situ heating of twin-roll cast Al-steel clad strip

Šlapáková M.[1], Křivská B.[1]

[1]Department of Physics of Materials, Charles University, Prague, Czech Republic

Email of the presenting author: slapakova@karlov.mff.cuni.cz

Aluminium-steel clad composite was manufactured by twin-roll casting, which ensures high quality bonding of the materials. An intermetallic layer of orthorhombic Al_5Fe_2 and monoclinic $Al_{13}Fe_4$ phase grew at the Al-Fe interface upon annealing above 500 °C. Those phases can deteriorate mechanical properties of the bond, if the thickness of the intermetallics exceeds a critical value. Thus understanding the formation and growth of the interface phases is of high importance.
The Al_5Fe_2 phase, which is closer to the steel side, has equiaxed grains, whereas the grains of the $Al_{13}Fe_4$ phase are elongated and perpendicular to the interface. Moreover, $Al_{19}Fe_4MnSi_2$ phase formed inhomogeneously on the Al13Fe4-Al interface.
During in-situ annealing in transmission electron microscope at 540 °C, the layer grew on the surface towards the steel side of the interface. A study of furnace-annealed samples revealed, that the bulk growth of the interface phase proceeds towards the aluminium side. The growth towards steel is a surface effect that takes place simultaneously with the bulk growth towards aluminium. The calculations of bulk diffusion indicate growth towards aluminium. The kinetics of growth of the intermetallic layer follows parabolic law in both cases – bulk and surface.

Acknowledgement: This research was funded by the GAČR project 20-00355Y and by SVV-260582.

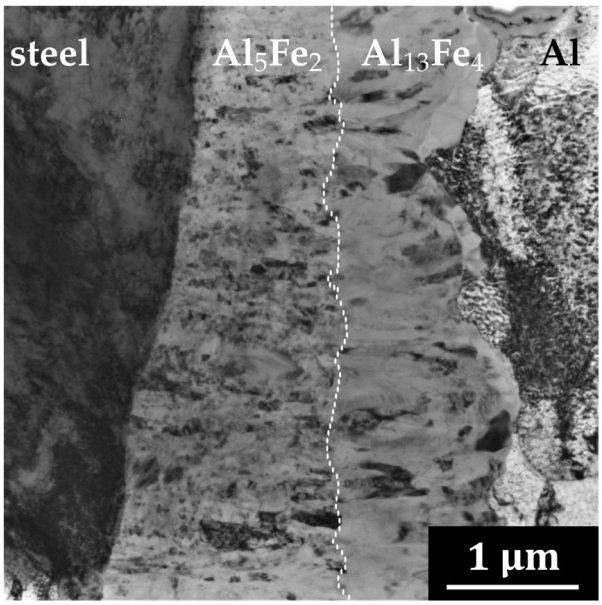

Fig. 1: TEM image of the Al-steel interface after 16 h annealing at 500 °C. Identified phases from left: steel, Al_5Fe_2, $Al_{13}Fe_4$ and Al.

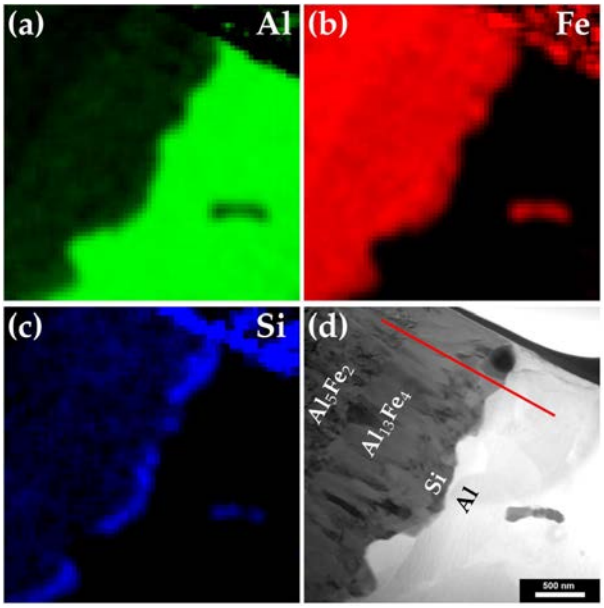

Fig. 2: Mapping of chemical elements by EDS in TEM across the intermetallic phases. (a) Al, (b) Fe, (c) Si, (d) respective STEM image, where Si denotes the $Al_{19}Fe_4MnSi_2$.

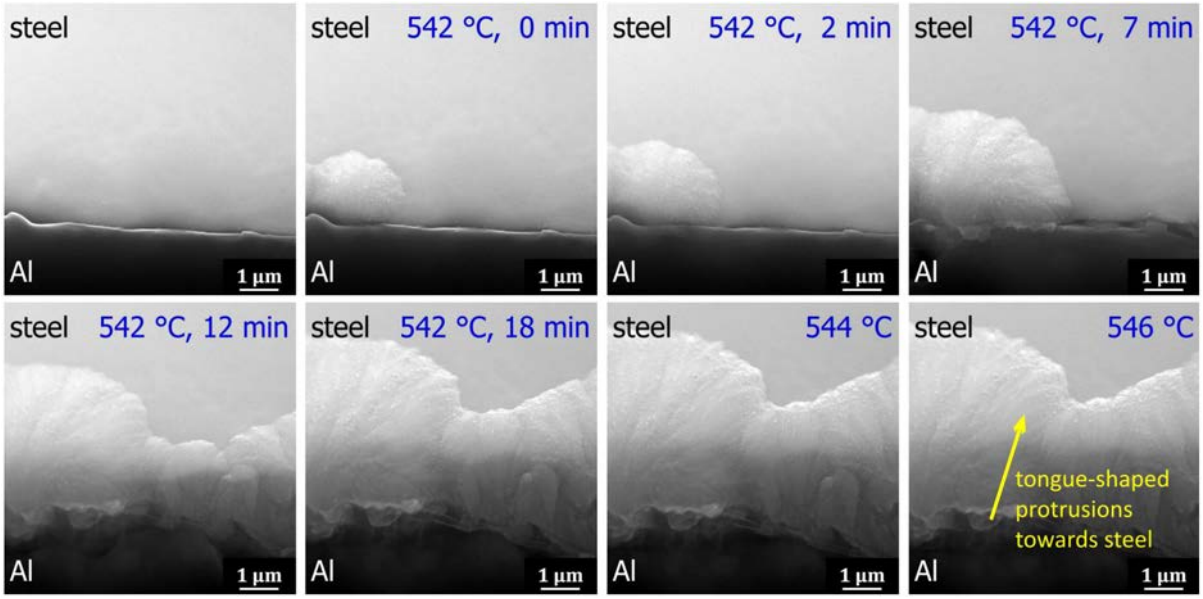

Fig. 3: TEM images taken in the MAG I mode (using SEI-COMPO contrast) of the intermetallics layer growth during in-situ annealing at 542 °C.

Type of presentation: Poster

MS1-P-2689 Thermal stability of hydro-extruded aluminum: Judging the distribution of amorphous and crystalline aluminum-oxide via plasmon mapping.

Švec P.[1, 2], Sadeghi B.[2], Skiba J.[3], Balog M.[2, 4]

[1]Institute of Physics, Slovak Academy of Sciences, Bratislava, Slovak Republic, [2]Centre of Excellence for Advanced Materials Application, Slovak Academy of Sciences, Bratislava, Slovak Republic, [3]Institute of High Pressure Physics, Polish Academy of Sciences, Warsaw, Poland, [4]Institute of Materials and Machine Mechanics, Slovak Academy of Sciences, Bratislava, Slovak Republic

Email of the presenting author: peter-svec@savba.sk

In the present work we will discuss the exceptionally high thermal stability of the HITEMAL [1] material and the strengthening mechanisms arising from the presence of two forms of aluminum oxide – amorphous and crystalline. The ultrafine-grained (UFG) aluminum material was fabricated by powder metallurgy techniques of blending, cold isostatic pressing and hydroextrusion under three distinct ratios (1:20, 1:96 and 1:626). The thermal stability was tested in the as received and annealed states. Different annealing temperatures were selected to satisfyingly map the future application temperature range. The heat-treatment temperatures were set to 300, 400 and 450°C for 24 hours. To address the outstanding thermal stability, the microstructural evolution of the HITEMAL material with respect to the size and distribution of the aluminum oxide disperzoids vs. UFG Al matrix was examined in detail after each treatment using EELS and EDS mapping. Multiple linear least squares fitting [2] was used to satisfyingly map and differentiate among the two present aluminum oxide forms and thus more precise calculations with respect to the Zenner drag phenomena [3] could be carried out.

[1] Balog M., Poletti C., Simancik F., Walcher M., Rajner W. The effect of native Al2O3 skin disruption on properties of fine Al powder compacts, Journal of Alloys and Compounds. 2011; 509(1):235-238.
[2] Leapman RD, Swyt CR. Separation of overlapping core edges in electron energy loss spectra by multiple-least-squares fitting. Ultramicroscopy. 1988;26(4):393-403.
[3] Nes E., Ryum N., Hunderi O. On the Zener drag. Acta Metallurgica 1985;33:11-22.

Acknowledgement: CEMEA project: ITMS project code 313021T081 supported by the Integrated Infrastructure Operational Programme funded by the ERDF.

Type of presentation: Poster

MS1-P-2702 Phase evolution clarification in Al86Ni8Gd6 amorphous alloy: A spotlight on Al20Ni6Gd4 phase and its peculiarities

Švec P.[1, 2], Mihalkovič M.[1], Janičkovič D.[1], Švec Sr P.[1]

[1]Institute of Physics, Slovak Academy of Sciences, Dúbravská Cesta 9, 845 11 Bratislava, Slovak Republic, [2]Centre of Excellence for Advanced Materials Application, Slovak Academy of Sciences, Dúbravská Cesta 9, 845 11 Bratislava, Slovak Republic

Email of the presenting author: peter-svec@savba.sk

Metallic ribbon with $Al_{86}Ni_8Gd_6$ composition was produced by standard planar flow casting method in amorphous state. Phase transformation follows upon heat treatment in 4 distinct crystallization stages. Detailed microstructural characterizations were carried out to explain unusual phenomenon shown in x-ray diffraction data, calorimetric and complementary resistometry measurements bound to the second transformation stage. The observed phenomenon was proven to be connected to a observed reordering on the sub-nanometer scale without previous chemical rearrangement forming from amorphous matrix surrounding fcc-Al(Ni) nanocrystals, appearing as a second and single transformation step. During the third transformation stage a new phase was observed. The unknown phase was clarified by density functional theory (DFT) calculations. The starting DFT input of atomic coordinates was extracted from a single structural projection by the means of high angle annular dark filed (HAADF, 101-200 mrad) and corresponding annular bright filed (ABF, 13-20 mrad) micrographs. Resulting structural model/phase composition was stated to be $Al_{20}Ni_6Gd_4$, further confirmation was achieved by x-ray diffraction refinement. The newly observed $Al_{20}Ni_6Gd_4$ phase possesses few peculiarities with respect to 180 deg in-plane rotation in [010] as shown in Fig. 1, most prominent in Ni site position. The full transformation sequence up to 850 K is explained by X-ray diffraction and supported with detailed scanning transmission electron microscopy and energy dispersive spectroscopy observations. Moreover, detailed phase diagram was calculated to clarify the computed results.

Acknowledgement: CEMEA project: ITMS project code 313021T081 supported by the Integrated Infrastructure Operational Programme funded by the ERDF. APVV-19-0369, VEGA 2/0144/21.

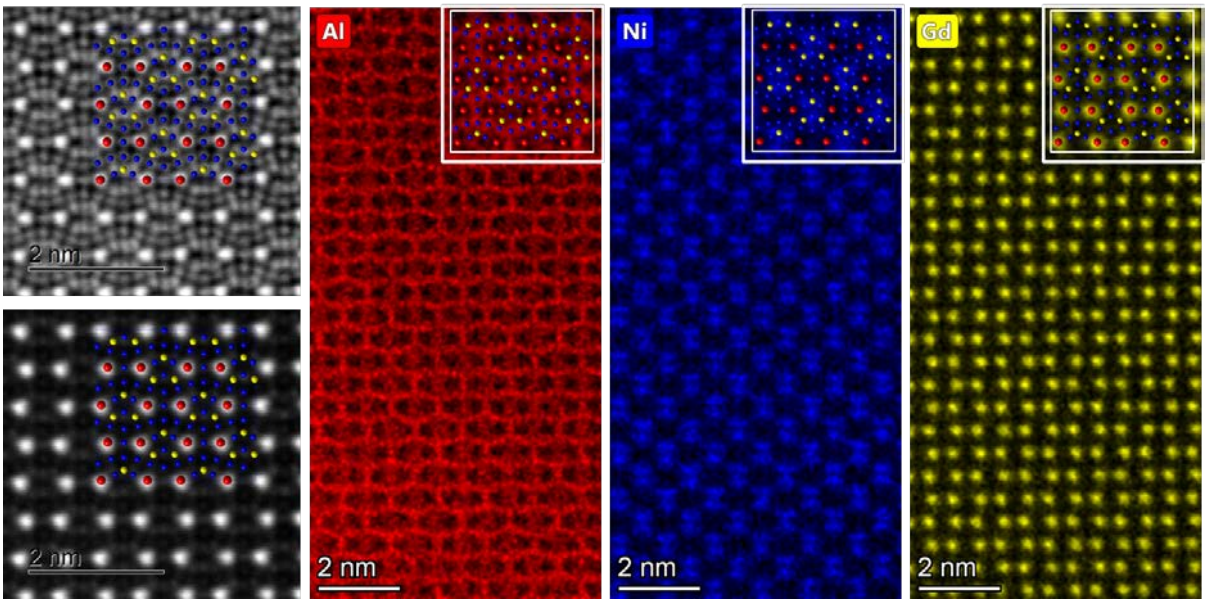

Fig. 1: $Al_{86}Ni_8Gd_6$ alloy annealed to 636K (10K/min). Inverted ABF (top left), HAADF (bottom left) micrographs and corresponding EDS maps. 2x2 unit cell overlay, $Al_{20}Ni_6Gd_4$, [010]. Al blue, Ni yellow, Gd red.

Type of presentation: Poster

MS1-P-2803 Modification of local ordering in Fe-B based metallic glasses during long-term room temperature ageing

Janotová I.[1, 2], Švec P.[1, 2], Janičkovič D.[1], Švec Sr P.[1]

[1]Institute of Physics, Slovak Academy of Sciences, 845 11 Bratislava, Slovakia, [2]2Centre of Excellence for Advanced Materials Application, Slovak Academy of Sciences, 845 11 Bratislava, Slovakia

Email of the presenting author: fyzisvec@savba.sk

Rapidly quenched amorphous Fe-B based system belongs to one of the most and longest studied amorphous alloy system which appeared since the report of discovery of Au-Si metallic glass in 1960 [1]. Research on preparation, stability and transformation to crystalline state in amorphous Fe-B ranges from 1970's, e. g. [2] till recent period. While most of the studies and developments were performed on ternary and more component alloys, Fe-B still remains a model system from which most of the nanocrystalline magnetic materials were developed by suitable alloying, e. g. Finemet, Nanoperm and several others. In all these systems both the stability of amorphous state as well as the transformation to stable crystalline state are of scientific and technical interest.

Transformation kinetics and especially differences in second-stage transformation reaction in long-term room-temperature aged rapidly quenched hypoeutectic Fe-B metallic glasses were investigated on amorphous $Fe_{86}B_{14}$ ribbons prepared by planar flow casting. Three sets of amorphous ribbons in different stage of ageing were considered: (1) ribbon prepared in 1995, (2) ribbon produced in 2005 and (3) freshly prepared ribbon.

Preliminary analysis of the three sets of samples by differential scanning calorimetry and electrical resistivity measurements as a function of temperature in linear heating regime indicated minimal changes in the kinetics of first-stage of crystallization and no detectable differences in the crystaline structure embedded in the remaining amorphous matrix. The second crystallization stage which involves the amorphous remains, however, exhibited significant differences in the kinetics of the process for the three sample sets. Details of these differences were further investigated by kinetic and diffraction methods and by STEM/EDS techniques analogous to those used in [3]. Changes in the stability of the amorphous remains due to prolonged room-temperature ageing were correlated with local ordering of the original amorphous matrix and with the mass transport mechanisms controlling nucleation and growth processes upon devitrification.

[1] Klement, W., Willens, R. H., and Duwez, P. O. L., Nature 187 (1960) 869–870.

[2] O'Handley, R. C., Hasegawa, R., Ray, R., and Chou C.-P., Appl. Phys. Lett. 29 (1976) 330.

[3] P. Svec et al., Journal of Alloys and Compounds 876 (2021) 160109.

Acknowledgement: APVV-20-0124, VEGA 2/0144/21, M-ERA.Net COSMAG, CEMEA project ITMS 313021T081 supp. by the Integrated Infrastructure Operational Programme funded by the ERDF.

Type of presentation: Poster

MS1-P-2813 Microanalyses for a better understanding of active soldering processes

Zobačová J.[1], Motlová T.[1], Vlček I.[1], Dupák L.[1], Zobač M.[1]

[1]Electron and Plasma Technologies, Institute of Scientific Instruments of the CAS, Brno, Czech Republic

Email of the presenting author: zobacova@isibrno.cz

Sapphire is a brittle, non-conductive material with excellent dielectric and thermal properties. It is used in advanced designs e.g. as part of an ion trap in extremely precise atomic clocks [1]. For these designs would be very beneficial to join sapphire dielectrics permanently to metallic electrodes. Standard soldering techniques fail when used with non-metallic surfaces but so-called active soldering overcomes problems with the wettability of dielectrics. Different thermal expansion coefficients of the sapphire and metal can induce very high stresses if not properly controlled. One way is to use a ductile solder with a low working temperature. Active solders contain active elements such as titanium as part of a pre-prepared soldering alloy or can be added during the soldering process [2]. Diffusion through solder can be sufficient to successfully wet the sapphire surface.

The aim of this work is an investigation of titanium sapphire bonding using indium based solder activated by titanium. Different sample configurations were prepared according to Figure 1. Pure In is very ductile and has a low melting point of 156 °C which avoids the use for higher working temperatures. However, diffusion of the Ti during processing rises dramatically the melting temperature (see [3]). The bonding quality of the joints was examined by electron microscopy (see Figure 2). EDX analysis reveals the diffusion rate and distribution of the Ti during processing.

For example, the scanning electron micrograph in Figure 3 shows differences between samples with and without additional Ti foil. The top row reveals the titanium foil did not melt uniformly in indium solder. The EDX microanalysis proved the presence of titanium beyond a few per cent in solder. The resulting solid-state solution may be detrimental concerning solder plasticity. The cracks on the interface of the sapphire surface may indicate the presence of plastic deformation, which, however, should be confirmed by future investigations.

Future research will look for connections between process parameters, diffusion rates and resulting material properties and microstructure to find out the optimal combination of the above. The goal is a strong vacuum-tight joint with a working temperature range from cryogenic temperature up to at least 200 °C. Also, more complex alloys such as InAg20Ti2 are considered for further investigation.

[1] P. Obšil et al., Multipath interference from large trapped-ion chains, New Journal of Physics. 21 (2019) 093039.
[2] J. Dupák et al., Pájení tvárnými aktivními pájkami, Zváranie-Svařování 48 (1999) 130–132.
[3] L.D. Gulay, J.C. Schuster, Investigation of the titanium–indium system, Journal of Alloys and Compounds. 360 (2003) 137–142.

Acknowledgement: The paper was created with the institutional support RVO:68081731.

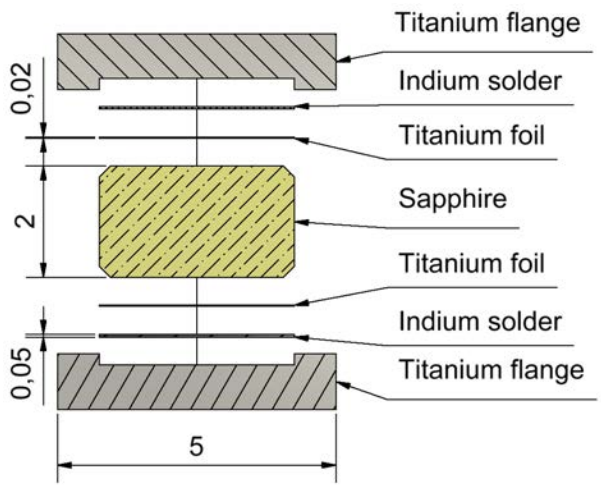

Fig. 1: Arrangement of the samples and their dimensions

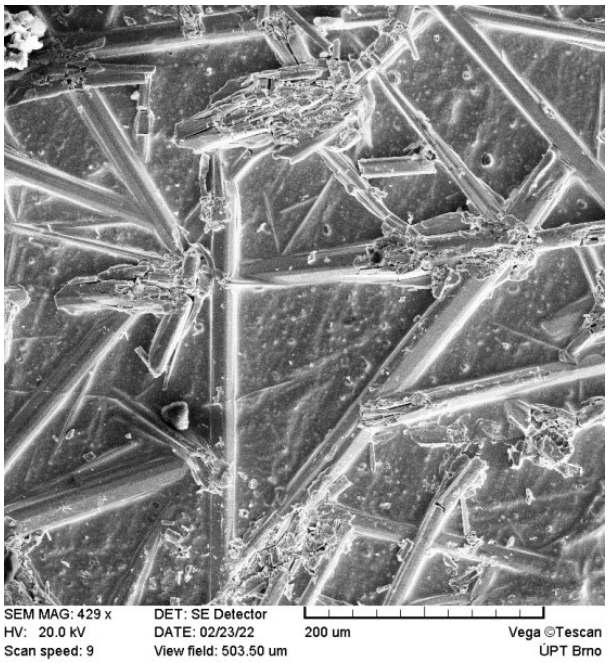

Fig. 2: Indium crystals formed in the cavity of the failed joint

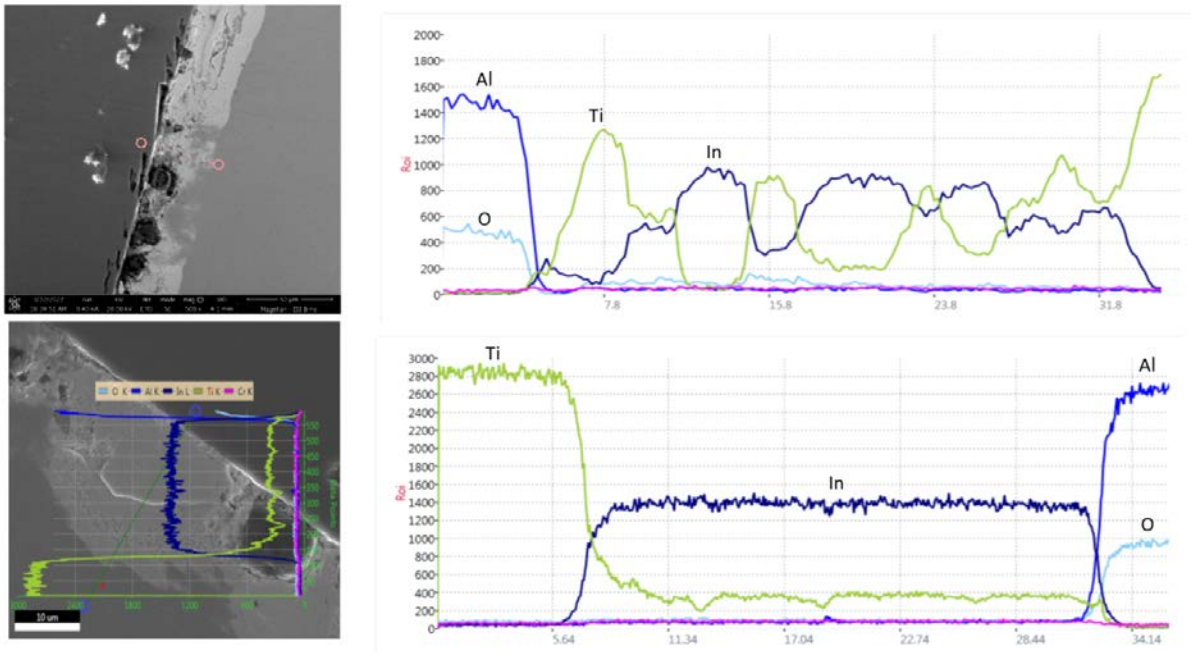

Fig. 3: EDX microanalysis of joint with (top) and without (bottom) titanium foil.

MS2 Ceramics, rocks and minerals

Type of presentation: Invited

MS2-IN-2596 A key to develop novel ceramics: Microstructural design

Kaya P.[1]

[1]Materials Research Institute (IMFAA), Aalen University, Aalen, Germany

Email of the presenting author: pinar.kaya@hs-aalen.de

The functionality of the materials used for model applications, such as batteries [1], fuel cells [2] thermoelectric devices [3], is strongly influenced by their microstructure. Therefore, understanding the microstructure–property relationship and the design of the microstructure at different length scales can improve the functionalities for many applications. Ceramics are promising candidates that can be used as a key component in thermoelectric generators, solid oxide fuel cells (SOFCs), and all-solid-state batteries (ASSBs). For large-scale production of these materials, not only the transport properties but also mechanical and electrochemical stability are of significance. For instance, electrical transport along the grain boundaries (TiCN/SiAlON composites and AlN ceramics [4,5]), designed interfaces (La2CuO4-based interfaces [6,7]) and particular crystallographic directions (polycrystalline PdCoO2 [8]) can be tuned, even by several orders of magnitudes. Apart from this, aging of the components under certain temperatures and/or pressure can change the microstructure and influence the mechanical properties, which are crucial for SOFC applications. Moreover, surface-near microstructural modification of NCM-based cathodes in Li-ion batteries enhances the rate capability [9]. In this talk, I will give several examples of the aforementioned microstructural aspects to tune the properties of materials for novel functionalities in energy applications.

References

[1] Wilson, J.R., Cronin, J.S., Barnett, S.A. and Harris, S.J, Journal of Power Sources 196, 7, 3443–34473 (2011).
[2] Prakash, B.S., Kumar, S.S. and Aruna, S.T., Renewable and Sustainable Energy Reviews, 36, 149–179 (2014)
[3] Mori, T. &, Toru, H., Scripta Materialia, 111, 44-48 (2016).
[4] Kaya, P., Gregori, G., Yordanov, P., Ayas, E., Habermeier, H.U., Maier, J. and Turan, S., J. Eur. Ceram. Soc, 37, 10, 3367-3373 (2017).
[5] Kaya, P., Suyolcu, Y.E., van Aken, P.A., Turan, S., Gregori, G. and Maier, J., J. Eur. Ceram. Soc. 41, 9, 4870-4875 (2021).
[6] Kaya, P., Gregori, G., Baiutti, F., Yordanov, P., Suyolcu, Y.E., Cristiani, G., Wrobel, F., Benckiser, E., Keimer, B., van Aken, P.A. and Habermeier, H.U., Logvenov, G., Maier, J., ACS Appl. Mater. Interfaces 10, 22786–22792 (2018).
[7] Suyolcu, Y. E., Christiani, G., van Aken, P. A, et al., J. Supercond. Nov. Magn, 33 1 107-120 (2020).
[8] Yordanov, P., Gibbs, A.S., Kaya, P., Bette, S., Xie, W., Xiao, X., Weidenkaff, A., Takagi, H. and Keimer, B, Physical Review Materials, 5, 1, 015404 (2021).
[9] Bolsinger, M., Weller, M., Ruck, S., Kaya, P., Riegel, H. and Knoblauch, V., Electrochimica Acta, 330, 135163 (2020).

Acknowledgement: I would like to thank all co-authors for their significant contributions to the works presented. Especially to Prof. J. Maier, Dr. E. Suyolcu, Prof. P.v. Aken.

Type of presentation: Oral

MS2-O-2843 Quantifying Ordering Phenomena at the Atomic Scale in Rare Earth Oxide Ceramics via EELS Elemental Mapping

Lammer J.[1,2], Berger C.[3], Löffler S.[4], Knez D.[1], Bucher E.[3], Haberfehlner G.[1], Kothleitner G.[1,2], Hofer F.[1], Sitte W.[3], Grogger W.[1,2]

[1]Institute of Electron Microscopy and Nanoanalysis (FELMI), Graz University of Technology, [2]Graz Centre for Electron Microscopy (ZFE), Graz, Austria, [3]Chair of Physical Chemistry, Montanuniversitaet Leoben, Leoben, Austria, [4]University Service Centre for Transmission Electron Microscopy (USTEM), TU Wien, Vienna, Austria

Email of the presenting author: judith.lammer@felmi-zfe.at

Oxide ceramics qualify for multiple applications for future energy technologies: small changes in the concentration of the elements already lead to changes of the macroscopic properties such as electronic and ionic conductivity and catalytic activity. Precise characterization techniques, e.g. EELS or EDX in STEM, help to uncover these secrets of the nanoworld. Our investigations on new oxide ceramics – promising materials as triple conducting oxides (proton-, oxygen ion- and electron-conducting) – revealed interesting correlations visible within high-resolution EELS elemental maps: perovskite- and Ruddlesden-Popper phases containing rare earth elements exhibit variations of their element distributions within equivalent crystal sites. This behaviour is vividly observable in lanthanum barium ferrate, a second order Ruddlesden-Popper phase where both La and Ba occupy the A-sites within the crystal. Our experiments show that La favours sites in the rock salt layer, whereas Ba prefers the perovskite block. Moreover, the Ba/La distribution varies from atomic column to atomic column within both rock salt and perovskite layers.

Unfortunately, acquiring elemental maps at atomic scale is always prone to channelling effects, which lead to additional intensities stemming from neighbouring atomic columns – a circumstance which renders a straightforward, reliable quantification impossible. We address this issue by using inelastic multislice calculations based on Slater-type orbitals in order to overcome the problem with unknown neighbouring off-axis intensities. After subtracting the additional off-axis intensity we successfully performed a column-by-column quantification: through taking advantage of the large changes in the elemental distribution from column to column we introduced a quantification technique which substitutes inelastic scattering cross sections during the quantification step by parameters obtained from the actual experiment [1]. We revealed that (in terms of crystal structure) equivalent atomic columns within either the rock salt layer or the perovskite layer do not exhibit distinct La/Ba ratios but a broad variation in concentration.

[1] J. Lammer, C. Berger, S. Löffler, et al., Ultramicroscopy, 234, 11347 (2022)

Acknowledgement: Financed by FFG (853538), Klima- und Energiefonds within "Energieforschung (e!MISSION)", EU Horizon 2020 programme (823717-ESTEEM3) and FWF (I4309-N36)

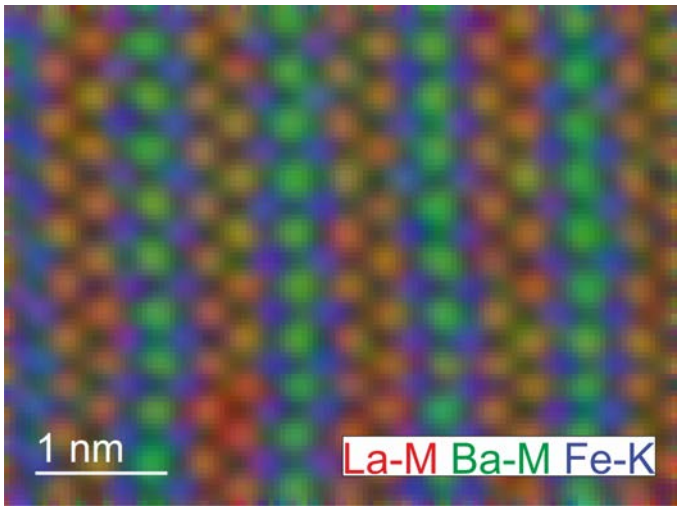

Fig. 1: Experimental EELS elemental map of barium lanthanum ferrate.

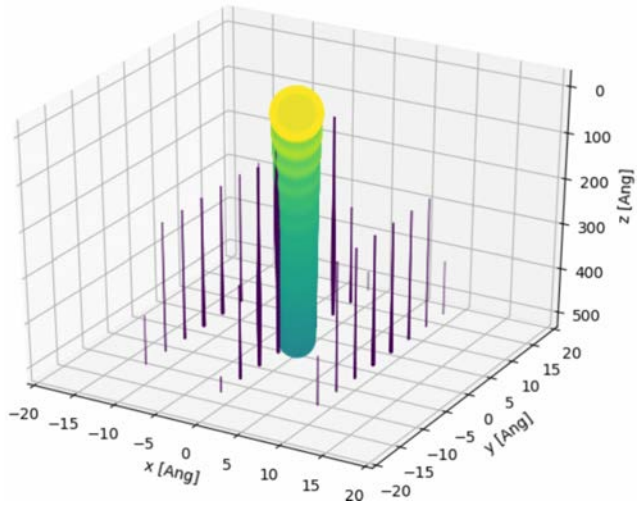

Fig. 2: Simulated EELS Ba-M_{45} intensity (at 781 eV) showing contributions from on-axis atoms (green/yellow) and neighbouring atomic columns (purple).

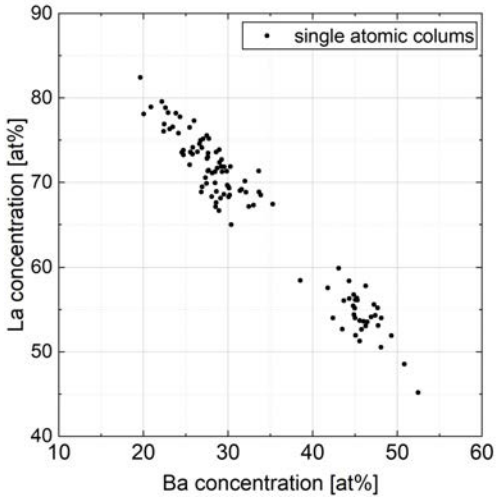

Fig. 3: Ba and La concentrations for each atomic column extracted from the region shown in Fig. 1.

Type of presentation: Oral

MS2-O-2578 Atomic-scale characterization of polytypic defects in Li0.33La0.56TiO3

Borštnar P.[1,2], Spreitzer M.[1], Dražič G.[3], Daneu N.[1]

[1]Advanced Materials Department, Jožef Stefan Institute, Ljubljana, Slovenia, [2]Jožef Stefan International Postgraduate School, Ljubljana, Slovenia, [3]Inorganic Chemistry and Technology, National Institute of Chemistry, Ljubljana, Slovenia

Email of the presenting author: petrusa.borstnar@ijs.si

The development of Li-ion all-solid-state batteries demands a stable and highly conductive solid electrolyte such as $Li_{0.33}La_{0.56}TiO_3$ (LLTO) [1]. To obtain high conductivity in this material and reduce the effect of the grain boundaries [2],[3], we altered the La/Ti ratio in the starting compositions of the ceramic LLTO. In a sufficiently La-rich sample (La:Ti ratio 0.61) we observed exaggerated grain growth triggered by the nucleation of Ruddlesden-Popper-type phase $Li_2La_2Ti_3O_{10}$. To understand its role in microstructure development, we thoroughly investigated the structural characteristics of polytypic lamellae by STEM.

$Li_2La_2Ti_3O_{10}$ was present as in-grain non-periodic lamellae and less commonly as individual lamellar grains. The typical structure of this phase consists of 2 atomic columns of La that interchange with Ti columns, forming $(La_2Ti_3O_{10})^{2-}$ pseudo-perovskite block. Each such block is shifted in the [100] direction for ½ of the unit cell and separated by Li-rich layer. Blocks with a higher number of La-rich layers were also observed. In these sequences, the intermediate La-rich layers show a darker contrast than the edge ones (74% relative intensity), indicating a lower occupancy of La. As the charge of the two neighbouring edge layers $(LaO)^{1+}$ is compensated by $(Li_2O_2)^{2-}$ layer, the intermediate layers must be charge neutral. Such lamellae are composed of the two end-members: $Li_2La_2Ti_3O_{10}$ and LLTO perovskite that corresponds to one of the compositions $Li_{3x}La_{2/3-x}TiO_3$. A comparison of experimental and simulated images showed a weak contrast in the Li_2O_2 layers in the HAADF-STEM images that should not be present if the layers would be occupied only by O and Li. This suggests that these layers contain a low concentration of La, which is a result of an ionic exchange between the Li-layers and the neighbouring La-layers. Furthermore, we believe that pronounced La-Li exchange occurs in the LaO-Li_2O_2-LaO sequences of the blocks with higher n-values. Using the simulations, we were able to estimate the degree of ionic exchange in the polytypic lamellae. At higher sintering temperatures $Li_2La_2Ti_3O_{10}$ sequences were recrystallized to LLTO due to Li evaporation and a radical ionic exchange.

This study provides a novel insight into the $Li_2La_2Ti_3O_{10}$ phase and its modulated structures that have a significant impact on LLTO grain growth and microstructure. By comparing the experimental images with simulations, we were able to quantify compositional changes between the layers of LLTO and $Li_2La_2Ti_3O_{10}$.

References:
[1] Y. Inaguma et al. Solid State Commun., 1993, 86(10),689–693.
[2] C. Ma et al. Energy Environ. Sci., 2014, 7(5),1638–1642.
[3] S. Sasano, R. Ishikawa, G. Sánchez-Santolino, H. Ohta, N. Shibata, and Y. Ikuhara. Nano Lett., 2021, 21(14),6282–6288.

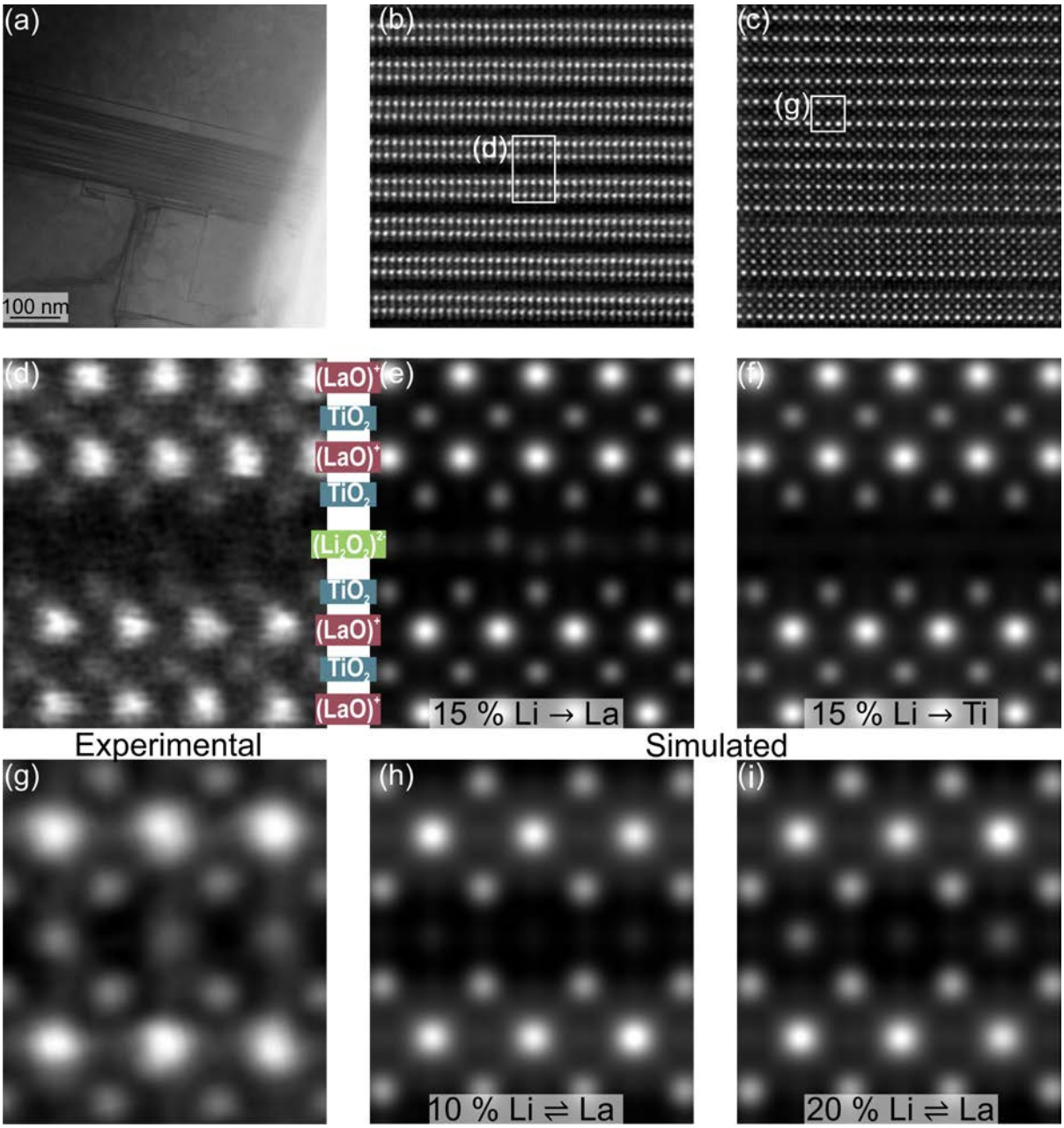

Fig. 1: a) In-grain lamella. b) HAADF image of $Li_2La_2Ti_3O_{10}$ and c) blocks with a higher number of La-rich layers followed by LLTO. d) Exp. image of $Li_2La_2Ti_3O_{10}$ compared with a simulation where 15% of Li is exchanged with e) La and f) Ti. g) Exp. image of LLTO compared with a simulation where h) 10% and i) 20% of Li and La are exchanged.

Type of presentation: Oral

MS2-O-2789 Stacking faults dominant strengthening mechanism behind the anomalous hardness variation of TaN/TiN multilayer films

Huang Y.[1,2], Zhuo C.[1], Terziyska V.[2], Mitterer C.[2], Zhang Z.[1,2]

[1]Erich Schmid Institute of Material Science, Austrian Academy of Sciences, [2]Department of Materials Science, Montanuniversität Leoben

Email of the presenting author: yong.huang@oeaw.ac.at

Multilayered materials, which consist of the periodic alternation of different layers, can realize drastic hardness enhancement when the individual layer thickness decrease to the nanoscale. Lots of literature suggested that the bilayer period plays a key role in determining the enhancement of hardness and elastic modulus for multilayer films. Extensive investigations also reveal several commonly accepted strengthening mechanisms including dislocation pile-ups, coherent stresses, misfit dislocations, elastic moduli mismatch or Koehler stress, and the confined layer slip (CLS) model [1–4]. Among superlattice transition metal nitrides systems TaN/TiN show great potential due to their high hardness and good wear resistance.
In this work, TaN/TiN superlattice films with four bilayer periods Λ were synthesized by reactive magnetron sputtering. The hardness measurement by nanoindentation (Fig.1(b)) and X-ray diffraction (XRD) patterns (Fig.1(c)) both show that these TaN/TiN multilayer films exhibit an inverse trend in hardness and interfacial coherency compared to previous studies. These thin films were then characterized by spherical aberration-corrected (Cs-corrected) transmission electron microscopy (TEM, JEOL 2100F). Detailed high-resolution TEM (HRTEM) studies revealed that a high density of stacking faults (SFs) appeared in Λ= 20 nm sample and abundant SFs cannot only enhance the hardness but also relieve the interfacial stress. There are at least two types of intrinsic SFs including and (Fig.2). Besides, two stacking sequences, which was predicted by DFT calculation [5], have also been observed (Fig.3). Different leading partials inside TaN layers meet and form sessile dislocations, like well-known Lomer-Cottrell lock (Fig.4). This well explains the hardness variation of these multilayers and points out a good direction for designing multilayer nitrides.

Acknowledgement: Kindly acknowledge the financial support by the Austrian Science Fund (FWF): No. P 33696. Thanks to Stanislav Žák and Megan J. Cordill on hardness measurement.

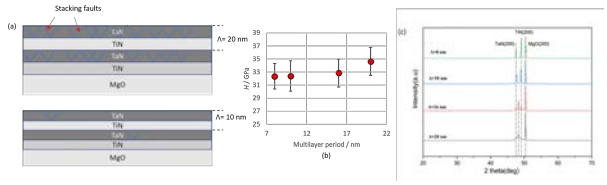

Fig. 1: (a) Schematic of TaN/TiN multilayer films with Λ= 20 nm and Λ= 10 nm (b) nanoindentation hardness and (c) XRD patterns of TaN/TiN films with different bilayer period

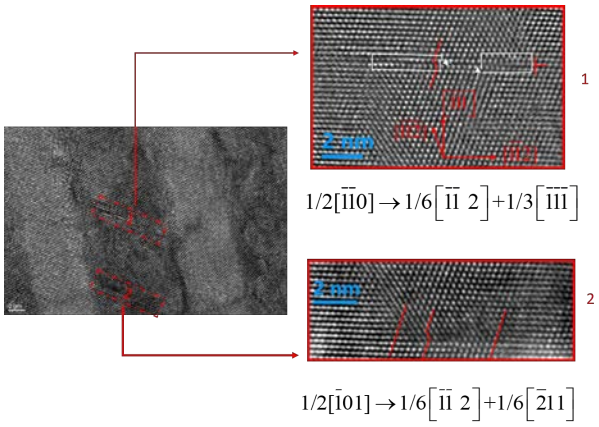

Fig. 2: Stacking faults configuration in Λ=20 nm multilayer

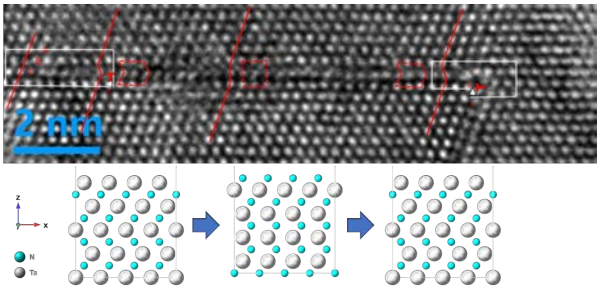

Fig. 3: Two different stacking sequences of the stacking fault

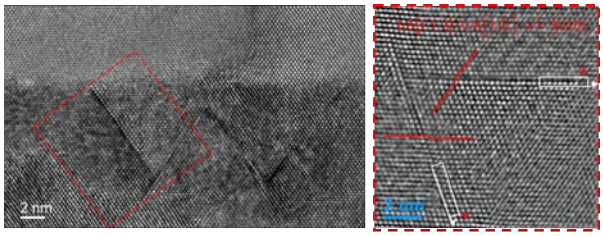

Fig. 4: Lomer-Cottrell lock bounded by two Shockley partials

Type of presentation: Oral

MS2-O-2667 High resolution CT study of microstructure defects behaviour in deformed NiTi prepared by spark plasma sintering

Šimek D.[1], Samal S. M.[1], Ahmed U.[1], Kopeček J.[1]

[1]FZU Institute of Physcis, Academy of Sciences of the Czech Republic, Prague, Czech Republic

Email of the presenting author: simek@fzu.cz

Spark plasma sintered (SPS) nickel-titanium [1] contained intrinsical defects. Most of them being the pores (Figure 1) stemming from the technology of preparation, but also inclusions (Figure 2) were observed in smaller voluminar percentage in the resulting bulk material. Upon tensile loading the inclusions exhibit different efect on the surrounding matrix based on their stiffness difference. The effect of the deformation of pores and inclusions can be evaluated on the statistical basis and compared with the mean bulk material. We utilized the method of high resolution X-ray computed tomography (micro-CT) to visualize the distribution of pores and heavy inclusions in the specimen and employed in-situ loading in combination with the CT scanning. Statistical parametrization of the deformation of defects based on their absorption was then employed to estimate the stiffnes of the inclusions. The CT, as well, allowed to locate the defects for their more thorough inspection using scanning electron microscopy (SEM) and energy-dispersive analysis of their X-ray spectra (EDAX) to identify possible source of the impurities.

Reference:

[1] S. Samal, O. Molnárová, F. Pruša, J, Kopeček, M. Škodová, L. Abate, L. Heller, P. Šittner, I. Blanco: Net-Shape NiTi Shape Memory Alloy by Spark Plasma Sintering Method, Appl. Sci. 2021, 11, 1802. https://doi.org/10.3390/app11041802

Acknowledgement: The work is supported by the Czech Ministry of Education, Youth and Sports (Project No. SOLID21 - CZ.02.1.01/0.0/0.0/16_019/0000760).

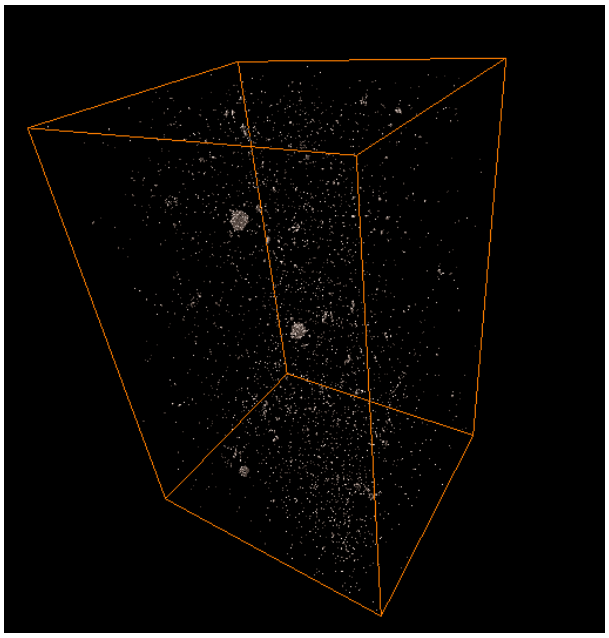

Fig. 1: Pores in the reconstructed 3d gauge volume

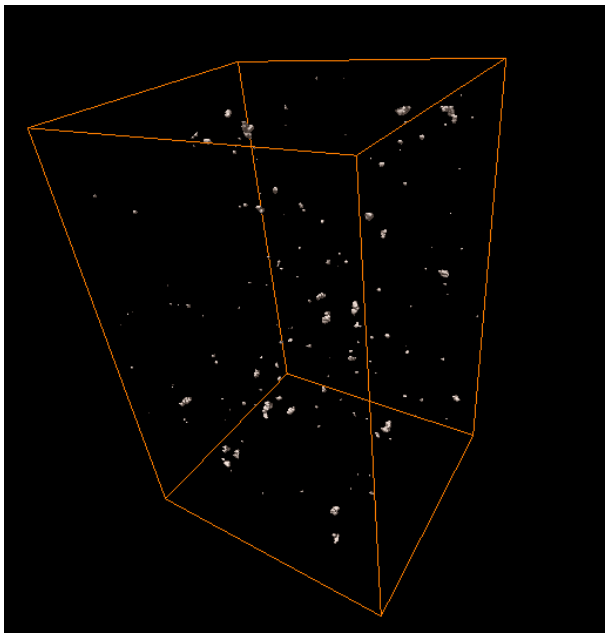

Fig. 2: Heavy inclusions in the reconstructed 3d gauge volume

Type of presentation: Invited

MS2-IN-3034 Nano crystallography from 3-dimensional electron diffraction: a powerful tool to uncover supergene minerals

Steciuk G.[1], Plašil J.[1], Hornfeck W.[1]

[1]Department of Structure Analysis, Institute of Physics ASCR, v.v.i., Na Slovance 2, CZ-182 21 Prague 8, Czechia

Email of the presenting author: steciuk@fzu.cz

Nowadays, the advancements in electron diffraction techniques allow us to take up new challenges in terms of structural characterization for samples that were previously overlooked [1]. In the mineralogy area, supergene minerals are great examples of samples that easily fail to be characterized by conventional analyses by X-ray methods (on single crystal or powder). Due to their formation conditions, they often form as an assembly of sub-micrometric crystals, poorly crystalline and they can present compositional or structural variations at the nanoscale. Moreover, the concomitant presence of other minerals makes them difficult to isolate. This is especially the case for uranium and arsenate-based supergene minerals.

The exploitation of uranium as a source of energy has not been just beneficial and today, there is a need to effectively cope with the aftermath of mining and processing of the U ores. On the other hand, the decomposition of primary As-containing sulfides and sulfosalts potentially leads to a release into the environment of significant amounts of arsenic, heavy metals, and metalloids. In ore deposits, supergene minerals are formed as resulting products of these reactions and they serve as a temporary or final sink for such toxic elements otherwise released into the groundwater systems. Therefore, to give proper answers and solutions to the environmental problems, the detailed knowledge of the structure combined with physical and chemical properties is of great importance as it can be used to assess and predict the behavior and the mobility of elements during weathering, both natural or anthropogenically induced.

To analyze the structure of supergene minerals, a recent approach consists in using one of the 3-dimensional electron diffraction techniques (3D ED) [1] under specific experimental conditions. In order to reach the finest structural details, accurate data analysis benefits from the latest developments of the software PETS2 used for the data reduction together with the application of the dynamical theory of diffraction in the refinement [2]. From the data collection to the analysis, the different crystallographic challenges specific to natural samples will be illustrated through recent examples of uranium (vyacheslavite and sedovite) and arsenate (kaatialaite and krupičkaite) supergene minerals [3-4].

[1] Gemmi, M. et al. ACS Cent. Sci. 5, 1315–1329 (2019), and Gemmi, M. & Lanza, A. Acta Cryst. B 75, 495–504 (2019). [2] Palatinus, L. et al. Acta Cryst. B 71, 740–751 (2015), and B 75, 512–522 (2019). [3] Steciuk, G. et al. American Mineralogist, 107, 131–137 (2022), and Steciuk, G. et al. Inorg. Chem. 60, 15169–15179 (2021). [4] Steciuk, G. et al. IUCrJ 8, 2052–2525 (2021), and Steciuk, G. et al. J. Geosci. 66, 37–50 (2021).

Acknowledgement: We acknowledge projects No. SOLID21 CZ.02.1.01/0.0/0.0/16_019/0000760, LM2018110, the GACR projects 17-09161S, 20-11949S, and 18-10438S.

Type of presentation: Poster

MS2-P-2706 Multimodal and multi-resolution approach for defects analysis on the example of Additively Manufactured healable aluminium alloy

Gheysen J.[1], Brinek A.[2], Winiarski B.[3], Chirazi A.[3], Pyka G.[1], Kaiser J.[2], Villanova J.[4], Simar A.[2]

[1]UCLouvain, Belgium, julie.gheysen@uclouvain.be, grzegorz.pyka@uclouvain.be, aude.simar@uclouvain.be, [2]CEITEC BUT, Czech Republic xbrine02@vutbr.cz, jozef.kaiser@ceitec.vutbr.cz, [3]ThermoFisher Scientific, France, bartlomiej.winiarski@thermofisher.com, ali.chirazi@thermofisher.com, [4]ESRF, Grenoble, France, julie.villanova@esrf.fr

Email of the presenting author: xbrine02@vutbr.cz

Aluminium alloys are widely used in aerospace and aeronautic industries because of their excellent strength-to-weight ratio. To increase the part's lifetime, a solution would be to use a material able to heal its damage and restore its continuity. The most advanced man-made self-healing materials are polymers [1]. Designing self-healing metals is more challenging because the mobility of the healing phase is insufficient at room temperature. It requires a heat treatment to trigger the migration of these healing agents towards the damage sites and allow their healing [2]. However, the damage and its healing are hard to quantify using only surface observations. Mostly due to the changing behaviour after the healing process (such as the oxidation of the surface during the healing heat treatment) and with limited access to tracking, the damages as the correlative task is somewhat more challenging because the volume of interest is typically hidden beneath the sample surface. Therefore, a multiscale and multimodal imaging approach is required to evidence the healing mechanism and efficiency.
Correlative tomography (CMT) [3] is a concept of spatial registration in two and three dimensions (2D and 3D) of many imaging modalities - light microscopy (LM), electron/ion microscopy (EM, IM), X-Ray tomography, 2D/3D EBSD [2], EDS, Raman, etc.) - that allows various types of information, and at different length-scale, to be collected for the same region of interest (ROI). Therefore, this research aimed to develop a precise, robust and controlled multiscale analysis workflow for the evaluation of the evolution of the cracks and pores dimensions during the healing of an AlMg alloy, using three-dimensional (3D) correlative microscopy/tomography (fig. 01).

Acknowledgement: We acknowledge Czech Nano Lab Research Infrastructure supported by MEYS CR (LM201811 0) and the Ministry of Health of the Czech Republic (17 –31276A).

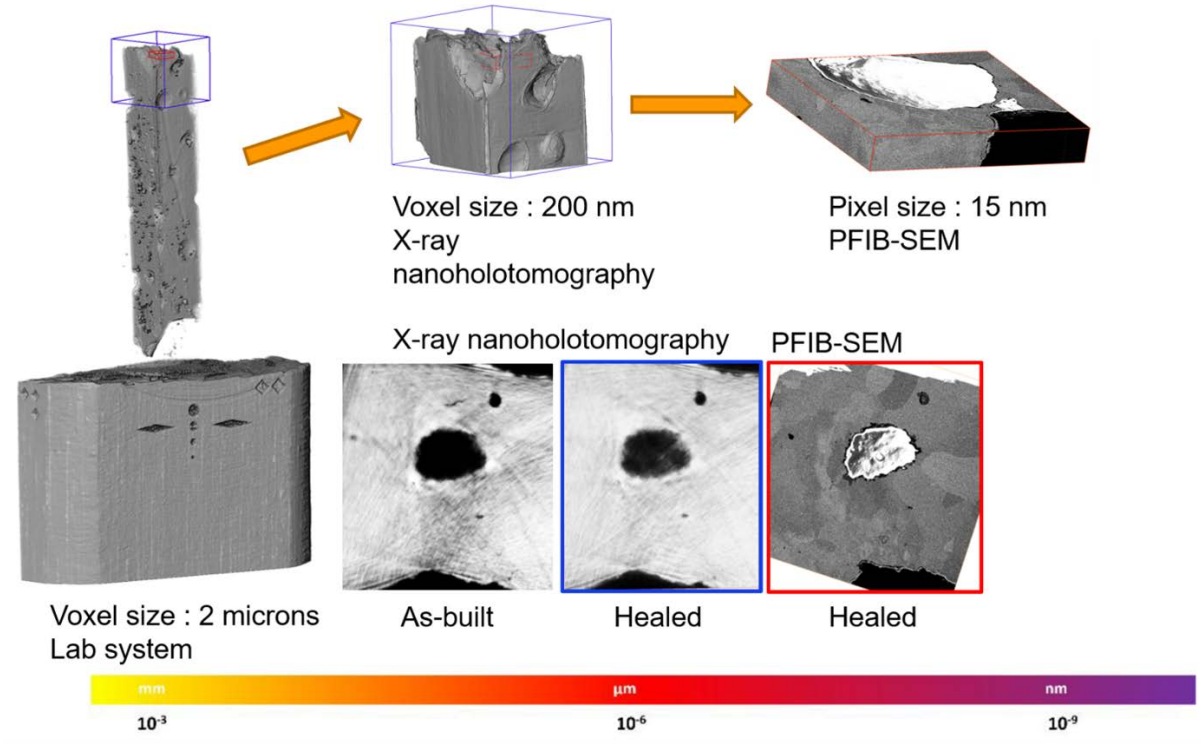

Fig. 1: Correlative microscopy approach for healable aluminium alloy

MS3 Polymers, biomaterials and soft materials

Type of presentation: Invited

MS3-IN-2878 Extracellular Vesicles and biomimetic membranes: an Atomic Force Microscopy point of view

Parisse P.[1,2]

[1]Istituto Officina dei Materiali - Italian National Research Council, [2]Elettra Sincrotrone Trieste

Email of the presenting author: parisse@iom.cnr.it

Extracellular vesicles (EVs) are tiny lipid-bilayers enclosed containers sending messages through their cargo and surface markers from one cell to another. Initially considered as “trash”, they are getting more and more recognized as intercellular mediators and actual players in the intercellular communications and extracellular matrix remodeling [1]. Due to their heterogeneity in size (from 30 nm to micrometer scale) and in origin (endosomal or from cell membrane budding) their isolation and characterization are not yet standardized hampering their actual use in diagnosis and/or therapy. Among the different characterization techniques of EVs, Atomic Force Microscopy starts to be a quite common tool for the direct visualization of single vesicles and for the evaluation of size distribution [2]. Moreover combined with force-spectroscopy can provide nanomechanical characterization helping in distinguishing vesicles from other co-isolated particles and in defining peculiar properties of specific subpopulations of EVs. Here together with the classical study of EVs immobilized on surfaces we will show how AFM can turn useful also for the investigation of the interaction of EVs with biomimetic membranes (resembling the plasma membrane) [3], giving morphological and structural insights on the fusion mechanisms.

References: [1] M. Mathieu, et al. Nat Cell Biol 2019, 21, 9 ; [2] P. Parisse et al. Eur. Biophys. 2017, 46, 813, [3]F. Perissinotto et al. , Nanoscale 2021 13, 5224

Type of presentation: Invited

MS3-IN-2935 Synergy of Scanning Electron and Light Microscopies in Visualization of Swollen Hydrogels and Effect of Hydrogel Parameters on the Image: Artifacts and Reality

Dušková-Smrčková M.[1], Kaberova Z.[1], Karpushkin E.[1], Nevoralová M.[1], Vetrik M.[1], Šlouf M.[1]

[1]Institute of Macromolecular Chemistry, Czech Academy of Sciences, Prague

Email of the presenting author: m.duskova@imc.cas.cz

Open macroporosity is a crucial geometrical property of many hydrogel scaffolds in tissue engineering. The exact knowledge of hydrogel microstructure, mainly its pore topology, is a critical issue
in hydrogel engineering. For visualization of the swollen hydrogels, cryogenic or high vacuum scanning electron microscopies (cryo-SEM or HVSEM) are frequently used. At the same time, the possibility of artifact-biased images is frequently underestimated. The major cause of artifacts is the formation of ice crystals upon freezing of the hydrated gel. Some porous hydrogels can be visualized with SEM without the danger of artifacts because the growing crystals are accommodated within already existing primary pores of the gel. However, the possibility of secondary pores formed in soft gel matrix is linked to matrix swelling ratio, its mechanical strength, and its primary morphological structure.

We have determined semiquantitatively the limits of the swelling degree and mechanical strength within which the true reproduction of the hydrogel morphology is evidenced. To link hydrogel's primary structure and investigate a series of methacrylate hydrogels made by crosslinking polymerization of glycerol monomethacrylate and 2-hydroxyethyl methacrylate including their interpenetrating networks. The hydrogel morphology was studied using cryo-SEM, HVSEM, environmental scanning electron microscopy (ESEM), laser scanning confocal microscopy (LSCM), and classical wide-field light microscopy (LM). The cryo-SEM and HVSEM yielded artifact-free micrographs for a limited range of non-porous hydrogels and for macroporous gels. A true non-porous structure was observed free of artifacts only for hydrogels exhibiting relatively low swelling and high elastic modulus above 0.5 MPa, whereas for highly swollen and/or
mechanically weak hydrogels the cryo-SEM/HVSEM experiments resulted in secondary porosity. In this contribution, we present several cases of severe artifact formation in PHEMA and PGMA hydrogels during their visualization by cryo-SEM and HVSEM. We also put forward an empirical correlation between hydrogel morphological and mechanical parameters and the occurrence and intensity of artifacts.

Acknowledgement: Czech Science Foundation No. 17-08531S (MD, ZK, MV), Technology Agency of the Czech Republic TE01020118 and TN01000008 (experimental equipment at IMC)

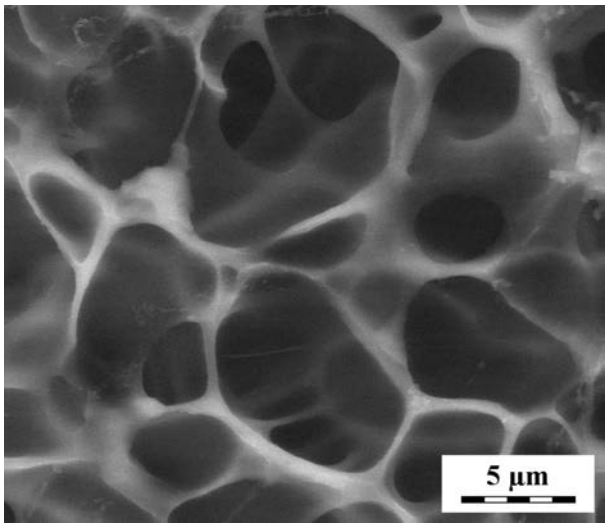

Fig. 1: Cryo-SEM micrograph of the water-swollen hydrogel prepared from lightly crosslinked glycerol monomethacrylate (water content 85 wt.%).

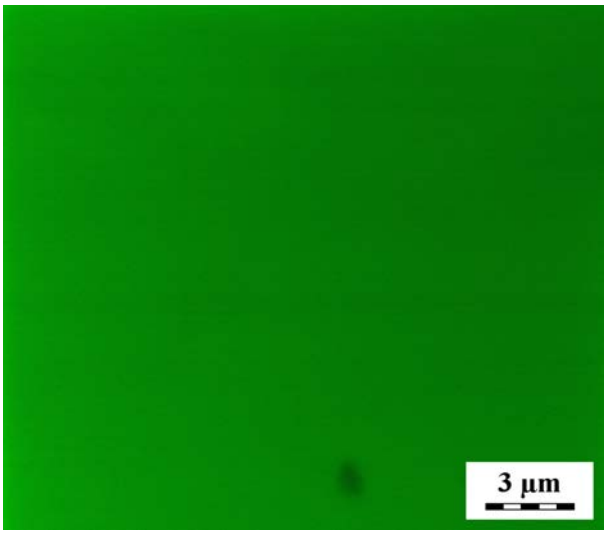

Fig. 2: Laser scanning confocal microscopy image of the same hydrogel as shown in Fig. 1 (contrasted with fluorescein).

Type of presentation: Oral

MS3-O-2798 Ultrastructural analysis of hydrogels and its contribution to understanding their mechanical and transport performance

Sedlacek P.[1], Smilek J.[1], Trudicova M.[1], Pekar M.[1]

[1]Brno University of Technology, Faculty of Chemistry

Email of the presenting author: sedlacek-p@fch.vut.cz

When something is soft, it is not necessarily weak as well. It is especially true for hydrogels as outstandingly powerful class of soft matter. Since the first appearance of the term “hydrogel” in scientific literature in 1894, these materials have continuously attracted substantial attention in science and technology. Currently available gels are materials of versatile composition, preparation, and properties, successfully utilized in numerous applications including biomedical, environmental, or in the fields of personal care and bioseparations. In general, the very essence of their functionality is rooted in their structure, i.e. network architecture, mesh or pore size, pore distribution etc., and in their binding ability based on a combination of chemical and physical structural features. We have put a considerable effort to develop a complex methodology for revealing the causal relationship between chemical and morphological structure of hydrogels and their application-relevant properties, especially the mechanical and transport (i.e. barrier and/or release) performances. This contribution will summarize this original methodology and illustrate its usefulness on the specific example of semi-interpenetrating polymer network hydrogels – modern gel-based controlled release systems with tailorable ultrastructure and material properties.

Type of presentation: Oral

MS3-O-2810 Nanobubble-assisted nanostructuring of water-immersed solid surfaces

Janda P.[1], Tarábková H.[1]

[1]J. Heyrovský Institute of Physical Chemistry, CAS, Dept. of Electrochemical Materials

Email of the presenting author: pavel.janda@jh-inst.cas.cz

Gaseous nanobubbles populating water-immersed solid surfaces were found to act as surface nanostructuring tools. The nanostructuring mechanism relies on tension forces FST = πdNBΓwa derived from surface tension water/air (Γwa ≈ 0.072 N/m). Externally applied short mild pressure drop (-10kPa/sec) triggers nanobubble expansion. Nanobubble energy minimization leads to an increase of its curvature, reflected by decreasing the apparent contact angle θa and consequently, by increasing the longitudinal component of surface tension FL = FST cos(180 − θ) with stress/strain impact predominantly in surface layers. Thus, the nanomorphology of materials, which surface strength falls below the magnitude of tension/stress imposed by forces acting at nanobubble ternary interface, is modified at locations occupied by nanobubbles. Paraffin, PTFE (Teflon) and polystyrene surfaces were nanostructured by nanobubbles and the magnitude of nanostructures correlates with surface Young modulus. Depending on the experimental arrangement, nanopinholes or nanoprotrusions (Fig. 1) with relatively narrow size distribution (rmean ~ 10 nm) and high appearance density (~ 600/μm2) were created by nanobubbles on water-immersed polystyrene film(1)(2). Nanobubble-assisted nanostructuring can find prospective application for low-cost manufacturing of nanoporous membranes and nanoscaffolds for biomedical applications. Besides nanopatterning, the nanobubble-created imprints can serve for ex-post, ex-situ examination of nanobubble appearance on immersed surface, representing significant simplification compared to direct nanobubble imaging in liquids. The nanobubble imprint technique combined with ex-situ AFM imaging allowed us to reveal existence of water-immersed quasi-2D nano- and micro-foams (Fig. 2) (3), which imaging in situ is difficult.

References

[1] Hana Tarábková, Pavel Janda: Surface Rearrangement of Water-Immersed Hydrophobic Solids by Gaseous Nanobubbles, Langmuir 2014, 30, 14522−14531

[2] Hana Tarábková, Pavel Janda: Single-Step Nanoporation of Water-Immersed Polystyrene Film by Gaseous Nanobubbles, Langmuir 2016, 32, 11221−11229

[3] Hana Tarábková, Pavel Janda: Nanobubble-Assisted Nanopatterning Reveals the Existence of Liquid Quasi-Two-Dimensional Foams Pinned to a Water-Immersed
Surface, Langmuir 2020, 36, 7200−7209

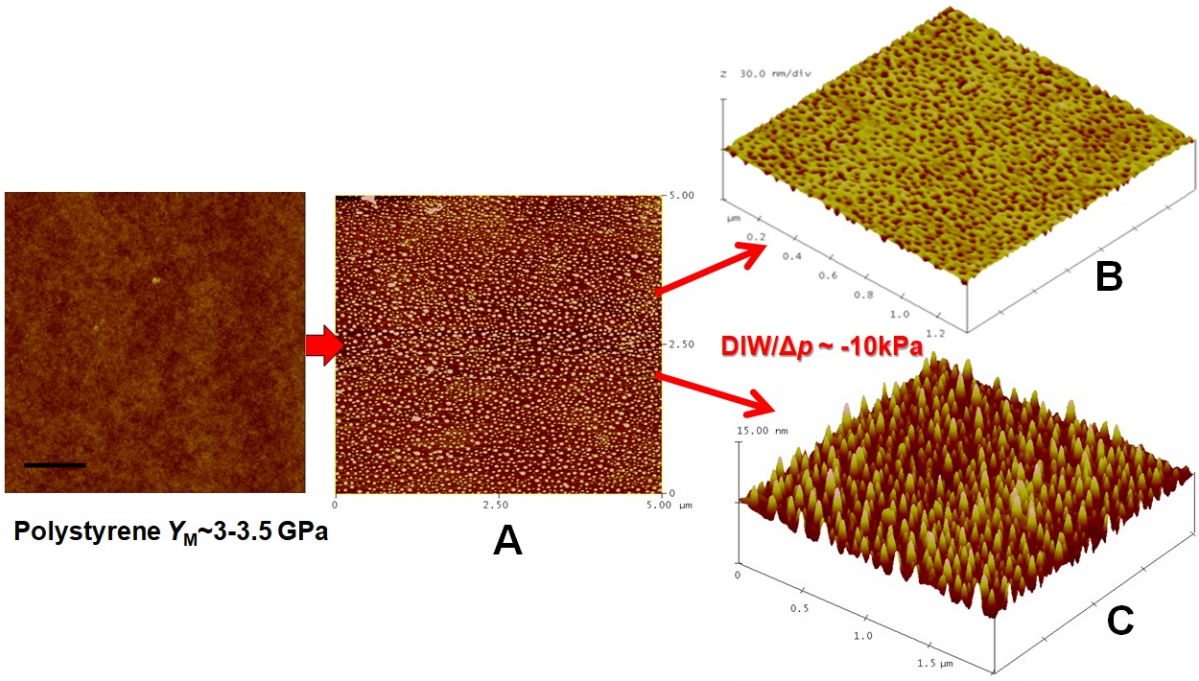

Fig. 1: In-situ AFM image of nanobubbles on water-immersed polystyrene surface (A) and ex-situ AFM images of nanobubble-created pinholes (B) and nanoprotrusions (C) in polystyrene film.

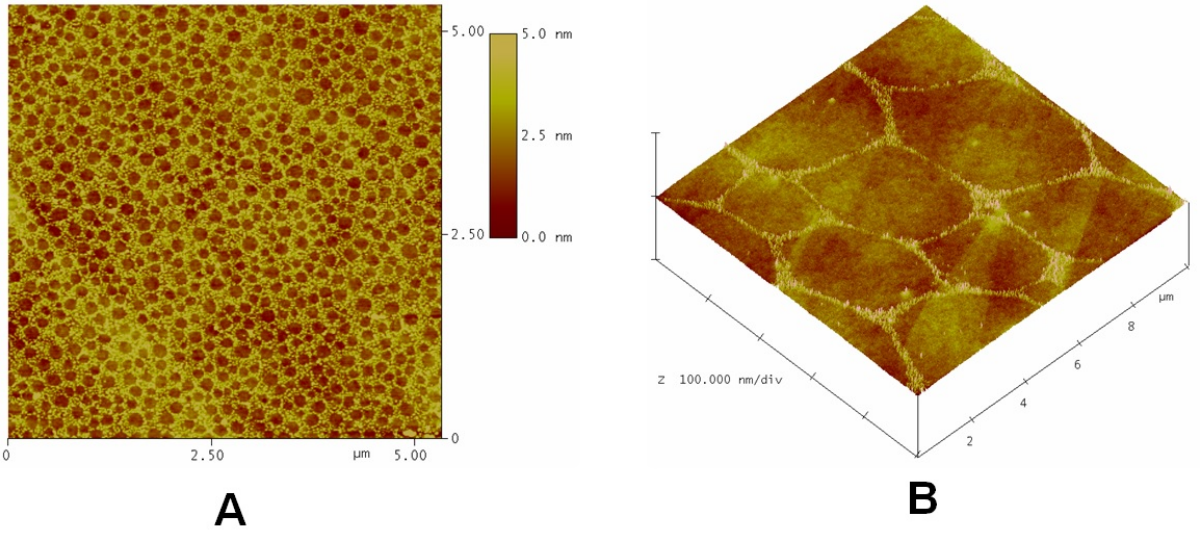

Fig. 2: Ex-situ AFM images of quasi-2D nanofoam (A) and microfoam (B) imprinted in polystyrene matrix during immersion in water.

Type of presentation: Oral

MS3-O-2846 Sub-Ångstrom resolution imaging of 2D conjugated metal-organic frameworks enabled by unconventional resilience against electron radiation

Qi H.[1,2], Liang B.[1], Mücke D.[1], Cooley I.[3], Besley E.[3], Kaiser U.[1]

[1]Central Facility of Materials Science Electron Microscopy, Universität Ulm, 89081 Ulm, Germany, [2]Faculty of Chemistry and Food Chemistry, Technische Universität Dresden, 01062 Dresden, Germany, [3]School of Chemistry, University of Nottingham, NG7 2RD Nottingham, UK

Email of the presenting author: haoyuan.qi@uni-ulm.de

Recent years have witnessed the rise of two-dimensional conjugated metal-organic frameworks (2D c-MOFs) [1]. 2D c-MOFs with strong in-plane π-d conjugation are of particular interest because of their intrinsic conductivity, anisotropic charge transport, and potential (opto-)electronic applications. However, the structural determination of 2D c-MOFs, particularly that down to the atomic scale, remains a formidable task. Aberration-corrected high-resolution transmission electron microscopy (AC-HRTEM) is capable of direct imaging with sub-Ångstrom resolution. Nonetheless, electron radiation damage, i.e., atomic displacement, bond scission, and chemical etching, leads to instantaneous amorphization of organic materials, severely limiting the achievable resolution [2].

We envisage that enhancing the intrinsic electron resilience of MOFs is vital to circumventing this physical limitation. However, no systematic study has been conducted to identify the structural features contributing to MOF stability under electron radiation. In this regard, empirical rules from crystals of organic polymers may offer a reference point. For example, aromatic compounds are more electron resilient than aliphatics due to π electron delocalization and conjugation, suggesting higher stability of conductive 2D c-MOFs than conventional insulating ones. In addition, organic polymers are prone to crosslinking after carbon-hydrogen bond scission, which leads to the loss of long-range order. Exchanging protium for chlorine on coronene molecules has increased the crosslinking dose by two orders of magnitude due to the reduced displacement cross-section of chlorine, indicating a potential negative correlation between hydrogen content and electron resilience in MOFs. Nevertheless, the effects of organometallic bonds on MOF stability remain unexplored.

Following the sketchy roadmap, we investigate the electron resilience of 2D c-MOFs with systematically altered structural attributes, including hydrogen content, framework density, and organometallic bonding. The experimental demonstration is quantitatively explicated by ab initio quantum calculation. Highly conductive 2D c-MOFs demonstrate exceptional stability, allowing information transfer to the sub-Ångstrom regime.

References

[1] M. Wang, R. Dong, X. Feng, Two-dimensional conjugated metal–organic frameworks (2D c-MOFs): chemistry and function for MOFtronics. Chem. Soc. Rev. 50, 2764–2793 (2021).

[2] C. J. Russo, R. F. Egerton, Damage in electron cryomicroscopy: Lessons from biology for materials science. MRS Bull. 44, 935–941 (2019).

Acknowledgement:

Deutsche Forschungsgemeinschaft (DFG) – 492191310; 426572620; 424798828; 417590517 (SFB-1415)

European Union GrapheneCore3 (881603)

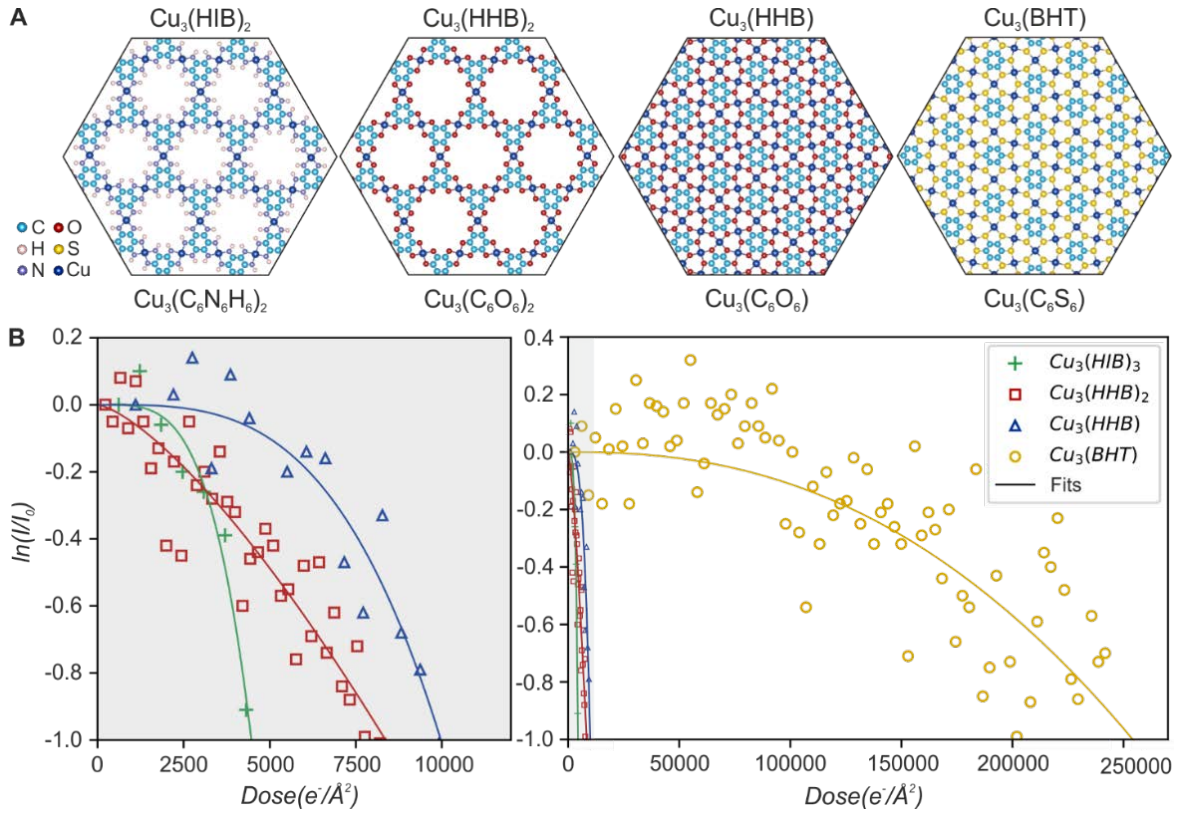

Fig. 1: (A) Atomic models of 2D c-MOFs. (B) Intensity profile of the first-order reflections in 2D c-MOFs as a function of accumulated electron dose.

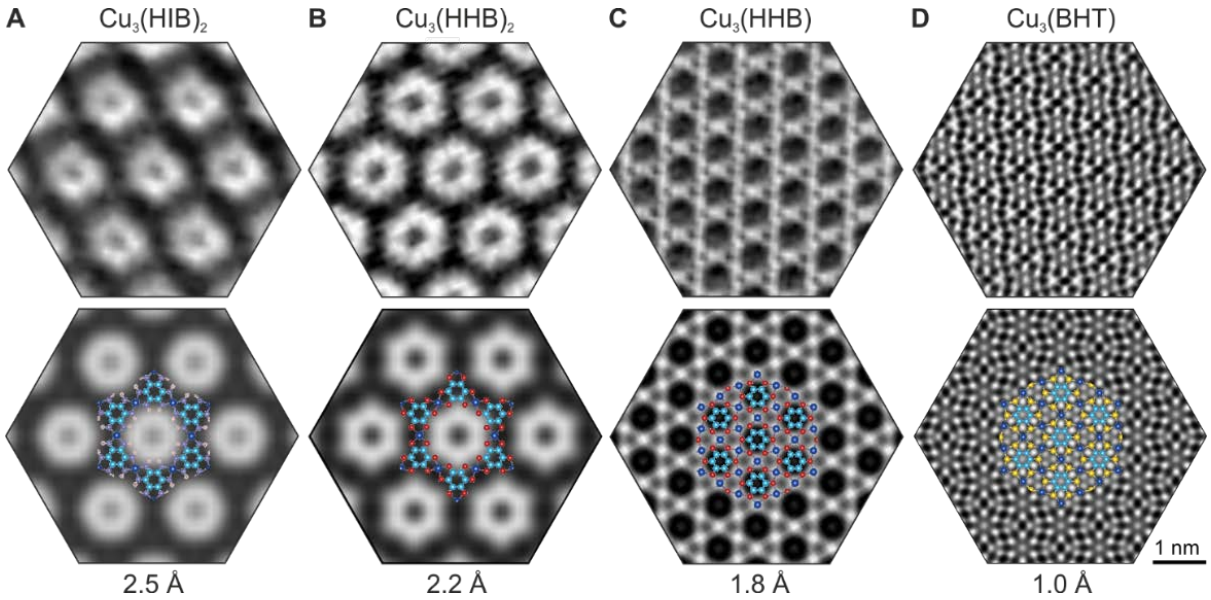

Fig. 2: Cs-corrected imaging at 300 kV. Upper row: experimental AC-HRTEM images. Lower row: simulated AC-HRTEM images with atomic models overlaid and achieved resolution specified. Image acquisition dose: A: 100e^- Å^{-2}, B−C: 200 e^- Å^{-2}; D: 5.6 × 10^3 e^- Å^{-2}.

Type of presentation: Oral

MS3-O-2538 Extreme scale-dependent tensile properties of epoxy fibers and a polarized micro-Raman study

Sui X. M.[1, 2], Tiwari M.[3], Pinkas I.[1], Wagner H. D.[2]

[1]Chemical Research Support, Weizmann Institute of Science, Rehovot, Israel, [2]Department of Molecular Chemistry and Materials Science, Weizmann Institute of Science, Rehovot, Israel, [3]3. Department of Mechanical Engineering, Indian Institute of Technology, Rupnagar, India

Email of the presenting author: xiaomeng.sui@weizmann.ac.il

Abstract

It has long been known that the strength of materials depends on the volume of stressed material and on the nature of the stress distribution. Materials with reduced size and dimensionality such as thin fibers and films, nanotubes and nanowires, indeed often exhibit exceptionally high mechanical properties compared to their macroscopic counterparts. However, only very few studies deal with size effects in epoxy resins, in spite of the relevance of the potentially higher mechanical properties. These studies also reported, without further discussion, the observation of a highly ductile behavior of their epoxy fibers. Thus, evidence on the size effect in epoxy fibers is scarce, and physical explanation is absent or just descriptive. It is therefore our aim to meticulously explore the size effects on stiffness, strength and failure strain for a wide range of fiber sizes, and to suggest possible mechanisms that may account for such cross-properties effects.

In this work, epoxy fibers with different diameters were prepared by hot drawing and their mechanical properties were measured under tension. The stiffness, strength, ultimate strain, and toughness revealed substantial scale-dependent effects as they all significantly increased with a decrease in size. Compared to bulk epoxy, an intrinsically brittle material, thin epoxy fibers displayed a highly ductile behavior under tension. Necked fiber segments tested in tension were found to have even higher strength and modulus compared to the initial as-prepared fibers [1]. Here we used confocal polarized Raman spectroscopy to monitor the deformation of epoxy fibers. The apparent molecular reorientation induced by plastic deformation of epoxy fibers, both qualitatively and quantitatively. Based on these results and X-ray diffraction measurements, we find that highly cross-linked necked epoxy fibers exhibit partial macromolecular anisotropy which likely explains the observed high mechanical characteristics [2].

[1] X.M. Sui, M. Tiwari, I. Greenfeld, R.L. Khalfin, H. Meeuw, B. Fiedler, H.D. Wagner, “Extreme scale-dependent tensile properties of epoxy fibers”. Express Polymer Letters, 13 (11), 993-1003, 2019.

[2] X.M. Sui, I. Pinkas, H.D. Wagner*, A polarized micro-Raman study of necked epoxy fibers, Polymer, 2021, 230, 124034.

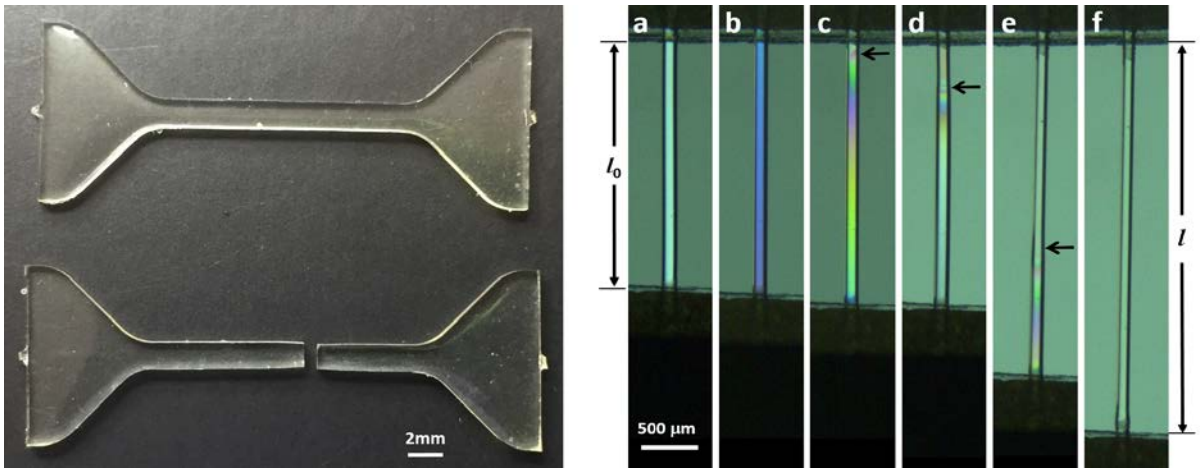

Fig. 1: (left) Bulk epoxy specimen before and after a tensile test, note a beginning of necking at the fractured sides; (right) typical tensile test of as-prepared epoxy fiber (arrows designate the nucleation and propagation of necking), displaying the large elongation of the specimen (from l_0 to l).

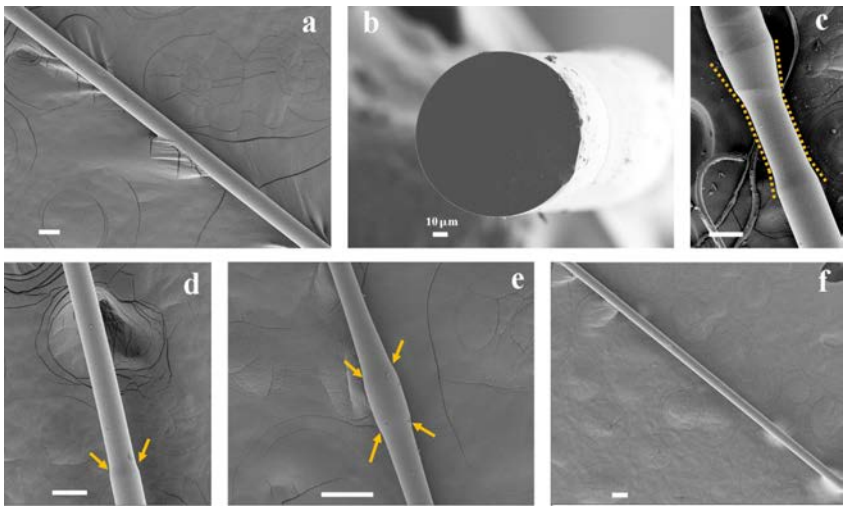

Fig. 2: SEM images of the as-prepared (a) and necked fibers (b-f). Yellow dash lines and arrows indicates the dogbone shape and kinks of the stretched fibers, respectively. Scale bars are 100 um in all images, except in (b) the scale bar is 10 um.

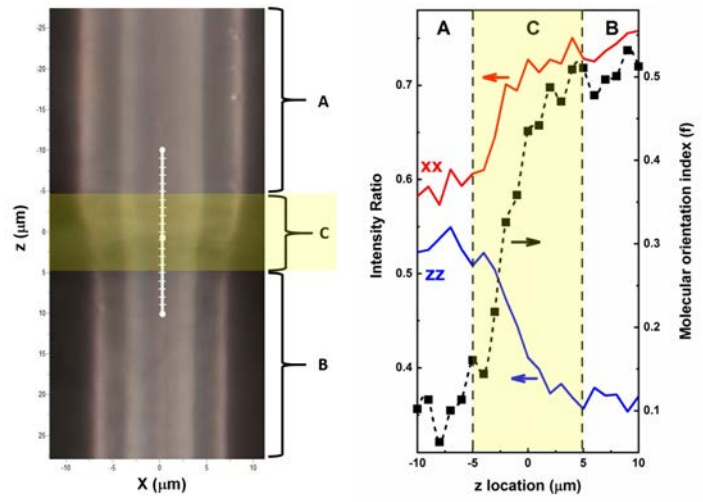

Fig. 3: Polarized Raman scanning of a necked fiber. Scanning with a step size of 1 um along the white line was performed in xx and zz configurations. The I_{1184}/I_{1610} ratio in each configuration was calculated and plotted. The transition region (C) was marked on the ratio map. The black dash line with symbols is the molecular orientation index (*f*).

Type of presentation: Poster

MS3-P-2653 Simple, fast and reliable method of UHMWPE accelerated aging

Gajdosova V.[1], Hodan J.[1], Dybal J.[1], Krejcikova S.[1], Sloufova I.[2], Fulin P.[3], Pokorny D.[3], Slouf M.[1]

[1]Institute of Macromolecular Chemistry AS CR, Heyrovského nam. 2, 162 06 Prague 6, Czech Republic, [2]Charles University, Faculty of Science, Hlavova 2030, 128 40 Prague 2, Czech Republic , [3]1st Orthopedics Clinic of the 1st Faculty of Medicine UK, Hospital Motol, V Uvalu 84, 156 06 Prague 5, Czech Republic

Email of the presenting author: gajdosova@imc.cas.cz

Ultra-high molecular weight polyethylene (UHMWPE) is employed as a key bearing component of total joint replacements (TJR) for five decades [1]. Over the years, UHMWPE itself has been modified mainly to increase its resistance to wear and oxidative degradation. The study of new UHMWPE modifications comprises the accelerated aging that simulates in vivo conditions in order to estimate the modified material lifespan. The aging methods used in the field of UHMWPE for TJR can be divided into two main groups: (i) thermooxidative degradation and (ii) the accelerated aging in solutions. The accelerated aging in the solutions is considered closer to the in vivo conditions. On the other hand, the solution accelerated aging methods tend to be time-consuming and some protocols were reported to yield “unnatural” peaks in infrared (IR) spectra [2].

In this work, we introduce a novel, simple and fast method of UHMWPE accelerated aging in solution, in which UHMWPE samples are submerged in water solution containing 0.1 % of H_2O_2 at 70 °C. The method exhibits two main advantages: (i) it is at least 2.5-times faster than the methods published previously and (ii) the IR spectrum of the oxidation products does not contain unnatural oxidation peaks corresponding to aldehydes or other compounds, which has been observed by some other authors [2,3]. Two types of the UHMWPE samples were selected for testing: virgin UHMWPE (PE/0) and UHMWPE stabilized with the 0.1% of vitamin E (PE/VitE). The samples were characterized by several independent microscale methods: SEM microscopy, IR microspectroscopy, DSC and microindentation hardness testing (MH).

All characterization methods (Figs. 1–3) were in agreement that the virgin polymer (PE/0) exhibited lower resistance to oxidative degradation than stabilized material (PE/VitE): SEM micrographs documented surface cracks on PE/0 surface, IR profiles of proved higher (sub)surface oxidation of PE/0, and microindentation measurements confirmed that the oxidative degradation of PE/0 changed the mechanical behaviour of the surface layer, in agreement with our previous studies [4,5]. The fact that all three independent methods confirmed higher oxidation resistance of stabilized material (PE/VitE) confirmed the reliability of our method. We conclude that our method of UHMWPE accelerated aging is faster than previously published techniques and provides reliable results without formation of “unnatural” peaks in infrared spectra.

References:
[1] UHMWPE Biomaterials Handbook. 3rd ed., London, Elsevier 2016.
[2] J. Biomed. Mater. Res. B, 2009, 369 – 372.
[3] J. Biomed. Mater. Res. B, 2006, 79 – 85.
[4] J. Biomed. Mat. Res. B, 2008, 240 - 251
[5] Polym. Degrad. Stabil, 2021, 109735

Acknowledgement: Technology Agency of the Czech Republic (TA CR; project TN01000008) and Czech Health Research Council (AZV CR; project NU21-06-00084) is gratefully acknowledged

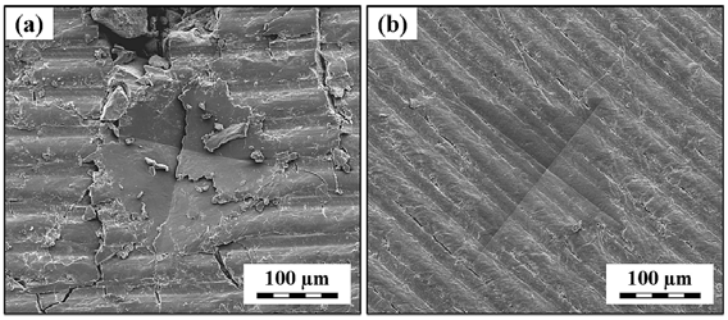

Fig. 1: SEM micrographs of the indent on the PE/0 (a) and PE/VitE (b) surfaces after 80 days of accelerated aging in H_2O_2 solution. The surface of PE/0 sample shows changes (microcracks and sample fragments) due to oxidative degradation.

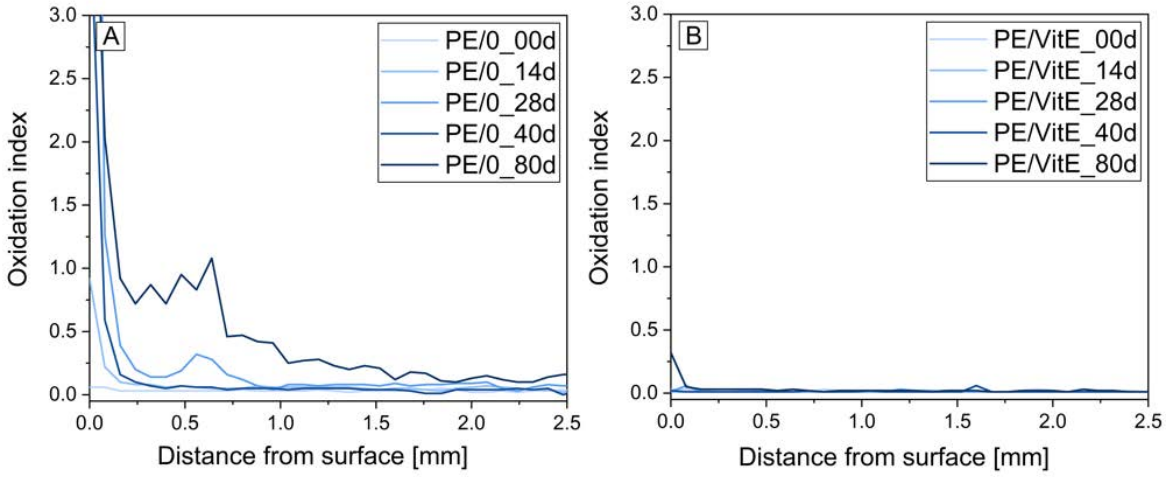

Fig. 2: IR microspectroscopy results: the oxidation index (OI, ref. [3]) profiles of (a) PE/0 and (b) PE/VitE samples during the accelerated aging in H_2O_2 solution. The profiles are shown for various times of accelerated aging (0, 14, 28, 40 and 80 days).

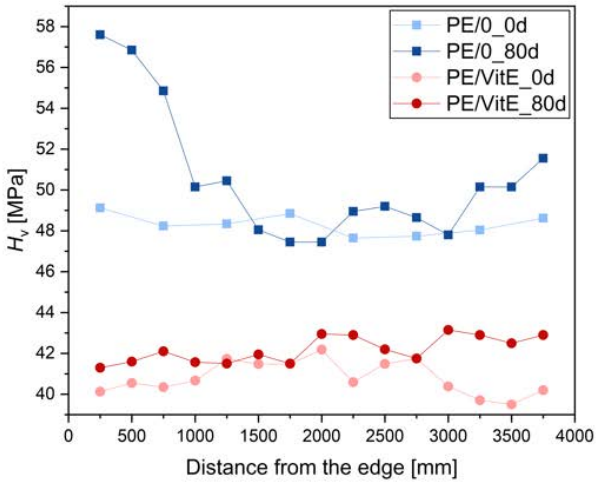

Fig. 3: Vickers microhardness (HV) profiles of PE/0 (blue lines) and PE/VitE (red lines) before and after the accelerated aging in H_2O_2 solution. Profiles were measured from the cross-section of the PE sample (from one oxidized side to the opposite oxidized side).

Type of presentation: Poster

MS3-P-2990 BioAFM imaging and mechanics tracking

Obořilová R.[1,2], Přibyl J.[1], Uher M.[1,2], Skládal P.[1,2]

[1]CEITEC MU, Masaryk University, Kamenice 5, 625 00 Brno, Czech Republic, [2]Department of Biochemistry, Faculty of Science, Masaryk University, Kamenice 5, 625 00 Brno, Czech Republic

Email of the presenting author: Radka.Oborilova@ceitec.muni.cz

Atomic force microscopy for live sciences (BioAFM) plays an important role in imaging under physiological conditions. It works in liquid (buffer, growth medium) and can be tempered to the required temperature. The most common examples used in our CF include imaging a DNA double helix, determining the change in collagen in bone tissue after treatment, both the topography and mechanics are evaluated, monitoring the formation and interactions of the bilayer by observing its rupture.
Another example is the monitoring of bacterial lysis using bacteriophages in real time or bacterial biofilm imaging. Finally, fast and gentle visualization of the sensor surface after specific detection can be mentioned.
BioAFM technique moves the visualization of biological structures and physiological processes closer to real conditions. In addition to imaging topography, it is possible to monitor other properties of materials, biomolecules and more complex structures (stiffness, elasticity, etc.).
[1] Obořilová R., Šimečková H., Pastucha M., Klimovič M., Víšová I, Přibyl J., Vaisocherová-Lísalová H., Pantůček R., Skládal P., Mašlaňová I., Farka Z. Nanoscale, 2021,13, 13538-13549
[2] Horáčková, V., Pribyl, J., & Skládal, P. (2016). Study of DNA immobilization on mica surface by atomic force microscopy. Monatshefte Für Chemie - Chemical Monthly, 147

Acknowledgement: „We acknowledge CF Nanobiotechnology of CIISB, Instruct-CZ Centre, supported by MEYS CR (LM2018127).“

Type of presentation: Poster

MS3-P-2814 Commonly used vs novel embedding resins for 3D-SEM microscopy with higher resistance to e-beam damage.

Pavlova E.[1], Strachota B.[1], Strachota A.[1], Skoupy R.[2], Krzyzanek V.[2], Tyc J.[3], Nebesarova J.[3], Slouf M.[1]

[1]Institute of Macromolecular Chemistry CAS, Heyrovskeho nam. 2, 162 06 Prague 6, Czech Republic, [2]Institute of Scientific Intruments CAS, Kralovopolska 147, 612 64 Brno, Czech Republic, [3]Institute of Parasitology, Biology Centre CAS, Branisovska 31, 37005 Ceske Budejovice, Czech Republic

Email of the presenting author: ewapavlova@seznam.cz

Electron microscopy (EM) is one of the key techniques for characterization of soft biological materials, such as tissues, cells and their components. Embedding of biological samples in polymer matrices provides an efficient protection and fixation of their structure and, as a result, it has become one of the preferred preparation methods for EM.

Nevertheless, traditional embedding resins are optimized for 2D-TEM imaging at high accelerating voltages and not for recently introduced modern 3D-SEM visualization techniques. At lower energies and higher doses, which are typical of 3D-SEM imaging, the embedding resins tend to suffer from charging, electron beam damage, and subsequent deterioration of image quality.

We have developed two new types of polymer resins with expected higher resistance to e-beam damage: (I) the resins with chemical stabilizing agent and (II) the resins based on more e-beam resistant polymer. The resins with chemical stabilizing agent (novel resins type I; not shown) have a similar chemical composition and similar contrast like commercial resins (such as HARD PLUS resin 812). The resins based on more e-beam resistant polymers (novel resins type II) show lower charging in comparison with commercial resins, overall quality of the micrographs is very good, contrast is high but their mechanical properties, cuttability and volume contraction upon cure are yet to be optimized.

In this contribution, we compare four types of resins with embedded mouse brain tissue. The resins are: commercial epoxy resin (HARD PLUS resin 812; sample 1), resin with novel stabilizing agent (novel resin type I; sample 2), two types of novel resins with different chemical composition (two novel resins type II; samples 3 and 4). The resins are characterized in details and compared from the point of view of their homogeneity, cuttability, contrast in both TEM and SEM, and stability under electron beam (charging at specific electron doses).
We conclude that both novel types of resins seem to be promising embedding media for 3D-SEM. Therefore, their chemical composition is not revealed at the moment due to possible patent applications. Further development and optimization of the materials and preparation protocols for 3D-SEM is a subject of our ongoing research.

Acknowledgement: Financial support through grant TN01000008 (TA CR) is gratefully acknowledged.

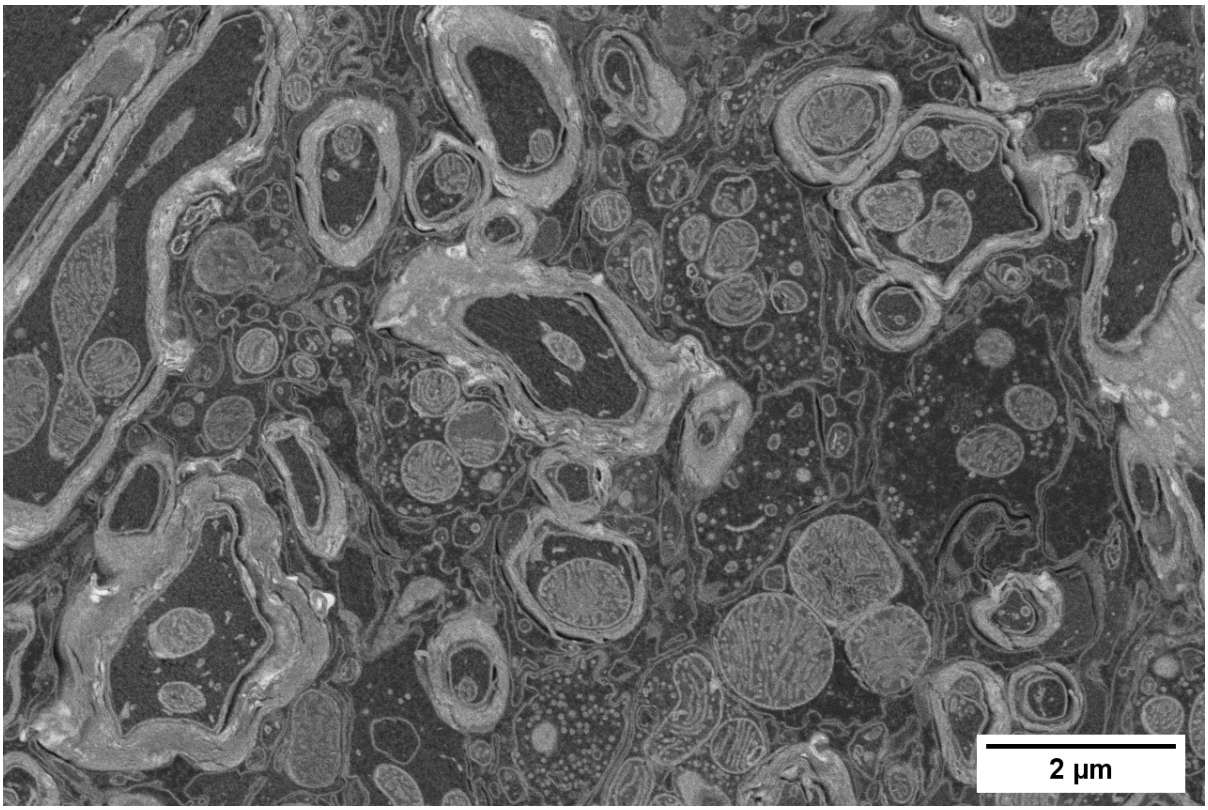

Fig. 1: SEM microphotograph showing mouse brain issue embedded in a novel embedding resin type II. The micrograph was taken with a SEM microscope Apreo (Thermo Fisher Scientific) at 2 kV using backscattered electron detector T1.

Type of presentation: Poster

MS3-P-2834 Low Dose Transmission Electron Microscopy Imaging on Sensitive Colloidal Covalent-Organic Frameworks

Pelaez-Fernandez M.[1,2,3], Salaun P.[1], Marinova M.[1], De la Peña F.[1], Le Fer G.[1]

[1]Université de Lille, Unité Matériaux et Transformations, Lille, France, [2]Laboratorio de Microscopías Avanzadas, Universidad de Zaragoza, Zaragoza, Spain, [3]Instituto de Nanociencia y Materiales de Aragón, Zaragoza, Spain

Email of the presenting author: Mario.pelaezfernandez@univ-lille.fr

Covalent-organic frameworks (COFs) are currently gaining a growing amount of interest due to their tunability and many possible applications, which range from gas storage to optoelectricity or even catalysis[1]. Within this realm, the recent synthesis of single-crystal colloidal COF suspensions has opened a new realm of possibilities for these materials[2].

The characterisation of these COFs, most notably their dispersion, morphology and crystallinity, is essential for the development of this research. However, transmission electron microscopy (TEM) characterisation in these samples is difficult due to the sensitivity of such samples to the electron beam. In this sense, colloidal COF nanoparticles (NPs) have already been imaged using TEM[2,3], although this imaging has consistently been performed in CryoTEMs in order to lower the beam damage on the samples.

A different path to lower this beam damage is the utilisation of direct detectors in the TEM. Novel studies[4] show that the usage of said detectors, like TimePix3, allow for much lower doses when imaging.

These works show the possibility to image colloidal COFs in a regular TEM. This imaging has been performed at low doses using a cryoholder and a Timepix3 detector. Results will be discussed with respect to previous studies.

[1] S.-Y. Ding and W. Wang, Chem. Soc. Rev. 42, 548 (2013).

[2] A. M. Evans et al, Science 361, 52 (2018).

[3] I. Castano et al, ACS Cent. Sci. 5, 1892 (2019).

[4] D. Jannis et al, Ultramicroscopy 233, 113423 (2022).

Acknowledgement: These works have been funded by the "Ayudas Margarita Salas para la formación de jóvenes doctores", the TemAster project and the ANR (ANR-21-CE06-0021)

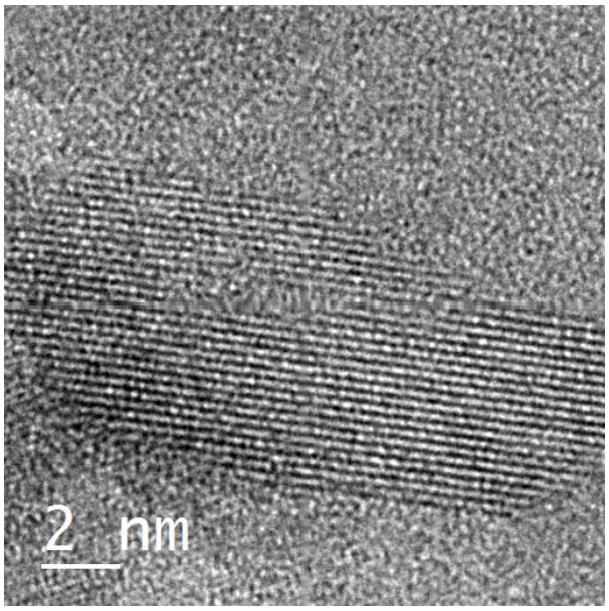

Fig. 1: TEM image of a single COF nanoparticle taken on the TimePix3 detector

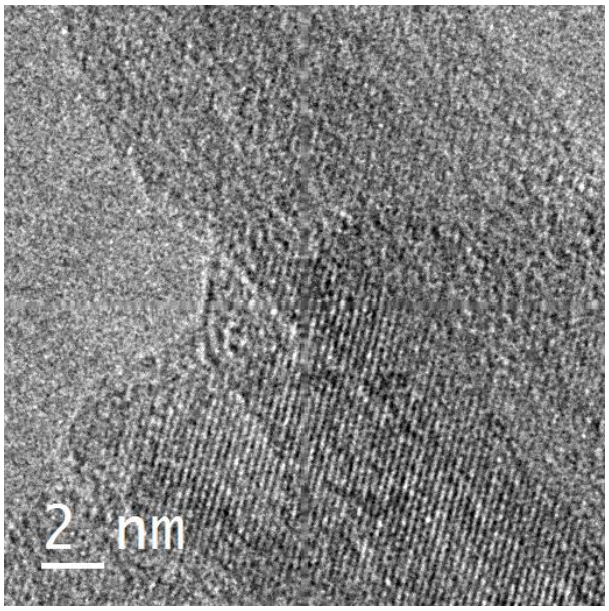

Fig. 2: TEM image of a COF nanoparticle bundle taken on the TimePix3 detector

Type of presentation: Poster

MS3-P-2829 Characterization of particle-filled polymer composites

Siedlaczek P.[1], Sinn G.[1], Lichtenegger H.[1]

[1]University of Natural Resources and Life Sciences, Institute of Phyics and Material Science, Vienna, Austria

Email of the presenting author: philipp.siedlaczek@boku.ac.at

High-performance composite materials are widely used in the aerospace, marine, and automotive industry due to their excellent specific mechanical properties and fast adaptability to new application fields. The potential of composites has been noticed by the civil engineering industry, leading to a steady increase in new applications. Particle-filled composites are often found at the construction site as adhesives in rehabilitation, strengthening, and post-installed fastenings.
These applications demand high mechanical properties, which are dependent on particle loading, particle shape, matrix-particle interface, chemical composition, and quality of dispersion. It is, therefore, important to characterize the embedding of the fillers to develop an understanding of each of the before-mentioned factors on mechanical properties.
3 commercially available polymer composites were analyzed under an electron microscope with secondary electron imaging, backscattered electron imaging, and energy dispersive x-ray analysis. These methods revealed particle size distribution, particle density, the occurrence of pores, and filler composition.
For each sample, an area of 4.36x2.58 mm was scanned with backscattered electron imaging (Z-Contrast), followed by ImageJ particle analysis. After contrast and brightness adaptions, a threshold was set to filter particles from the matrix, and in the final step, particles were outlined. This approach allows to calculate the average particle size, ferret diameter, and shape factor. Furthermore, particle density and a size distribution function could also be extracted.
The elemental composition and the distribution of elements in fillers and matrix were obtained from elemental mapping via EDX detected. These findings contributed to the identification of filler materials and were supported by X-Ray diffraction analysis.
From secondary electron images, plastic deformation, crack propagation, and interface of matrix and particle were qualitatively determined.

Acknowledgement: This work was financially supported by the Austrian Science Fund-FWF [grant number P 31203]

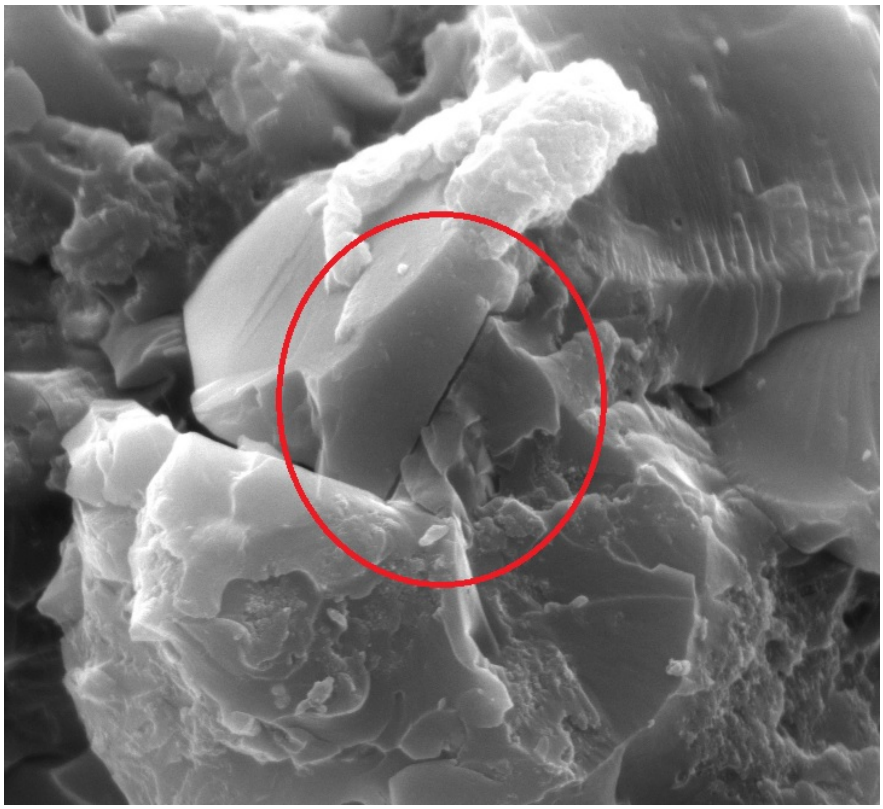

Fig. 1: Matrix-Particle Interface

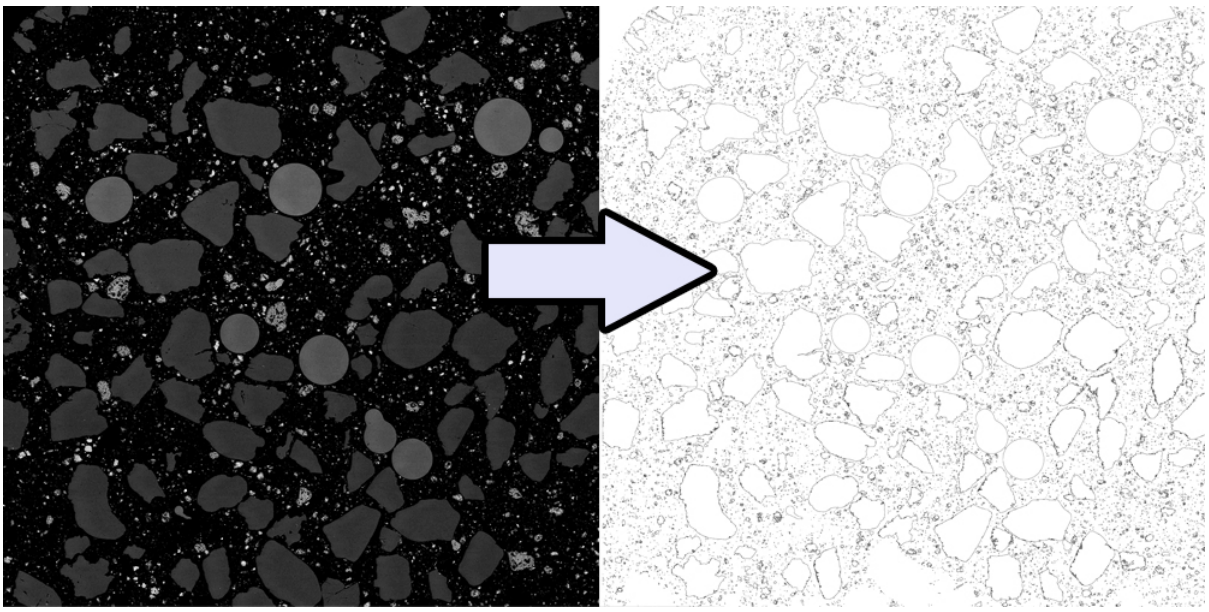

Fig. 2: Z-Contrast image transformation to outlined particles

Type of presentation: Poster

MS3-P-2828 Visualization of internal morphology of hydrogels based on polyvinyl alcohol in comparison with the indirect method of structural characterization

Trudicova M.[1], Zahradka J.[1], Mrazova K.[2], Hrubanova K.[2], Smilek J.[1], Sedlacek P.[1], Pekar M.[1]

[1]Faculty of Chemistry, Brno University of Technology, Purkynova 118, 61200 Brno, Czech Republic, [2]Institute of Scientific Instruments of the Czech Academy of Sciences, Kralovopolska 147, 61264 Brno, Czech Republic

Email of the presenting author: xctrudicova@vutbr.cz

The functionality of hydrogels, determining their potential use in a wide range of applications, is defined by a combination of their crucial material properties, such as swelling dynamics, elasticity, and mechanical strength. The essence of these properties guaranteeing hydrogels' unique qualities is rooted in their structure. Therefore, the ability to analyze these parameters in high resolution plays a significant role in the optimization and control of the functionality of hydrogels. In general, possibilities to characterize hydrogels' internal architecture can be divided into two groups, indirect and direct methods. Indirect methods cannot provide information about appearance (e.g., pore shapes); however, they can present some information about internal architecture. Direct methods are convenient techniques since we can observe internal architecture, shape, and size of pores, etc. However, common and available methods (e.g., scanning electron microscopy – SEM) require samples in a dry state. That is undesirable since the process of dehydration commonly leads to an increased likelihood of creating structural artifacts and providing misleading information. Alternatively, atomic force microscopy (AFM) can be used to image the topography of soft biological materials in their native environments.
In this work, the main aim was to compare direct visualization with results obtained from the indirect method, specifically calculating mesh sizes from viscoelastic moduli from rheology [1]. We chose a model hydrogel network based on polyvinyl alcohol prepared by the freeze-thaw method with different values of molecular weight. We tested different approaches of visualization based on microscopy, i.e. AFM, cryo-SEM with plunge freezing (swift immersion into liquid nitrogen), and SEM (after shock freezing in liquid nitrogen and freeze-drying). Images from these observations were analyzed using the ImageJ open-source image processing toolbox [2]. These results were eventually compared with results obtained from rheology. The usability of these methods on a particular system was evaluated.

Type of presentation: Poster

MS3-P-2819 STEM damage of Acrylic-based Materials for Stereolithography: Degradation Mechanism

Valencia L. M.[1], de la Mata M.[1], Herrera M.[1], Molina S. I.[1]

[1]Departamento de Ciencia de los Materiales e Ingeniería Metalúrgica y Química Inorgánica, IMEYMAT, Facultad de Ciencias, Universidad de Cádiz, Campus Río San Pedro s/n, 11510 Puerto Real (Cádiz), Spain

Email of the presenting author: luisamaria.valencia@uca.es

Transmission electron microscopy (TEM) plays a key role in materials science, while its performance strongly depends on the material under study [1]. The interaction of electrons with materials, especially dealing with soft systems, such as polymer-based materials, causes different types of radiation damage, e.g., electrostatic charging, radiolysis and knock-on damage [2], imposing a physical limit which determines the attainable resolution. Importantly, polymer-based systems, particularly acrylic resins, are appealing candidates for the development of novel materials, whose TEM characterization is limited by their sensitivity to the electron irradiation. Therefore, understanding the underlying mechanisms inducing the material degradation upon electron exposure is essential to pave the way towards an accurate analysis by means of TEM techniques.

The resolution limit achievable in electron beam sensitive materials depends, among other parameters, on the total accumulated electron dose before meaningful damage [3]. It is well-known that the material changes during TEM analyses can be monitored under a variety of techniques, such as Electron Energy Loss Spectroscopy (EELS). EELS studies allow addressing thickness variations of the specimen due to degradation or contamination during the measurements, as well as chemical, bonding or coordination changes [4].

In this work, we report the effect of the electron beam in acrylic resins under STEM-EELS conditions, combining low-loss and core-loss EELS sequential analyses for increasing exposure times (i.e., accumulated electron doses) (Figure 1). In particular, the target material is an acrylic resin based composite containing WS2, suitable for the fabrication of pieces by Stereolithography. Based on the evolution of the C and O signal during the beam irradiation, including the inspection of the spectral shape, as well as the thickness reduction, we propose likely underlying mechanisms explaining the acrylic resin degradation. The results obtained allow the optimization of the working conditions for structural characterization experiments, such as electron tomography, which are extremely important in the development of these materials.

[1] Williams, D.B.; Carter, C.B. Transmission Electron Microscopy. A textbook for Materials Science; Springer New York, NY, 2009; ISBN 9780387765006

[2] Egerton, R.F. Radiation damage to organic and inorganic specimens in the TEM. Micron 2019, 119, 72–87, doi:10.1016/j.micron.2019.01.005.

[3] Jiang, N.; Spence, J.C.H. On the dose-rate threshold of beam damage in TEM. Ultramicroscopy 2012, 113, 77–82, doi:10.1016/j.ultramic.2011.11.016.

[4] Singh, P.K.; Venugopal, B.R.; Nandini, D.R. Effect of electron beam irradiation on polymers. J. Mod. Mater. 2018, 5, 24–33, doi:10.1063/1.4710140.

Acknowledgement: 2014-2020 ERDF; national project FEDER-UCA 18-106586; TEP-946 INNANOMAT research group; DME-SC-ICyT/ELECMI-UCA; co-funding from EU is also acknowledged.

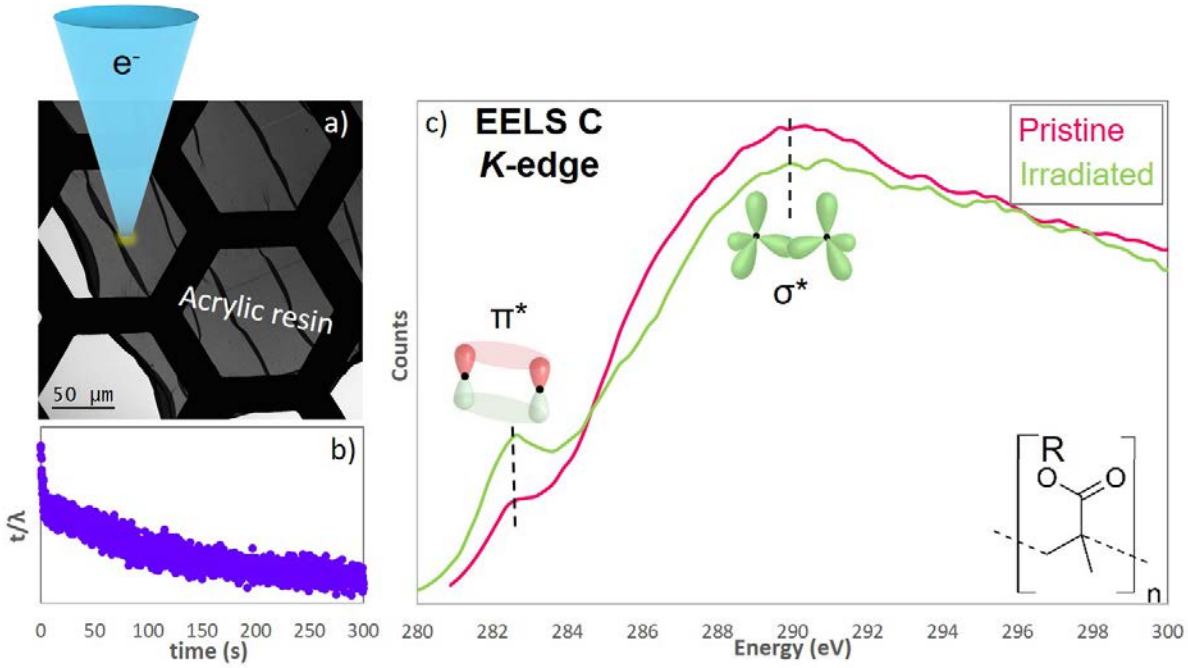

Fig. 1: a) TEM image of an acrylic-based composite TEM specimen; b) thickness variation of the acrylic-based composite specimen during electron beam exposure obtained from low-loss EELS spectra; c) EELS C K-edge of (almost) pristine material (red) and damaged material (green) obtained by increasing the accumulated dose.

Type of presentation: Poster

MS3-P-2592 Advanced microstructure analysis of tire polymer materials using cutting edge multi scale electron microscopy technologies

Wu M.[1]

[1]Thermo Fisher Scientific

Email of the presenting author: min.wu@thermofisher.com

Additive particles and agglomerates serve multiple functions in tires such as antioxidants, heat resisting elements, binders and others. The morphology, size and chemical distribution of these additive materials determine overall tire materials properties such as strength, elasticity, fuel efficiency, wear resistance and wet grip, etc. Meanwhile, since construction materials such as steel wires are used for reinforcement in tires, the microstructure of metal cords and adjacent rubber interface has been in significant ongoing research interests because gradual degradation of polymer metal interface fundamentally affects tire lifetime.

In this abstract we present the results of two multi scale electron microscopic characterizations on tire materials using cutting edge instruments. In the first dataset we investigated the 3D morphology and chemical distribution of additive particles in tire rubber volume using advanced multiple ion species plasma focused beam system integrated with femtosecond laser beam, the Helios Laser Hydra. The cut face quality on tire rubber and additive particles using different ion species with various beam parameters is also compared and analysed. In the second dataset the polymer metal interface microstructure has been characterized using Helios Hydra system. A piece of lamella was extracted from the interface and subsequently analyzed using transmission electron microscopy (TEM) equipped with energy dispersive X-ray spectroscopy (EDS).

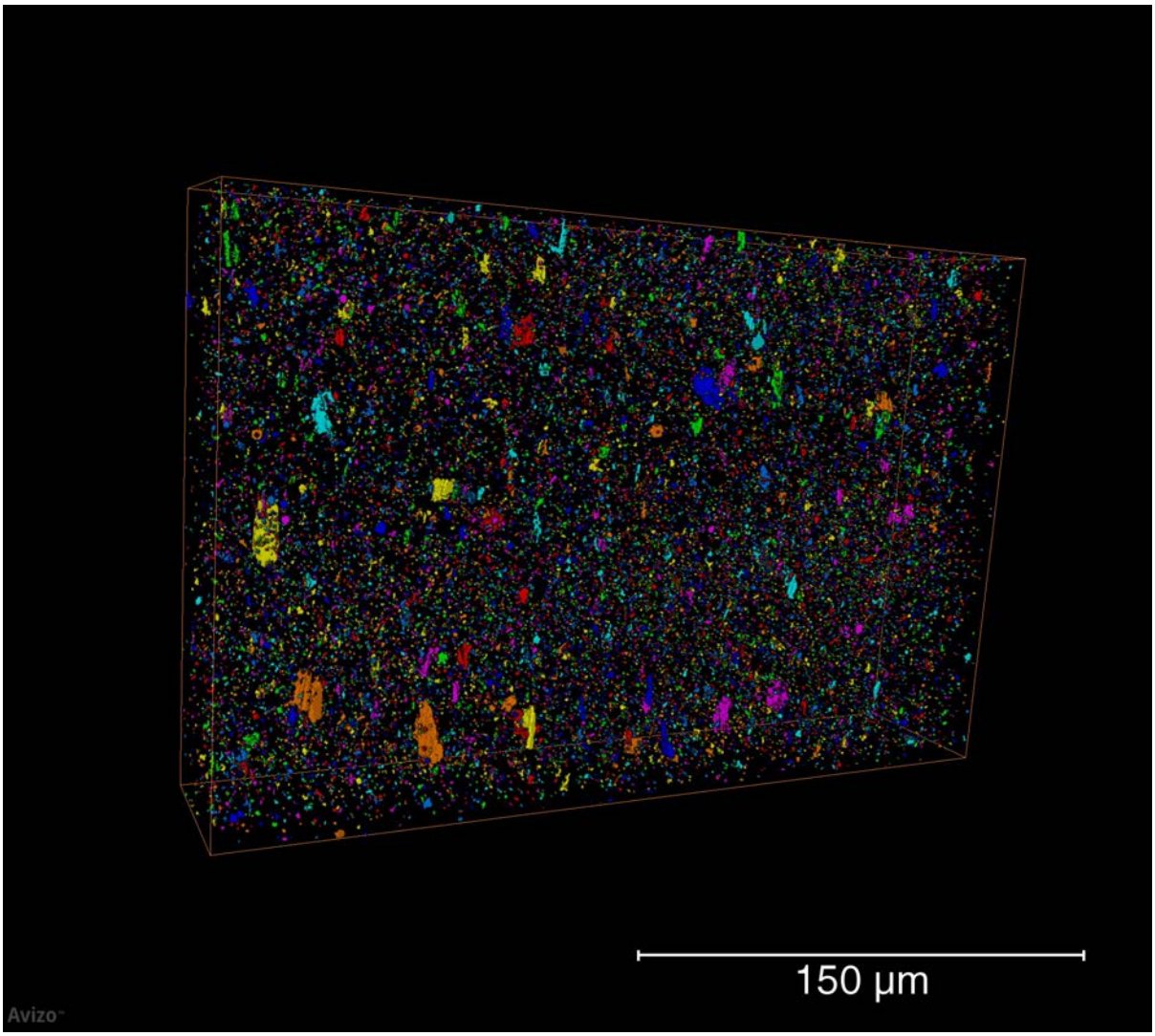

Fig. 1: 3D reconstruction of particle analysis in tire materials

MS4 2D-materials, thin films, coatings, surfaces and interfaces

Type of presentation: Invited

MS4-IN-2994 Low energy electron emission from surfaces and 2D-Materials and 2-D electron cascade in the scanning field electron microscope

Werner W. S.[1]

[1] Institut für Angewandte Physik, TU Vienna, Wiedner Hauptstraße 8-10/134, Vienna, Austria

Email of the presenting author: werner@iap.tuwien.ac.at

Emission of secondary electrons (SEs) upon electron impact is a phenomenon of overwhelming importance in many areas of science and technology, for example for visualisation of nanostructures the Secondary Electron Microscope (SEM), for charged particle detectors, plasma display panels, plasma stability in fusion reactors, etc. Low Energy Electrons (LEE) cause damage to bio materials leading to tumour formation, but can also be used for therapeutic purposes. The mechanism of SE-emission is far from understood presently[1].
The mechanism leading to emission emission of low energy electrons can be elucidated by means of spectroscopy with correlated electron pairs. With this technique one can identify the spectrum of emitted secondary electrons differential with respect to the energy loss suffered by the primary electrons, by measuring the two interaction partners in coincidence. Bulk plasmon decay leads to emission of secondary electrons in a Markovian process while the invacuo-excitation of surface plasmons leads to SE emission from the very surface of a material.
In 2-D van der Waals materials, plasmon decay breaks the D6h honeycomb-symmetry leading to a hybridisation of interlayer states with atom-like states, opening a gateway for characteristic electrons in graphitic materials to escape from the surface[2]
The final part of my lecture concerns the formation of a 2-D electron cascade in the scanning tunnelling microscope, operated in the field emission regime. In view of the fact that a 3D-electron cascade has been a paradigm in electron microscopy over the past century, the prediction of a 2D-cascade [3], followed by its recent experimental verification opens novel avenues for electron microscopy and other electron beam techniques in nanotechnology.

References
[1] W S M Werner and C Walker. Sources, Interaction with Matter, detection and Analysis of Low Energy Electrons (SIMDALEE2). Elsevier, J. Electron Spectrosc. Rel. Phen., (Vol 241), Amsterdam, 2020.
[2] W. S. M. Werner, V. Astasauskas, P. Ziegler, A. Bellissimo, G. Stefani, L. Linhart, and F. Libisch Phys. Rev. Lett., page 196603, 2020.
[3] W. S. M. Werner, M. Oral, T Radlicka, J. Zelinka, I. Müllerova, A. Bellissimo, G. Bertolini, H. Cabrera, and O. Gürlü. Applied Physics Letters, 115(25):251604, 2019.

Acknowledgement: Financial support by the FP7 People: Marie-Curie Actions Initial Training Network (ITN) SIMDALEE2 (Grant No. PITN 606988) is gratefully acknowledged.

Type of presentation: Oral

MS4-O-2647 Ordered electronic states in 2D quantum materials: Imaging effects of hydrostatic pressure at the atomic scale.

Kinyanjui M. K.[1], Ebad-Allah J.[2,3], Krotemüller M.[2], Kuntscher C. A.[2]

[1]Electron Microscopy Group of Materials Sciences, Ulm University, Ulm, Germany, [2]Experimental Physics II, Institute of Physics, University of Augsburg, Augsburg, Germany, [3]Department of Physics, Tanta University, Tanta, Egypt

Email of the presenting author: michael.kinyanjui@uni-ulm.de

Two dimensional (2D) quantum materials often show remarkable properties arising as a result of a complex interplay of charge, lattice, spin, orbital degrees of freedom. This interplay gives rise numerous collective phenomena including superconductivity, spin and charge density waves, among others [1-3]. Understanding the interplay between these orders is currently one of the most challenging areas in materials research.

To understand the nature of this interplay dimensionality, pressure, and introduction of controlled disorder are useful tuning knobs [2-5]. In cases, where 2D quantum materials show co-existing and/or competing electronic phases these knobs can used to either promote or suppress one of the existing electronic phases. This may lead to an atomic-scale spatial distribution of different electronic phases in the same crystal. This has prompted interest in using these tuning knobs to design atomic-scale landscapes to tune electronic phases [6]. However, this requires a better atomic-scale understanding of the effects these parameters have on the structure of the materials as well as the respective electronic phases [1, 3, 6].

We have investigated the atomic-scale response of the charge density waves (CDW) and the underlying atomic lattice in 1T-TaS2 exposed to hydrostatic pressure of up to 2.5 GPa in a Diamond Anvil Cell (Fig.1) [7]. Thin layers of pressurized 1T-TaS2 for TEM investigations were then prepared through mechanical exfoliation. Subsequent atomic-scale transmission electron microscopy imaging shows that the CDW order parameter responds to pressure-induced stacking faults and dislocations in the lattice with an elastic-like strain response. This response is characterized by a proliferation of phase defects in the electronic phase including vortices/dislocations, discommensurations, and domain walls. Our results show the importance of pressure-induced lattice deformations and defects in modulating, stabilizing or destroying electronic phases at the atomic scale.

References

[1] B. Keimer, and J. E. Moore, Nat. Phys. 13, 1045 (2017)
[2] E. Fradkin, S. A. Kivelson, and J. M. Tranquada, Rev. Mod. Phys. 2015,87, 457
[3] D. N. Basov, R. D. Averitt, and D. Hsieh, Nat. Mater. 2017, 16, 1077
[4] B. Sipos, A. F. Kusmartseva,A. Akrap, H. Berger, L. Forro, and E. Tutis, Nat. Mater. 2008, 7, 960
[5] T. Ritschel, J. Trinckauf, G. Garbarino, M. Hanfland, M. V. Zimmermann, H. Berger, B. Büchner, and J. Geck, Phys. Rev. B 2013, 87, 124135
[6] C. Bronholm, I. Fisher, J. Moore, M. Murnane, Basic Research needs Workshop on Quantum Materials for Energy Relevant Technology, US Department of Energy, Office of Science, 2017
[7] M.K. Kinyanjui, J.Ebad-Allah, M. Krotenmüller, and C. A. Kuntscher, Phys. Rev. B 104, 125106(2021)

Acknowledgement: M.K.K acknowledges funding from the Deutsche Forschungsgemeinschaft (DFG) within the project DFG: KI 2546/1-1.

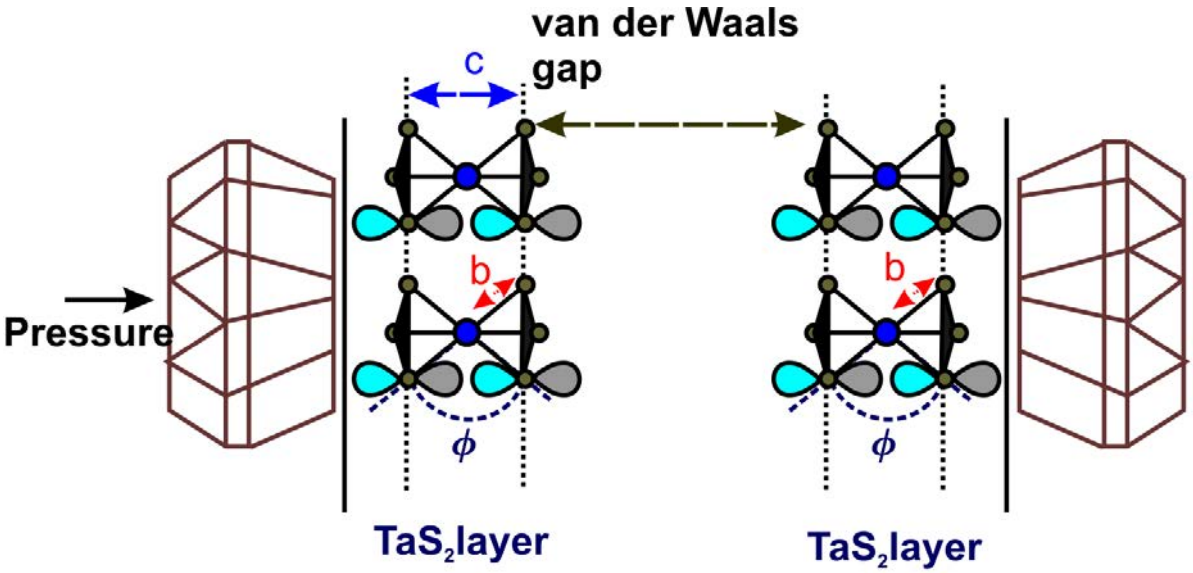

Fig. 1: Schematic diagrams of Diamond anvil cell set-up for hydrostatic pressure experiments on 1T-TaS2

Type of presentation: Oral

MS4-O-2807 Correlated AFM/STEM study on the Mechanical Stiffness of Defect-Engineered Graphene

Joudi W.[1], Trentino A.[1], Mustonen K.[1], Mangler C.[1], Kotakoski J.[1]

[1]Faculty of Physics, University of Vienna

Email of the presenting author: wael.joudi@univie.ac.at

The first isolation of a single layer graphene sheet from graphite via the adhesive tape method in 2004 [1] triggered an avalanche of experiments studying this two-dimensional (2D) material, including investigations on the unique electronic as well as mechanical properties. Since these macroscopically observed properties are a result of elemental composition and atomic structure, the 2D nature of graphene allows for a direct correlation by linking atomic resolution scanning transmission electron microscopy (STEM) images to the observed macroscopic properties. Moreover, this structure-to-property correlation permits investigations on alterations of material properties through defect-engineering. In this study, the in-plane mechanical stiffness of graphene in its pristine state is compared to a defective state in the form of vacancies by correlating atomic force microscopy (AFM) nano-indentation measurements to atomic resolution STEM images. Both instruments, as well as the target chamber where the vacancies are created, are part of the Controlled Alteration of Nano-materials in Vacuum down to the Atomic Scale (CANVAS) system at the University of Vienna, which provides an ultra-high vacuum environment permitting direct correlation. The vacancy density is precisely determined by 2D STEM scan maps, which combine individual small FOV atomic resolution images into one large area, followed by processing of the data set by a convolutional neural network [2]. With a vacancy density of around 1×10^{13} cm^{-2} the 2D elastic modulus decreases by approximately 40%. The STEM images reveal strain-induced surface corrugation caused by the vacancies [3], which might play a role in the weakening mechanism.

[1] K. S. Novoselov et al., Science, 306 (5696), 666-669 (2004)
[2] A. Trentino et al., Nano Letters, 21 (12) 5179-5185 (2021)
[3] J. Kotakoski, F. R. Eder, J. C. Meyer, Phys. Rev. B, 89 201406 (2014)

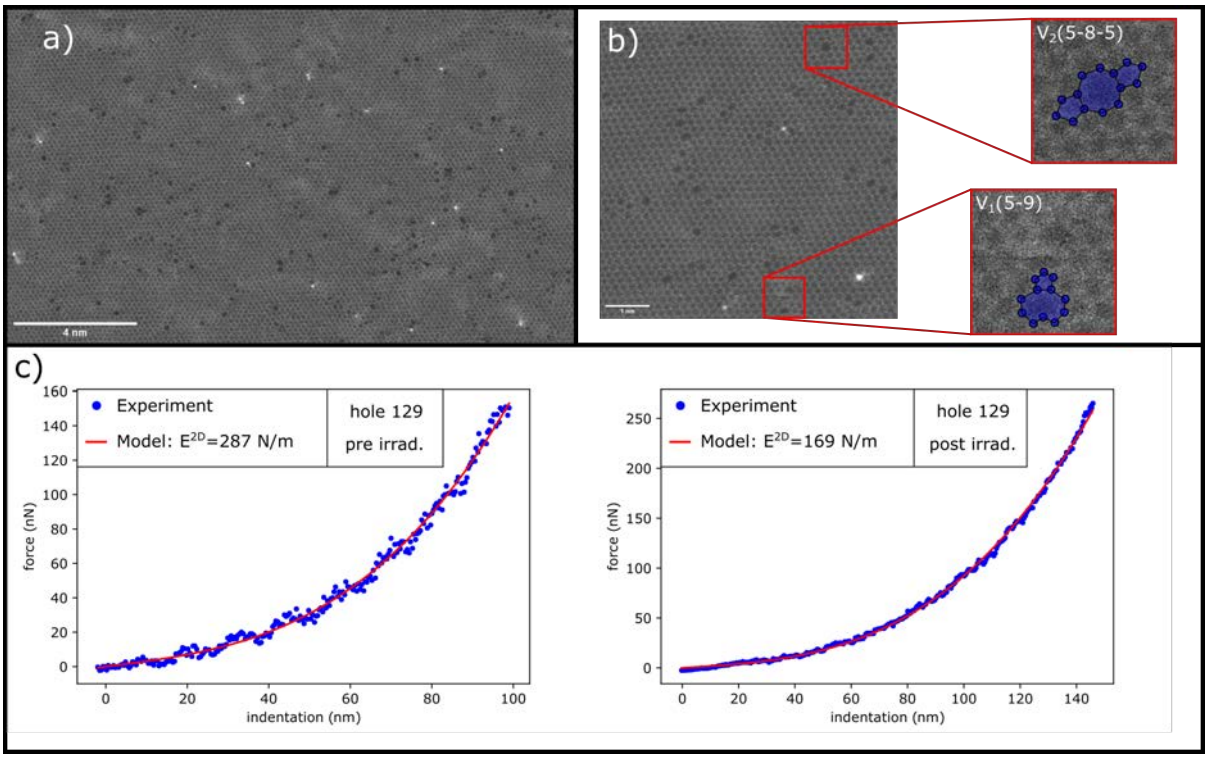

Fig. 1: Atomic resolution STEM image (a) and corresponding magnification (b) revealing the introduced vacancies. AFM nano-indentation curves of the same graphene drumhead before and after irradiation (c).

Type of presentation: Oral

MS4-O-2837 Optimal acceleration voltage for near-atomic resolution imaging of layer-stacked 2D polymer thin films

Liang B.[1], Leist C.[1], Kaiser U.[1], Qi H.[1]

[1]Central Facility of Materials Science Electron Microscopy, Universität Ulm, 89081 Ulm, Germany

Email of the presenting author: baokun.liang@uni-ulm.de

In recent years, two-dimensional polymers (2DPs) have attracted many research interests, and their potential for various applications, such as organic field-effect transistors (OFET), gas filtration, and catalysis, is unfolding in a broad spectrum (1, 2). Therefore, probing the internal construction of organic 2D crystals, ultimately down to the atomic scale, has been a long-sought goal of materials scientists. However, despite superb instrumental resolution in modern transmission electron microscopes (TEM), high-resolution imaging of organic two-dimensional (2D) materials is a formidable task.

In this work, we systematically evaluated the electron accelerating voltages for AC-HRTEM imaging of 2D polymer thin films, exemplified by 2D-PI-BPDA and 2D-PI-DhTPA (Fig. 1). We reached an image resolution of 1.9 Å at 120 kV. This improvement in image resolution has been achieved by maximizing the efficiency of electron usage, among the acceleration voltages of 300 kV, 200 kV, 120 kV, and 80 kV. As not only the resolution but also the image contrast is enhanced at 120 kV, sufficient structure visibility could be obtained under low defocus values (i.e., 40 – 50 nm) to mitigate the detrimental effects of contrast delocalization/blurring. This allows one-to-one mapping of the framework structures. Not only could the porphyrin pores be clearly resolved, but linkers with and without hydroxyl groups could also be distinguished. Surprisingly, we occasionally observed abnormal contrast in the vicinity of the porphyrin cores in both materials, which conflicts with their previously reported structures. Quantum mechanical calculations revealed that the additional contrast could be attributed to molecular interstitial defects – a defect type that had not been discovered in 2D polymers before. We envisage that our results will bring new insights into the defect types and pore interfaces in organic 2D crystals and promote a deeper understanding of pore engineering in future studies. Besides imaging highly crystalline 2D polymers, employing the optimized acceleration voltage also allowed the elucidation of the structures in amorphous organic 2D materials. Image analysis via a U-net-based neural network provided access to a full spectrum of datasets, enabling quantitative description of medium and short-range-order in 2D crystalline and amorphous organic thin films.

Reference

1. X. Feng, A. D. Schlüter, Towards macroscopic crystalline 2D polymers. Angew. Chemie Int. Ed. 57, 13748–13763 (2018).

2. S. Y. Ding, W. Wang, Covalent organic frameworks (COFs): From design to applications. Chem. Soc. Rev. 42, 548–568 (2013).

Acknowledgement: Deutsche Forschungsgemeinschaft 492191310; 426572620; 424798828; 417590517 (SFB-1415), European Union GrapheneCore3 No. 881603.

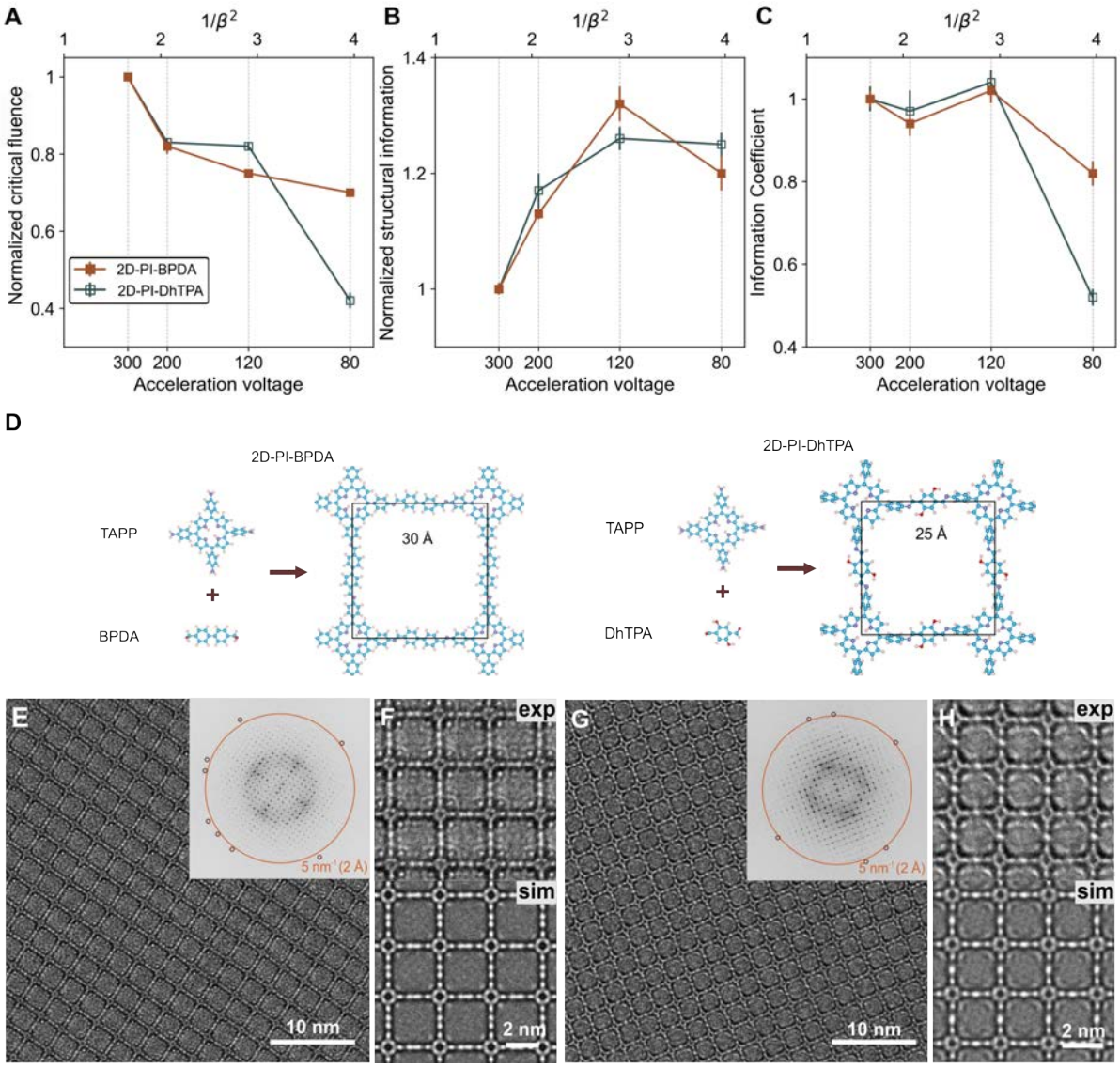

Fig. 1: A-C, Information coefficient determination. D, The reaction scheme of 2D-PI-BPDA and 2D-PI-DhTPA. E-G Unprocessed AC-HRTEM images. Scale bar: 10 nm. Insets: FFT patterns. F-H, upper: magnified images from E-G, respectively. The images have been denoised using Wiener filtering. Down: simulated images with TAPP interstitials.

Type of presentation: Oral

MS4-O-2859 Atomic insights into the structures and properties of nitride thin films

Zhang Z.[1], Chen Z.[1], Koutná N.[2], Holec D.[3], Bartosik M.[3], Mayrhofer H. P.[2]

[1]Erich Schmid Institute of Materials Science, Austrian Academy of Sciences, Leoben, Austria, [2]Institute of Materials Science and Technology, TU Wien, A-1060 Vienna, Austria , [3]Department of Materials Science, Montanuniversität Leoben, A-8700 Leoben, Austria

Email of the presenting author: zaoli.zhang@oeaw.ac.at

Transition metal nitrides have found widespread applications in the cutting- and machining-tool industry due to their extreme hardness, thermal stability, and resistance to corrosion. The increasing demand for these nitrides requires an in-depth understanding of their structures at the atomic level. This has led to numerous experimental and theoretical researches [1-3]. Particularly, with the development of the characterization tool, i.e., aberration-corrected electron microscopy, the understanding of this type of material's structure and property relationships has significantly advanced.

In this paper, we will first present the results of the atomic and electronic structure characterization of the defects in magnetron-sputtered TiN nanocrystalline films (synthesized using different negative bias potentials). We show that the structure of the film (including electronic structures, as revealed by ELNES, **Figure 1**) evolves with deposition conditions due to the defect density changes. Such defects significantly affect the mechanical properties of materials. Along with the structural evolution and point defect changes, the electrical conductivity and the fracture toughness of TiN are improved. Furthermore, the fracture toughness, Young's modulus, cleavage energy, and stresses for TiN films with different point defect structures are calculated. The experimental data is in excellent agreement with first-principle calculations. Our results directly correlate the point defect structure with TiN films' mechanical properties [2].

Secondly, we will present an example of a nitride multilayer (TiN/AlN) study through coupling uses of different microscopy techniques. A surprising intermixing phenomenon in nanoscale nitride multilayers under loads has been detected by detailed advanced TEM investigations. Close examination reveals that a new phase could be created during deformation, which could be observed and mapped via the fine structure difference (i.e., Ti-$L_{2,3}$). Using spherical aberration-corrected HRTEM and HAADF-STEM, we further corroborated such a homogenous solid-state phase has formed in the process of applied loads. Atomic-resolution EDXS analysis exhibits homogenous elemental distributions. The present study provides atomic-scale insights into the extraordinary strength mechanisms pertaining to this nanoscale multilayer [3].

References

[1] Zaoli Zhang, et al., Physical Review B 95, 155305 (2017)
[2] Zaoli Zhang, et al., Materials & Design, 207 (2021)109844.
[3] Zhuo Chen, et al., Acta Materialia, 214(2021) 117004.

Acknowledgement: This work is financially supported by the Austrian Science Fund (FWF P 33696-N).

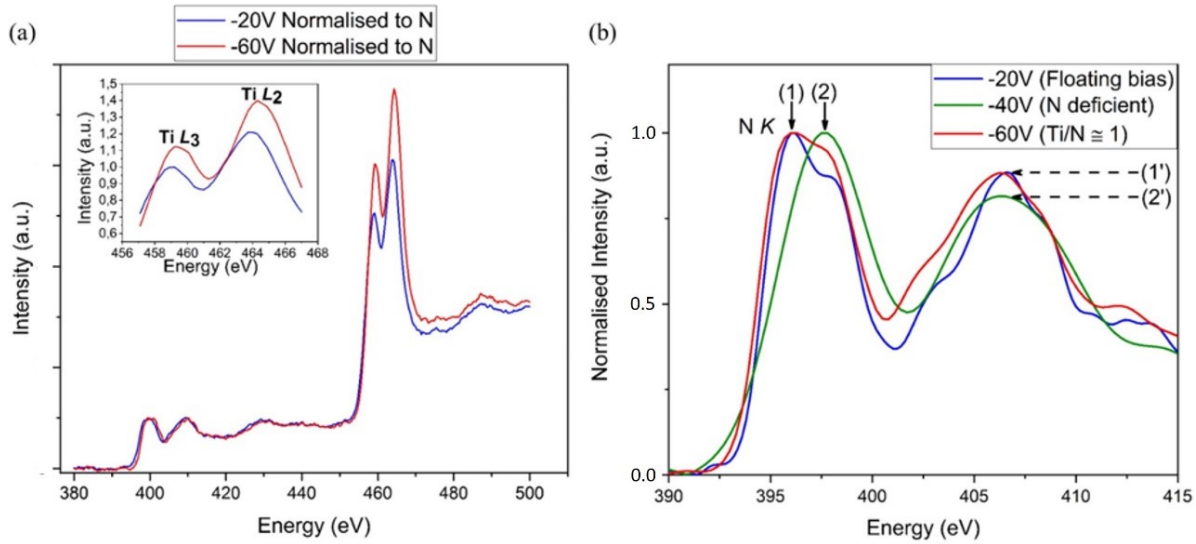

Fig. 1: (a) EELS spectra of Ti L2,3 and N K edges of samples grown with Ub = -20, and -60 V in blue and red. Magnified Ti L2,3 peaks inset. (b) N K of samples grown with Ub = -20, -40, and -60 V in blue, green, and red, respectively. The first N K of the sample with -40 V (green) shows an energy shift to higher values while the second peak drops.

Type of presentation: Oral

MS4-O-2594 Orbital mapping of the LaAlO3-TiO2 interface by STEM-EELS

Oberaigner M.[1], Knez D.[1], Ederer M.[2], Chaluvadi S. K.[3], Orgiani P.[3], Ciancio R.[3], Löffler S.[2], Kothleitner G.[1,4]

[1]Institute of Electron Microscopy and Nanoanalysis, Graz University of Technology, Graz, Austria, [2]University Service Centre for Transmission Electron Microscopy, TU Wien, Vienna, Austria, [3]Istituto Officia dei Materiali-CNR, Area Science Park, Trieste, Italy, [4]Graz Centre for Electron Microscopy, Graz, Austria

Email of the presenting author: michael.oberaigner@felmi-zfe.at

Oxide interfaces can give rise to and exhibit interesting phenomena, like magnetism, ferroelectricity and superconductivity. For the particular example of the interface between anatase TiO_2 and lanthanum aluminate $LaAlO_3$ also the presence of a two-dimensional electron gas (2DEG) has been discussed. [1] Different studies attribute the mechanism for 2DEG formation to an internal electrical potential, which requires a critical thickness, or to structural imperfections by oxygen vacancies. Despite of the technical potential, however, such emergent phenomena at the TiO_2/$LaAlO_3$ interface are still not fully understood.
The $LaAlO_3$-TiO_2 system exhibits two kinds of interfaces, which have different electronic properties predicted by first-principles calculations. The La-terminated interface shows metallic character in the first two TiO_2-layers (Figure 1 (a)), whereas the Al-terminated one remains semiconducting [1]. Both atomic structures have been observed by aberration corrected scanning transmission electron microscopy (STEM). However, for mapping out the electronic information from the interface, electron energy loss spectroscopy (EELS) is required.
Löffler et al. [2] and Bugnet et al. [3] have demonstrated the real-space mapping of individual electronic states in bulk materials by STEM-EELS. Although they could prove feasibility in rutile and graphene, the inherently poor signal-to-noise ratio (SNR) for such experiments imposes a major challenge in terms of general applications. Apart from instrumental parameters, the reason for this is the small usable integration window for orbital mapping with EELS signals. The relevant energy region for 2DEG related phenomena in $LaAlO_3$-TiO_2 is around the onset of the titanium core-loss edge, which marks the electronic states near the Fermi-level (Figure 1 (b)).
Despite the low intensity at the onset, we were able to map individual electronic states at the $LaAlO_3$-TiO_2 interface by using a direct electron detection camera and special post-processing procedures that included multicell averaging and denoising via principal component analysis. For the La-terminated interface, two layers near the titanium are visible, which might indicate the presence of a 2DEG (Figure 1 (c)), as predicted by [1].
This contribution aims to discuss the details of acquisition and data processing of the interface of TiO_2 and $LaAlO_3$ to yield spatially resolved orbital information. Such experiments, combined with simulations, can help clarifying the mechanisms behind 2DEG formation and related phenomena, potentially applicable to other complex oxide heterostructures as well.

[1] Z. Wang et. al, J. Appl. Phys., vol. 108, no. 11, 2010.
[2] S. Löffler et al," Ultramicroscopy, vol. 177, 2017.
[3] M. Bugnet et al., Phys. Rev. Lett., vol. 128, 2022

Acknowledgement: The authors acknowledge financial support by the Austrian Science Fund (FWF) under grant nr. I4309-N36.

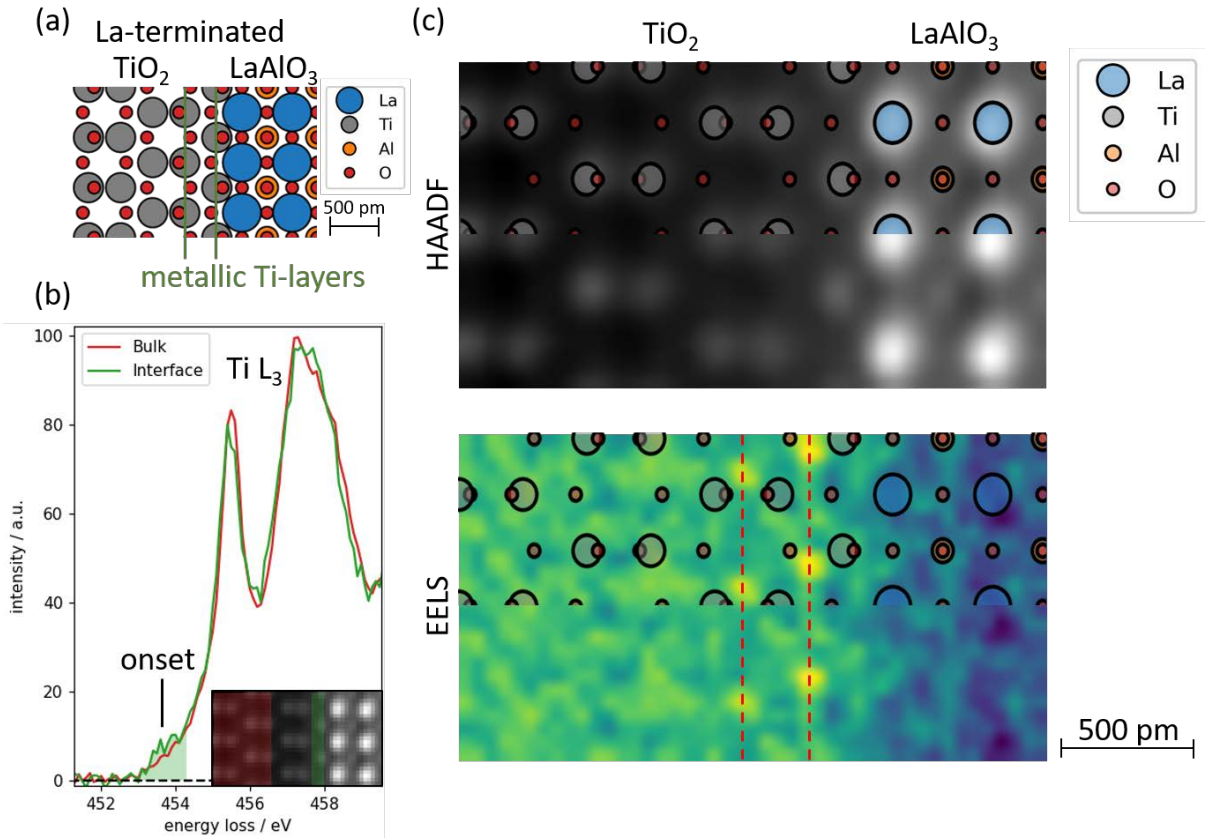

Fig. 1: (a) La-terminated interface of TiO2-LaAlO3. (b) Averaged EELS spectrum at the titanium L3-edge with the marked area used for the 2DEG mapping. (c) Mapped electronic states at La-terminated interface, indicating the 2DEG.

Type of presentation: Oral

MS4-O-2619 Aberration-Corrected STEM Characterisation of Mn-ion Structural Displacements in La0.7Sr0.3MnO3 Interfacial Dead-Layers

Rajak P.[1], Knez D.[2], Chaluvadi S. K.[1], Orgiani P.[1], Rossi G.[1,3], Méchin L.[4], Ciancio R.[1]

[1]Istituto Officina dei Materiali-CNR, Area Science Park, S.S.14, Km 163.5, 34149 Trieste, Italy, [2]Institute of Electron Microscopy and Nanoanalysis, Graz University of Technology, Steyrergasse 17, 8010 Graz, Austria, [3]Dipartimento di Fisica, Università degli Studi di Milano, Via Celoria 16, 20133 Milano, Italy, [4]Normandie University, UNICAEN, ENSICAEN, CNRS, GREYC, 14000 Caen, France

Email of the presenting author: rajak@iom.cnr.it

Due to half-metallicity and room-temperature ferromagnetism, colossal magnetoresistive manganite films with composition $La_{0.7}Sr_{0.3}MnO_3$ (LSMO) are of great interest for investigating oxide spintronic applications. Bulk LSMO is a metallic ferromagnet, but when thickness of LSMO film is less than a critical value of 4 unit cells, ultrathin films become insulators with drastically reduced magnetism and metallicity; known as "dead layer". It has shown that controling oxygen coordination, interfacial oxygen octahedral rotation, interfacial strain, and oxygen defect concentration can modify not only dead layer thickness but also magnetic characteristics of epitaxially grown LSMOs.

Using high resolution scanning/transmission electron microscopy (HR-S/TEM), strain analysis, electron energy loss spectrum (EELS) and density functional theory (DFT) calculations, we provide evidence of Mn ion displacement correlated with reduction of Mn valence state in the vicinity of film/substrate interface in LSMO thin films grown on (001) oriented $(LaAlO3)_{0.3}$-$(Sr2AlTaO6)_{0.7}$ (LSAT) substrates using pulsed laser deposition [1].

HRTEM and geometrical phase analysis are used to assess the quality and strain state of LSMO/LSAT heterostructure. It shows +2.4± 0.5% elongation of out of plane lattice spacing at first 7 nm interfacial region. Aberration-corrected STEM imaging with low angle annular dark-field (ADF) detector reveals enhanced defect contrast indicating formation of 7 nm thick interfacial region that is structurally different from the bulk of the film and can be associated with magnetic dead layers. EELS shows that Mn valence state gradually increases from +3.1±0.05 to +3.3±0.05 towards the surface of the film, indicating that oxygen vacancies occur at interfacial area with substrate compared to rest of the film, accompanied by an out-of-plane lattice expansion. In interfacial region, STEM imaging with high-angle (HA) ADF detector indicates that Mn ions are displaced by 29±10 pm from its centrosymmetric positions. DFT calculations and STEM image simulation show that Mn ion displacement is connected to a decrease in Mn valence state at interface. Using STEM-ADF imaging instead of STEM-HAADF imaging, which is mostly used for thin-film characterization, allowed us to emphasize the defect contrast due to the cumulative effect of Mn ions displacement and oxygen vacancies at the interfacial layer and relate it to changes in valence states of Mn measured by EELS.

Our results provide that structural symmetry loss is linked to reduced Mn valence state at the interfacial region, opening up new options for modifying the magnetic anisotropy of LSMO thin films using strain-driven thin-film technology.

[1] Rajak, P. et al. (2021). ACS Applied Materials and Interfaces, 13, 55666–55675

Acknowledgement: This project has received funding from the European Union's Horizon 2020 research and innovation program under grant No 823717– ESTEEM3.

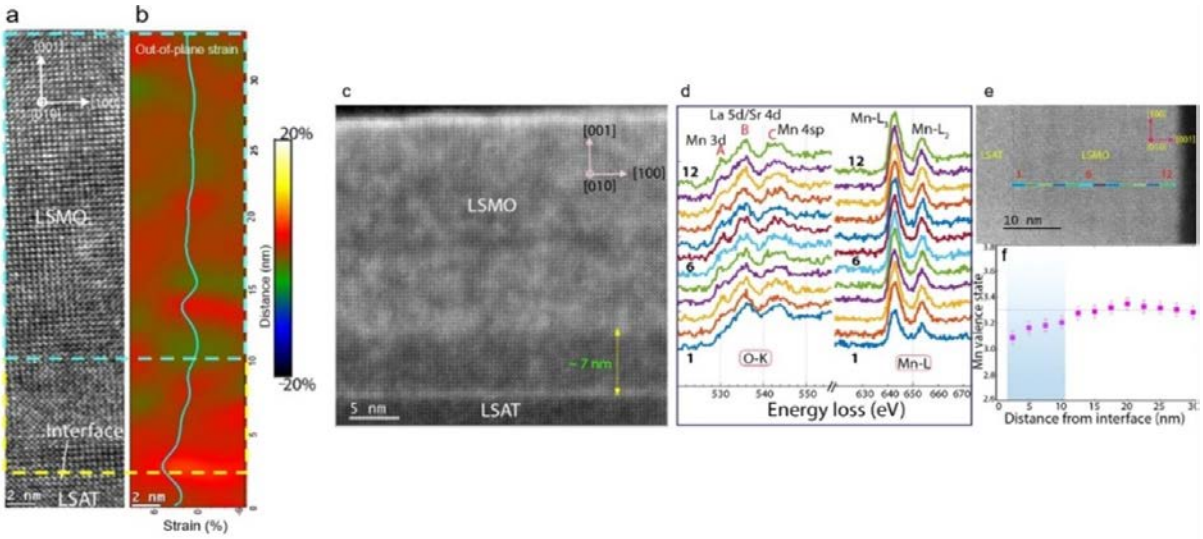

Fig. 1: (a) HRTEM image of [001] oriented LSMO film (b) out-of-plane lattice strain map and line profile of the strain is overlaid (c) STEM-ADF image showing contrast variation at 7 nm distance from interface (d) EELS fine structures (e) STEM-HAADF image of area where EELS line profiles were collected (f) estimated Mn valence as a function of distance.

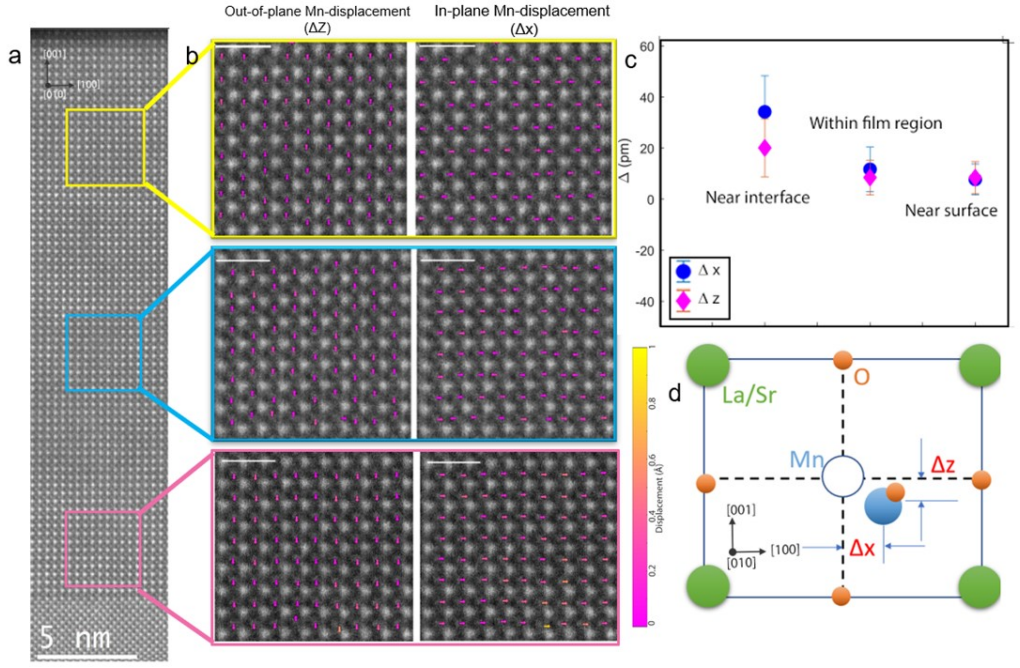

Fig. 2: (a) The regions used to map the displacement of Mn ions are indicated in a different color on STEM-HAADF image. (b) Map of atomic displacement vectors superimposed on STEM-HAADF (c) variation in magnitude of Δz and Δx from different regions. (d) Projection of LSMO unit cell along [010] direction.

Type of presentation: Invited

MS4-IN-2613 In and ex situ (S)TEM manipulation of 2D materials without air exposure

Kotakoski J.[1]

[1]University of Vienna, Faculty of Physics, Austria

Email of the presenting author: jani.kotakoski@univie.ac.at

Avoiding ambient exposure is typically impossible in the context of transmission electron microscopy due to the air gap between other experimental stations and the microscope. While this is only a limited problem for bulk samples that have a low surface-to-bulk ratio, the situation is more severe for 2D materials since they consist only of surface. This leads to significant problems with surface contamination and material degradation due to oxidation.

In this contribution, I will introduce the CANVAS (controlled alteration of nanomaterials in vacuum down to the atomic scale) system in Vienna, which we have built over the past several years to allow correlative experimentation on 2D materials combining different microscopes, a plasma ion source, evaporators, an argon glove box and even a protective atmosphere transfer possibility between two universities.

One recent example of the use of the CANVAS system is provided by defect-engineering of graphene [1], where we first pre-characterize graphene samples through Raman spectroscopy before entering them to the vacuum system, after which all following steps are carried out without air exposure. The samples are first imaged to confirm their quality, after which practically all remaining contamination is removed with a laser pulse in the microscope column. Next, they are exposed to low energy ion irradiation at the plasma ion source to create vacancies, which is subsequently confirmed (see Figure 1) by large-scale automated atomic resolution imaging [2] After this, the defect-engineered sample can be subjected to mechanical testing at the exact same sample locations, allowing for the first time a direct correlation of the defective atomic structure with its macroscopic elastic properties. As expected, but in contrast to some recent literature, the defected graphene shows significant softening (2D elastic modulus decreases by ca. 40% at a defect density of ca. 1e13 cm−2). Alternatively, the introduced defects can be used as anchoring sites for evaporated species allowing heteroatom doping via intermittent vacancies [2]. This technique is similar to the two-step implantation process we also recently demonstrated for Au in graphene [3], except
that now the whole process can be carried out within the same vacuum system containing also the atomic resolution microscope.
Overall, the CANVAS system demonstrates that the air gap can be eliminated between transmission electron microscopes and techniques typically used in surface science, paving the way for experiments that have until now remained impossible.

[1] A. Trentino et al., Nano Lett. 21, 5179-5185 (2021).
[2] H. Inani et al., J. Phys. Chem. C 123, 13136-13140 (2019).
[3] A. Trentino et al., 2D Mater. 9, 025011 (2022).

Acknowledgement: We thank the Austrian Science fund for funding through projects I3181-N36 and P31605-N36, and Vienna Scientific Cluster for computational time.

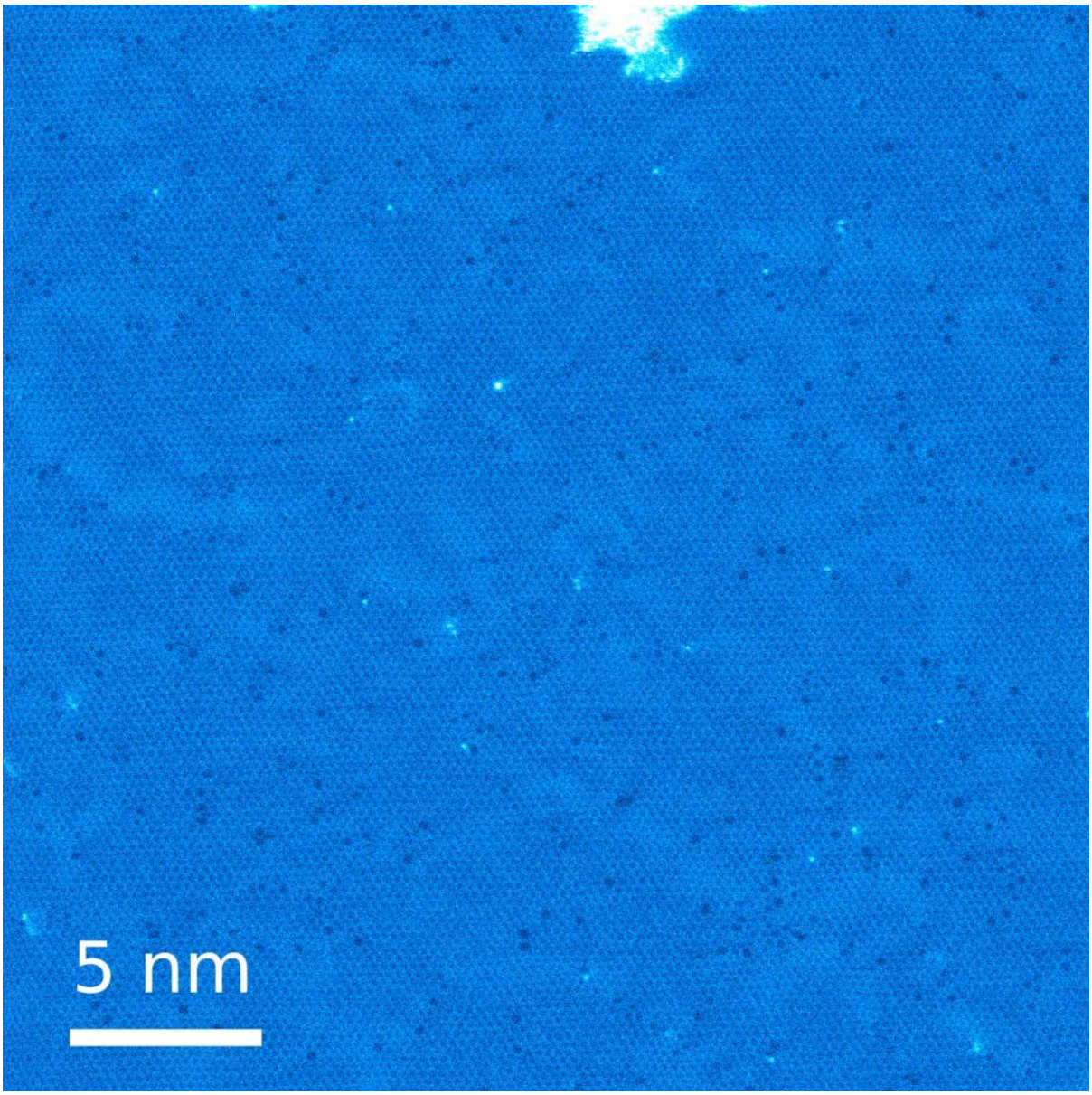

Fig. 1: Atomic-resolution STEM-MAADF image of atomically clean defect-engineered graphene.

Type of presentation: Oral

MS4-O-2792 Insights into tribology of TMD-based coatings from TEM experiments

Bondarev A.[1], Polcar T.[1]

[1]Department of Control Engineering, Faculty of Electrical Engineering, Czech Technical University in Prague, Technicka 2, Prague 6, Czech Republic

Email of the presenting author: bondaan2@fel.cvut.cz

The TMD coatings are widely used in tribological applications. Meanwhile, two main drawbacks of the MoS_2 solid lubricants, low load-bearing capacity, and fast degradation in the terrestrial atmosphere became a driving force for their improvement. To enhance mechanical and tribological properties, TMDs have been fabricated with gradient structure or combined with different additives to obtain composite structure, such as metallic (Ti , Zr, Cr, Au, Ni, Fe, Cu, Ag, Nb, Pb) and non-metallic elements (C, N, F, O). Mechanical properties are improved significantly when nanocomposite or amorphous structure is formed, and the sensitivity to environment can be reduced, although it is still a limitation even for complex compositions of the coatings.
In the early studies of sputtered TMDs, a friction-induced reorientation of the basal planes at the sliding interface of the coating was proposed as the reason for exceptional tribological behavior. The formation of a low friction interface was also studied for alloyed TMD coatings. Using a cross-sectional high-resolution transmission electron microscopy, researchers observed basally oriented MoS_2 layers on the surface of both friction bodies. Meanwhile, in the bulk of the coating, the structure was amorphous, therefore formation of a low-friction interface occurred due to crystallization of the MoS_2 during sliding. It is generally accepted that under the load, this crystallization/reorientation of the TMD crystals takes place near the tribocontact interface. The (0 0 2) basal planes are aligned parallel to the sliding direction, and weak van der Waals bonding between these basal planes in a lattice provides low shear stress values under sliding conditions and thus a low friction coefficient. However, the role of dopants and chemical interactions in a tribolayer are not completely understood so far.
Going beyond conventional TEM, in the present work, it is shown that by using state-of-the-art EDS detectors and EELS a deeper understanding of the tribological performance can be gained. Our results give insights into tribological behavior of unique Mo-S-O coatings. Collected EDX and EELS data on the nanoscale give a starting point for the MD and DFT calculations of the structures. It is found experimentally and by MD simulations, that the triboactivated separation of molybdenum oxide and sulfide phases occurs. The presence of so-called “undesired” oxygen in the structure of crystalline MoS_2 tribolayers does not hinder its lubricious properties. Also, TEM analysis allows to establish the missing relationship between the routes for the formation of the low-friction interface and the chemical composition of the doped TMD coatings.

Acknowledgement: The work was supported by MEYS CR (project CZ.02.2.69/0.0/0.0/20_079/0017983)

Type of presentation: Oral

MS4-O-2580 Nanoscale characterization of van der Waals-bonded GeTe/Sb2Te3 phase-change memory superlattices grown by pulsed laser deposition

Lotnyk A.[1,2], Hilmi I.[1], Behrens M.[1], Rauschenbach B.[1]

[1]Leibniz Institute of Surface Engineering (IOM), Permoserstr. 15, 04318 Leipzig, Germany,
[2]Laboratory of Infrared Materials and Devices, The Research Institute of Advanced Technologies, Ningbo University, Ningbo, Zhejiang 315211, China

Email of the presenting author: andriy.lotnyk@iom-leipzig.de

Ge-Sb-Te (GST) phase-change materials have attracted much attention due to their unique technologically relevant properties. The high importance of this class of materials has been recently demonstrated by Intel, which introduced several memory products based on GST layers. While the conventional phase-change memory technology uses amorphous-to-crystalline phase transitions, the advanced memory technology is based on the crystalline-to-crystalline phase transitions within of GeTe/Sb2Te3-based superlattices (SLs). Depending on the sequence of Ge-Te layers at the SLs interface, the SLs-based device can be either in high-resistance or low resistance state. However, switching mechanism in the SLs is still under debate. Since the local structure of GeTe/Sb_2Te_3-based SLs might have strong implications in the design and reliability of future memory devices, the knowledge of relevant structural properties is of high importance. While epitaxial growth of GeTe/Sb_2Te_3 SLs on Si (111) by sputter deposition and MBE require substrate temperatures (Ts) >230 °C, pulsed laser deposition (PLD) has an advantage in the growth of phase change thin films at lower Ts. This work aims to study the impact of substrate temperature and the thickness of GeTe layers on possible intermixing within of epitaxial GeTe/Sb_2Te_3 SLs grown on Si(111) substrates by PLD at substrate temperatures ranging between 100°C and 220°C. Atomic-resolution Cs-corrected STEM and atomic-scale EDX analysis are used to reveal structure changes in the SLs at the atomic scale [1,2].
The results showed huge intermixing at the interfaces of GeTe/Sb_2Te_3 SLs. The formation of Ge-rich GST units intercalated with Sb_2Te_3 building units were observed at low Ts (100-120 °C). Interestingly, the units are bonded to the Sb_2Te_3 layers by weak van der Waals (vdW) forces, while no pure GeTe layers were formed in the SLs. EDX analysis revealed disordered Ge/Sb cation layers within GST units and the formation of intermixed Sb/Ge cation layers in the 1st and 2nd outermost cation layers. However, the growth of thermodynamically stable vdW-bonded GST structures was found at higher Ts (185-200 °C), while continues layered $GeSb_2Te_4$ thin film was formed at Ts=220°C.

Overall, this work demonstrates that the formation of vdW-bonded GST structures is thermodynamically driven process, which cannot be suppressed at high growing temperatures, regardless of deposition technique. The results should also be considered when investigating the switching mechanism in phase-change SLs. However, diffusivity of Ge and Sb atoms can be largely restricted at low deposition temperatures, opening a way to further optimize the SLs microstructure.

[1] A. Lotnyk et al., Nano Res. 11 (2018) 1676
[2] A. Lotnyk et al., Appl. Surf. Sci. 536 (2021) 147959

Acknowledgement: We would like to thank Mrs. Agnes Mill for her assistance in the preparation specimens for TEM analysis.

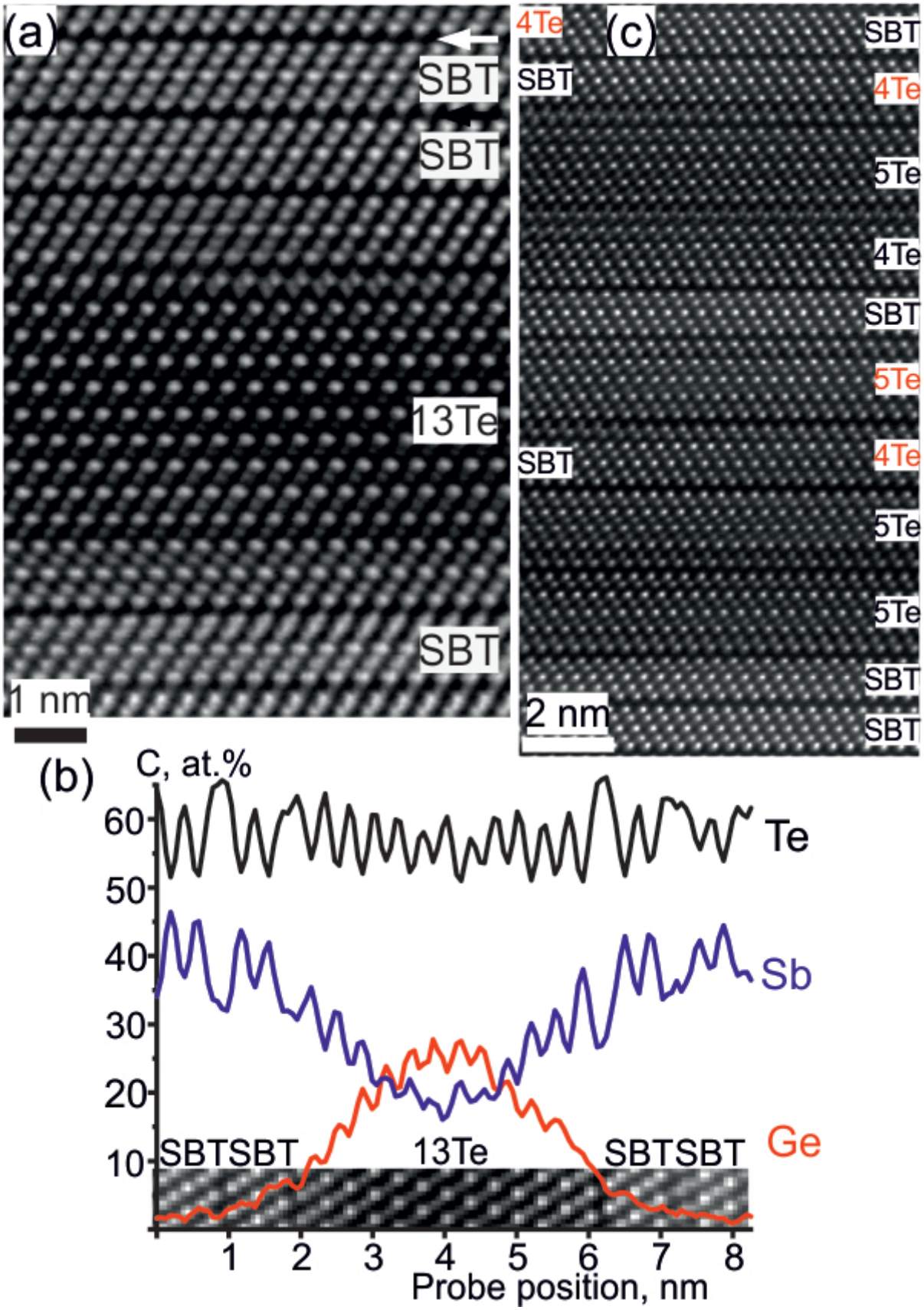

Fig. 1: Atomic-resolution HAADF-STEM images of $GeTe/Sb_2Te_3$ SLs grown at a substrate temperature of (a) 100°C and (c) 200°C. Individual building Sb_2Te_3 (SBT) and GST units (numbers in the images) are stacked along the [0001] direction and are separated by vdW gaps (dark lines). (b) Quantitative line profiles for Ge, Sb and Te chemical elements.

Type of presentation: Oral

MS4-O-2511 Microscopy of CVD grown MoS2 layers compared to layers obtained by the sulphurization of Mo

Pecz B.[1], Panasci S. E.[2,3], Koos A.[1], Schilirò E.[2], Franco S. D.[2], Greco G.[2], Fiorenza P.[2], Roccaforte F.[2], Agnello S.[4,2], Cannas M.[4], Gelardi F. M.[4], Sulyok A.[1], Nemeth M.[1], Giannazzo F.[2]

[1]Centre for Energy Research, Institute of Technical Physics and Materials Science, [2]Consiglio Nazionale delle Ricerche – Istituto per la Microelettronica e Microsistemi (CNR-IMM), Strada VIII 5, 95121 Catania (Italy), [3]Department of Physics and Astronomy, University of Catania, 95123 Catania, Italy, [4]Department of Physics and Chemistry Emilio Segrè, University of Palermo, 90123 Palermo, Italy

Email of the presenting author: pecz.bela@ek-cer.hu

MoS2 is one of the most promising transition metal dichalogenides (TMDs) as a semiconductor layer for new devices. The growth of MoS2 can be carried out with CVD (Chemical vapour Deposition) and results in high quality individual crystallites, which have to reach a certain size for real applications. Another method promises to cover the whole surface of the substrate by MoS2 when sputtered Mo layer is annealed at high temperature (700 or 800oC) for relatively long time (one hour) in sulphur atmosphere. The first results are promising despite the polycrystalline nature of the continuous film obtained on SiO2/Si substrate.
The grown and annealed layers were investigated by transmission electron microscopy (using a Thermofisher THEMIS 200 aberration corrected TEM/STEM), and XPS photoelectron spectroscopy. Electrical characterization was also carried out.
HREM images showed the layers with different thickness, while HAADF images taken in STEM mode show in a more direct way the number of layers via the Z-contrast in which the Mo sheets are bright. It is obvious that typically 1-3 layer thick MoS2 could be grown on different substrates including single crystalline SiC, sapphire and GaN.
Figure 1 shows the shape and size of the small MoS2 triangulars grown onto the carbon foil of a TEM grid. The crystallites are in the range of 50 nm size. They are not oriented because of the amorphous substrate. However, on the counterpart specimen grown in the same cycle they show the same size crystallites with oriented triangular shape. Being the crystallites small provide the possibility to take a high resolution (HREM) image of a whole triangular, which is shown in the next image (Fig.2). The lattice spacings seen are of 100 type and are about 0.27 nm.
The another approach via the deposition of thin continuous, sputtered Mo layer results in specimen completely buried by MoS2 after annealing that in sulphur at 700oC for one hour. One example is shown in Fig. 3 and 4. As the substrate is amorphous again (this case SiO2) we can not expect single crystalline layers. XPS analysis of the as deposited Mo layer shows that it is composed of MoO3 phase. Nevertheless, the same method proves that after sulphurization that is turned to stoichiometric MoS2 (probably with a very low oxygen content is also present in the layer). On the other hand, the CVD grown MoS2 crystallites does not contain any oxygen. Conductive AFM characterization showed submicron size inhomogeneity in the current map. The bandgap was also measured and 1.0 eV was evaluated what indicates that the layer is doped.

Acknowledgement: This work was funded, by project ETMOS in the framework of the FlagERA-JTC 2019.

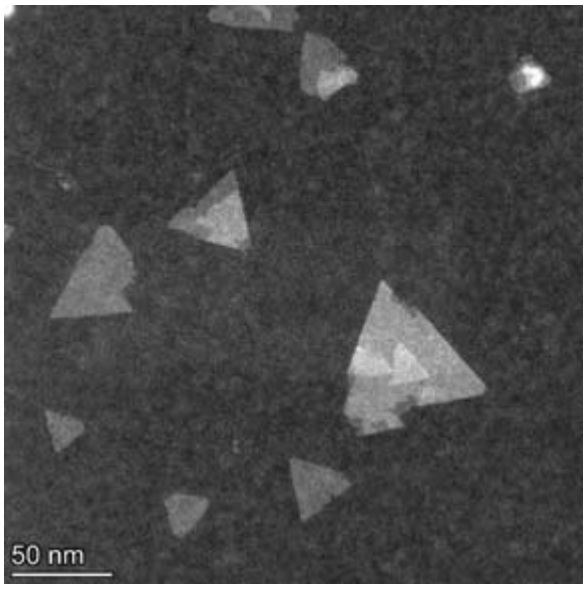

Fig. 1: HAADF plan view image of CVD grown MoS2 on TEM grid

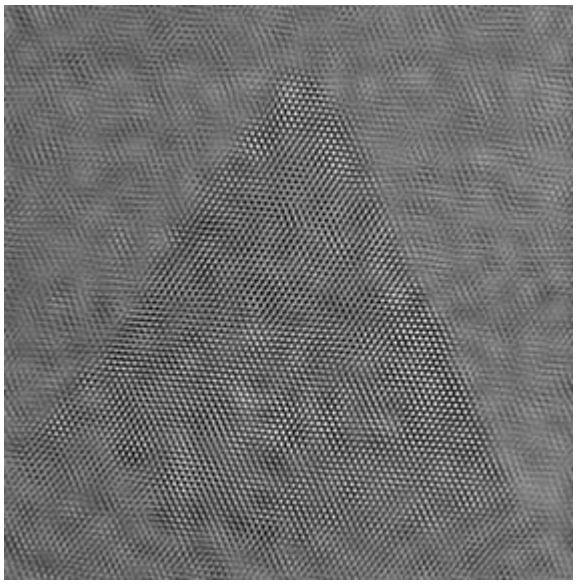

Fig. 2: One of the triangular shaped MoS2 island in high resolution and Fourier filtered (the lattice around the triangular is an artefact).

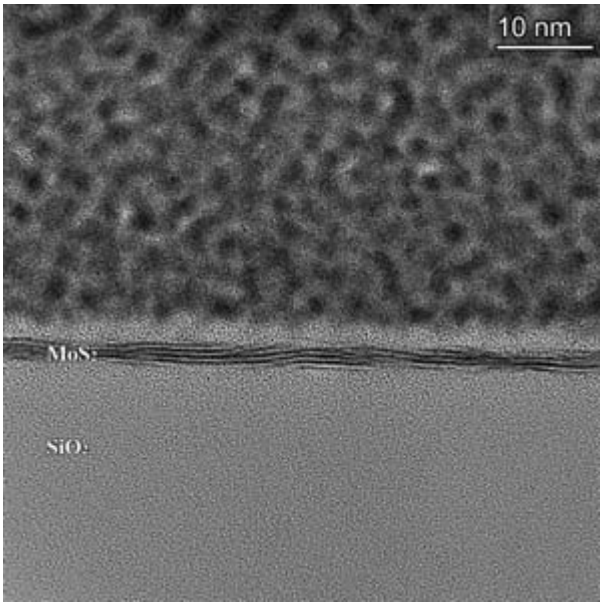

Fig. 3: TEM image of MoS2 obtained by sulphurization of Mo.

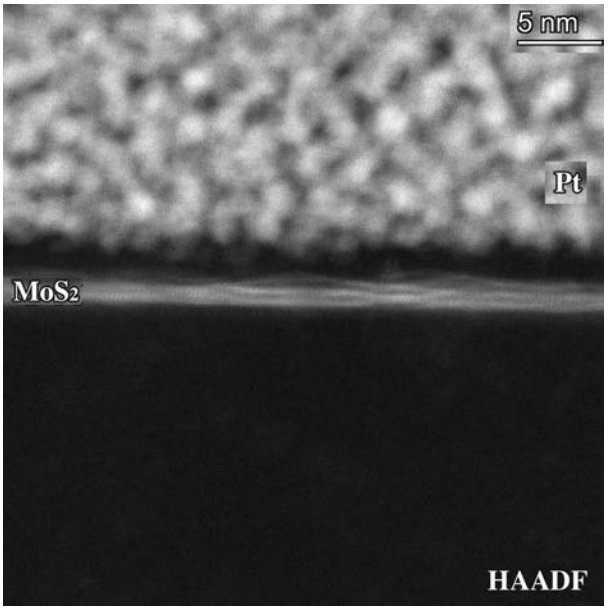

Fig. 4: HAADF image of the same specimen shown in Fig2.a. The MoS2 of 3 layers is clearly seen.

Type of presentation: Oral

MS4-O-2842 Thickness dependency of critical dose for extremely beam-sensitive two-dimensional polymer

Mücke D.[1], Kaiser U.[1], Qi H.[1]

[1]Central Facility of Material Science Electron Microscopy, Universität Ulm, Germany

Email of the presenting author: david.muecke@uni-ulm.de

AC-HRTEM imaging has been proven a powerful tool to probe the local structures in organic 2D crystals, such as, 2D polymers and metal organic frameworks[1]. However, the achievable image resolution is typically limited by the low electron resilience of organic materials. The critical dose for amorphization is material-dependant, which can be as low as only a few electrons per square Ångstrom. In order to enhance the signal-to-noise ratio in HRTEM images, increasing the critical dose is of vital importance. The common techniques dedicated to this purpose however lack a comprehensive understanding. Especially the effect of sample thickness is only vaguely understood [2,3]. It is believed that a higher thickness leads to a self-encapsulating effect, which reduces the loss of radicals, leading to a self-healing of the material. Our study, however, reveals that the caging effect reported in literature may not be generalized to more sophisticated polymer systems. In this work, the critical dose of a triazine-based 2D polymer[4] has been measured as a function of the sample thickness (Fig. 1). Mechanical exfoliation has been employed to fabricate nanoflakes with thicknesses ranging from 15 nm to 85 nm. We found that, although the Bragg reflection intensity increased with thickness due to more elastic scattering, the total dose for amorphization was invariable. The extremely low critical dose at 1-2 e-/□2 rendered HRTEM imaging significantly challenging if not impossible. The absence of caging effect has been attributed to the pore channels in the framework structure, serving as escape routes for free radicals (Fig. 2). To further prove our assumption, graphene encapsulation has been applied to prevent radical escape. This has led to an unambiguous increase of the critical dose (Fig. 3), allowing for HRTEM imaging on a direct electron detector with unit-cell resolution.

References

[1] Haoyuan, Q. *et al.* Near–atomic-scale observation of grain boundaries in a layer-stacked two-dimensional polymer. *Sci. Adv.* **6**, eabb5976 (2022).
[2] Fryer, J. R. Radiation damage in organic crystalline films. *Ultramicroscopy* **14**, 227–236 (1984).
[3] Egerton, R. F. Control of radiation damage in the TEM. *Ultramicroscopy* **127**, 100–108 (2013).
[4] Hu, F. *et al.* Highly Efficient Preparation of Single-Layer Two-Dimensional Polymer Obtained from Single-Crystal to Single-Crystal Synthesis. *J. Am. Chem. Soc.* **143**, 5636–5642 (2021).

Acknowledgement: We acknowledge the funding from Deutsche Forschungsgemeinschaft (DFG) – 492191310; 426572620; 417590517 (SFB-1415), and European Union GrapheneCore3 (881603).

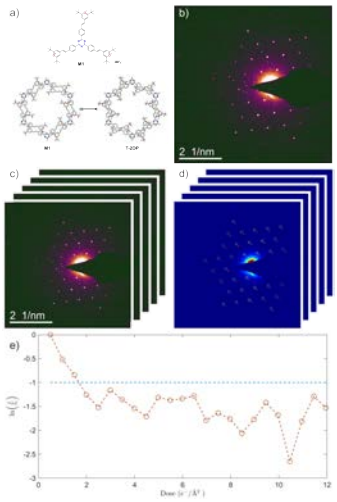

Fig. 1: a) Model of the 2DP. b) Diffraction pattern of the polymer. c) In order to obtain the critical dose of the polymer a series of diffraction patterns has to be obtained. e) With the intensity in every image d), the relation between intensity and accumulated dose can be obtained. If the intensity drops below 1/e the critical dose is reached.

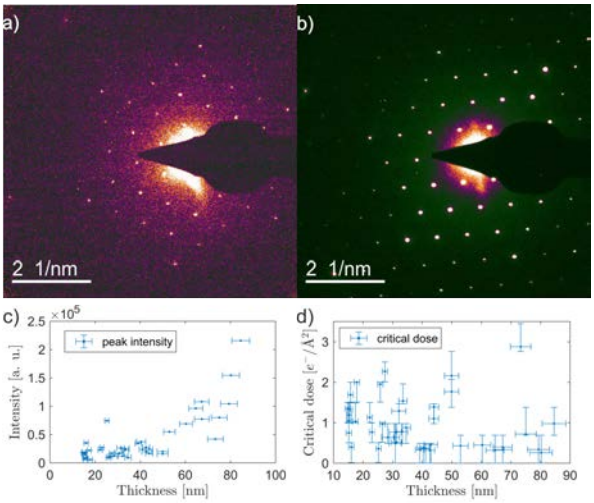

Fig. 2: a) Diffraction pattern of a (15.8 ± 0.9) nm thick polymer area. b) Diffraction pattern of a (85 ± 4) nm thick area. c) Measured first order peak intensity of the first image of the dose series normalized with the electron dose per image, over the thickness of the polymer. d) Critical dose over the thickness of the 2DP.

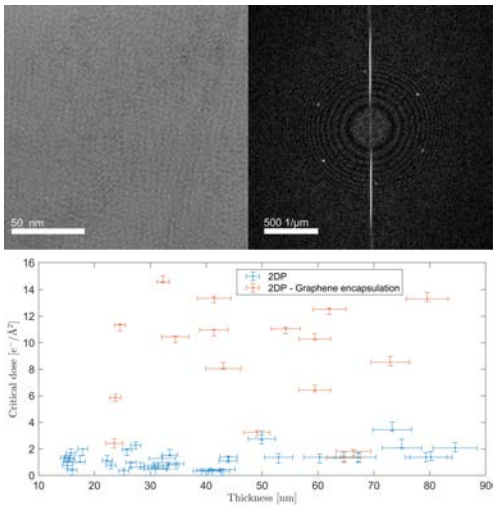

Fig. 3: a) Real space averaged image of the polymer obtained with only 5 e-/Å2 on the direct electron detector. b) Fourier transform of the raw image of a). c) Comparison of the critical dose of the in graphene encapsulated polymer sample and the pristine sample over the measured thickness range.

Type of presentation: Poster

MS4-P-2609 Imaging of structural deformations of gas-phase synthesized graphene by intermediate energy electrons

Jurmanová J.[1], Jašek O.[1], Toman J.[1], Nejezchleba D.[1]

[1]Department of Physical Electronics, Faculty of Science, Masaryk University, Brno, Czech Republic

Email of the presenting author: janar@physics.muni.cz

Microwave-plasma-based decomposition of organic precursors represents a simple, environmentally friendly bottom-up approach for the synthesis of few-layer graphene [1]. The decomposition of hydrocarbons and alcohols to C atoms and C2 molecules leads to the growth of the hexagonal network forming the graphene layer [2,3]. The formed layers are overlapping, individual nanosheets corrugating and curving of the nanosheet's edges. For detailed information about these structural features various techniques of scanning electron microscopy will be used for their the imaging - the different acceleration voltage (HV) or working distance (WD), beam deceleration mode (BDM), and the Scanning Transmission Electron Microscopy (STEM). The brightness and contrast of obtained images will be compared for these methods, and it will be chosen as the best method of imagining such samples. We further evaluate the relationship between the results of the high-resolution imaging and material analysis results obtained by Raman spectroscopy.
To display the corrugations and curving of the few-layer nanosheets, the large working distance (WD) in combination with beam deceleration mode (BDM), 2 - 3 kV acceleration voltage proved to be the best choice. The large WD proposed by the authors of the article [5] ensures an increase in the contrast visibility (CV) of corrugation due to the removal of the unwanted SE3 signal by a more suitable position of the sample relative to the detector. In addition, if we replace the traditional view with the BDM view, this guarantees better electron beam shaping and greater electron scattering in the sample than the normal mode, which further improves the contrast visibility of the nanosheets structure (Fig. 2 shows better visibility of edges and wrinkles emerging compared to Fig. 1).
The use of a STEM gives a unique opportunity to visualize the thickness of individual nanosheets and to make structural deformations visible by selecting different acceleration voltages. From the set of images in Fig. 3, the number of individual layers and their structural deformations can be determined approximately by calculating the CV. These results can be correlated with values of D, G, and 2D band intensity obtained by Raman spectroscopy analysis of few-layer graphene and will be the subject of our further research.

References

[1] A. Dato, Journal of Materials Research, 34 (2019) 214–230
[2] O. Jasek et al., J. Phys. D: Appl. Phys., 54 (2021) 165201
[3] O. Jasek et al., Nanotechnology, 32 (2021) 505608
[4] J. Jurmanova et al., Proceedings 11th International Conference on Nanomaterials - Research & Application, 85-90. (2020)
[5] Huang, L., Zhang, D., Zhang, F.-H., Feng, Z.-H., Huang, Y.-D., Gan, Y., Small 2018, 14, 1704190. https://doi.org/10.1002/smll.201704190

Acknowledgement: This work was supported by project LM2018097 funded by the Ministry of Education, Youth, and Sports of the Czech Republic.

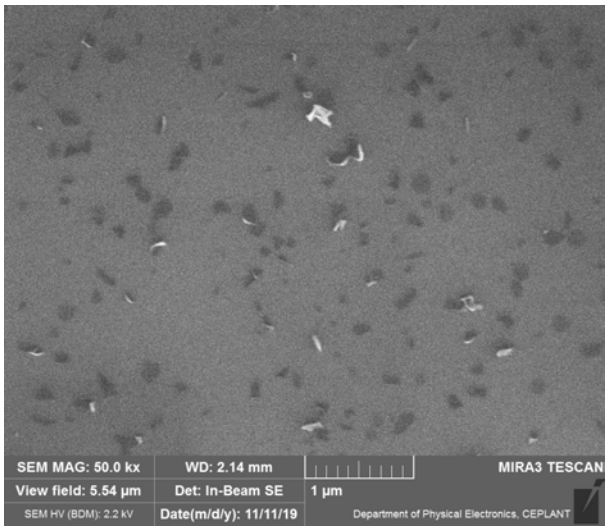

Fig. 1: Few-layer graphene was synthesized by decomposition of ethanol in a dual-channel microwave plasma torch deposited on a silicon wafer. The graphene sheets are displayed using Beam deceleration mode (BDM) at a working distance of 2 mm.

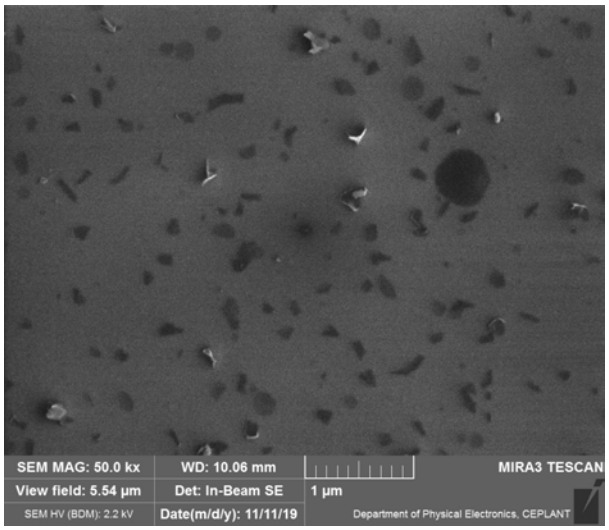

Fig. 2: The same sample is displayed using Beam deceleration mode (BDM) at a working distance of 10 mm.

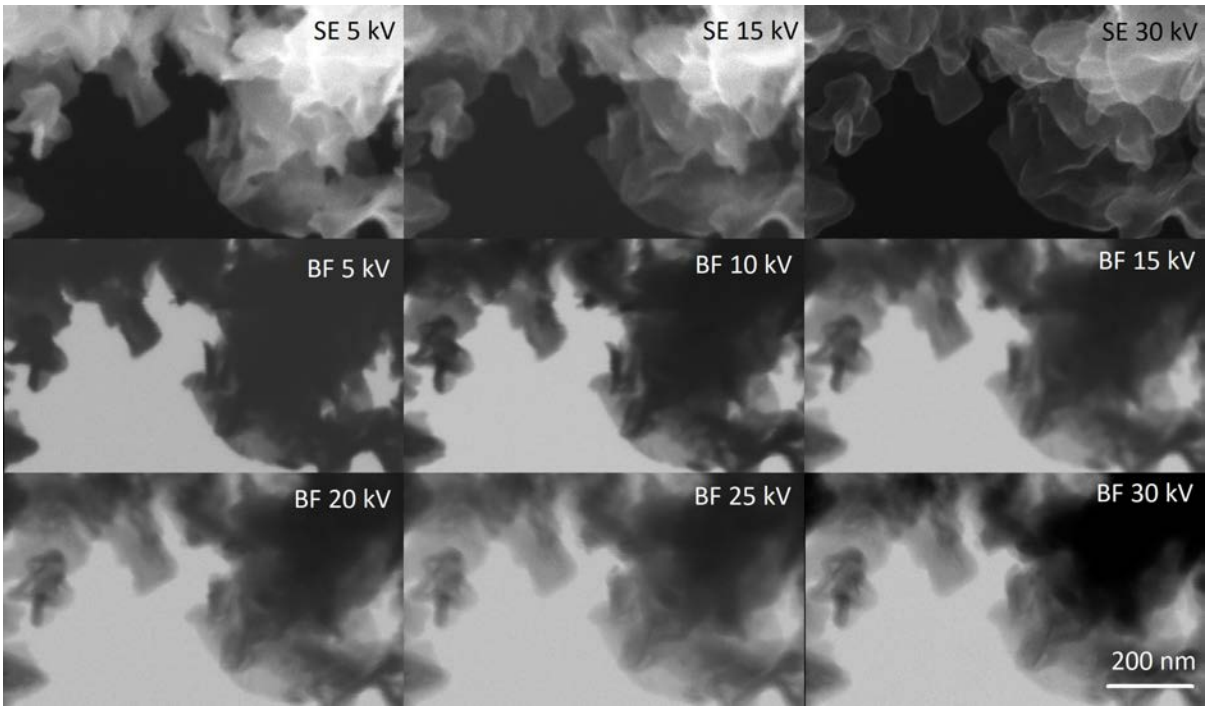

Fig. 3: The few-layer graphene nanosheets - a study of contrast visibility in the dependence on the acceleration voltage. The first row shows the secondary electron image (SE, topographical contrast) of the sheets, and the second and third resolute the thickness and visualize the corrugations by means of the bright field (BF) detector in STEM mode.

Type of presentation: Poster

MS4-P-2750 In-situ observation of 2D materials growth on liquid substrates

Bukvišová K.[1], Mahel V.[2], Kodambaka S.[3], Novák L.[4], Šikola T.[1,2], Kolíbal M.[1,2]

[1]CEITEC BUT, Brno University of Technology, Purkyňova 123, 612 00 Brno, Czech Republic, [2]Institute of Physical Engineering, Brno University of Technology, Technická 2, 616 69 Brno, Czech Republic, [3]Department of Materials Science and Engineering, University of California Los Angeles, Los Angeles, CA 90095 USA, [4]Thermo Fisher Scientific Brno. Vlastimila Pecha 12, 627 00 Brno, Czech Republic

Email of the presenting author: kolibal.m@fme.vutbr.cz

The isolation of graphene in 2004 raised an enormous excitement in the community, bringing to light a fundamentally new class of low-dimensional materials. Soon after, the graphene's insulating cousin – hexagonal boron nitride – was introduced, initiating a burst of papers speculating about a new electronics era. Process scalability, which is necessary for the utilisation of 2D materials on a larger scale, excludes the mechanical exfoliation and significantly narrows the choice of suitable growth techniques. In this regard, the most promising approach is that of chemical vapour deposition (CVD), in which the precursors are delivered from a gas phase to the substrate, where they react and form the growing layer. However, in contrast to exfoliated layers, those prepared by CVD exhibit a significantly higher concentration of various structural defects, which are detrimental to many quantum effects and device functionalities the physicists and engineers search for. The defect family in 2D materials includes domain boundaries (GBs) and twin defects, together with many types of vacancies and anti-sites. GBs were identified to play a critical role in many aspects. The mitigation strategies include specific sample preparation techniques or the use of single-crystal substrates.

Developing a more general strategy to avoid the formation of GBs within a footstep of the intended 2D-material-based device (and, preferably, at a wafer-scale) is desirable. Rheotaxy (growth on a liquid substrate) has been proposed as a viable method to achieve domain ordering and self-assembly already in 2012 for graphene [1]. However, it remains poorly explored due to a lack of in-situ experimental techniques that confirm or disprove hypotheses raised concerning the formation mechanisms [2]. Only recently, experimental studies started to pop-out [3].

While the growth of 2D materials on solid substrate inside SEM is straightforward, liquid substrate presents a significant challenge. We have utilised μReactor [4] in SEM to grow graphene on liquid gold. In our contribution, we experimentally demonstrate some aspects of the graphene growth on liquid substrate, that have been only hypothesized so far, namely movement and ordering of the graphene domains on liquid surface (Fig. 1). We will discuss peculiarities of our observations, and compare them with similar material systems reported so far.

[1] Geng, D. et al. PNAS **2012**, 109, 7992-7996.
[2] Tsakonas, C.; Dimitropoulos, M.; Manikas, A. C.; Galiotis, C. Nanoscale **2021**, 13, 3346-3373.
[3] Jankowski M. et al., ACS Nano **2021**, 15, 9638-9648.
[4] Novák, L., Wandrol, P., Vesseur J. R. Micr.&Microanal. **2020**, 26 (S2), 1144-1145.

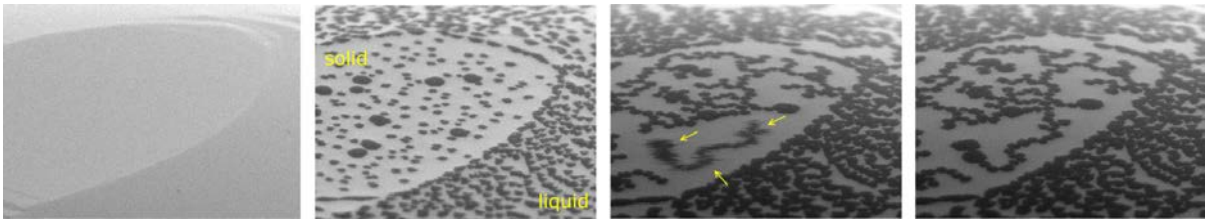

Fig. 1: Graphene growth from ethylene at 950 °C (first two images) and 1050 °C on a large quasi-melted Au. After melting the whole droplet at 1050 °C, free-floating graphene domains perform rapid oscilatory motion. The motion stops immediately if the domains are attached to a stable domain cluster. Horizontal field of view is 3 μm.

Type of presentation: Poster

MS4-P-2660 Noble gas clusters in a graphene sandwich

Längle M.[1,2], Pesenhofer C.[1], Mizohata K.[3], Terntino A.[1,2], Mangler C.[1], Mustonen K.[1], Åhlgren E. H.[1], Kotakoski j.[1]

[1]University of Vienna, Faculty of Physics, Physics of Nanostructured Materials, Boltzmanngasse 5, 1090 Vienna, Austria, [2]University of Vienna, Vienna Doctoral School in Physics, Boltzmanngasse 5, 1090 Vienna, Austria, [3]University of Helsinki, Department of Physics, P.O. Box 43, FI-00014 Helsinki, Finland

Email of the presenting author: manuel.laengle@univie.ac.at

Due to their chemical inertness, noble gases are in gas phase under normal conditions. When trapped between two graphene sheets, however, the exerted pressure presses noble gas atoms together leading to the formation of clusters [1]. We create such clusters by implanting singly charged low energy ions into suspended bi- and double layer graphene, which allows their direct imaging through (scanning) transmission electron microscopy (figure 1) inside the graphene sandwich [2]. While all small clusters (up to at least 14 atoms) remain solid, larger clusters can exhibit either solid- or liquid-like structures depending on their size, chemical element and possibly local microscopic environment. In general, Xe clusters appear more solid than Kr ones (figure 2).

[1] Längle, M., Mizohata, K., Åhlgren, E., Trentino, A., Mustonen, K., & Kotakoski, J., Microscopy and Microanalysis, 26(S2), 1086-1089
[2] Rasim Mirzayev, Kimmo Mustonen, Mohammad R. A. Monazam, Andreas Mittelberger,Timothy J. Pennycook, Clemens Mangler, Toma Susi, Jani Kotakoski, Jannik C. Meyer, Science Advances 3, e1700176 (2017)

Acknowledgement: Funding through the Austrian Science Fund (FWF) within projects P31605 and M2596 and computational resources from the Vienna Scientific Cluster are acknowledged

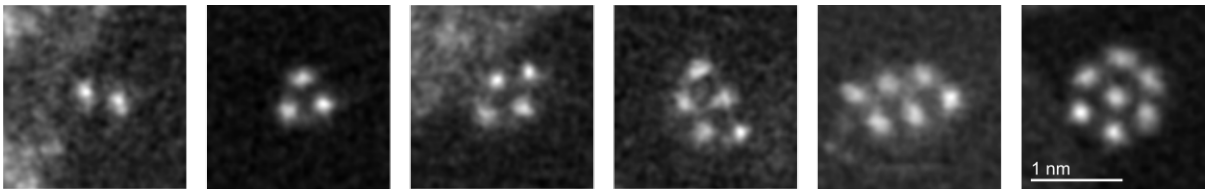

Fig. 1: Filtered annular dark field scanning transmission electron microscopy images of Xe clusters to up to seven atoms.

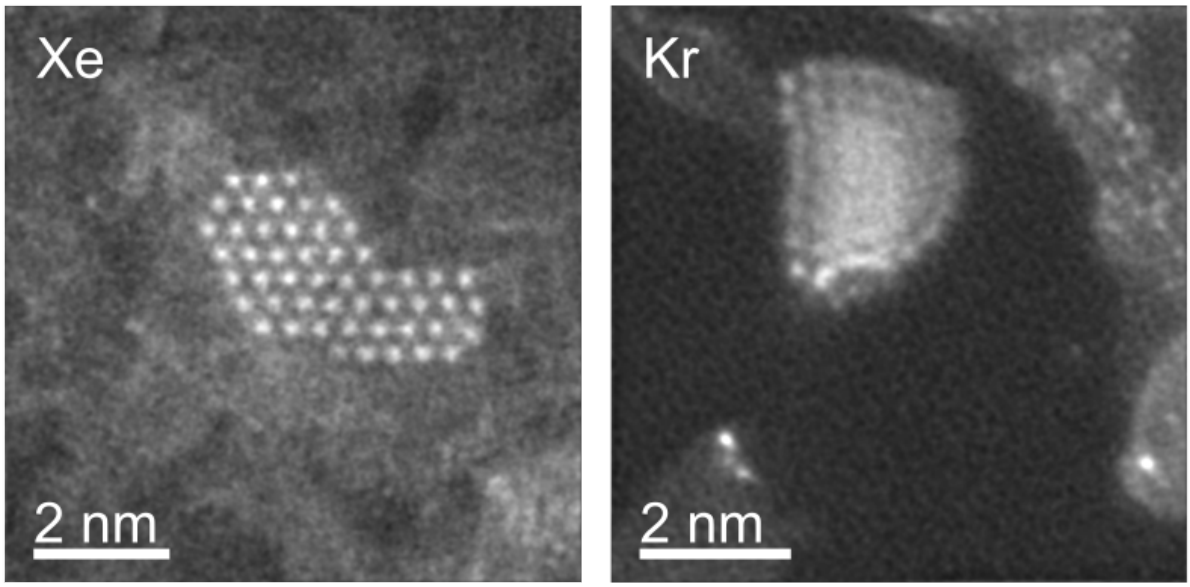

Fig. 2: Filtered annular dark field scanning transmission electron microscopy images of a Xe51 cluster and a Kr cluster of a comparable size.

Type of presentation: Poster

MS4-P-2835 Deep learning pipeline for statistical quantification of amorphous two-dimensional materials

Leist C.[1], Kaiser U.[1], Qi H.[1]

[1]Central Facility of Electron Microscopy Group of Materials, Universität Ulm, Germany

Email of the presenting author: christopher.leist@uni-ulm.de

Since 2004, the discovery of graphene has triggered an explosive development of two-dimensional (2D) materials with fascinating properties and exceptional application potential The research interest soon extended beyond the monolayer crystalline carbon into non-carbon 2D materials, including transition metal dichalcogenides, hexagonal boron nitride, black phosphorous. Although crystallinity is essential to these materials, recent years have witnessed the rise of their amorphous counterparts, namely amorphous 2D (a-2D) materials. The combination of atomic thinness and lack of long-range order has endowed a-2D materials with unique characteristics, such as ultra-high uniformity, excellent mechanical and chemical stability, and abundance in catalytic-active sites, promoting their applications in flexible electronics, electrocatalysis, and energy storage. Aberration corrected high-resolution transmission electron microscopy (AC-HRTEM) allows for unambiguous elucidation of atomic structures in amorphous two-dimensional (2D) materials. However, image analysis of short-range-ordered structures remains a great challenge due to laborious manual evaluation and lack of statistical significance.
In this work, we automated image analysis of amorphous 2D materials via a deep learning approach. The neural network is capable of atom identification and segmentation of evaluation-suitable regions with high precision. This has been achieved by training the U-net network exclusively on simulated images. A semi-random atomic model with porous and bilayer areas led to the successful recognition of complex attributes in experimental images, including disorder, micropore, and surface contaminations. The neural network robustness against intensity inhomogeneity was further enhanced by introducing background gradients in the training datasets. Implementation on the experimental images of monolayer amorphous carbon and amorphous polymer provided multifold datasets with statistical significance and direct visualization of the short-range-ordered structures. Although designed for amorphous materials, our deep learning pipeline is readily generalizable to crystalline samples, enabling the identification of local defects and grain boundaries, as well as strain mapping. We envisage that automated quantification of short-range order will bring new insights into the structural understanding of a-2D systems, laying the foundation for the establishment of structure-property correlation in this rising class of materials. The deep learning approach may also pave the way for probing dynamic processes with efficiency and precision, e.g., amorphous-crystalline transition, amorphization, nucleation and crystal growth, etc., where human endeavour no longer suffice.

Acknowledgement: We acknowledge the funding from DFG – 424798828, as well as the support the European Union's Horizon2020 research and innovation program - 881603.

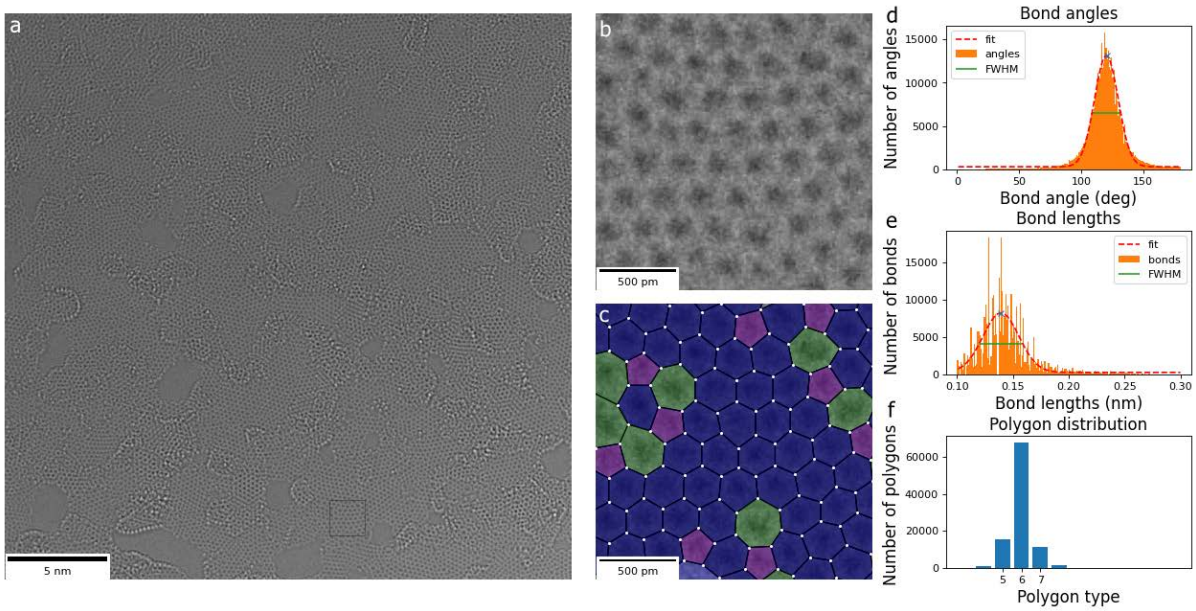

Fig. 1: Automated image evaluation. a, AC-HRTEM image of monolayer amorphous carbon. b, Enlarged image from the boxed region in (a). c, Neural network real-space mapping of polygons . d-f, Statistical histogram of bond angles, bond lengths and polygons. TEM experiments were performed on the Cc/Cs-corrected SALVE instrument operated at 80kV.

Type of presentation: Poster

MS4-P-2861 Electron tomography for measurement of buried interface roughness in thin films

Manjeshwar Sathyanath S. K.[1], Warnatz T.[2], Hjörvarsson B.[2], Leifer K.[1]

[1]Department of Materials Science and Engineering, Uppsala University, Box 35, 75103 Uppsala, Sweden, [2]Department of Physics and Astronomy, Uppsala University, Box 516, 75120 Uppsala, Sweden

Email of the presenting author: sharath.kumar@angstrom.uu.se

Interface roughness in thin films grown plays a vital part in the subsequent properties of these materials. One of the challenges associated with such structures is the uncertainties associated when measuring the roughness of the cross-sectional samples in the TEM [1]. Alternative methods exist, such as AFM and X-ray diffraction. Whereas in the AFM, only the surface roughness can be determined, using XRD, the buried interfacial roughness can be determined. Though, this measurement needs a model to relate the diffractogram to the interfacial roughness, especially in the analysis of multilayers. Electron tomography allows for the complete three-dimensional roughness analysis even for the buried interface. The only mathematical operation needed for tomography is the Radon transform.

In this work we have carried out STEM electron tomography to evaluate the roughness and the interfacial width of the Fe film grown on a MgO substrate. From the roughness analysis at the interface between the film and the substrate, the RMS roughness was around 2 nm. The surface RMS roughness of the Fe film was also around 2 nm. The interfacial width was around 4 nm.

[1] Misa Hayashida. et al. Tomographic measurement of buried interface roughness, Journal of Vacuum Science & Technology B 33, 040605 (2015); https://doi.org/10.1116/1.4926975.

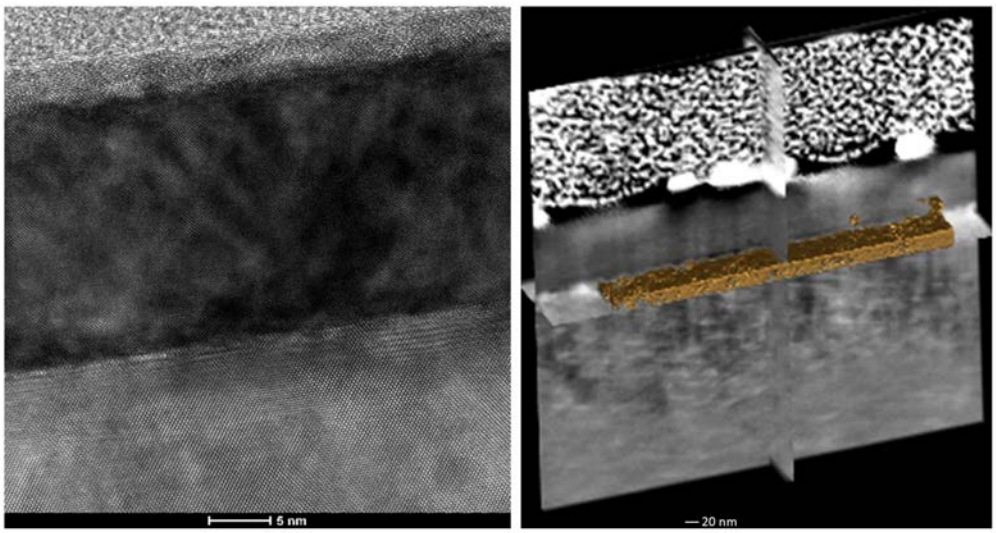

Fig. 1: HRTEM image of Fe thin film on MgO substrate (left). Tomogram showing the Fe film (right).

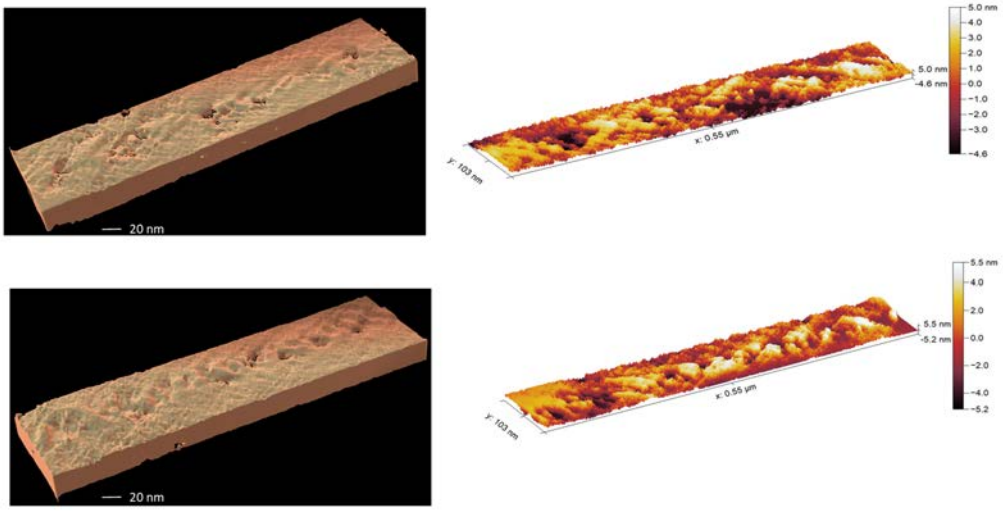

Fig. 2: Roughness of the Fe film at the substrate/film interface (top). Surface roughness of the Fe film (bottom).

Type of presentation: Poster

MS4-P-2610 In situ TEM annealing: comparison of thin GeSn layers grown by MBE and CVD

Martínez K.[1], Minenkov A.[1], Aberl J.[2], Vukušić L.[2], Brehm M.[2], Groiss H.[1]

[1]Christian Doppler Laboratory for Nanoscale Phase Transformations, Center for Surface and Nanoanalytics, Johannes Kepler University Linz, Linz, Austria, [2]Institute of Semiconductor and Solid-State Physics, Johannes Kepler University Linz, Linz, Austria

Email of the presenting author: kari.martinez_reyna@jku.at

The continuing interest in studying the properties of epitaxial $Ge_{1-x}Sn_x$ films is motivated by their great potential in high-performance Si-based electronics and optoelectronics. Even though Ge originally has an indirect band gap, incorporating Sn above 6 at% [1] permits a transition to the direct band gap. Nevertheless, the low eutectic temperature and a very limited Sn solubility in Ge of 1%, make the GeSn layers dramatically nonequilibrium, resulting in phase separation and decomposition processes at quite low temperatures [2,3]. The thermal stability of these systems is not fully clear yet. Therefore, for detailed insights into the decomposition process, *in situ* transmission electron microscopy (TEM) experiments have been performed. This technique allows the observation of dynamic processes in materials under external stimuli, such as temperature. To track real-time changes during annealing, micro-electro-mechanical system (MEMS) devices are used. Significant efforts were given to the comparison of the thermal stability of GeSn thin layers grown by molecular beam epitaxy (MBE) and chemical vapor deposition (CVD).

To trace the samples' structural evolution upon annealing, cross-sectional lamellae were cut from specimens and installed on micro-electro-mechanical system (MEMS) heating chips with a focused ion beam (FIB)-assisted approach as presented in Fig. 1. Heating experiments were carried out from 25 to 600°C. A combination of complementary TEM techniques and energy-dispersive X-ray spectroscopy (EDX) has provided valuable information on the thermal stability and decomposition of the specimens under investigation.

The thermal stability of GeSn samples grown by MBE, with a layer thickness of 50 nm and Sn concentrations of 10 and 14 at% has been compared. For the $Ge_{0.9}Sn_{0.1}$ sample, Pt was used as a capping layer in the lamella preparation. It was found that Pt is not stable for temperatures above 460°C. For this reason, in the $Ge_{0.86}Sn_{0.14}$ sample W was used as a protecting layer.

The $Ge_{0.9}Sn_{0.1}$ sample was found to have a higher thermal stability compared to the $Ge_{0.86}Sn_{0.14}$ sample. The $Ge_{0.9}Sn_{0.1}$ alloy is stable up to 460°C. At 470°C Pt diffusion from a capping layer induces a decomposition (Fig. 2). The $Ge_{0.86}Sn_{0.14}$ sample is stable up to 300°C. At 350°C, a clear Sn segregation was observed, resulting in the emergence of Sn-rich precipitates (Fig. 3). Additional data on the thermal properties of CVD-grown GeSn samples with 10 at% Sn will be presented and discussed in comparison with MBE-grown ones.

[1] J. Doherty et al., Chem. Mater., 32, pp. 4383–4408 (2020)
[2] H. Groiss et al., Sci. Rep., 7, pp. 1–12 (2017)
[3] A. Minenkov, H. Groiss, J. Alloys Compd., 859, 157763 (2021)

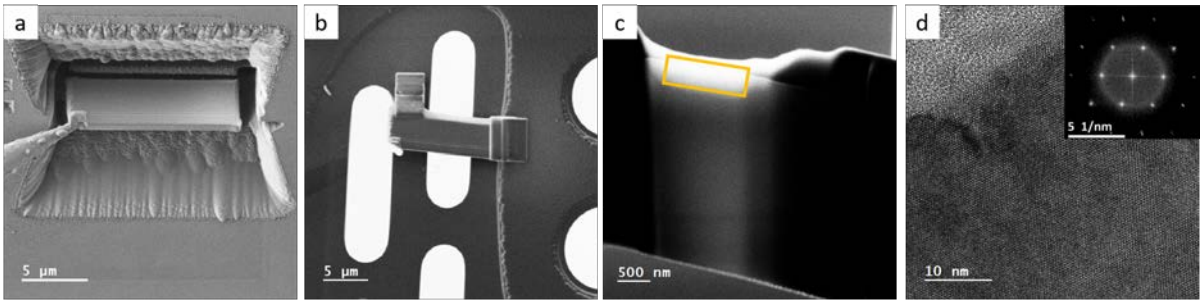

Fig. 1: Preparation of a MEMS heating chip: a) lift-out; b) installation of the lamella on the MEMS chip; c) final thinning of the sample to electron transparency, the region of interest is highlighted with the orange rectangle; and d) high-resolution TEM image of the sample cross-section along with the corresponding Fast Fourier Transform (FFT) pattern.

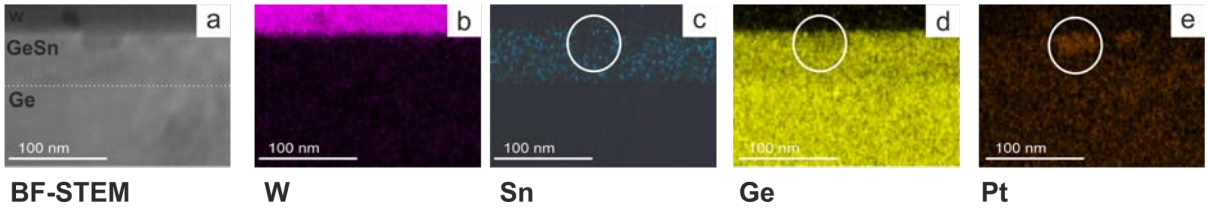

Fig. 2: EDX maps of the $Ge_{0.9}Sn_{0.1}$ sample at 470°C: a) BF-STEM image of the sample cross-section; elemental maps of b) W capping layer, c) Sn, d) Ge and e) Pt. The decomposition of the GeSn layer, which is readily visible in the Sn and Ge maps might be influenced by Pt diffusion.

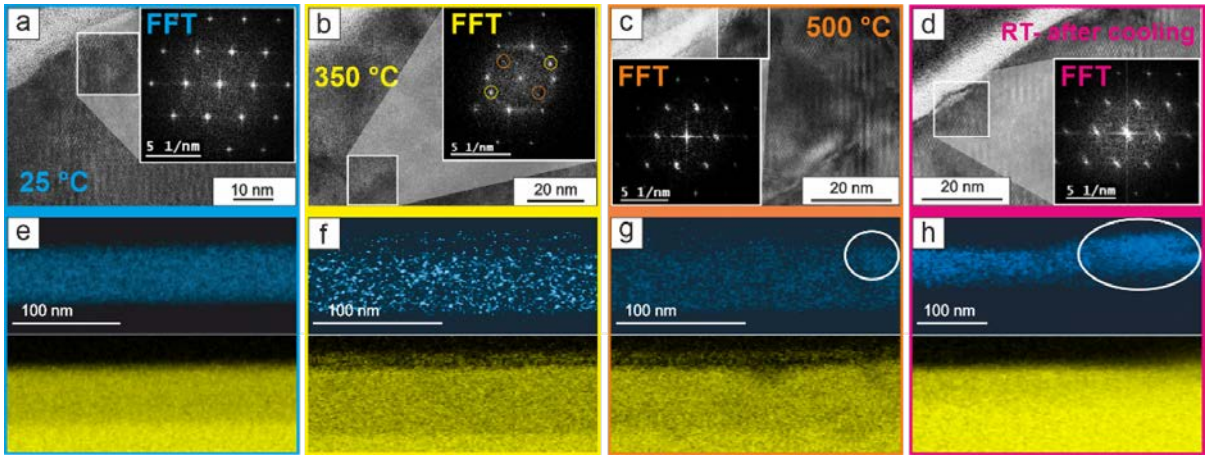

Fig. 3: Thermal evolution of a $Ge_{0.86}Sn_{0.14}$ layer. (a-d) High resolution (HR) TEM images and FFT patterns of highlighted areas. At 350°C, extra reflexes appear in the FFT. (e-h) EDX maps of Ge, in yellow, and Sn, in blue. Sn precipitates at 500°C and at RT-after cooling are highlighted with white ovals.

Type of presentation: Poster

MS4-P-2595 Native surface oxide characterization with S/TEM on PM metal powders

Nagy Š.[1], Krížik P.[1], Nagy Trembošová V.[1], Hájovská Z.[1], Orovčík Ľ.[1], Nosko M.[1]

[1]Institute of Materials and Machine Mechanics SAS, Dúbravská cesta 9/6319, 845 13 Bratislava

Email of the presenting author: nagy.stefan@savba.sk

Most powder metallurgy (PM) metals are manufactured with atomization technology. On the powder surface, native oxidation is inevitable. This native surface oxide layer can affect the processing technology and the final functional properties of the product, therefore investigating the nature of this surface quality is important and challenging. With a further surface modification or coating of the powders, this native oxide must be taken into account also.
In this study, we investigated the microstructural features of the native oxide surface on metallic industrial PM materials (Al, Zn, Mg, Ni) and the different preparation methods for S/TEM observation. Preparation of sample from pressed bulk powder material finished by ion milling, epoxy embedding of examined powders, and direct observation of metallic powders regarding native oxide layer on Cu grids with carbon film are presented.
Bulk aluminium PM powders investigated with HR-STEM indicate a consistent amorphous oxide layer with 10 nm thickness between two powder interfaces which can ensure higher temperature stability of the material (Fig.1)[1]. The deformation of powders and the surface oxide should be taken into account for the bulk material preparation technique. Embedment of examined powders in epoxy resin enable the cross-section observation of the powder (Fig.2) but with powders of significant native oxide surface, the epoxy resin can also affect the observation quality. Moreover, the preparation of embedded powders is also very demanding. Observation of the native oxide surface layer on PM powders of the range of nano to hundreds of micrometer-sized powders is possible directly with any metallographic preparation (Fig.2). The native oxide on metallic powders is electron transparent in some cases and can be directly observed in the TEM. Magnesium and zinc powders investigated with this method indicate crystalline native oxide (MgO, ZnO) with a non-homogenous oxide thickness. Powder surface stability in a different environment can be also investigated with this observation method.
[1] Martin Balog, Tao Hu, Peter Krizik, Maria Victoria Castro Riglos, Brandon D. Saller, Hanry Yang, Julie M. Schoenung, Enrique J. Lavernia, On the thermal stability of ultrafine-grained Al stabilized by in-situ amorphous Al2O3 network, Materials Science and Engineering: A, Volume 648, 2015, Pages 61-71, ISSN 0921-5093, https://doi.org/10.1016/j.msea.2015.09.037.
[2] M. Čavojský, V. Trembošová , N. Beronská, Š. Nagy, M. Nosko, Microstructure and mechanical properties of extruded profiles made from pure magnesium powders, Kovové Mater. 57 2019 371–376, DOI: 10.4149/km 2019 6 371

Acknowledgement: VEGA 2/0143/22 and ITMS project (code 313021T081), supported by Research & Innovation Operational Programme funded by the ERDF are gratefully acknowledged.

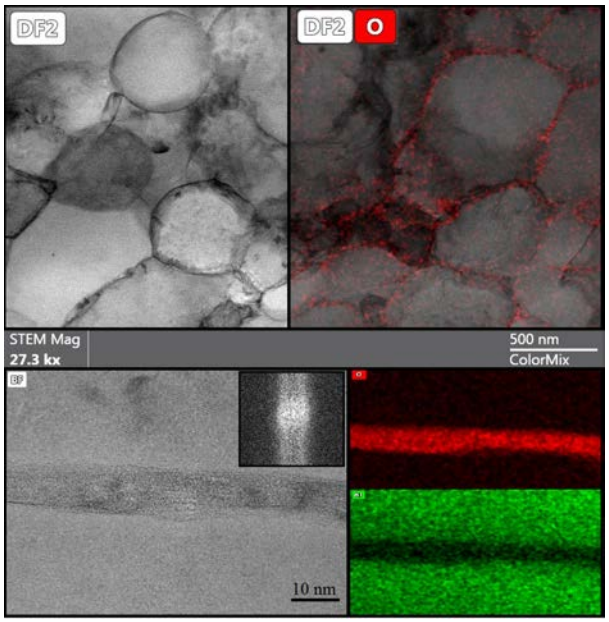

Fig. 1: Aluminium powder interface with amorphous native oxide revealed by STEM and EDS analysis.

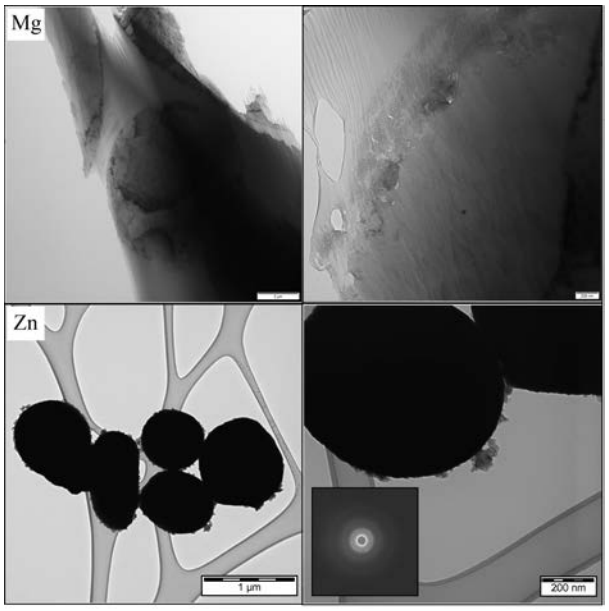

Fig. 2: Cross-section TEM observation of magnesium powders and native oxid surface layer prepared with epoxy embedment [2]. Direct TEM observation of zinc PM powders regarding native oxide surface.

Type of presentation: Poster

MS4-P-2670 Graphene-coated scintillators for low-energy electron detection

Lalinský O.[1], Průcha L.[1], Skoupý R.[2, 3]

[1]Department of Electron Microscopy, Institute of Scientific Instruments of the CAS, Královopolská 147, 612 64 Brno, Czech Republic, [2]Department of Bionanoscience, Kavli Institute of Nanoscience Delft University of Technology, Delft, The Netherlands, [3]Department of Imaging Physics, Delft University of Technology, Delft, The Netherlands

Email of the presenting author: coud.is.my.idol@gmail.com

Low-energy electron imaging has seen increased popularity nowadays. Such imaging has the advantage over higher-energy imaging in higher surface resolution, i.e. smaller primary beam (PB) penetration depth, and therefore less sample damage depth. However, the problem can occur especially in the detection of backscattered electrons (BSE), which are usually not accelerated compared to the secondary electrons (usually to 10 keV) and impinge on the scintillator with energy close to the energy of the PB. This is because slower BSE can cause lower cathodoluminescence (CL) response of the detector [1]. First, the CL efficiency (integral CL intensity divided by the energy of the incident electrons) of the scintillator generally decreases with the BSE energy. Second, slower BSE lose more of their energy or may not pass through the scintillator coating at all. It is therefore necessary to find the ideal combination of coating + scintillator for maximum CL efficiency.
Scintillators of various compositions were supplied by CRYTUR™. The scintillators were grown by the Czochralski method as single-crystals. The studied coating materials were Al, Sc, Indium Tin Oxide (ITO), and graphene. Al, Sc, and ITO were prepared by magnetron sputtering. Graphene was prepared by chemical vapor deposition with methane as a precursor. The graphene was grown on the Cu foil according to the recipe described in [2]. The graphene was then transferred with the help of PMMA onto a 5.7 mm diameter and 0.5 mm thick CRY018™ sample.
The graphene on the CRY018™ was studied by Raman spectroscopy, see Fig. 1. Graphene is characterized by 2 peaks in the spectrum — G (approx. 1583 cm^{-1}) and 2D (approx. 2660 cm^{-1}). For a single carbon layer, the 2D peak should be at least 2× larger than the G peak, as confirmed by the Figure.
To study the CL efficiency, a specialized CL apparatus located at our institute was used [3]. The primary energy (PE) was in the range of 0.6 to 10 keV. The CL spectra were studied, from which the CL efficiency was calculated. This was plotted as a function of the PE.
Fig. 2 shows the results of CRY018™ sample with various coatings. The CRY018™ with 50 nm Al has the highest CL efficiency for PE ≥ 5 keV. However, BSE slower than 1.9 keV cannot pass through such a coating. Graphene is the best coating for slow BSE. Such a system should be able to detect BSE up to 400 eV.
Although graphene is not yet possible to deposit in large quantities on scintillators, it is certainly a very promising way to effectively dissipate charge from the scintillator surface while maintaining the maximum CL efficiency of the scintillator.

[1] Garlick G. F. J., *Brit. J. Appl. Phys.* **13**, 541 (1962).
[2] Li X., et al., *Science* **324**, 1312 (2009).
[3] Bok J., Schauer P., *Rev. Sci. Instrum.* **82**, 113109 (2011).

Acknowledgement: The research was supported by TACR (TN01000008), MIT CR (TRIO FV30271). We thank the company CRYTUR™ for supplying with the samples of bulk single-crystals.

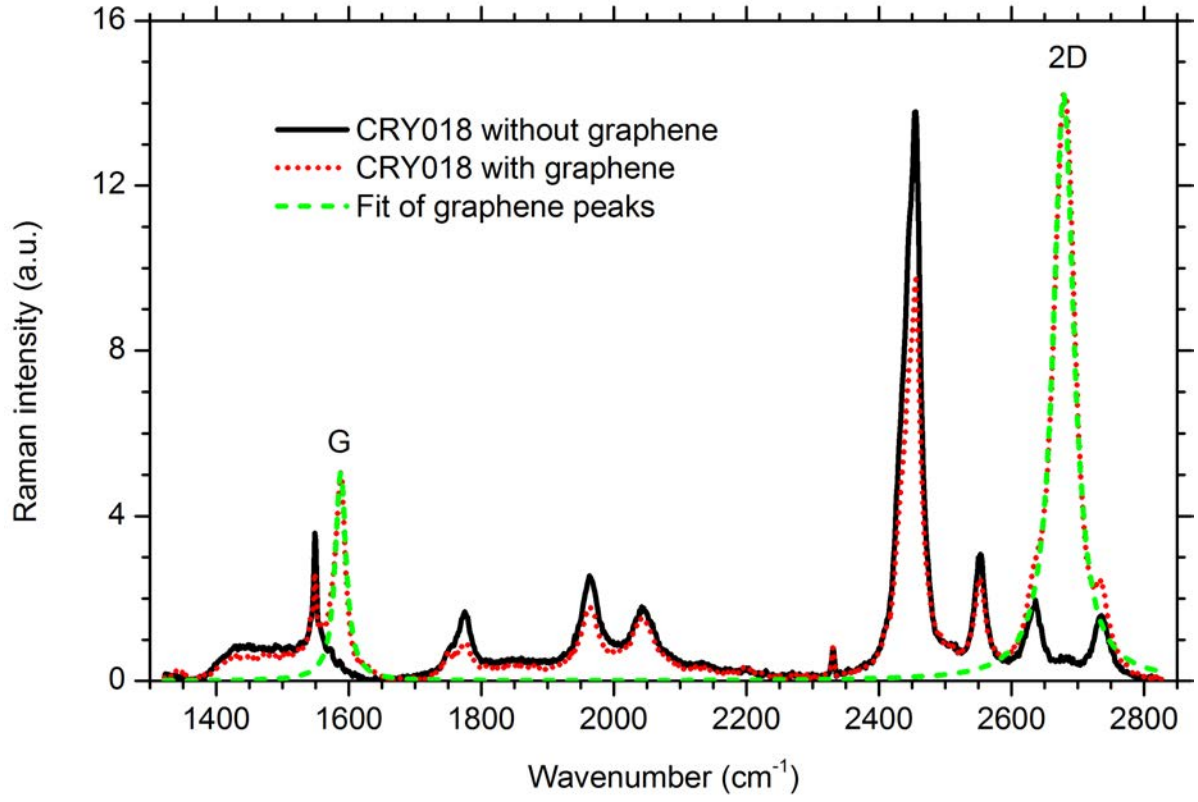

Fig. 1: Raman spectra of CRY018™ before and after graphene deposition. Significant peaks to demonstrate the existence of graphene (G and 2D) are highlighted by fit.

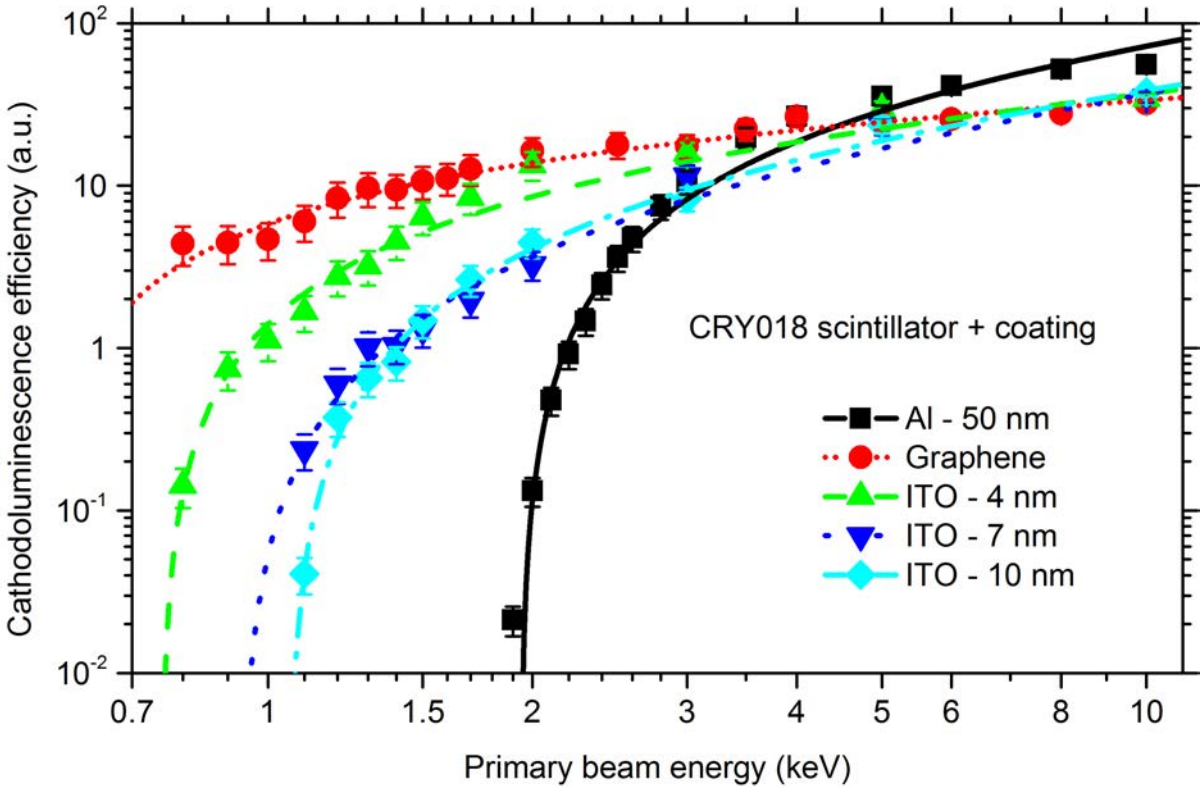

Fig. 2: CL efficiency of CRY018™ scintillation material coated by various layers.

Type of presentation: Poster

MS4-P-2823 STEM analysis of freestanding monolayer h-BN irradiated with slow highly charged ions

Propst D.[1], Speckmann C.[1], Niggas A.[2], Wilhelm R. A.[2], Kotakoski J.[1]

[1]Faculty of Physics, University of Vienna, Vienna, Austria, [2]Institute of Applied Physics, Technical Unviersity of Vienna, Vienna Austria

Email of the presenting author: diana.propst@univie.ac.at

Two-dimensional (2D) materials and their applications play a large role in the development of new technologies. However, the manufacturing of specific features on such limited scales is a challenge that requires precise, definite and reproducible methods of fabrication. Perforations of few to single atomic layers are of high interest, due to their possible applications in the fields of DNA-sequencing and water desalination. Slow highly charged ions (HCIs) have shown to produce well defined pores of regular density in 2D materials, such as MoS_2 [1] and carbon nanomembranes [2]. The pore sizes can be tuned by the charge state of the ions. Hexagonal boron nitride (h-BN) has been proposed as a suitable 2D material for the applications mentioned above, due to its favorable properties of chemical stability and oxidation resistance. It also has many similarities to graphene, being considered its non-conducting counterpart. But the research on freestanding ion-irradiated h-BN is lacking, partially due to difficulties in the preparation of a suitable sample. Therefore, the effects of slow highly charged xenon ions with charge states 20 and 38 impinging on freestanding monolayer h-BN are investigated by Scanning Transmission Electron Microscopy (STEM), in regard to nanoscopic pore formation in the material. The CCD and MAADF detectors are used for the analysis, collecting a multitude of images. Two monolayer h-BN samples prepared on Quantifoil Transmission Electron Microscopy (TEM) grids are pre-characterized by STEM, then irradiated with the highly charged ions. After irradiation the samples are then characterized by STEM again. From the STEM images the post-irradiation pore sizes are collected and the mean pore radius for both charge states is determined. The samples exhibit pore formations with a larger mean pore size for the higher charge state, showing that monolayer h-BN is susceptible to perforation by HCI irradiation.

[1] Kozubek, R. et al., Perforating freestanding molybdenum disulfide monolayers with highly charged ions. The Journal of Physical Chemistry Letters 10, 904–910 (2019)

[2] Ritter, R. et al. Fabrication of nanopores in 1nm thick carbon nanomembranes with slow highly charged ions. Applied Physics Letters 102, 63112 (2013)

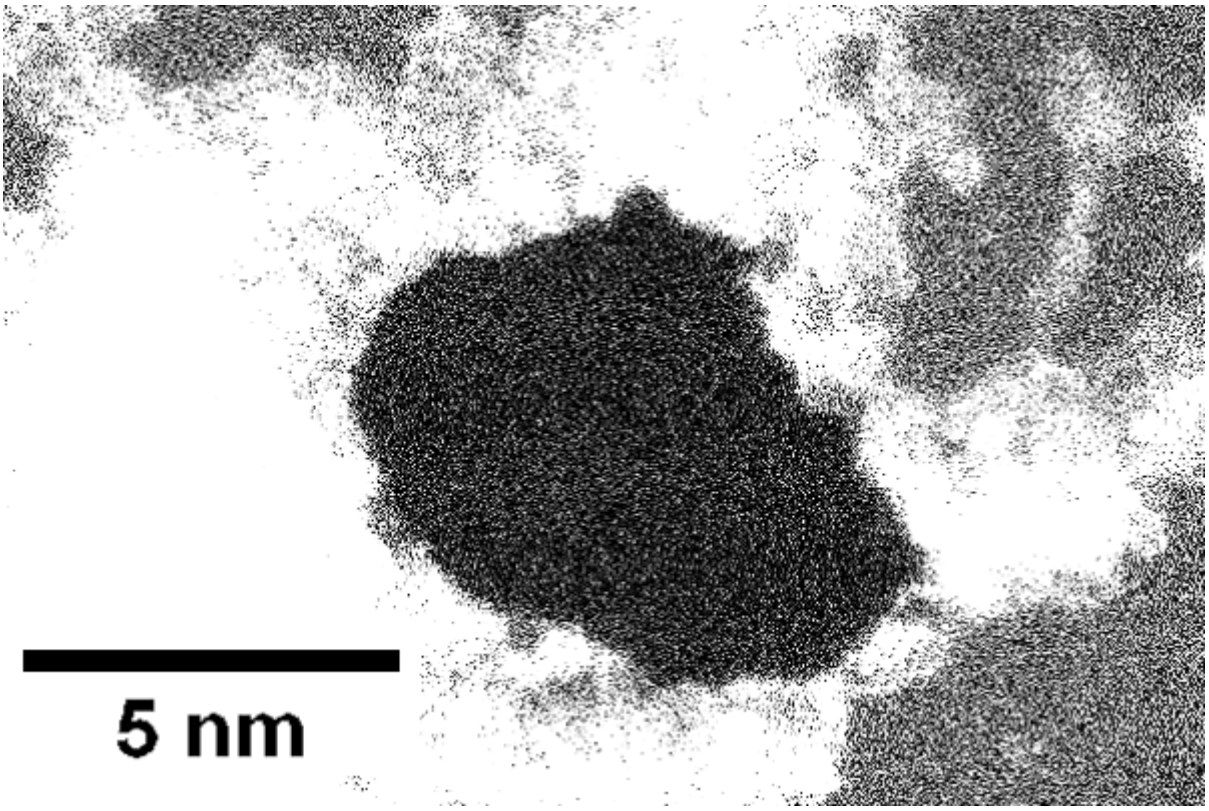

Fig. 1: **h-BN after Xe^{+20} ion irradiation**: MAADF STEM image of a pore (black) in the h-BN layer (grey), with surrounding contamination (white).

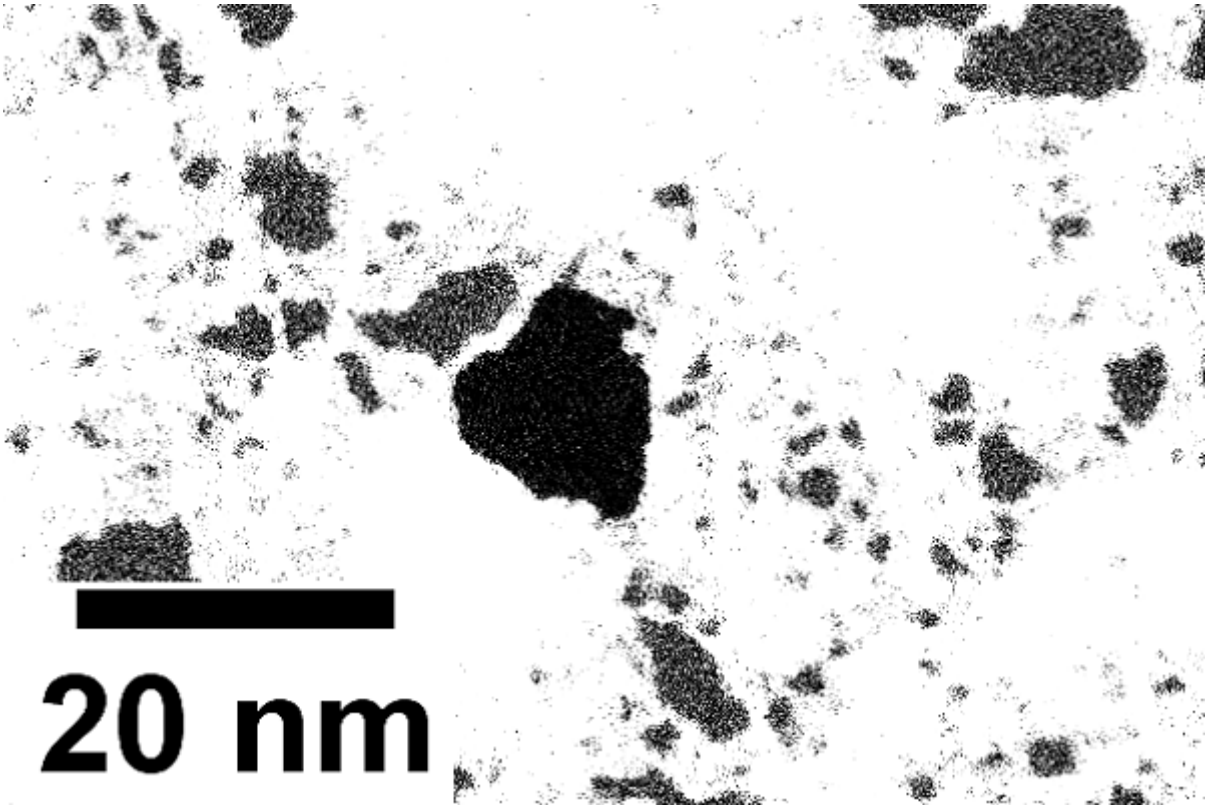

Fig. 2: **h-BN after Xe^{+38} ion irradiation**: MAADF STEM image of a pore (black) in the h-BN layer (grey), with contamination (white).

Type of presentation: Poster

MS4-P-2640 Transmission electron microscopy characterization of quasicrystal approximants in SrTiO3 thin films grown on Pt(111)/Al2O3(0001)

Semsari Parapari S.[1,3], Ruano Merchan C.[2,3], Trevizam Dorini T.[2,3], Podlogar M.[1,3], Brix F.[2,3], Pasquier L.[2], Jullien M.[2], Pierre D.[2], Andrieu S.[2], Dumesnil K.[2], Ledieu J.[2,3], Sicot M.[2,3], Copie O.[2], Gaudry E.[2,3], Fournée V.[2,3], Šturm S.[1,3]

[1]Department for Nanostructured Materials, Jožef Stefan Institute, Ljubljana, Slovenia, [2]Institut Jean Lamour, Université de Lorraine – CNRS, Nancy, France, [3]International Associated Laboratory PACS2, CNRS Université de Lorraine, Nancy, France and Jožef Stefan Institute, Ljubljana, Slovenia

Email of the presenting author: sorour.semsari.parapari@ijs.si

Ternary oxides with perovskite structures ABO_3 have two cationic species (A and B) that can be chosen among many transition metals, simple metals, rare earths or even alkalis. Due to this compositional diversity, various properties such as superconductivity, magnetoresistance, and metal-insulator transitions can be obtained within this large class of materials. As it was recently shown [1], synthesizing these materials in the form of ultra thin films with peculiar 2D structures with varying complexities could open the avenue towards new yet unexplored materials with functional properties.

In this work, an all-thin-film approach has been used to investigate ABO_3/Metal systems in a more versatile and less expensive way than using single crystal metal substrates [2]. A Pt(111) buffer layer was grown epitaxially on an Al_2O_3(0001) substrate by the molecular beam epitaxy method, on which $SrTiO_3$ thin films were deposited by pulsed laser deposition. A combination of TEM, STM, LEED, and XRD has been used to study the structure of the deposited layers and their interfaces. To directly visualize and assess the film thickness, atomic structure and orientation relationship of the thin layers in the film stacking, probe-corrected Scanning Transmission Electron Microscopy was used. For the cross-sectional study of these layers, an electron-transparent lamella was prepared using a focused ion beam scanning electron microscope. The high-angle annular dark-field STEM (HAADF-STEM) images were obtained using a JEM-ARM 200CF JEOL microscope operated at 200 keV. The FIB lamella was cut perpendicular to the $[10\text{-}10]_{Al2O3}$ direction. Figure 1 presents the HAADF-STEM image showing all three layers of the thin film stacking. The measured thickness of the Pt buffer layer in the cross-sectional view is about 12 nm and that of the $SrTiO_3$ film is 10 nm. Various crystalline grains are present in the $SrTiO_3$ layer, corresponding to different variants, whose average grain size lies at around 15 nm. Atomically resolved noise-filtered HAADF-STEM images of the two interfaces at their corresponding zone axes are shown as the figure insets. The Al_2O_3, Pt and $SrTiO_3$ layers are viewed along the $[10\text{-}10]_{Al2O3}$, $[110]_{Pt}$, and $[110]_{SrTiO3}$ zone axes, respectively. Atomically sharp interface is present between the Al_2O_3/Pt, and also Pt/$SrTiO_3$ layers. The structural analysis shows that the $(111)_{Pt}$ lattice planes are parallel to the $(111)_{STO}$ planes. The deduced orientation relationship between Pt and $SrTiO_3$ layers is $(111)_{Pt}[110]_{Pt} \parallel (111)_{SrTiO3}[110]_{SrTiO3}$, which is in agreement with the epitaxial growth of the thin film on the buffer layer.

[1] G. Barcaro and A. Fortunelli, Phys. Chem. Chem. Phys., 2019, 21, 11510–11536

[2] C. Ruano Merchan et al., Phys. Chem. Chem. Phys., 2022, 24, 7253

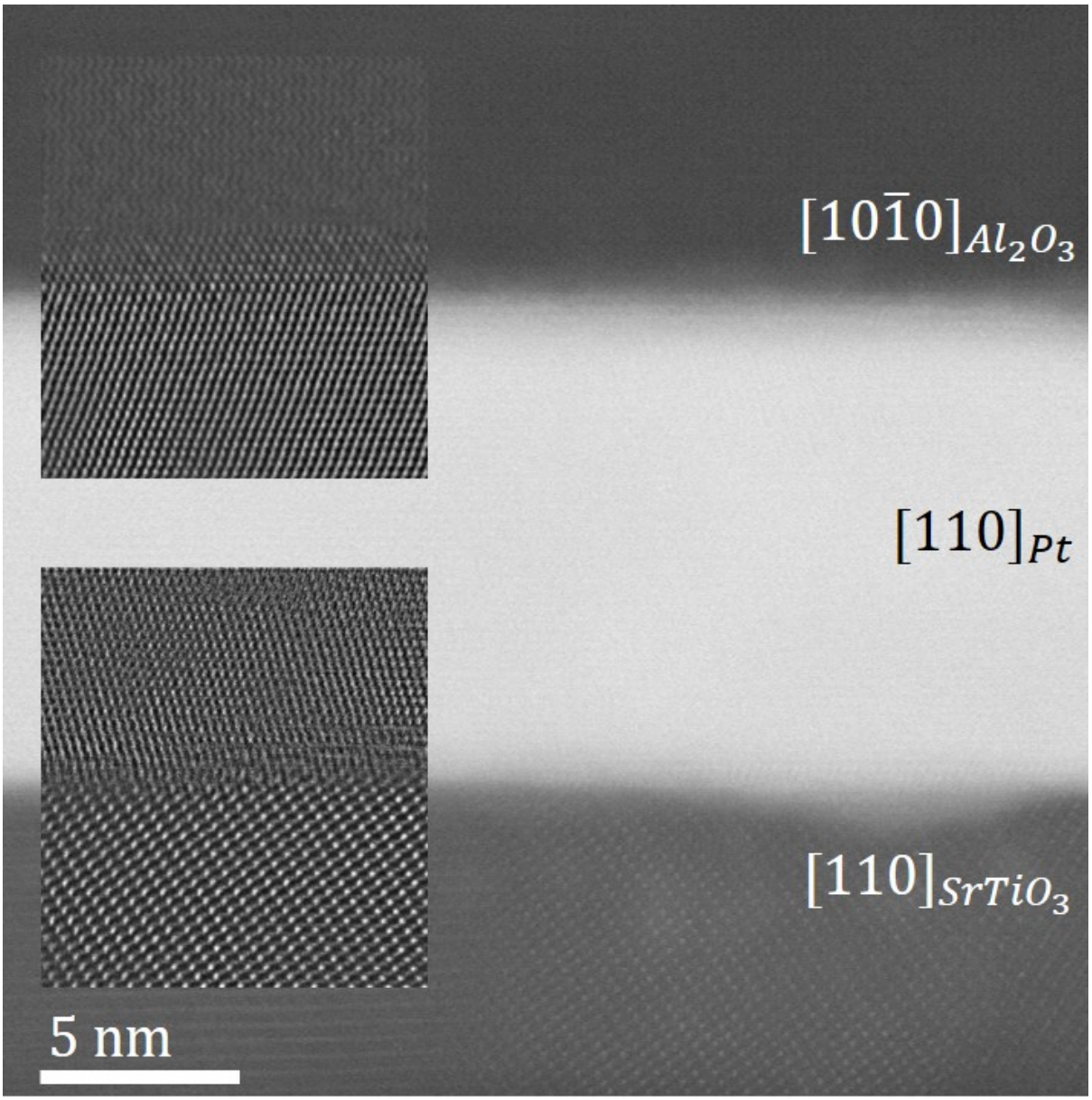

Fig. 1: HAADF-STEM image of the Al_2O_3/Pt/$SrTiO_3$ film stacking. The insets show the atomically resolved interfacial regions.

Type of presentation: Poster

MS4-P-2669 Energy-based calibration for quantitative STEM measurements and comparison with 2D-PAD

Zouhar M.[1], Paták A.[1], Konvalina I.[1], Fořt T.[1], Materna-Mikmeková E.[1]

[1]Department of Electron Microscopy, Institute of Scientific Instruments of the CAS, v. v. i., Brno, Czech Republic

Email of the presenting author: zouharm@isibrno.cz

We present a new calibration method of STEM device equipped with a segmented detector consisting of concentric annuli. The core idea of this method is to perform an additional measurement of gray-scale dependence $g(E)$ on incident energy E for each segment, so called calibration curves (CCs). The resulting profiles, see Fig. 1, exhibit suppressed response of the HAADF segment. We compare the measured experimental results with Monte-Carlo simulations (MC-sim) by Geant4 [1] and traced using EOD [2]. We utilise 4 different imaging modes, including ultra-high resolution (UHR) mode with beam deceleration (BD). We scale the data to a reference segment in order to avoid the necessity to measure the incident beam current precisely. The MC-sim provide access to detailed information such as electron count, total energy dose and energies E_i of individual electrons per each segment of the detector. Furthermore, we use the CCs to convert the E_i of simulated detected electrons to partial gray-scale values. These values are summed up and they provide a calibrated theoretical gray-scale G. We discuss how these quantities compare with the observed gray-scale intensity. The data are displayed in Fig. 2. The experimental error-bars stem from intensity variations in the region of interest and they are quantified using standard deviation. The errors in theoretical data originate from statistical analysis of an artificial random split into 10 batches. It turns out that the theoretical gray-scale G (obtained using traced MC-sim and experimental CCs) leads to the best agreement with the directly measured gray-scale. We validate this method on several thin foil samples for high and low values of atomic-number Z [3].

We complement the aforementioned results obtained using a 2-dimensional (2D) pixel-array detector (PAD). They are displayed in Fig. 3 with the corresponding MC-sim. The 2D-PAD provides finer angular resolution when compared to the segmented STEM and hence it represents a technological evolution of the segmented detector. On the other hand, data acquisition is faster in the case of the segmented STEM. The calibration of the 2D-PAD turns out to be much simpler. The intensity angular profiles exhibit sensitivity to both Z and sample thickness in the case of the two detectors [3]. This means that if one knows either the composition or the sample thickness, the MC-sim can be used to estimate the other. Thus the MC-sim provide a valuable tool to extract additional information from the measurements.

[1] S. Agostinelli et al.: Nucl. Instr. Meth. Phys. Res. A Accel. Spectrom. Detect. Assoc. Equip. 2003, 506, 250-303
[2] J. Zlámal, B. Lencová: Nucl. Instr. Meth. A 2011, 645, 278-282
[3] I. Konvalina et al.: Nanomaterials 2022, 12(1), 71

Acknowledgement: This research was funded by the Technology Agency of the Czech Republic, grant number TN01000008.

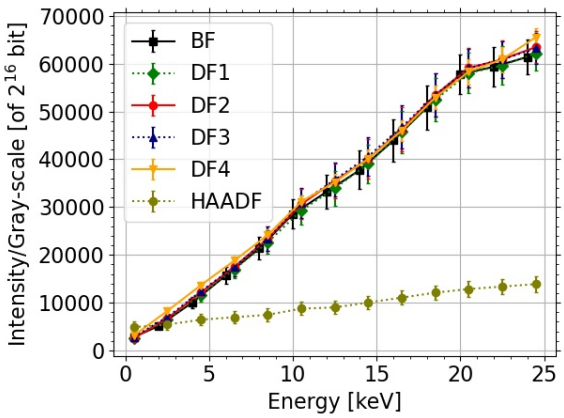

Fig. 1: Calibration curves for individual annular segments of the detector acquired with a particular setting.

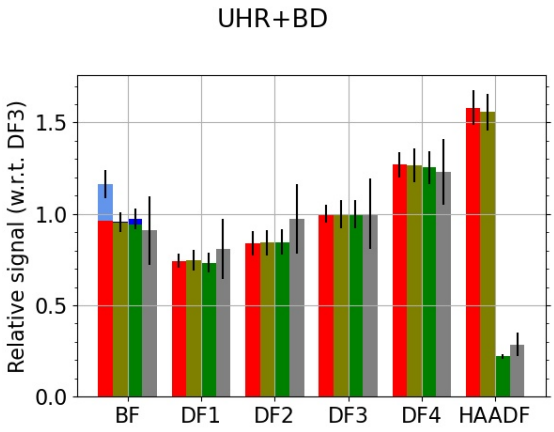

Fig. 2: Different quantities, contributions from forescattered + secondary electrons (SE) highlighted, in the case of carbon and both UHR and BD mode. Right to left: experimental gray-scale (gray), simulated gray-scale *G* via CCs (green + blue), total energy dose (grayish green + navy) and electron count (red + light-blue). Data scaled to the segment DF3.

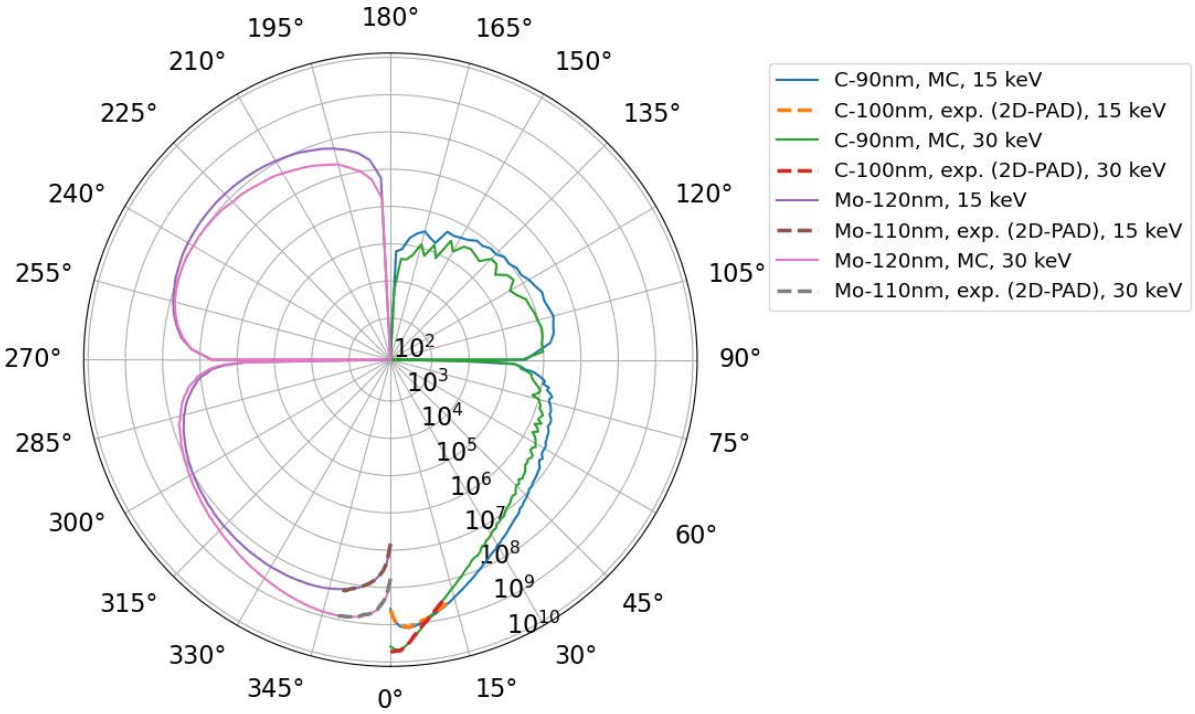

Fig. 3: Polar plot of total energy dose (within 1 deg bins) from simulations (solid) and scaled experimental 2D-PAD intensity (dashed). For carbon (right) and molybdenum (left), the latter mirrored to larger values of polar angle. Both elements measured and simulated at landing energies 15 keV and 30 keV.

MS5 1D-materials (nanowires, nanotubes, nanorods etc.), nanoparticles and nanostructures

Type of presentation: Invited

MS5-IN-3044 In situ microscopy of nanowires: From fundamental properties to functional applications

Vogl L. M.[1], Moninger M.[1], Schrenker N.[1], Schweizer P.[1], Spiecker E.[1]

[1]Institute of Micro- and Nanostructure Research (IMN) & Center for Nanoanalysis and Electron Microscopy (CENEM), University of Erlangen-Nürnberg, Erlangen, Germany

Email of the presenting author: erdmann.spiecker@fau.de

Nanowires can be fabricated with high structural quality resulting in excellent functional properties. The high mechanical strength and extreme bendability of nanowires make them ideal candidates for transparent electrodes in flexible devices. Moreover, nanowires show a high surface-to-volume ratio making them well suited for sensing applications. In order to understand the properties of individual nanowires and nanowire networks application of in situ microscopy techniques is absolutely key.

In this contribution we provide an overview of in situ microscopy studies of functional nanowires carried out at the CENEM in Erlangen. Special emphasis is dedicated to the correlative use of in situ electron and light microscopy. While light microscopy cannot provide structural details of nanowires it is well suited to image individual nanowires and their structural evolution or dynamics, e.g. during nanowire growth or resonance vibration. Combined with the high-resolution capabilities of electron microscopes this enables flexible studies in vacuum and different environments. In the presentation the following topics will be covered: (i) How correlative in situ light and electron microscopy can be used to unravel the growth kinetics of MoO2 nanowires during controlled oxidation of single crystal MoS2 [1], (ii) How in situ resonance measurements and bending tests in SEM/TEM enabled uncovering “size and shape” effects on the elastic properties of Au nanowires [2], (iii) How individual nanowires can be used for gas sensing through correlative in situ quality factor determination in light and electron microscopy [3] (iv) How nanowires dispersed on polymer substrate deform under tensile and (cyclic) compressive loading, (v) How mechanical and electrical failure of flexible Ag nanowire electrodes are interrelated and how the integrity of such electrodes can be enhanced through network anisotropy [4], and (vi) How in situ electrical probing of nanowire junctions helps to understand the impact of nanowire coating on junction resistance and environmental stability [5,6].

References

[1] L.M. Vogl, P. Schweizer, M. Wu, E. Spiecker, Nanoscale 11 (2019) 11687.
[2] L.M. Vogl, P. Schweizer, G. Richter, E. Spiecker, MRS Advances 6 (2021) 665–673.
[3] L.M. Vogl, P. Schweizer, P. Denninger, G. Richter, E. Spiecker, under review.
[4] N. Schrenker, Z. Xie, P. Schweizer, M. Moninger, F. Werner, N. Karpstein, M. Mackovic, G. Spyropoulos, M. Göbelt, S.H. Christiansen, C. Brabec, E. Bitzek, E. Spiecker, ACS Nano 15 (2021) 362–376.
[5] V. Kalancha, A. These, L. Vogl, I. Levchuk, X. Zhou, M. Barr, M. Bruns, J. Bachmann, S. Virtanen, E. Spiecker, A. Osvet, C. Brabec, K. Forberich, Advanced Electronic Materials (2022) 2100787.
[6] L.M. Vogl, Dissertation, University of Erlangen-Nürnberg (2021)

Acknowledgement: Financial support from the DFG through the Doctoral Program GRK1896 “In situ microscopy with electrons, X-rays and scanning probes” is gratefully acknowledged.

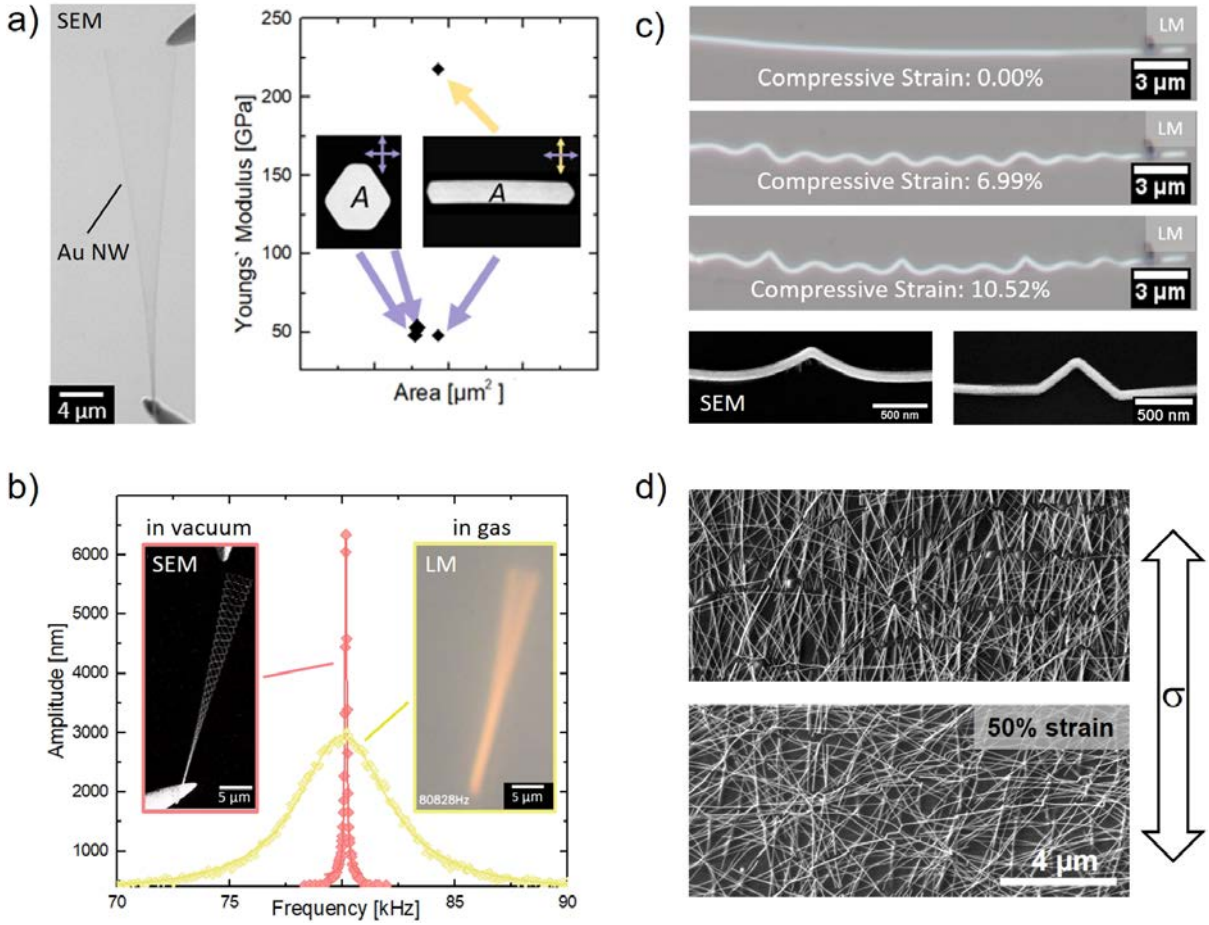

Fig. 1: a) Resonance measurements reveal size & shape dependent elastic properties of Au NWs [2]. b) Correlative Q-factor analysis of Au NW in LM and SEM for gas sensing [3,6]. c) Compressive testing of Ag NW on polymer showing transition from elastic buckling to plastic kinking. d) Mechanical testing of anisotropic Ag NW electrodes [4].

Type of presentation: Invited

MS5-IN-3031 Application of electron microscopy in development of sensor elements for detection of toxic organic compounds

Žagar Soderžnik K.[1,2], Korent A.[1,2], Trafela Š.[1], Krishnamurthy A.[1,2], Samardžija Z.[1], Rožman T.[1,2], Šturm S.[1,2]

[1]Departmenr for Nanostructured Materials, Jožef Stefan Institute, Jamova cesta 39, 1000 Ljubljana, Slovenia, [2]Jožef Stefan International Postgraduate School, Jamova cesta 39, 1000 Ljubljana, Slovenia

Email of the presenting author: kristina.zagar@ijs.si

We develop sensor elements for electrochemical detection of variety toxic organic components (TOC) and biomolecules such as SARS-CoV-2 virus. The emphasis on development of sensor elements is on synthesis and characterization of conductive and catalytic materials which boost the performance of working electrode on sensor element that this finally incorporated into sensor system. The portable, inexpensive, easy to use sensor should be fast, sensitive and selective to be able to detect TOCs, such as; formaldehyde, acrylamide, benzendiols etc.
In the present work we focus on importance of correlative characterization combining different electron microscopy techniques with electrochemical and spectroscopy techniques in order to develop materials with desirable properties, such as; high conductivity, high electron transfer, electrochemical activity and/or catalytical activity. The focus of presentation will be on synthesis, characterisation and application of conductive polymer materials (polyaniline) and carbon-basted materials functionalized with Au, Pt and Pt-Au nanoparticles. The SEM/STEM with EDXS (FEG-SEM Verios G4 HP, Thermo Fisher Scientific) and TEM (JEOL JEM-2100, Jeol Ltd.) were applied and compared with electrochemical and spectroscopic results. As an example; the development of electrochemical biosensor element for detection of acrylamide (AA) will be discussed were at each step the SEM and or TEM was applied to observe the morphology, composition and conductivity of the material. The sensors' receptor element was based on a modified commercial screen-printed electrodes (SPE). As an electrochemical transducer, conductive polyaniline (PANI) decorated with Au nanoparticles was applied, which enables high sensitivity and limit of detection below 10-6 M range. As biological component, enzyme amidase was selected, since it is known that it catalyses the hydrolysis of acrylamide into carboxyl acid and ammonia. The ammonia is finally detected using chronoamperometry. The chemical interaction between PANI and ammonia is well-known and was used as a base for the fabrication of an amperometric sensory platform for its aqueous detection at neutral pH. Understanding AA and amidase interaction and decomposition into ammonia, PANI electrochemical synthesis and redox behaviour in acidic and neutral media was used to study the mechanism for the AA indirect detection.

Acknowledgement: The authors acknowledge the ARRS for funding of projects and programme: PR-08337, J2-1739, J2-3051, Z2-3206 and P2-0084.

Type of presentation: Oral

MS5-O-2636 Expanded Design Flexibility in 3D-Nanoprinting via Focused Electron Beam Induced Deposition

Seewald L. M.[1], Winkler R.[1], Weitzer A.[2], Kothleitner G.[3], Plank H.[1,2,3]

[1]Christian Doppler Laboratory for Direct-Write Fabrication of 3D Nano-Probes, Graz University of Technology, 8010 Graz, Austria, [2]Institute of Electron Microscopy and Nanoanalysis, Graz University of Technology, 8010 Graz, Austria, [3]Graz Centre for Electron Microscopy, Steyrergasse 17, 8010 Graz, Austria

Email of the presenting author: lukas.seewald@felmi-zfe.at

While the miniaturization trend in research and industry is still unbroken, there is a rising demand on fabrication technologies, which allow fabrication of 3-dimensional architectures with gradually decreasing dimensions. Among a small pool of technologies, which enable 3D fabrication at the nanoscale, Focused Electron Beam Induced Deposition (FEBID) is a highly promising candidate due to both, its capabilities and increasing reliability [1]. Based on the working principle, which relies on the beam induced dissociation of surface adsorbed, gaseous precursor molecules, FEBID has very low demands on substrate materials and morphologies. Together with its additive character and a constantly increasing precursor material pool, FEBID reached the status of a 3D-nanoprinter for a wide range of novel applications, including 3D sensors, plasmonics, -nanomagnetics or SPM nanoprobes. Most 3D designs in the past were of mesh-like character by means of nanowires connected in 3D space (Fig 1). While desired for many applications, the small nanowire dimensions can entail limitations to relevant properties. Consequently, that expansion of design possibilities is of high relevance, which includes fully closed structures, sheet-like elements or their combination with the mesh-like architectures (Fig 2).
Following that motivation, this contribution focuses on two different approaches: (1) controlled diameter tuning of individual nanowires and (2) fabrication of closed, sheet-like elements. The former strategy uses the introduction of a deliberate beam defocus, which has manifold implications during growth aside of the originally intended diameter widening [2]. We discuss those results from a practical point of view and demonstrate the enhanced design flexibility of varying or even dynamically changing nanowire-dimensions. The second approach forms the baseline for 3D nanoprinting of objects, composed of sheet-like base-elements. Here, we discuss the basic implications when changing from nanowires to quasi-2D sheets, based on the more complex thermal situation. We present an unified compensation model, taking those effects into account, leading to very high precision [3]. Both together consequently form the basis for enhanced design flexibility of 3D-FEBID, which is stepwise leveraged into the status of a true 3D nanoprinter for yet unknown applications in 3D space.

[1] Plank, H. et al. Focused electron beam-based 3D nanoprinting for scanning probe microscopy: A review. Micromachines 2020, 11
[2] Seewald, L.M. et al. Expanding 3d nanoprinting performance by blurring the electron beam. Micromachines 2021, 12
[3] Weitzer, A. et al. Expanding FEBID-Based 3D-Nanoprinting toward Closed High-Fidelity Nanoarchitectures. ACS Appl. Electron. Mater. 2022, 4

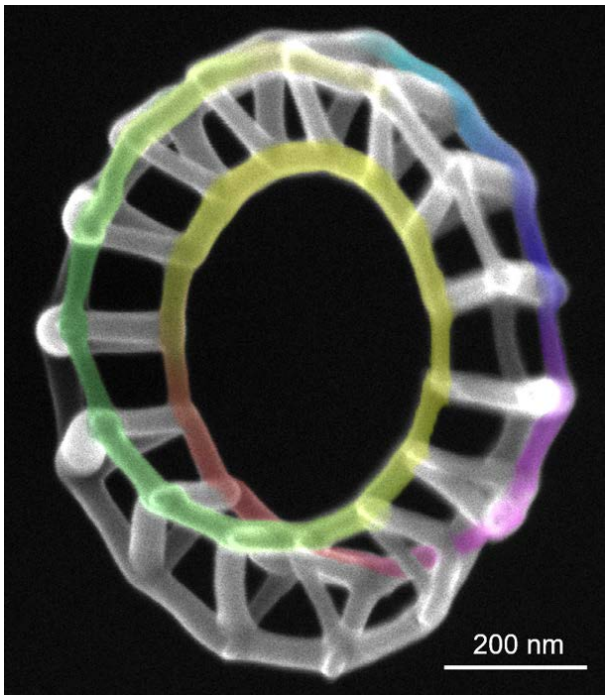

Fig. 1: Mesh-like structure of a moebius formed from connected nanowires.

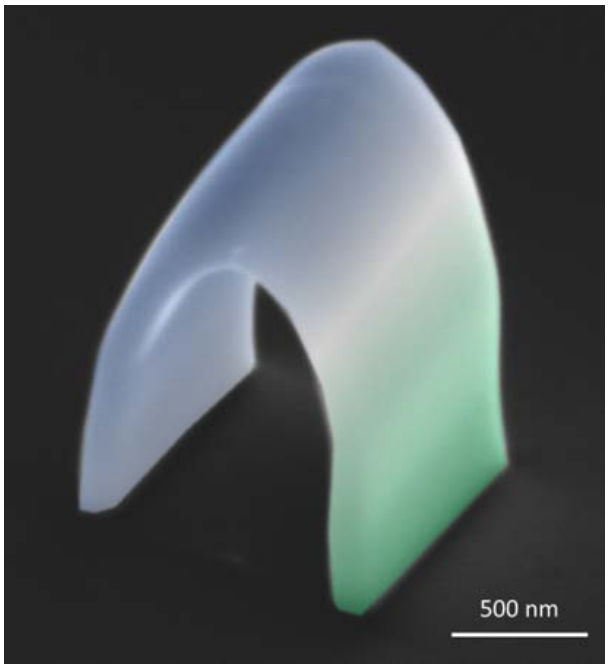

Fig. 2: Arch-like structure based on 2D sheet-like elements.

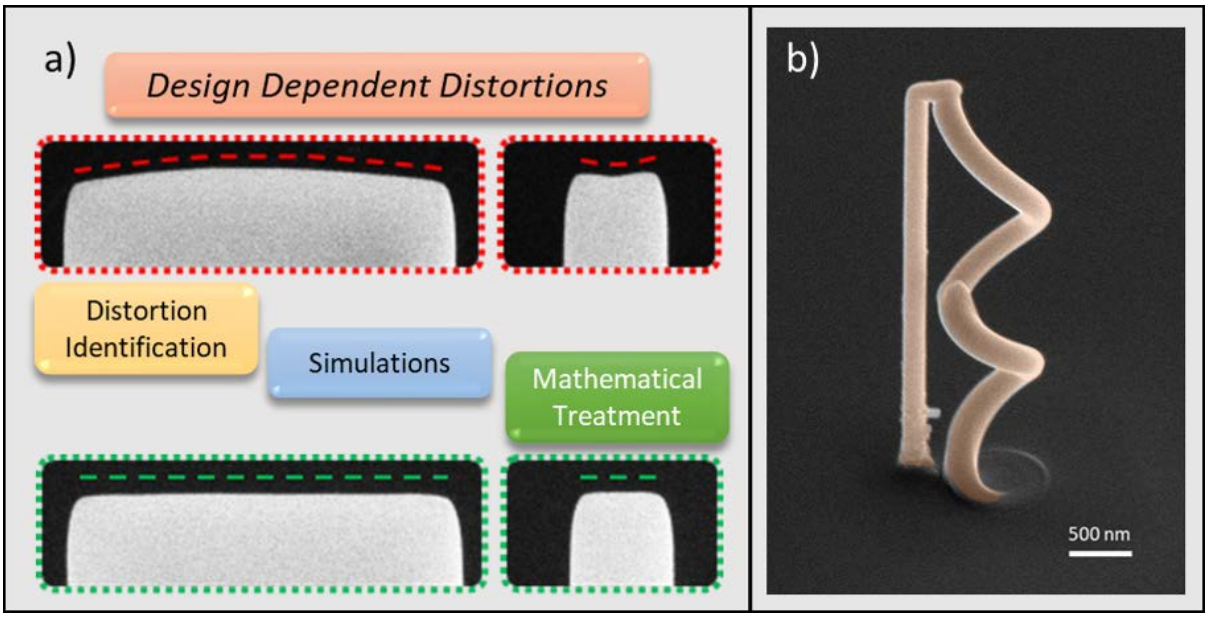

Fig. 3: a) Workflow to account for design dependent distortions for the fabrication of 2D structures. b) Helical structure illustrating deliberately tuned wire dimensions via beam defocus.

Type of presentation: Oral

MS5-O-2501 Plasmon resonances in biocompatible nanoparticles

Horák M.[1], Ligmajer F.[1], Čalkovský V.[1], Daňhel A.[2], Mach J.[1], Šikola T.[1]

[1]Brno University of Technology, Brno, Czech Republic, [2]Institute of Biophysics of the Czech Academy of Sciences, Brno, Czech Republic

Email of the presenting author: michal.horak2@ceitec.vutbr.cz

Localized surface plasmons (LSP) are self-sustained collective oscillations of free electrons in metal nano- and microstructures coupled to the local electromagnetic field. Moving apart from standard plasmonic materials, like gold, silver, and aluminum, opens a way to utilize plasmonic nanoparticles with special properties which are represented, for example, by a wide spectral range of LSP resonances from ultraviolet to infrared, biocompatibility, or good electrochemical properties. We present a study of biocompatible nanoparticles made of gallium and silver amalgam using STEM-EELS on a single particle level.

Gallium is commonly known as a metal with a melting temperature of 29.7 °C. It has several solid-state phases which enables a variety of phase-changing systems which are under investigation. Bulk plasmon energy of gallium is 13.7 eV and it has no strong interband transitions in a wide region from ultraviolet to infrared, which makes it an ideal plasmonic candidate. We have explored the plasmonic nature of its nanoparticles and shown that plasmon resonances can be tuned from ultraviolet to visible spectral region by changing the size of the nanoparticle, see Figure 1 and 2.

Silver amalgam is one of the most suitable solid electrode materials in electroanalysis of various reducible organic and inorganic compounds. The main advantage of silver amalgam within this context is its wide cathodic potential window, high mechanical stability, adequate sensitivity, and advantageous strong interaction with biopolymers. Nanostructuring the amalgam promises improved electrochemical performance and brings along the prospect of plasmonic activity. Our results show that silver amalgam, apart from its proven usefulness in electroanalytic chemistry, can be also regarded as a novel plasmonic material with promising optical properties. Silver amalgam nano- and micro-particles exhibit strong plasmon resonances in ultraviolet to mid-infrared regions depending on the particle size, see Figure 2. These findings establish silver amalgam nanoparticles as promising candidates for applications within photochemistry and spectroelectrochemistry, where the synergy between their plasmonic and electrochemical qualities can be fully utilized [1].

[1] F. Ligmajer et al., J. Phys. Chem. C **123**, 16957−16964 (2019).

Acknowledgement: Supported by Czech Science Foundation (17-23634Y), MEYS CR (CzechNanoLab, LM2018110), and Thermo Fisher Scientific and CSMS scholarship 2019.

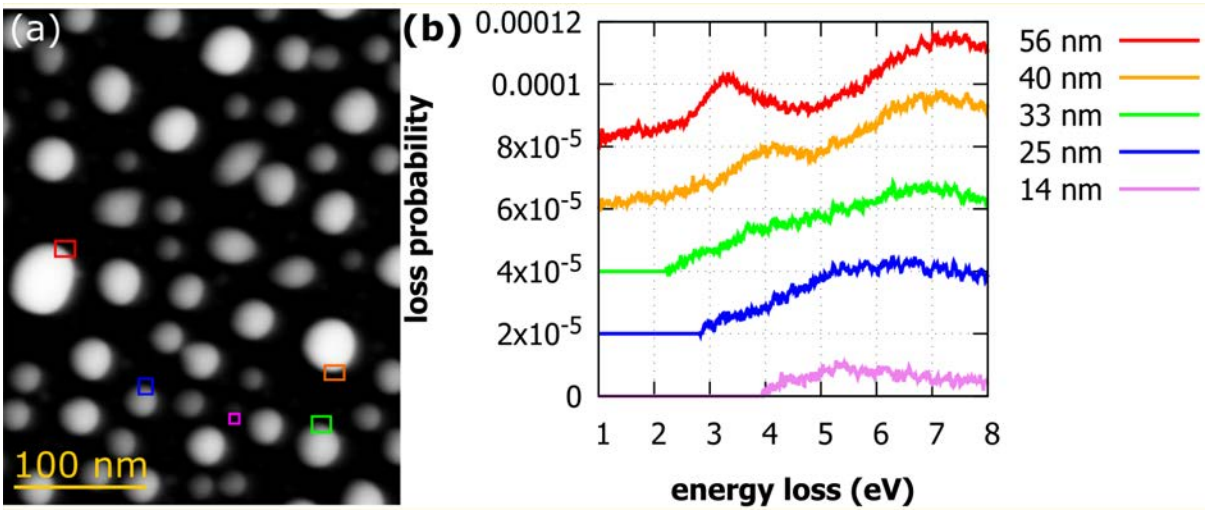

Fig. 1: (a) STEM HAADF image of gallium nanoparticles on silicon nitride membrane, (b) EEL spectra showing the dipole plasmon resonance in individual gallium nanoparticles integrated over marked areas in (a). Note that the first peak in the EEL spectra, corresponding to the dipole mode, is shifting with increasing the diameter of the nanoparticle.

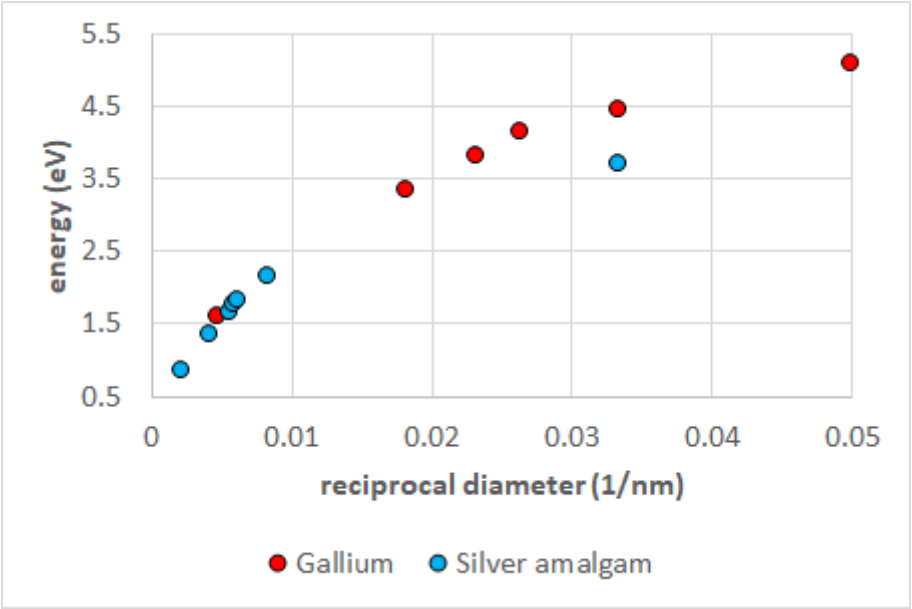

Fig. 2: Dispersion relation of gallium and silver amalgam nanoparticles proving the wide range tunability of the dipole LSP mode from ultraviolet to near-infrared spectral range.

Type of presentation: Oral

MS5-O-2808 Towards Laser-Induced Tuning of Plasmonic Response in High Aspect-Ratio Au Nanowires: A STEM/EELS study

Pelaez Fernandez M.[1,2,3], Majerus B.[4], Dufour R.[4], Funes-Hernando D.[5], Duvail J. L.[5], Henrard L.[4], Arenal R.[1,2,6]

[1]Laboratorio de Microscopias Avanzadas, Universidad de Zaragoza, Spain, [2]Instituto de Nanociencia y Materiales de Aragon (INMA), CSIC-U. de Zaragoza, Spain, [3]Unité de Matériaux et Transformations, Université de Lille, France, [4]Department of Physics, University of Namur, Belgium, [5]Institut des Matériaux Jean Rouxel, CNRS –Université de Nantes -France, [6]ARAID Foundation, 50018 Zaragoza, Spain.

Email of the presenting author: Mario.pelaezfernandez@univ-lille.fr

Plasmonics has been gaining an increasing amount of interest in research, given its broad range of applications. Within plasmonics, the characterisation and tuning of localized surface plasmon resonances (LSPRs) in metallic nanowires has been particularly fruitful considering their applications, ranging from photonics to electronics, sensors, or even chemical analysis through surface-enhanced light spectroscopies[1].

Furthermore, recent works show it is possible modify the morphology of metallic nanowires by laser irradiation producing nanoparicles through the melting of the metal in the nanowire. This provides a new realm of high aspect-ratio nanostructures with potential new properties[2].

Low-loss electron energy loss spectroscopy (EELS) is a very adequate tool to characterise these novel nanostructures, combining both spatial resolution and spectral resolution[3]. The EELS studies shown in this work, combined with discrete dipole approximation modelling, show how the plasmonic response of high aspect ratio gold 1D nanostructures can be tuned by means of nanoparticles attached to the tips of gold nanowires, that is, high aspect-ratio half-dumbbells and dumbbells.The investigation of the surface plasmon resonances has been developed using component analysis (particularly, non-negative factorisation) on the EELS spectrum images to be able to decompose the different spectral components.

These studies shed light on the properties of this kind of nanostructures and their potential tuning, enhancing their potential future applications..

[1] M. Moskovits, Journal of Raman Spectroscopy. 36, 485–496 (2005).
[2] S. v. Makarov et al., Laser and Photonics Reviews. 11, 1–25 (2017).
[3] M. Kociak et al, Plasmonics: Metallic Nanostructures and Their Optical Properties III. 5927, 592711 (2005).

Acknowledgement: Supported by the Spanish MICINN, Government of Aragon (project DGA E13-20R) and EU H2020 programs “ESTEEM3" (823717) and MSC Grant agreement No. 642742

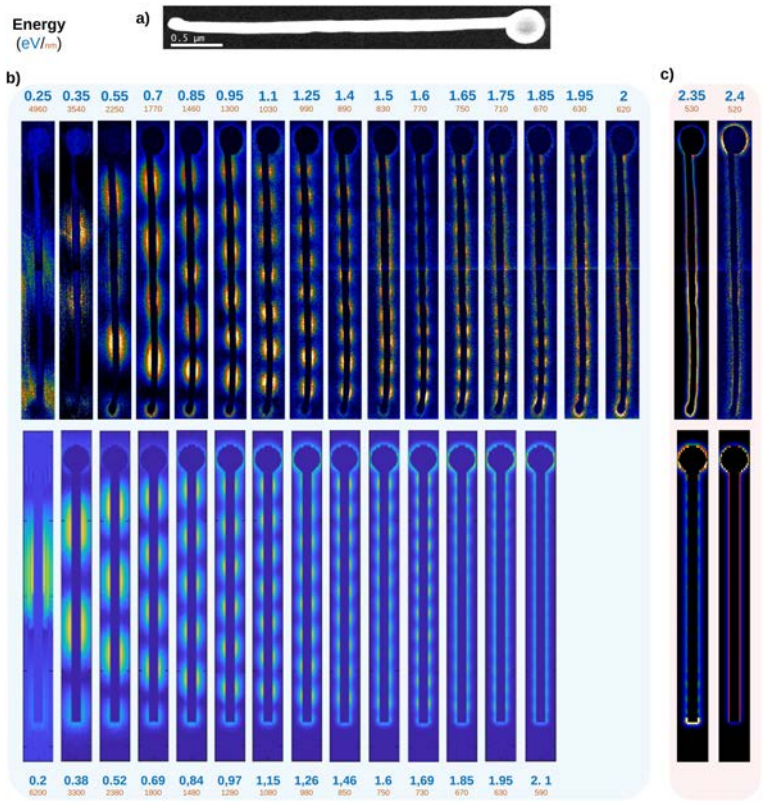

Fig. 1: Plasmonic modes of an Au half-Dumbbell (hdB) (a) STEM-HAADF micrograph, (b) Top: NMF components of the FP modes in ascending order of resonance energy. Bottom: DDA simulations corresponding to the same FP modes. (c) Top: NMF components of the transversal mode of the NW and the Au NP attached to the system, respectively. Bottom: DDA simulations.

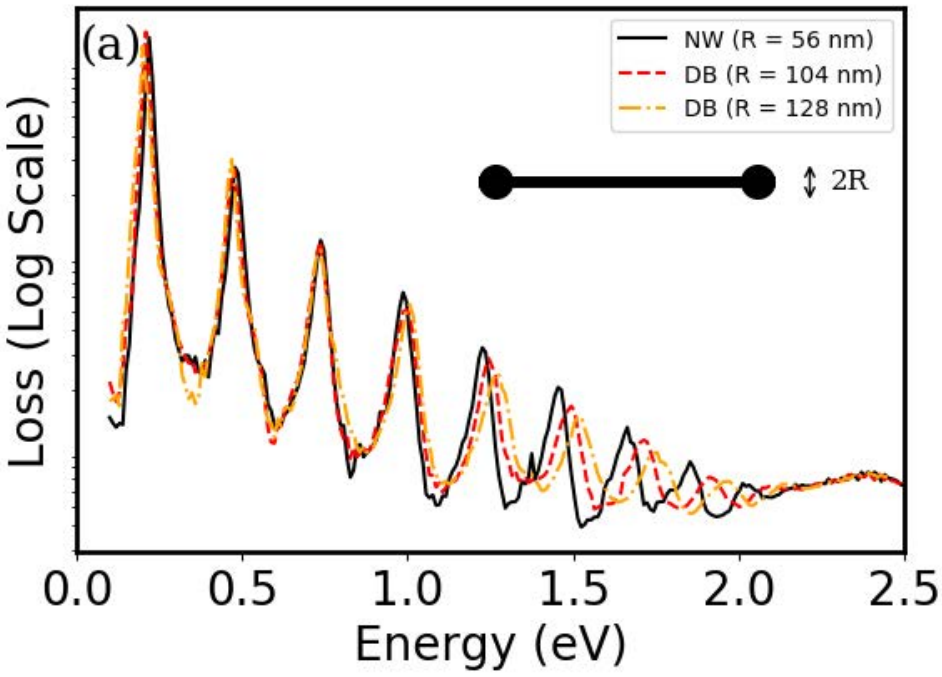

Fig. 2: Simulated EELS spectra of plain NW and of dumbell shape structures of total length L = 4140 nm with varius radii of the spheres at the ends of the NW (R = 104 nm and R = 128 nm.)

Type of presentation: Oral

MS5-O-2567 Ni-Ti Nanoparticles for Self-Propagating Reactions

Cieslar M.[1], Bajtošová L.[1], Hanuš J.[1], Křivská B.[1], Králík R.[1]

[1]Faculty of Mathematics and Physics, Charles University, Prague, Czechia

Email of the presenting author: cieslar@met.mff.cuni.cz

Metallic nanostructures have broad use in microelectronic devices and micro-electro-mechanical systems. The increasing complexity of these devices demands strict requirements for the individual components and their joints. Self-propagating reaction in reactive multilayer films is an option to produce reliable joints on the nanoscale. The same reaction could be achieved with nanoparticles. Their simple deposition could further increase the applicability of the process. Metallic nanoparticles could be conveniently prepared by vacuum techniques based on gas aggregation sources (GAS) with planar magnetrons. Additional planar magnetron positioned below the GAS allows the production of nanoparticles with heterogeneous core-shell structures where the direct contact between the layers favors the self-propagating synthesis. Thus, these nanoparticles could exhibit suitable material bonding and component joining properties.
The present work investigated the microstructure and thermal stability of core-shell Ni-Ti nanoparticles. The microstructure of nanoparticles was studied by transmission electron microscopy (TEM), including high-resolution TEM (HRTEM), scanning TEM (STEM), and chemical analysis by energy dispersive spectroscopy (EDS). The core-shell structure of the prepared nanoparticles with Ni core and Ti shell was confirmed by both STEM bright-field (BF) and high angle annular dark-field (HAADF) images and EDS maps (Figure 1). The thermal stability of the nanoparticles was studied by in-situ heating in TEM. The specimen was annealed up to 950 ºC, and the microstructural changes and transformations of nanoparticle aggregates (Figure 2) were monitored during this annealing.

Acknowledgement: Financial support from the Czech Science Foundation under the project 22-22572S is gratefully acknowledged.

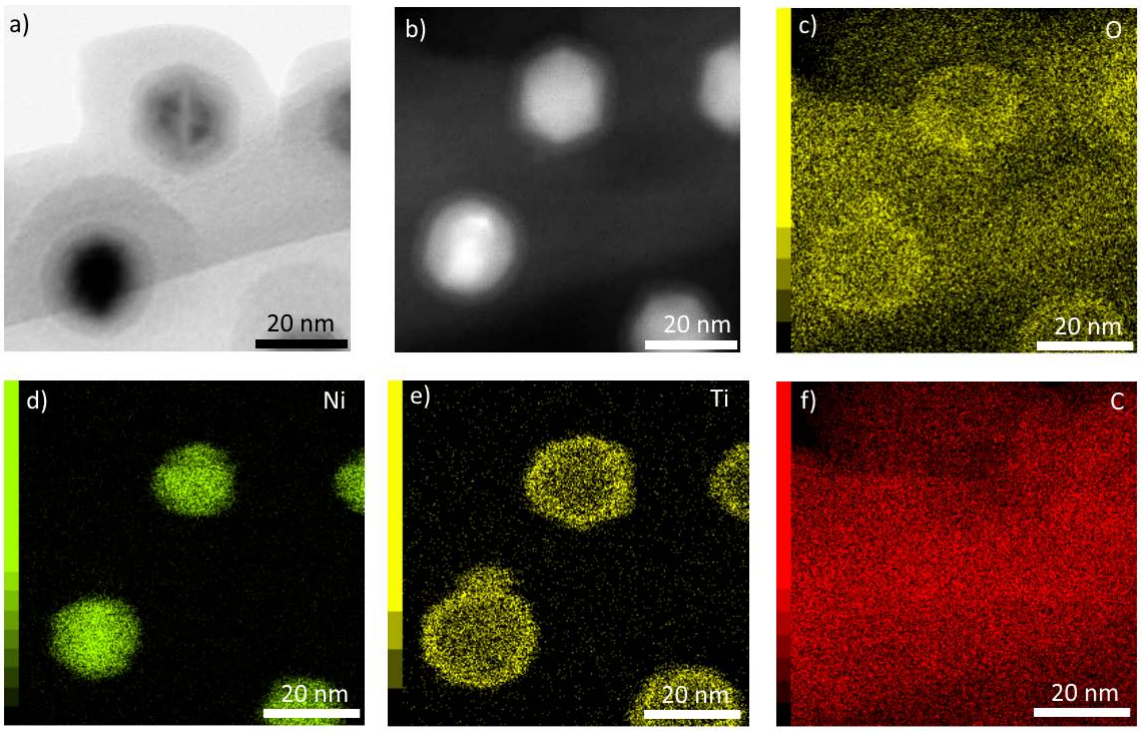

Fig. 1: Ni-Ti core shell nanoparticles: a) STEM BF, b) STEM HAADF, c-f) EDS maps.

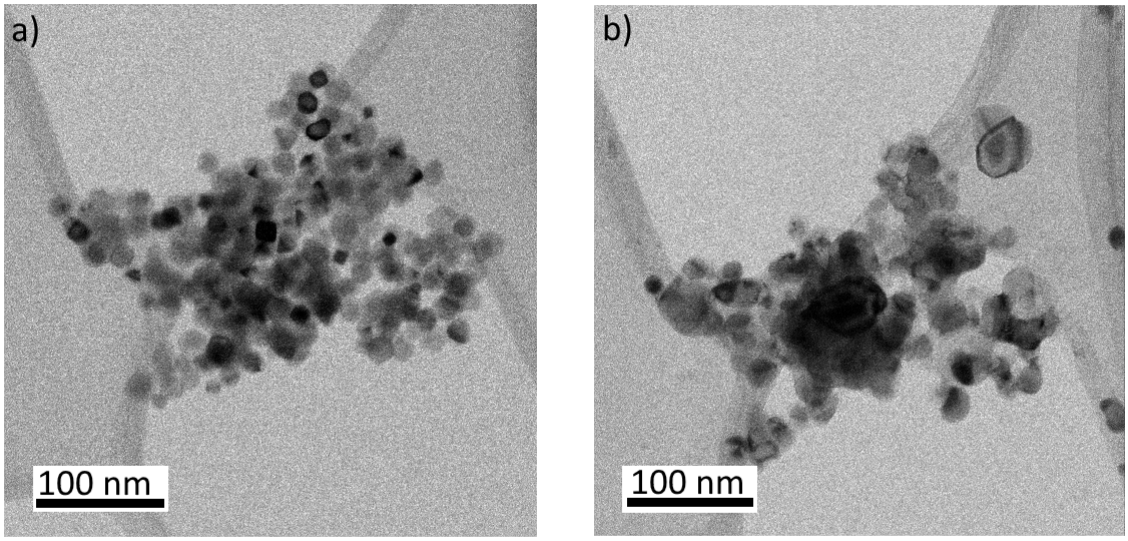

Fig. 2: TEM image of an aggregate of Ni-Ti nanoparticles a) before, b) after annealing up to 950 ºC.

Type of presentation: Poster

MS5-P-2618 Uranium reduction by magnetite – mechanism of UO2 formation monitored by STEM, SAED and STEM-EELS

Bártová B.[1,2], Pan Z.[1], LaGrange T.[3], Butorin S. M.[4], Hyatt N. C.[5], Stennett M. C.[5], Kvashinina K. O.[6,7], Bernier-Latmani R.[1]

[1]EML, EPFL, Lausanne, Switzerland , [2]CIME, EPFL, Lausanne, Switzerland , [3]LUMES, EPFL, Lausanne, Switzerland, [4]Department of Physics and Astronomy, Uppsala University, Uppsala, Sweden, [5]University of Sheffield, S10 2TN, UK, [6]The Rossendorf Beamline at ESRF, Grenoble Cedex 9, France, [7]HZDR, Institute of Resource Ecology, Dresden, Germany

Email of the presenting author: barbora.bartova@epfl.ch

Uranium (U) is a ubiquitous element in the Earth's crust and its biogeochemical behavior is largely constrained by its redox transformation from soluble uranium (U) hexavalent species (U(VI)) to sparingly soluble tetravalent species (U(IV)) under anoxic conditions. U(VI) reduction by mineral phases, most commonly ferrous iron-bearing minerals, has been shown to produce crystalline U in the form of UO2 as the end product at circumneutral pH values. However, there is increasing evidence for the presence of pentavalent U (U(V)). Theoretical calculations reported the reduction from U(VI) to U(V) by aqueous Fe(II) to be facile and demonstrated that the incorporation of U in solid phases widens the stability field of U(V) species in the reduction by magnetite [1]. Studies have shown that the co-precipitation of U(VI) and magnetite/green rust resulted in the formation of a stable uranate(V) coordination in the iron oxide mineral phases [2]. Furthermore, our recent study [3] showed the presence of U(V) as a result of U(VI) reduction by preformed magnetite and its persistence prior to further reduction to U(IV)O2 nanoparticles under neutral pH conditions. However, uncertainty about the role of U(V) in the reduction pathways involving iron oxides remains.

We reported the formation of single U oxide nanocrystals (1-5 nm) followed by the formation of nanowires that extended from the magnetite surface outward. Over time, the nanowires collapsed into ordered UO2 nanoclusters, resembling those previously reported for the final product after U(VI) reduction by magnetite. U(IV) was suggested as the dominant valence state in the nanowires based on both Fast Fourier Transform (FFT) on specific regions of HAADF-STEM images of the nanowires and the branching ratios obtained from M4/M5 peaks from U TEM-EELS spectra. Due to the sensitivity of U(V) under the beam, reduction of U(V) species may occur, and the presence of mixed valence states may be overlooked by using the branching ratios acquired from U EELS spectra under high beam current. Besides the beam sensitivity issue, differences between UO2 and UO2+x ($0<x<1$, representing uranium oxides with mixed valence states, such as U3O8) are too small to be robustly differentiated with FFT. Based on recent microscopic evidence for a range of crystallinity and order in the nanoparticles, we acquired the O K-edge EELS spectra from individual nanoparticles within the nanowires and compared the edge feature to that of U oxide reference standards in order to characterize the valence state of nanocrystals.

[1] Collins &Rosso, J.Phys. Chem. A 121, 6603-6613 (2017)
[2] Roberts et al., Environ. Sci. Technol. Lett. 4, 421–426 (2017)
[3] Pan et al., Nat Commun 11, 4001 (2020)

Acknowledgement: The work at EPFL was supported by Swiss National Science Foundation Grant 200021E-164209 and European Research Council Consolidator Grant 725675 (UNEARTH).

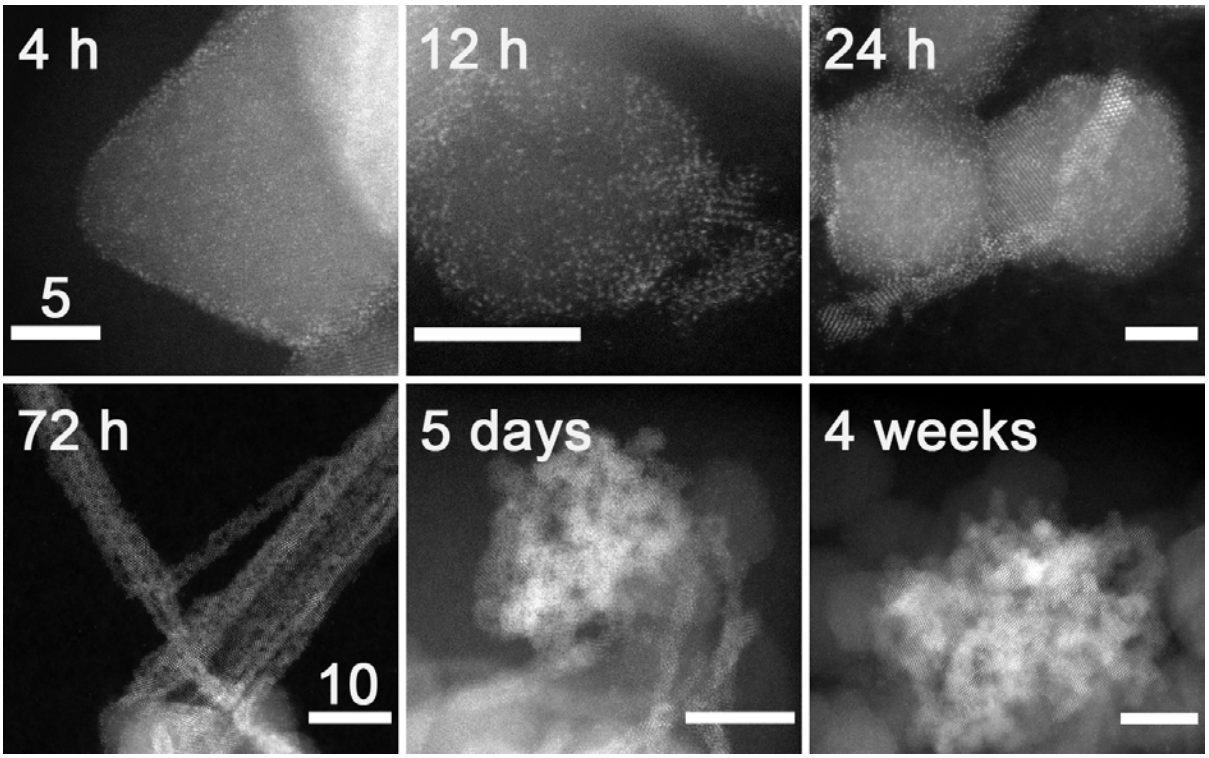

Fig. 1: HAADF-STEM images show the structure evolution during the reduction process. Scale bar in nm.

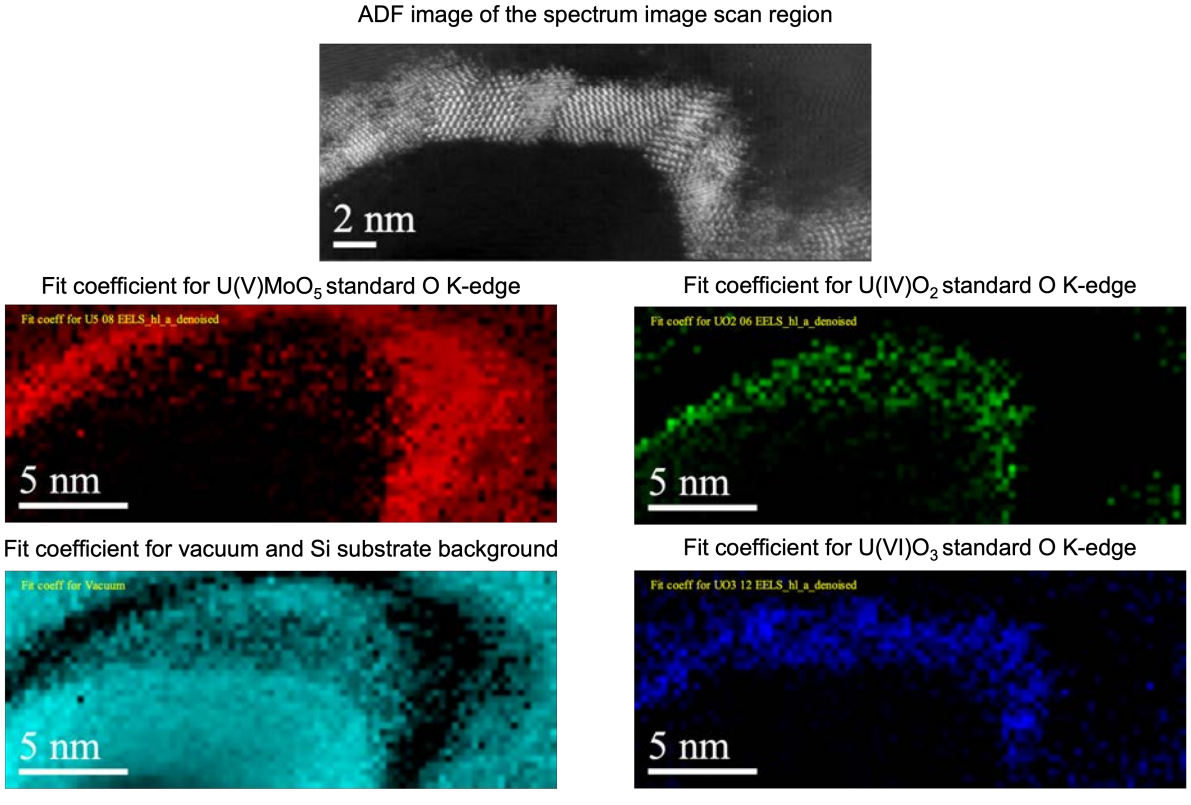

Fig. 2: The colorized images show the Mean Linear Least Squares fit of the spectrum image data obtained at the O-K-edge to those of Urania standards.

Type of presentation: Poster

MS5-P-2539 Real-time observation of vapor transport synthesis in the scanning electron microscope

Bukvisova K.[1,2,3], Rothman A.[4], Novak L.[3], Joselevich E.[4], Sikola T.[1,2], Kolibal M.[1,2]

[1]CEITEC Brno University of Technology, Purkynova 123, Brno 61200, Czech Republic, [2]Institute of Physical Engineering, Brno University of Technology, Technicka 2, Brno 61669, Czech Republic, [3]Thermo Fisher Scientific, Vlastimila Pecha 12, Brno 62700, Czech Republic, [4]Department of Molecular Chemistry and Materials Science, Weizmann Institute of Science, Rehovot 76100, Israel

Email of the presenting author: bukvisova@vutbr.cz

Vapor transport reactions are commonly used to synthesize a wide range of nanostructured materials. However, ex-situ observations of the reaction products are often not sufficient to understand the growth processes in detail, which sometimes leads to difficulty in producing high-quality nanomaterials. This work presents the results of real-time SEM imaging of CVD of selenide-based compounds.

Fig. 1 shows a schematic of the SEM reactor we have prototyped. A carefully calibrated heater allows vaporizing precursor powder, which is carried by a selected gas towards an independent substrate heater. The lid with an aperture for SEM imaging partly prevents contamination of the SEM chamber and protects the electron optics from heat as well.

The first studied reaction is the guided growth of zinc selenide (ZnSe) nanowires, a semiconductor with a direct bandgap (2.7 eV) in the visible range, which is interesting for applications in blue–UV photodetectors [1]. Guided growth of aligned in-plane nanowires catalyzed by gold nanoparticles has been reported on faceted sapphire in a two-zone tube furnace system [2], including modeling-based extraction of kinetic coefficients from the ex-situ data [3]. Our approach allows us to observe the nanowire growth in-situ, and thus, the experiments offer complementary data to create a complete picture of the reaction mechanism. Fig. 2 shows a sequence that revealed that the variations in nanowire diameter are a direct consequence of small changes in gold droplet shape as it moves along the nanogroove. Our latest results on different selenide-based compounds will be presented as well.

[1] Nanotechnology, 17(22), 5561-5564,
[2] Advanced Materials, 27(27), 3999-4005,
[3] Proceedings of the National Academy of Sciences of the United States of America, 117(1), 152-160.

Acknowledgement: H2020-Twinning project No. 810626 – SINNCE

CzechNanoLab project LM2018110 funded by MEYS CR

Brno Ph.D. Talent scholarship

Israel Science Foundation (2444/19)

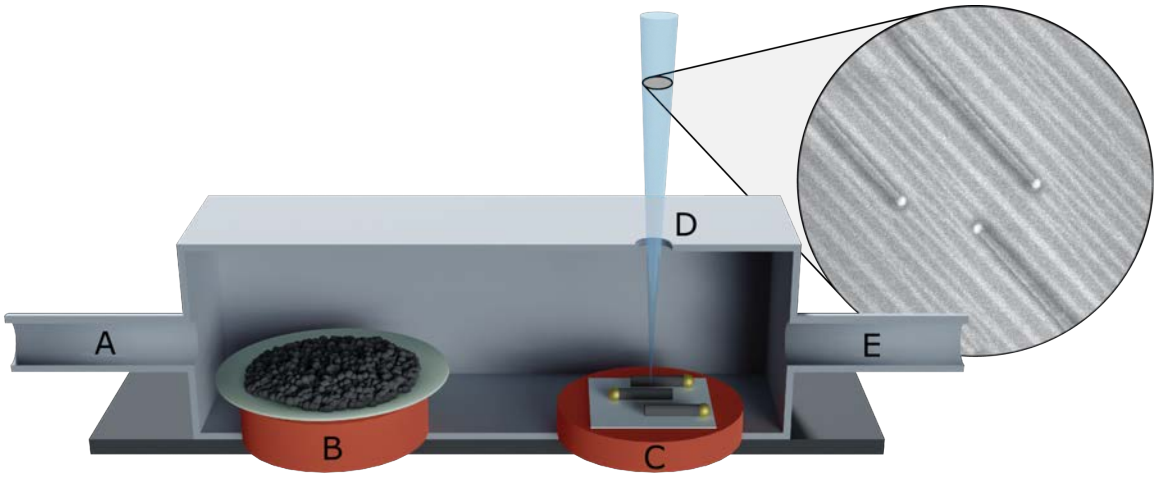

Fig. 1: A schematic of the SEM-compatible CVD reactor. Carrier gas flows through an inlet (A) and carries a precursor which is vaporized by the first heater (B). The vapor then condenses on a substrate kept at a different, lower temperature by the second heater (C). The lid has an aperture (D) for observation above the substrate and an outlet (E).

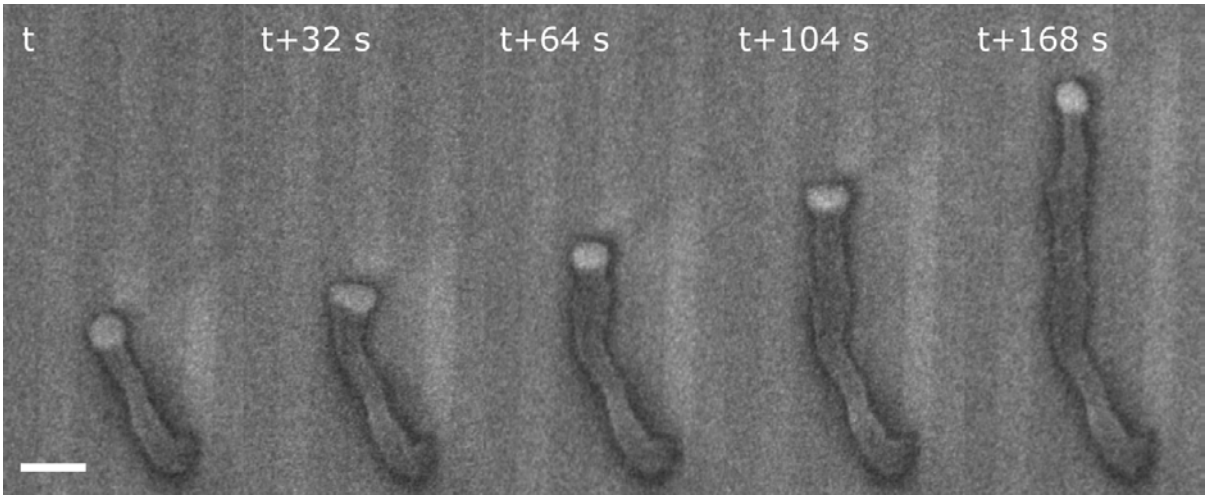

Fig. 2: Real-time SEM sequence showing growth of a ZnSe nanowire catalyzed by a gold nanoparticle. The carrier gas was pure hydrogen (pressure $1.1 \cdot 10^{-2}$ Pa), precursor ZnSe powder was held at 990 °C, and substrate, annealed R-plane sapphire, at 640 °C. The scale bar is 200 nm.

Type of presentation: Poster

MS5-P-2851 Effect of Nanoparticle Size on Phase Stability in ZrO2 System

Pizúrová N.[1], Buršík J.[1], Roupcová P.[1,2], Sokovnin S. Y.[3]

[1]Institute of Physics of Materials, Czech Academy of Sciences, Žižkova 22, 616 62, Brno, Czech Republic, [2]CEITEC - Central European Institute of Technology, Brno University of Technology, Purkyňova 123, 612 00, Brno, Czech Republic, [3]Institute of Electrophysics, UB RAS, Amundsen street 106, 620016, Yekaterinburg, Russia

Email of the presenting author: bursik@ipm.cz

Zirconium oxide nanoparticles are used in biomedical, catalytic, and electronic applications. They have high chemical stability, corrosion, chemical, and microbial resistance, and they also found uses in solid oxide fuel cells [1]. The ZrO_2 is formed with three crystal lattice types under normal pressure: cubic, tetragonal, and monoclinic (Fig. 1). The monoclinic phase is stable up to 1100°C. The tetragonal phase is stable in the temperature range of 1100-2370°C and the cubic phase at temperatures exceeding 2370°C. In small material volumes, these temperature ranges can be different. An inverse linear relationship between crystallite size and monoclinic-tetragonal transformation was found by Mayo et al. [2]. They suggested that the transformation temperature can be lower by hundreds of degrees. Regarding their results, high-temperature phases can become stable under ambient conditions in small crystalline volumes.

Inspired by these results, we tried to find high-temperature polymorphs in the ZrO_2 nanoparticle system. The ZrO_2 nanopowder was synthesized using electron beam evaporation technique [3]. The high-resolution transmission electron micrographs were taken with a Talos 200i transmission electron microscope; Fast Fourier transform patterns were evaluated with the JEMS software (P. Stadelmann).

The observed clusters contained nanoparticles of a wide range of sizes. It was supposed that larger crystalline areas arose with a coalescence process of the smaller nanoparticles. On the border of the clusters, part of the smallest nanoparticles kept their original sizes. We analysed randomly chosen crystalline areas and nanoparticles and identified monoclinic and tetragonal ZrO_2 polymorphs. The dominant phase in the larger crystalline areas was monoclinic Baddeleyite. The smaller nanoparticles (2-10 nm) were formed with the ZrO_2 tetragonal phase (Fig. 2). These results correspond with the previous experimental and thermodynamic studies [2], suggesting an influence of the nanoparticle size on the phase constitution. We confirmed the existence of nanoparticles with the high-temperature tetragonal crystal structure at temperatures significantly below 1100°C.

[1] S. Yu. Sokovnin et al., Ceramics International, 48 (2022) 17703-17713
[2] M. J. Mayo et al., Rev. Adv. Mater. Sci. 5 (2003) 100-109
[3] V. G. Ilves et al., Nanotechnol. Russ. 7 (2012) 213

Acknowledgement: The work was supported by the Czech Science Foundation, project No. 21-31852J, and by the CzechNanoLab project LM2018110 funded by MEYS CR.

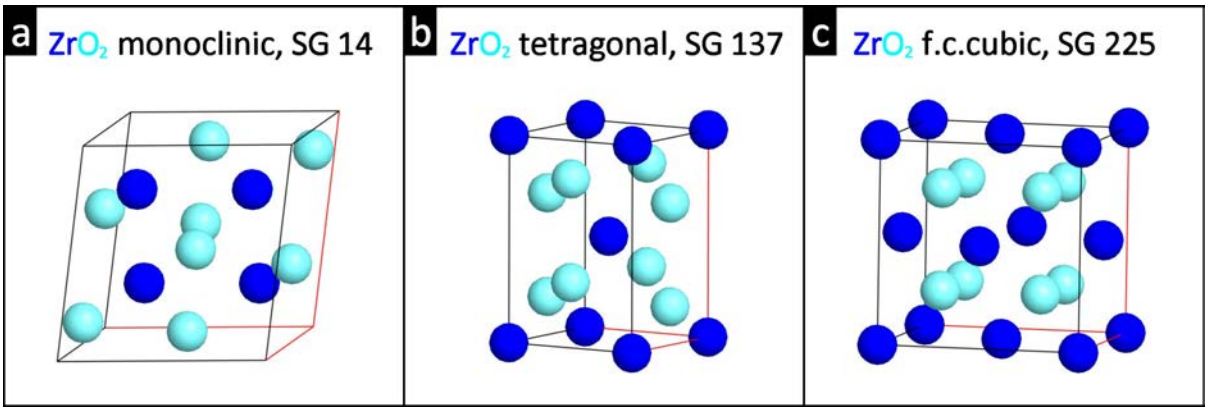

Fig. 1: Unit cells of the three polymorphs of ZrO_2 with their space groups: the monoclinic structure (ICSD entry #26488) (a), the body centred tetragonal structure (ICSD entry #23928) (b), and the face centred cubic structure (ICSD entry #105553) (c).

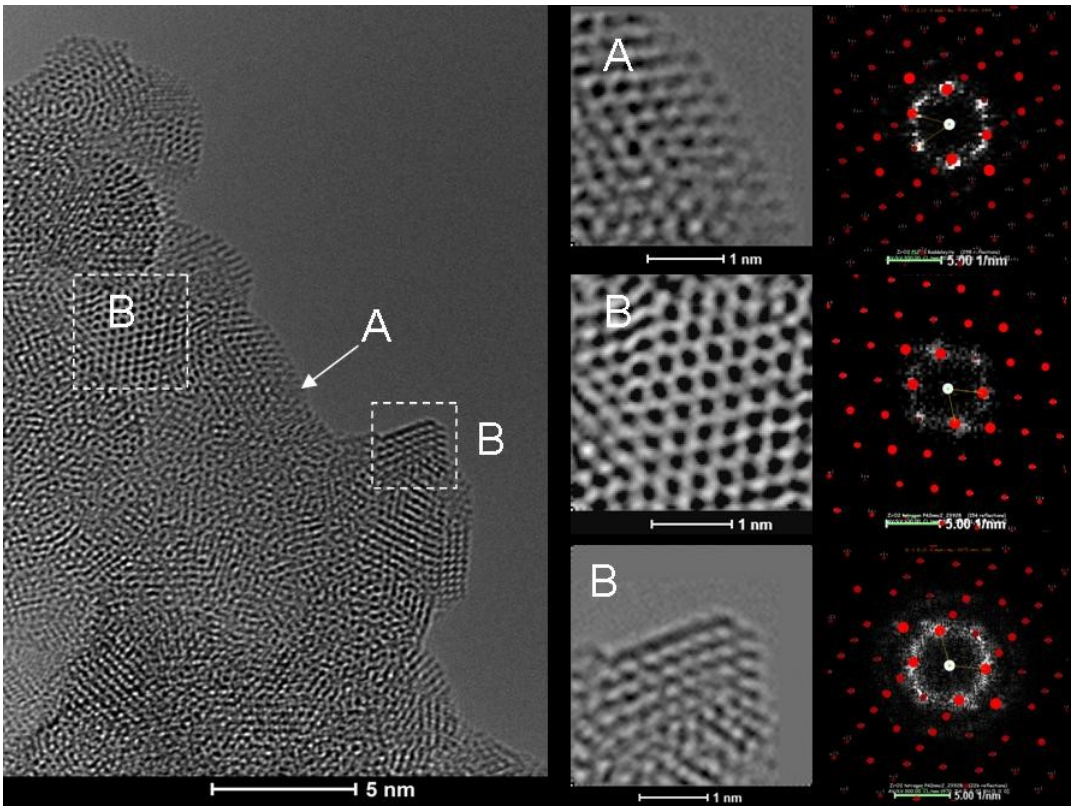

Fig. 2: High-resolution TEM micrograph showing a nanoparticle cluster containing two ZrO_2 polymorphs. The area of the Baddeleyite is dominant and signed as A. B corresponds to the tetragonal polymorph. Investigated areas are visible in more detail on the right hand side, including their evaluated FFT patterns.

Type of presentation: Poster

MS5-P-2982 Classification of Metal Nanoclusters Using Convolutional Neural Networks

Dearg M.[1,2], Hoddinott H. P.[3], Niu Y.[3], Palmer R. E.[3], Slater T.[1,2,3]

[1]Cardiff Catalysis Institute, School of Chemistry, Cardiff University, Cardiff, UK, [2]ePSIC, Diamond Light Source, Oxfordshire, UK, [3]Nanomaterials Lab, Swansea University, Bay Campus, Swansea, UK

Email of the presenting author: deargm@cardiff.ac.uk

Catalysis happens only at the surface of materials, this makes nanoparticles of particular interest in the field of catalysis because of their high surface-to-volume ratio. The exact atomic structure of nanoparticle surfaces is of great importance in catalysis, and the expression of surface facets is largely governed by their overall structure. Typically, 1-5nm metal particles will adopt decahedral, icosahedral or fcc structures (Fig. 1) – with glassy structures also common. The structural isomer of a nanoparticle can be determined using HAADF-STEM [1,2] in an aberration-corrected instrument. The isomer identification depends on comparison with a Simulation Atlas [1]. Here we focus on size-selected “magic number” gold clusters which have a complete closed outer shell of atoms; produced by a magnetron sputtering, gas-condensation source [3]. One innovation is video imaging of the fluctuations of a single cluster over time; the second is an automated approach to classifying the structures – e.g., to calculate the relative abundance of each structure and determine their relative potential energies [1,2].

Machine learning has become popular in electron microscopy [4]. Here we turn this approach to the cluster structure classification problem. We use a convolutional neural network (CNN), a class of machine learning algorithm that can be trained to recognize image features [5]. Specifically, a CNN is trained using HAADF-STEM images of particles (simulated using the plane-wave reciprocal-space interpolated scattering matrix (PRISM) algorithm, Fig. 1 d-u) to recognize the different shapes and patterns of nanocluster images from HAADF-STEM [6]. Manual identification of such nanoparticles is a time-consuming process, the neural network can rapidly determine the proportion of different isomers. The speed improvements afforded by the CNN approach will allow us to process multiple videos of individual clusters, determining the structure in each frame. This concept is demonstrated using the manual classification approach of Fig. 2. Video-rate imaging versus temperature [2] will determine both isomer energies and branching ratios (thus energy barriers) between the different structures.

[1] D. M. Wells, et al., Nanoscale 7 6498 (2015). doi: 10.1039/C4NR05811A
[2] D. M. Foster, R. Ferrando & R. E. Palmer, Nat. Comms. 9 1323 (2018). doi: 10.1038/s41467-018-03794-9
[3] S. Pratontep, et al., Rev Sci. Instr. 76 045103 (2005). doi: 10.1063/1.1869332
[4] J. M. Ede, Mach. Learn.: Sci. Technol. 2 011004 (2021). doi: 10.1088/2632-2153/abd614
[5] A. Dhillon & G. K. Verma, Prog. Artif. Intell. 9 85 (2020). doi: 10.1007/s13748-019-00203-0
[6] L. Rangel DaCosta, et al., Micron 151 103141 (2021). doi: 10.1016/j.micron.2021.103141

Acknowledgement: The authors acknowledge funding from the EPSRC (EP/V029797/1), and thank Diamond Light Source for access to ePSIC (Proposal No.: MG28449).

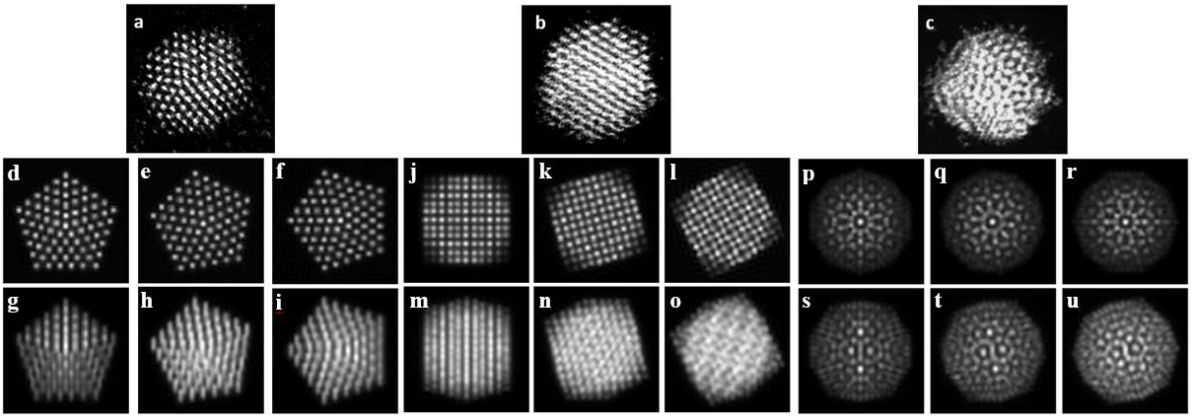

Fig. 1: (a) HAADF-STEM image of decahedral nanocluster. (b) HAADF-STEM image of cuboctahedral (fcc) nanocluster. (c) HAADF-STEM image of icosahedral nanocluster. (d-i) Simulations used for identification of decahedral motifs. (j-o) Simulations used for identification of cuboctahedral motifs. (p-u) Simulations used for identification of icosahedral motifs.

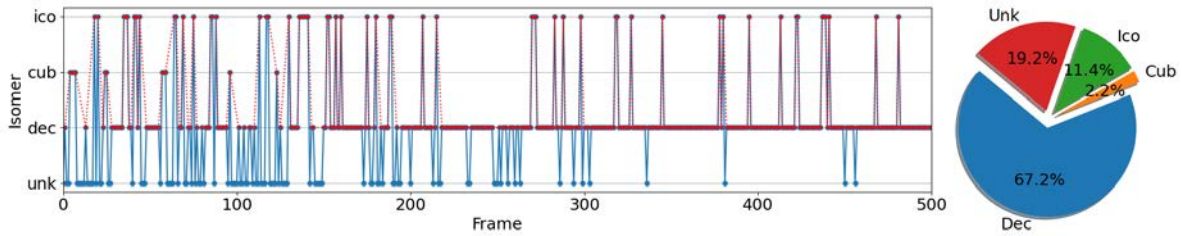

Fig. 2: Manual classification results from an HAADF-STEM video of one Au309 cluster on carbon at room temp. Icosahedral (ico), decahedral (dec), cuboctahedral (cub), unknown/amorphous (unk).

Type of presentation: Poster

MS5-P-2858 Study of barium titanate on transparent titania nanotubes arrays

Bohač M.[1], Kojić V.[1], Juraić K.[1], Čižmar T.[1], Pavić L.[2], Bafti A.[2], Gajović A.[1]

[1]Division of materials Physics, Ruđer Bošković Institute, Zagreb, Croatia, [2]Division of materials Chemistry, Ruđer Bošković Institute, Zagreb, Croatia

Email of the presenting author: gajovic@irb.hr

$BaTiO_3$ (BTO) has been a extensively investigated material over the past 60 years due to its attractive properties, such as mechanical and chemical stability and ferroelectricity at room temperature. Due its high dielectric constant and low-loss, BTO has been used in a wide range of applications, including multilayer ceramic capacitors, gate dielectrics, piezoelectric devices, waveguide modulators, IR detectors, and for holographic memories. The dielectric properties of BTO are controlled by purity and microstructure which are dependent on the methods of preparation Moreover, it was shown recently that BTO nanostructures have humidity sensing properties [1, 2].

In this work $BaTiO_3$ on TiO_2 nanotubes arrays (BTO@TNT) were synthesized by hydrothermal processing of transparent titania based precursor, TiO_2 nanotube arrays (TNT), with the aim to prepare transparent humidity sensor.

TNT were prepared by anodization of titanium thin films deposited on glass by magnetron sputtering. To obtain the thin film TNT the Ti thin films were anodized in an ethylene glycol electrolyte, containing ammonium fluoride and water until it become semi-transparent. To increase the transparency of the TNT thin films and to obtain the TiO2 anatase crystalline phase, the samples were annealed at 450°C for 2 h in air. Hydrothermal synthesis of BTO on TNT (BTO@TNT) was conducted for 2 h at 200 °C in 20 mL of aqueous solutions containing 15, 20, 30 or 40 mM $Ba(OH)_2$. The samples were subsequently annealed in air at 450 °C for 2 h. Structural properties were investigated by XRD, SEM, EDX, TEM, HRTEM, SAED and Raman spectroscopy (RS), transparency and optical properties by UV-Vis, while humidity sensing was studied by electric measurements using impendence spectroscopy (IS).

The BTO was observed by XRD and RS only in samples prepared using solutions with 30 or 40 mM $Ba(OH)_2$. SEM measurements of that samples show nanocubes/nanoparallelepiped at the surface of TNT (Fig. 1a) indicating BTO (in cubic/tetragonal structure). In samples prepared with lower concentration of $Ba(OH)_2$, BTO was not observed by XRD and RS, although nanoobjects containing high percentage of Ba was observed by SEM and EDS at the surface of TNT indicating unfinished reaction toward formation of BTO (Fig 1b). IS measurements show response for samples prepared with higher concentration of Ba(OH), but transparency of these samples was lower. Therefore, optimisation will be discussed in the view of structure and morphology of formed BTO@TNT.

References:

[1] A. Reynolds and J. Conboy, Sensors and Actuators: B. Chemical 273 (2018) 921-926, doi.org/10.1016/j.snb.2018.07.004.

[2] K. Zagar Soderznik et. al., Proceedings 15 (2019) 9; doi:10.3390/proceedings2019015009.

Acknowledgement: Supported by the Croatian Science Foundation project HrZZ-IP-2018-01-5246 and Centre of Excellence for Advanced Materials and Sensing Devices, KK.01.1.1.01.0001

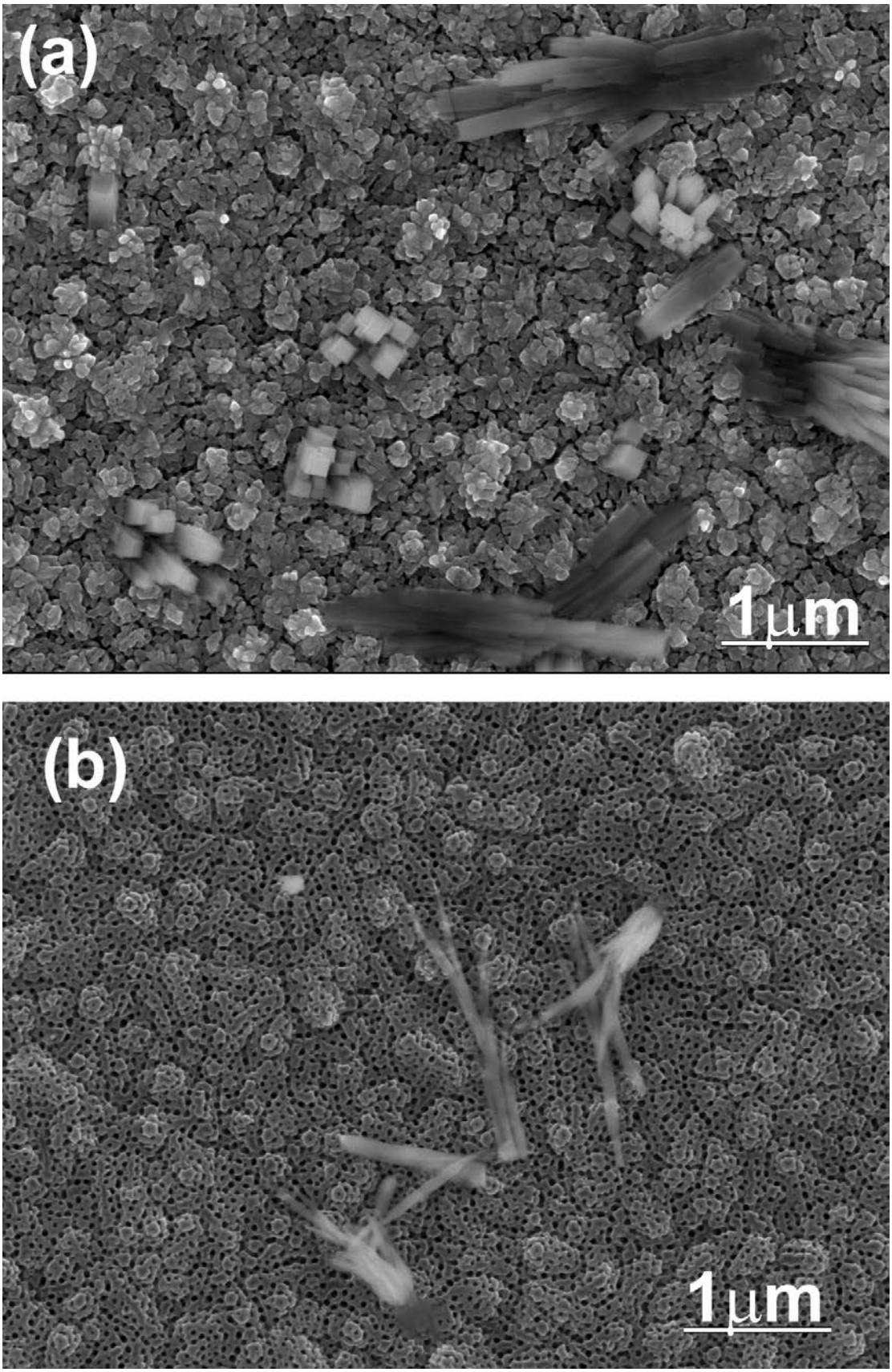

Fig. 1: BTO@TNT synthesized using (a) 40 mM $Ba(OH)_2$, (b) 15 mM $Ba(OH)_2$.

Type of presentation: Poster

MS5-P-2568 Structural and optical investigation of Fe-ZnO nanoarchitectures: from inversion domain boundaries to ZnO/ZnFe2O4 heterostructures

García-Fernández J.[1], Kjeldby S. B.[1], Nguyen P. D.[1], Haug K.[1], Galeckas A.[1], Jensen I. J.[2], Thøgersen A.[2], Vines L.[1], Prytz Ø.[1]

[1]Department of Physics and Center for Materials Science and Nanotechnology, University of Oslo, PO Box 1048 Blindern, N-0316 Oslo, Norway, [2]SINTEF Materials Physics, P.O. Box 124 Blindern, N-0314 Oslo, Norway

Email of the presenting author: j.g.fernandez@smn.uio.no

ZnO is a wide band gap semiconductor that has a broad range of potential applications, for example as a transparent conductive oxide (TCO) in photovoltaic devices. Hence, ZnO film could be used as a transparent front contact to enhance the charge carrier collection from a photovoltaic cell avoiding shadowing effects. Highly conductive, but still transparent, ZnO can be obtained through doping with e.g. aluminum or gallium. A possible route to further enhance the functionality of the TCO is to modify it in such a way that it can produce charge carriers by absorbing light of shorter wavelengths, which are less efficiently used by the main photovoltaic. One way to achieve this is to embed optically absorbing nanoparticles with a suitable band gap in the TCO. The $ZnFe_2O_4$ spinel has a band gap of ~1.9 eV, and according to the ZnO-Fe_2O_3 phase diagram, it is energetically favorable at temperatures below ~1200°C and/or at higher Fe concentrations [1]. $ZnFe_2O_4$ is therefore a well-suited candidate for the synthesis of optically absorbing nanoparticles embedded in a ZnO matrix. When Fe is incorporated in ZnO, lead to the formation of periodic nanostructures known as inversion domain boundaries (IDBs), decorated with Fe [2]. The IDBs are seen to consist of a network of essentially atomic layers of Fe intergrown with ZnO wurtzite blocks which could exhibit intriguing optoelectronic properties. For example, as the IDBs are essentially two-dimensional sheets of dopants, it has been reported that while IDBs play a fundamental role in charge generation, wurtzite blocks are responsible for charge collection in photocatalytic processes [3].

In this work, we use a solid state powder synthesis route to form nanoparticles of $ZnFe_2O_4$ embedded in ZnO (Figure 1) or 2D structures formed by iron decorated IDBs (Figure 2) with similar cation ratio. We use a combination of (Scanning) Transmission Electron Microscopy (STEM), electron energy loss spectroscopy (EELS), and Energy Dispersive X-ray spectroscopy (EDS) to investigate the structure and chemistry of the particles and the IDBs (Figure 3). The optical properties are measured using diffuse reflectance spectroscopy and cathodoluminescence in a scanning electron microscope (CL). The possibility of forming such different nanostructures offers the opportunity to exploit and tune the physical properties of these systems.

[1] Sergei A. Degterov et al. Metallurgical and Materials Transactions B, 32, 643– 657, (2001)
[2] O. Köster-Scherger et al. J. Am. Ceram. Soc., 90, 12, 3984– 3991, (2007)
[3] M. Lv et al. ACS Appl. Mater. Interfaces, 8, 42, 28700–28708, (2016)

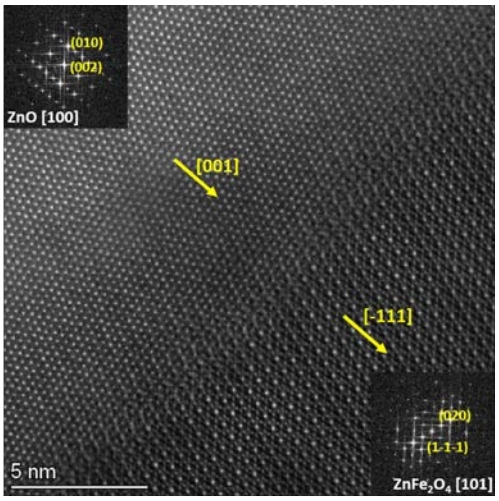

Fig. 1: High resolution high-angle annular dark-field STEM image of the interface between a ZnO and a $ZnFe_2O_4$ particle. Insets show Fourier-transforms of the image indexed according to the ZnO [100] and $ZnFe_2O_4$ [101] projection.

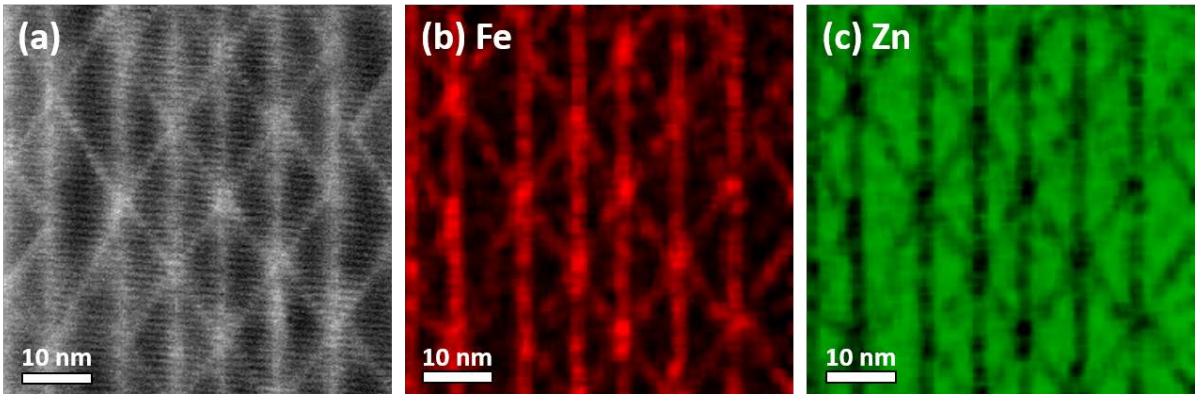

Fig. 2: (a) Annular dark field STEM image of the sample with IDBs structure and (b-c) EDS maps corresponding to Fe and Zn confirming the high concentration of Fe at the IDBs.

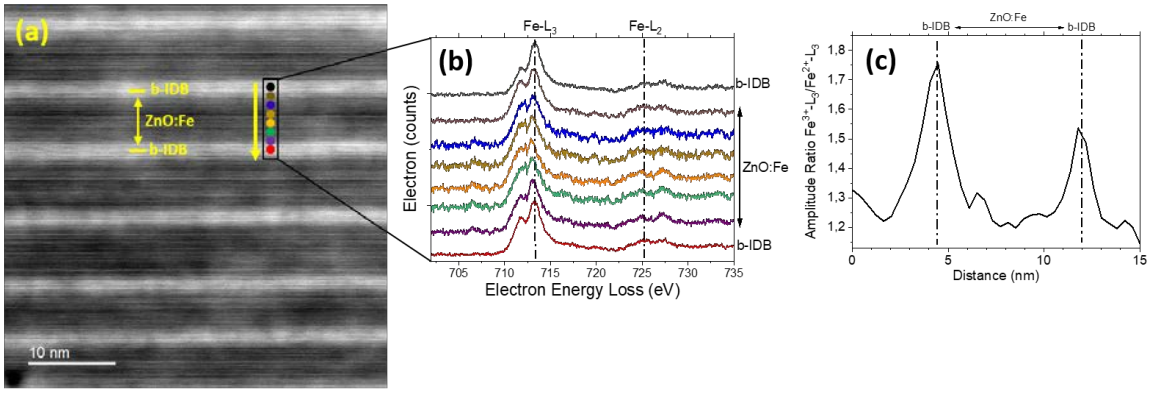

Fig. 3: (a) ADF STEM image of the sample with IDBs structure. (b) EELS spectra at different sites along the yellow arrow extracted from spectrum image of Fe-$L_{2,3}$ edges. (c) Estimated Fe^{3+}/ Fe^{2+} ratios increase to a maximum of around 1.7 on the Fe-rich IDB sites and around 1.2 on the ZnO matrix.

Type of presentation: Poster

MS5-P-2648 Imaging the atomic-scale effects of electron irradiation on charge density waves in 1D O-TaS3

Kinyanjui M. K.[1], Matsuura T.[2]

[1]Electron Microscopy Group of Materials Sciences, Ulm University, Ulm, Germany, [2]Department of Electrical and Electronic Engineering, National Institute of Technology, Fukui College, Fukui, Japan

Email of the presenting author: michael.kinyanjui@uni-ulm.de

Use of controlled disorder in low-dimensional quantum materials to design electronic states at the atomic scale is a major goal in quantum materials research [1]. 2D quantum materials often show remarkable properties arising as a result of a complex interplay of charge, lattice, spin, and orbital degrees of freedom. This interplay gives rise numerous electronic phases including superconductivity, anti-ferromagnetism, charge-density waves (CDW), spin-density waves, Mott-insulating among others [2-4]. Systematic introduction of external perturbations such as controlled disorder through doping or irradiation is one approach that has been used to probe this interplay [5-7]. However, the influence of induced disorder coupled with the intricate interaction between electronic and lattice degrees of freedom can trigger complex structural evolution and distribution of various electronic phases at the atomic scale [1, 4]. It's therefore necessary to understand how disorder-induced changes in the atomic lattice and the electronic ordered states are correlated at the atomic scale.

We have investigated the correlation between the atomic-scale responses of the charge density wave electronic state and the underlying atomic lattice in 1D O-TaS3 exposed to controlled electron irradiation. Atomic-scale transmission electron microscopy imaging supported by electron energy loss spectroscopy shows that the CDW electronic phase responds with an elastic-like strain response to irradiation induced defects and deformations in the atomic lattice. This is characterized by a proliferation of phase defects including CDW dislocations, discommensurations, and domain walls. Our results show the importance of disorder-induced defects in modulating, stabilizing or destroying electronic phases at the atomic scale in 2D quantum materials.

References

[1] C. Bronholm et al., Basic Research needs Workshop on Quantum Materials for Energy Relevant Technology, US Department of Energy, Office of Science, 2017
[2] B. Keimer, and J. E. Moore, Nat. Phys., 2017, 13, 1045
[3] E. Fradkin, S. A. Kivelson, and J. M. Tranquada, Rev. Mod. Phys., 2015,87, 457
[4] D. N. Basov, R. D. Averitt, and D. Hsieh, Nat. Mater. ,2017, 16, 1077
[5] K. Cho et al., Nat. Commun., 2018, 9, 2796
[6] E. Morosan et al., Nat. Phys., 2006, 2, 544
[7] J. Okamoto, C. J. Arguello, E. P. Rosenthal, A. N. Pasupathy, and A. J. Millis, Phys. Rev. Lett., 2015, 114, 026802

Acknowledgement: M.K.K acknowledges funding from the Deutsche Forschungsgemeinschaft (DFG) within the project DFG: KI 2546/1-1.

Type of presentation: Poster

MS5-P-2680 Latest TEM investigation of nanostructured CoS2 and Co2CuS4 based films with Fenton catalytic properties

Medlín R.[1], Vála L.[1], Koštejn M.[2], Vavruňková V.[1], Karatodorov S.[3], Jandová V.[2], Křenek T.[1]

[1]New Technologies - Research Centre, University of West Bohemia, Univerzitni 8, 306 14 Pilsen, Czech Republic, [2]Institute of Chemical Process Fundamentals, Academy of Sciences of the Czech Republic, Rozvojová 135, 160 00 Prague, Czech Republic, [3]Georgi Nadjakov Institute of Solid State Physics, Bulgarian Academy of Sciences, 72 Tzarigradsko Chaussee, 1784 Sofia, Bulgaria

Email of the presenting author: medlin@ntc.zcu.cz

Polymorphic cobalt sulfide is wery versatile material with attractive and unique electronic, optical, magnetic, mechanical and catalitic properties. Deposited by pulsed laser deposition from solid CoS2 target results in deposition of thin films on various substrates. Analysed by TEM, Raman and FTIR together with SEM reveals that films on Ta substrate consist of parent cubic CoS2 and films on Cu were more complex with multiphase structure containing Co2CuS4. Ternary materials are known as active electrode material with higher energy density for electrochemical capacitors and in this case proves interdiffusion events at Cu substrate. This process is first example of one step Co2CuS4 formation through reactive ablation process. Analysed films were examined for catalitic properties in Fenton degradation of methylene blue (MB) and their catalitic effect is compared and discussed.

Vála, Lukáš, et al. "Formation of catalytic nanoparticles via laser ablation in various environments and their degradation activity on methylene blue." (2021).

Acknowledgement: CEDAMNF CZ.02.1.01/0.0/0.0/15_003/0000358, CENTEM CZ.1.05/2.1.00/03.0088 through CENTEM PLUS (LO1402), MetaCentrum LM2010005 and CERIT-SC CZ.1.05/3.2.00/08.0144

Type of presentation: Poster

MS5-P-2832 Exploring the role of fuel on the microstructure of VOx/MgO powders prepared using solution combustion synthesis

Olivier E. J.[1], Ntola P.[2], Friedrich H. B.[2], Mahomed A. S.[2], Singh S.[2]

[1]Centre for HRTEM, Physics Department, Nelson Mandela University, Port Elizabeth, South Africa, [2]School of Chemistry, University of KwaZulu Natal, Private Bag X54001, Durban 4000, South Africa

Email of the presenting author: jolivier303@gmail.com

Vanadium magnesium oxide (V/MgO) is highly desirable in its use as catalyst for the oxidative dehydrogenation (ODH) of alkanes. Its shows high activity with a reported ability to form minimum oxygenates and/or cracking products during reaction with adequate selectivity towards desired ODH products [1]. Preparation of V/MgO catalysts has typically been done using a variety of different synthesis methods which include impregnation using ammonium metavanadate solutions onto supports, and co-precipitation methods [2,3]. In this paper, we present findings from a study of V/MgO catalysts synthesized using solution combustion synthesis (SCS), a previously unexplored method. The use of SCS for synthesis allows for a novel one-step synthesis of V/MgO catalysts. This provides benefits in synthesis time, reproducibility and the introduction of oxygen vacancies into catalytically active phases, which is hypothesized as beneficial for the Mars-Van Krevelen mechanism.

The V/MgO catalysts were prepared by combustion (400 ºC in a muffle furnace) of stoichiometric solutions (1:1 fuel to oxidant) of magnesium nitrate hexahydrate (MgNO3.6H2O) and ammonium metavanadate (NH4VO3), as metal precursors, with different fuels (urea, citric acid, hydrazine hydrate, oxalyl dihydrazide and glycine). Each reaction had a unique temperature-time profile during combustion.

Characterization of the formed nanomaterials was done using aberration-corrected TEM and STEM imaging, electron energy loss spectroscopy (EELS) and energy-dispersive X-ray spectroscopy (EDS) spectrum imaging (eg. FIG. 1), electron diffraction and related techniques. The acquired data was processed to extract structural parameters describing the abundance, composition, distribution, and structural morphology of V/MgO phases for each powder formed. These obtained parameters were subsequently used as input quantities for the development of a basic thermodynamic model to predict the microstructure of V/MgO catalysts prepared by solution combustion.

References

[1] E. A. Elkhalifa and H. B. Friedrich, Catalysis Letters, 2011, 141, 554-564.
[2] V. Soenen, J. M. Herrmann and J. C. Volta, Journal of Catalysis, 1996, 159, 410-417.
[3] J.M. Dejoz et al., Applied Catalysis A: General, 1999, 180, 83-94.

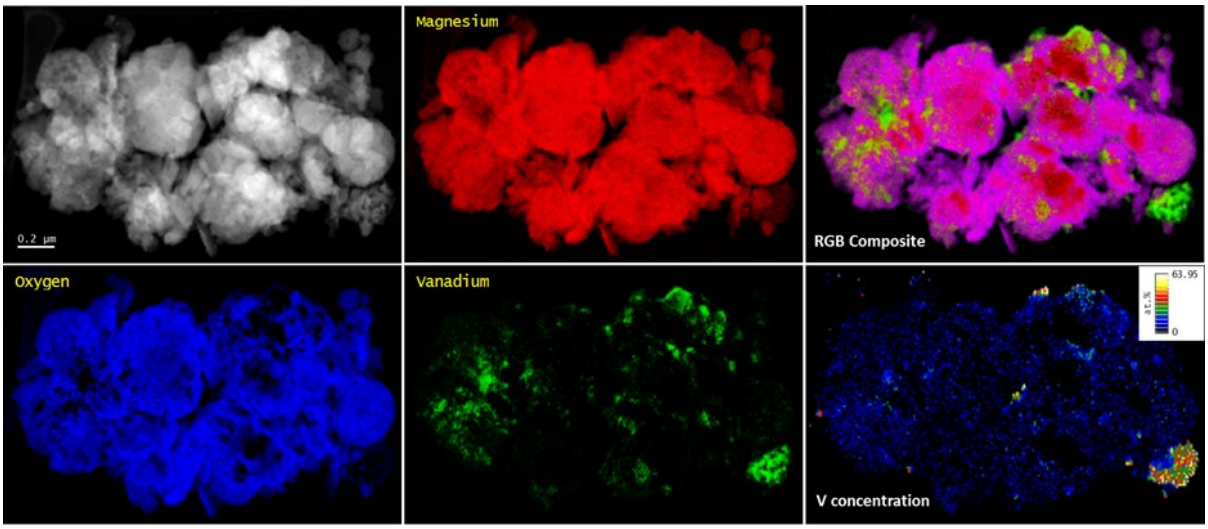

Fig. 1: Quantitative EELS spectrum image mapping of V/MgO(Urea) catalyst

Type of presentation: Poster

MS5-P-2844 In-situ Carbon Nanoribbon Formation by TEM Manipulation of a C59N Derivative

Pelaez-Fernandez M.[1,2,3], Stergiou A.[4], Tagmatarchis N.[4], Ewels C.[5], Arenal R.[1,2,6]

[1]Laboratorio de Microscopias Avanzadas, Universidad de Zaragoza, Spain , [2]Instituto de Nanociencia y Materiales de Aragón, Spain, [3]Université de Lille, Unité de Matériaux et Transformations, France, [4]Theoretical and Physical Chemistry Institute, NHRF, Athens, Greece, [5]Institut de Matériaux de Nantes Jean Rouxel, CNRS – Université de Nantes - France, [6]Fundación ARAID, Zaragoza – Spain

Email of the presenting author: Mario.pelaezfernandez@univ-lille.fr

The development of new kinds of functionalized carbon nanostructures is certainly a growing interest in solid-state physics research due to their wide range of potential applications [1]. Controlled electron irradiation within a transmission electron microscope (TEM) is a great tool for in-situ studies on these structures while they are being formed at their specific scale.

In this context, carbon 'peapods' (fullerenes encapsulated in SWNT)[2] have been proven to be a tool of interest regarding the controlled formation, into or on the SWNT, of nanostructures. A good example of this are graphene nanoribbons (GNRs) templated by the encapsulated fullerenes upon heating or beam irradiation [3]. Functionalized C59N-derivatives using dithiolane molecules, containing both sulphur and oxygen [4] may give rise to the creation of fine S, O, N or S-O-N co-doped GNRs within SWNTs under beam irradiation.

In this work, these derivatives (C59N-DT) have been introduced into SWNTs and irradiated *in situ* viaTEM. Results seem to point out to the formation of passivated GNRs. In order to delve deeper into the passivation on the edges of these materials, DFT calculations have been performed on these structures to discern the energetic viability of different GNR edges. Preliminary results seem to show that stochiometrically favourable configurations, such as S-O co-doped edges, are more energetically stable than S-doped edges, contrary to what has been shown in the literature [3].

Further insight on these nanostructures is vital to fully understand their structure, behaviour and possible future applications.

[1] Celis A et al. J. Phys. D. Appl. Phys. 49(14):143001, 2016
[2] Smith, B. W. et al, Nature 1998, 396, 323-324
[3] Chuvilin, A. et al, Nature Materials 2011, 10, 687-692.
[4] G. Rotas and N. Tagmatarchis, Chem. Eur. J. 2016, 22, 1206 – 1214

Acknowledgement: Research supported by the European Union's Horizon 2020 research and innovation programme under the Marie Sklodowska-Curie grant agreement No. 642742.

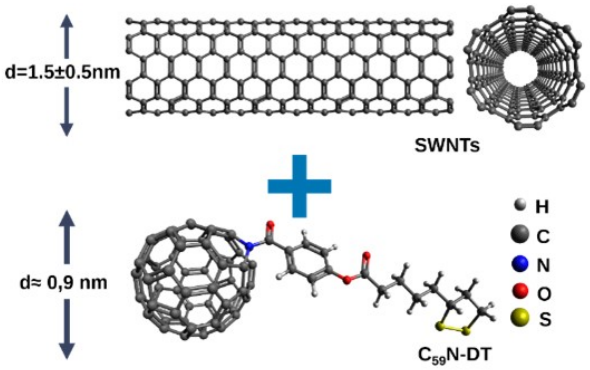

Fig. 1: structure of the different components of the DT-C59N@SWNT

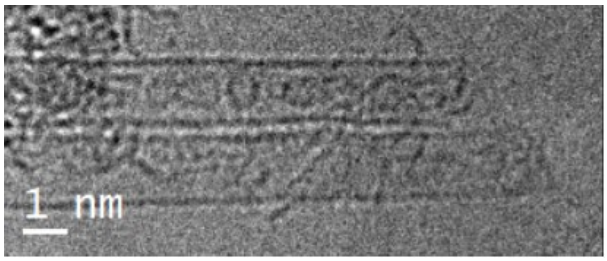

Fig. 2: TEM images of DT- C59N@SWNT before irradiation

Type of presentation: Poster

MS5-P-2524 Quantification and morphological analysis of nanofibers for exposure control and material characterization purposes using electron microscopy and advanced image

Peters T.[1], Schumann J.[2], Meyer-Plath A.[3], Plitzko S.[4]

[1]Unit 4.5 Particulate Hazardous Substances, Advanced Material, Federal Institute for Occupational Safety and Health (BAuA), Nöldnerstr. 40-42 D-10317 Berlin, Germany

Email of the presenting author: peters.torben@baua.bund.de

Airborne fibre exposure control requires sampling and quantification of fibres in a finite air volume. The visual recognition and manual determination of fibre morphologies in SEM images of sampling filters is a tedious and time-consuming task. Its workload increases quadratically with decreasing fibre diameter as reliable recognition requires the pixel resolution for imaging to be well below the detectable fibre diameter. For nanoscale fibres and exposure limits in the order of 10000 nanofibres/m³, it is practically unmanageable to determine concentrations of fibres thinner than about 40 nm and to test exposure limit compliance for fibres thinner than 20 nm by visual and manual evaluation [1]. Fortunately, the development of Convolutional Neural Networks (CNNs) and availability of powerful vector computing units enabled tremendous progress in the field of computer vision in recent years. Here, we present our approach to fully automated fibre concentration determination that combines CNNs for fibre recognition by semantic segmentation with classic image processing algorithms that perform fibre tracing and morphological analysis. To evaluate the reliability of our approach, we compare automated and manual image evaluation results from CNNs and human evaluators for a set of different nanofibre materials.
[1] A. Meyer-Plath et al. 10.3390/atmos11111254

Type of presentation: Poster

MS5-P-2685 CeO2 Morphology Study – Nanoparticles Prepared by Electron Beam Evaporation

Pizúrová N.[1], Hlaváček A.[2], Buršík J.[1], Sokovnin S. Y.[3]

[1]Institute of Physics of Materials, Czech Academy of Sciences, Žižkova 22, Brno 616 62, Czech Republic, [2]Department of Bioanalytical Instrumentation, Institute of Analytical Chemistry, Czech Academy of Sciences, Veveří 967/97, Brno 602 00, Czech Republic, [3]Institute of Electrophysics, Ural Branch RAS, Amundsen St. 106, 620016 Yekaterinburg, Russia

Email of the presenting author: pizurova@ipm.cz

Cerium oxide nanoparticles are a promising material for catalysis and various biomedical applications. Their use has brought new opportunities for safer and more efficient treatment of serious diseases, especially cancer. Their properties are significantly affected by the surface oxygen vacancies causing the oxygen off-stoichiometry [1]. The formation of oxygen vacancies leads to the reduction of Ce^{4+} ions to the Ce^{3+} state on the nanoparticle surface and affects CeO_2 properties usable for the radioprotection of healthy tissues during radiation therapy or to make radiotherapy more efficient in tumors [2].

The nanoparticle size, shape, and surface facet types affect material reactivity [3] and the ease of surface vacancy creation [4]. This structural-sensitive behavior can be affected in the synthesis process.

The purpose of this study was the surface quality and facet type evaluation of the CeO_2 nanoparticles produced using electron beam evaporation [5]. The nanoparticles arose in a one-step process, including nanoparticle creation followed by the break irradiation damaging the sample surface. TEM samples were prepared with electrophoresis to decrease the nanoparticle cluster size and make more facets visible. The sample was analyzed with the HRTEM method using analyses of the FFT patterns with the JEMS software (created by P. Stadelmann). The measurement was conducted using a Titan Themis 60-300 cubed transmission electron microscope working at 300 kV.

We analyzed 200 nanoparticles with a typical size of about 2 - 5 nm. We observed nanoparticles formed with shapes close to the truncated octahedrons containing {111}, {100}, and many small {100} and {110} facets. The typical octahedron contains most {111} facet types, unsuitable for oxygen vacancy formation [4]. Nonequilibrium conditions during the nanoparticle synthesis process caused the formation of many {100} and {110} small facets that are beneficial for an oxygen vacancy formation. The braking irradiation arising during the synthesis process can create defective surfaces on these facets and surface edges more easily. These results confirmed the used synthesis method is beneficial for the suggested applications.

References

[1] R. A. Vazirov et al., IOP Conf. Series: Journal of Physics: Conf. Series 1115 (2018), 032094
[2] M.V. Ulitko et al., AIP Conference Proceedings 2313 (2020), 080031
[3] Ning-Chao Zheng et al., Journal of Colloid and Interface Science, 525 (2018), 225-233
[4] P. Pérez-Bailac et al., Journal of Physics: Condensed Matter, 33 (2021), 504003
[5] V. G. Il'ves et al., Nanotechnol. Russ. 7 (2012), 213

Acknowledgement: The work was supported by the Czech Science Foundation, project No. 21-31852J, and by the CzechNanoLab project LM2018110 funded by MEYS CR.

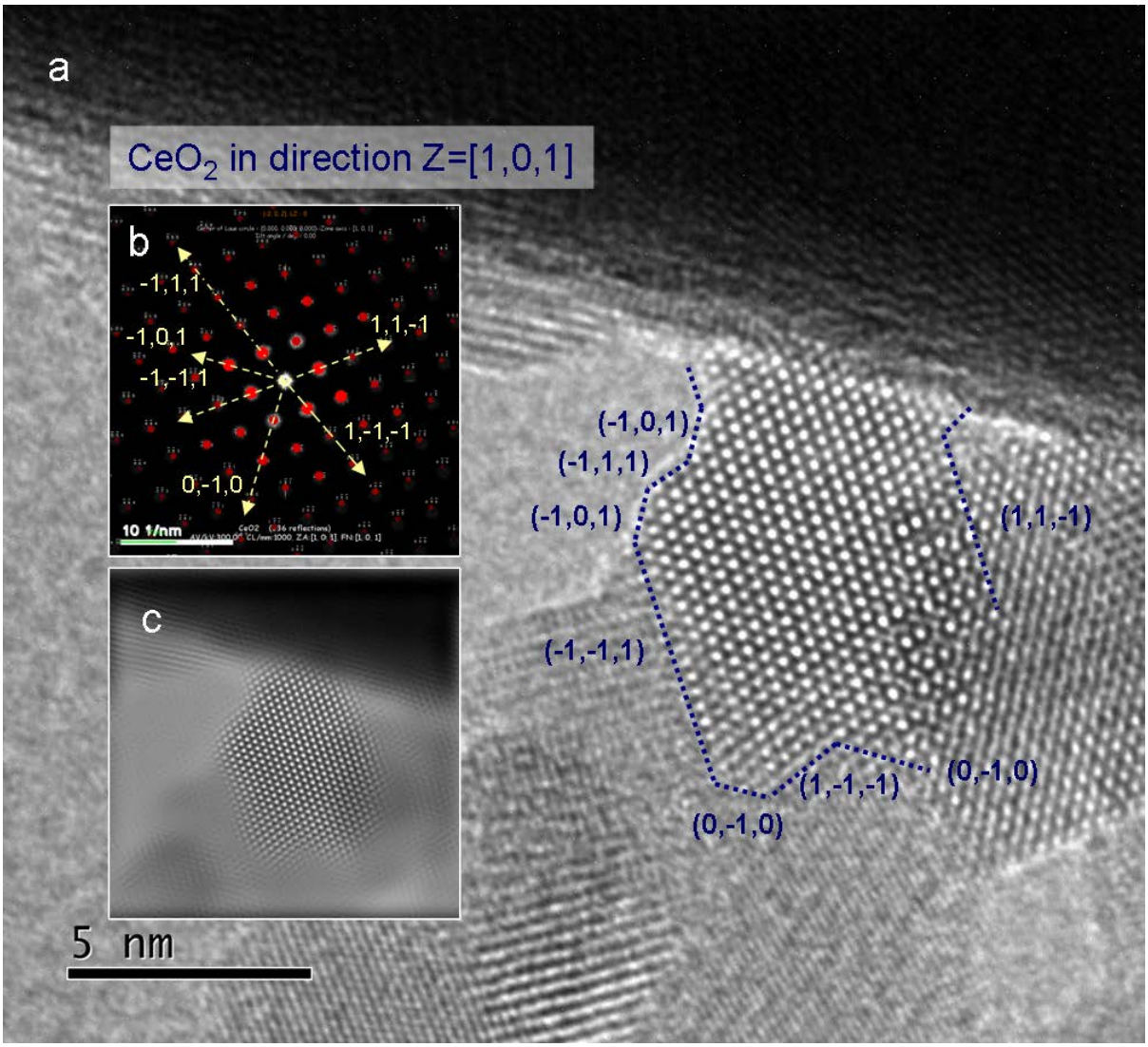

Fig. 1: a) HRTEM image shows an irregular nanoparticle shape. The evaluation of edges suggests the shape is close to the truncated octahedron with many additional {100} and {110} surface facets; b) Filtered Fast Fourier transform pattern evaluated with the JEMS software; c) Inverse filtered Fast Fourier transform of the evaluated nanoparticle

MS6 Materials for energy related applications

Type of presentation: Invited

MS6-IN-2562 In situ Scanning Transmission Electron Microscopy of Lead-Free Ferroelectrics with Atomic Resolution

Bencan Golob A.[1,2], Condurache O.[1,2], Ursic H.[1,2], Rojac T.[1,2], Damjanovic D.[3], Drazic G.[4]

[1]Electronic Ceramics Department, Jozef Stefan Institute, Ljubljana, Slovenia , [2] Jozef Stefan International Postgraduate School, Slovenia, [3]Group for Ferroelectrics and Functional Oxides, Institute of Materials, Ecole Polytechnique Fédérale de Lausanne, Switzerland, [4]Department of Materials Chemistry, National Institute of Chemistry, Ljubljana,Slovenia

Email of the presenting author: andreja.bencan@ijs.si

A comprehensive approach to ferroelectric materials design requires an understanding of local structures such as domain walls (DWs), polar nanoclusters, and other structural imperfections. All of these local structural features, which can be altered during the synthesis of ferroelectrics, have a major impact on the macroscopic responses of application-relevant ferroelectric materials. Recent technological improvements in scanning transmission electron microscopy (STEM) can resolve these local structures and allow direct observation and analysis down to the atomic level. Moreover, thanks to the development of high-resolution in situ techniques, we can perform structural studies under external stimuli and take another step towards understanding the behaviour of ferroelectrics under dynamic conditions.

In the first part of the talk, we will show that we can directly visualize polar nanoclusters in the paraelectric phase of BaTiO3-based ceramics by measuring the displacement of oxygen atoms relative to the Ba/Sr and Ti sublattices. In the presentation, we will provide evidence and discuss the possible origin of these polar nanoclusters [1].

Second, we will focus on the dynamics of DWs under externally applied voltage in ferroelectric BiFeO3 (BFO) and (K,Na)NbO3 single crystals. DWs are two-dimensional interfaces between ferroelectric domains with different polarization orientations that move when an external electric field is applied. We obtain information about polarization indirectly from the displacement of the B-site atoms with respect to the center of the A-site sublattice. We will show down to the atomic level that DW motion is complex and involves a change in the DW plane, a change in the distribution of charge, a distortion of the unit cell, and thus a redistribution of strain at DW.

[1] Bencan et al., Nat. Comm 12. 3509, 2021

Type of presentation: Oral

MS6-O-2514 Correlative Microscopy Techniques for Defect-Property-Correlation of Thermoelectric Materials

Abdellaoui L.[1], Zhiwei C.[3], Bueno-Villoro R.[2], Riley H.[4], Luo T.[2], Gault B.[2], Rodenkirchen C.[5], Yu Y.[5], Cojocaru-Mirédin O.[5], Yanzhong P.[3], Snyder J.[4], Amouyal Y.[6], Raabe D.[2], Scheu C.[2], Zaefferer S.[2], Zhang S.[2]

[1]Carl Zeiss Microscopy GmbH, Oberkochen, Germany, [2]MPIE GmbH, Düsseldorf, Germany, [3]School of Materials Science & Engineering, Tongji University, Shanghai, China, [4]Department Materials Science & Engineering, Northwestern University, Evanston, USA, [5]Institute of Physics IA, RWTH Aachen University, Aachen, Germany, [6]Materials Science & Engineering, Technion Institute of Technology, Haifa, Israel

Email of the presenting author: lamya.abdellaoui@zeiss.com

Complex chalcogenides are promising thermoelectric materials with a high efficiency, and suitable for thermoelectric power generation in the low-to mid-temperature range (e.g. 600-800 K). Thermoelectric materials directly convert spatial temperature gradients into electricity through the Seebeck effect. The conversion efficiency is determined by the dimensionless figure of merit, ZT, which scales with the thermal conductivity κ, electrical conductivity σ, the Seebeck coefficient S and the temperature T. Attempts to optimize ZT require reducing κ, while maintaining relatively high values of σ and S.

The thermal conductivity consists of an electronic part κe and a lattice part κL, which can be reduced by crystallographic defects such as stacking faults and dislocations. In this work, we investigated various microstructural features in the as-quenched δ-phase of $Ag_{16.7}Sb_{30}Te_{53.3}$ [1-3]. We applied correlative microscopy methods to study the microstructure from the scale of grains (sub-mm) down to the atomic scale. Specifically, we used electron contrast channeling imaging (ECCI) in a scanning electron microscope, high angle annular dark field (HAADF) imaging in an aberration corrected scanning transmission electron microscope and atom probe tomography [1-3]. Notably the as-quenched material showed a distinct mosaic- microstructure with abundant low angle grain boundaries, where planar fault networks are accumulated [1]. We found a high density of 2.7×107 m^{-1} at grain boundaries compared to the interior of the grain and observed a change in stoichiometry within the planar faults compared to their adjacent bulk regions [2,3] in which would lower thermal conductivity.

Moreover, we used the same corelative approach mentioned above to study dislocations network in the p-type $Eu_{0.03}Na_{0.025}Pb_{0.945}Te$ compound which has a κ_L reduction to the amorphous limit of 0.36 $W \cdot m^{-1} \cdot K^{-1}$, and a high zT of 2.2 was achieved at 850 K [4]. The arrangement and the character of the dislocations as well as the chemistry on the nanometre-scale were investigated. The results reveal that the dislocation cores are decorated by Na (see Fig. 1). We demonstrate the effect of both the parallel alignment and Cottrell atmospheres of dislocations on the low thermal conductivity by the Callaway transport model [5,6]. When dislocation arrangement and local chemistry are considered the phonon dislocation scattering strength increases which provides an explanation for the significant reduction in k_L and improvement in zT measured experimentally, even at moderate dislocation densities near 1 x 10^{10} cm^{-2}.

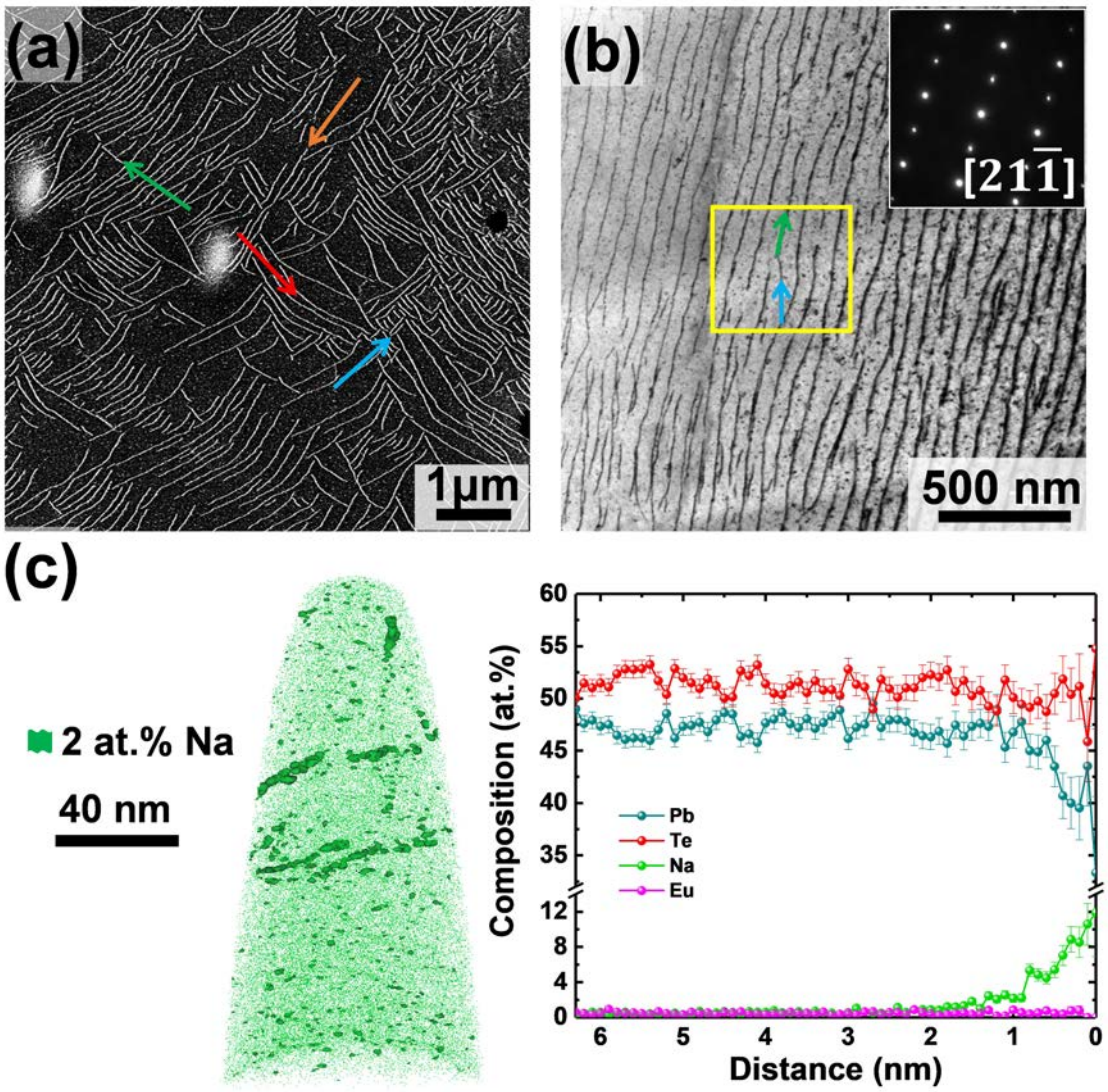

Fig. 1: (a) Overview of dislocation lines revealed by ECCI; the dislocations are lying on the [111] directions (b)BF micrographs of an area contain visible dislocation tilted toward g=(22 0̄)"-g3g" WBDF condition. (c)3D APT reconstruction of dislocations with Iso-composition surfaces of 2 at.% Na are highlighted in green;

Type of presentation: Oral

MS6-O-2577 Study of failure modes in two sulphide-based solid electrolyte all-solid-state batteries via in-situ SEM

YADAV N. G.[1,2], FOLASTRE N.[1,2], BOLMONT M.[1,2], JAMALI A.[3], MORCRETTE M.[1,2], DAVOISNE C.[1,2]

[1]Laboratoire de Réactivité et Chimie des Solides (LRCS), CNRS UMR 7314, Université de Picardie Jules Verne, 33 rue Saint Leu, 80039 Amiens Cedex, France, [2]Réseau sur le Stockage Electrochimique de l'Energie (RS2E), FR CNRS 3459, France, [3]Plateforme Microscopie Electronique (PME), Université de Picardie Jules Verne, 33 rue Saint Leu, 80039 Amiens Cedex, France

Email of the presenting author: neelamyadavg111@gmail.com

Lithium metal was left unemployed for a long time in conventional liquid-based batteries, with a fear of catching fire for safety reasons. However, with advancements in solid electrolytes, it was considered as the holy grail in the development of Li metal-based all-solid-state batteries (ASSBs) alongside NMC, considered as the next-generation cathode materials. Unfortunately, Li metal faces tremendous challenges when brought in contact with many currently considered promising Solid Electrolytes (SEs). The associated challenges are electrical, electro-(chemical) and mechanical instabilities1. Surprisingly, if one studies the literature thoroughly, it seems that batteries based on SEs show much faster dendrites formation than liquid electrolytes,2. For this particular study, thanks to in-situ and operando SEM, we studied these sulfides-based SE, viz β-Li3PS4 (LPS) and Li6PS5Cl (LPSCl) highlighting the key differences in failure modes by keeping the anode (Li metal) and cathode (NMC111) constant. For both the SEs, initially, electro-chemo-mechanical stress is induced, due to volumic expansion of active materials and plating during cycling. However, in the case of LPS, this leads to electrical failure causing a short circuit, whereas in the case of LPSCl it leads to further mechanical damage-causing delamination of the cathode. Thus, the porous structure of SEs heavily determines the mechanical behaviour of the ASSB, the distribution of the induced electro-chemo-mechanical stress and in turn, the mechanism of ASSB failure. We demonstrate that differences in cycling performance and mode of failure is due to the differences in SEs. We also highlight that the key limitation in implementing the Li metal as an anode in ASSB is the dendrite formation and mechanical instability. These findings, again emphasize the importance of coating of active materials, the introduction of a buffer layer between the SE/Li metal interface3, coating of SE, or the need of using composite/hybrid or bilayer solid electrolytes at least.

[1] Lewis, J. A., Tippens, J., Cortes, F. J. Q. & McDowell, M. T. Chemo-Mechanical Challenges in Solid-State Batteries. Trends in Chemistry 1, 845 (2019).
[2] Wood, K. N. et al. Dendrites and pits: Untangling the complex behaviour of lithium metal anodes through operando video microscopy. ACS Central Science 2, 790–801 (2016).
[3] Chen, K. et al. Effect of introducing interlayers into electrode/electrolyte interface in the all-solid-state battery using sulfide electrolyte. Solid State Ionics 327, 150–156 (2018).

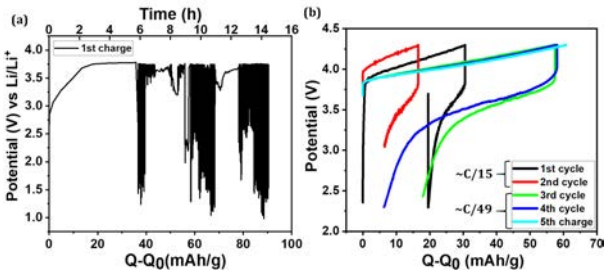

Fig. 1: Electrochemistry inside *In-situ* cell with a) Li_3PS_4 (LPS) b) Li_6PS_5Cl (LPSCl)

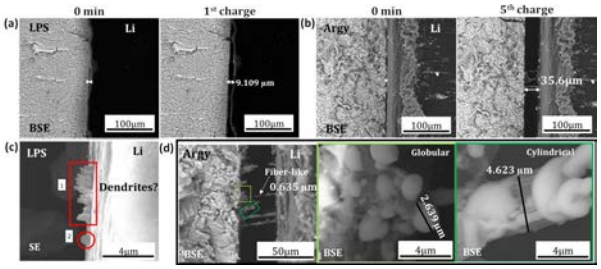

Fig. 2: Anode interface: a) and b) backscattered electrons images (BSE) at the lithium interface for LPS and LPSCl solid electrolyte respectively showing the loss of contact. Li dendrite morphologies observed in c) LPS (secondary electrons - SE) and d) LPSCl (black outlined, backscattered electrons BSE).

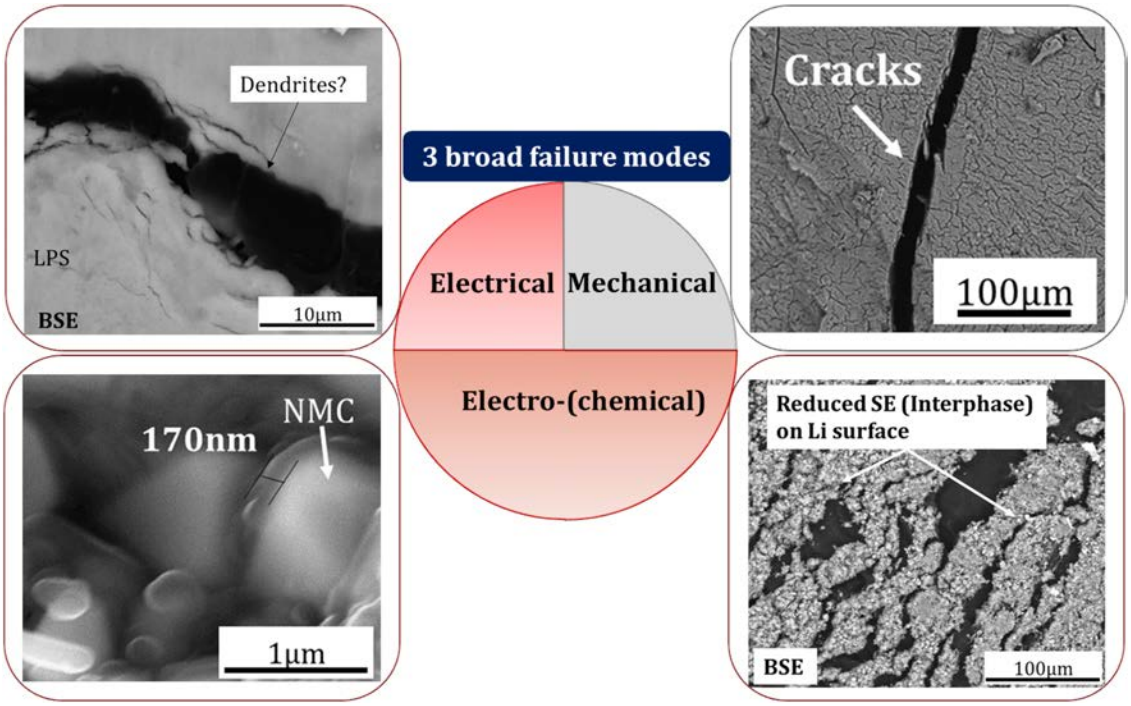

Fig. 3: Summary of observed failure modes

Type of presentation: Invited

MS6-IN-2913 Can the Wet Win the Bet? The case of Energy Harvesting and Storage

Radmilovic V. V.[1], Mijailovic D.[1], Hou Y.[2], Uskokovic P. S.[1], Brabec C. J.[3], Spiecker E.[4], Radmilovic V. R.[5]

[1]Faculty of Technology and Metallurgy, University of Belgrade, Serbia, [2]National University of Singapore, Singapore, [3]Institute of Materials for Electronics and Energy Technology, Friedrich-Alexander-University Erlangen-Nuremberg, Germany, [4]Center for Nanoanalysis and Electron Microscopy, Friedrich –Alexander-University of Erlangen-Nuremberg, Germany, [5]Serbian Academy of Sciences and Arts, Serbia

Email of the presenting author: vukradmilovic@tmf.bg.ac.rs

Perovskite solar cells have been one of the hottest topics as they have shown enormous potential for reaching high power conversion efficiency (PCE), currently above 25% [1] due to very efficient light harvesting, fast charge separation ability, etc. coupled with the low cost of materials and their ease of synthesis/processing from liquid phase. In our work, a novel organic mesoporous interfacial (OMI) layer was produced in a cost efficient and ecofriendly manner making scalable organics the most promising alternatives to porous inorganic interfaces, which although efficient, struggle with certain limitations. With this novel layer, the perovskite effectively infiltrates into OMI, and with enhanced wetting of the surface, the perovskite dramatically increases its homogeneity, thus leading to PCE enhancement and thermal stability [2]. For their ease and cost-effectiveness of wet synthesis and processing, silver nanowires (AgNWs) have been extensively studied as a transparent electrode alternative to conventional solutions like indium tin oxide in optoelectronic devices like solar cells. The main focus of this research was elucidating the solid-state wetting and welding mechanisms that occur during annealing of AgNWs before a layer of aluminum doped zinc oxide is deposited on them, for the enhancement of properties essential for an electrode in a solar cell [3]. Microstructural characterization using (S)TEM revealed that solid-state wetting and subsequent welding occurred only between nanowires whose contact geometry is characterized by an enormous difference in radii of curvature [4]. Energy harvesting and energy storage are equal parts of the energy sustainability equation, thus, simple and cheap yet efficient storage must exist as well. In such systems, one of the key aspects of improving overall performance is adequate material selection for electrodes [5]. Mixed transition metal oxides with a spinel structure have been shown to be promising candidates for high-performance pseudocapacitive and battery-type electrodes. The aim of this work was to design a mesoporous structure from liquid phase and subsequent post-processing, with highly conductive carbon fibers and redox-active Co/Mn based mixed oxide spinels [6,7] with highly developed surface area. Electrochemical results in aqueous systems showed high specific capacitance, excellent rate capability and cycling stability.

[1] H. Min et al., Nature 598 (2021) 444. [2] Y. Hou et al., Adv. Mater. 31 (2019) 1806516. [3] Goebelt et al., Nano Energy 16 (2015) 196. [4] V.V.Radmilovic et al., Nanotechnology (2017) 385701. [5] P. Simon et al., Nat. Mater. 19 (2020) 1151. [6] D.M. Mijailovic et al., Appl. Surf. Sci. 534 (2020) 147678. [7] D.M. Mijailovic et al., Dalton Trans. 50 (2021) 15669.

Acknowledgement: Ministry of Education, Science and Technological Development of Serbia, Serbian Academy of Sciences and Arts as well as Deutsche Forschungsgemeinschaft (DFG).

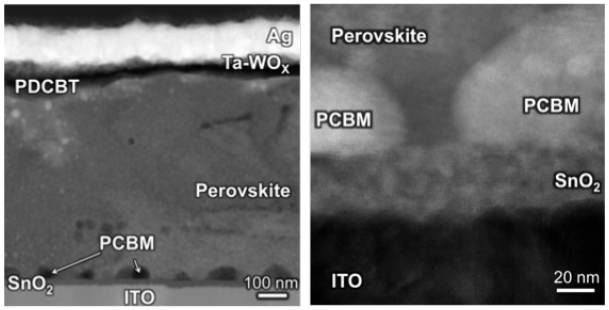

Fig. 1: STEM HAADF of whole cell (left) and TEM of area around mesoporous interface (right).

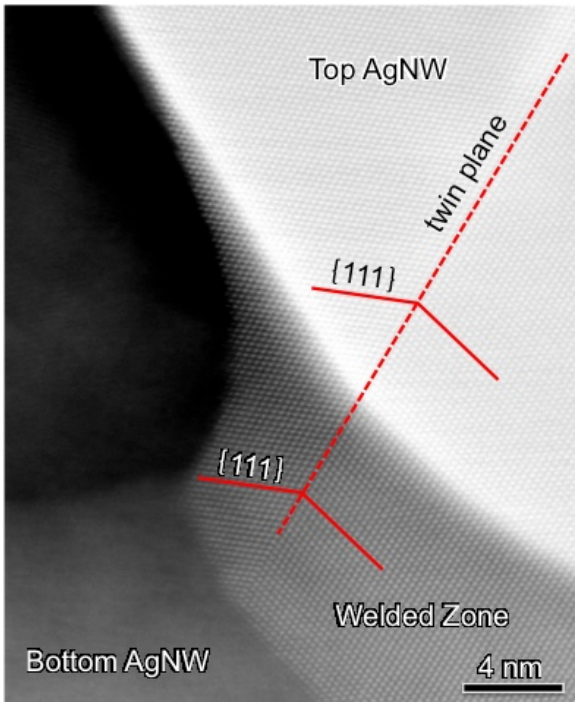

Fig. 2: HRTEM of two welded showing continuation of {111} planes from the top NW into the welded zone.

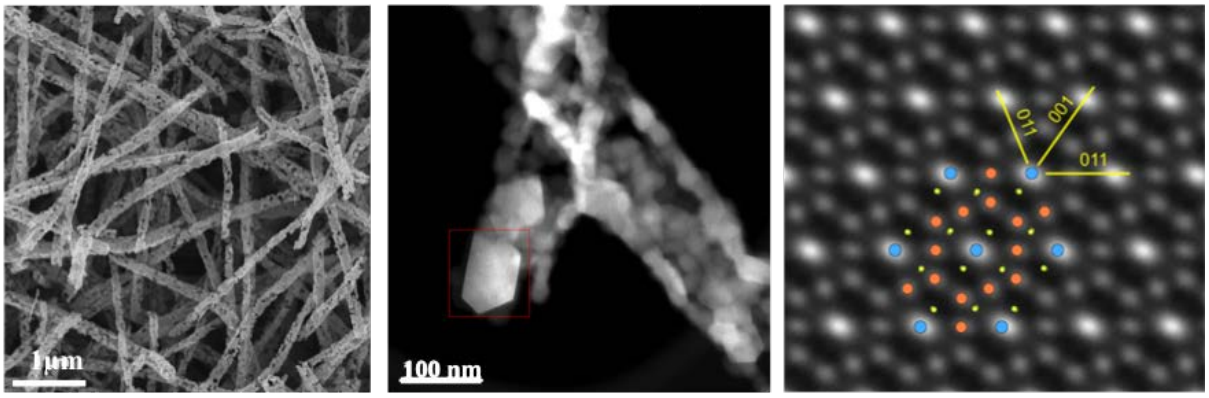

Fig. 3: Low mag STEM of C/Co1.5Mn1.5O4 fibers (left), STEM HAADF of C/Co1.5Mn1.5O4 fiber (center), atomic resolution STEM HAADF of nanocrystal noted in center image with atomistic model of Co1.5Mn1.5O4 (right).

Type of presentation: Oral

MS6-O-2793 Morphology related energy losses in small molecule organic solar cells

Radovanović-Perić F.[1], Panžić I.[1], Bafti A.[1], Rath T.[2], Mandić V.[1]

[1]Faculty of Chemical Engineering and Technology, University of Zagreb, [2]Institute of Chemistry and Technology, Technical University of Graz

Email of the presenting author: fradovano@fkit.hr

Small molecule organic solar cells have achieved PCE values up to an order of magnitude higher in the past decade, which further signifies their potential for light-weight, cost efficient flexible solar panel fabrication. A promising group of small molecule electron donors for photovoltaic application were shown to be squaraine derivatives (SQ), as they have tunable bandgaps, easy synthesis routes and excellent absorption coefficient as well as good thermal stability. Here we report on hybrid organic solar cells fabricated from various squaraine derivatives synthesized without catalysts. Laboratory scale devices (ITO/ZnO/SQ:PC71BM/MoO3/Ag) were fabricated with various morphologies of the active layer and characterized to gain deeper insight into the charge carrier transport through the cell. Electrical characterization (J/V measurements, light intensity dependence measurements, impendance spectroscopy) confirmed that the degree of phase separation and domain size influence greatly the charge accumulation and recombination mechanisms in the cells. Furthermore, the morphology and phase separation of the thin films were studied by TEM, AFM (KPFM, phase and height) and ToF-SIMS which were, coupled with X-ray scattering, diffraction and UV-VIS spectra, correlated to electrical data and overall performance.

Acknowledgement: Financial support by the projects UIP-2019-04-2367 SLIPPERY SLOPE and PZS-2019-02-1555 PV-WALL of the Croatian Science Foundation is gratefully acknowledged.

Type of presentation: Oral

MS6-O-2505 Multi-scale, high-resolution, time-resolved residual stress in laser-welded Eurofer97 using plasma focused ion beam-digital image correlation method

Zhu B.[1], Wang Y.[2], Dluhoš J.[3], London A. J.[3], Gorley M.[3], Whiting M. J.[1], Sui T.[1]

[1]School of Mechanical Engineering Sciences, University of Surrey, Guildford, Surrey, GU2 7XH, UK., [2]United Kingdom Atomic Energy Authority, Culham Centre for Fusion Energy, Culham Science Centre, Abingdon, Oxon, OX14 3DB, UK., [3]TESCAN ORSAY HOLDING, a.s., Libušina třída 21, 623 00 Brno, Czech Republic.

Email of the presenting author: t.sui@surrey.ac.uk

Nuclear fusion power is a clean and inexhaustible source of electricity production to reduce and the carbon emissions and achieve the net-zero. A series of fusion tokamaks have been developed, from the Joint European Torus (JET), the International Thermonuclear Experimental Reactor (ITER) to the DEMOnstration power plant (DEMO). Eurofer97, which is modified by adding lower activation elements like W and Ta, is a primary construction material for critical tokamaks components, such as coolant pipes, breeding blanket, vacuum vessel and divertor cassette. The design of these in-vessel structures imposes inherent assembly difficulties because of the internal grid structure and the irradiated circumstances require an autonomous operation. Laser welding performed by a robotic device is one of the most promising techniques, which could reduce welding distortion and enable a narrow heat affected zone (HAZ) with full penetration in thick sections. It could serve both the assembly and maintenance works [1]. However, the laser welding induces significant residual stresses, up to c.800 MPa, as a result of the thermal distortion and the martensite phase transformation incurred during welding [2]. Detrimental residual stresses can cause premature catastrophic failure of critical components and the replacement or repair can be costly and time-consuming. To optimise welding processes for in-service time extension of tokamaks components, it is necessary to quantify the residual stress with a high-resolution and multi-scale method and reveal the relationship between residual stress, microstructures and mechanical properties. Here, a Xe+ plasma focused ion beam, with digital image correlation (PFIB-DIC) are used to quantify the macro-scale residual stress distribution across the weldment. A high-resolution and time-resolved residual strain is obtained at a finer scale, which provides critical information to develop micro-mechanical rationale for failure analysis. Nanoindentation was also used to cross-validate the residual stress distribution from the Xe+ PFIB-DIC technique. The stress ratio (k) gained from PFIB-DIC technique overcomes the key limitation of nanoindentation residual stress measurement [3]. The multi-scale residual strain distribution is correlated with microstructure characterisation and mechanical property using electron backscatter diffraction (EBSD), micro-hardness and nano-indentation mapping. Insights obtained will contribute to building up a predictable model to predict the mechanical properties and lifetime of components.

[1] S. Kirk, et al, Fusion Eng. Des.. (2018).
[2] B. Zhu, et al, J. Mater. Sci. Technol. 114 (2022) 249–260.
[3] B. Zhu, Sci. Adv. 8 (2022) eabl4592.

Type of presentation: Poster

MS6-P-2963 Self-sustained oscillatory dynamics of ethylene to syngas by operando SEM and XPS

Colbea C.[1 3], Plodinec M.[1 3], Artiglia L.[2], van Bokhoven J. A.[2 3], Willinger M.[1]

[1]Scientific Center for Optical and Electron Microscopy, ScopeM ETH Zürich, 8093, Zürich, Switzerland, [2]Laboratory for Catalysis and Sustainable Chemistry, Paul Scherrer Institute, 5232, Villigen, Switzerland, [3]Institute for Chemical and Bioengineering, Department of Chemistry and Applied Biosciences, ETH Zurich, 8093, Zürich, Switzerland

Email of the presenting author: ccolbea@ethz.ch

Despite its importance and numerous scientific efforts, the working state of catalysts is still subject to debate. Apart from the simplest model reactions, the majority of the scientific community is still unable to fully comprehend the underlying mechanism of catalysis and the atomistic details of the active state. The main issue resides in the lack of techniques that enable a direct view of a catalyst's functioning state and is often coupled with non-equilibrium processes that involve multi-scale dynamics. Here, by studying the partial oxidation of ethylene, we obtained insights into the mechanistic details of hydrocarbons to syngas conversion. Our operando approach combines real-time imaging of structural dynamics with complementary surface-sensitive spectroscopy and mass spectrometry to offer a comprehensive surface characterization of a polycrystalline nickel catalyst. The environmental scanning electron microscope (ESEM) [1], represents a promising platform for operando material characterization. We were able to extend the functionality of a commercially available TFS Quattro S ESEM by developing a mobile in-situ unit. This enabled the ambient pressure x-ray photoemission spectroscopy and operando scanning electron microscopy study to be performed under identical conditions. This mobile unit is composed of a modified sample holder that can achieve working temperatures of up to 1250oC in reactive gas atmospheres, an automated heating unit that allows precise temperature regulation and a high purity, automated gas feeding system. Using the above-mentioned characterization toolbox, we gained insight into the gas-phase and temperature-induced dynamics relevant to the formation of catalytic activity in ethylene to syngas conversion on a model polycrystalline nickel sample. In non-stoichiometric conditions, we identified the active species that form protective surface intermediates. We were able to pinpoint the catalytic behavior down to competing species that influence catalyst deactivation with excellent spatial resolution. We were able to discriminate between local and non-local mechanisms that impact the collective dynamics usually reported using traditional approaches. Using a combination of specialized secondary electron, high-temperature 3D BSE and an EBAC detectors, we can visually assess the state of the active catalyst under reaction conditions in real-time, at high spatial resolution. Direct observation coupled with on-line gas-phase mass spectroscopic analysis and surface sensitive chemical information from APXPS, we enable structure-reactivity correlations under relevant operating conditions.

[1] Cao, Jing, et al. "In situ observation of oscillatory redox dynamics of copper." Nature communications 11.1 (2020): 1-11

Acknowledgement: The authors thank ScopeM and SLS for the beamtime 20201856 at the X07DB beamline. C.C, J.v.B, and M.W. thank the ETH Grant-36 18-2: Bridging Scales in Catalysis

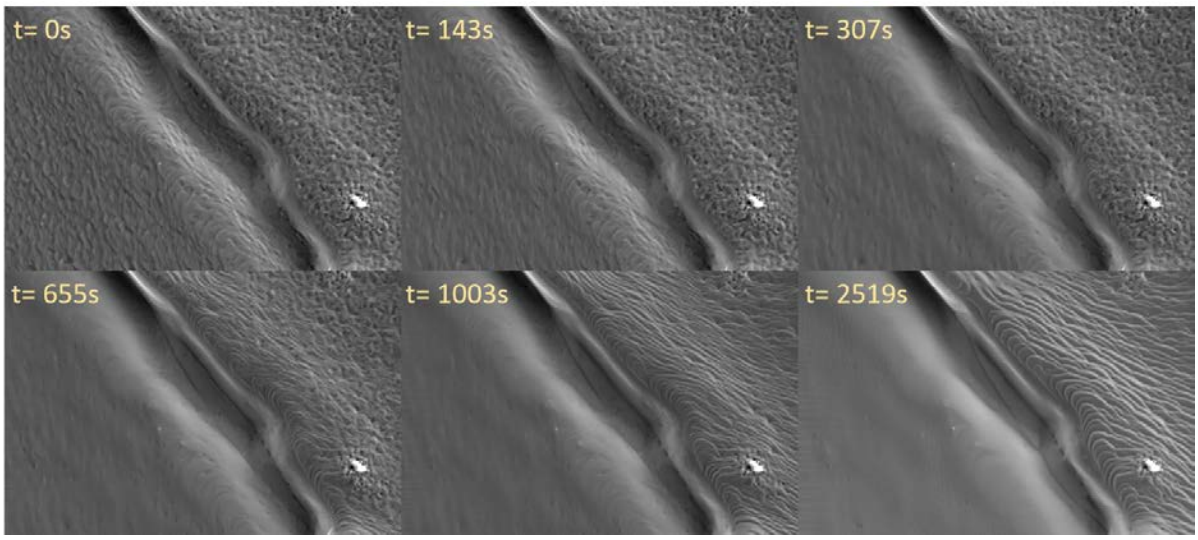

Fig. 1: Time series of a Ni surface during ethylene to syngas conversion. HFOV is 33.5µm.

Type of presentation: Poster

MS6-P-2847 Are FIB-prepared hybrid perovskite cross-sections still luminescent?

Kosasih F. U.[1], Divitini G.[1,2], Ferrer Orri J.[1,3], Tennyson E. M.[3], Kusch G.[1], Oliver R. A.[1], Stranks S. D.[3,4], Ducati C.[1]

[1]Department of Materials Science and Metallurgy, University of Cambridge, UK, [2]Istituto Italiano di Tecnologia, Genoa, Italy, [3]Cavendish Laboratory, University of Cambridge, UK, [4]Department of Chemical Engineering, University of Cambridge, UK

Email of the presenting author: giorgio.divitini@iit.it

Hybrid perovskites, beginning from methylammounium lead iodide, have been extremely popular in research in the last decade due to their great promise for optoelectronic applications, leading to a broad variety of chemical compositions suitable for solar cells and light emitting devices with efficiencies comparable to established technologies [1]. The macroscopic properties are strongly influenced by the nanoscale structure, including the morphology, quality of the layers and chemical distribution, which can all be tweaked during synthesis. As devices age, due to environmental factors or to operation, those properties can change further, and the understanding of such phenomena is crucial to the realisation of viable, robust commercial applications.
The study of structure and chemical inhomogeneities is typically carried out using transmission electron microscopy on cross-sectional samples produced via focused ion beam (FIB) milling [2]. The FIB process is known to significantly affect the sample in the case of other materials through amorphisation, implantation of Ga+ ions and local heating, and such effects should be taken into account. In this work [3], we determine the extent of the induced changes by using luminescence as a proxy for the local properties that are relevant to the operation of an optoelectronic device. We perform spectrally-resolved cathodoluminescence on FIB-prepared lamellae, and correlate the effect of FIB preparation on the surviving luminescent properties of the film.
[1] Kim, J. Y., Lee, J.-W., Jung, H. S., Shin, H., & Park, N.-G. (2020). High-efficiency perovskite solar cells. Chemical Reviews,120(15), 7867–7918
[2] Kosasih, F. U., Cacovich, S., Divitini, G., & Ducati, C. (2020). Nanometric chemical analysis of beam-sensitive materials: A case study of STEM-EDX on perovskite solar cells.Small Methods, 2000835
[3] Felix U. Kosasih, Giorgio Divitini, Jordi Ferrer Orri, Elizabeth M. Tennyson, Gunnar Kusch, Rachel A. Oliver, Samuel D. Stranks, Caterina Ducati (2022). Optical emission from focused ion beam milled halide perovskite device cross-sections. Microscopy Research & Technique

Acknowledgement: FUK: Jardine Foundation, Cambridge Trust. GK, RAO: EPSRC EP/R025193/1 and Attolight. JFO, SDS: ERC HYPERION, 756962. CD: EU2020 823717–ESTEEM3

Type of presentation: Poster

MS6-P-2621 Influence of sample tilt on measurement of atomic column position

Drazic G.[1, 2], Bencan Golob A.[2, 3]

[1]Department of Materials Chemistry, National Institute of Chemistry, Ljubljana, Slovenia, [2]Jožef Stefan International Postgraduate School, Ljubljana, Slovenia, [3]Electronic Ceramics Department, Jožef Stefan Institute, Ljubljana, Slovenia

Email of the presenting author: goran.drazic@ki.si

In ferroelectric materials, the structure changes from centrosymmetric (cubic) to noncentrosymmetric (tetragonal, rhombohedral, or orthorombic) when the temperature falls below the Curie temperature. During this phase transformation, individual atomic columns undergo small displacements, which are the reason for the spontaneous polarisation. Direct measurement of these shifts would allow us to determine the local polarisation at the atomic level.
From high-angle annular dark-field (HAADF) and annular bright-field (ABF) images acquired with a Cs-corrected scanning transmission electron microscope (STEM), the position of individual atomic columns can be extracted with very high precision. In the $BiFeO_3$ perovskite system, we were able to determine the position of the Bi and Fe/O columns in the [100] zone from HAADF images with an accuracy of 5 pm [1]. HAADF micrographs are used for imaging atoms with higher atomic number, for lighter elements like oxygen ABF micrographs should be used. The position of the oxygen atoms is very important for the correct determination of the spontaneous polarisation.
The problem is that the measured position of the oxygen columns on ABF micrographs depends strongly on the tilt with respect to the exact zone axis [2]. Despite careful tilting of the sample, a tilt of a few tenths of a degree may occur due to heating of the sample and the resulting bending.
In the present work, we have developed a method to test the potential mistilt of ABF images.
Simulated HAADF and ABF images of $Ba_{0.6}Sr_{0.4}TiO_3$ using the multi-slice frozen phonon simulation code (QSTEM) [3] were calculated for 0° and 0.5° sample mistilt for different thicknesses. It was found that the sample mistilt of 0.5° did not affect the Ti/O atomic column displacements measured from the HAADF images. However, the sample mistilt strongly affected both the magnitude and direction of the oxygen and Ti/O atomic column displacements measured from ABF images, and we found that the displacements were different for different sample thicknesses [4].
To verify that our experimental ABF images were taken at a certain mistilt, we should analyse two nearby regions with different thicknesses and take displacement measurements. If we obtain similar (identical) displacements in magnitude and direction, we can assume that the sample mistilt is negligible. If this is not the case, the ABF images were not taken exactly on the zone axis and should not be used to measure the displacement of atomic columns.

[1] T. Rojac, et al, Nature Materials, 16, 322-327, 2017
[2] P. Gao, et al, Ultramicroscopy, 184, 177, 2018
[3] C. Koch, PhD thesis, Arizona State University, 2002
[4] A. Bencan et al, Nature Communications, 11, 1762, 2020

Acknowledgement: This work was supported by the Slovenian Research Agency under programmes P2-0393 and P2-0105 and projects J2-2497 and J2-3041.

Type of presentation: Poster

MS6-P-2600 Description of Ageing of Soldering Materials by Means of Electron Microscopy

Michalcová A.[1], Msallamová Š.[1]

[1]Department of Metals and Corrosion Engineering, University of Chemistry and Technology in Prague, Technicka 5, Prague 6, 166 28, Czech Republic

Email of the presenting author: michalca@vscht.cz

The ageing of soldering materials has an important role in outdoor devices (e.g., energy related). The very first Sn-Pb soldering alloy had good resistance but contained high amount of Pb, which is not suitable for the environment. Reduction of the Pb content raised again a problem know from the history – a tin pest. This phenomenon causes the degradation of Sn- rich materials by transformation of β-Sn (metal like) to powder α-Sn at temperatures about 10 °C (depending on the exact composition). Very often the tin pest effect is used for degradation explanation of almost all Sn-rich materials. In our research we want to prove also other type of degradation mechanism – decrease of mechanical properties by precipitation of secondary phase e.g., in the Sn-Pb and Sn-Cu materials. The Sn samples with 1 wt. % of Pb were annealed at 60 °C (temperature that might be easily obtained at sun exposed surface in the summer) and observed by TEM. Even after 24 h of annealing, the Pb precipitates occurred. Fig. 1 demonstrates the unsuitable presence of Pb particles and Kirkendall pores at the grain boundary, which weakens the aged material.

Acknowledgement: This research was funded by Czech Science Foundation, project No. 22-05801S.

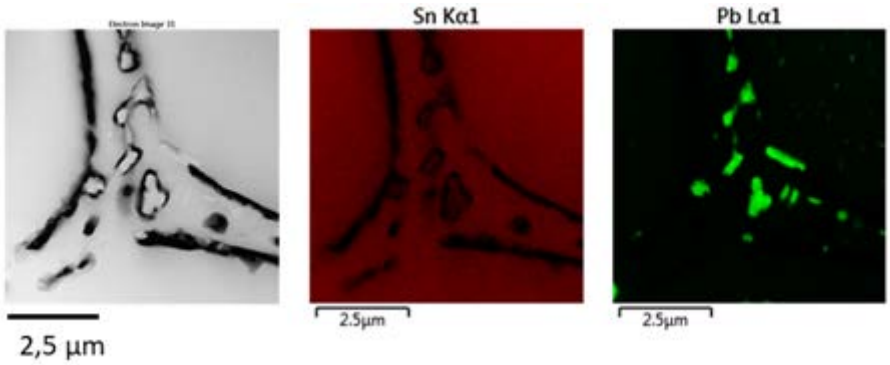

Fig. 1: Microstructure of model alloy Sn1.8Pb (wt.%)

Type of presentation: Poster

MS6-P-2630 Combined Microstructural and Electrochemical Studies of Sputtered Ni Thin Layers as Catalysts for Hydrogen Evolution Reaction

Neumüller D.[1], Rafailovic L. D.[1], Lassnig A.[2], Pašti I. A.[3], Jovanović A. Z.[3], Eckert J.[1, 2], Gammer C.[2]

[1]Department Materials Science, Chair of Materials Physics, Montanuniversität Leoben, Leoben, Austria, [2]Erich Schmid Institute of Materials Science, Austrian Academy of Sciences, Leoben, Austria, [3]Faculty of Physical Chemistry, University of Belgrade, Belgrade, Serbia

Email of the presenting author: daniela.neumueller@unileoben.ac.at

The decarbonization of energy and industry in order to limit climate change is an essential aim of current generations. A challenge, however, is the temporal and local dependency of renewable energies. To overcome the fluctuation, the use of the energy vector hydrogen, produced by green electrolysis of water, is promising. Thus, there is great interest in developing, highly efficient and cost-effective catalysts for hydrogen production.
This work focuses on the synthesis of thin layer, non-noble metallic materials, and their catalytic efficiency for the hydrogen evolution reaction (HER). The main aim is the investigation of intrinsic catalytic properties of smooth Ni layers obtained by magneton sputtering and the possible role of the substrate. In combination with efficiency studies, material modifications during different electrode processes are monitored. Therefore, we carry out structural characterization including Transmission Electron Microscopy (TEM) to identify reaction sites, presenting the ultimate goal of these studies.
Methods
Materials used as cathodes for HER are produced by magnetron sputtering in a way to reduce the roughness to a minimum. This should exclude the influence of deviations from geometric area on catalytic efficiency and reveal intrinsic catalytic properties.
The electrodes and changes thereof are evaluated according to their efficiency, chemistry, structure and morphology using laser microscopy (LEXT), Scanning Electron Microscopy (SEM), Energy Dispersive X-Ray Analysis (EDX) as well as TEM. Electrochemical characterization is done by steady-state polarization curves and EIS using a three-electrode setup. The direct effects of thin layer oxidation on the catalytic efficiency and material structure and morphology, are demonstrated. It is shown that combining TEM and electrochemical measurements allows to visualize changes during reduction and oxidation reaction on the electrode surface.
Results
The studies revealed an influence of layer thickness on the electrode reaction. These findings might suggest an interaction between the substrate and electrolytically active Ni layer as well as the oxide formation being relevant for enhancing HER activity (Fig. 1). Surface analysis shows that magnetron sputter deposition leads to very smooth layers with roughness factors similar to the used substrates. TEM confirms, that the metal layers are nanocrystalline with grain sizes depending on the processing parameters (Fig. 2).
Another advantage of magnetron sputtering is the possibility of simultaneous co-deposition from different targets. The aim is to analyze metals and alloys of different composition according to their intrinsic catalytic properties and also to find the most relevant alloys and systems for latter surface modification.

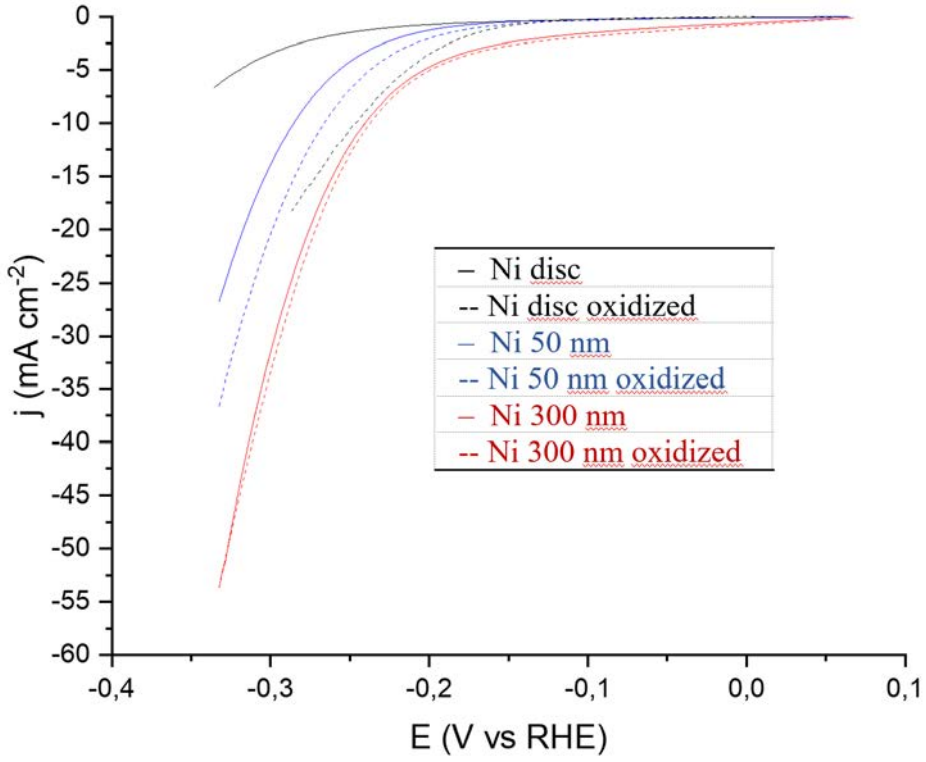

Fig. 1: Cyclic voltammetry curves of Ni thin layer catalysts of different thickness on Cu substrate as well as a bulk Ni disk, before and after oxidation, in 1 M KOH (sweep rate of 10 mV/s). For comparison, only back curves are displayed. The data shows an increase of HER activity with increasing Ni layer thickness and the effect of material oxidation.

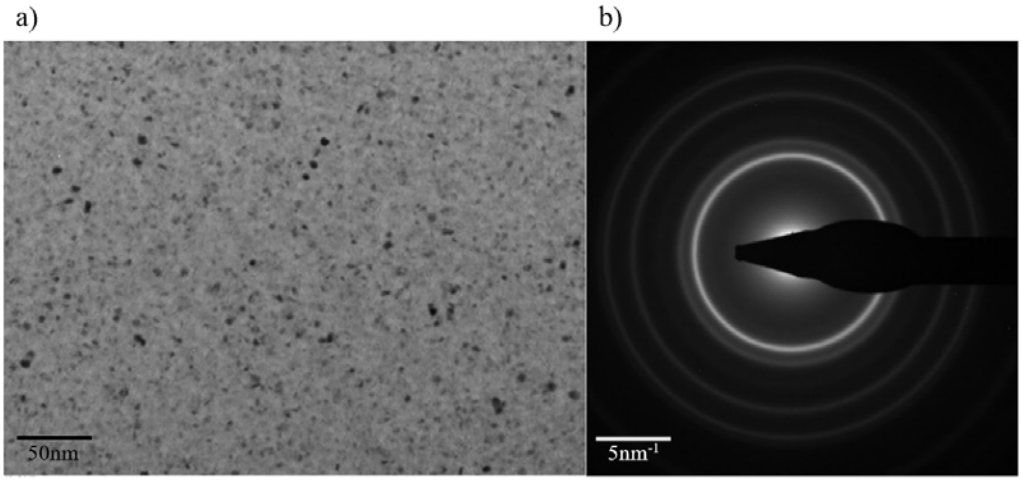

Fig. 2: a) TEM image of sputter deposited Ni (HV=120 kV) and b) corresponding selective area diffraction pattern.

Type of presentation: Poster

MS6-P-2682 Studying electrochemical degradation in nanocatalysts with identical location STEM

Ruiz-Zepeda F.[1,2], Hrnjić A.[1], Kamšek A.[1], Pavlišič A.[1], Smiljanić M.[1], Lončar A.[1], Gatalo M.[1], Bele M.[1], Jovanovič P.[1], Dražić G.[1], Gaberšček M.[1,3], Hodnik N.[1]

[1]National Institute of Chemistry, Hajdrihova 19, SI-1000 Ljubljana, Slovenia , [2]Institute of Metals and Technology, Lepi pot 11, SI-1000 Ljubljana, Slovenia, [3]University of Ljubljana, Vecna pot 113, SI-1000 Ljubljana, Slovenia

Email of the presenting author: francisco.ruizzepeda@ki.si

The generation and utilization of hydrogen in electrolyzers and fuel cells have gained recent interest and popularity as a promising alternative option in the need for better and greener sources of energy. However, the activity and stability of the catalysts employed are affected due to the harsh environment occurring in a regular cycle workload or during activation protocols since the catalysts materials are typically formed of precious metals based (i.e. Pt-M) nanoparticles on a conductive support, and suffer from dissolution and dealloying (and other related events). In order to understand such phenomena a study that targets the structure-properties relationship during degradation is needed. Identical location which consists in examining the same area of interest of the sample in the microscope before and after a reaction or an electrochemical process has taken place fits properly for this purpose [1]. In this work, we explore the degradation effects in nanocatalysts arising during electrochemical processes by using identical location-aberration corrected STEM. And by recording the same individual nanoparticles at high resolution we are able to observe specific changes, such as missing and/or appearing kinks or steps, hence discerning whether a particular facet has experienced dissolution or redeposition, as well as analyzing precise information from the distribution of strain in the nanoparticle's lattice. Different catalysts, including Pt, PtCo and PtNi, are analyzed with this methodology shedding light on the undergoing mechanisms induced by the electrocatalytic processes.

References

[1] K. J. J. Mayrhofer, J. C. Meier, S. J. Ashton, G. K. H. Wiberg, F. Kraus, M. Hanzlik, M. Arenz. Fuel cell catalyst degradation on the nanoscale. Electrochem. Commun. 10 (2008) 1144-1147.

Acknowledgement: Authors would like to thank the European Research Council (ERC) Starting Grant 123STABLE (Grant agreement ID: 852208) for funding the study in progress.

Type of presentation: Poster

MS6-P-2566 The implementation of microscopic and spectroscopic techniques in characterisation of the spinel ferrite for photocatalytic reduction of CO2

Spilarewicz-Stanek K.[1], Urbanek K.[1], Macyk W.[1]

[1]Jagiellonian University, Faculty of Chemistry, Gronostajowa 2, 30-387 Krakow, Poland

Email of the presenting author: kaja.spilarewicz-stanek@uj.edu.pl

The CO2 from the air can be considered a free chemical compound for the obtaining of CO, which after mixing with H2 creates syngas. One of the strategies which can be applied to this approach is photocatalysis. Spinel ferrites are promising materials for photocatalytic reduction of CO2 [1]. They belong to a class of materials with the crystal structure of the natural spinel MgAl2O4. Their composition can be described as AB2X4, and where A and B cations have different oxidation states and depending on the material can occupy tetrahedral or octahedral coordination sites [2]. However, there is a possibility of different cation distributions in the tetrahedral and octahedral interstices, which determine A and B positions. Therefore, a more accurate formula A1 λBλ(AλB2 λ)X4 can be used [3]. The spinels can be divided into three types: λ = 0 is regarded as “normal” spinel, λ = 1 is the “inverse” spinel, and 0 < λ < 1 reflects the complex spinels. The occupancy of positions depends on the preparation method and influences the material properties. Especially, the chemical composition and structure determine the photoactivity.

In this work, the SnFe2O4 with TiO2 composite was designed for photocatalytic reduction of CO2 in the gas phase. The spinel with the expected structure of SnFe2O4 was prepared by a newly developed hydrothermal method. Since Fe3+ and Sn2+ constitute a strong redox pair, there is a possibility of introducing Fe2+ and Sn4+ cations into the crystal structure. To elucidate the obtained material structure, several microscopic and spectroscopic techniques were utilised for the complex analysis (Fig. 1). Scanning electron microscopy (SEM) was used for the verification of the material’s morphology, which shows octahedral shaped microcrystals with a deposited additional nanoparticulate phase. Additionally, high-angle annular dark-field scanning transmission electron microscopy (HAADF STEM) was used to confirm the homogeneity of the material. The crystal structure was studied by X-ray diffraction analysis (XRD). Furthermore, X-ray photoelectron spectroscopy (XPS) and X-ray fluorescence (XRF) examinations were used to define the chemical composition of the obtained material. Collected data indicate that obtained spinel formula is SnxFe1 xFe2O4 (where x < 1), showing that the positions of Sn2+ are partially replaced by Fe2+. Therefore, the obtained material might be classified as a normal spinel with defects. It was found that this type of material combined with TiO2 has a potential for selective reduction of CO2 to CO.

[1] Jia Y, Zhang W, Do J Y, Kang M, Liu C 2020 Chem. Eng. J. 420 126193

[2] Galvão W S, Neto D M A, Freire R M, Fechine P B A 2016 Solid State Phenom. 241 139-176

[3] Zhao Q, Yan Z, Chen C, Chen J 2017 Chem. Rev. 117 10121-10211

Acknowledgement: Acknowledgement: This work was financially supported by the National Science Centre, Poland, within the research grant NCN 2018/30/Q/ST5/00776 (SHENG-1).

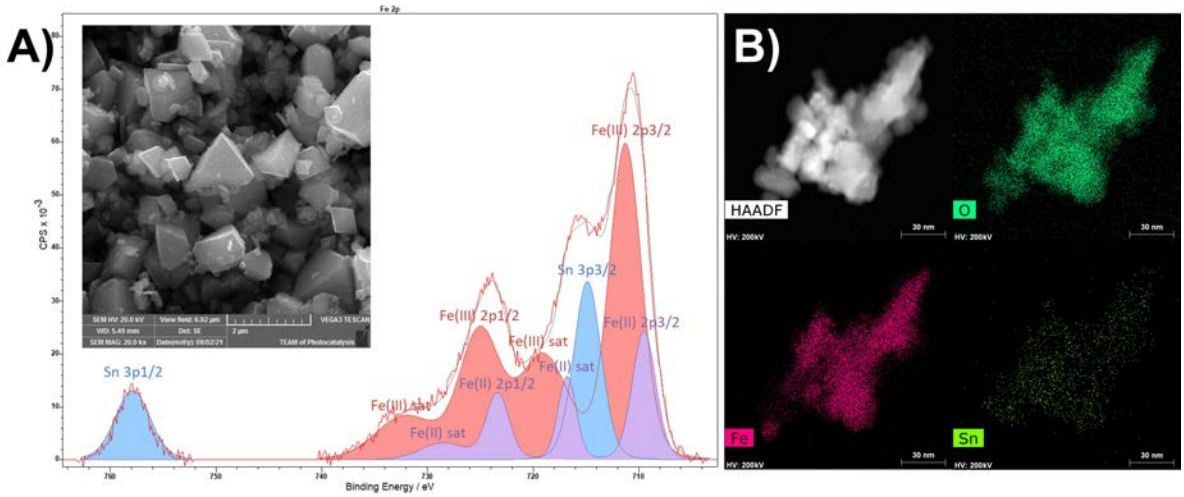

Fig. 1: Deconvoluted XPS spectra of core level binding energies of Fe 2p and Sn 3p (A), SEM image (A insert), HAADF-STEM image and EDX maps of Fe, Sn and O (B) of studied spinel ferrite.

Type of presentation: Poster

MS6-P-2806 Advanced STEM insights into atomic and electronic structure evolution of corncob-derived hard carbon anode materials for sustainable sodium-ion batteries

Tchernychova E.[1], Tratnik B.[1,2], Kapun G.[1], Tomšič M.[2], Vižintin A.[1], Dominko R.[1,2,3]

[1]National Institute of Chemistry, Ljubljana, Slovenia, [2]Faculty of Chemistry and Chemical Technology, University of Ljubljana, Ljubljana, Slovenia, [3]ALISTORE-European Research Institute, CNRS FR 3104, Amiens Cedex, France

Email of the presenting author: elena.tchernychova@ki.si

Sustainable raw materials-based sodium ion batteries (SIBs) offer a high competition to current lithium ion batteries (LIBs) technology due to the low cost, raw material abundance and its global homogenous distribution. The SIB technology, however, requires different materials design for both anode and cathode compared to that of LIB. A number of cathode materials for SIB has already been successfully employed, however, the options for the anode are still under consideration. Here, a graphite that is commonly used as a LIBs anode does not form binary graphite intercalation compounds upon Na intercalation. This incapacitates proper battery functioning. Currently, most feasible material's option is represented by a family of non-graphitizable carbons. These can be derived from a number of sustainable biomass precursors such as banana peels, chestnuts, nut shells, etc.[1] However, the electrochemical properties of such biomass-derived anode material strongly depend on the precursor choice and processing parameters. Both tremendously influence final non-graphitizable carbon microstructure and electronic properties from micro- down to the atomic level.[2]
We have investigated the relationship between structural properties and electrochemical performance of the anodes made from corncob derived non-graphitizable carbons. The materials were prepared at different carbonization T using a combination of structural characterization methodology unique for the SIB field. We have followed structure development upon the increase in carbonization temperature with thorough structural characterization and electrochemical testing. With increase in carbonization temperature from 900 °C to 1600 °C, our prepared materials exhibited a trend toward increasing structural order, increase in specific surface area of micropores, development of ultramicroporosity, and increase in conductivity. This was clearly demonstrated by a synergy of different examination techniques. Furthermore, doping with Bi_2S_3 nanorods was introduced and structural changes in corncob derived non-graphitizable carbons upon Na (de)insertion were studied. The use of scanning transmission electron microscopy (STEM) imaging and electron-energy loss spectroscopy (EELS) analysis allowed a systematic insight into the materials' atomic structure and electronic properties evolution. Subsequently, a strong correlation between the determined structural properties and the electrochemical behavior was established.

References:
1. J. Zhu, J. Roscow, S. Chandrasekaran, L. Deng, P. Zhang, T. He, K. Wang, L. Huang, Chem. Sus. Chem. 2020, 13, 1275-1295.
2. C. del M. Saavedra Rios, L. Simonin, A. de Geyer, C. Matei Ghimbeu, C. Dupont, Energies 2020, 13, 3513.

Acknowledgement: EU Horizon 2020 grant 875629 NAIMA, M-ERA.NET NOEL, ARRS P2-0423, P2-0393, P1-201, P1-0175 and N1-0139, CENN Nanocenter Slovenia (FIB-SEM Helios NanoLab 650)

MS7 Micro- and nanomechanical characterization of materials

Type of presentation: Invited

MS7-IN-2666 Recent advances in in-situ SEM nanomechanical testing: extreme temperatures, ultra-high strain rates, in-situ electron diffraction and digital image correlation

Schwiedrzik J.[1], Maeder X.[1], Edwards T.[1], Michler J.[1]

[1]Empa, Swiss Federal Laboratories for Materials Science and Technology

Email of the presenting author: johann.michler@empa.ch

We've developed recently a universal nanomechanical testing platform that allows for variable temperature and variable strain rate testing of micro-sized specimen in situ in the scanning electron microscope. By utilizing an intrinsically displacement-controlled micro-compression setup, which applies displacement using a miniaturized piezoactuator, we've recently extended the attainable range of strain rates to up to 10^4 s^{-1}, and enabled cyclic loading up to 10^7 cycles. Stable, variable temperature indentation/micro-compression in the range of -150°C to 1000°C is achieved through independent heating/cooling and temperature monitoring of both the indenter tip and sample and by cooling the instrument frame.
At room temperature micro-compression experiments were combined with in-situ EBSD measurements. In situ EBSD allows for the determination of crystallographic orientation with sub-100 nm spatial resolution. Thereby, it provides highly localized information on phenomena such as elastic bending of the micropillar or the formation of deformation twins and plastic orientation gradients due to geometrically necessary dislocations. The deformation of all materials can be separated into elastic and plastic parts. Mapping of total strain with nanoscale resolution is achieved through digital image correlation (DIC) methods, which track the movement of a pattern deposited by focused electron beam induced deposition and imaged by SEM. In combination with EBSD based measurements of elastic strains the plastic strain components during deformation can be assessed.
We are currently developing with partners a novel stand alone in situ device that combines high-resolution nanomechanical testing with high-speed Differential Phase Contrast (DPC) imaging inside a scanning electron microscope. The new device will allow for the dynamic in situ study of structural changes within samples during nanomechanical testing at extreme conditions including strain rates of up to 1000 s^{-1}.
Using these new capabilities, we examine the plasticity and fracture at small length scales. Application examples ranging from cryogenic behavior of nanocrystalline metals, high temperature deformation, twinning in Magnesium and fracture of Tungsten will be presented.

Type of presentation: Oral

MS7-O-2644 Automated In-Situ Mechanical Testing of heavily textured Ti 6Al 4V to Obtain High Spatial and Temporal Resolution Strain Maps

Smith A. D.[1,3], Lunt D.[2,3], Curran P.[3], Donoghue J. M.[3]

[1]TESCAN-UK, Wellbrook Court, Cambridge, UK, [2]United Kingdom Atomic Energy Authority (UKAEA), Culham Science Centre, Abingdon, UK, [3]Henry Royce Institute, Department of Materials, University of Manchester, UK

Email of the presenting author: albert.smith@tescan.com

Typically, performing statistically relevant in-situ thermo-mechanical testing is a labour-intensive process, e.g. incrementing the load, re-acquiring and re-focusing the field of view and imaging the region, which is also limited by working hours. Through the introduction of automation, the continuous running of experiments is possible. The fully integrated system dramatically improves temporal resolution and/or expanding the region of interest during in-situ experiments, all with no cost to spatial resolution whilst also increasing sample throughput. The high spatial resolution enables the capture of highly localised deformation and/or failure events. When combined with digital image correlation (DIC), it can be used to quantify shear strain of discrete slip traces and heterogeneous deformation at the grain scale (with nanoscale resolution).

The presented applied example is a multi-field investigation of a Ti-6Al-4V alloy, heat treated to produce an equiaxed microstructure, focussing on the interfaces of two regions of localised texture in the same sample. These interfaces separate regions with randomly textured grains from those with a common orientation, where the response of the two is expected to be different due to the relative ease of slip transfer across grain boundaries and the similar stress required to activate slip in the region with similarly oriented grains. By recreating the complex loading program outlined in ref. [1] and utilising automation, it has been possible to capture the onset of yielding over a large area of interest, at a temporal and spatial resolution that is not possible using a manual approach. Carrying out the experiment at regular displacement increments within the elastic range up to and including the proof stress (Fig. 1) revealed the very early slip band formation and subsequent progression before it is washed out by the activation of alternate slip systems at higher strains. The DefDap python analysis package was utilised to determine the active slip mode within individual grains, where the relative displacement ratio (RDR) was used to differentiate the actual Burgers vector along which slip had occurred. Having the opportunity to study the early slip system formation and using newly developed analysis tools has confirmed prior research that early slip occurs along the basal plane and is then dominated by prismatic slip. Furthermore, by covering statistically relevant areas and observing the deformation in multiple regions the transgranular slip patterning due to heavily textured regions can be described with confidence and used to inform Crystal Plasticity simulations.

[1] Dichtl,C. et al. (2022) 229, p. 117691. doi: 10.1016/j.actamat.2022.117691.

Acknowledgement: The authors are grateful to the Henry Royce Institute for Advanced Materials, funded through EPSRC grants EP/R00661X/1, EP/S019367/1, EP/P025021/1 & EP/P025498/

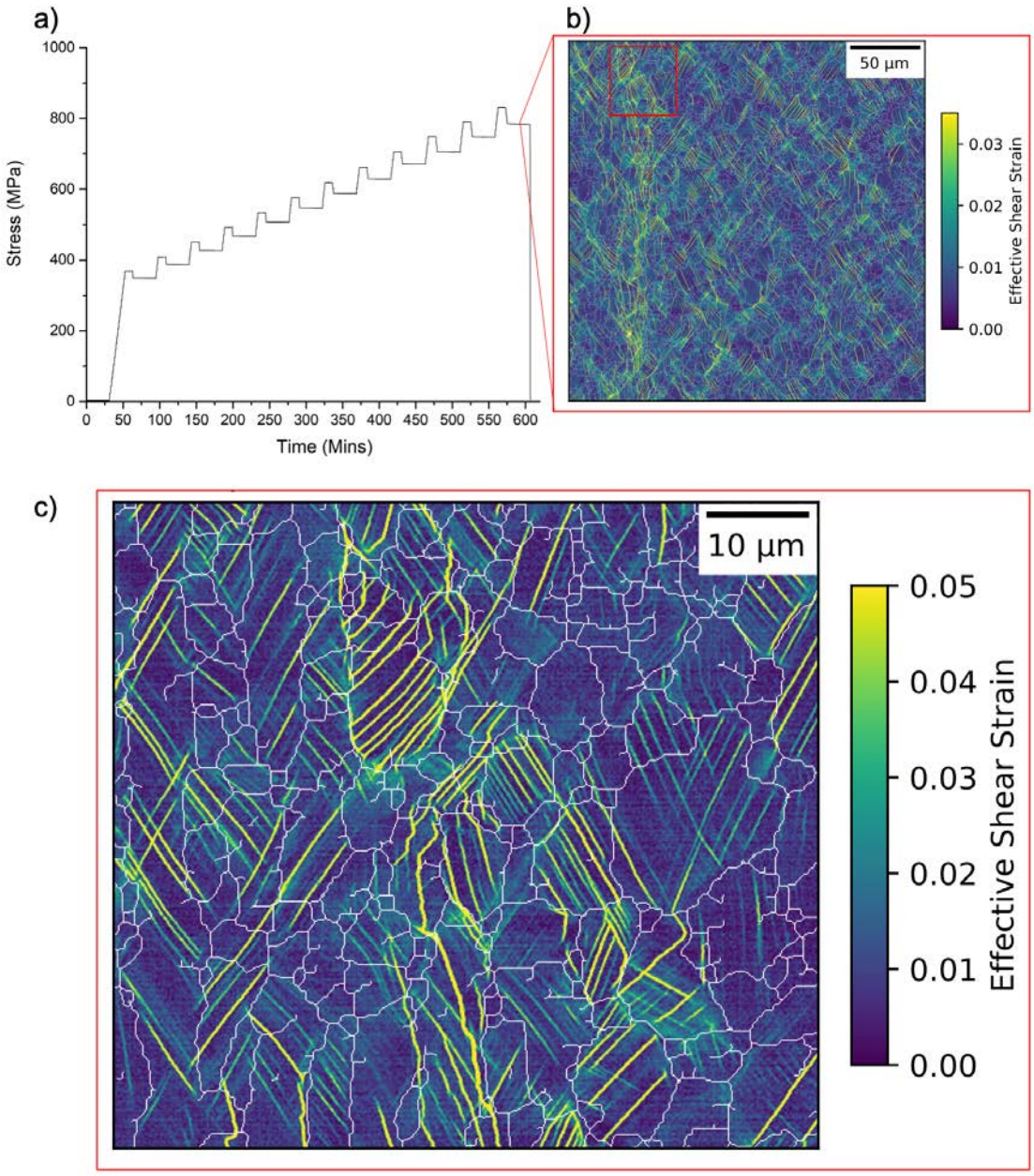

Fig. 1: a) Automated loading regime of the experiment over 10 hours, loaded up to hold point and allowed to relax for 10 mins before at 5% unload and automated mapping; b) Effective shear strain map with overlaid grain boundaries from linked orientation map; c) Inlay of high strain region to illustrate resolution of processed strain maps.

Type of presentation: Oral

MS7-O-2700 Analysis of dislocation evolution in cerium oxide nanocubes using in situ transmission electron microscopy

Zhang R.[1], Joly-Pottuz L.[1], Laurens G.[2], Albaret T.[2], Amodeo J.[1], Masenelli-Varlot K.[1]

[1]Univ Lyon, INSA-Lyon, MATEIS CNRS UMR5510, 69621 Villeurbanne, France, [2]Univ Lyon, UCB Lyon 1, ILM UMR 5306, 69621 Villeurbanne, France

Email of the presenting author: Karine.Masenelli-Varlot@insa-lyon.fr

As one of the most important ceramic materials, cerium oxide nanoparticles is widely used in many applications, such as in solid oxide fuel cell electrodes, catalysis, or as superior abrasive particles in chemical mechanical planarization. However, there are only few experiments regarding their structural evolution when cerium oxides are tested under loading. One possible reason is its sensitivity to the electron beam, as it may undergo phase transformation under electron irradiation [1]. In this study, we will focus on the effect of electron beam irradiation on the mechanical behavior of cerium oxide nanocubes.
Cerium oxides nanocubes (20-130 nm in size) are compressed using a dedicated Hysitron PI 95 sample holder in an environmental transmission electron microscope (ETEM). Plastic deformation of the nanocubes is analyzed using live High-Resolution TEM imaging. Two main phases of cerium oxides are investigated in this study: CeOx has a fluorite structure (space group Fm-3m) when x ranges between around 1.75 and 2, while it crystallizes in bixbyite (space group Ia-3) when x is less than about 1.75.
We will first determine the plasticity mechanism in CeOx. [110]{100} are considered as primary slip systems in materials with fluorite structure. In this study, the slip systems are determined by observing the dislocation movement during compression. By using different tilt axis, we will show – in agreement with simulations - that [110]{111} is the main slip system in CeO2 nanocubes with the fluorite structure. Moreover, results will be shown on cubes irradiated using a high dose rate, completely reduced into CeO1.5, and compressed along the same axis <110>. Many stacking faults have been produced during compression. To better compare both phases, a sequence of compression of an isolated cube under different electron doses have been performed (Figure 1). From the mechanical curves obtained, the yield stress is significantly increased when the electron beam change from high dose to low dose. This repeatable and reversible process will also be discussed.
[1] L. A. J. Garvie and P. R. Buseck, “Determination of Ce4+ / Ce3+ in electron-beam-damaged CeO2 by electron energy-loss spectroscopy,” J. Phys. Chem. Solids, vol. 60, no. 1999, pp. 1943–1947, 1999.

Acknowledgement: This work was funded by ANR (projet ANR-18-CE42-0009) and CSC.
Acknowledged to CLYM for microscope access and D.D. Stauffer (Bruker) for his help.

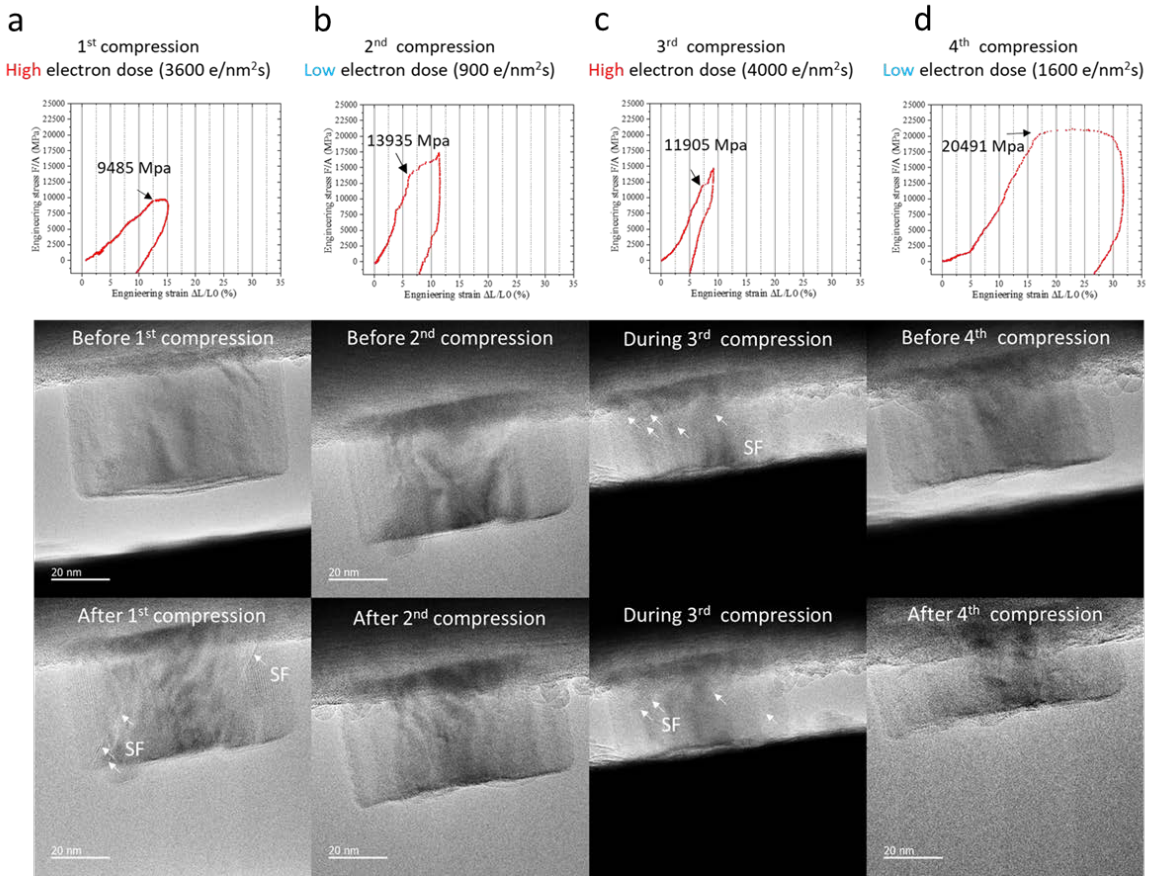

Fig. 1: Stress-strain curves obtained from four successive compressions tests on the same CeOx nanocube under different electron dose rates (the black arrow represents the yield stress). Bright field images recorded are shown below each curve. Under high dose, more stacking faults are created and the yield stress decreases. This process is reversible.

Type of presentation: Oral

MS7-O-2565 Al nanocrystalline thin film deformation by in situ TEM and molecular dynamics

Bajtošová L.[1], Křivská B.[1], Králík R.[1], Veselý J.[1], Hanuš J.[1], Harcuba P.[1], Fikar J.[2], Yadav A.[2], Cieslar M.[1]

[1]Charles University, Faculty of Mathematics and Physics Ke Karlovu 3, 12116 Prague, Czech Republic, [2]Czech Academy of Sciences, Institute of Physics of Materials, Žižkova 22, 61600 Brno, Czech Republic

Email of the presenting author: lucibajtos@gmail.com

Nanocrystalline thin films are widely applicable in various micro-electro-mechanical systems. Restricted grain sizes and film dimensions cause activation of deformation mechanisms different from the bulk materials and change of mechanical properties. In-situ deformation in a transmission electron microscope (TEM) allows direct observation of the sample and measurement of mechanical properties. This experimental method was combined with results of simulations by molecular dynamics (MD).

150 nm thick films were prepared by a DC magnetron sputtering from Al-3wt%Mg alloy. The film was sputtered onto a polymer tape, which was then dissolved. The film was in-situ annealed up to 400 °C in transmission electron microscope. A dog-bone shape specimen was cut from the film in a scanning electron microscope using focused ion beam and fixed onto a Push-to-Pull device with stiffness 150 N/m by a layer of Pt deposited by the gas injection system. The deformation was realised by a Hysitron PI 95 TEM PicoIndenter. During straining, rapid contrast changes in bright field (BF) (Figs. 1a and 1b) and very low dislocation density, both suggesting grain boundary-related deformation mechanisms were observed. ASTAR orientation maps were taken before the deformation and after the failure (Figs. 1c and 1d). The maps confirmed the possibility of grain rotations during the deformation. Moreover, the intergranular character of the crack propagation can be deduced from ASTAR images taken after the failure (Figs. 1b and 1d).

For MD simulations using ATOMSK software, a polycrystal structure was constructed in an orthogonal box with dimensions x = 400 nm, y = 400 nm, z = 200 nm. Twelve hexagonal grains with [110] parallel to z-direction and random orientation in x and y were created in the box. Periodic boundary conditions were employed in x- and y-directions. The MD simulations were performed using a large-scale atomic/molecular massively parallel simulator (LAMMPS). The polycrystal was deformed in the y-direction at a strain rate of 2.109 s-1 and a temperature of 300 K up to 20 % strain. Open visualisation tool (OVITO) was employed to visualise the atomic structure. Visualisation of simulation results is shown in Fig. 2. Common features with experimental results are visible: Restricted dislocation activity, deformation by grain boundary mechanisms, namely dislocations inside grain boundaries, and intergranular crack propagation. However, measurements of grain rotations showed no significant changes in misorientations at the beginning and the end of the simulation.

Acknowledgement: Authors would like to acknowledge the support from the Grant Agency of Charles University under project 574120.

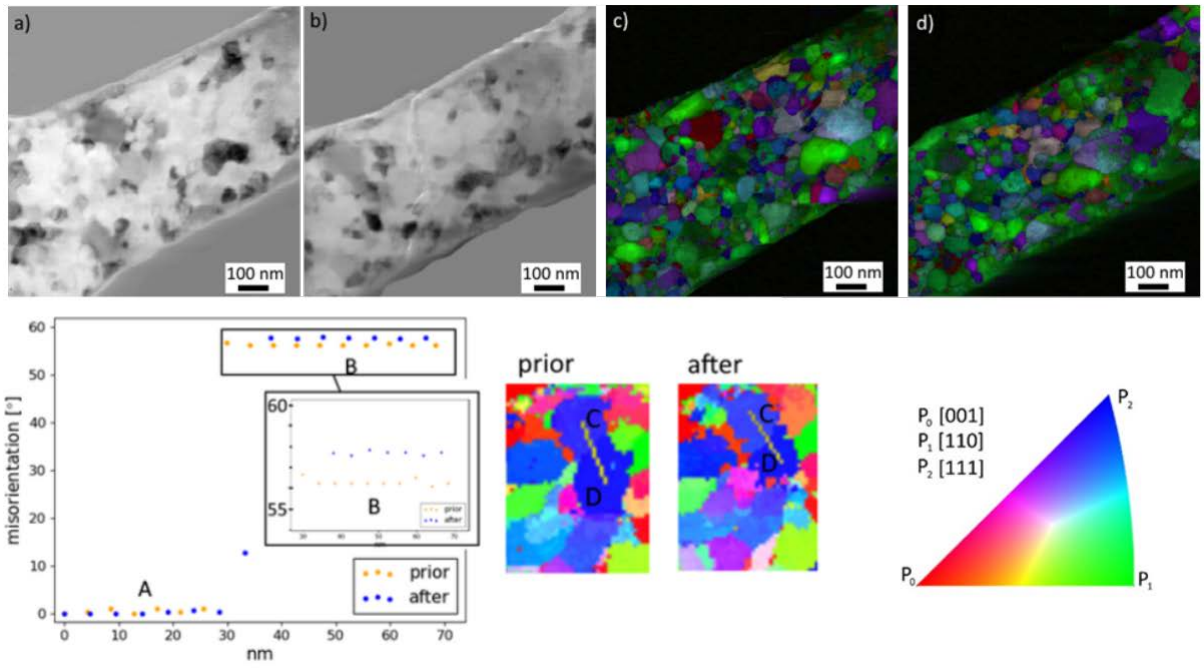

Fig. 1: ASTAR images of dog bone shape sample before (a, c) and after (b, d) deformation; a and b) constructed BF image; c and d) orientation maps; e) disorientations along the marked line.

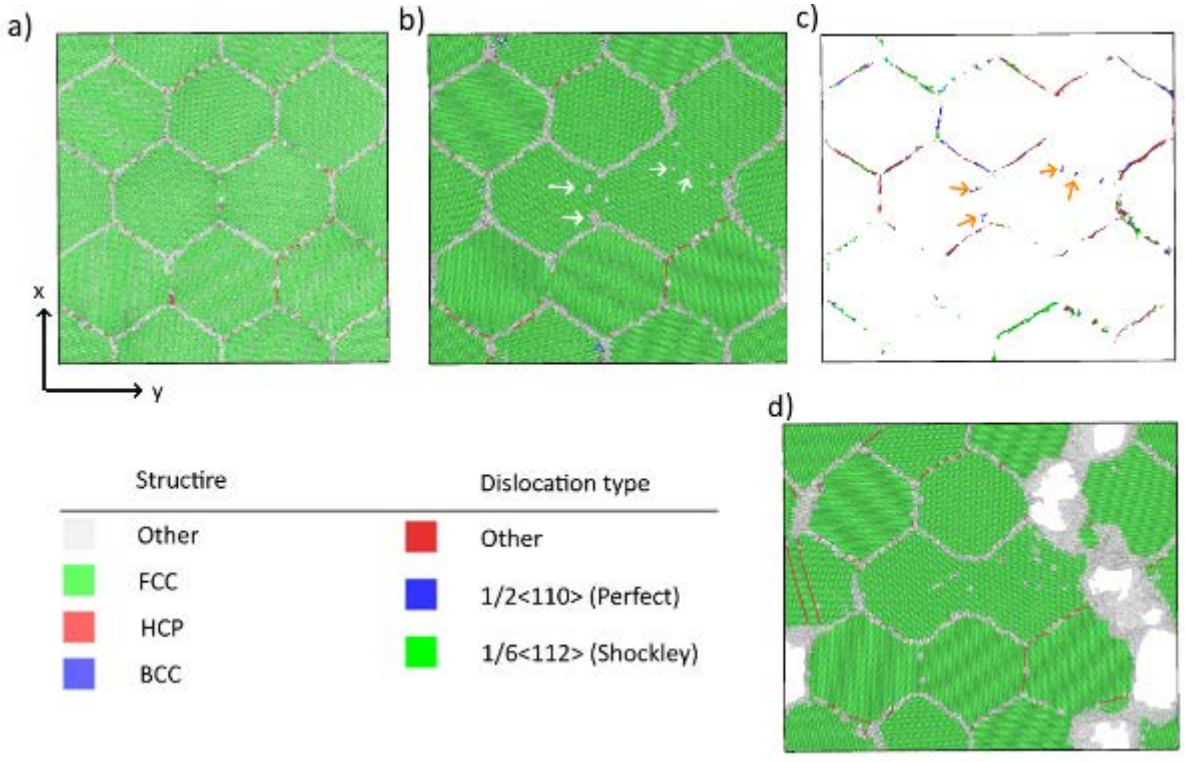

Fig. 2: Visualisation of MD simulation results, a) 0 %; b and c) 9 %; d) 18 %; a, b and d) common neighbour analysis; c) dislocation analysis. Dislocations propagating inside grains are marked by arrows.

Type of presentation: Invited

MS7-IN-2739 Fracture behavior of distinct interfaces of two intermetallic TiAl alloys

Burtscher M.[1], Alfreider M.[1], Clemens H.[1], Gammer C.[2], Kiener D.[1]

[1]Department of Materials Science, Montanuniversität Leoben, Franz Josef-Straße 18, Leoben 8700, Austria, [2]Erich Schmid Institute of Materials Science, Austrian Academy of Sciences, Jahnstaße 12, Leoben 8700, Austria

Email of the presenting author: michael.burtscher@unileoben.ac.at

Modern TiAl alloys are commonly used as structural materials for turbine blades in aero engines or vents in advanced motorsport applications. Understanding the ductility and fracture behaviour at ambient temperatures before and during warm-up of these components is thus of prime importance for a safe operation. In this study, the *J*-Integral and conditional fracture toughness were determined via notched microcantilever experiments at room temperature. To this end, specimens were cut via focused ion beam processing at predefined positions within the microstructure as displayed in Fig. 1a, b. Consequently, testing distinct interfaces and phases in two different TNM alloys allowed to identify the fracture properties at micron scale, see Fig. 1c. These two alloys differ only in the Si and C content of 0.3 at.% each and an adjusted Al content. Secondary electron microscopy videos were recorded during the experiments and subsequently, computer vision methods were used to analyze the crack propagation. The complementary continuous stiffness measurement allowed to track the actual crack propagation through respective phases or along specific interfaces during the experiments. Furthermore, strain maps of distinct interfaces of the different alloys were realized by 4D scanning transmission electron microscopy (see Fig. 2). This allows to determine the effects of additional alloying elements such as C and Si on the fracture properties of the TNM system at the micron scale. Hence, a connection between the different strains analyzed along the interfaces and the resulting fracture properties is established. The results presented in this study allow to take a further step towards optimized alloy design with optimized interface types for the respective application.

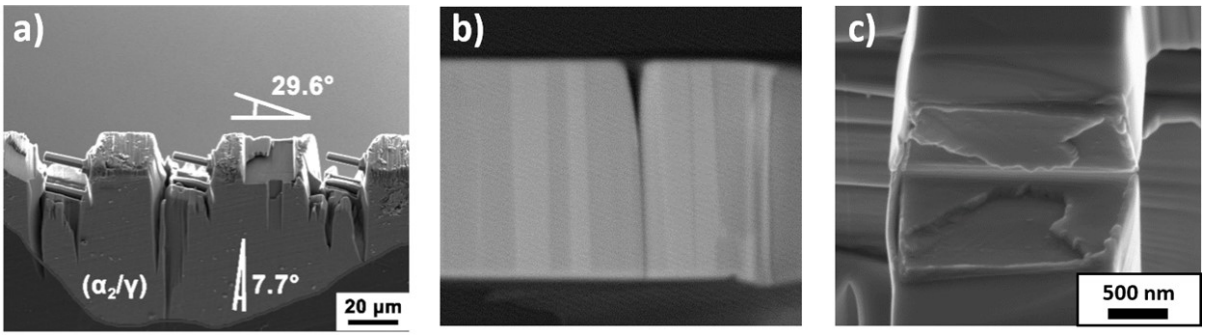

Fig. 1: In a), an overview image of cantilevers machined within an α2/γ colony is displayed. The side view in b) unveils the type of the notched interface within the lamellar structure. After in-situ testing, the fractured surfaces were visualized by secondary electron contrast and respective lamellae were identified (see c)).

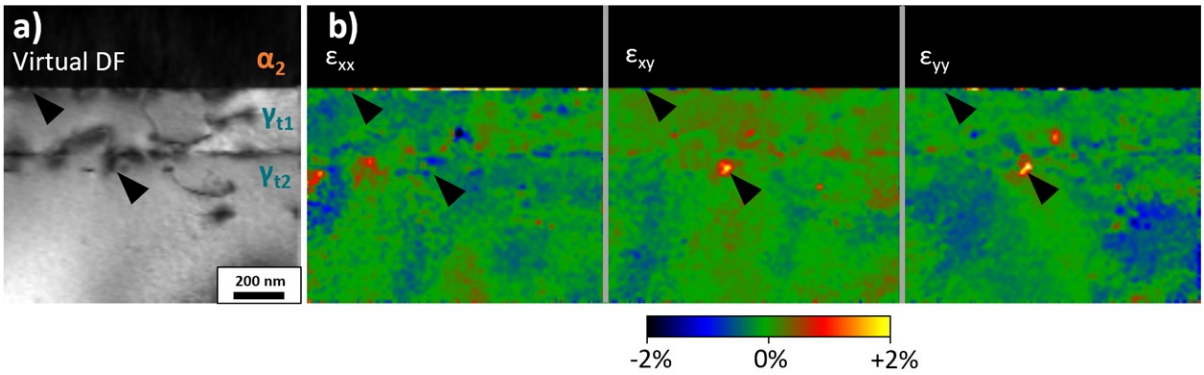

Fig. 2: Experimental data from 4D scanning transmission electron microscopy investigations of different interface types within an α2/γ colony. The virtual dark field and designated strain maps are displayed in a) and b), respectively. Here, the two black arrows indicate misfit dislocations along the α2/γ interface and a potential silicide particle.

Type of presentation: Oral

MS7-O-2694 Liquid cell TEM electrodeposition of PtNi alloy nanoparticle film

Parlinska-Wojtan M.[1], Sobczak K.[2], Depciuch J.[1], Tarnawski T.[1], Pawlyta M.[3], Schäublin R.[4]

[1]Institute of Nuclear Physics Polish Academy of Sciences, PL-31-342 Krakow, Poland, [2]Faculty of Chemistry, Biological and Chemical Research Centre, Warsaw, Poland, [3]Silesian University of Technology, Institute of Engineering Materials and Biomaterials, Konarskiego 18A, 44100 Gliwice, Poland, [4]ScopeM-Scientific Center for Optical and Electron Microscopy, ETH Zürich, 8093 Zürich, Switzerland

Email of the presenting author: magdalena.parlinska@ifj.edu.pl

There are many ways to synthesize PtNi NPs, one of them is electrodeposition [1]. In this study, liquid cell transmission electron microscopy (LC-TEM) was used to grow alloyed PtNi nanoparticle films in order to reveal the fundamental mechanisms at play. Generally, in electrodeposition the voltage is applied to the solution of metal precursors via three electrodes. As the voltage varies from reductive to oxidative potential, precursors dissociate, metal ions reduce (or oxidize) into atoms and adsorb as such on the working glassy carbon electrode surface. The potential range for PtNi electrodeposition was established during ex-situ experiments where the following parameters were varied: the potential range was varied between E1 = 1.2 V and E2, = -0.8 V The potential range was varied between E1 and E2, the scanning rate dE/dt was changed between 70 and 100 mV/s and the process was stopped after n = 5, 7, 10 or 15 potential cycles, while two Pt:Ni ratios were tested 25:75 and 35:65, respectively. The morphology of the PtNi films deposited at different conditions were analyzed by scanning electron microscopy (SEM). In the LC-TEM experiment, the potential ranged from -0.8 V to 0.8 V, the scanning rate was 80 mV/s, the number of cycles 7 and the Pt:Ni precursor ratio 35:65. These parameters resulted in a monolayer of nanostructured, crack-free PtNi film with a highly porous structure, see SEM image in Fig. 1. The spherical nanoparticles are composed of needle-like structures. The NPs exhibit a large spread in size distribution, from several nanometers to single NPs with a diameter reaching 500 nm.
The films were electrodeposited from a liquid precursor on a carbon electrode in a 3 electrodes configuration on the large e-chip of the Poseidon Protochips TEM holder. The synthesis process can be affected by the electron beam as it may cause radiolysis, atomic replacements, gas bubbles [2], pH fluctuations and an uncontrolled temperature increase [3]. In our LC-TEM experiment, directly after switching the current on, Fig. 1a, burst-like growth of the PtNi NPs film occurred, Fig. 2b-f. The electron beam enhanced the growth, as the PtNi NPs formed in the liquid in the vicinity of the film in addition to the dendritic structure growing directly on the film coated electrode Fig. 2 d-e. The growth of the films was the fastest during the first 4 cycles, while no differences in film thickness between cycle 4 to 7 was observed, Fig.3.

References:

[1] Xiu, R. et al. (2015) RSC Advances, 5(105), pp. 86578–86583. doi: 10.1039/C5RA13728D.
[2] Egerton, R. F., Li, P. and Malac, M. (2004) Micron, 35(6), pp. 399–409. doi: 10.1016/J.MICRON.2004.02.003.
[3] Cazaux, J. (1995) Ultramicroscopy, 60(3), pp. 411–425. doi: 10.1016/0304-3991(95)00077-1.

Acknowledgement: This research was founded by the grant from the National Science Foundation 2019/35/B/ST5/04140. Many thanks for partial financial support by Pik-Instruments

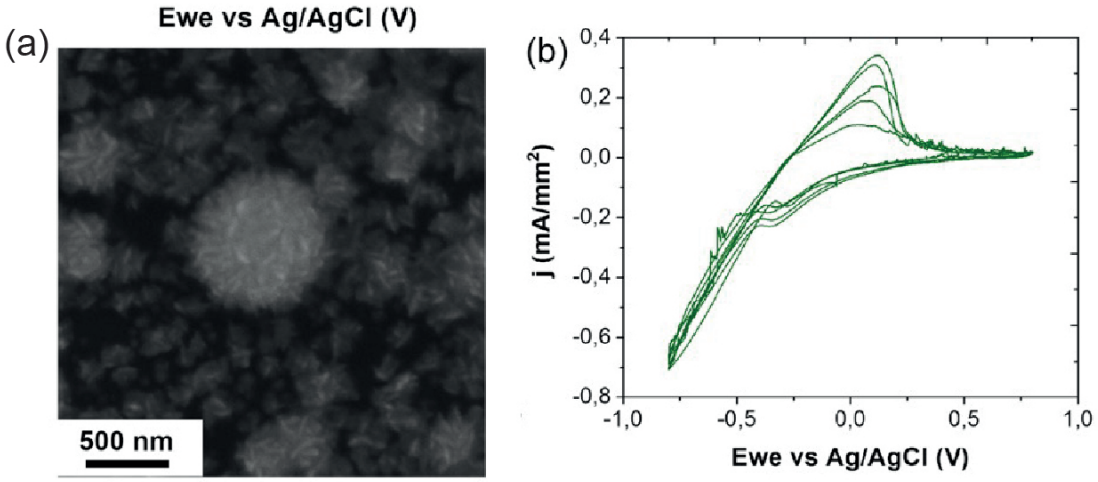

Fig. 1: a) SEM image of the surface of the ex-situ deposited PtNi NPs sample; b) Corresponding voltammogram.

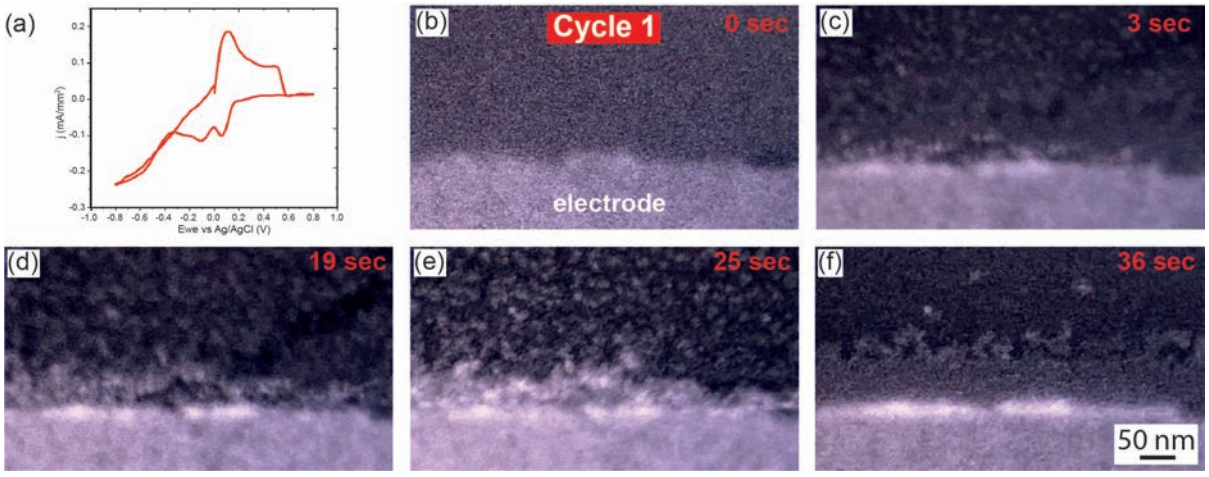

Fig. 2: a) First cycle of the electrodeposition voltammogram; b) – f) HAADF STEM still frames from the in-situ LC-TEM movie recorded during the first electrodeposition cycle of the PtNi film on the edge of the electrode.

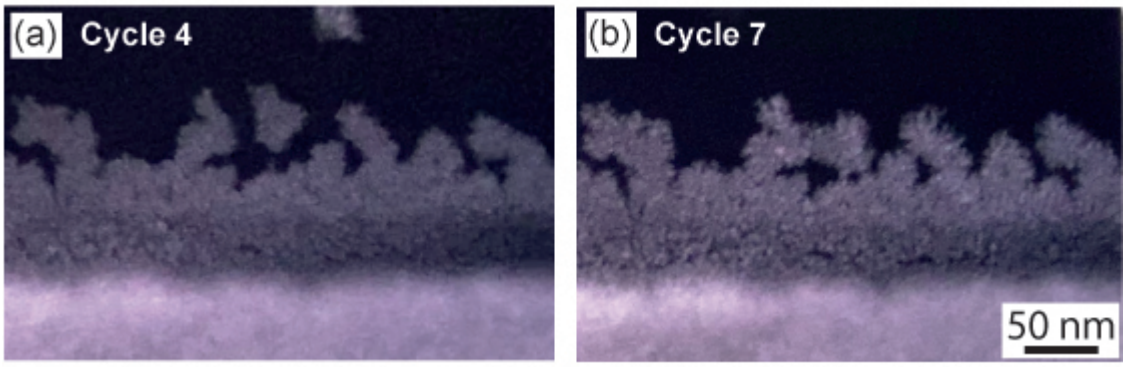

Fig. 3: Comparison between PtNi NPs film thickness in: a) Cycle 4; b) Cycle 7.

Type of presentation: Poster

MS7-P-2687 Impact behaviour of the industrially sputtered AlCrN coatings prepared using cathodic arc glow discharge

Alishahi M.[2,3], Daniel J.[1], Žemlička R.[4], Jílek M.[3], Souček P.[2], Klusoň J.[3], Bolvardi H.[4], Lümkemann A.[4], Vašina P.[2]

[1]Institute of Scientific Instruments of the Czech Academy of Sciences, Královopolská 147, CZ-612 64 Brno, Czech Republic, [2]Department of Physical Electronics, Faculty of Science, Masaryk University, Kotlářská 2, CZ-61137 Brno, Czech Republic, [3]Platit a.s., Průmyslová 3020/3, CZ-78701 Šumperk, Czech Republic, [4]Platit AG, Eichholzstrasse 9, CH-2545 Selzach, Switzerland

Email of the presenting author: jdaniel@isibrno.cz

Two sets of the AlCrN coating were prepared in the magnetron sputtering based system SCIL® deposition technology. In this technology, the sample is deposited by sputtering of the central cathode and simultaneously the second discharge, lateral glow discharge (LGD®), is ignited between two lateral cathodes [1]. This technology enables to control the ion density in sputtering discharge and ion-deposition flux ratio (J_i/J_d) by driving the LGD parameters. The ion-deposition flux ratio and the ion energy (E_i) define the average ion energy per deposited atom (E_d) [2].

Two sets of the AlCrN coatings were prepared using sputtering of the Al-Cr target in the argon/nitrogen mixture atmosphere. One set of samples was prepared in metallic regime of the cathode; second set was prepared in poisoned regime of the cathode. The samples in each set was prepared with various E_d. Structure and chemical composition of the coatings were analysed by a TESCAN MIRA 3 SEM equipped with an EDX detector from Oxford Instruments. Mechanical properties were estimated using nanoindentation tester with the applied maximum force of 20, 30, and 50 mN. It was shown that mechanical hardness of the coating depends strongly on the E_d, while young modulus strongly dependent mainly on the coatings microstructure [2].

Aim of this work was to study the impact behaviour of the AlCrN coating under repetitive impact load. For this study, the impact tester invented in ISI CAS was used. Impact frequency of 8 Hz, impact loads of 200 N and 400 N and WC/Co ball (Ø 5 mm) were used as impact parameters. Impact craters were investigated using laser confocal microscope Keyence and SEM TESCAN MIRA 3. Dependence of the behaviour of the AlCrN coatings under the repetitive impact on the coatings microstructure and hardness was discussed.

[1] HYBRID LACS® TECHNOLOGY, https://www.platit.com/en/coating-know-how/coating-technologies/, (accessed 12 April 2022).

[2] Žemlička, R., Alishahi, M., Jílek, M., Souček, P., Daniel, J., Kluson, J., Bolvardi H, Lümkemann A., Vašina, P. (2021). Enhancing mechanical properties and cutting performance of industrially sputtered AlCrN coatings by inducing cathodic arc glow discharge. Surface and Coatings Technology, 422, 127563.

Acknowledgement: This research was supported by the project LM2018097 funded by the Ministry of Education Youth and Sports of the Czech Republic.

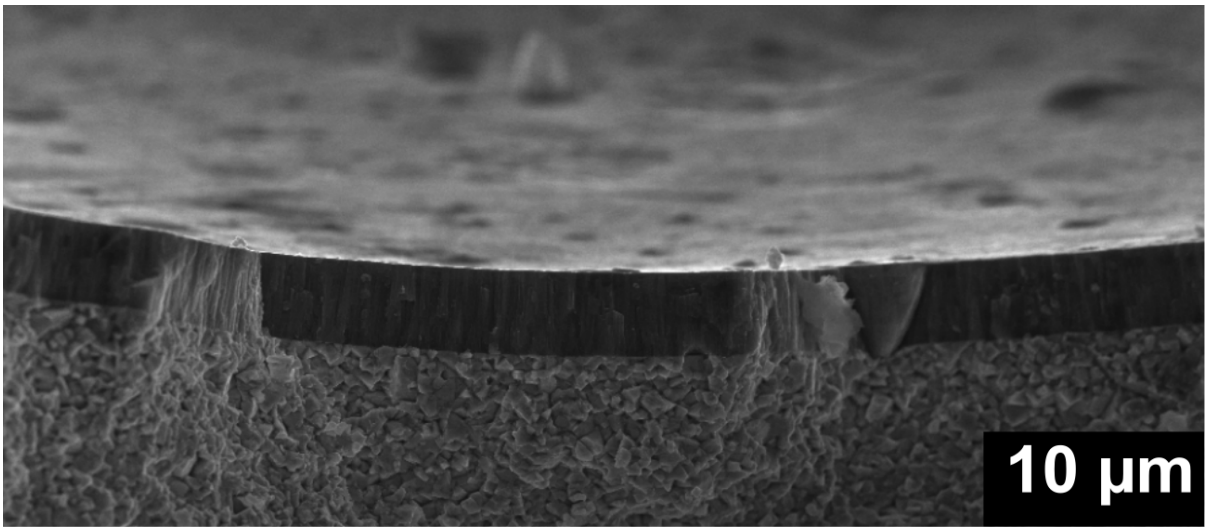

Fig. 1: Example of the cross-section of impact crater on AlCrN coating.

Type of presentation: Poster

MS7-P-2603 Nanohardness and toughness of multicomponent TiNbVTaZrHf-N coatings deposited by reactive DC magnetron sputtering and High Target Utilization Sputtering

Lofaj F.[1], Csanádi T.[1], Kvetková L.[1], Hviščová P.[1], Kabátová M.[1], Kovalčíková A.[1], Girman V.[1]

[1]Institute of Materials Research of the Slovak Academy of Sciences

Email of the presenting author: flofaj@saske.sk

Multicomponent ceramic coating systems based on refractory metals from 3rd and 4th group of elements in the periodic table and forming structures analogous to high entropy alloys are expected to represent a new class of materials with improved high level of mechanical properties combined with high thermal stability and resistance in extreme conditions [1]. Among them, high entropy nitrides (HEN) can be relatively easy produced by reactive sputtering, mostly arc and or DC magnetron (co)sputtering [2]. However, novel sputtering methods with higher level of ionization of sputtered species like High Power Impulse Magnetron Sputtering and High Target Utilization Sputtering (HiTUS) were not applied in these systems. Moreover, it is even not clear if HiTUS can principally produce homogeneous solid solutions from multicomponent metals and corresponding nitrides and in the positive case, what would be the mechanical properties of HiTUS coatings in comparison with conventional DCMS made coatings. Therefore, the aim of the current work was to investigate structure and mechanical properties (hardness, elastic modulus and fracture toughness) of multicomponent TiZrHfNbVTa–N coatings involving strong nitride formers and produced by reactive DCMS and HiTUS over wide range of nitrogen additions into sputtering Ar atmosphere. Coating structures were investigated using high resolution TEM, mechanical properties by nanoindentation and pillar splitting technique [3] on micropillars produced by FIB. TEM confirmed that both DCMS and HiTUS are able to produce homogeneous solid solutions which can be attributed to HEN. Near-stoichiometric nitrides consisted of textured fcc nanocolumns (Fig. 1) however, the structure and mechanical properties (Fig. 2) were strongly affected by the amount of nitrogen. The highest hardness values in HiTUS coatings, were in the range 28 - 33 GPa at around 6 sccm N2 (in DCMS coatings it was 32 - 35 GPa) and the indentation moduli were 350 - 400 GPa (vs. 460 - 490 GPa in DCMS made coatings). The corresponding fracture toughness values were in the range 2-3 MPa.m1/2 (Fig. 3). Thus, reactive HiTUS was found to be suitable for the preparation of hard HEA and HEN coatings.

References

[1] Oses C., Toher C., Curtarolo S.: Nat Rev Mater 5 (2020) 295–309. https://doi.org/10.1038/s41578-019-0170-8.
[2] Lewin E.: J. Appl. Phys. 127 (2020) 160901. https://doi.org/10.1063/1.5144154
[3] Sebastiani M., Johanns K. E., Herbert E.G., Carassiti F., Pharr G.M.: Phil. Mag. 95 (2015) 1928-1944. https:/dx./doi.org/10.1080/14786435.2014.913110.

Acknowledgement:
This work was supported by SAS via Int. Visegrad Fund (JP39421, V4-Japan Joint Research Program) and by APVV (APVV 17-0059, APVV-17-0320 and APVV-17-0049).

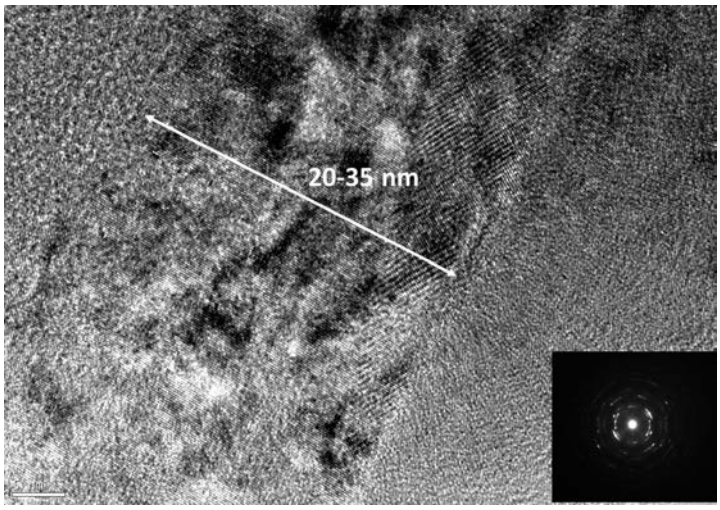

Fig. 1: HRTEM of HiTUS TiZrHfNbVTa–N coating deposited with 6 sccm N2 in the sputtering atmosphere exhibiting columnar structure with the column diameter around 30 nm. Microdiffraction (see insert) suggest textured fcc structure.

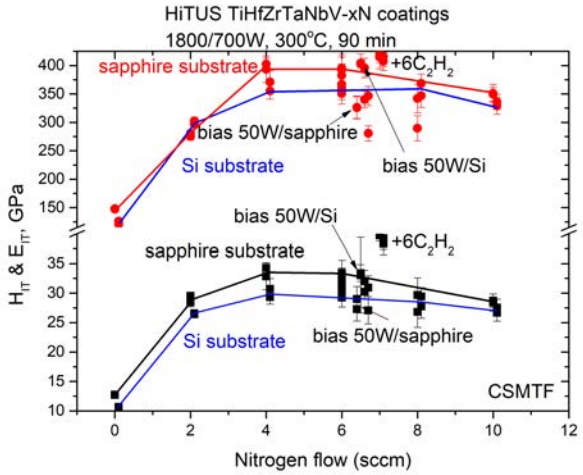

Fig. 2: Dependence of hardness and elastic modulus of the studied HiTUS TiZrHfNbVTa–N coatings on the amount of nitrogen in the Ar sputtering atmosphere.

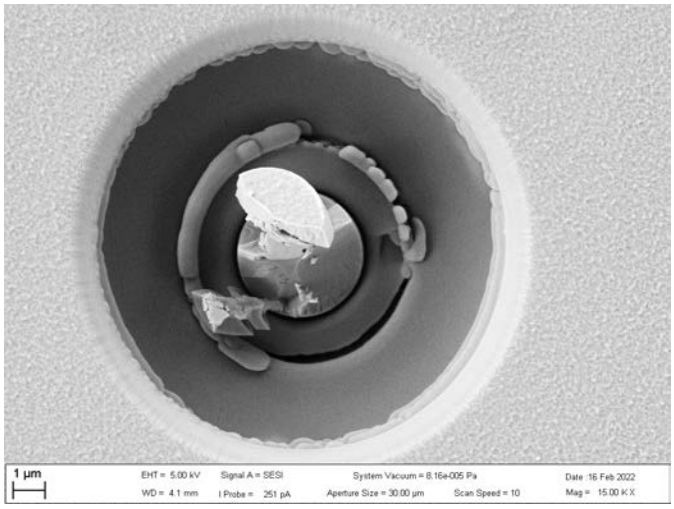

Fig. 3: Micropillar in HiTUS TiZrHfNbVTa–N coatings with 6 sccm N2 after pillar splitting tests.

Type of presentation: Poster

MS7-P-2840 Characterization of Mechanical and Topographical Properties of Nanocomposite Thin Films with Plasma Polymer Structure

Václavik R.[1], Buršíková V.[1], Charvátová Campbell A.[2], Havlíček M.[2, 3], Klapetek P.[2]

[1]Department of Physical Electronics, Faculty of Science, Masaryk University, Brno, Czech Republic, [2]Czech Metrology Institute, Brno, Czech Republic, [3]CEITEC BUT, Brno, Czech Republic

Email of the presenting author: richardvaclavik96@gmail.com

The main aim of the present work was to study the topographical and mechanical properties of nanocomposite thin films with plasma polymer structures. Plasma polymers were deposited in a capacitively coupled radiofrequency discharge from a mixture of monomer hexamethyldisiloxane (HMDSO) and oxygen as carrier gas. The flow rate of HMDSO was 3.5 sccm, the flow of oxygen was 10 sccm and the power supply of CCP was 25 W. Deposition time varied in the range 1 – 90 minutes, what resulted in thicknesses in the range 0.4 – 15 micrometers. Atomic force microscopy in both topography and phase shift imaging mode has been used to study surface morphology. To obtain a comprehensive and complex analysis of surface mechanical properties, nanocomposites underwent measurements by various indentation methods (partial unloading, creep tests, dynamic nanoindentation, etc.) with changing indentation parameters (duration of individual segments, loading/unloading rate, oscillation frequency, etc.). The nanoindentation tip is capable of ultrahigh-speed high-resolution mapping, which was utilized to obtain maps and distribution histograms of mechanical properties. Moreover, local surface mechanical properties were investigated by AFM in Hybrid mode using compositional mapping of local adhesion and stiffness.

Acknowledgement: The research has been supported by the Czech Science Foundation under project GACR 19-15240S.

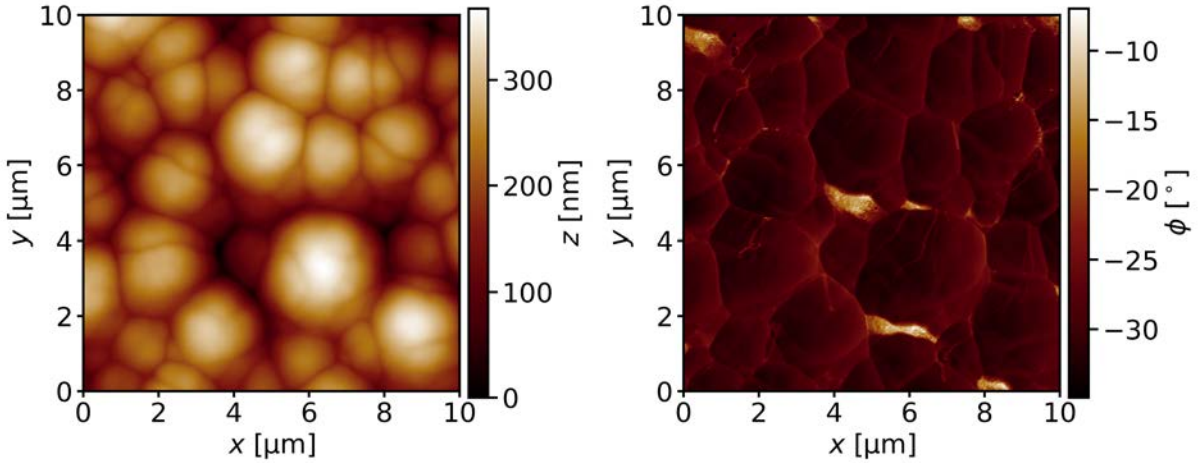

Fig. 1: Topography (left) and phase shift (right) AFM images, which allow distinguish dusty particles and matrix of nanocomposite plasma polymer.

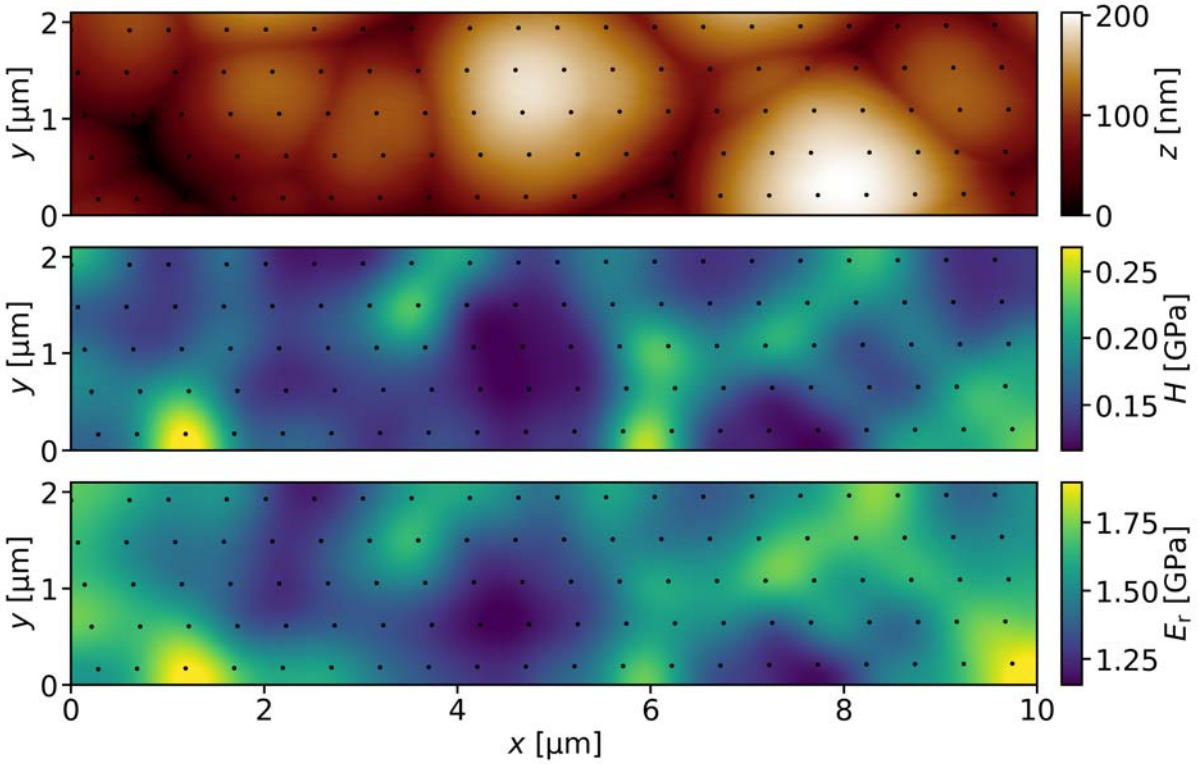

Fig. 2: Local mechanical properties. From the top: topography obtained by scanning with indentation tip, distribution of indentation hardness, and elastic modulus.

Type of presentation: Poster

MS7-P-2540 Mechanical response of domain walls in lead-free ferroelectrics

Žiberna K.[1, 2], Drnovšek A.[3], Koblar M.[1], Rojac T.[1, 2], Uršič H.[1, 2], Benčan A.[1, 2]

[1]Electornic Ceramics Department, Jožef Stefan Institute, Ljubljana, Slovenia, [2]Jožef Stefan International Postgraduate School, Ljubljana, Slovenia, [3]Department of Thin Films and Surfaces, Jožef Stefan Institute, Ljubljana, Slovenia

Email of the presenting author: katarina.ziberna@ijs.si

Domain walls (DWs) in ferroelectric materials are nanoscale topological defects separating regions of homogeneous orientation of spontaneous polarization, whose properties often differ from those of the matrix material. In contrast to a large body of research on the functionally of DWs, less is known about their mechanical properties. The development of new techniques for measuring mechanical responses at the nanoscale, such as *in situ* nanoindentation in the scanning electron microscope (SEM) or amplitude modulated - frequency modulated mapping and contact resonance frequency mapping in the atomic force microscope (AFM), have enabled the study of the mechanical response of individual DWs. For example, mechanically softer ferroelectric 180° DWs in ferroelectric single crystals and thin films compared to the matrix material have been recently reported [1].

In this work, we will present and compare the results of mechanical investigation of DWs in environmentally friendly ferroelectric $BiFeO_3$ ceramics and in (K, Na)NbO_3 single crystal using the above mentioned techniques. The resolution of the techniques used in the investigation will be discussed. The type and structure of DWs will be determined by electron backscattered diffraction method (EBSD) and transmission electron microscopy methods. The mechanical properties of DWs as a function of their local structure will be presented.

References:

[1] C. Stefani et al., Phys. Rev. X 2020, 10, 041001.

Late poster

Type of presentation: Poster

Late-P-3026 In-situ analysis of graphene and its derivatives by combined SEM/AFM method

Hošek J.[1], Čépe K.[1], Otyepka M.[1, 2]

[1]Regional Centre of Advanced Technologies and Materials, Czech Advanced Technology and Research Institute (CATRIN), Palacký University Olomouc, Šlechtitelů 27, 779 00 Olomouc, Czechia, [2]IT4Innovations, VSB – Technical University of Ostrava, 17. listopadu 2172/15, 708 00 Ostrava-Poruba, Czech Republic

Email of the presenting author: jiri.hosek@upol.cz

Graphene and its derivatives are due to their unique properties (size, thickness, mechanical properties, conductivity, etc.) one of the most examined material in the field of the science. Graphene derivatives are promising materials because of the diversity of functional groups, which could have different applications to a wide variety of fields. Each sample needs to be characterized by microscopic methods in order to know its basic properties before it is applied in the next research. Scanning Electron Microscopy (SEM) brings the information about the size, shape and the surface characterization of the sheets. In the case of graphene and its derivates, it is almost impossible to distinguish the thickness and number of the layers from SEM images. For complete characterization of graphene sheets, it is necessary to use Atomic Force Microscope (AFM), which gives information about the thickness and number of layers. Litescope AFM is integrated into the SEM chamber and creates unique microscopic system based on the combination of SEM and AFM. Litescope is eqquiped with unique Correlative Probe and Electron Microscopy (CPEMTM) technique, which allows simoultaneous measurement SEM and AFM of the same object at the same time in the same conditions. Therefore, combined SEM/AFM method (Scios 2/Litescope) was used as the tool for complex in-situ analysis.

Acknowledgement: The authors gratefully acknowledge support from the Technology Agency of the Czech Republic, Program TRENDGEFSEM, FW01010183).

Type of presentation: Poster

Late-P-3036 Microstructural analysis of Inconel 625 superalloy manufactured by laser powder bed fusion with remelting

Ledwig P.[1], Gola K.[1], Dubiel B.[1]

[1]Faculty of Metals Engineering and Industrial Computer Science. AGH University of Science and Technology, al. Adama Mickiewicza 30, 30-059 Kraków, Poland

Email of the presenting author: pledwig@agh.edu.pl

Inconel 625 produced by laser powder bed fusion (LPBF) exhibits improved properties than the wrought superalloy, which result from the hierarchical microstructure formed during rapid solidification [1].
In this work, the effect of remelting on the microstructure of Inconel 625 manufactured by laser powder-bed fusion was investigated by means of light microscopy (LM) and scanning electron microscopy (SEM). Electron backscattered diffraction (EBSD) method was used to determine the orientation of the grains.
The laser remelting was achieved by the application of the double laser scan routes in one layer. During the first scan, the powder was melted and the liquid metal was rapidly solidified, while the aim of the second scan was to remelt and solidify the deposit, without adding another layer of powder.
The aim of such a procedure was reduction of porosity, homogenization of the chemical composition, and obtaining of the crystallographic texture [2]. The series of Inconel 625 samples were manufactured by LPBF applying a single laser scan and a double laser scan with remelting.
Figure 1 a-b shows the LM images of the microstructure in plane parallel to the build direction (BD). It was indicated that the microstructure of Inconel 625 after a single scan consisted of melt pools arranged according to the laser scan strategy. Between the melt pools sparse lack of fusion porosity was also observed (Fig. 1a). In the specimens subjected to remelting, the shape of the melt pools was more regular and the lack of fusion was negligible (Fig. 1b).
SEM observations revealed that after a single scan the grains were equiaxial or elongated in shape (Fig. 1c), while after remelting the elongated columnar grains dominated (Fig. 1d). The submicrometer cellular-dendritic substructure was formed within grains, as shown in the inserts in Fig. 1 c-d. EBSD analysis revealed the crystallographic orientation of grains along the BD. No preferred orientation of grains was determined after a single scan, while after remelting most of grains were <001> oriented (Fig. 2b). In case of remelting, a higher amount of small angle boundaries was noticed, which was related to the formation of the columnar structure of grains (Fig. 2c).
The results show that application of remelting allowed to reduce lack of fusion porosity and obtain columnar grain structure in LPBF Inconel 625 superalloy.

References:

1. Gola, K., Dubiel, B., Kalemba-Rec, I., 2020. J. Mater. Eng. Perform. 29, 1528–1534.
2. Yu, Z., Zheng, Y., Chen, J., Wu, C., Xu, J., Lu, H., Yu, C., 2020. J. Mater. Process. Technol. 284, 116738.

Acknowledgement: The study was supported by AGH UST Project No. 16.16.110.663.7

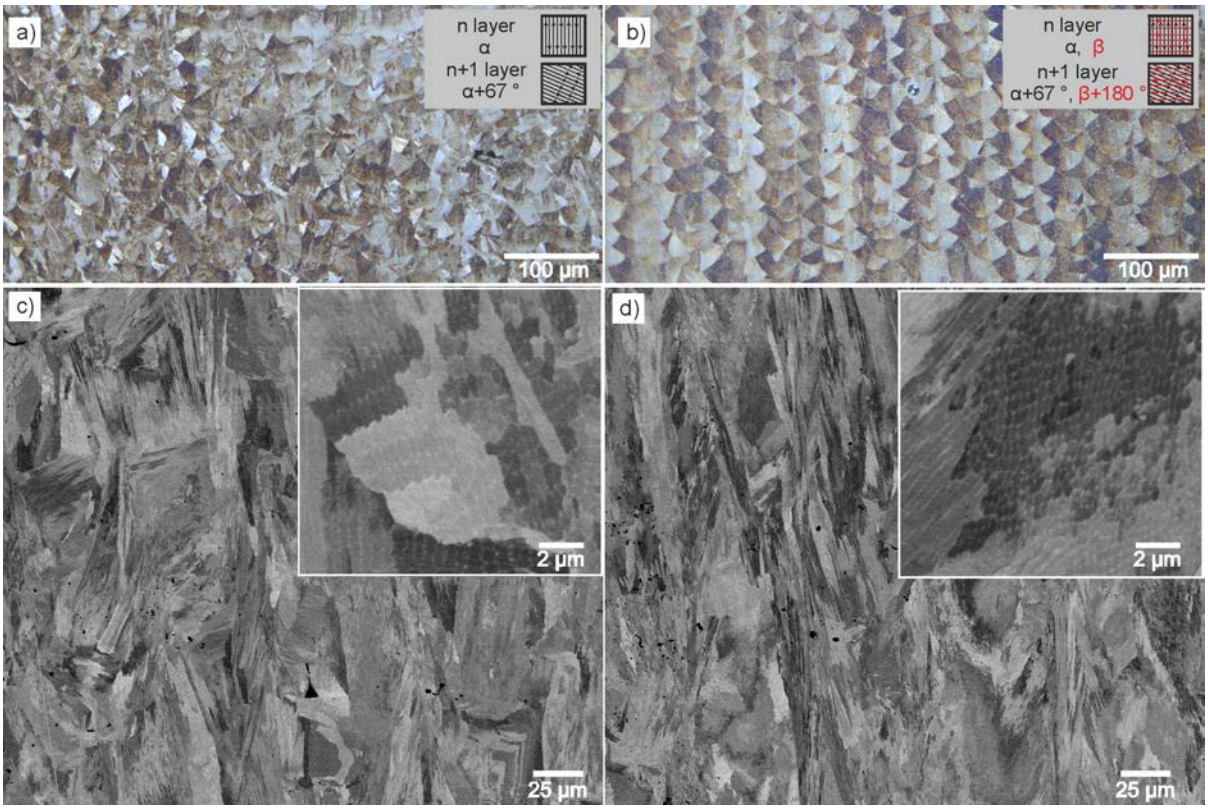

Fig. 1: LM and SEM BSE images of Inconel 625 obtained by LPBF using a, c) single laser scan, and b, d) double laser scan with remelting.

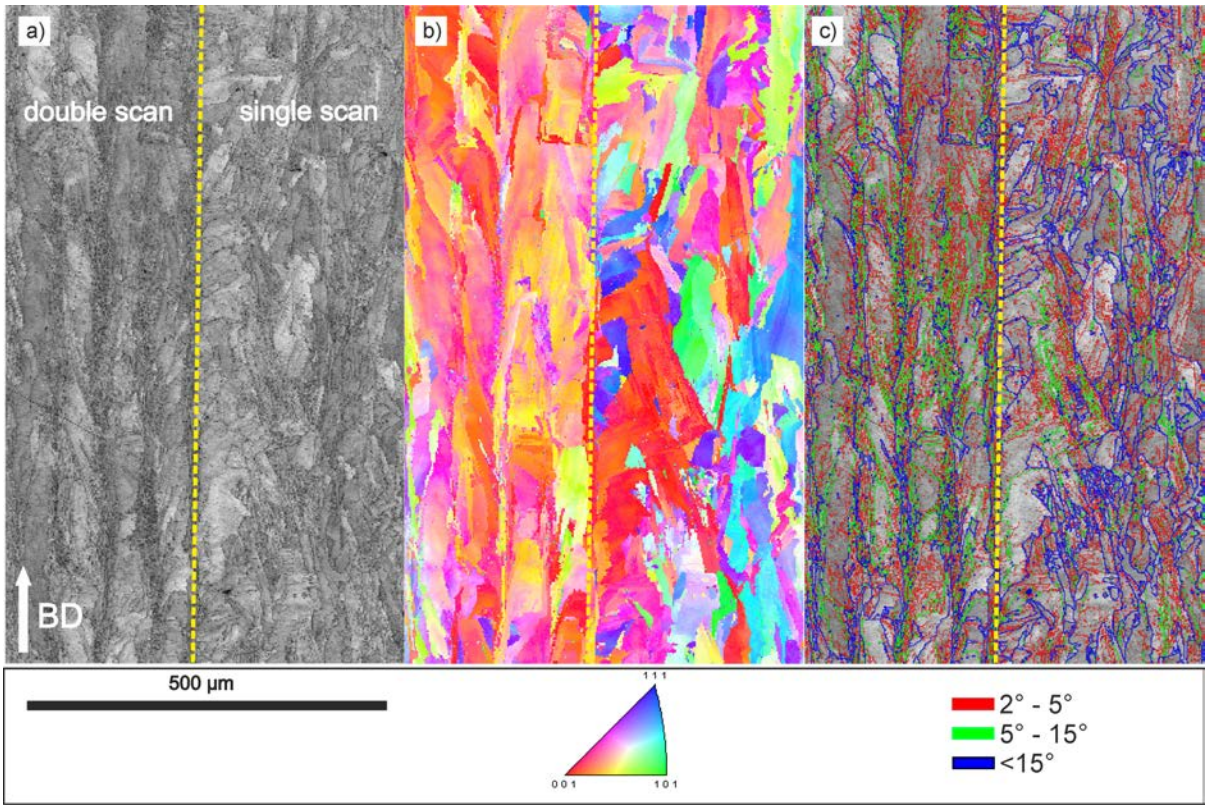

Fig. 2: a) Image quality, b) inverse pole figures and c) grain boundary maps of Inconel 625 with and without remelting. SEM EBSD

Type of presentation: Poster

Late-P-3032 Electron beam irradiation induced Brownmillerite – perovskite phase transition in La_{0.6} Sr_{0.4} CoO_{3-ð}

Ražnjević S.[1,2], Böhme C.[3], Riedl C.[3], Siebenhofer M.[3], Kubicek M.[3], Zhang Z.[1,2]

[1]Erich Schmid Institute of Material Science, Austrian Academy of Sciences, 8700, Austria, [2]Montanuniversität Leoben, Franz-Jozef-Straße, 8700, Leoben, Austria, [3]Institute of Chemical Technologies and Analytics Vienna University of Technology, Getreidemarkt 9, A-1060 Vienna, Austria

Email of the presenting author: Sergej.Raznjevic@oeaw.ac.at

Perovskite structure is often described with a chemical formula ABO3 where A is usually the bigger ion and B is the smaller one. In the perovskite structure, every B site is surrounded by an oxygen octahedral. There are a large number of oxygen-deficient perovskites AmBmO3m-ð that have a wide variety of oxygen vacancy ordering pattern. Brownmillerite structure is chemically described as A2B2O5 and here, unlike perovskites, oxygen atoms form alternating planes of octahedral and tetrahedral along the [100] direction.
Lanthanum Strontium Cobaltite has been heavily studied in the past decade because of its promising properties that can be used in solid oxide fuel cells, oxygen transport membranes and gas sensors.
In this work we investigate how the electron beam influences the oxygen vacancy ordering in epitaxial Lanthanum Strontium Cobaltite thin films.
Using pulsed laser deposition (PLD) 40nm of epitaxial La0.6Sr0.4CoO3-ð (LSCO) was grown on a (100) Yttrium stabilized Zirconia (YSZ) with a 10nm buffer layer of Ce0.8Gd0.2O2-ð (GDC). TEM-sample was prepared using a Focused Ion Beam (FIB) cutting technique.
Atomic structure evolution under electron beam was investigated using a JEOL 2100F microscope equipped with an image-side Cs-corrector. The film was continuously illuminated for 8min with a beam current density of 64.8pA/cm2. Before illumination, from the atomic structure image, darker stripe contrast in every other CoO plane are present, which indicates the presence of the Brownmillerite phase. This ordering trend in every other plane effectively doubles the cell parameters. During illumination, the difference in contrast between the planes gradually fades and, finally, disappears completely. Doubling of the lattice parameter of the Brownmillerite structure is usually visible in the diffraction pattern as half-integer reflections. Therefore, the local fast Fourier transform (FFT) analysis was performed on the HRTEM images. An FFT pattern before illumination in which half-integer reflections are present further confirms the existence of the Brownmillerite phase. After illumination, half-integer reflections disappear, indicating that the lattice doubling is no longer present, thus ensuring the transition to the perovskite phase. The analytical investigation was further carried out using electron energy-loss spectroscopy (EELS). Oxygen K-edge before illumination shows two peaks with an energy difference of about 6 eV are distinguished. The first peak corresponds to the interactions of O 2p and La 5d orbitals, while the second peak is due to the interaction of O 2p and hybrid La/Sr 4sp orbital5. After illumination, the peak with the higher energy is not present anymore, thus indicating the change in the oxygen bounds in the film.

Acknowledgement: The authors acknowledge the financial support from the Austrian Science Fund (FWF P31654-N37)

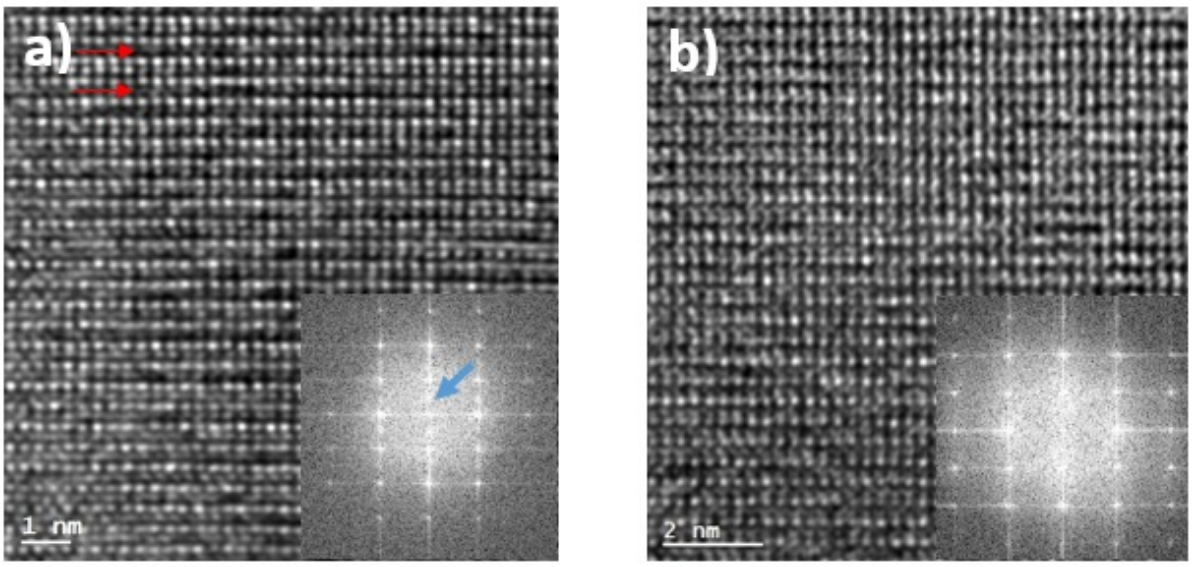

Fig. 1: NL-Filtered HRTEM images along [011] zone axis, showing the evolution of LSCO film under electron beam illumination. The current density of the electron beam was 64.8pA/cm2. The images were recorded before (a) and after 8min illumination (b). The inserts show corresponding FFT patterns. The blue arrow in (a) shows half-integer reflection.

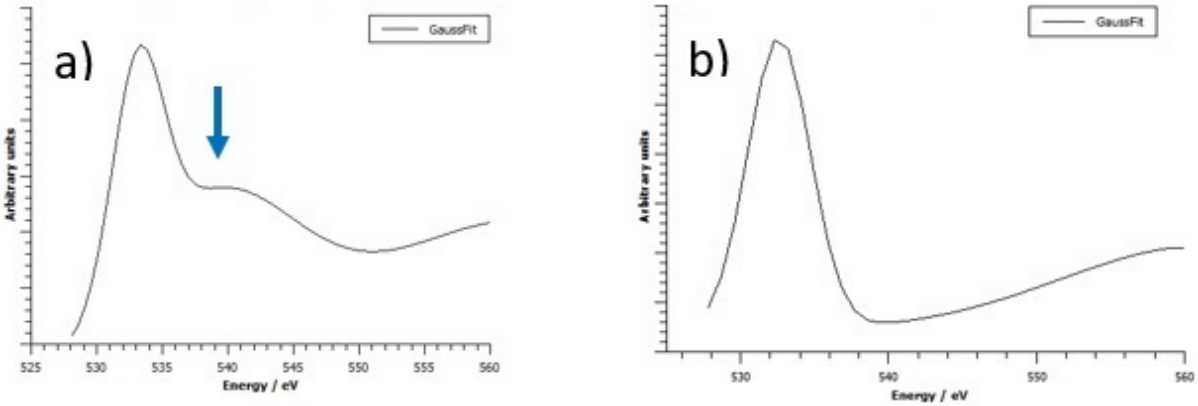

Fig. 2: Gaussian fit of O-K-edge EELS-spectrum before (a) and after illumination (b).

Type of presentation: Poster

Late-P-3055 Non-Invasive Imaging Method for Evaluating Effect of Migrastatics on Tumor Cells In Vitro Based on Coherence - Controlled Holographic Microscopy

Šuráňová M.[1,2], Zábranská M.[1], Kolínková V.[1], Muchová N.[1], Jůzová V.[2], Chmelík R.[1,2], Veselý P.[2]

[1]Institute of Physical Engineering (IPE), Faculty of Mechanical Engineering, Brno University of Technology, Brno, Czech Republic, [2]CEITEC - Central European Institute of Technology, Brno University of Technology, Brno, Czech Republic

Email of the presenting author: 213727@vutbr.cz

Live cancer cell lines H1299, A549, and HT1080 in vitro were exposed to selected drugs with a presumed antimigration activity that implies antimetastatic potential and time-lapse examined with holographic incoherent light Quantitive Phase Imaging (hiQPI) by Coherence Controlled Holography Microscopy (CCHM – Q-PHASE by Telight). It is a methodology that directly evaluates the dynamics of morphology, migration, phenotype, and the growth of tumor cells by weighing them.
Eight putative migrastatics, vincristine (VIN, 100 nM) as the positive control, 4-hydroxyacetophenone (4HAP, 4 μM), niclosamide (NICL, 1 μM), belumosudil (BEL, 1 μM), doxycycline (DOXY, 1 mg/ml), pimozide (PIM, 10 μM), midostaurin (MID, 1 μM) and fasudil (FAS, 10 μM) were tested with human non-small cell lung carcinoma cell lines, A549 and H1299, and human fibrosarcoma cell line HT1080, using Ibidi μ-Slide VI 0.4 , for 20 hours recording with an objective lens of 10x0.3 and 20x0.5.
The dynamic of migratory behavior of the whole cell population after medicaments application was evaluated by motility rose graphs. This parameter was measured using an objective 10x0.3 and is amenable to statistical evaluation.
Analysis of morphological changes in living cells was evaluated with Q-PHASE objective lens 20x0.5 to demonstrate apoptosis, necrosis, and division as a warning against the unwanted cytopathogenic activity of the tested medicament though marginal.
Following parameters were set to take hold of rare single cells escaping tested migrastatics inducing slow down of migration capability or even showing stimulation of migration. The position of their circularity symbol in the scatter plot is defined by the meandering index (y) and the Euclidean distance (x), which in the case of the invasive phenotype indicates that the cell has low % circularity, a high meandering index, and a higher Euclidean distance. The additional purpose is to refine the way to the classification of the cancer cell invasive phenotype.

Acknowledgement: This research was supported by the Czech-Bioimaging: National Infrastructure for Biological and Medical Imaging (LM2018129).

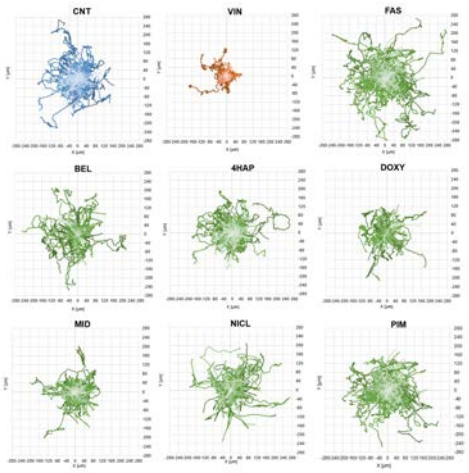

Fig. 1: Fig.1: Motility rose graphs of cell lines HT1080 with eight stative migrastatics. Cell trajectory graphs from hiQPI records. The individual tracks of the 20-hour scan were shifted to a common origin [0,0]. Axis represents distances in µm and using by objective lens 10x0.3.

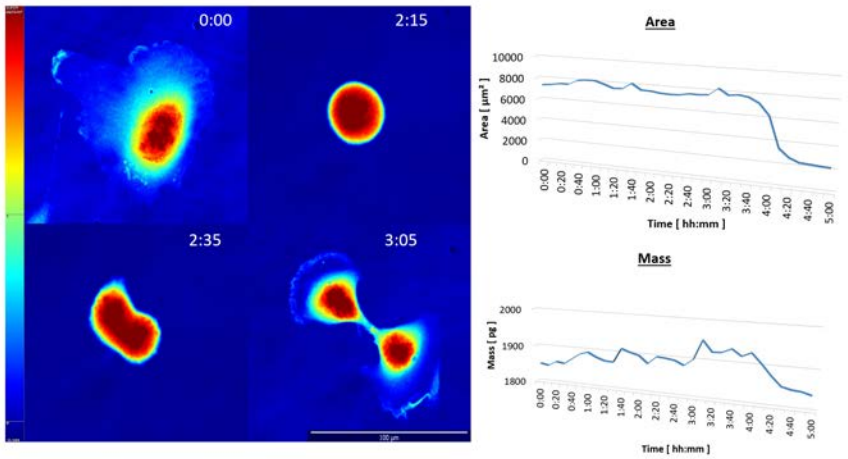

Fig. 2: Fig. 2. Demonstration of cell A549 during its division by CCHM without any medicaments. An objective of 20x0.5. Graphs of the dependence of the changes of area and mass of the analyzed cell on time.

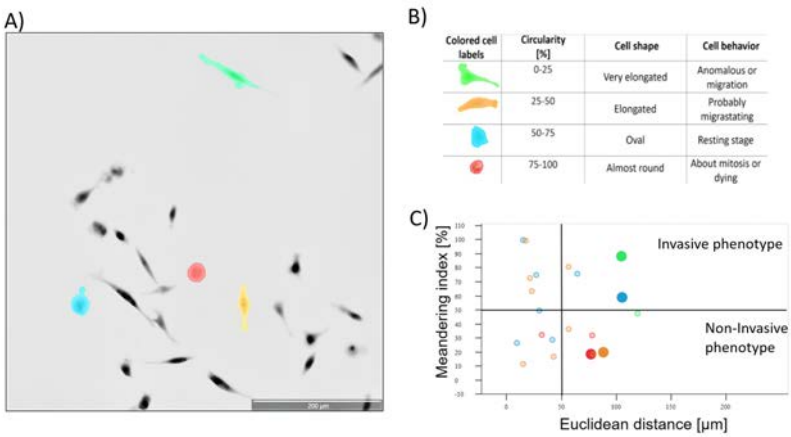

Fig. 3: Fig.3: Phenotype analysis of the four HT1080 cells after NICL. A) and B) Cells are color-coded according to the percentage of circularity in the table using by software SophiQ. An objective lens 10x0.3. C) The scatter plot of the HT1080 cells with color cell segmentation based on circularity value and graph evaluating the type of phenotype.

Type of presentation: Poster

Late-P-3052 FROM A CLINICAL CASE TO A GENERAL METHODOLOGY TO ANALYZE PROSTHETIC JOINT FAILURE BY MICRO- AND NANO-CHARACTERIZATION OF INTRA-TISSUE WEAR DEBRIS

Tarter S.[1], Gialanella S.[1], Tessarolo F.[2], Nollo G.[1,2], Molinari A.[3]

[1]Department of Industrial Engineering, University of Trento, 38123, Trento, Italy , [2]BIOtech Center for Biomedical Technologies, Department of Industrial Engineering, Università di Trento, 38123 Trento, Italy, [3]Division of Othopaedics and Traumatology at Fiemme Hospital, A.P.S.S. , Trento, Italy

Email of the presenting author: stefania.tarter@unitn.it

Between 4% and 8% of shoulder, hip and knee joint prostheses requires premature replacement due to septic or aseptic loosening. A major reason for these phenomena is the presence of debris at the tissue-implant interface, often observed at the revision surgery.

We report on the composition and micro-nanostructure of intra-tissue debris in periprosthetic tissue samples obtained at revision surgery. We focused on a clinical case of metal-on-polymer total hip prosthesis revision following misalignment of the acetabular components, drastic wearing of the polyethylene acetabular insert and final impingement and wear of the and Cr-Co base alloy femoral head on the Ti-6Al-4V acetabular cup.

The purpose of the study is to outline, starting from an extremely complex and specific case, a general modus operandi for the analysis of intra-tissue wear debris originated at joint prostheses.

Five micron thick sections of paraffin-embedded periprosthetic tissues were deposited on 0.2 micron polyurethane filter membranes and tissues were partially digested using a KOH solution to expose intra-tissue debris.
Debris and explanted prosthetic components were analysed by Scanning Electron Microscopy (SEM) collecting secondary and backscattered electron signals. Elemental composition was investigated by Energy Dispersive X-rays Spectroscopy (EDXS).

This multi-technique approach, allows to obtain compositional data and microstructural features of the debris, reporting about the tribological processes originating the debris and their subsequent aggregation-compartimentalization within tissue and cellular structures.

The methodology for understanding and identifying the tribological phenomena underlying debris production is discussed, including also the mechanisms of biological interaction between the prosthesis fragments and the surrounding biological environment. The results achieved so far lay the foundation for further methodological studies that delve into the best digestive techniques to adopt for isolating intra-tissue debris microscopy samples, with possible application in nanotoxicology or simulation-based studies in nanotribology that may deepen the understanding of debris generation mechanisms.

[1] N. Espallargas, A. Fischer, A. Igual Muñoz, S. Mischler, M.A. Wimmer, *In-situ generated tribomaterial in metal/metal contacts: Current understanding and future implications for implants* Biotribology 10 (2017) 42–50

[2]ASTM F561 − 19 (2022), *Standard Practice for Retrieval and Analysis of Medical Devices and Associated Tissues and Fluids*

[3] ASTM F1877 – 05 (2005), *Standard Practice for Characterization of Particles*

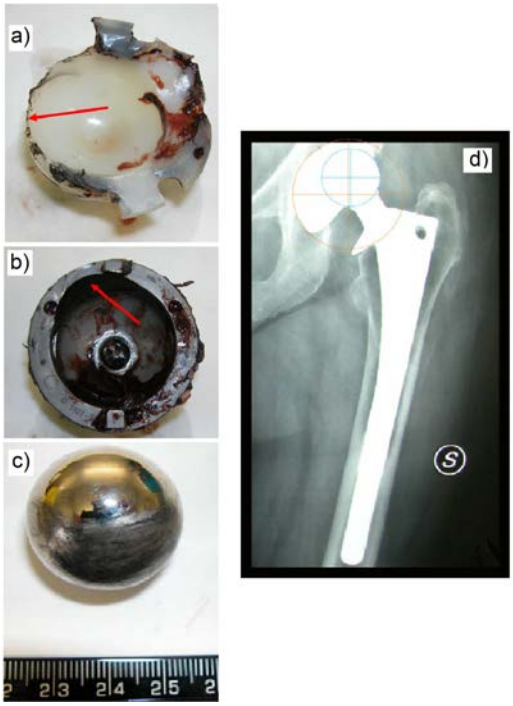

Fig. 1: Components of the implant removed from clinical case RO008: polyethylene insert (a), Ti acetabular cup (b), Cr-Co metal head (c).
The arrows in (a) and (b) highlight the areas of wear.
Pre-implantation X-ray of patient, with schematic of the displacement of the prosthesis, obtained by AUTOCAD technique for evaluation of implant wear (d).

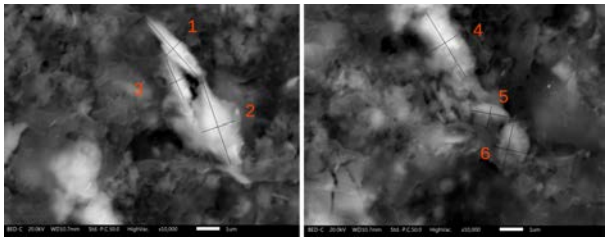

Fig. 3: Example of axis length characterization of titanium particles, identified in the collected BED images. The lengths of the two axes were used to calculate the Aspect Ratio for each particle.

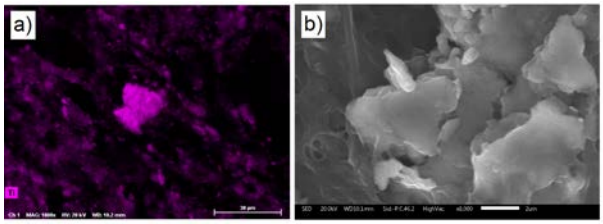

Fig. 2: Images of an agglomerate of Ti particles in partially digested body tissue:
a) EDXS full-field map revealing the presenxe of Ti
B) detail of the agglomerate at higher magnification (SEM image obtainde with Secondary Electrons Detector)

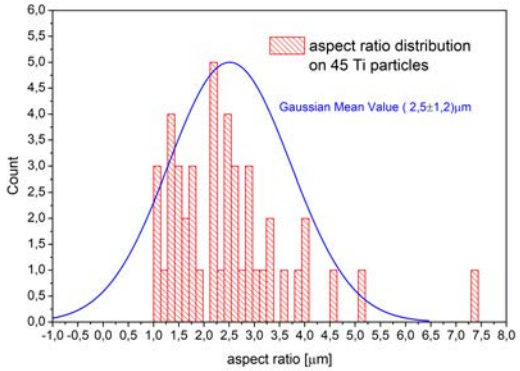

Fig. 4: The identified Ti particles have an Average Aspect Ratio of (2.5±1.2)µm.
Their morphology is granular, irregular and rather elongated. Their surfaces are rough.

Type of presentation: Poster

Late-P-3047 An Alternative Approach For The EELS Analysis Of Noble Gases

Savaci U.[1], Turan S.[1,2]

[1]Department of Materials Science and Engineering, Eskisehir Technical University, Eskisehir, Turkey, [2]Ceramic Research Center Inc., Eskişehir, 26555, Turkey

Email of the presenting author: sturan@eskisehir.edu.tr

Electron energy loss spectroscopy (EELS) is one of the most important analysis technique in transmission electron microscopy (TEM) to obtain not only qualitative and quantitative chemical information but also structural data. In the literatüre, it was reported that, EELS analysis of noble gases can only be carried out by the use of limited methods. These methods were; (i) formation of gas bubbles filled with noble (He-50keV, Ne-500keV) gas within metallic alloys [1], (ii) bombardment of semiconductor structures with high energy (50keV) ions [1] and (iii) thin film deposition of noble gases on an amorphous layer [2]. In this study, a new and alternative low energy methodology have been proposed for the EELS analysis of noble gases by the use of nanoplatelets such as hexagonal boron nitride (hBN) and graphene (GNP). Nanoplatelets have been extensively used in many applications, due to their superior properties, either in pure state or as an additive to form composites. The addition of these particles to engineering ceramic matrices resulted in improved electrical or mechanical properties [3]. In addition to the use of nanoplatelets as a property modifier, these particles can also be used to capture noble gas ions, thus EELS analysis of these elements. For this purpose, in this study, crystallographically oriented hBN particles were in-situ synthesized within SiC matris by the use of spark plasma sintering method. The low energy (<6 keV) Ar ions were then embedded within the planes of crystallographically oriented hBN particles and EELS analysis of the embedded Ar ions were carried out by using TEM. The results showed that Ar ions can be embedded within the planes of nanoplatelets at relatively low energies without any damage, if the specific orientation relation condition with respect to ion beam was satisfied. EELS results showed that Ar-M2-3 edge at 12 eV was present in the particles which satisfy the orientation relation condition. In this study, results showed that low energy Ar ion embedding to the nanoplatelets can be used for the EELS analysis of Ar element, furthermore this methodology can also be used for the EELS analysis of other noble gases embedded at low energies without damaging the crystalline structure.

[1] Marochov, N. and P.J. Goodhew, A comparison of the growth of helium and neon bubbles in nickel. Journal of Nuclear Materials, 1988. 158: p. 81-86.
[2] Colliex, C. and B. Jouffrey, Pertes d'énergie dans des couches minces de gaz solidifiés. J. Phys. France, 1971. 32(5-6): p. 461-466.
[3] Yılmaz, Z., et al., The effect of in-situ formed layered hBN on the machinability and mechanical properties of SPS sintered SiC. Ceramics International, 2022. 48(1): p. 1047-1056.

Acknowledgement: Authors would like to thank Dr.Zuhal YILMAZ for SiC-hBN samples, Anadolu University (grant numbers: 1406F321 and 1504F168) and TUBITAK 2211 Ph.D scholarship.

Type of presentation: Poster

Late-P-3048 Effect of in-situ Conductive TiB2 3D-Network Structure on the Thermoelectric Properties of SiC

Arslan K.[1], Ozer S. C.[1], Savaci U.[1], Turan S.[1,2]

[1]Department of Materials Science and Engineering, Eskisehir Technical University, Eskisehir, Turkey, [2]Ceramic Research Center Inc., Eskişehir, Turkey

Email of the presenting author: sturan@eskisehir.edu.tr

Among the research for cleaner, sustainable and productive energy resources, thermoelectric (TE) materials have increasing interest due to their potential application areas such as power plants, automobiles, and computers1. The thermoelectric phenomenon is established on the basis of the direct conversion of heat energy to electrical energy using the Seebeck effect. The efficiency of a TE material can be calculated by using the dimensionless figure of merit (ZT) formulation:
$ZT=(S^2\sigma T)/\kappa$
where S, σ, κ, and T are the Seebeck coefficient, electrical conductivity, thermal conductivity and temperature, respectively. SiC ceramics possess remarkable properties such as excellent thermal stability and oxidation resistance, low cost of manufacturing, and relatively good Seebeck coefficient, making SiC a promising material for TE applications for elevated temperatures2. On the other hand, increasing the electrical conductivity and concurrently reducing the thermal conductivity of SiC is one of the main challenges to improve the TE performance of the material. The aim of this study is to improve the TE efficiency of SiC by surrounding the matrix granules with a mixture of B4C and TiC powders, resulting in in-situ synthesised TiB2 3D network structures. Microstructures of sintered SiC composites were investigated by using scanning electron microscopy (SEM) techniques. Phase contents of the sintered samples were analysed by the X-ray diffraction (XRD) method. Temperature-dependent electrical conductivities and Seebeck coefficients of the samples were measured between 323 and 923 K using the 4-point probe technique. Thermal conductivity values of the samples were calculated by measuring the thermal diffusivity, heat capacity and density, by laser flash technique, differential scanning calorimetry (DSC) and Archimedes method, respectively. Electrical conductivity values increased dramatically with increasing TiB2 content due to the continuous conductive network structure as seen in Figure 1. Thermal conductivity decreased as well, due to increased phonon scattering with increased grain boundary density. In spite of these positive outcomes, it has been observed that ZT deteriorates with increasing TiB2 content due to the n-type behaviour and low Seebeck coefficient of TiB2. The sample with 1% TiB2 addition showed higher ZT than monolithic SiC, whereas samples with 5 to 10% TiB2 showed higher ZT at temperatures below 523 K.

[1] M. H. Elsheikh, et al. Renewable and Sustainable Energy Reviews, 2014, 30, 337.
[2] Y. Okamoto, et al. J. Jpn. Soc. Powder Metall., 2008, 56, 477.

Acknowledgement: The authors would like to express their gratitude to TUBITAK for their financial support for the project numbered 219M514.

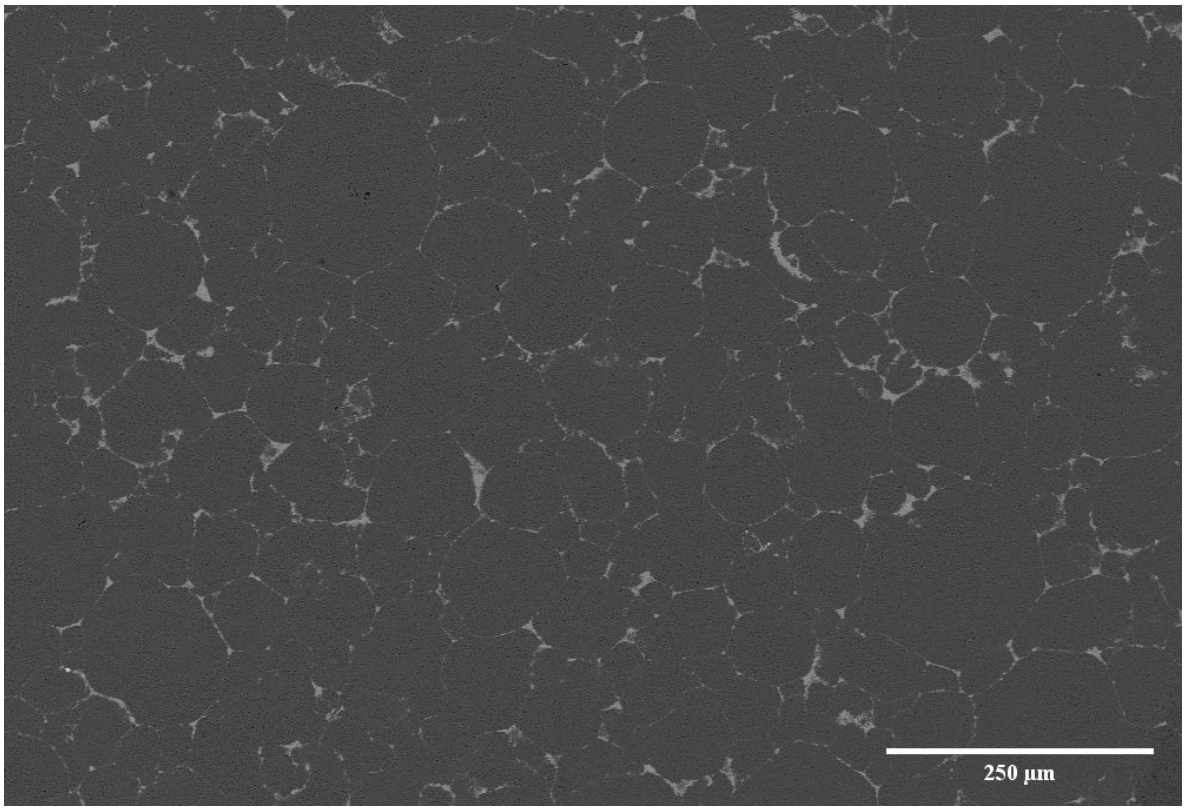

Fig. 1: BSE-SEM images of SiC samples with 5% TiC addition.

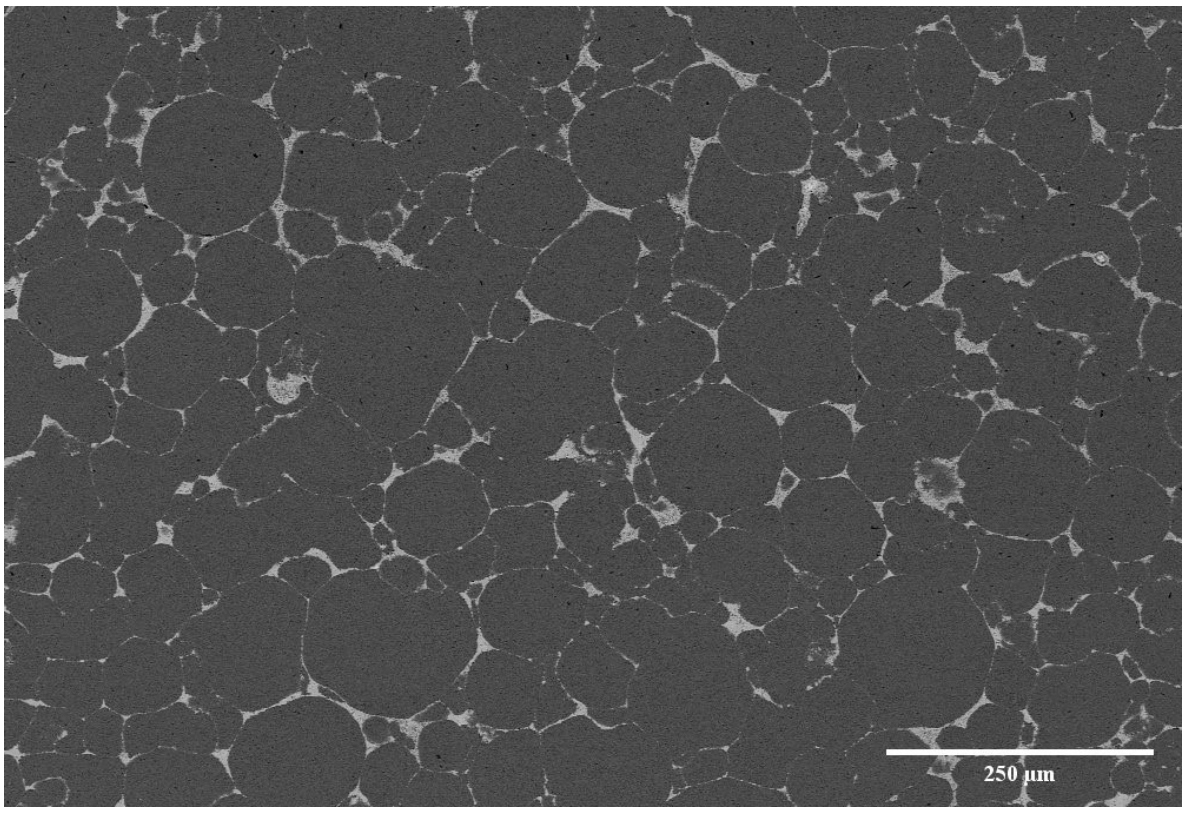

Fig. 2: BSE-SEM images of SiC samples with 10% TiC addition.

Type of presentation: Poster

Late-P-3058 Identification of Tumor Cells Behavior Changes by Holographic Incoherent Quantitative Phase Imaging Focuses on Migrastatics

Horák T.[1], Šuráňová M.[1,2], Netíková I. Š.[3], Zicha D.[1,2], Juzova V.[2], Chmelík R.[1,2], Veselý P.[2]

[1]Institute of Physical Engineering (IPE), Faculty of Mechanical Engineering, Brno University of Technology, Brno, Czech Republic, [2]CEITEC—Central European Institute of Technology, Brno University of Technology, Brno, Czech Republic, [3]General University Hospital in Prague, Department of Clinical Pharmacology and Pharmacy, Prague, Czech Republic.

Email of the presenting author: horto2310@gmail.com

The methodology and process of migrastatic discovery can be effectively supported by dynamic time-lapse analysis of living human cancer cells using Holographic Incoherent Quantitative Phase Imaging (hiQPI) obtained by Coherence-Controlled Holographic Microscopy (CCHM). This approach allows for the most reliable and accurate automatic cell segmentation and monitors morphological and positional changes over time. Analysis of the rate of migration of individual cells and evaluation of their migratory behavior is a key aspect of building a better-personalized medicine because current anticancer therapy does not include a specific category of anti-invasive and antimetastatic drugs.
We present a methodology that can quickly evaluate the viability of tumor cells and evaluate morphological and dynamic changes in tumor cell behavior in migrastatic treatment with CCHM.
Live cancer cell line HT1080 was exposed to selected drugs with a presumed antimigration activity that implies antimetastatic potential. Four such migrastatic - niclosamide (NICL, 1 μM), belumosudil (BEL, 1μM), midostaurin (MID, 1 μM) and vincristine (VIN, 100 nM) as the positive control were tested.
The 20 hours - timelapse method with an objective lens of 10x0.3 was chosen for a gradual regeneration test 3-times after gaps w/s treatment achieving thus the long-term monitoring of tumor cell activity. The dynamic of migratory behavior of the whole cell population after medicaments application was evaluated by motility rose graphs and time graphs, which allow us to monitor parameters such as circularity, dry mass, and area over time.

Tomáš Slabý, Pavel Kolman, Zbyněk Dostál, Martin Antoš, Martin Losťák, and Radim Chmelík, "Off-axis setup taking full advantage of incoherent illumination in coherence-controlled holographic microscope," Opt. Express 21 , 14747-14762 (2013)

Gandalovičová A, Rosel D, Fernandes M, Veselý P, Heneberg P, Čermák V, Petruželka L, Kumar S, Sanz-Moreno V, Brábek J. Migrastatics-Anti-metastatic and Anti-invasion Drugs: Promises and Challenges. Trends Cancer. 2017 Jun;3(6):391-406. doi: 10.1016/j.trecan.2017.04.008. PMID: 28670628; PMCID: PMC5482322.

Acknowledgement: This research was supported by the Czech-Bioimaging: National Infrastructure for Biological and Medical Imaging (LM2018129).

Index of Authors

Abdellaoui L.

MS6-O-2514 Correlative Microscopy Techniques for Defect-Property-Correlation of Thermoelectric Materials (page 487)

Abellan P.

IM5-O-2894 Graphene liquid cell for electron microscopy analysis of nanoparticle interaction with solutions: the case of titanium oxide nanoparticles and phosphates (page 123)

IM7-O-2888 Imaging the Hard-Soft Bone Interface in near native conditions using Cryo FIB/SEM (page 177)

Aberl J.

MS4-P-2610 In situ TEM annealing: comparison of thin GeSn layers grown by MBE and CVD (page 440)

Abrescia N. G.

LS2-P-2658 Preliminary morphological characterization of Schmallenberg Virus using cryo-TEM techniques (page 225)

Ačkar L.

LS3-P-2654 NME6, a member of the NME/NDPK family resides in complexes at the interface of mitochondrial inner membrane and matrix (page 247)

Adamski Z.

LS6-P-2881 A beetle that was a flea. Comparison of morphological adaptations in external parasites among Coleoptera and Siphonaptera, using light and scanning electron mic (page 300)

Addadi L.

LS7-P-2625 Characterization of the Growth Plate-Bone Interphase Region Using Cryo-FIB SEM 3D Volume Imaging (page 320)

Addadi L.

IM5-P-2782 Cryo Volume Imaging: from cell nucleus to extracellular structure. (page 146)

Aebischer A.

LS2-P-2658 Preliminary morphological characterization of Schmallenberg Virus using cryo-TEM techniques (page 225)

Agnello S.

MS4-O-2511 Microscopy of CVD grown MoS2 layers compared to layers obtained by the sulphurization of Mo (page 426)

Agudo-Jácome L.

MS1-IN-2503 Quantitative STEM in the diffraction contrast regime (page 323)

Åhlgren E. H.

MS4-P-2660 Noble gas clusters in a graphene sandwich (page 434)

Ahmadian A.

MS1-O-2601 Co-segregation of zinc, carbon and boron in a Σ5 iron grain boundary resolved by correlating atomic resolution STEM, APT and first-principles calculations (page 326)

Ahmed U.

MS2-O-2667 High resolution CT study of microstructure defects behaviour in deformed NiTi prepared by spark plasma sintering (page 377)

Akbari E.

MS1-O-2796 An in-depth investigation of liquid metal embrittlement sensitive grain boundaries in TBF steels (page 328)

Akdemir A. S.

LS3-P-2704 Vitamin-D combined with resveratrol regulates islets hemostasis, β-cell regeneration, ER-stress and inflammation in fructose-fed diet/STZ-induced diabetic rats (page 255)

Akgul B.

LS5-IN-3045 Quantitative super-resolution microscopy of nuclear antigens in cells and tissues (page 283)

Albaret T.

MS7-O-2700 Analysis of dislocation evolution in cerium oxide nanocubes using in situ transmission electron microscopy (page 511)

Alfreider M.

MS7-IN-2739 Fracture behavior of distinct interfaces of two intermetallic TiAl alloys (page 515)

Alishahi M.

MS7-P-2687 Impact behaviour of the industrially sputtered AlCrN coatings prepared using cathodic arc glow discharge (page 519)

Altingövde O.

IM1-O-2853 4D-STEM Imaging for 3D Stereo Reconstruction by Deep Learning Neural Networks (page 16)

Ambrož O.

MS1-P-2794 Phase determination of dual phase steel using backscattered electron images and image analysis techniques (page 335)

MS1-P-2826 Deep learning powered optical microscopy for steel research (page 347)

Amodeo J.

MS7-O-2700 Analysis of dislocation evolution in cerium oxide nanocubes using in situ transmission electron microscopy (page 511)

Amouyal Y.

MS6-O-2514 Correlative Microscopy Techniques for Defect-Property-Correlation of Thermoelectric Materials (page 487)

Amunts K.

IM2-O-2612 Proof-of-Concept study for high-resolution correlative multimodal imaging and big data of a mouse brain (page 35)

LS6-O-2615 The BUILD project: A multi-modal cross-scale approach to reveal characteristics of the human brain’s nested connectome (page 297)

Anapali M.

LS3-P-2704 Vitamin-D combined with resveratrol regulates islets hemostasis, β-cell regeneration, ER-stress and inflammation in fructose-fed diet/STZ-induced diabetic rats (page 255)

Andrieu S.

MS4-P-2640 Transmission electron microscopy characterization of quasicrystal approximants in SrTiO3 thin films grown on Pt(111)/Al2O3(0001) (page 448)

Aoyama T.

IM6-IN-2513 Contrast mechanism and its application at landing energy near 0 eV in super low energy SEM (page 155)

Arenal R.

MS5-O-2808 Towards Laser-Induced Tuning of Plasmonic Response in High Aspect-Ratio Au Nanowires: A STEM/EELS study (page 460)

MS5-P-2844 In-situ Carbon Nanoribbon Formation by TEM Manipulation of a C59N Derivative (page 480)

Argun Kurum G.

LS3-P-2756 Differentiation of DDR1+ progenitor cells into β cells in neonatal rat diabetes (page 257)

Arndt M.

MS1-O-2796 An in-depth investigation of liquid metal embrittlement sensitive grain boundaries in TBF steels (page 328)

Arslan K.

Late-P-3048 Effect of in-situ Conductive TiB2 3D-Network Structure on the Thermoelectric Properties of SiC (page 537)

Artiglia L.

MS6-P-2963 Self-sustained oscillatory dynamics of ethylene to syngas by operando SEM and XPS (page 495)

Axer M.

IM2-O-2612 Proof-of-Concept study for high-resolution correlative multimodal imaging and big data of a mouse brain (page 35)

LS6-O-2615 The BUILD project: A multi-modal cross-scale approach to reveal characteristics of the human brain’s nested connectome (page 297)

Ayanzadeh A.

IM1-IN-2752 Image Analysis Workflow for Phase-Contrast Optical Microscopy Images (page 20)

Aydemir D.

LS3-P-2704 Vitamin-D combined with resveratrol regulates islets hemostasis, β-cell regeneration, ER-stress and inflammation in fructose-fed diet/STZ-induced diabetic rats (page 255)

Babinský T.

MS1-P-2722 Microstructural changes in DLMS IN939 due to low cycle fatigue investigated by advanced electron microscopy. (page 345)

Bábor P.

IM5-O-2703 In-situ Microscopy of Catalytic Oxidation of CO to CO2 over Platinum Surfaces. (page 128)

Bačovský J.

IM4-O-2867 Concept of Aberration Corrected Low-Voltage Transmission Electron Microscope (page 114)

IM6-O-2862 Delta – Detector for Scanning Electron Mirror Microscopy (page 163)

Bačovský V.

LS4-P-2839 Comparison of CLMS and super-resolution techniques to study meiotic proteins in plants (page 270)

Bafti A.

MS5-P-2858 Study of barium titanate on transparent titania nanotubes arrays (page 472)

MS6-O-2793 Morphology related energy losses in small molecule organic solar cells (page 493)

Bajletić M. I.

LS1-IN-3008 Transmission electron microscopy in research and diagnostics - new challenges in the omics era (page 201)

Bajtošová L.

MS5-O-2567 Ni-Ti Nanoparticles for Self-Propagating Reactions (page 462)

MS7-O-2565 Al nanocrystalline thin film deformation by in situ TEM and molecular dynamics (page 513)

Balboni R.

IM4-O-2591 Enhancing Electron Computational Ghost Imaging Using Artificial Neural Networks (page 116)

Bale H.

IM5-P-2530 In situ deformation observation via EBSD and EDS during high temperature tensile testing (page 140)

Balıkçi M.

IM1-IN-2752 Image Analysis Workflow for Phase-Contrast Optical Microscopy Images (page 20)

Balog M.

MS1-P-2689 Thermal stability of hydro-extruded aluminum: Judging the distribution of amorphous and crystalline aluminum-oxide via plasmon mapping. (page 363)

Balos S.

MS1-P-2855 Morphological characterization of mill scales iron oxides products by SEM (page 355)

MS1-P-2856 Characterization of oil pipe weld localized corrosion and perforation (page 357)

Bartosik M.

MS4-O-2859 Atomic insights into the structures and properties of nitride thin films (page 415)

Bártová B.

MS5-P-2618 Uranium reduction by magnetite – mechanism of UO2 formation monitored by STEM, SAED and STEM-EELS (page 464)

Basak S.

IM7-O-2590 FIB-based lamella preparation for in-situ TEM gas experiment (page 176)

Batra N.

IM5-O-2894 Graphene liquid cell for electron microscopy analysis of nanoparticle interaction with solutions: the case of titanium oxide nanoparticles and phosphates (page 123)

Beer M.

LS2-P-2658 Preliminary morphological characterization of Schmallenberg Virus using cryo-TEM techniques (page 225)

Behrens M.

MS4-O-2580 Nanoscale characterization of van der Waals-bonded GeTe/Sb2Te3 phase-change memory superlattices grown by pulsed laser deposition (page 424)

Bekel A.

LS7-O-2698 3D reconstruction of hydrated samples at the sub-micrometer scale using Liquid-Phase STEM at low voltage (page 315)

Bele M.

MS6-P-2682 Studying electrochemical degradation in nanocatalysts with identical location STEM (page 503)

Belevich I.

LS7-IN-3024 Chasing for efficacy: from manual and semi-automatic tools to convolutional neural networks in segmentation of microscopy datasets (page 307)

Belli Ö. N.

IM1-IN-2752 Image Analysis Workflow for Phase-Contrast Optical Microscopy Images (page 20)

Benčan A.

MS7-P-2540 Mechanical response of domain walls in lead-free ferroelectrics (page 525)

Bencan Golob A.

MS6-IN-2562 In situ Scanning Transmission Electron Microscopy of Lead-Free Ferroelectrics with Atomic Resolution (page 486)

MS6-P-2621 Influence of sample tilt on measurement of atomic column position (page 498)

Benda A.

IM2-O-2791 Correlative super-resolution and electron microscopy in plant samples (page 39)

Berecki M.

IM2-P-2800 Microscopy and in vivo imaging in aid for visualization of dynamic processes - example of brain damage evolution after ischemic brain stroke (page 68)

IM7-P-2801 Washing brains or how to see things more clearly - Fluorescence microscopy can be used for visualization of blood vessels and neurons in the cleared mouse brain (page 181)

Berger C.

MS2-O-2843 Quantifying Ordering Phenomena at the Atomic Scale in Rare Earth Oxide Ceramics via EELS Elemental Mapping (page 371)

Bernatova S.

IM2-P-2699 Assembly for Cryo-SEM/Raman Microspectroscopy sample analysis (page 63)

Bernier-Latmani R.

MS5-P-2618 Uranium reduction by magnetite – mechanism of UO2 formation monitored by STEM, SAED and STEM-EELS (page 464)

Beronská N.

MS1-P-2624 Modification of native oxide on magnesium powders for enhanced corrosion resistance (page 349)

Beronská N.

MS1-P-2589 Microstructural characterization of sintered Iron and observation of oxides reduction after different conditions of sintering process (page 350)

Bertoni G.

IM4-O-2506 Measurement and Correction of Phase Aberrations in Scanning Transmission Microscopy by Artificial Neural Networks (page 112)

Besley E.

MS3-O-2846 Sub-Ångstrom resolution imaging of 2D conjugated metal-organic frameworks enabled by unconventional resilience against electron radiation (page 389)

Bettge D.

IM1-O-2679 Integrated topographic SEM imaging for software assisted fractography (page 18)

Biagi G.

LS7-O-2827 Deep learning approaches for electron tomography under limited data acquisition conditions (page 313)

Bideau J. L.

IM7-O-2888 Imaging the Hard-Soft Bone Interface in near native conditions using Cryo FIB/SEM (page 177)

Bilušić T.

LS2-P-2585 Expression of the enzyme myrosinase type 1 in the root, the stem and the leaves of the plant nasturtium (Tropaeolum majus L.) (page 229)

Bílý T.

LS2-P-2665 3D organization of photosynthetic membranes in cells of photosynthetic bacterium Sediminicoccus rosea (page 224)

LS5-O-2521 Novel method for simultaneous visualization and distinguishing Au nanoparticles on both sides of the ultrathin sections using low-energy STEM and BSE in HRSEM (page 285)

LS5-O-2715 Correlative cathodoluminescence scanning electron microscopy for identification of cellular structures within vitrified samples at low electron beam energies (page 289)

Birinji A.

LS3-P-2504 Effect of arsenic(III) oxide on reproductive organs of female mices (page 242)

Bočina I.

LS2-P-2585 Expression of the enzyme myrosinase type 1 in the root, the stem and the leaves of the plant nasturtium (Tropaeolum majus L.) (page 229)

Boese M.

IM5-P-2530 In situ deformation observation via EBSD and EDS during high temperature tensile testing (page 140)

IM7-P-2607 Imaging of uncoated samples with secondary electrons using in lens detection under optimum conditions – ‘sweet spot’ imaging (page 179)

Bogataj U.

LS3-P-2643 Insect midgut epithelium architecture – focus on gut stem cells in larvae and adults (page 259)

Bogdanović L.

LS1-IN-3008 Transmission electron microscopy in research and diagnostics - new challenges in the omics era (page 201)

Bohač M.

MS5-P-2858 Study of barium titanate on transparent titania nanotubes arrays (page 472)

Bohačiaková D.

IM7-P-2790 Nanopatterned Surface for Super-resolution Microscopy localization of Cell Interactions (page 191)

Bohak C.

LS7-O-2860 Volume electron microscopy and automatic segmentation of intracellular compartments in the urinary bladder umbrella cells (page 310)

Böhme C.

Late-P-3032 Electron beam irradiation induced Brownmillerite – perovskite phase transition in La_{0.6} Sr_{0.4} CoO_{3-ð} (page 530)

BOLMONT M.

MS6-O-2577 Study of failure modes in two sulphide-based solid electrolyte all-solid-state batteries via in-situ SEM (page 489)

Boltje D. B.

IM2-O-2719 Integrated light-4D-STEM: from fluorescence microscopy and sample thickness mapping to powder diffraction analysis (page 45)

Bolvardi H.

MS7-P-2687 Impact behaviour of the industrially sputtered AlCrN coatings prepared using cathodic arc glow discharge (page 519)

Bondarev A.

MS4-O-2792 Insights into tribology of TMD-based coatings from TEM experiments (page 423)

Boneš E.

LS7-O-2860 Volume electron microscopy and automatic segmentation of intracellular compartments in the urinary bladder umbrella cells (page 310)

Borkovcová K.

MS1-P-2623 Aluminothermally reduced deep-sea concretion and its phase structure (page 341)

Borštnar P.

MS2-O-2578 Atomic-scale characterization of polytypic defects in Li0.33La0.56TiO3 (page 373)

Bosch C.

IM2-O-2938 From mammalian neuronal circuits to synapses: correlative multimodal imaging using hard X-rays (page 51)

Boshra H.

LS2-P-2658 Preliminary morphological characterization of Schmallenberg Virus using cryo-TEM techniques (page 225)

Botsch B.

IM1-O-2679 Integrated topographic SEM imaging for software assisted fractography (page 18)

Bouchal P.

Plenary-3049 Mature Holographic Microscopy (page 10)

Bozkurt E.

LS3-IN-2605 Time-lapse microscopy reveals induction of entosis by TRAIL signalling (page 234)

Brabec C. J.

MS6-IN-2913 Can the Wet Win the Bet? The case of Energy Harvesting and Storage (page 491)

Brabencova S.

LS3-P-2924 Active transcription-translation coupling at the early translation elongation stages (page 248)

Brehm M.

MS4-P-2610 In situ TEM annealing: comparison of thin GeSn layers grown by MBE and CVD (page 440)

Brinek A.

MS2-P-2706 Multimodal and multi-resolution approach for defects analysis on the example of Additively Manufactured healable aluminium alloy (page 380)

Brix F.

MS4-P-2640 Transmission electron microscopy characterization of quasicrystal approximants in SrTiO3 thin films grown on Pt(111)/Al2O3(0001) (page 448)

Brontvein O.

IM3-P-2650 Investigation the origin of TiO2 nanoparticles in human pancreas using different TEM techniques (page 84)

Brozyniak A.

IM3-P-2631 Precession Electron Diffraction and its Applications in Semiconductor Heterostructures (page 86)

Brugger-Hatzl M.

IM2-O-2635 3D-Nanoprinting of Magnetic Force Microscopy Tips (page 37)

Bublík A.

LS4-P-2673 Integrated Fluorescent Light Microscope (iFLM) - Applications Workflows (page 279)

Bucher E.

MS2-O-2843 Quantifying Ordering Phenomena at the Atomic Scale in Rare Earth Oxide Ceramics via EELS Elemental Mapping (page 371)

Buchta D.

LS3-O-2732 Endosome disruption enables enteroviruses to reach cell cytoplasm (page 236)

Bueno-Villoro R.

MS6-O-2514 Correlative Microscopy Techniques for Defect-Property-Correlation of Thermoelectric Materials (page 487)

Bukvišová K.

MS4-P-2750 In-situ observation of 2D materials growth on liquid substrates (page 432)

Bukvisova K.

MS5-P-2539 Real-time observation of vapor transport synthesis in the scanning electron microscope (page 466)

Burg T. P.

IM2-P-2604 Towards correlating light and electron microscopy with immersion objectives at cryogenic temperatures (page 57)

IM5-IN-2999 Microsystems for in situ cryofixation and correlative cryomicroscopy (page 127)

LS4-P-2645 High-stability stage for cryo-light microscopy with immersion objectives (page 272)

Bürger D.

MS1-IN-2503 Quantitative STEM in the diffraction contrast regime (page 323)

Burnett T. L.

LS6-O-2639 Correlative 3D imaging workflow using X-ray micro-computed tomography and laser plasma focussed ion beam electron microscopy on biological soft tissues (page 298)

Buršík J.

MS1-P-2657 Incommensurate structure of τ phase in the Al-Cu-Zn system (page 337)

MS5-P-2851 Effect of Nanoparticle Size on Phase Stability in ZrO2 System (page 468)

MS5-P-2685 CeO2 Morphology Study – Nanoparticles Prepared by Electron Beam Evaporation (page 483)

Buršíková V.

MS7-P-2840 Characterization of Mechanical and Topographical Properties of Nanocomposite Thin Films with Plasma Polymer Structure (page 523)

Burtscher M.

MS7-IN-2739 Fracture behavior of distinct interfaces of two intermetallic TiAl alloys (page 515)

Busch R.

IM7-O-2593 High-Throughput TEM Sample Preparation with iNotch Technique (page 174)

Butorin S. M.

MS5-P-2618 Uranium reduction by magnetite – mechanism of UO2 formation monitored by STEM, SAED and STEM-EELS (page 464)

Čalkovský V.

MS5-O-2501 Plasmon resonances in biocompatible nanoparticles (page 458)

Camacho R.

IM2-O-2612 Proof-of-Concept study for high-resolution correlative multimodal imaging and big data of a mouse brain (page 35)

LS6-O-2615 The BUILD project: A multi-modal cross-scale approach to reveal characteristics of the human brain’s nested connectome (page 297)

Camara O.

IM7-O-2590 FIB-based lamella preparation for in-situ TEM gas experiment (page 176)

Cannas M.

MS4-O-2511 Microscopy of CVD grown MoS2 layers compared to layers obtained by the sulphurization of Mo (page 426)

Carton F.

LS1-IN-2535 Hyaluronic acid based nanoparticles are suitable carriers to muscle cells: the ultrastructural evidence (page 195)

Casares A.

IM2-O-2612 Proof-of-Concept study for high-resolution correlative multimodal imaging and big data of a mouse brain (page 35)

IM2-P-2633 Multimodal Microscopy for very large 2D & 3D Imaging (page 54)

LS6-O-2615 The BUILD project: A multi-modal cross-scale approach to reveal characteristics of the human brain’s nested connectome (page 297)

Castro M.

MS1-P-2624 Modification of native oxide on magnesium powders for enhanced corrosion resistance (page 349)

Cechmanek M.

LS1-P-2817 Tundra TEM: tool ‘easy of use’ for new commers to Cryo EM (page 209)

Čeh M.

IM7-P-2822 Conventional TEM preparation of thin films by the method of "cross-section" (page 180)

LS2-O-2690 The use of SEM imaging and elemental mapping in the research of artificial bacterial aggregates (page 220)

Čépe K.

Late-P-3026 In-situ analysis of graphene and its derivatives by combined SEM/AFM method (page 527)

Čermák J.

MS1-P-2794 Phase determination of dual phase steel using backscattered electron images and image analysis techniques (page 335)

MS1-P-2826 Deep learning powered optical microscopy for steel research (page 347)

Cervinkova M.

LS1-P-2817 Tundra TEM: tool ‘easy of use’ for new commers to Cryo EM (page 209)

Ćetković H.

LS3-P-2654 NME6, a member of the NME/NDPK family resides in complexes at the interface of mitochondrial inner membrane and matrix (page 247)

Chaluvadi S. K.

IM5-P-2628 Field induced oxygen vacancy migration in anatase thin films studied by in situ biasing TEM (page 138)

MS4-O-2594 Orbital mapping of the LaAlO3-TiO2 interface by STEM-EELS (page 417)

MS4-O-2619 Aberration-Corrected STEM Characterisation of Mn-ion Structural Displacements in La0.7Sr0.3MnO3 Interfacial Dead-Layers (page 419)

Charvátová Campbell A.

IM6-IN-2598 Ab initio study of angle-resolved electron spectroscopy of graphene (page 156)

MS7-P-2840 Characterization of Mechanical and Topographical Properties of Nanocomposite Thin Films with Plasma Polymer Structure (page 523)

Chauvier A.

LS3-P-2916 Translation initiation stages of coupled transcription-translation (page 246)

Chen S. Y.

IM2-P-2604 Towards correlating light and electron microscopy with immersion objectives at cryogenic temperatures (page 57)

IM5-IN-2999 Microsystems for in situ cryofixation and correlative cryomicroscopy (page 127)

Chen Z.

IM5-P-2797 Real-time atomic-resolution observation of coherent twin boundary migration in rocksalt transition metal nitride (page 136)

MS4-O-2859 Atomic insights into the structures and properties of nitride thin films (page 415)

Chirazi A.

MS2-P-2706 Multimodal and multi-resolution approach for defects analysis on the example of Additively Manufactured healable aluminium alloy (page 380)

Chmelík R.

Plenary-3049 Mature Holographic Microscopy (page 10)

Late-P-3055 Non-Invasive Imaging Method for Evaluating Effect of Migrastatics on Tumor Cells In Vitro Based on Coherence - Controlled Holographic Microscopy (page 532)

Late-P-3058 Identification of Tumor Cells Behavior Changes by Holographic Incoherent Quantitative Phase Imaging Focuses on Migrastatics (page 539)

Chmelíková E.

MS1-P-2656 The Use of Titanothermic Reduction for Processing of Deep-Sea Nodules (page 339)

Chorvát D.

IM1-P-2686 Deep-learning model for automatic detection of cells in microscopy images (page 24)

Ciancio R.

IM5-P-2628 Field induced oxygen vacancy migration in anatase thin films studied by in situ biasing TEM (page 138)

MS4-O-2594 Orbital mapping of the LaAlO3-TiO2 interface by STEM-EELS (page 417)

MS4-O-2619 Aberration-Corrected STEM Characterisation of Mn-ion Structural Displacements in La0.7Sr0.3MnO3 Interfacial Dead-Layers (page 419)

Cieslar M.

MS5-O-2567 Ni-Ti Nanoparticles for Self-Propagating Reactions (page 462)

MS7-O-2565 Al nanocrystalline thin film deformation by in situ TEM and molecular dynamics (page 513)

Citterbardová K.

LS4-P-2673 Integrated Fluorescent Light Microscope (iFLM) - Applications Workflows (page 279)

Ciuciu P.

LS7-O-2827 Deep learning approaches for electron tomography under limited data acquisition conditions (page 313)

Čižmar T.

MS5-P-2858 Study of barium titanate on transparent titania nanotubes arrays (page 472)

Čižmár T.

LS4-O-2597 High-resolution structural and functional deep brain imaging using holographic endo-microsocpy (page 266)

LS4-P-2606 Fluorescence confocal imaging via holographic endo-microscopy (page 278)

Clemens H.

MS7-IN-2739 Fracture behavior of distinct interfaces of two intermetallic TiAl alloys (page 515)

Cmiel V.

LS3-P-2805 Mitochondria activity evaluation under osmotic conditions (page 244)

LS6-P-2849 Monitoring the endothelial cell behavior during flow stress induction using digital holographic microscopy. (page 304)

Cojocaru-Mirédin O.

MS6-O-2514 Correlative Microscopy Techniques for Defect-Property-Correlation of Thermoelectric Materials (page 487)

Colbea C.

MS6-P-2963 Self-sustained oscillatory dynamics of ethylene to syngas by operando SEM and XPS (page 495)

Condello M.

LS1-P-2519 Electron microscopy in the study of nanomaterial-cell interaction: involvement of autophagy (page 206)

Condurache O.

MS6-IN-2562 In situ Scanning Transmission Electron Microscopy of Lead-Free Ferroelectrics with Atomic Resolution (page 486)

Conlan A. P.

IM2-O-2520 In-situ electrical analysis with EBIC STEM: developments and applications (page 33)

Cooley I.

MS3-O-2846 Sub-Ångstrom resolution imaging of 2D conjugated metal-organic frameworks enabled by unconventional resilience against electron radiation (page 389)

Cooper D.

IM2-O-2520 In-situ electrical analysis with EBIC STEM: developments and applications (page 33)

Copie O.

MS4-P-2640 Transmission electron microscopy characterization of quasicrystal approximants in SrTiO3 thin films grown on Pt(111)/Al2O3(0001) (page 448)

Coroianu A. M.

LS7-O-2632 What does SARS-CoV-2 do to the lungs – what can 3D electron microscopy tell us (page 312)

Cottet C.

LS3-P-2654 NME6, a member of the NME/NDPK family resides in complexes at the interface of mitochondrial inner membrane and matrix (page 247)

Csanádi T.

MS7-P-2603 Nanohardness and toughness of multicomponent TiNbVTaZrHf-N coatings deposited by reactive DC magnetron sputtering and High Target Utilization Sputtering (page 521)

Čunderlíková B.

IM1-P-2686 Deep-learning model for automatic detection of cells in microscopy images (page 24)

Curran P.

MS7-O-2644 Automated In-Situ Mechanical Testing of heavily textured Ti 6Al 4V to Obtain High Spatial and Temporal Resolution Strain Maps (page 509)

Cyran N.

IM2-P-2850 Imidazole-osmium reduces elution of lipids from cryofixed rat hepatic tissue for correlative TEM/NanoSIMS analysis (page 55)

Dadosh T.

LS4-O-2587 Localization of Bacteria in Tumor Cells using Correlative Light and Electron Microscopy (page 268)

Damborský J.

IM7-P-2790 Nanopatterned Surface for Super-resolution Microscopy localization of Cell Interactions (page 191)

Damjanovic D.

MS6-IN-2562 In situ Scanning Transmission Electron Microscopy of Lead-Free Ferroelectrics with Atomic Resolution (page 486)

Daneu N.

MS2-O-2578 Atomic-scale characterization of polytypic defects in Li0.33La0.56TiO3 (page 373)

Daňhel A.

MS5-O-2501 Plasmon resonances in biocompatible nanoparticles (page 458)

Daniel B.

IM6-O-2820 Time-of-Flight Spectrometer for Low Landing Energies (page 160)

IM6-P-2599 Effective IMFP of thin samples via the time-of-flight method (page 168)

Daniel J.

MS7-P-2687 Impact behaviour of the industrially sputtered AlCrN coatings prepared using cathodic arc glow discharge (page 519)

Dao R.

IM2-P-2527 AFM-in-SEM solution for correlative microscopy in material sciences (page 65)

DAVOISNE C.

MS6-O-2577 Study of failure modes in two sulphide-based solid electrolyte all-solid-state batteries via in-situ SEM (page 489)

De Felipe J.

IM2-O-2612 Proof-of-Concept study for high-resolution correlative multimodal imaging and big data of a mouse brain (page 35)

LS6-O-2615 The BUILD project: A multi-modal cross-scale approach to reveal characteristics of the human brain’s nested connectome (page 297)

de Kloe R.

MS1-P-2923 Reconstructing parent microstructures from EBSD based orientation measurements (page 333)

de la Mata M.

MS3-P-2819 STEM damage of Acrylic-based Materials for Stereolithography: Degradation Mechanism (page 403)

De la Peña F.

MS3-P-2834 Low Dose Transmission Electron Microscopy Imaging on Sensitive Colloidal Covalent-Organic Frameworks (page 398)

De Rubeis M.

LS1-P-2518 Ultrastructure analysis in the male reproductive system of different mammals exposed to ionizing radiation after the Fukushima accident: a comparative study (page 208)

Dearg M.

MS5-P-2982 Classification of Metal Nanoclusters Using Convolutional Neural Networks (page 470)

Deev D.

LS2-O-2690 The use of SEM imaging and elemental mapping in the research of artificial bacterial aggregates (page 220)

Dehm G.

MS1-O-2601 Co-segregation of zinc, carbon and boron in a Σ5 iron grain boundary resolved by correlating atomic resolution STEM, APT and first-principles calculations (page 326)

Dellby N.

IM4-P-2584 Simplified electron vortex generator with aberration correction (page 118)

Demo G.

LS3-P-2916 Translation initiation stages of coupled transcription-translation (page 246)

LS3-P-2924 Active transcription-translation coupling at the early translation elongation stages (page 248)

Depciuch J.

LS6-O-2627 In-situ observations of metal nanoparticles interactions with living cells, in liquid environments directly in the Nanolive 3D CX-A microscope (page 294)

MS7-O-2694 Liquid cell TEM electrodeposition of PtNi alloy nanoparticle film (page 517)

Descloux A. C.

LS4-IN-3001 Combining Super-resolution Optical Fluctuation Imaging (SOFI) With Structure Illumination and 3D Imaging (page 264)

Dienemann C.

IM2-P-2604 Towards correlating light and electron microscopy with immersion objectives at cryogenic temperatures (page 57)

Dienstleder M.

IM5-P-2628 Field induced oxygen vacancy migration in anatase thin films studied by in situ biasing TEM (page 138)

IM7-IN-2701 Rise to the occasion – high quality sample preparation for high resolution TEM (page 170)

Ding Z.

IM3-IN-3015 Pushing at the limits of low-dose in 4D-STEM and electron ptychography (page 74)

Divitini G.

MS1-O-2765 Rejuvenation/relaxation in bulk metallic glasses: high-resolution transmission electron microscopy study (page 332)

MS6-P-2847 Are FIB-prepared hybrid perovskite cross-sections still luminescent? (page 497)

Dlouhý A.

MS1-IN-2503 Quantitative STEM in the diffraction contrast regime (page 323)

Dluhoš J.

MS6-O-2505 Multi-scale, high-resolution, time-resolved residual stress in laser-welded Eurofer97 using plasma focused ion beam-digital image correlation method (page 494)

Dolezal V.

LS1-P-2817 Tundra TEM: tool ‘easy of use’ for new commers to Cryo EM (page 209)

Dolinšek J.

MS1-O-2857 Correlative electron microscopy and magnetism of CoCrFeNiZr high-entropy allos (page 330)

Dolník M.

LS4-P-2673 Integrated Fluorescent Light Microscope (iFLM) - Applications Workflows (page 279)

Dominko R.

MS6-P-2806 Advanced STEM insights into atomic and electronic structure evolution of corncob-derived hard carbon anode materials for sustainable sodium-ion batteries (page 506)

Donik Č.

MS1-P-2852 Influence of melting and AM-SLM processing on microtexture of Fe-Si soft magnetic materials – Is one-step manufacturing of electrical steels possible? (page 359)

Donoghue J. M.

IM5-O-2649 Integration of EBSD acquisition into fully automated in-situ thermo-mechanical testing for high temporal and spatial resolution (page 125)

LS6-O-2639 Correlative 3D imaging workflow using X-ray micro-computed tomography and laser plasma focussed ion beam electron microscopy on biological soft tissues (page 298)

MS7-O-2644 Automated In-Situ Mechanical Testing of heavily textured Ti 6Al 4V to Obtain High Spatial and Temporal Resolution Strain Maps (page 509)

Đorđević A.

LS1-IN-3008 Transmission electron microscopy in research and diagnostics - new challenges in the omics era (page 201)

Dostál Z.

Plenary-3049 Mature Holographic Microscopy (page 10)

Doulab R. A.

LS1-O-2870 Evaluation of elements impurities in drugs according to pharmacopoeia by use FESEM-EDS technique. (page 204)

Downing C.

IM6-O-2572 The Retrofittable Photoelectron Source: A Potential Improvement to Low Voltage SEM Imaging (page 158)

Dramicanin M.

MS1-P-2856 Characterization of oil pipe weld localized corrosion and perforation (page 357)

Dražić G.

MS6-P-2682 Studying electrochemical degradation in nanocatalysts with identical location STEM (page 503)

Drazic G.

MS6-IN-2562 In situ Scanning Transmission Electron Microscopy of Lead-Free Ferroelectrics with Atomic Resolution (page 486)

MS6-P-2621 Influence of sample tilt on measurement of atomic column position (page 498)

Dražič G.

MS2-O-2578 Atomic-scale characterization of polytypic defects in Li0.33La0.56TiO3 (page 373)

Drev S.

IM7-P-2822 Conventional TEM preparation of thin films by the method of "cross-section" (page 180)

Drnovšek A.

MS7-P-2540 Mechanical response of domain walls in lead-free ferroelectrics (page 525)

Dubiel B.

Late-P-3036 Microstructural analysis of Inconel 625 superalloy manufactured by laser powder bed fusion with remelting (page 528)

Ducati C.

MS6-P-2847 Are FIB-prepared hybrid perovskite cross-sections still luminescent? (page 497)

Dufour R.

MS5-O-2808 Towards Laser-Induced Tuning of Plasmonic Response in High Aspect-Ratio Au Nanowires: A STEM/EELS study (page 460)

Dumesnil K.

MS4-P-2640 Transmission electron microscopy characterization of quasicrystal approximants in SrTiO3 thin films grown on Pt(111)/Al2O3(0001) (page 448)

Dupák L.

IM5-P-2833 Cryogenic Sample Holder with Electrical Contacts for UHV SEM/SPM (page 142)

IM5-P-2845 Low conductive thermal insulation pad with high mechanical stiffness (page 152)

MS1-P-2813 Microanalyses for a better understanding of active soldering processes (page 367)

Durinova E.

IM7-P-2818 Distribution of staining agents in samples of mice soft tissues prepared for Serial Block Face SEM. (page 189)

Ďurinová E.

IM2-O-2571 Combining Light, Raman, and Electron Microscopy in Imaging Viral Factories of Avian Reovirus (page 31)

LS5-O-2715 Correlative cathodoluminescence scanning electron microscopy for identification of cellular structures within vitrified samples at low electron beam energies (page 289)

Ďuriš M.

Plenary-3049 Mature Holographic Microscopy (page 10)

Dürr S.

IM2-P-2850 Imidazole-osmium reduces elution of lipids from cryofixed rat hepatic tissue for correlative TEM/NanoSIMS analysis (page 55)

Dušková-Smrčková M.

MS3-IN-2935 Synergy of Scanning Electron and Light Microscopies in Visualization of Swollen Hydrogels and Effect of Hydrogel Parameters on the Image: Artifacts and Reality (page 384)

Duvail J. L.

MS5-O-2808 Towards Laser-Induced Tuning of Plasmonic Response in High Aspect-Ratio Au Nanowires: A STEM/EELS study (page 460)

Dvořáčková M.

IM2-O-2791 Correlative super-resolution and electron microscopy in plant samples (page 39)

Dvořák P.

MS1-P-2656 The Use of Titanothermic Reduction for Processing of Deep-Sea Nodules (page 339)

MS1-P-2623 Aluminothermally reduced deep-sea concretion and its phase structure (page 341)

Dybal J.

MS3-P-2653 Simple, fast and reliable method of UHMWPE accelerated aging (page 393)

Dziurowitz N.

IM2-O-2528 Analysis of sampled airborne particles by correlative microscopy (page 47)

Ebad-Allah J.

MS4-O-2647 Ordered electronic states in 2D quantum materials: Imaging effects of hydrostatic pressure at the atomic scale. (page 409)

Eberle A. L.

IM2-O-2612 Proof-of-Concept study for high-resolution correlative multimodal imaging and big data of a mouse brain (page 35)

LS6-O-2615 The BUILD project: A multi-modal cross-scale approach to reveal characteristics of the human brain’s nested connectome (page 297)

Eckert J.

MS6-P-2630 Combined Microstructural and Electrochemical Studies of Sputtered Ni Thin Layers as Catalysts for Hydrogen Evolution Reaction (page 501)

Ederer M.

IM1-O-2681 Precipitate size estimation using image feature detection (page 22)

MS4-O-2594 Orbital mapping of the LaAlO3-TiO2 interface by STEM-EELS (page 417)

Edwards T.

MS7-IN-2666 Recent advances in in-situ SEM nanomechanical testing: extreme temperatures, ultra-high strain rates, in-situ electron diffraction and digital image correlation (page 508)

Ehret V.

IM2-P-2850 Imidazole-osmium reduces elution of lipids from cryofixed rat hepatic tissue for correlative TEM/NanoSIMS analysis (page 55)

Eichel R. A.

IM7-O-2590 FIB-based lamella preparation for in-situ TEM gas experiment (page 176)

Eklund A. S.

LS4-IN-2948 A DNA origami-based biointerface for probing the spatial requirements of cell surface receptor triggering (page 262)

Erdem Y. S.

IM1-IN-2752 Image Analysis Workflow for Phase-Contrast Optical Microscopy Images (page 20)

Ewels C.

MS5-P-2844 In-situ Carbon Nanoribbon Formation by TEM Manipulation of a C59N Derivative (page 480)

Ezati M.

LS3-P-2805 Mitochondria activity evaluation under osmotic conditions (page 244)

Fabbro R.

IM5-IN-2617 Do you know the relevant conditions for in situ heating experiments in the TEM? (page 121)

Fairclough S. M.

IM3-P-2683 Scanning electron diffraction study of TiFeAl alloy microstructure (page 100)

Fajkus J.

IM2-O-2791 Correlative super-resolution and electron microscopy in plant samples (page 39)

Faul N. A.

IM2-P-2604 Towards correlating light and electron microscopy with immersion objectives at cryogenic temperatures (page 57)

IM5-IN-2999 Microsystems for in situ cryofixation and correlative cryomicroscopy (page 127)

LS4-P-2645 High-stability stage for cryo-light microscopy with immersion objectives (page 272)

Fernandez-Rodriguez J.

IM2-O-2612 Proof-of-Concept study for high-resolution correlative multimodal imaging and big data of a mouse brain (page 35)

LS6-O-2615 The BUILD project: A multi-modal cross-scale approach to reveal characteristics of the human brain’s nested connectome (page 297)

Ferrer Orri J.

MS6-P-2847 Are FIB-prepared hybrid perovskite cross-sections still luminescent? (page 497)

Fikar J.

MS7-O-2565 Al nanocrystalline thin film deformation by in situ TEM and molecular dynamics (page 513)

Filić V.

LS6-O-2622 Oscillatory intracellular patterns of the small GTPase Rac1 (page 292)

Filimonenko V.

IM1-P-2696 Project „Pattern“ – an online tool for spatial analysis of immunolabeling in electron microscopy (page 27)

IM7-O-2668 Faster Cryo TEM lamella preparation using optimised conditions and advanced workflows (page 173)

Filimoněnko V.

IM7-P-2676 IMG Electron Microscopy Core Facility (page 192)

Fintová S.

MS1-P-2722 Microstructural changes in DLMS IN939 due to low cycle fatigue investigated by advanced electron microscopy. (page 345)

Fiorenza P.

MS4-O-2511 Microscopy of CVD grown MoS2 layers compared to layers obtained by the sulphurization of Mo (page 426)

Fisslthaler E.

IM3-IN-2626 Challenges in the characterization of complex nanomaterials with analytical STEM (page 80)

IM5-IN-2617 Do you know the relevant conditions for in situ heating experiments in the TEM? (page 121)

IM5-P-2651 The power of speed: DED EELS for analytical in situ TEM (page 132)

IM7-IN-2701 Rise to the occasion – high quality sample preparation for high resolution TEM (page 170)

Fitzek H.

IM2-O-2563 Correlative Raman microscopy, SEM and EDS – The combined evaluation of a whole sample mapping of a Chelyabinsk meteorite fragment (page 43)

LS2-O-2684 Pyroplastics: A new Approach (page 222)

Fodor F.

LS2-P-2532 Utilization of haematite nanoparticles by a flavin mediated iron uptake of roots (page 227)

FOLASTRE N.

MS6-O-2577 Study of failure modes in two sulphide-based solid electrolyte all-solid-state batteries via in-situ SEM (page 489)

Fořt T.

IM5-P-2833 Cryogenic Sample Holder with Electrical Contacts for UHV SEM/SPM (page 142)

MS4-P-2669 Energy-based calibration for quantitative STEM measurements and comparison with 2D-PAD (page 450)

Fournée V.

MS4-P-2640 Transmission electron microscopy characterization of quasicrystal approximants in SrTiO3 thin films grown on Pt(111)/Al2O3(0001) (page 448)

Frabboni S.

IM4-O-2591 Enhancing Electron Computational Ghost Imaging Using Artificial Neural Networks (page 116)

Franco S. D.

MS4-O-2511 Microscopy of CVD grown MoS2 layers compared to layers obtained by the sulphurization of Mo (page 426)

Francolini M.

LS7-IN-2525 Moving from two- to three- dimensional electron microscopy in the study of the synapse: a lesson from neurodevelopmental disorder models (page 309)

Franek M.

IM2-O-2791 Correlative super-resolution and electron microscopy in plant samples (page 39)

Frank L.

MS1-P-2588 Real Time Observation of strain in the SEM copper sample (page 351)

Friedrich H. B.

MS5-P-2832 Exploring the role of fuel on the microstructure of VOx/MgO powders prepared using solution combustion synthesis (page 478)

Fua P.

IM1-O-2853 4D-STEM Imaging for 3D Stereo Reconstruction by Deep Learning Neural Networks (page 16)

Fulin P.

MS3-P-2653 Simple, fast and reliable method of UHMWPE accelerated aging (page 393)

Funes-Hernando D.

MS5-O-2808 Towards Laser-Induced Tuning of Plasmonic Response in High Aspect-Ratio Au Nanowires: A STEM/EELS study (page 460)

Fürnsinn C.

IM2-P-2850 Imidazole-osmium reduces elution of lipids from cryofixed rat hepatic tissue for correlative TEM/NanoSIMS analysis (page 55)

Füzik T.

LS3-O-2732 Endosome disruption enables enteroviruses to reach cell cytoplasm (page 236)

LS6-P-2802 In situ cryo-electron tomography of enterovirus cell entry (page 303)

Gabalcová Z.

MS1-P-2589 Microstructural characterization of sintered Iron and observation of oxides reduction after different conditions of sintering process (page 350)

Gaberšček M.

MS6-P-2682 Studying electrochemical degradation in nanocatalysts with identical location STEM (page 503)

Gajdosova V.

MS3-P-2653 Simple, fast and reliable method of UHMWPE accelerated aging (page 393)

Gajić D. M.

LS3-P-2799 Beneficial effects of ferroptosis inhibitor ferrostatin-1 on pancreatic islets in streptozotocin-induced diabetes (page 251)

LS3-P-2812 Beneficial effects of ferroptosis inhibitor ferrostatin-1 in diabetes-induced liver damage (page 253)

Gajović A.

MS5-P-2858 Study of barium titanate on transparent titania nanotubes arrays (page 472)

Gajović S.

IM2-P-2800 Microscopy and in vivo imaging in aid for visualization of dynamic processes - example of brain damage evolution after ischemic brain stroke (page 68)

IM7-P-2801 Washing brains or how to see things more clearly - Fluorescence microscopy can be used for visualization of blood vessels and neurons in the cleared mouse brain (page 181)

Gal A.

IM5-P-2782 Cryo Volume Imaging: from cell nucleus to extracellular structure. (page 146)

Galeckas A.

MS5-P-2568 Structural and optical investigation of Fe-ZnO nanoarchitectures: from inversion domain boundaries to ZnO/ZnFe2O4 heterostructures (page 474)

Galvani A.

IM7-O-2888 Imaging the Hard-Soft Bone Interface in near native conditions using Cryo FIB/SEM (page 177)

Gammer C.

MS6-P-2630 Combined Microstructural and Electrochemical Studies of Sputtered Ni Thin Layers as Catalysts for Hydrogen Evolution Reaction (page 501)

MS7-IN-2739 Fracture behavior of distinct interfaces of two intermetallic TiAl alloys (page 515)

Ganeeva G.

IM1-O-2853 4D-STEM Imaging for 3D Stereo Reconstruction by Deep Learning Neural Networks (page 16)

Garbowski T.

LS6-O-2615 The BUILD project: A multi-modal cross-scale approach to reveal characteristics of the human brain’s nested connectome (page 297)

García-Fernández J.

MS5-P-2568 Structural and optical investigation of Fe-ZnO nanoarchitectures: from inversion domain boundaries to ZnO/ZnFe2O4 heterostructures (page 474)

Gardian Z.

LS3-O-2608 Bacteriophage φ8 protein P4, an RNA binding molecular motor, studied by Cryo-EM (page 237)

Gardiner A. T.

LS2-P-2665 3D organization of photosynthetic membranes in cells of photosynthetic bacterium Sediminicoccus rosea (page 224)

Garel J.

IM1-O-2569 Making Every Electron Count: Improving STEM Quantification, Speed, and Data Throughput with Solid State Detectors and Pulse Counting Hardware (page 14)

Gatalo M.

MS6-P-2682 Studying electrochemical degradation in nanocatalysts with identical location STEM (page 503)

Gatti M.

LS1-P-2518 Ultrastructure analysis in the male reproductive system of different mammals exposed to ionizing radiation after the Fukushima accident: a comparative study (page 208)

Gaudry E.

MS4-P-2640 Transmission electron microscopy characterization of quasicrystal approximants in SrTiO3 thin films grown on Pt(111)/Al2O3(0001) (page 448)

Gault B.

MS1-O-2601 Co-segregation of zinc, carbon and boron in a Σ5 iron grain boundary resolved by correlating atomic resolution STEM, APT and first-principles calculations (page 326)

MS6-O-2514 Correlative Microscopy Techniques for Defect-Property-Correlation of Thermoelectric Materials (page 487)

Gautron E.

IM5-O-2894 Graphene liquid cell for electron microscopy analysis of nanoparticle interaction with solutions: the case of titanium oxide nanoparticles and phosphates (page 123)

Gelardi F. M.

MS4-O-2511 Microscopy of CVD grown MoS2 layers compared to layers obtained by the sulphurization of Mo (page 426)

Gemmi M.

IM3-P-2579 3D Electron Diffraction on Ferroelectric Perovskites. (page 88)

Geoffroy V.

IM7-O-2888 Imaging the Hard-Soft Bone Interface in near native conditions using Cryo FIB/SEM (page 177)

Gheysen J.

MS2-P-2706 Multimodal and multi-resolution approach for defects analysis on the example of Additively Manufactured healable aluminium alloy (page 380)

Ghilardi A.

LS7-IN-2525 Moving from two- to three- dimensional electron microscopy in the study of the synapse: a lesson from neurodevelopmental disorder models (page 309)

Gholina A.

LS6-O-2639 Correlative 3D imaging workflow using X-ray micro-computed tomography and laser plasma focussed ion beam electron microscopy on biological soft tissues (page 298)

Gholinia A.

IM5-O-2649 Integration of EBSD acquisition into fully automated in-situ thermo-mechanical testing for high temporal and spatial resolution (page 125)

Gialanella S.

Late-P-3052 FROM A CLINICAL CASE TO A GENERAL METHODOLOGY TO ANALYZE PROSTHETIC JOINT FAILURE BY MICRO- AND NANO-CHARACTERIZATION OF INTRA-TISSUE WEAR DEBRIS (page 534)

Giannazzo F.

MS4-O-2511 Microscopy of CVD grown MoS2 layers compared to layers obtained by the sulphurization of Mo (page 426)

Giepmans B. N.

LS5-IN-3002 Multimodal microscopy in Type 1 diabetes research (page 282)

Girman V.

MS7-P-2603 Nanohardness and toughness of multicomponent TiNbVTaZrHf-N coatings deposited by reactive DC magnetron sputtering and High Target Utilization Sputtering (page 521)

Glasnović A.

IM2-P-2800 Microscopy and in vivo imaging in aid for visualization of dynamic processes - example of brain damage evolution after ischemic brain stroke (page 68)

Gloesmann M.

IM2-O-2612 Proof-of-Concept study for high-resolution correlative multimodal imaging and big data of a mouse brain (page 35)

LS6-O-2615 The BUILD project: A multi-modal cross-scale approach to reveal characteristics of the human brain's nested connectome (page 297)

Godec M.

MS1-P-2852 Influence of melting and AM-SLM processing on microtexture of Fe-Si soft magnetic materials – Is one-step manufacturing of electrical steels possible? (page 359)

Gola K.

Late-P-3036 Microstructural analysis of Inconel 625 superalloy manufactured by laser powder bed fusion with remelting (page 528)

Gomes A.

LS4-O-2597 High-resolution structural and functional deep brain imaging using holographic endo-microsocpy (page 266)

Gorley M.

MS6-O-2505 Multi-scale, high-resolution, time-resolved residual stress in laser-welded Eurofer97 using plasma focused ion beam-digital image correlation method (page 494)

Greco G.

MS4-O-2511 Microscopy of CVD grown MoS2 layers compared to layers obtained by the sulphurization of Mo (page 426)

Greer A. L.

MS1-O-2765 Rejuvenation/relaxation in bulk metallic glasses: high-resolution transmission electron microscopy study (page 332)

Griesi A.

IM3-P-2579 3D Electron Diffraction on Ferroelectric Perovskites. (page 88)

Grigorov I. I.

LS3-P-2799 Beneficial effects of ferroptosis inhibitor ferrostatin-1 on pancreatic islets in streptozotocin-induced diabetes (page 251)

LS3-P-2812 Beneficial effects of ferroptosis inhibitor ferrostatin-1 in diabetes-induced liver damage (page 253)

Grillo V.

IM4-IN-2672 Advanced measuring schemes using new electron optics ideas (page 108)

IM4-O-2506 Measurement and Correction of Phase Aberrations in Scanning Transmission Microscopy by Artificial Neural Networks (page 112)

IM4-O-2591 Enhancing Electron Computational Ghost Imaging Using Artificial Neural Networks (page 116)

Grinkevich P.

LS3-O-2608 Bacteriophage φ8 protein P4, an RNA binding molecular motor, studied by Cryo-EM (page 237)

Gröger R.

IM2-P-2544 High-resolution electron beam induced current study of AlN epitaxial layer (page 69)

Grogger W.

IM3-IN-2626 Challenges in the characterization of complex nanomaterials with analytical STEM (page 80)

IM3-P-2510 Phase Analysis of (Li)FePO4 by Selected Area Electron Diffraction in Transmission Electron Microscopy (page 98)

IM5-IN-2617 Do you know the relevant conditions for in situ heating experiments in the TEM? (page 121)

IM5-P-2651 The power of speed: DED EELS for analytical in situ TEM (page 132)

MS2-O-2843 Quantifying Ordering Phenomena at the Atomic Scale in Rare Earth Oxide Ceramics via EELS Elemental Mapping (page 371)

Groiss H.

IM3-P-2631 Precession Electron Diffraction and its Applications in Semiconductor Heterostructures (page 86)

IM5-P-2664 Efficient preparation of MEMS carriers with plan-view specimens: a case study of in situ TEM experiments with thin epitaxial layers (page 134)

MS1-O-2796 An in-depth investigation of liquid metal embrittlement sensitive grain boundaries in TBF steels (page 328)

MS4-P-2610 In situ TEM annealing: comparison of thin GeSn layers grown by MBE and CVD (page 440)

Gruber D.

IM2-P-2850 Imidazole-osmium reduces elution of lipids from cryofixed rat hepatic tissue for correlative TEM/NanoSIMS analysis (page 55)

Gruber M.

MS1-O-2796 An in-depth investigation of liquid metal embrittlement sensitive grain boundaries in TBF steels (page 328)

Grussmayer K. S.

LS4-IN-3001 Combining Super-resolution Optical Fluctuation Imaging (SOFI) With Structure Illumination and 3D Imaging (page 264)

Gryčová L.

IM2-P-2677 Miro proteins and their role in horizontal transfer of mitochondria via tunneling nanotubes in cancer cells (page 67)

Grydin O.

MS1-P-2602 Phase Identification in Twin-Roll Cast Al-Steel Clad Composite (page 343)

Grzęda J.

IM5-O-2542 Transmission electron microscope modification for light-induced in situ imaging of specimens in liquid on example of photodynamic therapy (page 130)

Guerra G. S.

LS2-P-2658 Preliminary morphological characterization of Schmallenberg Virus using cryo-TEM techniques (page 225)

Guim H.

MS1-O-2857 Correlative electron microscopy and magnetism of CoCrFeNiZr high-entropy allos (page 330)

Guo S.

MS1-O-2857 Correlative electron microscopy and magnetism of CoCrFeNiZr high-entropy allos (page 330)

Habart D.

IM1-P-2611 Estimation of Pancreatic Islets Volume from Single Projection. (page 26)

Haberfehlner G.

IM3-O-2555 Tomography of surface phonon polarition fields by electron energy loss spectroscopy (page 82)

IM3-P-2642 Analytical electron tomography of CuNiFe magnetic spinodal alloys (page 90)

MS2-O-2843 Quantifying Ordering Phenomena at the Atomic Scale in Rare Earth Oxide Ceramics via EELS Elemental Mapping (page 371)

Haberfehnler G.

IM3-IN-2626 Challenges in the characterization of complex nanomaterials with analytical STEM (page 80)

Hadraba D.

IM2-P-2691 IPHYS Bioimaging Facility (page 59)

Hage F. S.

Plenary-2901 Recent Progress in High-Resolution Electron Energy Loss Spectroscopy in the Scanning Transmission Electron Microscope (page 4)

Haider H.

IM2-P-2545 Extensive material characterization for series production of 3D printer components (page 71)

Haimov H.

LS7-P-2625 Characterization of the Growth Plate-Bone Interphase Region Using Cryo-FIB SEM 3D Volume Imaging (page 320)

Hájovská Z.

MS1-P-2589 Microstructural characterization of sintered Iron and observation of oxides reduction after different conditions of sintering process (page 350)

MS4-P-2595 Native surface oxide characterization with S/TEM on PM metal powders (page 442)

Hamer D.

IM2-P-2800 Microscopy and in vivo imaging in aid for visualization of dynamic processes - example of brain damage evolution after ischemic brain stroke (page 68)

IM7-P-2801 Washing brains or how to see things more clearly - Fluorescence microscopy can be used for visualization of blood vessels and neurons in the cleared mouse brain (page 181)

Hammer R.

IM2-O-2520 In-situ electrical analysis with EBIC STEM: developments and applications (page 33)

Hampl A.

IM7-P-2790 Nanopatterned Surface for Super-resolution Microscopy localization of Cell Interactions (page 191)

Handschuh S.

IM2-O-2612 Proof-of-Concept study for high-resolution correlative multimodal imaging and big data of a mouse brain (page 35)

LS6-O-2615 The BUILD project: A multi-modal cross-scale approach to reveal characteristics of the human brain’s nested connectome (page 297)

Hanuš J.

MS5-O-2567 Ni-Ti Nanoparticles for Self-Propagating Reactions (page 462)

MS7-O-2565 Al nanocrystalline thin film deformation by in situ TEM and molecular dynamics (page 513)

Hanzelka P.

IM5-P-2838 Effect of thermal radiation on the measurement of the sample holder temperature over the cryogenic range for various types of temperature sensor installations (page 150)

IM5-P-2845 Low conductive thermal insulation pad with high mechanical stiffness (page 152)

Hanzu I.

IM3-P-2510 Phase Analysis of (Li)FePO4 by Selected Area Electron Diffraction in Transmission Electron Microscopy (page 98)

Harcuba P.

MS7-O-2565 Al nanocrystalline thin film deformation by in situ TEM and molecular dynamics (page 513)

Hashemi A.

LS3-P-2805 Mitochondria activity evaluation under osmotic conditions (page 244)

LS6-P-2849 Monitoring the endothelial cell behavior during flow stress induction using digital holographic microscopy. (page 304)

Haslinger P.

IM3-P-2678 Temporal correlations in coherent cathodoluminescence (page 94)

Hassan A. H.

LS3-P-2916 Translation initiation stages of coupled transcription-translation (page 246)

Hatmanstorfer A.

LS7-O-2632 What does SARS-CoV-2 do to the lungs – what can 3D electron microscopy tell us (page 312)

Hauer R.

IM3-O-2555 Tomography of surface phonon polarition fields by electron energy loss spectroscopy (page 82)

Haug K.

MS5-P-2568 Structural and optical investigation of Fe-ZnO nanoarchitectures: from inversion domain boundaries to ZnO/ZnFe2O4 heterostructures (page 474)

Hauschild R.

LS2-IN-2966 Shedding new light on plant biology – automated long-term vertical-stage microscopy at high resolution (page 213)

Havlíček M.

MS7-P-2840 Characterization of Mechanical and Topographical Properties of Nanocomposite Thin Films with Plasma Polymer Structure (page 523)

Havrankova J.

IM7-O-2668 Faster Cryo TEM lamella preparation using optimised conditions and advanced workflows (page 173)

IM7-P-2662 Solutions for preparation and visualization of vitrified biological samples at IMG Electron Microscopy Core Facility (page 193)

Hawlicek V.

LS7-O-2632 What does SARS-CoV-2 do to the lungs – what can 3D electron microscopy tell us (page 312)

Haybäck J.

LS1-O-2804 Neurons and glial cells appear to store and release human brain ferritin at different rates (page 202)

Hébert C.

IM1-O-2853 4D-STEM Imaging for 3D Stereo Reconstruction by Deep Learning Neural Networks (page 16)

Hegrova V.

IM2-P-2527 AFM-in-SEM solution for correlative microscopy in material sciences (page 65)

Hellmeier J.

LS4-IN-2948 A DNA origami-based biointerface for probing the spatial requirements of cell surface receptor triggering (page 262)

Helmberger F. J.

IM6-P-2879 Determination of the inelastic mean free path of electrons in selected Polymers, indenpent from optical data, considering surface excitations (page 165)

Hemmleb M.

IM1-O-2679 Integrated topographic SEM imaging for software assisted fractography (page 18)

Henderson R.

Plenary-3051 The electron cryomicroscopy revolution in structural biology (page 2)

Henrard L.

MS5-O-2808 Towards Laser-Induced Tuning of Plasmonic Response in High Aspect-Ratio Au Nanowires: A STEM/EELS study (page 460)

Henrichs V.

IM2-P-2677 Miro proteins and their role in horizontal transfer of mitochondria via tunneling nanotubes in cancer cells (page 67)

Herak Bosnar M.

LS3-P-2654 NME6, a member of the NME/NDPK family resides in complexes at the interface of mitochondrial inner membrane and matrix (page 247)

Herrera M.

MS3-P-2819 STEM damage of Acrylic-based Materials for Stereolithography: Degradation Mechanism (page 403)

Herten D.

LS4-IN-3001 Combining Super-resolution Optical Fluctuation Imaging (SOFI) With Structure Illumination and 3D Imaging (page 264)

Hesser G.

MS1-O-2796 An in-depth investigation of liquid metal embrittlement sensitive grain boundaries in TBF steels (page 328)

Hilmi I.

MS4-O-2580 Nanoscale characterization of van der Waals-bonded GeTe/Sb2Te3 phase-change memory superlattices grown by pulsed laser deposition (page 424)

Hinterdorfer P.

LS2-O-2638 Borrelia – host interactions: zoom in on the big picture (page 216)

Hiriyur Nagaraj P.

LS3-P-2924 Active transcription-translation coupling at the early translation elongation stages (page 248)

Hjörvarsson B.

MS4-P-2861 Electron tomography for measurement of buried interface roughness in thin films (page 438)

Hlaváček A.

MS5-P-2685 CeO2 Morphology Study – Nanoparticles Prepared by Electron Beam Evaporation (page 483)

Hlavenkova Z.

LS1-P-2817 Tundra TEM: tool ‘easy of use’ for new commers to Cryo EM (page 209)

Hoboth P.

LS5-IN-3045 Quantitative super-resolution microscopy of nuclear antigens in cells and tissues (page 283)

Hodan J.

MS3-P-2653 Simple, fast and reliable method of UHMWPE accelerated aging (page 393)

Hoddinott H. P.

MS5-P-2982 Classification of Metal Nanoclusters Using Convolutional Neural Networks (page 470)

Hodnik N.

MS6-P-2682 Studying electrochemical degradation in nanocatalysts with identical location STEM (page 503)

Hoeche T.

IM7-O-2593 High-Throughput TEM Sample Preparation with iNotch Technique (page 174)

Hofer F.

IM2-O-2563 Correlative Raman microscopy, SEM and EDS – The combined evaluation of a whole sample mapping of a Chelyabinsk meteorite fragment (page 43)

IM3-IN-2626 Challenges in the characterization of complex nanomaterials with analytical STEM (page 80)

MS1-P-2531 Exploring the magnetic microstructure of spinodal alloys with differential phase contrast scanning transmission electron microscopy (DPC-STEM) (page 353)

MS2-O-2843 Quantifying Ordering Phenomena at the Atomic Scale in Rare Earth Oxide Ceramics via EELS Elemental Mapping (page 371)

Hohenester U.

IM3-O-2555 Tomography of surface phonon polarition fields by electron energy loss spectroscopy (page 82)

Holec D.

IM5-P-2797 Real-time atomic-resolution observation of coherent twin boundary migration in rocksalt transition metal nitride (page 136)

MS4-O-2859 Atomic insights into the structures and properties of nitride thin films (page 415)

Hoogenboom J. P.

IM2-O-2719 Integrated light-4D-STEM: from fluorescence microscopy and sample thickness mapping to powder diffraction analysis (page 45)

Horák M.

IM2-P-2502 Magnetic field imaging with electron energy loss spectroscopy based on Babinet's principle (page 60)

MS5-O-2501 Plasmon resonances in biocompatible nanoparticles (page 458)

Horák T.

Late-P-3058 Identification of Tumor Cells Behavior Changes by Holographic Incoherent Quantitative Phase Imaging Focuses on Migrastatics (page 539)

Horáková L.

LS4-P-2839 Comparison of CLMS and super-resolution techniques to study meiotic proteins in plants (page 270)

Hornfeck W.

MS2-IN-3034 Nano crystallography from 3-dimensional electron diffraction: a powerful tool to uncover supergene minerals (page 379)

Horodyský P.

LS5-O-2715 Correlative cathodoluminescence scanning electron microscopy for identification of cellular structures within vitrified samples at low electron beam energies (page 289)

Hošek J.

Late-P-3026 In-situ analysis of graphene and its derivatives by combined SEM/AFM method (page 527)

Hou Y.

MS6-IN-2913 Can the Wet Win the Bet? The case of Energy Harvesting and Storage (page 491)

Hovádková Z.

IM7-P-2790 Nanopatterned Surface for Super-resolution Microscopy localization of Cell Interactions (page 191)

Hovorka M.

LS4-P-2673 Integrated Fluorescent Light Microscope (iFLM) - Applications Workflows (page 279)

Hozak P.

IM1-P-2696 Project „Pattern" – an online tool for spatial analysis of immunolabeling in electron microscopy (page 27)

IM7-O-2668 Faster Cryo TEM lamella preparation using optimised conditions and advanced workflows (page 173)

IM7-P-2662 Solutions for preparation and visualization of vitrified biological samples at IMG Electron Microscopy Core Facility (page 193)

LS5-IN-3045 Quantitative super-resolution microscopy of nuclear antigens in cells and tissues (page 283)

Hrabovský M.

IM7-P-2790 Nanopatterned Surface for Super-resolution Microscopy localization of Cell Interactions (page 191)

Hrebík D.

LS3-O-2732 Endosome disruption enables enteroviruses to reach cell cytoplasm (page 236)

Hreščak J.

LS2-O-2690 The use of SEM imaging and elemental mapping in the research of artificial bacterial aggregates (page 220)

Hrnjić A.

MS6-P-2682 Studying electrochemical degradation in nanocatalysts with identical location STEM (page 503)

Hrtoň M.

IM2-P-2502 Magnetic field imaging with electron energy loss spectroscopy based on Babinet's principle (page 60)

Hrubanova K.

IM2-P-2699 Assembly for Cryo-SEM/Raman Microspectroscopy sample analysis (page 63)

LS2-P-2663 Ultrastructural changes in prokaryotic microorganisms caused by long-term exposure to high salt and copper ion concentrations (page 231)

MS3-P-2828 Visualization of internal morphology of hydrogels based on polyvinyl alcohol in comparison with the indirect method of structural characterization (page 402)

Hrůza D.

IM5-O-2703 In-situ Microscopy of Catalytic Oxidation of CO to CO2 over Platinum Surfaces. (page 128)

Huang C.

IM3-O-2896 A New Approach for 3D Quantitative STEM Using Defocus Corrected Electron Ptychography (page 78)

Huang Y.

MS2-O-2789 Stacking faults dominant strengthening mechanism behind the anomalous hardness variation of TaN/TiN multilayer films (page 375)

Hudoklin S.

LS7-O-2860 Volume electron microscopy and automatic segmentation of intracellular compartments in the urinary bladder umbrella cells (page 310)

Hughes L.

LS7-P-2659 Modern SEM allows high-throughput 2D and 3D analyses on a single platform (page 317)

Huntosova V.

LS4-P-2498 Targeted photobiomodulation of cancer cells at 808 nm may improve efficacy of photodynamic therapy (page 274)

LS4-P-2499 Imaging of autophagic and mitochondrial proteins in 3D spheroids of U87 MG cancer cells during photodynamic therapy mediated with hypericin (page 276)

Huppa J. B.

LS4-IN-2948 A DNA origami-based biointerface for probing the spatial requirements of cell surface receptor triggering (page 262)

Hviščová P.

MS7-P-2603 Nanohardness and toughness of multicomponent TiNbVTaZrHf-N coatings deposited by reactive DC magnetron sputtering and High Target Utilization Sputtering (page 521)

Hyatt N. C.

MS5-P-2618 Uranium reduction by magnetite – mechanism of UO2 formation monitored by STEM, SAED and STEM-EELS (page 464)

Idrobo J. C.

IM2-O-2695 Atomically Sharp Domain Walls in an Antiferromagnet (page 41)

Iheme L. O.

IM1-IN-2752 Image Analysis Workflow for Phase-Contrast Optical Microscopy Images (page 20)

Ishemgulova A.

LS3-O-2732 Endosome disruption enables enteroviruses to reach cell cytoplasm (page 236)
LS6-P-2802 In situ cryo-electron tomography of enterovirus cell entry (page 303)

Ister R.
IM2-P-2800 Microscopy and in vivo imaging in aid for visualization of dynamic processes - example of brain damage evolution after ischemic brain stroke (page 68)

Ivanov Y. P.
MS1-O-2765 Rejuvenation/relaxation in bulk metallic glasses: high-resolution transmission electron microscopy study (page 332)

Jaeger C.
IM2-O-2612 Proof-of-Concept study for high-resolution correlative multimodal imaging and big data of a mouse brain (page 35)
LS6-O-2615 The BUILD project: A multi-modal cross-scale approach to reveal characteristics of the human brain’s nested connectome (page 297)

Jagos J.
LS6-P-2849 Monitoring the endothelial cell behavior during flow stress induction using digital holographic microscopy. (page 304)

Jákl P.
LS4-O-2597 High-resolution structural and functional deep brain imaging using holographic endo-microsocpy (page 266)
LS4-P-2606 Fluorescence confocal imaging via holographic endo-microscopy (page 278)

Jakobi A. J.
IM2-O-2719 Integrated light-4D-STEM: from fluorescence microscopy and sample thickness mapping to powder diffraction analysis (page 45)

JAMALI A.
MS6-O-2577 Study of failure modes in two sulphide-based solid electrolyte all-solid-state batteries via in-situ SEM (page 489)

Janáček J.
IM1-P-2611 Estimation of Pancreatic Islets Volume from Single Projection. (page 26)

Janacek J.
IM1-P-2696 Project „Pattern“ – an online tool for spatial analysis of immunolabeling in electron microscopy (page 27)

Janák M.
IM5-O-2703 In-situ Microscopy of Catalytic Oxidation of CO to CO2 over Platinum Surfaces. (page 128)

Janda P.
MS3-O-2810 Nanobubble-assisted nanostructuring of water-immersed solid surfaces (page 387)

Jandová V.
MS5-P-2680 Latest TEM investigation of nanostructured CoS2 and Co2CuS4 based films with Fenton catalytic properties (page 477)

Janičkovič D.
MS1-P-2702 Phase evolution clarification in Al86Ni8Gd6 amorphous alloy: A spotlight on Al20Ni6Gd4 phase and its peculiarities (page 364)
MS1-P-2803 Modification of local ordering in Fe-B based metallic glasses during long-term room temperature ageing (page 366)

Janjatovic P.
MS1-P-2856 Characterization of oil pipe weld localized corrosion and perforation (page 357)

Janković R. M.

LS1-IN-3008 Transmission electron microscopy in research and diagnostics - new challenges in the omics era (page 201)

Janotová I.

MS1-P-2803 Modification of local ordering in Fe-B based metallic glasses during long-term room temperature ageing (page 366)

Jánský P.

IM4-O-2867 Concept of Aberration Corrected Low-Voltage Transmission Electron Microscope (page 114)

IM6-O-2862 Delta – Detector for Scanning Electron Mirror Microscopy (page 163)

Jaroš A.

IM5-O-2703 In-situ Microscopy of Catalytic Oxidation of CO to CO2 over Platinum Surfaces. (page 128)

Jaroš J.

IM7-P-2790 Nanopatterned Surface for Super-resolution Microscopy localization of Cell Interactions (page 191)

Jašek O.

MS4-P-2609 Imaging of structural deformations of gas-phase synthesized graphene by intermediate energy electrons (page 430)

Javurek J.

IM7-O-2668 Faster Cryo TEM lamella preparation using optimised conditions and advanced workflows (page 173)

LS7-P-2659 Modern SEM allows high-throughput 2D and 3D analyses on a single platform (page 317)

Jelen A.

MS1-O-2857 Correlative electron microscopy and magnetism of CoCrFeNiZr high-entropy allos (page 330)

Jelínková A.

LS2-IN-2966 Shedding new light on plant biology – automated long-term vertical-stage microscopy at high resolution (page 213)

Jensen I. J.

MS5-P-2568 Structural and optical investigation of Fe-ZnO nanoarchitectures: from inversion domain boundaries to ZnO/ZnFe2O4 heterostructures (page 474)

Jezek J.

IM2-P-2699 Assembly for Cryo-SEM/Raman Microspectroscopy sample analysis (page 63)

Jílek M.

MS7-P-2687 Impact behaviour of the industrially sputtered AlCrN coatings prepared using cathodic arc glow discharge (page 519)

Jokitalo E.

LS7-IN-3024 Chasing for efficacy: from manual and semi-automatic tools to convolutional neural networks in segmentation of microscopy datasets (page 307)

Joly-Pottuz L.

MS7-O-2700 Analysis of dislocation evolution in cerium oxide nanocubes using in situ transmission electron microscopy (page 511)

Jones L.

IM1-O-2569 Making Every Electron Count: Improving STEM Quantification, Speed, and Data Throughput with Solid State Detectors and Pulse Counting Hardware (page 14)

IM4-O-2570 A User Adjustable Pole-piece Gap as a Route to Improve the Sustainability of TEM Infrastructure (page 110)

IM6-O-2572 The Retrofittable Photoelectron Source: A Potential Improvement to Low Voltage SEM Imaging (page 158)

Jones N. G.

IM3-P-2683 Scanning electron diffraction study of TiFeAl alloy microstructure (page 100)

Joselevich E.

MS5-P-2539 Real-time observation of vapor transport synthesis in the scanning electron microscope (page 466)

Josić P.

IM2-P-2800 Microscopy and in vivo imaging in aid for visualization of dynamic processes - example of brain damage evolution after ischemic brain stroke (page 68)

Joudi W.

MS4-O-2807 Correlated AFM/STEM study on the Mechanical Stiffness of Defect-Engineered Graphene (page 411)

Jovanović A. Z.

MS6-P-2630 Combined Microstructural and Electrochemical Studies of Sputtered Ni Thin Layers as Catalysts for Hydrogen Evolution Reaction (page 501)

Jovanovič P.

MS6-P-2682 Studying electrochemical degradation in nanocatalysts with identical location STEM (page 503)

Jozefovič P.

MS1-P-2794 Phase determination of dual phase steel using backscattered electron images and image analysis techniques (page 335)

MS1-P-2826 Deep learning powered optical microscopy for steel research (page 347)

Juffmann T.

IM4-IN-2573 Electrons and Light: Ponderomotive Beam Shaping and Optical Near-field Electron Microscopy (page 107)

IM6-O-2496 Imaging optical near-fields using a low energy electron microscope (page 162)

Jullien M.

MS4-P-2640 Transmission electron microscopy characterization of quasicrystal approximants in SrTiO3 thin films grown on Pt(111)/Al2O3(0001) (page 448)

Jungmann R.

LS4-IN-2948 A DNA origami-based biointerface for probing the spatial requirements of cell surface receptor triggering (page 262)

Jungwirth T.

IM2-O-2695 Atomically Sharp Domain Walls in an Antiferromagnet (page 41)

Juraić K.

MS5-P-2858 Study of barium titanate on transparent titania nanotubes arrays (page 472)

Jurásek M.

IM7-P-2790 Nanopatterned Surface for Super-resolution Microscopy localization of Cell Interactions (page 191)

Jurmanová J.

MS4-P-2609 Imaging of structural deformations of gas-phase synthesized graphene by intermediate energy electrons (page 430)

Jůzová V.

Late-P-3055 Non-Invasive Imaging Method for Evaluating Effect of Migrastatics on Tumor Cells In Vitro Based on Coherence - Controlled Holographic Microscopy (page 532)

Juzova V.

Late-P-3058 Identification of Tumor Cells Behavior Changes by Holographic Incoherent Quantitative Phase Imaging Focuses on Migrastatics (page 539)

Kabanov D.

LS6-P-2898 Correlation of Atomic Force Microscopy with other techniques: application on biosamples (page 301)

Kabátová M.

MS7-P-2603 Nanohardness and toughness of multicomponent TiNbVTaZrHf-N coatings deposited by reactive DC magnetron sputtering and High Target Utilization Sputtering (page 521)

Kaberova Z.

MS3-IN-2935 Synergy of Scanning Electron and Light Microscopies in Visualization of Swollen Hydrogels and Effect of Hydrogel Parameters on the Image: Artifacts and Reality (page 384)

Kaczmarczyk O.

IM5-O-2542 Transmission electron microscope modification for light-induced in situ imaging of specimens in liquid on example of photodynamic therapy (page 130)

LS1-O-2543 Antimicrobial photodynamic therapy effects on Gram-negative and Gram-positive bacteria observed using light-induced in-situ TEM (page 197)

Kaftan D.

LS2-P-2665 3D organization of photosynthetic membranes in cells of photosynthetic bacterium Sediminicoccus rosea (page 224)

Kahil K.

LS7-P-2625 Characterization of the Growth Plate-Bone Interphase Region Using Cryo-FIB SEM 3D Volume Imaging (page 320)

Kaiser J.

MS2-P-2706 Multimodal and multi-resolution approach for defects analysis on the example of Additively Manufactured healable aluminium alloy (page 380)

Kaiser U.

MS3-O-2846 Sub-Ångstrom resolution imaging of 2D conjugated metal-organic frameworks enabled by unconventional resilience against electron radiation (page 389)

MS4-O-2837 Optimal acceleration voltage for near-atomic resolution imaging of layer-stacked 2D polymer thin films (page 413)

MS4-O-2842 Thickness dependency of critical dose for extremely beam-sensitive two-dimensional polymer (page 428)

MS4-P-2835 Deep learning pipeline for statistical quantification of amorphous two-dimensional materials (page 436)

Kaiser U. A.

Plenary-3038 Determining and modifying properties of two-dimensional inorganic and organic materials using low-voltage TEM - challenges and solutions (page 6)

Kamšek A.

MS6-P-2682 Studying electrochemical degradation in nanocatalysts with identical location STEM (page 503)

Kapun G.

MS6-P-2806 Advanced STEM insights into atomic and electronic structure evolution of corncob-derived hard carbon anode materials for sustainable sodium-ion batteries (page 506)

Karatodorov S.

MS5-P-2680 Latest TEM investigation of nanostructured CoS2 and Co2CuS4 based films with Fenton catalytic properties (page 477)

Karia D.

LS1-P-2817 Tundra TEM: tool ‘easy of use’ for new commers to Cryo EM (page 209)

Karpushkin E.

MS3-IN-2935 Synergy of Scanning Electron and Light Microscopies in Visualization of Swollen Hydrogels and Effect of Hydrogel Parameters on the Image: Artifacts and Reality (page 384)

Kaščáková B.

IM2-O-2571 Combining Light, Raman, and Electron Microscopy in Imaging Viral Factories of Avian Reovirus (page 31)

LS3-O-2608 Bacteriophage φ8 protein P4, an RNA binding molecular motor, studied by Cryo-EM (page 237)

Kashkan I.

LS2-IN-2966 Shedding new light on plant biology – automated long-term vertical-stage microscopy at high resolution (page 213)

Kašpar Z.

IM2-O-2695 Atomically Sharp Domain Walls in an Antiferromagnet (page 41)

Katanić K. R.

LS3-P-2799 Beneficial effects of ferroptosis inhibitor ferrostatin-1 on pancreatic islets in streptozotocin-induced diabetes (page 251)

Kaya P.

MS2-IN-2596 A key to develop novel ceramics: Microstructural design (page 370)

Kaya-Dagistanli F.

LS3-P-2704 Vitamin-D combined with resveratrol regulates islets hemostasis, β-cell regeneration, ER-stress and inflammation in fructose-fed diet/STZ-induced diabetic rats (page 255)

LS3-P-2756 Differentiation of DDR1+ progenitor cells into β cells in neonatal rat diabetes (page 257)

Kazda T.

IM5-P-2864 Batteries in situ testing in SEM (page 144)

Kepaptsoglou D. M.

Plenary-2901 Recent Progress in High-Resolution Electron Energy Loss Spectroscopy in the Scanning Transmission Electron Microscope (page 4)

Keresztes Á.

LS2-P-2532 Utilization of haematite nanoparticles by a flavin mediated iron uptake of roots (page 227)

Kević N.

LS2-P-2585 Expression of the enzyme myrosinase type 1 in the root, the stem and the leaves of the plant nasturtium (Tropaeolum majus L.) (page 229)

Kiener D.

MS7-IN-2739 Fracture behavior of distinct interfaces of two intermetallic TiAl alloys (page 515)

Kim H. J.

MS1-O-2857 Correlative electron microscopy and magnetism of CoCrFeNiZr high-entropy allos (page 330)

Kinyanjui M. K.

MS4-O-2647 Ordered electronic states in 2D quantum materials: Imaging effects of hydrostatic pressure at the atomic scale. (page 409)

Kinyanjui M. K.

MS5-P-2648 Imaging the atomic-scale effects of electron irradiation on charge density waves in 1D O-TaS3 (page 476)

Kirkland A. I.

IM3-IN-3015 Pushing at the limits of low-dose in 4D-STEM and electron ptychography (page 74)

IM3-O-2896 A New Approach for 3D Quantitative STEM Using Defocus Corrected Electron Ptychography (page 78)

Kitzberger F.

IM7-P-2818 Distribution of staining agents in samples of mice soft tissues prepared for Serial Block Face SEM. (page 189)

LS5-O-2521 Novel method for simultaneous visualization and distinguishing Au nanoparticles on both sides of the ultrathin sections using low-energy STEM and BSE in HRSEM (page 285)

Kizovský M.

IM6-P-2620 Combining Low Energy Electron Microscopy and Thermal Raman Spectroscopy for Graphene Analysis (page 166)

Kizovsky M.

IM2-P-2699 Assembly for Cryo-SEM/Raman Microspectroscopy sample analysis (page 63)

Kjeldby S. B.

MS5-P-2568 Structural and optical investigation of Fe-ZnO nanoarchitectures: from inversion domain boundaries to ZnO/ZnFe2O4 heterostructures (page 474)

Klapetek P.

MS7-P-2840 Characterization of Mechanical and Topographical Properties of Nanocomposite Thin Films with Plasma Polymer Structure (page 523)

Klebowski B.

LS6-O-2627 In-situ observations of metal nanoparticles interactions with living cells, in liquid environments directly in the Nanolive 3D CX-A microscope (page 294)

Klementová M.

MS1-P-2657 Incommensurate structure of τ phase in the Al-Cu-Zn system (page 337)

Klencsár Z.

LS2-P-2532 Utilization of haematite nanoparticles by a flavin mediated iron uptake of roots (page 227)

Klimovič Š.

LS6-P-2898 Correlation of Atomic Force Microscopy with other techniques: application on biosamples (page 301)

Klimša L.

MS1-P-2656 The Use of Titanothermic Reduction for Processing of Deep-Sea Nodules (page 339)

MS1-P-2623 Aluminothermally reduced deep-sea concretion and its phase structure (page 341)

Klusáček J.

IM3-P-2825 Improved mapping algorithms: combating data sparsity in SEM EDS (page 102)

Klusoň J.

MS7-P-2687 Impact behaviour of the industrially sputtered AlCrN coatings prepared using cathodic arc glow discharge (page 519)

Klvač O.

IM5-P-2864 Batteries in situ testing in SEM (page 144)

Knaislová A.

MS1-IN-2915 Titanium-aluminide-silicide based alloys (page 325)

Knez D.

IM3-IN-2626 Challenges in the characterization of complex nanomaterials with analytical STEM (page 80)

IM3-P-2510 Phase Analysis of (Li)FePO4 by Selected Area Electron Diffraction in Transmission Electron Microscopy (page 98)

IM5-P-2651 The power of speed: DED EELS for analytical in situ TEM (page 132)

IM5-P-2628 Field induced oxygen vacancy migration in anatase thin films studied by in situ biasing TEM (page 138)
IM7-IN-2701 Rise to the occasion – high quality sample preparation for high resolution TEM (page 170)
MS2-O-2843 Quantifying Ordering Phenomena at the Atomic Scale in Rare Earth Oxide Ceramics via EELS Elemental Mapping (page 371)
MS4-O-2594 Orbital mapping of the LaAlO3-TiO2 interface by STEM-EELS (page 417)
MS4-O-2619 Aberration-Corrected STEM Characterisation of Mn-ion Structural Displacements in La0.7Sr0.3MnO3 Interfacial Dead-Layers (page 419)

Knippenberg B.
LS1-P-2817 Tundra TEM: tool ‘easy of use’ for new commers to Cryo EM (page 209)

Koban M.
LS7-P-2659 Modern SEM allows high-throughput 2D and 3D analyses on a single platform (page 317)

Koblar M.
MS7-P-2540 Mechanical response of domain walls in lead-free ferroelectrics (page 525)

Koblížek M.
LS2-P-2665 3D organization of photosynthetic membranes in cells of photosynthetic bacterium Sediminicoccus rosea (page 224)

Kociak M.
IM3-O-2555 Tomography of surface phonon polarition fields by electron energy loss spectroscopy (page 82)
IM4-P-2584 Simplified electron vortex generator with aberration correction (page 118)

Kodambaka S.
MS4-P-2750 In-situ observation of 2D materials growth on liquid substrates (page 432)

Kojić V.
MS5-P-2858 Study of barium titanate on transparent titania nanotubes arrays (page 472)

Kolařík V.
IM4-O-2867 Concept of Aberration Corrected Low-Voltage Transmission Electron Microscope (page 114)
IM6-O-2862 Delta – Detector for Scanning Electron Mirror Microscopy (page 163)

Kolbábková P.
LS4-O-2597 High-resolution structural and functional deep brain imaging using holographic endo-microsocpy (page 266)

Kolíbal M.
IM2-P-2816 KPFM in SEM - Simultaneous Kelvin Probe Force Microscopy and Scanning Electron Microscopy (page 62)
IM5-O-2703 In-situ Microscopy of Catalytic Oxidation of CO to CO2 over Platinum Surfaces. (page 128)
MS4-P-2750 In-situ observation of 2D materials growth on liquid substrates (page 432)

Kolibal M.
MS5-P-2539 Real-time observation of vapor transport synthesis in the scanning electron microscope (page 466)

Kolínková V.
Late-P-3055 Non-Invasive Imaging Method for Evaluating Effect of Migrastatics on Tumor Cells In Vitro Based on Coherence - Controlled Holographic Microscopy (page 532)

Kolouch A.
LS5-O-2715 Correlative cathodoluminescence scanning electron microscopy for identification of cellular structures within vitrified samples at low electron beam energies (page 289)

Komazec B.

LS2-O-2661 Surface Coating-Modulated Phytotoxic Responses of Silver Nanoparticles in Chlorella vulgaris (page 218)

Komis G.

LS2-IN-2688 Recent advances in plant development and plant-microbe interactions employing light-sheet and super-resolution microscopy (page 215)

Konečná A.

IM2-P-2502 Magnetic field imaging with electron energy loss spectroscopy based on Babinet's principle (page 60)

Konečný M.

IM2-P-2816 KPFM in SEM - Simultaneous Kelvin Probe Force Microscopy and Scanning Electron Microscopy (page 62)

Konvalina I.

IM6-IN-2598 Ab initio study of angle-resolved electron spectroscopy of graphene (page 156)

IM6-O-2820 Time-of-Flight Spectrometer for Low Landing Energies (page 160)

IM6-P-2599 Effective IMFP of thin samples via the time-of-flight method (page 168)

MS1-P-2826 Deep learning powered optical microscopy for steel research (page 347)

MS4-P-2669 Energy-based calibration for quantitative STEM measurements and comparison with 2D-PAD (page 450)

Konwerski S.

LS6-P-2881 A beetle that was a flea. Comparison of morphological adaptations in external parasites among Coleoptera and Siphonaptera, using light and scanning electron mic (page 300)

Koos A.

MS4-O-2511 Microscopy of CVD grown MoS2 layers compared to layers obtained by the sulphurization of Mo (page 426)

Kopeček J.

MS1-P-2656 The Use of Titanothermic Reduction for Processing of Deep-Sea Nodules (page 339)

MS1-P-2623 Aluminothermally reduced deep-sea concretion and its phase structure (page 341)

MS2-O-2667 High resolution CT study of microstructure defects behaviour in deformed NiTi prepared by spark plasma sintering (page 377)

Kopejtka K.

LS2-P-2665 3D organization of photosynthetic membranes in cells of photosynthetic bacterium Sediminicoccus rosea (page 224)

Koptašíková L.

IM2-O-2791 Correlative super-resolution and electron microscopy in plant samples (page 39)

Korenjak Jausnik S.

LS2-O-2684 Pyroplastics: A new Approach (page 222)

Korent A.

MS5-IN-3031 Application of electron microscopy in development of sensor elements for detection of toxic organic compounds (page 455)

Kormilina T. K.

IM3-P-2642 Analytical electron tomography of CuNiFe magnetic spinodal alloys (page 90)

Kosasih F. U.

MS6-P-2847 Are FIB-prepared hybrid perovskite cross-sections still luminescent? (page 497)

Koštejn M.

MS5-P-2680 Latest TEM investigation of nanostructured CoS2 and Co2CuS4 based films with Fenton catalytic properties (page 477)

Kotakoski J.

IM7-P-2755 CANVAS: A System for Controlled Alteration of Nanomaterials in Vacuum Down to the Atomic Scale (page 183)

MS4-O-2807 Correlated AFM/STEM study on the Mechanical Stiffness of Defect-Engineered Graphene (page 411)

MS4-IN-2613 In and ex situ (S)TEM manipulation of 2D materials without air exposure (page 421)

MS4-P-2823 STEM analysis of freestanding monolayer h-BN irradiated with slow highly charged ions (page 446)

Kotakoski j.

MS4-P-2660 Noble gas clusters in a graphene sandwich (page 434)

Kotecha A.

IM7-P-2848 High-Throughput Cryo-Electron Tomography with a next generation platform (page 187)

Kothleitner G.

IM2-O-2635 3D-Nanoprinting of Magnetic Force Microscopy Tips (page 37)

IM3-IN-2626 Challenges in the characterization of complex nanomaterials with analytical STEM (page 80)

IM3-O-2555 Tomography of surface phonon polarition fields by electron energy loss spectroscopy (page 82)

IM3-P-2642 Analytical electron tomography of CuNiFe magnetic spinodal alloys (page 90)

IM5-P-2628 Field induced oxygen vacancy migration in anatase thin films studied by in situ biasing TEM (page 138)

IM7-IN-2701 Rise to the occasion – high quality sample preparation for high resolution TEM (page 170)

MS1-P-2531 Exploring the magnetic microstructure of spinodal alloys with differential phase contrast scanning transmission electron microscopy (DPC-STEM) (page 353)

MS2-O-2843 Quantifying Ordering Phenomena at the Atomic Scale in Rare Earth Oxide Ceramics via EELS Elemental Mapping (page 371)

MS4-O-2594 Orbital mapping of the LaAlO3-TiO2 interface by STEM-EELS (page 417)

MS5-O-2636 Expanded Design Flexibility in 3D-Nanoprinting via Focused Electron Beam Induced Deposition (page 456)

Koutná N.

MS4-O-2859 Atomic insights into the structures and properties of nitride thin films (page 415)

Kovács Kis V.

LS2-P-2532 Utilization of haematite nanoparticles by a flavin mediated iron uptake of roots (page 227)

Kovalčíková A.

MS7-P-2603 Nanohardness and toughness of multicomponent TiNbVTaZrHf-N coatings deposited by reactive DC magnetron sputtering and High Target Utilization Sputtering (page 521)

Kovařík M.

IM2-P-2816 KPFM in SEM - Simultaneous Kelvin Probe Force Microscopy and Scanning Electron Microscopy (page 62)

Koželj P.

MS1-O-2857 Correlative electron microscopy and magnetism of CoCrFeNiZr high-entropy allos (page 330)

Králík R.

MS1-P-2602 Phase Identification in Twin-Roll Cast Al-Steel Clad Composite (page 343)

MS5-O-2567 Ni-Ti Nanoparticles for Self-Propagating Reactions (page 462)

MS7-O-2565 Al nanocrystalline thin film deformation by in situ TEM and molecular dynamics (page 513)

Králík T.

IM5-P-2838 Effect of thermal radiation on the measurement of the sample holder temperature over the cryogenic range for various types of temperature sensor installations (page 150)

Křápek V.

IM2-P-2502 Magnetic field imaging with electron energy loss spectroscopy based on Babinet's principle (page 60)

Krause M.

IM7-O-2593 High-Throughput TEM Sample Preparation with iNotch Technique (page 174)

Krauss S.

IM7-P-2607 Imaging of uncoated samples with secondary electrons using in lens detection under optimum conditions – 'sweet spot' imaging (page 179)

Krauß S.

IM5-P-2530 In situ deformation observation via EBSD and EDS during high temperature tensile testing (page 140)

Krbková B.

LS4-O-2597 High-resolution structural and functional deep brain imaging using holographic endo-microsocpy (page 266)

Krčmarský V.

LS4-P-2673 Integrated Fluorescent Light Microscope (iFLM) - Applications Workflows (page 279)

Krejčí J.

LS4-O-2597 High-resolution structural and functional deep brain imaging using holographic endo-microsocpy (page 266)

LS4-P-2606 Fluorescence confocal imaging via holographic endo-microscopy (page 278)

Krejcikova S.

MS3-P-2653 Simple, fast and reliable method of UHMWPE accelerated aging (page 393)

Křenek T.

MS5-P-2680 Latest TEM investigation of nanostructured CoS2 and Co2CuS4 based films with Fenton catalytic properties (page 477)

Krishnamurthy A.

MS5-IN-3031 Application of electron microscopy in development of sensor elements for detection of toxic organic compounds (page 455)

Krisper R.

IM3-IN-2626 Challenges in the characterization of complex nanomaterials with analytical STEM (page 80)

IM5-IN-2617 Do you know the relevant conditions for in situ heating experiments in the TEM? (page 121)

IM5-P-2651 The power of speed: DED EELS for analytical in situ TEM (page 132)

IM5-P-2628 Field induced oxygen vacancy migration in anatase thin films studied by in situ biasing TEM (page 138)

IM7-IN-2701 Rise to the occasion – high quality sample preparation for high resolution TEM (page 170)

Kristianová E.

MS1-P-2656 The Use of Titanothermic Reduction for Processing of Deep-Sea Nodules (page 339)

Křivská B.

MS1-P-2602 Phase Identification in Twin-Roll Cast Al-Steel Clad Composite (page 343)

MS1-P-2490 In-situ heating of twin-roll cast Al-steel clad strip (page 361)

MS5-O-2567 Ni-Ti Nanoparticles for Self-Propagating Reactions (page 462)

MS7-O-2565 Al nanocrystalline thin film deformation by in situ TEM and molecular dynamics (page 513)

Křížek F.

IM2-O-2695 Atomically Sharp Domain Walls in an Antiferromagnet (page 41)

Krížik P.

MS4-P-2595 Native surface oxide characterization with S/TEM on PM metal powders (page 442)

Křížová A.

LS3-O-2746 Exploring the unseen: quantitative phase imaging in cancer research (page 240)

Krotemüller M.

MS4-O-2647 Ordered electronic states in 2D quantum materials: Imaging effects of hydrostatic pressure at the atomic scale. (page 409)

Kršňák M.

IM2-P-2850 Imidazole-osmium reduces elution of lipids from cryofixed rat hepatic tissue for correlative TEM/NanoSIMS analysis (page 55)

Krutil V.

IM5-P-2833 Cryogenic Sample Holder with Electrical Contacts for UHV SEM/SPM (page 142)

IM5-P-2845 Low conductive thermal insulation pad with high mechanical stiffness (page 152)

Krzyžánek V.

IM5-P-2845 Low conductive thermal insulation pad with high mechanical stiffness (page 152)

LS5-O-2715 Correlative cathodoluminescence scanning electron microscopy for identification of cellular structures within vitrified samples at low electron beam energies (page 289)

Krzyzanek V.

IM2-P-2699 Assembly for Cryo-SEM/Raman Microspectroscopy sample analysis (page 63)

IM3-O-2671 High-resolution Powder Nano-Beam Diffraction in Scanning Electron Microscopy (page 76)

LS2-P-2663 Ultrastructural changes in prokaryotic microorganisms caused by long-term exposure to high salt and copper ion concentrations (page 231)

MS3-P-2814 Commonly used vs novel embedding resins for 3D-SEM microscopy with higher resistance to e-beam damage. (page 396)

Kuba J.

LS4-P-2673 Integrated Fluorescent Light Microscope (iFLM) - Applications Workflows (page 279)

Kuběna I.

MS1-P-2722 Microstructural changes in DLMS IN939 due to low cycle fatigue investigated by advanced electron microscopy. (page 345)

Kubicek M.

Late-P-3032 Electron beam irradiation induced Brownmillerite – perovskite phase transition in La_{0.6} Sr_{0.4} CoO_{3-ð} (page 530)

Kumagai K.

IM6-IN-2513 Contrast mechanism and its application at landing energy near 0 eV in super low energy SEM (page 155)

Kunčič K.

LS3-P-2652 Formation of cell junctions during integument morphogenesis in crustacean Porcellio scaber (page 249)

Kundrát V.

IM5-P-2864 Batteries in situ testing in SEM (page 144)

Kungl H.

IM7-O-2590 FIB-based lamella preparation for in-situ TEM gas experiment (page 176)

Kuntscher C. A.

MS4-O-2647 Ordered electronic states in 2D quantum materials: Imaging effects of hydrostatic pressure at the atomic scale. (page 409)

Kurić L.

LS2-P-2585 Expression of the enzyme myrosinase type 1 in the root, the stem and the leaves of the plant nasturtium (Tropaeolum majus L.) (page 229)

Kürnsteiner P.

MS1-O-2796 An in-depth investigation of liquid metal embrittlement sensitive grain boundaries in TBF steels (page 328)

Kusch G.

MS6-P-2847 Are FIB-prepared hybrid perovskite cross-sections still luminescent? (page 497)

Kvashinina K. O.

MS5-P-2618 Uranium reduction by magnetite – mechanism of UO2 formation monitored by STEM, SAED and STEM-EELS (page 464)

Kvetková L.

MS7-P-2603 Nanohardness and toughness of multicomponent TiNbVTaZrHf-N coatings deposited by reactive DC magnetron sputtering and High Target Utilization Sputtering (page 521)

Lábár J. L.

IM3-P-2781 Application of the DiffMap program to PtSi thin films (page 92)

Labudović Borović M. M.

LS1-IN-3008 Transmission electron microscopy in research and diagnostics - new challenges in the omics era (page 201)

LaGrange T.

MS5-P-2618 Uranium reduction by magnetite – mechanism of UO2 formation monitored by STEM, SAED and STEM-EELS (page 464)

Lalinský O.

MS4-P-2670 Graphene-coated scintillators for low-energy electron detection (page 444)

Lalošević D.

LS3-P-2504 Effect of arsenic(III) oxide on reproductive organs of female mices (page 242)

Lamberz C.

IM2-P-2604 Towards correlating light and electron microscopy with immersion objectives at cryogenic temperatures (page 57)

IM5-IN-2999 Microsystems for in situ cryofixation and correlative cryomicroscopy (page 127)

Lammer J.

IM3-IN-2626 Challenges in the characterization of complex nanomaterials with analytical STEM (page 80)

IM7-IN-2701 Rise to the occasion – high quality sample preparation for high resolution TEM (page 170)

MS2-O-2843 Quantifying Ordering Phenomena at the Atomic Scale in Rare Earth Oxide Ceramics via EELS Elemental Mapping (page 371)

Längle M.

MS4-P-2660 Noble gas clusters in a graphene sandwich (page 434)

Lánský Z.

IM2-P-2677 Miro proteins and their role in horizontal transfer of mitochondria via tunneling nanotubes in cancer cells (page 67)

Lanza A.

IM3-P-2579 3D Electron Diffraction on Ferroelectric Perovskites. (page 88)

Lapanje A.

LS2-O-2690 The use of SEM imaging and elemental mapping in the research of artificial bacterial aggregates (page 220)

Lassnig A.

MS6-P-2630 Combined Microstructural and Electrochemical Studies of Sputtered Ni Thin Layers as Catalysts for Hydrogen Evolution Reaction (page 501)

Lau A. J.

IM4-P-2584 Simplified electron vortex generator with aberration correction (page 118)

Laufek F.

MS1-P-2656 The Use of Titanothermic Reduction for Processing of Deep-Sea Nodules (page 339)

MS1-P-2623 Aluminothermally reduced deep-sea concretion and its phase structure (page 341)

Laurens G.

MS7-O-2700 Analysis of dislocation evolution in cerium oxide nanocubes using in situ transmission electron microscopy (page 511)

Lawson M. J.

LS6-O-2639 Correlative 3D imaging workflow using X-ray micro-computed tomography and laser plasma focussed ion beam electron microscopy on biological soft tissues (page 298)

Laznicka T.

IM2-P-2699 Assembly for Cryo-SEM/Raman Microspectroscopy sample analysis (page 63)

Le Caer S.

IM5-O-2894 Graphene liquid cell for electron microscopy analysis of nanoparticle interaction with solutions: the case of titanium oxide nanoparticles and phosphates (page 123)

Le Fer G.

MS3-P-2834 Low Dose Transmission Electron Microscopy Imaging on Sensitive Colloidal Covalent-Organic Frameworks (page 398)

Lebas L.

LS7-O-2698 3D reconstruction of hydrated samples at the sub-micrometer scale using Liquid-Phase STEM at low voltage (page 315)

Ledieu J.

MS4-P-2640 Transmission electron microscopy characterization of quasicrystal approximants in SrTiO3 thin films grown on Pt(111)/Al2O3(0001) (page 448)

Ledwig P.

Late-P-3036 Microstructural analysis of Inconel 625 superalloy manufactured by laser powder bed fusion with remelting (page 528)

Lefloch F.

IM3-P-2781 Application of the DiffMap program to PtSi thin films (page 92)

Leifer K.

MS4-P-2861 Electron tomography for measurement of buried interface roughness in thin films (page 438)

Leist C.

MS4-O-2837 Optimal acceleration voltage for near-atomic resolution imaging of layer-stacked 2D polymer thin films (page 413)

MS4-P-2835 Deep learning pipeline for statistical quantification of amorphous two-dimensional materials (page 436)

Leitinger G.

LS1-O-2804 Neurons and glial cells appear to store and release human brain ferritin at different rates (page 202)

Lejeune M.

IM6-P-2620 Combining Low Energy Electron Microscopy and Thermal Raman Spectroscopy for Graphene Analysis (page 166)

Letofsky-Papst I.

IM7-P-2537 The Hidden Power of Coffee – An Exceptional Replacement for Uranyl Acetate for Staining Biological Specimens in Transmission Electron Microscopy (page 185)

Levin-Zaidman S.

LS4-O-2587 Localization of Bacteria in Tumor Cells using Correlative Light and Electron Microscopy (page 268)

Li X.

IM3-O-2555 Tomography of surface phonon polarition fields by electron energy loss spectroscopy (page 82)

IM4-P-2584 Simplified electron vortex generator with aberration correction (page 118)

Liang B.

MS3-O-2846 Sub-Ångstrom resolution imaging of 2D conjugated metal-organic frameworks enabled by unconventional resilience against electron radiation (page 389)

MS4-O-2837 Optimal acceleration voltage for near-atomic resolution imaging of layer-stacked 2D polymer thin films (page 413)

Liberti E.

IM3-O-2896 A New Approach for 3D Quantitative STEM Using Defocus Corrected Electron Ptychography (page 78)

Lichtenegger H.

LS1-O-2655 Why do Schwann cells like spider silk? (page 199)

MS3-P-2829 Characterization of particle-filled polymer composites (page 400)

Liebscher C. H.

MS1-O-2601 Co-segregation of zinc, carbon and boron in a Σ5 iron grain boundary resolved by correlating atomic resolution STEM, APT and first-principles calculations (page 326)

Ligmajer F.

MS5-O-2501 Plasmon resonances in biocompatible nanoparticles (page 458)

Lingbo Y.

LS1-P-2817 Tundra TEM: tool ‘easy of use’ for new commers to Cryo EM (page 209)

Lipovsek S.

LS1-O-2804 Neurons and glial cells appear to store and release human brain ferritin at different rates (page 202)

Lofaj F.

MS7-P-2603 Nanohardness and toughness of multicomponent TiNbVTaZrHf-N coatings deposited by reactive DC magnetron sputtering and High Target Utilization Sputtering (page 521)

Löffler M.

IM2-O-2693 Micro X-ray computed tomography as an extension to light microscopy and FIB/SEM (page 49)

Löffler S.

IM1-O-2681 Precipitate size estimation using image feature detection (page 22)

MS2-O-2843 Quantifying Ordering Phenomena at the Atomic Scale in Rare Earth Oxide Ceramics via EELS Elemental Mapping (page 371)

MS4-O-2594 Orbital mapping of the LaAlO3-TiO2 interface by STEM-EELS (page 417)

Löfler L.

IM5-P-2797 Real-time atomic-resolution observation of coherent twin boundary migration in rocksalt transition metal nitride (page 136)

Lollo G.

LS1-IN-2535 Hyaluronic acid based nanoparticles are suitable carriers to muscle cells: the ultrastructural evidence (page 195)

Lonc̆ar A.

MS6-P-2682 Studying electrochemical degradation in nanocatalysts with identical location STEM (page 503)

London A. J.

MS6-O-2505 Multi-scale, high-resolution, time-resolved residual stress in laser-welded Eurofer97 using plasma focused ion beam-digital image correlation method (page 494)

Lopes C.

LS3-IN-2769 Spheroids: in vitro 3D cell cultures of brown trout liver as a model for ecotoxicology research (page 235)

Losonczy A.

Plenary-2872 Watching and shaping memories in the brain with optical methods (page 9)

Lotnyk A.

MS4-O-2580 Nanoscale characterization of van der Waals-bonded GeTe/Sb2Te3 phase-change memory superlattices grown by pulsed laser deposition (page 424)

Lukes T.

LS4-IN-3001 Combining Super-resolution Optical Fluctuation Imaging (SOFI) With Structure Illumination and 3D Imaging (page 264)

Lümkemann A.

MS7-P-2687 Impact behaviour of the industrially sputtered AlCrN coatings prepared using cathodic arc glow discharge (page 519)

Lunt D.

IM5-O-2649 Integration of EBSD acquisition into fully automated in-situ thermo-mechanical testing for high temporal and spatial resolution (page 125)

MS7-O-2644 Automated In-Situ Mechanical Testing of heavily textured Ti 6Al 4V to Obtain High Spatial and Temporal Resolution Strain Maps (page 509)

Luo T.

MS6-O-2514 Correlative Microscopy Techniques for Defect-Property-Correlation of Thermoelectric Materials (page 487)

Lyons D. M.

LS2-O-2661 Surface Coating-Modulated Phytotoxic Responses of Silver Nanoparticles in Chlorella vulgaris (page 218)

Macálka A.

IM5-P-3010 New TDS software for computer-based optimisation of thermodynamic conditions in Advanced Environmental Scanning Electron Microscopy (A-ESEM) (page 148)

Macchiarelli G.

LS1-P-2518 Ultrastructure analysis in the male reproductive system of different mammals exposed to ionizing radiation after the Fukushima accident: a comparative study (page 208)

Mach J.

MS5-O-2501 Plasmon resonances in biocompatible nanoparticles (page 458)

Machalkova M.

LS7-P-2659 Modern SEM allows high-throughput 2D and 3D analyses on a single platform (page 317)

Macyk W.

MS6-P-2566 The implementation of microscopic and spectroscopic techniques in characterisation of the spinel ferrite for photocatalytic reduction of CO2 (page 504)

Madureira T. V.

LS3-IN-2769 Spheroids: in vitro 3D cell cultures of brown trout liver as a model for ecotoxicology research (page 235)

Maeder X.

MS7-IN-2666 Recent advances in in-situ SEM nanomechanical testing: extreme temperatures, ultra-high strain rates, in-situ electron diffraction and digital image correlation (page 508)

Mahecic D.

LS4-IN-3001 Combining Super-resolution Optical Fluctuation Imaging (SOFI) With Structure Illumination and 3D Imaging (page 264)

Mahel V.

MS4-P-2750 In-situ observation of 2D materials growth on liquid substrates (page 432)

Mahomed A. S.

MS5-P-2832 Exploring the role of fuel on the microstructure of VOx/MgO powders prepared using solution combustion synthesis (page 478)

Maiellano G.

LS7-IN-2525 Moving from two- to three- dimensional electron microscopy in the study of the synapse: a lesson from neurodevelopmental disorder models (page 309)

Majerus B.

MS5-O-2808 Towards Laser-Induced Tuning of Plasmonic Response in High Aspect-Ratio Au Nanowires: A STEM/EELS study (page 460)

Malatesta M.

LS1-IN-2535 Hyaluronic acid based nanoparticles are suitable carriers to muscle cells: the ultrastructural evidence (page 195)

Malínská K.

LS2-IN-2966 Shedding new light on plant biology – automated long-term vertical-stage microscopy at high resolution (page 213)

Malinsky M.

LS1-P-2817 Tundra TEM: tool ‘easy of use’ for new commers to Cryo EM (page 209)

Malínský M.

LS3-O-2821 Extending Capabilities of 120 kV LaB6 TEMs to Cryo-EM Reconstructions at Subnanometer Resolution (page 238)

Maliszewska I.

LS1-O-2543 Antimicrobial photodynamic therapy effects on Gram-negative and Gram-positive bacteria observed using light-induced in-situ TEM (page 197)

Man O.

IM2-O-2695 Atomically Sharp Domain Walls in an Antiferromagnet (page 41)

Mandić V.

MS6-O-2793 Morphology related energy losses in small molecule organic solar cells (page 493)

Mangler C.

IM7-P-2755 CANVAS: A System for Controlled Alteration of Nanomaterials in Vacuum Down to the Atomic Scale (page 183)

MS4-O-2807 Correlated AFM/STEM study on the Mechanical Stiffness of Defect-Engineered Graphene (page 411)

MS4-P-2660 Noble gas clusters in a graphene sandwich (page 434)

Manjeshwar Sathyanath S. K.

MS4-P-2861 Electron tomography for measurement of buried interface roughness in thin films (page 438)

Manley S.

LS4-IN-3001 Combining Super-resolution Optical Fluctuation Imaging (SOFI) With Structure Illumination and 3D Imaging (page 264)

Marček Chorvátová A.

IM1-P-2686 Deep-learning model for automatic detection of cells in microscopy images (page 24)

Marin M.

LS3-P-2504 Effect of arsenic(III) oxide on reproductive organs of female mices (page 242)

Marinova M.

MS3-P-2834 Low Dose Transmission Electron Microscopy Imaging on Sensitive Colloidal Covalent-Organic Frameworks (page 398)

Marinović M.

LS6-O-2622 Oscillatory intracellular patterns of the small GTPase Rac1 (page 292)

Mark P.

LS3-P-2643 Insect midgut epithelium architecture – focus on gut stem cells in larvae and adults (page 259)

Markelić M. B.

LS3-P-2799 Beneficial effects of ferroptosis inhibitor ferrostatin-1 on pancreatic islets in streptozotocin-induced diabetes (page 251)

LS3-P-2812 Beneficial effects of ferroptosis inhibitor ferrostatin-1 in diabetes-induced liver damage (page 253)

Marolt M.

LS7-O-2860 Volume electron microscopy and automatic segmentation of intracellular compartments in the urinary bladder umbrella cells (page 310)

Marsmans D.

IM4-O-2506 Measurement and Correction of Phase Aberrations in Scanning Transmission Microscopy by Artificial Neural Networks (page 112)

Martinez F.

IM5-O-2649 Integration of EBSD acquisition into fully automated in-situ thermo-mechanical testing for high temporal and spatial resolution (page 125)

Martínez K.

MS4-P-2610 In situ TEM annealing: comparison of thin GeSn layers grown by MBE and CVD (page 440)

Martinović V. I.

LS3-P-2812 Beneficial effects of ferroptosis inhibitor ferrostatin-1 in diabetes-induced liver damage (page 253)

Martinů P.

IM5-P-3010 New TDS software for computer-based optimisation of thermodynamic conditions in Advanced Environmental Scanning Electron Microscopy (A-ESEM) (page 148)

Mascitti I. A.

LS1-P-2518 Ultrastructure analysis in the male reproductive system of different mammals exposed to ionizing radiation after the Fukushima accident: a comparative study (page 208)

Masenelli-Varlot K.

LS7-O-2698 3D reconstruction of hydrated samples at the sub-micrometer scale using Liquid-Phase STEM at low voltage (page 315)

MS7-O-2700 Analysis of dislocation evolution in cerium oxide nanocubes using in situ transmission electron microscopy (page 511)

Masiulis S.

LS3-O-2821 Extending Capabilities of 120 kV LaB6 TEMs to Cryo-EM Reconstructions at Subnanometer Resolution (page 238)

Matczyszyn K.

IM5-O-2542 Transmission electron microscope modification for light-induced in situ imaging of specimens in liquid on example of photodynamic therapy (page 130)

LS1-O-2543 Antimicrobial photodynamic therapy effects on Gram-negative and Gram-positive bacteria observed using light-induced in-situ TEM (page 197)

Mateašík A.

IM1-P-2686 Deep-learning model for automatic detection of cells in microscopy images (page 24)

Matějka M.

IM5-P-2833 Cryogenic Sample Holder with Electrical Contacts for UHV SEM/SPM (page 142)

Materna J.

MS1-P-2826 Deep learning powered optical microscopy for steel research (page 347)

Materna-Mikmeková E.

IM6-IN-2598 Ab initio study of angle-resolved electron spectroscopy of graphene (page 156)

IM6-P-2599 Effective IMFP of thin samples via the time-of-flight method (page 168)

MS1-P-2826 Deep learning powered optical microscopy for steel research (page 347)

MS4-P-2669 Energy-based calibration for quantitative STEM measurements and comparison with 2D-PAD (page 450)

Matsuura T.

MS5-P-2648 Imaging the atomic-scale effects of electron irradiation on charge density waves in 1D O-TaS3 (page 476)

Mayalı B.

IM1-IN-2752 Image Analysis Workflow for Phase-Contrast Optical Microscopy Images (page 20)

Mayrhofer C.

IM2-P-2545 Extensive material characterization for series production of 3D printer components (page 71)

IM7-P-2537 The Hidden Power of Coffee – An Exceptional Replacement for Uranyl Acetate for Staining Biological Specimens in Transmission Electron Microscopy (page 185)

Mayrhofer H. P.

MS4-O-2859 Atomic insights into the structures and properties of nitride thin films (page 415)

McBean P.

IM4-O-2570 A User Adjustable Pole-piece Gap as a Route to Improve the Sustainability of TEM Infrastructure (page 110)

McGuinness C.

IM6-O-2572 The Retrofittable Photoelectron Source: A Potential Improvement to Low Voltage SEM Imaging (page 158)

Méchin L.

MS4-O-2619 Aberration-Corrected STEM Characterisation of Mn-ion Structural Displacements in La0.7Sr0.3MnO3 Interfacial Dead-Layers (page 419)

Meden A.

MS1-O-2857 Correlative electron microscopy and magnetism of CoCrFeNiZr high-entropy allos (page 330)

Medlín R.

MS5-P-2680 Latest TEM investigation of nanostructured CoS2 and Co2CuS4 based films with Fenton catalytic properties (page 477)

Meffert M.

IM3-P-2815 Hybrid-pixel detectors for TEM (page 96)

Mellor R. F.

IM3-P-2683 Scanning electron diffraction study of TiFeAl alloy microstructure (page 100)

Merchan A.

IM2-O-2612 Proof-of-Concept study for high-resolution correlative multimodal imaging and big data of a mouse brain (page 35)

Merchan-Perez A.

LS6-O-2615 The BUILD project: A multi-modal cross-scale approach to reveal characteristics of the human brain’s nested connectome (page 297)

Meschini S.

LS1-P-2519 Electron microscopy in the study of nanomaterial-cell interaction: involvement of autophagy (page 206)

Meyer J. C.

IM7-P-2755 CANVAS: A System for Controlled Alteration of Nanomaterials in Vacuum Down to the Atomic Scale (page 183)

Meyer-Plath A.

IM2-O-2528 Analysis of sampled airborne particles by correlative microscopy (page 47)

MS5-P-2524 Quantification and morphological analysis of nanofibers for exposure control and material characterization purposes using electron microscopy and advanced image (page 482)

Micaroni M.

IM2-O-2612 Proof-of-Concept study for high-resolution correlative multimodal imaging and big data of a mouse brain (page 35)

LS6-O-2615 The BUILD project: A multi-modal cross-scale approach to reveal characteristics of the human brain’s nested connectome (page 297)

Michalcová A.

MS1-P-2656 The Use of Titanothermic Reduction for Processing of Deep-Sea Nodules (page 339)

MS1-P-2623 Aluminothermally reduced deep-sea concretion and its phase structure (page 341)

MS6-P-2600 Description of Ageing of Soldering Materials by Means of Electron Microscopy (page 499)

Michalička J.

IM2-O-2695 Atomically Sharp Domain Walls in an Antiferromagnet (page 41)

Michler J.

MS7-IN-2666 Recent advances in in-situ SEM nanomechanical testing: extreme temperatures, ultra-high strain rates, in-situ electron diffraction and digital image correlation (page 508)

Midgley P. A.

IM3-P-2683 Scanning electron diffraction study of TiFeAl alloy microstructure (page 100)

Migliori A.

IM4-O-2591 Enhancing Electron Computational Ghost Imaging Using Artificial Neural Networks (page 116)

Mihalkovič M.

MS1-P-2702 Phase evolution clarification in Al86Ni8Gd6 amorphous alloy: A spotlight on Al20Ni6Gd4 phase and its peculiarities (page 364)

Mijailovic D.

MS6-IN-2913 Can the Wet Win the Bet? The case of Energy Harvesting and Storage (page 491)

Mikmeková E. M.

IM6-O-2820 Time-of-Flight Spectrometer for Low Landing Energies (page 160)

IM6-P-2620 Combining Low Energy Electron Microscopy and Thermal Raman Spectroscopy for Graphene Analysis (page 166)

Mikmeková Š.

IM6-IN-2513 Contrast mechanism and its application at landing energy near 0 eV in super low energy SEM (page 155)

MS1-P-2794 Phase determination of dual phase steel using backscattered electron images and image analysis techniques (page 335)

MS1-P-2826 Deep learning powered optical microscopy for steel research (page 347)

Minárik P.

MS1-P-2602 Phase Identification in Twin-Roll Cast Al-Steel Clad Composite (page 343)

Minenkov A.

IM5-P-2664 Efficient preparation of MEMS carriers with plan-view specimens: a case study of in situ TEM experiments with thin epitaxial layers (page 134)

MS4-P-2610 In situ TEM annealing: comparison of thin GeSn layers grown by MBE and CVD (page 440)

Mitchels J.

LS4-P-2673 Integrated Fluorescent Light Microscope (iFLM) - Applications Workflows (page 279)

Mitchels J. M.

IM7-P-2848 High-Throughput Cryo-Electron Tomography with a next generation platform (page 187)

Mittelberger A.

IM7-P-2755 CANVAS: A System for Controlled Alteration of Nanomaterials in Vacuum Down to the Atomic Scale (page 183)

Mitterer C.

MS2-O-2789 Stacking faults dominant strengthening mechanism behind the anomalous hardness variation of TaN/TiN multilayer films (page 375)

Mizohata K.

MS4-P-2660 Noble gas clusters in a graphene sandwich (page 434)

Mlčoušková J.

IM7-P-2790 Nanopatterned Surface for Super-resolution Microscopy localization of Cell Interactions (page 191)

Mojzeš P.

IM2-O-2571 Combining Light, Raman, and Electron Microscopy in Imaging Viral Factories of Avian Reovirus (page 31)

Moldovan G.

IM1-O-2569 Making Every Electron Count: Improving STEM Quantification, Speed, and Data Throughput with Solid State Detectors and Pulse Counting Hardware (page 14)

IM2-O-2520 In-situ electrical analysis with EBIC STEM: developments and applications (page 33)

IM7-O-2593 High-Throughput TEM Sample Preparation with iNotch Technique (page 174)

Molina S. I.

MS3-P-2819 STEM damage of Acrylic-based Materials for Stereolithography: Degradation Mechanism (page 403)

Molinari A.

Late-P-3052 FROM A CLINICAL CASE TO A GENERAL METHODOLOGY TO ANALYZE PROSTHETIC JOINT FAILURE BY MICRO- AND NANO-CHARACTERIZATION OF INTRA-TISSUE WEAR DEBRIS (page 534)

Moninger M.

MS5-IN-3044 In situ microscopy of nanowires: From fundamental properties to functional applications (page 453)

MORCRETTE M.

MS6-O-2577 Study of failure modes in two sulphide-based solid electrolyte all-solid-state batteries via in-situ SEM (page 489)

Moreau P.

IM5-O-2894 Graphene liquid cell for electron microscopy analysis of nanoparticle interaction with solutions: the case of titanium oxide nanoparticles and phosphates (page 123)

Mostaed A.

IM3-O-2896 A New Approach for 3D Quantitative STEM Using Defocus Corrected Electron Ptychography (page 78)

Motlová T.

MS1-P-2813 Microanalyses for a better understanding of active soldering processes (page 367)

Mrak P.

LS3-P-2652 Formation of cell junctions during integument morphogenesis in crustacean Porcellio scaber (page 249)

Mrazova K.

IM2-P-2699 Assembly for Cryo-SEM/Raman Microspectroscopy sample analysis (page 63)

LS2-P-2663 Ultrastructural changes in prokaryotic microorganisms caused by long-term exposure to high salt and copper ion concentrations (page 231)

MS3-P-2828 Visualization of internal morphology of hydrogels based on polyvinyl alcohol in comparison with the indirect method of structural characterization (page 402)

Msallamová Š.

MS6-P-2600 Description of Ageing of Soldering Materials by Means of Electron Microscopy (page 499)

Muchová N.

Late-P-3055 Non-Invasive Imaging Method for Evaluating Effect of Migrastatics on Tumor Cells In Vitro Based on Coherence - Controlled Holographic Microscopy (page 532)

Mücke D.

MS3-O-2846 Sub-Ångstrom resolution imaging of 2D conjugated metal-organic frameworks enabled by unconventional resilience against electron radiation (page 389)

MS4-O-2842 Thickness dependency of critical dose for extremely beam-sensitive two-dimensional polymer (page 428)

Mukhamedova L.

LS6-P-2802 In situ cryo-electron tomography of enterovirus cell entry (page 303)

Mukhamedova M.

LS3-O-2732 Endosome disruption enables enteroviruses to reach cell cytoplasm (page 236)

Mullarkey T.

IM1-O-2569 Making Every Electron Count: Improving STEM Quantification, Speed, and Data Throughput with Solid State Detectors and Pulse Counting Hardware (page 14)

Müllerová I.

IM6-IN-2598 Ab initio study of angle-resolved electron spectroscopy of graphene (page 156)

IM6-O-2820 Time-of-Flight Spectrometer for Low Landing Energies (page 160)

Murphy P.

IM4-O-2570 A User Adjustable Pole-piece Gap as a Route to Improve the Sustainability of TEM Infrastructure (page 110)

Mustonen K.

IM7-P-2755 CANVAS: A System for Controlled Alteration of Nanomaterials in Vacuum Down to the Atomic Scale (page 183)

MS4-O-2807 Correlated AFM/STEM study on the Mechanical Stiffness of Defect-Engineered Graphene (page 411)

MS4-P-2660 Noble gas clusters in a graphene sandwich (page 434)

Mynář M.

IM4-O-2867 Concept of Aberration Corrected Low-Voltage Transmission Electron Microscope (page 114)

IM6-O-2862 Delta – Detector for Scanning Electron Mirror Microscopy (page 163)

Nachtnebel M.

IM2-O-2563 Correlative Raman microscopy, SEM and EDS – The combined evaluation of a whole sample mapping of a Chelyabinsk meteorite fragment (page 43)

IM2-O-2629 Automated and correlative SEM-EDX-Raman particle analysis on fine dust filters of extreme events: New Year’s Eve and Sahara dust (page 52)

Nagaraj P. H.

LS3-P-2916 Translation initiation stages of coupled transcription-translation (page 246)

Naghilou A.

LS1-O-2655 Why do Schwann cells like spider silk? (page 199)

Nagy Š.

MS1-P-2624 Modification of native oxide on magnesium powders for enhanced corrosion resistance (page 349)

MS1-P-2589 Microstructural characterization of sintered Iron and observation of oxides reduction after different conditions of sintering process (page 350)

MS4-P-2595 Native surface oxide characterization with S/TEM on PM metal powders (page 442)

Nagy Trembošová V.

MS1-P-2624 Modification of native oxide on magnesium powders for enhanced corrosion resistance (page 349)

MS4-P-2595 Native surface oxide characterization with S/TEM on PM metal powders (page 442)

Nahácka Z.

IM2-P-2677 Miro proteins and their role in horizontal transfer of mitochondria via tunneling nanotubes in cancer cells (page 67)

Navarro-Quezada A.

IM3-P-2631 Precession Electron Diffraction and its Applications in Semiconductor Heterostructures (page 86)

Navikas V.

LS4-IN-3001 Combining Super-resolution Optical Fluctuation Imaging (SOFI) With Structure Illumination and 3D Imaging (page 264)

Nebesářová J.

LS2-O-2638 Borrelia – host interactions: zoom in on the big picture (page 216)

LS5-O-2521 Novel method for simultaneous visualization and distinguishing Au nanoparticles on both sides of the ultrathin sections using low-energy STEM and BSE in HRSEM (page 285)

LS5-O-2715 Correlative cathodoluminescence scanning electron microscopy for identification of cellular structures within vitrified samples at low electron beam energies (page 289)

Nebesarova J.

IM7-P-2818 Distribution of staining agents in samples of mice soft tissues prepared for Serial Block Face SEM. (page 189)

LS2-P-2663 Ultrastructural changes in prokaryotic microorganisms caused by long-term exposure to high salt and copper ion concentrations (page 231)

MS3-P-2814 Commonly used vs novel embedding resins for 3D-SEM microscopy with higher resistance to e-beam damage. (page 396)

Neděla V.

IM5-P-3010 New TDS software for computer-based optimisation of thermodynamic conditions in Advanced Environmental Scanning Electron Microscopy (A-ESEM) (page 148)

Nejezchleba D.

MS4-P-2609 Imaging of structural deformations of gas-phase synthesized graphene by intermediate energy electrons (page 430)

Nejman D.

LS4-O-2587 Localization of Bacteria in Tumor Cells using Correlative Light and Electron Microscopy (page 268)

Nellist P.

IM3-O-2896 A New Approach for 3D Quantitative STEM Using Defocus Corrected Electron Ptychography (page 78)

Nellist P. D.

IM3-IN-3015 Pushing at the limits of low-dose in 4D-STEM and electron ptychography (page 74)

Němeček D.

LS3-O-2821 Extending Capabilities of 120 kV LaB6 TEMs to Cryo-EM Reconstructions at Subnanometer Resolution (page 238)

Nemeth M.

MS4-O-2511 Microscopy of CVD grown MoS2 layers compared to layers obtained by the sulphurization of Mo (page 426)

Nemouchi F.

IM3-P-2781 Application of the DiffMap program to PtSi thin films (page 92)

Netíková I. Š.

Late-P-3058 Identification of Tumor Cells Behavior Changes by Holographic Incoherent Quantitative Phase Imaging Focuses on Migrastatics (page 539)

Neuman J.

IM2-P-2527 AFM-in-SEM solution for correlative microscopy in material sciences (page 65)

Neumüller D.

MS6-P-2630 Combined Microstructural and Electrochemical Studies of Sputtered Ni Thin Layers as Catalysts for Hydrogen Evolution Reaction (page 501)

Neužil J.

IM2-P-2677 Miro proteins and their role in horizontal transfer of mitochondria via tunneling nanotubes in cancer cells (page 67)

Nevolová Š.

IM7-P-2790 Nanopatterned Surface for Super-resolution Microscopy localization of Cell Interactions (page 191)

Nevoralová M.

MS3-IN-2935 Synergy of Scanning Electron and Light Microscopies in Visualization of Swollen Hydrogels and Effect of Hydrogel Parameters on the Image: Artifacts and Reality (page 384)

Nguyen P. D.

MS5-P-2568 Structural and optical investigation of Fe-ZnO nanoarchitectures: from inversion domain boundaries to ZnO/ZnFe2O4 heterostructures (page 474)

Niggas A.

MS4-P-2823 STEM analysis of freestanding monolayer h-BN irradiated with slow highly charged ions (page 446)

Niu Y.

MS5-P-2982 Classification of Metal Nanoclusters Using Convolutional Neural Networks (page 470)

Nohýnková E.

IM7-IN-2978 CLEM for FIB/SEM: A workflow for characterization of low-abundant samples on example of a parasitic flagellate Giardia intestinalis. (page 172)

Nollo G.

Late-P-3052 FROM A CLINICAL CASE TO A GENERAL METHODOLOGY TO ANALYZE PROSTHETIC JOINT FAILURE BY MICRO- AND NANO-CHARACTERIZATION OF INTRA-TISSUE WEAR DEBRIS (page 534)

Nord M.

IM1-IN-2973 Writing and sustaining analysis tools for large and complex microscopy data (page 12)

Nosko M.

MS1-P-2624 Modification of native oxide on magnesium powders for enhanced corrosion resistance (page 349)

MS1-P-2589 Microstructural characterization of sintered Iron and observation of oxides reduction after different conditions of sintering process (page 350)

MS4-P-2595 Native surface oxide characterization with S/TEM on PM metal powders (page 442)

Nottola S. A.

LS1-P-2518 Ultrastructure analysis in the male reproductive system of different mammals exposed to ionizing radiation after the Fukushima accident: a comparative study (page 208)

Nováček D.

MS1-P-2656 The Use of Titanothermic Reduction for Processing of Deep-Sea Nodules (page 339)

MS1-P-2623 Aluminothermally reduced deep-sea concretion and its phase structure (page 341)

Nováček J.

LS3-O-2732 Endosome disruption enables enteroviruses to reach cell cytoplasm (page 236)

LS6-P-2802 In situ cryo-electron tomography of enterovirus cell entry (page 303)

Novackova I.

LS2-P-2663 Ultrastructural changes in prokaryotic microorganisms caused by long-term exposure to high salt and copper ion concentrations (page 231)

Novák J.

IM2-P-2677 Miro proteins and their role in horizontal transfer of mitochondria via tunneling nanotubes in cancer cells (page 67)

Novak L.

MS5-P-2539 Real-time observation of vapor transport synthesis in the scanning electron microscope (page 466)

Novák L.

IM5-P-2864 Batteries in situ testing in SEM (page 144)

MS4-P-2750 In-situ observation of 2D materials growth on liquid substrates (page 432)

Novák P.

MS1-IN-2915 Titanium-aluminide-silicide based alloys (page 325)

MS1-P-2656 The Use of Titanothermic Reduction for Processing of Deep-Sea Nodules (page 339)

MS1-P-2623 Aluminothermally reduced deep-sea concretion and its phase structure (page 341)

Nováková Z.

LS3-O-2746 Exploring the unseen: quantitative phase imaging in cancer research (page 240)

Novotná P.

LS4-P-2839 Comparison of CLMS and super-resolution techniques to study meiotic proteins in plants (page 270)

Ntola P.

MS5-P-2832 Exploring the role of fuel on the microstructure of VOx/MgO powders prepared using solution combustion synthesis (page 478)

Oberaigner M.

IM3-IN-2626 Challenges in the characterization of complex nanomaterials with analytical STEM (page 80)

MS4-O-2594 Orbital mapping of the LaAlO3-TiO2 interface by STEM-EELS (page 417)

Oberhumer P.

MS1-O-2796 An in-depth investigation of liquid metal embrittlement sensitive grain boundaries in TBF steels (page 328)

Obořilová R.

MS3-P-2990 BioAFM imaging and mechanics tracking (page 395)

Obruca S.

IM2-P-2699 Assembly for Cryo-SEM/Raman Microspectroscopy sample analysis (page 63)

LS2-P-2663 Ultrastructural changes in prokaryotic microorganisms caused by long-term exposure to high salt and copper ion concentrations (page 231)

Oh Y.

LS2-O-2638 Borrelia – host interactions: zoom in on the big picture (page 216)

Oliver R. A.

MS6-P-2847 Are FIB-prepared hybrid perovskite cross-sections still luminescent? (page 497)

Olivier E. J.

MS5-P-2832 Exploring the role of fuel on the microstructure of VOx/MgO powders prepared using solution combustion synthesis (page 478)

Olšinová M.

IM2-O-2791 Correlative super-resolution and electron microscopy in plant samples (page 39)

Önal S.

IM1-IN-2752 Image Analysis Workflow for Phase-Contrast Optical Microscopy Images (page 20)

Ondráčková P.

LS4-O-2597 High-resolution structural and functional deep brain imaging using holographic endo-microsocpy (page 266)

LS4-P-2606 Fluorescence confocal imaging via holographic endo-microscopy (page 278)

Ong Khac Q.

IM1-O-2853 4D-STEM Imaging for 3D Stereo Reconstruction by Deep Learning Neural Networks (page 16)

Orgiani P.

IM5-P-2628 Field induced oxygen vacancy migration in anatase thin films studied by in situ biasing TEM (page 138)

MS4-O-2594 Orbital mapping of the LaAlO3-TiO2 interface by STEM-EELS (page 417)

MS4-O-2619 Aberration-Corrected STEM Characterisation of Mn-ion Structural Displacements in La0.7Sr0.3MnO3 Interfacial Dead-Layers (page 419)

Orlandi F.

IM3-P-2579 3D Electron Diffraction on Ferroelectric Perovskites. (page 88)

Orlova L.

LS6-P-2849 Monitoring the endothelial cell behavior during flow stress induction using digital holographic microscopy. (page 304)

Orovčík Ľ.

MS4-P-2595 Native surface oxide characterization with S/TEM on PM metal powders (page 442)

Orovčík L.

MS1-P-2589 Microstructural characterization of sintered Iron and observation of oxides reduction after different conditions of sintering process (page 350)

Orzechowska B.

LS6-O-2627 In-situ observations of metal nanoparticles interactions with living cells, in liquid environments directly in the Nanolive 3D CX-A microscope (page 294)

Otašević V. M.

LS3-P-2799 Beneficial effects of ferroptosis inhibitor ferrostatin-1 on pancreatic islets in streptozotocin-induced diabetes (page 251)

LS3-P-2812 Beneficial effects of ferroptosis inhibitor ferrostatin-1 in diabetes-induced liver damage (page 253)

Otyepka M.

Late-P-3026 In-situ analysis of graphene and its derivatives by combined SEM/AFM method (page 527)

Ovečka M.

LS2-IN-2688 Recent advances in plant development and plant-microbe interactions employing light-sheet and super-resolution microscopy (page 215)

Oveisi E.

IM1-O-2853 4D-STEM Imaging for 3D Stereo Reconstruction by Deep Learning Neural Networks (page 16)

Ozer S. C.

Late-P-3048 Effect of in-situ Conductive TiB2 3D-Network Structure on the Thermoelectric Properties of SiC (page 537)

Ozturk M.

LS3-P-2704 Vitamin-D combined with resveratrol regulates islets hemostasis, β-cell regeneration, ER-stress and inflammation in fructose-fed diet/STZ-induced diabetic rats (page 255)

LS3-P-2756 Differentiation of DDR1+ progenitor cells into β cells in neonatal rat diabetes (page 257)

Paciu I.

LS4-P-2645 High-stability stage for cryo-light microscopy with immersion objectives (page 272)

Pala J.

LS4-O-2854 Time resolved spectral detection for autofluorescence studies (page 269)

Palatinus L.

Plenary-2891 When microscopy meets crystallography: Crystal structure analysis by 3D electron diffraction (page 7)

MS1-P-2657 Incommensurate structure of τ phase in the Al-Cu-Zn system (page 337)

Palmer R. E.

MS5-P-2982 Classification of Metal Nanoclusters Using Convolutional Neural Networks (page 470)

Palmerini M. G.

LS1-P-2518 Ultrastructure analysis in the male reproductive system of different mammals exposed to ionizing radiation after the Fukushima accident: a comparative study (page 208)

Palus M.

LS7-O-2632 What does SARS-CoV-2 do to the lungs – what can 3D electron microscopy tell us (page 312)

Pan Z.

MS5-P-2618 Uranium reduction by magnetite – mechanism of UO2 formation monitored by STEM, SAED and STEM-EELS (page 464)

Panasci S. E.

MS4-O-2511 Microscopy of CVD grown MoS2 layers compared to layers obtained by the sulphurization of Mo (page 426)

Pankaczi F.

LS2-P-2532 Utilization of haematite nanoparticles by a flavin mediated iron uptake of roots (page 227)

Panžić I.

MS6-O-2793 Morphology related energy losses in small molecule organic solar cells (page 493)

Parisse P.

MS3-IN-2878 Extracellular Vesicles and biomimetic membranes: an Atomic Force Microscopy point of view (page 383)

Park J.

IM7-O-2590 FIB-based lamella preparation for in-situ TEM gas experiment (page 176)

Parlinska-Wojtan M.

LS6-O-2627 In-situ observations of metal nanoparticles interactions with living cells, in liquid environments directly in the Nanolive 3D CX-A microscope (page 294)

MS7-O-2694 Liquid cell TEM electrodeposition of PtNi alloy nanoparticle film (page 517)

Paruch K.

IM7-P-2790 Nanopatterned Surface for Super-resolution Microscopy localization of Cell Interactions (page 191)

Pasquier L.

MS4-P-2640 Transmission electron microscopy characterization of quasicrystal approximants in SrTiO3 thin films grown on Pt(111)/Al2O3(0001) (page 448)

Pašti I. A.

MS6-P-2630 Combined Microstructural and Electrochemical Studies of Sputtered Ni Thin Layers as Catalysts for Hydrogen Evolution Reaction (page 501)

Paták A.

IM6-IN-2598 Ab initio study of angle-resolved electron spectroscopy of graphene (page 156)

IM6-O-2820 Time-of-Flight Spectrometer for Low Landing Energies (page 160)

IM6-P-2599 Effective IMFP of thin samples via the time-of-flight method (page 168)

MS4-P-2669 Energy-based calibration for quantitative STEM measurements and comparison with 2D-PAD (page 450)

Paulin I.

MS1-P-2852 Influence of melting and AM-SLM processing on microtexture of Fe-Si soft magnetic materials – Is one-step manufacturing of electrical steels possible? (page 359)

Pavić L.

MS5-P-2858 Study of barium titanate on transparent titania nanotubes arrays (page 472)

Pavin N.

LS6-O-2622 Oscillatory intracellular patterns of the small GTPase Rac1 (page 292)

Pavlišič A.

MS6-P-2682 Studying electrochemical degradation in nanocatalysts with identical location STEM (page 503)

Pavlova E.

IM3-O-2671 High-resolution Powder Nano-Beam Diffraction in Scanning Electron Microscopy (page 76)

MS3-P-2814 Commonly used vs novel embedding resins for 3D-SEM microscopy with higher resistance to e-beam damage. (page 396)

Pavone F.

LS6-IN-2950 Large Area Brain Imaging (page 296)

Pawlyta M.

MS7-O-2694 Liquid cell TEM electrodeposition of PtNi alloy nanoparticle film (page 517)

Pécz B.

IM3-P-2781 Application of the DiffMap program to PtSi thin films (page 92)

Pecz B.

MS4-O-2511 Microscopy of CVD grown MoS2 layers compared to layers obtained by the sulphurization of Mo (page 426)

Peharec Štefanić P.

LS2-O-2661 Surface Coating-Modulated Phytotoxic Responses of Silver Nanoparticles in Chlorella vulgaris (page 218)

Pekar M.

MS3-O-2798 Ultrastructural analysis of hydrogels and its contribution to understanding their mechanical and transport performance (page 386)

MS3-P-2828 Visualization of internal morphology of hydrogels based on polyvinyl alcohol in comparison with the indirect method of structural characterization (page 402)

Pelaez Fernandez M.

MS5-O-2808 Towards Laser-Induced Tuning of Plasmonic Response in High Aspect-Ratio Au Nanowires: A STEM/EELS study (page 460)

Pelaez-Fernandez M.

MS3-P-2834 Low Dose Transmission Electron Microscopy Imaging on Sensitive Colloidal Covalent-Organic Frameworks (page 398)

MS5-P-2844 In-situ Carbon Nanoribbon Formation by TEM Manipulation of a C59N Derivative (page 480)

Pesen Okvur D.

IM1-IN-2752 Image Analysis Workflow for Phase-Contrast Optical Microscopy Images (page 20)

Pesenhofer C.

MS4-P-2660 Noble gas clusters in a graphene sandwich (page 434)

Peter K.

LS1-O-2655 Why do Schwann cells like spider silk? (page 199)

Peters J.

IM1-O-2569 Making Every Electron Count: Improving STEM Quantification, Speed, and Data Throughput with Solid State Detectors and Pulse Counting Hardware (page 14)

Peters T.

IM2-O-2528 Analysis of sampled airborne particles by correlative microscopy (page 47)

MS5-P-2524 Quantification and morphological analysis of nanofibers for exposure control and material characterization purposes using electron microscopy and advanced image (page 482)

Petrášek J.

LS2-IN-2966 Shedding new light on plant biology – automated long-term vertical-stage microscopy at high resolution (page 213)

Petrinec D.

IM2-P-2800 Microscopy and in vivo imaging in aid for visualization of dynamic processes - example of brain damage evolution after ischemic brain stroke (page 68)

IM7-P-2801 Washing brains or how to see things more clearly - Fluorescence microscopy can be used for visualization of blood vessels and neurons in the cleared mouse brain (page 181)

Petrun M.

MS1-P-2852 Influence of melting and AM-SLM processing on microtexture of Fe-Si soft magnetic materials – Is one-step manufacturing of electrical steels possible? (page 359)

Pevna V.

LS4-P-2498 Targeted photobiomodulation of cancer cells at 808 nm may improve efficacy of photodynamic therapy (page 274)

LS4-P-2499 Imaging of autophagic and mitochondrial proteins in 3D spheroids of U87 MG cancer cells during photodynamic therapy mediated with hypericin (page 276)

Philimonenko V.

IM7-P-2662 Solutions for preparation and visualization of vitrified biological samples at IMG Electron Microscopy Core Facility (page 193)

Philippe C.

IM2-P-2850 Imidazole-osmium reduces elution of lipids from cryofixed rat hepatic tissue for correlative TEM/NanoSIMS analysis (page 55)

Piazza L.

IM3-P-2815 Hybrid-pixel detectors for TEM (page 96)

Pierre D.

MS4-P-2640 Transmission electron microscopy characterization of quasicrystal approximants in SrTiO3 thin films grown on Pt(111)/Al2O3(0001) (page 448)

Pikálek T.

LS4-O-2597 High-resolution structural and functional deep brain imaging using holographic endo-microsocpy (page 266)

LS4-P-2606 Fluorescence confocal imaging via holographic endo-microscopy (page 278)

Piksa M.

IM5-O-2542 Transmission electron microscope modification for light-induced in situ imaging of specimens in liquid on example of photodynamic therapy (page 130)

Pinkas D.

IM1-P-2696 Project „Pattern“ – an online tool for spatial analysis of immunolabeling in electron microscopy (page 27)

IM7-O-2668 Faster Cryo TEM lamella preparation using optimised conditions and advanced workflows (page 173)

IM7-P-2676 IMG Electron Microscopy Core Facility (page 192)

IM7-P-2662 Solutions for preparation and visualization of vitrified biological samples at IMG Electron Microscopy Core Facility (page 193)

Pinkas I.

MS3-O-2538 Extreme scale-dependent tensile properties of epoxy fibers and a polarized micro-Raman study (page 391)

Piňos J.

IM6-O-2820 Time-of-Flight Spectrometer for Low Landing Energies (page 160)

IM6-P-2599 Effective IMFP of thin samples via the time-of-flight method (page 168)

MS1-P-2588 Real Time Observation of strain in the SEM copper sample (page 351)

Pizúrová N.

MS5-P-2851 Effect of Nanoparticle Size on Phase Stability in ZrO2 System (page 468)

MS5-P-2685 CeO2 Morphology Study – Nanoparticles Prepared by Electron Beam Evaporation (page 483)

Plank H.

IM2-O-2635 3D-Nanoprinting of Magnetic Force Microscopy Tips (page 37)

MS5-O-2636 Expanded Design Flexibility in 3D-Nanoprinting via Focused Electron Beam Induced Deposition (page 456)

Plašil J.

MS2-IN-3034 Nano crystallography from 3-dimensional electron diffraction: a powerful tool to uncover supergene minerals (page 379)

Platzer R.

LS4-IN-2948 A DNA origami-based biointerface for probing the spatial requirements of cell surface receptor triggering (page 262)

Plevka P.

LS3-O-2732 Endosome disruption enables enteroviruses to reach cell cytoplasm (page 236)

LS6-P-2802 In situ cryo-electron tomography of enterovirus cell entry (page 303)

Plitzko S.

MS5-P-2524 Quantification and morphological analysis of nanofibers for exposure control and material characterization purposes using electron microscopy and advanced image (page 482)

Plodinec M.

MS6-P-2963 Self-sustained oscillatory dynamics of ethylene to syngas by operando SEM and XPS (page 495)

Ploszczanski L.

LS1-O-2655 Why do Schwann cells like spider silk? (page 199)

Podlogar M.

MS4-P-2640 Transmission electron microscopy characterization of quasicrystal approximants in SrTiO3 thin films grown on Pt(111)/Al2O3(0001) (page 448)

Poizot P.

IM5-O-2894 Graphene liquid cell for electron microscopy analysis of nanoparticle interaction with solutions: the case of titanium oxide nanoparticles and phosphates (page 123)

Pokorny D.

MS3-P-2653 Simple, fast and reliable method of UHMWPE accelerated aging (page 393)

Polcar T.

MS4-O-2792 Insights into tribology of TMD-based coatings from TEM experiments (page 423)

Pongrácz J.

IM2-P-2544 High-resolution electron beam induced current study of AlN epitaxial layer (page 69)

Pospíšil J.

IM7-P-2790 Nanopatterned Surface for Super-resolution Microscopy localization of Cell Interactions (page 191)

Preimesberger A.

IM3-P-2678 Temporal correlations in coherent cathodoluminescence (page 94)

Přibyl J.

MS3-P-2990 BioAFM imaging and mechanics tracking (page 395)

Přibyl J.

LS6-P-2898 Correlation of Atomic Force Microscopy with other techniques: application on biosamples (page 301)

Propst D.

MS4-P-2823 STEM analysis of freestanding monolayer h-BN irradiated with slow highly charged ions (page 446)

Proust B.

LS3-P-2654 NME6, a member of the NME/NDPK family resides in complexes at the interface of mitochondrial inner membrane and matrix (page 247)

Průcha L.

IM6-IN-2598 Ab initio study of angle-resolved electron spectroscopy of graphene (page 156)

IM6-O-2820 Time-of-Flight Spectrometer for Low Landing Energies (page 160)

IM6-P-2620 Combining Low Energy Electron Microscopy and Thermal Raman Spectroscopy for Graphene Analysis (page 166)

MS4-P-2670 Graphene-coated scintillators for low-energy electron detection (page 444)

Prytz Ø.

MS5-P-2568 Structural and optical investigation of Fe-ZnO nanoarchitectures: from inversion domain boundaries to ZnO/ZnFe2O4 heterostructures (page 474)

Pyka G.

MS2-P-2706 Multimodal and multi-resolution approach for defects analysis on the example of Additively Manufactured healable aluminium alloy (page 380)

Qi H.

MS3-O-2846 Sub-Ångstrom resolution imaging of 2D conjugated metal-organic frameworks enabled by unconventional resilience against electron radiation (page 389)

MS4-O-2837 Optimal acceleration voltage for near-atomic resolution imaging of layer-stacked 2D polymer thin films (page 413)

MS4-O-2842 Thickness dependency of critical dose for extremely beam-sensitive two-dimensional polymer (page 428)

MS4-P-2835 Deep learning pipeline for statistical quantification of amorphous two-dimensional materials (page 436)

Quigley F.

IM6-O-2572 The Retrofittable Photoelectron Source: A Potential Improvement to Low Voltage SEM Imaging (page 158)

Raabe D.

MS6-O-2514 Correlative Microscopy Techniques for Defect-Property-Correlation of Thermoelectric Materials (page 487)

Raabova H.

IM1-P-2696 Project „Pattern“ – an online tool for spatial analysis of immunolabeling in electron microscopy (page 27)

IM7-P-2662 Solutions for preparation and visualization of vitrified biological samples at IMG Electron Microscopy Core Facility (page 193)

Raabová H.

IM7-P-2676 IMG Electron Microscopy Core Facility (page 192)

Radenovic A.

LS4-IN-3001 Combining Super-resolution Optical Fluctuation Imaging (SOFI) With Structure Illumination and 3D Imaging (page 264)

Radić M.

LS3-P-2654 NME6, a member of the NME/NDPK family resides in complexes at the interface of mitochondrial inner membrane and matrix (page 247)

Radlinger T.

IM3-IN-2626 Challenges in the characterization of complex nanomaterials with analytical STEM (page 80)

IM3-P-2642 Analytical electron tomography of CuNiFe magnetic spinodal alloys (page 90)

MS1-P-2531 Exploring the magnetic microstructure of spinodal alloys with differential phase contrast scanning transmission electron microscopy (DPC-STEM) (page 353)

Radmilović M.

IM2-P-2800 Microscopy and in vivo imaging in aid for visualization of dynamic processes - example of brain damage evolution after ischemic brain stroke (page 68)

Radmilovic V. R.

MS6-IN-2913 Can the Wet Win the Bet? The case of Energy Harvesting and Storage (page 491)

Radmilovic V. V.

MS6-IN-2913 Can the Wet Win the Bet? The case of Energy Harvesting and Storage (page 491)

Radochová B.

IM1-P-2611 Estimation of Pancreatic Islets Volume from Single Projection. (page 26)

Radovanović-Perić F.

MS6-O-2793 Morphology related energy losses in small molecule organic solar cells (page 493)

Radtke C.

LS1-O-2655 Why do Schwann cells like spider silk? (page 199)

Radulovic S.

LS1-O-2804 Neurons and glial cells appear to store and release human brain ferritin at different rates (page 202)

Rafailovic L. D.

MS6-P-2630 Combined Microstructural and Electrochemical Studies of Sputtered Ni Thin Layers as Catalysts for Hydrogen Evolution Reaction (page 501)

Rajak P.

MS4-O-2619 Aberration-Corrected STEM Characterisation of Mn-ion Structural Displacements in La0.7Sr0.3MnO3 Interfacial Dead-Layers (page 419)

Rajnovic D.

MS1-P-2855 Morphological characterization of mill scales iron oxides products by SEM (page 355)

MS1-P-2856 Characterization of oil pipe weld localized corrosion and perforation (page 357)

Ramasse Q. M.

Plenary-2901 Recent Progress in High-Resolution Electron Energy Loss Spectroscopy in the Scanning Transmission Electron Microscope (page 4)

Raschdorf O.

LS3-O-2821 Extending Capabilities of 120 kV LaB6 TEMs to Cryo-EM Reconstructions at Subnanometer Resolution (page 238)

Rašić D. M.

LS1-IN-3008 Transmission electron microscopy in research and diagnostics - new challenges in the omics era (page 201)

Raskovic B.

LS3-IN-2769 Spheroids: in vitro 3D cell cultures of brown trout liver as a model for ecotoxicology research (page 235)

Rath T.

MS6-O-2793 Morphology related energy losses in small molecule organic solar cells (page 493)

Rattenberger J.

IM2-O-2563 Correlative Raman microscopy, SEM and EDS – The combined evaluation of a whole sample mapping of a Chelyabinsk meteorite fragment (page 43)

IM2-O-2629 Automated and correlative SEM-EDX-Raman particle analysis on fine dust filters of extreme events: New Year's Eve and Sahara dust (page 52)

LS2-O-2684 Pyroplastics: A new Approach (page 222)

Rauschenbach B.

MS4-O-2580 Nanoscale characterization of van der Waals-bonded GeTe/Sb2Te3 phase-change memory superlattices grown by pulsed laser deposition (page 424)

Razinger J.

LS3-P-2643 Insect midgut epithelium architecture – focus on gut stem cells in larvae and adults (page 259)

Ražnjević S.

Late-P-3032 Electron beam irradiation induced Brownmillerite – perovskite phase transition in La_{0.6} Sr_{0.4} CoO_{3-ð} (page 530)

Rechav K.

IM5-P-2782 Cryo Volume Imaging: from cell nucleus to extracellular structure. (page 146)

LS7-P-2625 Characterization of the Growth Plate-Bone Interphase Region Using Cryo-FIB SEM 3D Volume Imaging (page 320)

Rego R.

LS2-O-2638 Borrelia – host interactions: zoom in on the big picture (page 216)

Reimers S.

IM2-O-2695 Atomically Sharp Domain Walls in an Antiferromagnet (page 41)

Reipert S.

IM2-P-2850 Imidazole-osmium reduces elution of lipids from cryofixed rat hepatic tissue for correlative TEM/NanoSIMS analysis (page 55)

Rellinghaus B.

IM2-O-2693 Micro X-ray computed tomography as an extension to light microscopy and FIB/SEM (page 49)

Repellin M.

LS1-IN-2535 Hyaluronic acid based nanoparticles are suitable carriers to muscle cells: the ultrastructural evidence (page 195)

Restović I.

LS2-P-2585 Expression of the enzyme myrosinase type 1 in the root, the stem and the leaves of the plant nasturtium (Tropaeolum majus L.) (page 229)

Reyntjens S.

IM7-P-2848 High-Throughput Cryo-Electron Tomography with a next generation platform (page 187)

Riedl C.

Late-P-3032 Electron beam irradiation induced Brownmillerite – perovskite phase transition in La_{0.6} Sr_{0.4} CoO_{3-ð} (page 530)

Righi L.

IM3-P-2579 3D Electron Diffraction on Ferroelectric Perovskites. (page 88)

Rigort A.

IM7-P-2848 High-Throughput Cryo-Electron Tomography with a next generation platform (page 187)

Rijavec T.

LS2-O-2690 The use of SEM imaging and elemental mapping in the research of artificial bacterial aggregates (page 220)

Riley H.

MS6-O-2514 Correlative Microscopy Techniques for Defect-Property-Correlation of Thermoelectric Materials (page 487)

Roccaforte F.

MS4-O-2511 Microscopy of CVD grown MoS2 layers compared to layers obtained by the sulphurization of Mo (page 426)

Rocha E.

LS3-IN-2769 Spheroids: in vitro 3D cell cultures of brown trout liver as a model for ecotoxicology research (page 235)

Rodenkirchen C.

MS6-O-2514 Correlative Microscopy Techniques for Defect-Property-Correlation of Thermoelectric Materials (page 487)

Roiban L.

LS7-O-2698 3D reconstruction of hydrated samples at the sub-micrometer scale using Liquid-Phase STEM at low voltage (page 315)

Rojac T.

MS6-IN-2562 In situ Scanning Transmission Electron Microscopy of Lead-Free Ferroelectrics with Atomic Resolution (page 486)

MS7-P-2540 Mechanical response of domain walls in lead-free ferroelectrics (page 525)

Romaner L.

MS1-O-2601 Co-segregation of zinc, carbon and boron in a Σ5 iron grain boundary resolved by correlating atomic resolution STEM, APT and first-principles calculations (page 326)

Romih R.

LS7-O-2860 Volume electron microscopy and automatic segmentation of intracellular compartments in the urinary bladder umbrella cells (page 310)

Ropele S.

LS1-O-2804 Neurons and glial cells appear to store and release human brain ferritin at different rates (page 202)

Rosi P.

IM4-O-2591 Enhancing Electron Computational Ghost Imaging Using Artificial Neural Networks (page 116)

Rossi G.

MS4-O-2619 Aberration-Corrected STEM Characterisation of Mn-ion Structural Displacements in La0.7Sr0.3MnO3 Interfacial Dead-Layers (page 419)

Rossy J.

LS6-IN-3013 Quantitative visualisation of membrane dynamics through photoactivation of fluorescent proteins (page 291)

Rothman A.

MS5-P-2539 Real-time observation of vapor transport synthesis in the scanning electron microscope (page 466)

Rotunno E.

IM4-O-2506 Measurement and Correction of Phase Aberrations in Scanning Transmission Microscopy by Artificial Neural Networks (page 112)

IM4-O-2591 Enhancing Electron Computational Ghost Imaging Using Artificial Neural Networks (page 116)

Roupcová P.

MS5-P-2851 Effect of Nanoparticle Size on Phase Stability in ZrO2 System (page 468)

Rožman T.

MS5-IN-3031 Application of electron microscopy in development of sensor elements for detection of toxic organic compounds (page 455)

Ruano Merchan C.

MS4-P-2640 Transmission electron microscopy characterization of quasicrystal approximants in SrTiO3 thin films grown on Pt(111)/Al2O3(0001) (page 448)

Ruiz-Zepeda F.

MS6-P-2682 Studying electrochemical degradation in nanocatalysts with identical location STEM (page 503)

Ruland S.

IM2-O-2612 Proof-of-Concept study for high-resolution correlative multimodal imaging and big data of a mouse brain (page 35)

LS6-O-2615 The BUILD project: A multi-modal cross-scale approach to reveal characteristics of the human brain’s nested connectome (page 297)

Rusz J.

IM2-O-2695 Atomically Sharp Domain Walls in an Antiferromagnet (page 41)

Růžek D.

LS7-O-2632 What does SARS-CoV-2 do to the lungs – what can 3D electron microscopy tell us (page 312)

Sabotič J.

LS3-P-2643 Insect midgut epithelium architecture – focus on gut stem cells in larvae and adults (page 259)

Sadeghi B.

MS1-P-2689 Thermal stability of hydro-extruded aluminum: Judging the distribution of amorphous and crystalline aluminum-oxide via plasmon mapping. (page 363)

Sag F. B.

LS1-P-2811 Histopathological and ultrastructural effects of chronic administrated high dose dehydroepiandrosterone on liver and kidney of male rats (page 211)

Sagawa R.

IM4-O-2570 A User Adjustable Pole-piece Gap as a Route to Improve the Sustainability of TEM Infrastructure (page 110)

Saghi Z.

LS7-O-2827 Deep learning approaches for electron tomography under limited data acquisition conditions (page 313)

Sahin H.

LS1-P-2811 Histopathological and ultrastructural effects of chronic administrated high dose dehydroepiandrosterone on liver and kidney of male rats (page 211)

Saksida T. A.

LS3-P-2799 Beneficial effects of ferroptosis inhibitor ferrostatin-1 on pancreatic islets in streptozotocin-induced diabetes (page 251)

LS3-P-2812 Beneficial effects of ferroptosis inhibitor ferrostatin-1 in diabetes-induced liver damage (page 253)

Salaun P.

MS3-P-2834 Low Dose Transmission Electron Microscopy Imaging on Sensitive Colloidal Covalent-Organic Frameworks (page 398)

Šamaj J.

LS2-IN-2688 Recent advances in plant development and plant-microbe interactions employing light-sheet and super-resolution microscopy (page 215)

Šamajová O.

LS2-IN-2688 Recent advances in plant development and plant-microbe interactions employing light-sheet and super-resolution microscopy (page 215)

Samal S. M.

MS2-O-2667 High resolution CT study of microstructure defects behaviour in deformed NiTi prepared by spark plasma sintering (page 377)

Samardžija Z.

MS5-IN-3031 Application of electron microscopy in development of sensor elements for detection of toxic organic compounds (page 455)

Šantić N.

IM5-P-2664 Efficient preparation of MEMS carriers with plan-view specimens: a case study of in situ TEM experiments with thin epitaxial layers (page 134)

Savaci U.

Late-P-3047 An Alternative Approach For The EELS Analysis Of Noble Gases (page 536)

Late-P-3048 Effect of in-situ Conductive TiB2 3D-Network Structure on the Thermoelectric Properties of SiC (page 537)

Schachinger T.

IM3-P-2678 Temporal correlations in coherent cathodoluminescence (page 94)

Schachinger T.

IM4-P-2584 Simplified electron vortex generator with aberration correction (page 118)

Schaper M.

MS1-P-2602 Phase Identification in Twin-Roll Cast Al-Steel Clad Composite (page 343)

Schattschneider P.

IM4-P-2584 Simplified electron vortex generator with aberration correction (page 118)

Schatz M.

LS5-IN-3045 Quantitative super-resolution microscopy of nuclear antigens in cells and tissues (page 283)

Schäublin R.

MS7-O-2694 Liquid cell TEM electrodeposition of PtNi alloy nanoparticle film (page 517)

Scheiber D.

MS1-O-2601 Co-segregation of zinc, carbon and boron in a Σ5 iron grain boundary resolved by correlating atomic resolution STEM, APT and first-principles calculations (page 326)

Scherer T.

IM2-P-2850 Imidazole-osmium reduces elution of lipids from cryofixed rat hepatic tissue for correlative TEM/NanoSIMS analysis (page 55)

Scheu C.

MS6-O-2514 Correlative Microscopy Techniques for Defect-Property-Correlation of Thermoelectric Materials (page 487)

Scheucher M.

IM3-P-2678 Temporal correlations in coherent cathodoluminescence (page 94)

Schilirò E.

MS4-O-2511 Microscopy of CVD grown MoS2 layers compared to layers obtained by the sulphurization of Mo (page 426)

Schintlmeister A.

IM2-P-2850 Imidazole-osmium reduces elution of lipids from cryofixed rat hepatic tissue for correlative TEM/NanoSIMS analysis (page 55)

Schlattner U.

LS3-P-2654 NME6, a member of the NME/NDPK family resides in complexes at the interface of mitochondrial inner membrane and matrix (page 247)

Schlichthärle T.

LS4-IN-2948 A DNA origami-based biointerface for probing the spatial requirements of cell surface receptor triggering (page 262)

Schmidt R.

IM2-O-2563 Correlative Raman microscopy, SEM and EDS – The combined evaluation of a whole sample mapping of a Chelyabinsk meteorite fragment (page 43)

Schmies L.

IM1-O-2679 Integrated topographic SEM imaging for software assisted fractography (page 18)

Schneider M.

MS1-IN-2503 Quantitative STEM in the diffraction contrast regime (page 323)

Schrenker N.

MS5-IN-3044 In situ microscopy of nanowires: From fundamental properties to functional applications (page 453)

Schroettner H.

IM2-O-2563 Correlative Raman microscopy, SEM and EDS – The combined evaluation of a whole sample mapping of a Chelyabinsk meteorite fragment (page 43)

IM2-O-2629 Automated and correlative SEM-EDX-Raman particle analysis on fine dust filters of extreme events: New Year’s Eve and Sahara dust (page 52)

IM2-P-2545 Extensive material characterization for series production of 3D printer components (page 71)

LS2-O-2684 Pyroplastics: A new Approach (page 222)

Schumann J.

IM2-O-2528 Analysis of sampled airborne particles by correlative microscopy (page 47)

MS5-P-2524 Quantification and morphological analysis of nanofibers for exposure control and material characterization purposes using electron microscopy and advanced image (page 482)

Schürrer M. W.

IM6-P-2879 Determination of the inelastic mean free path of electrons in selected Polymers, indenpent from optical data, considering surface excitations (page 165)

Schusser G.

IM7-O-2593 High-Throughput TEM Sample Preparation with iNotch Technique (page 174)

Schweizer P.

MS5-IN-3044 In situ microscopy of nanowires: From fundamental properties to functional applications (page 453)

Schwiedrzik J.

MS7-IN-2666 Recent advances in in-situ SEM nanomechanical testing: extreme temperatures, ultra-high strain rates, in-situ electron diffraction and digital image correlation (page 508)

Searle S.

LS7-P-2659 Modern SEM allows high-throughput 2D and 3D analyses on a single platform (page 317)

Sebesta O.

LS5-IN-3045 Quantitative super-resolution microscopy of nuclear antigens in cells and tissues (page 283)

Sedlacek P.

MS3-O-2798 Ultrastructural analysis of hydrogels and its contribution to understanding their mechanical and transport performance (page 386)

MS3-P-2828 Visualization of internal morphology of hydrogels based on polyvinyl alcohol in comparison with the indirect method of structural characterization (page 402)

Seewald L.

IM2-O-2635 3D-Nanoprinting of Magnetic Force Microscopy Tips (page 37)

Seewald L. M.

MS5-O-2636 Expanded Design Flexibility in 3D-Nanoprinting via Focused Electron Beam Induced Deposition (page 456)

Seke M.

LS1-IN-3008 Transmission electron microscopy in research and diagnostics - new challenges in the omics era (page 201)

Šembera O.

IM3-P-2825 Improved mapping algorithms: combating data sparsity in SEM EDS (page 102)

Semsari Parapari S.

MS4-P-2640 Transmission electron microscopy characterization of quasicrystal approximants in SrTiO3 thin films grown on Pt(111)/Al2O3(0001) (page 448)

Senturk G. E.

LS1-P-2811 Histopathological and ultrastructural effects of chronic administrated high dose dehydroepiandrosterone on liver and kidney of male rats (page 211)

Sevcsik E.

LS4-IN-2948 A DNA origami-based biointerface for probing the spatial requirements of cell surface receptor triggering (page 262)

Sever T.

MS1-P-2852 Influence of melting and AM-SLM processing on microtexture of Fe-Si soft magnetic materials – Is one-step manufacturing of electrical steels possible? (page 359)

Sezer Z.

LS1-P-2811 Histopathological and ultrastructural effects of chronic administrated high dose dehydroepiandrosterone on liver and kidney of male rats (page 211)

Shav-Tal Y.

LS4-O-2712 RNA export through the nuclear pore complex is directional (page 265)

Sheratt M. J.

LS6-O-2639 Correlative 3D imaging workflow using X-ray micro-computed tomography and laser plasma focussed ion beam electron microscopy on biological soft tissues (page 298)

Sicot M.

MS4-P-2640 Transmission electron microscopy characterization of quasicrystal approximants in SrTiO3 thin films grown on Pt(111)/Al2O3(0001) (page 448)

Siebenhofer M.

Late-P-3032 Electron beam irradiation induced Brownmillerite – perovskite phase transition in La_{0.6} Sr_{0.4} CoO_{3-ð} (page 530)

Siedlaczek P.

MS3-P-2829 Characterization of particle-filled polymer composites (page 400)

Sienkiewicz P.

LS6-P-2881 A beetle that was a flea. Comparison of morphological adaptations in external parasites among Coleoptera and Siphonaptera, using light and scanning electron mic (page 300)

Sierlinger R.

MS1-O-2796 An in-depth investigation of liquid metal embrittlement sensitive grain boundaries in TBF steels (page 328)

Šikola T.

IM2-P-2502 Magnetic field imaging with electron energy loss spectroscopy based on Babinet’s principle (page 60)

IM2-P-2816 KPFM in SEM - Simultaneous Kelvin Probe Force Microscopy and Scanning Electron Microscopy (page 62)

IM5-O-2703 In-situ Microscopy of Catalytic Oxidation of CO to CO2 over Platinum Surfaces. (page 128)

MS4-P-2750 In-situ observation of 2D materials growth on liquid substrates (page 432)

MS5-O-2501 Plasmon resonances in biocompatible nanoparticles (page 458)

Sikola T.

MS5-P-2539 Real-time observation of vapor transport synthesis in the scanning electron microscope (page 466)

Šiler M.

LS4-O-2597 High-resolution structural and functional deep brain imaging using holographic endo-microsocpy (page 266)

LS4-P-2606 Fluorescence confocal imaging via holographic endo-microscopy (page 278)

Simar A.

MS2-P-2706 Multimodal and multi-resolution approach for defects analysis on the example of Additively Manufactured healable aluminium alloy (page 380)

Šimek D.

MS2-O-2667 High resolution CT study of microstructure defects behaviour in deformed NiTi prepared by spark plasma sintering (page 377)

Šimić N.

IM3-IN-2626 Challenges in the characterization of complex nanomaterials with analytical STEM (page 80)

IM3-P-2510 Phase Analysis of (Li)FePO4 by Selected Area Electron Diffraction in Transmission Electron Microscopy (page 98)

IM5-P-2651 The power of speed: DED EELS for analytical in situ TEM (page 132)

Singh S.

MS5-P-2832 Exploring the role of fuel on the microstructure of VOx/MgO powders prepared using solution combustion synthesis (page 478)

Singhal N.

LS2-P-2665 3D organization of photosynthetic membranes in cells of photosynthetic bacterium Sediminicoccus rosea (page 224)

Sinn G.

LS1-O-2655 Why do Schwann cells like spider silk? (page 199)

MS3-P-2829 Characterization of particle-filled polymer composites (page 400)

Sitte W.

MS2-O-2843 Quantifying Ordering Phenomena at the Atomic Scale in Rare Earth Oxide Ceramics via EELS Elemental Mapping (page 371)

Siwy R.

LS1-P-2817 Tundra TEM: tool ‘easy of use’ for new commers to Cryo EM (page 209)

Skiba J.

MS1-P-2624 Modification of native oxide on magnesium powders for enhanced corrosion resistance (page 349)

MS1-P-2689 Thermal stability of hydro-extruded aluminum: Judging the distribution of amorphous and crystalline aluminum-oxide via plasmon mapping. (page 363)

Skládal P.

MS3-P-2990 BioAFM imaging and mechanics tracking (page 395)

Škokić S.

IM2-P-2800 Microscopy and in vivo imaging in aid for visualization of dynamic processes - example of brain damage evolution after ischemic brain stroke (page 68)

Skoupy R.

IM2-O-2719 Integrated light-4D-STEM: from fluorescence microscopy and sample thickness mapping to powder diffraction analysis (page 45)

IM3-O-2671 High-resolution Powder Nano-Beam Diffraction in Scanning Electron Microscopy (page 76)

IM7-P-2818 Distribution of staining agents in samples of mice soft tissues prepared for Serial Block Face SEM. (page 189)

MS3-P-2814 Commonly used vs novel embedding resins for 3D-SEM microscopy with higher resistance to e-beam damage. (page 396)

Skoupý R.

IM5-P-2845 Low conductive thermal insulation pad with high mechanical stiffness (page 152)

LS5-O-2715 Correlative cathodoluminescence scanning electron microscopy for identification of cellular structures within vitrified samples at low electron beam energies (page 289)

MS4-P-2670 Graphene-coated scintillators for low-energy electron detection (page 444)

Škrobot Vidaček N.

LS3-P-2654 NME6, a member of the NME/NDPK family resides in complexes at the interface of mitochondrial inner membrane and matrix (page 247)

Škubník K.

LS3-O-2732 Endosome disruption enables enteroviruses to reach cell cytoplasm (page 236)

Skukan L.

IM2-P-2800 Microscopy and in vivo imaging in aid for visualization of dynamic processes - example of brain damage evolution after ischemic brain stroke (page 68)

IM7-P-2801 Washing brains or how to see things more clearly - Fluorescence microscopy can be used for visualization of blood vessels and neurons in the cleared mouse brain (page 181)

Slamkova D.

LS7-P-2582 Plasma FIB applications in Life Science: from large volumes to cryo-lamella preparation (page 318)

Slamova L.

LS3-P-2924 Active transcription-translation coupling at the early translation elongation stages (page 248)

Šlapáková M.

MS1-P-2602 Phase Identification in Twin-Roll Cast Al-Steel Clad Composite (page 343)

MS1-P-2490 In-situ heating of twin-roll cast Al-steel clad strip (page 361)

Slater T.

MS5-P-2982 Classification of Metal Nanoclusters Using Convolutional Neural Networks (page 470)

Slouf M.

MS3-P-2653 Simple, fast and reliable method of UHMWPE accelerated aging (page 393)

Šlouf M.

MS3-IN-2935 Synergy of Scanning Electron and Light Microscopies in Visualization of Swollen Hydrogels and Effect of Hydrogel Parameters on the Image: Artifacts and Reality (page 384)

Slouf M.

IM3-O-2671 High-resolution Powder Nano-Beam Diffraction in Scanning Electron Microscopy (page 76)

MS3-P-2814 Commonly used vs novel embedding resins for 3D-SEM microscopy with higher resistance to e-beam damage. (page 396)

Sloufova I.

MS3-P-2653 Simple, fast and reliable method of UHMWPE accelerated aging (page 393)

Šmerdová L.

LS3-O-2732 Endosome disruption enables enteroviruses to reach cell cytoplasm (page 236)

LS6-P-2802 In situ cryo-electron tomography of enterovirus cell entry (page 303)

Smilek J.

MS3-O-2798 Ultrastructural analysis of hydrogels and its contribution to understanding their mechanical and transport performance (page 386)

MS3-P-2828 Visualization of internal morphology of hydrogels based on polyvinyl alcohol in comparison with the indirect method of structural characterization (page 402)

Smiljanić M.

MS6-P-2682 Studying electrochemical degradation in nanocatalysts with identical location STEM (page 503)

Smith A. D.

IM5-O-2649 Integration of EBSD acquisition into fully automated in-situ thermo-mechanical testing for high temporal and spatial resolution (page 125)

MS7-O-2644 Automated In-Situ Mechanical Testing of heavily textured Ti 6Al 4V to Obtain High Spatial and Temporal Resolution Strain Maps (page 509)

Snyder J.

MS6-O-2514 Correlative Microscopy Techniques for Defect-Property-Correlation of Thermoelectric Materials (page 487)

Sobczak K.

MS7-O-2694 Liquid cell TEM electrodeposition of PtNi alloy nanoparticle film (page 517)

Sojka J.

LS2-IN-2688 Recent advances in plant development and plant-microbe interactions employing light-sheet and super-resolution microscopy (page 215)

Sokovnin S. Y.

MS5-P-2851 Effect of Nanoparticle Size on Phase Stability in ZrO2 System (page 468)

MS5-P-2685 CeO2 Morphology Study – Nanoparticles Prepared by Electron Beam Evaporation (page 483)

Solti Á.

LS2-P-2532 Utilization of haematite nanoparticles by a flavin mediated iron uptake of roots (page 227)

Sonntag U.

IM1-O-2679 Integrated topographic SEM imaging for software assisted fractography (page 18)

Šoštar M.

LS6-O-2622 Oscillatory intracellular patterns of the small GTPase Rac1 (page 292)

Souček P.

MS7-P-2687 Impact behaviour of the industrially sputtered AlCrN coatings prepared using cathodic arc glow discharge (page 519)

Speckmann C.

MS4-P-2823 STEM analysis of freestanding monolayer h-BN irradiated with slow highly charged ions (page 446)

Spiecker E.

MS5-IN-3044 In situ microscopy of nanowires: From fundamental properties to functional applications (page 453)

MS6-IN-2913 Can the Wet Win the Bet? The case of Energy Harvesting and Storage (page 491)

Spielauer T.

IM3-P-2678 Temporal correlations in coherent cathodoluminescence (page 94)

Spilarewicz-Stanek K.

MS6-P-2566 The implementation of microscopic and spectroscopic techniques in characterisation of the spinel ferrite for photocatalytic reduction of CO2 (page 504)

Spreitzer M.

MS2-O-2578 Atomic-scale characterization of polytypic defects in Li0.33La0.56TiO3 (page 373)

Srakočić S.

IM2-P-2800 Microscopy and in vivo imaging in aid for visualization of dynamic processes - example of brain damage evolution after ischemic brain stroke (page 68)

Srnka A.

IM5-P-2833 Cryogenic Sample Holder with Electrical Contacts for UHV SEM/SPM (page 142)

IM5-P-2838 Effect of thermal radiation on the measurement of the sample holder temperature over the cryogenic range for various types of temperature sensor installations (page 150)

IM5-P-2845 Low conductive thermal insulation pad with high mechanical stiffness (page 152)

Stančić A. T.

LS3-P-2799 Beneficial effects of ferroptosis inhibitor ferrostatin-1 on pancreatic islets in streptozotocin-induced diabetes (page 251)

LS3-P-2812 Beneficial effects of ferroptosis inhibitor ferrostatin-1 in diabetes-induced liver damage (page 253)

Staníček J.

LS3-O-2821 Extending Capabilities of 120 kV LaB6 TEMs to Cryo-EM Reconstructions at Subnanometer Resolution (page 238)

Steciuk G.

MS2-IN-3034 Nano crystallography from 3-dimensional electron diffraction: a powerful tool to uncover supergene minerals (page 379)

Steineder K.

MS1-O-2796 An in-depth investigation of liquid metal embrittlement sensitive grain boundaries in TBF steels (page 328)

Steiner Petrovič D.

MS1-P-2852 Influence of melting and AM-SLM processing on microtexture of Fe-Si soft magnetic materials – Is one-step manufacturing of electrical steels possible? (page 359)

Stellacci F.

IM1-O-2853 4D-STEM Imaging for 3D Stereo Reconstruction by Deep Learning Neural Networks (page 16)

Stennett M. C.

MS5-P-2618 Uranium reduction by magnetite – mechanism of UO2 formation monitored by STEM, SAED and STEM-EELS (page 464)

Stéphan O.

IM3-O-2555 Tomography of surface phonon polarition fields by electron energy loss spectroscopy (page 82)

Stephens S.

IM3-P-2825 Improved mapping algorithms: combating data sparsity in SEM EDS (page 102)

Stergiou A.

MS5-P-2844 In-situ Carbon Nanoribbon Formation by TEM Manipulation of a C59N Derivative (page 480)

Stibůrek M.

LS4-O-2597 High-resolution structural and functional deep brain imaging using holographic endo-microsocpy (page 266)

Stöger-Pollach M.

IM3-O-2824 The choice of the right beam energy for analytical (scanning) transmission electron microscopy (page 81)

IM3-P-2678 Temporal correlations in coherent cathodoluminescence (page 94)

Stolbchenko M.

MS1-P-2602 Phase Identification in Twin-Roll Cast Al-Steel Clad Composite (page 343)

Stone H. J.

IM3-P-2683 Scanning electron diffraction study of TiFeAl alloy microstructure (page 100)

Strachota A.

MS3-P-2814 Commonly used vs novel embedding resins for 3D-SEM microscopy with higher resistance to e-beam damage. (page 396)

Strachota B.

MS3-P-2814 Commonly used vs novel embedding resins for 3D-SEM microscopy with higher resistance to e-beam damage. (page 396)

Stranks S. D.

MS6-P-2847 Are FIB-prepared hybrid perovskite cross-sections still luminescent? (page 497)

Straussman R.

LS4-O-2587 Localization of Bacteria in Tumor Cells using Correlative Light and Electron Microscopy (page 268)

Strnad M.

LS2-O-2638 Borrelia – host interactions: zoom in on the big picture (page 216)

Stroppa D. G.

IM3-P-2815 Hybrid-pixel detectors for TEM (page 96)

Šturm S.

MS4-P-2640 Transmission electron microscopy characterization of quasicrystal approximants in SrTiO3 thin films grown on Pt(111)/Al2O3(0001) (page 448)

MS5-IN-3031 Application of electron microscopy in development of sensor elements for detection of toxic organic compounds (page 455)

Sui T.

MS6-O-2505 Multi-scale, high-resolution, time-resolved residual stress in laser-welded Eurofer97 using plasma focused ion beam-digital image correlation method (page 494)

Sui X. M.

MS3-O-2538 Extreme scale-dependent tensile properties of epoxy fibers and a polarized micro-Raman study (page 391)

Šulák I.

MS1-P-2722 Microstructural changes in DLMS IN939 due to low cycle fatigue investigated by advanced electron microscopy. (page 345)

Šulcová L.

MS1-P-2623 Aluminothermally reduced deep-sea concretion and its phase structure (page 341)

Sulyok A.

MS4-O-2511 Microscopy of CVD grown MoS2 layers compared to layers obtained by the sulphurization of Mo (page 426)

Sunkara S.

LS1-O-2804 Neurons and glial cells appear to store and release human brain ferritin at different rates (page 202)

Šuráňová M.

Late-P-3055 Non-Invasive Imaging Method for Evaluating Effect of Migrastatics on Tumor Cells In Vitro Based on Coherence - Controlled Holographic Microscopy (page 532)

Late-P-3058 Identification of Tumor Cells Behavior Changes by Holographic Incoherent Quantitative Phase Imaging Focuses on Migrastatics (page 539)

Susi T.

IM7-P-2755 CANVAS: A System for Controlled Alteration of Nanomaterials in Vacuum Down to the Atomic Scale (page 183)

Švec P.

MS1-P-2689 Thermal stability of hydro-extruded aluminum: Judging the distribution of amorphous and crystalline aluminum-oxide via plasmon mapping. (page 363)

MS1-P-2702 Phase evolution clarification in Al86Ni8Gd6 amorphous alloy: A spotlight on Al20Ni6Gd4 phase and its peculiarities (page 364)

MS1-P-2803 Modification of local ordering in Fe-B based metallic glasses during long-term room temperature ageing (page 366)

Švec Sr P.

MS1-P-2702 Phase evolution clarification in Al86Ni8Gd6 amorphous alloy: A spotlight on Al20Ni6Gd4 phase and its peculiarities (page 364)

MS1-P-2803 Modification of local ordering in Fe-B based metallic glasses during long-term room temperature ageing (page 366)

Szabo G. V.

IM5-IN-2999 Microsystems for in situ cryofixation and correlative cryomicroscopy (page 127)

Sztacho M.

LS5-IN-3045 Quantitative super-resolution microscopy of nuclear antigens in cells and tissues (page 283)

Tagmatarchis N.

MS5-P-2844 In-situ Carbon Nanoribbon Formation by TEM Manipulation of a C59N Derivative (page 480)

Tanriverdi G.

LS3-P-2704 Vitamin-D combined with resveratrol regulates islets hemostasis, β-cell regeneration, ER-stress and inflammation in fructose-fed diet/STZ-induced diabetic rats (page 255)

Tarábková H.

MS3-O-2810 Nanobubble-assisted nanostructuring of water-immersed solid surfaces (page 387)

Tarnawski T.

MS7-O-2694 Liquid cell TEM electrodeposition of PtNi alloy nanoparticle film (page 517)

Tarter S.

Late-P-3052 FROM A CLINICAL CASE TO A GENERAL METHODOLOGY TO ANALYZE PROSTHETIC JOINT FAILURE BY MICRO- AND NANO-CHARACTERIZATION OF INTRA-TISSUE WEAR DEBRIS (page 534)

Taylor M.

IM5-O-2649 Integration of EBSD acquisition into fully automated in-situ thermo-mechanical testing for high temporal and spatial resolution (page 125)

Taylor M. S.

IM5-P-2634 Cryo-SEM to access the Microstructure of Colloidal Dispersions (page 147)

Tchernychova E.

MS6-P-2806 Advanced STEM insights into atomic and electronic structure evolution of corncob-derived hard carbon anode materials for sustainable sodium-ion batteries (page 506)

Tempel H.

IM7-O-2590 FIB-based lamella preparation for in-situ TEM gas experiment (page 176)

Tennyson E. M.

MS6-P-2847 Are FIB-prepared hybrid perovskite cross-sections still luminescent? (page 497)

Terntino A.

MS4-P-2660 Noble gas clusters in a graphene sandwich (page 434)

Terziyska V.

MS2-O-2789 Stacking faults dominant strengthening mechanism behind the anomalous hardness variation of TaN/TiN multilayer films (page 375)

Tessarolo F.

Late-P-3052 FROM A CLINICAL CASE TO A GENERAL METHODOLOGY TO ANALYZE PROSTHETIC JOINT FAILURE BY MICRO- AND NANO-CHARACTERIZATION OF INTRA-TISSUE WEAR DEBRIS (page 534)

Thiem D.

IM5-IN-2999 Microsystems for in situ cryofixation and correlative cryomicroscopy (page 127)

Thim C.

IM2-O-2528 Analysis of sampled airborne particles by correlative microscopy (page 47)

Thøgersen A.

MS5-P-2568 Structural and optical investigation of Fe-ZnO nanoarchitectures: from inversion domain boundaries to ZnO/ZnFe2O4 heterostructures (page 474)

Tichá M.

LS2-IN-2688 Recent advances in plant development and plant-microbe interactions employing light-sheet and super-resolution microscopy (page 215)

Tiemeijer P.

IM4-O-2506 Measurement and Correction of Phase Aberrations in Scanning Transmission Microscopy by Artificial Neural Networks (page 112)

Tihlaříková E.

IM5-P-3010 New TDS software for computer-based optimisation of thermodynamic conditions in Advanced Environmental Scanning Electron Microscopy (A-ESEM) (page 148)

Tiwari M.

MS3-O-2538 Extreme scale-dependent tensile properties of epoxy fibers and a polarized micro-Raman study (page 391)

Tokarska-Schlattner M.

LS3-P-2654 NME6, a member of the NME/NDPK family resides in complexes at the interface of mitochondrial inner membrane and matrix (page 247)

Tolnai G.

LS2-P-2532 Utilization of haematite nanoparticles by a flavin mediated iron uptake of roots (page 227)

Toman J.

MS4-P-2609 Imaging of structural deformations of gas-phase synthesized graphene by intermediate energy electrons (page 430)

Tomasch J.

LS2-P-2665 3D organization of photosynthetic membranes in cells of photosynthetic bacterium Sediminicoccus rosea (page 224)

Tomkova S.

LS4-P-2498 Targeted photobiomodulation of cancer cells at 808 nm may improve efficacy of photodynamic therapy (page 274)

Tomšič M.

MS6-P-2806 Advanced STEM insights into atomic and electronic structure evolution of corncob-derived hard carbon anode materials for sustainable sodium-ion batteries (page 506)

Tordoff B.

IM5-P-2530 In situ deformation observation via EBSD and EDS during high temperature tensile testing (page 140)

Töreyin B. U.

IM1-IN-2752 Image Analysis Workflow for Phase-Contrast Optical Microscopy Images (page 20)

Trafela Š.

MS5-IN-3031 Application of electron microscopy in development of sensor elements for detection of toxic organic compounds (page 455)

Tratnik B.

MS6-P-2806 Advanced STEM insights into atomic and electronic structure evolution of corncob-derived hard carbon anode materials for sustainable sodium-ion batteries (page 506)

Trebichalská Z.

LS3-O-2732 Endosome disruption enables enteroviruses to reach cell cytoplasm (page 236)

LS6-P-2802 In situ cryo-electron tomography of enterovirus cell entry (page 303)

Trentino A.

MS4-O-2807 Correlated AFM/STEM study on the Mechanical Stiffness of Defect-Engineered Graphene (page 411)

Trevizam Dorini T.

MS4-P-2640 Transmission electron microscopy characterization of quasicrystal approximants in SrTiO3 thin films grown on Pt(111)/Al2O3(0001) (page 448)

Trudicova M.

MS3-O-2798 Ultrastructural analysis of hydrogels and its contribution to understanding their mechanical and transport performance (page 386)

MS3-P-2828 Visualization of internal morphology of hydrogels based on polyvinyl alcohol in comparison with the indirect method of structural characterization (page 402)

Truglas T.

IM3-P-2631 Precession Electron Diffraction and its Applications in Semiconductor Heterostructures (page 86)

Tsepeleva A.

MS1-P-2656 The Use of Titanothermic Reduction for Processing of Deep-Sea Nodules (page 339)

MS1-P-2623 Aluminothermally reduced deep-sea concretion and its phase structure (page 341)

Tučková T.

LS4-O-2597 High-resolution structural and functional deep brain imaging using holographic endo-microsocpy (page 266)

LS4-P-2606 Fluorescence confocal imaging via holographic endo-microscopy (page 278)

Tůma R.

LS3-O-2608 Bacteriophage φ8 protein P4, an RNA binding molecular motor, studied by Cryo-EM (page 237)

Tůma R.

IM2-O-2571 Combining Light, Raman, and Electron Microscopy in Imaging Viral Factories of Avian Reovirus (page 31)

Tůma T.

IM3-P-2825 Improved mapping algorithms: combating data sparsity in SEM EDS (page 102)

Tůmová P.

IM7-IN-2978 CLEM for FIB/SEM: A workflow for characterization of low-abundant samples on example of a parasitic flagellate Giardia intestinalis. (page 172)

Turan S.

Late-P-3047 An Alternative Approach For The EELS Analysis Of Noble Gases (page 536)

Late-P-3048 Effect of in-situ Conductive TiB2 3D-Network Structure on the Thermoelectric Properties of SiC (page 537)

Turtaev S.

LS4-O-2597 High-resolution structural and functional deep brain imaging using holographic endo-microsocpy (page 266)

LS4-P-2606 Fluorescence confocal imaging via holographic endo-microscopy (page 278)

Tyc J.

IM7-P-2818 Distribution of staining agents in samples of mice soft tissues prepared for Serial Block Face SEM. (page 189)

MS3-P-2814 Commonly used vs novel embedding resins for 3D-SEM microscopy with higher resistance to e-beam damage. (page 396)

Týč J.

LS2-P-2665 3D organization of photosynthetic membranes in cells of photosynthetic bacterium Sediminicoccus rosea (page 224)

LS5-O-2521 Novel method for simultaneous visualization and distinguishing Au nanoparticles on both sides of the ultrathin sections using low-energy STEM and BSE in HRSEM (page 285)

LS7-O-2632 What does SARS-CoV-2 do to the lungs – what can 3D electron microscopy tell us (page 312)

Uçar M.

IM1-IN-2752 Image Analysis Workflow for Phase-Contrast Optical Microscopy Images (page 20)

Uher M.

MS3-P-2990 BioAFM imaging and mechanics tracking (page 395)

Uhlířová H.

LS4-O-2597 High-resolution structural and functional deep brain imaging using holographic endo-microsocpy (page 266)

LS4-P-2606 Fluorescence confocal imaging via holographic endo-microscopy (page 278)

Ulusu N. N.

LS3-P-2704 Vitamin-D combined with resveratrol regulates islets hemostasis, β-cell regeneration, ER-stress and inflammation in fructose-fed diet/STZ-induced diabetic rats (page 255)

Ulutin T.

LS3-P-2704 Vitamin-D combined with resveratrol regulates islets hemostasis, β-cell regeneration, ER-stress and inflammation in fructose-fed diet/STZ-induced diabetic rats (page 255)

Ünay D.

IM1-IN-2752 Image Analysis Workflow for Phase-Contrast Optical Microscopy Images (page 20)

Unčovský M.

IM3-P-2831 New possibilities enabled by correlative low-kV STEM-in-SEM imaging and Transmission Electron Diffraction (page 104)

Upadhyay A.

IM7-O-2888 Imaging the Hard-Soft Bone Interface in near native conditions using Cryo FIB/SEM (page 177)

Urban P.

IM5-P-2833 Cryogenic Sample Holder with Electrical Contacts for UHV SEM/SPM (page 142)

IM5-P-2838 Effect of thermal radiation on the measurement of the sample holder temperature over the cryogenic range for various types of temperature sensor installations (page 150)

IM5-P-2845 Low conductive thermal insulation pad with high mechanical stiffness (page 152)

Urbanek K.

MS6-P-2566 The implementation of microscopic and spectroscopic techniques in characterisation of the spinel ferrite for photocatalytic reduction of CO2 (page 504)

Uršič H.

MS7-P-2540 Mechanical response of domain walls in lead-free ferroelectrics (page 525)

Ursic H.

MS6-IN-2562 In situ Scanning Transmission Electron Microscopy of Lead-Free Ferroelectrics with Atomic Resolution (page 486)

Uskokovic P. S.

MS6-IN-2913 Can the Wet Win the Bet? The case of Energy Harvesting and Storage (page 491)

Vacek P.

IM2-P-2544 High-resolution electron beam induced current study of AlN epitaxial layer (page 69)

IM3-P-2683 Scanning electron diffraction study of TiFeAl alloy microstructure (page 100)

Václavik R.

MS7-P-2840 Characterization of Mechanical and Topographical Properties of Nanocomposite Thin Films with Plasma Polymer Structure (page 523)

Vála L.

MS5-P-2680 Latest TEM investigation of nanostructured CoS2 and Co2CuS4 based films with Fenton catalytic properties (page 477)

Valencia L. M.

MS3-P-2819 STEM damage of Acrylic-based Materials for Stereolithography: Degradation Mechanism (page 403)

van Bokhoven J. A.

MS6-P-2963 Self-sustained oscillatory dynamics of ethylene to syngas by operando SEM and XPS (page 495)

Vaňatka M.

IM3-P-2825 Improved mapping algorithms: combating data sparsity in SEM EDS (page 102)

Vancová M.

LS2-O-2638 Borrelia – host interactions: zoom in on the big picture (page 216)

LS5-O-2715 Correlative cathodoluminescence scanning electron microscopy for identification of cellular structures within vitrified samples at low electron beam energies (page 289)

LS7-O-2632 What does SARS-CoV-2 do to the lungs – what can 3D electron microscopy tell us (page 312)

Vařeka K.

IM5-O-2703 In-situ Microscopy of Catalytic Oxidation of CO to CO2 over Platinum Surfaces. (page 128)

Varsano N.

IM5-P-2782 Cryo Volume Imaging: from cell nucleus to extracellular structure. (page 146)

LS7-P-2625 Characterization of the Growth Plate-Bone Interphase Region Using Cryo-FIB SEM 3D Volume Imaging (page 320)

Vašina P.

MS7-P-2687 Impact behaviour of the industrially sputtered AlCrN coatings prepared using cathodic arc glow discharge (page 519)

Vaverka O.

IM3-P-2825 Improved mapping algorithms: combating data sparsity in SEM EDS (page 102)

Vavruňková V.

MS5-P-2680 Latest TEM investigation of nanostructured CoS2 and Co2CuS4 based films with Fenton catalytic properties (page 477)

Veličković K. D.

LS3-P-2799 Beneficial effects of ferroptosis inhibitor ferrostatin-1 on pancreatic islets in streptozotocin-induced diabetes (page 251)

LS3-P-2812 Beneficial effects of ferroptosis inhibitor ferrostatin-1 in diabetes-induced liver damage (page 253)

Veselá K.

LS5-O-2697 Methods of leaf preparations for microscopic measurements of stomata and other epidermal cells (page 287)

Veselý J.

MS1-P-2602 Phase Identification in Twin-Roll Cast Al-Steel Clad Composite (page 343)

MS7-O-2565 Al nanocrystalline thin film deformation by in situ TEM and molecular dynamics (page 513)

Veselý P.

Plenary-3049 Mature Holographic Microscopy (page 10)

Late-P-3055 Non-Invasive Imaging Method for Evaluating Effect of Migrastatics on Tumor Cells In Vitro Based on Coherence - Controlled Holographic Microscopy (page 532)

Late-P-3058 Identification of Tumor Cells Behavior Changes by Holographic Incoherent Quantitative Phase Imaging Focuses on Migrastatics (page 539)

Vethaak T. D.

IM3-P-2781 Application of the DiffMap program to PtSi thin films (page 92)

Vetrik M.

MS3-IN-2935 Synergy of Scanning Electron and Light Microscopies in Visualization of Swollen Hydrogels and Effect of Hydrogel Parameters on the Image: Artifacts and Reality (page 384)

Viani L.

IM4-O-2591 Enhancing Electron Computational Ghost Imaging Using Artificial Neural Networks (page 116)

Vihinen H.

LS7-IN-3024 Chasing for efficacy: from manual and semi-automatic tools to convolutional neural networks in segmentation of microscopy datasets (page 307)

Villanova J.

MS2-P-2706 Multimodal and multi-resolution approach for defects analysis on the example of Additively Manufactured healable aluminium alloy (page 380)

Vines L.

MS5-P-2568 Structural and optical investigation of Fe-ZnO nanoarchitectures: from inversion domain boundaries to ZnO/ZnFe2O4 heterostructures (page 474)

Vit V.

IM3-P-2579 3D Electron Diffraction on Ferroelectric Perovskites. (page 88)

Vižintin A.

MS6-P-2806 Advanced STEM insights into atomic and electronic structure evolution of corncob-derived hard carbon anode materials for sustainable sodium-ion batteries (page 506)

Vlčák E.

IM7-P-2676 IMG Electron Microscopy Core Facility (page 192)

Vlcak E.

IM1-P-2696 Project „Pattern“ – an online tool for spatial analysis of immunolabeling in electron microscopy (page 27)

IM7-P-2662 Solutions for preparation and visualization of vitrified biological samples at IMG Electron Microscopy Core Facility (page 193)

Vlček I.

IM5-P-2833 Cryogenic Sample Holder with Electrical Contacts for UHV SEM/SPM (page 142)

IM5-P-2845 Low conductive thermal insulation pad with high mechanical stiffness (page 152)

MS1-P-2813 Microanalyses for a better understanding of active soldering processes (page 367)

Vogl L. M.

MS5-IN-3044 In situ microscopy of nanowires: From fundamental properties to functional applications (page 453)

Vrbovská V.

LS4-P-2673 Integrated Fluorescent Light Microscope (iFLM) - Applications Workflows (page 279)

Vrca I.

LS2-P-2585 Expression of the enzyme myrosinase type 1 in the root, the stem and the leaves of the plant nasturtium (Tropaeolum majus L.) (page 229)

Vrtnik S.

MS1-O-2857 Correlative electron microscopy and magnetism of CoCrFeNiZr high-entropy allos (page 330)

Vu N. H.

MS1-P-2623 Aluminothermally reduced deep-sea concretion and its phase structure (page 341)

Vukušić L.

MS4-P-2610 In situ TEM annealing: comparison of thin GeSn layers grown by MBE and CVD (page 440)

Vystavěl T.

IM3-P-2831 New possibilities enabled by correlative low-kV STEM-in-SEM imaging and Transmission Electron Diffraction (page 104)

Wadley P.

IM2-O-2695 Atomically Sharp Domain Walls in an Antiferromagnet (page 41)

Wagner H. D.

MS3-O-2538 Extreme scale-dependent tensile properties of epoxy fibers and a polarized micro-Raman study (page 391)

Wagnieres G.

LS4-P-2498 Targeted photobiomodulation of cancer cells at 808 nm may improve efficacy of photodynamic therapy (page 274)

Walter N. G.

LS3-P-2916 Translation initiation stages of coupled transcription-translation (page 246)

Wandrol P.

IM3-P-2825 Improved mapping algorithms: combating data sparsity in SEM EDS (page 102)

Wang Y.

MS6-O-2505 Multi-scale, high-resolution, time-resolved residual stress in laser-welded Eurofer97 using plasma focused ion beam-digital image correlation method (page 494)

Wanner G.

IM7-IN-2978 CLEM for FIB/SEM: A workflow for characterization of low-abundant samples on example of a parasitic flagellate Giardia intestinalis. (page 172)

Warnatz T.

MS4-P-2861 Electron tomography for measurement of buried interface roughness in thin films (page 438)

Weber I.

LS6-O-2622 Oscillatory intracellular patterns of the small GTPase Rac1 (page 292)

Weiner S.

LS7-P-2625 Characterization of the Growth Plate-Bone Interphase Region Using Cryo-FIB SEM 3D Volume Imaging (page 320)

Weiner S.

IM5-P-2782 Cryo Volume Imaging: from cell nucleus to extracellular structure. (page 146)

Weitzer A.

MS5-O-2636 Expanded Design Flexibility in 3D-Nanoprinting via Focused Electron Beam Induced Deposition (page 456)

Werner W. S.

IM6-P-2879 Determination of the inelastic mean free path of electrons in selected Polymers, indenpent from optical data, considering surface excitations (page 165)

MS4-IN-2994 Low energy electron emission from surfaces and 2D-Materials and 2-D electron cascade in the scanning field electron microscope (page 408)

Whiting M. J.

MS6-O-2505 Multi-scale, high-resolution, time-resolved residual stress in laser-welded Eurofer97 using plasma focused ion beam-digital image correlation method (page 494)

Wilhelm R. A.

MS4-P-2823 STEM analysis of freestanding monolayer h-BN irradiated with slow highly charged ions (page 446)

Willinger M.

MS6-P-2963 Self-sustained oscillatory dynamics of ethylene to syngas by operando SEM and XPS (page 495)

Winiarski B.

MS2-P-2706 Multimodal and multi-resolution approach for defects analysis on the example of Additively Manufactured healable aluminium alloy (page 380)

Winkler R.

IM2-IN-2637 Combining AFM with FIB/SEM in Nanofabrication (page 29)

IM2-O-2635 3D-Nanoprinting of Magnetic Force Microscopy Tips (page 37)

MS5-O-2636 Expanded Design Flexibility in 3D-Nanoprinting via Focused Electron Beam Induced Deposition (page 456)

Withers P. J.

LS6-O-2639 Correlative 3D imaging workflow using X-ray micro-computed tomography and laser plasma focussed ion beam electron microscopy on biological soft tissues (page 298)

Wombacher R.

LS4-IN-3001 Combining Super-resolution Optical Fluctuation Imaging (SOFI) With Structure Illumination and 3D Imaging (page 264)

Wright S. I.

MS1-P-2923 Reconstructing parent microstructures from EBSD based orientation measurements (page 333)

Wu M.

MS3-P-2592 Advanced microstructure analysis of tire polymer materials using cutting edge multi scale electron microscopy technologies (page 405)

Yadav A.

MS7-O-2565 Al nanocrystalline thin film deformation by in situ TEM and molecular dynamics (page 513)

YADAV N. G.

MS6-O-2577 Study of failure modes in two sulphide-based solid electrolyte all-solid-state batteries via in-situ SEM (page 489)

Yalçın Özyusal Ö.

IM1-IN-2752 Image Analysis Workflow for Phase-Contrast Optical Microscopy Images (page 20)

Yamashiro H.

LS1-P-2518 Ultrastructure analysis in the male reproductive system of different mammals exposed to ionizing radiation after the Fukushima accident: a comparative study (page 208)

Yang S. M.

LS5-O-2521 Novel method for simultaneous visualization and distinguishing Au nanoparticles on both sides of the ultrathin sections using low-energy STEM and BSE in HRSEM (page 285)

Yang Z.

IM5-O-2649 Integration of EBSD acquisition into fully automated in-situ thermo-mechanical testing for high temporal and spatial resolution (page 125)

Yanzhong P.

MS6-O-2514 Correlative Microscopy Techniques for Defect-Property-Correlation of Thermoelectric Materials (page 487)

Yserentant K.

LS4-IN-3001 Combining Super-resolution Optical Fluctuation Imaging (SOFI) With Structure Illumination and 3D Imaging (page 264)

Yu Y.

MS6-O-2514 Correlative Microscopy Techniques for Defect-Property-Correlation of Thermoelectric Materials (page 487)

Zábranská M.

Late-P-3055 Non-Invasive Imaging Method for Evaluating Effect of Migrastatics on Tumor Cells In Vitro Based on Coherence - Controlled Holographic Microscopy (page 532)

Zachej S.

IM7-O-2668 Faster Cryo TEM lamella preparation using optimised conditions and advanced workflows (page 173)

IM7-P-2662 Solutions for preparation and visualization of vitrified biological samples at IMG Electron Microscopy Core Facility (page 193)

LS7-P-2659 Modern SEM allows high-throughput 2D and 3D analyses on a single platform (page 317)

Zaefferer S.

MS6-O-2514 Correlative Microscopy Techniques for Defect-Property-Correlation of Thermoelectric Materials (page 487)

Žagar Soderžnik K.

MS5-IN-3031 Application of electron microscopy in development of sensor elements for detection of toxic organic compounds (page 455)

Zahradka J.

MS3-P-2828 Visualization of internal morphology of hydrogels based on polyvinyl alcohol in comparison with the indirect method of structural characterization (page 402)

Žak A. M.

IM5-O-2542 Transmission electron microscope modification for light-induced in situ imaging of specimens in liquid on example of photodynamic therapy (page 130)

LS1-O-2543 Antimicrobial photodynamic therapy effects on Gram-negative and Gram-positive bacteria observed using light-induced in-situ TEM (page 197)

Zakopal P.

IM3-P-2831 New possibilities enabled by correlative low-kV STEM-in-SEM imaging and Transmission Electron Diffraction (page 104)

Záležák T.

MS1-IN-2503 Quantitative STEM in the diffraction contrast regime (page 323)

Zandonella R.

IM7-P-2537 The Hidden Power of Coffee – An Exceptional Replacement for Uranyl Acetate for Staining Biological Specimens in Transmission Electron Microscopy (page 185)

Zankel A.

IM2-O-2563 Correlative Raman microscopy, SEM and EDS – The combined evaluation of a whole sample mapping of a Chelyabinsk meteorite fragment (page 43)

Zemanek P.

IM2-P-2699 Assembly for Cryo-SEM/Raman Microspectroscopy sample analysis (page 63)

Žemlička R.

MS7-P-2687 Impact behaviour of the industrially sputtered AlCrN coatings prepared using cathodic arc glow discharge (page 519)

Žerovnik Mekuž M.

LS7-O-2860 Volume electron microscopy and automatic segmentation of intracellular compartments in the urinary bladder umbrella cells (page 310)

Zhang R.

MS7-O-2700 Analysis of dislocation evolution in cerium oxide nanocubes using in situ transmission electron microscopy (page 511)

Zhang S.

MS6-O-2514 Correlative Microscopy Techniques for Defect-Property-Correlation of Thermoelectric Materials (page 487)

Zhang Z.

IM5-P-2797 Real-time atomic-resolution observation of coherent twin boundary migration in rocksalt transition metal nitride (page 136)

MS2-O-2789 Stacking faults dominant strengthening mechanism behind the anomalous hardness variation of TaN/TiN multilayer films (page 375)

MS4-O-2859 Atomic insights into the structures and properties of nitride thin films (page 415)

Late-P-3032 Electron beam irradiation induced Brownmillerite – perovskite phase transition in La_{0.6} Sr_{0.4} CoO_{3-δ} (page 530)

Zhiwei C.

MS6-O-2514 Correlative Microscopy Techniques for Defect-Property-Correlation of Thermoelectric Materials (page 487)

Zhou F.

IM7-P-2607 Imaging of uncoated samples with secondary electrons using in lens detection under optimum conditions – ‘sweet spot’ imaging (page 179)

Zhou X.

MS1-O-2601 Co-segregation of zinc, carbon and boron in a Σ5 iron grain boundary resolved by correlating atomic resolution STEM, APT and first-principles calculations (page 326)

Zhu B.

MS6-O-2505 Multi-scale, high-resolution, time-resolved residual stress in laser-welded Eurofer97 using plasma focused ion beam-digital image correlation method (page 494)

Zhuo C.

MS2-O-2789 Stacking faults dominant strengthening mechanism behind the anomalous hardness variation of TaN/TiN multilayer films (page 375)

Žiberna K.

MS7-P-2540 Mechanical response of domain walls in lead-free ferroelectrics (page 525)

Zicha D.

Plenary-3049 Mature Holographic Microscopy (page 10)

Late-P-3058 Identification of Tumor Cells Behavior Changes by Holographic Incoherent Quantitative Phase Imaging Focuses on Migrastatics (page 539)

Žigon P.

LS3-P-2643 Insect midgut epithelium architecture – focus on gut stem cells in larvae and adults (page 259)

Žnidaršič N.

LS3-P-2652 Formation of cell junctions during integument morphogenesis in crustacean Porcellio scaber (page 249)

LS3-P-2643 Insect midgut epithelium architecture – focus on gut stem cells in larvae and adults (page 259)

Zobač M.

MS1-P-2813 Microanalyses for a better understanding of active soldering processes (page 367)

Zobač O.

MS1-P-2657 Incommensurate structure of τ phase in the Al-Cu-Zn system (page 337)

Zobačová J.

MS1-P-2813 Microanalyses for a better understanding of active soldering processes (page 367)

Zouhar M.

IM6-IN-2598 Ab initio study of angle-resolved electron spectroscopy of graphene (page 156)

IM6-O-2820 Time-of-Flight Spectrometer for Low Landing Energies (page 160)

IM6-P-2599 Effective IMFP of thin samples via the time-of-flight method (page 168)

MS1-P-2826 Deep learning powered optical microscopy for steel research (page 347)

MS4-P-2669 Energy-based calibration for quantitative STEM measurements and comparison with 2D-PAD (page 450)

Zumberg I.

LS3-P-2805 Mitochondria activity evaluation under osmotic conditions (page 244)

LS6-P-2849 Monitoring the endothelial cell behavior during flow stress induction using digital holographic microscopy. (page 304)

delong instruments®

… your way to electron microscopy

Compact Transmission Electron Microscopes

The smallest transmission electron microscopes (TEM) in the world

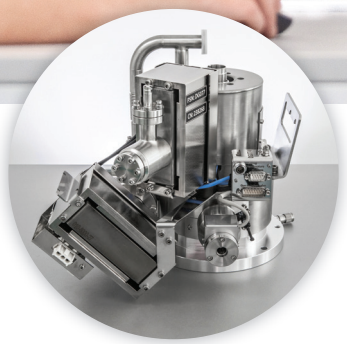

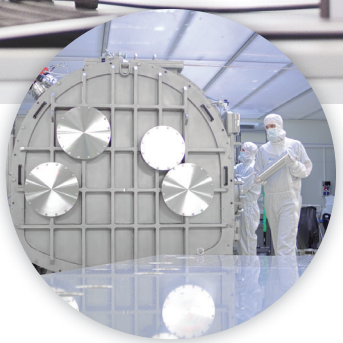

Microscopes

Compact and powerful TEMs for every lab. Robust and user friendly instruments that help you in your everyday tasks.

DIGUN

Schottky electron gun: cornerstone of your electron microscope or custom electron optic solution, quick to install and remove.

Custom Solutions

Development and engineering, OEM solutions and special components from first proposal to proven prototype.

www.delong.cz

Palackého třída 3019/153 b, 602 00 Brno, Czech Republic

LVEM 25E

Low Voltage Electron Microscope

All-in-One EM

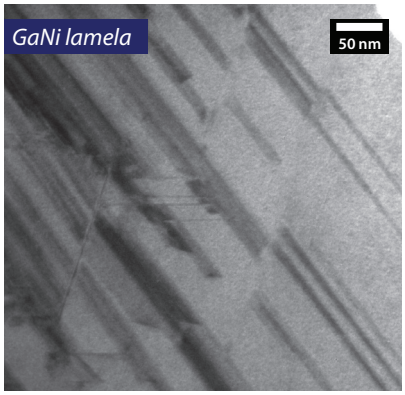

TEM

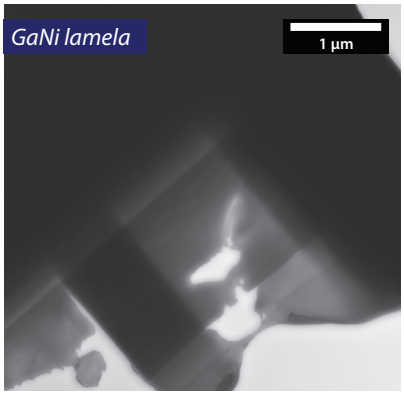

STEM

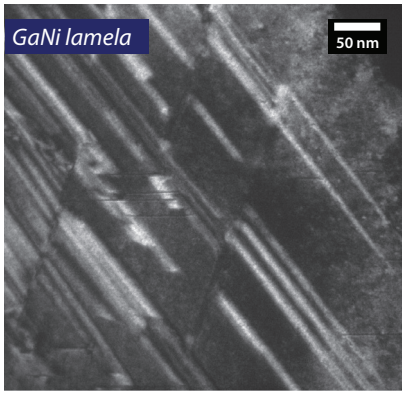

Dark Field

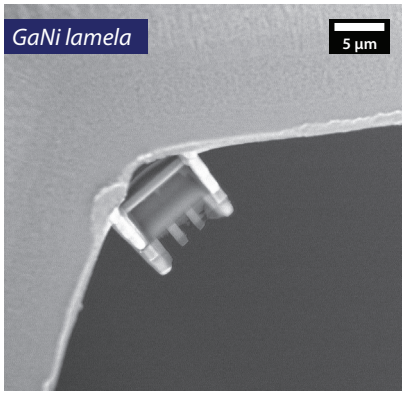

SEM

ED

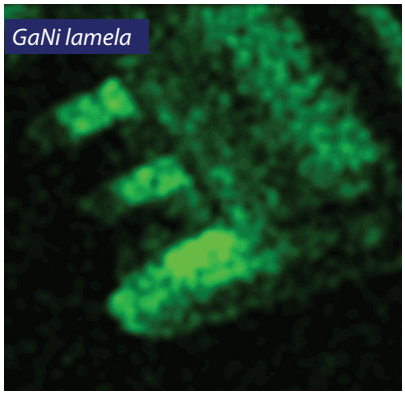

EDS

Compact and Versatile

- Availability of five modes in one device: TEM, SEM, STEM, ED, EDS
- Image resolution as good as 1.0 nm
- Fully integrated and portable design
- Enhanced contrast and resolution for conventionally prepared samples

delong instruments®

… your way to electron microscopy

DECTRIS
detecting the future

DECTRIS ARINA

Fast hybrid-pixel electron-counting detector for 4D STEM applications